



Proceedings of 13th SIRM: The 13th International Conference on Dynamics of Rotating Machinery

Santos, Ilmar

Publication date:
2019

Document Version
Publisher's PDF, also known as Version of record

[Link back to DTU Orbit](#)

Citation (APA):
Santos, I. (Ed.) (2019). *Proceedings of 13th SIRM: The 13th International Conference on Dynamics of Rotating Machinery*. Technical University of Denmark.

General rights

Copyright and moral rights for the publications made accessible in the public portal are retained by the authors and/or other copyright owners and it is a condition of accessing publications that users recognise and abide by the legal requirements associated with these rights.

- Users may download and print one copy of any publication from the public portal for the purpose of private study or research.
- You may not further distribute the material or use it for any profit-making activity or commercial gain
- You may freely distribute the URL identifying the publication in the public portal

If you believe that this document breaches copyright please contact us providing details, and we will remove access to the work immediately and investigate your claim.

Proceedings of 13th SIRM

The 13th International Conference on Dynamics of Rotating Machinery



DTU Mechanical Engineering

Section of Solid Mechanics

Technical University of Denmark

ISBN 978-87-7475-568-5

Proceedings of 13th SIRM
The 13th International Conference on
Dynamics of Rotating Machinery
13-15 February 2019

Ilmar Ferreira Santos (editor)

Scientific Committee

N. Bachschmid, Italy
H. Ecker, Austria
K. Ellermann, Austria
F. Heitmeir, Austria
R. Liebich, Germany
E. Malenovsky, Czech Republic
R. Markert, Germany
R. Nordmann, Germany
T. Pumhössel, Austria
S. Rinderknecht, Germany
I. F. Santos, Denmark
J. Schmied, Switzerland
B. Schweizer, Germany
J. Strackeljan, Germany
T. Szolc, Poland
J. Wallaschek, Germany

Local Chairman for SIRM 2019

I. F. Santos

Sponsors



Foreword

Motivated by the continuous development of turbo machines ranging in both size and complexity, vibration problems in rotating machinery are still a theme of high interest in both industry and academia. Large rotors of wind turbines and flywheel energy storage systems as well as small turbochargers in automotive applications highlight the spectrum of turbo machinery sizes. The thematic of the 13th International Conference on Dynamics of Rotating Machinery (SIRM 2019) held at the Technical University of Denmark from February 13th till 15th, 2019, fits perfectly within the context of Industry 4.0, and includes:

- the deep, fundamental understanding of the vibration causes and effects;
- the development of computer models based on Multiphysics approaches for describing and predicting abnormal vibrational behaviors;
- the mitigation and the control of vibration levels via passive and active systems;
- the usage of sensor signals and big-data for mining machines' normal and abnormal behaviors aimed at monitoring and diagnosing failures, as well as validating complex Multiphysics computer models (digital twins)

The proceedings of the 13th International Conference on Dynamics of Rotating Machinery (SIRM 2019) are structured exactly like the conference program. The 10 main topics are: 1 Gas-foil Bearings, 2 Journal Bearings, 3 Magnetic Bearings, 4 Rotor Fluid Interaction & Instability, 5 Rotor-Foundation Dynamics, 6 Balancing, 7 Advanced Numerical Tools & Nonlinearities, 8 Active Control, 9 Analysis – Monitoring – Diagnose & Prognosis, and 10 Case Studies & Application Tools. The technical contributions and participants come from 17 different countries, namely, Australia, Austria, Brazil, Chile, Czech Republic, Denmark, France, Germany, Greece, Israel, Netherlands, Poland, Russia, Sweden, Switzerland, United Kingdom, and the USA.

As chairman of SIRM 2019, I sincerely thank all colleagues from the Department of Mechanical Engineering Department, especially Gerda Helene Fogt, Torben Bender Christensen, Frederik Bredal Merser, Magnus Bech Schouw, and Jacob Andersen Trolle, for their support with the organization of the event. I also express my gratitude to all members of my research team, namely Ph.D. students, research assistants, Master's students, and postdocs, for their assistance and help with all technical and practical issues involved with the conference organization and laboratory visit: Michael Gani, Vergílio Torean, Alejandro de Miguel, Thomas Thougard Paulsen, Mikael Mosbech Eronen, Sebastian von Osmanski, Nikolaj Dagnæs-Hansen, Simon Bo Jensen, Svend Erik Andersen, Troy Snyder, Massimiliano Deon, Maria Gomez-Polo, Ignacio Escudero, Alvaro Brandes Gorrioz, Aleksander Andersen, and Josephine Villefrance.

The sponsorships of GEA, Bently Nevada, and Technical University of Denmark are acknowledged and very much appreciated.

I wish you all a fruitful and inspiring time at the SIRM 2019 and at the Technical University of Denmark.



Ilmar Ferreira Santos, Professor, Dr.-Ing., dr.techn., Livre-Docte
Department of Mechanical Engineering
Technical University of Denmark
Building 404, Room 006
2800 Lyngby, Denmark

Table of Contents

Gas-foil Bearings

A new method for the calculation of the Campbell diagram of a foil-air bearing rotor model, <i>Philip Bonello</i>	4
Modelling of compliant-type gas bearings: A numerical recipe, <i>Sebastian von Osmanski & Jon S. Larsen & Ilmar F. Santos</i>	14
Analysis of displacements in a gas foil bearing using an ultra-high-speed camera, <i>Lukasz Breńkacz & Paweł Bagiński & Grzegorz Żywica</i>	28
Impact of bump height manufacturing errors on the unbalance response of a 4 DoF rigid rotor, <i>Omar Benchekroun & Mihai Arghir</i>	36
Bifurcation analysis of rotors on refrigerant-lubricated gas foil bearings, <i>Tim Leister & Wolfgang Seemann & Benyebka Bou-Saïd</i>	46

Analysis, Monitoring, Diagnosis and Prognosis

Motor-bearing damage detection based on vibration data, <i>John J. Yu & Nicolas Péton</i>	60
Using measured transmission error for diagnostics of gears, <i>Robert B Randall & Dikang Peng & Wade A Smith</i>	68
Rotor model reduction for wireless sensor node based monitoring systems, <i>Samuel Krügel & Johannes Maierhofer & Thomas Thümmel & Daniel J. Rixen</i>	78
Automated wind turbine gearbox bearing diagnosis algorithm based on vibration data analysis and signal pre-whitening, <i>Meik Schlechtingen & Ilmar Ferreira Santos</i>	88
Torsional vibration measurement and model-based monitoring in today's reality of power generation business, <i>Mateusz Golebiowski & Eric Knopf & Thomas Krueger</i>	116
Using autoresonance for in-situ identification in rotating structures, <i>Izhak Bucher & Solomon Davis & Shachar Tresser</i>	122

Journal Bearings

Advanced measurements and model update of an automotive turbocharger with full-floating journal bearings, <i>Sebastian Leichtfuß & Martin Kreschel & Loic Durbiano & Tobias Dielenschneider & Rainer Nordmann & Heiko Atzrodt & Rafael Pilotto & Heinz-Peter Schiffer</i>	132
Simulation and measurement of ring speed of full floating ring bearing in an automotive turbo charger, <i>Christian Daniel & Elmar Woschke & Steffen Nitzschke</i>	142

Transient simulation of a rotor supported in herringbone grooved journal bearings using the narrow groove theory, <i>Steffen Nitzschke & Elmar Woschke & Christian Daniel & Thorsten Sporbeck</i>	150
Transient thermo-hydrodynamic analysis of a laval rotor supported by journal bearings with respect to calculation times, <i>Cornelius Irmischer & Steffen Nitzschke & Elmar Woschke</i>	162
Systematic stability investigation of a rotor system involving journal bearings with variable, oval geometry, <i>Kai Becker & Wolfgang Seemann</i>	174
An extension of the bearing database method to implement enhanced models of fixed geometry bearings in transient rotordynamic analysis, <i>Athanasios Chasalevris</i>	184

Active Control

Active vibration control actuator placement for a planetary gearbox based on operational modal analysis, <i>Ellis C. Kessler & Daniel F. Plöger & Philipp Zech & Stephan Rinderknecht</i>	196
Comparative study of active control applied to hydrodynamic supported rotor, <i>Matheus Freire Wu & Katia Lucchesi Cavalca & Richard Markert</i>	206
Evaluation of vibration energy harvesters in tilting pad journal bearings, <i>André Rodrigues Garcia da Silveira & Gregory Bregion Daniel</i>	216
Vibration of rigid rotors supported by hydrodynamic bearings controlled by magnetically sensitive oils, <i>Jaroslav Zapoměl & Jan Kozánek & Petr Ferfecki</i>	226
Control analysis of wind turbine blade vibration with SMA actuators in thermal equilibrium, <i>Rodrigo Nicoletti & Robert Liebich</i>	234
Experimental and theoretical study of an actively lubricated LEG tilting pad bearing, <i>Alejandro Cerda Varela & Ilmar Ferreira Santos & Jorge González Salazar & Cristóbal Ponce Salazar</i>	244

Magnetic Bearings

Using the dynamics of active magnetic bearings to perform an experimental modal analysis of a rotor system, <i>Johannes Maierhofer & Max Gille & Thomas Thümmel & Daniel Rixen</i>	262
The design of a combined, self-stabilizing electrodynamic passive magnetic bearing supporting high-speed rotors, <i>Tomasz Szolc & Krzysztof Falkowski</i>	272
Overview of mobile flywheel energy storage systems state-of-the-art, <i>Nikolaj A. Dagnaes-Hansen & Ilmar F. Santos</i>	282

Rotor-fluid Interaction & Instability

Oil whirl instability on gearbox and gas turbine unbalance, <i>Sergey Dyrgin & Nicolas Péton & Syauqi Ahmad</i>	298
---	-----

Optimization of the bearing system for a micro-power turbogenerator with a rotational speed up to 120,000 rpm, <i>Grzegorz Zywica & Lukasz Brenkacz & Malgorzata Bogulicz</i>	308
Steam instability, <i>Sergey Drygin & Nicolas Péton</i>	318

Advanced Numerical Tools & Nonlinearities

Numerical schemes for quasi-periodic oscillations and synchronisation in rotordynamics, <i>Simon Bäeuerle & Harmut Hetzler</i>	330
Numerical description of a rotor supported by gas polymer bearings for time domain simulations – implementation and parametrisation of the structure model, <i>Gregor Schilling & Katja Bäuerlein & Robert Liebich</i>	340
Quasiperiodic motions in unbalanced rotor systems with simultaneous self- or forced excitation, <i>Robert Fiedler & Hartmut Hetzler</i>	350
Model correlation for special types of rotor systems, <i>Gudrun Mikota, Horst Ecker</i>	360
SHBT based modeling of a composite hollow shaft regarding its dynamic behavior prediction, <i>Paulo C. P. F. Barbosa & Vergílio T. S. Del Claro & Marcelo S. Sousa Jr. & Aldemir A. Cavalini Jr. & Valder Steffen Jr.</i>	370
Validation of the generalized polynomial chaos expansion to approximate the stochastic frequency response of a multi-fault rotor, <i>Gabriel Y. Garoli & Lais B. Visnadi & Helio F. de Castro</i>	380

Rotor-foundation Dynamics

On the multiphysics modelling of rotor-bearing-foundation dynamics & the model-based control design of active fluid film bearings, <i>Michael Gani & Ilmar F. Santos</i>	394
Investigation on the rotor-bearing-foundation interaction, <i>Leonardo Biagiotti Saint Martin & Ricardo Ugliara Mendes & Kátia Luchesi Cavalca</i>	408
Dynamics of a flexible mobile flywheel energy storage system - modeling and analysis, <i>Frederik T. Hansen & Nikolaj A. Dagnæs-Hansen & Ilmar F. Santos</i>	418

Balancing

Balancing high-speed gyroscopic systems at low rotation speeds, <i>Izhak Bucher & Shachar Tresser & Amit Dolev</i>	432
Two plane generator balancing with support of lateral analysis, <i>Guillaume Christin & Nicolas Péton</i>	442
Low speed balancing via parametric combination resonance, <i>Ricardo Ugliara Mendes & Fadi Dohnal</i>	452

Case Studies & Application Tools

Case study on resolving high vibration on a vertical motor, <i>Sanker Ganesh & Mustafa Shalabi</i>	462
Case study on resolving structural vibration issues on a multi stage pump, <i>Nicolas Péton & Sanker Ganesh</i>	472
Turbocharger dynamic analysis: concept-phase simulation in frequency domain, <i>Tigran Parikyan & Saša Bukovnik</i>	482
Application of MADYN 2000 to rotor dynamic problems of industrial machinery, <i>Joachim Schmied</i>	490
Vibration analysis of a rotor of an electrical machine with stochastically distributed input parameters, <i>Marcel S. Prem & Michael Klanner & Katrin Ellermann</i>	502

Gas-foil Bearings

A new method for the calculation of the Campbell diagram of a foil-air bearing rotor model

Philip Bonello¹

¹ School of Mechanical, Aerospace and Civil Engineering, University of Manchester, Manchester M13 9PL, United Kingdom, philip.bonello@manchester.ac.uk

Abstract

Campbell diagrams (describing free linearised vibration) of rotor/foil-air bearing (FAB) systems are currently based on the linearised force coefficients (FC) method, which eliminates the air film and foil state variables from the eigenvalue analysis. Individual modes of FC-based Campbell diagrams have not been verified by transient nonlinear dynamic analysis (TNDA) at low amplitudes and significant discrepancies between FC and TNDA stability predictions have been reported. This paper introduces a new method that avoids the FC method by extracting the Campbell diagram directly from the nonlinear state-space model. Through appropriate scaling of the eigenvectors and the application of a minimum journal amplitude criterion, it is found that the multitude of eigenvalues/eigenvectors of the state Jacobian could be filtered to extract the relevant modes. Where appropriate, a maximum damping criterion should also be applied. Each extracted mode is precisely verified using TNDA with mode-specific initial conditions. The methodology is successfully applied to a symmetric rigid rotor on single-pad FABs with the pad modelled by the simple equivalent foundation model. The simulation results correlate well with observations reported in an independent study that used a more advanced foil model but was restricted to TNDA (no Campbell diagram).

1 Introduction

The dynamics of FAB-rotor systems are governed by the nonlinear interaction between the air film, foil structure, and rotor domains, where each domain is governed by time-based differential equations [1]. Such systems can therefore be cast into the non-linear state-space format used to represent generic dynamical systems [1, 2]:

$$\mathbf{s}' = \boldsymbol{\chi}(\boldsymbol{\tau}, \mathbf{s}) \quad (1)$$

where $(\)'$ denotes differentiation with respect to the time variable τ , \mathbf{s} is the state vector which contains state variables from all three domains (air film, foil and rotor), and $\boldsymbol{\chi}$ is a vector of nonlinear functions of τ and \mathbf{s} . The explicit presence of τ arises from the vector of unbalance excitation forces \mathbf{f}_u .

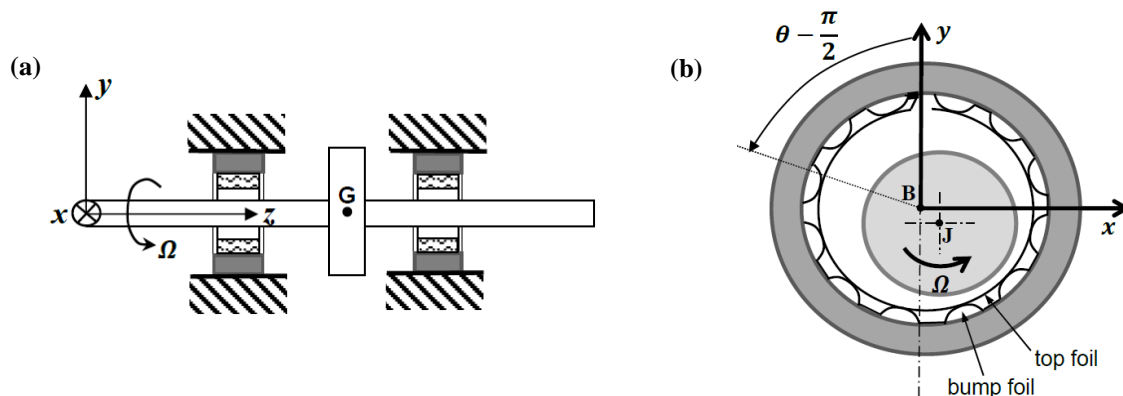


Figure 1. System considered: (a) symmetric rigid rotor/FAB system; (b) single-pad FAB (configuration shown is for a clamped leading edge/free trailing edge (CLE/FTE)).

A rotordynamic system with FABs was first expressed as a dynamical system (eq. (1)) in 2013/14 by Bonello and Pham [3-5]. For the case of the symmetric rigid rotor-FAB system running in single-pad FABs (Figure 1), with foil pad modelled using the simple equivalent foundation model (SEFM) [6], and air film modelled by the finite difference (FD) method, as considered in [4] and the present paper, the state vector \mathbf{s} is given by

$$\mathbf{s} = [\boldsymbol{\Psi}^T \quad \tilde{\mathbf{w}}^T \quad \boldsymbol{\varepsilon}^T \quad \boldsymbol{\varepsilon}'^T]^T \quad (2)$$

where the subvectors $\boldsymbol{\Psi}$, $\tilde{\mathbf{w}}$, $(\boldsymbol{\varepsilon}, \boldsymbol{\varepsilon}')$ respectively contain state variables relating to the air film, the foil, and the rotor, where $\boldsymbol{\varepsilon} = [x/c \quad y/c]^T$ is the journal eccentricity vector (c is the radial clearance). Bonello and Pham [3-5] then used readily available implicit integrator routines to obtain the nonlinear response for given initial conditions $\mathbf{s}(0)$ i.e. performed the *simultaneous* time domain solution by applying transient nonlinear dynamic analysis (TNDA) to the *complete* system in eq. (1). Bonello and Pham [4, 5] also devised a rapid method for computing the static equilibrium condition $\mathbf{s} = \mathbf{s}_E$, and assessing the stability of small free perturbations $\Delta \mathbf{s}$ about this condition, for each given speed within a range. This process was referred to as static equilibrium stability analysis (SESA) [5]. In the first part of SESA, the static equilibrium condition $\mathbf{s} = \mathbf{s}_E$ can be obtained by setting $\mathbf{s}' = \mathbf{0}$ for $\mathbf{f}_u = \mathbf{0}$ in eq. (1) and solving the resulting set of nonlinear algebraic equations:

$$\boldsymbol{\chi}(0, \mathbf{s})|_{\mathbf{f}_u=0} = \mathbf{0} \quad (3)$$

In the second part of the current form of SESA, the stability of the dynamical system (eq. (1)) to small (linear) free perturbations $\Delta \mathbf{s}$ about $\mathbf{s} = \mathbf{s}_E$ is determined by performing an eigenvalue analysis of the state Jacobian matrix

$$\mathbf{J} = \partial \boldsymbol{\chi} / \partial \mathbf{s}|_{\mathbf{f}_u=0, \mathbf{s}=\mathbf{s}_E} \quad (4)$$

A change in sign (from negative to positive) of the real part of one of the eigenvalues marks the birth of self-excited vibration (Hopf bifurcation) [2].

The purpose of this paper is to develop the eigenvalue analysis of the Jacobian to determine the Campbell diagrams, which describe the variation with speed of the free linearised vibration modes about the static equilibrium condition, and are an important tool that is used to aid the interpretation of the full nonlinear response e.g. [7-9]. The novel contribution lies in the fact that, in contrast to the current method for deriving Campbell diagrams, the proposed method avoids the use of linear force coefficients (FC) [10, 11]. There are two reasons that motivate the development of such a method, which is directly based on the Jacobian:

- The FC-method eliminates the air film and foil state variables from the eigenvalue analysis through an assumption that relates them to the journal motion [10-12].
- The above assumption has not been tested by verifying individual modes by (low amplitude) TNDA of the original system (eq. (1)). Indeed, significant discrepancies have been reported between FC and (low amplitude) TNDA predictions for the onset of instability speed (OIS) for certain conditions [12]. This contrasts with the invariable consistency between TNDA and SESA results for the OIS [1, 4, 5].

The FC method, as used in FAB-rotor systems, is based on Lund's method [10], who used the procedure on gas bearings with rigid sleeves (no foil) and oil-lubricated bearings [12]. It was extended to FAB-rotor systems by Peng and Carpino [11] and since then has been used extensively (e.g. [7-9]) to predict features of the linear dynamics of FAB-rotor systems, such as stability, Campbell diagrams, and synchronous unbalance response, as reported in [12]. Lund's FC method assumes that the air-film pressure p is a function of $(\boldsymbol{\varepsilon}, \boldsymbol{\varepsilon}')$, which are assumed to be harmonic of assumed frequency (whirl frequency), and p is then approximated by a first-order Taylor series expansion [10-12]. The harmonic foil deflection is similarly eliminated. Having found the FC (stiffness and damping coefficients), the dynamics of small perturbations about the static condition are investigated by considering *only* the linearized rotor equations since the FC effectively replace the air film and foil domains.

The use of the Jacobian (eq. (4)) for stability analysis, and its presently proposed use for Campbell diagram derivation, has only been made possible fairly recently. Prior to the work of Bonello and Pham [3-5], it has been the practice to decouple the air film, foil and rotor equations by approximating the air film equations as algebraic, rather than differential, equations e.g. [13]. This traditional solution technique for the full nonlinear response was therefore a non-simultaneous "time lagging" approach that did not preserve the true simultaneous coupling between the three domains, since it was not based on the dynamical system representation (eq. (1)) [4].

Although the state-space formulation introduced in [3-5] has now been taken up by a growing number of researchers e.g. [6, 12, 14, 15], these have used it only for TNDA, even for small perturbation analysis. For example, the same OIS determined by Larsen and Santos [12] through TNDA from initial conditions $\mathbf{s}(0) = \mathbf{s}_E$ could have been more rapidly determined using the SESA approach introduced in [4, 5].

Unlike the FC method, the new method of this paper retains the air film and foil state variables within the eigenvalue analysis. It shall be shown that each mode so computed can be verified by TNDA of the original dynamical system (eq. (1)) using mode-specific initial conditions. The new method is tested on a two-degree-of

freedom system comprising a rigid symmetric rotor-FAB system with single-pad FABs. The pad is modelled using the simple equivalent foundation model (SEFM) [6] and air film conditions appropriate for two alternative pad configurations: (i) clamped leading edge/free trailing edge (CLE/FTE, Figure 1(b)); (ii) free leading edge and clamped trailing edge (FLE/CTE). The CLE/FTE configuration is unusual for single pad-FABs [1], but is considered since the results of the simulation can be correlated with those of an independent study by Nielsen and Santos [14] which used a more advanced foil model (allowing top foil detachment) incorporated into the state-space format (eq. (1)). The study in [14] was restricted to TNDA and did not derive the Campbell diagram, but made certain observations that can be correlated with the findings of this paper.

2 Dynamical System Model

The differential equations governing the nonlinear dynamics of the symmetric rotor-FAB system in Figure 1 are expressed in the dynamical system form of eq. (1) as follows [4]:

$$\boldsymbol{\Psi}' = \mathbf{g}_{RE}(\boldsymbol{\Psi}, \tilde{\mathbf{w}}, \boldsymbol{\varepsilon}) \quad (5a)$$

$$\tilde{\mathbf{w}}' = 2(\mathbf{p}_{g,\theta}(\boldsymbol{\Psi}, \tilde{\mathbf{w}}, \boldsymbol{\varepsilon})/(cK_b) - \tilde{\mathbf{w}})/\eta \quad (5b)$$

$$\begin{bmatrix} \boldsymbol{\varepsilon}' \\ \boldsymbol{\varepsilon}' \end{bmatrix} = \begin{bmatrix} \boldsymbol{\varepsilon}' \\ \frac{4}{Mc\Omega^2} \{ \mathbf{f}_u(\tau) + \mathbf{f}_s + \mathbf{f}_j(\boldsymbol{\Psi}, \tilde{\mathbf{w}}, \boldsymbol{\varepsilon}) \} \end{bmatrix} \quad (5c)$$

where the non-dimensional time is defined as $\tau = \Omega t/2$ (Ω being the rotational speed) and the equations (5a), (5b), (5c) relate to the coupled domains of the air film, foil and the rotor respectively.

In equation (5c), \mathbf{f}_u , \mathbf{f}_s , \mathbf{f}_j are 2×1 vectors containing the Cartesian components of the unbalance force, static load and air film force respectively, acting on one half of the symmetric rotor of total mass of $2M$.

Equations (5b) govern the pad deflection according to the SEFM, which is based entirely on the bump foil i.e. the stiffness and inertia of the top foil are neglected and it is assumed to be in contact with the bumps at all times for the purpose of determining the local radial deflection w of the top foil. It is additionally assumed that w is a function of θ only. $\tilde{\mathbf{w}}$ is the $N_\theta \times 1$ vector of values $\tilde{w}_j = \tilde{w}(\theta_j)$, where $\tilde{w} = w/c$ and $\theta_j, j = 1, \dots, N_\theta$, are discrete values of θ according to the Finite Difference (FD) grid used to discretize the Reynolds Equation (RE). K_b is the stiffness per unit area of the bump foil and η is the damping loss factor, for which the equivalent viscous damping coefficient is assumed to be $C_{damp,eq} = K_b\eta/\Omega$. $\mathbf{p}_{g,\theta}$ is the vector of the averages of the gauge pressure p_g over the axial direction for discrete values of θ .

Equations (5a) are obtained by using the FD method to discretize the RE, as described in [1]. The RE is formulated in terms of the combined state variable $\boldsymbol{\psi} \equiv \tilde{p}\tilde{h}$ where \tilde{p} and \tilde{h} are the non-dimensional air film pressure and thickness at a position (ξ, θ) where ξ is the non-dimensional axial coordinate. The FD grid has $N_\xi \times N_\theta$ points spaced by $\Delta\xi, \Delta\theta$ in the axial and angular directions respectively, where $\xi = \xi_i, i = 1, \dots, N_\xi$ and $\theta = \theta_j, j = 1, \dots, N_\theta$. Hence, in eqs. (5a), $\boldsymbol{\Psi}$ is the $N_\xi N_\theta \times 1$ vector of variables $\psi_{i,j} = \psi(\xi_i, \theta_j, \tau)$. The grid covers only half the axial length of the FAB due to symmetry (bearing is open at both ends). Following the work in [1], for the single-pad FAB with CLE/FTE, a ‘‘finite θ ’’ air film model with Gumbel condition [1] is used. The Gumbel condition truncates subatmospheric pressures when integrating p_g for \mathbf{f}_j [6]. It is a retrospective correction for the detachment of the top foil that is good for CLE/FTE [16], but not FLE/CTE [16, 1]. For FLE/CTE, a ‘‘continuous θ ’’ air film model with no Gumbel condition was considered satisfactory in [1].

3 Extraction of Campbell Diagrams

The dynamical system of eq. (1) is linearised as follows [5]:

$$(\boldsymbol{\Delta s})' = \mathbf{J}(\boldsymbol{\Delta s}) \quad (6)$$

where the Jacobian \mathbf{J} is given by eq. (4). The eigenvalue analysis of the matrix \mathbf{J} yields N_s eigenvalues that comprise N_e real eigenvalues and N_o pairs of complex conjugate eigenvalues $\lambda_{n,Re} \pm j\lambda_{n,Im}$, $\lambda_{n,Im} > 0$ ($n = 1 \dots N_o$). The complex conjugate eigenvalues have associated conjugate eigenvectors $\boldsymbol{\rho}^{(n)}, \boldsymbol{\rho}^{(n)*}$. The *oscillatory* part of the general solution of eq. (6) is:

$$\boldsymbol{\Delta s} = \sum_{n=1}^{N_o} c_n e^{-\zeta_n \varpi_{u,n} t} \text{mod}\{\boldsymbol{\rho}^{(n)}\} .* \cos(\varpi_{d,n} t + \arg\{\boldsymbol{\rho}^{(n)}\} + \alpha_n) \quad (7)$$

In eq. (7): c_n, α_n are arbitrary real scalar constants; $\text{mod}\{\mathbf{v}\}, \arg\{\mathbf{v}\}$ respectively denote the vectors of moduli and phases of the complex elements of vector \mathbf{v} ; $\mathbf{a}.*\mathbf{b}$ denotes a vector containing the products of corresponding elements of two vectors \mathbf{a}, \mathbf{b} ; $\varpi_{d,n}, \zeta_n, \varpi_{u,n}$ are, respectively, the damped natural circular frequency, equivalent viscous damping ratio, and the undamped natural circular frequency of (oscillatory) mode no. n :

$$\varpi_{d,n} = \Omega \lambda_{n,Im}/2, \quad \zeta_n = -\lambda_{n,Re}/(\lambda_{n,Re}^2 + \varpi_{d,n}^2)^{0.5}, \quad \varpi_{u,n} = \varpi_{d,n}/(1 - \zeta_n^2)^{0.5} \quad (8a-c)$$

The number of oscillatory modes N_o at each given rotational speed Ω is typically very high since the dimension of the Jacobian is very high (due to the discretisation of air film spatial domain). Hence, as shall be revealed later, the eigenfrequency vs speed map is a dense accumulation of dots, but most of these dots do not represent any significant vibration (*whirl*) of the rotor. The Campbell diagram of the FAB-rotor system therefore needs to be extracted from the eigenfrequency vs speed map by applying a filtering criterion.

The eigenvectors $\boldsymbol{\rho}^{(n)}$ first need to be scaled by an appropriate factor $\kappa^{(n)}$, which is chosen so that, for mode no. n , the greatest non-dimensional amplitude of vibration within the FAB (considering both journal and pad vibration) is a prescribed fraction σ of the nominal radial clearance:

$$\kappa^{(n)} = \sigma / \tilde{A}^{(n)} \quad (9)$$

where $\tilde{A}^{(n)}$ is the greatest non-dimensional vibration amplitude within the FAB:

$$\tilde{A}^{(n)} = \max\left(\text{mod}\{\boldsymbol{\rho}_{\boldsymbol{\varepsilon}}^{(n)}\}, \text{mod}\{\boldsymbol{\rho}_{\boldsymbol{\tilde{w}}}^{(n)}\}\right) \quad (10)$$

where $\boldsymbol{\rho}_{\boldsymbol{\varepsilon}}^{(n)}$, $\boldsymbol{\rho}_{\boldsymbol{\tilde{w}}}^{(n)}$ are the complex amplitudes of the damped harmonic perturbations $\Delta\boldsymbol{\varepsilon}^{(n)}$, $\Delta\boldsymbol{\tilde{w}}^{(n)}$ respectively, which, from eq. (7), are given by:

$$\Delta\boldsymbol{\varepsilon}^{(n)}(t) = c_n e^{-\zeta_n \varpi_{u,n} t} \text{mod}\{\boldsymbol{\rho}_{\boldsymbol{\varepsilon}}^{(n)}\} .* \cos\left(\varpi_{d,n} t + \arg\{\boldsymbol{\rho}_{\boldsymbol{\varepsilon}}^{(n)}\} + \alpha_n\right) \quad (11)$$

$$\Delta\boldsymbol{\tilde{w}}^{(n)}(t) = c_n e^{-\zeta_n \varpi_{u,n} t} \text{mod}\{\boldsymbol{\rho}_{\boldsymbol{\tilde{w}}}^{(n)}\} .* \cos\left(\varpi_{d,n} t + \arg\{\boldsymbol{\rho}_{\boldsymbol{\tilde{w}}}^{(n)}\} + \alpha_n\right) \quad (12)$$

The complex vectors $\boldsymbol{\rho}_{\boldsymbol{\varepsilon}}^{(n)}$, $\boldsymbol{\rho}_{\boldsymbol{\tilde{w}}}^{(n)}$ are obtained by partitioning the eigenvector $\boldsymbol{\rho}^{(n)}$ into its constituent sub-vectors according to the composition of \mathbf{s} (eq. (2)). The scaled eigenvectors are denoted by $\tilde{\boldsymbol{\rho}}^{(n)}$ where

$$\tilde{\boldsymbol{\rho}}^{(n)} = \kappa^{(n)} \boldsymbol{\rho}^{(n)} \quad (13)$$

The sub-vectors of the scaled eigenvectors $\tilde{\boldsymbol{\rho}}^{(n)}$ are given similar notation i.e. $\tilde{\boldsymbol{\rho}}_{\boldsymbol{\varepsilon}}^{(n)}$, $\tilde{\boldsymbol{\rho}}_{\boldsymbol{\tilde{w}}}^{(n)}$, ...etc. and the result of eq. (10) using these vectors becomes $\tilde{A}^{(n)} = \sigma$.

Let $\tilde{A}_{\boldsymbol{\varepsilon}}^{(n)}$ denote the mean of the x, y non-dimensional scaled vibration amplitudes of the FAB journal:

$$\tilde{A}_{\boldsymbol{\varepsilon}}^{(n)} = \text{mean}\left(\text{mod}\{\tilde{\boldsymbol{\rho}}_{\boldsymbol{\varepsilon}}^{(n)}\}\right) \quad (14a,b)$$

The filtering criterion to be adopted sets a minimum journal amplitude such that mode no. n will be rejected from the Campbell diagram unless $\tilde{A}_{\boldsymbol{\varepsilon}}^{(n)}$ is greater than C times σ , where C is a cut-off threshold:

$$\tilde{A}_{\boldsymbol{\varepsilon}}^{(n)} > C\sigma \quad (15)$$

In this work, $\sigma = 0.2$ and $C = 0.1$. In other words, the eigenvector of the mode no. n is scaled so that the greatest vibration amplitude within the FAB, considering both pad and journal, is 20% of the radial clearance, and the scaled mode is rejected if the amplitude of the journal vibration (average of x, y vibrations) it is not greater than 2% (i.e. 0.1 of 20%) of the radial clearance.

The journal and pad vibrations in mode no. n , and the whirl direction, are determined by plotting $\boldsymbol{\varepsilon}^{(n)} = \boldsymbol{\varepsilon}_{\mathbf{E}} + \Delta\boldsymbol{\varepsilon}^{(n)}$ and $\boldsymbol{\tilde{w}}^{(n)} = \boldsymbol{\tilde{w}}_{\mathbf{E}} + \Delta\boldsymbol{\tilde{w}}^{(n)}$ at a number of discrete times covering the period $2\pi/\varpi_{d,n}$ (where $\Delta\boldsymbol{\varepsilon}^{(n)}$, $\Delta\boldsymbol{\tilde{w}}^{(n)}$ are from eqs. (11, 12) using scaled eigenvectors $\tilde{\boldsymbol{\rho}}_{\boldsymbol{\varepsilon}}^{(n)}$, $\tilde{\boldsymbol{\rho}}_{\boldsymbol{\tilde{w}}}^{(n)}$, and $\boldsymbol{\varepsilon}_{\mathbf{E}}$, $\boldsymbol{\tilde{w}}_{\mathbf{E}}$ are from the static solution (eq. (3)).

The initial conditions to induce the dynamical system defined by eq. (1) to respond in one specific mode *only* (with no unbalance excitation applied) are given by:

$$\mathbf{s}(\tau = 0) = \mathbf{s}_{\mathbf{E}} + c_n \text{mod}\{\tilde{\boldsymbol{\rho}}^{(n)}\} .* \cos\left(\arg\{\tilde{\boldsymbol{\rho}}^{(n)}\} + \alpha_n\right) \quad (16)$$

4 Discussion of Simulation Results

The parameters of the system (Figure 1) are as in [4] and negligibly different from [14]: $M = 3.061$ kg; $\mathbf{f}_{\mathbf{s}} = [0 \quad -3.061 \times 9.81]^T$; $c = 32 \times 10^{-6}$ m; radius $R = 19.05 \times 10^{-3}$ m; length $L = 38.1 \times 10^{-3}$ m; air viscosity $\mu = 1.95 \times 10^{-5}$ Pa·s; $p_a = 101325$ Pa; $K_b = 4.739$ GN/m³; $\eta = 0.25$. In the simulations performed, the grid size (covering half axial length of FAB) was 7×71 in the case of the finite θ model (CLE/FTE) and 7×72 in the case of the continuous θ model (FLE/CTE), as per procedure explained in [1]. The dimension of the Jacobian \mathbf{J} was therefore 572×572 for the CLE/FTE case (section 4.1) and 580×580 for the FLE/CTE case (section 4.2). In all TNDA simulations presented, the unbalance force $\mathbf{f}_{\mathbf{u}} = \mathbf{0}$.

4.1 FAB with SEFM/Finite θ Gmbel Air Film (appropriate for CLE/FTE)

The first task was to verify that the model used here (SEFM/finite θ FD air film/Gmbel condition) agreed with TNDA results presented in [14] for the same rotor-FAB system. Figure 2 shows the TNDA result for the journal trajectory at 12 krpm over 20 revolutions from initial conditions corresponding to $\boldsymbol{\varepsilon}, \boldsymbol{\varepsilon}' = \mathbf{0}, \tilde{\boldsymbol{w}} = \mathbf{0}$ and air film at atmospheric pressure. The journal trajectory in Figure 2 agrees very closely with those calculated by the two models used in Figure 3 of Nielsen and Santos [14] i.e.

- 1) the detachable top foil/bilinear bump foil/Finite Element (FE) air film model,
- 2) the SEFM/FE air film/Gmbel model used to validate model (1) at 12 krpm.

With regards to pad deformation, the present model (SEFM/finite θ FD air film/Gmbel) gives the same result as model (2), whereas model (1) naturally gives a different result in the upper right hand quadrant due to the detachment of the top foil.

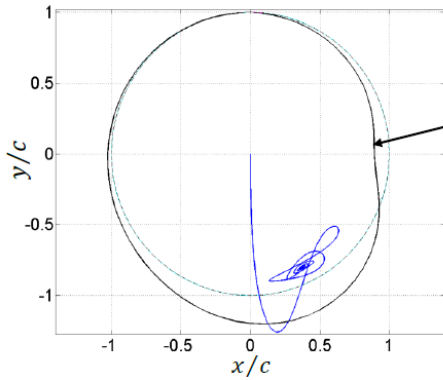


Figure 2. TNDA result journal trajectory over 20 revolutions from initial conditions corresponding to $\boldsymbol{\varepsilon}, \boldsymbol{\varepsilon}' = \mathbf{0}, \tilde{\boldsymbol{w}} = \mathbf{0}$ (SEFM/Finite θ Gmbel) (compare with Figure 3 of Nielsen and Santos [14]).

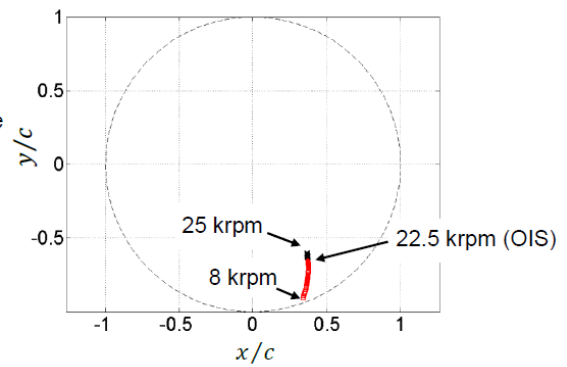


Figure 3. Loci of static equilibrium journal positions over a range of speeds for SEFM/Finite θ Gmbel (CLE/FTE) (stable – red squares).

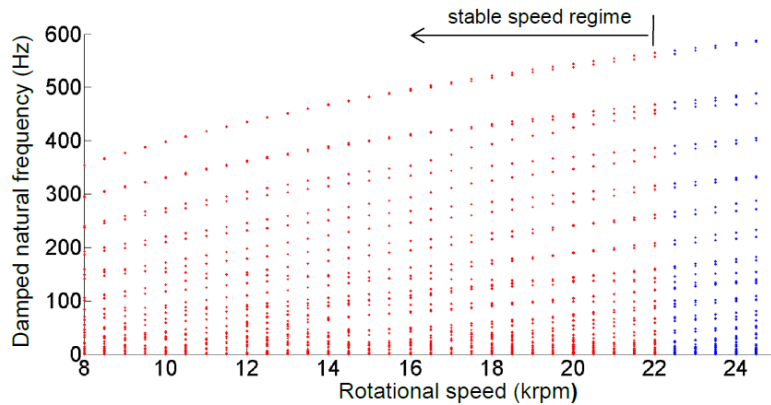


Figure 4. Unfiltered eigenfrequency $\varpi_{d,n}/(2\pi)$ vs speed map for SEFM/Finite θ Gmbel (CLE/FTE).

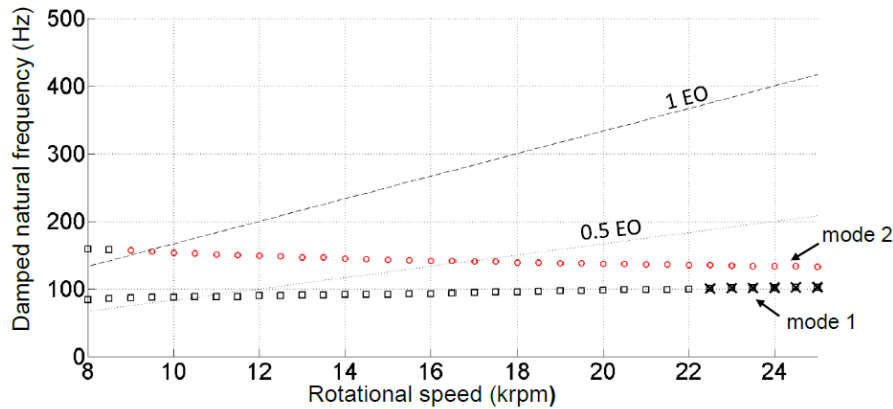


Figure 5. Campbell diagram for SEFM/Finite θ Gmbel (CLE/FTE), extracted from the unfiltered eigenfrequency vs speed map of Figure 4 using minimum journal amplitude criterion, eq. (15) with $C = 0.1$: forward whirl (black squares); reverse whirl (red circles); unstable mode points overlaid with a cross; EO (engine order).

Figure 3 shows the loci of the static equilibrium positions of the journal for the speed range 8-25 krpm. The onset of instability speed (OIS) in this paper is defined as the first speed, in increments of 500 rpm, to register a negative damping ratio in one of the modes. The OIS in this case is 22.5 krpm and compares well with the OIS of ~ 20 krpm reported from the TNDA simulations by Nielsen and Santos [14], considering that they used the detachable top foil/bilinear bump foil/FE air film model (in [14], the latter model was compared with the SEFM/FE air film/Gümbel model at only one speed).

The free vibration about the static equilibria in Figure 3 is next considered. Figure 4 shows the unfiltered eigenfrequency ($\varpi_{d,n}/(2\pi)$) vs speed map, which is seen to comprise a multitude of eigenmodes. However, the application of the minimum journal amplitude (eq. (15)) to Figure 4 results in the extraction of the “clean” Campbell diagram of Figure 5. The two modes (“mode points”) at individual speeds each lie on distinct curves (labelled “mode 1” and “mode 2”) covering the speed range. This is consistent with the system having two degrees of freedom. Figure 6 shows two examples of modes that were rejected from the Campbell diagram by the minimum journal amplitude criterion. In these modes, the vibration in the FAB is virtually entirely in the pad, with negligible vibration of the journal. Such modes were also found to be highly damped, although still oscillatory (as evident by the non-zero frequencies).

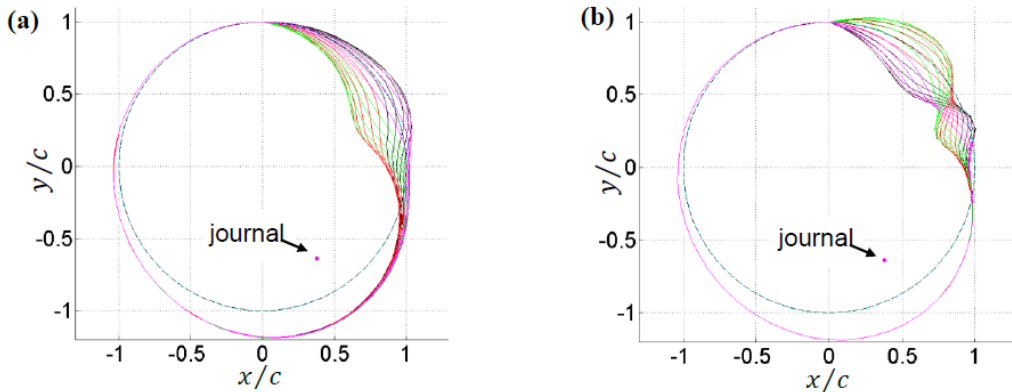


Figure 6. Two examples of modes rejected by the minimum journal amplitude criterion, eq. (15), for SEFM/Finite θ Gümbel (CLE/FTE): (a) mode at 22 krpm with $f_{d,n} = \varpi_{d,n}/(2\pi) = 141.97$ Hz, $\zeta_n = 0.96288$; (b) mode at 22 krpm with $f_{d,n} = 67.60$ Hz, $\zeta_n = 0.99801$ (NB: for clarity of display, the exponential decay factor $e^{-\zeta_n \varpi_{u,n} t}$ in eqs. (11), (12) was omitted when calculating the modal vibration).

The Campbell diagram of Figure 5 indicates the direction of whirl and the state of stability of the two modes. Mode 1 is forward whirl over the entire speed range and becomes unstable beyond 22 krpm. The frequency of mode 1 varies from 84 Hz at 8 krpm to 98 Hz at 20 krpm. This correlates well with the following observation made by Nielsen and Santos [14]: “This frequency increases slightly from approximately 80 Hz at 8,000 r/min to around 100 Hz at 20,000 r/min”. This observation from [14] related to a subharmonic frequency observed in the waterfall diagram of the initial 0.22s of the simulated transient response (as the rotor was dropped from the centralised initial conditions) with 5 g-mm unbalance, using the detachable top foil/bilinear bump foil/FE air film model (Figure 13 in Nielsen and Santos [14]). This subharmonic frequency was *transient* and, therefore, a *mode* i.e. it was absent from the waterfall diagram of the steady-state vibration (Figure 12 of [14]). Figure 5 shows that mode 2 is in reverse whirl for most of the speed range. Evidence for the existence of mode 2 is not provided in the transient unbalance response result of [14], but this is to be expected since reverse whirl modes are not normally excited by the unbalance [17]. However, mode 2 shall be verified by TNDA in the present paper.

Figure 7 shows modes 1 and 2 at 22 krpm i.e. just before the OIS (22.5 krpm). Mode 2 is seen to be considerably more damped than mode 1. The two modes in Figure 7 were verified by TNDA using mode-specific initial conditions (eq. (16)), which caused the unforced nonlinear dynamical system (eq. (1)) to respond in mode 1 only (Figure 8(a), (b)) or mode 2 only (Figure 8(c), (d)). The orbital trajectories in Figures 8(a), 8(c) confirm the stability, orientation and direction of whirl of the orbits in Figures 7(a), 7(b) respectively (orbit in Figure 8(a) winds anticlockwise, whereas orbit in Figure 8(c) winds clockwise, as predicted in Figure 7). The time histories in Figures 8(b), (d) were used to check the values for damped frequency $f_{d,n} = \varpi_{d,n}/(2\pi)$ and the damping ratio ζ_n given in the captions of Figure 7 (that were calculated from eigenvalue analysis and eqs. (8a-c)). The estimates for $f_{d,n}$ and ζ_n shown in Figure 8(b), (d) were determined by calculating the period and applying the logarithmic decrement method [18] and are seen to be reasonably close those of Figure 7: 0.4%, 2.1% difference in frequency for modes 1, 2 respectively; 8.75%, -0.53% difference in damping ratio for modes 1, 2 respectively. The higher discrepancy in the damping ratio at mode 1 is attributed to the inherent accuracies in the application of the logarithmic decrement method to the time history of Figure 8(b), considering its light damping, uneven time steps and higher frequency.

Figure 9 shows the TNDA simulation of the journal trajectory using initial conditions specific to mode 1 at 22.5 krpm (for which this mode is unstable, Figure 5). As predicted by the Campbell diagram, the trajectory is seen to diverge. The estimates for $f_{d,n}$ and ζ_n from the time history in Figure 9(b) agree closely with the eigenvalue analysis values in the caption (0.4%, 6.15% difference in $f_{d,n}$ and ζ_n respectively). Figure 10 shows the TNDA journal trajectory at two unstable speeds – 22.5 krpm (onset of instability speed OIS) and 25 krpm – from initial conditions specific to mode 2 which is *stable* at both these speeds. At 22.5 krpm (Figures 10(a,b)), the degree of instability ($|\zeta_n|$) of mode 1 is very low and the trajectory can still converge unhindered along mode 2 to the static equilibrium position - the integration errors in the TNDA time steps (equivalent to physical perturbations) do not reach a sufficient level to excite mode 1 and diverge the trajectory. However, at 25 krpm (Figures 10(c,d)), where the degree of instability of mode 1 is 10 times higher than at the OIS, the trajectory *initially* converges along mode 2 (reverse whirl) but then starts diverging along mode 1 (forward whirl).

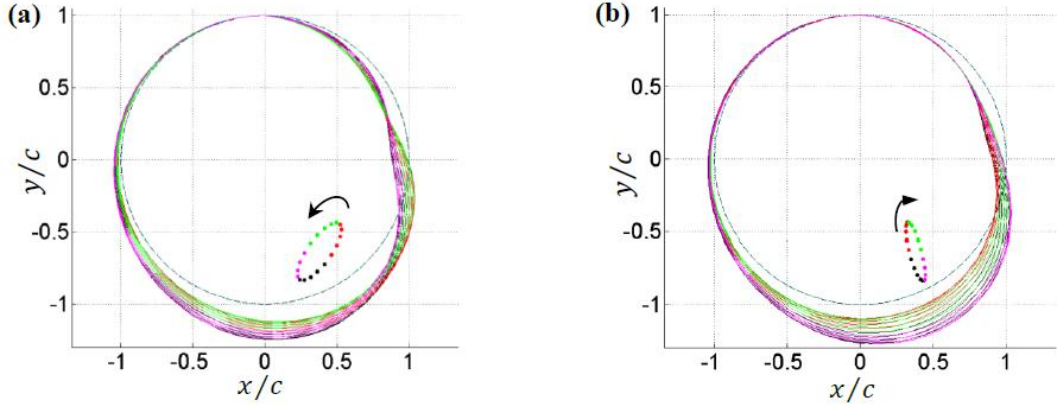


Figure 7. Modes at 22 krpm taken from Campbell diagram in Figure 5: (a) mode 1 ($f_{d,n} = 99.59$ Hz, $\zeta_n = 0.002533$, forward whirl); (b) mode 2 ($f_{d,n} = 135.33$ Hz, $\zeta_n = 0.14976$, reverse whirl) (NB: for readers of digital version, temporal sequence of vibration is indicated by colour sequence black-red-green-magenta; for clarity of display, the exponential decay factor $e^{-\zeta_n \omega_{u,n} t}$ in eqs. (11), (12) was omitted when calculating the modal vibration).

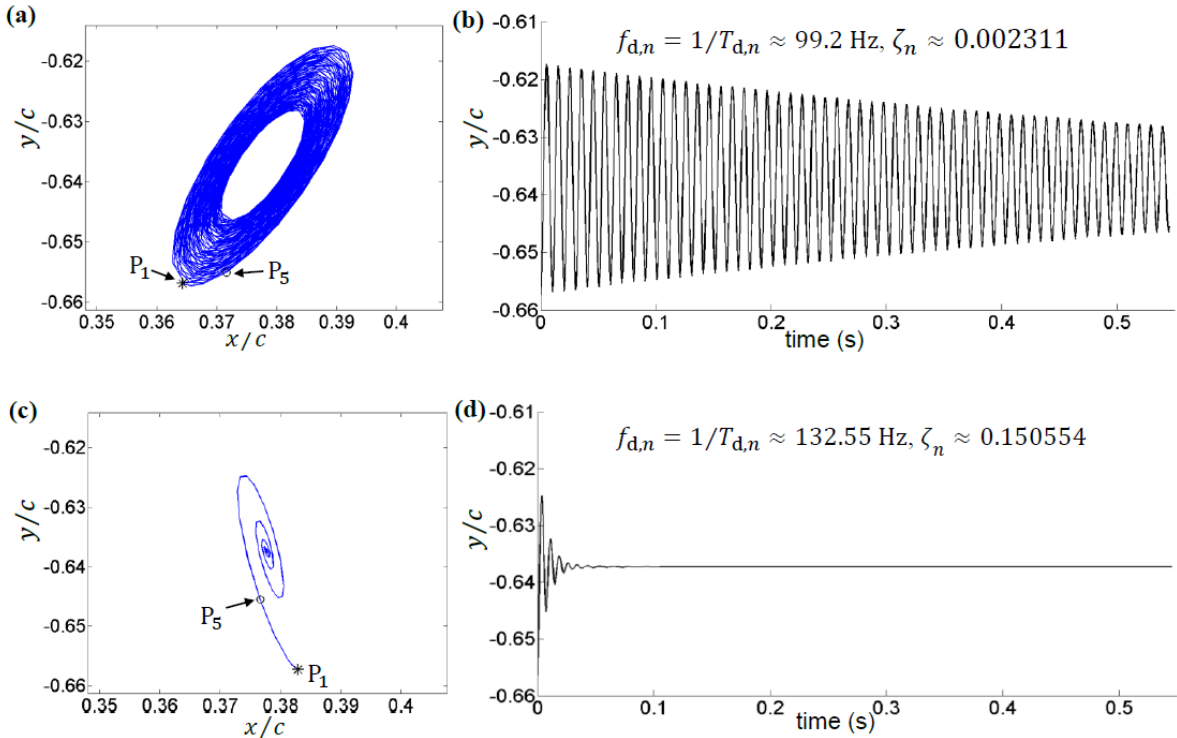


Figure 8. Transient nonlinear dynamic analysis (TNDA) journal trajectories and time histories at 22 krpm using mode-specific initial conditions (eq. (16)) taken from Campbell diagram of Figure 6: (a), (b) mode 1; (c), (d) mode 2; (P_1 : point at $t = 0$; P_5 : point four time steps later; displayed estimates for $f_{d,n}$, ζ_n were determined from the corresponding time histories and should be compared with the Campbell diagram analysis values in caption of Figure 7).

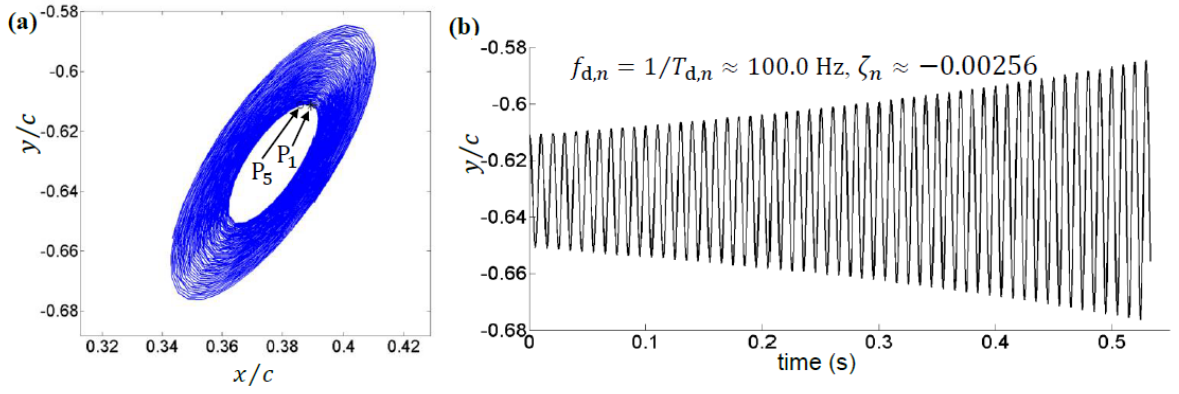


Figure 9. Transient nonlinear dynamic analysis (TNDA) journal trajectory and time history at 22.5 krpm using mode-specific initial conditions (eq. (16)) taken from mode 1 @ 22.5 krpm (unstable) on Campbell diagram of Figure 5 (P_1 : point at $t = 0$; P_5 : point four time steps later; displayed estimates for $f_{d,n}$, ζ_n were determined from the time history and should be compared with the values output from the Campbell diagram analysis $f_{d,n} = 100.4$, $\zeta_n = -0.00273$).

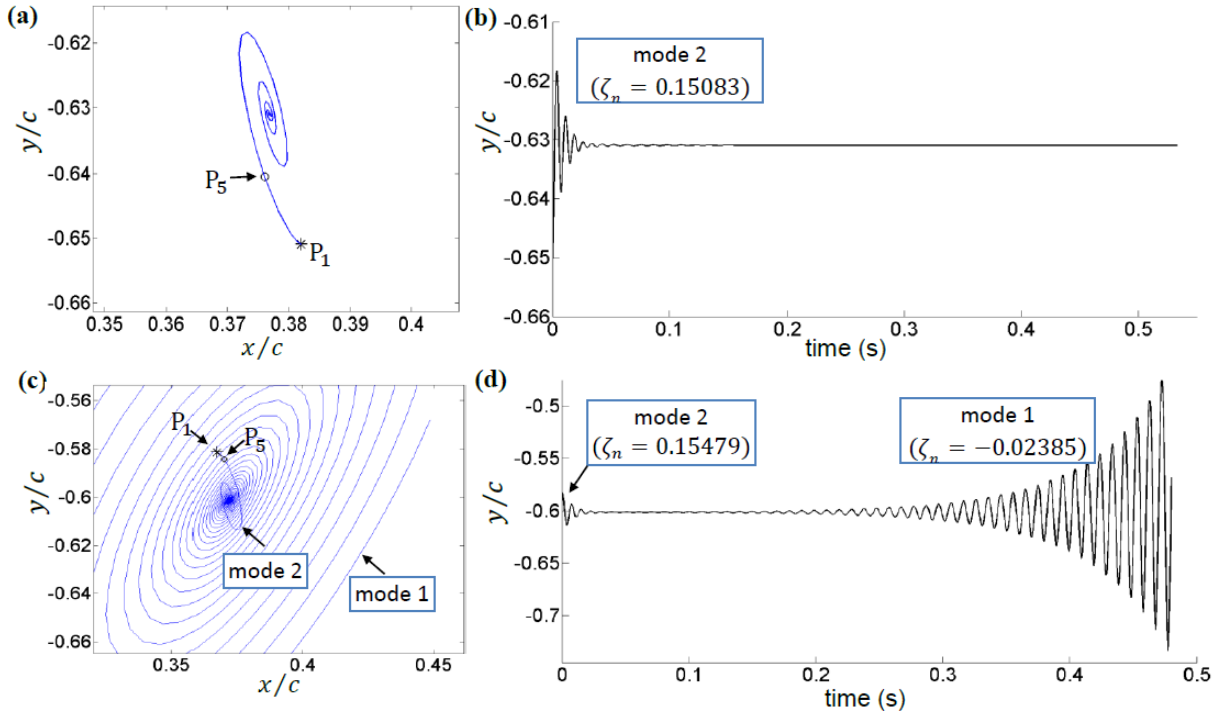


Figure 10. Transient nonlinear dynamic analysis (TNDA) journal trajectories and time histories at two speeds, one at the onset of instability (22.5 krpm: (a), (b)) and the other above this (25 krpm: (c), (d)), for mode-specific initial conditions (eq. (16)) taken from *stable* mode 2 on Campbell diagram of Figure 5 (P_1 : point at $t = 0$; P_5 : point four time steps later; values of ζ_n in figures are taken from Campbell diagram analysis).

4.2 FAB with SEFM/Continuous θ non-Gümbel Air Film (appropriate for FLE/CTE)

Figure 11 shows the loci of the static equilibrium positions of the journal for the speed range 8-25 krpm. Comparing with Figure 3, the static equilibria are at a higher level and the OIS is considerably lower (15 krpm, as reported in [4]). The removal of constraints on the air film is seen to lower the OIS, as observed in [1].

Figure 12 shows the unfiltered eigenfrequency ($\omega_{d,n}/(2\pi)$) vs speed map for free vibration about the static equilibria, from which the Campbell diagram of Figure 13 is extracted by the minimum journal amplitude criterion (eq. (15)). Like the previous one of Figure 5, the Campbell diagram of Figure 13 shows two modes that describe significant rotor whirl – one in forward whirl that becomes unstable at 15 krpm, the other in reverse whirl that is stable over the speed range considered. These two modes are depicted in Figures 14(a,b) and are seen to have similar orientations to those in Figures 7(a,b). However, the Campbell diagram of Figure 13 also shows a low journal amplitude mode that manages to pass the minimum journal amplitude criterion with

$C = 0.1$. An example of such a mode is given in Figure 14(c), where it is seen that the vibration is mainly in the pad (as in the rejected modes e.g. Figure 6). The low journal amplitude mode in Figure 13 was found to have a high damping ratio (above 0.7) over the entire speed range and therefore would have little practical significance. Therefore, rather than raising the value of the threshold C in the minimum journal amplitude criterion (eq. (15)), a better way of eliminating such a mode from the Campbell diagram of Figure 13 would be to apply a *maximum modal damping* criterion in conjunction with the minimum journal amplitude criterion.

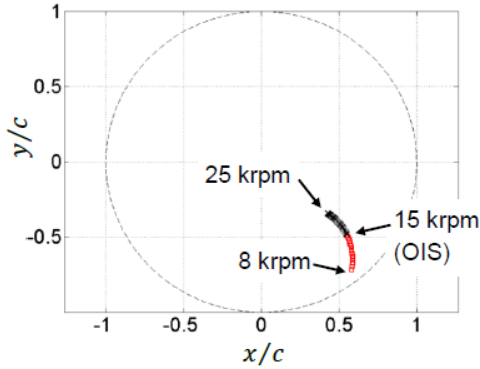


Figure 11. Loci of static equilibrium journal positions over a range of speeds for continuous θ non-Gümbel (FLE/CTE) (stable – red squares).

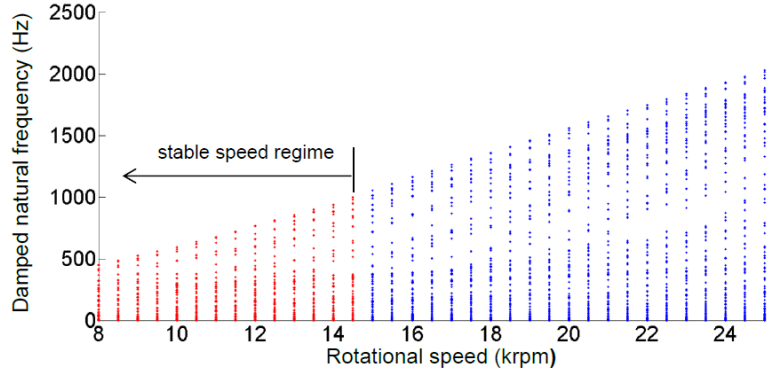


Figure 12. Unfiltered eigenfrequency $\omega_{d,n}/(2\pi)$ vs speed map for continuous θ non-Gümbel (FLE/CTE).

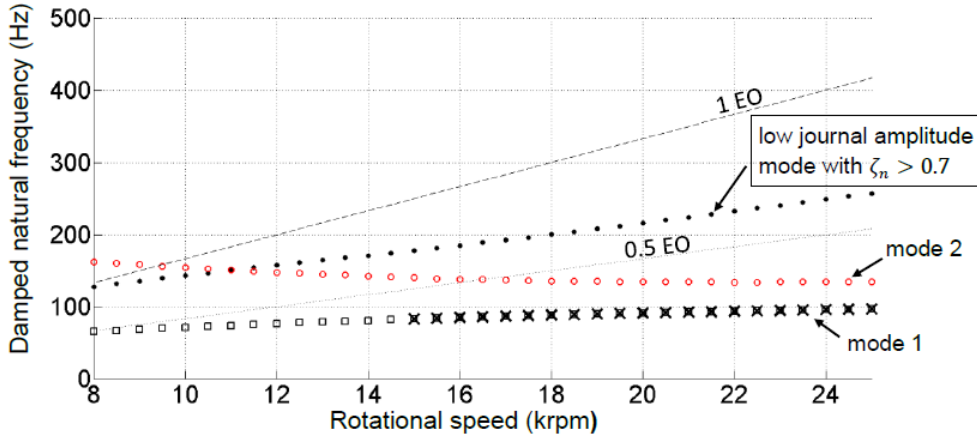


Figure 13. Campbell diagram for continuous θ non-Gümbel (FLE/CTE), extracted from the unfiltered eigenfrequency vs speed map of Figure 12 using minimum journal amplitude criterion, eq. (15) with $C = 0.1$: forward whirl (black squares); reverse whirl (red circles); unstable mode points overlaid with a cross; EO (engine order).

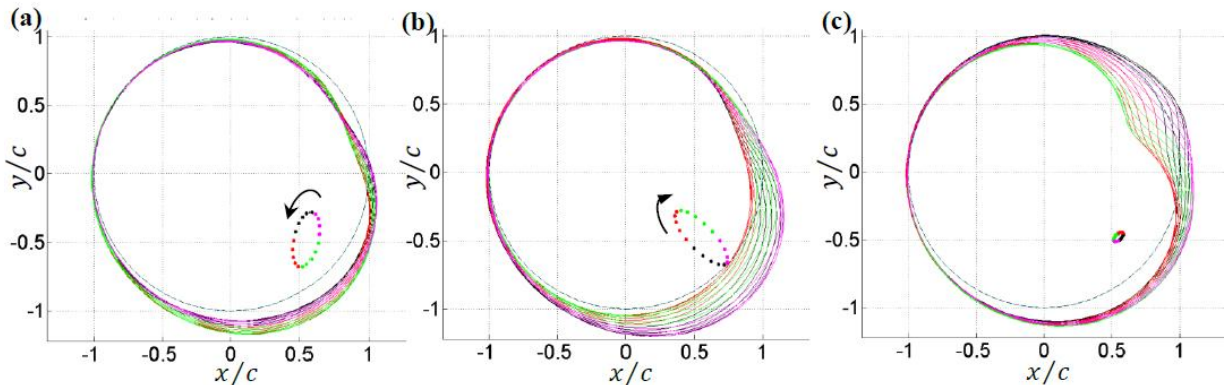


Figure 14. Modes at 15 krpm taken from Campbell diagram in Figure 13: (a) mode 1 ($f_{d,n} = 82.97$ Hz, $\zeta_n = -0.000166$ i.e. unstable, forward whirl); (b) mode 2 ($f_{d,n} = 140.05$ Hz, $\zeta_n = 0.25546$, reverse whirl); (c) low journal amplitude mode ($f_{d,n} = 178.11$ Hz, $\zeta_n = 0.81155$) (NB: for readers of digital version, temporal sequence of vibration is indicated by colour sequence black-red-green-magenta; for clarity of display, the exponential decay factor $e^{-\zeta_n \omega_{u,n} t}$ in eqs. (11), (12) was omitted when calculating the modal vibration).

7 Conclusions

This paper has introduced a new method for deriving the Campbell diagram of a rotor/foil-air bearing (FAB) that does not depend on Lund's linearised force coefficient (FC) method. It was based on the eigenvalue analysis of the state Jacobian of the dynamical system (nonlinear state-space) representation of the fully coupled air film/foil/rotor model. Through appropriate scaling of the eigenvectors and the application of a minimum journal amplitude criterion, the multitude of eigenvalues/eigenvectors of the Jacobian could be filtered in order to extract only the relevant modes. Where appropriate, a maximum damping criterion should also be applied. Each extracted mode could be precisely verified using transient nonlinear dynamic analysis (TNDA) with mode-specific initial conditions derived directly from the eigenvalue analysis. The methodology was successfully applied to a two-degree-of freedom (rigid-symmetric) rotor on single-pad FABs with the pad modelled by the simple equivalent foundation model. Two types of air film conditions were considered, respectively suitable for alternative pad configurations. The simulation results correlated well with observations reported in an independent study in the literature that used a more advanced foil model but was restricted to TNDA (no Campbell diagram). A forthcoming journal paper shall present this method for a generic rotor-FAB system.

References

- [1] Bonello, P. and Bin Hassan, M.F. (2018): An experimental and theoretical analysis of a foil-air bearing rotor system. *JSV*, **413**, pp. 395–420.
- [2] Ott, E. (1993): *Chaos in Dynamical Systems*. Cambridge University Press, Cambridge.
- [3] Pham, H.M. and Bonello, P. (2013): Efficient Techniques for the Computation of the Nonlinear Dynamics of a Foil-Air Bearing-Rotor System. In *Proc. ASME Turbo Expo*. San Antonio, Texas, USA, paper no. GT-2013-94389.
- [4] Bonello, P. and Pham, H.M. (2014): The efficient computation of the nonlinear dynamic response of a foil-air bearing rotor system. *JSV*, **333**(15), pp. 3459-3478.
- [5] Bonello, P. and Pham, H.M. (2014): Nonlinear dynamic analysis of high speed oil-free turbomachinery with focus on stability and self-excited vibration. *J. Tribology*, **136**(4), 041705.
- [6] Larsen, J.S. and Santos, I.F. (2015): On the nonlinear steady-state response of rigid rotors supported by air foil bearings – Theory and experiments. *JSV*, **346**, pp. 284-297.
- [7] Hoffmann, R. and Liebich, R. (2018): Characterisation and calculation of nonlinear vibrations in gas foil bearing systems – An experimental and numerical investigation. *JSV*, **412**, pp. 389-409.
- [8] Sim, K., Lee, Y.-B., Kim, T.-H., and Lee, J. (2012): Rotordynamic performance of shimmed gas foil bearings for oil-free turbochargers. *J. Tribology*, **134**, 031102.
- [9] Guo, Z., Peng, L., Feng, K. and Liu, W. (2018): Measurement and prediction of nonlinear dynamics of a gas foil bearing supported rigid rotor system. *Measurement*, **121**, pp. 205-217.
- [10] Lund, J.W.. (1968): Calculation of stiffness and damping properties of gas bearings. *J. Lubrication Technology*, pp. 793–804.
- [11] Peng, J.P. and Carpino, M. (1993): Calculation of stiffness and damping coefficients for elastically supported gas foil bearings. *J. Tribology*, **115**, pp. 20-27.
- [12] Larsen, J.S., Santos, I.F. and von Osmanski, S. (2016): Stability of rigid rotors supported by air foil bearings: Comparison of two fundamental approaches. *JSV*, **381**, pp. 179-191.
- [13] Kim, D. (2007): Parametric studies on static and dynamic performance of air foil bearings with different top foil geometries and bump stiffness distributions. *J. Tribology*, **129**(2), pp. 354-364.
- [14] Nielsen, B.B.. and Santos, I.F. (2017): Transient and steady state behaviour of elasto-aerodynamic air foil bearings, considering bump foil compliance and top foil inertia and flexibility: a numerical investigation. *Proc. IMechE Part J: J. Eng. Trib.*, doi: 10.1177/1350650117689985.
- [15] Leister, T., Baum, C., and Seemann, W. (2017): On the importance of frictional energy dissipation in the prevention of undesirable self-excited vibrations in gas foil bearing rotor systems. *Technische Mechanik*, **37**, 2-5, pp. 280-290.
- [16] Nielsen, B. B. (2017): *Combining Gas Bearing and Smart Material Technologies for Improved Machine Performance: Theory and Experiment*. Dissertation, Technical University of Denmark, Lyngby, Denmark.
- [17] Kramer, E. (1993): *Dynamics of Rotors and Foundations*. Springer-Verlag, Berlin.
- [18] Rao, S.S. (2011): *Mechanical Vibrations (Fifth Edition)*. Prentice Hall, N.J.

Modelling of Compliant-type Gas Bearings: A Numerical Recipe

Sebastian von Osmanski¹, Jon S. Larsen², Ilmar F. Santos¹

¹ Dept. of Mechanical Engineering, Technical University of Denmark, 2800 Kgs. Lyngby, Denmark

² GEA Process Engineering A/S, 2860 Søborg, Denmark

E-mail addresses: asvosm@mek.dtu.dk (S. von Osmanski), jonsteffen.larsen@gea.com (J.S. Larsen),
and ifs@mek.dtu.dk (I.F. Santos)

Abstract

Despite its merits, the Gas Foil Bearing (GFB) suffers from several inherent limitations which could likely be overcome using active radial injection. This hence represents a natural next step, even though several issues relating to the foil structure modelling remain unresolved. A prerequisite for the development of any model-based feedback control scheme is a model capturing the effects of gas injection on the system dynamics. The currently presented work on a generic numerical recipe for GFB simulation is intended as a step towards such a model.

The aim of the present work is to consolidate the existing state of the art knowledge on GFB modelling into a generic framework that can act as an efficient platform for further research. By creating a structure where the same pieces of code can be applied for simulation of a wide range of rotors supported by any number of rigid or compliant type gas bearings — with or without injection — the available experimental results can be utilized optimally for validation. Furthermore, the programming intensive optimizations necessary to obtain tolerable solution times can be more easily reused.

The framework consists of three domains treating the rotor, the foil structure and the fluid film respectively, along with clear-cut domain interfaces based on linear mappings. In the fluid domain, the film is modelled using the Modified Reynolds Equation discretised using finite volume, leaving the injection flow to an auxiliary model. Both the rotor and the compliant structure are represented in generic state-space formats facilitating various different models for both domains. The global system is solved both statically and in time using efficient general purpose routines exploiting e.g. analytical Jacobian matrices and sparse direct linear solvers.

Nomenclature

BC	Boundary Condition	(\cdot)	Non-dimensional quantity
CDS	Central Differencing Scheme	$\nabla \cdot$	Divergence
CFD	Computational Fluid Dynamics	∇	Gradient
CSR	Compressed Sparse Row	A_b	Bearing surface area $A_b = [0, L] \times [0, 2\pi]$
CV	Control Volume	A_i	In-film area of the i -th CV
DAE	Differential/Algebraic Equation	L, \tilde{L}	Bearing length, $\tilde{L} = L/R$
DOF	Degree of Freedom	M_g	Molar mass of gas
EOM	Equation of Motion	$M_{inj,i}$	Integrated injection flux for the i -th CV
FD	Finite Difference	R	Journal radius
FE	Finite Element	R_u	Universal gas constant
FV	Finite Volume	S_i	In-film circumference of the i -th CV
GFB	Gas Foil Bearing	S_τ	Non-dimensional group, $S_\tau = \frac{6R^2\mu\omega_\tau}{C^2\rho_a}$
IC	Initial Condition	T_{iso}	Isothermal gas temperature
IVP	Initial Value Problem	U	Unbalance, mass \times eccentricity
LUDS	Linear Upwind Differencing Scheme	a_j	FV stencil coefficients constituting \mathbf{A}_{FV}
MRE	Modified Reynolds Equation	f_{tol}	Global force tolerance
ODE	Ordinary Differential Equation	h, \tilde{h}	Film height, $\tilde{h} = h/C$
SEFM	Simple Elastic Foundation Model	l_{tol}	Global length tolerance
UDS	Upwind Differencing Scheme (1 st order)	l_f	Foil domain length scale
(\cdot)	Time derivative, $d^2/d\tau^2$	l_r	Rotor domain length scale
(\cdot)	Time derivative, $d/d\tau$	m_r	Rotor domain mass scale

m_{inj}	Injection flux field	\mathbf{n}	Outward pointing unit normal vector
n_{cv}	Number of CVs (per bearing)	$\mathbf{p}_\alpha, \tilde{\mathbf{p}}_\alpha$	Bearing α CV centre pressures, $\mathbf{p}_\alpha = p_a \tilde{\mathbf{p}}_\alpha$
n_{rdof}	Number of rotor domain DOFs	\mathbf{r}_{scale}	Nondimensionalization scalings for \mathbf{r}_r
n_{ub}	Number of unbalance masses	\mathbf{r}_{tol}	Dimensional system residual tolerances
n_b	Number of GFBs	\mathbf{r}_r	Rotor residual vector
p, \tilde{p}	Film pressure, $\tilde{p} = p/p_a$	$\mathbf{r}_{FV,\alpha}$	FV residual vector for bearing α
p_{tol}	Global (derived) pressure tolerance	$\mathbf{r}_{f,\alpha}$	Foil structure residual in bearing α
p_a	Ambient pressure, fluid pressure scaling	$\mathbf{u}_g, \tilde{\mathbf{u}}_g$	Gas in-film velocity vector, $\mathbf{u}_g = \{u_\theta \ u_z\}^T$
p_f	Foil domain pressure scale	$\mathbf{x}_r, \tilde{\mathbf{x}}_r$	Rotor DOF vector
p_i	Pressure at i -th CV centre	$\mathbf{x}_{f,\alpha}, \tilde{\mathbf{x}}_{f,\alpha}$	Foil structure DOF vector for bearing α
$r_{FV,i}$	FV equation residual for i -th CV	\mathbf{z}_r	Rotor state vector
t	Physical time	$\mathbf{z}_{f,\alpha}$	Foil structure state vector for bearing α
x_g, y_g, z_g	Fluid film coordinates, y_g is curvilinear	\mathbf{A}_f	Foil structure state-space inertia
x_r, y_r, z_r	Rotor coordinates	\mathbf{A}_r	Rotor state-space inertia
$\Omega, \tilde{\Omega}$	Angular velocity $\tilde{\Omega} = \Omega/\omega_\tau$	\mathbf{A}_{FV}	FV coefficient matrix, Couette & Poiseuille
Ξ	FV stencil, i.e. a set of CV indices	\mathbf{B}_f	Foil structure state-space stiffness/damping
α	Bearing index, $\alpha = 1, \dots, n_b$	\mathbf{B}_r	Rotor state-space stiffness/damping
μ	Dynamic gas viscosity	\mathbf{B}_{FV}	FV coefficient matrix, squeeze term
ω_τ	Characteristic frequency	\mathbf{C}_r	Rotor state-space gyroscopic matrix
ϕ	Phase of unbalance	\mathbf{C}_{FV}	FV coefficient matrix, local expansion term
ρ_g	Density of gas	$\mathbf{D}_f, \tilde{\mathbf{D}}_f$	Foil structure damping matrix
τ	Dimensionless time, $\tau = \omega_\tau t$	$\mathbf{D}_r, \tilde{\mathbf{D}}_r$	Rotor damping matrix
θ	Circumferential angle	$\mathbf{G}_r, \tilde{\mathbf{G}}_r$	Rotor gyroscopic matrix
$\tilde{\theta}$	Circumferential coordinate, $\tilde{\theta} = y_g/R$	$\mathbf{H}_{cvc,f}$	Mapping from $\tilde{\mathbf{x}}_{f,\alpha}$ to $\mathbf{h}_{c,cvc}$
\mathbf{f}_{ub}	Rotor unbalance force vector	$\mathbf{H}_{cvc,r}$	Mapping from $\tilde{\mathbf{x}}_r$ to $\mathbf{h}_{r,cvc}$
$\mathbf{f}_{\mu,\alpha}$	Foil structure friction forces in bearing α	$\mathbf{H}_{cve,f}$	Mapping from $\tilde{\mathbf{x}}_{f,\alpha}$ to $\mathbf{h}_{c,cve}$
\mathbf{f}_b	Bearing force vector	$\mathbf{H}_{cve,r}$	Mapping from $\tilde{\mathbf{x}}_r$ to $\mathbf{h}_{r,cve}$
$\mathbf{f}_{fw,\alpha}$	Foil structure static loads in bearing α	$\mathbf{H}_{fb,p}$	Mapping from bearing pressures to $\mathbf{T}_r \tilde{\mathbf{f}}_b$
$\mathbf{f}_{p,\alpha}$	Foil structure pressure loads in bearing α	$\mathbf{H}_{fp,p}$	Mapping from \mathbf{p}_α to $\mathbf{T}_f \tilde{\mathbf{f}}_{p,\alpha}$
\mathbf{f}_{rw}	Rotor static force vector	\mathbf{I}	Identity matrix
$\mathbf{h}_{0,cvc}$	Initial film heights at CV centres	$\mathbf{K}_f, \tilde{\mathbf{K}}_f$	Foil structure stiffness matrix
$\mathbf{h}_{0,cve}$	Initial film heights at CV edges	$\mathbf{K}_r, \tilde{\mathbf{K}}_r$	Rotor stiffness matrix
$\mathbf{h}_{c,cvc}$	Compliant film heights at CV centres	$\mathbf{M}_f, \tilde{\mathbf{M}}_f$	Foil structure mass matrix
$\mathbf{h}_{c,cve}$	Compliant film heights at CV edges	$\mathbf{M}_r, \tilde{\mathbf{M}}_r$	Rotor mass matrix
$\mathbf{h}_{r,cvc}$	Rigid film heights at CV centres	\mathbf{T}_f	Foil structure DOF to state-space mapping
$\mathbf{h}_{r,cve}$	Rigid film heights at CV edges	\mathbf{T}_r	Rotor DOF to state-space mapping

1 Introduction

Rotor-bearing systems supported by Gas Foil Bearings (GFBs) often display complex dynamics originating from the non-linear behaviour of the compressible gas film and its interaction with the compliant structure. To understand and predict such a behaviour, several researchers have contributed improvements to the available GFB modelling tools over the recent years. These include the introduction of the simultaneous solution approach [2] and work on various foil structure models [11, 19, 15]. Even though several issues remain unresolved for conventional GFBs, especially regarding the foil structure damping, a natural next step concerns active radial injection. This could potentially overcome some of the passive GFB's inherent issues and work on hybrid GFBs have been presented [21, 22].

The aim of the present work is to generate a fast and versatile simulation tool for radial GFBs. This should be capable of modelling an arbitrary number of rigid or compliant type gas bearings supporting a variety of rigid or flexible rotors. The tool should rely on fast and readily available general purpose solvers to provide simultaneous steady-state solutions as well as time integrations while reusing as much code as possible. This allows the available base of experimental and theoretical gas bearing results from the literature to be utilised optimally for validation purposes.

A prerequisite for the development of any model-based feedback control scheme would be a model capturing the effects of gas injection on the system dynamics. The currently presented work on a generic numerical recipe for GFB simulation is intended as a step towards such a model.

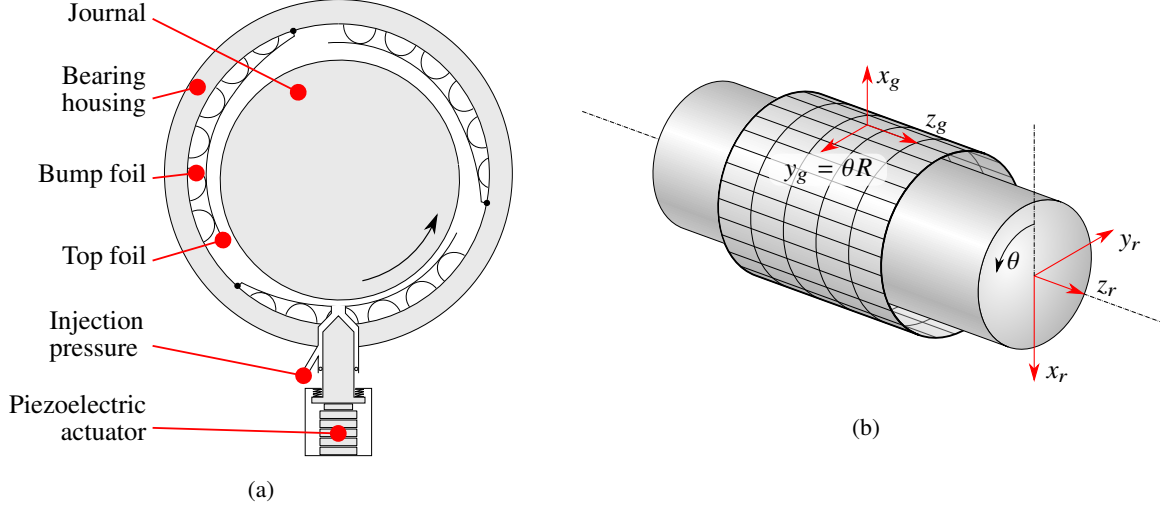


Figure 1: (a): A three-pad GFB augmented with a single injector. (b): Illustration of the discretized fluid film along with its coordinate system and the rotor. Notice that the fluid film is unwrapped meaning that y_g is curvilinear in the illustration.

2 Rotor Domain

The model is build to support any type of rotor representable in a general state-space form using the rotor Degree of Freedom (DOF) vector $\tilde{\mathbf{x}}_r$ as

$$\underbrace{\begin{bmatrix} \mathbf{0} & \tilde{\mathbf{M}}_r \\ \mathbf{I} & \mathbf{0} \end{bmatrix}}_{\mathbf{A}_r} \underbrace{\begin{Bmatrix} \dot{\tilde{\mathbf{x}}}_r \\ \tilde{\mathbf{x}}_r \end{Bmatrix}}_{\dot{\mathbf{z}}_r} + \underbrace{\begin{bmatrix} \tilde{\mathbf{K}}_r & \tilde{\mathbf{D}}_r \\ \mathbf{0} & -\mathbf{I} \end{bmatrix}}_{\mathbf{B}_r} + \underbrace{\tilde{\Omega} \begin{bmatrix} \mathbf{0} & -\tilde{\mathbf{G}}_r \\ \mathbf{0} & \mathbf{0} \end{bmatrix}}_{\mathbf{C}_r} \underbrace{\begin{Bmatrix} \tilde{\mathbf{x}}_r \\ \dot{\tilde{\mathbf{x}}}_r \end{Bmatrix}}_{\mathbf{z}_r} - \underbrace{\begin{bmatrix} \mathbf{I} \\ \mathbf{0} \end{bmatrix}}_{\mathbf{T}_r} (\tilde{\mathbf{f}}_{rw} + \tilde{\mathbf{f}}_b + \tilde{\mathbf{f}}_{ub}) = \mathbf{r}_r, \quad (1)$$

where $\tilde{\mathbf{M}}_r$, $\tilde{\mathbf{D}}_r$, $\tilde{\mathbf{G}}_r$ and $\tilde{\mathbf{K}}_r$ are the non-dimensional rotor mass, damping, gyroscopic and stiffness matrices, respectively. The static forces are kept in $\tilde{\mathbf{f}}_{rw}$, while $\tilde{\mathbf{f}}_{ub}$ represents the unbalance forcing and $\tilde{\mathbf{f}}_b$ holds the bearing forces. No restrictions are made on the origin of the rotor equations which could represent a point mass with just two linear displacement DOFs in $\tilde{\mathbf{x}}_r$, a rigid rotor with a mix of rotational and linear displacement DOFs or a Finite Element (FE) based rotor with potentially hundreds of DOFs. For some models, involving e.g. a reduced order rotor, a more complicated \mathbf{T}_r would be required. Notice that the momentum balance in eq. (1) is equated to a rotor residual \mathbf{r}_r , which should be minimized when solving the non-linear system either in time as an IVP or as an algebraic system in steady-state.

All quantities in the rotor domain are non-dimensionalized using a global characteristic frequency ω_τ , a rotor length scale l_r and a rotor mass scale m_r . The frequency ω_τ gives a non-dimensional angular velocity $\tilde{\Omega} = \Omega/\omega_\tau$ which is shared between the domains. It will often be sensible to define ω_τ simply as the angular velocity implying $\tilde{\Omega} = 1$, but other choices could be advantageous for some simulations [12, 2]. The choice of rotor length and mass scales depends on the specific rotor and the underlying mathematical model, but these can be tuned to enhance the numerical properties of the rotor matrices. A point mass rotor supported by a single GFB will have $\tilde{\mathbf{D}}_r$, $\tilde{\mathbf{G}}_r$ and $\tilde{\mathbf{K}}_r$ equal to zero, hence the scales could be chosen to provide $\tilde{\mathbf{M}}_r = \mathbf{I}$ while maintaining sensible numerical force values. For a more complex rotor, based on e.g. FE discretization with beam elements, a good choice is less obvious.

The force vector \mathbf{f}_b contains the vertical x_r and horizontal y_r components of the fluid film forces on the rotor stemming from all GFBs in the system and hence has $2n_b$ non-zero elements. For each bearing, the forces are found from the usual integration of the projected fluid film pressures as

$$\begin{Bmatrix} f_{b,x_r} \\ f_{b,y_r} \end{Bmatrix} = \iint_{A_b} (p - p_a) \begin{Bmatrix} \cos \theta \\ \sin \theta \end{Bmatrix} R dA \quad \text{where} \quad A_b = [0, L] \times [0, 2\pi]. \quad (2)$$

The force vector $\tilde{\mathbf{f}}_{ub}$ contains the components of the unbalance forces due to each unbalance mass U attached to the rotor and hence has $2n_{ub}$ non-zero elements. For one particular unbalance mass attached to a node of the

rotor, the unbalance forces are found using the usual projections as

$$\begin{Bmatrix} \tilde{f}_{ub,x_r} \\ \tilde{f}_{ub,y_r} \end{Bmatrix} = \begin{Bmatrix} \cos(\tilde{\Omega}\tau + \phi) \\ \sin(\tilde{\Omega}\tau + \phi) \end{Bmatrix} \tilde{U}\tilde{\Omega}^2, \quad (3)$$

where the non-dimensional unbalance mass is given as $\tilde{U} = U/(m_r l_r)$.

3 Foil Domain

Various different foil structure models are available in the literature of which the majority are based on variations over the Simple Elastic Foundation Model (SEFM). The available models include purely algebraic equation systems (stiffness only), first order systems (including stiffness and damping) as well as full second order systems including also mass and possibly friction. In the current implementation, a format capable of containing all these variations is desirable. Therefore the foil structural model in a bearing α is represented using the non-dimensional foil DOF vector $\tilde{\mathbf{x}}_{f,\alpha}$ in the general state-space residual format as

$$\underbrace{\begin{bmatrix} \mathbf{0} & \tilde{\mathbf{M}}_f \\ \mathbf{I} & \mathbf{0} \end{bmatrix}}_{\mathbf{A}_f} \underbrace{\begin{Bmatrix} \dot{\tilde{\mathbf{x}}}_{f,\alpha} \\ \tilde{\mathbf{x}}_{f,\alpha} \end{Bmatrix}}_{\dot{\mathbf{z}}_{f,\alpha}} + \underbrace{\begin{bmatrix} \tilde{\mathbf{K}}_f & \tilde{\mathbf{C}}_f \\ \mathbf{0} & -\mathbf{I} \end{bmatrix}}_{\mathbf{B}_f} \underbrace{\begin{Bmatrix} \tilde{\mathbf{x}}_{f,\alpha} \\ \dot{\tilde{\mathbf{x}}}_{f,\alpha} \end{Bmatrix}}_{\mathbf{z}_{f,\alpha}} + \underbrace{\begin{bmatrix} \mathbf{I} \\ \mathbf{0} \end{bmatrix}}_{\mathbf{T}_f} (\tilde{\mathbf{f}}_{fw,\alpha} + \tilde{\mathbf{f}}_{p,\alpha} + \tilde{\mathbf{f}}_{\mu,\alpha}) = \mathbf{r}_{f,\alpha}, \quad (4)$$

which is suitable for the most general class of foil models. The non-dimensional foil structure mass, damping and stiffness matrices are given as $\tilde{\mathbf{M}}_f$, $\tilde{\mathbf{D}}_f$, $\tilde{\mathbf{K}}_f$ respectively, while the static loads are represented in $\tilde{\mathbf{f}}_{fw,\alpha}$, the fluid film pressure loads are contained in $\tilde{\mathbf{f}}_{p,\alpha}$ and the friction forces (if any) are held by $\tilde{\mathbf{f}}_{\mu,\alpha}$. For a non-zero mass matrix, this represents a system of Ordinary Differential Equations (ODEs), but for many models, such as the widely applied case of an inertialess SEFM incorporating a structural loss factor, eq. (4) turns into a system of Differential/Algebraic Equations (DAEs). If friction forces are not included, the DAE structure could still be used directly as discussed in [20], but this is unnecessarily complicated. Instead, the implementation also supports a decayed version of eq. (4) given simply as

$$\underbrace{\tilde{\mathbf{C}}_f}_{\mathbf{A}_f} \underbrace{\dot{\tilde{\mathbf{x}}}_{f,\alpha}}_{\dot{\mathbf{z}}_{f,\alpha}} + \underbrace{\tilde{\mathbf{K}}_f}_{\mathbf{B}_f} \underbrace{\tilde{\mathbf{x}}_{f,\alpha}}_{\mathbf{z}_{f,\alpha}} + \underbrace{\mathbf{I}}_{\mathbf{T}_f} (\tilde{\mathbf{f}}_{fw,\alpha} + \tilde{\mathbf{f}}_{p,\alpha}) = \mathbf{r}_{f,\alpha}, \quad (5)$$

representing a system of first order ODEs for non-zero damping matrices or an algebraic equation system in the case of zero damping. As for the rotor domain equations, all quantities in the foil domain are non-dimensionalized. This is achieved using the characteristic frequency ω_τ , a foil domain length scale l_f and a foil domain pressure scale p_f . For an SEFM-like model, the obvious choices for these would be the clearance and ambient pressure, but for more complex models other scales might be advantageous.

4 Fluid Film Domain

To model the gas film separating the journal from the rigid or compliant surfaces of the bearing, we will apply the Modified Reynolds Equation (MRE) under the assumption of isothermal, isoviscous conditions. The compressibility is introduced by assuming ideal gas behaviour providing the relation for the gas density ρ_g

$$\rho_g = \frac{M_g}{R_u T_{\text{iso}}} p, \quad (6)$$

where M_g , R_u and T_{iso} are the (average) molar mass of the gas, the universal gas constant and the isothermal gas temperature, respectively. A natural extension would be to drop the assumption of isothermal conditions and simultaneously solve the energy equation. This has been done for rigid gas bearings, at least using non-simultaneous approaches [16], but for foil bearings the thermal BCs are less clearly defined. The maximum temperature differences in the circumferential and axial directions were found experimentally by Żywica et al.

[23] for a specific GFB to be approximately 35 °C and 2 °C, respectively. This would imply density variations on the order of $\pm 5\%$, which is not considered sufficient to justify the inclusion of the energy equation. If this was nevertheless to be attempted, experimental validation of the resulting temperature field would be necessary to adjust the applied thermal BCs.

4.1 The Modified Reynolds Equation in Terms of Flows

To formulate a discretization scheme for the MRE, it is convenient to consider the underlying velocity profiles. Expressing the journal surface velocity as $u_\theta(x_g = 0) = \Omega R$ and assuming the pressure and viscosity to be constant across the film thickness h , the velocity profiles can be derived from the Navier–Stokes equations using an order of magnitude analysis followed by an integration across the film thickness [7] as

$$\mathbf{u}_g = \{u_\theta \ u_z\}^T = \left\{ -x_g \frac{h-x_g}{2\mu} \frac{\partial p}{\partial y_g} + \Omega R \frac{h-x_g}{h} \quad -x_g \frac{h-x_g}{2\mu} \frac{\partial p}{\partial z_g} \right\}^T, \quad (7)$$

giving the in–film fluid velocities in m/s as functions of the pressure gradients and the journal surface velocity. Note that the axial velocity of the journal is neglected leaving only the Poiseuille component in this direction.

The MRE can be obtained by inserting the velocity profiles into the continuity equation augmented with a source term to represent injection and integrating it across the film thickness as

$$\int_0^h \left(\frac{\partial \rho_g}{\partial t} + \nabla \cdot (\rho_g \mathbf{u}_g) \right) dx_g = m_{\text{inj}}, \quad (8)$$

where ρ_g is the fluid density and $m_{\text{inj}} = m_{\text{inj}}(y_g, z_g)$ represents an injection source term field in $\text{kg}/(\text{m}^2 \text{s})$. The inflow due to injection could be obtained using analytical expressions, possibly including empirical correction factors, as suggested by various authors [1, 14, 17, 21] or by an external Computational Fluid Dynamics (CFD) routine, but this is outside the present scope.

Replacing the fluid density by its average across the film thickness and applying Leibniz’ rule, eq. (8) produces the MRE on the form

$$-\frac{\partial}{\partial y_g} \left(\frac{\rho_g h^3}{12\mu} \frac{\partial p}{\partial y_g} \right) - \frac{\partial}{\partial z_g} \left(\frac{\rho_g h^3}{12\mu} \frac{\partial p}{\partial z_g} \right) + \frac{\omega R}{2} \frac{\partial \rho_g h}{\partial y_g} + \frac{\partial (\rho_g h)}{\partial t} = m_{\text{inj}}, \quad (9)$$

which can alternatively be expressed in terms of the flow vector \mathbf{q}_g with units $\text{kg}/(\text{m s})$ [3] as

$$\nabla \cdot \mathbf{q}_g = -\frac{\partial (\rho_g h)}{\partial t} + m_{\text{inj}} \quad \text{where} \quad \mathbf{q}_g = \{q_\theta \ q_z\}^T = -\frac{\rho_g h^3}{12\mu} \nabla p + \frac{\Omega R}{2} \rho_g h \{1 \ 0\}^T. \quad (10)$$

Equation (10) can be non-dimensionalised using the clearance C and radius R as through-film and in-film length scales respectively, the ambient pressure p_a as the pressure scale and a frequency ω_τ as time scale. Assuming isothermal conditions in the fluid film, the viscosity can be assumed constant and the gas density can be expressed using the ideal gas law. This gives the version of the MRE implemented in the model

$$\nabla \cdot \tilde{\mathbf{q}}_g = -2S_\tau \frac{\partial (\tilde{p}\tilde{h})}{\partial \tau} + \tilde{m}_{\text{inj}}, \quad (11)$$

where

$$S_\tau = \frac{6R^2 \mu \omega_\tau}{C^2 p_a}, \quad \tilde{\mathbf{q}}_g = \{\tilde{q}_\theta \ \tilde{q}_z\}^T = \left(-\tilde{p}\tilde{h}^3 \nabla \tilde{p} + S_\tau \tilde{\Omega} \tilde{p}\tilde{h} \{1 \ 0\}^T \right) \quad \text{and} \quad \tilde{m}_{\text{inj}} = \frac{12R^2 \mu R_u T_{\text{iso}}}{p_a^2 C^3 M_g} m_{\text{inj}}. \quad (12)$$

Notice that before eq. (11) is non-dimensionalised, insertion of the ideal gas law and multiplication by $R_u T_{\text{iso}}/M_g$ changes its units into $\text{J}/(\text{m}^2 \text{s})$, such that the conserved quantity is rather energy than mass. Subsequently, the equation is divided by the viscosity μ resulting in the rather awkward unit $\text{J Pa s}/(\text{m}^2 \text{s})$ or N^2/m^3 .

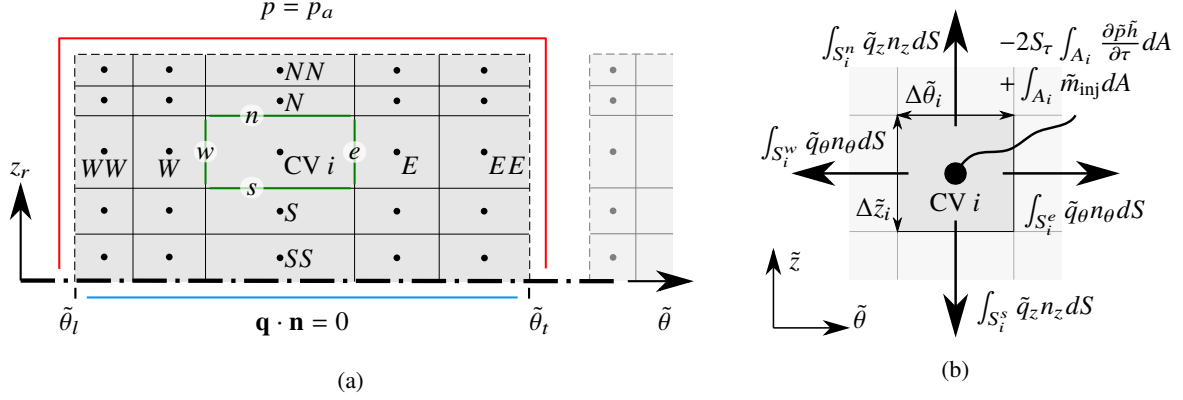


Figure 2: The fluid film discretization. (a): Mesh of a single pad showing the BCs and the naming convention for the neighbours and faces of the i -th CV. (b): Contributions to the integrated conservation equation for the i -th CV.

4.2 Finite Volume Discretization

Having the MRE represented in terms of flows as given in eq. (11), the Finite Volume (FV) method can be applied and implemented following an intuitive approach. Equation (11) represents the differential form of the conservation equation which can be integrated over a Control Volume (CV) i with in-film area A_i and circumference S_i . Applying the divergence theorem, this can be written as

$$\int_{S_i} \tilde{\mathbf{q}}_g \cdot \mathbf{n} dS = -2S_\tau \iint_{A_i} \frac{\partial}{\partial \tau} (\tilde{p}\tilde{h}) dA + \iint_{A_i} \tilde{m}_{inj} dA, \quad (13)$$

where the three terms represent the flux across the CV boundary to the neighbouring cells, the accumulation within the CV and the injection influx, respectively. Limiting the implementation to rectilinear non-uniform grids, i.e. grids of quadrilateral CVs, the integral over the CV circumference in eq. (13) can be split into four components as illustrated in fig. 2b. Representing the flow $\tilde{\mathbf{q}}_g$ at each face by its midface value and the unsteady term $\frac{\partial}{\partial \tau} (\tilde{p}\tilde{h})$ by its cell centre value (both being second order approximations), the FV residual equation for the i -th CV can be written as

$$\Delta\tilde{z}_i (\tilde{q}_\theta|_e - \tilde{q}_\theta|_w) + \Delta\tilde{\theta}_i (\tilde{q}_z|_n - \tilde{q}_z|_s) + 2S_\tau \Delta\tilde{z}_i \Delta\tilde{\theta}_i \left(\tilde{p}_i \frac{\partial \tilde{h}_i}{\partial \tau} + \tilde{h}_i \frac{\partial \tilde{p}_i}{\partial \tau} \right) - \tilde{M}_{inj,i} = r_{FV,i}, \quad (14)$$

where $\Delta\tilde{\theta}_i$, $\Delta\tilde{z}_i$ are the CV dimensions, \tilde{p}_i , \tilde{h}_i are the CV centre pressure and film height and \tilde{q}_θ , \tilde{q}_z are the flow components evaluated at the midpoint of the respective CV faces as indicated in fig. 2a. For now, the integrated value of the injection flux over the cell area is denoted simply as $\tilde{M}_{inj,i}$ since its treatment depends on the applied injection model.

4.3 Cell Face Fluxes

To evaluate eq. (14), the components of the flow must be known at the CV faces. These are given from eq. (12) and hence depend on the face pressure, face pressure gradient and face film height. The gradient at the midpoint of each face is reconstructed using linear interpolation between the centres of the two CVs sharing the face following a Central Differencing Scheme (CDS). This approximation is of second order on a uniform mesh, but formally decays to first order for a non-uniform mesh. For reasonable grid expansion rates it will, however, still produce convergence characteristics close to that of a second order scheme [5]. Referring to fig. 2a, the gradient at the eastern face is thus reconstructed using the CV centre values i and E . If formal second order accuracy was requested, one could apply the "Quadratic Upstream Interpolation for Convective Kinematics" scheme or a fourth-order CDS using three or four cell centres, respectively.

The face pressure values could likewise be reconstructed using CDS to provide a second order accurate approximation. It is, however, argued by Arghir et al. [1] that these "convected pressures" should be treated using an upwind procedure to stabilize the numerical solution. The approach presented in [1] is intended for unstructured grids where the implementation of higher order upwind schemes is complicated, thus the Upwind Differencing Scheme (UDS) relying on a single upstream cell is used. The current work is limited to structured grids where

it is straightforward to include an additional upwind cell in the stencil to produce the Linear Upwind Differencing Scheme (LUDES). This provides second order accuracy for the face pressure, but has the potential to produce unbounded solutions when used without limiters.

Considering the structure of the resulting equation system, the combination of CDS for face pressure gradients and UDS for face pressure values gives a computational molecule for each cell with five contributions: the cell itself and its four immediate neighbours E , N , W and S . Using LUDES for the face pressures, four additional contributions from the next set of neighbours EE , NN , WW and SS should furthermore be included.

Prior to applying any of the upwind schemes, the flow direction at the given face must be evaluated. Noting that the pressure is always positive, the sign of the flow vector components can be judged from eq. (12) as

$$\text{sign}(\tilde{q}_\theta) = \text{sign}\left(-\tilde{h}^3 \frac{\partial \tilde{p}}{\partial \tilde{\theta}} + S_\tau \tilde{\Omega} \tilde{h}\right) \quad \text{and} \quad \text{sign}(\tilde{q}_z) = \text{sign}\left(-\tilde{h}^3 \frac{\partial \tilde{p}}{\partial \tilde{z}}\right), \quad (15)$$

where the CDS approximations for the pressure gradients are used while the film height at the face is supplied by the rotor and foil models. Knowing the sign of the flow, the face pressure itself can be reconstructed using cell centres in the upwind direction only.

At the outer boundaries where ambient pressure is prescribed (see fig. 2a), corresponding to a Dirichlet type Boundary Condition (BC), only the face gradient needs reconstruction. This is achieved using a one-sided FD scheme relying on two CV centres into the mesh. If a symmetry condition is imposed at the bearing mid plane, corresponding to a Neumann type BC, the flux at these faces should simply be set to zero. Both types of BCs are used if the LUDES is requested to reconstruct face pressures too close to a boundary for two upstream CV centres to be available.

Lastly, the model implements a cyclic condition which is physically meaningful for rigid and single-pad foil bearings. In this case, the cyclic boundary face fluxes are reconstructed exactly as for the internal faces using the corresponding CVs from the opposite end of the mesh.

4.4 Finite Volume Residual Equation

Using the FD schemes described in the preceding section to evaluate the fluxes across each CV face and plugging these into eq. (14), one obtains a residual equation on the form

$$\sum_{\xi \in \Xi} a_j \tilde{p}_j + 2S_\tau \Delta \tilde{z}_i \Delta \tilde{\theta}_i \left(\tilde{p}_i \dot{\tilde{h}}_i + \tilde{h}_i \dot{\tilde{p}}_i \right) - \tilde{M}_{\text{inj},i} = r_{\text{FV},i}, \quad (16)$$

where Ξ is the set of stencil members making up the computational molecule, e.g. $\Xi = \{i, E, N, W, S\}$ for the case of a CDS+UDS combination. The stencil coefficients a_j depend on the present pressure values across the stencil, the current film heights at the cell faces and the dimensions of the cell. In a steady-state simulation, the cell centre temporal pressure derivative $\dot{\tilde{p}}_i$ is zero, while it is directly available in a time integration. The film heights at the cell centre and faces as well as the temporal derivative at the cell centre $\dot{\tilde{h}}_i$ are given from the rotor and foil domains.

For a bearing α discretized using n_{cv} CVs, the pressure state vector holding all CV centre pressures can be written

$$\mathbf{p}_\alpha = \{\tilde{p}_1, \dots, \tilde{p}_{n_{\text{cv}}}\}^T, \quad (17)$$

using which the FV residual vector can be assembled for the entire bearing as

$$\underbrace{\mathbf{A}_{\text{FV}}(\mathbf{p}_\alpha, \mathbf{x}_r, \mathbf{x}_{f,\alpha}) \mathbf{p}_\alpha}_{\sum_{\xi \in \Xi} a_j \tilde{p}_j} + \underbrace{\mathbf{B}_{\text{FV}}(\dot{\mathbf{x}}_r, \dot{\mathbf{x}}_{f,\alpha}) \mathbf{p}_\alpha}_{2S_\tau \Delta \tilde{z}_i \Delta \tilde{\theta}_i \dot{\tilde{h}}_i \tilde{p}_i} + \underbrace{\mathbf{C}_{\text{FV}}(\mathbf{x}_r, \mathbf{x}_{f,\alpha}) \dot{\mathbf{p}}_\alpha}_{2S_\tau \Delta \tilde{z}_i \Delta \tilde{\theta}_i \tilde{h}_i \dot{\tilde{p}}_i} + \underbrace{\mathbf{f}_{\text{FV}}}_{\tilde{M}_{\text{inj},i}} = \mathbf{r}_{\text{FV},\alpha}, \quad (18)$$

where \mathbf{A}_{FV} holds the FV coefficients originating from the Couette and Poiseuille terms of the MRE, while the coefficients in \mathbf{B}_{FV} and \mathbf{C}_{FV} represent the squeeze and local expansion terms respectively. The injection contribution is represented by \mathbf{f}_{FV} which will generally depend on the bearing pressure and possibly variables from the rotor and fluid domains.

5 Domain Interfaces

To evaluate the FV residuals from eq. (16), the film height \tilde{h} is required at all CV edges and centres. This contains three contributions: (a) a constant describing the initial geometry such as clearance and pad inlet slopes; (b) a rigid contribution stemming from the movement of the rotor; and (c) the compliant contribution due to deformation of the foil structure (if simulating a compliant bearing).

Recalling the rigid contributions to be given merely as trigonometric projections of the eccentricity components, written usually like $e_x \cos \theta + e_y \sin \theta$, this can be represented as a constant linear mapping applied to the rotor DOF vector $\tilde{\mathbf{x}}_r$. Collecting the rigid film heights from all CV centres and edges across all bearings in the vectors $\mathbf{h}_{r,\text{cvc}}$ and $\mathbf{h}_{r,\text{cve}}$ respectively, these can be calculated as

$$\mathbf{h}_{r,\text{cvc}} = \mathbf{H}_{\text{cvc},r} \tilde{\mathbf{x}}_r \quad \text{and} \quad \mathbf{h}_{r,\text{cve}} = \mathbf{H}_{\text{cve},r} \tilde{\mathbf{x}}_r, \quad (19)$$

where the mapping matrices can be assembled offline knowing: (a) the angular positions of the CV centres/edges; (b) the indices of the rotor DOFs representing the eccentricity components in each bearing; and (c) the length scaling between the two domains. The row dimensions correspond to the combined number of CV centres/edges across all bearings while the column dimensions equal the number of rotor DOFs n_{rdof} , but only $2n_b$ columns will contain non-zero elements.

Analogously to the rigid contributions in eq. (19), the compliant film heights at all CV centres and edges can be represented as constant linear mappings from the foil DOF vectors $\tilde{\mathbf{x}}_{f,\alpha}$. This can be written as the linear combinations

$$\mathbf{h}_{c,\text{cvc}} = \mathbf{H}_{\text{cvc},f} \left\{ \tilde{\mathbf{x}}_{f,1}^T \dots \tilde{\mathbf{x}}_{f,n_b}^T \right\}^T \quad \text{and} \quad \mathbf{h}_{c,\text{cve}} = \mathbf{H}_{\text{cve},f} \left\{ \tilde{\mathbf{x}}_{f,1}^T \dots \tilde{\mathbf{x}}_{f,n_b}^T \right\}^T \quad (20)$$

but the content of the mapping matrices will be dependent on the applied foil model. The currently implemented SEFM places one foil node for each circumferential CV centre position. In this case, $\mathbf{H}_{\text{cvc},f}$ maps each foil DOF directly to all CV centres sharing the same circumferential position and applies a length scaling. The mapping to CV edges $\mathbf{H}_{\text{cve},f}$, on the contrary, will furthermore contain FD coefficients interpolating from the foil DOFs locations to the CV edges. Having prebuild the mapping matrices and the constant contribution vectors $\mathbf{h}_{0,\text{cvc}}$ and $\mathbf{h}_{0,\text{cve}}$, the film heights can hence be found at runtime simply as

$$\mathbf{h}_{\text{cvc}} = \mathbf{h}_{0,\text{cvc}} + \mathbf{H}_{\text{cvc},r} \tilde{\mathbf{x}}_r + \mathbf{H}_{\text{cvc},f} \left\{ \tilde{\mathbf{x}}_{f,1}^T \dots \tilde{\mathbf{x}}_{f,n_b}^T \right\}^T \quad \text{and} \quad \mathbf{h}_{\text{cve}} = \mathbf{h}_{0,\text{cve}} + \mathbf{H}_{\text{cve},r} \tilde{\mathbf{x}}_r + \mathbf{H}_{\text{cve},f} \left\{ \tilde{\mathbf{x}}_{f,1}^T \dots \tilde{\mathbf{x}}_{f,n_b}^T \right\}^T. \quad (21)$$

To evaluate the rotor residual from eq. (1), the bearing forces must be obtained by integration of the pressure as given in eq. (2). For a single bearing, this is evaluated numerically by summing the projected force contributions from all CVs as

$$\begin{Bmatrix} \tilde{f}_{b,x} \\ \tilde{f}_{b,y} \end{Bmatrix} = \frac{p_a R^2}{l_r m_r \omega_r^2} \sum_i^{n_{\text{cv}}} \Delta \tilde{\theta}_i \Delta \tilde{z}_i (\tilde{p}_i - 1) \begin{Bmatrix} \cos \theta_{\text{cvc},i} \\ \sin \theta_{\text{cvc},i} \end{Bmatrix}, \quad (22)$$

where \tilde{p}_i and $\theta_{\text{cvc},i}$ are the the i -th CV centre pressure and circumferential position respectively, while $\frac{p_a R^2}{l_r m_r \omega_r^2}$ is the inter-domain force scaling. Notice that eq. (22) effectively applies the midpoint rule within each CV, but a higher order numerical integration scheme could likewise have been applied. This would require the trigonometric functions to be sampled and the pressure value to be reconstructed using FD at a number of locations within each CV, thus making the force contribution from each CV dependent also on the neighbouring cells. Regardless of the integration scheme applied within each CV, the scaling, integration and summation can be represented using a constant linear mapping

$$\mathbf{T}_r \tilde{\mathbf{f}}_b = \mathbf{H}_{\tilde{f}_b,p} \left\{ \mathbf{p}_1^T - 1, \dots, \mathbf{p}_{n_b}^T - 1 \right\}^T, \quad (23)$$

calculating the state-space sized bearing force vector as a single matrix–vector product. $\mathbf{H}_{\tilde{f}_b,p}$ has row dimension equal to the rotor state-space, i.e. $2n_{\text{rdof}}$, and column dimension matching the combined number of CVs across all

bearings, i.e. $n_b n_{cv}$. Generally, each bearing will give rise to two bearing force components, meaning that $\mathbf{H}_{f_b,p}$ will contain $2n_b n_{cv}$ non-zero elements. For GFBs it is common to apply the Gmbel condition such that sub-ambient pressures are discarded during the integration. In this case, $\mathbf{H}_{f_b,p}$ becomes non-constant as the columns corresponding to CVs with sub-ambient pressures should be zeroed. In practice, this is achieved by prebuilding the full non-Gmbel $\mathbf{H}_{f_b,p}$ and continuously restoring a copy of this before zeroing out the sub-ambient columns.

Lastly, the pressure forces on the foil structure should be integrated to calculate $\tilde{\mathbf{f}}_{p,\alpha}$ in eq. (4) or eq. (5). For each bearing α , this can be achieved analogously to the bearing force integration in eq. (23) using a constant linear mapping as

$$\mathbf{T}_f \tilde{\mathbf{f}}_{p,\alpha} = \mathbf{H}_{f_p,p} \mathbf{p}_\alpha, \quad (24)$$

where the exact content of $\mathbf{H}_{f_p,p}$ depends on the foil model. For the currently implemented SEFM, the mapping will simply calculate the average pressure at each circumferential position multiplied by the surface area ascribed to each foil DOF and the inter-domain force scaling $\frac{p_a R^2}{\rho_f l_f^2}$. The row dimension should match the number of foil states while the column dimension is n_{cv} , but the number of non-zero elements depends on the foil model.

The mapping matrices introduced in this section usually have sparse structures and are used mostly for calculating matrix–vector products. They are hence build and stored in Compressed Sparse Row (CSR) format to lower the storage requirements and provide efficient matrix–vector products.

6 System Assembly

For a rotor–bearing system comprising n_b GFBs, the coupled state-space and residual vectors are defined as

$$\mathbf{z} = \left\{ \mathbf{p}_1^T \cdots \mathbf{p}_{n_b}^T \mid \mathbf{z}_{f,1}^T \cdots \mathbf{z}_{f,n_b}^T \mid \tilde{\mathbf{x}}_r^T \dot{\tilde{\mathbf{x}}}_r^T \right\}^T \quad \text{and} \quad \mathbf{r} = \left\{ \mathbf{r}_{FV,1}^T \cdots \mathbf{r}_{FV,n_b}^T \mid \mathbf{r}_{f,1}^T \cdots \mathbf{r}_{f,n_b}^T \mid \mathbf{r}_r^T \right\}^T \quad (25)$$

using which the global non-linear system of equations can be written on fully implicit form like

$$\mathbf{f}_G(\tau, \mathbf{z}, \dot{\mathbf{z}}) = \mathbf{f}_{G,t}(\tau, \mathbf{z}, \dot{\mathbf{z}}) + \mathbf{f}_{G,s}(\mathbf{z}) + \mathbf{f}_{G,0} = \mathbf{r}, \quad (26)$$

with a global residual function $\mathbf{f}_G(\tau, \mathbf{z}, \dot{\mathbf{z}})$ which can be partitioned into its transient, steady and constant components $\mathbf{f}_{G,t}(\tau, \mathbf{z}, \dot{\mathbf{z}})$, $\mathbf{f}_{G,s}(\mathbf{z})$ and $\mathbf{f}_{G,0}$ respectively. The main advantage of this partitioning is to clearly separate out all time dependent terms such that $\mathbf{f}_{G,t}(\tau, \mathbf{z}, \dot{\mathbf{z}}) = \mathbf{0}$ at steady-state, thus allowing the exact same implementation of $\mathbf{f}_{G,s}(\mathbf{z})$ and $\mathbf{f}_{G,0}$ to be used for steady-state solutions as well as in time integrations.

It is common to treat IVPs for ODE systems on explicit first order form where a system function evaluates the temporal derivative of the state vector directly. In the current model, the fluid film FV equations could have been formulated explicitly in terms of the alternative variable $\psi = \tilde{p}\tilde{h}$, if this had been substituted into eq. (11) as demonstrated by Bonello and Pham [2]. For many cases, explicit forms of the rotor and foil equations could likewise have been obtained by inverting \mathbf{A}_r and \mathbf{A}_f in eqs. (1), (4) and (5). In the GFB models by Larsen and Santos [10] and Gu et al. [6], the global systems are formulated on linearly implicit form where the product of a ”mass” matrix and the state vector derivative is provided by the system function. In [10], this matrix is constant such that the system can be solved on explicit form by evaluating and inverting it, while a dedicated solver for the linearly implicit form is used in [6] where the ”mass” matrix is state dependent. In the present work, the fully implicit form is maintained for several reasons. It allows the implementation to span the largest possibly variety of foil structure models, including those resulting in a DAE system. Any explicit matrix inversions can be avoided and the use of only physically meaningful variables simplifies the implementation of BCs as well as the interpretation of errors and intermediate results. Furthermore, it is an advantage when it comes to friction models that the variable $\dot{\mathbf{z}}$ is available when evaluating the residual. The disadvantages of using the fully implicit form are mainly the added complexity of defining consistent Initial Conditions (ICs) and a smaller selection of available time integrators.

Assembling the contributions from the three domains, the global equation system can be written on the fully

implicit format of eq. (26) as

$$\underbrace{\begin{pmatrix} \mathbf{B}_{\text{FV}}(\tilde{\mathbf{x}}_r, \tilde{\mathbf{x}}_{f,1}) \mathbf{p}_1 + \mathbf{C}_{\text{FV}}(\tilde{\mathbf{x}}_r, \tilde{\mathbf{x}}_{f,1}) \dot{\mathbf{p}}_1 \\ \vdots \\ \mathbf{B}_{\text{FV}}(\tilde{\mathbf{x}}_r, \tilde{\mathbf{x}}_{f,n_b}) \mathbf{p}_{n_b} + \mathbf{C}_{\text{FV}}(\tilde{\mathbf{x}}_r, \tilde{\mathbf{x}}_{f,n_b}) \dot{\mathbf{p}}_{n_b} \\ \hline \mathbf{A}_f \dot{\mathbf{z}}_{f,1} + \mathbf{T}_f \tilde{\mathbf{f}}_\mu(\mathbf{p}_1, \mathbf{z}_{f,1}) \\ \vdots \\ \mathbf{A}_f \dot{\mathbf{z}}_{f,n_b} + \mathbf{T}_f \tilde{\mathbf{f}}_\mu(\mathbf{p}_{n_b}, \mathbf{z}_{f,n_b}) \\ \hline \mathbf{A}_r \dot{\mathbf{z}}_r + \mathbf{T}_r \tilde{\mathbf{f}}_{\text{ub}}(\tau) \end{pmatrix}}_{\mathbf{f}_{G,t}(\tau, \mathbf{z}, \dot{\mathbf{z}})} + \underbrace{\begin{pmatrix} \mathbf{A}_{\text{FV}}(\mathbf{p}_1, \tilde{\mathbf{x}}_r, \tilde{\mathbf{x}}_{f,1}) \mathbf{p}_1 \\ \vdots \\ \mathbf{A}_{\text{FV}}(\mathbf{p}_{n_b}, \tilde{\mathbf{x}}_r, \tilde{\mathbf{x}}_{f,n_b}) \mathbf{p}_{n_b} \\ \hline \mathbf{B}_f \mathbf{z}_{f,1} + \mathbf{T}_f \tilde{\mathbf{f}}_p(\mathbf{p}_1) \\ \vdots \\ \mathbf{B}_f \mathbf{z}_{f,n_b} + \mathbf{T}_f \tilde{\mathbf{f}}_p(\mathbf{p}_{n_b}) \\ \hline (\mathbf{B}_r + \tilde{\Omega} \mathbf{C}_r) \mathbf{z}_r + \mathbf{T}_r \tilde{\mathbf{f}}_b(\mathbf{p}_1, \dots, \mathbf{p}_{n_b}) \end{pmatrix}}_{\mathbf{f}_{G,s}(\mathbf{z})} + \underbrace{\begin{pmatrix} \mathbf{f}_{\text{FV},1} \\ \vdots \\ \mathbf{f}_{\text{FV},n_b} \\ \hline \mathbf{T}_f \tilde{\mathbf{f}}_{fw,1} \\ \vdots \\ \mathbf{T}_f \tilde{\mathbf{f}}_{fw,n_b} \\ \hline \mathbf{T}_r \tilde{\mathbf{f}}_{rw} \end{pmatrix}}_{\mathbf{f}_{G,0}} = \mathbf{r}, \quad (27)$$

where the upper rows represent the non-linear FV equations governing the fluid film while the midmost rows can either be left out (to model a rigid bearing) or represent a linear/non-linear foil structure. The lowermost rows hold the rotor model. Notice that the injection contributions, if any, are currently located in the constant part $\mathbf{f}_{G,0}$, while most injection models would be state dependent and hence should be relocated to the non-constant parts.

Depending on the system size, ranging potentially from a few hundred to tens of thousands of states, and the system stiffness, it is advantageous or downright necessary to formulate analytical expressions for the Jacobian matrices. This is the case for steady-state solutions, but particularly when integrating in time. For the steady-state case where $\mathbf{f}_{G,t}(\tau, \mathbf{z}, \dot{\mathbf{z}}) = \mathbf{0}$, the Jacobian with respect to the state vector \mathbf{z} is given as

$$\mathbf{J}_{\mathbf{z},s} = \frac{\partial \mathbf{f}_{G,s}}{\partial \mathbf{z}} = \begin{bmatrix} \frac{\partial \mathbf{A}_{\text{FV}} \mathbf{p}_1}{\partial \mathbf{p}_1} \dots \mathbf{0} & \frac{\partial \mathbf{A}_{\text{FV}} \mathbf{p}_1}{\partial \mathbf{z}_{f,1}} \dots \mathbf{0} & \frac{\partial \mathbf{A}_{\text{FV}} \mathbf{p}_1}{\partial \tilde{\mathbf{x}}_r} \mathbf{0} \\ \vdots \ddots \vdots & \vdots \ddots \vdots & \vdots \vdots \\ \mathbf{0} \dots \frac{\partial \mathbf{A}_{\text{FV}} \mathbf{p}_{n_b}}{\partial \mathbf{p}_{n_b}} & \mathbf{0} \dots \frac{\partial \mathbf{A}_{\text{FV}} \mathbf{p}_{n_b}}{\partial \mathbf{z}_{f,n_b}} & \frac{\partial \mathbf{A}_{\text{FV}} \mathbf{p}_{n_b}}{\partial \tilde{\mathbf{x}}_r} \mathbf{0} \\ \hline \mathbf{H}_{f,p} \dots \mathbf{0} & \mathbf{B}_f \dots \mathbf{0} & \\ \vdots \ddots \vdots & \vdots \ddots \vdots & \mathbf{0} \\ \mathbf{0} \dots \mathbf{H}_{f,p} & \mathbf{0} \dots \mathbf{B}_f & \\ \hline \mathbf{H}_{f,b,p} & \mathbf{0} & \mathbf{B}_r + \tilde{\Omega} \mathbf{C}_r \end{bmatrix}. \quad (28)$$

The upper left and midmost blocks reflect the changes in FV residuals within each bearing as the pressure and foil deflection (governing the compliant film height) vary within that same bearing. The upper right block gives the FV residual changes due to the rotor position (governing the rigid film height). These blocks are all state-dependent, i.e. non-constant. The blocks in the midmost rows are constant and represent the changes in foil residuals within each bearing due to changes in pressure and foil states within that same bearing. If a friction model was included, this would likely cause additional non-constant contribution to the left and midmost of these blocks. Notice that the foil residuals are not directly affected by the rotor states, which is physically meaningful since the rotor and foil domains are only coupled through the fluid film. The lower left block governs the change in rotor residuals due to pressure changes across all bearings. As discussed in relation to eq. (23), this block is pressure dependent if the Gumbel condition is applied, but constant if the full bearing surface is included in the pressure integration. The lower right block is constant and contains the rotor stiffness, damping and gyroscopic contributions governing the change in rotor residuals due to changes in rotor states. Again, the nature of the foil–rotor coupling is evident, as the rotor residuals are not directly affected by the foil states.

For the transient case, the Jacobian with respect to both the state vector and to its temporal derivative are necessary. The Jacobian with respect to \mathbf{z} is now the sum of $\mathbf{J}_{\mathbf{z},s} = \partial \mathbf{f}_{G,s} / \partial \mathbf{z}$ from eq. (28) and an additional

contribution $\partial \mathbf{f}_{G,t} / \partial \mathbf{z}$ given as

$$\frac{\partial \mathbf{f}_{G,t}}{\partial \mathbf{z}} = \begin{bmatrix} \mathbf{B}_{\text{FV}} \cdots \mathbf{0} & \frac{\partial \mathbf{C}_{\text{FV}} \mathbf{p}_1}{\partial \mathbf{z}_{f,1}} \cdots \mathbf{0} & \frac{\partial \mathbf{C}_{\text{FV}} \mathbf{p}_1}{\partial \bar{\mathbf{x}}_r} \mathbf{0} \\ \vdots \ddots \vdots & \vdots \ddots \vdots & \vdots \vdots \\ \mathbf{0} \cdots \mathbf{B}_{\text{FV}} & \mathbf{0} \cdots \frac{\partial \mathbf{C}_{\text{FV}} \mathbf{p}_{n_b}}{\partial \mathbf{z}_{f,n_b}} & \frac{\partial \mathbf{C}_{\text{FV}} \mathbf{p}_{n_b}}{\partial \bar{\mathbf{x}}_r} \mathbf{0} \\ \hline \mathbf{0} & \mathbf{0} & \mathbf{0} \\ \hline \mathbf{0} & \mathbf{0} & \mathbf{0} \end{bmatrix}, \quad (29)$$

which represents the additional pressure and film height dependencies originating from the local expansion and squeeze terms of the MRE. If a friction model was included, this would possibly give rise to additional contributions in this matrix. Since $\partial \mathbf{f}_{G,s} / \partial \dot{\mathbf{z}} = \mathbf{0}$ by definition, the Jacobian with respect to the temporal derivative of the state vector $\dot{\mathbf{z}}$ is given as

$$\mathbf{J}_{\dot{\mathbf{z}}} = \frac{\partial \mathbf{f}_{G,t}}{\partial \dot{\mathbf{z}}} = \begin{bmatrix} \mathbf{C}_{\text{FV}} \cdots \mathbf{0} & \frac{\partial \mathbf{B}_{\text{FV}} \mathbf{p}_1}{\partial \mathbf{z}_{f,1}} \cdots \mathbf{0} & \frac{\partial \mathbf{B}_{\text{FV}} \mathbf{p}_1}{\partial \bar{\mathbf{x}}_r} \mathbf{0} \\ \vdots \ddots \vdots & \vdots \ddots \vdots & \vdots \vdots \\ \mathbf{0} \cdots \mathbf{C}_{\text{FV}} & \mathbf{0} \cdots \frac{\partial \mathbf{B}_{\text{FV}} \mathbf{p}_{n_b}}{\partial \mathbf{z}_{f,n_b}} & \frac{\partial \mathbf{B}_{\text{FV}} \mathbf{p}_{n_b}}{\partial \bar{\mathbf{x}}_r} \mathbf{0} \\ \hline \mathbf{0} & \mathbf{A}_f \cdots \mathbf{0} & \mathbf{0} \\ \hline \mathbf{0} & \mathbf{0} \cdots \mathbf{A}_f & \mathbf{0} \\ \hline \mathbf{0} & \mathbf{0} & \mathbf{A}_r \end{bmatrix}, \quad (30)$$

where the FV residual derivatives in the uppermost blocks are, once again, stemming from the MRE's local expansion and squeeze terms. \mathbf{A}_f represents either foil inertia or damping depending on whether eq. (4) or eq. (5) is employed and \mathbf{A}_r holds the rotor inertia. Notice that the content of eq. (30) is decisive to the overall system structure. When $\mathbf{J}_{\dot{\mathbf{z}}}$ has full rank, the model is a system of ODEs, while a singular $\mathbf{J}_{\dot{\mathbf{z}}}$ implies a DAE system.

7 Steady-state and Transient Solution

The entire model is implemented in C where eq. (27) is solved in steady-state using the general purpose non-linear algebraic solver "KINSOL" and integrated in time using the ODE/DAE IVP solver "IDA". Both are readily available and part of the "SUNDIALS: SUite of Nonlinear and Differential/ALgebraic Equation Solvers" developed by the Lawrence Livermore National Laboratory [8]. In both cases, a Modified Newton iteration is employed to solve the non-linear equation systems using the Jacobian matrices given in eqs. (28) to (30). Like the mapping matrices, the Jacobians are constructed in the CSR format and the linear equation systems emerging from the Newton iterations are solved using sparse LU factorization provided by the KLU sparse solver library [4].

7.1 Ill-conditioning and Tolerances

Equation (27) presents a multi-domain problem, hence the numerical quantities involved will have varying orders of magnitude. To some extent, this can be alleviated using the scaling parameters within each domains, but the specification of meaningful solver tolerances still requires each equation to be assessed separately. Rotordynamics codes are often organized in a segregated fashion using an inner routine to solve for the pressure distribution (and related fields, such as temperature) while an independent outer routine searches for the rotor static equilibrium or steps the dynamic rotor equations forward in time. In these constructions, separate equation systems are solved for each domain and the solver tolerances should hence also be set separately. This can usually be achieved using scalar values as the variables/residuals within each domain are homogeneous. In the present model, all equations are solved simultaneously by a single solver, meaning that a vector of absolute tolerances must be supplied.

This is achieved by supplying global absolute force and length tolerances f_{tol} [N] and l_{tol} [m] which are then used to construct equivalent tolerances for each state and residual quantity involved. As an example, the fluid film state variables physically represent pressure with unit Pa. Assuming the absolute tolerances to be specified in the vicinity of 1 N and 1 m respectively, the corresponding relative tolerances can be added and multiplied by the

derived base value for the relevant quantity as

$$p_{\text{tol}} = \frac{1 \text{ N}}{(1 \text{ m})^2} \left(\frac{f_{\text{tol}}}{1 \text{ N}} + \frac{2l_{\text{tol}}}{1 \text{ m}} \right), \quad (31)$$

which for realistic values $f_{\text{tol}} = 1 \times 10^{-3} \text{ N}$ and $l_{\text{tol}} = 1 \times 10^{-8} \text{ m}$ is completely dominated by the force tolerance and gives $p_{\text{tol}} = 1.00002 \times 10^{-3} \text{ Pa}$. One could argue that other base values than 1 N and 1 m should be used, but for now this is utilized as a systematic way of producing tolerances across the equation system. This approach is beneficial since the tolerances on some quantities, such as the FV residual given in $\text{J Pa s}/(\text{m}^2 \text{ s}) = \text{N}^2/\text{m}^3$, are challenging to define based on physical intuition.

Collecting the system residual scaling factors implied by the non-dimensionalizations in the vector $\mathbf{r}_{\text{scale}}$ and the corresponding absolute tolerances derived as shown above in the vector \mathbf{r}_{tol} , the convergence criterion used for steady-state solutions can be written as

$$\|\text{diag}(\mathbf{r}_{\text{scale}}) \text{diag}(\mathbf{r}_{\text{tol}})^{-1} \mathbf{r}\|_{\infty} < 1, \quad (32)$$

where $\|\cdot\|_{\infty}$ denotes the infinity norm. When integrating in time using the IDA solver, the tolerances are set on the local truncation error as estimated by the integration routine within each time step [9]. This is done in a way similar to the well-known Matlab integrators using a vector of absolute tolerances and a scalar relative tolerance. The first is here calculated as $\text{diag}(\mathbf{r}_{\text{scale}})^{-1} \mathbf{r}_{\text{tol}}$ consistently to eq. (32), while the latter is set to around 1×10^{-6} .

8 Results

The current implementation has been validated against two previously presented codes treating rigid and compliant gas bearings respectively.

In the case of a rigid bearing, the midmost rows representing the foil structure in eqs. (25) and (27), along with the corresponding Jacobian rows and columns in eqs. (28) to (30), are simply left out. The same is the case for the compliant film height contribution in eq. (21). In this configuration, the code has been used to simulate the rotor–bearing system presented in [18]. This comprises a flexible rotor weighing approximately 4 kg modelled using FE which is supported by a ball bearing and a single rigid gas bearing. Placing an unbalance of 10 g mm at the disc, this system has been integrated in time to obtain the forced steady-state orbit at 5 kRPM. The same has been simulated using the code presented in [13] utilising an FD discretization of the fluid film, a reduced order rotor and an explicit time integration scheme. The resulting orbits are very similar, as it can be seen from the comparison in fig. 3a.

To validate the full model including a foil structure, the test rig presented in [10] has been simulated. This is composed of a rigid shaft with a mass of 21.1 kg supported by two identical three-pad GFBs. The SEFM is employed to model the foil structure under the assumption of an axially uniform displacement field. For the present code, this is implemented by locating foil nodes at each circumferential CV position and to incorporate the calculation of the average pressure at each of these locations in the pressure–foil mapping matrix from eq. (24).

Simulating in time at 15 kRPM with unbalances of 40 g mm and -2.5 g mm at the bearing locations, the forced steady-state orbits measured in the two bearings are obtained as shown in fig. 3b. These are compared to results from the code presented in [10], where a FE discretized fluid film is used, and the orbits are seen to agree well for both bearings.

9 Conclusions & Future Aspects

In the paper, a recipe for a simultaneously formulated model for simulation of rigid as well as compliant type gas bearings supporting a wide variety of rotor configurations has been treated. This has included the mathematical formulation as well as selected aspects of the numerical implementation.

Two main features of the presented model are the full coupling between the domains and the residual form of the system. For steady-state solutions, the presented formulation allows a single general purpose non-linear algebraic solver to be used while given full system knowledge through the Jacobian. This is not possible in the more common segregated solution approaches involving (at least) two independent solvers. For time integrations, the same formulation allows all state variables to be solved simultaneously in time using a general purpose IVP solver. The residual, or fully implicit, form of the equation system has numerical advantages as no explicit matrix

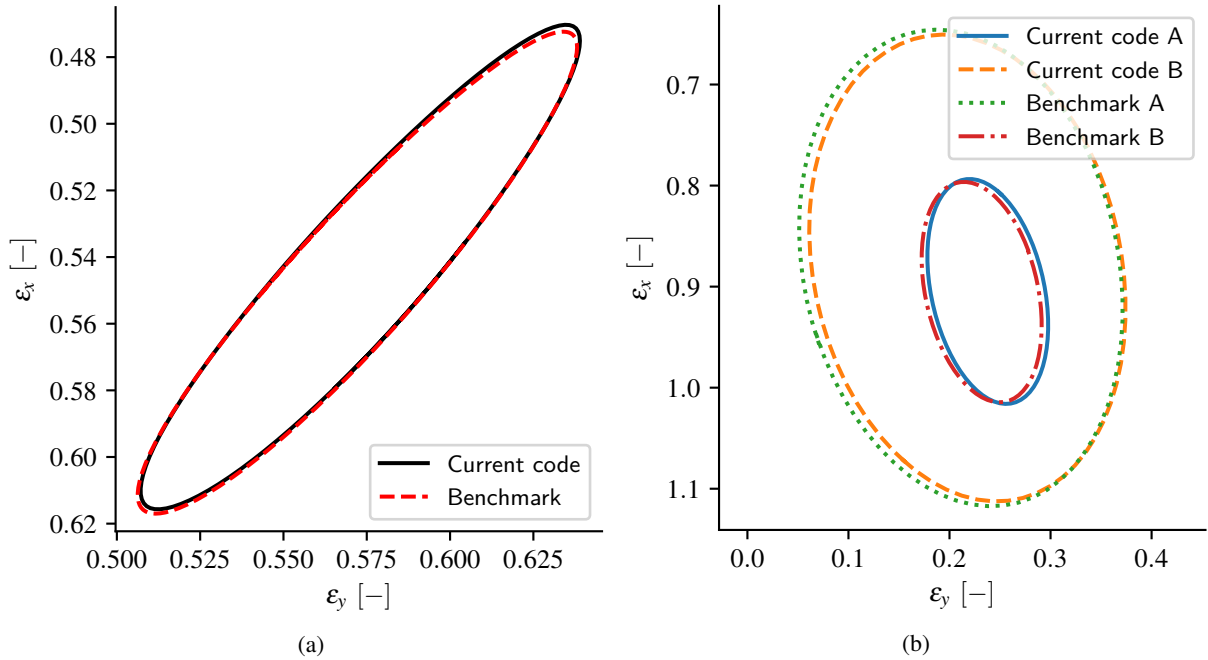


Figure 3: Time integrated unbalance driven steady-state orbits compared to benchmark codes: (a): Flexible rotor supported by a rigid gas bearing as described in [18] simulated as given in [13] at 5 kRPM with a 10 g mm unbalance at the disc. (b): Rigid rotor supported by two identical GFBs ("A" and "B") using the geometry and code described in [10] at 15 kRPM with 40 g mm and -2.5 g mm unbalances at the bearings.

inversions are necessary, but it is mainly chosen to allow a wider variety of foil models. Unfortunately, a limited number of IVP solvers are available for this form, and calculation of consistent ICs is required, something which is not generally necessary for explicitly formulated systems.

In the future, several extensions to the model should be made. One is the inclusion of reduced order rotors, e.g. through modal truncation, which will primarily require the left eigenvectors or similar to be included in the \mathbf{T}_r matrix of eq. (1). The resulting reduction in overall system size would usually be limited, as even the full rotor would most often require much fewer states than the fluid film, but removing the high frequency modes of a full FE rotor model would allow the IVP solver to take much larger time steps. Another interesting extension would be to include a bump foil model with frictional dissipation as described in [19], possibly coupled to a top foil as described in [15].

The original and main motivation for developing the presented model has been to prepare an efficient platform for research into GFBs with active radial injection. For rigid bearings, several analytical expressions are available in the literature, but the additional compliance–injection interaction in GFBs complicates the identification of the empirical correction factors, or "discharge coefficients", most often involved. This could possibly be circumvented by simultaneously solving a miniature CFD model for the injection zones, but this has not yet been proven feasible.

REFERENCES

- [1] Arghir, M., Le Lez, S. and Frene, J. [2006]. Finite-volume solution of the compressible Reynolds equation: linear and non-linear analysis of gas bearings, *Proc. Inst. Mech. Eng. Part J J. Eng. Tribol.* **220**(7): 617–627.
- [2] Bonello, P. and Pham, H. M. [2014]. The efficient computation of the nonlinear dynamic response of a foil-air bearing rotor system, *J. Sound Vib.* **333**(15): 3459–3478.
- [3] Crastan, V. and Devos, J. [1972]. Finite element solution of the three-dimensional flow problem and of reynold's equation for incompressible and compressible fluids, *Nucl. Eng. Des.* **22**(2): 225–232.
- [4] Davis, T. A. and Natarajan, E. P. [2010]. Algorithm 907, *ACM Trans. Math. Softw.* **37**(3): 1–17.
- [5] Ferziger, J. H. and Peric, M. [2002]. Computational methods for fluid dynamics, *Comput. Math. with Appl.* **46**(2-3): 503–504.
- [6] Gu, Y., Ma, Y. and Ren, G. [2017]. Stability and vibration characteristics of a rotor-gas foil bearings system with high-static-low-dynamic-stiffness supports, *J. Sound Vib.* .

- [7] Hamrock, B. J., Schmid, S. R. and Jacobson, B. O. [2004]. *Fundamentals of Fluid Film Lubrication*, 2 edn, Marcel Dekker.
- [8] Hindmarsh, A. C., Brown, P. N., Grant, K. E., Lee, S. L., Serban, R., Shumaker, D. E. and Woodward, C. S. [2005]. SUNDIALS: Suite of Nonlinear and differential/algebraic equation solvers, *ACM Trans. Math. Softw.* **31**(3): 363–396.
- [9] Hindmarsh, A. C., Serban, R. and Collier, A. [2018]. *User Documentation for ida v3.1.2*, ucrl-sm-20 edn, Center for Applied Scientific Computing Lawrence Livermore National Laboratory.
- [10] Larsen, J. S. and Santos, I. F. [2015]. On the nonlinear steady-state response of rigid rotors supported by air foil bearings Theory and experiments, *J. Sound Vib.* **346**: 284–297.
- [11] Le Lez, S., Arghir, M. and Frêne, J. [2009]. Nonlinear Numerical Prediction of Gas Foil Bearing Stability and Unbalanced Response, *J. Eng. Gas Turbines Power* **131**(1): 012503.
- [12] Leister, T., Baum, C. and Seemann, W. [2017]. On the Importance of Frictional Energy Dissipation in the Prevention of Undesirable Self-Excited Vibrations in Gas Foil Bearing Rotor Systems, *Tech. Mech.* **37**(2-5): 280–290.
- [13] Morosi, S. and Santos, I. F. [2011a]. Active lubrication applied to radial gas journal bearings. Part 1: Modeling, *Tribol. Int.* **44**(12): 1949–1958.
- [14] Morosi, S. and Santos, I. F. [2011b]. On the modelling of hybrid aerostatic-gas journal bearings, *J. Eng. Tribol.* **225**(7): 641–653.
- [15] Nielsen, B. B. and Santos, I. F. [2017]. Transient and steady state behaviour of elastoaerodynamic air foil bearings, considering bump foil compliance and top foil inertia and flexibility: A numerical investigation, *Proc. Inst. Mech. Eng. Part J J. Eng. Tribol.* **231**(10): 1235–1253.
- [16] Paulsen, B. T., Morosi, S. and Santos, I. F. [2011]. Static, Dynamic, and Thermal Properties of Compressible Fluid Film Journal Bearings, *Tribol. Trans.* **54**(2): 282–299.
- [17] Pierart, F. G. and Santos, I. F. [2015]. Steady state characteristics of an adjustable hybrid gas bearing - Computational fluid dynamics, modified Reynolds equation and experimental validation, *Proc. Inst. Mech. Eng. Part J J. Eng. Tribol.* **229**(7): 807–822.
- [18] Pierart, F. G. and Santos, I. F. [2016]. Active lubrication applied to radial gas journal bearings. Part 2: Modelling improvement and experimental validation, *Tribol. Int.* **96**: 237–246.
- [19] von Osmanski, S., Larsen, J. S. and Santos, I. F. [2017a]. A fully coupled air foil bearing model considering friction Theory & experiment, *J. Sound Vib.* **400**: 660–679.
- [20] von Osmanski, S., Larsen, J. and Santos, I. [2017b]. On the incorporation of friction into a simultaneously coupled time domain model of a rigid rotor supported by air foil bearings, *Tech. Mech.* **37**(2-5): 291–302.
- [21] Yazdi, B. Z. and Kim, D. [2017]. Rotordynamic Performance of Hybrid Air Foil Bearings With Regulated Hydrostatic Injection, *J. Eng. Gas Turbines Power* **140**(1): 012506.
- [22] Zamanian Yazdi, B. and Kim, D. [2018]. Effect of Circumferential Location of Radial Injection on Rotordynamic Performance of Hybrid Air Foil Bearings, *Vol. 7B Struct. Dyn.*, ASME, p. V07BT34A029.
- [23] Żywica, G., Bagiński, P. and Kiciński, J. [2017]. Selected operational Problems of high-speed Rotors supported by Gas Foil Bearings, *Tech. Mech.* **37**(2-5): 339–346.

Analysis of displacements in a gas foil bearing using an ultra-high-speed camera

Łukasz Breńkacz¹, Paweł Bagiński², Grzegorz Żywica³

¹ Department of Turbine Dynamics and Diagnostics, Institute of Fluid Flow Machinery, Polish Academy of Sciences, 80-231, Gdansk, Poland, lbrenkacz@imp.gda.pl

² Department of Turbine Dynamics and Diagnostics, Institute of Fluid Flow Machinery, Polish Academy of Sciences, 80-231, Gdansk, Poland, pbaginski@imp.gda.pl

³ Department of Turbine Dynamics and Diagnostics, Institute of Fluid Flow Machinery, Polish Academy of Sciences, 80-231, Gdansk, Poland, gzywica@imp.gda.pl

Abstract

The article discusses the analysis of displacements of the structural supporting layer in a gas foil bearing. Instead of a traditional measurement of the displacements of the bearing journal, the measurement was done using an ultra-high-speed camera. It turned out that doing so can give a far richer picture of what is happening in gas foil bearings during their operation. When recordings are watched in slow-motion, one can observe displacements of the journal and of the bump foils. Furthermore, vibrations of small fragments of the bump foil are clearly visible. The registered motion of the journal and of particular fragments of the foil can be compared with results obtained from numerical models, thus allowing their further development.

1 Introduction

An evaluation of displacements in fluid-flow machinery is often done using accelerometers, eddy current sensors, laser sensors or other types of sensors. High-speed cameras are rarely used for that purpose. Our article aims at filling this gap. At the same time, we want to show that a high-speed camera can serve as a useful tool to analyse the operation of a foil bearing. In addition to tracking the motion of the bearings's journal or sleeve (which can easily be done using traditional sensors), it is possible to analyse displacements of the bump foil (which is impossible for the great majority of above-mentioned sensor types). In this section of the article, we will present a few methods that can be used for performing tests of foil bearings and discuss several examples of the application of high-speed cameras for the purposes of conducting research on similar structures. Based on our observations deriving from the literature review, we are in a position to claim that the use of high-speed cameras in different fields of science is rising.

A foil bearing is the type of bearing that is relatively new but growing very fast. A coupled thermo-elastohydrodynamic model has been developed by Aksoy and Aksit [1] to predict three-dimensional thermal, structural and hydrodynamic performance of foil bearings. The bearing's deformations and pressure of the lubricating film were coupled in a FEM model that considers thermal/centrifugal growths as well as thermo-mechanical material properties. The authors solved the energy equation for the temperature of the lubricating film using the finite difference method, and it was also incorporated into the FEM model via successive iterations. The augmented Lagrangian method and thermal contact models were applied to solve mechanical and thermal contacts. The predicted values were compared with published measurement results and it turned out that a significant correlation exists between them. Moreover, a parametric study was conducted for various rotational speeds of the shaft and various load conditions to assess the performance of the bearing.

Bagiński et al. [2] presented the results of experimental research carried out on foil bearings operating under elevated temperature. Dynamic properties of the bearings were also investigated when a cooling system was turned on. In order to protect rotors and foil bearings operating at high temperatures from being overheated and damaged. This article presents various methods for cooling foil bearings and discusses the impact of these methods on dynamic parameters of the rotating system equipped with such bearings. To be able to assess the

temperature inside such a bearing, there was a need to apply a reliable measurement method. The authors of the article measured the temperature of the top foil using thermocouples and showed that their measurement method does not exert any significant impact on the operation of the rotor-bearings system.

Żywica et al. [3] wrote an article in which they discussed experimental research and simulation testing on prototypical foil bearings. All experimental tests were conducted on a special test rig which makes it possible to operate in various conditions and within a wide range of speeds. As a result of the study, it turned out that adverse operating conditions caused almost instant bearing damage, accompanied by a significant rise in temperature. The main factors affecting the durability of foil bearings were material covering mating surfaces, bearing geometry, way of assembling the bearing, rotational speed and load. To better understand the physical phenomena occurring in foil bearings, a numerical model has been developed which allowed carrying out thermal analyses. The research showed that the development of a new foil bearing is a very difficult task and requires many aspects to be taken into account, including the aspects directly related to the operation of the bearing itself, as well as those related to the rotor's operation and characteristics of the machine.

A fast-speed camera works particularly well in research on cavitation occurring in hydrodynamic bearings. The effect of viscosity on the cavitation characteristics of a high-speed sleeve bearing was investigated theoretically and experimentally by Wang and Lu and described in article [4]. The cavitation characteristics, the cavitation shape and the cavitation location of a spiral oil wedge hydrodynamic bearing were investigated experimentally by using the transparent bearing and the high-speed camera. The generalised Reynolds equation was established with considerations of the cavitation mechanism based on the modified Elrod method and the cavitation of different viscosity sleeve bearings was analysed and compared. The experiment results (measured by high-speed camera) in general are consistent with the theoretical results.

In order to accurately estimate deformations of the test object, it is sometimes necessary to prepare recordings in two different planes using a high-speed camera. In such cases, a high-speed camera is used in combination with a mirrors, and one of those cases is described in article [5] by Yu and Pan. They carried out full-frame, high-speed 3D shape and deformation measurements using stereo-digital image correlation (stereo-DIC) technique and a single high-speed colour camera. Compared with existing two-camera high-speed stereo-DIC or four-mirror-adaptor-assisted single-camera high-speed stereo-DIC, the proposed single-camera high-speed stereo-DIC technique offers prominent advantages of full-frame measurements using a single high-speed camera but without sacrificing its spatial resolution.

High-speed cameras are also used for registering fast-changing processes. Staudt et al. [6] presented results from observations of deep penetration laser welding process using a hyperspectral imaging (HSI) technique. For In today's business environment, the trend towards more product variety and customization is unbroken. Due to this trend there is the need for monitoring different types of laser-based material processing. Staudt et al. developed an appropriate high-speed camera-based HSI system. This systems agile and reconfigurable production systems emerged to cope with various products and product families. To design and optimize production enables us to derive spectra of the deep penetration welding process with high time resolution.

Research using high-speed cameras is often conducted during flow analyses, which was shown by Miles in article [7]. Since 2000 there has been a revolution in diagnostics of high-speed air flows. The foundations for this revolution were laid over the past few decades, but with the development of new short pulse and pulse burst laser technologies, higher laser powers and higher pulse energies, new high-speed cameras, better laser control and improved detection and laser delivery methodologies, many very effective new capabilities have been developed. Newly developed methods for molecular tagging velocimetry provide high fidelity visualization of transport properties and may be extended to simultaneous temperature measurements.

The impingement dynamics of water drops onto solid substrates at high velocities was investigated numerically by Cimpeanu and Papageorgiou [8]. Current methodologies in the aircraft industry estimating water collection on aircraft surfaces are based on particle trajectory calculations and empirical extensions thereof in order to approximate the complex fluid-structure interactions. Cimpeanu and Papageorgiou performed direct numerical simulations (DNS) using the volume-of-fluid method in three dimensions, for a collection of drop sizes and impingement angles. The high-speed background air flow was coupled with the motion of the liquid in the framework of oblique stagnation-point flow. Qualitative and quantitative features were studied in both pre- and post-impact stages. Drop deformation, collision, coalescence and microdrop ejection and dynamics, all typically neglected or empirically modelled, were accurately accounted for. In particular, they identified new morphological features in regimes below the splashing threshold in the modelled conditions. An experimental setup consisting of a monosize droplet dispenser, a rotating arm with a model wing fixed at its end, as well as associated motor and camera equipment were used to capture the drop dynamics as the solid body approached the liquid droplets at velocities of up to 100 m/s.

Applications of an easy-to-implement, compact but practical single-camera high-speed (SCHS) stereo-digital image correlation (DIC) technique for full-field transient 3D deformation measurement during ballistic impact were shown by Pan et al. [9]. The established SCHS stereo-DIC system relies on a four-mirror adapter to convert a single high-speed camera into two virtual high-speed cameras, which view a specimen from different angles and record the surface images of the test object onto two halves of the camera sensor. The system configuration, measurement principles and experimental procedures of the proposed SCHS stereo-DIC technique for full-field transient 3D deformation measurement were described first. Then, the effectiveness and accuracy of the established system were verified by measuring the static deformation of a stationary carbon fibre reinforced polymer (CFRP) panel and transient deformation of an aluminium panel under the impact of a cylindrical foam projectile. Finally, full-field in-plane and out-of-plane deformations of the CFRP panel under rigid steel sphere impact were determined using this system, which shed light on the deformation behaviour and failure mechanism of the CFRP panel under transient ballistic impact. The results confirm that the SCHS stereo-DIC is a cost-effective and practical technique for full-field transient 3D deformation measurement.

2 Research equipment

We carried out research on the foil bearing's structure on a specially prepared test rig, located in the Vibrodiagnostics Laboratory of the Institute of Fluid-Flow Machinery of the Polish Academy of Sciences (IMP PAN), in Gdańsk (Poland). The tested bearing was mounted on the shaft with a diameter of 34 mm. The shaft was put in rotational motion using an electro-spindle whose maximal speed is 24,000 rpm. A diagram that shows how the bearing is mounted on the shaft is presented in **Figure 1**.

During the research, the shaft's journal was inserted into the bearing sleeve. If the shaft rotated at a high enough speed, a gaseous lubricating film was formed between the top foil and the bearing journal. During the research, the bearing sleeve was not able to rotate.

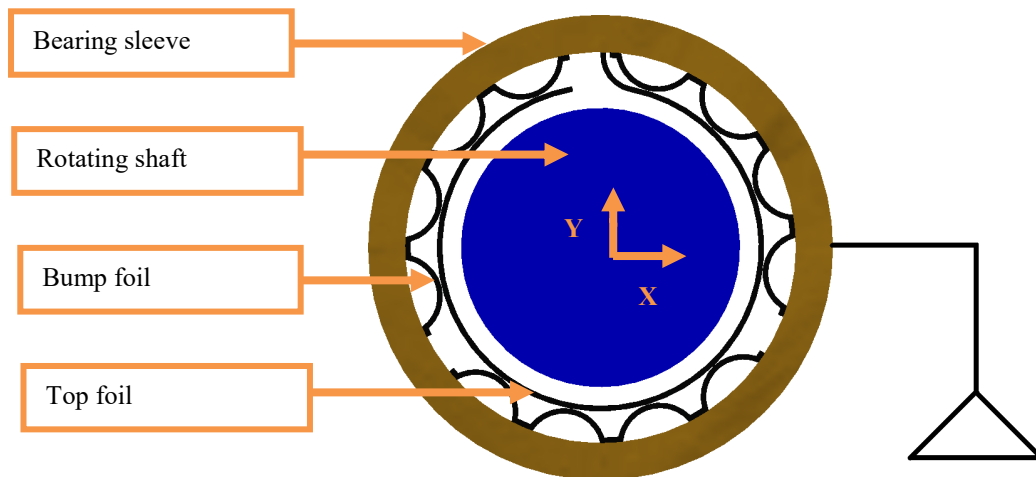


Figure 1: The way of mounting a foil bearing on the shaft.

Within the framework of the research described herein, an impulse excitation force was applied to the sleeve during operation of the bearing. The Vision Research's v2511 ultrahigh-speed camera (shown on the left-hand side of **Figure 2**) recorded what happened during the impact. An analysis of the recording in slow-motion followed. The camera is equipped with a CMOS sensor that allows capturing high-resolution images at very high speeds (offering full megapixel resolution of 1280 x 800). Moreover, the CMOS sensor has pixels with a diameter of 28 μm . Acquiring around 25 gigapixels-per-second of data enables frame rates up to 1,000,000 fps at 128 x 32 resolution. When recording with maximal resolution, the maximal frame rate is 25,600 frames-per-second. We connected the camera with the measurement computer using the Ethernet communication interface. Phantom Camera Control (PCC) is the Vision Research's software that allows controlling every camera function. We also used TEMA Motion, produced by Image Systems, which is the software for advanced motion analysis. For recording purposes, we used a Zeiss 100mm f/2 macro lens whose main features are the following: maximum reproduction ratio is 1:2 and minimum focusing distance is 0.4 m.



Figure 2: Vision Research's v2511 ultrahigh-speed camera (left). Extension tubes that enable achieving higher macro magnification (right).

Two sets of extension tubes (shown on the right-hand side of **Figure 2**) were placed between the lens and the camera. The extension tubes do not include any magnifying lenses but can be combined if we want to increase the reproduction ratio. As a matter of fact, those adapter rings enable increasing the distance between the focal plane of the lens and the CMOS sensor, thus increasing the reproduction ratio. In practice, the farther we move the lens away from the camera (using the extension tubes), the better magnification of the test object we get. One set of extension tubes includes rings with three widths (7 mm, 14 mm and 28 mm) and two bayonet fixings between the camera and the lens. After assembling two such sets, the distance between the lens and the camera was 128 mm.

Figure 3 shows the laboratory test rig with an ultrahigh-speed camera. The camera was controlled by the measurement computer that is also shown in this figure. We used two 60W LED lamps (PRO 2X Oscon 60 model, manufactured by Easy LED) for better illumination of the tested bearing. Each lamp can deliver light output up to 6,000 lumens.

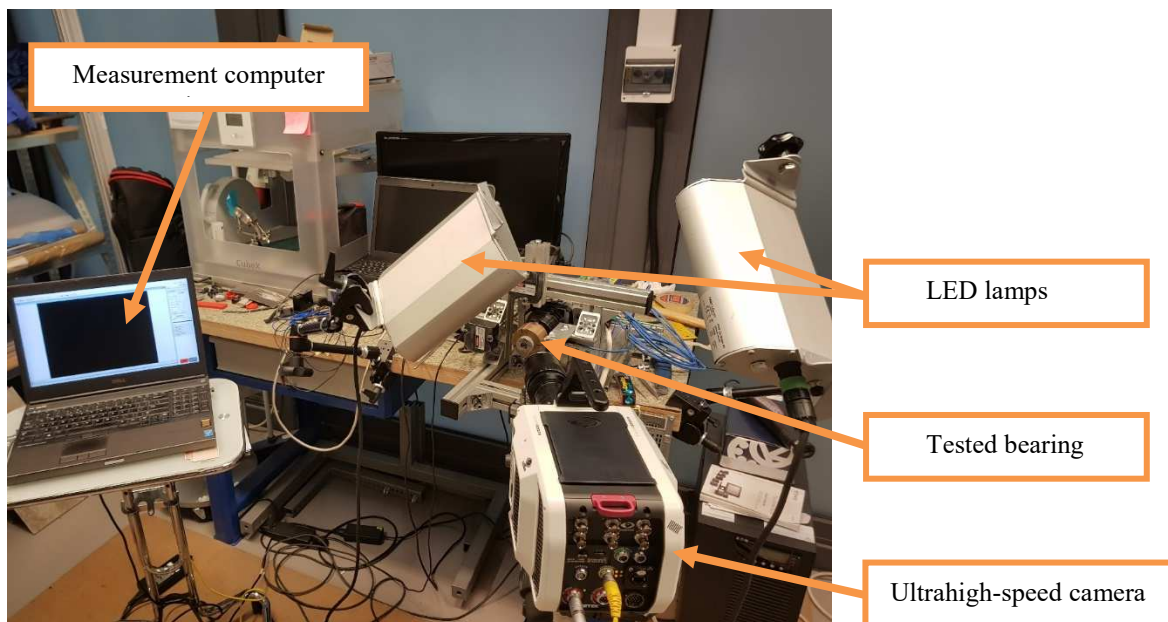


Figure 3: Test rig with the foil bearing and computer-controlled camera

For the purposes of analysing the motion of the foil bearing's components, we employed the TEMA Motion software, developed by Image Systems. A dialogue box that enables setting relevant parameters to track a chosen point on the bearing is demonstrated in **Figure 4**. Parameters of the recording were reciprocally coupled with each other.

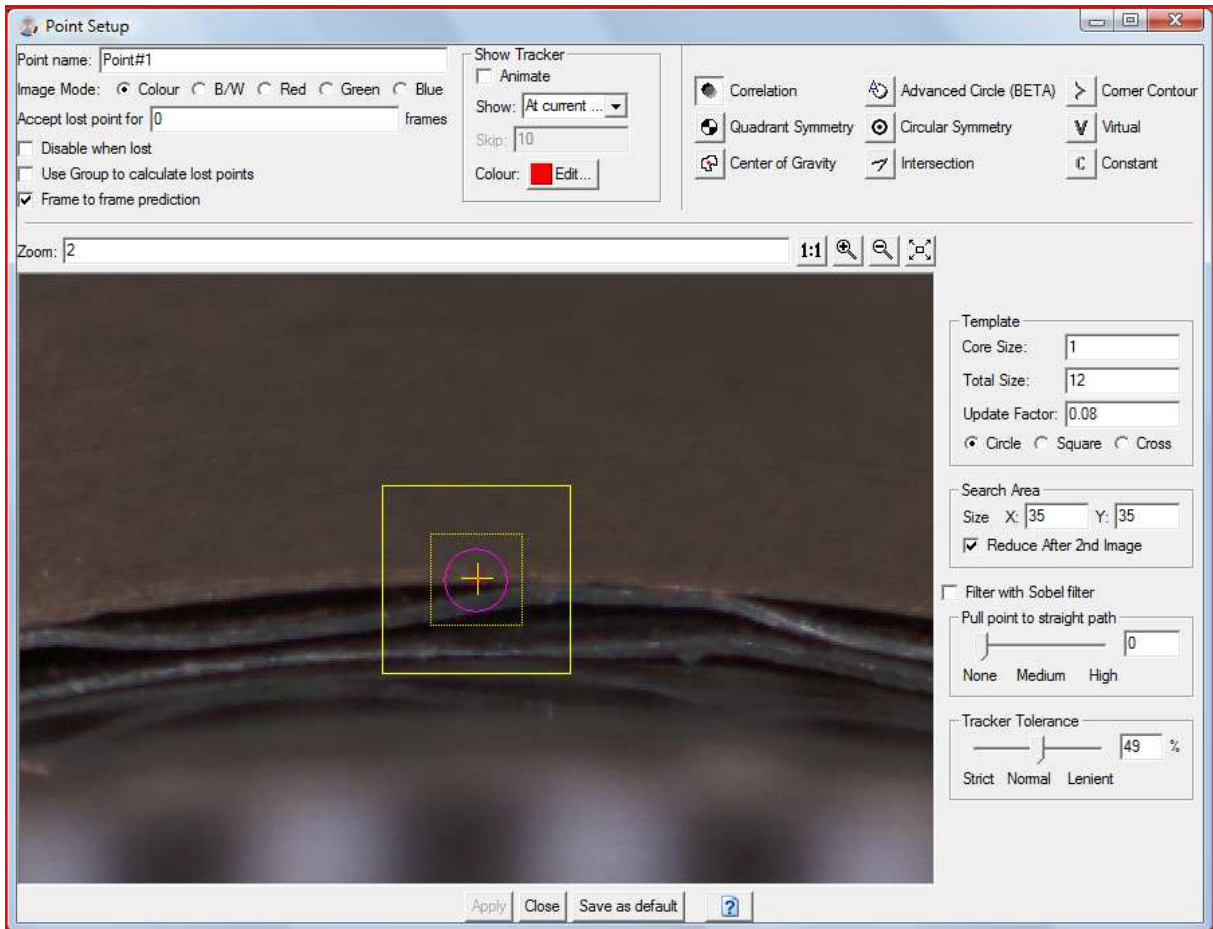


Figure 4: The dialogue box that enables setting relevant parameters to track the motion of a point located on the outer surface of the bearing sleeve after an impulse excitation was applied.

3 Research results

Figure 5 shows a portion of the tested bearing at two different points in time after an impulse excitation was applied. On the left-hand side, we can see the maximum deflection of the foils due to the impact and it was the moment when the distance between the bearing sleeve and the rotating rotor was the shortest. The biggest deflection was observed for the bump foil, whose height was approx. 400 μm before the excitation and decreased by around 50 per cent after it. On the right-hand side of **Figure 5**, we presented a photo of the bearing which was taken after its operation became stable again. The bearing was overloaded only for a short period of time and then the journal returned to its previous position.

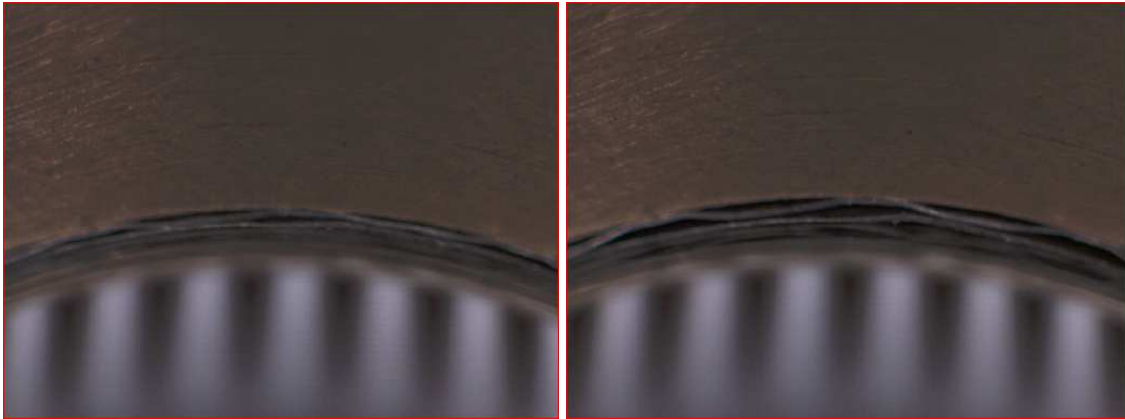


Figure 5: Maximum deflection of the foils caused by an impulse excitation (left). Stable operation of the bearing (right).

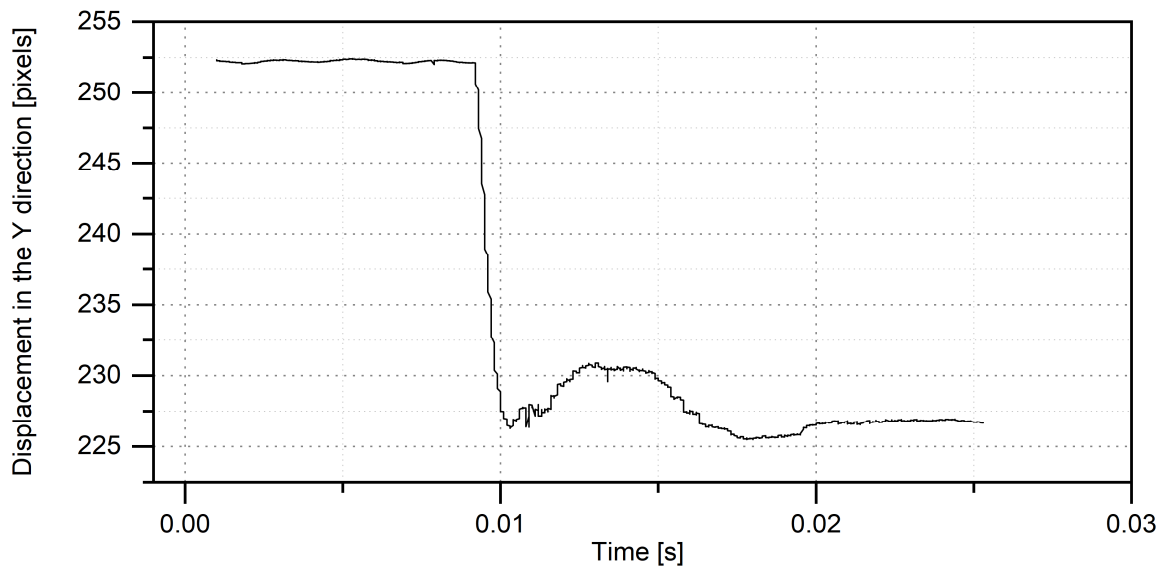


Figure 6: Displacement of the bearing sleeve in the Y direction (vertical direction), registered after an impulse excitation was applied vs. time.

In **Figure 6**, we showed the displacement of the bearing sleeve versus time, registered after an impulse excitation was applied during operation at a rotational speed of 24,000 rpm (maximum speed). This time, the magnitude of the excitation force was higher than the magnitude of the force used in the case shown in **Figure 5**. It turns out that when the magnitude of the excitation force was too large, plastic deformation of the bump foil took place. Even though the bearing was still able to operate, its operational characteristics changed.

In a foil bearing, the pre-clamp is a very important parameter. If the pre-clamp is not firm enough, the entire space between the top foil and the bearing sleeve will not be filled properly by the bump foil. In such a case, during operation at the nominal speed, the rotor (due to the unbalance) keeps pressing against the top foil that can deflect in places in which the bump foil is not tightened strongly. The vibration amplitude of the rotor is then significantly increased. We observed such behaviour only in several cases when we used the bump foil whose bumps were not high enough.

During operation at a constant speed, we noticed the vibration of the portion of the top foil, which was situated between the bump foil's bumps. The vibration frequency was the same as the frequency of rotational speed of the rotor. We observed one cycle of the sinusoidal waveform per one complete revolution of the rotor. Such vibrations were not present in each configuration of the tested bearing. Łagodziński and Miazga [10] have already conducted an investigation into this phenomenon using numerical simulations. In addition to numerical research, they carried out experimental research that showed how making the foils assembly more rigid (by mounting an additional intermediate foil) improved dynamic parameters of the bearings. Another way of

improving the dynamic properties of a foil bearing is to make its top foil more rigid. The phenomenon observed by other scientists cannot be viewed with the naked eye. Only after the preparation of recordings using an ultrahigh-speed camera, it was possible to thoroughly analyse the phenomenon perceived before based on numerical research.

4 Conclusion

Within the framework of the research presented herein, we conducted a visual analysis of displacements of the foil bearing's subassemblies. Recording video images using the set including only an ultrahigh-speed camera and a macro lens did not permit a high enough magnification to see details on the foils and, therefore, it was not possible to use it for analysing the motion of components of the foil bearing during its operation. Nevertheless, we also used two sets of extension tubes during our research. They allowed increasing the distance between the lens and the CMOS sensor, thus decreasing the minimum focusing distance and increasing the reproduction ratio. After we used six extension tubes, the distance between the lens and the CMOS sensor increased by 128 mm. As a result of using these accessories, 2 or 3 bumps of the bump foil were visible in each display frame. The magnification was high enough to analyse their motion and observe particular portions of the bearing.

We observed different portions of the bearing (e.g. its top part, side and the lock). Recordings presented various regimes such as a stable operation of the bearing at the nominal speed, a beginning of the operation and a run-up (during which the rotational speed was increased gradually). We also carried out several tests that were aimed to check the behaviour of the bearing after it was subjected to an impulse excitation. Depending on the magnitude of the excitation force, the bearing was able to function normally again (if the impact was not strong) or plastic deformation of its structural supporting layer occurred (after a strong impact).

During the research, we noticed something that was very interesting to us, namely the vibration of the portion of the top foil which was located between bumps of the bump foil. During operation at the maximum rotational speed (24,000 rpm), the vibration frequency of the top foil was equal to the frequency corresponding to the current rotational speed.

Acknowledgement

The research presented in this article was carried out within the framework of project No. 2016/21/D/ST8/01711, entitled "Examination and modelling of anti-vibration processes occurring in high-speed bearings with variable geometry", which is financed by the National Centre for Science (NCN).

The research was made using the equipment of KEZO research center in Jablonna.

References

- [1] Aksoy, S. and Aksit, M.F. (2015): A fully coupled 3D thermo-elastohydrodynamics model for a bump-type compliant foil journal bearing. *Tribology International*. **82**, pp. 110–122.
- [2] Bagiński, P., Żywica, G., Lubieniecki, M., and Roemer, J. (2018): The effect of cooling the foil bearing on dynamics of the rotor-bearings system. *Journal of Vibroengineering*. **20**(2), pp. 843–857.
- [3] Żywica, G., Bagiński, P., and Andrearczyk, A. (2017): Analysis of Thermal Damage in the High-Speed Foil Bearing. *Solid State Phenomena*. **260**, pp. 266–277.
- [4] Wang, L.L. and Lu, C.H. (2015): The effect of viscosity on the cavitation characteristics of high speed sleeve bearing. *Journal of Hydrodynamics*. **27**(3), pp. 367–372.
- [5] Yu, L. and Pan, B. (2017): Full-frame, high-speed 3D shape and deformation measurements using stereo-digital image correlation and a single color high-speed camera. *Optics and Lasers in Engineering*. **95**(03), pp. 17–25.
- [6] Staudt, T., Eschner, E., Tenner, F., and Schmidt, M. (2018): Deriving spectral information upon the laser welding process employing a hyperspectral imaging technique. *Procedia CIRP*. **74**, pp. 636–639.
- [7] Miles, R.B. (2015): Optical diagnostics for high-speed flows. *Progress in Aerospace Sciences*. **72**, pp. 30–36.
- [8] Cimpeanu, R. and Papageorgiou, D.T. (2018): Three-dimensional high speed drop impact onto solid surfaces at arbitrary angles. *International Journal of Multiphase Flow*. **107**, pp. 192–207.
- [9] Pan, B., Yu, L., Yang, Y., Song, W., and Guo, L. (2016): Full-field transient 3D deformation measurement of 3D braided composite panels during ballistic impact using single-camera high-speed stereo-digital image correlation. *Composite Structures*. **157**, pp. 25–32.
- [10] Łagodziński, J. and Miazga, K. (2018): Influence of intermediate foil on air-foil bearings performance and exploitation properties. *Advances in Technical Diagnostics*. pp. 401–410.

Impact of bump height manufacturing errors on the unbalance response of a 4dof rigid rotor

Omar Benchekroun ¹, Mihai Arghir ²

¹ Institut PPRIME, ISAE ENSMA, 86962 Futuroscope Chasseneuil, France, omar.benchekroun@univ-poitiers.fr

² Institut PPRIME, Université de Poitiers, 86962 Futuroscope Chasseneuil, France, mihai.arghir@univ-poitiers.fr

Abstract

The paper presents the synchronous amplitudes of unbalance responses of a rigid rotor supported by an aerodynamic foil bearing and a ball bearing. The foil bearing is affected by bump height manufacturing errors. The paper describes the main points of the theoretical model dealing with foil manufacturing errors. The model is based on contact mechanics algorithms and uses an augmented Lagrangian approach for dealing with normal contact forces and penalties for the Coulomb friction forces. The top and the bump foils are described by individual stiffness matrices. The equations of motion of the rigid rotor are integrated by using an explicit Euler algorithm where the mass and the structural damping of the foils are neglected. Unbalance response results are calculated for speeds comprised between 5 krpm and 55 krpm. The results show that the presence of bump height manufacturing errors modifies the value of the resonance speed and has a non-negligible impact on the damping introduced by the foil bearing.

Nomenclature

C_r , design radial clearance, [m]	X, Y , axes of the Cartesian coordinates system
C , damping, [Ns/m]	μ , dynamic viscosity, [Pa·s]
E , Young modulus of elasticity, [Pa]	ε , penalty parameter, [N/m]
e , foil thickness, [m]	η , structural damping coefficient
F, \mathbf{F} , force and force vector, [N]	σ , standard deviation, [m]
f , friction coefficient	$\tilde{\lambda}$, augmented Lagrange multiplier, [N]
g , gap, [m]	θ , angular coordinate, [rad]
h , film thickness, [m]	σ , standard deviation, [m]
h_b , bump height, [m]	Π , potential energy, [j]
I_p, I_d , polar and diametral moment of inertia, [kgm ²]	ν , Poisson coefficient
\mathbf{K} , stiffness matrix, [N/m]	Ω , rotation speed, [rad/s]
\mathbf{L} , matrix, [N/m]	
M, \mathbf{M} , mass [kg] and mass matrix	<i>Subscripts</i>
L , bearing length, [m]	ALM , augmented Lagrange multiplier
l_0 , bump half width, [m]	ax , axially averaged
N , number of contacts	b , bump
n , number of iterations in eqs. and	$cntct$, contact
nb , number of bumps	ext , external ambient
nx , number of circumferential discretization points	f , friction
P, \bar{P} , pressure, [Pa]	i, j , bump number
p_b , bump pitch, [m]	n , normal
R , bearing radius, [m]	p , pressure
T , rotation period, [s]	r, R , rotor
$t, \Delta t$, time and time step, [s]	rlt , ball bearing
u, \mathbf{u} , displacement and displacement vector, [m]	t , top foil
$W_{x,y}$, static load, [N]	ub , unbalance
x, y, z , Cartesian coordinates	0 , initial value

1 Introduction

Figure 1 depicts a first generation aerodynamic foil bearing of the kind used in the present work. The first foil bearing models consider the compliant structure as a Winkler foundation [6]. The stiffness of an isolated, single bump of infinite length was calculated from a simplified model using Castigliano's method and was uniformly distributed over the bearing surface. The model is very convenient being economic and easy to code but has some weaknesses. First, the structure has uniform stiffness in the axial direction. This supposes that the predicted deformations of the foils are constant in the axial direction. The second drawback is discarding the interactions between bumps. By assimilating the compliant structure to a Winkler foundation, the model supposes that all bumps respond in the same way when loaded. This is not true because the friction forces between the bumps and the top foil and the bumps and the sleeve may restrict displacements through stick-slip effects. The third drawback is the fact that these simplified models cannot reproduce the damping effect due to structural friction forces. An ad-hoc structural loss coefficient has been introduced to overcome this limitation [3, 8, 10]. The values of the structural loss coefficient were triggered from experiments but they are correct only for single frequency excitations while foil bearings may experience multiple frequencies responses even for simple excitations. However, the simplified models were and still are extensively used and enable at least the qualitative characterisation of foil bearing dynamic responses.

At the opposite side of the scale are approaches where the compliant structure is described by using complex, non-linear elasticity, finite element models [4, 5, 12, 15]. Commercial codes are generally used for this purpose. The numerical solution of Reynolds equation describing the thin film compressible flow and the time integration of the rotor-bearing dynamic model are treated by independent user-defined subroutines that are linked to the code solver. The resulting models are quite complex and need important investments but they offer the best insight into the physics of the foil bearing. One of the analysis made possible by the use of these very complex approaches was the impact of manufacturing errors on the operating characteristics of foil bearings. Indeed, the foil bearing structure results from a complex manufacturing process involving plastic deformations and heat treatments of the thin, highly allied foils. Therefore, the manufacturing process is inevitably accompanied by errors [11]. The theoretical manufacturing errors were considered by introducing gaps between different parts of the foil bearing. The impact of these errors on the stiffness of the foil structure and on the unbalance response of a two-dimensional rotor-bearing system was shown in [4] and [5], respectively.

Another category of models lies between the two previously exposed. They try to eliminate some (but not all) of the drawbacks of the very simplified models while introducing approaches simpler than those based on non-linear finite element analyses. One of the first models of the kind was introduced in [9]. The bump foil was modelled by a system of spring/trusses (**Figure 2**). The elasticity of the bump foil was still constant in the axial direction but a stiffness matrix could be assembled in a manner very similar to finite elements models. Friction forces were considered by using a first order differential equation based on a regularization of the Coulomb law. The model could therefore consider the interactions between bumps and showed clearly stick/slip transitions of the contacts. Similar models were subsequently introduced and used for the dynamic analysis of foil bearings [7, 13]. The top foil was discarded in [9] because its stiffness was supposed negligible compared to bumps and it was assumed that all contacts were closed. The results of complex finite element analyses presented in [4] showed this is not the case even for foil structures free of manufacturing errors. The static loading of an ideal foil structure by an impinging rotor lead to close/loose contacts between the bump and the top foil and between the bump and the sleeve.

The model introduced in [9] was therefore extended for considering these effects [1]. The structure of the top foil and an additional degree of freedom per bump were added to the model.

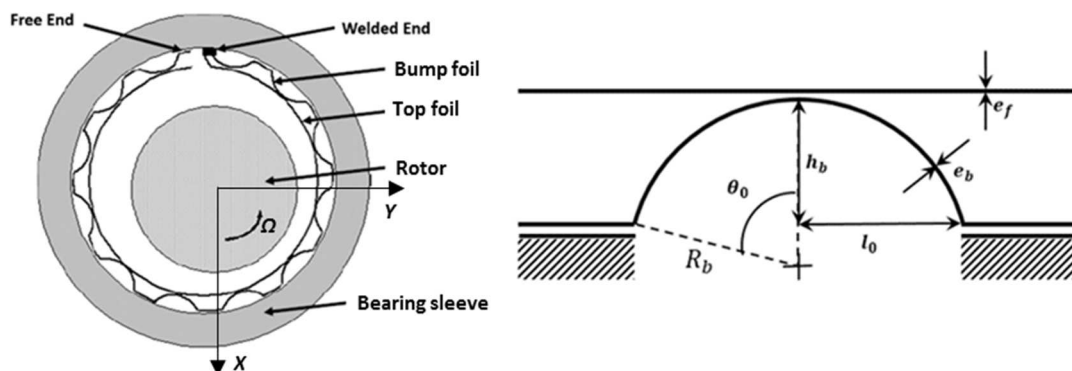


Figure 1. First generation bump foil bearing

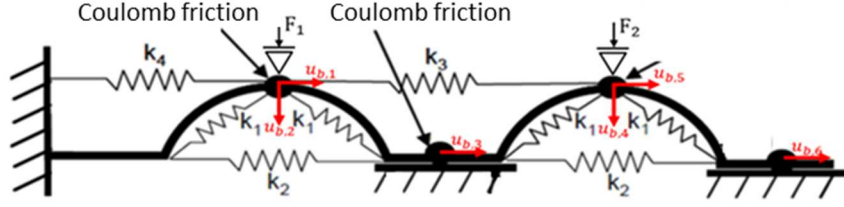


Figure 2. Structural model of the bump foil used in [9]

These additions enabled the definitions of gaps between the elements of the foil bearing. Normal contact forces were calculated with the augmented Lagrangian multipliers method while friction forces were treated with penalties. The results of the new model were extensively confronted with the model introduced in [9] as well as with the full non-linear analysis presented in [4] for bump height manufacturing errors. Start-up torque and lift-off speed calculations as well as results obtained for full operating speeds and high static loads were presented in [2] and systematically compared with experimental data.

The present work introduces the unbalance response results of a rotor-bearing system with four degrees of freedom (4dof). The rotor is rigid and is supported by an aerodynamic foil bearing and a ball bearing. The results show the impact of bump height manufacturing errors of the foil bearing on the unbalance response. The main traits of the computational model are presented before discussing the unbalance results of the rotor-bearing system.

2 The foil bearing model

The main improvement of the new model is its capacity to deal with gaps i.e. with open/loose contacts between the foils of the compliant structure, the bearing sleeve and the rotor. The bump foil is discretized following the same model than in [9] but each bump has now four degrees of freedom as depicted in **Figure 3**: two displacements of its top ($u_{b,1/2}$, $u_{b,5/6}$, etc.) and two displacements of its bottom ($u_{b,3/4}$, $u_{b,7/8}$, etc.). The radial displacements of the bump bottom ($u_{b,4}$ and $u_{b,8}$ in **Figure 3**) are newly introduced compared to the model in [9]. The top foil is now also considered. Its degrees of freedom in **Figure 3** are $u_{t,1}$ and $u_{t,2}$ and correspond to the top of the bumps.

The gaps taken into account by the model are:

- the gap between the rotor and the top foil: $g_{r,i} = C_r + x_r \cos \theta_i + y_r \sin \theta_i + u_{t,i} \geq 0$ (1)
- the gap between the top foil and the bump foil: $g_{t,i} = g_{0,t,i} - u_{t,i} + u_{b,1+2(i-1)} \geq 0$ (2)
- the gap between the bump foil and the sleeve: $g_{b,i} = g_{0,b,i} - u_{b,2+2(i-1)} \geq 0$ (3)

If non-zero, the initial gaps, $g_{0,t,i}$ and $g_{0,b,i}$ can describe manufacturing errors of the foil structure. Following the non-interference condition, all gaps must be positive (open/loose) or null (closed). This is mathematically described by the Signorini-Moreau condition [14]

$$g_i \geq 0 \wedge F_{n,i} \leq 0 \wedge g_i F_{n,i} = 0$$

The potential energy of the structure with gaps must consider these constraints. The normal contact forces are calculated by using the augmented Lagrange multipliers method for the bump/top foil contacts and for the bump/sleeve contacts and the penalty method for the rotor/top foil contacts. The potential energy of the foil structure is then:

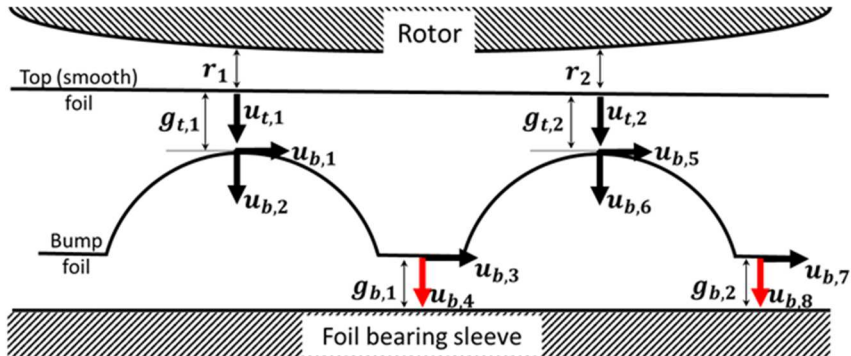


Figure 3. Gaps and degrees of freedom of the new structural model

$$\begin{aligned} \Pi_{ALM} = & \frac{1}{2} \mathbf{u}_b^T \mathbf{K}_b \mathbf{u}_b + \frac{1}{2} \mathbf{u}_t^T \mathbf{K}_t \mathbf{u}_t + \sum_{i=1}^{N_{cntct}} (\bar{\lambda}_i g_i + \frac{1}{2} \varepsilon_{ALM} g_i^2) + \frac{1}{2} \sum_{i=1}^{N_{Rotor}} \varepsilon_r g_{r,i}^2 \\ & + \frac{1}{2} \sum_{i=1}^{N_{stick}} \varepsilon_f (u_{b,i} - u_{b,i}^{(0)})^2 - \sum_{i=1}^{N_{slip}} \frac{f \bar{\lambda}_i \text{sign}(\dot{u}_{b,i})}{F_{f,i}} (u_{b,i} - u_{b,i}^{(0)}) \end{aligned} \quad (4)$$

Friction forces at closed bump/top foil and bump/sleeve contacts are also added to the potential energy. They are calculated with the penalty method for stick contacts and with the Coulomb law for slip contacts. The Lagrange multipliers in eq. (4) correspond to normal contact forces, $\bar{\lambda}_i = F_{n,i} \leq 0$.

The equations obtained by minimizing the potential energy (4) yield:

$$\begin{bmatrix} \mathbf{K}_b + \mathbf{L}_{bb} & \mathbf{L}_{bt} \\ \mathbf{L}_{bt}^T & \mathbf{K}_t + \mathbf{L}_{tt} \end{bmatrix} \begin{Bmatrix} \mathbf{u}_b \\ \mathbf{u}_t \end{Bmatrix} = \begin{Bmatrix} \mathbf{F}_b \\ \mathbf{F}_t \end{Bmatrix} \quad (5)$$

The bump and the top foil stiffness matrices were presented in [1, 2] and are now omitted for brevity. The coupling matrices \mathbf{L}_{bb} , \mathbf{L}_{bt} , \mathbf{L}_{tt} and the vectors \mathbf{F}_b and \mathbf{F}_t contain the Lagrange multipliers and the penalties. Equation (5) is non-linear because the vector \mathbf{F}_b contains terms of the kind $\bar{\lambda}_i \text{sign}(\dot{u}_{b,i})$.

The second part of the foil bearing model is the compressible thin film flow between the rotor and the top foil. The thin flow is modelled by using the compressible Reynolds equation. For an isothermal flow of an ideal gas obeying the state law this yields:

$$\frac{\partial}{\partial x} \left(\frac{\bar{P} h^3}{12\mu} \frac{\partial P}{\partial x} \right) + \frac{\partial}{\partial z} \left(\frac{\bar{P} h^3}{12\mu} \frac{\partial P}{\partial z} \right) = \frac{R\Omega}{2} \frac{\partial(\bar{P}h)}{\partial x} + \frac{\partial(\bar{P}h)}{\partial t} \quad (6)$$

where \bar{P} are ‘‘upwinded’’ pressures. Ambient pressure is imposed along the axial welding (**Figure 1**) and at the two ends of the bearing. The equation is discretized following the finite volume method on a rectangular grid corresponding to the unwrapped bearing. The discretized system of equations is non-linear due to \bar{P} and is solved by using the Newton-Raphson method. Equation (6) is not sufficient for modelling the pressures between the top and the rotor. If the local film thickness is smaller than three times the equivalent standard deviation of the roughness heights, then contacts between roughness asperities may occur. The mixed lubrication regime is then considered by calculating a local contact pressure following a statistical contact model [2].

Coupling the structural model with Reynolds equation is another important point. First, the structural model considers the variation of the foils stiffness only in the circumferential direction and discards the axial direction. The pressure field calculated from Reynolds equation and from the contact model is two-dimensional; the pressure varies in the circumferential and the axial direction. The first step for coupling the present foil structure model with the pressure field is to consider that axially averaged pressures load the top foil.

$$P_{ax} = \frac{1}{L} \int_0^L (P + P_{cntct}) dz \quad (7)$$

and the corresponding radial force is:

$$dF = (P_{ax} - P_{ext}) R d\theta L \quad (8)$$

The forces acting on the rotor are:

$$F_x = \int_0^{2\pi} dF \cos\theta, F_y = \int_0^{2\pi} dF \sin\theta \quad (9)$$

The assumption that axially averaged pressure forces load the top foil is coherent with the foil structure model but it supposes that the thin film thickness is constant in the axial direction. This is not exactly true in aerodynamic foil bearings where the pressure varies axially from the mid plane to the bearing ends for satisfying the boundary condition, $P = P_{ext}$ @ $z = \pm L/2$. The real film thickness has a similar variation, decreasing from a maximum value at the bearing mid plane to a minimum value at the bearing ends. Experimental results showed a systematic wear of the foils at the bearing ends. Considering the axial direction in the structural model of the foils would lead to approaches of the kind presented in [4] while the goal of the present work is to introduce a model requiring less calculation time. The modelling assumption of an axially constant thin film thickness is the condition for a simple structural model and the thin film thickness will then be the gap given by eq. (1).

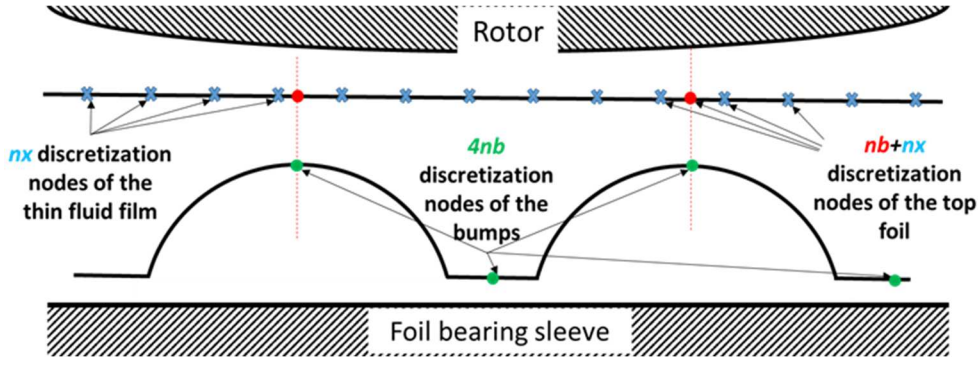


Figure 4. Circumferential discretization of the top and bump foils

The second point in coupling the foil structure model with the thin film pressure field is the fact that the circumferential discretization points of Reynolds equation are more numerous and do not correspond to the top of the bumps. This situation is depicted in **Figure 4**. The number of circumferential discretization points of Reynolds equation is at least the double of the number of bumps, nb . In the present structural model, the stiffness matrix of the bump foil has $4nb$ lines and columns. The stiffness matrix of the top foil is obtained by considering the nb bumps and the nx discretization lines of Reynolds equation organized for the increasing circumferential coordinate. However, the contact algorithm requires a clear distinction between the nb nodes where contacts may occur and the rest. Therefore, after its calculation, the stiffness matrix and the degrees of freedom of the top foil are re-organized as its follows.

$$[K_t] = \begin{bmatrix} K_{t11} & K_{t12} \\ K_{t12}^T & K_{t22} \end{bmatrix}, \{u_t\} = \begin{Bmatrix} u_{t1} \\ u_{t2} \end{Bmatrix} \quad (10)$$

where u_{t1} are the nb degrees of freedom of the top foil associated to the bumps (where gaps are defined and contacts may occur) and u_{t2} are the nx degrees of freedom associated with the discretization lines of the Reynolds equation. The complete non-linear system of equation replacing eq. (5) is now:

$$\begin{bmatrix} K_b + L_{bb} & L_{bt} & \mathbf{0} \\ L_{tb}^T & K_{t11} + L_{tt} & [K_{t12}]_{nb,nx} \\ \mathbf{0} & K_{t12}^T & K_{t22} \end{bmatrix} \begin{Bmatrix} u_b \\ u_{t1} \\ u_{t2} \end{Bmatrix} = \begin{Bmatrix} F_b \\ F_{t1} + F_{p1} \\ F_{p2} \end{Bmatrix} \quad (11)$$

For solving, the system is decomposed into two sub-systems:

$$\underbrace{(K_{bt1} - L_{t12}K_{t22}^{-1}L_{t21})}_{K_{bt}} u_{bt1} = \underbrace{F_{bt1} - L_{t12}K_{t22}^{-1}F_{p2}}_{F_{bt}} \quad (12)$$

$$K_{bt1} = \begin{bmatrix} K_b + L_{bb} & L_{bt} \\ L_{tb}^T & K_{t11} + L_{tt} \end{bmatrix}, u_{bt1} = \begin{Bmatrix} u_b \\ u_{t1} \end{Bmatrix}, F_{bt1} = \begin{Bmatrix} F_b \\ F_{t1} + F_{p1} \end{Bmatrix} \quad (13)$$

$$u_{t2} = K_{t22}^{-1}(F_{p2} - L_{t21}u_{bt1}) \quad (14)$$

where eq. (12) and (14) represent systems of non-linear and linear systems of equations, respectively.

For given pressure loading, the system is solved following a special algorithm that detects closed/loose gaps and stick/slip contacts. The algorithm first detects if the gaps are closed or loose depending on the initial values of the displacements. The augmented Lagrange multipliers λ have zero initial values. If gaps are closed, then they are supposed to be in stick state and a first estimation of the friction forces is calculated using the penalty method.

$$F_f^{trial} = \varepsilon_f(u_b - u_b^{(0)}) \quad (15)$$

where $u_b^{(0)}$ is the displacement at the previous loading step. The non-linear system of equations (12) is solved using a Newton-Raphson algorithm. This is the innermost loop of the algorithm. The solution yields the new values of the displacements, u_b , u_{t1} and u_{t2} .

The algorithm then checks if the contacts are in stick or slip state.

$$\begin{cases} \text{if } |F_f^{trial}| < f|\bar{\lambda}| \text{ then } F_f^{(k)} = F_f^{trial}, \text{ stick state} \\ \text{otherwise } F_f^{(k)} = f\bar{\lambda}\text{sign}(\dot{u}_{tg}^{(k)}), \text{ slip state} \end{cases} \quad (16)$$

and the solution of the non-linear system of equations (12) is repeated until the convergence of the friction forces. This is the second loop of the algorithm. The values of the augmented Lagrange multipliers are kept constant during the calculation of the friction forces. Once the friction forces are converged, the augmented Lagrange multipliers are updated:

$$\bar{\lambda}_i^{(n+1)} = \bar{\lambda}_i^{(n)} + \varepsilon_{ALM} g_i^{(n+1)} \quad (17)$$

and the whole algorithm is repeated until convergence. This is the third loop of the algorithm. After the convergence of the augmented Lagrange multipliers the close/loose state of the contacts is checked. The whole calculation is repeated if the initial assumption of close/loose state of the is not verified.

The algorithm consists of four embedded loops and proceeds in an iterative manner. The key point ensuring the robustness of the contact algorithm is keeping the augmented Lagrange multipliers (i.e. the normal contact forces) constant while calculating the friction forces.

Once the algorithm is converged the film thickness is calculated in all points following eq. (1), i.e. $h_i = g_{r,i}$. It should be underlined that defining the film thickness as a gap and treating it subsequently avoids any artificial (i.e. numerical) interpenetration between the top foil and the rotor.

2 The dynamic analysis of the foil bearing

The foil bearing is analysed in the context of a dynamic system. Traditional methods for dynamic analysis of bearings involve the use of rotordynamic coefficients. For bearings lubricated with oil or water (i.e. with incompressible lubricants), the rotordynamic coefficients are defined by using the small perturbation assumption and do not depend on the excitation frequency and amplitude. For bearings lubricated with compressible fluids, the perturbed forces (i.e. bearing impedances) depend on the excitation frequency. The dependence of the perturbed forces on the excitation frequency can be more or less important depending on the compressibility of the fluid and on the values of the analysed frequencies. If the dependence is too strong, then rotordynamic coefficients can be replaced by transfer functions. Nevertheless, the small perturbation assumption is supposed to be valid. For foil bearings, the situation is different because their characteristics depend also on the excitation amplitude. Simple experiments have shown that the stiffness of the foil structure is non-linear. Moreover, the friction damping introduced by the compliant structure depends on the amplitude of dynamic displacements. It is therefore quite difficult to apply the small perturbation approach to foil bearings and to define rotordynamic coefficients or transfer functions. This problem is still an open discussion in the literature.

The remaining possibility is the full non-linear analysis. Following the orbit method, the equations of motion of the dynamic system are time integrated together with the model of the foil bearing. For example, the equations of motion of the two degrees of freedom (2dof) rotor-bearing system are:

$$M_R \begin{Bmatrix} \ddot{x} \\ \ddot{y} \end{Bmatrix} = \begin{Bmatrix} F_x \\ F_y \end{Bmatrix}_{(x,y,\dot{x},\dot{y})} + M_R e_B \Omega^2 \begin{Bmatrix} \cos(\Omega t) \\ \sin(\Omega t) \end{Bmatrix} + \begin{Bmatrix} W_x \\ W_y \end{Bmatrix} \quad (18)$$

with the initial conditions,

$$x = y = \dot{x} = \dot{y} = 0 @ t = 0 \quad (19)$$

This system of equations can be time integrated by using either implicit or explicit methods. Foil bearing forces must be calculated at least once at every time step. This means that Reynolds equation (6) and the dynamic model of the foil structure are time integrated in a coupled manner. A dynamic model of the foil structure could be simply developed, for example:

$$\mathbf{M}_{bt} \ddot{\mathbf{u}}_{bt1} + \mathbf{C}_{bt} \dot{\mathbf{u}}_{bt1} + \mathbf{K}_{bt} \mathbf{u}_{bt1} = \mathbf{F}_{bt} \quad (20)$$

where \mathbf{K}_{bt} , \mathbf{u}_{bt1} and \mathbf{F}_{bt} where defined in eqs. (12, 13). A diagonal mass matrix could be estimated from a lumped model of the foils while the damping matrix could be estimated by using a structural damping. However, a more simple approach was adopted.

Implicit methods are often preferred because they do not suffer from time step stability limitations. The time step is controlled only by the desired accuracy of the result. In the meantime, the bearing forces are non-linear

Table 1. Geometry of the journal bearing and of the foil structure

Rotor radius, R	19.05 mm	Bump height, h_b	0.508 mm
Axial length, L	38.1 mm	Foil thickness, $e_b=e_t$	0.102 mm
Radial clearance, C_r	31.8 μm	Young modulus, E	214 GPa
Bump pitch, p	4.572 mm	Poisson's ratio, ν	0.29
Bump length, $2l_0$	3.556 mm	Friction coefficient, f	0.25

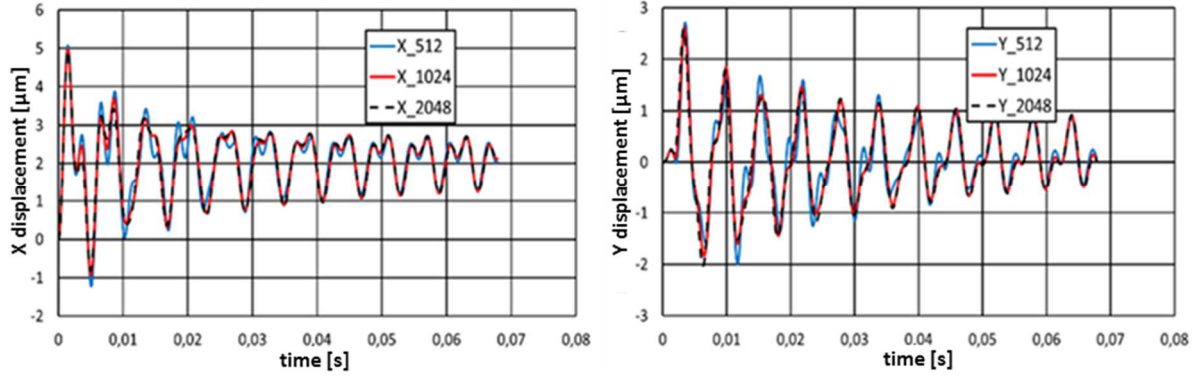


Figure 5. Dynamic displacements of the rotor calculated with different time steps

because they depend on the state variables x, y, \dot{x}, \dot{y} . This means that a non-linear algorithm must be applied at every time step of the implicit time integration. Repeated calculations of the bearing forces proved to be very time consuming and therefore the implicit algorithm was abandoned.

The explicit algorithm requires only a single estimation of the bearing forces per time step. However the time step is limited because the algorithm must deal with all time scales of the model. The dynamic structural model (20) may introduce very small time scales because the mass of the foils is very small compared to their stiffness. Experience showed that explicit dynamic models of foil bearings based on complex finite element analysis are submitted to very strong time step limitations. The necessity of accurately dealing with the eigenmodes of the top and bump foils in the context of rotor-bearing dynamics can be questioned. In the present work, the dynamic model of the foils described by eq. (20) was not used. The mass and the structural damping of the foils were discarded and only the static equation (10) was integrated at each time step. The explicit integration could then use reasonably large time steps.

However, the numerical accuracy of an explicit time integration algorithm is more difficult to control than of an implicit one. For a rigorous control, the calculations should be repeated at each step with different values of the time increment and the results compared. This would lead again to repeated calculations of foil bearing forces at each time step. Therefore, the accuracy of the time integration was only a posteriori verified for a 2dof rigid rotor supported by two identical foil bearings with characteristics given in **Table 1**. **Figure 5** depicts the dynamic displacements obtained for $M_R=1$ kg, $W_x=30$ N, $W_y=0$, $\Omega=30$ krpm, $e_{ub}=0$ (i.e. a non-linear stability analysis) and the initial conditions given by (19). The results were obtained for three different time steps $\Delta t=T/512$, $T/1024$ and $T/2048$. The results obtained with $\Delta t=T/1024$ and $T/2048$ are very close at all time steps. The results obtained with $\Delta t=T/512$ show differences in the first time steps when the accelerations are large but tend to the same values of the displacements when time progresses. The results obtained with $\Delta t=T/1024$ were therefore considered accurate enough.

2 Unbalance response of a 4DOF rotor-bearing system

The impact of bump height manufacturing errors is presented for the unbalance response of a rigid rotor supported by a foil bearing and a ball bearing (**Figure 6**). The e.o.m of the 4dof rotor are:

$$\begin{cases} M_R \ddot{x}_G = F_x^1 + F_x^2 + W_x + M_R e_B \Omega^2 \cos(\Omega t) \\ M_R \ddot{y}_G = F_y^1 + F_y^2 + W_y + M_R e_B \Omega^2 \sin(\Omega t) \\ I_d \ddot{\theta}_r + I_p \Omega \dot{\psi} = \delta_1 F_y^1 + \delta_2 F_y^2 + M_R e_B \Omega^2 \delta_b \sin(\Omega t) \\ I_a \ddot{\psi} - I_p \Omega \dot{\theta}_r = -\delta_1 F_x^1 - \delta_2 F_x^2 - M_R e_B \Omega^2 \delta_b \cos(\Omega t) \end{cases} \quad (21)$$

The displacements at the bearings centers are:

$$x_k \approx x_G + \delta_k \psi, y_k \approx y_G - \delta_k \theta_r, k = \{1,2\} \quad (22)$$

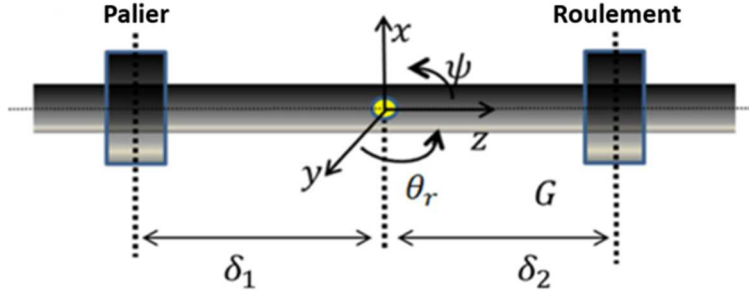


Figure 6. Notations and coordinate system for a rigid rotor

where it was supposed that $\sin\psi \approx \psi$ and $\sin\theta_r \approx \theta_r$. Similar relations hold for velocities at the bearings centers. The e.o.m (22) are expressed as a system of first order differential equations.

$$\begin{Bmatrix} \dot{q} \\ \ddot{q} \end{Bmatrix} = \begin{bmatrix} \mathbf{0} & \mathbf{I}^{4 \times 4} \\ \mathbf{0} & -\mathbf{M}^{-1}\mathbf{G} \end{bmatrix} \begin{Bmatrix} q \\ \dot{q} \end{Bmatrix} + \begin{Bmatrix} \{0\}_4 \\ F_x^1 + F_x^2 + W_X + M_R e_B \Omega^2 \cos(\Omega t) \\ F_{y1} + F_{y2} + W_Y + M_R e_B \Omega^2 \sin(\Omega t) \\ \delta_1 F_y^1 + \delta_2 F_y^2 + M_R e_B \Omega^2 \delta_b \sin(\Omega t) \\ -\delta_1 F_x^1 - \delta_2 F_x^2 - M_R e_B \Omega^2 \delta_b \cos(\Omega t) \end{Bmatrix} \quad (23)$$

$$\mathbf{q} = \begin{Bmatrix} x_G \\ y_G \\ \theta_r \\ \psi \end{Bmatrix}, \quad \mathbf{M} = \begin{bmatrix} M_R & 0 & 0 & 0 \\ 0 & M_R & 0 & 0 \\ 0 & 0 & I_d & 0 \\ 0 & 0 & 0 & I_d \end{bmatrix}, \quad \mathbf{G} = \begin{bmatrix} 0 & 0 & 0 & 0 \\ 0 & 0 & 0 & 0 \\ 0 & 0 & 0 & I_p \Omega \\ 0 & 0 & -I_p \Omega & 0 \end{bmatrix} \quad (24)$$

that is integrated following an explicit Euler method with initial conditions:

$$\mathbf{q} = \dot{\mathbf{q}} = 0 \text{ @ } t = 0 \quad (25)$$

The inertia characteristics of the rotor are $M_R=2 \text{ kg}$, $I_p=0.0175 \text{ kgm}^2$, $I_d=0.0032 \text{ kgm}^2$. The foil bearing and the ball bearing are equally spaced from the centre of inertia, $\delta_1 = -\delta_2 = 0.1 \text{ ym}$. An unbalance $e_{ub}=0.32 \text{ gmm}$ was considered at the rotor centre of inertia.

The ball bearing has a stiffness $K_{rit}=2.5 \cdot 10^8 \text{ N/m}$ and a structural damping $\eta_{rly} = 0.5\%$, both constant with the rotation speed.¹

The geometry of the foil bearing is described in **Table 1**. Bump height manufacturing errors are depicted in **Figure 7**. It is supposed that the manufacturing errors have a natural distribution of given standard deviation while the average bump height is the design value. A random number generator is used for obtaining a set of nb values of unit average and 1% or 2% standard deviation. These values are then scaled to the design value of the bump height. This corresponds to $5 \mu\text{m}$ or $10 \mu\text{m}$ of standard deviation. Only two sets of random bump heights errors (HBE1 and HBE2) both with $5 \mu\text{m}$ and $10 \mu\text{m}$ standard deviations were used in the present study. A systematic, statistical analysis would require a much larger number of random bump height sets.

Calculations were performed for distinct rotation speeds comprised between 5 krpm and 55 krpm. Each calculation was performed for a time interval corresponding to 200 periods of the rotation speeds. Generally, the

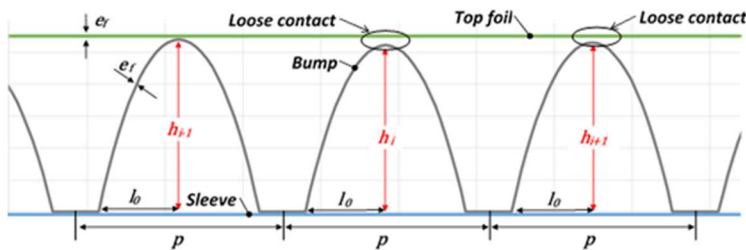


Figure 7. Bump height manufacturing errors

¹ Introducing a structural damping coefficient is equivalent of using a rotation speed dependent damping, $C_{rit} = \eta_{rit} K_{rit} / \Omega$.

orbits became stabilized after 100 periods and in all cases the stabilized orbits showed only synchronous responses. The X synchronous amplitudes of the 5 calculations cases (no manufacturing errors i.e. HBE0, $HBE1/\sigma_{hb} = 5 \mu m$, $HBE2/\sigma_{hb} = 5 \mu m$, $HBE1/\sigma_{hb} = 10 \mu m$, $HBE2/\sigma_{hb} = 10 \mu m$) are depicted in **Figure 8**.

The top left **Figure 8** compares the amplitudes in the foil bearing obtained for cases HBE0, $HBE1/\sigma_{hb} = 5 \mu m$ and $HBE2/\sigma_{hb} = 5 \mu m$. The resonance of the conical forward mode is visible just before 30 krpm for the HBE0 case. Adding 5% bump height manufacturing errors modifies the resonance speed either increasing or decreasing it but most noticeable the resonance amplitude is higher. This means the foil bearing brings less damping to the rotor-bearing system. This observation is reinforced by the top right **Figure 8** showing the amplitudes in the foil bearing for the cases HBE0, $HBE1/\sigma_{hb} = 10 \mu m$ and $HBE2/\sigma_{hb} = 10 \mu m$. Compared to the $5 \mu m$ bump height errors, the resonance speeds are not modified but the resonance amplitudes increased considerably with increasing the standard deviation of manufacturing errors. These figures show that the damping of the foil bearing decreases non-linearly with the increase of the bump height manufacturing errors.

The amplitudes in the ball bearing are depicted in the lower left and right part of **Figure 8**. The values of the synchronous amplitudes are much smaller than in the foil bearing and increase continuously with the rotation speed. The remarks made for the foil bearing hold also for the ball bearing amplitudes.

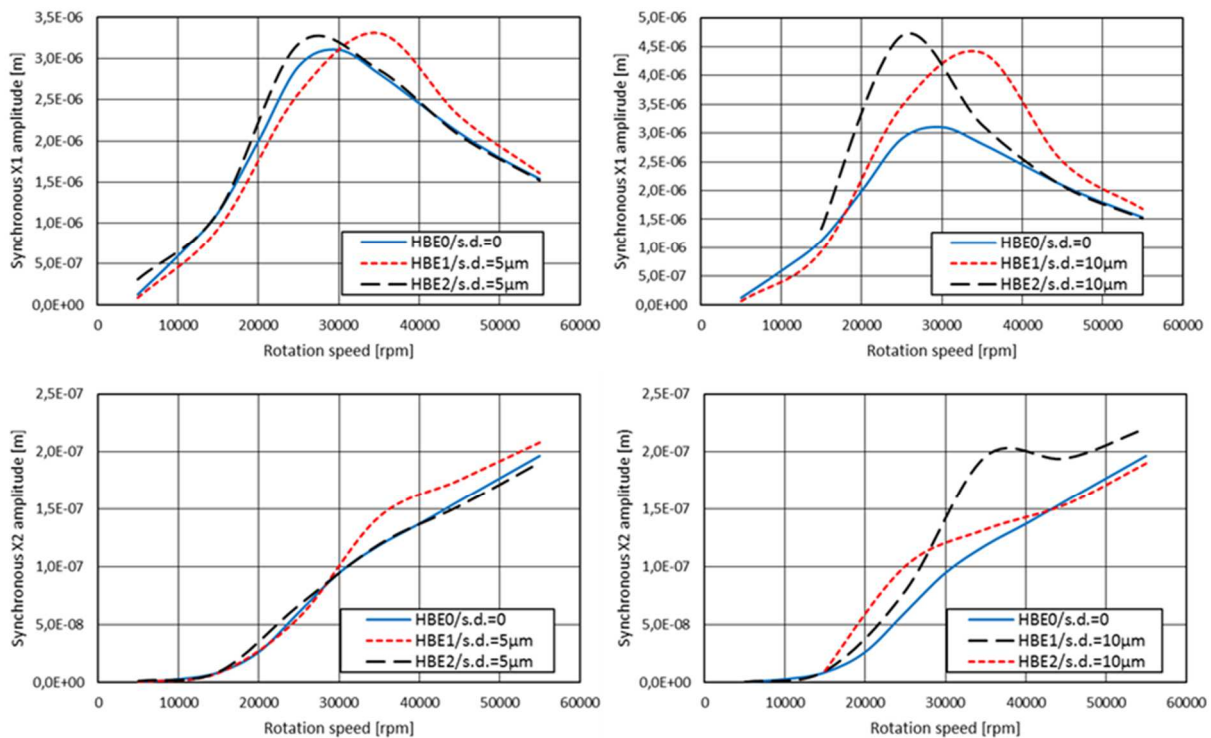


Figure 8. Synchronous amplitudes of the unbalance response of the 4dof rotor-bearing system

7 Conclusion

The bump height errors influence the unbalance response of rotors supported by aerodynamic foil bearings. The present results showed that the value of the resonance speed is moderately modified by the manufacturing errors. This indicates that the stiffness of the foil bearing might either increase or decrease due to manufacturing errors. On the other hand, the values of the resonance amplitudes are always higher when manufacturing errors are present and they increase non-linearly with the magnitude of the errors. This indicates that the damping introduced by the foil bearing decreases with bump height manufacturing errors.

Acknowledgement

The authors are grateful to Centre National d'Etudes Spatiales (CNES) and to Airbus Safran Launchers for supporting this work.

References

- [1] Arghir, M, Benchekroun, O., 2018, "A simplified structural model of bump-type foil bearings based on contact mechanics including gaps and friction", manuscript submitted to Tribol. Int.

- [2] Arghir, M, Benchekroun, O., 2019, "A New Structural Bump Foil Model With Application from Start-up to Full Operating Conditions", accepted for the ASME Turbo Expo 2019.
- [3] Bonello, P., Pham, H. M., 2014, "The efficient computation of the nonlinear dynamic response of a foil-air bearing rotor system", *J. Sound and Vibration*, 333(15): 3459-3478.
- [4] Fatu, A., Arghir, M., 2018, "Numerical Analysis of the Impact of Manufacturing Errors on the Structural Stiffness of Foil Bearings", *ASME J. Eng. Gas Turbines Power*, 140(4): 041506.
- [5] Fatu, A., Arghir, M., 2018, "Influence of Manufacturing Errors on the Unbalance Response of Aerodynamic Foil Bearings", *Proceedings of the 10th International Conference on Rotor Dynamics – IFToMM*.
- [6] Heshmat, H., Walowit, J. A., and Pinkus, O., 1983, "Analysis of Gas-Lubricated Foil Journal Bearings", *ASME J. of Lub. Tech*, 105, pp. 647-655.
- [7] Hoffmann, R., Munz, O., Pronobis, T., Barth, E., Liebich, R., 2016, "A valid method of gas foil bearing parameter estimation: A model anchored on experimental data", *J. Mechanical Engineering Science*, 0(0): 1-18.
- [8] Kim, D., Park, S., 2009, "Hydrostatic Air Foil Bearings: Analytical and Experimental Investigations", *Tribol. Int.*, 42(3): 413-425.
- [9] Le Lez, S., Arghir, M., Frêne, J., 2007, "A New Bump-Type Foil Bearing Structure Analytical Model", *ASME J. Eng Gas Turbines Power*, 129(4): 1047-1057.
- [10] Rubio, D., San Andres, L. Structural Stiffness, 2007, "Dry Friction Coefficient, and Equivalent Viscous Damping in a Bump-Type Foil Gas Bearing", *ASME J. Eng. Gas Turbines Power*, 129(2): 494-502.
- [11] Shalash, K., Schiffmann, J., 2017, "On the manufacturing of compliant foil bearings", *J. Manufacturing Processes*, 25 : 357-368.
- [12] Temis, Y.M., Temis, M.Y., Meshcheryakov, A.B., 2013, "Gas-dynamics Foil Bearing Model", *J. Friction and Wear*, 32(3): 212-220.
- [13] Von Osmanski, S., Larsen, J.S., Santos, I.F., 2017, "A fully coupled air foil bearing model considering friction – Theory & experiment", *J. of Sound and Vibration*, 400: 660-679.
- [14] Wriggers, P, Zavarise, G., 2006, "Computational Contact Mechanics", Springer-Verlag Berlin Heidelberg, Second Edition: 518: 195-226.
- [15] Zywicki G., 2011, "The static performance analysis of the foil bearing structure", *Acta Mechanica et Automatica*, 5(4): 119-122.

Bifurcation Analysis of Rotors on Refrigerant-Lubricated Gas Foil Bearings

Tim Leister^{1,2}, Wolfgang Seemann¹, Benyebka Bou-Said²

¹Institute of Engineering Mechanics (ITM), Karlsruhe Institute of Technology (KIT),
Kaiserstraße 10, 76131 Karlsruhe, Germany, {tim.leister, wolfgang.seemann}@kit.edu

²Contact and Structure Mechanics Laboratory (LaMCoS UMR 5259), INSA Lyon,
27bis, avenue Jean Capelle, 69621 Villeurbanne CEDEX, France, benyebka.bou-said@insa-lyon.fr

Abstract

This paper discusses a comprehensive modeling approach for the fully coupled analysis of rotating machinery using refrigerant-lubricated gas foil bearings (GFBs). To account for possible vapor–liquid phase transitions in the lubricant, a fluid model for non-ideal gases is established by coupling a Peng–Robinson equation of state to a generalized Reynolds equation. Knowing that GFBs are particularly sensitive to energy dissipation in the foil structure, the presented bump foil model captures dry friction by implementing an elasto-plastic bristle friction law. Completed by an adapted Jeffcott–Laval rotor model, the resulting nonlinear dynamical system is investigated making use of numerical bifurcation and stability analysis combined with solution continuation techniques.

1 Introduction and Motivation

With the growing awareness of energy efficiency and environmental sustainability in aeronautics and space engineering, an important technological breakthrough of the 21st century is expected from the further development and promotion of oil-free turbomachinery with high-speed rotors supported by self-acting gas foil bearings (GFBs). Due to the absence of solid-to-solid contact between the bearing structure and the gas-borne rotor journal, GFBs are characterized by almost wear-free operation, an outstandingly low power loss, and the ability to overcome speed, temperature, size, weight, and cleanliness limitations of conventional rolling-element or oil bearings [6]. The remarkable potential of this technology has been confirmed by successful applications in vapor-compression refrigeration systems within air cycle machines of commercial aircraft. In order to reduce the complexity of such systems and thus the susceptibility to failure, it is an obvious choice to simply deploy the surrounding refrigerant (for instance, 1,1,1,3,3-pentafluoropropane) as the lubricating fluid instead of supplying the GFBs with ambient air [5]. Unfortunately, rotors supported by GFBs often suffer from different instability phenomena and tend to exhibit self-excited vibrations with large amplitudes, which may ultimately lead to machine failure [2, 7]. As a countermeasure, the compliant and slightly movable bump foil inside the lubrication gap of most GFBs acts as a passive vibration control device, which dissipates some of the excessive energy by deliberately introduced dry friction [9, 11].

In recent years, research on GFBs has gained a remarkable scientific interest mainly focused on computational analysis, given the complexity and costliness of experiments. Computational time being a highly critical aspect in simulating coupled fluid–structure–rotor interaction models, the lubricant pressure is typically described by a rather simple Reynolds equation for compressible ideal gases [12, 15]. Moreover, it is often avoided to establish realistic foil structure models considering dry friction energy dissipation, knowing that excessively elaborate approaches prove inapplicable for a transient analysis of the dynamical system. However, most notably when investigating refrigerant-lubricated GFBs under severe loading, neither thermodynamic effects such as phase transitions nor dissipative effects inside the foil structure can be neglected without introducing substantial inaccuracies [5, 7].

In this perspective, the present study establishes a fluid model for non-ideal gases by coupling a Peng–Robinson equation of state to a generalized Reynolds equation, thus enabling the prediction of liquid condensation and two-phase flow. Moreover, the novel bump foil model described in this paper captures the true nature of dry friction assuming either regularized Coulomb friction or elasto-plastic bristle friction, the latter being capable of reproducing stiction. Completed by an adapted Jeffcott–Laval rotor model, the resulting nonlinear dynamical system is thoroughly investigated using a monolithic simulation approach. Since brute-force time integration is time-consuming and only of limited suitability for systematic insight into the vast variety of relevant phenomena, this work is the first to make use of bifurcation analysis and solution continuation techniques applied to a refrigerant-lubricated GFB rotor model.

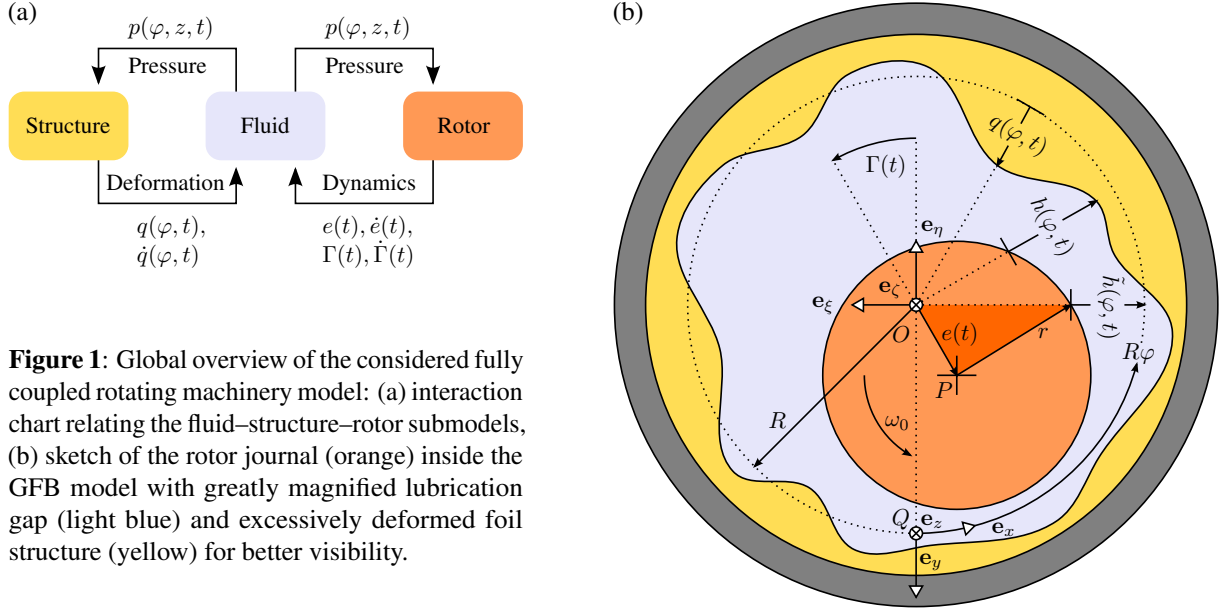


Figure 1: Global overview of the considered fully coupled rotating machinery model: (a) interaction chart relating the fluid–structure–rotor submodels, (b) sketch of the rotor journal (orange) inside the GFB model with greatly magnified lubrication gap (light blue) and excessively deformed foil structure (yellow) for better visibility.

2 Theory and Modeling

The presented rotating machinery model is composed of three mechanical submodels, which are a fluid model for non-ideal gases (see Sec. 2.1), a foil structure model considering dry friction (see Sec. 2.2), and an adapted Jeffcott–Laval rotor model (see Sec. 2.3). Knowing that the pressurized fluid film in the lubrication gap interacts strongly with both the compliant foil structure and the movable rotor shaft [2, 7, 10], a realistic prediction of the nonlinear system dynamics requires a monolithic simulation approach. To this effect, as illustrated by the interaction chart in Fig. 1a, all submodels are fully coupled to each other and, as previously discussed in [1, 2, 8], all governing equations are solved simultaneously. In other words, the ultimate goal is a mathematical description of the entire dynamical system using one single autonomous first-order ordinary differential equation (ODE) system of the form

$$\frac{d\mathbf{x}(\tau)}{d\tau} = \frac{d}{d\tau} \begin{bmatrix} \mathbf{x}_F(\tau) \\ \mathbf{x}_S(\tau) \\ \mathbf{x}_R(\tau) \end{bmatrix} = \mathbf{f} \left\{ \begin{bmatrix} \mathbf{x}_F(\tau) \\ \mathbf{x}_S(\tau) \\ \mathbf{x}_R(\tau) \end{bmatrix}, \Lambda \right\} = \mathbf{f}\{\mathbf{x}(\tau), \Lambda\}. \quad (1)$$

In Eq. (1), the nonlinear vector field $\mathbf{f}: \mathbb{R}^n \times \mathbb{R} \rightarrow \mathbb{R}^n$ depends on the fluid–structure–rotor (FSR) state vector $\mathbf{x}(\tau)$ itself and on the nondimensional rotational speed Λ , which is subsequently considered the bifurcation parameter.

2.1 Fluid Model for Non-Ideal Gases

The bearing geometry is described by the axial length L and by the inner radius R of the undeformed foil structure. Depending on the outer radius r of the rotor journal, the height of the lubrication gap is characterized by a nominal clearance parameter $C = R - r$. Under the thin-film assumption $C/R \ll 1$, any radial dependence of the fluid properties as well as the curvature of the lubrication gap can be neglected, reducing the latter to a two-dimensional, rectangular domain. According to the schematic sketch of the overall model depicted in Fig. 1b, the nondimensional thickness of the fluid film (at any nondimensional instant of time $\tau = t/t_0$) is given by

$$H = H(\varphi, \tau) = \frac{h(\varphi, \tau t_0)}{C} = \overbrace{1}^{\text{Clearance}} - \overbrace{Q(\varphi, \tau)}^{\text{Structure deformation}} - \overbrace{\varepsilon(\tau) \cos[\varphi - \gamma(\tau)]}^{\text{Rotor journal displacement}}, \quad (2)$$

which is a superposition of the nominal clearance, the foil structure deformation field $Q = Q(\varphi, \tau) = q(\varphi, \tau t_0)/C$, and a sinusoidal contribution of the rotor journal displacement obtained by linearization w.r.t. the eccentricity $\varepsilon(\tau) = e(\tau t_0)/C$, whereas the attitude angle is denoted by $\gamma(\tau) = \Gamma(\tau t_0)$. It is evident that Eq. (2) is independent of the axial coordinate Z under the widely accepted assumptions of plane deformations [13, 14] and perfectly aligned

journals [2, 14]. When the bearing is operated within the full fluid film lubrication regime with a continuous gas film thick enough to completely separate the surfaces, the compressible flow in the lubrication gap is governed by

$$\frac{1}{2} \left\{ \overbrace{\frac{\partial}{\partial \varphi} \left[\frac{DH^3}{V(T)} \frac{\partial P(D, T)}{\partial \varphi} \right]}^{\text{Poiseuille flow}} + \kappa^2 \frac{\partial}{\partial Z} \left[\frac{DH^3}{V(T)} \frac{\partial P(D, T)}{\partial Z} \right] - \overbrace{\Lambda \frac{\partial(DH)}{\partial \varphi}}^{\text{Couette flow}} \right\} = \frac{\partial(DH)}{\partial \tau}$$

$$= \underbrace{\frac{\partial D}{\partial \tau}}_{\text{Fluid compression}} H + D \left\{ \underbrace{-\frac{\partial Q}{\partial \tau}}_{\text{Structure squeeze}} - \underbrace{\varepsilon'(\tau) \cos[\varphi - \gamma(\tau)] - \varepsilon(\tau) \gamma'(\tau) \sin[\varphi - \gamma(\tau)]}_{\text{Rotor journal squeeze}} \right\}, \quad (3)$$

which is a generalized, transient form of the classical Reynolds equation [12, 15] with the nondimensional rotational speed (bearing number) $\Lambda = t_0 \omega_0 = 6\mu_0 \omega_0 / p_0 (R/C)^2$. At each of the N_G foil fixation gaps ($\varphi = \varphi_0, \dots, \varphi_{N_G-1}$) and at the unsealed bearing edges ($Z = \pm 1/2$), ambient density is prescribed by appropriate Dirichlet boundary conditions. Given that Eq. (3) involves both the nondimensional density field $D = D(\varphi, Z, \tau) = \rho(\varphi, ZL, \tau t_0) / \rho_0$ and the nondimensional pressure field $P = P(\varphi, Z, \tau) = p(\varphi, ZL, \tau t_0) / p_0$, an additional constitutive equation is required for the solution of this partial differential equation (PDE). Moreover, the nondimensional viscosity field $V = V(\varphi, Z, \tau) = \mu(\varphi, ZL, \tau t_0) / \mu_0$ is directly obtained from the nondimensional temperature field $T = T(\varphi, Z, \tau) = \vartheta(\varphi, ZL, \tau t_0) / \vartheta_0$ by application of Sutherland's law, which is based on an idealized kinetic theory [5].

According to Gibbs' phase rule $N_{\text{DoF}} = 3 - N_{\text{Phases}}$ for a single-component system in thermodynamic equilibrium, the local condition of the fluid is entirely determined by knowledge of at most two independent state variables. Hence, the relation between pressure, density, and temperature is always given by a thermal equation of state, commonly written in the pressure-explicit form $P = P(D, T)$. For the simplest case of an ideal gas law with $P \propto DT$, the resulting phase diagram is shown in Fig. 2a with three exemplary isothermal curves. While this might be a sufficient model for high-temperature applications or when considering GFBs operated with ambient air, the use of a refrigerant such as 1,1,1,3,3-pentafluoropropane typically demands a more sophisticated real gas law. Considering the phase diagram depicted in Fig. 2b, it is evident that such a nonlinear equation of state must be capable of reproducing phase boundaries and phase transitions at constant equilibrium vapor pressure. Following a proposition by Garcia et al. [5], the considered refrigerant can be modeled in good approximation by the cubic Peng–Robinson equation of state

$$P_{\text{PR}}(D, T) = \frac{1}{p_0} \left[\frac{R_m \vartheta_0 T}{\left(\frac{M_m}{\rho_0 D} \right) - b} - \frac{a(\vartheta_0 T)}{\left(\frac{M_m}{\rho_0 D} \right)^2 + 2b \left(\frac{M_m}{\rho_0 D} \right) - b^2} \right], \quad (4)$$

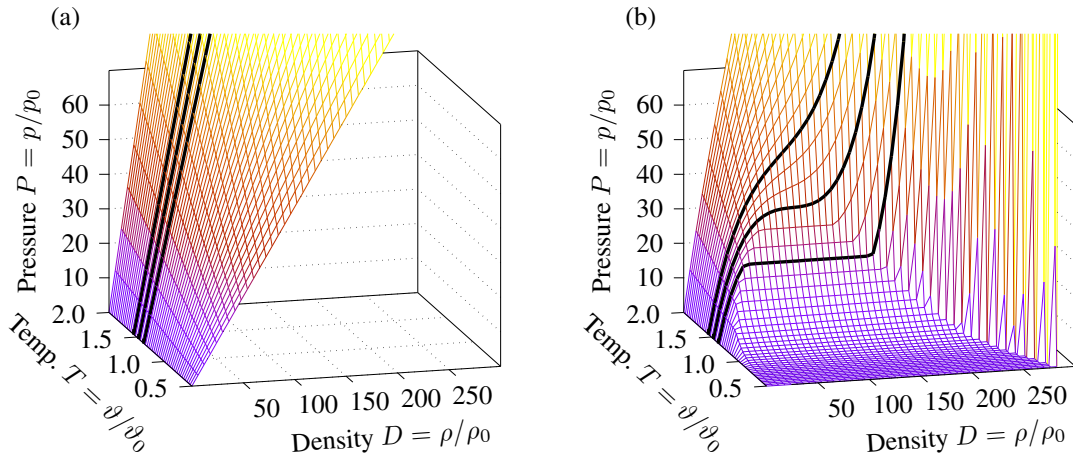


Figure 2: P, D, T phase diagrams based on (a) an ideal gas law and (b) a real gas law.

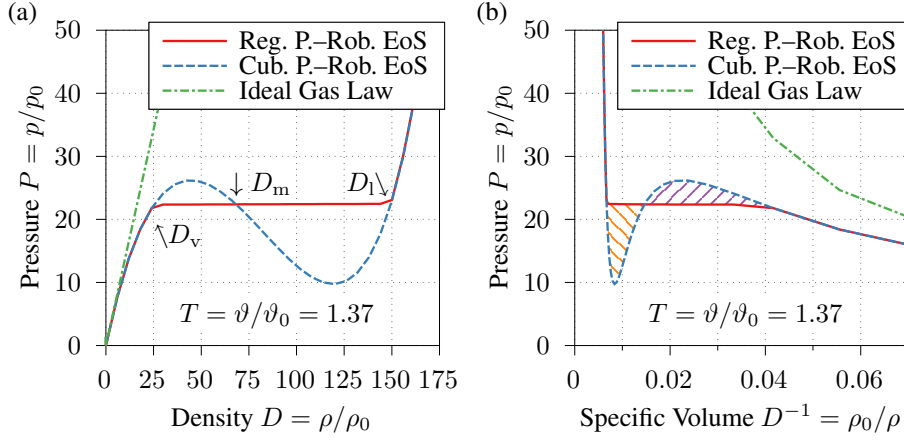


Figure 3: Efficient phase transition regularization of the Peng–Robinson eq. of state visualized in (a) the P, D phase diagram and (b) the P, D^{-1} phase diagram with inverted abscissa.

with the temperature-dependent molecular cohesion parameter

$$a(\vartheta_0 T) \approx 0.46 R_m^2 \frac{\vartheta_c^2}{p_c} \left[1 + \left(0.38 + 1.5 \omega_a - 0.17 \omega_a^2 + 0.020 \omega_a^3 \right) \left(1 - \sqrt{\frac{\vartheta_0 T}{\vartheta_c}} \right) \right] \quad (5)$$

and the constant molecular covolume $b \approx 0.078 R_m \vartheta_c / p_c$. In these expressions, the molar gas constant R_m , the molar mass M_m , the critical pressure p_c , the critical temperature ϑ_c , and the acentric factor ω_a are readily obtained from a suitable database of fluid properties [5].

For temperatures inferior to the critical temperature (i.e., $T < \vartheta_c / \vartheta_0$), the cubic function from Eq. (4) takes a characteristic s-shape as shown in Fig. 3a by the dashed blue curve. The resulting negative slopes with $\partial P / \partial D < 0$ violate a necessary condition for thermodynamic stability, thus making the analytical model nonphysical in such regions. To overcome this deficiency, the pure vapor and the pure liquid zones must be connected by straight two-phase coexistence curves at the temperature-dependent equilibrium vapor pressure $P_{\text{sat}}(T)$. According to the classical Maxwell construction, the equilibrium vapor pressure must be such that the orange and the purple areas in the phase diagram with inverted abscissa in Fig. 3b become equal. However, computational times can be improved without significant loss of accuracy by fitting the solution of a simplified Clausius–Clapeyron equation

$$P_{\text{sat}}(T) = \exp\left(C_0 - C_1 T^{-1} - C_2 \ln T\right) \quad (6)$$

to values obtained from a database of fluid properties [5]. When setting equal Eqs. (4) and (6), the resulting cubic equation $P_{\text{PR}}(D, T) = P_{\text{sat}}(T)$ has up to three real roots $D_v(T) < D_m(T) < D_l(T)$, which can be calculated algebraically. Eventually, the strictly increasing solid red curve in Fig. 3a is found by introducing a very small regularization slope. Knowing the roots $D_v(T)$ and $D_l(T)$, the mass fraction of liquid is obtained by the lever rule

$$W_l(D, T) = \frac{D - D_v(T)}{D_l(T) - D_v(T)}. \quad (7)$$

Using the regularized Peng–Robinson equation of state, pressure can be eliminated in Eq. (3) and the Reynolds equation is then solved for the time derivative of density $\partial D / \partial \tau$ (fluid compression). All spatial derivatives are approximated by a finite difference upwind scheme on a uniform computational grid with $\Delta \varphi = 2\pi / (N_\varphi - 1)$ and $\Delta Z = 1 / (N_Z - 1)$. After splitting the domain according to the number of foil fixation gaps N_G and taking advantage of the axial symmetry, a reduced number of discrete density values $D_{i,j}(\tau)$ is collected in the state vector

$$\mathbf{x}_F(\tau) = \left[\cdots D_{i,j}(\tau) D_{i,j+1}(\tau) \cdots D_{i+1,j}(\tau) D_{i+1,j+1}(\tau) \cdots \right]^\top \in \mathbb{R}^{\frac{1}{2}(N_\varphi - N_G - 1)(N_Z - 1)}. \quad (8)$$

This approach is original in the sense that it integrates the non-ideal gas law directly into the simultaneously solved dynamical system from Eq. (1) instead of treating the Peng–Robinson eq. of state and the Reynolds eq. in a sequential procedure. As this paper focuses on qualitative effects of the non-ideal fluid behavior, the energy equation is ignored and only isothermal conditions with prescribed average temperature throughout the film are considered.

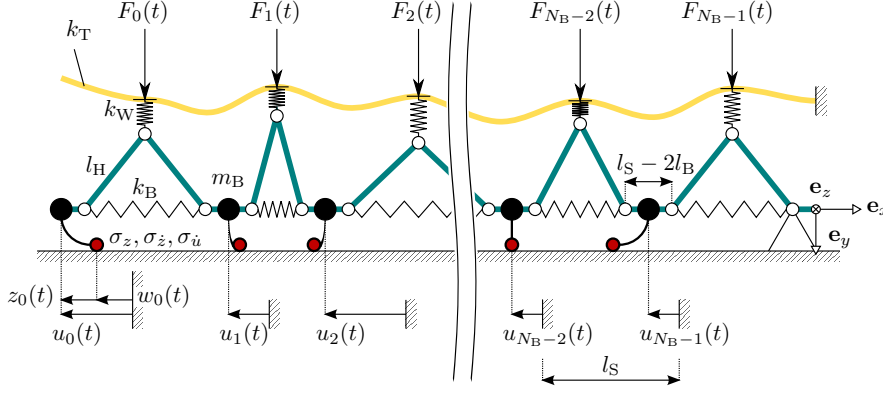


Figure 4: Sketch of the lumped-element foil structure model, which implements dry friction based on an elasto-plastic bristle friction law.

2.2 Foil Structure Model Considering Dry Friction

The sketch in Fig. 4 shows the lumped-element foil structure model, in which each of the N_B bumps (width $2l_B$, undeformed apices spaced by $l_S = 2\pi R/N_B$) is modeled as a triangular arrangement of two massless rods (length l_H) and a horizontal spring (stiffness k_B). Despite the foil mass being negligible even in a transient analysis of the overall model [10], discrete particles (mass m_B) are introduced under the bumps for the sole purpose of obtaining a system of ODEs instead of differential-algebraic equations (DAEs). Taking into account the fixation of the foil strip and the interaction between adjacent bumps, the nondimensional apex deflection of the n -th triangle is a function of two mass particle displacements $U_n(\tau) = u_n(\tau t_0)/C$ and $U_{n+1}(\tau) = u_{n+1}(\tau t_0)/C$, giving the kinematic relation

$$Q_n(\tau) = \frac{q_n(\tau t_0)}{C} = \frac{1}{2} \sqrt{4L_H^2 - [2L_B + U_n(\tau) - U_{n+1}(\tau)]^2} - \sqrt{L_H^2 - L_B^2}. \quad (9)$$

On top of each triangle, another spring (stiffness k_W) accounts for possible deformations even when both ends of a bump are stuck due to friction. As indicated by the yellow curve in the sketch, the top foil is represented by a segmented beam model superposed to the bump foil model, according to an earlier publication by the authors [8].

For the consideration of dry friction in a transient GFB analysis based on numerical time integration, the authors have proposed [9] the implementation of an elasto-plastic bristle friction law according to Dupont et al. [4], which allows to capture presliding displacements and true stiction without spurious drift. Using such a dynamic friction model, the elastic deformation of the n -th bristle (stiffness σ_z) is described by the nondimensional displacement $Z_n(\tau) = z_n(\tau t_0)/C$, whereas the corresponding plastic deformation, obviously identified with the covered sliding distance in Fig. 4, writes $W_n(\tau) = w_n(\tau t_0)/C = U_n(\tau) - Z_n(\tau)$. Resulting from the pressurized fluid film and from a constant nondimensional preload force $f_{\perp,p}$ due to mounting, the nondimensional normal force acting on the n -th contact zone between bump foil and bearing sleeve is approximated by

$$f_{\perp,n}(\tau) = \max \left\{ 0, \int_{(n-\frac{1}{2})L_S}^{(n+\frac{1}{2})L_S} \int_{-\frac{1}{2}}^{+\frac{1}{2}} [P(\varphi, Z, \tau) - P_0] dZ d\varphi + f_{\perp,p} \right\}, \quad (10)$$

with the maximum function ensuring that nonphysical negative normal forces are cut off in the case of foil detachment. The dynamics of the internal state variables $Z_n(\tau)$ being governed by N_B additional ODEs, the nondimensional friction forces are finally retrieved from the elastic restoring forces of the deformed bristles. Despite the elasto-plastic friction model being superior to most other friction models in quantitative simulations of the isolated foil structure, it appears unreasonably complex for the identification of qualitative effects concerning the overall system dynamics. As a matter of fact, comparisons between different friction models reveal that it is usually sufficient to assume a regularized Coulomb friction law with sliding friction coefficient μ_C , which neglects the existence of true stiction and the accompanying non-uniqueness of solutions. In this case, friction forces between bump foil and bearing sleeve are obtained after smoothing the sign-change discontinuity around zero-velocity by

$$\text{sgn } U'_n(\tau) \approx \tanh \Xi U'_n(\tau), \quad \Xi \gg 1. \quad (11)$$

The generic foil structure model can be adapted to multi-pad GFBS with N_G foil fixation gaps oriented by some angle χ . However, to keep formulas short and clear, only equations obtained for a GFB with one foil strip fixed at $\varphi = 0$ (i.e., $\chi = 0$) are stated in this paper. According to the classical Euler–Lagrange equations evaluated for the discussed lumped-element model, the dynamics of the bump foil structure are governed by the equations of motion

$$\begin{aligned} \begin{bmatrix} U_0(\tau) \\ U_1(\tau) \\ \vdots \\ U_{N_B-2}(\tau) \\ U_{N_B-1}(\tau) \end{bmatrix}'' + \Omega_B^2 \begin{bmatrix} +1 & -1 & & 0 \\ -1 & +2 & -1 & \\ & \ddots & \ddots & \ddots \\ & & -1 & +2 & -1 \\ 0 & & & -1 & +2 \end{bmatrix} \begin{bmatrix} U_0(\tau) \\ U_1(\tau) \\ \vdots \\ U_{N_B-2}(\tau) \\ U_{N_B-1}(\tau) \end{bmatrix} \\ = \frac{1}{M_B} \left\{ \begin{bmatrix} \phi_0(\tau) \\ \phi_1(\tau) - \phi_0(\tau) \\ \vdots \\ \phi_{N_B-2}(\tau) - \phi_{N_B-3}(\tau) \\ \phi_{N_B-1}(\tau) - \phi_{N_B-2}(\tau) \end{bmatrix} - \mu_C \begin{bmatrix} f_{\perp,0}(\tau) \tanh \Xi U'_0(\tau) \\ f_{\perp,1}(\tau) \tanh \Xi U'_1(\tau) \\ \vdots \\ f_{\perp,N_B-2}(\tau) \tanh \Xi U'_{N_B-2}(\tau) \\ f_{\perp,N_B-1}(\tau) \tanh \Xi U'_{N_B-1}(\tau) \end{bmatrix} \right\}, \quad (12) \end{aligned}$$

with the effective fluid pressure leading to the generalized force components

$$\phi_n(\tau) = \frac{1}{2} \frac{2L_B + U_n(\tau) - U_{n+1}(\tau)}{\sqrt{4L_H^2 - [2L_B + U_n(\tau) - U_{n+1}(\tau)]^2}} \int_{nL_S}^{(n+1)L_S} \int_{-\frac{1}{2}}^{+\frac{1}{2}} [P(\varphi, Z, \tau) - P_0] dZ d\varphi. \quad (13)$$

For the computational analysis, a state-space representation of Eq. (12) is established introducing the state vector

$$\mathbf{x}_S(\tau) = [U_0(\tau) \ U'_0(\tau) \ \cdots \ U_{N_B-1}(\tau) \ U'_{N_B-1}(\tau)]^T \in \mathbb{R}^{2N_B}. \quad (14)$$

2.3 Adapted Jeffcott–Laval Rotor Model

To capture a possible maximum of relevant rotordynamic phenomena while still being computationally efficient, an adapted Jeffcott–Laval rotor model with unbalanced disk is considered in the following. As visualized by the sketch in Fig. 5, the shaft of stiffness k is symmetrically mounted on two GFBS and the horizontal rotor is exposed to gravity. In contrast to the classical Jeffcott–Laval rotor model, a small proportion $\alpha/2$ (with $0 < \alpha \ll 1$) of the total mass m is shifted from the disk to each of the journals such that a system of ODEs instead of DAEs can be stated [1]. Possible dissipative effects caused by the working fluid, which circulates around the rotor disk, are represented by a stationary (i.e., nonrotating) viscous damping b .

The journal positions are described by the Cartesian coordinates $X(\tau) = \xi(\tau t_0)/C$ and $Y(\tau) = \eta(\tau t_0)/C$, whereas the coordinates of the disk are denoted by $X_D(\tau) = \xi_D(\tau t_0)/C$ and $Y_D(\tau) = \eta_D(\tau t_0)/C$. For coupling the journal motion to the fluid model via the film thickness expression from Eq. (2), the Cartesian coordinates must be transformed to polar coordinates. When assessing the dynamics of the rotor, it is sufficient to analyze only the

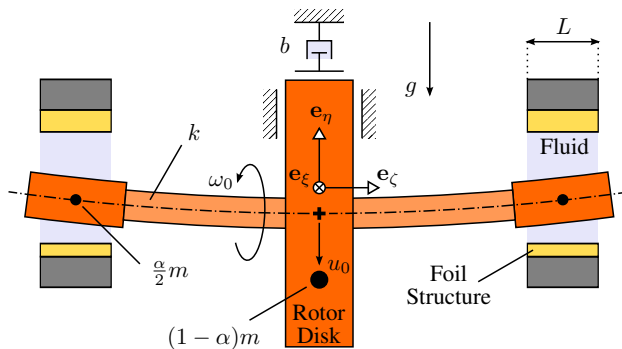


Figure 5: Sketch of the adapted Jeffcott–Laval rotor model, which is mounted on two GFBS.

bearing force created by one of the GFBs due to the assumption of symmetry, giving the equations of motion

$$\begin{aligned}
\begin{bmatrix} X(\tau) \\ Y(\tau) \\ X_D(\tau) \\ Y_D(\tau) \end{bmatrix}'' + \frac{2B\Omega}{1-\alpha} \begin{bmatrix} 0 & 0 & 0 & 0 \\ 0 & 0 & 0 & 0 \\ 0 & 0 & 1 & 0 \\ 0 & 0 & 0 & 1 \end{bmatrix} \begin{bmatrix} X(\tau) \\ Y(\tau) \\ X_D(\tau) \\ Y_D(\tau) \end{bmatrix}' + \Omega^2 \begin{bmatrix} \frac{1}{\alpha} & 0 & -\frac{1}{\alpha} & 0 \\ 0 & \frac{1}{\alpha} & 0 & -\frac{1}{\alpha} \\ -\frac{1}{1-\alpha} & 0 & \frac{1}{1-\alpha} & 0 \\ 0 & -\frac{1}{1-\alpha} & 0 & \frac{1}{1-\alpha} \end{bmatrix} \begin{bmatrix} X(\tau) \\ Y(\tau) \\ X_D(\tau) \\ Y_D(\tau) \end{bmatrix} \\
= \underbrace{\frac{2}{\alpha M} \int_0^{2\pi} \begin{bmatrix} \sin \varphi \\ \cos \varphi \\ 0 \\ 0 \end{bmatrix} \int_{-\frac{1}{2}}^{+\frac{1}{2}} P(\varphi, Z, \tau) dZ d\varphi}_{\text{Scaled bearing force}} - \underbrace{G \begin{bmatrix} 0 \\ 1 \\ 0 \\ 1 \end{bmatrix}}_{\text{Gravity}} - \underbrace{U_0 \Lambda^2 \begin{bmatrix} 0 \\ 0 \\ \sin(\Lambda\tau) \\ \cos(\Lambda\tau) \end{bmatrix}}_{\text{Disk unbalance}}. \quad (15)
\end{aligned}$$

When deriving a state-space representation of Eq. (15), the rotor disk unbalance obviously violates the requirement of an autonomous ODE system stated in Eq. (1). Following a common approach to solve this issue, two coupled nonlinear and self-excited oscillators [3]

$$\begin{aligned}
s_\Lambda'(\tau) &= +\Lambda c_\Lambda(\tau) - s_\Lambda(\tau) \left[s_\Lambda(\tau)^2 + c_\Lambda(\tau)^2 - 1 \right], \\
c_\Lambda'(\tau) &= -\Lambda s_\Lambda(\tau) - c_\Lambda(\tau) \left[s_\Lambda(\tau)^2 + c_\Lambda(\tau)^2 - 1 \right]
\end{aligned} \quad (16)$$

are artificially added to the equations of motion, knowing that they possess asymptotically stable solution components $s_\Lambda(\tau) = \sin(\Lambda\tau)$ and $c_\Lambda(\tau) = \cos(\Lambda\tau)$. Consequently, the periodic forcing terms in Eq. (15) can be directly substituted by two newly introduced state variables in order to obtain an autonomous ODE system. Altogether, an appropriate state-space representation is found using the state vector

$$\mathbf{x}_R(\tau) = \left[X(\tau) \ X'(\tau) \ Y(\tau) \ Y'(\tau) \ X_D(\tau) \ X_D'(\tau) \ Y_D(\tau) \ Y_D'(\tau) \ s_\Lambda(\tau) \ c_\Lambda(\tau) \right]^\top \in \mathbb{R}^{10}. \quad (17)$$

3 Results and Discussion

The numerical results presented hereafter are based on data of a bump-type GFB with three pads, similar to GFBs discussed in a great number of both experimental and numerical investigations [13, 14]. In the code, following an object-oriented modular concept, the right-hand side \mathbf{f} of Eq. (1) is assembled by calling a submodel library implemented in C++ according to Eqs. (3), (12), and (15). For the bifurcation and stability analysis, this submodel library is then linked to AUTO 2000, a widely-used software package written in C, which implements an orthogonal collocation method for the continuation of periodic solutions [3]. The use of compiled programming languages makes it possible to explore even high-dimensional state-spaces \mathbb{R}^n with $n \gg 100$ within only a few minutes.

3.1 Classification of Possible Bifurcation Scenarios

Prior to looking at some important effects due to non-ideal gas behavior, dry friction, and rotor shaft deformations, it appears indispensable to firstly understand in principle what kind of bifurcation scenarios can possibly be observed for 3-pad GFB rotor systems. Therefore, in the first part of this study, the limiting case of a rigid rotor in rigid GFBs is considered under high-temperature conditions, which legitimates the use of an ideal gas law with $P \propto DT$.

The bifurcation diagram in Fig. 6a visualizes stationary and periodic solutions found for the simplified system by plotting minima and maxima of the vertical rotor displacement as a function of rotational speed. Moreover, the a priori unknown subsynchronous frequencies of the periodic solutions are traced in Fig. 6b in relation to the speed-synchronous frequency. For a rather lightweight rotor (green curve: $m = 50$ g), the initially stable equilibrium points become unstable at some critical speed Λ_c via a supercritical Hopf bifurcation (HB). At the bifurcation point, a branch of limit cycle oscillations, stable according to the Floquet multipliers, is born and causes the characteristic half-frequency whirling with $\Lambda_{\text{sub}} \approx \Lambda/2$. Looking at a mediumweight rotor (orange curve: $m = 250$ g), the occurring HB is now identified as being subcritical, which means that limit cycle oscillations directly emerging from the bifurcation point are unstable. Following the branch, however, these periodic solutions become stable via a limit point of cycles bifurcation (LP) at some speed inferior to the critical speed Λ_c at the HB, suggesting that one

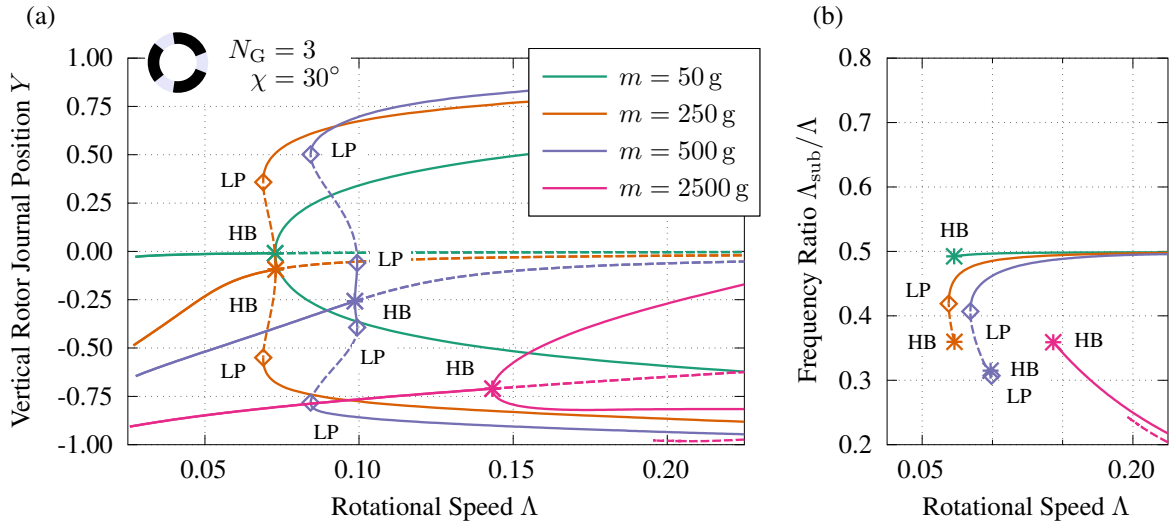


Figure 6: Bifurcation diagrams showing (a) vertical rotor journal displacements and (b) vibration frequency ratios for different rotor masses found by numerical solution continuation with rot. speed Λ as bifurcation parameter (solid lines: stable solutions, dashed lines: unstable solutions, HB: Hopf bifurcation, LP: limit point of cycles bifurcation). The symbol in the upper left corner visualizes the foil fixation gap orientation of the vertically loaded 3-pad GFBs.

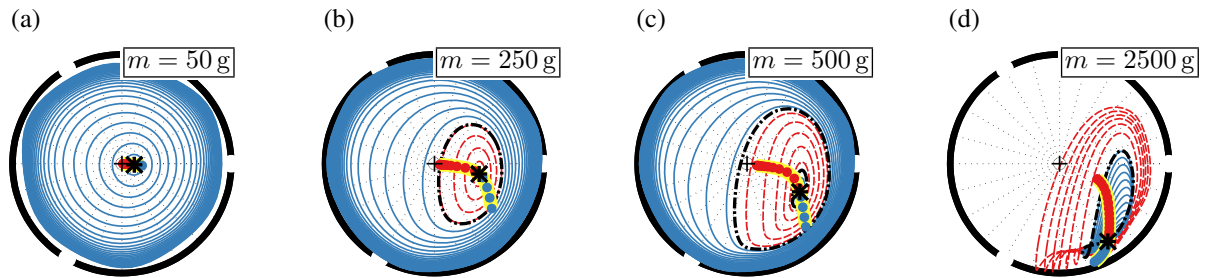


Figure 7: Rotor journal operating points and orbits for (a)–(d) different rotor masses (blue dots: stable stationary solutions, red dots: unstable stationary solutions, black asterisk: Hopf bifurcation, blue solid lines: stable periodic solutions, red dashed lines: unstable periodic solutions, black chain-dotted lines: limit point of cycles bifurcation).

stationary and one periodic solution may coexist in the phase-space. From the frequency ratio diagram, it can be observed that half-frequency whirling motions slow down as the rotor mass is increased. When considering a rather heavyweight rotor (blue curve: $m = 500$ g), the HB becomes supercritical again, but is now followed by a double LP. In this very interesting case, there is a possible coexistence of two periodic solutions in the phase-space with very distinct amplitudes and frequencies. The primary periodic branch gains influence with growing rotor mass (magenta curve: $m = 2500$ g), whereas the secondary branch finally goes undetected when the fluid film collapses.

Projecting some of the n -dimensional solutions onto the rotor journal coordinate subspace as shown in Figs. 7a–d, it becomes even more obvious that varying the rotor mass may have strong qualitative effects on the stationary operating point locus curve (dots on yellow background) and the shapes of periodic orbits. Interestingly, stable limit cycle oscillations with vibration amplitudes small enough to be tolerable for operation seem to be possible throughout the investigated range of rotor masses, notwithstanding the structural change of the underlying phase-space.

3.2 Influence of Rotor Shaft Flexibility

As is generally known, the flexibility of any real rotor shaft may add important effects to the dynamics of rotating machinery, which cannot be reproduced by considering perfectly rigid rotor models. Therefore, the second part of this study compares the behavior of the flexible Jeffcott–Laval rotor model ($m = 500$ g) with varying stiffness k to results from Sec. 3.1 based on a rigid rotor model. During the comparison, the simplifying assumptions of an ideal gas law and of rigid GFBs are maintained so that all sensitivities can be directly attributed to the stiffness parameter.

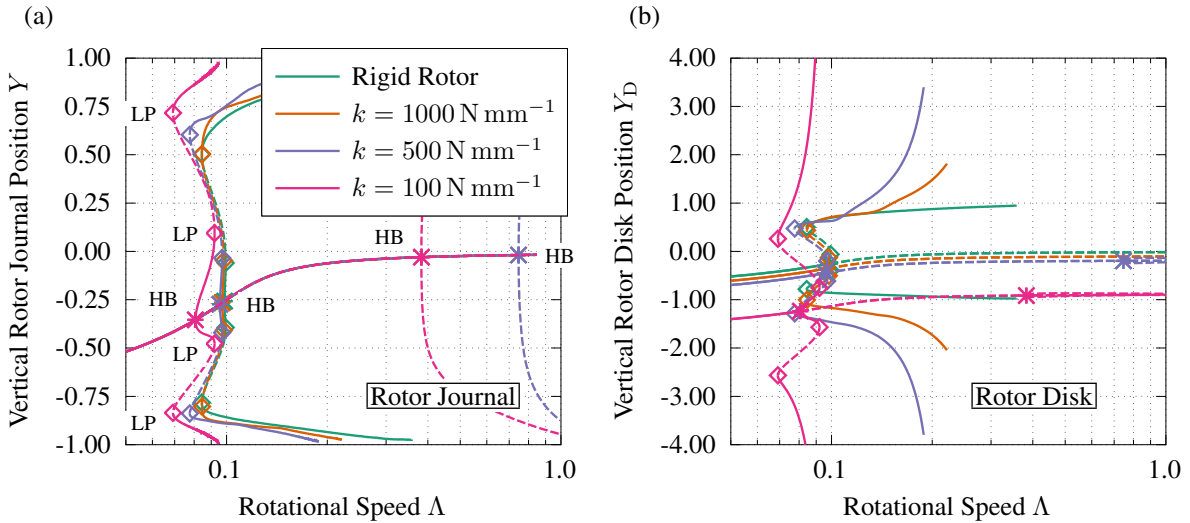


Figure 8: Bifurcation diagrams showing vertical (a) rotor journal displacements and (b) rotor disk displacements for different rotor shaft flexibilities found by numerical solution continuation (see Fig. 6 for line types and symbols).

The vertical displacements of the rotor journal are visualized by the bifurcation diagram in Fig. 8a, whereas the plot in Fig. 8b shows the corresponding behavior of the rotor disk. Coming from the limiting case of a rigid rotor (green curve), it can be observed that the double limit point of cycles bifurcation (LP) becomes more important as the rotor shaft is getting more flexible. For an extremely low shaft stiffness (magenta curve: $k = 100 \text{ N mm}^{-1}$), the equilibrium point is destabilized at a significantly lower speed, but the onset of self-excited vibrations is stable over a relatively wide range and exhibit only small amplitudes. However, the secondary branch of periodic solutions shows a sudden critical rise in amplitudes directly related to the natural frequency of the rotor. The occurrence of a second Hopf bifurcation (HB) is not further investigated in the present study as this happens only at rotational speeds beyond the interesting operating range.

3.3 Significance of Fluid Model Refinements

It becomes evident from Eqs. (13) and (15) that both structural dynamics and rotor dynamics are strongly influenced by the actual shape of the pressure field. In this regard, the implications of a non-ideal gas behavior merit a closer look in the following third part of the analysis, in which the considered equation of state is varied.

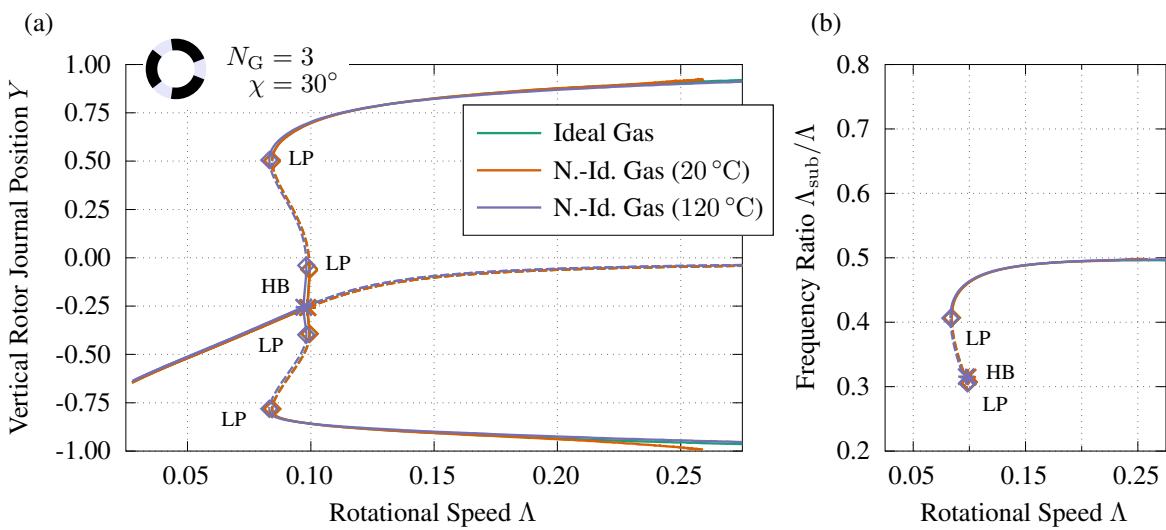


Figure 9: Bifurcation diagrams showing (a) vertical rotor journal displacements and (b) vibration frequency ratios for different equations of state found by numerical solution continuation (see Fig. 6 for line types and symbols).

According to the bifurcation diagrams in Figs. 9a–b, there seem to be only slight and purely quantitative differences between the results predicted by an ideal gas law (green curve) and the results obtained with the regularized Peng–Robinson equation of state (orange and blue curves). However, when the non-ideal gas law is parameterized with a rather low temperature such as 20 °C, it turns out that the rotor journal is actually predicted to suddenly collide with the lower part of the bearing structure at $\Lambda \approx 0.25$ (orange curve). This can be explained by the fact that the pressure field is obviously bounded by the temperature-dependent equilibrium vapor pressure, at which liquid droplet formation begins abruptly once the (mostly dynamic) loading induces a critical pressurization. Notwithstanding the importance of this pressure-limiting effect, the evaluation of the mass fraction of liquid reveals that only less than 1 % of the fluid are actually condensed in the concerned regions. Moreover, taking into account that heat transfer typically leads to elevated fluid temperatures such as 120 °C under heavy loading conditions (blue curve), this detrimental effect of the refrigerant behavior may be compensated due to the increasing vapor pressure.

3.4 Passive Vibration Control by Dry Friction

In the last part of the analysis, the ability of the foil structure to dissipate excessive energy by deliberately introduced dry friction is investigated by considering the lumped-element model with varying friction coefficient μ_C in the regularized Coulomb friction law. The essential question is whether and to what extent this passive mechanism stabilizes the system and if it is therefore capable of avoiding or mitigating unwanted self-excited vibrations.

The bifurcation diagram in Fig. 10a suggests that already by the simple addition of structural compliance, with or without friction, the characteristic supercritical HB succeeded by a double LP vanishes and only subcritical HBs are possible. In addition to the resulting delay of vibration onset, there is also an amplitude reduction compared to rigid GFBs (magenta curve) if the friction coefficient is chosen appropriately (e.g., blue curve: $\mu_C = 0.8$). Plotted in Fig. 10b, the frequencies of periodic solutions also show a strong dependence on the friction coefficient.

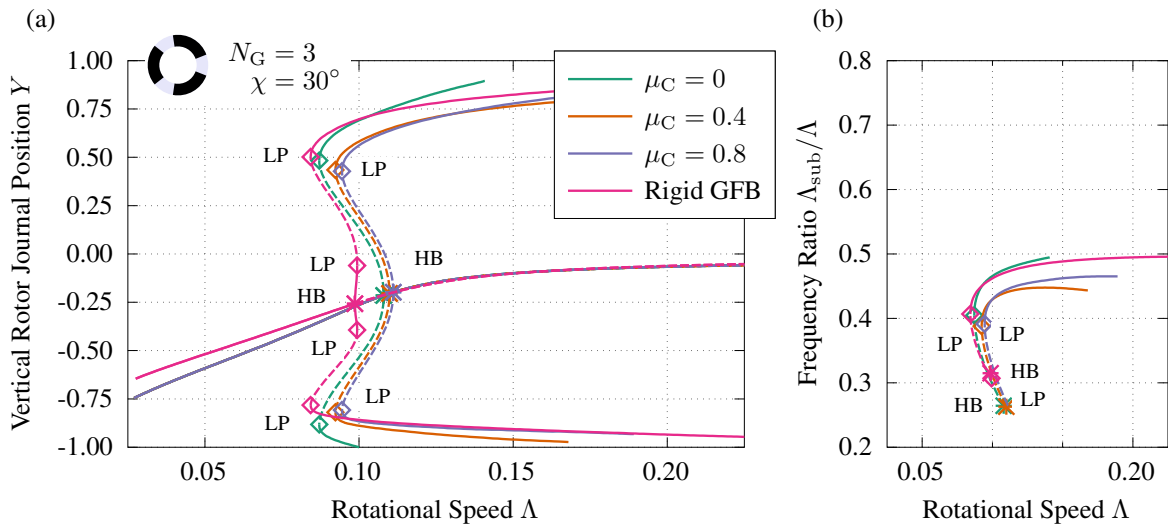


Figure 10: Bifurcation diagrams showing (a) vertical rotor journal displacements and (b) vibration frequency ratios for different friction coefficients found by numerical solution continuation (see Fig. 6 for line types and symbols).

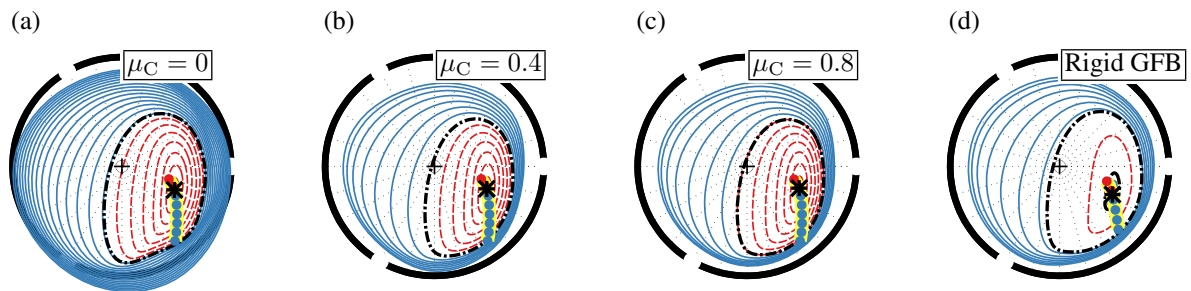


Figure 11: Rotor journal op. points and orbits for (a)–(d) diff. friction coeff. (see Fig. 7 for line types and symbols).

The importance of frictional energy dissipation within the foil structure is confirmed by the rotor orbits visualized in Figs. 11a–d. Apparently, compliant GFBs exhibiting a minimum amount of vibration can only be constructed if a properly designed foil structure adds an adequate amount of energy dissipation to the system. Even though the rigid model also performs well, excessively stiff GFBs are of limited practical use because structural compliance stabilizes stationary operating points (see above), increases manufacturing tolerances, and improves thermal resistance.

4 Conclusion and Perspective

This paper discusses the bifurcation and stability analysis of rotating machinery using refrigerant-lubricated gas foil bearings (GFBs) by implementing three fully coupled submodels for the fluid, the foil structure, and the rotor. Depending on system parameters such as rotor mass or shaft flexibility, qualitatively different bifurcation scenarios may lead to the occurrence of either harmless or dangerous self-excited vibrations. When reproducing a realistic refrigerant behavior by a regularized Peng–Robinson equation of state, it can be observed that the lubricant pressurization is bounded by the temperature-dependent equilibrium vapor pressure, thus limiting the operating range. Finally, the consideration of a lumped-element foil structure model proves that GFB rotor systems benefit from structural compliance as long as an adequate amount of frictional energy dissipation can be passively provided.

Future work will focus on an extension of the fluid model with regard to non-isothermal conditions and heat transfer inside the lubrication gap. Moreover, the presented fluid–structure–rotor model will be subject to more detailed analyses considering further bifurcation scenarios and mechanisms preventing subsynchronous vibrations.

References

- [1] C. Baum, T. Leister, and W. Seemann. Foil air bearing rotor interaction – Bifurcation analysis of a Laval rotor. In *Proceedings of the EUROMECH Colloquium 573*, Lyon, France, 2015.
- [2] P. Bonello and H. M. Pham. The efficient computation of the nonlinear dynamic response of a foil-air bearing rotor system. *Journal of Sound and Vibration*, 333(15):3459–3478, 2014. doi:10.1016/j.jsv.2014.03.001.
- [3] E. J. Doedel, R. C. Paffenroth, A. R. Champneys, T. F. Fairgrieve, Y. A. Kuznetsov, B. E. Oldeman, B. Sandstede, and X. Wang. AUTO 2000: Continuation and bifurcation software for ordinary differential equations (with HomCont). Technical report, California Institute of Technology, USA, 2002.
- [4] P. Dupont, V. Hayward, B. Armstrong, and F. Altpeter. Single state elastoplastic friction models. *IEEE Transactions on Automatic Control*, 47(5):787–792, 2002. doi:10.1109/TAC.2002.1000274.
- [5] M. Garcia, B. Bou-Saïd, J. Rocchi, and G. Grau. Refrigerant foil bearing behavior – A Thermo-HydroDynamic study (Application to rigid bearings). *Tribology International*, 65:363–369, 2013. doi:10.1016/j.triboint.2012.12.006.
- [6] H. Heshmat, J. A. Walowit, and O. Pinkus. Analysis of gas-lubricated foil journal bearings. *Journal of Lubrication Technology*, 105(4):647–655, 1983. doi:10.1115/1.3254697.
- [7] T. Leister, C. Baum, and W. Seemann. On the importance of frictional energy dissipation in the prevention of undesirable self-excited vibrations in gas foil bearing rotor systems. *Technische Mechanik*, 37(2–5):280–290, 2017. doi:10.24352/UB.OVGU-2017-104.
- [8] T. Leister, C. Baum, and W. Seemann. Computational analysis of foil air journal bearings using a runtime-efficient segmented foil model. *Journal of Fluids Engineering*, 140(2):021115, 2018. doi:10.1115/1.4037985.
- [9] T. Leister, W. Seemann, and B. Bou-Saïd. Passive vibration control by frictional energy dissipation in refrigerant-lubricated gas foil bearing rotor systems. *Proc. Appl. Math. Mech.*, 18(1), 2018.
- [10] S. von Osmanski, J. S. Larsen, and I. F. Santos. A fully coupled air foil bearing model considering friction – Theory & experiment. *Journal of Sound and Vibration*, 400:660–679, 2017. doi:10.1016/j.jsv.2017.04.008.
- [11] J.-P. Peng and M. Carpino. Calculation of stiffness and damping coefficients for elastically supported gas foil bearings. *Journal of Tribology*, 115(1):20–27, 1993. doi:10.1115/1.2920982.
- [12] O. Reynolds. On the theory of lubrication and its application to Mr. Beauchamp Tower’s experiments, including an experimental determination of the viscosity of olive oil. *Philosophical Transactions of the Royal Society of London*, 177:157–234, 1886.
- [13] D. Ruscitto, J. McCormick, and S. Gray. Hydrodynamic air lubricated compliant surface bearing for an automotive gas turbine engine, I – Journal bearing performance. Technical Report NASA CR-135368, National Aeronautics and Space Administration, USA, 1978.
- [14] L. San Andrés and T. H. Kim. Analysis of gas foil bearings integrating FE top foil models. *Tribology International*, 42(1):111–120, 2009. doi:10.1016/j.triboint.2008.05.003.
- [15] A. Z. Szeri. *Fluid film lubrication*. Cambridge University Press, Cambridge, UK, 2nd edition, 2010.

Analysis, Monitoring, Diagnose & Prognosis

Motor Bearing Damage Detection Based on Vibration Data

John J. Yu¹, **Nicolas Péton**²

¹Machinery Diagnostics Technical Leader, Baker Hughes a GE Company (Bently Nevada), 30339, Atlanta, USA, john.yu@bhge.com

²MDS Global Director, Baker Hughes a GE Company (Bently Nevada), 44300, Nantes, France, nicolas.peton@bhge.com

Abstract

This case study shows that rolling element bearing damage on an extruder was detected from on-line remote monitoring vibration data. Though vibration level was well below the acceptable limit, its abnormal signatures warranted a shutdown action. It was then observed that for each bearing, the whole outer raceway was spalled circumferentially into a “washboard” pattern. This was caused by electrical corrosion or fluting due to poor insulation resulted from damaged insulating washers. After replacing the bearings with insulated ones, vibration level and signatures have then become normal ever since its restart.

1 Introduction

It is often a practice in the field that vibration level determines whether a machine is safe to operate or not. This may not be true for rolling element bearing machines. Besides the magnitude of direct (broadband) vibration, its signatures should be reviewed carefully that includes its spectrum and/or timebase data. Its vibration trending should also be monitored closely. Otherwise, unanticipated machine failure would occur. The current case study discusses a rolling element bearing failure on a motor where vibration amplitude was still far below the acceptable level.

Rolling element bearings are widely used in many machines, especially on electrical motors where they can be crucial for daily operations in some petrochemical plants. Harris addressed all aspects of rolling element bearings from design to maintenance in [1]. Numerous research papers in detecting rolling element bearing defects have been published. The author even developed defect detection methodology using high-gain displacement transducers in [6]. Most researchers have used casing-mounted transducers to diagnose the rolling element bearing defects, as shown in [2] and [5]. Qiu, etc. explained bearing defects and lifespan from spectrum plots in [3]. Case studies have often been presented to show how defects would look like as shown in [4].

In the current case, velocity transducers were installed on motor bearing casing for monitoring vibration. When vibration level was found trending up slightly but still well below the acceptable limit, in-depth review of vibration data was carried out, which led to successful detection of severe outer race damage. Its root-cause of outer race failure was also found with a good action plan.

2 Case Study

This was a pelletizer motor supported by two deep groove ball bearings at a petrochemical facility, as shown in Figure 1. Motor was running at 350-390 rpm. Vibration was monitored by velocity transducers at each end of bearing housing. Continuous safe operation of its extruder and pelletizer is crucial to daily petrochemical processing. When all vibration data was reviewed on this machine, it was observed that both DE and NDE motor vibration readings slightly trended up but still were very low. Could the machine still be operated continuously without any action? It would be a big loss if a malfunction developed to destroy the machine and have an unscheduled forced outage. However, shutdown of the unit for inspection with lost production without finding anything malfunctions would be very costly as well.

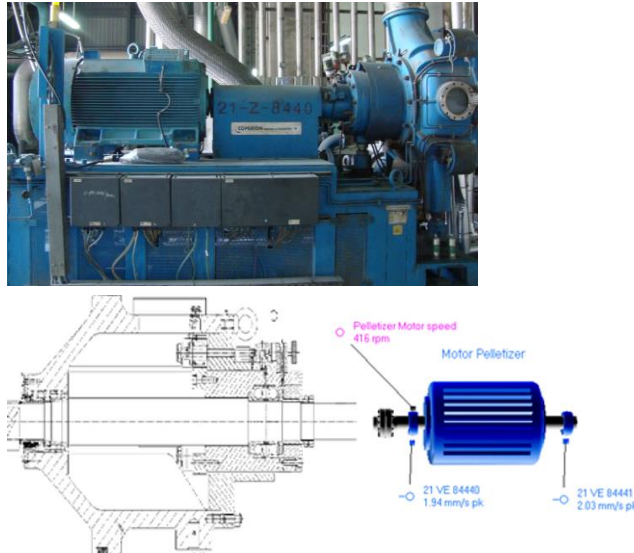


Figure 1: Pelletizer motor supported by rolling element bearings

2.1 Problem Statement

Vibrations on this machine including motor bearings were measured by casing-mounted velocity transducers with an on-line remote monitoring system. High vibration readings triggered alarm events on this extruder. The alarms, however, occurred in other locations, not on motor bearings. These alarms were later found to be due to signal noise issues. When vibrations at adjacent locations were also examined at that time, direct amplitudes were found trending up from two velocity sensors mounted on DE and NDE bearings of the motor, as shown in Figure 2. It was observed that vibration readings had slowly trended up from approximately 2 mm/s pk to 3 mm/s pk at running speed of about 380 rpm. The readings were still within the acceptable limit. Would the machine still be safe to keep its running, or need to shut down for some actions?

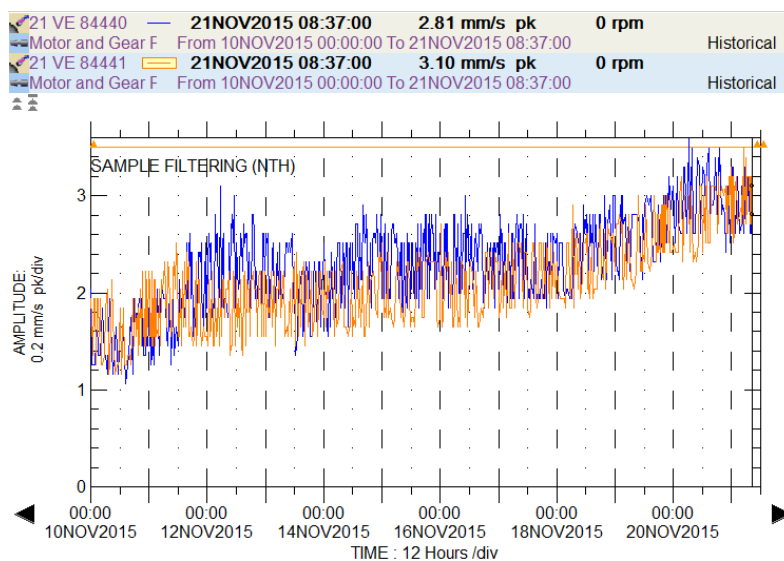


Figure 2: Motor bearing vibration trending up but still within the acceptable limit

2.2 Data review

The motor speed was fairly stable, and varied only with slight step changes due to changes in operational condition, as shown in Figure 3. The vibration trend did not seem to match speed trend completely. From 14NOV2015 to 20 NOV2015, speed was almost constant, but vibration amplitude slowly increased if comparing speed and vibration trends. In order to know the root-cause of growing vibration, waterfall plots at DE and NDE bearings were reviewed. Figures 4 and 5 shows their corresponding waterfall plots within this time period. At DE bearing as shown in Figure 4, spectrum was fairly clean at the very beginning besides speed-related components and possible low-frequency noise from the transducer. But a frequency component at around 233-237 Hz plus rich harmonics of 26-26.3 Hz later appeared and gradually increased. The step change in frequency was due to the step change in running speed from 380 to 385 rpm. These components seemed to be real, not due to any signal noise issue. The 237 Hz happened to be approximately 9 times 26.3 Hz at speed of 385 rpm. Similar vibration signatures were also observed at NDE bearing as shown in Figure 5.

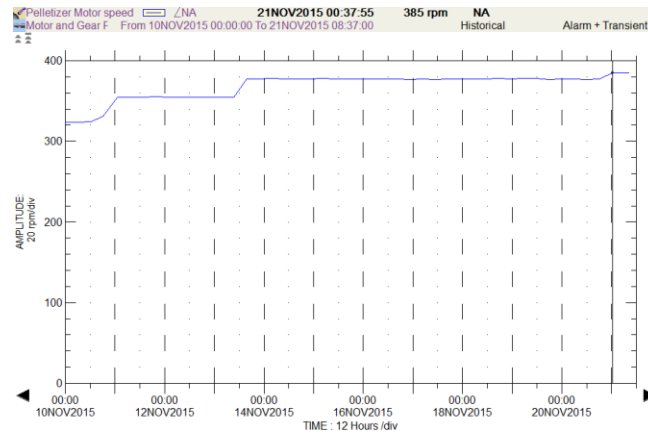


Figure 3: Motor speed trend, comparison with vibration trends in Figure 2

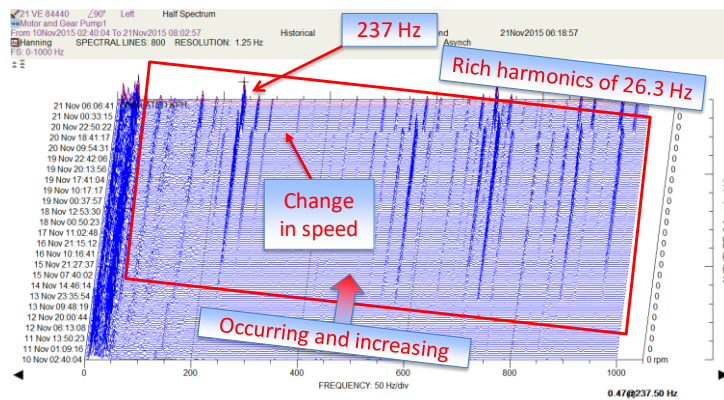


Figure 4: Waterfall plot at DE bearing

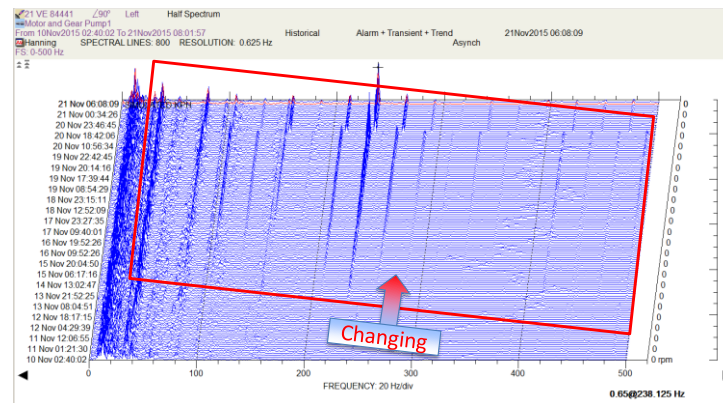


Figure 5: Waterfall plot at NDE bearing

Spectrum plots at 385 rpm were reviewed at both bearings, as shown in Figures 6 and 7. It was found that increasing vibration was due to 26.3 Hz harmonics, which was about 4.1 times shaft speed. The 237 Hz (9x26.3 Hz) component could be close to one of the natural frequencies of the rotor/bearing system of the motor.

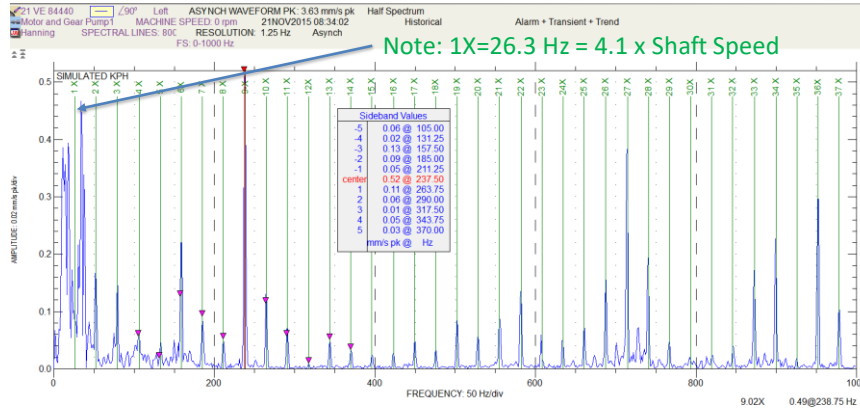


Figure 6: Spectrum plot at DE bearing, showing vibration climbing due to 26.3 Hz harmonics

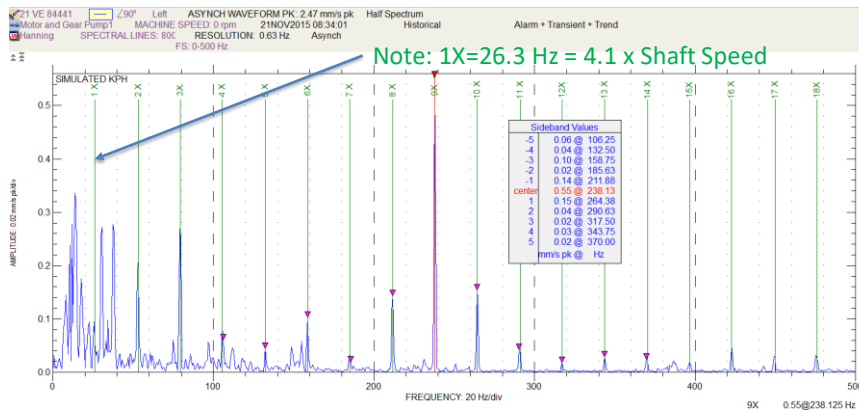


Figure 7: Spectrum plot at NDE bearing, showing vibration climbing due to 26.3 Hz harmonics

Rolling element bearing defects, are usually associated with fault frequencies in spectrum plot. These excitation frequencies are dependent of bearing geometry and shaft speed. If the bearing dimensions are known, these frequencies can be calculated. There are four defect frequencies: Ball-Pass-Frequency of Inner race (BPIF), Ball-Pass-Frequency of Outer race (BPFO), Fundamental Train Frequency (FTF) or cage frequency, and Ball Spin Frequency (BSF). Their expressions are as below:

$$BPIF = \frac{z}{2}(1 + \gamma)(\Omega_i - \Omega_o) \quad (1)$$

$$BPFO = \frac{z}{2}(1 - \gamma)(\Omega_i - \Omega_o) \quad (2)$$

$$FTF = \frac{1}{2}[\Omega_i(1 - \gamma) + \Omega_o(1 + \gamma)] \quad (3)$$

$$BSF = \frac{1}{2} \frac{d}{D}(1 - \gamma^2)(\Omega_i - \Omega_o) \quad (4)$$

where

z = number of balls

$$\gamma = \frac{D}{d} \cos \alpha$$

D = ball diameter

d = pitch diameter

α = contact angle

Ω_i = inner race speed

Ω_o = outer race speed (0 if outer race is fixed, and negative if opposite to Ω_i)

For this bearing, its defect frequencies can be obtained as shown in Table 1. If expressed in terms of shaft speed, its outer race defect frequency can be given in the following format:

$$BPFO = 4.1 \times \text{shaft speed}$$

Table 1: Bearing fault frequencies at 385 rpm

Bearing Data		Output
SKF bearing designation*	6220 Search	<input checked="" type="radio"/> Hertz <input type="radio"/> CPM <input type="radio"/> Orders
Measurement system	<input checked="" type="radio"/> Metric <input type="radio"/> Imperial	Shaft speed frequency 6.417 Hz
Bearing type*	DGGB	Inner race defect frequency (BPFI) 37.904 Hz
Pitch diameter*	140 mm	Outer race defect frequency (BPFO) 26.263 Hz
Rolling element diameter*	25.4 mm	Cage defect frequency (FTF) 2.626 Hz
Number of rolling elements (per row)*	10	Ball spin frequency (BSF) 17.102 Hz
Contact angle*	0.0 degrees	Rolling element defect frequency 34.203 Hz
Rotational speed*	385 rpm	
Rotating ring*	<input checked="" type="radio"/> inner <input type="radio"/> outer	

Therefore, Figures 4 to 7 clearly indicates outer race damage. Could the unit still run continuously without shutdown now?

2.3 Bearing life estimation

Reference [3] discusses about four stages of bearing remaining life in terms of frequency zones (A, B, C, and D). They can be summarised as shown in Figures 8 and 9.

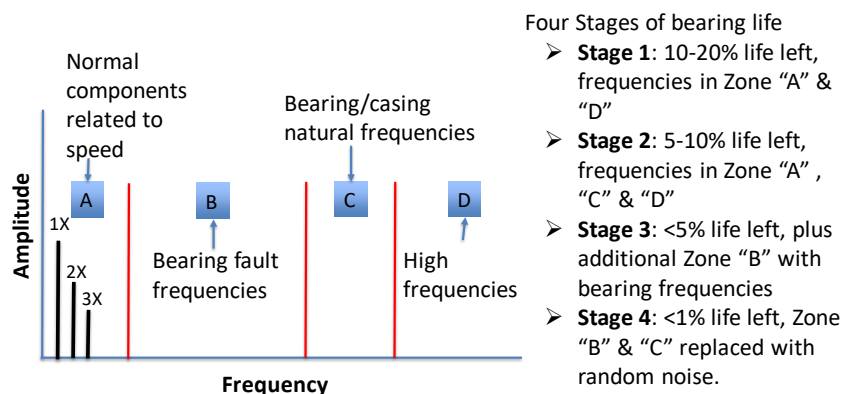


Figure 8: Four frequency zones (A, B, C, and D) related to four stages of bearing life

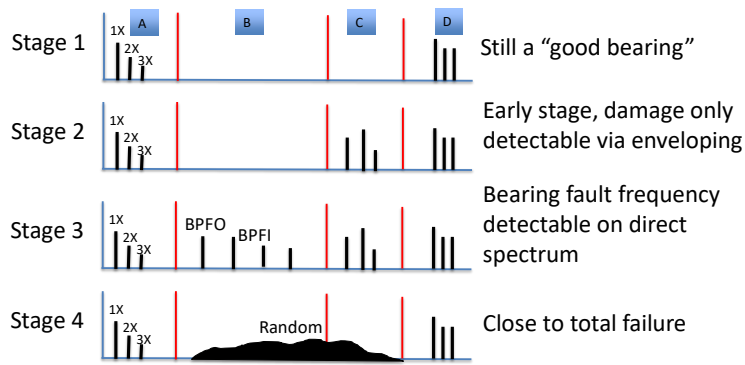


Figure 9: Four stages of bearing life based on frequency zones

The current outer race damage seemed to be in later Stage 3, towards Stage 4, as BPFO frequency and its harmonics could be seen clearly in classical spectrum, without having to utilize enveloping techniques. Its progression of damage appeared to be fast as shown in waterfall plots (See Figures 4 and 5).

2.4 Recommendations

After on-line remote data review and diagnosis, similar vibration signatures were measured via off-line portable devices. The following recommended actions were made quickly:

- Stop the machine within a few days
- Inspect the two bearings to confirm the damage
- Find the root-cause of the damage
- Install the new bearings

2.5 Inspection and findings

The machine was shut down 3 days after the initial diagnosis and recommendations. It was observed that both inboard and outboard rolling element bearings were severely damaged. For each bearing, the whole outer raceway was spalled circumferentially into a unique “wash-boarding” pattern plus worn balls and inner race, as shown in Figures 10 and 11.



Figure 10: DE bearing damage during inspection

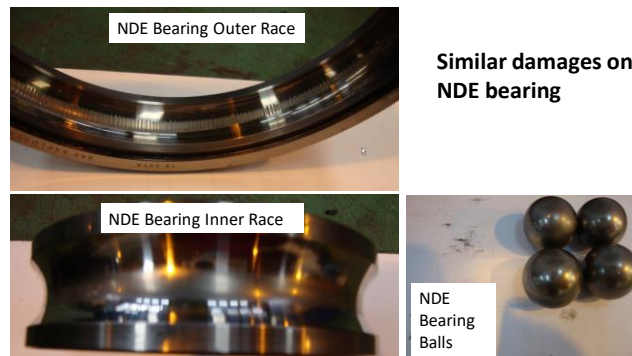


Figure 11: NDE bearing damage during inspection

This “washboarding” pattern damage seemed to indicate that electrical erosion was the culprit, likely due to poor insulation to prevent electric currents from passing through. Further investigation found that insulated washers were damaged on the end cover of NDE bearing, as shown in Figure 12.



Figure 12: Insulated washers damaged on end cover of NDE bearing

The root-cause can be explained as shown in Figure 13. The presumed insulation was broken due to damaged insulation washers. Then the stator and rotor generated charge accumulation, which passed through the motor shaft to the bearings and discharged from the balls with enough energy to pit the outer race, resulting in electrical corrosion or fluting.

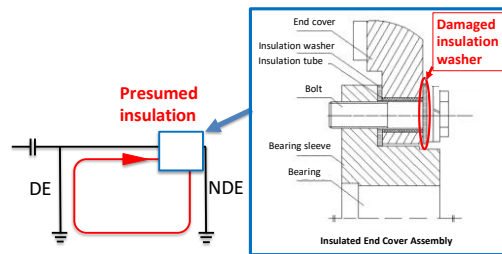


Figure 13: Illustration of root-cause of the bearing damage

The bearings were then replaced with insulated bearings. Vibration levels and signatures have then become normal ever since its restart.

2.6 Resolution and final vibration results

Since the insulation washer had not been reliable to prevent electrical corrosion, insulated bearings were installed to replace the previously damaged ones. On these insulated bearings, aluminum oxide is coated on the external surface of outer ring for electrical resistance. As shown in Figure 14, no loop can be formed for electrical current with insulated bearings.

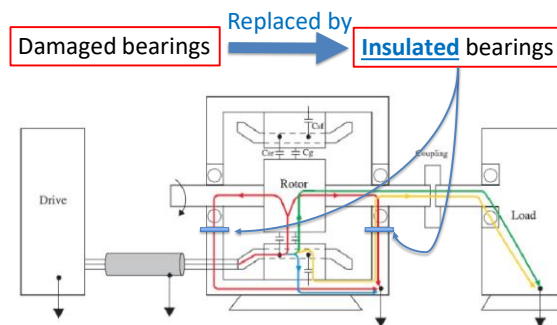


Figure 14: Replacement with insulated bearings as resolution

After the bearing replacement, the machine was started with low but stable vibration readings as shown in Figure 15. Abnormal 26.3 Hz and its rich harmonics totally disappeared as shown in Figure 16.

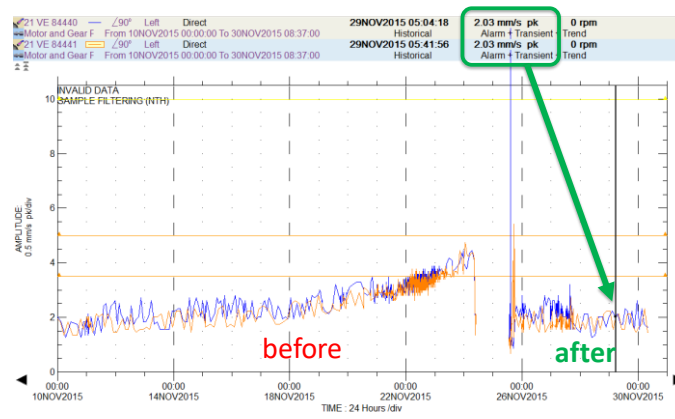


Figure 15: Vibration trend before and after bearing replacement

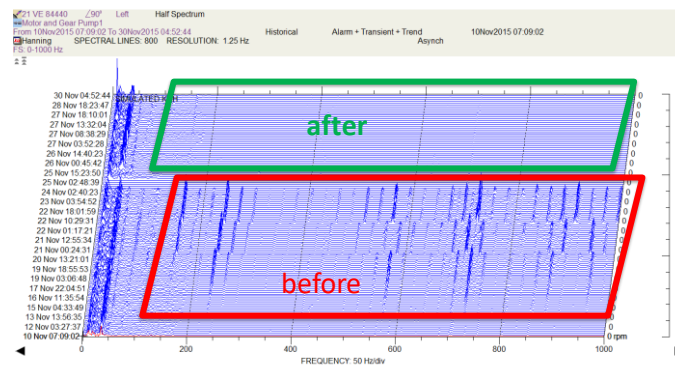


Figure 16: Vibration spectrum before and after bearing replacement

3 Discussions and Summary

If the machine had continued its operation with the damaged bearings while maintaining electric arcing without knowledge, further deterioration would have led to complete bearing failure, and unscheduled equipment downtime and unanticipated maintenance costs would have likely followed. Electric erosion can damage bearings very fast, and rolling elements can be welded to the raceways.

It is shown in this case that even if vibration is still within the acceptable level, it cannot warrant no malfunction. A change in vibration is more important than vibration level itself. Examining and understanding of the change are crucial to ensure a safe reliable operation of the machine.

References

- [1] Harris, T.A. (1991): Rolling Element Bearing Analysis. John Wiley & Sons, Inc.
- [2] Mathew, J., and Alfredson, R. J., (1984): The Condition Monitoring of Rolling Element Bearings Using Vibration Analysis, Transactions of the American Society of Mechanical Engineers, Journal of Vibration and Acoustics, (106), pp. 447– 453.
- [3] Qiu, H., Luo, H. and Eklund, N. (2009): On-board bearing prognostics in aircraft engine: Enveloping analysis or FFT? AFRL-RX- WP - TP -2009-4141, Air Force Research Laboratory, USA.
- [4] Upadhyay R.K., Kumaraswamidhas, L.A., and Sikandar Azam, Md. (2013): Rolling element bearing failure analysis: A case study. Case Studies in Engineering Failure Analysis (1) 15–17.
- [5] Wang, D., and Miao, Q. (2015): Some Improvements on a General Particle Filter Based Bayesian Approach for Extracting Bearing Fault Features. Transactions of the American Society of Mechanical Engineers, Journal of Vibration and Acoustics, (137), 041016-1.
- [6] Yu, J. J., Bently, D.E, Goldman, P., Dayton, K.P., and Van Slyke, B.G. (2002): Rolling Element Bearing Defect Detection and Diagnostics Using Displacement Transducers. Transactions of the American Society of Mechanical Engineers, Journal of Engineering for Gas Turbines and Power, (124), pp.517-527.

Using measured transmission error for diagnostics of gears

Robert B Randall¹, **Dikang Peng**², **Wade A Smith**³

¹ School of Mechanical and Manufacturing Engineering, UNSW Sydney, 2052 Sydney, Australia,
b.randall@unsw.edu.au

² dikang.peng@unsw.edu.au

³ wade.smith@unsw.edu.au

Abstract

It was shown many years ago that gear transmission error (TE) could be measured very accurately using high quality shaft encoders on the free ends of the shafts on which the gears are mounted. TE is defined as the difference in torsional vibration of the gears, scaled so as to represent linear motion along the line of action. The torsional vibration can be measured most accurately using phase demodulation of the encoder pulse signals, since the accuracy of the encoders themselves corresponds to fractions of a micron of TE. The main intended application at the time was to measure the TE in operation at different speeds and loads. We are now applying TE measurement to a wider range of diagnostic applications, such as measuring the geometric TE (low speed, low load), and loaded TE, including elastic deformation of teeth etc (low speed, full torque), and finally dynamic TE, including dynamic effects at higher speed (full speed, full torque). This can be used to update simulation models which should be much simpler for torsional models than for complete models, including lateral DOFs and many irrelevant resonances. Torsional models are also much less susceptible to modulations due to the passage of faults past a fixed transducer. Even where only the overall TE can be measured, between the input and output of a gear train, the TE for an individual stage can be extracted by synchronous averaging.

1 Introduction

It was shown as long ago as 1996 [1] that the simplest and most accurate way of measuring gear transmission error (TE) is by using phase demodulation of the pulse signals from high quality shaft encoders on the free ends of the shafts on which the gears are mounted. TE is defined as the difference in torsional vibration of the gears, scaled so as to represent linear motion along the line of action, this being common to the two gears in mesh, as opposed to the angular deviations, directly obtained by phase demodulation, which are scaled according to the pitch radius of the gears. It is convenient to divide TE up into three categories, (1) Geometric TE (GTE), obtained when the load is only sufficient to keep the gear teeth in contact, and thus tending to be dominated by local high spots on individual teeth, (2) Static TE (STE), which takes into account static (ie stiffness controlled) elastic deformations of the teeth, and (3) Dynamic TE (DTE), where the loads on the teeth, and thus tooth deflections, are dependent on dynamic loads, due to inertial effects at higher speeds where the stiffness controlled deformations are no longer dominant.

It has recently been realised that these three types of TE can be measured experimentally, as long as it is possible to make measurements over a sufficiently wide range of speeds and loads. GTE can be measured at low speed, low load; STE at low speed, high load; and DTE at high speed, high load, and the purpose of this paper is to demonstrate some of the advantages to be gained from this.

Firstly, the TE signal itself is much closer to the source than response vibration measurements, and does not have the wide variation of the latter (through different transmission paths) and so provides a very robust condition indicator. Secondly, simulation models of the rotational degrees-of-freedom (DOFs) are much simpler than those involving much more numerous lateral DOFs, and even when the latter are included, the rotational DOFs are often largely decoupled, and not influenced by resonances such as many that are primarily related to the casing. Thirdly, simulation models often require an estimate of GTE as an input to the dynamic model, and this can be directly measured at several stages through the operation of the gearbox, rather than just assuming a typical (random)

pattern scaled according to the gear quality, or requiring the modified profile to be inferred from vibration measurements, a much more difficult proposition.

Note that the concept of using the measured TE as a diagnostic parameter has been suggested before, and is summarised in Section 5.4.2 of [2], but was only described for the TE encountered under operating conditions.

2 Test setups and measurements

Two gearbox test rigs were used to illustrate different aspects of the topic. The first is a single stage spur gear reduction gearbox, with 19 teeth on the input pinion and 52 teeth on the driven gear, with module 2. It is shown in Fig. 1.

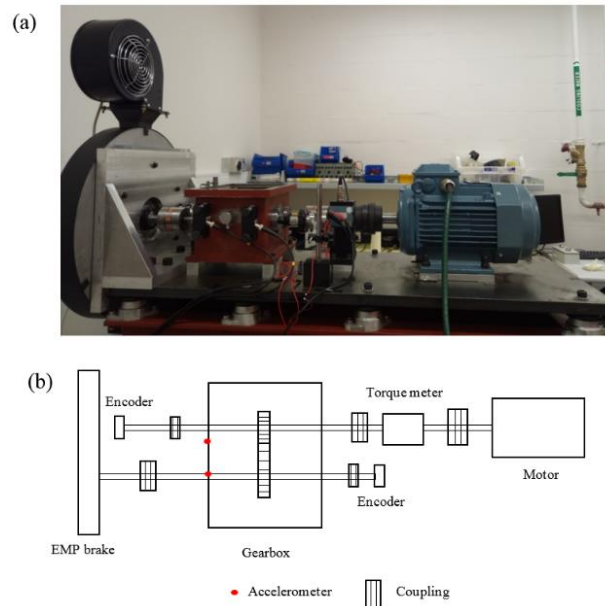


Figure 1: The spur gear test rig at UNSW. (a) photo; (b) schematic diagram

The 4 kW drive motor has a variable frequency drive (VFD) and variable torque load is applied by an electromagnetic particle (EMP) brake. The “encoders” are actually slip rings with a built-in encoder, but it was discovered in doing the measurements that there is a resonance at just over 200 Hz which limits the use of the encoders for high frequency measurements. The highest input shaft rotational speed for which TE could be measured up to a reasonable number of harmonics of the gearmesh frequency was 2 Hz, even though measurements had been done for speeds up to 20 Hz. The results from this rig are thus limited to measurements of GTE and STE, since inertial effects were only significant at higher speeds. Vibration responses at higher speeds can, however, be shown.

The two encoders give a once-per-rev tachometer signal as well as 512 per rev encoder pulses, and recordings were made of all these as well as vibration signals from two accelerometers (B&K type 4394 and 4396) mounted on the upper rim of the casing above the bearings at the brake end of the gearbox. The initial sample rate was 100 kHz on all channels.

The second test rig is shown in Figure 2 and has a planetary gear set driven by an input parallel gear reduction stage with ratio 42T:55T. The planet carrier forms the input to the planetary gear set, which consists of three equi-spaced 23T planets, a fixed 80T ring gear and a 34T sun gear (output). All planetary stage gears are module 2. The AC induction motor has a VFD, but the circulating power hydraulic motor/pump system is able to apply considerably higher torque to the gearbox, than that delivered by the electric motor itself. The two timing belt drives, introduced for alignment purposes, are in fact 1:1 ratio, and do not change the overall transmission ratio from motor to brake.

The two encoders mounted on the free ends of the input and output shafts of the gearbox are both Heidenhain type ROD 426, but that on the input shaft gives 900 pulses per rev (ppr) and that on the output shaft gives 225 ppr, and both also give once-per-rev tachometer signals. Accelerometer measurements are taken from the top of the ring gear.

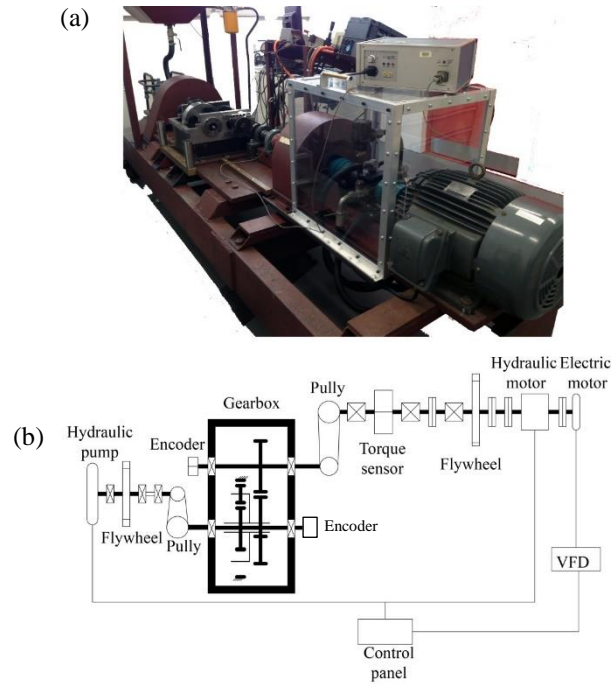


Figure 2: The planetary gear test rig at UNSW. (a) photo; (b) schematic diagram

3 Results and discussion

3.1 Parallel gear rig

A series of experiments was carried out on this rig to develop natural faults. The gears were of mild steel, whose properties were such that they would fail through surface distress before developing tooth root cracks. The gears were run at a series of different speeds and loads, and periodically through the series, moulds were taken of a number of teeth around both the pinion and gear, in order to monitor the development of surface pits. The impressions could be made in situ during the tests, without dismantling the gearbox.

The surface profile of the impressions could be measured using a laser scanner, but here only microscopic photographs of the tooth flanks are used to show the development of the surface. Pits often develop close to the pitchline, because this is where the sliding velocity is zero, and thus the oil film has the greatest likelihood of breaking down. It is also usually where the whole load is taken by a single tooth pair rather than shared between two. However, in this case the pitting first occurred close to the base of the pinion tooth, where the tip of the mating tooth comes into mesh, possibly because there was no tip relief, and an impulsive contact would occur. Figure 3 shows a series of stages of the development of this pitting on the pinion, each of whose teeth had a greater number of contacts in proportion to the rotational speed. The results are for a particular tooth (aligned to show the same section), but the deterioration was fairly uniform around the gear. Pitting on the gear was similar but more sparse, and it occurred much later in the test.

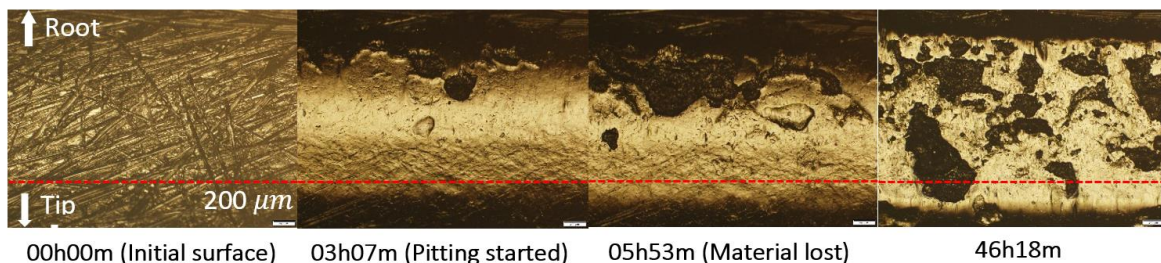


Figure 3: Development of pitting after different times of operation. Horizontal dotted line shows pitchline.

The encoder signals were first order tracked using the tacho signals as reference, and using the phase demodulation method described in [2]. The TEs between the input and output shaft were then measured by first phase demodulating each encoder signal, as described in [1]. Rather than scaling the TE to the distance along the line of action, it has been scaled as equivalent rotation of the input shaft (in radians) by multiplying that of the output

shaft by the gear ratio before subtraction, and then detrended. When performing the demodulation, the bandwidth was reduced to the total spread of the sidebands around each carrier frequency (the rotational speed of each shaft multiplied by the number of ppr of the encoder), and was resampled to give a fixed number of samples per tooth spacing (20) and thus be the same for both gears.

The TE for each gear could then be extracted by synchronous averaging over an integer number of rotations for that gear, this corresponding to a different total number of samples because of the different tooth numbers and “hunting tooth” design (no common factors). The records were truncated symmetrically by one rotation to remove wrap-around errors caused by the FFT processing. Most results were obtained for the pinion, this being the most damaged. Because of the relatively short records available (19 rotations of the pinion) the averaging was accomplished by an efficient procedure involving comb filtering in the frequency spectrum. Since there was an integer number of periods of the gear in question, the harmonics of that gear’s rotation were located in single lines of the FFT spectrum, and all other frequency lines could be set to zero. Noise at those harmonics is reduced by the same amount as if the averaging were done conventionally in the time domain [4], but was very low in this case. The harmonics of the other gear, though smeared because of the non-integer number of periods in the record, were almost entirely removed, except in the very small number of cases where they overlapped with the other discrete harmonics, and so were reduced to a larger extent than from time domain averaging [4]. This worked very well even for the gear, with a much smaller number of rotations, although this paper concentrates on the results for the pinion.

As mentioned in section 2, only the GTE and STE could be measured, at an input speed of 2 Hz, the GTE with a load close to zero, and the SE with an input torque of 20 Nm. Figure 4 shows the TEs for these two loads, at times approximately 0 hrs, 3 hrs, 6 hrs and 45 hrs, corresponding roughly to the four stages in Fig. 3. Note that two rotations are depicted in each case, although the starting phase is not matched. The latter can be judged from the low frequency (once per rev) fluctuation in each case, which does not change with wear, and is presumably dominated by slight eccentricity of the pitch circle with respect to the centre of rotation. The higher frequency ripple in each case corresponds to the toothmesh frequency, and becomes clearer as the wear progresses. It is interesting that the application of the load, to give the STE, decreases the toothmesh component for the first three stages of wear. This is not unexpected, as the GTE is dominated by high spots on the teeth, whose effect tends to be smoothed (lowpass filtered) by preferential deflection of the high spots by Hertzian deformation, but with not a great change in the mean tooth profile, except near the root where the initial wear occurs. The reverse situation at the final stage of wear, after 45 hrs, where the STE is now bigger than the GTE, is likely because the pitting is so widespread, including the zone near the pitch circle, that it does change the mean profile, and the load now serves to force the mating gear into “holes” in the profile, deforming local high spots.

It is interesting to compare the results for TE with those for acceleration. Figure 5 shows acceleration power spectra, but only for the initial condition (0 hrs) and final condition (45 hrs). The figures have a harmonic cursor set to the gearmesh frequency, and it is obvious that this does not dominate the spectrum at this low speed, even for the high load. The origin of the high vibration levels in the vicinity of multiples of 50 Hz, is not fully known but appears to be a function of the VFD at this very low speed. They were not prominent in vibration signals at higher speed. In contrast to the TEs in Fig. 4, there is very little difference in the first harmonic of gearmesh frequency from initial to final condition, which can be explained by the fact that at low speed there is little resistance to angular motions by inertial effects. On the other hand, there is a considerable increase in this first harmonic with increase in load from zero to 20 Nm, and this is probably because it is the tooth deflection rather than the GTE component of the overall TE which dominates the mesh forces under load. The fact that the STE has actually decreased with load for the first three wear stages shows that the information given by TE and vibration is quite different, although there may be more similarity between vibration and DTE, at higher speed, where it was not possible to make comparisons in this case.

It is also interesting that the TE measurements in Fig. 4 were little affected by the above-mentioned disturbances from the VFD, even though they made it difficult to extract synchronously averaged signals from the acceleration signals with such a small number of averages at the rotational frequency. It is an illustration of the fact that TE is not very sensitive to many forces causing substantial lateral vibrations.

The actual vibration response spectra for 20 Hz input speed are given in Figure 6, for both zero and 20 Nm torque load, for initial and final wear conditions, for comparison with the equivalent cases in Fig. 5 for 2 Hz speed. As in that case, there is little increase in the first two harmonics of gearmesh frequency with increasing pitting, but the higher harmonics (3-5) have increased by about 10 dB.

Unfortunately, it has not yet been possible to give results for simulation, to compare with the measurements, or for higher speed responses, as explained above, but these are part of work to be carried out in the near future, when the new encoders are mounted.

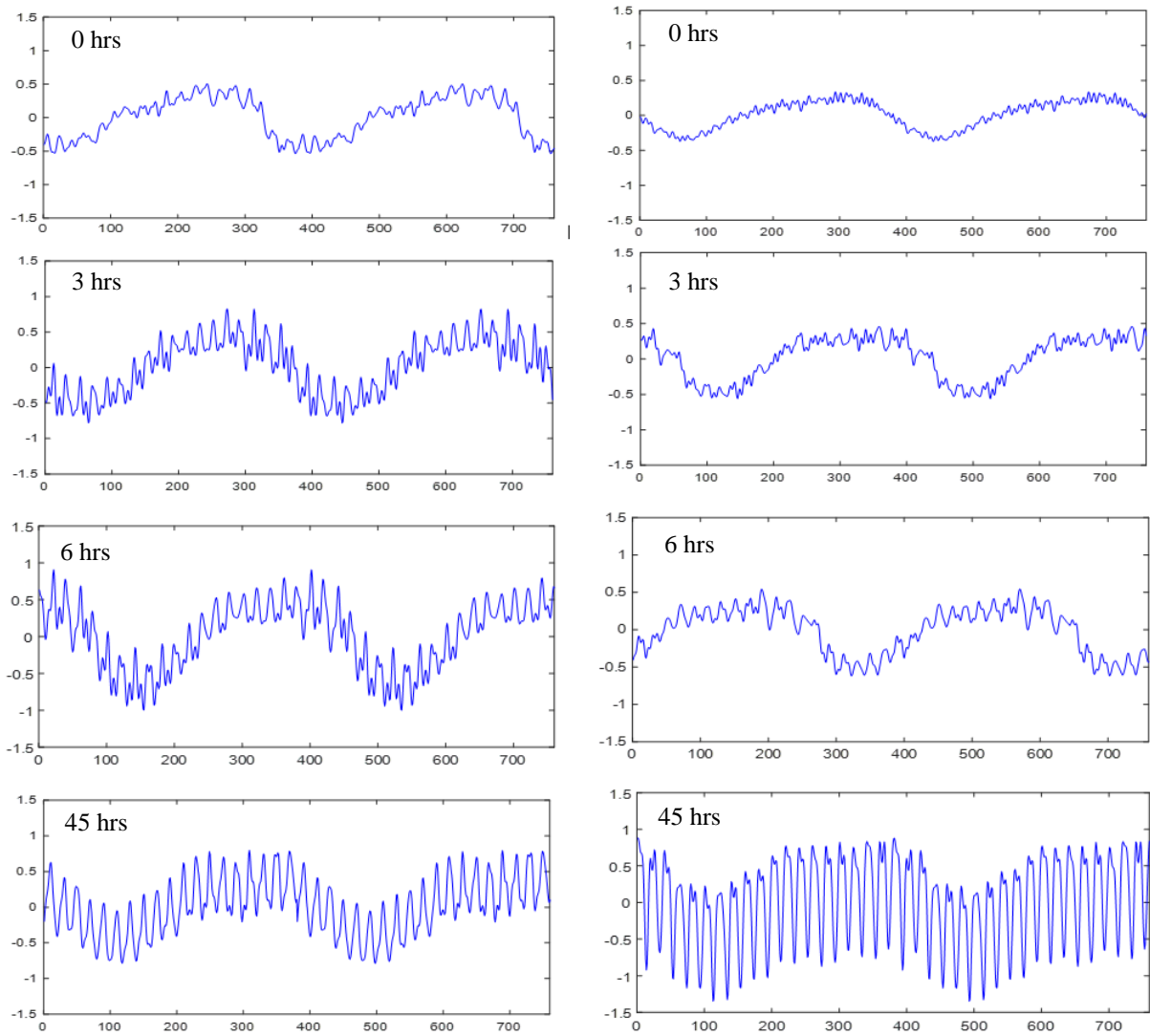


Figure 4: Development of TE with wear. (Left – GTE, 0 Nm); (Right – STE, 20 Nm)

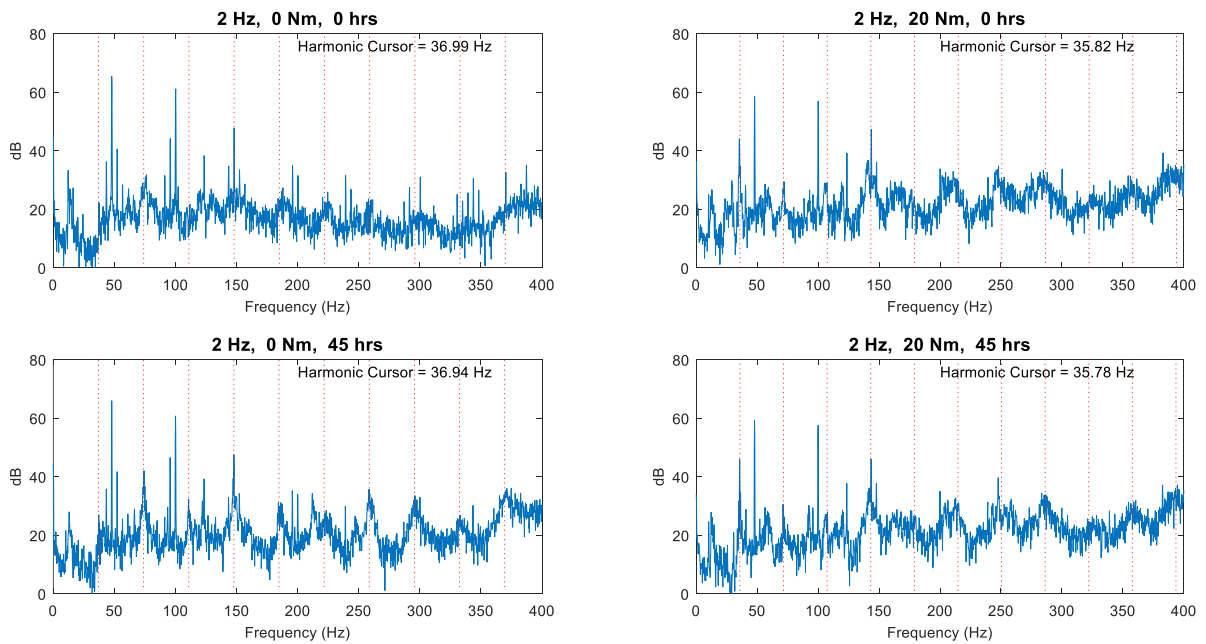


Figure 5: Comparison of vibration spectra at 2 Hz, load 0 Nm and 20 Nm, for initial and final wear

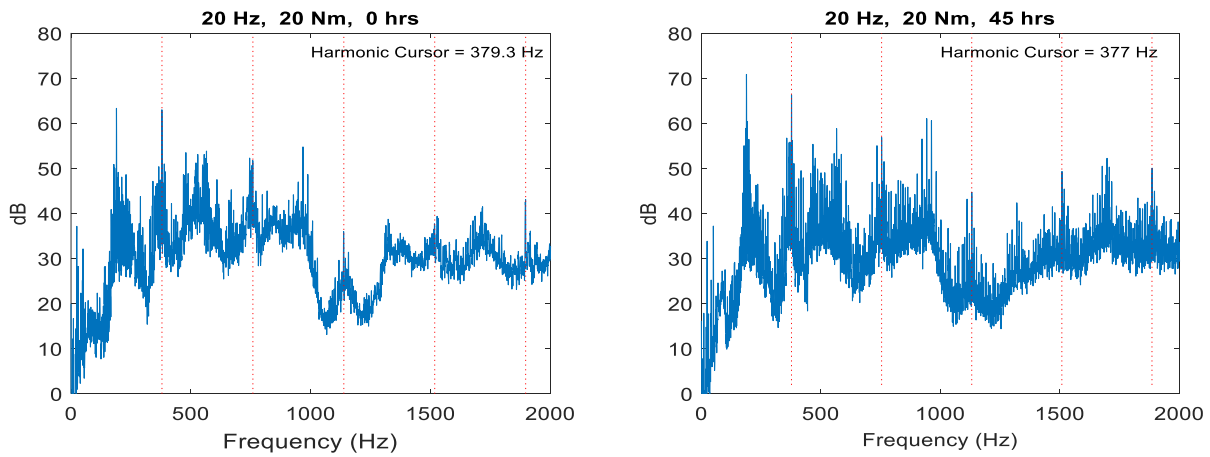


Figure 6: Comparison of vibration spectra at 20 Hz, load 20 Nm, for initial and final wear

3.2 Planetary gear rig

Comparisons can be made between simulations and measurements for the planetary gear rig, but only for relatively low speed, where dynamic effects are not pronounced. This is a limitation of the drive motor and its VFD. The simulations presented here are similar to those presented at a recent international rotor dynamics conference [5], but are here compared with measured TEs. A major goal of the project is to develop diagnostic techniques to distinguish between tooth root cracks and spalls, to follow the work initiated for single stage parallel gears in [6, 7], and continued for planetary gearsets in [8-10]. In the latter case, the difference was clarified between faults on a single flank of a planet gear tooth, such as a spall, which only contacts either the ring gear or sun gear, and a fault, such as a cracked or chipped tooth, which affects bending stiffness in both directions, and so has an effect when meshing with both sun and ring gear. These two contacts can be quite different, however, both because of different stiffness for a crack opening or closing, but also because of the very different contact ratio for the two meshes, giving a large difference in the ratio of time intervals for single tooth pair and double tooth pair contact.

Results are compared here in Figure 7 for a spall interacting with the sun gear, a spall interacting with the ring gear, and a tooth root crack, with input shaft speed close to 2 Hz (planet carrier speed 1.53 Hz, sun gear output speed 5.31 Hz). The input stage to the planetary section was not included in the simulation model, so simulated TE results were estimated and are given for the planetary stage directly, ie the TE from the planet carrier shaft to the sun shaft. On the other hand, there was no encoder mounted on the planet carrier shaft, so the measured TE was between the input shaft and the output shaft, and included the input parallel gear stage. However, it was found to be possible to extract the TE of the planetary stage by using synchronous averaging synchronised with the rotation speed of the planet gears, ie a period corresponding to the meshing of 23 teeth. It is necessarily a composite overall TE for the three planet gears, and cannot indicate on which planet gear the fault is located. If there were a fault on more than one gear, they would all show up in this composite average.

Firstly, before making a detailed comparison of the results, there is an immediate obvious difference in the background ripple frequency related to the gearmesh frequency. Because of the tooth numbers in the gearset, it has so-called sequential tooth-meshing, with the meshing of the teeth on one planet offset by 1/3 of a tooth spacing compared with each of the others. For there to be synchronous tooth meshing, the numbers of teeth on all three components (sun, planet, ring) would have to all be divisible by 3. Since the simulation is for initially perfect teeth on all gears, apart from that on which each fault was introduced, the background ripple for the simulations has a fundamental frequency corresponding to the third harmonic of the gearmesh frequency (ie 69 periods per gear rotation).

It was therefore at first surprising that the measured results had clear background ripple at gearmesh frequency (23 periods per rotation), but then it was realised that this could be ascribed to the limited resolution given by the encoder on one shaft, the output shaft, with only 225 ppr, compared with 900 ppr for the other. Originally, both gave 900 ppr, but one had been modified for an earlier experiment, with the pulse count divided by 4. It will be possible to correct this in future work, but it does not significantly detract from the results of this paper showing the effects of local faults on one gear. Even though the TE signal was resampled during the analysis to a higher sample rate, the TE signal was effectively lowpass filtered prior to this at less than three times the gearmesh frequency, because of the small number of pulses per tooth spacing. Since the second harmonic of gearmesh frequency was virtually not present in any case, the background ripple is dominated by the fundamental gearmesh frequency.

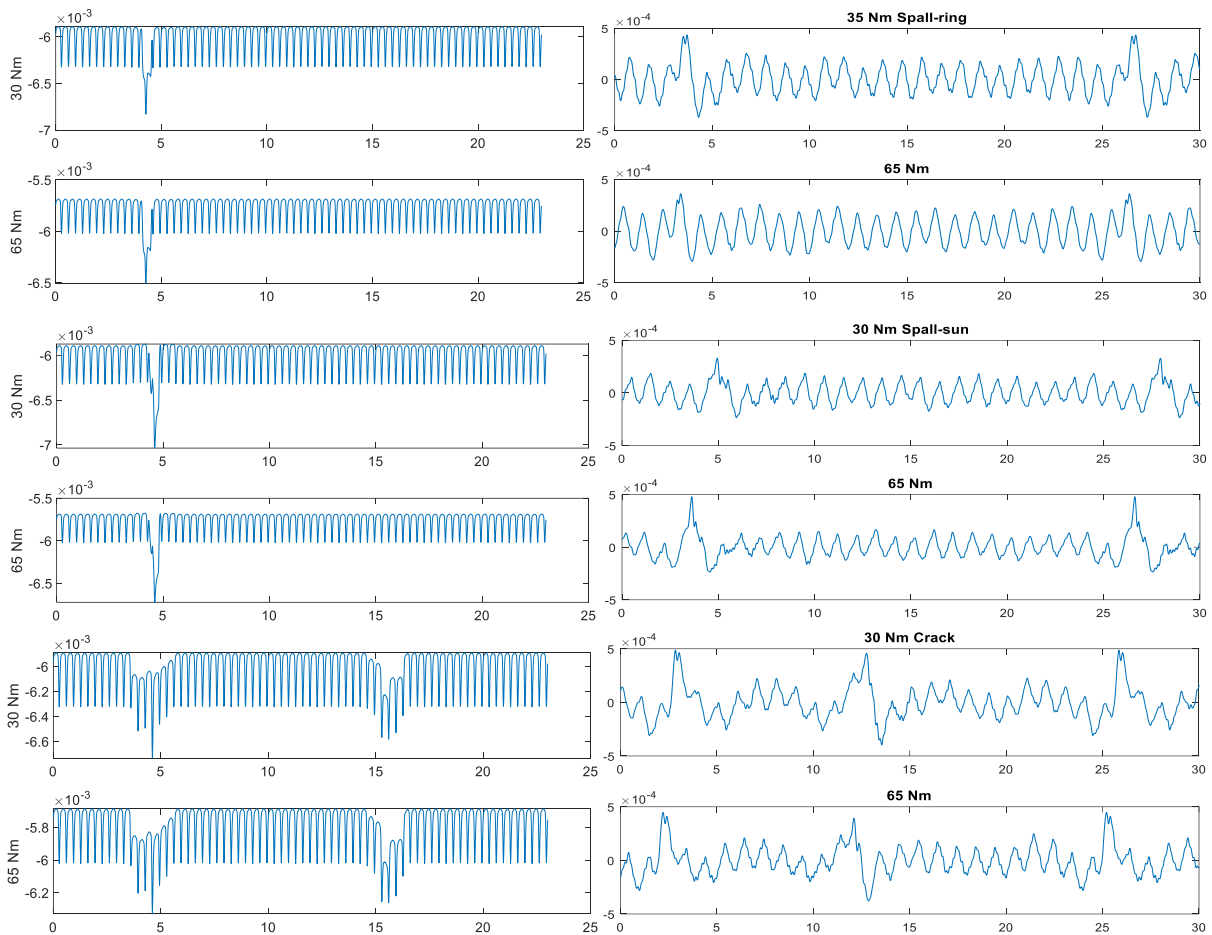


Figure 7: Simulated vs measured TE for planetary gear faults (Left) Simulations (Right) Measurements (Top - 2 loads) Spall – ring gear (Mid – 2 loads) Spall – sun gear (Bottom – 2 loads) Crack

It should be noted that the scaling of the TEs has not been unified for the two cases of simulation vs measurement, although attention will be paid to this point in future work, particularly after the lumped parameter simulation model has been updated to correct natural frequencies etc. This should in fact be much simpler for the torsional natural frequencies than the much greater number of lateral natural frequencies, which all require updating for a full model. The other obvious difference is that the TE has been measured in the inverse direction for the two cases.

The simulation records are for exactly one planet rotation (23 teeth) so show only one pulse per record for the spalls, but two for the crack, whereas the records for the measurements are displayed over thirty teeth, with a once-per-rotation spacing of 23 teeth.

Comparing now the upper two sets of curves in Fig. 7, for the spall interacting with the ring gear, and for two different applied loads (30 Nm and 65Nm at the input shaft), there is seen to be a similar pattern for simulation and measurement, and not much effect of load. This can be explained, as the spall primarily gives a change in GTE, but little change in tooth stiffness, which might be load dependent. In this case, the spall was narrow, and didn't enter into the region with double tooth pair meshing, but the latter would happen with a somewhat wider spall, even though it might stay in the single tooth pair meshing region for the sun-planet interaction.

For the next two sets of curves, with the spall interacting with the sun gear, the results are very similar, though the TE deviations are more triangular, as in [10]. If the spall were wider, and stayed within the single tooth pair meshing region, as mentioned above, this might give more differentiation between the two interactions [10].

The bottom two sets of curves, for a simulated tooth root crack, show obvious differences compared with the spalls. In both simulations and measurements there are now two responses per revolution, one with the sun gear and one with the ring gear, though these are not the same. Neither are they uniformly spaced, both because of the odd number of teeth and the fact that the effective contact points with sun and ring are on the same side of a diametral line through the planet gear. The length of interaction is now greater than for a spall, as it corresponds to the entire time the faulty tooth is engaged, ie longer than the tooth spacing, in accordance with [5, 10], although the part with larger deviation extends further for contact with the sun than with the ring [5, 10].

It should be mentioned that the regularly repeating part of the signal can be removed from simulations, to give a so-called “residual TE” or RTE, as shown in [5, 10], and something similar can be achieved in measurements, by using linear prediction, as shown in [11]. This will be tested in future work.

4 Conclusion

This paper gives a number of examples of how measured gear TE can be useful in gear diagnostics, as an alternative, or supplement, to vibration measurements. It explains for the first time how GTE, STE and DTE can be measured if it is possible to run the machine at low speed and low load (GTE), low speed and high load (STE) and high speed and high load (DTE), although the latter case could not be demonstrated here because of equipment limitations, which will be overcome in the near future. It is also shown how the TE for a hidden internal stage can be extracted using synchronous averaging from the overall TE from input to output if shaft encoders can only be mounted on the input and output shafts. Another point demonstrated is that where the major disturbance of the effects of a particular gear is from other gears, or other discrete frequency sources, the synchronous averaging can often be carried out more effectively by comb filtering in the frequency domain, in particular when there is a limited record length.

Potential advantages of using TE for gear diagnostics are:

- 1) The measurement is closer to the source, and less disturbed by transfer function effects than vibration responses, which not only vary considerably between different positions, but can also be time-varying.
- 2) It is easier to get a good correspondence with simulations, because the torsional parts of simulated systems are simpler, and affected by fewer resonances than lateral vibrations, so model updating should be simpler.
- 3) The measurement of GTE at different times during the life of a gearbox, as well as giving a more direct measurement of wear, will make possible the inclusion of more accurate versions of this parameter in simulation models, including those giving lateral vibrations as outputs.

The technique does require the mounting of accurate encoders on at least the input and output shafts of the gear transmission, but does not necessarily require them to be mounted on all shafts, which can be difficult for internal components. However, the inclusion of such encoders is already implemented in some machines, for operational purposes, and this is likely to increase with the wider implementation of the Internet of Things.

It is hoped in future work to overcome some of the limitations caused by equipment, which is in the process of being updated, so that, for example, it will be possible to demonstrate the differences with GTE at different speeds, and better comparisons with vibration measurements over a wider range of conditions. It should also be possible to demonstrate the inclusion of measured GTE in simulation results.

Acknowledgement

The authors would like to thank Mr Jacky Chin, for providing the measurements on the single stage test rig, and Mr Haichuan Chang for acquiring the impressions and providing illustrations of the gear tooth surfaces, for the same tests, at different stages of the wear process.

References

- [1] Sweeney, P.J. and Randall, R.B., (1996): Gear Transmission Error Measurement using Phase Demodulation. *Proc. IMechE., Part C, J.Mech.Eng.Sci.* **210**(C3), pp. 201-213.
- [2] Randall, R.B., (2011): *Vibration-based Condition Monitoring: Industrial, Aerospace and Automotive Applications*. Wiley, Chichester, UK.
- [3] Coats, M.D. and Randall, R.B. (2014): Single and multi-stage phase demodulation based order-tracking. *Mechanical Systems and Signal Processing* **44**, pp. 86–117.
- [4] McFadden, P.D., (1987), A Revised Model for the Extraction of Periodic Waveforms by Time Domain Averaging, *Mechanical Systems and Signal Processing*, **1**(1), pp 83-95.
- [5] Peng, D., Smith, W.A., Randall, R.B., and Peng, Z. (2018): Differentiating tooth root cracks and spalls in planet gears from changes in the transmission error. IFToMM International Conference on Rotor Dynamics, Rio de Janeiro, September 23-27.
- [6] Endo, H., Randall, R.B. and Gosselin, C. (2004) Differential Diagnosis of Spalls vs Cracks in the Gear Tooth Fillet Region, *J. Failure Analysis and Prevention*, **4**(5), pp. 57-65.
- [7] Endo, H., Randall, R.B., Gosselin, C. (2009) Differential diagnosis of spall vs. cracks in the gear tooth fillet region: Experimental validation. *Mechanical Systems and Signal Processing*, **23**(3), pp. 636-651.
- [8] Smith, W., Deshpande, L., Randall, R., and Li, H. (2013). Gear diagnostics in a planetary gearbox: a study using internal and external vibration signals. *Int. Journal of Condition Monitoring*, **3**(2), pp.36-41.

- [9] Deshpande, L., Randall, R., and Smith, W. (2014). Diagnostics of planet gear faults from the effects of meshing with the ring and sun gears. In *Proceedings of the 21st International Congress on Sound and Vibration*, Beijing, pp. 13-17.
- [10] Peng, D., Smith, W.A., Borghesani, P., Randall, R.B. and Peng, Z. (2018) Comprehensive planet gear diagnostics: use of transmission error and mesh phasing to distinguish fault types and identify faulty gears. Paper MSSP 18-1875, submitted to *Mechanical Systems and Signal Processing*.
- [11] Endo, H., Randall, R.B., (2007) Enhancement of autoregressive model based gear tooth fault detection technique by the use of minimum entropy deconvolution filter. *Mechanical Systems and Signal Processing*, **21**, pp. 906–919.

Rotor Model Reduction for Wireless Sensor Node Based Monitoring Systems

Samuel Krügel¹, **Johannes Maierhofer**², **Thomas Thümmel**², **Daniel J. Rixen**²

¹ Siemens Corporate Technology, Siemens AG, 91058, Erlangen, Germany, samuel.kruegel@siemens.com

² Chair of Applied Mechanics, Technical University of Munich, 85748, Garching, Germany,

² j.maierhofer@tum.de, thuemmel@tum.de, rixen@tum.de

Abstract

Model based monitoring using wireless sensor nodes gains in importance for industry, but standard high order models are not applicable on these micro-controlled systems. Consequently, an efficient, validated rotor model is required as a base for holistic digital twins. Here, we propose a modelling method for a common rotor type with reduced degrees of freedom. It represents the core of a cage motor with overhung impeller as characteristic feature, whereby the transition between shaft and impeller constitutes the principal point.

Within a reference simulation, we create a detailed finite element model. Subsequently, we build up a reduced one, considering radial displacement and axial bending degrees of freedom only. Therefore, we split the rotor into three substructures and use Timoshenko beam theory except for the transition between shaft and impeller. That junction represents a thin, circular plate and shows pronounced deformation at the first two bending mode shapes. For identification of this plate stiffness, we use an analogous model. The outcome is implemented into the rotor model via a connecting element stiffness matrix. Thereupon, the first two mode shapes and natural frequencies of the resulting model match with the reference. Finally, the simulations are validated by experimental modal analysis.

1 Introduction

Monitoring systems are rarely applied to rotating machinery in drives and plants despite their broad impact. A valid reason for that is the price for condition monitoring sensor technology. A possible solution of this cost issue may be provided by MEMS¹ accelerometers. This sensor technology offers the advantage of cost-efficient methods for machines, which are not monitored up to now, because their price including signal condition unit is about 10 % or less compared with conventional accelerometer systems [1]. An extension option is the MEMS integration into wireless sensor nodes. Here, the brief signal chain due to the accelerometer's digital interfaces supplies huge benefits. Hence, local signal processing on these micro-controlled systems and subsequent wireless transfer of preprocessed data snapshots or key performance indicators with less file size is possible. Apart from that, entirely signal based assessment cannot serve as a solution for tasks, where the fault quantification plays a role and big operational data is not available. Therefore, combined model and signal aided monitoring implies an expedient approach. However, calculation power and wireless transmission speed of micro-controlled sensor nodes is strictly limited. Hence, an applied model has to be very efficient while containing only few degrees of freedom. Although several model reduction techniques as described in [3] are well established and have great benefits in decreasing calculation time, we are aiming at a simple solution for modelling a common kind of rotor. Therefore, we do not use a classical numeric approach for model order reduction, but rather split it into substructures and apply appropriate, section specific methods.

For this purpose, we use an exemplary blower application, which is shown in figure 1. The regarded rotor type sucks air axially, displaces it radially and subsequently redirects it axially along the housing of pumps and blowers. Within our application, the rotor is responsible for air cooling of drives.

¹Micro-Electro-Mechanical System

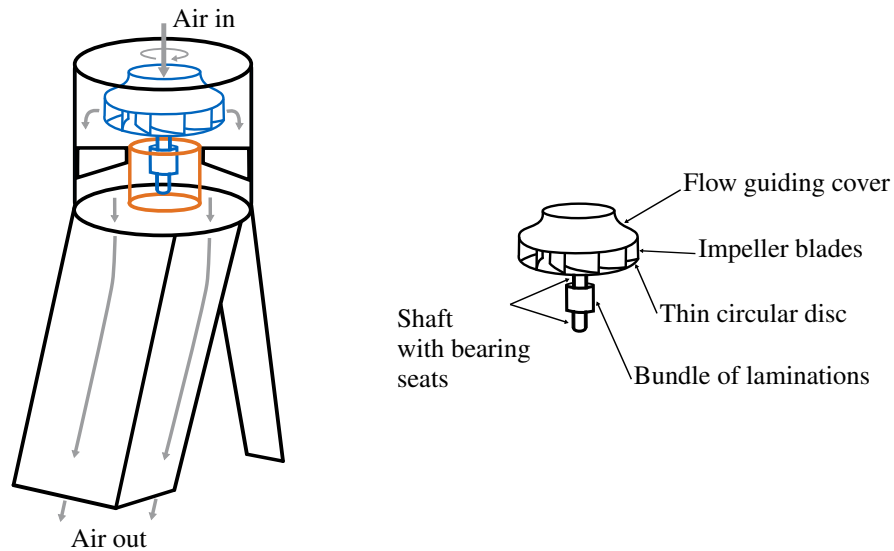


Figure 1: Left: Drive cooling blower as exemplary application with housing (black), cage motor (orange) and rotor (blue). Right: Extracted rotor with characterized main parts.

The depicted application consists of the housing with struts (black), cage motor (orange) and the rotor (blue), at which we have a closer look hereinafter. On the right hand side of the picture, referring to modelling, the extracted rotor is outlined by its main sections:

1. Shaft with bundle of laminations and bearing seats at the bottom and beneath the impeller,
2. A thin, circular disc as transition between shaft and impeller blades and
3. The impeller blades, extending to the flow guiding cover.

2 Reference Model of the Rotor

We start with a rotor reference finite element model using ANSYS SOLID 187, tetrahedral volume elements and a fine mesh with 575 718 degrees of freedom. In order to later compare simulation and experimental results, we assume "free-free" boundary conditions. In detail, we use the experimentally determined, elastic threads stiffness approximation explained in section 4. For axial flexibility approach, we divide the thread stiffness in relation to the active surface, which is defined by the impeller underside. Similarly, the twice, radially projected cross-sectional area of the impeller disc is used. By this, radial, soft "clamping" is realized in order to obtain the base stiffness in N/m^3 needed by ANSYS for the eigenvalue calculation. In figure 2, the first two resulting bending mode shapes are mapped.

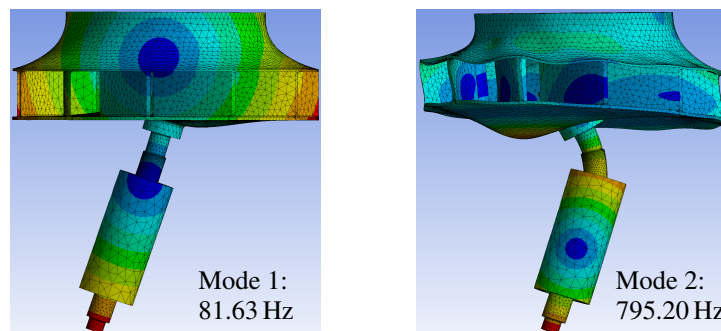


Figure 2: First and second bending mode shape at associated resonance frequencies.

The first mode shows pronounced bending at the plate between shaft and impeller. This thin disc also plays an important role at the second natural frequency, where furthermore, the upper bearing seat undergoes large deflection. These effects must be properly accounted for in subsequent modelling of the reduced rotor.

3 Reduced Model

Hereinafter, we set the origin of global coordinate system at the lower shaft end and orientate the z-coordinate along the rotor axis. Radial x- and y-orientations are illustrated in figure 3. For the subsequent finite element modelling programmed in MATLAB, we split the rotor into three substructures, enumerated in section 1. Thereby, we apply a thread stiffness used for boundary conditions described in section 4, which is analogue to the base stiffness of the reference model.

3.1 Rotor Shaft Discretization

The rotor shaft is described by Timoshenko beam elements along the z-axis [6]. It contains bearing seats and bundle of laminations as components of the cage motor. For discretizing the beam elements, cross-sectional areas and geometrical moments of inertia are key variables. The general axial (I_x, I_y), polar (I_p) and mixed (I_{xy}) geometrical moments of inertia [2], are defined as

$$I_x = \int_A y^2 dx, \quad I_y = \int_A x^2 dy \quad I_p = I_x + I_y \quad \text{and} \quad I_{xy} = - \int_A xy dA. \quad (1)$$

Here, the geometrical and polar moments of inertia $I_x = I_y$ and I_p are characterized by circle and ring sections (outer and inner diameter D_o and D_i) as

$$I_x = \frac{\pi \cdot (D_o^4 - D_i^4)}{64}, \quad I_p = 2 \cdot I_x, \quad (D_{i,circle} = 0). \quad (2)$$

3.2 Impeller Blades Discretization

Considering the impeller blades, we have sections with constant and variable cutting areas depending on the z-coordinate. Henceforth, we derive their geometrical moments of inertia regarding the global coordinate system. The geometry required for transformations is depicted in figure 3.

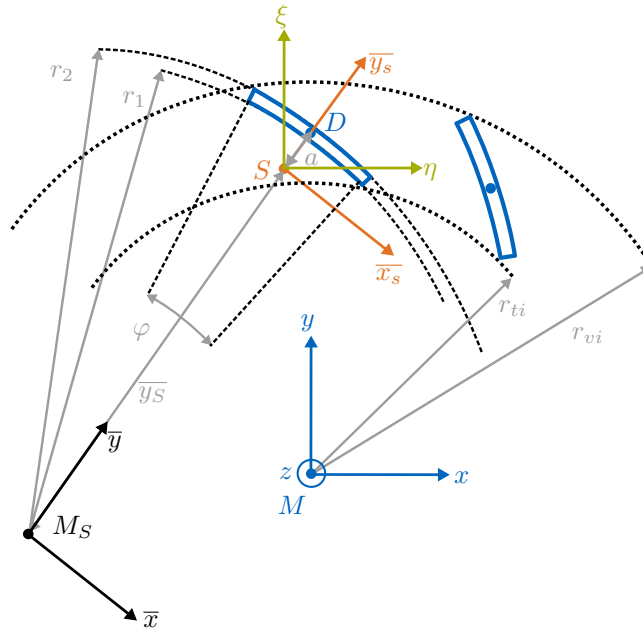


Figure 3: Rotor section plane extract with two marked blades and global coordinate system (blue) besides relative systems and geometrical parameters for blade transformation.

For the following considerations, just one single blade with constant cross-section area is regarded. It spreads over φ with its circle center M_S . When splitting it into two circle segments with radii r_1, r_2 and distances to each centroid $\bar{y}_{S1/2}$ with areas $A_{1/2}$,

$$\bar{y}_{S1/2} = \frac{4 \cdot \sin\left(\frac{\varphi}{2}\right) \cdot r_{1/2}}{3 \cdot \varphi} \quad \text{and} \quad A_{1/2} = r_{1/2}^2 \cdot \frac{\varphi}{2}, \quad (3)$$

we get the resulting \bar{y}_S -distance to the blade centroid according to [4] in the form of

$$\bar{y}_S = \frac{\bar{y}_{S2} \cdot A_2 - \bar{y}_{S1} \cdot A_1}{A_2 - A_1} = \frac{4 \cdot \sin\left(\frac{\varphi}{2}\right) \cdot (r_2^3 - r_1^3)}{r_2^2 - r_1^2}. \quad (4)$$

The geometrical moments of inertia $I_{\bar{x}_s}$, $I_{\bar{y}_s}$ and $I_{\bar{x}_s \bar{y}_s}$ relating to the centroid S are

$$I_{\bar{x}_s} = \frac{\left(\sin\left(\frac{\varphi}{2}\right)\right)^3}{3} \cdot \left((r_2 - \bar{y}_s)^3 - (r_1 - \bar{y}_s)^3\right) \cdot \cos\left(\frac{\varphi}{2}\right) \cdot (r_1 + r_2), \quad (5)$$

$$I_{\bar{y}_s} = \frac{\left(\cos\left(\frac{\varphi}{2}\right)\right)^3}{3} \cdot (r_1^3 + r_2^3) \cdot \sin\left(\frac{\varphi}{2}\right) \cdot (r_2 - r_1 - 2\bar{y}_s), \quad \text{and} \quad (6)$$

$$I_{\bar{x}_s \bar{y}_s} = -\frac{\left(\sin\left(\frac{\varphi}{2}\right)\right)^2}{2} \cdot \left((r_2 - \bar{y}_s)^2 - (r_1 - \bar{y}_s)^2\right) \cdot \frac{\left(\cos\left(\frac{\varphi}{2}\right)\right)^2}{2} \cdot (r_1^2 + r_2^2). \quad (7)$$

Now, we can rotate the blade to η, ξ -axes around the centroid S . The resulting geometrical moments of inertia I_η and I_ξ can be written as

$$I_\eta = \frac{1}{2} (I_{\bar{x}_s} + I_{\bar{y}_s}) + \frac{1}{2} (I_{\bar{x}_s} - I_{\bar{y}_s}) \cdot \cos(2\varphi_n) + I_{\bar{x}_s \bar{y}_s} \cdot \sin(2\varphi_n), \quad \text{and} \quad (8)$$

$$I_\xi = \frac{1}{2} (I_{\bar{x}_s} + I_{\bar{y}_s}) - \frac{1}{2} (I_{\bar{x}_s} - I_{\bar{y}_s}) \cdot \cos(2\varphi_n) - I_{\bar{x}_s \bar{y}_s} \cdot \sin(2\varphi_n) \quad \text{with} \quad (9)$$

$$\varphi_n = \varphi_{n0} + n \cdot \frac{2 \cdot \pi}{N}, \quad (10)$$

where φ_{n0} is the start angle for the first regarded blade referred to $\eta - \xi$ -axes, $n = 0 \dots N - 1$ stands for the further, respective blade index and N for the total amount of blades. Finally, we shift the rotated moments of inertia via $\bar{\eta}$ and $\bar{\xi}$ to absolute coordinates x and y . Hence we get

$$I_x = I_\eta + \bar{\eta}^2 \cdot A \quad \text{and} \quad I_y = I_\xi + \bar{\eta}^2 \cdot A \quad \text{using} \quad A = (r_2^2 - r_1^2) \cdot \frac{\varphi}{2} \quad \text{and} \quad (11)$$

$$x_s = a \cdot \sin\left(\frac{\varphi}{2}\right) \quad \text{and} \quad y_s = \frac{r_{vi} + r_{ti}}{2} - a + a \cdot \left(1 - \cos\left(\frac{\varphi}{2}\right)\right), \quad \text{where} \quad a = \frac{r_1 + r_2}{2} - \bar{y}_s. \quad (12)$$

In the next step, we consider the variable, z-coordinate dependent cutting plane areas. Therefore, we introduce the angle $\varphi_{vn}(z)$ to deduct it from φ in order to obtain the angle $\varphi_v(z)$ as substitute for φ . The reason is, that the blades cut surface lessens along rotor axis in the tapering flow guiding cover part. In figure 4, the corresponding approximation with required geometry is pictured.

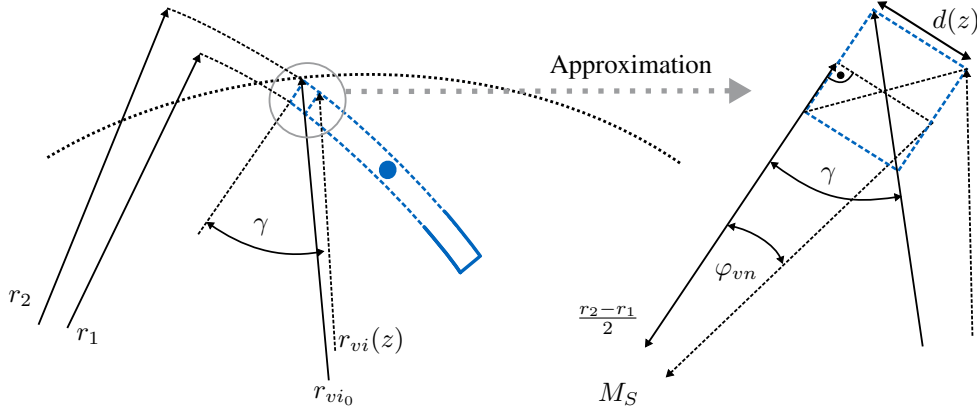


Figure 4: Illustration of a blade with decreasing cross-sectional area (blue) along the z-coordinate and geometrical assumptions for φ_{vn} approximation.

Thus, we get the new blades spread angle $\varphi_v(z)$ using the subtrahend $\varphi_{vn}(z)$ over the length $d(z)$

$$\varphi_v(z) = \varphi - \varphi_{vn}(z) \quad \text{with} \quad \varphi_{vn}(z) = \arctan\left(\frac{2 \cdot d}{r_1 + r_2}\right), \quad d(z) = \sin(\gamma) \cdot (r_{vi0} - r_{vi}(z)). \quad (13)$$

3.3 Flow Guiding Coverage Discretization

In connection with the blades, a flow guiding cap covers the impeller. To obtain sufficiently correct ring radii approximations $a_{vo}(z)$ and $a_{vi}(z) = a_{vo}(z) - d_w$, we divide it into four segments (z_0 to z_1 , z_1 to z_2 , z_2 to z_3 , z_3 to z_4) with sectionally defined discretization laws (geometry in figure 5).

At the first section, a_{vo} is constant. We define for the second segment

$$a_{vo}(z) = a_{vo}(z_0) - r_{a1} \cdot (\sin \varphi_d(z) - \sin \varphi_{d0}), \quad (14)$$

$$\varphi_d(z) = \arccos\left(\frac{z_0 - z}{r_{i1}} + \cos(\varphi_{d0})\right) - \varphi_{d0}, \quad (15)$$

for the third segment

$$a_{vo}(z) = a_{vo}(z_2) - r_{a2} \cdot (\sin \varphi_d(z) - \sin \varphi_d(z_2) - \sin \varphi_{d0}), \quad (16)$$

$$\varphi_d(z) = \arccos\left(\frac{z_2 - z}{r_{i2}} + \cos(\varphi_d(z_2))\right) - \varphi_d(z_2), \quad (17)$$

and for the last, that a_{vo} is constant. As concluding remark regarding the discretization, note that the rotor mass differences due to volume depending on discretization step width of the impeller along the z-axis. Therefore, we set the increment dz to 20 mm. At this threshold, the overall volume deviation to the reference model is less than 2% with a resulting overall mass of 22.20 kg and the degrees of freedom result in a small amount of 136.

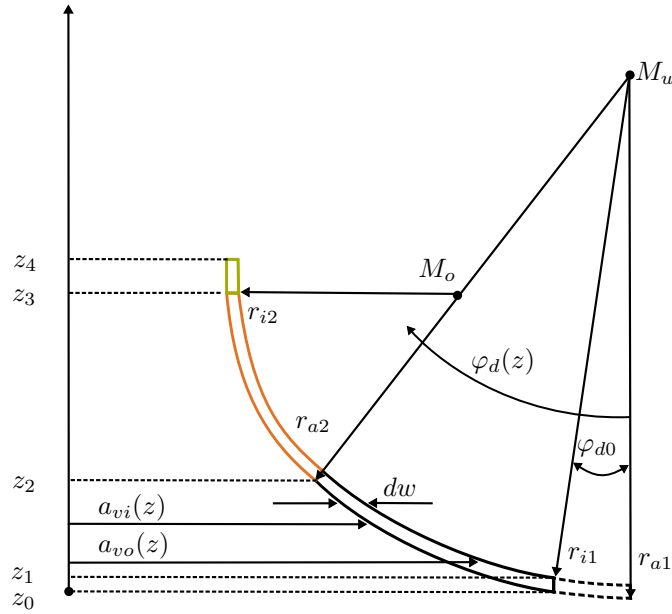


Figure 5: Sectional view of the flow guiding coverage in x-z plane.

3.4 Transition Stiffness Approximation

At the transition between shaft and impeller, we need an analogous stiffness for the thin, circular plate. For this purpose, we simulate a load condition with fine mesh, similar to section 2 (mapped in figure 6).

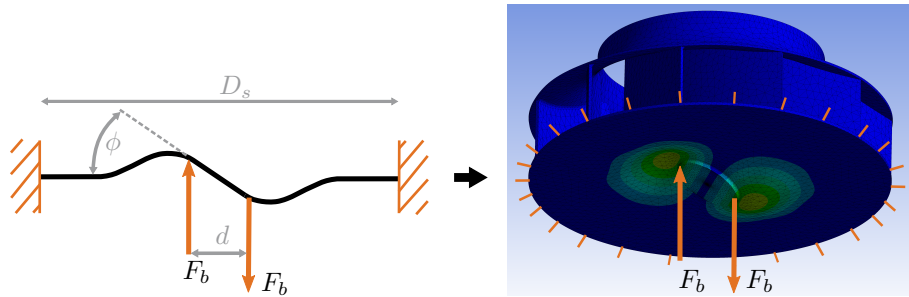


Figure 6: Left: Schematic drawing of the deformed, circular plate with circumferential, rigid clamping at outer diameter D_s and axial bending moment generating forces F_b at a distance of d , generating a bending angle ϕ . Right: Corresponding impeller finite element model (ANSYS) with labelled clamping and bending forces

Two oppositely orientated unit forces F_b are applied at the interface between shaft and impeller at a distance of d . Meanwhile, the disc is clamped circumferential at the outer diameter D_s . Based on the resulting bending moment $M = F_b \cdot d$ and -angle ϕ , we obtain the stiffness $k_b = M/\phi$, which is essential for the rotor model completion. Furthermore, we assume the stiffness against lateral force k_{inf} towards infinity due to the short length and high diameter of the finite element representing the disc. This is necessary, because the disc is represented by an element and not by a constraint between two axial degrees of freedom. In detail, we take the corresponding stiffness value of the adjoining shaft element (diameter d) and multiply it with 10^6 to get the approximation of the plate's stiffness against lateral force. In summary, we neglect the coupling terms between rotational ϕ and translational u degrees of freedom and obtain the element lateral forces F as well as bending moments M approximation in the formulation

$$\begin{bmatrix} F_1 \\ M_1 \\ F_2 \\ M_2 \end{bmatrix} = \begin{bmatrix} k_{inf} & 0 & -k_{inf} & 0 \\ 0 & k_b & 0 & -k_b \\ -k_{inf} & 0 & k_{inf} & 0 \\ 0 & -k_b & 0 & k_b \end{bmatrix} \begin{bmatrix} u_1 \\ \phi_1 \\ u_2 \\ \phi_2 \end{bmatrix}. \quad (18)$$

Finally, we link the adjoining shaft and impeller nodes by this element stiffness matrix.

3.5 Results

By solving the eigenvalue problem using the axial and radial stiffnesses evoked by the elastic threads (derived in section 4), we get the first two bending mode shapes at eigenfrequencies 82.12 Hz and 812.96 Hz (figure 7).

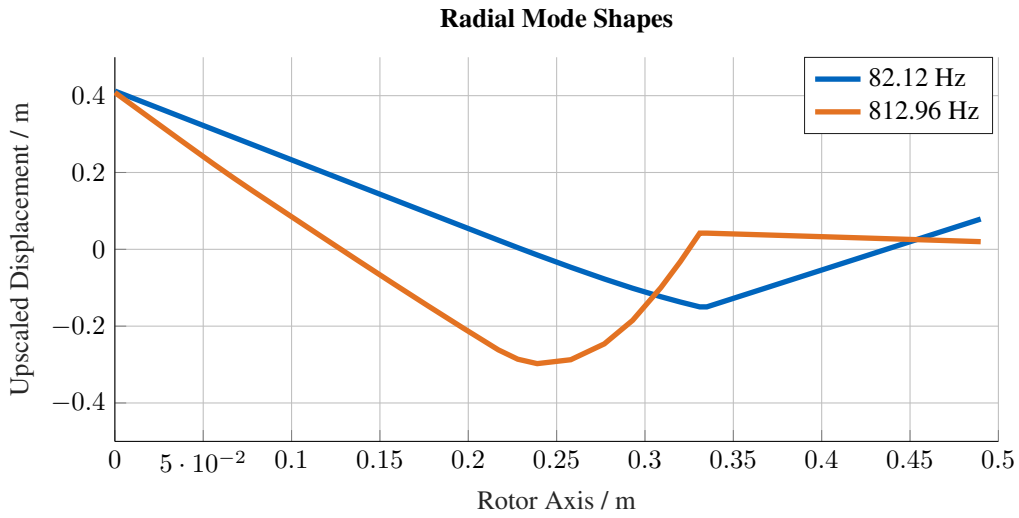


Figure 7: First (blue) and second (orange) bending mode shape of the reduced model with horizontally aligned rotor axis.

The first bending mode shape has its antinode at 0.335 m rotor axis position, which complies exactly with the disc location. Similarly, the second mode shape shows this pronounced bending at the same point, but in opposite direction. Comparing the results with figure 2, we note the same qualitative axis displacement. Moreover, the second mode shape antinode at upper bearing seat ($z = 0.27$ m) behaves equally. The first natural frequency is 0.6 % and the second one 2.3 % higher compared to the reference result. This deviation can be justified by differing element types and -sizes (see [5], p.316) besides all above described approximations and is, however situated in an acceptable range.

4 Experimental Validation

For simulation validation, we use experimental modal analysis with multiple inputs (x , y , and z -direction) and multiple outputs at 21 measurement points, spread over the whole rotor, in all three measurement directions. We apply the excitation force (F_e in figure 8) with an impact hammer (Brüel & Kjaer 8204) at the lower bearing seat position in two orthogonal radial directions and measure the response using piezoelectric accelerometers (Kistler 8688A) acquired by LMS Test Lab. For the modal analysis, we use the roving accelerometer method (3 sets with 7 accelerometers each) in order to obtain a completely defined Matrix containing the Frequency response functions. On behalf of post processing and modal parameter estimation, we employ the LMS PolyMAX frequency domain tool.

4.1 Test Set Up

In order to approximate "free-free" boundary conditions with minimum stiffness of the suspension, we hang up the rotor on four elastic threads. In order gain this approximation, we calculate the thread stiffness. The set in angle φ_s of each thread due to radius r_a , original length l_0 , gravity F_g and elongation δl is marked in figure 8. Thus, we get the approximated, linearised stiffnesses against axial and radial Forces $F_{ax} = F_g$ and $F_r = F_g \cdot \tan(\varphi_s)$ for the model boundary conditions in sections 2 and 3.

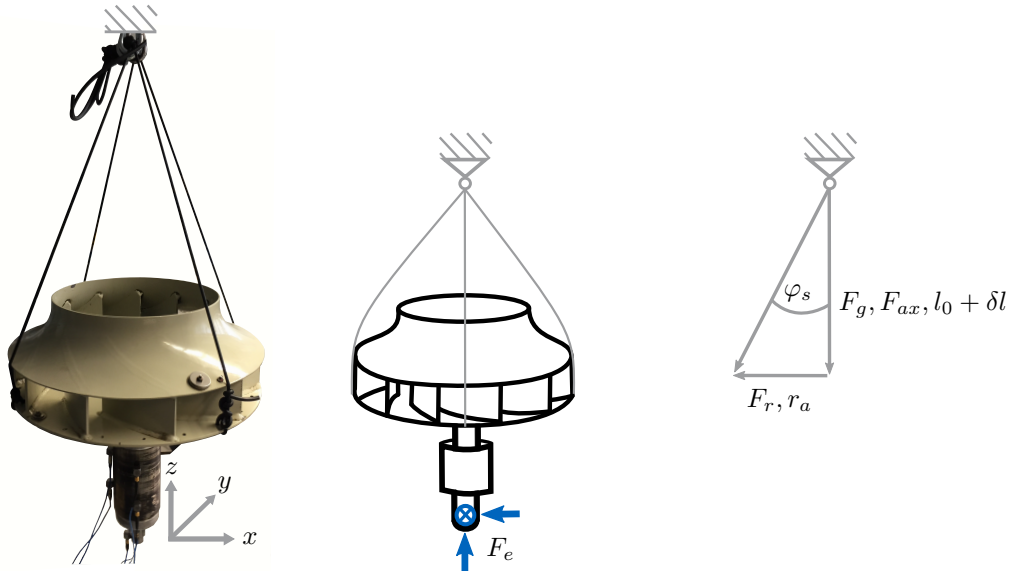


Figure 8: Left: Hung rotor, supported by four elastic threads, first set of attached accelerometers below and global coordinates. Middle: Schematic drawing with excitation force F_e . Right: Force and geometry sketch for thread stiffness approximation.

4.2 Results

By way of illustration, the resonance frequencies of the first two bending mode shapes, the averaged x- and y- frequency response functions (FRFs) are plotted in figure 9. In detail, the mean value of all FRFs between x-acceleration at 21 measurement points and x-excitation at the reference point (marked as force application at figure 8) is plotted in black. The same measurement results are shown for the y-direction (grey plot in figure 9). Besides the two resonance peaks, f_1 at 79.86 Hz and f_2 at 810.34 Hz we see a third, small one at about 523 Hz. This magnification has its origin in impeller bending around x- as well as y-axis and consequently does not show in our reduced simulation model. Furthermore, not only peak level but also narrow width of the relevant resonances is striking. Thus, damping ratio is very low (0.07 % at f_1 and 0.52 % at f_2). Additionally, the discrepancy between x- and y-FRFs is conspicuous. This deviation can be justified by the impeller asymmetry, since the rotor blade amount is 11 and consequently, particularly the stiffness depends on x-y axis alignment.

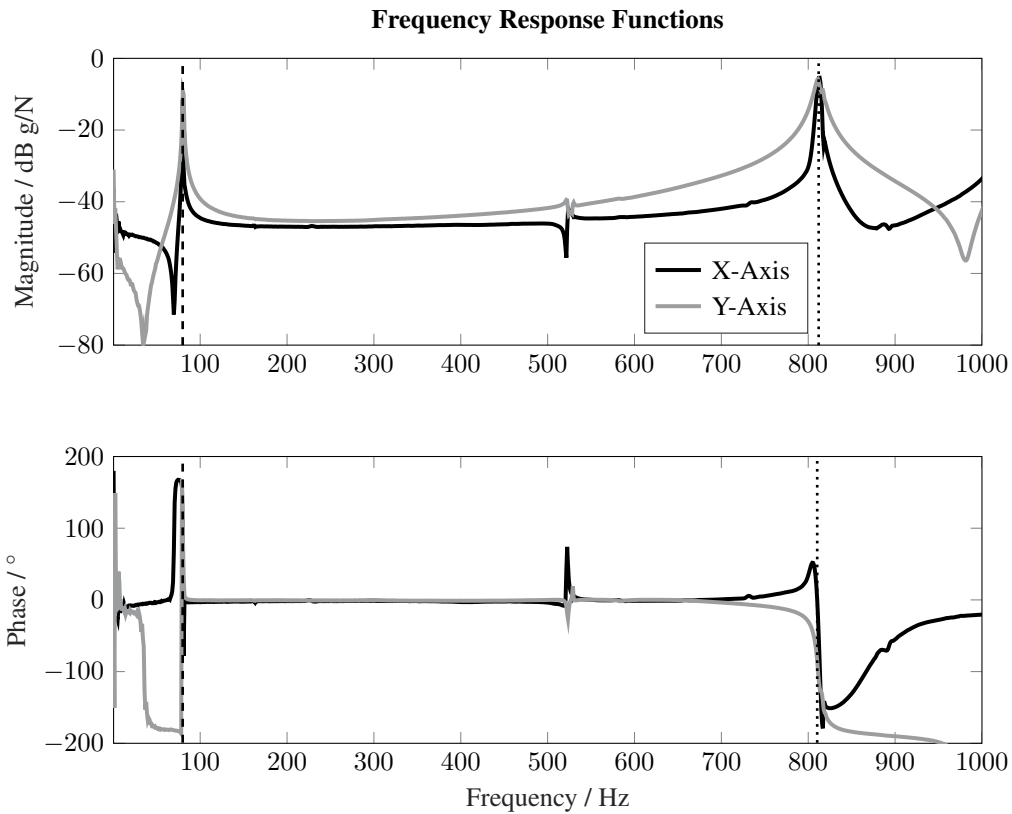


Figure 9: Averaged frequency response functions in x- and y-direction with marked resonance frequencies f_1 at 79.86 Hz (dashed line) and f_2 at 810.34 Hz (dotted line).

In figure 10, we see the x-axis projection of the first two mode shapes. Apparent measurement points are plotted and connections delineated. We recognize the undeformed geometry in black for relative displacement illustration.

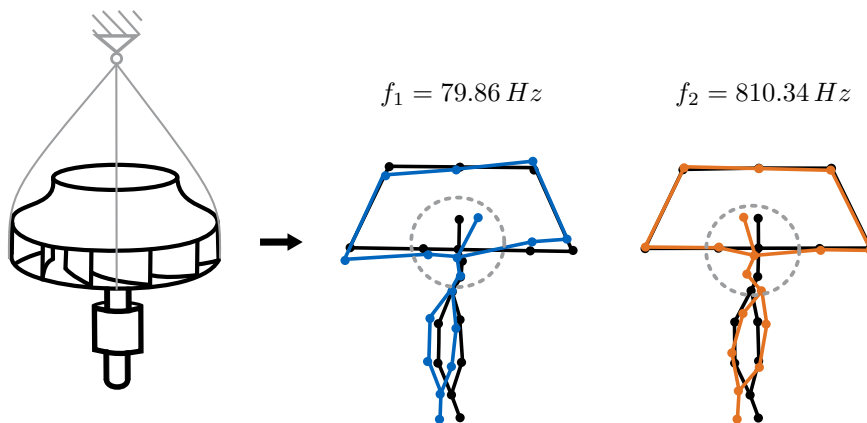


Figure 10: Experimentally determined, axial bending mode shapes at resonance frequencies f_1 and f_2 . Marked leftwards impeller tilt at mode shape 1 and marked antinode at upper bearing seat position at mode shape 2

The frequency related to the first mode shows a deviation to the reference model of 2.2 % and 2.8 % to the reduced one. Deflections are particularly distinct at excitation point as well as at shaft extension inside the impeller. Striking bending occurs at the thin, circular disc, qualitatively equal to the simulation results. Thus, the impeller

tilts leftwards in figure 10. The second relevant natural frequency is 1.9 % away from the reference and differs 0.3 % from the reduced model. Its mode shape deflection at the disc is in accordance with the simulation results. Furthermore, we see the similar antinode at upper bearing seat position tightly below the impeller, displaced to the left. The natural frequency deviations between simulation and experiment could be explained by the mass distribution. Although we checked the reference and reduced model masses and corrected them especially at the bundle of laminations, the mass distribution might differ from reality. Moreover, the corrosion protection paint is not included in the simulations. Additionally, approximated stiffnesses notably at the impeller contains errors, because of numerous welding seams which reinforce the structure. In sum, the natural frequency deviations between simulation and experiment are low and the mode shapes similarly, representing a satisfactory quality of the reduced rotor model despite of huge degrees of freedom reduction from 575 718 to 136. Particularly, a deviation up to 10 % between finite element simulation and experimental modal analysis is within a standard range ([5], p.316), therefore the results can be valued very positively. Table 1 shows a final comparison.

Table 1: Simulated and experimental identified axial bending resonance frequencies f_1 and f_2

Resonance Frequencies	<i>Reference</i>	<i>Reduced</i>	<i>Experimental</i>
f_1	81.63 Hz	82.12 Hz	79.86 Hz
f_2	795.20 Hz	812.96 Hz	810.34 Hz

5 Conclusion and Future Research

The new presented model reduction method constitutes a solution for building up a base for efficient simulations of a widely rotor type. A combination of Timoshenko beam theory and an analogous stiffness of the characteristic, circular impeller plate, represents the rotor structural dynamics, resulting in nearly the same first two axial bending resonance frequencies as identified by experimental modal analysis with just 136 degrees of freedom. For closing the gap to sensor positions of a condition monitoring system in future, we plan to couple the rotor model to remaining components of the application. Nevertheless, further supplements like the bearing stiffnesses and the operational, gyroscopic effects have to be implemented. Advanced model reduction may be realized by regarding the impeller as a ideally stiff, coupled mass. Subsequently, specific fault forces can be applied to the rotor. Henceforth, the optimized model is ready for a condition monitoring system based on wireless sensor nodes.

Acknowledgment

This work ist funded by the Federal Ministry of Education and Research within the project "AMELI 4.0: Micro-Electro-Mechanical Electronics System for Condition Monitoring in Industry 4.0" (ID: 16ES0442).

REFERENCES

- [1] Albarbar, A., Badri, A., Sinha, J. K., Starr, A. (2009): *Performance evaluation of mems accelerometers*, Measurement, **42**(5), pp. 790–795. DOI: 10.1016/j.measurement.2008.12.002
- [2] Altenbach, H., Meyer, H., Schumpich, G. (2018): *Technische Mechanik Festigkeitslehre*. Springer Vieweg, 13, pp. 81 ff. DOI: 10.1007/978-3-658-22854-5
- [3] Besselink, B., Tabak, U., Lutowska, A., Van De Wouw, N., Nijmeijer, H., Rixen, D. J., Hochstenbach, M. E. and Schilders, W. H. A. (2013): *A comparison of model reduction techniques from structural dynamics, numerical mathematics and systems and control*. Journal of Sound and Vibration, **332**(19), pp. 4403–4422. DOI: 10.1016/j.jsv.2013.03.025
- [4] Gross, D., Ehlers, W., Wriggers, P., Schröder, J., Müller, R. (2016): *Formeln und Aufgaben zur Technischen Mechanik 1 Statik*. Springer-Verlag Berlin Heidelberg, 12, p.36. DOI: 10.1007/978-3-662-52715-3
- [5] Klein, B. (2015): *FEM*. Springer Vieweg, Wiesbaden. DOI: 10.1007/978-3-658-06054-1
- [6] Timoshenko, S.P. (1921): *On the correction for shear of the differential equation for transverse vibrations of prismatic bars*. Philosophical Magazine, 41, pp. 774–746. DOI: 10.1080/14786442108636264

Automated wind turbine gearbox bearing diagnosis algorithm based on vibration data analysis and signal pre-whitening

Meik Schlechtingen¹, **Ilmar Ferreira Santos**²

¹ Department of Technical Operation, EnBW AG, 20095 Hamburg, Germany, m.schlechtingen@enbw.com,
Tel: +4940533268134

² Department of Mechanical Engineering, Section of Solid Mechanics, Technical University of Denmark,
Denmark

Abstract

In this paper an automated wind turbine gearbox bearing diagnosis algorithm is presented. The algorithm is based on most recent research results for separating discrete (gear) from random (bearing) frequency components using Cepstral Editing Procedure (CEP) based signal Pre-Whitening (PW). The proposed automated procedure builds up on the semi-automated procedure described by Sawalhi et al. in 2007. The procedure is updated with regards to the most recent achievements made concerning signal separation and extended with a frequency content identifier and rule based diagnosis to fully automate the diagnosis process. Furthermore, this paper gives a selection of important statements made in literature throughout the last decade to summarize the algorithms used and focus on the most important issues. Each of the involved processing steps is discussed with respect to its effectiveness based on real data.

The proposed procedure is applied to wind turbine data coming from seventeen wind turbines of the 2 MW class, for which vibration data are available containing both healthy and damaged states. Three application examples are given, where the automated procedure successfully diagnosed High Speed Shaft (HSS) bearing damages in the data sets.

Nomenclature

AIC	=	Akaikes entropy based information criterion
ANC	=	Adaptive noise cancellation
AR	=	Autoregressive
BPFI	=	Ball pass frequency inner race
BPFO	=	Ball pass frequency outer race
BSF	=	Ball spin frequency
CEP	=	Cepstral editing procedure
DRS	=	Discrete/random separation
FCI	=	Frequency content identifier
FL	=	Fuzzy logic
FFT	=	Fast Fourier transformation
FTF	=	Fundamental train frequency
FRF	=	Frequency response function
HSS	=	High speed shaft
IMS	=	Intermediate speed shaft
LP	=	Linear prediction
MED	=	Minimum entropy deconvolution
MF	=	Membership function
OT	=	Order tracking
PSD	=	Power spectral density
PW	=	Pre-whitening
RMS	=	Root mean squared
RPM	=	Revolutions per minute

SANC	=	Self adaptive noise cancellation
SCADA	=	Supervisory control and data acquisition
SK	=	Spectral kurtosis
SRM	=	Stochastic resonance model
STFT	=	Short time Fourier transform
TS	=	Time series
TSA	=	Time synchronous average
WTG	=	Wind turbine generator

1 Introduction

Wind turbine condition monitoring is of increasing importance as the wind turbines are built more and more in remote locations. A special challenge is the placement of wind turbines at sea (offshore). Here the energy yield is usually much higher than on land (onshore), but special (expensive) logistics is required for construction, service & maintenance and decommissioning. Although the higher energy yield is desirable, the cost of energy is still very high in comparison to onshore turbines. From a society perspective a sharp drop in cost of energy must be achieved in the coming years. Next to the usually high construction costs of wind power plants offshore, unexpected downtime due to component failure bears large potential for cost reduction, if faults can be foreseen.

Difficulties with effective monitoring of wind turbines arise from the number installed units, which is increasing rapidly. A 2 GW conventional power station may consist of four 500 MW units, which can be monitored constantly in a cost effective manner [1], but several hundred 3 MW offshore wind turbines would be required to achieve this installed capacity, each in need of monitoring. Hence, a high degree of automation is required to reduce monitoring costs.

Due to their crucial role the components main bearing, gearbox and generator are usually monitored via vibration measurements at offshore turbines. Vibration analysis is by far the most prevalent method for machine condition monitoring [2]. However, also other information sources can be considered such as Supervisory Control And Data Acquisition (SCADA) data, e.g. temperatures, currents, voltages, power output, etc. in case no vibration measurements are available or to enhance diagnostics [3]. In general, operators should consider all information at hand in order to schedule their service & maintenance and achieve their cost reduction targets. In this research the focus lies on automated wind turbine gearbox bearing diagnosis based on vibration data analysis using signal Pre-Whitening (PW).

A large part of condition monitoring consists of separating the mixed signals at each measurement point into components coming from individual sources [2]. Here the task is to separate the deterministic (e.g. originating from gears) from the random and cyclostationary (e.g. originating from rolling element bearings) components in the signal. Signal PW is a comparably new method and can be used for this separation.

In 2007 Sawalhi and Randall [4] proposed a semi-automated method for diagnosing bearing faults. Using three case studies Sawalhi and Randall show the applicability of their method. It consist of (I) removal of speed fluctuations (II) removal of discrete frequencies (III) removal of the smearing effect of the signal transfer path (IV) determination of the optimum band for filtering & demodulation and (V) determination of the fault characteristic frequencies.

In the same year Sawalhi et al. [5] studied the enhancement of fault detection and diagnosis in rolling element bearings using Minimum Entropy Deconvolution (MED) combined with Spectral Kurtosis (SK). This corresponds to step III and IV of the semi-automated procedure. The results show that using the MED technique dramatically sharpens the pulses originating from the impacts of the balls with the spall and increases the kurtosis value to a level that reflects the severity of the fault [5]. In this work a good match between the fault size and the Spectral Kurtosis (SK) value was found, when MED is applied to enhance the signals impulsiveness. The effect of MED as pre-process is further studied and a significant increase in diagnostic information found by Barszcz and Sawalhi [6] in 2012. These findings are further discussed in this research for the case of wind turbine gearbox bearings.

Using the same three test cases as described by Sawalhi and Randall [4], the proposed semi-automated method is summarized and further developed in 2011 by Randall and Antoni [7] who presented a tutorial for rolling element bearing diagnostics. In this tutorial different processing techniques for discrete and random separation are summarized (corresponding to step II of the semi-automated procedure), which are: Linear Prediction (LP), Adaptive Noise Cancellation (ANC), Self Adaptive Noise Cancellation (SANC), Discrete/Random Separation (DRS) and Time Synchronous Averaging (TSA).

In the LP approach an autoregressive linear model built with past values is used to model the current value. Such a model can only represent the deterministic part of the signal. The random part is given by the residual. However, the model order (number of previous values considered) is generally unknown, which requires some search for an optimum order.

The ANC algorithm requires a simultaneously measured coherent signal from a different location, for adjustment of the adaptive filter. Such synchronous data recordings are not always available for operators. In this case the SANC algorithm can be used, in which a delay of the input signal is taken for adoption of the adaptive filters. Antoni and Randall [8] show however, that the same effect could be achieved, but much more efficiently using DRS.

In DRS the efficient Fast Fourier Transformation (FFT) is used. The transfer function between the primary signal and its delayed version (representing only the deterministic part) is calculated in the same way as the H1 Frequency Response Function (FRF) [9]. This has a value near one at discrete frequencies and near zero at other frequencies [9]. This property is used to filter the signal by fast convolution in the frequency domain. However, it does give a notch filter of fixed width that can have detrimental effects at high and low frequencies [9]. At low frequencies (low harmonics of the bearing frequencies if they exist), the bearing harmonics may still be within the bandwidth of the comb filter, and they may be treated as discrete frequencies [9]. At high frequencies, some random modulation of the discrete frequency components may be left in the form of a narrow-band noise and not completely removed [9].

In TSA specific discrete frequency components can be removed by averaging together a series of signal segments each corresponding to one period of a synchronising signal [7]. The drawback is that it requires separate operation for every different harmonic in the signal including a separate resampling in each case so as to give a specified integer number of samples per period [7].

Further research was carried out by Sawalhi and Randall with regards to the separation of the discrete and random components (corresponding to step II of the semi-automated procedure). In 2011 a method based on cepstrum editing is proposed by Sawalhi and Randall [10] to remove selected components from a time signal. The cepstrum collects uniformly spaced harmonics and sideband families such as arise from gear mesh harmonics and modulations of these by the gear rotational speeds [10]. For removal of undesired components, the real cepstrum is computed, selected components (quefrecencies) are set to zero and the result inverse transformed back to the initial time domain.

Also in 2011 this procedure was given the name Cepstral Editing Procedure (CEP) by Randall and Sawalhi [9]. Further application examples are given and a performance comparison to the traditionally used TSA and DRS method is made. It is pointed out that this method has a number of advantages compared with alternative methods. Unlike TSA and DRS, it can remove sidebands as well as harmonics and also narrow-band noise peaks rather than just discrete frequency harmonics [9].

Sawalhi and Randall [11] presented an even more drastic editing in the cepstrum, by setting all components to zero except that at zero quefrecency.

In 2012 Niaoqing et al. [12] tested the method using test rig data and inner ring faults with different fault sizes. They used a Stochastic Resonance Model (SRM) to enhance the Envelope spectrum. The method proved to be robust and suitable for the application with more vibration interference. However, the stochastic resonance method requires tuning of the system parameters, which can be difficult in practical applications, involving a large number of units to be monitored. In this work, also the SK value as fault size indicator (first used by Dyer and Stewart [13]) was examined. Results show that the SK after signal processing, contains some fluctuations, but in general is sensible to the fault size. The findings confirm the findings from Sawalhi et al. [5], who conclude that the SK value can be used as fault size indicator after impulsiveness enhancement. In the case of Sawalhi et al. this was achieved by MED in contrast to the SRM algorithm used by Niaoqing et al. [12].

The main original contribution of this paper lies in the further evaluation of signal PW using the CEP in combination with the SK value as a fault size indicator for wind turbine gearbox bearings. Furthermore an automated method for bearing diagnosis is presented using the achievements made by Sawalhi and Randall, as well as own research results. In this respect the semi-automated method as proposed by Sawalhi and Randall is updated with regards to the most recent developments and further developed with regards to automated envelope spectra diagnosis as it is required for wind turbine gearbox bearing diagnosis.

For this purpose data from seventeen operating wind turbines are available, both in fault free states as well as in states where the fault signatures indicate bearing damage. Using these data the effectiveness of the automated procedure is shown. Additionally the use of the SK value as fault size indicator is discussed using the available data and faults.

In this paper many statements are collected from related papers in this research area in order to summarize the most important conclusions and findings necessary for the understanding of the automated procedure. These statements are consistently cited, allowing finding more information about the specific topics of interest in the original source.

In section 2 of this paper, the available data sets are introduced. In section 3 the automated procedure for bearing fault diagnosis is described in detail with a focus on the individual processing steps involved. Furthermore the efficiency and the effect the involved pre-processes are evaluated. Three application examples are given in section 4. Results and Discussion are made in section 5 and necessary future research discussed in section 6. Finally conclusions are drawn in section 7.

2 Data Set Descriptions

The data sets available come from seventeen Wind Turbine Generators (WTGs) of the 2 MW class, where vibration measurements are recorded cyclically every second week. The gearbox is equipped with three accelerometers (type: Gram&Juhl GJ1200M8), with one sensor placed at the planetary stage, one in the Intermediate Shaft (IMS) region and one in the High Speed Shaft (HSS) region (see Figure 1).

The cyclic measurements available for research are sampled with the settings as summarized in Table 1.

Table 1: Summary of recordings

Name	Sampling freq.	Sample lengths	Number of samples
#1	2.59 kHz	12.51 s	32000
#2	15.36 kHz	4.17 s	64100
#3	41.67 kHz	1.54s	64100

Around 32 measurements per turbine, sensor and sampling frequency are available from the past 1.5 years of operation. Thus in total around 1632 recordings are available. The recording system is set up to only record, when the turbine is operating under full load to allow comparison of measurements at different times (causing the slight differences in number of measurements available for each turbine).

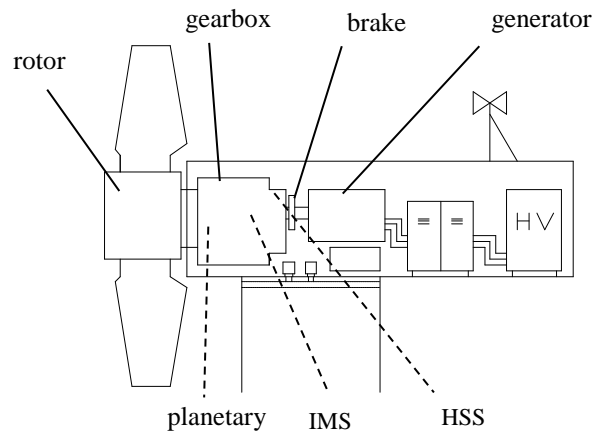


Figure 1: Wind turbine schematic

Due to their longer recording times of measurement #1 and #2, these time series are given by the system as tracked time series. By tracking, speed variations are encountered by resampling the signal synchronous to the speed of the shaft. Here these data are resampled to the nominal speed. For #3 resampling is not necessary as the recording length is short.

3 Automated procedure for bearing fault detection

The semi-automated procedure presented by Sawalhi and Randall [4] in 2007 consists of a five step strategy to arrive at the envelope spectrum to be interpreted for fault signatures. Due to recent advances made by the different researchers, this procedure requires an update with regards to the algorithms used and the signal processing steps involved.

The following update is proposed to fully automate diagnosis:

1. Order tracking – Remove speed fluctuations (optional)
2. Pre-Whitening (PW) based on CEP - Signal decomposition
3. Minimum Entropy Deconvolution (MED) – Remove smearing effect of the signal transfer path (optinal)
4. Spectral Kurtosis (SK) – Determine optimum band for filtering and demodulation (optional)

5. Envelope analysis – Determine fault characteristic frequencies
6. Frequency content identification – Identify frequency components and modulations

3.1 Order Tracking

Order Tracking (OT) means resampling the time series according to the angular position of the shaft. It is useful for variable speed machines in order to remove the rotational speed related frequency fluctuations. For OT generally a tacho signal or a once per revolution trigger is required that indicates the shafts angular position. In case no tacho signal is available Bonnardot and Randall [14] found it to be possible to extract the instantaneous speed information by phase demodulation of a number of gear mesh frequencies.

When applying digital or analog OT, frequency components which are independent of the shaft speed such as natural frequencies will shift and consequentially their amplitude in the spectra will decrease.

For the automated bearing diagnosis algorithm OT is recommended, but not necessarily mandatory, if the speed variations are limited and the CEP is used [9].

3.2 Pre-whitening

Decomposition of vibration signals into deterministic and nondeterministic parts is recommended for machinery diagnostics as it can be used for the separation of signals emitted from different machinery elements [15]. One of the major sources of masking the relatively weak bearing signals is discrete frequency “noise” from gears, since such signals are usually quite strong, even in the absence of gear faults [7]. Even in machines other than gearboxes, there will usually be strong discrete frequency components that may contaminate frequency bands where the bearing signal is otherwise dominant [7]. It is usually advantageous therefore to remove such frequency noise before proceeding with bearing diagnostic analysis [7].

The fundamental idea of separation is based on the assumption that gear related vibrations are phase locked to the rotational speed, i.e. after order tracking they will appear as discrete frequencies in the spectrum. However, bearings virtually always have some slip for the following reason: the load angle ϕ from the radial plane varies with the position of each rolling element in the bearing as the ratio of local radial to axial load changes, and thus each rolling element has a different effective rolling diameter and is trying to roll at a different speed [2]. The cage ensures that the mean speed of all rolling elements is the same, by causing some random slip [2]. This slip is typically of the order of 1-2%, both as deviation from the calculated value and as a random variation around the mean frequency [2]. The slip, while small, does give a fundamental change in character of the signal, and is the reason why envelope analysis extracts diagnostic information not available from frequency analysis of the raw signal [2].

The separation method here is signal PW for the reasons given in the introduction.

Basic element of the signal PW procedure is the real cepstrum. The cepstrum has a number of versions and definitions, but all can be interpreted as a “spectrum of a log spectrum” [9]. The complex cepstrum reads:

$$C(\tau) = \mathfrak{F}^{-1} \log[|\mathfrak{F}[x(t)]|] \quad (1)$$

$C(\tau)$ is the complex cepstrum; \mathfrak{F}^{-1} is the inverse Fourier transform; \mathfrak{F} is the Fourier transform; $x(t)$ is the time signal.

In order to arrive at the real cepstrum, only the real part of the complex cepstrum is considered. Information about the history of the cepstrum is summarized by Oppenheim and Schaffer [16]. Additional general information in the context of vibration analysis is given by Randall and Hee [17] and in the context of cepstrum editing by Randall and Sawalhi [9].

The procedure to achieve signal PW is depicted in Figure 2. In order to proceed from the real cepstrum to the edited cepstrum, all frequencies are set to zero, apart from the first, which is determining the mean value of the log spectrum and thus giving appropriate scaling of the resulting signals [9].

After editing, the edited log amplitude spectrum is exponentiated and recombined with the original phase spectrum to form the complex log spectrum [9]. When processing the signals with Matlab® the required polar to cartesian coordinate transformation can be done with the `pol2cart` function using the phase and the exponentiated edited log amplitude spectrum as input. The output can be interpreted as the real and imaginary part of the complex spectrum.

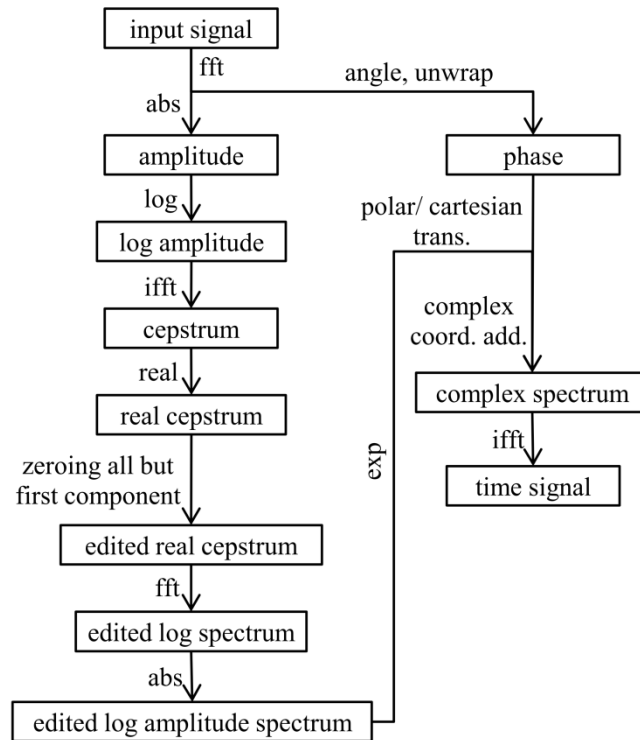


Figure 2: PW based on CEP schematic

Since the procedure is based on the efficient Fast Fourier Transformation (FFT), the whole editing procedure is very fast to calculate and can be fully automated without the need of parameter optimization. The real cepstrum before editing of #3, measurement 29 at WTG 02 is shown in Figure 3.

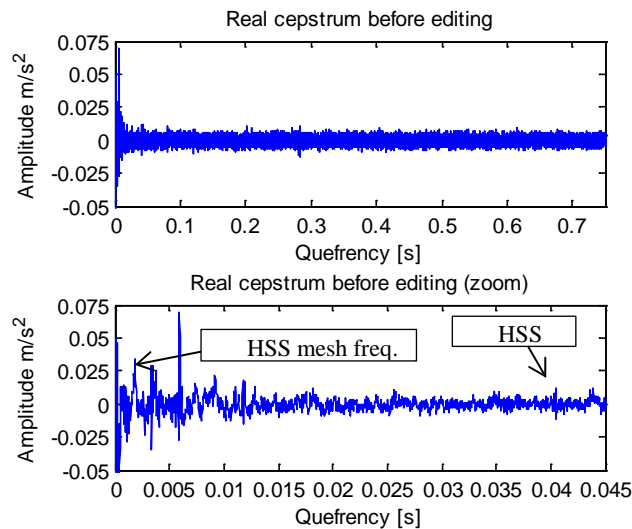


Figure 1: Real cepstrum before editing (#3, HSS, meas. 31, WTG 02)

The HSS mesh frequency as well as the HSS speed can be clearly identified, together with other deterministic components of unknown source. The effect of PW on the corresponding time series as well as the Root Mean Squared (RMS) spectrum is illustrated in Figure 4.

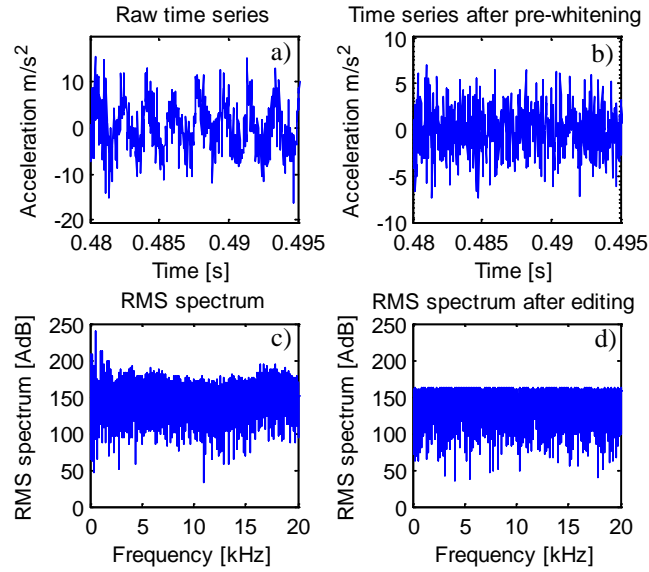


Figure 2: The effect of signal PW (#3, HSS, meas. 31, WTG 02)

Prior PW, the raw time series (a) was contaminated with deterministic components causing cyclical fluctuations. The PW procedure removed the dominance of these components and reduced them to the noise level (b). The RMS spectrum before PW contained dominating frequency components and frequency bands containing more energy (c). After PW the RMS spectrum has the same level for all frequencies (d).

3.3 Minimum Entropy Deconvolution

The Minimum Entropy Deconvolution (MED) method is designed to reduce the spread of impulse response functions, to obtain signals closer to the original impulses that gave rise to them [7]. It was first proposed by Wiggins [18] to sharpen the reflections from different subterranean layers in seismic analysis [7]. The basic idea is to find an inverse filter that counteracts the effect of the transmission path, by assuming that the original excitation was impulsive, and thus having high kurtosis [7].

(2)

K is the Kurtosis; s is the standard deviation; N is the number of data points; \bar{Y} is the mean.

The name MED derives from the fact that increasing entropy corresponds to increasing disorder, whereas impulsive signals are very structured, requiring all significant frequency components to have zero phase simultaneously at the time of each impulse [7]. Thus, minimizing the entropy maximizes the structure of the signal, and this corresponds to maximizing the kurtosis of the inverse filter output (corresponding to the original input to the system) [7]. The method might just as well be called maximum kurtosis deconvolution because the criterion used to optimize the coefficients of the inverse filter is maximization of the kurtosis (impulsiveness) of the inverse filter output [7]. The MED method was applied to bearing diagnostics by Sawalhi, Randall and H. Endo [5].

Using the MED method, the kurtosis can be increased, if impulses are present. Note that in case the discrete frequencies are not removed prior the MED, they will also be amplified.

The Matlab[®] code used for performing the MED was developed by G.McDonald [19] based on the algorithm proposed by Wiggins [18].

A critical choice using MED is the filter size. If the filter size is chosen too large, start-up and ending transients may occur, dominating the minimization method and leading to a loss of diagnostic information. The effect of the filter size on the time series is illustrated in Figure 5, for a time series with start-up and ending transients for large filter size (a) and medium filter size (b). For a low filter size (c) reasonable impulse amplification is achieved without transients. (d) shows the Time Series (TS) after PW without MED.

This is in contrast to the findings of Barszcz and Sawalhi [6] who found very large filters (filter size > 2000) to perform better in case of their surveyed wind turbine gearbox bearing inner ring damage.

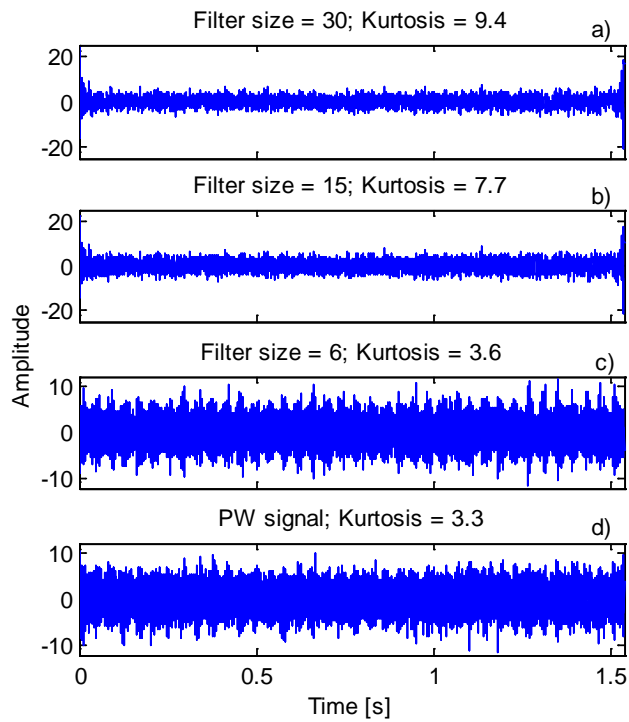


Figure 3: Time series after PW & MED a) filter size = 30; b) filter size = 15; c) filter size =6; d) signal after PW without MED (#3, HSS, meas. 19, WTG 05)

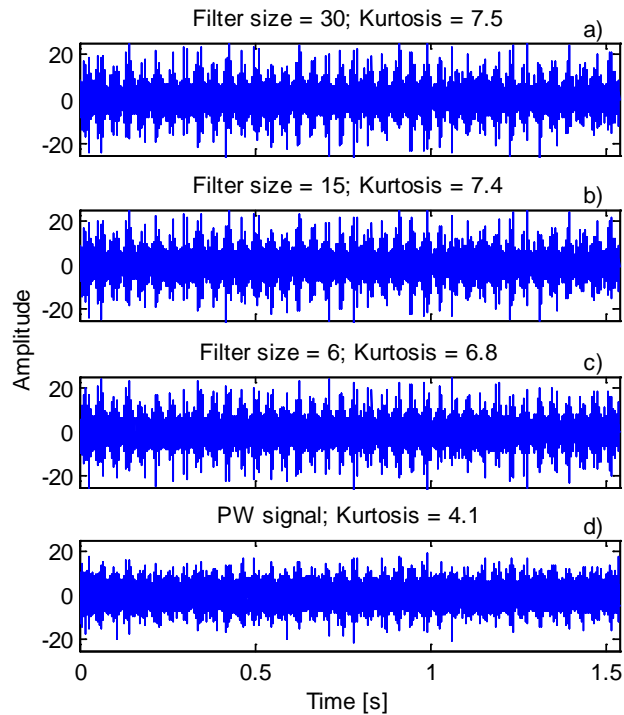


Figure 4: Time series after PW & MED a) filter size = 30; b) filter size = 15; c) filter size =6; d) signal after PW without MED (#3, HSS, meas. 32, WTG 05)

Their finding is based on the kurtosis values achieved, apparently using a TS where MED does did not lead to start-up and end transients. For blind analysis the filter size used should give reasonable results for all TS processed.

Figure 6 shows the effect of the filter size for a time series without transients. It is seen that choosing a filter size of six already gives a reasonable impulse amplification and increase in kurtosis, which is why this filter size is used throughout the research as a stable compromise.

Figure 7 illustrates the kurtosis as a function of the filter size for the TS with and without transients.

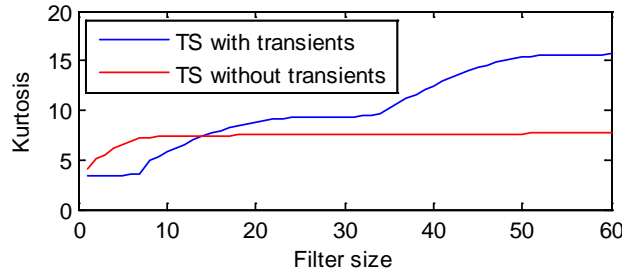


Figure 5: Kurtosis value as function of the filter size; blue (#3, HSS, meas. 19, WTG 05) and red (#3, HSS, meas. 32, WTG 05)

The kurtosis for the TS without transients occurring converges with increasing filter size, whereas the kurtosis values with transients stepwise increases. The transients are believed to be caused by the first and the last value in the time series. In case of their occurrence, these values may be modified or deleted to avoid the transients and obtain proper results. However, further root cause investigation is required, which is outside the scope of this paper.

For the proposed automated procedure, applying MED is not necessarily required, since after successful PW the impulsiveness of the TS is already enhanced, building a good basis for a consecutive envelope analysis. Figure 8 shows the effect of MED of the PW signal in the time domain.

In the raw time series (a) the individual impulses are visible, but they are embedded in the cyclic variations of the deterministic components. Signal PW removes the deterministic components, but leaves a high noise level embedding the impulses (b). Applying MED enhances the impulses and gives the clearest signal (c). The kurtosis increased from 4.5 after PW to 8.0 after PW & MED. After introduction of the envelope spectrum the influence of MED in the frequency domain will be discussed.

3.4 Spectral Kurtosis

Spectral kurtosis (SK) provides a means of determining which frequency bands contain a signal of maximum impulsivity [7]. The definition is given by equation 3.

$$SK = \frac{\langle H^4(t, f) \rangle}{\langle H^2(t, f) \rangle^2} - 2 \quad (3)$$

SK is the spectral kurtosis, $H(t, f)$ is the Amplitude envelope function.

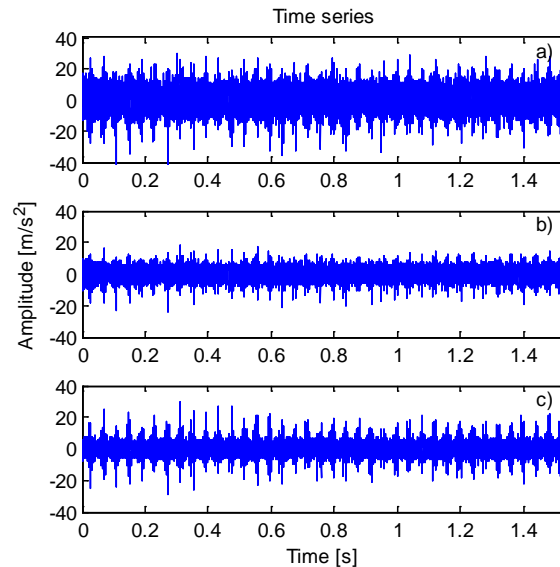


Figure 6: The time series a) no processing, b) PW, c) PW & MED (#3, HSS, meas. 31, WTG 02)

It was first used in the 1980s for detecting impulsive events in sonar signals [20]. It was based on the Short Time Fourier Transform (STFT) and gave a measure of the impulsiveness of a signal as a function of frequency [7]. The spectral kurtosis extends the concept of the kurtosis, which is a global value, to that of a function of frequency that indicates how the impulsiveness of a signal, if any, is distributed in the frequency domain [7]. The principle is analogous in all respects to the Power Spectral Density (PSD) which decomposes the power of a signal vs frequency, except that fourth-order statistics are used instead of second order [7]. This makes the spectral kurtosis a powerful tool for detecting the presence of transients in a signal, even when they are buried in strong additive noise, by indicating in which frequency bands these take place [7]. However, the optimal window length used for the STFT is generally unknown. To obtain a maximum value of kurtosis, the window must be shorter than the spacing between the pulses but longer than the individual pulses [2]. The center frequency and bandwidth (window length and center) is thus varied continuously from low to high values, while recording the SK of each window and thus arriving at a full kurtogram, which can be used to identify the optimum filter settings (center frequency and bandwidth). This procedure is used for bearing diagnosis by Antoni and Randall [21].

The signal is filtered according to the optimum filter settings determined, arriving at a signal that has maximum kurtosis for envelope analysis.

However, computation of the kurtogram for all possible combinations of center frequencies and bandwidths is obviously costly and not convenient for practical purposes [7]. Therefore the fast kurtogram was proposed by Antoni [22] in 2007. A „1/3-binary tree“ was used, where each halved-band is further split into three other bands, thus producing a frequency resolution in the sequence $1/2, 1/3, 1/4, 1/6, 1/8, 1/12, \dots, 2^{-k-1}$ with corresponding “scale levels” $k=0, 1, 1.6, 2, 2.6, \dots$ to compute the SK in this bands.

With this limited amount of combinations the computational time could be drastically decreased, but virtually the same result can be achieved than with using the full kurtogram. The fast kurtogram algorithm for detection of transient faults proposed by Antoni [22], was made available for public in terms of a Matlab[®] function [23], which is used here.

Figure 9 shows the kurtogram for the example wind turbine and time series after PW and PW & MED.

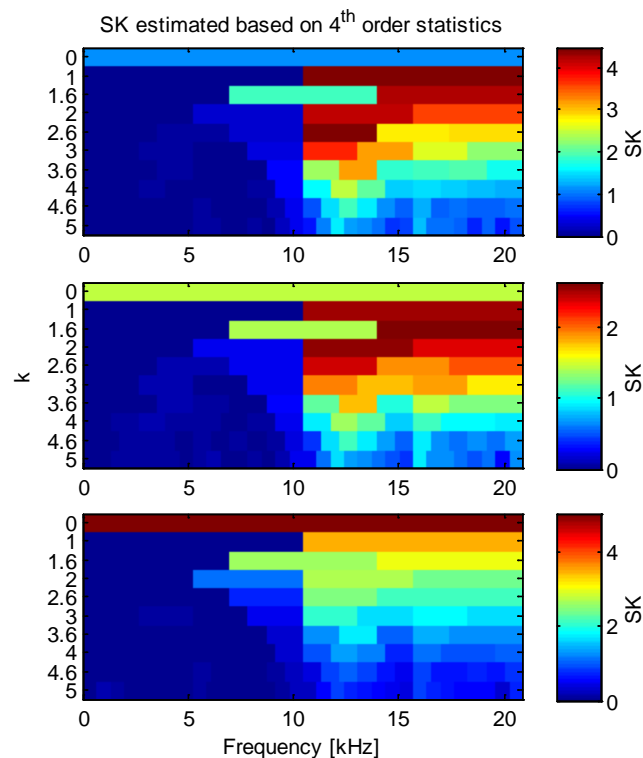


Figure 7: Kurtogram based on 4th order statistics a) raw time series, b) PW, c) PW & MED (#3, HSS, meas. 31, WTG 02)

The maximum SK is achieved at different frequency bands, depending on the processing involved. The kurtogram for the raw time series (a) has its maximum at $k = 2.6$, corresponding to a center frequency of 12.1 kHz and a bandwidth of 3.7 kHz. After PW (b) maximum SK is in the band with a center frequency of 17.6 kHz and a band width of 6.9 kHz ($k=1.6$). After PW & MED (c), maximum kurtosis is in the full frequency band.

Sawalhi and Randall [11] conclude in their research, based on a fault in a planetary bearing at a helicopter gearbox, that even without filtration in the optimum frequency band, complete whitening of the spectrum means that faults have a good chance of manifesting themselves in an envelope analysis covering the full frequency range, because the most impulsive bands will tend to dominate peaks in the time signal. It is further concluded, that if desired, spectral kurtosis can in any case be applied after cepstral PW, to give an optimal result. In general, a shift of the maximum kurtosis to a lower scale level (broader band) is desirable, as this allows a broader frequency spectrum to be analyzed in the envelope spectrum. A small bandwidth can cause problems in spectra interpretation as the higher harmonics may not be visible, due to the limited maximum frequency.

3.5 Envelope Analysis

Envelope analysis has become one of the prominent vibration signal processing techniques for detection and diagnosis of rolling element bearing incipient failure [24].

The envelope can be calculated by performing a Hilbert transform of the squared signal. The signal is band pass filtered according to the band width and center frequency identified through the SK and the kurtogram beforehand. The envelope is then further transformed via a FFT to the frequency domain to arrive at the squared envelope spectrum, which can be used to identify the damage frequencies. Next, the effect of the different pre-processing algorithms (PW, MED and SK) on the squared envelope spectrum is discussed.

3.5.1 The effect of PW

The focus lies on the improvement of the envelope spectra when the time series is pre-whitened. A comparison is made between the raw TS, the PW TS and the LP residual.

The LP (AutoRegressive (AR)) model used here for comparison takes the form

$$\hat{x}(n) = \sum_{k=1}^p a(k)x(k-n) \quad (3) [2]$$

$\hat{x}(n)$ is the predicted current value, p is the number of previous values (model order), $a(k)$ is the weighting coefficient and $x(k-n)$ is the previous value.

The weighting coefficients are obtained using the Yule-Walker equations model and Akaike's entropy-based Information Criterion (AIC) [25] to estimate the model order p .

Although the model order can be estimated using AIC it must be determined for each time series individually as the rotational speed can vary slightly, influencing the discrete frequency components and hence requires different model parameters. The model order can be quite high for time series with a high sampling frequency. The AIC lead to an optimum model order of 598 for the example TS used. Here PW gives some advantage as no parameter must be optimized, making PW a computationally very efficient method.

Figure 10 emphasizes that the PW procedure gives virtually the same result as LP (b and c for all WTGs are very similar). The fundamental IMS frequency (6.4 Hz), the IMS meshing frequency (115.1 Hz), the HSS meshing frequency (550 Hz) component as well as the modulations of the meshing frequency have been successfully removed by both methods at all WTGs (b,c), leaving the bearing damage frequency (297 Hz), its harmonics and shaft speed modulations (± 24.8 Hz) together with the fundamental shaft speed (24.8 Hz). The PW based on CEP thus gives good results in a very efficient manner.

Without separation, the envelope spectra can be dominated by the deterministic frequencies (compare WTG 04 (a) and WTG 10 (a)), making it impossible to diagnose the bearing defect reliably.

3.5.2 The effect of MED

It was already shown that the MED method can increase the kurtosis value in the time domain and enhance the impulsiveness of the signal. In this section it will now be investigated, whether or not this gives an advantage in respect of fault visibility in the envelope spectra using the available data sets. The fault visibility is increased, when typical fault patterns (e.g. damage frequencies) are enhanced, allowing a certain diagnosis. Figure 11 shows the squared envelope spectra of the TS with PW and PW & MED. The strongest improvement archived is at WTG 04. Here the shaft speed modulations around the damage frequency (297 Hz \pm 24.8Hz) are stronger pronounced with MED. The same is true for WTG 02. At the other turbines the improvement is marginal as (a) and (b) are very similar. However, the amplitudes of PW & MED are higher, which becomes evident by the lower noise level.

It can be concluded, that MED can improve the results and is thus recommended, but diagnosis should also be possible without MED.

3.5.3 The effect of band pass filtering using SK

The time series of the four example WTGs of Figure 10 and Figure 11, have the highest SK value in the full band after applying MED. Hence SK filtering does not give any improvement. Figure 12 compares the envelope spectra with and without optimal band pass filtering prior MED, but after PW.

Both spectra clearly show the present inner race damage signature, which consists of the Ball Pass Frequency Inner race (BPFI) (297 Hz) and present modulations at the shaft speed (24.8 Hz). Differences exist in the amplitudes and the higher modulation of the shaft speeds around the second harmonic of the BPFI. The results appear to be slightly better with band pass filtering. The conclusion drawn by Sawalhi and Randall [11] can thus be confirmed with the data at hand at least prior MED.

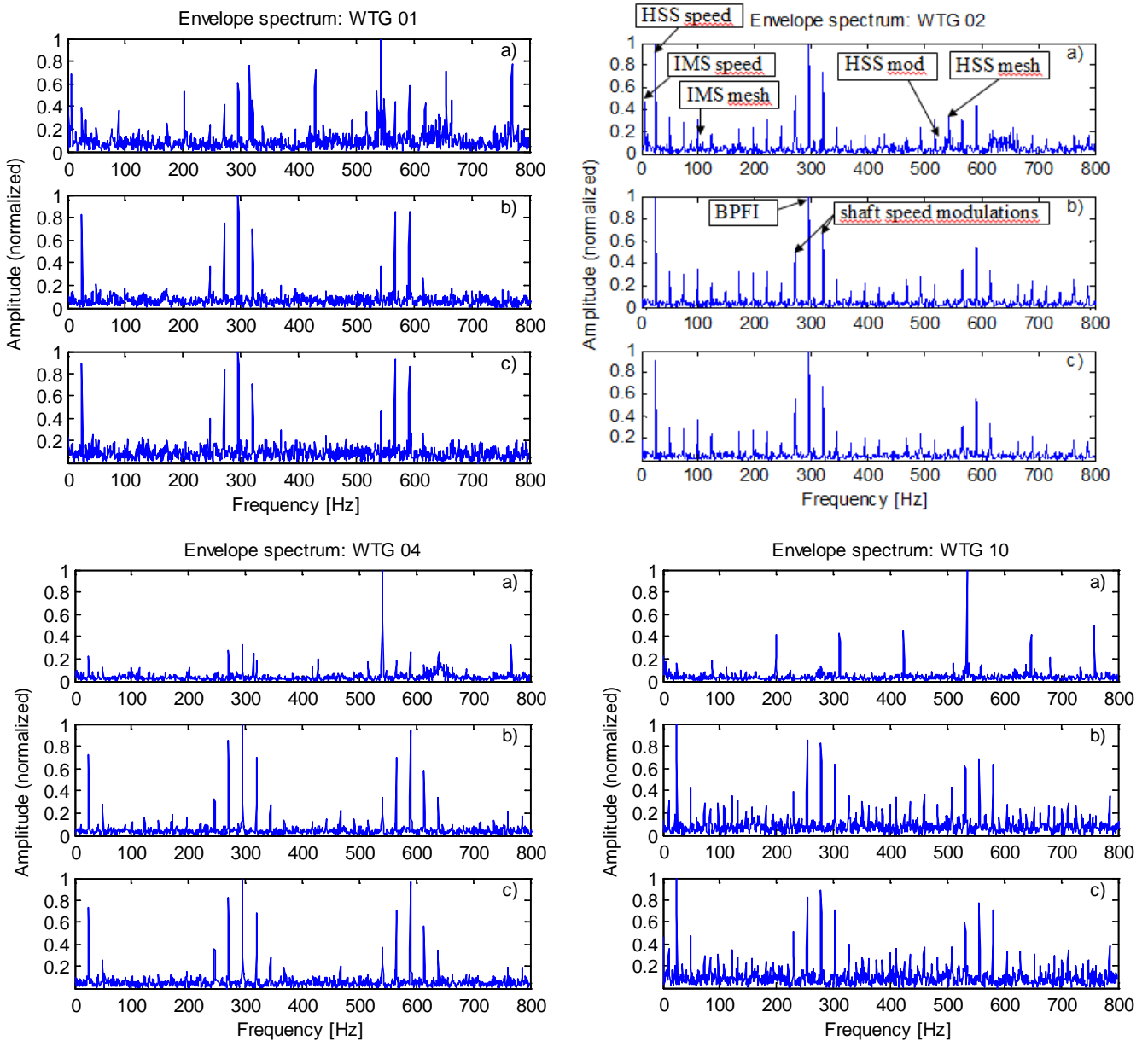


Figure 8: The effect of signal PW; a) no processing, b) linear prediction, c) PW (#3, HSS, meas. 31, WTG 01, 02, 04, 10)

The SK algorithm is fast to compute, (the kurtogram shown in Figure 9 was calculated in 0.5s using a regular 2.6 GHz processor). It is therefore recommended to apply optimal band filtering based on the SK, bearing in mind that in most cases, no improvement to the envelope spectra is made. However, a few cases existed in the data, where the maximum SK was not in full band. In these cases, it is expected that SK filtering improves the envelope spectrum in a fault situation.

3.6 Frequency content identification

For bearing diagnosis, the bearing damage frequencies as well as the individual shaft speeds are required. This information is usually available, either through theoretical calculations based on the geometry and design or in terms of damage frequencies coming from the bearing manufacturer (potentially originating from experimental studies). For further analysis it is assumed that these frequencies are available. In case those frequencies are not at hand, estimation methods can be applied.

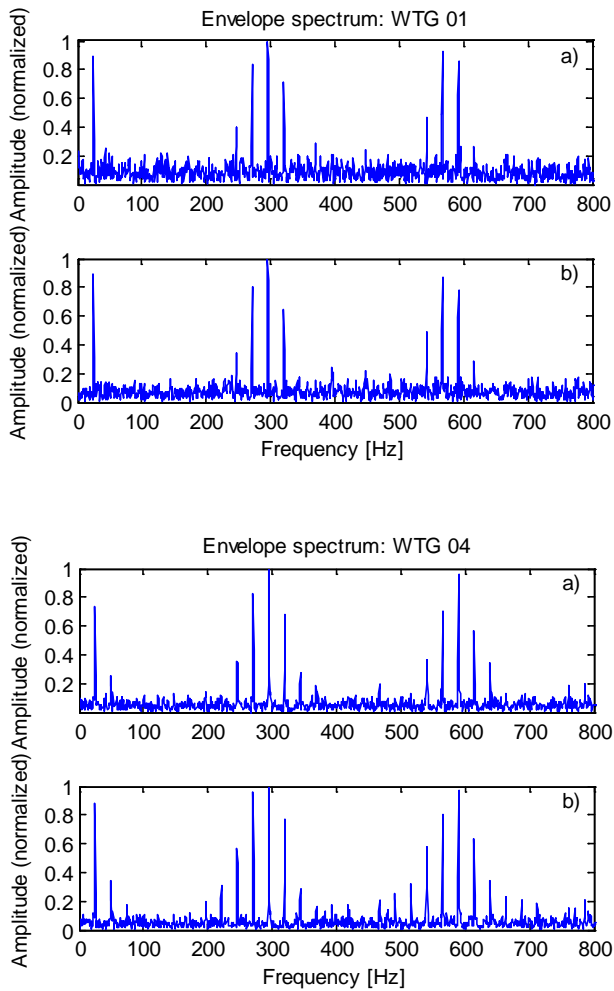


Figure 11: The effect of MED; a) PW without MED, b) PW & MED (#3, HSS, meas. 31, WTG 01, 02, 04, 10)

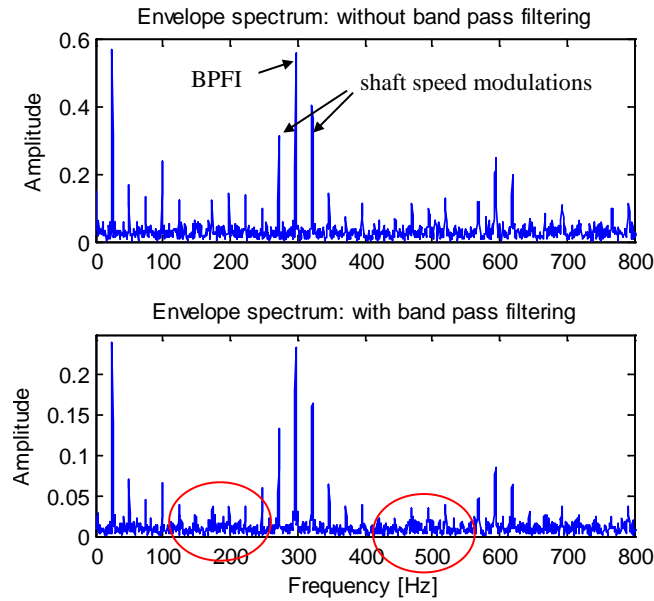


Figure 9: Envelope spectra with and without band pass filtration (PW without MED) (#3, HSS, meas. 31, WTG 02)

As pointed out by Randall and Antoni [7], the deviations from the theoretical values of the damage frequencies may be in the range of 1-2%. Any algorithms developed must therefore be capable of dealing with variations of this order, without affecting the diagnosis.

The Frequency Content Identifier (FCI) developed here deals with this by applying a tolerance band around the known damage frequency with a variation tolerance of 2%. Next to the pure damage frequencies, the presence of modulation sidebands is of interest, too. The developed concepts of damage and modulation frequency identification are visualized in Figure 13.

Before applying the FCI the envelope spectrum must first be checked for present peaks.

A data point is a local peak if (a) it is large and locally a maximum value within a window; the value need not necessarily be large nor a global maximum; and (b) it is isolated i.e. not too many points in the window have similar values [26].

Using this definition two types of peak detectors are set up, which are visualized in Figure 14. Both detectors consist of a moving window shifting along the whole envelope spectrum.

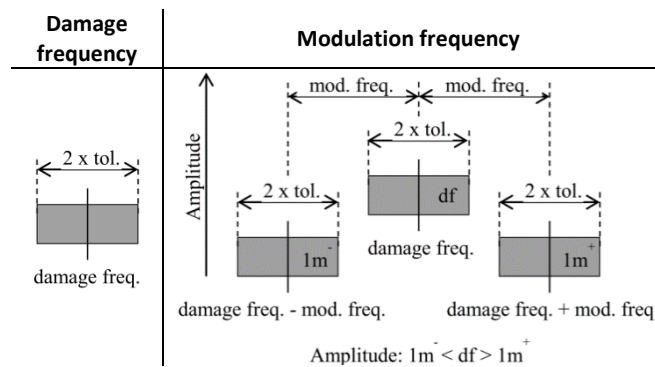


Figure 10: Frequency content identification principle

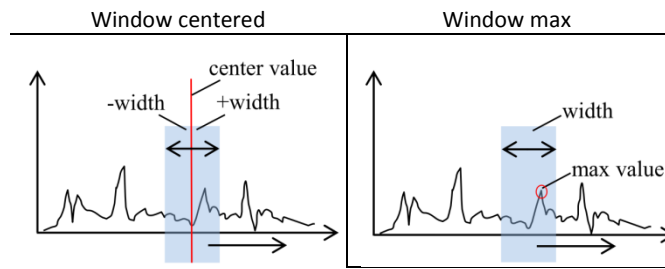


Figure 11: Two types of peak detectors

Differences exist in which of the values within the window is checked for being a peak. In the window centered method two conditions are checked, before the value is assigned a peak:

- Is the centered value larger than the maximum value in the window excluding itself?
- Is the centered value larger than the mean plus x times the standard deviation of the values in the window excluding itself?

In the window max method only one condition is checked, before the value is assigned a peak:

- Is the maximum value in the window larger than the mean plus x times the standard deviation of the values in the window excluding the maximum value?

The properties of these two peak detectors are quite different. While the window centered method cannot detect multiple values per peak, the window max detector has this property. In both methods the window is moving value by value. Dependent on which property appears to be more suitable either of the methods can be applied. For peak detection in the envelope spectrum the window max method is more suitable, since the peaks in the envelope spectrum can be spread over more than one spectral line, and the spectral components can be close to each other.

Since the peaks used for analysis should be clearly distinct, a tough bound with $x = 6$ (multiplier of the standard deviation) is chosen for peak definition here. In order to avoid false diagnosis, the detected peaks should be of reasonable magnitude. If it is assumed that the random noise in the envelope spectrum is normal distributed, it can be an option to mark detected peaks as true peaks only if they are larger than five times the standard deviation of the envelope values. This gives a high likelihood that the detected components are significant and thus carry some information. This filter is applied after peak detection here. Figure 15 illustrates a zoom of the squared envelope spectrum and the detected peaks using this setting.

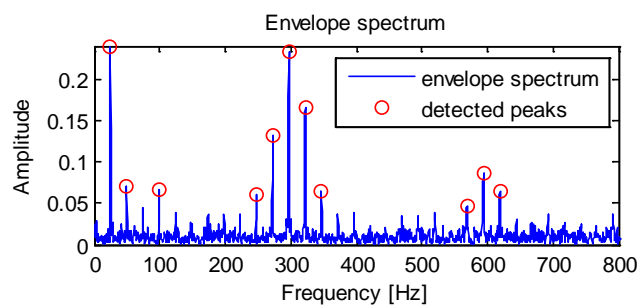


Figure 12: Envelope spectrum and detected peaks using window max method width = 15, $x = 6$ (#3, HSS, meas. 29, WTG 02)

In the following the true value of the envelope spectrum is only kept where a peak is detected and set to zero otherwise (see Figure 16).

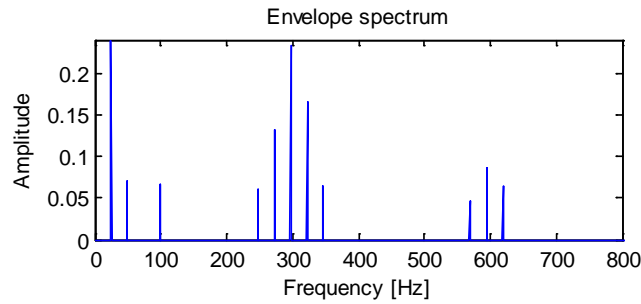


Figure 13: Envelope spectrum after peak filtering (#3, HSS, meas. 29, WTG 02)

The remaining envelope spectrum can now be analyzed for different frequency contents. For bearing diagnosis, the frequency contents given in Table 2 and Table 3 are checked for.

Table 1: Wanted frequency contents

Frequency	Harmonic
RPM	0, 1, 2, 3, 4 ^{*)}
BPFI	0, 1, 2, 3, 4 ^{*)}
BPFO	0, 1, 2, 3, 4 ^{*)}
FTF	0, 1, 2, 3, 4 ^{*)}
BSF	0, 1, 2, 3, 4 ^{*)}

^{*)} 0: fundamental frequency; 1: first harmonic;
2: second harmonic etc.

Table 2: Wanted modulation contents

		Modulation frequency				
		RPM	BPFI	BPFO	FTF	BSF
Fundamental frequency	RPM	-	0, 1 ^{*)}	0, 1 ^{*)}	0, 1 ^{*)}	0, 1 ^{*)}
	BPFI	0, 1 ^{*)}	-	0, 1 ^{*)}	0, 1 ^{*)}	0, 1 ^{*)}
	BPFO	0, 1 ^{*)}	0, 1 ^{*)}	-	0, 1 ^{*)}	0, 1 ^{*)}
	FTF	0, 1 ^{*)}	0, 1 ^{*)}	0, 1 ^{*)}	-	0, 1 ^{*)}
	BSF	0, 1 ^{*)}	0, 1 ^{*)}	0, 1 ^{*)}	0, 1 ^{*)}	-

In these tables RPM is the shaft speed; BPFI is the ball pass frequency inner race; BPFO is the ball pass frequency outer race; FTF is the fundamental train frequency and BSF is the ball spin frequency.

The result of the FCI for each component is stored in a matrix (see Table 4). If the frequency content is present (Pres.) the matrix entry will contain a one or zero otherwise. This matrix can afterwards be used to set up rules for automatic diagnosis. Note that the frequency contents labeled Mod_ are identified using the modulation frequency identifier and the other frequency contents are identified using the damage frequency identifier (compare Figure 13).

Table 3: Content matrix

No.	Freq. Cont.	Pres.	No.	Freq. Cont.	Pres.	No.	Freq. Cont.	Pres.
1	RPM_h0	0/1 ^{*)}	23	BSF_h2	0/1 ^{*)}	45	Mod_BPFO_h0_BPFI_h1	0/1 ^{*)}
2	RPM_h1	0/1 ^{*)}	24	BSF_h3	0/1 ^{*)}	46	Mod_BPFO_h0_FTF_h0	0/1 ^{*)}
3	RPM_h2	0/1 ^{*)}	25	BSF_h4	0/1 ^{*)}	47	Mod_BPFO_h0_FTF_h1	0/1 ^{*)}
4	RPM_h3	0/1 ^{*)}	26	Mod_RPM_h0_BPFI_h0	0/1 ^{*)}	48	Mod_BPFO_h0_BSF_h0	0/1 ^{*)}
5	RPM_h4	0/1 ^{*)}	27	Mod_RPM_h0_BPFI_h1	0/1 ^{*)}	49	Mod_BPFO_h0_BSF_h1	0/1 ^{*)}
6	BPFI_h0	0/1 ^{*)}	28	Mod_RPM_h0_BPFO_h0	0/1 ^{*)}	50	Mod_FTF_h0_RPM_h0	0/1 ^{*)}
7	BPFI_h1	0/1 ^{*)}	29	Mod_RPM_h0_BPFO_h1	0/1 ^{*)}	51	Mod_FTF_h0_RPM_h1	0/1 ^{*)}
8	BPFI_h2	0/1 ^{*)}	30	Mod_RPM_h0_FTF_h0	0/1 ^{*)}	52	Mod_FTF_h0_BPFI_h0	0/1 ^{*)}
9	BPFI_h3	0/1 ^{*)}	31	Mod_RPM_h0_FTF_h1	0/1 ^{*)}	53	Mod_FTF_h0_BPFI_h1	0/1 ^{*)}
10	BPFI_h4	0/1 ^{*)}	32	Mod_RPM_h0_BSF_h0	0/1 ^{*)}	54	Mod_FTF_h0_BPFO_h0	0/1 ^{*)}
11	BPFO_h0	0/1 ^{*)}	33	Mod_RPM_h0_BSF_h1	0/1 ^{*)}	55	Mod_FTF_h0_BPFO_h1	0/1 ^{*)}
12	BPFO_h1	0/1 ^{*)}	34	Mod_BPFI_h0_RPM_h0	0/1 ^{*)}	56	Mod_FTF_h0_BSF_h0	0/1 ^{*)}
13	BPFO_h2	0/1 ^{*)}	35	Mod_BPFI_h0_RPM_h1	0/1 ^{*)}	57	Mod_FTF_h0_BSF_h1	0/1 ^{*)}
14	BPFO_h3	0/1 ^{*)}	36	Mod_BPFI_h0_BPFO_h0	0/1 ^{*)}	58	Mod_BSF_h0_RPM_h0	0/1 ^{*)}

15	BPFO_h4	0/1 ^{*)}
16	FTF_h0	0/1 ^{*)}
17	FTF_h1	0/1 ^{*)}
18	FTF_h2	0/1 ^{*)}
19	FTF_h3	0/1 ^{*)}
20	FTF_h4	0/1 ^{*)}
21	BSF_h0	0/1 ^{*)}
22	BSF_h1	0/1 ^{*)}

37	Mod_BPFI_h0_BPFO_h1	0/1 ^{*)}
38	Mod_BPFI_h0_FTF_h0	0/1 ^{*)}
39	Mod_BPFI_h0_FTF_h1	0/1 ^{*)}
40	Mod_BPFI_h0_BSF_h0	0/1 ^{*)}
41	Mod_BPFI_h0_BSF_h1	0/1 ^{*)}
42	Mod_BPFO_h0_RPM_h0	0/1 ^{*)}
43	Mod_BPFO_h0_RPM_h1	0/1 ^{*)}
44	Mod_BPFO_h0_BPFI_h0	0/1 ^{*)}

59	Mod_BSF_h0_RPM_h1	0/1 ^{*)}
60	Mod_BSF_h0_BPFI_h0	0/1 ^{*)}
61	Mod_BSF_h0_BPFI_h1	0/1 ^{*)}
62	Mod_BSF_h0_BPFO_h0	0/1 ^{*)}
63	Mod_BSF_h0_BPFO_h1	0/1 ^{*)}
64	Mod_BSF_h0_FTF_h0	0/1 ^{*)}
65	Mod_BSF_h0_FTF_h1	0/1 ^{*)}

*) 0: Frequency component not present; 1: frequency component present

This setup allows for future addition of further contents in envelope spectra that may be checked for. This could be for instance higher harmonics of interest. In this case the content matrix can be extended.

For the application example used here the frequency content around the BPFI frequency together with the tolerance limits is shown in Figure 17.

In line with Figure 17, the entries: BPFI_h0 and Mod_RPM_h0_BPFI_h0 will contain a “1”, since the fundamental BPFI frequency as well as shaft speed modulations around this frequency are present.

3.7 Diagnosis

The FCI outputs the content matrix containing the indicators of whether a particular frequency or frequency pattern (modulation) is present in the envelope spectrum.

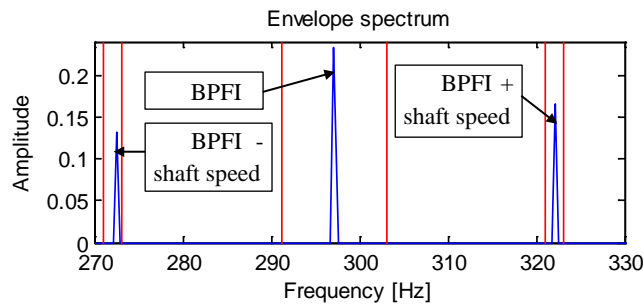


Figure 14: Envelope spectrum after peak filtering and the tolerance limits (#3, HSS, meas. 29, WTG 02)

Based on this matrix rules can be set up which allow the expert to implement his knowledge in fault diagnosis. Rules based on common knowledge about typical bearing damages are for instance:

- *When* BPFI frequency present & shaft speed modulations around BPFI present *then* Inner race damage
- *When* FTF frequency present *then* Rolling element damage
- *When* BPFO frequency present *then* Outer race damage
- *When* BPFO frequency present & shaft speed modulations around BPFO present *then* Outer race damage + unbalance or misalignment

Instead of formulating rules in a classical way, Fuzzy Logic (FL) is applied, since FL rules can be expressed in a very compact manner. Note that the advantages of fuzzification are not used here. Each line in the content matrix has its own input variable to the FL system. Because the content matrix does only contain two values - either “0” (frequency content not present) or “1” (frequency content present) - the shape of the Membership Function (MF) does not influence the result. The applicable MF has always full membership, due to the functions being centered around 0 and 1. The output is the diagnosis based on the rule evaluation. The initialized MFs are visualized in Figure 18 and Figure 19.

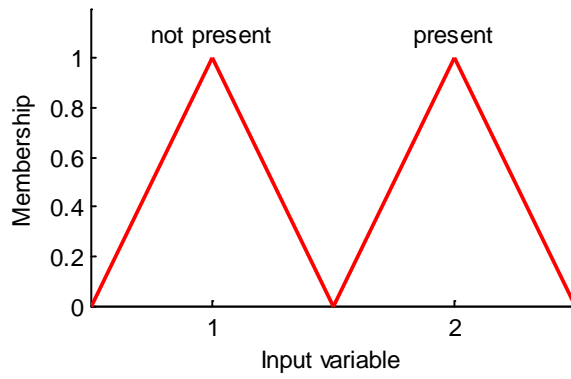


Figure 15: Membership functions initialized for each input variable

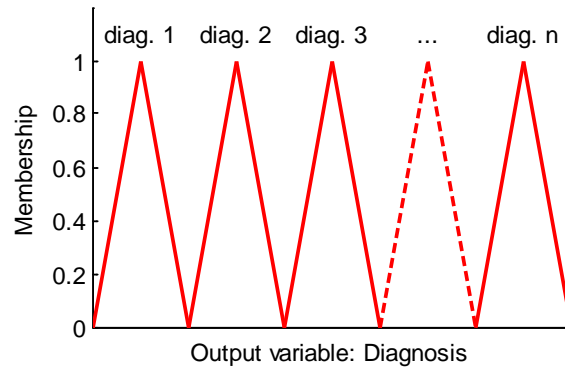


Figure 16: Membership functions initialized for each diagnosis

The rules are specified in a table whose structure is shown in Figure 20.

	RPM_h0	RPM_h1	RPM_h2	...	Mod_BSF_h0_FTF_h1	Diagnosis	Diagnosis code	weight	and/or
Rule1	-	-	-	...	-	Diagnosis 1	1	1	1
Rule2	1	-	0	...	-	Diagnosis 2	2	0.9	1
Rule3	-	-	-	...	-	Diagnosis 3	3	1	1
Rule4	1	1	-	...	-	Diagnosis 4	4	0.9	1
...

-: input not considered in rule
0: frequency content not present
1: frequency content present

Arbitrary text

Continuous number

Rule weight 0...1

0: logical or
1: logical and

Figure 20: Rule specification table structure

4. Application examples

From the seventeen wind turbines in the power plant, six have inner race damage at the high speed shaft bearing. Unfortunately this bearing cannot be inspected by endoscopic methods due its closed design. Hence tracking of the fault size was not possible. However, after bearing replacement factory investigations confirmed straight axial cracks.

In this section three application examples for the automated fault detection algorithm are given, using the proposed procedure.

4.1 Example 1

The available discontinuous measurements are evaluated for faults after PW & MED and SK processing. The envelope spectra after filtering are analyzed via the FCI and the rules specified. Figure 21 shows a waterfall plot of the envelope spectra together with the spectral kurtosis values of the full frequency band of the most recent ten measurements.

Rising amplitudes in the envelope spectra are visible. This corresponds nicely with the increase in SK of the full frequency band. Since March 2012 a rise in SK value can be observed. Although it is not proven here, the findings of Sawalhi et al. [5], Niaoqing et al. [12] and Sawalhi and Randall [27] make it very likely that the increase in SK can be linked to the crack growths at the inner ring.

Note that here the SK of the full band is plotted, instead of the SK of the band with maximum impulsiveness. This choice was made to avoid fluctuations in the SK trend, simply due to shifts in the frequency band with maximum SK. In this sense the same reference band is used.

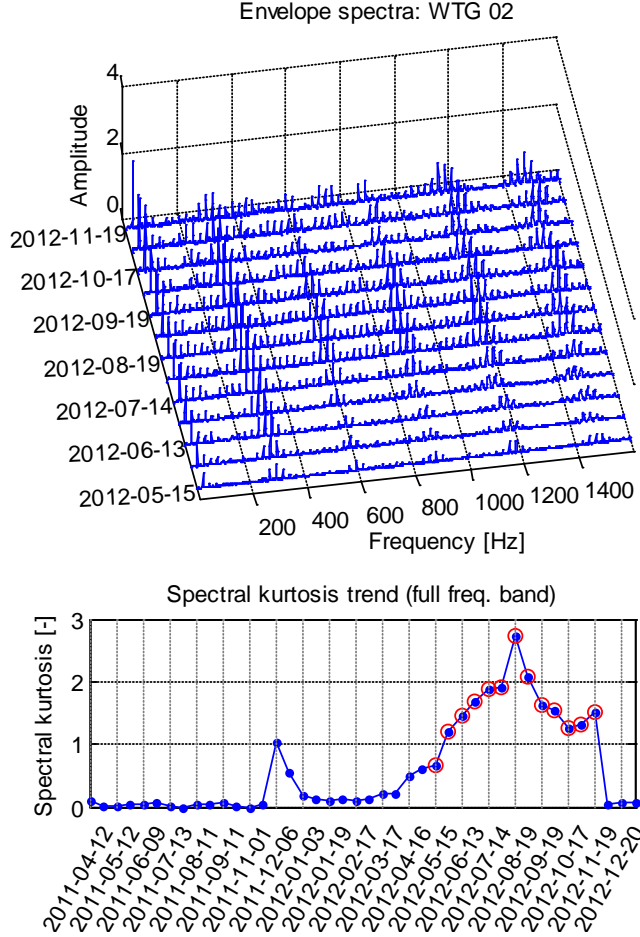
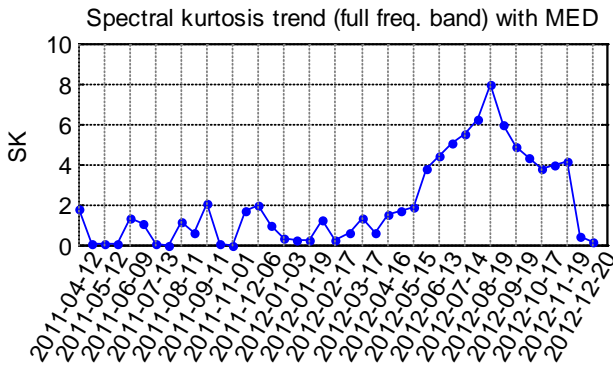


Figure 21: Envelope spectra and spectral kurtosis (WTG 02)

Moreover it was realized that the MED algorithm makes the SK values in a healthy state more fluctuating. Hence the SK trend in Figure 21 is based on SK values prior application of MED. It is visible that the SK trend corresponds with the envelope spectra. Repair took place in November 2012.

Figure 22 illustrates the SK trend after applying MED as a comparison. This figure presents a novelty as for the first time the SK evolution is shown over time covering both, the long healthy and the damaged period



The fluctuations in the healthy state are characterized by a large variation. Once the crack develops, the SK values stabilize and indicate a trend, most likely linked to the crack size. Beyond 2012-08-19 the SK values decrease. A similar behavior was observed by Sawalhi and Randall [28]. They suspected the decrease to be due to the fact that the entry and exit edges of the spall would tend to wear [2]. The actual fault here aids this presumption, as the characteristic fault frequency amplitude decreases in the later time series, but rich sideband modulations occur.

Differences in the SK trend with and without MED exist in the healthy period as well as in the overall amplitude level. The fluctuating pattern of the SK trend prior fault development makes the SK trend after MED a more difficult parameter to monitor, which is why the SK trend without MED is preferred.

A further difference can be observed at 2011-12-06, where the SK trend without MED shows a noticeable increase, whereas it is not as obvious in the SK trend after MED. The increase at 2011-12-06 has its reason, as in this period the envelope spectra gives indication of fault (see Figure 23), which disappear again after 2012-01-03. This phenomenon is potentially caused by flattening of the developing crack due to overrollment and a continuous crack growth beyond 2012-03-17.

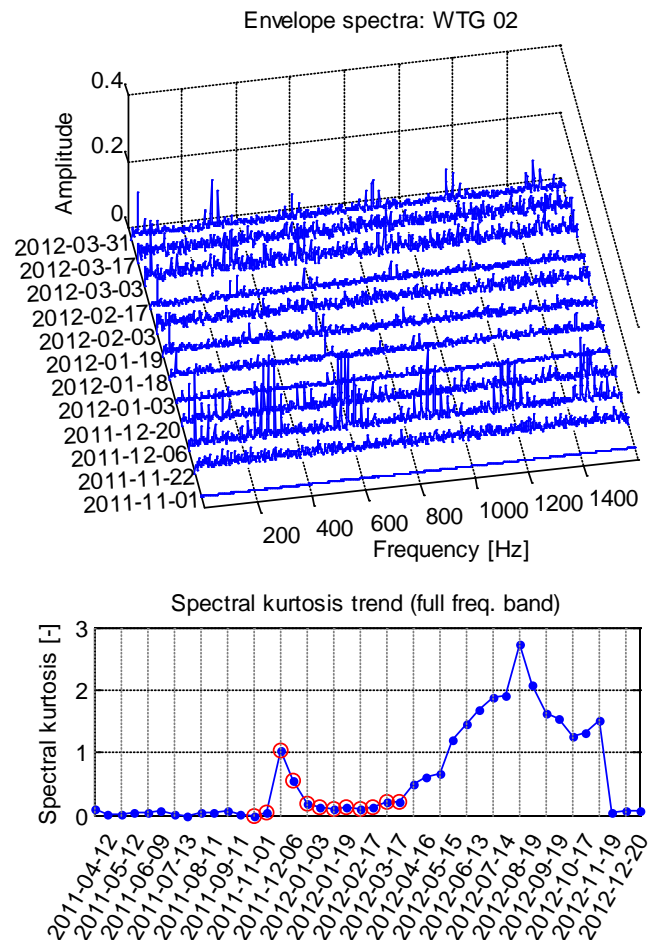


Figure 18: Envelope spectra and spectral kurtosis (WTG 02)

Figure 24 shows the envelope spectrum for the most recent measurement together with the most important frequency contents.

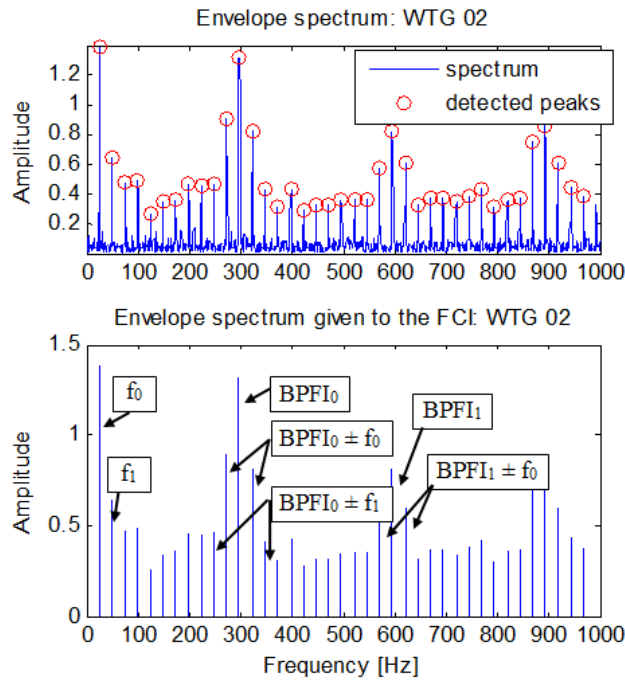


Figure 19: Envelope spectrum and detected peaks (top); envelope spectrum after peak filtering (#3, HSS, meas. 34, WTG 02)

The BPF_{I0} is around 297.8 Hz, f_0 around 24.8 Hz and BPF_{I1} 221.6 Hz. After FCI, the following entries in Table 4 contain a “1” for frequency content being present.

- RPM_h0 (f_0)
- RPM_h1 (f_1)
- BPF_{I0} (BPF_{I0})
- BPF_{I1} (BPF_{I1})
- BPF_{I2}
- BPF_{I3}
- BPF_{I4}
- BPF_{I5}
- BPF_{I6}
- BPF_{I7}
- BPF_{I8}
- BPF_{I9}
- BPF_{I10}
- BPF_{I11}
- BPF_{I12}
- BPF_{I13}
- BPF_{I14}
- BPF_{I15}
- BPF_{I16}
- BPF_{I17}
- BPF_{I18}
- BPF_{I19}
- BPF_{I20}
- BPF_{I21}
- BPF_{I22}
- BPF_{I23}
- BPF_{I24}
- BPF_{I25}
- BPF_{I26}
- BPF_{I27}
- BPF_{I28}
- BPF_{I29}
- BPF_{I30}
- BPF_{I31}
- BPF_{I32}
- BPF_{I33}
- BPF_{I34}
- BPF_{I35}
- BPF_{I36}
- BPF_{I37}
- BPF_{I38}
- BPF_{I39}
- BPF_{I40}
- BPF_{I41}
- BPF_{I42}
- BPF_{I43}
- BPF_{I44}
- BPF_{I45}
- BPF_{I46}
- BPF_{I47}
- BPF_{I48}
- BPF_{I49}
- BPF_{I50}
- BPF_{I51}
- BPF_{I52}
- BPF_{I53}
- BPF_{I54}
- BPF_{I55}
- BPF_{I56}
- BPF_{I57}
- BPF_{I58}
- BPF_{I59}
- BPF_{I60}
- BPF_{I61}
- BPF_{I62}
- BPF_{I63}
- BPF_{I64}
- BPF_{I65}
- BPF_{I66}
- BPF_{I67}
- BPF_{I68}
- BPF_{I69}
- BPF_{I70}
- BPF_{I71}
- BPF_{I72}
- BPF_{I73}
- BPF_{I74}
- BPF_{I75}
- BPF_{I76}
- BPF_{I77}
- BPF_{I78}
- BPF_{I79}
- BPF_{I80}
- BPF_{I81}
- BPF_{I82}
- BPF_{I83}
- BPF_{I84}
- BPF_{I85}
- BPF_{I86}
- BPF_{I87}
- BPF_{I88}
- BPF_{I89}
- BPF_{I90}
- BPF_{I91}
- BPF_{I92}
- BPF_{I93}
- BPF_{I94}
- BPF_{I95}
- BPF_{I96}
- BPF_{I97}
- BPF_{I98}
- BPF_{I99}
- BPF_{I100}
- BPF_{I101}
- BPF_{I102}
- BPF_{I103}
- BPF_{I104}
- BPF_{I105}
- BPF_{I106}
- BPF_{I107}
- BPF_{I108}
- BPF_{I109}
- BPF_{I110}
- BPF_{I111}
- BPF_{I112}
- BPF_{I113}
- BPF_{I114}
- BPF_{I115}
- BPF_{I116}
- BPF_{I117}
- BPF_{I118}
- BPF_{I119}
- BPF_{I120}
- BPF_{I121}
- BPF_{I122}
- BPF_{I123}
- BPF_{I124}
- BPF_{I125}
- BPF_{I126}
- BPF_{I127}
- BPF_{I128}
- BPF_{I129}
- BPF_{I130}
- BPF_{I131}
- BPF_{I132}
- BPF_{I133}
- BPF_{I134}
- BPF_{I135}
- BPF_{I136}
- BPF_{I137}
- BPF_{I138}
- BPF_{I139}
- BPF_{I140}
- BPF_{I141}
- BPF_{I142}
- BPF_{I143}
- BPF_{I144}
- BPF_{I145}
- BPF_{I146}
- BPF_{I147}
- BPF_{I148}
- BPF_{I149}
- BPF_{I150}
- BPF_{I151}
- BPF_{I152}
- BPF_{I153}
- BPF_{I154}
- BPF_{I155}
- BPF_{I156}
- BPF_{I157}
- BPF_{I158}
- BPF_{I159}
- BPF_{I160}
- BPF_{I161}
- BPF_{I162}
- BPF_{I163}
- BPF_{I164}
- BPF_{I165}
- BPF_{I166}
- BPF_{I167}
- BPF_{I168}
- BPF_{I169}
- BPF_{I170}
- BPF_{I171}
- BPF_{I172}
- BPF_{I173}
- BPF_{I174}
- BPF_{I175}
- BPF_{I176}
- BPF_{I177}
- BPF_{I178}
- BPF_{I179}
- BPF_{I180}
- BPF_{I181}
- BPF_{I182}
- BPF_{I183}
- BPF_{I184}
- BPF_{I185}
- BPF_{I186}
- BPF_{I187}
- BPF_{I188}
- BPF_{I189}
- BPF_{I190}
- BPF_{I191}
- BPF_{I192}
- BPF_{I193}
- BPF_{I194}
- BPF_{I195}
- BPF_{I196}
- BPF_{I197}
- BPF_{I198}
- BPF_{I199}
- BPF_{I200}
- BPF_{I201}
- BPF_{I202}
- BPF_{I203}
- BPF_{I204}
- BPF_{I205}
- BPF_{I206}
- BPF_{I207}
- BPF_{I208}
- BPF_{I209}
- BPF_{I210}
- BPF_{I211}
- BPF_{I212}
- BPF_{I213}
- BPF_{I214}
- BPF_{I215}
- BPF_{I216}
- BPF_{I217}
- BPF_{I218}
- BPF_{I219}
- BPF_{I220}
- BPF_{I221}
- BPF_{I222}
- BPF_{I223}
- BPF_{I224}
- BPF_{I225}
- BPF_{I226}
- BPF_{I227}
- BPF_{I228}
- BPF_{I229}
- BPF_{I230}
- BPF_{I231}
- BPF_{I232}
- BPF_{I233}
- BPF_{I234}
- BPF_{I235}
- BPF_{I236}
- BPF_{I237}
- BPF_{I238}
- BPF_{I239}
- BPF_{I240}
- BPF_{I241}
- BPF_{I242}
- BPF_{I243}
- BPF_{I244}
- BPF_{I245}
- BPF_{I246}
- BPF_{I247}
- BPF_{I248}
- BPF_{I249}
- BPF_{I250}
- BPF_{I251}
- BPF_{I252}
- BPF_{I253}
- BPF_{I254}
- BPF_{I255}
- BPF_{I256}
- BPF_{I257}
- BPF_{I258}
- BPF_{I259}
- BPF_{I260}
- BPF_{I261}
- BPF_{I262}
- BPF_{I263}
- BPF_{I264}
- BPF_{I265}
- BPF_{I266}
- BPF_{I267}
- BPF_{I268}
- BPF_{I269}
- BPF_{I270}
- BPF_{I271}
- BPF_{I272}
- BPF_{I273}
- BPF_{I274}
- BPF_{I275}
- BPF_{I276}
- BPF_{I277}
- BPF_{I278}
- BPF_{I279}
- BPF_{I280}
- BPF_{I281}
- BPF_{I282}
- BPF_{I283}
- BPF_{I284}
- BPF_{I285}
- BPF_{I286}
- BPF_{I287}
- BPF_{I288}
- BPF_{I289}
- BPF_{I290}
- BPF_{I291}
- BPF_{I292}
- BPF_{I293}
- BPF_{I294}
- BPF_{I295}
- BPF_{I296}
- BPF_{I297}
- BPF_{I298}
- BPF_{I299}
- BPF_{I300}
- BPF_{I301}
- BPF_{I302}
- BPF_{I303}
- BPF_{I304}
- BPF_{I305}
- BPF_{I306}
- BPF_{I307}
- BPF_{I308}
- BPF_{I309}
- BPF_{I310}
- BPF_{I311}
- BPF_{I312}
- BPF_{I313}
- BPF_{I314}
- BPF_{I315}
- BPF_{I316}
- BPF_{I317}
- BPF_{I318}
- BPF_{I319}
- BPF_{I320}
- BPF_{I321}
- BPF_{I322}
- BPF_{I323}
- BPF_{I324}
- BPF_{I325}
- BPF_{I326}
- BPF_{I327}
- BPF_{I328}
- BPF_{I329}
- BPF_{I330}
- BPF_{I331}
- BPF_{I332}
- BPF_{I333}
- BPF_{I334}
- BPF_{I335}
- BPF_{I336}
- BPF_{I337}
- BPF_{I338}
- BPF_{I339}
- BPF_{I340}
- BPF_{I341}
- BPF_{I342}
- BPF_{I343}
- BPF_{I344}
- BPF_{I345}
- BPF_{I346}
- BPF_{I347}
- BPF_{I348}
- BPF_{I349}
- BPF_{I350}
- BPF_{I351}
- BPF_{I352}
- BPF_{I353}
- BPF_{I354}
- BPF_{I355}
- BPF_{I356}
- BPF_{I357}
- BPF_{I358}
- BPF_{I359}
- BPF_{I360}
- BPF_{I361}
- BPF_{I362}
- BPF_{I363}
- BPF_{I364}
- BPF_{I365}
- BPF_{I366}
- BPF_{I367}
- BPF_{I368}
- BPF_{I369}
- BPF_{I370}
- BPF_{I371}
- BPF_{I372}
- BPF_{I373}
- BPF_{I374}
- BPF_{I375}
- BPF_{I376}
- BPF_{I377}
- BPF_{I378}
- BPF_{I379}
- BPF_{I380}
- BPF_{I381}
- BPF_{I382}
- BPF_{I383}
- BPF_{I384}
- BPF_{I385}
- BPF_{I386}
- BPF_{I387}
- BPF_{I388}
- BPF_{I389}
- BPF_{I390}
- BPF_{I391}
- BPF_{I392}
- BPF_{I393}
- BPF_{I394}
- BPF_{I395}
- BPF_{I396}
- BPF_{I397}
- BPF_{I398}
- BPF_{I399}
- BPF_{I400}
- BPF_{I401}
- BPF_{I402}
- BPF_{I403}
- BPF_{I404}
- BPF_{I405}
- BPF_{I406}
- BPF_{I407}
- BPF_{I408}
- BPF_{I409}
- BPF_{I410}
- BPF_{I411}
- BPF_{I412}
- BPF_{I413}
- BPF_{I414}
- BPF_{I415}
- BPF_{I416}
- BPF_{I417}
- BPF_{I418}
- BPF_{I419}
- BPF_{I420}
- BPF_{I421}
- BPF_{I422}
- BPF_{I423}
- BPF_{I424}
- BPF_{I425}
- BPF_{I426}
- BPF_{I427}
- BPF_{I428}
- BPF_{I429}
- BPF_{I430}
- BPF_{I431}
- BPF_{I432}
- BPF_{I433}
- BPF_{I434}
- BPF_{I435}
- BPF_{I436}
- BPF_{I437}
- BPF_{I438}
- BPF_{I439}
- BPF_{I440}
- BPF_{I441}
- BPF_{I442}
- BPF_{I443}
- BPF_{I444}
- BPF_{I445}
- BPF_{I446}
- BPF_{I447}
- BPF_{I448}
- BPF_{I449}
- BPF_{I450}
- BPF_{I451}
- BPF_{I452}
- BPF_{I453}
- BPF_{I454}
- BPF_{I455}
- BPF_{I456}
- BPF_{I457}
- BPF_{I458}
- BPF_{I459}
- BPF_{I460}
- BPF_{I461}
- BPF_{I462}
- BPF_{I463}
- BPF_{I464}
- BPF_{I465}
- BPF_{I466}
- BPF_{I467}
- BPF_{I468}
- BPF_{I469}
- BPF_{I470}
- BPF_{I471}
- BPF_{I472}
- BPF_{I473}
- BPF_{I474}
- BPF_{I475}
- BPF_{I476}
- BPF_{I477}
- BPF_{I478}
- BPF_{I479}
- BPF_{I480}
- BPF_{I481}
- BPF_{I482}
- BPF_{I483}
- BPF_{I484}
- BPF_{I485}
- BPF_{I486}
- BPF_{I487}
- BPF_{I488}
- BPF_{I489}
- BPF_{I490}
- BPF_{I491}
- BPF_{I492}
- BPF_{I493}
- BPF_{I494}
- BPF_{I495}
- BPF_{I496}
- BPF_{I497}
- BPF_{I498}
- BPF_{I499}
- BPF_{I500}
- BPF_{I501}
- BPF_{I502}
- BPF_{I503}
- BPF_{I504}
- BPF_{I505}
- BPF_{I506}
- BPF_{I507}
- BPF_{I508}
- BPF_{I509}
- BPF_{I510}
- BPF_{I511}
- BPF_{I512}
- BPF_{I513}
- BPF_{I514}
- BPF_{I515}
- BPF_{I516}
- BPF_{I517}
- BPF_{I518}
- BPF_{I519}
- BPF_{I520}
- BPF_{I521}
- BPF_{I522}
- BPF_{I523}
- BPF_{I524}
- BPF_{I525}
- BPF_{I526}
- BPF_{I527}
- BPF_{I528}
- BPF_{I529}
- BPF_{I530}
- BPF_{I531}
- BPF_{I532}
- BPF_{I533}
- BPF_{I534}
- BPF_{I535}
- BPF_{I536}
- BPF_{I537}
- BPF_{I538}
- BPF_{I539}
- BPF_{I540}
- BPF_{I541}
- BPF_{I542}
- BPF_{I543}
- BPF_{I544}
- BPF_{I545}
- BPF_{I546}
- BPF_{I547}
- BPF_{I548}
- BPF_{I549}
- BPF_{I550}
- BPF_{I551}
- BPF_{I552}
- BPF_{I553}
- BPF_{I554}
- BPF_{I555}
- BPF_{I556}
- BPF_{I557}
- BPF_{I558}
- BPF_{I559}
- BPF_{I560}
- BPF_{I561}
- BPF_{I562}
- BPF_{I563}
- BPF_{I564}
- BPF_{I565}
- BPF_{I566}
- BPF_{I567}
- BPF_{I568}
- BPF_{I569}
- BPF_{I570}
- BPF_{I571}
- BPF_{I572}
- BPF_{I573}
- BPF_{I574}
- BPF_{I575}
- BPF_{I576}
- BPF_{I577}
- BPF_{I578}
- BPF_{I579}
- BPF_{I580}
- BPF_{I581}
- BPF_{I582}
- BPF_{I583}
- BPF_{I584}
- BPF_{I585}
- BPF_{I586}
- BPF_{I587}
- BPF_{I588}
- BPF_{I589}
- BPF_{I590}
- BPF_{I591}
- BPF_{I592}
- BPF_{I593}
- BPF_{I594}
- BPF_{I595}
- BPF_{I596}
- BPF_{I597}
- BPF_{I598}
- BPF_{I599}
- BPF_{I600}
- BPF_{I601}
- BPF_{I602}
- BPF_{I603}
- BPF_{I604}
- BPF_{I605}
- BPF_{I606}
- BPF_{I607}
- BPF_{I608}
- BPF_{I609}
- BPF_{I610}
- BPF_{I611}
- BPF_{I612}
- BPF_{I613}
- BPF_{I614}
- BPF_{I615}
- BPF_{I616}
- BPF_{I617}
- BPF_{I618}
- BPF_{I619}
- BPF_{I620}
- BPF_{I621}
- BPF_{I622}
- BPF_{I623}
- BPF_{I624}
- BPF_{I625}
- BPF_{I626}
- BPF_{I627}
- BPF_{I628}
- BPF_{I629}
- BPF_{I630}
- BPF_{I631}
- BPF_{I632}
- BPF_{I633}
- BPF_{I634}
- BPF_{I635}
- BPF_{I636}
- BPF_{I637}
- BPF_{I638}
- BPF_{I639}
- BPF_{I640}
- BPF_{I641}
- BPF_{I642}
- BPF_{I643}
- BPF_{I644}
- BPF_{I645}
- BPF_{I646}
- BPF_{I647}
- BPF_{I648}
- BPF_{I649}
- BPF_{I650}
- BPF_{I651}
- BPF_{I652}
- BPF_{I653}
- BPF_{I654}
- BPF_{I655}
- BPF_{I656}
- BPF_{I657}
- B

4.2 Example 2

The automated analysis highlighted five more turbines with inner race signature and inner race damage. Figure 25 shows a waterfall plot of the envelope spectra together with the SK trend of the most recent ten measurements of WTG 05.

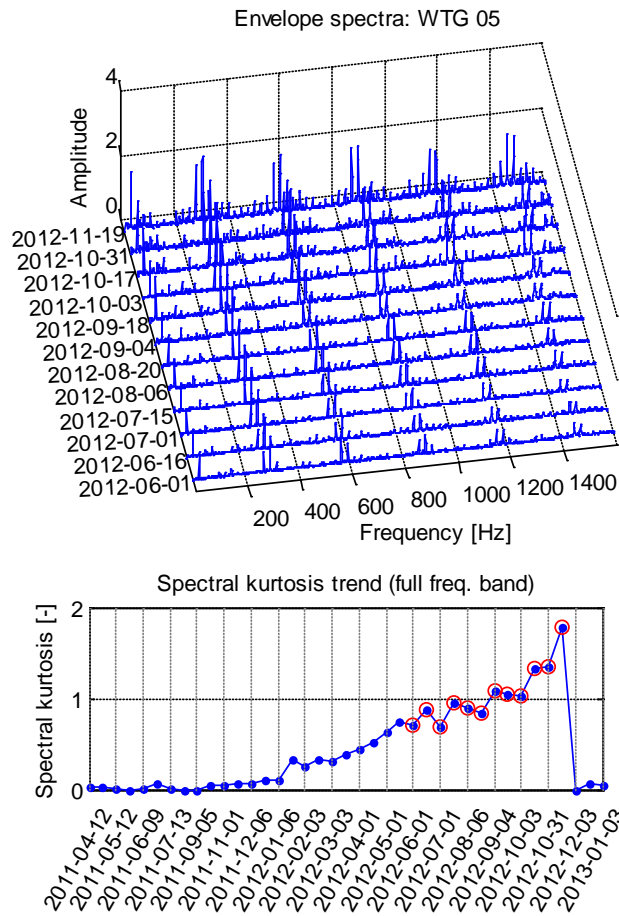


Figure 20: Envelope spectra and spectral kurtosis (WTG 05)

At this turbine a very clear trend in SK is visible since January 2012, with the recent measurements slightly fluctuating. The envelope spectra follow this trend, with rising amplitudes and more harmonics showing up. Repair took place in November 2012. Plotting the SK trend after MED gives the results presented in Figure 26. Also for this turbine the SK has a high variance in the healthy period. A trend first establishes at 2011-03-18, which is two month later than with the SK values without MED. Hence, for the data sets available, it appears preferable using the SK values without MED for trending. However, this is in contrast to the findings of Sawalhi et al. [5] in which a case is shown where SK trending was not possible without MED.

Figure 27 shows the most recent envelope spectrum, the detected peaks and the filtered spectrum passed to the FCI.

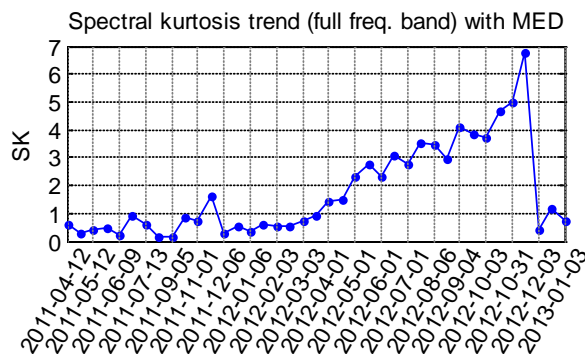


Figure 21: Spectral kurtosis trend after MED (WTG 05)

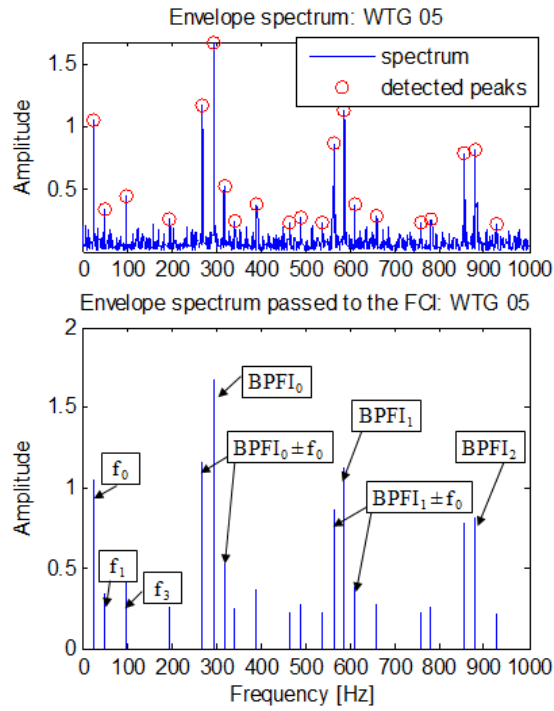


Figure 22: Envelope spectrum and detected peaks (top); envelope spectrum after peak filtering (#3, HSS, meas. 31, WTG 05)

The identified frequency contents by the FCI are:

- RPM_h0 (f_0)
- RPM_h1 (f_1)
- RPM_h3 (f_3)
- BPFI_h0 ($BPFI_0$)
- BPFI_h1 ($BPFI_1$)
- BPFI_h2 ($BPFI_2$)
- BPFI_h3
- BPFI_h4
- BPFO_h3
- BSF_h2
- Mod_RPM_h0_BPFI_h1
- Mod_RPM_h0_BPFI_h1
- Mod_BPFO_h0_BPFI_h2

The present frequency contents evaluated via the rules implemented highlight the inner race signature and the potential damage fully automatized, together with the correct diagnosis.

4.3 Example 3

Another turbine with detected inner race damage is WTG 04. Again the most recent ten envelope spectra and the spectral kurtosis trend is illustrated in Figure 28 and the SK trend with MED in Figure 29.

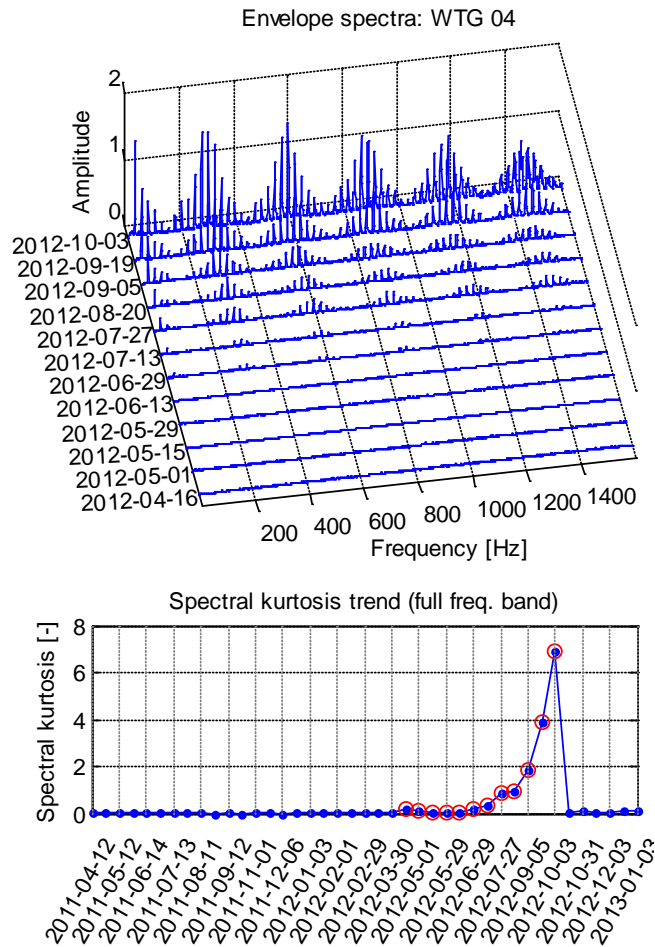


Figure 23: Envelope spectra and spectral kurtosis (WTG 04)

At this turbine many measurements in a healthy state exist, as the crack develops comparably late. However, the SK sharply increases 2012-06-29 again well in line with the envelope spectra amplitude rise. Bearing replacement took place in October 2012.

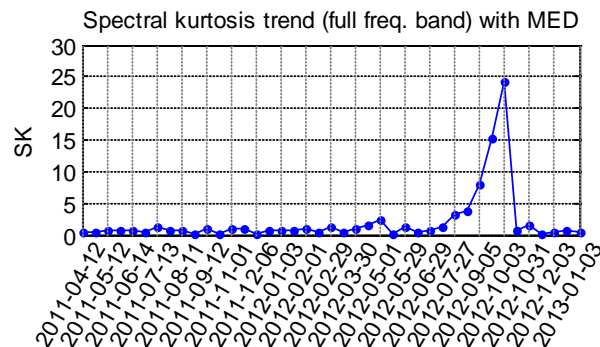


Figure 24: Spectral kurtosis trend after MED (WTG 04)

Also the SK after applying MED shows the steep rise. However, the healthy state is also for this turbine characterized by a larger variance. Because of this a trend is reliably detectable first at 2012-07-27, in contrast to trend establishment in the SK values without MED, where the trend can be identified two weeks earlier.

Figure 30 visualizes the most recent envelope spectrum and the detected beaks together with the envelope spectrum passed to the FCI and important frequency components.

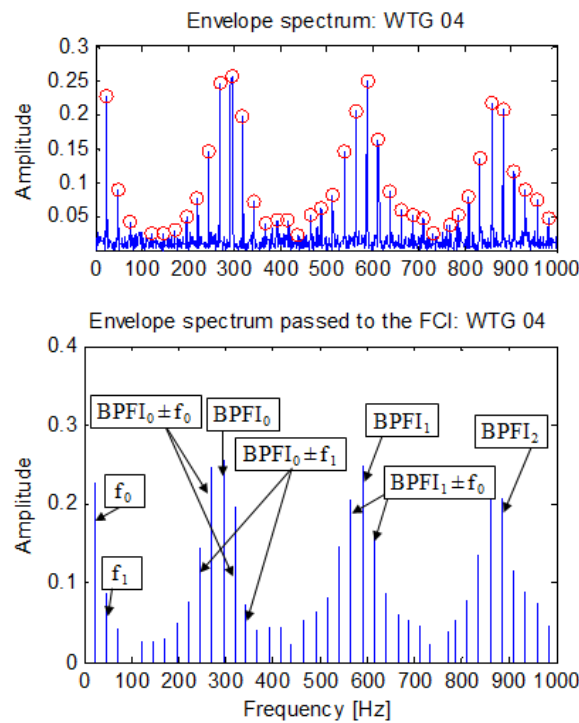


Figure 25: Envelope spectrum and detected peaks (top); envelope spectrum after peak filtering (#3, HSS, meas. 31, WTG 04)

The detected frequency content is:

- RPM_h0 (f_0)
- RPM_h1 (f_1)
- RPM_h2
- BPFI_h0 (BPFI₀)
- BPFI_h1 (BPFI₁)
- BPFI_h2 (BPFI₂)
- BPFI_h3
- BPFI_h4
- BPFO_h0
- BPFO_h2
- BPFO_h3
- BPFO_h4
- BSF_h2
- Mod_RPM_h0_BPFI_h0
- Mod_RPM_h0_BPFI_h1
- Mod_BPFO_h0_BPFI_h0
- Mod_BPFO_h0_BPFI_h1

Based on the frequency content present, an inner race signature was automatically detected, which is the correct diagnosis for the pattern existing.

5. Results and discussion

The given examples emphasize the successful application of the proposed procedure to real measured data and fault diagnosis.

Moreover research showed the benefits of using the CEP based signal PW for signal separation into deterministic and non-deterministic components. The performance of PW is close to the LP residual, but without the need of parameter optimization, which makes it an efficient method and very fast to compute.

Using MED as a further pre-process step prior envelope calculation proved useful to emphasizing present fault pattern both in the time and frequency domain. Attention must be paid, to the choice of filter order. It was found that a too high filter order can lead to start-up and end transients in the time series preventing successful diagnosis. For practical applications, it is thus recommended using a rather low filter order, accepting that the impulse amplification may be less effective than with a higher filter order, but avoiding the risk of transients.

Furthermore the effect of the spectral kurtosis based optimal filter band selection was studied. Results show that in many cases the combination of PW & MED lead to the situation that band pass filtering gives no improvement. However, in some cases a frequency band can be found that gives higher spectral kurtosis values and accordingly a clearer fault pattern in the envelope spectrum. By applying the fast kurtogram (proposed by

Antoni [22]) the search for an optimal frequency band is fast to compute and should thus supplement the automated procedure.

Finally the effect of MED on the SK values trend (used as a fault size indicator) was under research. A higher variance of the SK values was observed for bearings in a healthy state when MED is used prior SK value calculation. This variance lead in some cases to a later establishment of observable trends, but both methods (with and without MED) show trends in the fault state, potentially linked to the crack size. The SK without MED appears to be superior to use, because of the more direct link between present patterns in the envelope spectra and high SK values as well as lower variance in the values.

6. Future research

Identifying HSS bearing faults in wind turbine gearboxes is a comparably simple task, because of the high rotational speed. Future research will focus on the efficiency of the proposed method to automatically detect and diagnose faults in the IMS and the planetary stage of wind turbine gearboxes. At least for the IMS stage (rotating with approx. 350 rpm) it is expected that the proposed procedure will give good results. However, the available data sets did not contain any bearing damages of the IMS or the planetary stage. Hence the efficiency for intermediate and low speed bearings must still be evaluated and is left for future research.

7. Conclusions

The proposed procedure proved capable of automatically process and analyse vibration time series for bearing defect frequencies in the envelope spectra. The diagnosis is based on rules which are set up using common knowledge about typical bearing fault signatures. The rules are implemented using fuzzy logic, building the basis for flexible and reliable fault diagnosis.

The proposed technique is an extension of the semi-automated procedure for bearing diagnosis (originally proposed by Sawalhi and Randall [4]) with regards to the application of a frequency content identification and rule based diagnosis. Moreover state of the art pre-processing techniques, namely CEP based signal PW and MED have been successfully applied and their effectiveness shown. In comparison to LP models for separating random from discrete components, CEP based signal PW proved to be an efficient and fast to compute method for separation.

8. References

I. References

- [1] Ebersbach, S. and Peng, Z. (2008). "Expert system development for vibration analysis in machine condition monitoring. " *Expert system with Applications, Vol.34, pp.291-299.*
- [2] Crabtree, C.J. and Tavner, P.J. (2011). "Condition monitoring algorithm suitable for wind tubrine use. " *Renewable Power Generation (RPG 2011), Edinburgh .*
- [3] Randall, Robert B. (ISBN:978-0-470-74785-8, 2011). "Vibration-based Condition Monitoring. " *Wiley.*
- [4] Schlechtingen, M., Santos, I.F. and Achiche, S. (2012). "Wind turbine condition monitoring based on SCADA data using normal behavior models. Part 2: Application examples. " *Applied Soft Computing.*
- [5] Sawalhi, N. and Randall, R. B. (2007). "Semi-automated bearing diagnostics - three case studies. " *Proceedings of the Comadem Conference, Faro, Portugal.*
- [6] Sawalhi, N., Randall, R. B. and Endo, H. (2007). "The enhancement of fault detection and diagnosis in rolling element bearings using minimum entropy deconvolution combined with spectral kurtosis. " *Mechanical Systems and Signal Processing Vol.21, pp.2616-2633.*
- [7] Barszcz, T. and Sawalhi, N. (2012). "Fault detection enhancement in rolling element bearings using the minimum entropy deconvolution. " *Archives of Acoustics, Vol. 37-2, pp.131-141.*
- [8] Randall, R. B. and Antoni, J. (2011). "Rolling element bearing diagnosis - A tutorial. " *Mechanical Systems and Signal Processing Vol.25 pp.485-520.*
- [9] Antoni, J. and Randall, R.B. (2004). "Unsupervised noise cancellation for vibration signals: part II a novel frequency-domain algorithm. " *Mechanical Systems and Signal Processing Vol.18, pp.103-117.*
- [10] Randall, R. B. and Sawalhi, N. (2011). "A new method for seperating discrete components from a signal. " *Sound and Vibration Vol.May, pp.6-9.*
- [11] Randall, R. B. and Sawalhi, N. (2011). "Use of the cepstrum to remove selected discrete frequency components from a time signal. " *IMAC conference, Jocksonville.*
- [12] Sawalhi, N. and Randall, R.B. (2011). "Signal pre-whitening using cepstrum editing (liftering) to enhance fault detection in rolling element bearings. " *Proceedings of the 24th International Congress on Condition Monitoring and Diagnostics Engineering Management, pp.330-336.*
- [13] Niaoqing, H., et al. (2012). "Enhanced fault detection of rolling element bearing based on cepstrum and

- stochastic resonance. " *Journal of Physics: Conference Series Vol.364, pp.1-8.*
- [14] Dyer, D. and Stewart, R.M. (1978). "Detection of rolling element bearing damage by statistical vibration analysis. " *Journal of Mechanical Design Vol.100, pp.229-235.*
- [15] Bonnardot, F., Randall, R. B. and Antoni, J. (2004). "Enhanced unsupervised noise cancellation using angular resampling for planetary bearing fault diagnosis. " *International Journal of Acoustics and Vibration Vol.9-2 pp.51-60.*
- [16] Barszcz, T. (2009). "Decomposition of vibration signals into deterministic and nondeterministic components and its capabilities of fault detection and identification. " *International Journal of Applied Mathematical Computation Vol.19-2 pp.327-335.*
- [17] Oppenheim, A.V. and Schafer, R.W. (2004). "From frequency to quefrequency: a history of the cepstrum. " *IEEE Signal Processing Magazine, September, pp.95-104.*
- [18] Randall, R.B. and Hee, J. (1981). "Cepstrum analysis. " *Brüel & Kjær, Technical Reviel Vol.3, ISSN:0007-2621.*
- [19] Wiggins, R. A. (1978). "Minimum entropy deconvolution. " *Geoexploration Vol.16, pp.21-35.*
- [20] McDonald, G. *Minimum Entropy Deconvolution.* [Online] 04 2012. <http://www.mathworks.com/matlabcentral/fileexchange/29151-minimum-entropy-deconvolution-med-1d-and-2d/content/med2d.m>.
- [21] Dwyer, R. F. (1983). "Detection of non-Gaussian signals by frequency domain Kurtosis estimation. " *Acoustics, Speech, and Signal Processing, IEEE International Conference on ICASSP '83, pp.607-610.*
- [22] Antoni, J. and Randall, R. B. (2006). "The spectral kurtosis: application to the vibratory surveillance and diagnostics of rotating machines. " *Mechanical Systems and Signal Processing Vol.20, pp.308-331.*
- [23] Antoni, J. (2006). "Fast computation of the kurtogram for the detection of transient faults. " *Mechanical Systems and Signal Processing Vol.21, pp.108-124.*
- [24] Antoni. *Programmes.* [Online] 04 2012. <http://www.utc.fr/~antoni/programm.htm>.
- [25] Howard, I. (1994). "A Review of rolling element bearing vibration "detection, diagnosis and prognosis". " *Aeronautical and Maritime Research Laboratory, DSTO-RR-0013.*
- [26] Akaike, H. (1973). "Information theory and an extension of the maximum likelihood principle. " *Second International Symposium on Information Theory, pp.267-281, Budapest.*
- [27] Palshikar, G. K. (2009). "Simple algorithms for peak detection in time-series. " *Proceedings of 1st IIMA International Conference on Advanced Data Analysis, Business Analytics and Intelligence, Ahmedabad, India.*
- [28] Sawalhi, N. and Randall, R. B. (2008). "Helicopter gearbox bearing blind fault identification using a range of analysis techniques. " *Journal of Mechanical engineering Vol.5, pp.157-168.*
- [29] Sawalhi, N. and Randall, R.B. (2008). "Novel signal processing techniques to aid bearing prognosis. " *IEEE PHM Conference, Denver, Co, USA, Oktober.*

Torsional Vibration Measurement and Model-based Monitoring in Today's Reality of Power Generation Business

Mateusz Golebiowski, Eric Knopf, Thomas Krueger

GE Power (Steam Power), Brown Boveri Strasse, 5401 Baden, Switzerland, mateusz.golebiowski@ge.com

Abstract

Growing share of renewables and consequently increasing risk of sub-synchronous torsional interactions between electrical grid and power plant machinery, constitute a demand for a robust, reliable and accurate torsional vibration monitoring approach. In addition, the torsional vibration measurements are frequently required by customers to validate rotor dynamic models and to prove sufficient separation between shaft-line's torsional modes and the excitation frequencies (in case of rotor retrofits). This paper presents various case studies of torsional vibration measurements starting from component level validation tests to full shaft train operational measurements. It describes also application of a model-based torsional vibration monitoring, where numerical rotor dynamic models were used to predict stresses and vibration amplitudes in non-observable locations along the rotor (including stress estimation in subcomponents like blades or retaining rings of turbo-generators).

1 Introduction

Torsional vibration refers to oscillatory torsional deformations of the machine rotor sections. For large rotating machinery (power generation trains), the mechanical system will consist of several rotors that are joined by relatively slender intermediate shafts and couplings. Each rotor in the system will oscillate following a torsional disturbance resulting in twisting in the shafts and to a lesser extent in the large diameter rotor bodies themselves (see Figure 1).

These twisting motions following severe torsional excitations may be sufficient to cause fatigue or overload-related damage to machine couplings and other components (steam turbine blades, generator's retaining rings).

The electrical disturbance that causes torsional vibration of turbo-generator units comes from:

- faults (short circuits in the grid or at generator's terminals, failed auto-reclosing events)
- switching of transmission lines
- continuous oscillation due to unbalanced phases (so called "negative sequence currents")
- out-of-phase synchronisation of a generator

The above excitation mechanisms are typically included in the OEM design criteria. If the model quality is adequate, safe operation can be guaranteed by a sufficient separation between natural frequencies of the rotor and the harmonics of grid frequency (mainly 1x and 2x).

Component-level testing to validate the torsional models and leveraging fleet experience gives additional level of confidence for the machine manufacturer with respect to these torsional stimuli cases, especially needed when rotor retrofit studies are carried out. More information about these basic characteristic of torsional vibration in the context of turbomachinery can be found in [2, 6, 7, and 9].

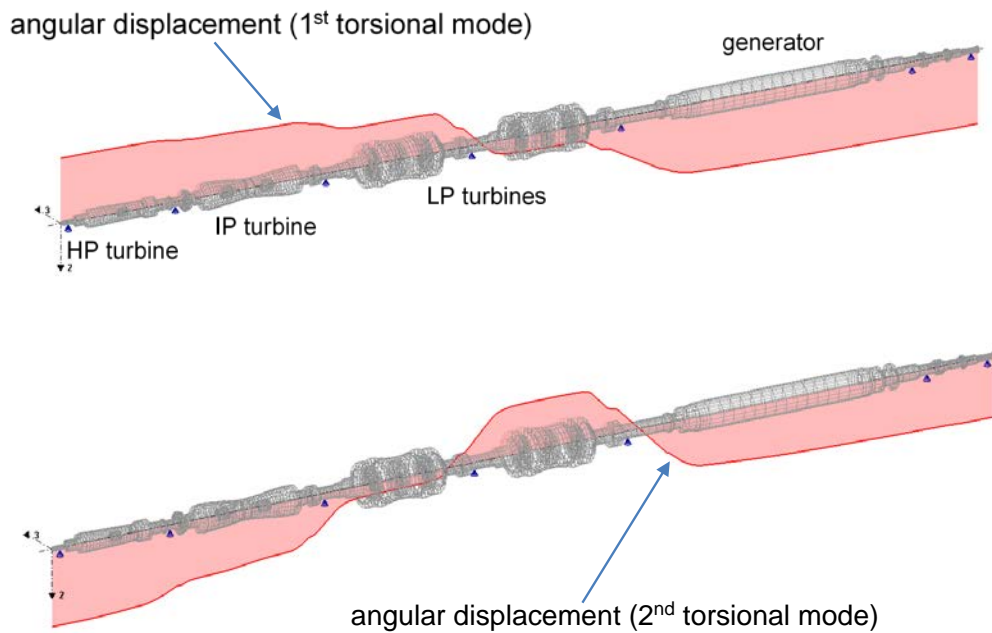


Figure 1 – Typical low-frequency mode-shapes of a turbo-generator shaft-line (1080MW coal fired power plant)

2 New Challenges

Changes in the electrical grid that can be observed today (triggered primarily by the growing share of renewables in the network), can have a big impact on torsional vibration risks adding new challenges for the owners of power plants.

The additional sources of torsional interaction between today's grid and power plant machinery are:

- application of power electronics (power stations located close to terminals of HVDC lines at risk)
- installation of series compensating capacitors in the transmission lines (risk of sub-synchronous resonance SSR; thermal power stations located far from load centres)
- large AC arc furnaces
- variable frequency electric drives (VFDs)

In all these situations, very high levels of torsional vibration can be induced by interactions between mechanical oscillations of the shaft-line and the electrical current oscillations in the grid (see [10] for more information).

Difficulty for power plant designers and machine manufacturers comes from the fact that these interactions can't be sufficiently handled on the power station level. As the turbo-generator's rotor interacts with the regulating system of the DC power converters the net torsional oscillation damping (representing coupled electro-mechanical system) can become very low or even negative. In such case the damaging fatigue cycles of the rotor accumulate much faster than assumed in the design or, in worst case, sub-synchronous instability leads to immediate failure.

Following some severe incidents, certain countermeasures were developed on the electrical side to protect against these problems (filters, excitation controllers, static VAR compensators). This protective equipment is designed to ensure that the harmful frequency components wouldn't enter the generator armature of the impacted machine.

On the mechanical side, the torsional vibration monitoring and protection systems are necessary to supervise the mechanical integrity of the shaft and detect the events, where the abnormal levels of torsional excitation impact the residual fatigue life of the rotor.

As the most endangered elements (i.e. turbine blades and generators' retaining rings) are not accessible for measurement in operation, it is critical to incorporate the OEM's component knowledge in the protection logic (model-based monitoring).

3 Measurement Technique

Most of the contemporary, industry-wide accepted measurement technologies (strain gage with telemetry, optical probes, laser) fit well the short-term test needs but their lack of robustness and durability as well as problematic installation, impacting machine operation do not allow considering them for the long-term monitoring applications (see [1, 3, 4, 9]).

Based on the experience of authors (summarized in [8]), these drawbacks are overcome with the use of encoder-based measurement technologies (i.e. incremental pulse timing technique). This digital measurement method for torsional vibration is based on sampling at equidistant angular intervals around the rotating shaft. This can be generally accomplished by one of three methods:

- mounting an incremental rotary encoder onto the shaft
- scanning a toothed wheel with a magnetic or eddy-current pickup
- targeting reflective/non-reflective (black/white) bar patterns ('zebra tape') with an optical sensor¹

The counter card together with edge detection circuitry identifies tooth tip (or zebra stripe) passing time (based on voltage thresholds fixed by the user). Assuming that the angular velocity is constant between adjacent pulses, the instantaneous angular velocity values may be calculated by dividing the actual angular spacing of the physical steps (between gear teeth or encoder lines) by the elapsed time from one positive edge to the next. Speed signal is then integrated to angular vibration waveform, which is filtered and re-sampled to obtain vibration values uniformly distributed in time. More detailed description of the processing routines and extensions of this measurement technique can be found in [5].

4 Case Study 1 (component-level testing)

Before a specific rotor model can be included in the torsional vibration monitoring algorithm, it is necessary to thoroughly study all torsional modes that could interact with the grid-related instabilities. In certain cases, it is necessary to confirm the numerical models with a test.

Figure 2 (left) shows a test arrangement that was used for a model validation of a generator rotor. As this machine was designed to be coupled with a dedicated frequency converter, the natural frequency of the local, component modes (twisting of a retaining ring for example, see Figure 2 right) had to be very accurately determined. In the numerical model, the retaining rings, and the main fan have been modelled as flexible components and the anticipated torsional modes were calculated as high as in the range of 1kHz.

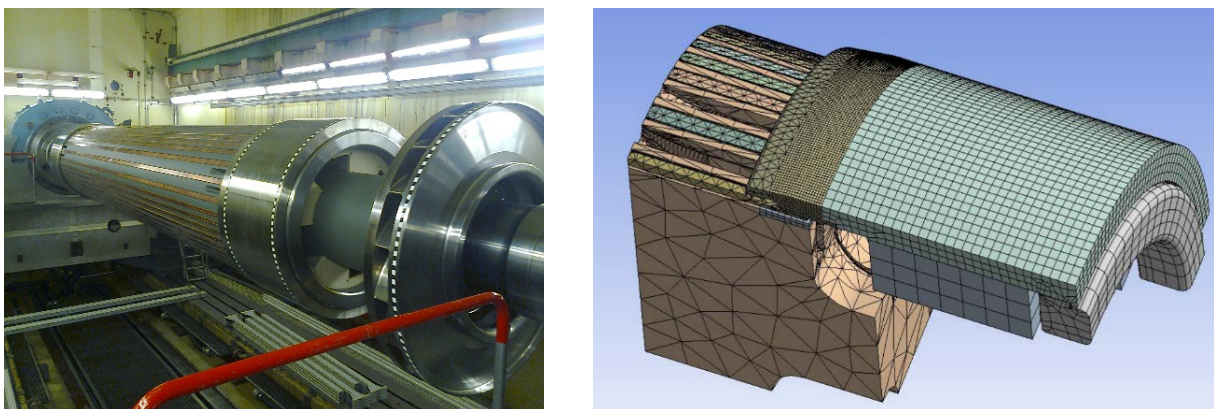


Figure 2 – Test arrangement (left) and FE model of a retaining ring (right)

¹ This last method is applicable for short-term testing mainly.

The torsional vibrations of this rotor have been measured at full operational speed in a high-speed balancing facility. The ‘zebra-tapes’ that have been glued on the surface of main fan and retaining rings where a target for a laser to capture rotational velocity fluctuations.

As there’s no special actuation to excite torsional modes (apart from the broadband, system-borne noise) the main challenge in this type of test comes from very low level of vibrations.

5 Case Study 2 (nuclear power plant)

A demand for a torsional vibration monitoring approach, which is sufficiently robust, reliable and accurate to be acceptable as a practical solution for power generation business, is particularly high in case of large steam turbine trains (fossil as well as nuclear power plants). To meet the most stringent safety requirements, the torsional vibration monitoring strategy must offer highest and proven reliability and accuracy.

This example demonstrates the use of model-based measurement approach that has been deployed in a 1300MW nuclear plant.

The torsional vibration was measured only in a single plane, utilizing existing speed wheel behind the generator’s exciter (see Figure 3). Combination of accurate measurement of angular vibration (high signal to noise ratio in 0-500Hz range; 0.01mrad/sec resolution) with a detailed rotordynamic model allows insight into every critical location along the shaft-line.

The spectrum of measured torsional vibration proves the accuracy and validity of the model. The modes of the low-pressure steam turbine blades (coupled with rotor modes) were successfully measured despite the distance between vibrating blades and sensor location (more than 25m).

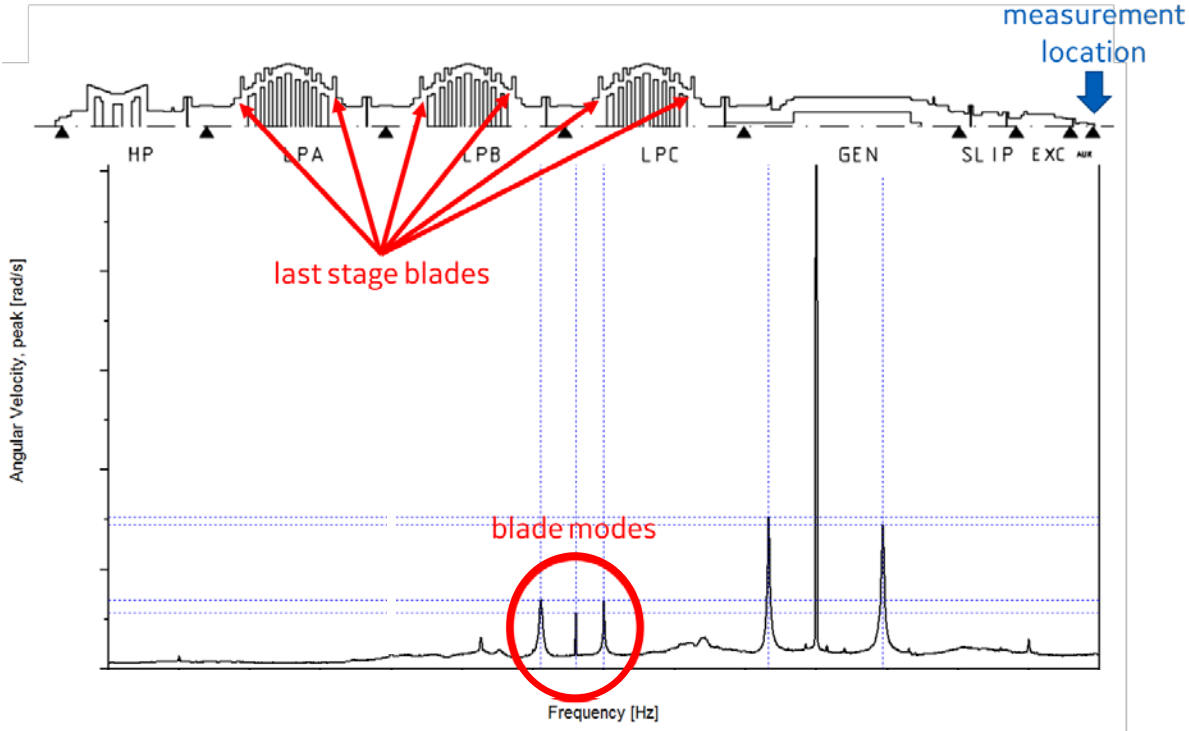


Figure 3 – Measured torsional vibration spectrum (frequency range around 2x grid frequency)

6 Case Study 3 (monitoring system)

The torsional vibration monitoring and diagnostics (TVMD) system has been developed to allow continuous, real-time insight into the torsional vibration state of the turbo-generator trains.

Applications that were industrialised and tailored to the needs of power plant operators enable collecting and analysing torsional data to:

- protect against abnormal excitation in off-design grid conditions (considering specific excitation mechanisms due to SSR, HVDC converters)
- support targeted maintenance and localisation of faults via model-based and comparative analytics (fleet outliers, anomalies)

The stability and reliability of the system were intensively tested in Birr Power Plant (Switzerland) where it was deployed to protect a heavy-duty gas turbine (~300MW output) driving a converter-controlled generator (4-pole, hydrogen cooled).



Figure 4 – Encoder wheel and measurement heads

The angular vibration was measured with a magnetic encoder installed on the non-drive-end side of the generator (see Figure 4). With the use of the detailed rotordynamic model, this single measurement plane allowed to accurately assess torsional vibration levels along the whole train (same approach as in the example described in the previous section).

The interface of the monitoring system (see Figure 5) gives a quick overview of the machine's condition. A list of events associated with abnormal levels of torsional vibration allows a very quick identification of the nature of the alarm:

- short time (possibly linked with transmission line switching)
- repetitive (e.g. load dependent for cycling unit)
- continuous (unbalance of voltage phases in electrical network)
- others

With the included OEM's component knowledge (i.e. insight into stresses of critical but non-observable components) a smarter, focused and predictive maintenance is enabled. The locations of the shaft-line (shaft-end between two LP rotors highlighted in red in the presented example) that have been exposed to higher stresses due to torsional vibration are easily identified and can be selected for inspection at the next service interval which leads to plant maintenance cost reduction.

Practically unlimited cloud-based storage solutions available today are being coupled with the advanced analytics (statistics, patterns recognition). Predix© platform creates opportunities that, only a couple of years ago, were not conceivable. Tracking and comparison of torsional characteristics of different turbo-generator trains that are monitored in the system will allow robust identification of anomalies and outliers and early fault detection and assessment (if accompanied by a change in torsional frequency response function for instance).

ASSET PERFORMANCE

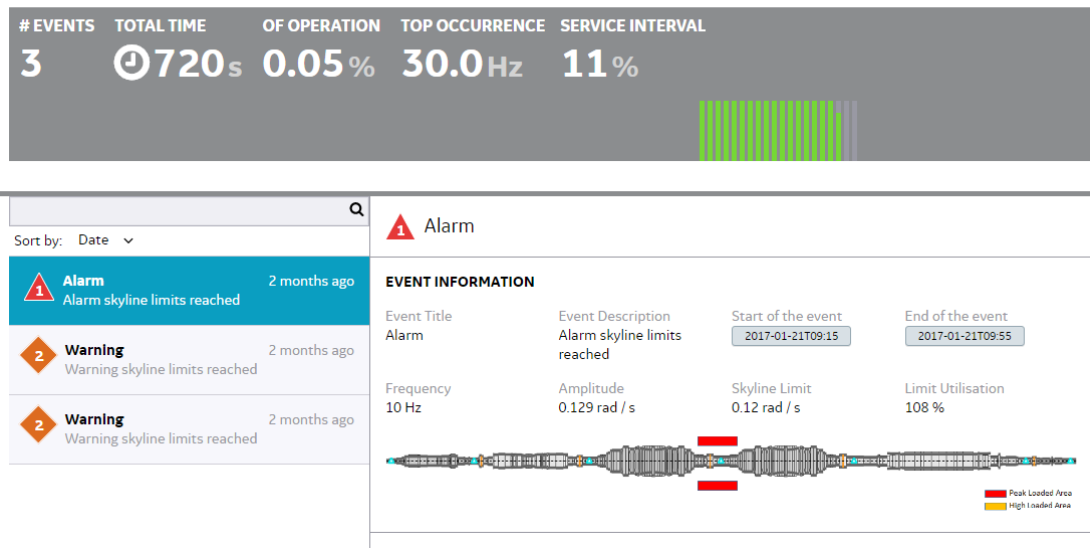


Figure 5 – Predix© screen of the torsional vibration monitoring system

7 Summary

As the risk of sub-synchronous interactions between the electrical grid and the power plant machinery increases, the manufacturers of rotating equipment must address these new challenges. In addition to the described mitigation measures on the grid side, robust torsional vibration monitoring solutions are necessary to guarantee the mechanical integrity of the turbo-generator shaft-lines.

An overview of the authors' experience gained from the development and implementation of the model-based measurement and monitoring systems for power generation trains' torsional vibration was presented.

It was shown that the combined use of the incremental pulse timing measurement technique together with the detailed model results (available for OEMs) allows reliable evaluation of the alternating torque levels in all machine sections, including critical subcomponents like blades or retaining rings of turbo-generators. The number of necessary signal sources was reduced to one, which is very important from a practical standpoint, as it makes the approach suitable for most existing turbomachinery (already equipped with an encoder-based speed measurement system).

Several permanent monitoring systems employing the described approach are currently being installed on a number of critical units.

References

- [1] Wachel J.C., Szenasi F.R., Field Verification of Lateral-Torsional Coupling Effects on Rotor Instabilities in Centrifugal Compressors, NASA Conference Publication No. 2147 (1980)
- [2] Duncan N. Walker, Torsional Vibration of Turbomachinery, The McGraw-Hill Companies, Inc. (2004)
- [3] Rossi V., Naldi L., Depau V., Torsional Vibration in Rotordynamic Systems: Smart Investigation Methods, Proceedings of ASME Turbo Expo 2009, Orlando
- [4] Naldi L., Biondi R., Rossi V., Torsional Vibration in Rotordynamic Systems, Identified by Monitoring Gearbox Behavior, Proceedings of ASME Turbo Expo 2008, Berlin
- [5] Wang P., Davies P., Starkey J.M., Routson R.L., A Torsional Vibration Measurement System, IEEE Transactions on Instrumentation and Measurement, Vol. 41, No. 6, December 1992
- [6] Den Hartog J.P., Mechanical Vibrations, Dover Publications, Inc., New York (1985)
- [7] Nestorides E.J., A Handbook on Torsional Vibration, British Internal Combustion Engine Research Association (BICERA), pp. 84-88 (1958)
- [8] Golebiowski M., Naldi L., Rossi V., Ponticelli S., Train Torsional Vibrations: Monitoring System Based On Model Result, Proceedings of ASME Turbo Expo 2010, Glasgow
- [9] Feese T., Hill C., Prevention of Torsional Vibration Problems in Reciprocating Machinery, 38th Turbomachinery Symposium, Houston (2009)
- [10] EPRI, Steam Turbine-Generator Torsional Vibration Interaction with the Electrical Network: Tutorial, Palo Alto, CA: 2005. 1011679.

Using Autoresonance for in-situ identification in rotating structures

Izhak Bucher, Solomon Davis, Shachar Tresser

Dynamics Laboratory, Mechanical Engineering, Technion Israel Institute of Technology, Haifa 320003, Israel

Abstract

Fast rotating structures can exhibit several vibration modes within their operating speeds; some of these modes become active only under specific circumstances and are therefore not visible by sensors during normal run-up.

The present paper combines Autoresonance and modal filtering [1,2] to actively excite one particular mode of vibration at a time, while speed of rotation and therefore the frequency are changing. Rotating structures exhibit forward or backward whirling motion that encapsulate potentially important physical features of the system. Autoresonance actively excites any mode of vibration in either forward or backward whirling direction and automatically tracks the change of natural frequency with speed of rotation, thereby identifying a specific branch of the Campbell diagram, in situ. Since rotating structures exhibit rich dynamics, some special filtering needs to be employed so as to eliminate the disturbances and the additional dynamics. The paper briefly describes the methodology and shows some numerical and experimental results.

1 Introduction and motivation

Fast rotating structure like turbo-chargers, gas-turbines and jet engines store a large amount of kinetic and strain energy and therefore can pose a great danger if not operated within safe regimes [1–6]. Obtaining a precise model is thus necessary to verify the model-based design and to ensure proper and safe operation. Identification is carried out via modal testing [7] or using in-situ, run-up measured data [8–10].

Several difficulties arise in implementing modal testing which is a comprehensive approach to extracting modal information from which a complete model can be assembled. Some of these difficulties are a) The model parameters, in particular the natural frequencies, vary with speed of rotation; b) The rotating parts are barely accessible for application of any external forces needed to excite hidden dynamics; c) A limited number of sensors can be placed on the structure. For these reasons a method using a small number of actuators and sensors that can track the changing dynamics with speed or rotation is sought.

The present paper develops a method whereby up to two actuators and two sensors are employed to quickly lock onto specific branches of the Campbell diagram while the system is undergoing speed variations. Because of the Autoresonance (AR) technique, one is not dependent on the imbalance forces to excite the various modes and both forward and backward whirling modes can be made visible. In order to obtain precise estimates of the natural frequencies, special phase-locked-loop style filtering is employed jointly with wide bandpass filtering illuminating the frequency range of interest.

The paper begins by describing the AR technique combined with modal filtering, later a simplified model of a gyroscopic system capable of performing whirling motions is described and the conditions for locking onto the natural frequencies are outlined. Some simulated and experimental results are shown to verify the proposed approach.

2 Autoresonance and modal filtering for automatic excitation of specific modes

Consider a multi-degrees of freedom system being excited by a monochromatic (single frequency) vector of forces. The equation of motion can be described by

$$\mathbf{M}\ddot{\mathbf{q}} + \mathbf{C}\dot{\mathbf{q}} + \mathbf{K}\mathbf{q} = \mathbf{b}f_0e^{i\omega t}, \quad \mathbf{b}, \mathbf{q}(t) \in \mathbb{R}^N \quad (1)$$

Now, at steady-state, the harmonic vibrations of the system can be described in terms of a modal summation

$$\mathbf{q}(t) = \left(\sum_{n=1}^N \frac{\phi_n \phi_n^T \mathbf{b} f_0 e^{i\omega t}}{\omega_n^2 - \omega^2 + i2\zeta_n \omega \omega_n} \right) e^{i\omega t}, \quad \phi_n \in \mathbb{R}^N \quad (2)$$

Consider a linear combination of the measured response as output, we obtain

$$y(t) = \mathbf{c} \left(\sum_{n=1}^N \frac{\phi_n \phi_n^T}{\omega_n^2 - \omega^2 + i2\zeta_n \omega \omega_n} \right) \mathbf{b} f_0 e^{i\omega t} \triangleq \mathbf{c}\mathbf{G}(\omega) f_0 e^{i\omega t}. \quad (3)$$

It has been shown before (see [11]) that for well-separated modes, one can make a structure vibrate at one of its natural frequencies by employing modal filtering. A modal filter measuring the p th mode is obtained by choosing $\mathbf{c} = \phi_p^T \mathbf{M}$, which by orthogonality of normal modes [6,7], isolated a single mode of the summation:

$$y(t) = \alpha \phi_p^T \mathbf{M} \mathbf{q}(t) = \alpha \frac{\phi_n \phi_p^T \mathbf{b}}{\omega_p^2 - \omega^2 + i2\zeta_p \omega \omega_p} f_0 e^{i\omega t}, \quad y(t) \in \mathbb{R}. \quad (4)$$

The AR combined with modal filtering replaces the right hand force in (1) with a 90 degrees shifted version of $y(t)$, e.g. a differentiator, fed to a relay nonlinear limiter [12]. In this case an ideal relay would yield a signal

$$f_p(t) = \text{sgn}[\Psi[y(t)]] = \begin{cases} 1 & \Psi[y(t)] \geq 0 \\ -1 & \Psi[y(t)] < 0 \end{cases}. \quad (5)$$

where $\Psi[y(t)]$ is 90 degrees shifted version of $y(t)$, realized in the present example by a derivative.

Now, combining modal filtering with AR, one can see, by employing the Describing Function (DF) approximate analysis (see [13][12]). It can be shown that (5) can be approximated for sinusoidal input, as

$$\text{sgn}[A \sin \omega t] \approx \frac{4}{\pi A} \sin \omega t, \quad \text{sgn}[\Psi(A \sin \omega t)] = \text{sgn}\left[\frac{d(A \sin \omega t)}{dt}\right] \approx \frac{4}{\pi A} \cos \omega t. \quad (6)$$

In the frequency domain, one obtains for the DF of $\frac{dy}{dt}$, passed through a relay,

$$\text{sgn}\left[\frac{dy}{dt}\right] \rightarrow \frac{4i}{\pi |\omega Y(\omega)|} Y(\omega). \quad (7)$$

The realization of a multi degrees of freedom system (MDOF) with Autoresonance (AR) in a loop is shown:

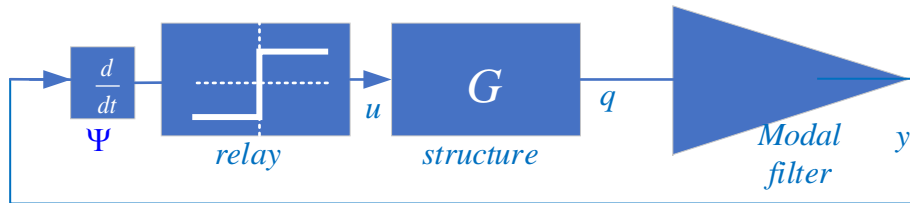


Figure 1: A MDOF system, $\mathbf{G}(\omega)$ in an Autoresonance closed loop with modal filtering

Examination of Fig.1, making use of (7), allows us to write

$$y(\omega) = \alpha \phi_p^T \mathbf{M} \mathbf{G}(\omega) \mathbf{b} u(\omega), \quad u(\omega) = \frac{4i}{\pi |\omega y(\omega)|} y(\omega). \quad (8)$$

Equation (8) holds if the system exhibits limit cycle oscillations, therefore

$$1 = \alpha \phi_p^T \mathbf{M} \mathbf{G}(\omega) \mathbf{b} \frac{4i}{\pi |\omega y(\omega)|} \quad (9)$$

Clearly, to maintain (9) we must have

$$\frac{4\alpha\phi_p^T \mathbf{M}\mathbf{G}(\omega)\mathbf{b}}{\pi|\omega y(\omega)|} = -i \quad (10)$$

So $\alpha\phi_p^T \mathbf{M}\mathbf{G}(\omega)\mathbf{b}$ is should be lagging by 90 degrees, which takes place for the natural frequency of mode p , i.e.

for $\omega = \omega_p$. And $y(\omega)$ is such that the vibrations amplitude is $|y(\omega)| = \frac{4\alpha\phi_p^T \mathbf{M}\mathbf{G}(\omega_p)\mathbf{b}}{\pi|\omega_p|}$.

This result is best illustrated by an example using the simplest gyroscopic system possible, i.e. the Stodola-Green model [1,5,14].

Auto resonance of a single mode gyroscopic system using a modal filter – an example

Consider a gyroscopic Stodola-Green model, obeying

$$\begin{bmatrix} 1 & 0 \\ 0 & 1 \end{bmatrix} \begin{pmatrix} \ddot{\theta}_x \\ \ddot{\theta}_y \end{pmatrix} + \Omega\mu \begin{bmatrix} 0 & 1 \\ -1 & 0 \end{bmatrix} \begin{pmatrix} \dot{\theta}_x \\ \dot{\theta}_y \end{pmatrix} + \omega_0^2 \begin{bmatrix} 1 & 0 \\ 0 & 1 \end{bmatrix} \begin{pmatrix} \theta_x \\ \theta_y \end{pmatrix} = \frac{1}{I_t} \begin{pmatrix} Q_x \\ Q_y \end{pmatrix}, \quad \mathbf{Q} \triangleq \frac{1}{I_t} \begin{pmatrix} Q_x \\ Q_y \end{pmatrix}, \quad \boldsymbol{\theta} \triangleq \begin{pmatrix} \theta_x \\ \theta_y \end{pmatrix} \quad (11)$$

where I_t, I_p are the diameter and polar moments of inertia, k is the bending stiffness and Ω spin speed. Q_x, Q_y are the generalized forces. Here we defined $\mu = \frac{I_p}{I_t}$, $\omega_0^2 = \frac{k}{I_t}$.

Nonrotating simulation

When the system is not rotating, $\Omega = 0$, we can employ the AR on, say θ_x and adding viscous damping, one has

$$\ddot{\theta}_x + 2\zeta\omega_0\dot{\theta}_x + \omega_0^2\theta_x = \frac{1}{I_t}Q_x, \quad \zeta = 0.01, \omega_0 = 10, I_t = 1, \quad (12)$$

Time domain simulation of the diagram in Fig.1, results in Fig.2

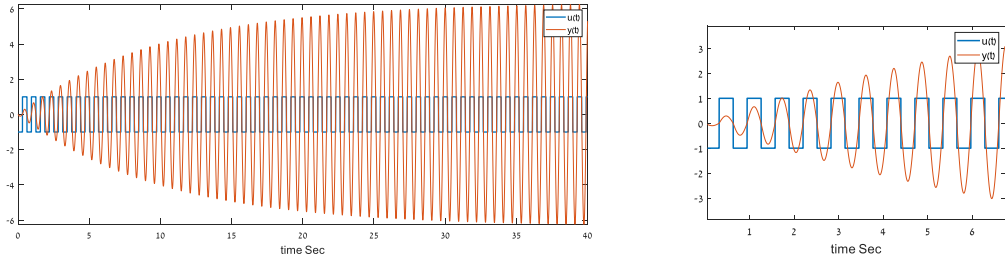


Figure 2: Non-rotating system under Autoresonance excitation. **Right:** zoomed area showing the excitation by the relay and the synchronized response. Response is exactly at 10Rad/s when it reaches steady-state

The intermediate conclusions from Fig.2 are that the system locks immediately onto the natural frequency from the first cycle, therefore allowing for a quick identification of the natural frequency. The steady state amplitude is 2% lower than the predicted amplitude from (10). The latter accounts for the numerical simulation accuracy and the approximate expression of the nonlinear relay DF.

Rotating case example

Once the system is rotating, there are two close natural frequencies that make the identification task more difficult. But by employing modal filtering, and making use of the natural 90 degrees phase shift between x and y , a modified approach can be used. The natural frequencies and eigenvectors are a function of rotation speed

$$\left\{ \omega_1 \triangleq \omega_- = \frac{1}{2} \left(-\mu\Omega + \sqrt{\mu^2\Omega^2 + 4\omega_0^2} \right), \phi_1 = \frac{1}{\sqrt{2}} \begin{pmatrix} 1 \\ i \end{pmatrix} \right\}, \left\{ \omega_2 \triangleq \omega_+ = \frac{1}{2} \left(+\mu\Omega + \sqrt{\mu^2\Omega^2 + 4\omega_0^2} \right), \phi_2 = \frac{1}{\sqrt{2}} \begin{pmatrix} 1 \\ -i \end{pmatrix} \right\} \quad (13)$$

Choosing a modal transformation,

$$\begin{pmatrix} \theta_x \\ \theta_y \end{pmatrix} = [\phi_1 \quad \phi_2] \begin{pmatrix} \eta_1 \\ \eta_2 \end{pmatrix} = \Phi \eta = \frac{1}{\sqrt{2}} \begin{pmatrix} 1 \\ i \end{pmatrix} \eta_1 + \frac{1}{\sqrt{2}} \begin{pmatrix} 1 \\ -i \end{pmatrix} \eta_2. \quad (14)$$

Equation (11) can be diagonalized and 2 independent equations are obtained (see [15])

$$\bar{\phi}_r^T \begin{bmatrix} 1 & 0 \\ 0 & 1 \end{bmatrix} \phi_r \ddot{\eta}_r + \Omega \mu \bar{\phi}_r^T \begin{bmatrix} 0 & 1 \\ -1 & 0 \end{bmatrix} \phi_r \dot{\eta}_r + \omega_0^2 \bar{\phi}_r^T \begin{bmatrix} 1 & 0 \\ 0 & 1 \end{bmatrix} \phi_r \eta_r = \frac{1}{I_r} \bar{\phi}_r^T \begin{pmatrix} Q_x \\ Q_y \end{pmatrix}, \quad r=1,2 \quad (15)$$

which leads to

$$\ddot{\eta}_1 + i\Omega \mu \dot{\eta}_1 + \omega_0^2 \eta_1 = \frac{1}{I_1} (Q_x - iQ_y), \quad \ddot{\eta}_2 - i\Omega \mu \dot{\eta}_2 + \omega_0^2 \eta_2 = \frac{1}{I_2} (Q_x + iQ_y). \quad (16)$$

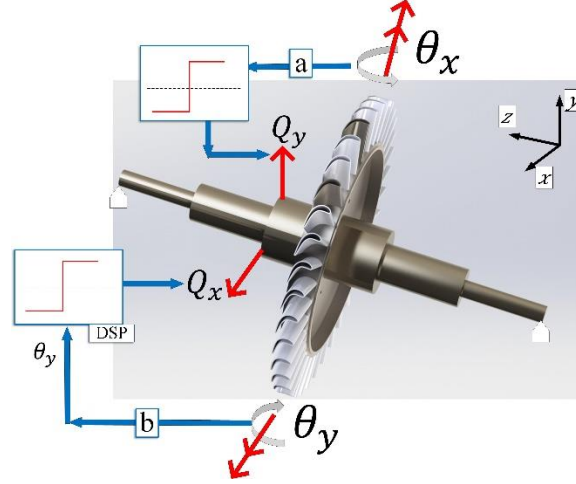


Figure 3: Schematic description of the proposed method showing 2 sensors and 2 actuators connected with a 'relay' (sign function) in a cross-coupled manner.

Let $Q_x = F_1 e^{i\omega t}$, $Q_y = F_2 e^{i\omega t}$ and thus $\eta_1 = A_1 e^{i\omega t}$, $\eta_2 = A_2 e^{i\omega t}$

$$\begin{pmatrix} \theta_x \\ \theta_y \end{pmatrix} = \frac{1}{2I_t} \begin{pmatrix} 1 \\ i \end{pmatrix} \frac{F_1 e^{i\omega t} - iF_2 e^{i\omega t}}{-\mu\Omega\omega + \omega_0^2 - \omega^2} + \frac{1}{2I_t} \begin{pmatrix} 1 \\ -i \end{pmatrix} \frac{F_1 e^{i\omega t} + iF_2 e^{i\omega t}}{\mu\Omega\omega + \omega_0^2 - \omega^2}. \quad (17)$$

Substituting (13), we have

$$\begin{pmatrix} \theta_x \\ \theta_y \end{pmatrix} = -\frac{1}{2I_t(\omega_- + \omega_+)} \begin{pmatrix} 1 \\ i \end{pmatrix} \frac{(F_1 - iF_2)e^{i\omega t}}{(\omega - \omega_-)} + \frac{1}{2I_t(\omega_- + \omega_+)} \begin{pmatrix} 1 \\ i \end{pmatrix} \frac{(F_1 - iF_2)e^{i\omega t}}{(\omega + \omega_+)} + \frac{1}{2I_t(\omega_- + \omega_+)} \begin{pmatrix} 1 \\ -i \end{pmatrix} \frac{F_1 e^{i\omega t} + iF_2 e^{i\omega t}}{(\omega + \omega_-)} - \frac{1}{2I_t(\omega_- + \omega_+)} \begin{pmatrix} 1 \\ -i \end{pmatrix} \frac{F_1 e^{i\omega t} + iF_2 e^{i\omega t}}{(\omega - \omega_+)}. \quad (18)$$

When the external force is rotating in a forward direction, i.e. $Q_x = F e^{i\omega t}$, $Q_y = -iF e^{i\omega t}$, we have

$$\begin{pmatrix} \theta_x \\ \theta_y \end{pmatrix} = \frac{1}{2I_t(\omega_- + \omega_+)} \begin{pmatrix} 1 \\ -i \end{pmatrix} \frac{2F e^{i\omega t}}{(\omega + \omega_-)} - \frac{1}{2I_t(\omega_+ + \omega_-)} \begin{pmatrix} 1 \\ -i \end{pmatrix} \frac{2F e^{i\omega t}}{(\omega - \omega_+)}. \quad (19)$$

This means that both the backward (ω_-) and the forward (ω_+) modes are excited, but when $\omega \rightarrow \omega_+$ the second term dominates and we have nearly pure forward whirl motion

$$\begin{pmatrix} \theta_x \\ \theta_y \end{pmatrix} \approx -\frac{\alpha_2^2 F}{I_t(\omega_+ + \omega_-)(\omega - \omega_+)} \begin{pmatrix} \cos \omega t \\ \sin \omega t \end{pmatrix}. \quad (20)$$

Alternatively, choosing a backward rotating force, i.e. $Q_x = F e^{i\omega t}$, $Q_y = iF e^{i\omega t}$, we obtain

$$\begin{pmatrix} \theta_x \\ \theta_y \end{pmatrix} = -\frac{1}{I_r(\omega_- + \omega_+)} \begin{pmatrix} 1 \\ i \end{pmatrix} \frac{F e^{i\omega t}}{(\omega - \omega_-)} + \frac{1}{2I_r(\omega_- + \omega_+)} \begin{pmatrix} 1 \\ i \end{pmatrix} \frac{F e^{i\omega t}}{(\omega + \omega_+)} . \quad (21)$$

Once more, when $\omega \rightarrow \omega_-$, in the presence of light damping, we would have

$$\begin{pmatrix} \theta_x \\ \theta_y \end{pmatrix} = -\frac{1}{I_r(\omega_- + \omega_+)} \begin{pmatrix} 1 \\ i \end{pmatrix} \frac{F e^{i\omega t}}{i2\zeta_- \omega_0^2} + \frac{1}{2I_r} \begin{pmatrix} 1 \\ i \end{pmatrix} \frac{F e^{i\omega t}}{(\omega_- + \omega_+)^2 + i2\zeta_- \omega_0^2} . \quad (22)$$

which is clearly dominated by the backward whirl.

Rotating case simulation example

To analyze the conditions for self-excitation at the natural frequency with the Autoresonance technique we employ a cross-connection scheme as illustrated in Fig.3. To analyze this case when we have 2 force inputs and 2 output degrees of freedom, we rewrite (17) in matrix form

$$\begin{pmatrix} \theta_x \\ \theta_y \end{pmatrix} = \frac{1}{2I_r} \left(\frac{1}{-\mu\Delta\Omega\omega + \omega_0^2 - \omega^2} \begin{bmatrix} 1 & -i \\ i & 1 \end{bmatrix} + \frac{1}{\mu\Delta\Omega\omega + \omega_0^2 - \omega^2} \begin{bmatrix} 1 & i \\ -i & 1 \end{bmatrix} \right) \begin{pmatrix} F_1 \\ F_2 \end{pmatrix} e^{i\omega t} . \quad (23)$$

Now, employing 2 relays, as shown in Fig.3 and substituting (6), assuming harmonic response

$$\begin{pmatrix} F_1 \\ F_2 \end{pmatrix} = \frac{4}{\pi} \begin{bmatrix} 0 & 1 \\ 1 & 0 \end{bmatrix} \begin{pmatrix} \frac{\alpha_x \theta_x(\omega)}{|\theta_x(\omega)|} \\ \frac{\alpha_y \theta_y(\omega)}{|\theta_y(\omega)|} \end{pmatrix} \quad (24)$$

where α_x, α_y are scalars to be selected later. Substituting (24) in (23), and adding the effect of small viscous damping, while neglecting its effect on the eigenvectors, one obtains

$$\begin{pmatrix} \theta_x \\ \theta_y \end{pmatrix} = \frac{1}{2I_r} \left(\frac{1}{-\mu\Delta\Omega\omega + \omega_0^2 - \omega^2 + 2i\zeta\omega\omega_0} \begin{bmatrix} 1 & -i \\ i & 1 \end{bmatrix} + \frac{1}{\mu\Delta\Omega\omega + \omega_0^2 - \omega^2 + 2i\zeta\omega\omega_0} \begin{bmatrix} 1 & i \\ -i & 1 \end{bmatrix} \right) \frac{4}{\pi} \begin{bmatrix} 0 & \frac{\alpha_y}{|\theta_y(\omega)|} \\ \frac{\alpha_x}{|\theta_x(\omega)|} & 0 \end{bmatrix} \begin{pmatrix} \theta_x \\ \theta_y \end{pmatrix} \quad (25)$$

By factoring out the response amplitudes, the limit cycle harmonic oscillations require here

$$\left[\mathbf{I} - \frac{1}{2I_r} \left(\frac{1}{-\mu\Delta\Omega\omega + \omega_0^2 - \omega^2 + 2i\zeta\omega\omega_0} \begin{bmatrix} 1 & -i \\ i & 1 \end{bmatrix} + \frac{1}{\mu\Delta\Omega\omega + \omega_0^2 - \omega^2 + 2i\zeta\omega\omega_0} \begin{bmatrix} 1 & i \\ -i & 1 \end{bmatrix} \right) \frac{4}{\pi} \begin{bmatrix} 0 & \frac{\alpha_y}{|\theta_y(\omega)|} \\ \frac{\alpha_x}{|\theta_x(\omega)|} & 0 \end{bmatrix} \right] \begin{pmatrix} \theta_x \\ \theta_y \end{pmatrix} = 0 \quad (26)$$

We can now examine 4 candidate frequencies for limit cycle oscillations, $\omega = \pm\omega_-, \pm\omega_+$.

Case $\omega = +\omega_+$, one has from (18)

$$\left| \mathbf{I} - \frac{1}{\pi I_r \zeta \omega_+ \omega_0} \begin{bmatrix} -i & 1 \\ -1 & -i \end{bmatrix} \begin{bmatrix} 0 & \frac{\alpha_y}{|\theta_y(\omega)|} \\ \frac{\alpha_x}{|\theta_x(\omega)|} & 0 \end{bmatrix} \right| \approx 0 \rightarrow \frac{1}{\pi I_r \zeta \omega_+ \omega_0} \frac{\alpha_y}{|\theta_y(\omega)|} - \frac{1}{\pi I_r \zeta \omega_+ \omega_0} \frac{\alpha_x}{|\theta_x(\omega)|} + 1 = 0 . \quad (27)$$

Once (27) is substituted in (26), we obtain

$$\begin{pmatrix} -\frac{\alpha_y}{\pi I_r \zeta \omega_+ \omega_0 |\theta_y(\omega)|} & -\frac{i\alpha_y}{\pi I_r \zeta \omega_+ \omega_0 |\theta_y(\omega)|} \\ 1 + \frac{i\alpha_y}{\pi I_r \zeta \omega_+ \omega_0 |\theta_y(\omega)|} & 1 + \frac{\alpha_y}{\pi I_r \zeta \omega_+ \omega_0 |\theta_y(\omega)|} \end{pmatrix} \begin{pmatrix} \theta_x \\ \theta_y \end{pmatrix} = 0 \quad (28)$$

that leads to

$$\theta_x = i\theta_y \quad (29)$$

which indicates perfect forward whirling motion. Clearly, this is accomplished by choosing $\alpha_x = a > 0$, $\alpha_y = -a$.

A similar exercise, choosing $\omega = +\omega_-$ would lead to the requirement $\alpha_x = a < 0$, $\alpha_y = -a$ that would lead to backward whirling motion under the same conditions.

Matlab Simulation

To assess the validity of the above analysis a Matlab™ /Simulink simulation was created with the system presented (11) in the configuration shown in Fig.3 and with added viscous damping of 0.5%.

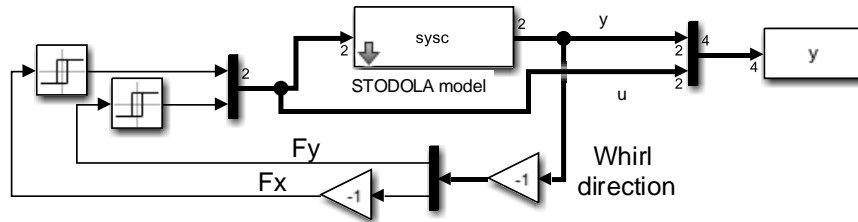


Figure 4: Simulink™ simulation of the Autoresonance method on the model in Fig.3

To verify the ability to drive the system such so it locks to the forward and backward whirling branches of the Campbell diagram, the whirl direction parameter shown in the diagram was switched at time $t=12$ from +1 to -1.

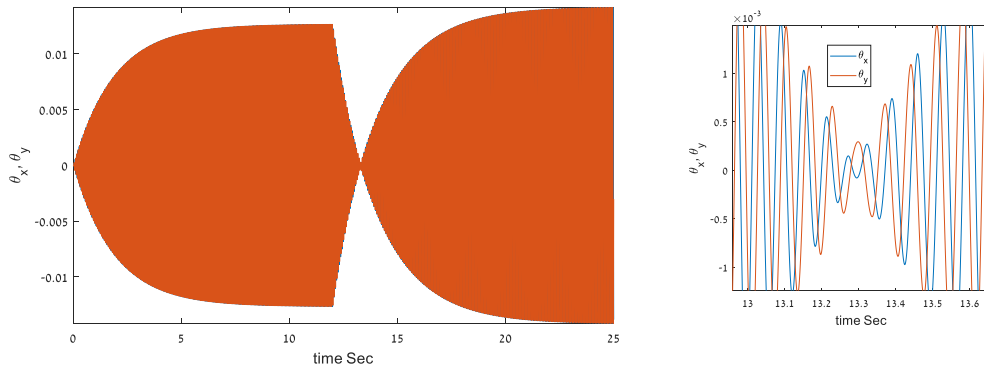


Figure 5: Left: Autoresonance forward response, converted to backward whirl at time=12 upon changing the sign of both AR feedbacks. Right: closer look at the switching area showing the change from x leading y by 90 degrees (forward) to y leading x by 90 (backward whirl)

2 Experimental verification

The proposed method was realized on a laboratory simulator of a fast-rotating engine, shown in Fig.6

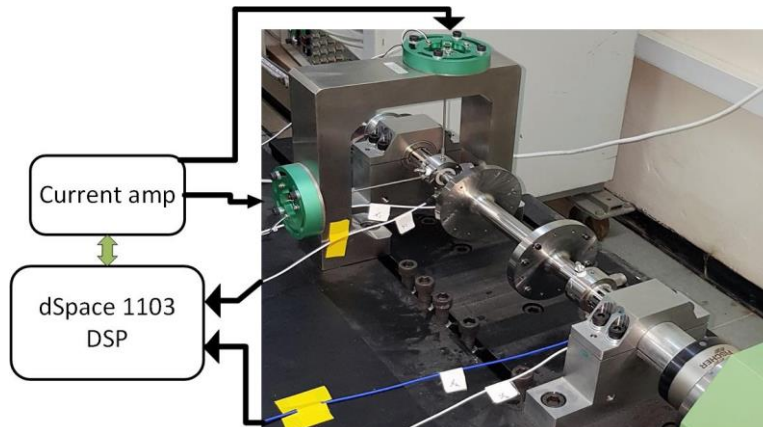


Figure 6: Experimental system showing 2 voice coil actuators applying the necessary F_x, F_y

In the laboratory system several difficulties have been observed concerning the imperfection of the current amplifiers (see Fig.6), additional dynamics and imperfect signal to noise ratio. To remedy these obstacles, some additional signal conditioning had to be applied and a detailed description of these actions are beyond the scope of this paper and are to appear in [16].

Before applying the method on the real system, a Finite element simulation in Ansys(tm) and Matlab was carried out. The procedure was set to identify the forward and backward modes of a higher mode as shown below.

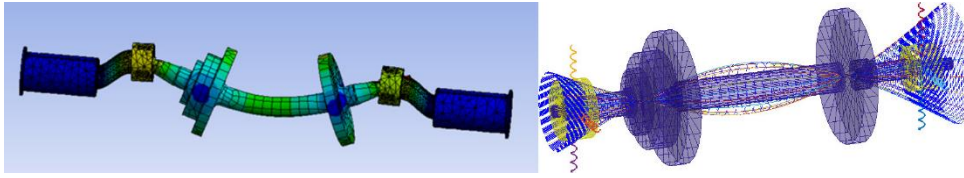


Figure 7: Left: ANSYS™ model of the rotor's third bending mode. Right: Matlab™ based simplified finite element model used in the time domain simulations.

The rotation speed was dictated by the PC in a for-loop. For each new iteration, the loop waited 30 seconds for the new speed to reach steady state. After the first branch was complete the for-loop was repeated for the second branch. The rotation speeds were increased from 500 to 5000 RPM in steps of 500 RPM. Two experimental Campbell Diagrams are presented in Fig.8 to show repeatability.

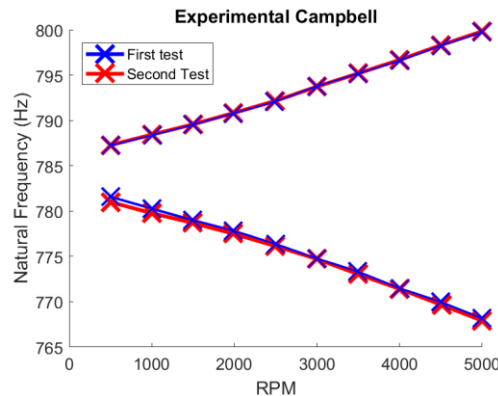


Figure 8: Two acquired Campbell Diagrams, third bending mode of the experimental system.

4 Conclusions

This paper presents a method to quickly lock on to a natural frequency of a gyroscopic, rotating system in-situ by employing an Autoresonance feedback.

The advantages of the demonstrated approach are fast locking to the true frequency and the ability to isolate close modes of forward and backward whirl that do not lend themselves to identification by natural imbalance excitation.

The proposed method can be used to excite gyroscopic or any other axisymmetric structure in its natural frequency while causing it to present a wave-like response, which is manifested by whirling motions in rotating shafts. The method was verified in theory in numerical simulations and on a dedicated experimental system.

References

- [1] Gasch, R., Nordmann, R., and Pfützner, H., 2006, *Rotordynamik*, Springer-Verlag.
- [2] Nguyen-Schäfer, H., 2012, *Rotordynamics of Automotive Turbochargers*, Springer Berlin Heidelberg, Berlin, Heidelberg.
- [3] Krämer, E., 1993, "Dynamics of Rotors and Foundations."
- [4] Vance, J. M., Zeidan, F. Y., and Murphy, B., *MACHINERY VIBRATION AND ROTORDYNAMICS*, John Wiley & Sons, Hoboken, New Jersey.
- [5] Genta, G., 2007, *Dynamics of Rotating Systems*, Springer Science & Business Media.
- [6] Geradin, M., and Rixen, D. J., 2015, *MECHANICAL VIBRATIONS THEORY AND APPLICATION TO STRUCTURAL DYNAMICS*.

- [7] Ewins, D. J., 1984, *Modal Testing: Theory and Practice*, Research studies press Letchworth.
- [8] Bucher, I., and Ewins, D. J., 2001, "Modal Analysis and Testing of Rotating Structures," *Philos. Trans. R. Soc. London A Math. Phys. Eng. Sci.*, **359**(1778), pp. 61–96.
- [9] Bucher, I., and Ewins, D. J., 1997, "Multidimensional Decomposition of Time-Varying Vibration Response Signals in Rotating Machinery," *Mech. Syst. Signal Process.*, **11**(4), pp. 577–601.
- [10] Bucher, I., 2013, "Directional Order Tracking in Rotating Machines," *J. Vib. Acoust.*, **135**(6), p. 61004.
- [11] Davis, S., and Bucher, I., 2018, "Automatic Vibration Mode Selection and Excitation; Combining Modal Filtering with Autoresonance," *Mech. Syst. Signal Process.*, **101**, pp. 140–155.
- [12] Gelb, A., and Velde, W. E. Vander, 1967, "Multiple-Input Describing Functions and Nonlinear System Design."
- [13] Davis, S., and Bucher, I., 2018, "Automatic Vibration Mode Selection and Excitation; Combining Modal Filtering with Autoresonance," *Mech. Syst. Signal Process.*, **101**, pp. 140–155.
- [14] Yukio, I., and Toshio, Y., 2012, *Linear and Nonlinear Rotordynamics*.
- [15] Bucher, I., and Ewins, D. J., 2001, "Modal Analysis and Testing of Rotating Structures," *Philos. Trans. R. Soc. A Math. Phys. Eng. Sci.*, **359**(1778), pp. 61–96.
- [16] Solomon, D., Tresser, S., Ferdiskoif, A., and Bucher, I., 2018, "In Situ Identification of Natural Frequency Branches in Gyroscopic Systems via Autoresonance and Phase Locked Loop," *J. Vib. Acoustics* - Submitt.

Journal Bearings

Advanced measurements and model update of an automotive turbocharger with full-floating journal bearings

Sebastian Leichtfuß¹, **Martin Kreschel**², **Loic Durbiano**³, **Tobias Dielenschneider**⁴,
Rainer Nordmann⁵, **Heiko Atzrodt**⁶, **Rafael Pilotto**⁷, **Heinz-Peter Schiffer**⁸

¹ Institute of Gas Turbines and Aerospace Propulsion, Technische Universität Darmstadt, Otto-Berndt-Str. 2, 64287 Darmstadt, Germany, leichtfuss@glr.tu-darmstadt.de

² IHI Charging Systems International GmbH, Haberstrasse 3-24, 69126 Heidelberg, Germany, m.kreschel@ihi-csi.de

³ IHI Charging Systems International GmbH, Haberstrasse 3-24, 69126 Heidelberg, Germany, l.durbiano@ihi-csi.de

⁴ Turbo Science GmbH, Robert-Bosch-Str. 7, 64293, Darmstadt, Germany, dielenschneider@turboscience.de

⁵ Fraunhofer Institute for Structural Durability and System Reliability LBF, Bartningstrasse 47, 64289 Darmstadt, Germany

⁶ Fraunhofer Institute for Structural Durability and System Reliability LBF, Bartningstrasse 47, 64289 Darmstadt, Germany, heiko.atzrodt@lbf.fraunhofer.de

⁷ Fraunhofer Institute for Structural Durability and System Reliability LBF, Bartningstrasse 47, 64289 Darmstadt, Germany, rafael.pilotto@lbf.fraunhofer.de

⁸ Institute of Gas Turbines and Aerospace Propulsion, Technische Universität Darmstadt, Otto-Berndt-Str. 2, 64287 Darmstadt, Germany, schiffer@glr.tu-darmstadt.de

Abstract

Full-floating journal bearings are commonly used in automotive turbochargers. Subsynchronous vibrations in such applications are often caused by oil-whirl and -whip phenomena. The small rotor weight in combination with very high rotational speeds provoke this unstable rotor-bearing behavior. This often leads to high vibration amplitudes, undesired noise or even risks rotor integrity. Models are commonly used to predict the complex nonlinear interaction of shaft, casing, floating-ring and oil film. Those models are based on basics of mechanics, experiences and are normally calibrated with simplified experiments.

In this paper a unique set of experimental data are compared to different simulation methods providing an overview of the physical behavior of a typical automotive turbocharger rotor and the model complexity needed to account for such phenomena. Experimental data are gathered at the hot gas test stand at Technische Universität Darmstadt. Intensive high-speed instrumentation is used providing information of the relative radial movement of the shaft at both ends of the rotor. Additionally, the rotational speed of both floating rings is monitored, and the axial movement of the shaft is recorded. The turbocharger is operated with realistic oil and gas temperatures and pressures. Acceleration and deceleration sweeps with different aerodynamic throttlings are recorded accounting for varying axial thrust.

Experimental results are compared with a model results presented by Köhl 2015 [1] and related to simulation results conducted by the Fraunhofer institute LBF with the simulation tool MADYN 2000. The rotor model by Köhl is using Ritz-Ansatz functions. These ansatz functions have to discretize the rotor eigenmodes and fulfill the geometrical boundary conditions of the rotor system. In MADYN 2000 the rotor is modelled by using the Timoshenko beam theory and Finite-Elements with Hermite polynomials to model properties of the rotor including gyroscopic effects. The forces in the floating bearing system are calculated by integration of the fluid film pressure. Those are derived from the solution of the Reynolds equations numerically solved using the Finite-Volume method.

Full-floating bearings in automotive turbochargers

Full-floating bearings are commonly used for high-speed rotor application because of their superior damping behavior and cost. A disadvantage nevertheless are undesired self-excited vibration in the bearing which can lead to noise emission or even risks rotor integrity. In figure 1 a typical rotor setup of a turbocharger rotor with shaft,

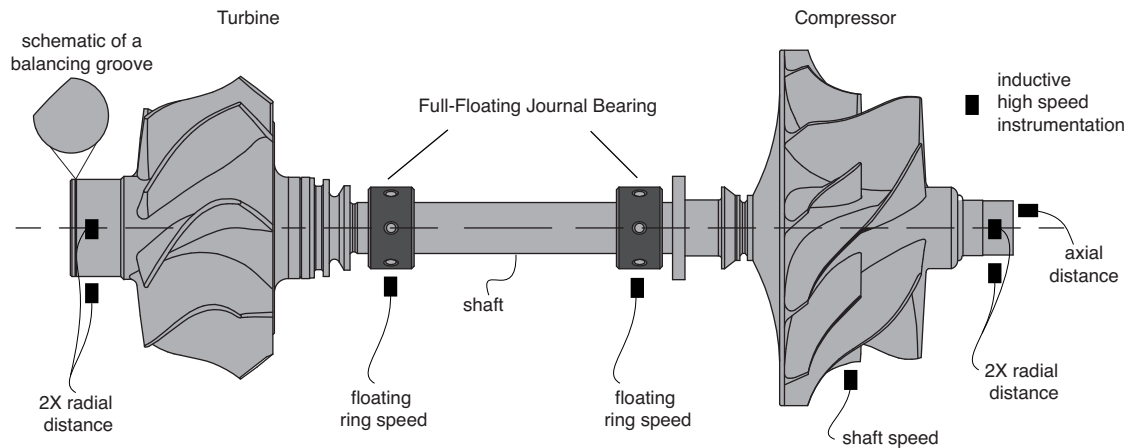


Figure 1: Turbocharger rotor with instrumentation (not to be scaled)

turbine, compressor wheel and radial bearings is visualized. The full-floating bearing consists of the bearing shell, a floating ring and the shaft (figure 2). Oil is induced through the casing and guided to the shaft with communication holes in the ring. The inner and outer oil film velocities lead to low friction losses and the double film induces extra damping in comparison to single oil film bearings. In the application at automotive turbocharger full-floating bearing on the other hand tend to induce Oil-Whirl and -Whip instabilities. The resultant subsynchronous vibration pattern with an almost constant frequency can cause tonal emissions typically in a range of 600 - 900 Hz. Oil-Whirl and -Whip instabilities are often reported (for example by Muszynska [2], Schweizer [3], [4], [5] and Woschke [6]). The low rotor weight in combination with very high rotational speed promote this phenomena at the outer and inner lubrication film of the radial bearings.

A schematic of the bearing system with inner and outer oil film is shown in figure 2. With some assumption and considering simple flow profile the right schematic in figure 2 shows a typical oil-whirl and oil-whip excitation. In this diagram possible frequencies of vibration are shown in dependence of the angular velocities of the shaft Ω_s . Beside the two usually harmless oil whirl frequencies (dotted lines) the more critical oil whip frequencies (full lines) have to be considered, when the two whirl frequencies are crossing and exciting the circular natural frequencies ω_{1+} and ω_{2+} and eigenmodes of the rotor system. Oil films show a log on effect by adopting rotor dynamic frequencies leading to a self excitation of the system. A shift of excitation frequencies and mechanisms are sometimes reported during rotor ramp ups. Those correspond to a change of excitation mechanism from the outer to the inner oil film.

As long as the whirl frequency of the lubrication films is not logged on to an eigenfrequency of the rotor, it is usually not a critical excitation mechanism. Nevertheless, it is typically visible in a frequency spectrum. In case of full-floating bearings two excitation whirl mechanisms coexist, which are correspondent to the inner and outer

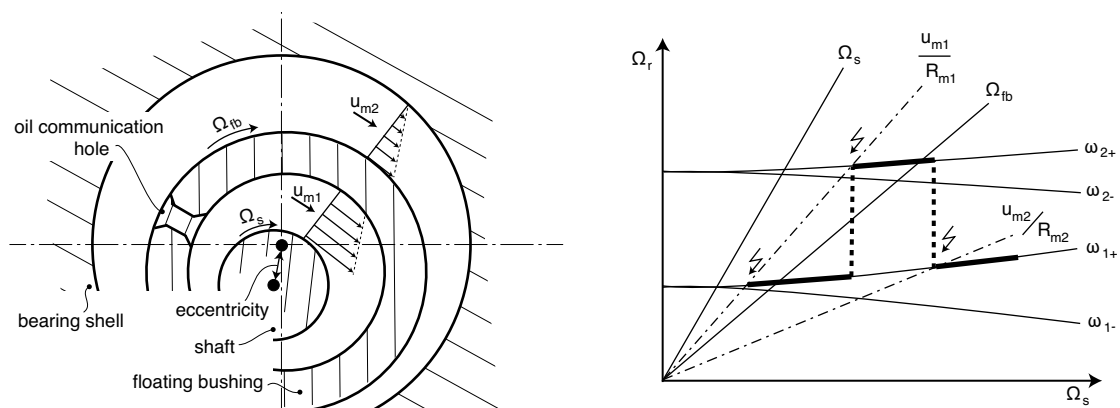


Figure 2: Schematic of a full-floating bearing (left) and correspondent excitation mechanisms (right) (not to be scaled)

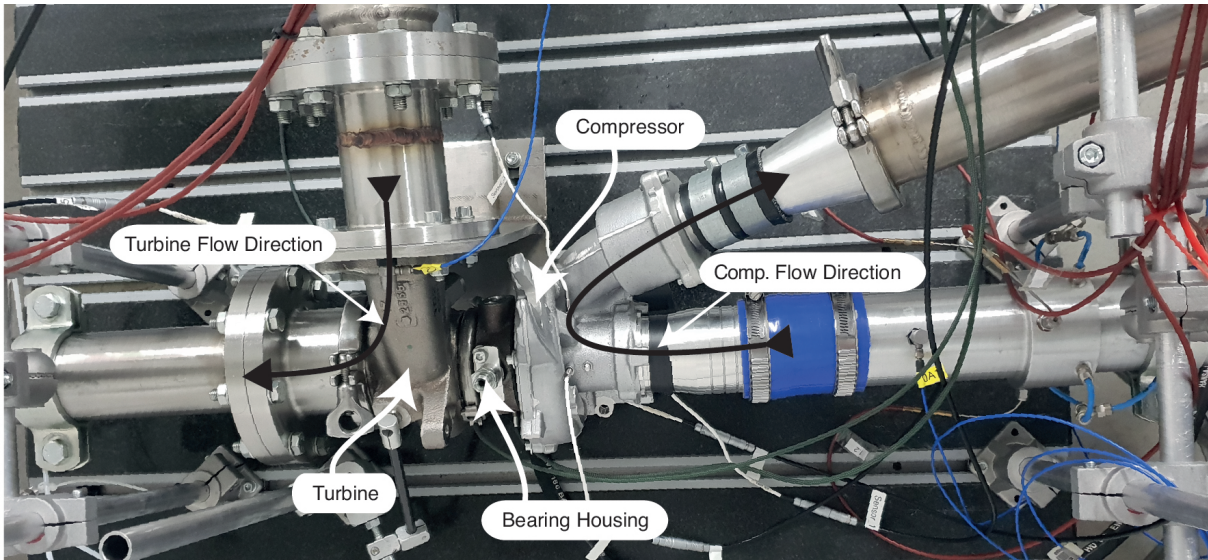


Figure 3: Experimental setup at the Institute of Gas Turbines and Aerospace Propulsion (GLR) at Technische Universität Darmstadt

oil film. The complexity of this coupled system between inner, outer oil film, rotor dynamics and motion of the floating ring is superimposed by complex boundary conditions.

Cavitation of oil and the correspondent effects on rotor stability are intensively investigated during recent years and modeling approaches are presented among others by Ausas et al. [7], Grando et al. [8] and Li et al. [9]. The influence of heat transfer is presented by many researchers and thermodynamic models accounting for its effects on compressor and turbine performance are available ([10], [11] and [12] for example). The interaction of heat transfer with oil, bearings and rotor dynamic is a topic already published by Han et al. [13] but nevertheless still of high importance. Finally the influence of axial load and therewith the aerodynamic operating point can influence the rotor dynamic behavior of a turbocharger significantly.

Therefore, the rotor dynamic simulation of a complete automotive turbochargers is complex and time consuming. To achieve results in an acceptable time during development processes, the complexity of the system is typically reduced. Models must be validated and calibrated with appropriate experimental results. The aim of this paper is to give an overview of a currently developed measurement setup for detailed investigations. The influence of aerodynamic throttling condition on oil-whirl and -whip is presented. Results are compared with results from modeling techniques and the limitation of these models are shown.

Experimental setup

After a major rebuild, the turbocharger laboratory at the Institute of Gas Turbines and Aerospace Propulsion (GLR) at Technische Universität Darmstadt was commissioned in 2014. Turbine and compressor are aerodynamically decoupled in the open loop test facility. A screw compressor, which delivers up to 0.3 kg s^{-1} mass flow rate at a maximum pressure of 4.5 bar is used to power the turbine and an electrical heater provides a constant and controllable turbine inlet temperature. This heater allows to vary turbine inlet temperature for sensitivity studies. On the other hand, the maximum turbine inlet temperature is limited to 573 K. The power limitation currently allows to measure a complete compressor map with a maximum compressor wheel diameter of 60 mm. Aerodynamic performance and operating point are monitored and controlled with a standard instrumentation in accordance with [14]. Therefore, four static pressure tappings and three thermocouples type K are located at five wheel diameters upstream and two wheel diameters downstream of the compressor. An orifice with corresponding pipe length and diameter is designed in accordance to DIN EN ISO 5167-1:2004-01 and DIN EN ISO 5167-3:2004-01 to determine mass flow rate of the compressor. Repeatability is ensured by controlling test cell and oil conditions.

For rotor dynamic investigations the turbocharger is mounted to a 500 kg table and flexible pipes are used for isolation to prevent from excitation (figure 3). The goal was to constrain the turbocharger casing, because sensors are attached to it and shaft movements are measured relative to the casing.

Inductive high speed sensors with a maximal resolution of 100 kHz, measurement range of 1 mm and accuracy of $2 \mu\text{m}$ are used to determine the relative displacement of the shaft at the compressor and turbine end (cf. figure 1).

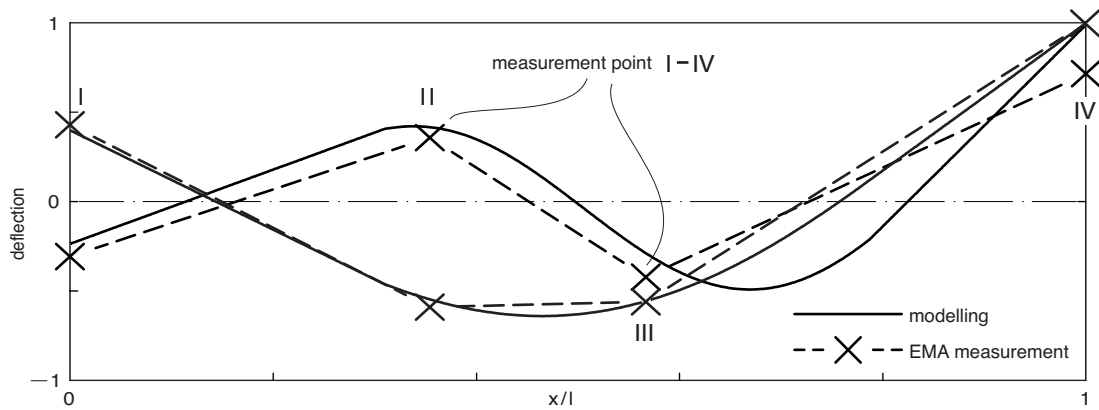


Figure 4: Experimentally determined bending eigenmodes of the rotor (EMA) and comparison to modeling approach by Köhl et al. [1] (not to be scaled)

The turbocharger wheel and floating ring speed at compressor and turbine end are measured with the same sensor type. In these cases only impulses at the sensor are counted which correspond to moving blades or communication holes in the floating ring. The application of this type of sensor at the turbine is only possible due to the low inlet temperature controlled by the electrical heater.

The turbocharger rotor system under investigation features two subsynchronous eigenfrequencies and corresponding rigid body modes, which depend on the stiffness of the bearing and bearing housing. In addition to those, two bending eigenfrequencies and -modes were determined with experimental modal analyses (EMA) by Köhl et al. [1] and compared to modeling approaches (cf. figure 4)

Experimental results

The aerodynamic compressor map of the turbocharger is shown in figure 5. The total pressure is plotted over corrected mass flow rate which corresponds to inlet Mach-number. Five speed lines with constant circumferential Mach-number are measured covering a range from low to high speed operation. The aerodynamic standard procedure of Mach-number reduction is used to account for varying inlet conditions, in particular day to day temperature

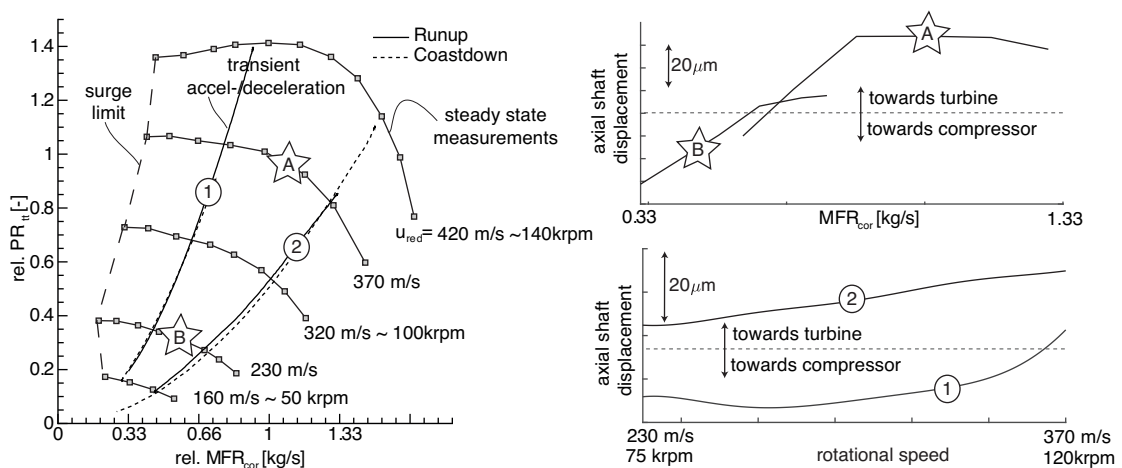


Figure 5: Aerodynamic compressor map with ramp up and down conditions (left) axial movement of the shaft for low (B) and high (A) speed operation (right top), axial displacement for transient runup close to surge (1) and close to choke operation (2)

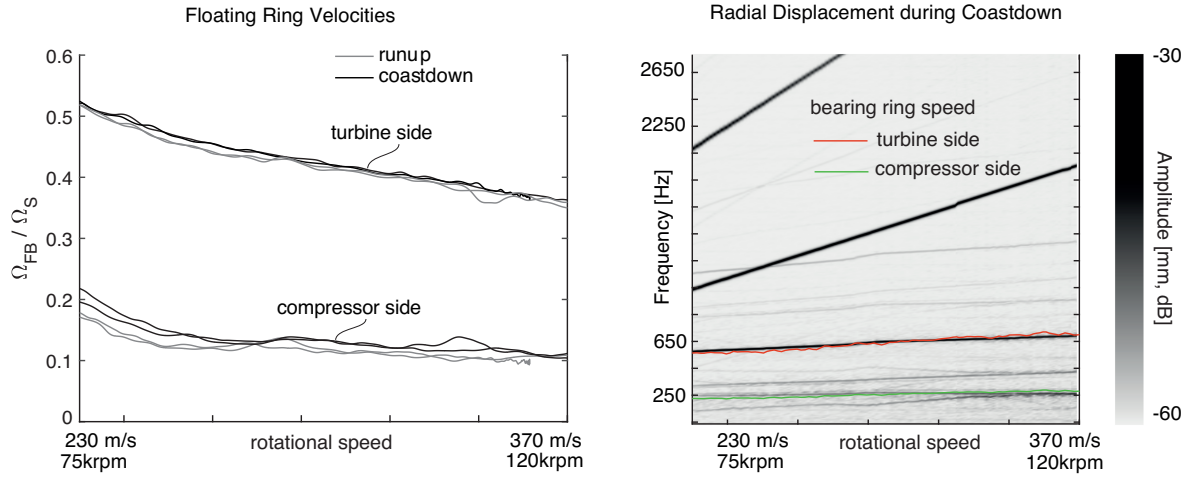


Figure 6: Measured floating ring speed for multiple runup and coastdown ((1) and (2) in figure 5) at left side, Campbell-Diagram for runup from approx. 230m/s to 370m/s ((1) in figure 5 right)

and humidity variations.

$$M_a = \frac{c}{\sqrt{\kappa RT}} \quad (1)$$

A constant speed line is determined by gradually closing a valve at the pressure side of the compressor while circumferential velocity of the turbocharger is controlled with the power input to the turbine (controlling of the mass flow rate through the turbine). The reduction of cross flow section in the valve increases the throttling pressure to the compressor. This leads to a gradual reduction of inlet velocity and correspondent Mach-number. At high mass flow rates and low circumferential Mach number, speed lines are limited by pressure losses. In case of high speed operation the flow is reaching supersonic conditions in the smallest cross section of the compressor which can lead to very high pressure drops.

At very low inlet velocity, compressor blades tend to suffer flow separation. At a certain point this leads to compressor surge at which flow is reversed and air is periodically discharging from exit of the compressor to its inlet. This phenomenon is well known and intensively investigated. From a mechanical point of view the periodic unloading of pressure leads to a very high fluctuating axial force normally not tolerable.

The resultant axial force of a turbocharger during normal operation depends mainly on turbine inlet and compressor outlet pressure. The exit pressure at the compressor manifests itself at the backside of the impeller and induces an axial force in direction to the compressor inlet. The inlet pressure of the turbine induces a force counteracting to that of the compressor side. The resultant force therefore depends on the operating condition of compressor and turbine.

In figure 5 the results of the axial distance measurements at the compressor end (c.f. figure 1) is shown to demonstrate the change of resultant axial force. At high compressor throttling (i.e. low inlet Mach-number) the pressure ratio of the compressor is high and the shaft moves towards the compressor end while for high mass flow rates the shaft moves towards the turbine and the distance to the sensor increases.

Transient acceleration and deceleration measurements

In addition to steady state experiments at certain operating points the equipment allows to perform transient maneuvers. Two examples are shown in the compressor map of figure 5 at which the turbocharger is accelerated and decelerated with a constant compressor throttling. The axial displacement of the shaft is monitored during these maneuvers and shown at the right side of figure 5.

A main result of these maneuvers is shown at the left side of figure 6. The circumferential speed of the floating ring at turbine and compressor end is visualized as the ratio of the shaft speed during acceleration and deceleration. In the range of investigation, the axial force has no influence on the speed of the floating rings. A significant difference between the ring velocity at compressor end to the ring at the turbine end is resolved. Furthermore, a

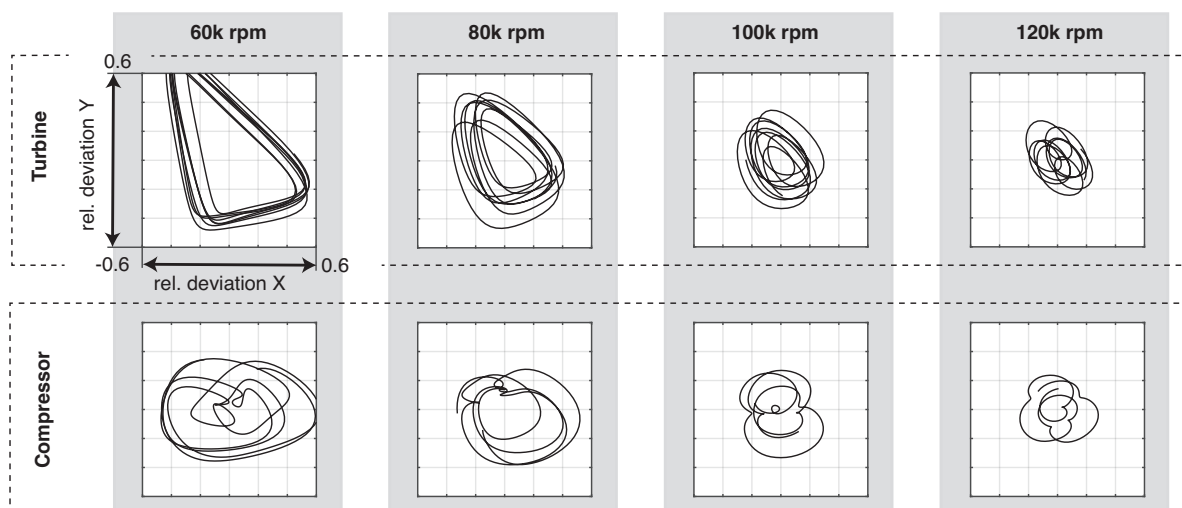


Figure 7: Subsynchronous ($< 750Hz$) experimentally determined shaft displacement at turbine and compressor measurement position (cf. figure 1)

small difference between acceleration and deceleration maneuvers is visible.

At the right side of figure 6 a Campbell diagram is shown based on the signal of the radial distance sensors at the turbine end. The signals of a deceleration maneuver are post-processed representative for all transient runs. A high signal strength is visible for synchronous rotational frequencies. Since the radial distance sensors are used for the Campbell diagram, a synchronous signal is expected due to the presence of a balancing groove (cf. figure 1). The rotor was dynamically balanced prior to testing with a residual field balancing quality and acceleration sensors show rather small signals at synchronous frequencies and the subsynchronous pattern is the predominant vibration phenomenon. Depending on the rotational speed, the amplitude of subsynchronous vibrations are 2-5 times higher than those of synchronous vibrations.

The subsynchronous vibration frequencies are equivalent to the rotational frequency of the floating ring at turbine and compressor end. Based on these observations it is obvious, that the subsynchronous frequencies are a self excited vibration patterns induced by the full floating bearings.

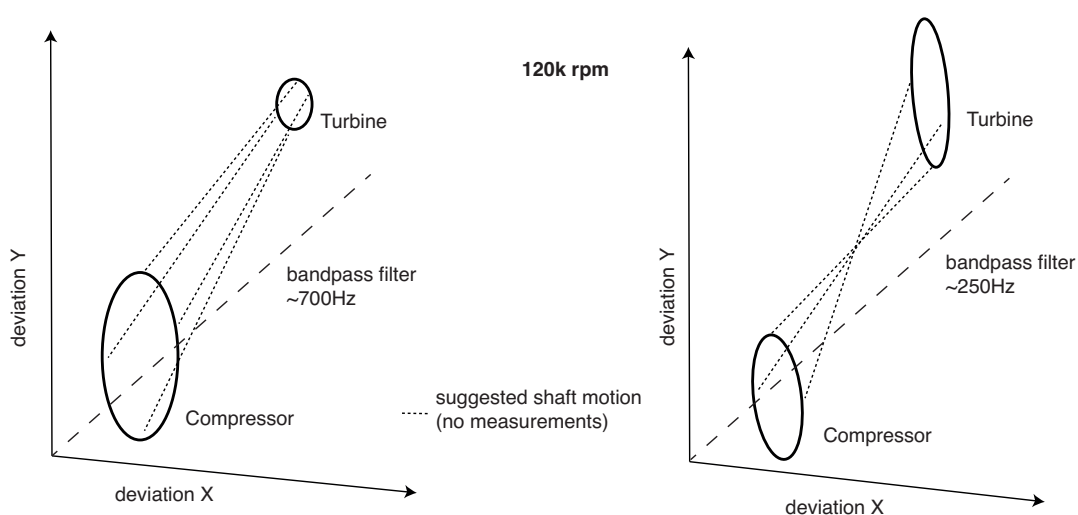


Figure 8: Subsynchronous shaft displacements bandpass filtered at the two predominant vibration modes. 3 Dimensional visualization including phase information.

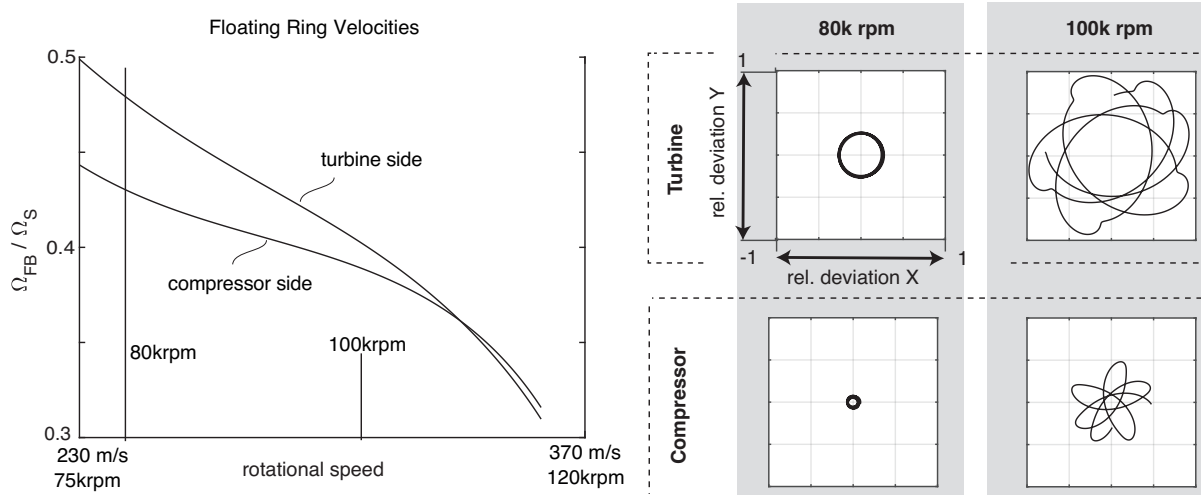


Figure 9: Simulation results with the simplified model presented by Köhl [1]. Floating ring speed (left), subsynchronous ($< 750Hz$) shaft displacement at turbine and compressor (right)

Subsynchronous orbits of the shaft at turbine and compressor end

Since the turbine can be operated at low temperatures it is possible to apply inductive sensors at the compressor and turbine end surfaces (cf. figure 1). At synchronous frequencies the signal of these sensors are corrupted by the balancing grooves. After filtering the signals, the subsynchronous orbit of the turbine and compressor can be visualized. In figure 7 the radial displacement due to subsynchronous vibrations of the shaft at the turbine and compressor end are shown for varying rotational speeds. The absolute displacement from peak to peak is limited which is in the expected range due to measured bearing clearances. In general, the displacement decreases with rotational speed which can be explained by the stiffening of the bearing system with rotational speed. The signals can be used to visualize the three dimensional displacement of the shaft. Therefore, phase information of compressor and turbine end are considered. Figure 8 shows the bandpass filtered shaft motion for the two predominant subsynchronous vibration patterns. The motion between compressor and turbine is not measured. Therefore, bending of the shaft can not be visualized here.

Simplified modeling results

Experimental results can be compared to the model presented by Köhl [1]. This model is using Ritz-Ansatz functions for modeling the rotor. The forces in the floating bearing system are calculated with a finite volume method resolving the Reynolds equations for the oil films. Some simplifications are applied which are:

1. constant oil viscosity (no temperature distribution or change of temperature)
2. incompressible fluid
3. pressure variations in the radial direction are neglected
4. no tilting of the bearing rings
5. rigid bearing housing and no deformation of the bearing rings
6. the influence of axial forces are neglected
7. Gümble boundary conditions

Details of the model can be found in the publication [1]. At this point only a qualitative comparison is visualized in figure 9. It is apparent, that the simulated floating ring speed of the turbine is in the same range as the measured one. The floating ring at the compressor end show a high discrepancy to experimental results and also the decline of rotational speed ratio for high speed is overestimated by the simulation. At the right side of figure 9 the shaft displacement due to subsynchronous vibrations at the turbine and compressor end are evaluated at the measurement positions. Till medium speed of approximately 80 krpm no relevant subsynchronous vibrations are predicted by the simulation model. Between 80krpm and 100krpm subsynchronous vibrations increase and the induced displacement of those is clearly visible in figure 9. In addition to the qualitative difference the predicted amplitude of shaft displacements is almost two times larger than the one observed in the experiments.

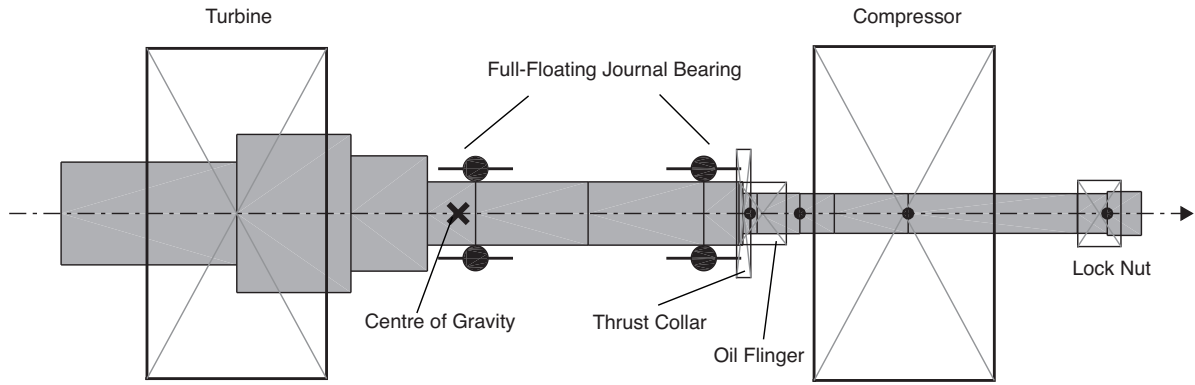


Figure 10: Madyn2000 rotordynamic model

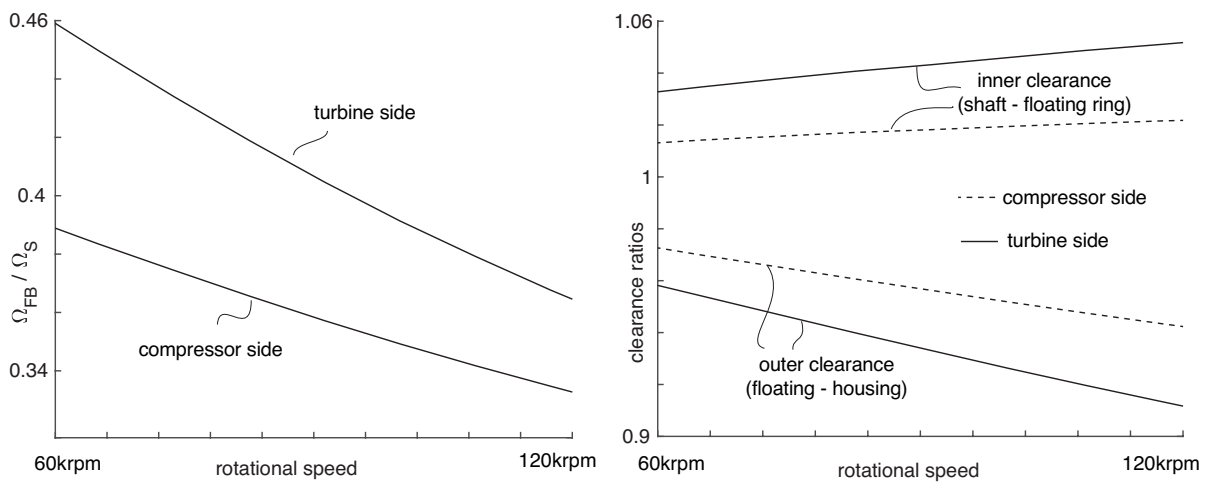


Figure 11: modeling result with Madyn2000, speed ratio of floating rings (left) and clearance ratio between shaft and floating ring as well as floating ring and housing (right)

A modeling approach with MADYN2000

With the intent to reproduce and understand the experimental results, a numerical model of the examined turbocharger was constructed using the commercial rotordynamic software MADYN2000. Using the geometrical data provided by IHI Charging Systems International GmbH, a simple model consisting of 16 shaft elements and 5 disc elements was created (figure 10). Since the detailed geometries of the turbine and compressor wheel are too complex to be modeled, they have been taken into account as simple cylindrical elements considering their mass moments of inertia.

Regarding the floating ring bearings, some assumptions have to be made. While the bearing housing has only one oil-outlet in the middle between both floating rings, the model consists of two radial outlets (one at each side). Outlet and inlet are modeled as radial holes in the bearing housing above the floating ring. They are placed with a definite circumferential distance from each other.

The Madyn2000 bearing model is based on the assumption of perfectly circular short bearings, the loads in both bearings (T-end and C-end) are calculated from a static analysis and applied as the only external force in the floating ring bearing. The unbalanced loads are located in the T-end and C-end with the same magnitude and a phase difference of 90° between them. Results for the floating ring at the turbine and compressor end, regarding speed ratio and clearances of the floating rings are visualized in figure 11.

According to Köhl 2015 [1], the speed ratio is related to the differences in viscosity of the oil and the clearances at the outer and inner gap between floating ring, shaft and housing. Since oil temperatures are very high, the dynamic viscosity is almost constant over the investigated speed range. Therefore, the only dominant effect causing the change in speed ratio of the floating rings and shaft is the variation of inner and outer clearance. This relation can

be observed in figure 11. While the outer clearance diminishes with increasing speed the inner clearance rises. At the same time the speed ratio of the floating rings drop with the rotational speed increasing.

Summary

Oil-whirl and -whip are two important excitation mechanisms to be considered during the design process of full-floating journal bearings. The resultant subsynchronous vibration can lead to noise emissions or even risks rotor integrity. The precise prediction is difficult since rotordynamic, fluid dynamic and thermodynamic mechanisms are coupled and induce a complex system to be resolved with numerical methods.

A new test rig for rotordynamic related turbo charger investigations at Technische Universität Darmstadt is presented. The infrastructure and measurement setup delivers highly resolved signals while the turbo charger is operated with realistic temperature, pressure and rotational speed. The radial shaft movement at compressor and turbine side as well as the floating ring speeds are resolved with inductive sensors. In addition the axial movement of the shaft is measured.

An aerodynamic map of the compressor is shown and the corresponding axial displacement of the shaft is visualized. This mainly depends on the static pressure at compressor outlet and turbine inlet varying for different rotational speeds and throttling conditions.

The subsynchronous vibration pattern observed during first experimental investigations causes a tonal noise emission between 600 and 750 Hz. Observations of several transient accelerations and deceleration procedures indicate that the axial displacement of the shaft does not influence the speed ratio of the floating rings in the radial bearings. The floating ring speeds at compressor and turbine are considerably different. The frequency of the subsynchronous vibration pattern is close to the rotational frequency of the floating ring at the turbine side.

The subsynchronous shaft orbits at compressor and turbine side are shown for several rotational speeds. Those can be compared to simulations results conducted with a simplified model presented by Köhl 2015. The model shows a decrease of speed ratio between floating ring and shaft speed with increasing rotational speed. A similar phenomenon was observed within the experiments. Nevertheless, considerable differences between modeling results and experiments are shown ascribed to the model assumptions applied.

In addition the system is modeled with the commercial software Madyn2000. Likewise the results show a decrease of floating ring speed ratio with increasing operation speed. The model depicts that the clearance between shaft and floating ring decreases with increasing speed and at the same time the clearance between floating ring and shaft is decreasing. This indicates that the ring is widened with rotational speed. The pressure difference between inner and outer oil film increasing with rotational speed causes this effect.

Acknowledgement

The authors would like to thank IHI Charging Systems International GmbH for provision of the necessary hardware for testing, financial support, for their continuing technical assistance as well as permission to publish this paper.

NOMENCLATURE

<i>Latin</i>		<i>Subscripts</i>	
u	oils speed	cor	corrected
R	radius	s	shaft
EMA	Experimental Modal Analysis	t	total to total
M_a	Mach number	fb	floating ring
MFR	Mass Flow Rate	1	inner oil film
PR	pressure ratio	2	outer oil film
R	gas constant	+	forward traveling
T	temperature	-	backward traveling
		m	median
<i>Greek</i>			
κ	isentropic exponent		
Ω	rotational speed		
ω	eigenfrequency		

REFERENCES

- [1] Köhl, W. and Kreschel, M. and Filsinger, D., 23. – 25. Februar 2015. “Modellabgleich eines turboladerrrotors in schwimmbuchsenlagerung anhand gemessener schwimmbuchsendrehzahlen”. *SIRM 2015 – 11. Internationale Tagung Schwingungen in rotierenden Maschinen, Magdeburg, Deutschland*,.
- [2] Muszynska, A., 1986. “Whirl and whip—rotor/bearing stability problems”. *Journal of Sound and Vibration*, **110**(3), pp. 443–462.
- [3] Schweizer, B., 2009. “Oil whirl, oil whip and whirl/whip synchronization occurring in rotor systems with full-floating ring bearings”. *Nonlinear Dynamics*, **57**(4), pp. 509–532.
- [4] Schweizer, B., 2009. “Total instability of turbocharger rotors—physical explanation of the dynamic failure of rotors with full-floating ring bearings”. *Journal of Sound and Vibration*, **328**(1-2), pp. 156–190.
- [5] Schweizer, B., 2010. “Dynamics and stability of turbocharger rotors”. *Archive of Applied Mechanics*, **80**(9), pp. 1017–1043.
- [6] Woschke, E., Daniel, C., and Nitzschke, S., 2017. “Excitation mechanisms of non-linear rotor systems with floating ring bearings - simulation and validation”. *International Journal of Mechanical Sciences*, **134**, pp. 15–27.
- [7] Ausas, R. F., Jai, M., and Buscaglia, G. C., 2009. “A mass-conserving algorithm for dynamical lubrication problems with cavitation”. *Journal of Tribology*, **131**(3), p. 031702.
- [8] Grando, F. P., Priest, M., and Prata, A. T., 2006. “A two-phase flow approach to cavitation modelling in journal bearings”. *Tribology Letters*, **21**(3), pp. 233–244.
- [9] Li, X.-s., Song, Y., Hao, Z.-r., and Gu, C.-w., 2012. “Cavitation mechanism of oil-film bearing and development of a new gaseous cavitation model based on air solubility”. *Journal of Tribology*, **134**(3), p. 031701.
- [10] Baines, N., Wygant, K. D., and Dris, A., 2010. “The analysis of heat transfer in automotive turbochargers”. *Journal of Engineering for Gas Turbines and Power*, **132**(4), p. 042301.
- [11] Shaaban, S., and Seume, J. R., 2006. “Analysis of turbocharger non-adiabatic performance”. In *8th International Conference on Turbochargers and Turbocharging*. Elsevier, pp. 119–130.
- [12] Bohn, D., Heuer, T., and Kusterer, K., 2005. “Conjugate flow and heat transfer investigation of a turbo charger”. *Journal of Engineering for Gas Turbines and Power*, **127**(3), p. 663.
- [13] Han, T., and Paranjpe, R. S., 1990. “A finite volume analysis of the thermohydrodynamic performance of finite journal bearings”. *Journal of Tribology*, **112**(3), p. 557.
- [14] Committee, E. P. T. C., 1995. “Turbocharger gas stand test code”. *SAE International*.

Simulation and measurement of ring speed of full floating ring bearing in an automotive turbocharger

Christian Daniel¹, Elmar Woschke¹, Steffen Nitzschke¹

¹Institute of Mechanics, Otto-von-Guericke University Magdeburg, 39106, Magdeburg, Germany,
{christian.daniel}{elmar.woschke}{steffen.nitzschke}@ovgu.de

Abstract

The rotating shaft of automotive turbo-chargers are commonly supported in floating ring bearings with two fluid films in serial connection. They are – due to the high rotational shaft speed – often designed as full floating ring bearings with a free rotating ring between shaft and housing. The ring is driven by the shear stresses on the inner and outer surface of the fluid films, which depend on the rotational speed gradient in the fluid and the pressure distribution in the fluid films. Furthermore the pressure distribution and the ring speed interdepend, because the oil speed determines the frequency of the oil whirl excitation. If this frequency meets a natural frequency of the system the oil-whirl locks in an oil-whip and causes a circular motion of the shaft in the bearing with very high amplitudes. Finding an optimal bearing design as a result of these nonlinear relations is a sophisticated task. Several parameters of the floating rings could be tuned to avoid such oil-whip effects. Hence, a holistic simulation approach is used to calculate the run-up of the turbocharger by using the simulation software EMD, which contains solution methods for the nonlinear fluid film equations in order to solve them in every time step. However, the simulation has to be validated against measurements. For this sake, the ring speed is measured using a miniature eddy-current sensor during an electric driven run-up on a test rig, yielding an integral quantity containing all relevant effects. Furthermore, the shaft motion is measured and compared to simulation in form of spectrograms.

1 Introduction

The bearing system of high speed rotating systems are often based on fluid bearings. Due to their simple and cheap design and good damping characteristics they are often used in automotive turbochargers (TC). To enlarge the damping of the fluid bearings a floating ring is introduced to add an additional outer fluid bearing. Depending on the rings capability to rotate either as full floating or as semi floating ring bearing results, whereat in the latter case, the outer fluid film acts as a squeeze film damper. This design has some advantages like higher damping but also some disadvantages like nonlinear behaviour caused by two fluid films which can both induce oil-whirl excitations. Therefore other bearing designs become more and more popular. Ball bearings can in some case replace the fluid bearings. The advantages are high stiffness and low friction, which decreases the power loss. The authors presented some different bearing designs, which have been compared for an automotive turbocharger [1]. Nevertheless the full floating ring design is still common in automotive turbochargers, since the production costs are low in case of pure cylindrical bearings. An integral state variable of these bearings is the ring speed. It depends on different bearing parameters like clearance, bearing width and of course the resulting pressure distribution in the fluid films. For comparison of simulation and measurement the ring speed is essential. Other researcher groups have also performed measurements of the floating ring speed. One of the first is from Kettleborough [2], which was published in 1954. On a relative large test rig for a single bearing, the ring speed was determined stroboscopically. Later, Domes [3] used a simple rotor, which was smaller, but still larger than an automotive turbocharger. The ring speed was obtained using a hall sensor in combination with a permanent magnet, which was glued in the rings surface. Köhl et al. [4] built a transparent printed housing to get the possibility to arrange a high speed camera on the area of the rings oil feed holes. By image processing the passing oil feed holes are counted and so the ring speed could be determined. The problem of the printed housing is the low stiffness and the temperature durability, which prohibits measurements with hot oil. Furthermore, air bubbles in the oil film impede the optical observation of the oil feed holes. Summarising, in the context of turbochargers, it is still a challenge to apply a speed sensor to a floating ring without changing the bearings behaviour significant. Finally the measured ring speed could be used

to validate the numerical simulation results of the TC.

2 Electric test rig for TC

The test rig used in the present study consist of a simplified turbocharger, where the turbine- and compressor wheel are substituted by equivalent cylindrical masses. This reduces the friction loss during run-up and neglects the majority of aerodynamic effects acting on the blades. The shaft and the bearing system are still in the original configuration. The run-up is realised by an electric synchronous motor with approx 2000W and an idle speed of 50000 rpm. This does not cover the whole speed range of this turbocharger, but it is enough to show the relevant effects like oil-whirling motions of the shaft. The shaft displacement is measured at the compressor side by two redundant displacement sensor, a laser triangulation sensor and a capacitive sensor for the sake of comparability. The first allow a large distance to the shaft, but optical reflections on the rotating surface can cause problems. Contrarily, the latter has to be arranged very near to the shaft surface, but is much cheaper. The shaft speed is measured by an optical speed sensor at the turbine side. The speed of one floating ring is measured by an eddy current sensor placed at the compressor side bearing - Fig. (3). The turbine side bearing was not measured because the housing is unfavourable for direct access with tapped hole. The connection from the motor to the turbocharger was realised with a steel wire to get a coupling with low bending stiffness, nevertheless the connection to the shaft of the turbocharger is difficult. The thread at the shafts end is used for the adapter with the collet chuck for the steel wire, but the thread is not able to center the adapter properly. This leads to a skewing of the adapter, which induces unintentional excitations to the turbocharger and of course limits the maximum speed. Fig. (3) shows the

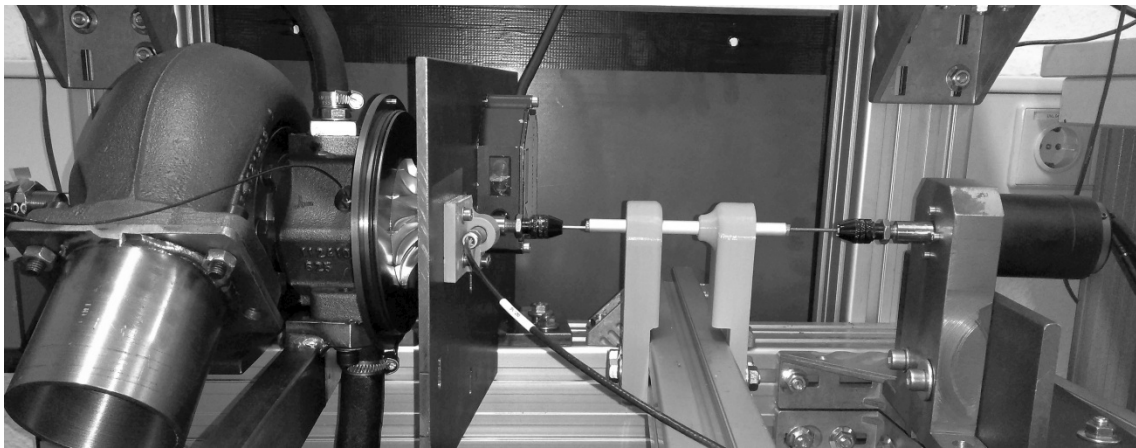


Figure 1: Electric driven test rig for TC.

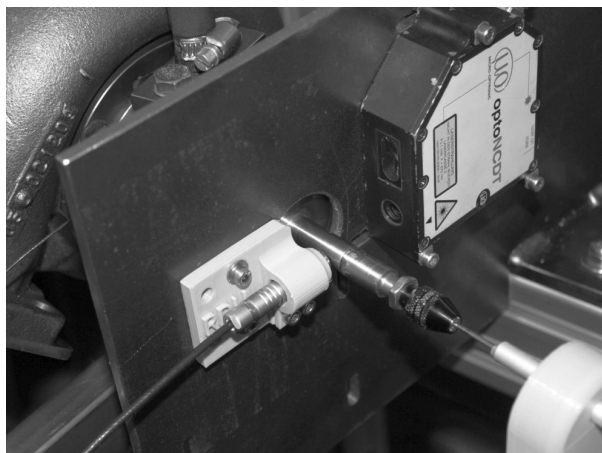


Figure 2: Position measurement at the compressor side with laser triangulation sensor and capacitive sensor.

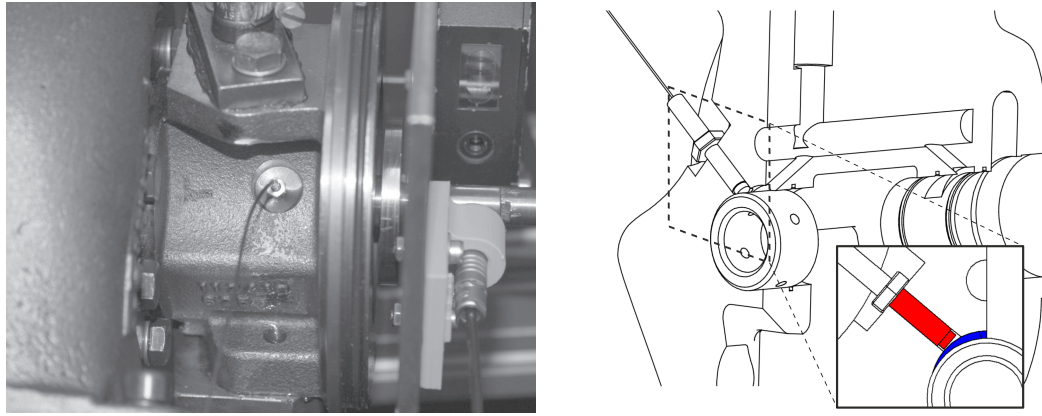


Figure 3: Ring speed measurement at bearing on the compressor side in the sickle groove.

installation of the eddy current sensor EU05 in the sickle groove of the oil inlet. This ensures that the tapped hole for the sensor has no hydrodynamical influence on the system. However, there is somewhat leakage at the sensor inlet, which is in comparison to the oil consumption of the bearing system very low.

3 Measurement of floating ring speed

The speed of the ring is measured by counting the oil feed holes in the floating ring. This is realised by measuring the position of the floating ring in the midplane using an eddy current sensor. The signal is disturbed by the oil feed holes in the floating ring. Fig. (4) illustrates the signal of the eddy current sensor. In regions of without oil inlet holes the sensor measures the position of the floating ring. The passing oil inlet hole disturbs the position signal and seemingly enlarges the distance measured by the sensor. The transition is continuously and not like a rectangular signal because the hole is much smaller compared to the surface of the sensor.

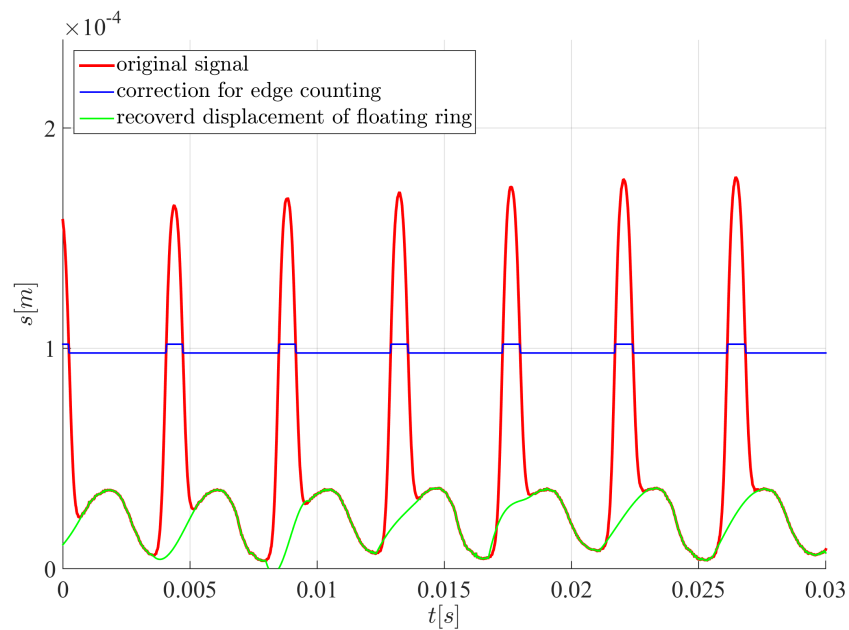


Figure 4: Signal from eddy current sensor.

Anyway, the signal could be easily converted into a rectangular signal in order to count the edges for speed measurement. With this information the time signal could be recovered by eliminating the regions of the holes. By

using a spline interpolation the leaks could be recovered in order to get a smooth function. Thus two signals could be obtained with the eddy current sensor at the same time, which will additionally help to compare with simulation results.

4 Simulation of run up

The equation of motion of the rotor dynamic system, which includes the rigid and elastic bodies – here considered as finite Timoshenko beam elements – form a system of second order equations

$$\underline{\underline{M}}_{\text{rigid}} \cdot \ddot{\underline{q}} + \underline{b}(q, \dot{q}) = \underline{h}(t, q, \dot{q}, x, \dot{x}) \quad (1)$$

$$\underline{\underline{M}}_{\text{elastic}} \cdot \ddot{\underline{x}} + (\underline{\underline{D}}_{\text{elastic}} + \Omega \underline{\underline{G}}_{\text{elastic}}) \cdot \dot{\underline{x}} + \underline{\underline{K}}_{\text{elastic}} \cdot \underline{x} = \underline{f}(t, q, \dot{q}, x, \dot{x}) \quad (2)$$

which is solved numerically in time domain using appropriate semi-implicit time integration solvers like [5, 6]. The pressure distribution in full floating ring bearing is represented by the Reynolds equation

$$\frac{\partial}{\partial x} \left(\frac{h^3}{\eta} \frac{\partial p}{\partial x} \right) + \frac{\partial}{\partial y} \left(\frac{h^3}{\eta} \frac{\partial p}{\partial y} \right) = 6(U_1 + U_2) \frac{\partial h}{\partial x} + 12 \frac{\partial h}{\partial t} \quad (3)$$

Eq. (3) is solved numerically in every time step for the input quantities h and $\partial h/\partial t$ for the inner and outer oil film. For this sake the finite volume method is used to build a system of equations. Due to the proposed cavitation algorithm the equation can either be linear or nonlinear. Daniel [7] shows an finite difference approach for Gumbel cavitation, which yields a linear equation. For Elrod [8] or Bi-Phase [9] cavitation models an iterative solution method based on fix-point iteration has to be used, which enlarges the numerical effort [10]. Stability problems of this algorithms could be bypassed using a regularisation approach, which additionally allows the application of Newton-Raphson leading to a remarkable speed-up [11–13]. A detailed description of the overall simulation approach including validation against experimental data is given in [14]. However, after the solution of Eq. (3) the pressure distribution $p(x, y)$ is known and the shear stresses at the radial bearing surface can be calculated

$$\tau_s = -\frac{h}{2} \cdot \frac{\partial p}{\partial x} + \eta \cdot \frac{\Delta u}{h} \quad (4)$$

The friction torque consists of two parts, the shear stress due to the velocity gradient and the shear stress due to the pressure gradient. Felscher [15] showed that the second part becomes important for high eccentricities and should not be neglected. For calculation of the resulting torque the reference point determines whether only shear stresses or additional normal stresses have to be taken into account. However, Vogelpohl [16] has shown that the result is the same regardless whether the centre of the shaft or the centre of the shell is used as reference. Here the formula is developed for the centre of the shell with the radius r_s

$$M_{fr} = \int \tau(x, y) \cdot r_s \, dA \quad (5)$$

The friction torque M_{fr} is acting on the inner side of the floating ring which accelerates the ring, the torque at the outer surface decelerates the ring. In addition to the friction torque at the radial surfaces, the friction torque at the axial side of the floating ring is present. It can be determined by integrating the shear stresses due to relative velocity

$$M_{fa_i} = \int_{r_i}^{r_a} 2\pi \cdot r^3 \cdot \frac{\eta}{s} \cdot \Omega_{\text{ring}} \, dr \quad (6)$$

Domes has mentioned this equation in his thesis [3] and has used it for comparison with measurements at a sample rotor. Here the sum of both acting friction torques on the axial sides of the floating ring are formulated as function of the axial gaps s_1 and s_2 . These values are usually unknown, and also depend on the axial thrust load acting on

the floating ring, which is hard to measure. So there is a kind of uncertainty by setting the parameter for the axial gaps

$$M_{fa} = M_{fa1} + M_{fa2} = \frac{\pi}{2} \cdot (r_a^4 - r_i^4) \cdot \eta \cdot \left(\frac{1}{s_1} + \frac{1}{s_2} \right) \cdot \Omega_{ring} \quad (7)$$

The resulting ring speed Ω_{ring} depends on all acting torques and inertias, which are a result of the numerical time integration process. The ring speed could hardly be estimated a-priori because it is a function of the pressure distribution and vice versa. Especially in regions of oil-whirl motions the friction torque rises immediately and could speed up or drag down the ring depending on whether the oil whirl is in the inner or outer bearing.

5 Comparison of predicted and measured ring speed

The boundary conditions of the system are well known. For the simulation the temperature and the pressure of the oil are set to the values which are pretended at the test rig. The clearances of the bearings were measured at room temperature (20°C) - Tab. (1).

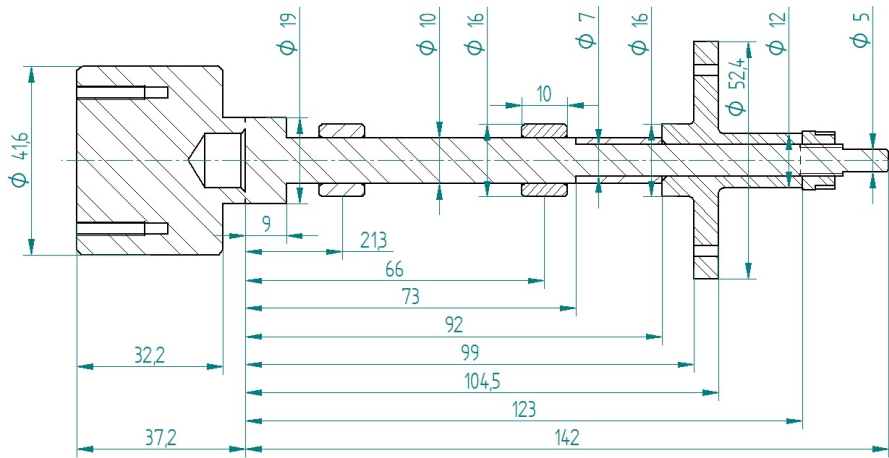


Figure 5: Geometry of TC

Table 1: Bearing parameter measured at 20°C.

parameter	inner bearing	outer Bearing
diameter	10.00 mm	16.00 mm
width	7.00 mm	10.00 mm
clearance (diameter)	30 μm	80 μm
clearance (axial)	300 μm	300 μm

The oil (FUCHS 600639273 10W-40) was fed with 3 bar and 60°C. The change of clearance due to the different bearing materials is regarded in the simulation, but the temperatures are assumed to be constant during the run up. Fig. (6) shows the results of measurement of shaft and ring speed. The measured shaft speed is a boundary condition for the shaft speed in the simulation. Only the ring speed is a result of the acting torques caused by the fluid films in the inner and outer bearing. The predicted ring speed meets the measurements pretty good. Only the harmonic changing in the measured ring speed can not be seen in the simulation, but the unbalance and eccentricity of the coupling to the electric motor unit was seriously high, which imposes large excitations of the shaft and the floating ring. This could lead to a periodical friction torque, which influences the rotational speed of the ring.

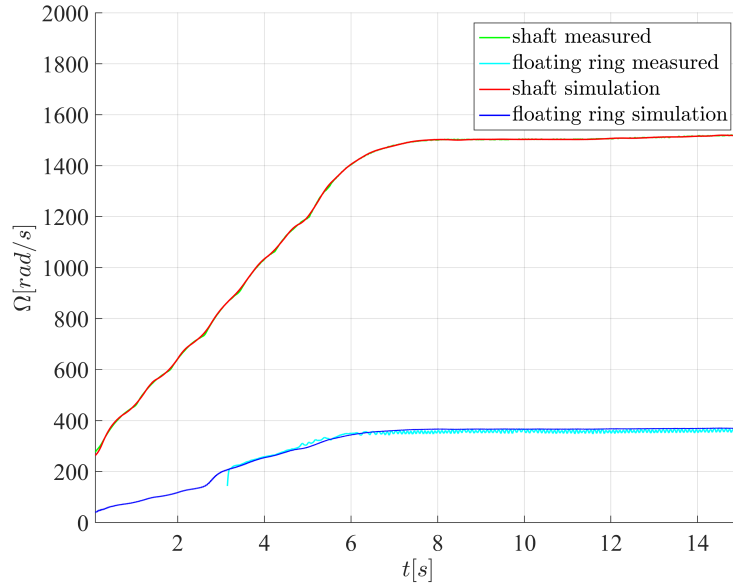


Figure 6: Comparison between measured and simulated floating ring speed (Elrod / $10\mu m$).

The prediction of the axial position of the ring also influences the resulting ring speed. The assumption of a mid position leads to the smallest friction torque and to the highest ring speed. If the ring moves to one axial border, the difference of the axial gap s_1 and s_2 becomes larger and due to Eq. (7) the axial friction torque rises. Fig. (7) shows the influence of the minimal axial gap on the resulting ring speed in case of a Gumbel cavitation model.

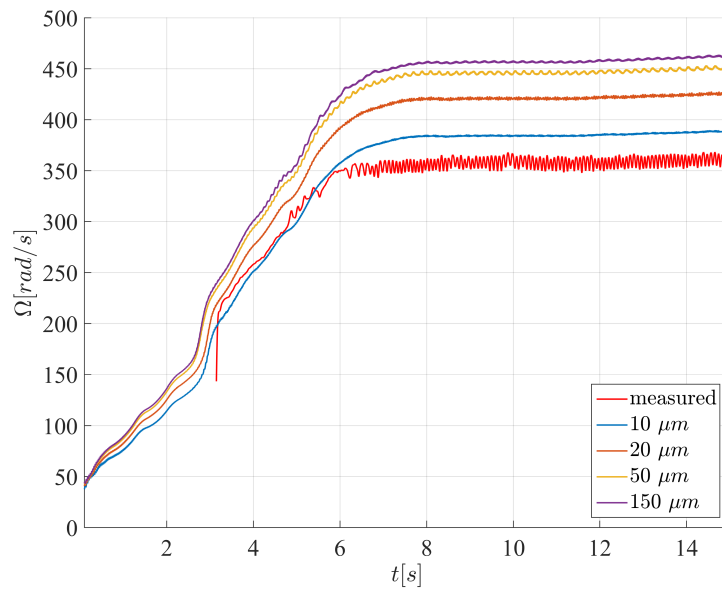


Figure 7: Influence of smallest axial gap of the floating ring (Gumbel).

The Gumbel approach used here assumes a totally filled gap in the cavitation domain. Due to outgas and pour in of air the gap in this domain is only partly filled, leading to a reduced surface, on which the shear stress can take

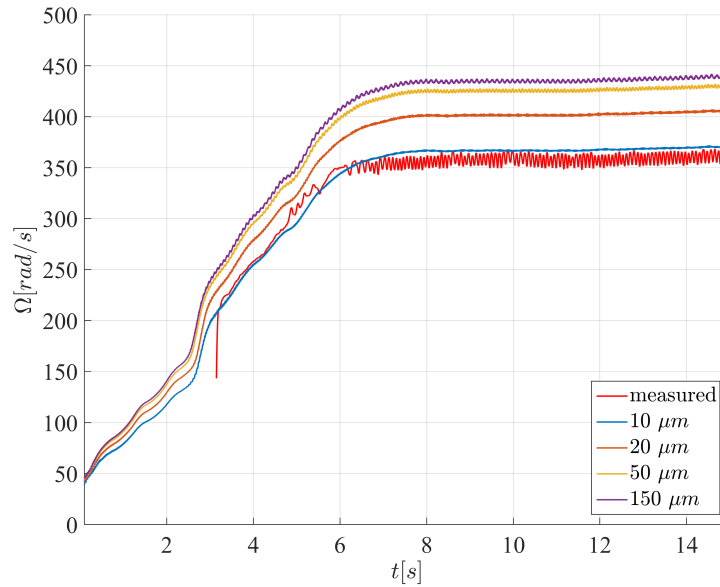


Figure 8: Influence of smallest axial gap of the floating ring (Elrod).

effect. This effect can be considered in the simulation using e.g. the Elrod cavitation algorithm.

Comparing Gumbel Fig. (7) and Elrod Fig. (8), the choice of cavitation model changes the absolute values but the qualitative results for the ring speed behaviour stays the same. Nevertheless with the Elrod algorithm, the simulation is able to follow the experimental results more precisely.

6 Conclusion

The paper showed a method for ring speed measurement of automotive turbochargers by using a small sized eddy current sensor. The oil feed holes in the floating ring influences the signal of displacement measurement if they are passing the sensor. Otherwise the position information is measured. It could be shown that a simple signal processing is able to separate the ring speed information from the position information of the ring. As a consequence of less information during passing of oil feed holes the position signal is a bit deranged but sufficient to analyse to movement of the ring. The advantage of using an eddy current sensor compared to other speed sensor concepts is the duality of measurement results and the possibility to use it on small bearings without disturbing the bearings behaviour.

The comparison to the nonlinear simulation with EMD shows a good prediction of the ring speed. The influence of the axial friction torque was studied w.r.t. the ring speed. It could be shown, that this torque has a significant influence depending on the axial position of the ring. Nevertheless the value of the axial position of the floating ring is not a priori known. An automatic axial arrangement of the ring by solution of the according equation of motion is difficult, because there are no directed forces on the ring.

In future work, the test rig will be improved. Therefore the steel wire between electrical drive and shaft will be replaced by a double flexible multi disc clutch. Hence, the operational speed range can be enlarged, which allows to observe further subharmonic vibrations and their interaction with the ring speed.

REFERENCES

- [1] Daniel, C., Göbel, S., Nitzschke, S., Woschke, E. and Strackeljan, J. (2013). Numerical simulation of the dynamic behaviour of turbochargers under consideration of full-floating-ring bearings and ball bearings, *ICOVP 2013 - 11th International Conference on Vibration Problems*.
- [2] Kettleborough, C. (1954). Frictional experiments on lightly-loaded fully floating journal bearings, *Australian J. Appl. Sci* 5: pp. 211–220.
- [3] Domes, B. (1980). *Amplituden der unwucht- und selbsterregten Schwingungen hochtouriger Rotoren mit rotierenden und nichtrotierenden schwimmenden Büchsen*, PhD thesis, Universität Karlsruhe.

- [4] Köhl, W., Kreschel, M. and Filsinger, D. (2015). Modellabgleich eines turboladerrotors in schwimmbuchsenlagerung anhand gemessener schwimmbuchsendrehzahlen, *Proceedings SIRM2015 11. Internationale Tagung Schwingungen in Rotierenden Maschinen*, Magdeburg, pp. 1–10.
URL: <http://tubiblio.ulb.tu-darmstadt.de/72538/>
- [5] Shampine, L. F. and Reichelt, M. W. (1997). The matlab ode suite, *SIAM J. Sci. Comput.* **18**(1): pp. 1–22.
- [6] Shampine, L. F., Reichelt, M. W. and Kierzenka, J. A. (1999). Solving index-1 daes in matlab and simulink, *SIAM J. Sci. Comput.* **41**(3): pp. 538–552.
- [7] Daniel, C. (2013). *Simulation von gleit- und wälzgelagerten Systemen auf Basis eines Mehrkörpersystems für rotordynamische Anwendungen.*, PhD thesis, Otto-von-Guericke Universität Magdeburg.
- [8] Elrod, H. G. (1981). A cavitation algorithm, *Journal of Tribology* **103**(3): pp. 350–354.
- [9] Schweizer, B. (2008). ALE formulation of reynolds fluid film equation, *ZAMM* **88**(9): pp. 716–728.
- [10] Nitzschke, S., Woschke, E., Daniel, C. and Strackeljan, J. (2013). Einfluss der masseerhaltenden Kavitation auf gleitgelagerte Rotoren unter instationärer Belastung, *10. Internationale Tagung Schwingungen in rotierenden Maschinen*.
- [11] Nitzschke, S., Woschke, E., Schmicker, D. and Strackeljan, J. (2016). Regularised cavitation algorithm for use in transient rotordynamic analysis, *International Journal of Mechanical Sciences* **113**: pp. 175–183.
- [12] Nitzschke, S., Woschke, E. and Daniel, C. (2017). Dynamic behaviour of ehd-contacts using a regularised, mass conserving cavitation algorithm, *Technische Mechanik* **37**(2-5): pp. 181–195.
- [13] Nitzschke, S., Woschke, E. and Daniel, C. (2019). Application of regularised cavitation algorithm for transient analysis of rotors supported in floating ring bearings, in K. L. Cavalca and H. I. Weber (eds), *Proceedings of the 10th International Conference on Rotor Dynamics – IFToMM*, Springer International Publishing, Cham, pp. 371–387.
- [14] Woschke, E., Daniel, C. and Nitzschke, S. (2017). Excitation mechanisms of non-linear rotor systems with floating ring bearings - simulation and validation, *International Journal of Mechanical Sciences* .
- [15] Felscher, P. (2016). *Rückwirkung des Gleitlagermoments auf die Drehbewegung des Rotors*, PhD thesis, Technische Universität, Darmstadt.
URL: <http://tuprints.ulb.tu-darmstadt.de/5545/>
- [16] Vogelpohl, G. (1943). Zur Integration der Reynoldschen Gleichung für das Zapfenlager endlicher Breite, Ingenieur-Archiv, Abteilung Reibungsforschung Berlin des Kaiser Wilhelm-Institutes für Strömungsforschung, Göttingen.

Transient simulation of a rotor supported in herringbone grooved journal bearings using the narrow groove theory

Steffen Nitzschke¹, Elmar Woschke¹, Christian Daniel¹, Thorsten Sporbeck²

¹ Institute of Mechanics, Otto-von-Guericke University Magdeburg, 39106 Magdeburg, Germany,
{steffen.nitzschke}{elmar.woschke}{christian.daniel}@ovgu.de

² Siemens Healthcare GmbH, 91058 Erlangen, Germany, thorsten.sporbeck@siemens-healthineers.com

Abstract

The paper describes the application of the narrow groove theory to transient rotor dynamics. The presented approach is verified against literature. Furthermore, a comparison to a numerical solution with local discretised groove-ridge pairs is given, whereat differences in the results are discussed in the context of computational costs.

1 Introduction

A herringbone grooved journal bearing (HGJB) is a special case of journal bearing with groove-ridge pairs in the surface, which are arranged in a herringbone configuration. Additionally to the circumferential fluid transport of a plain journal bearing this configuration causes a fluid transport towards the bearings centerline. This kind of bearing is mainly used in hard disk drives and optical drives (CD, DVD) [1] and for miniature fan motors [2]. Here they are replacing ball bearings because of their long life, low noise and low friction.

In other applications, where it might be difficult to ensure an external fluid supply, another property of HGJBs is the decisive factor: If properly engineered, self-sealing behaviour can be realised, so a single initially filled fluid amount is sufficient for the whole lifetime. Such applications are e.g. the support of gyroscope flywheels in spacecraft [3] or in medical devices as support of the rotating anode inside an X-ray tube [4].

Due to the X-ray principle the anode and therefore the rotor has to be driven in a vacuum, which is one reason for the application of HGJB. The rotating anode is necessary to distribute the heat generated by the impact of the electron beam on a larger area, cf. Fig. (1). The induced heat has to be transferred through the bearings, which is why liquid metal (mixture of Indium, Gallium and Tin) is used as fluid [5].

For design purposes, the pressure distribution in the fluid film has to be known. Hence, the Reynolds partial differential equation (R-PDE) has to be solved, which is nowadays done via Finite Difference- [6, 7], Finite

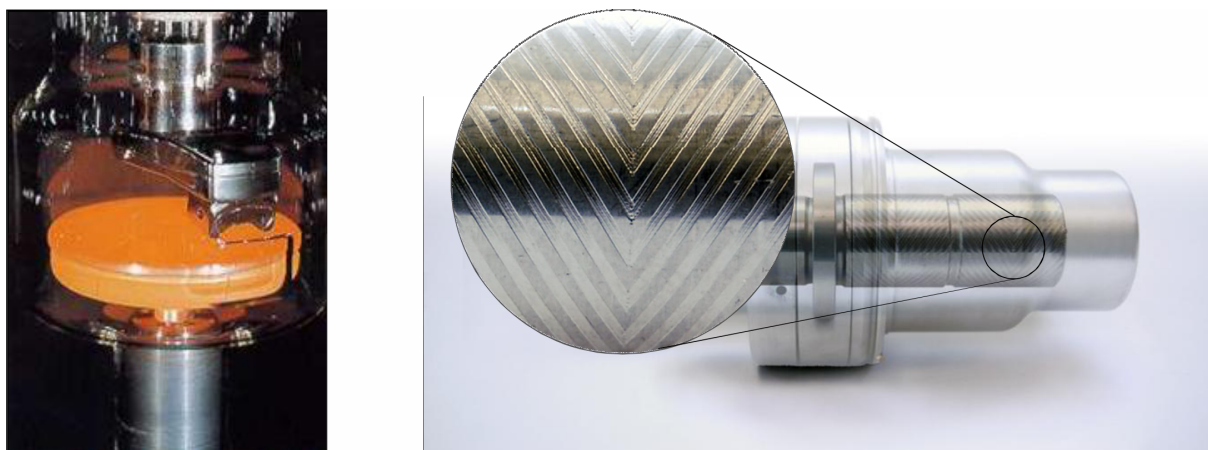


Figure 1: Temperatures in a rotating anode: 1200°C on anode base, 2000°C on burn trace and upto 2600°C on the focal spot (left). Typical HGJB profile on a rotating anode (right). [5]

Volume- [1, 8] or Finite Element Method [9–12]. In order to map the the groove-ridge pairs accurately, a fine mesh with a high number of unknowns is necessary. While the resulting computational effort is acceptable under steady state conditions, it is not under transient conditions within a rotor dynamic research. In this case, a numerical time integration in combination with an online solution of R-PDE leads to very high computational time.

At this point, a review of papers from the early days of HGJB-computations is helpful: Since the computational power was low at that time, the narrow groove theory (NGT) was developed, which enables a possibility to calculate a mean pressure over a groove-ridge pair if a sufficient number of such pairs exist [13–15]. Therefore, the R-PDE can be reformulated in terms of the smoothed pressure, which afterwards has also to be solved numerically, but on a considerable coarser mesh. Hence, bearing forces needed for the rotor dynamics can be calculated much faster, resulting in a reduction of the overall effort.

In case of bearings driven with fluids instead of gas, the question of cavitation effects arises. For this sake, Jang and Chang [1] as well as Lee et al. [6] used Elrod's cavitation algorithm [16] in combination with local discretised groove-ridge pairs.

They found, that the influence of cavitation on the load capacity is lower compared to plain journal bearings because it starts at high eccentricity values. Nevertheless, a handling of cavitation is necessary, since the effect of side leakage has to be mapped.

As the NGT was developed, Elrod's cavitation algorithm was not yet invented. Instead, researchers at that time tried to map the so called side effect by modifying the gap geometrically in order to influence the pressure there [17, 18] or by adapting the film width numerically in order to satisfy the mass conservation [15].

In the present paper the NGT is used and will be combined with a modern form of Elrod's cavitation algorithm, which was proposed by the authors [19–22]. The resulting algorithm is then applied to a transient rotor dynamic or multi body simulation, as described in [23], whereat the bearing forces are calculated via an online approach.

2 Reynolds Equation for Narrow Groove Theory

The Reynolds PDE assuming the NGT is given by Bootsma [15] for radial, axial and combined bearings as

$$\begin{aligned} & \frac{1}{r} \frac{\partial}{\partial \Theta} \left(\rho \left(-\frac{(\Delta R)^3}{12\eta} \left(\frac{A}{r} \frac{\partial p_0}{\partial \Theta} + B \frac{\partial p_0}{\partial s} \right) + \frac{1}{2}(\omega_p - \omega_g)r\Delta R F' \right) \right) \\ & + \frac{1}{r} \frac{\partial}{\partial s} \left(\rho r \left(-\frac{(\Delta R)^3}{12\eta} \left(\frac{B}{r} \frac{\partial p_0}{\partial \Theta} + C \frac{\partial p_0}{\partial s} \right) + \frac{1}{2}(\omega_p - \omega_g)r\Delta R G' \right) \right) \\ & + \Delta R \frac{\partial}{\partial t}(\rho I_1) = 0 \quad , \end{aligned} \quad (1)$$

wherein p_0 denotes the pressure averaged over a groove-ridge pair

$$p_0 = \lim_{\bar{b} \rightarrow 0} \frac{1}{\bar{b}} \int_{-\bar{b}/2}^{+\bar{b}/2} p \, d\zeta \quad \text{with} \quad b = b_r + b_g. \quad (2)$$

The rotational speeds of the plain and the grooved surface are named ω_p and ω_g respectively. For further use, the relations

$$\bar{\omega}_p = \omega_p/\omega \quad , \quad \bar{\omega}_g = \omega_g/\omega \quad \text{and} \quad \omega = |\omega_p - \omega_g| \quad (3)$$

are introduced. Restriction to radial bearings ($r = \text{const}$) and transformation of Eq. (1) to the inertial frame, ($\Theta \rightarrow \varphi$) according to [24], yields

$$\begin{aligned} & \frac{\partial}{\partial \varphi} \left(\rho \frac{(\Delta R)^3}{12\eta} \left(\frac{A}{r} \frac{\partial p}{\partial \varphi} + B \frac{\partial p}{\partial s} \right) - \frac{1}{2} \rho \omega r \Delta R F \right) + \\ & r \frac{\partial}{\partial s} \left(\rho \frac{(\Delta R)^3}{12\eta} \left(\frac{B}{r} \frac{\partial p}{\partial \varphi} + C \frac{\partial p}{\partial s} \right) - \frac{1}{2} \rho \omega r \Delta R G \right) = r \frac{\partial(\rho h_r)}{\partial t} \quad . \end{aligned} \quad (4)$$

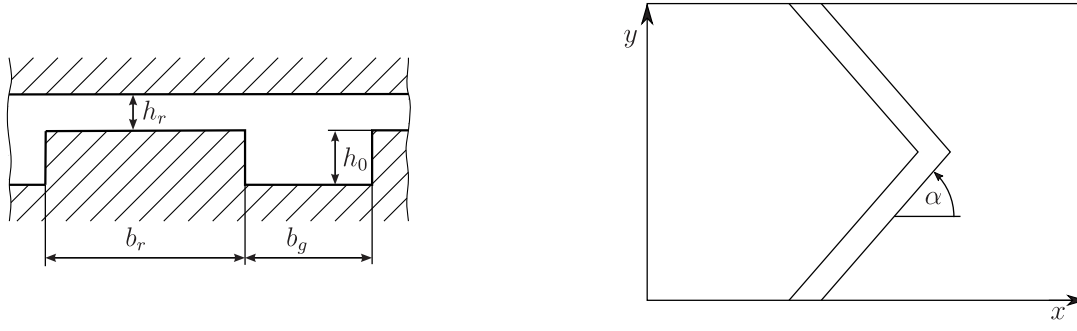


Figure 2: Geometry of herringbone profile: Definition of groove-ridge pair (left) and orientation angle (right) [24].

Due to the averaging process of Eq. (2), some mainly geometrical quantities are introduced

$$\begin{aligned}
 A &= \sin^2(\alpha) \frac{1}{I_{-3}} + \cos^2(\alpha) I_3 & G' &= \sin(\alpha) \cos(\alpha) \left(I_1 - \frac{I_{-2}}{I_{-3}} \right) \\
 B &= \sin(\alpha) \cos(\alpha) \left(I_3 - \frac{1}{I_{-3}} \right) & F &= (\bar{\omega}_p - \bar{\omega}_g) F' + 2\bar{\omega}_g I_1 \\
 C &= \cos^2(\alpha) \frac{1}{I_{-3}} + \sin^2(\alpha) I_3 & G &= (\bar{\omega}_p - \bar{\omega}_g) G' \\
 F' &= \sin^2(\alpha) \frac{I_{-2}}{I_{-3}} + \cos^2(\alpha) I_1 & & ,
 \end{aligned}$$

which are on the one hand determined by the orientation angle α between the groove-ridge pattern and the direction of rotation and on the other hand by the function I_j , which reads for a rectangular groove cross section according to Fig. (2)

$$I_j = \frac{\gamma h_r^j + (h_o + h_r)^j}{(\Delta R)^j (1 + \gamma)} \quad \text{with} \quad \gamma = \frac{b_r}{b_g} . \quad (5)$$

3 Application of regularised Elrod cavitation algorithm

Assuming incompressibility would lead to tensile stresses inside the fluid in regions, where the fluidfilm height increases w.r.t. the direction of rotation. In practice, gas enters the gap from the axial boundaries or is dissolved from the fluid, which yields a mixture of gas and fluid. In the bearings context this behaviour is known as cavitation. Based on the ideas of Elrod [16], Kumar and Booker [25] introduced the film fraction ϑ in order to describe density ρ and viscosity η of the mixture

$$\rho = \vartheta \rho_{liq} + (1 - \vartheta) \rho_{gas} \approx \vartheta \rho_{liq} \quad \text{and} \quad \eta = \vartheta \eta_{liq} + (1 - \vartheta) \eta_{gas} \approx \vartheta \eta_{liq} . \quad (6)$$

Introducing Eq. (6) into R-PDE, Eq. (4), reads

$$\begin{aligned}
 & \frac{\partial}{\partial \varphi} \left(\frac{(\Delta R)^3}{12\eta_{liq}} \left(\frac{A}{r} \frac{\partial p}{\partial \varphi} + B \frac{\partial p}{\partial s} \right) - \frac{1}{2} \vartheta \omega r \Delta R F \right) + \\
 & r \frac{\partial}{\partial s} \left(\frac{(\Delta R)^3}{12\eta_{liq}} \left(\frac{B}{r} \frac{\partial p}{\partial \varphi} + C \frac{\partial p}{\partial s} \right) - \frac{1}{2} \vartheta \omega r \Delta R G \right) = r \frac{\partial(\vartheta h_r)}{\partial t}
 \end{aligned} \quad (7)$$

with the complementary unknowns p and ϑ : In regions where $p > p_{cav}$, the film fraction is known $\vartheta \stackrel{!}{=} 1$; otherwise $p \stackrel{!}{=} p_{cav}$ holds and the film fraction varies $0 < \vartheta < 1$. At this point it is convenient to introduce dimensionless

quantities

$$H = \frac{h_r}{\Delta R}, \quad X = \frac{r \varphi}{r}, \quad Y = \frac{s}{r}, \quad \bar{\eta} = \frac{\eta_{liq}}{\eta^*}, \quad \omega_m = \frac{\omega_{shaft} + \omega_{shell}}{2}, \quad P = \frac{p (\Delta r)^2}{\eta^* \omega_m r^2}, \quad T = t \omega_m, \quad \bar{\omega} = \frac{\omega}{\omega_m} \quad (8)$$

and, following Shi and Paranjpe [26], a universal unknown Π as well as a switch function g in the way that

$$\Pi(X, Y) \stackrel{!}{=} \begin{cases} \vartheta(X, Y) - 1 & (X, Y) \in \Omega_\theta \\ P(X, Y) & (X, Y) \in \Omega_p \end{cases} \iff \begin{cases} \vartheta(X, Y) = (1-g)(\Pi(X, Y)+1) + g \\ P(X, Y) = g \Pi(X, Y) \end{cases} \quad (9)$$

Inserting Eq. (8) and Eq. (9) into Eq. (7) and reordering w.r.t. terms of the switch function g yields the final R-PDE under the conditions of the NGT and considering cavitation effects

$$\underbrace{\left[\frac{\partial}{\partial X} \left(\frac{1}{12\bar{\eta}} \left(A \frac{\partial(g\Pi)}{\partial X} + B \frac{\partial(g\Pi)}{\partial Y} \right) \right) + \frac{\partial}{\partial Y} \left(\frac{1}{12\bar{\eta}} \left(B \frac{\partial(g\Pi)}{\partial X} + C \frac{\partial(g\Pi)}{\partial Y} \right) \right) - \frac{\bar{\omega}}{2} \left(\frac{\partial F}{\partial X} + \frac{\partial G}{\partial Y} \right) - \frac{\partial H}{\partial T} \right]}_{\text{pressure region}} + \underbrace{\left[\frac{\bar{\omega}}{2} \left(\frac{\partial((g-1)\Pi F)}{\partial X} + \frac{\partial((g-1)\Pi G)}{\partial Y} \right) + \frac{\partial((g-1)\Pi H)}{\partial T} \right]}_{\text{cavitation region}} = 0 \quad (10)$$

Depending on the design of the axial boundary, certain boundary conditions can be assumed. Either ambient pressure Π_{amb} holds or the boundary is sealed

$$\Pi = \Pi_{amb} \quad \text{or} \quad \frac{\partial \Pi}{\partial Y} = 0 \quad (11)$$

Eq. (10) and Eq. (11) build an initial boundary value problem with elliptical character. Due to the partial derivatives, an analytical solution is not known. Hence, a solution has to be obtained via a numerical method. Here, the Finite Volume Method according to Patankar [27] is used to derive a system of equations. For this sake, the fluid film is discretized with a 2-D mesh in circumferential and axial direction with a number of volumes n . Due to the mixed derivatives, a nine-point stencil results from the discretisation procedure. In the pressure region central differences are suitable while in the cavitation region upwinding is necessary, which leads to backward differences there. Finally, the nonlinear system of equations

$$\underline{A}(g) \underline{p} = \underline{r}(g) \quad \text{with} \quad \underline{p} = \Pi_1 \dots \Pi_n \quad (12)$$

results, wherein the asymmetric system matrix \underline{A} shows a sparsity pattern with eight secondary diagonals.

The nonlinearity results from the switch function g , which is usually chosen to be the Heaviside function, what induces some drawbacks. This choice necessarily leads to the application of fix point iteration and in some load cases causes oscillatory solutions with, if at all, a poor convergence rate. The root cause is the discontinuity between the two regions and the necessity, that the border between them is bounded to the numerical grid.

In a transient simulation in rotor dynamics or multi body dynamics, where a lot of online solution steps of R-PDE are necessary, the convergence must be guaranteed, even on a somewhat coarse mesh. Hence, the authors have developed a regularised algorithm, with a smooth switch function

$$g(\Pi) = \frac{1}{\pi} \arctan \left(\frac{\Pi}{1 - \Pi^*} \right) + \frac{1}{2} \quad (13)$$

This enables a finite volume to be a part of both regions at the same time – the mentioned border is no longer bounded to the grid. This ensures the existence of the solution and allows for the application of a Newton-Raphson

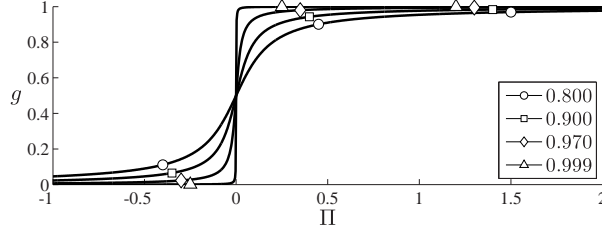


Figure 3: Switch function of sigmoid type according to Eq. (13) for different values of parameter Π^* . For $\Pi^* \rightarrow 1$ a transition to Heaviside function takes place.

scheme, leading to a much higher convergence rate [19–22]. Therefore, Eq. (12) has to be interpreted as a function of Π or \underline{p} , respectively

$$\underline{f}(\underline{p}) \mapsto \underline{r}(\underline{p}) - \underline{A}(\underline{p}) \underline{p} = 0 \quad . \quad (14)$$

The Newton-Raphson scheme, starting from an initial guess $\underline{p}^{(0)}$, yields the increment

$$\underline{p}^{(i+1)} = \underline{p}^{(i)} - \underline{J}(\underline{p}^{(i)})^{-1} \underline{f}(\underline{p}^{(i)}) \quad (15)$$

with the Jacobian

$$\underline{J}(\underline{p}^{(i)}) = \left. \frac{\partial \underline{f}}{\partial \underline{p}} \right|_{\underline{p}^{(i)}} = \left. \frac{\partial \underline{r}}{\partial \underline{p}} \right|_{\underline{p}^{(i)}} - \left(\underline{A}(\underline{p}^{(i)}) + \left. \frac{\partial \underline{A}}{\partial \underline{p}} \right|_{\underline{p}^{(i)}} \underline{p}^{(i)} \right), \quad (16)$$

whereat the derivatives can be expressed analytically.

4 Validation and numerical studies

Neglecting the derivative w.r.t. time in Eq. (10), a stationary problem remains. Under this assumption, the described method is compared to results from Bootsma [15], which were achieved with the Finite Difference Method. The relevant bearing parameters are listed in Tab. (1). The dimensionless load capacity

$$\bar{W} = \frac{W (\Delta R)^2}{\eta \omega R^4} \quad (17)$$

is plotted against increasing values of the bearings relative eccentricity ε for two different values of groove depth h_0 in Fig. (4). As can be expected, with increasing groove depth, the load capacity is decreasing. However, the agreement between both methods is very good for moderate eccentricities $\varepsilon = 0 \dots 0.6$, but for higher values some differences occur, which are acceptably small and may occur due to different cavitation handling.

Table 1: Bootsma FDM

parameter	value set 1	value set 2	unit
B/D	1	1	[–]
α	33	33	[°]
ω_g	0	0	[rad/s]
ω_p	ω	ω	[rad/s]
γ	1	1	[–]
$h_0/\Delta R$	1.0	3.0	[–]

Table 2: Bootsma measurement

parameter	value set 1	value set 2	unit
B/D	2	2	[–]
α	14.2	14.2	[°]
ω_g	0	ω	[rad/s]
ω_p	ω	0	[rad/s]
γ	1	1	[–]
$h_0/\Delta R$	5.0	5.0	[–]

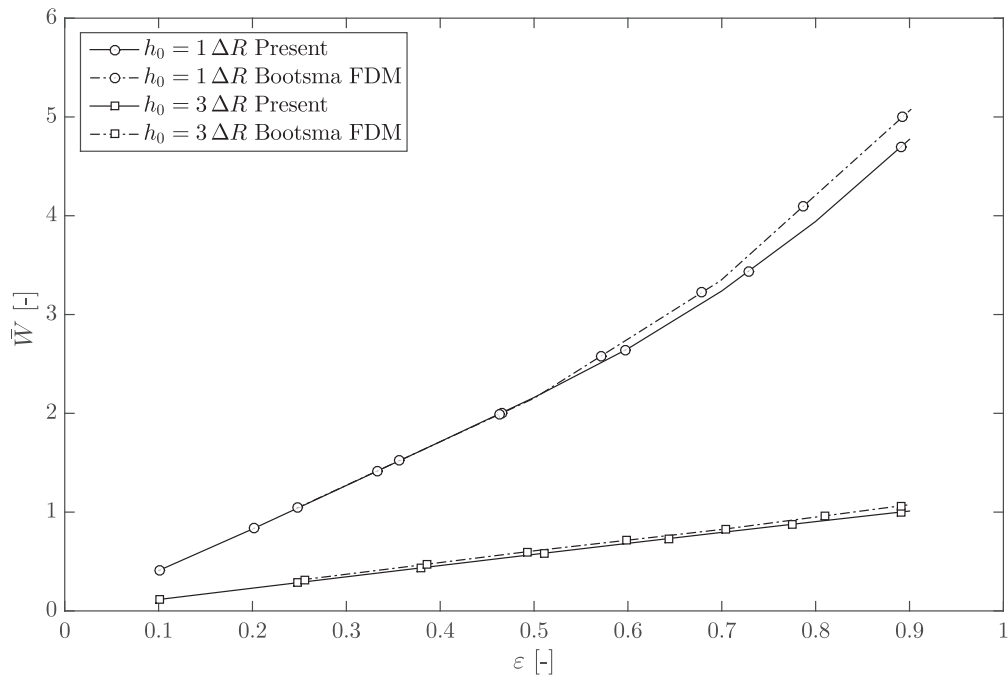


Figure 4: Dimensionless load capacity \bar{W} vs. eccentricity ε for different values of groove depth h_0 .

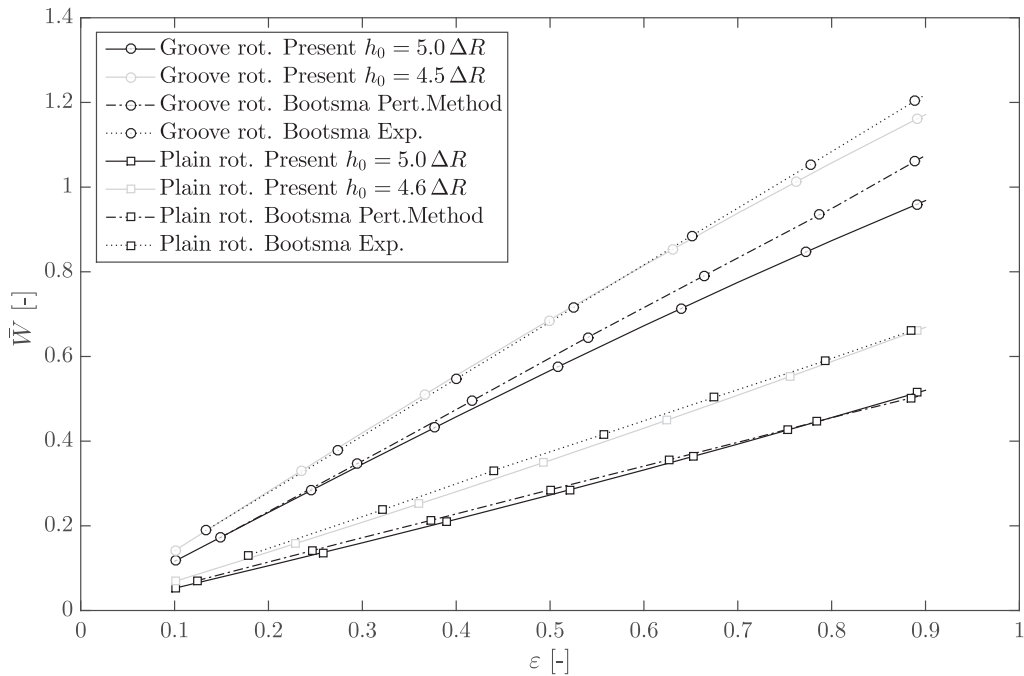


Figure 5: Dimensionless load capacity \bar{W} vs. eccentricity ε . Comparison to measurements, where either the grooved part or the plain part rotates. For the present model, a grid of 90x60 with 5220 unknowns was used.

Another configuration, taken also from Bootsma [15], allows the comparison to experimental obtained data. Here, a comparatively large groove depth was chosen, cf. Tab. (2), because in this case differences in the load capacity occur depending on whether the plain member or the grooved member rotates.

For the sake of comparability, simulation results from the reference were also plotted, which in this case are obtained by a perturbation method based on the NGT. Again the simulation results show a good accordance, but the difference to the measurement results are quite large. When comparing to measurements, the production accuracy and error of measurements should be considered. Unfortunately, in the reference no information concerning this matter is present. Nevertheless, the influences of orientation angle α and groove depth h_0 were investigated. Whereas the orientation angle has a minor influence on the load capacity, the groove depth shows a major one. Diminishing the groove depth by $\approx 10\%$ yields a much better congruence of simulation and measurements, cf. Fig. (5).

Before the method is used in further analyses, the convergence properties should be investigated. Hence, the numerical grid was refined successive and the change in load capacity was observed w.r.t. a quasi exact solution obtained with 30000 unknowns. As mentioned earlier, the HGJB behaviour differs related to the part, which is rotating – the grooved or the plain one. Therefore, the convergence study was performed for both cases, cf. Fig. (6).

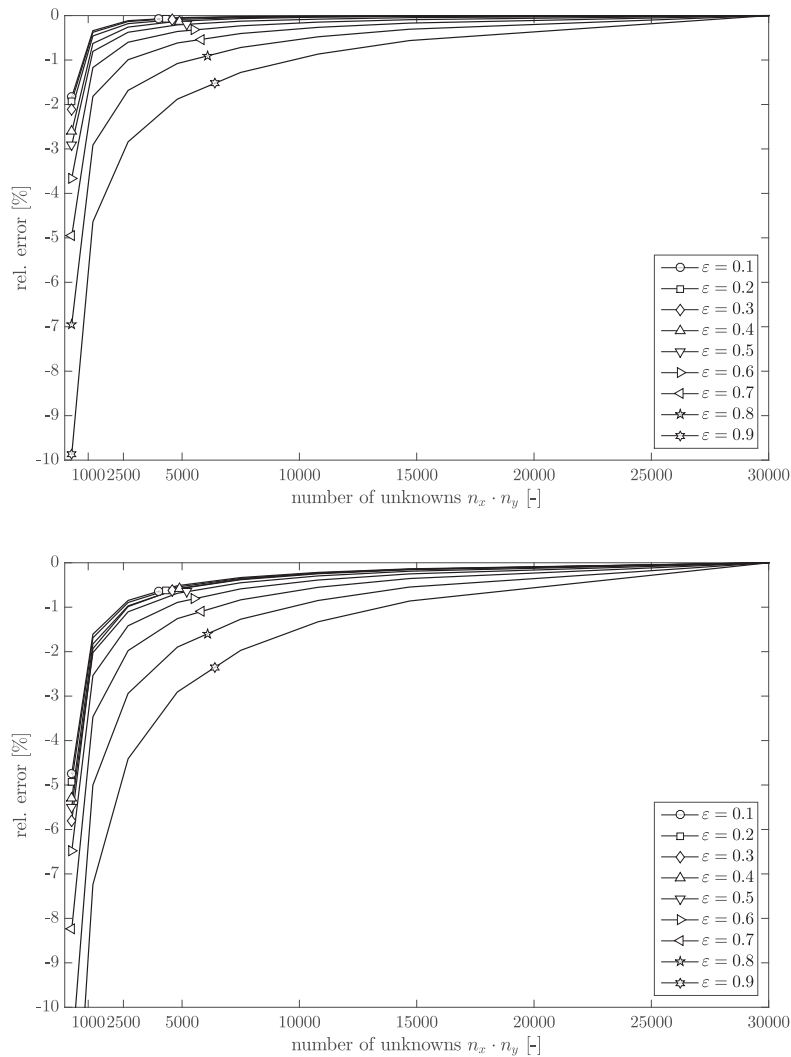


Figure 6: Relative error $e_{\text{rel}} = \frac{\bar{W}_{n_x n_y} - \bar{W}_{\text{quasiexact}}}{\bar{W}_{n_x n_y}}$ for different grids ($n_x \cdot n_y$) and different values of bearing eccentricity ε . Grooved member rotates (top), plain member rotates (bottom). Bearing parameters according to Tab. (1) with $H_0/\Delta R = 1$.

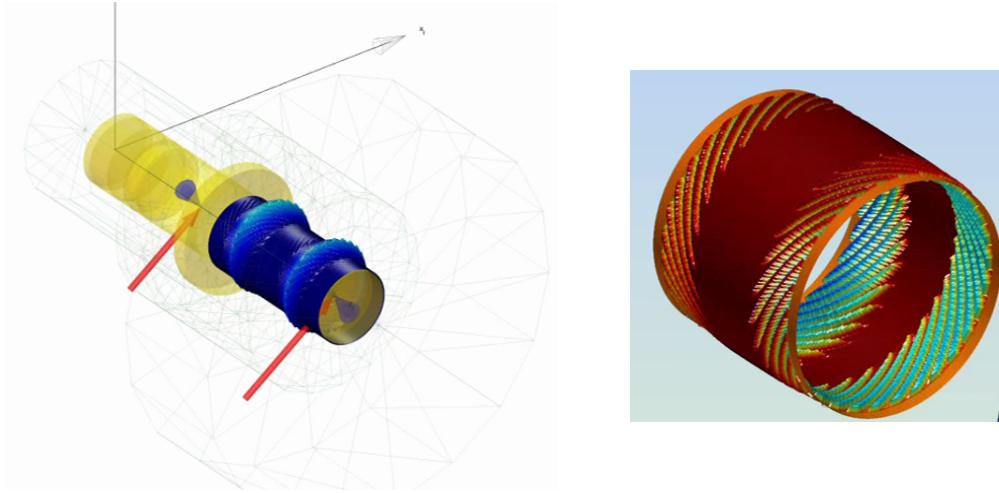


Figure 7: MBS/rotor dynamic model of rotating anode inside a X-ray device with pressure distribution due to herringbone bearings and forces caused by unbalance distribution (left). Film content of HGJB with partial initial filling (right).

Additionally, the bearing eccentricity was varied between a weak load state $\varepsilon = 0.1$ and a heavy load state $\varepsilon = 0.9$. For use in rotor dynamics, it should be convenient, if the relative error concerning the bearing force is about 1%. Assuming moderate load states this is the case if approximately 2500 unknowns are used, whereas the failure is slightly higher when the plain member rotates.

5 Comparison of NGT-algorithm with conventional R-PDE within rotor dynamics

In order to demonstrate the possibilities of the developed NGT algorithm, the differences compared to a solution, which uses online R-PDE with local discretisation of the herringbone grooves, are studied. Therefore, the bearings are discretised with a relatively fine rectangular mesh of 395×120 finite volumes, which causes high computational effort. On the contrary, using the NGT, a mesh of 60×22 is sufficient. The model consists of a cantilever shaft, which holds the herringbone profile for the two bearings and the rotor, which is designed as outside runner, cf. Fig. (7). The remaining model parameters are given in Tab. (3).

The computed rotor orbits of both methods are compared in Fig. (8). It can be seen that the NGT orbit is somewhat smaller and its midpoint is closer to the bearing center, which both induces a higher stiffness. In this context it should be mentioned that the conventional R-PDE method on a rectangular mesh has a limited capability to map the herringbone grooves with the orientation angle α accurately. A further refinement of the mesh shows a trend towards smaller orbits.

Additionally, the pressure distribution for a given time is compared in Fig. (9) between both methods. The global form and also locus as well as value of maximum pressure coincide very well, while the size of the cavitation region (white areas) differs. Due to the averaging character of the NGT the film content has to be interpreted as a mean value over the grooved area. Hence, the NGT solution yields a smaller cavitation area.

However, on the same machine (a I7-7820X desktop PC, using a single core), the conventional R-PDE method requires ≈ 3.7 hours, while the NGT method needs only ≈ 100 seconds which underlines the effectiveness of the described algorithm.

Table 3: Parameters of rotor and bearings for comparison between NGT and conventional R-PDE.

Parameter	Value	Unit	Parameter	Value	Unit	Parameter	Value	Unit
B	0,026	[m]	$r_{\text{unbalance}}$	0.0001	[m]	$\Delta R/R$	0.001	[-]
D	0,024	[m]	ω	500	[rad/s]	$h_0/\Delta R$	1.166	[-]
m_{rotor}	5	[kg]	g_y	-9,81	[m/s ²]	η	0,0015	[Pa s]

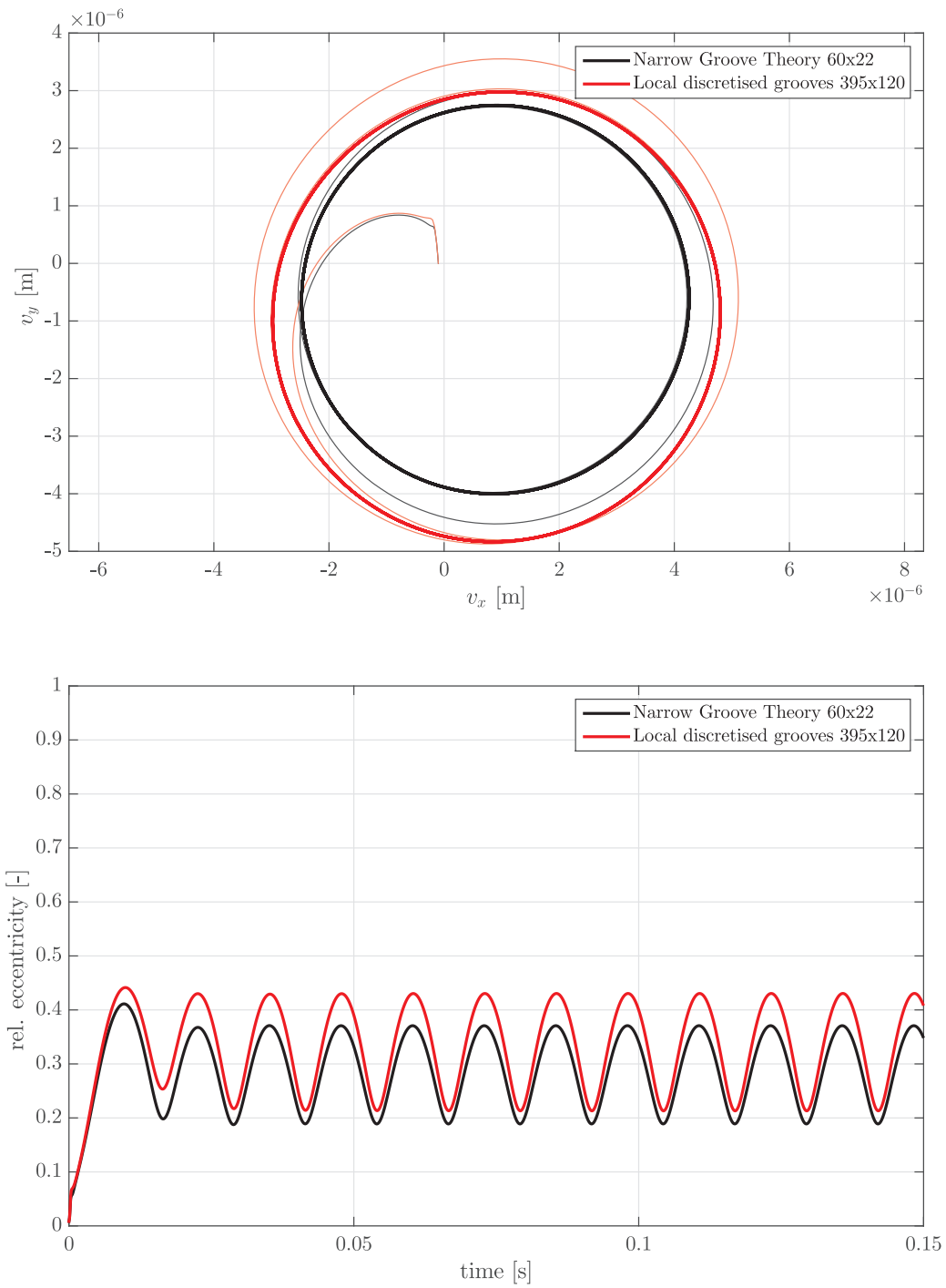


Figure 8: Comparison of rotor orbit (top) and relative eccentricity (bottom) between conventional R-PDE method with local discretised grooves and NGT based method.

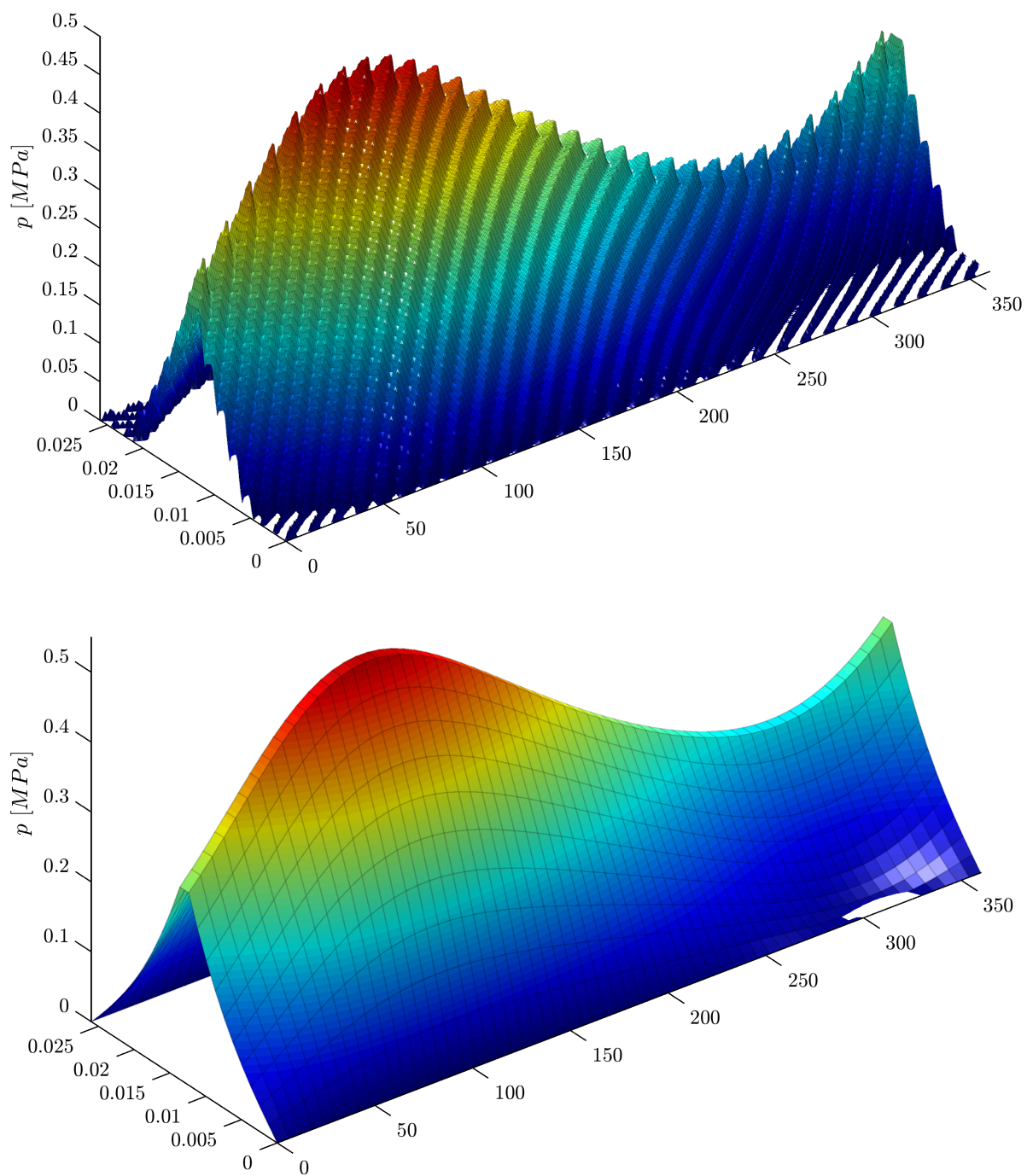


Figure 9: Comparison of pressure distribution between conventional R-PDE method with local discretised grooves (top) and NGT based method (bottom). White areas indicate the occurrence of cavitation.

6 Conclusion

The application of the NGT for herringbone grooved journal bearings within the transient rotor dynamic simulation was shown. In order to take cavitation effects into account, the NGT was combined with a regularised variant of the Elrod algorithm, which ensures both, numerical stability and low computational costs. The described algorithm was verified and validated against measurements and calculations present in the literature, which showed good congruence. Finally, the method was compared to a conventional R-PDE with local mapping of the herringbone profile.

Acknowledgment

The results were partially generated in the framework of the project WO 2085/2 „Numerische Analyse des transienten Verhaltens dynamisch belasteter Rotorsysteme in Gleit- und Schwimmbuchsenlagern unter Berücksichtigung kavitativer Effekte“, which is supported by the DFG (Deutsche Forschungsgemeinschaft / German Research Foundation). This support is gratefully acknowledged.

REFERENCES

- [1] Jang, G. H. and Chang, D. I. (2000). Analysis of a hydrodynamic herringbone grooved journal bearings considering cavitation, *Journal of Tribology* **122**: pp. 103–109.
- [2] Chen, C.-Y., Liu, C.-S. and Li, Y.-C. (2015). Design and characterization of miniature fluid dynamic bearing using novel multi-step elliptical grooves, *Microsystem Technologies* **21**(1): pp. 91.
- [3] Muijderman, E. A. (1993). Fettgeschmierte Spiralrillenlager - neue hydrodynamische Gleitlager, in W. J. Bartz (ed.), *Selbstschmierende und wartungsfreie Gleitlager*, Expert Verlag, Ehningen bei Böblingen, pp. 86–133.
- [4] Dössel, O. (2016). *Bildgebende Verfahren in der Medizin - Von der Technik zur medizinischen Anwendung*, Springer Vieweg, Berlin, Heidelberg.
- [5] Schörner, K., Stephan, J. and Watzl, C. (2014). Schnelle CT mit medizinischer high-power Röntgenröhre, *Vortrag zur DGZfP-Jahrestagung*, Siemens AG München.
- [6] Lee, T. S., Liu, Y. G. and Winoto, S. H. (2004). Analysis of liquid-lubricated herringbone grooved journal bearings, *International Journal of Numerical Methods for Heat & Fluid Flow* **14**(3): pp. 341–365.
- [7] Chao, P. and Huang, J. (2005). Calculating rotordynamic coefficients of a ferrofluid-lubricated and herringbone-grooved journal bearing via finite difference analysis, *Tribology Letters* **19**(2): pp. 99.
- [8] Kobayashi, T. (1999). Numerical analysis of herringbone-grooved gas-lubricated journal bearings using a multigrid technique, *Journal of Tribology* **121**: pp. 148–156.
- [9] Bonneau, D. and Absi, J. (1994). Analysis of aerodynamic journal bearings with small number of herringbone grooves by finite element method, *Journal of Tribology* **116**: pp. 698–704.
- [10] Zirkelback, N. and San Andrés, L. (1998). Finiten element analysis of herringbone grooved journal bearings: A parametric study, *Journal of Tribology* **120**: pp. 234–240.
- [11] Park, S.-W. and Rhim, Y.-C. (2001). A study on the air-lubricated herringbone grooved journal bearing by finite element method, *KSTLE International Journal* **2**: pp. 46–54.
- [12] Jang, G. H. and Yoon, J. W. (2002). Nonlinear dynamic analysis of hydrodynamic journal bearings considering the effect of a rotation or stationary herringbone groove, *Journal of Tribology* **124**: pp. 297–304.
- [13] Hirs, G. G. (1965). The load capacity and stability characteristics of hydrodynamic grooved journal bearings, *ASLE Transactions* **8**: pp. 396–305.
- [14] Vohr, J. H. and Chow, C. Y. (1965). Characteristics of herringbone-grooved gas-lubricated journal bearings, *ASME Journal of Basic Engineering* **87**(3): pp. 568–578.
- [15] Bootsma, J. (1975). *Liquid-Lubricated Spiral-Groove Bearings*, PhD thesis, Technische Hogeschool Delft.
- [16] Elrod, H. G. (1981). A cavitation algorithm, *Journal of Tribology* **103**(3): pp. 350–354.
- [17] Muijderman, E. (1964). *Spiral Groove Bearings*, PhD thesis, TU Delft.
- [18] Elrod, H. G. (1973). Some refinements on the theory of the viscous screw pump., *Journal of Lubrication Technology* **95**(1): pp. 82–93.
- [19] Nitzschke, S., Woschke, E., Schmicker, D. and Strackeljan, J. (2016). Regularised cavitation algorithm for use in transient rotordynamic analysis, *International Journal of Mechanical Sciences* **113**: pp. 175–183.
- [20] Nitzschke, S. (2016). *Instationäres Verhalten schwimmbuchsenlagerter Rotoren unter Berücksichtigung masseerhaltender Kavitation*, PhD thesis, Otto-von-Guericke Universität Magdeburg.
- [21] Nitzschke, S., Woschke, E. and Daniel, C. (2017). Dynamic behaviour of ehd-contacts using a regularised, mass conserving cavitation algorithm, *Technische Mechanik* **37**(2-5): pp. 181–195.

- [22] Nitzschke, S., Woschke, E. and Daniel, C. (2019). Application of regularised cavitation algorithm for transient analysis of rotors supported in floating ring bearings, in K. L. Cavalca and H. I. Weber (eds), *Proceedings of the 10th International Conference on Rotor Dynamics – IFToMM*, Springer International Publishing, Cham, pp. 371–387.
- [23] Woschke, E., Daniel, C. and Nitzschke, S. (2017). Excitation mechanisms of non-linear rotor systems with floating ring bearings - simulation and validation, *International Journal of Mechanical Sciences* .
- [24] Röber, M. (2017). *Dynamische Analyse von Fischgrätenlagern*, Master's thesis, Otto-von-Guericke Universität Magdeburg.
- [25] Kumar, A. and Booker, J. F. (1991). A finite element cavitation algorithm, *Journal of Tribology* **113**(2): pp. 279–284.
- [26] Shi, F. and Paranjpe, R. (2002). An implicit finite element cavitation algorithm, *Computer modeling in engineering and sciences* **3**(4): pp. 507–516.
- [27] Patankar, S. (1980). *Numerical heat transfer and fluid flow*, Hemisphere Publishing Corp.

Transient thermo-hydrodynamic analysis of a laval rotor supported by journal bearings with respect to calculation times

Cornelius Irmischer¹, Steffen Nitzschke¹, Elmar Woschke¹

¹ Institute of Mechanics, Otto-von-Guericke University Magdeburg, 39106 Magdeburg, Germany,
{cornelius.irmscher} {steffen.nitzschke} {elmar.woschke}@ovgu.de

Abstract

The work at hand presents simulation results for the motion of a laval rotor supported by hydrodynamic journal bearings with a detailed model to represent the instationary thermo-hydrodynamic behaviour of the system. This model incorporates a transient solution of the full three-dimensional energy equation in the lubricating films as well as transient solutions of the heat conduction equations for the bushing and the shaft. The comparison of the simulation results with measurement data clearly shows, that the comprehensive temperature algorithm yields better results than isoviscous approaches. However, the calculation times are significantly longer. Therefore, different strategies are tested in the second part of this paper to accelerate the calculations. The combination of suitable strategies enables to limit the increase of computational time to 30 %.

1 Introduction and motivation

Hydrodynamic bearings are commonly used to support high speed rotors because of their low production costs and wearlessness, as long as the surfaces of rotor and bearing are fully separated. On the downside, these bearings are characterised by non-linear stiffness and damping matrices, which are unsymmetric and lead to self-induced vibrations known as oil-whirl and oil-whip, cf. [20]. Moreover, the bearing behaviour is determined by cavitation phenomena, where a rupture in the oil-film takes place, and thermal effects, which can result from frictional heat in the lubricating film or thermal boundary conditions. Thermal effects can lead to a distinct alteration of the lubricant properties, especially the viscosity. All these influences cause an extremely non-linear behaviour of hydrodynamic bearings.

Nevertheless, precise and robust simulation algorithms are needed to predict the behaviour of high-speed rotor systems such as exhaust turbochargers reliably. This does not only help to ensure safe operation in the long-term, but also to exploit existing potentials for optimisation, e.g. regarding efficiency (smaller gaps in gas-carrying structures) and noise reduction (lower vibrations).

The modelling approach used in this paper is based on a time integration of the equation of motion of the (flexible) rotor with non-linear force elements which solve the Reynolds partial differential equation (Reynolds PDE) to account for the hydrodynamic bearings. It has been presented in various publications (see section 2) and is enhanced by a temperature algorithm in this paper (see section 3). The calculation results of the isothermal as well as the enhanced, non-isothermal models are compared to measurement results by Eling for a laval rotor in plain journal bearings presented in [8].

The first goal of this paper is to show that non-isothermal calculations yield more realistic results than isothermal calculations (see section 4). Due to the increased modelling depth, there is a significant increase in calculation times. Therefore, the second goal of the paper is to explore different approaches to reduce the numerical effort for the thermo-hydrodynamic model without reducing the quality of the results (see section 5).

2 Simulation methods and state of research on thermally extended rotordynamics

2.1 Simulation approaches

Various approaches have been used to model rotor systems supported by hydrodynamic bearings, starting with linearised stiffness- and damping coefficients around single operating points [17]. These linearised coefficients are not suitable for the description of non-linear lubricating-film-induced vibrations, but can provide a reasonable

approximation of the resonance frequencies of a bearing-rotor-system if the elastic properties of the rotor are taken into account for the analysis [9].

It is possible to calculate stiffness and damping coefficients for a multitude of rotor positions and store them in a lookup-table for subsequent use in rotordynamic analyses such as the simulation of a rotor run-up, which is also known as mobility method [4] or impedance method [5]. Therein, interpolations are carried out to account for intermediate shaft positions. This lookup-table-approach has been used commonly, for instance in [19, 13, 18, 32, 11]. However, the numerical effort increases substantially if additional effects are to be modelled. These effects include rotor deflection, which causes a resulting torque on the rotor and has a major influence on the minimal fluid film gap [7], cavitation phenomena, thermal influences or additional lubricating films. The latter appear in floating ring bearings, where a (non-)rotating ring is positioned between shaft and bushing. If more effects are incorporated, the lookup-table approach loses its advantage in performance compared to a transient approach.

Therefore, a third approach utilises a solution of the equation of motion of the (flexible) rotor in the time domain while taking the non-linear bearing forces into consideration by an online-solution of the Reynolds PDE in every time step. With this method, retroactions of the hydrodynamic forces on the kinematic state of the rotor are fully represented. Such an approach has been described in [21, 34, 2, 37, 26] for instance and is enhanced by a detailed thermal model in the publication at hand.

2.2 Thermally extended rotordynamics

The long history of thermo-hydrodynamic modelling of journal bearings is thoroughly reviewed in [15, 16, 10]. In older publications, thermal considerations are usually restricted to stationary solutions, whereas thermally extended rotordynamics require instationary approaches to account for frictional heat and the comparatively slow (not instantaneous) warming of the surrounding parts of the lubricating film. A number of lumped thermal models have been proposed to account for temperature changes in the lubricating films during rotor run-up, for instance in [6] and [31]. Keogh and Morton presented one of the first non-steady-state approaches to model the thermo-hydrodynamic behaviour of a journal bearing in the context of rotordynamics [14]. The analysis was restricted to stationary forward and backward synchronous orbits. Paranjpe and Han [28] presented a more general approach including solutions of the generalized Reynolds PDE and the full three-dimensional energy equation for unsteady load. They showed that the temperature in the lubricating film will react to changes of the load almost instantaneously and considered different time scales for the different bearing parts leading to a quasi-steady state formulation for the journal and the bushing. Therefore, the lubricating film was not directly coupled to the surrounding parts. There are many works, which include stationary solutions of the (full) energy equation, but not a single publication is known to the authors, where all describing equations are solved in their full form for general non-steady-state conditions to investigate the thermo-hydrodynamic performance of journal bearings for rotors. The dissertation of Eling [8] and preliminary works [1, 9] describe the most sophisticated model known, which is based on a time integration and contains transient, online solutions of the Reynolds PDE including shaft tilting and a mass-conserving cavitation model developed by Alakhransing [1]. Furthermore, the model uses online solutions of a 2D-formulation of the energy equation with constant temperature over the gap height and incorporates these into a lumped thermal network model to account for temperature changes of the shaft and the bushing. This lumped thermal network model was parametrised using conjugate heat transfer models and the approach was used to conduct rotordynamic analyses, however with quite long calculation times.

Therefore, a fully transient approach including a solution of the three-dimensional energy equation in the fluid film and heat equations for shaft and bushing is unknown to the authors and will be presented here with regard to calculation times.

3 Theory

As mentioned above, the core of the simulation is the transient solution of the equations of motion with a numerical time integration scheme like [30, 33] or similar. The equation of motion can be derived using either multi body dynamics, structure dynamics or rotor dynamics depending on the kind of application. Here the latter was chosen, leading to

$$\underline{\underline{M}} \cdot \ddot{\underline{x}} + (\underline{\underline{D}} + \Omega \underline{\underline{G}}) \cdot \dot{\underline{x}} + \underline{\underline{K}} \cdot \underline{x} = \underline{f}(t, \underline{x}, \dot{\underline{x}}) \quad . \quad (1)$$

The mass-, stiffness- and gyroscopic matrices are derived using finite beam elements for rotor dynamic analy-

ses, cf. Nelson [22]. Usually and also in this work, the damping matrix is obtained using the Rayleigh approach

$$\underline{D} = \alpha \underline{M} + \beta \underline{K} \quad . \quad (2)$$

The bearings' behaviour enters in Eq. (1) in terms of the right hand side f , which thereby depends on time, shaft position and orientation as well as its translational and rotational velocity. The correlating bearing forces and moments (due to friction and tilting) are obtained by an online solution of the Reynolds PDE in every time step of the time integration. This equation, including cavitation effects [24] and expressed in terms of the non-dimensional pressure Π , reads

$$\begin{aligned} & \left[\frac{\partial}{\partial X} \left(\frac{H^3}{12\bar{\eta}} \frac{\partial(g\Pi)}{\partial X} \right) + \frac{\partial}{\partial Y} \left(\frac{H^3}{12\bar{\eta}} \frac{\partial(g\Pi)}{\partial Y} \right) - \text{sgn}(u_m) \frac{\partial H}{\partial X} - \frac{\partial H}{\partial T} \right] \\ & + \left[\text{sgn}(u_m) \frac{\partial((g-1)\Pi H)}{\partial X} + \frac{\partial((g-1)\Pi H)}{\partial T} \right] = 0 \quad . \end{aligned} \quad (3)$$

Therein, the first bracket accounts for the pressure region while the second bracket is active in the cavitation region, depending on the value of the switch function g . The Eq. (3) is discretised in the bearing domain using the finite volume method, leading to a non-linear system of equations, which can be solved with a Newton-Raphson approach, if the switch function is of sigmoid type instead of the usually used Heaviside type. By means of integration w.r.t. the bearing domain, the current forces and moments can be computed depending on the rotor surface velocity u_m , the gap function H and its time derivative $\partial H/\partial T$. The corresponding coordinate system in the lubricating gap is shown in Figure 1.

Besides this direct link to the rotor motion, the force values depend on thermal expansion of the bearing partners as well as the current viscosity of the fluid, which varies due to the temperature distribution T in the film. Moreover, the film temperature is influenced by the heat fluxes from the shaft and from the bearing housing. Hence, the energy transport equation has to be solved in the fluid film and the surrounding structure. This equation is derived from the change of energy in an infinitesimal control volume with respect to time, cf. [27] or [36], and is stated as

$$\underbrace{\frac{\partial T}{\partial t}}_{\text{Instat. t.}} + \underbrace{u \frac{\partial T}{\partial x} + v \frac{\partial T}{\partial y} + w \frac{\partial T}{\partial z}}_{\text{Convective term}} = \underbrace{\frac{\lambda}{\rho c_p} \left[\frac{\partial}{\partial x} \left(\frac{\partial T}{\partial x} \right) + \frac{\partial}{\partial y} \left(\frac{\partial T}{\partial y} \right) + \frac{\partial}{\partial z} \left(\frac{\partial T}{\partial z} \right) \right]}_{\text{Conductive term}} + \underbrace{\frac{\eta}{\rho c_p} \left[\left(\frac{\partial u}{\partial z} \right)^2 + \left(\frac{\partial v}{\partial z} \right)^2 \right]}_{\text{Dissipative term}} \quad (4)$$

in Cartesian coordinates with the indicated mechanisms of energy transport. Main input properties are the hydrodynamic pressure, which determines the fluid flow velocities u, v, w and the lubricant fraction, which is obtained from the cavitation model and which is essential for solving the energy equation to calculate the effective physical properties ρ, λ and c_p of the fluid. Otherwise, the temperatures calculated are too high, because the dissipation function is over-estimated. To solve this equation on an equidistant, time-invariant mesh, it is transformed to a cuboid domain using the relation $\tilde{z} = \frac{z}{h(x,y)}$, which is depicted on the right of Figure 1.

The frictional heat leads to a warming of the shaft and the bushing, which in turn leads to even higher temperatures in the lubricating gap. Because of this mutual influence, constant temperatures cannot be assumed for these surrounding parts and they are accounted for by solving the respective heat conduction equation which results from Eq. (4) by removing all velocity dependent terms and reads

$$\frac{\partial T}{\partial t} = \frac{\lambda}{\rho c_p} \left(\frac{1}{r^2} \frac{\partial^2 T}{\partial \varphi^2} + \frac{\partial^2 T}{\partial y^2} + \frac{1}{r} \frac{\partial}{\partial r} \left(r \frac{\partial T}{\partial r} \right) \right) \quad (5)$$

in cylindric coordinates. The shaft temperature is assumed to be constant over the circumference because of the high sliding velocity. Similar to Eq. (3), Eqs. (4) and (5) are solved using the finite volume method, which is extensively described in [29] and the solution is stabilised with the hybrid scheme that is also described therein. At the interfaces between fluid film and surrounding parts, it is presumed that the oil sticks to the respective surface

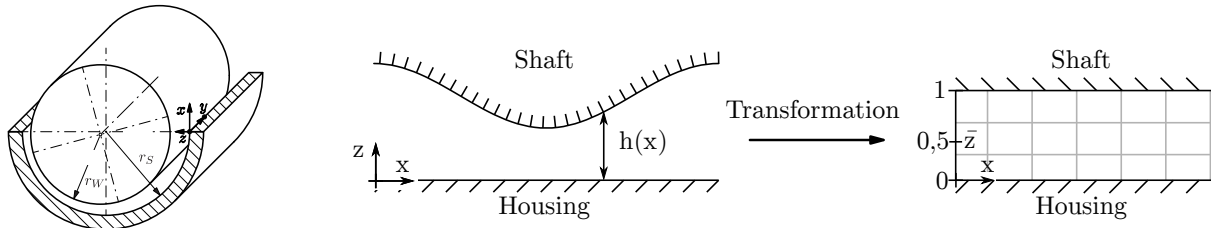


Figure 1: *Left:* Plain journal bearing with coordinate system. *Middle to right:* Transformation of the lubricating gap to a cuboid domain with the dimensionless coordinate \tilde{z} .

which allows to model the heat transfer over these interfaces as pure heat conduction. This leads to a single equation system for all three domains, which is solved in every time step for the full non-isothermal approach.

The resulting temperatures in the lubricating film T can be used to calculate the following input parameters for the solution of the Reynolds PDE: oil viscosity η (obligatory for thermo-hydrodynamic models), oil density ρ (small influence, not considered in this work) and changes in gap height due to thermal expansion Δh_{therm} (small influence for the system considered in this work, see section 4.3, but not generally).

4 Case Study: Laval rotor in cylindric hydrodynamic bearings

4.1 Technical data of the analysed rotor system

It is reasonable to test new calculation models using simple systems with an overseeable number of (measurable) input parameters to keep the uncertainties of the input as low as possible. In the field of rotordynamics, the laval rotor is such a simple system. Eling conducted measurements for a laval rotor supported by two identical plain journal bearings, which were documented in [9, 8] alongside with simulation models of varying modelling depth. It was stated in [8], that the calculation of a run-up experiment ($t_{sim} = 20$ s) takes 100-200 hours on four processors for the most sophisticated model, which was outlined in section 2.2.

The rotor analysed by Eling is depicted in Figure 3 and has three disks: One main disk, where different unbalances can be mounted and two small disks adjacent to the bearings. Various run-up experiments from 250 rpm to 52 000 rpm were conducted with an acceleration of 1000 rpm per second and the rotor displacements were measured at each disk. The reference operating conditions were defined as

- $T_{ambient} = 298$ K
- $T_{Oil\ supply} = 298$ K
- $p_{Oil\ supply} = 2.8$ bar
- $m_{Unbalance} = 250$ mg mm

and the properties of the rotor-bearing-system are listed in Figure 2.

4.2 Measurements by Eling

During the run-ups, various parameters were recorded from which especially the rotor displacement at the main disk will be analysed. The left part of Figure 4 depicts the measured displacements at the main disk during a run-up from 250 rpm to 52000 rpm at reference operating conditions as recorded by Eling. Right at the start of the recording, the displacements are greater than zero indicating that the measurement started from an eccentric rotor position. With increasing rotational speed, the rotor drifts to a more centric position, which is typical for hydrodynamically supported systems. Furthermore, two characteristic areas can be identified in both graphs (x-direction and y-direction). Firstly, the rotor passes the resonance after approximately 23 s at a rotational frequency of approximately 380-390 Hz. At this point, the excitation frequency of the rotating unbalance force equals a (current) eigenfrequency of the bearing-rotor system. Beyond the resonance, the amplitudes decline until secondly a sudden jump occurs at approximately 42 s (700 Hz). This point marks the onset of subharmonic vibrations (the frequency content can be examined by representing the measurement data as spectrogram, cf. [8]), which are excited by the lubricating films in both bearings. From 42-52 seconds, there is a very steep increase of the vibrational amplitudes reaching maximal values of +40 μ m/-50 μ m in the x-direction and +50 μ m/-60 μ m in the y-direction during the last two seconds of the plot, where the rotational speed was supposedly held constant, and are therefore quite asymmetric. However, Figure 4 shows that there seems to be a drift in the measurement signal, which can be regarded as an explanation why this asymmetric behaviour is reproduced only very slightly

Figure 2: Physical parameters of the rotor system according to [8] in comparison with current simulation model

	Name	Value nominal	Value current sim.
Bearings	d_{bear}	6.022 mm	6.022 mm
	d_{shaft}	6.000 mm	6.000 mm
	b	3.6 mm	3.6 mm
	ψ	$3.6533 e - 03$	$3.6533 e - 03$
Rotor	m	105.8 g	106.9 g
Steel 1.2379	I_{pol}	$10.4 e - 06 \text{ kg m}^2$	$10.27 e - 06 \text{ kg m}^2$
	E	–	226 GPa
	f_{crit}	764 Hz	780.3 Hz
	$unbal.$	50...350 mg mm	250 mg mm
	Oil	ϑ_{in}	298...348 K
Mobil 15W30	p_{in}	1.0...5.0 bar	2.8 bar

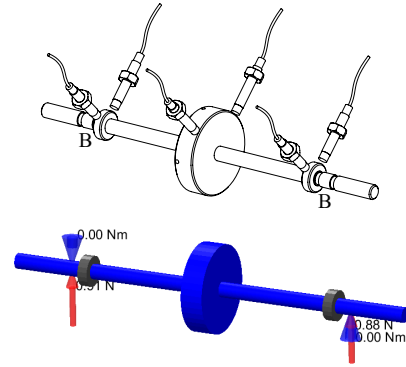


Figure 3: Top: Rotor used for experiments, 'B' marks the bearing positions [35], Bottom: Current simulation model, red arrows mark the bearing positions

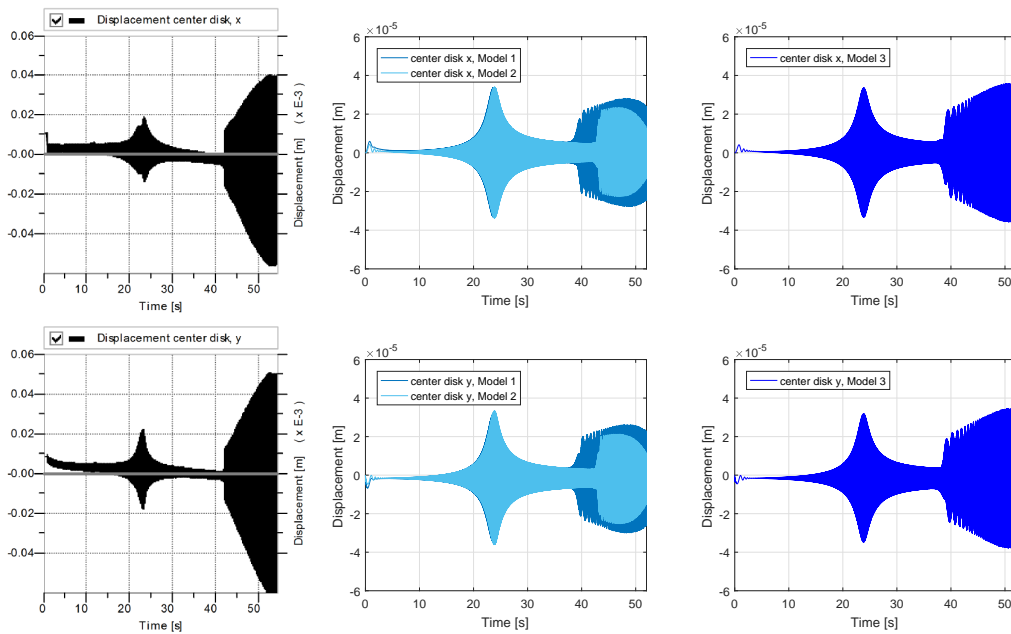


Figure 4: *Left:* Measurement results published in [8] at ref. conditions, gray line added by author. *Middle:* Simulation with isoviscous models. *Right:* Simulation with enhanced model as described in section 3, three-dimensional distribution of the oil viscosity.

in the simulations in y-direction (because of the gravitational load). The plots show that the amplitudes of the subharmonic vibrations can reach significantly higher values than the resonance amplitudes and this highlights the fact that they have to be looked at closely when designing rotor systems supported by hydrodynamic bearings. This requires efficient and realistic models to allow for suitable simulations of the dynamic behaviour.

To parametrise a heat transfer model for the surrounding parts, Eling conducted detailed conjugate heat transfer analyses. An important result of these analyses was that the changes in gap height due to thermal expansion lie in the order of $0.5 \mu m$, which is fairly small compared to the nominal height of the lubricating gap ($11 \mu m$) and it was concluded that these changes are negligible. The same assumption is made for all simulations presented in the following sections, which were therefore carried out with constant bearing clearance.

Figure 5: Overview of the different simulation models presented in chapters 4 and 5

Number	Thermal model	Remarks	Section
Model 1	Isothermal, therefore also isoviscous	$T_{\text{film}} = T_{\text{supply}}$	4.4
Model 2	Isoviscous, but not isothermal	Film temp. taken from measurement as shown in Figure 12. The temp. is constant over the film, but not constant over time.	4.4
Model 3	Full non-isothermal model	Transient solution of the energy and heat eq. in every time step.	4.5
Model 4	non-isothermal model with piecewise constant temperatures in lubricant film	Transient solution of the energy and heat eq. NOT in every time step.	5.1
Model 5	non-isothermal model with coarser mesh	Transient solution of the energy and heat eq. in every time step, but with coarser mesh than in Model 3.	5.2
Model 6	combination of model 4 and model 5	–	5.3

4.3 Simulation model

All simulation results which are presented in this work are based on the same basic model: The rotor is modelled as an elastic beam with finite elements based on the Timoshenko-theory, cf. for instance [22, 23]. Mass, polar mass moment of inertia and first eigenfrequency (free-free condition) of the model agree very well with the measured data, see Figure 2. The first eigenfrequency was adapted by a slight alteration of the Young's modulus because otherwise the resonance would occur too early in the simulations. The two bearings are modelled according to the geometric data given in [9] and are located at the prescribed axial positions. Oil is supplied from one circular hole at the top of each bearing. The solution of the Reynolds PDE includes the rotor deflection and the mass-conserving regularised Elrod Algorithm published in [26, 25] is used to account for cavitation. As mentioned in the previous section, the bearing clearance is assumed to be constant. Besides the bearing forces, which are calculated by integration of the discrete pressure values over the bearing surface, gravitation and unbalance act on the rotor. In analogy to the measurements, run-up simulations were conducted from 250 rpm up to 52000 rpm. The simulation time was set to 5 s with the rotor being located in a centered position initially. For better comparability with the measurements, all simulation results shown in Figure 4 were scaled to an end-time of 52 s. The table in Figure 5 shows an overview of the different models that are presented in this paper.

4.4 Simulation results with isoviscous models

Isothermal approach (Model 1) As a reference for calculation time, simulations were carried out with an isothermal model at first. With this modelling approach, the oil temperature does not change with increases of rotational speed, it is equal in the whole fluid film and the approach is therefore also called an isoviscous model. The oil supply temperature is the only thermal boundary condition which has to be defined. It was set to 323 K and therefore 25 °C higher than the value defined in the reference operating conditions because a major temperature increase was reported to occur in the oil supply channel [8].

The dark curve in the middle of Figure 4 shows the results of this isothermal calculation. Because the rotor starts from a centered position, there is no bearing force at the beginning, which leads to a slight drop of the rotor in the first second of the calculation. The two characteristic areas which were pointed out in the measurements are visible in the simulation results as well. The calculated resonance frequency of the rotor-bearing systems matches the measured resonance frequency: Both lie at 23.7 s (approximately 380-390 Hz). However, the rotor amplitude is over-predicted and, as already mentioned, asymmetries of the displacements in x-direction are not reproduced by the model. More importantly, the vibration amplitudes of the subharmonics are predicted to be smaller than the resonance amplitudes, which is a major disadvantage of this model. The calculated maximal displacements at maximal rotational speed reach roughly 50 % of the measured displacements. The calculation takes 52 minutes on a single processor with a comparatively coarse mesh of 60x16 for the solution of the Reynolds PDE equation in each bearing.

Temperature boundary conditions from measurement, constant viscosity in lubricating gap (Model 2) The second isoviscous model utilises the comprehensive data basis of the case study and uses the measured oil temperatures (see black plot in Figure 12) as boundary conditions with linear interpolations in between. This enables an examination of the correctness of lumped thermal models as the measured data should be close to the real temperatures, even if some changes in oil temperature might occur between the lubricating film and the thermocouple position at the outlet. The simulation results obtained with these boundary conditions are shown in the middle of

Figure 4 as the light blue curve. Regarding the resonance, the calculation results are very similar to the results obtained with the isothermal approach. However, the predicted amplitudes in the subharmonic domain are considerably lower than predicted by the isothermal model. Clearly, this was not expected, as the boundary conditions are more realistic than with the isothermal ansatz. On the other hand, the onset of the subharmonic vibrations is predicted at about 43 s and therefore noticeably closer to the measurements, where the onset was recorded at 42 s.

4.5 Simulation results with full non-isothermal approach (Model 3)

Results For distinction between the non-isothermal reference model, which incorporates a solution of the energy equation in every time step and the reduced models presented in chapter 5, the former will be called 'full non-isothermal approach'. The simulation results attained with the full non-isothermal model are depicted on the right-hand side of Figure 4. Just as in the isothermal results, a slight drop of the rotor can be observed in the first second of the calculation. However, contrary to the isothermal calculation, this initial displacement leads to vibrations during the first seconds of the calculation. A possible explanation is given by the boundary conditions: In opposition to the isothermal simulation, the non-isothermal simulation starts at cold conditions and therefore with a comparatively high oil viscosity, which connotes higher bearing stiffness. As a result, the rotor is pushed back closer to the bearing center than in the isothermal calculation and drops again. This is repeated several times with decreasing amplitudes. The same behaviour can be observed at the results of the non-isothermal, isoviscous model and the same explanation applies.

The transition through the resonance and the onset of the subharmonic oscillations are clearly visible in this simulation as well. Neither the maximal amplitude nor the passing time of the resonance differ from the isoviscous calculations, probably because the mean temperatures do not differ significantly at that time (323 K vs. 312 K, compare black and blue curve in Figure 12 at approximately 23 000 rpm).

However, significant differences exist regarding the prediction of the subharmonics. The increase of the vibrational amplitudes is steeper and the maximal displacement in the positive x-direction matches the measured displacements at this point much better than the isothermal solution.

Deviances remain regarding the displacements in the negative x- and in the y-direction compared to the measurements and the asymmetry that was recorded in the measurements is only slightly represented in the y-direction. Moreover, no considerable change is visible regarding the onset of the subharmonic oscillations compared to the isothermal solution, which is still predicted too early.

Boundary conditions As the full non-isothermal approach implies a thermo-hydrodynamic model for the bearings including heat conduction equations for the bearing housing and the shaft, more temperature boundary conditions are required.

1. Initial temperatures have to be defined – these are set to the ambient temperature (25 °C).
2. Interfaces of fluid film and surrounding parts: As explained in section 3, pure heat conduction is assumed at the interfaces between fluid film and surrounding parts, which means that no explicit boundary conditions have to be defined at these locations.
3. Axial boundaries of the shaft: The heat flow at the axial boundaries of the shaft is not known. However, steep axial temperature gradients were reported outside of the bearings in [8]. To keep the system boundaries as large as possible, this is modelled by defining an isothermal system boundary ($T = T_{amb}$), which is positioned in a reasonable distance l_{amb} to each axial bearing-edge. Heat is conducted from the axial bearing boundaries to these system boundaries. By choosing the distance to be $l_{amb} \geq b$, the temperatures in the lubricating film are not influenced significantly by the ambient temperature and can adjust almost freely. In the current work, the distance was defined to be equal to the bearing width $l_{amb} = b$ at each axial boundary of the calculation domain.
4. Axial boundaries of the lubricating film: It is assumed, that the oil can leave the bearing freely at the axial boundaries, which leads to the requirement that the temperature gradient must be zero there [29].
5. Axial boundaries of the bushing: The bushing is quite narrow [8] and therefore, free convection is assumed at this boundary. This results in the calculation of a heat transfer coefficient α_{FC} [3], which is then incorporated in the calculations as a heat flow boundary condition.
6. Radial boundary of the bushing: This boundary condition is equivalent to the condition formulated for the shaft's axial boundaries (item 3), because the heat flow over the radial boundaries is not known. Therefore, a system boundary d_{sys} was defined outside of the calculation boundary d_{calc} and the following values were chosen: $d_{calc} = 45 \text{ mm}$, $d_{sys} = 2 \cdot d_{calc} = 90 \text{ mm}$.
7. Oil mixing in the inlet: It is difficult to state the boundary condition of the effective temperature in the oil inlet area in the lubricating film, because a part of the hot oil sticks to the shaft and rotates over this area, whereas

another part of the hot oil mixes with the fresh oil from the oil supply channel. The proportion of these parts is strongly dependent on load and rotational speed. Presently, an investigation to find a good compromise is still pending and therefore, the simplest possible approach has been chosen: A heat balance in the oil supply region without empirical parameters as stated by Heshmat and Pinkus in [12].

These boundary conditions are used to solve the energy equation in each time step of the time integration, which causes a heavy increase in calculation time: The calculation takes 25.4 hours with a mesh size of $60 \times 16 \times 25$ in the lubricating films and $60 \times 16 \times 11$ in the bushing. The gap height of the fluid film was meshed with a comparatively large number of elements to account for the high temperature gradients which can occur across the fluid film. As mentioned before, all calculations were carried out on a single processor.

4.6 Conclusion of the simulations

The calculation results show clearly, that the enhanced temperature algorithm yields a better prediction of the rotor amplitudes than both isoviscous approaches. The growth of the amplitudes of the subharmonic vibrations is predicted more correctly and the maximal amplitudes are close to the maximal measured amplitudes. It is very surprising that the non-isothermal, isoviscous model performs significantly worse. Because the changes in gap height as a result of thermal expansion are neglected, there are only two possible explanations:

1. The local temperatures in the lubricating film are higher than the measured temperatures at the outlet. This would mean that the viscosity of the oil is actually lower in the lubricating film leading to lower damping and therefore higher vibrational amplitudes at high rotor speeds.
2. It is essential to calculate locally resolved temperatures and viscosities respectively to achieve a valid approximation of the subharmonic oscillations. This explanation seems to be more likely to be correct at first, as the simulation model of Eling also contained locally resolved viscosity and did also match the measurements better than the non-isothermal, isoviscous approach presented in section 4.4.

By averaging the temperatures resulting from the full non-isothermal approach and using them as boundary condition for the simulations, significantly better results are achieved (not shown). Therefore, explanation 1. applies and this means that the calculation results are exceptionally sensible to the temperatures.

The full non-isothermal model is the only approach, which does not predict a decline of the subharmonics at high rotational speeds and does therefore match their global behaviour best. The onset is calculated a little bit too early (measurement: 42 s, simulation: 38.7 s), but it is essential for the safety of a machine to predict the critical operating points correctly and a late prediction would be potentially more harmful. Therefore, the full non-isothermal approach yields much more reliable results.

5 Speed-up of thermally extended rotordynamics: Approach and results

Due to the increased modelling depth of the full non-isothermal model, there is a significant increase in calculation times. Therefore, different approaches to reduce the numerical effort for the thermo-hydrodynamic model will be explored in this section of the paper. All calculation results will be compared to the rotor displacements calculated with the full non-isothermal approach in x-direction.

5.1 Piecewise constant temperatures in lubricating film (Model 4)

The thermal processes in hydrodynamic bearings show significant differences regarding the time scales. On the one hand, the temperature rises very quickly in the lubricating film and very slowly in the surrounding parts. On the other hand, the temperatures in the lubricating film are strongly dependent on the wall temperatures. Therefore it is reasonable to solve the energy equation not in every time step because low changes in the wall temperatures are expectable after small time increments. Simulations were conducted with the number of time steps n until a new solution is carried out = 10, 25, 50, 100.

The simulation results shown in Figure 7 illustrate clearly, that this procedure is valid for the system investigated in this work. There are only very slight deviations regarding the onset of the subharmonic oscillations as shown in the detail on the right of Figure 7, where a slight phase-shift between the rotor responses can be seen, possibly due to slight differences in the temperatures. The amplitudes reached at the final rotor speed are the same and there are vast savings in computational time up to a speedup of 14 (see Figure 6). However, the factor $n = 100$ is rather high. With a maximal time step size in the magnitude 10^{-5} s and a maximal rotational frequency of 866.7 Hz in this model, the temperatures are solved approximately once in every revolution at maximal rotor speed. Choosing $n = 25$ leads to 4-5 solutions of the thermal model at maximal speed and still allows for major savings in computational time with a speedup of 7.

Figure 6: Calc. times for model 4

	Calc. time
$n = 1$	25.4 h
$n = 10$	7.7 h
$n = 25$	3.7 h
$n = 50$	2.4 h
$n = 100$	1.8 h

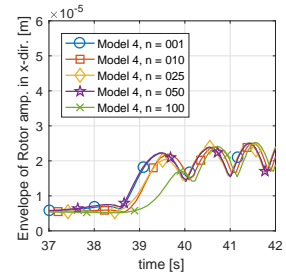
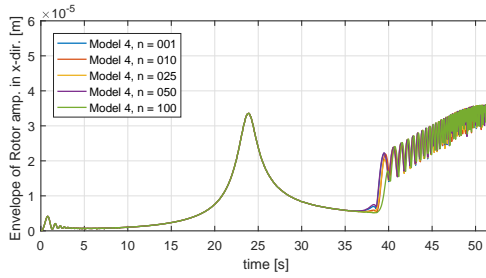


Figure 7: *Left:* Sim. results for different numbers of time steps n between each solution of the thermal model. The upper envelope of the rotor displacements is shown for better distinction between the curves. *Right:* Detail of the onset of subharmonic vibrations.

Figure 8: Calc. times for model 5

nz_{film}	Calc. time
25 (ref.)	25.4 h
15	11.8 h
10	7.6 h
5	5.0 h

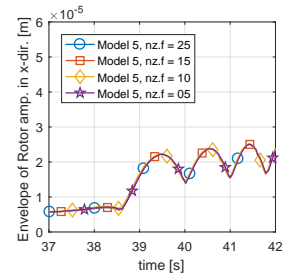
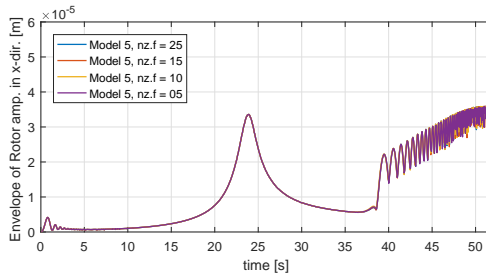


Figure 9: *Left:* Sim. results for different meshes. The upper envelope of the rotor displacements is shown for better distinction between the curves. *Right:* Detail of the onset of subharmonic vibrations.

5.2 Coarsening of the mesh (Model 5)

The same mesh has been used for all of the previously shown simulations: $60 \times 14 \times 25$ nodes in the lubricating film and $60 \times 14 \times 11$ nodes in the bushing with constant radial spacing. A coarsening of the mesh could be possible without significant changes in the results, especially with regards to the simple oil-supply model, which was described in item 7 in section 4.5. It leads to constant film temperatures over the gap height in the oil-supply region and this means that fine meshing in radial direction is not required there. Secondly, it is not necessary to use a mesh with constant radial spacing for the bushing as only the temperatures on the inside of the bushing are relevant for the oil film temperature. As an alternative, progressive radial spacing can be used for the bushing with a constant growth factor of the radial increment. This has two advantages: Firstly, the inner elements can be made smaller which leads to a better prediction of the friction induced heating on the inner side of the bushing and secondly, using less elements leads to smaller equation systems and therefore faster calculation times. All simulations shown in this section were carried out with a solution of the thermal model in every time step.

Coarsening of the mesh in the lubricating film only The following element numbers across the height of the lubricating film were used: $nz_{film} = 15, 10, 5$. Figures 8 and 9 show the calculation times and the rotor vibrations, respectively. With the simple boundary condition for the oil mixing in the inlet, the mesh size over the lubricating gap has no visible influence on the calculation results at all. However, the calculation times drop significantly and a speedup of 5 is achieved.

Coarsening of the the lubricating film and in the bushing with progressive radial spacing To achieve progressive radial spacing in the bushing, the radial increment of the first element in the bushing next to the oil film was fixed to the value $\Delta r_1 = \frac{r_{bushing}}{100}$ and is therefore smaller than before: $\Delta r_{konst} \approx \frac{8 \cdot r_{bushing}}{100}$. The simulation results are shown in Figure 11 for different meshes. All results with the coarser mesh are similar, but differ considerably from the reference solution as the subharmonic vibrations start much earlier. This can be explained by the smaller mesh size of the bushing next to the lubricating film and leads to the following conclusion: 1.) The mesh size of the reference solution is not fine enough 2.) The boundary conditions have to be reviewed because the temperatures

Figure 10: Calc. times

for model 5

nz _{film} + nz _{bushing}	Calc. time
25 + 11 (ref.)	25.4 h
25 + 4	33.3 h
20 + 4	22.0 h
15 + 4	13.9 h
5 + 4	5.1 h

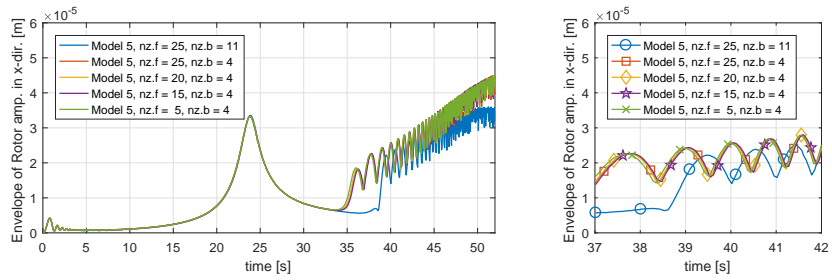


Figure 11: *Left:* Sim. results for different meshes. The upper envelope of the rotor displacements is shown for better distinction between the curves. *Right:* Detail of the onset of subharmonic vibrations.

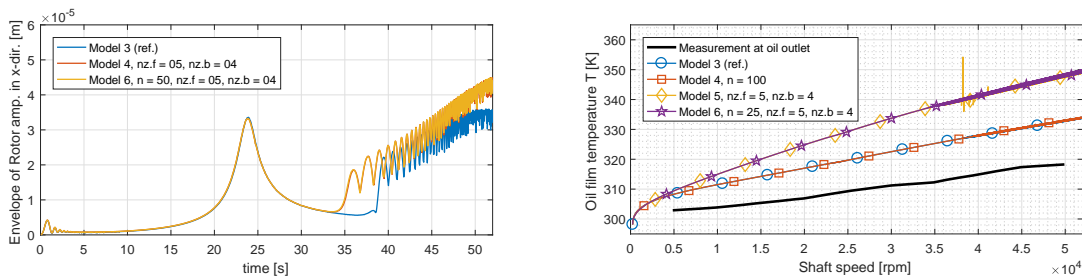


Figure 12: *Left:* Upper envelope of the calculated rotor displacements for model 6. *Right:* Average temperature in the lubricating film as measured by Eling [8] compared to different simulation models.

become distinctly higher than in the measurement as shown in Figure 12. Figure 10 shows the calculation times for various mesh sizes. It has to be pointed out, that the solution times become longer for mesh sizes similar to the reference mesh and an investigation of this showed that more time is needed to solve the equation system. Probably, the system is not as well-conditioned as before because of the different element sizes in the bushing. Nevertheless, a speedup of approximately 5 has been achieved between the reference solution and the coarsest mesh.

5.3 Combination (Model 6)

It is obvious that the greatest speedup can be achieved if the approaches shown sections 5.1 and 5.2 are combined. The following parameters were chosen for that calculation: $n = 25$, $nz_{film} = 5$ and $nz_{bushing} = 4$. The left part of Figure 12 shows the calculation results in comparison to a) the reference solution from section 4.5 and b) the last variant of the model with coarser mesh ($nz_{film} = 5$ and $nz_{bushing} = 4$) from section 5.2. There are no differences visible between the latter and the simulations results achieved with the combination of both approaches. The same applies to the calculated temperatures, which are shown in the right part of Figure 12. Therefore, the differences are caused only by the different mesh sizes at the inner side of the bushing.

The calculation times for the last model amounts to 1.1 h (67 min), which means a very high **speedup of 23**. In fact, this calculation takes only 30% more time than the isothermal model presented in section 4.4 while maintaining the increased modelling depth of the full model. As mentioned before, the boundary conditions for the thermal model will have to be reviewed.

6 Conclusion

This work presents simulation results for the motion of a laval rotor supported by hydrodynamic journal bearings. The thermo-hydrodynamic behaviour of these bearings is described in very high modelling depth, which has not been presented before and it is shown, that this model enables much better results regarding subharmonic vibrations than isoviscous models. This approach is associated with very long computational times which can be handled by two simple approaches and it becomes clear, that it is not necessary to solve the thermal model in every time step because of the widely differing time scales of lubricating film and surrounding parts. Moreover, it is acceptable to use few elements over the gap height if simple thermal boundary conditions are used to model the oil supply. With these approaches, the increase in calculation time can be limited to a factor of two compared to the

isothermal model. The thermal boundary conditions of the model will have to be reviewed, but this work still offers a very good perspective for a better description of hydrodynamically supported rotor systems. Further possibilities to reduce simulation times include a scaling of the instationary terms in the heat equation to speed up the heating in the surrounding parts. Preliminary work on this topic has shown that the results might not be equivalent, but the reason for this remains unclear.

Other than that, future work will include the adaptation of the shown procedure to full floating ring bearings, where it might have an even greater impact because the ring speed has a major influence on the bearing's behaviour and the correct prediction of the ring speed requires reliable knowledge of the temperatures in both oil films.

Acknowledgment

The authors thankfully acknowledge the funding of this research work by the Bundesministerium für Wirtschaft und Energie, AiF Otto von Guericke and DFG. We would also like to thank Rob Eling very much for his valuable tips regarding the simulation models and his interest in this work.

REFERENCES

- [1] Alakhramsing, S., van Ostayen, R. and Eling, R. [2015]. Thermo-hydrodynamic analysis of a plain journal bearing on the basis of a new mass conserving cavitation algorithm, *Lubricants* **3**(2): 256–280.
URL: <https://dx.doi.org/10.3390/lubricants3020256>
- [2] Ausas, R. F., Jai, M. and Buscaglia, G. C. [2009]. A mass-conserving algorithm for dynamical lubrication problems with cavitation, *Journal of Tribology* **131**(3): 031702–031702.
- [3] Baehr, H. D. and Stephan, K. [2016]. *Wärme- und Stoffübertragung*, Springer-Verlag Berlin Heidelberg.
- [4] Booker, J. F. [1971]. Dynamically-loaded journal bearings: numerical application of the mobility method, *Journal of Lubrication Technology* **93**(1): 168–174.
URL: <https://dx.doi.org/10.1115/1.3451507>
- [5] Boyaci, A., Backhaus, K. and Koch, R. [2009]. Mehrkörpersimulation des Hochlaufverhaltens von ATL-Rotoren mit nichtlinear modellierten Schwimmbuchsenlagern, *Abschlussbericht Vorhaben 912 Heft 889*, FVV.
- [6] Clarke, D., Fall, C., Hayden, G. and Wilkinson, T. [1992]. A steady-state model of a floating ring bearing, including thermal effects, *Journal of tribology* **114**(1): 141–149.
URL: <https://dx.doi.org/10.1115/1.2920852>
- [7] Daniel, C., Woschke, E. and Strackeljan, J. [2009]. Modellierung von Gleitlagern in rotordynamischen Modellen, *8th International Conference on Vibrations in Rotating Machines*.
- [8] Eling, R. P. T. [2018]. *Towards robust design optimization of automotive turbocharger rotor-bearing systems*, PhD thesis, Delft University of Technology.
URL: <https://dx.doi.org/10.4233/uuid:fdb0da19-0ef2-4bb6-92a7-8a7acbb05dd2>
- [9] Eling, R., te Wierik, M., van Ostayen, R. and Rixen, D. [2016]. Towards accurate prediction of unbalance response, oil whirl and oil whip of flexible rotors supported by hydrodynamic bearings, *Lubricants* .
URL: <https://dx.doi.org/10.3390/lubricants4030033>
- [10] Fillon, M., Frêne, J. and Boncompain, R. [1987]. Historical aspects and present development on thermal effects in hydrodynamic bearings, *Proc. of 13th Leeds-Lyon Symposium on Tribology*, pp. 27–47.
- [11] Hagemann, T. [2012]. *Ölzuführungseinfluss bei schnelllaufenden, hoch belasteten Radialgleitlagern unter Berücksichtigung des Lagerdeformationsverhaltens*, Diss, Technische Universität Clausthal.
- [12] Heshmat, H. and Pinkus, O. [1986]. Mixing inlet temperatures in hydrodynamic bearings, *Journal of tribology* **108**(2): 231–244.
URL: <https://doi.org/10.1115/1.3261168>
- [13] Holt, C., San Andrés, L., Sahay, S., Tang, P., La Rue, G. and Gjika, K. [2003]. Test response of a turbocharger supported on floating ring bearings: Part ii comparisons to nonlinear rotordynamic predictions, *19th Biennial Conference on Mechanical Vibration and Noise, Parts A, B, and C*, Vol. 5, pp. 975–980.
- [14] Keogh, P. and Morton, P. [1993]. Journal bearing differential heating evaluation with influence on rotor dynamic behaviour, *Proc. R. Soc. Lond. A* **441**(1913): 527–548.
URL: <https://dx.doi.org/10.1098/rspa.1993.0077>
- [15] Khonsari, M. M. [1987a]. A review of thermal effects in hydrodynamic bearings part i: Slider and thrust bearings, *A S L E Transactions* **30**(1): 19–25.
URL: <https://doi.org/10.1080/05698198708981725>
- [16] Khonsari, M. M. [1987b]. A review of thermal effects in hydrodynamic bearings. part ii: Journal bearings, *A*

S L E Transactions **30**(1): 26–33.

URL: <https://doi.org/10.1080/05698198708981726>

- [17] Lang, O. R. and Steinhilper, W. [1978]. *Gleitlager - Berechnung und Konstruktion von Gleitlagern mit konstanter und zeitlich veränderlicher Belastung*, Springer Berlin Heidelberg.
- [18] Mermertas, Ü. [2007]. *Nichtlinearer Einfluss von Radialgleitlagern auf die Dynamik schnelllaufender Rotoren*, Dissertation, Technische Universität Clausthal.
- [19] Mittwollen, N. [1990]. *Betriebsverhalten von Radialgleitlagern bei hohen Umfangsgeschwindigkeiten und hohen thermischen Belastungen - Theoretische Untersuchungen*, Dissertation, Technische Universität Braunschweig.
- [20] Muszynska, A. [2010]. *Rotordynamics*, CRC Press.
- [21] Myrick, S. T. and Rylander, H. G. [1976]. Analysis of flexible rotor whirl and whip using a realistic hydrodynamic journal bearing model, *Journal of Manufacturing Science and Engineering* **98**(4): 1135–1143.
- [22] Nelson, H. D. [1980]. A finite rotating shaft element using timoshenko beam theory, *Journal of Mechanical Design* **102**(4): 793–803.
- [23] Nitzschke, S. [2016]. *Stationäres Verhalten schwimmbuchsenlagerter Rotoren unter Berücksichtigung masseerhaltender Kavitation*, PhD thesis, Otto-von-Guericke-Universität Magdeburg.
- [24] Nitzschke, S., Woschke, E. and Daniel, C. [2017]. Dynamic behaviour of ehd-contacts using a regularised, mass conserving cavitation algorithm, *Technische Mechanik* **37**(2-5): 181–195.
- [25] Nitzschke, S., Woschke, E. and Daniel, C. [2018]. Application of regularised cavitation algorithm for transient analysis of rotors supported in floating ring bearings, *International Conference on Rotor Dynamics*, Springer, pp. 371–387.
- [26] Nitzschke, S., Woschke, E., Schmicker, D. and Strackeljan, J. [2016]. Regularised cavitation algorithm for use in transient rotordynamic analysis, *International Journal of Mechanical Sciences* **113**: 175–183.
URL: <https://dx.doi.org/10.1016/j.ijmecsci.2016.04.021>
- [27] Oertel jr, H., Böhle, M. and Reviol, T. [2011]. *Strömungsmechanik: Grundlagen-Grundgleichungen-Lösungsmethoden-Softwarebeispiele*, Springer-Verlag.
- [28] Paranjpe, R. S. and Han, T. [1995]. A transient thermohydrodynamic analysis including mass conserving cavitation for dynamically loaded journal bearings, *Journal of tribology* **117**(3): 369–378.
URL: <https://dx.doi.org/10.1115/1.2831261>
- [29] Patankar, S. [1980]. *Numerical heat transfer and fluid flow*, Hemisphere Publishing Corp.
- [30] Petzold, L. [1982]. Description of dassl: a differential/algebraic system solver, *10. International mathematics and computers simulation congress on systems simulation and scientific computation, Montreal, Canada, 9 Aug 1982*.
- [31] San Andrés, L. and Kerth, J. [2004]. Thermal effects on the performance of floating ring bearings for turbochargers, *Proceedings of the Institution of Mechanical Engineers, Part J: Journal of Engineering Tribology* **218**(5): 437–450.
URL: <https://doi.org/10.1243/1350650042128067>
- [32] Schweizer, B. [2009]. Total instability of turbocharger rotors—physical explanation of the dynamic failure of rotors with full-floating ring bearings, *Journal of Sound and Vibration* **328**(1-2): 156–190.
URL: <https://dx.doi.org/10.1016/j.jsv.2009.03.028>
- [33] Shampine, L. F. and Reichelt, M. W. [1997]. The matlab ode suite, *SIAM J. SCI. COMPUT.* **18**(1): 1–22.
- [34] Shi, F. and Paranjpe, R. [2002]. An implicit finite element cavitation algorithm, *Computer modeling in engineering and sciences* **3**(4): 507–516.
- [35] Te Wierik, M. [2016]. *Modeling and experimental validation of a laval rotor on plain journal-and turbocharger floating ring bearings-the behavior of high speed rotors on fluid film bearings*, Master’s thesis, TU Delft.
URL: <https://repository.tudelft.nl/islandora/object/uuid%3Aa5fac91c-2ad7-419e-aa79-84e9c5d48519>
- [36] Woschke, E. [2013]. *Simulation gleitlagerter Systeme in Mehrkörperprogrammen unter Berücksichtigung mechanischer und thermischer Deformationen*, Dissertation, Otto-von-Guericke-Universität Magdeburg.
- [37] Woschke, E., Daniel, C. and Nitzschke, S. [2017]. Excitation mechanisms of non-linear rotor systems with floating ring bearings - simulation and validation, *International journal of mechanical sciences* **134**: 15–27.
URL: <https://doi.org/10.1016/j.ijmecsci.2017.09.038>

Systematic stability investigation of a rotor system involving journal bearings with variable, oval geometry

Kai Becker¹, Wolfgang Seemann²

^{1,2} Institute of Engineering Mechanics, Karlsruhe Institute of Technology, 76131, Karlsruhe, Germany

¹ kai.becker@kit.edu, ² seemann@kit.edu

Abstract

The improvement of rotor-dynamic systems being supported by oil-lubricated journal bearings represents an ongoing field of research. As the rotational speed of the rotor is increased instability phenomena of the 'oil-whirl' and/or 'oil-whip' type can be detected. In order to suppress or at least to decrease the resulting oscillations of these unwanted effects, various modifications have been proposed in literature. The present work deals with the improvement of the rotor system by applying a variable change in geometry of the supporting journal bearings. Starting from an initially circular profile the bearing is elastically deformed by an appropriate actuation mechanism to an oval shape. The effect of this change in geometry is investigated by means of a systematic stability analysis in dependence of various system parameters. It can be shown that the change in geometry can have positive effects depending on the respective parameter set, such that the admissible rotational speed can be shifted to even higher values. In addition to a static deformation a small harmonic variation of the bearing's geometry is superimposed in order to improve the system's behaviour even further. The harmonic geometry variation leads to a system with parametric and self-excitation, which shows interesting stability properties in case of certain combination frequencies. As the self-excitation phenomena destabilize the equilibrium solution, a suitable choice of the parametric excitation frequency can lead to a stabilization, which is most probably caused by an interaction of the involved modes.

1 Introduction

The non-linear fluid-solid interaction within journal bearings represents a self-excitation mechanism, which can lead under certain circumstances to tremendously increasing oscillation amplitudes of the rotor-dynamic system. These phenomena are often referred to as 'oil-whirl' and/or 'oil-whip' and are well explained in literature (cf. [6, 9]). Various countermeasures for suppressing or at least for decreasing these unwanted effects have been developed, some of which are shortly listed below. It is thereby focused on concepts which are based on the general idea of adjustable, non-cylindrical bearing geometries, as these have shown to have a significant influence on the dynamic behaviour of the rotor system.

Journal bearings with non-cylindrical geometries like multi-lobe [1, 16, 18] or tilting pad bearings [17] have proved themselves to have a stabilizing effect for certain parameter configurations. As these concepts are considered to be rather passive, an active intervention from outside is not possible.

More recent works focus on the idea of actively adjustable journal bearings. An insight into the current state of the art can be found in [24]. Some of these concepts focus on the introduction of additional elements which lead to a change of the bearing's geometry. By actively modifying the properties of these elements, the system can successfully be influenced. E.g. CHASALEVRIS ET AL. [7, 8] suggest a displaceable lobe which is connected to a visco-elastic element. KRODKIEWSKI ET AL. [15] present a modification via an elastic element, whose displacement can be partly controlled by means of a hydraulic pressure unit.

Other concepts with an even more actively controlled change in geometry can be found as well. PRZYBYLOWICZ [22] or TŮMA ET AL. [29] introduce the idea of a rigid cylindrical bearing which can actively be displaced. Another approach is given by so-called active tilting pad bearings, which are investigated in the works of SANTOS [23], DECKLER ET AL. [10] or WU ET AL. [31]. Their concept is based on the radial displacement of the pivot points of the single tilting pads in order to influence the pressure distribution in a desired way. Among different other aspects the design of an appropriate controller represents one of the main objective in these works.

In all of the previously mentioned cases it has been shown (experimentally and/or numerically) that the behaviour of the rotor system can be improved significantly by using these active journal bearings.

The following work rather considers the systematic analysis of the solution evolution of a rotor system involving a slightly modified approach of an active journal bearing without covering the question of an appropriate controller.

Like captured by PFAU ET AL. [20] who investigate a two-lobe bearing with harmonically changing geometry, it is thereby focused on the theoretical aspects from the mathematical/mechanical point of view. The whole rotor system should therefore be interpreted as some kind of coupled non-linear oscillators with a harmonic parametric excitation, caused by a time-dependent change of the bearing's geometry. Various examples (e.g. [13, 20, 27]) revealed a stabilizing effect caused by an appropriate choice of the frequency of this parametric excitation for similar systems.

A more elaborated model of an actively deformable journal bearing is presented in section 2.1, for which the geometry adjustment is realised, in contrast to the above mentioned concepts, by an elastic deformation of an initially cylindrical bearing. The overall rotor model is presented in section 2.2 and the corresponding computational results can be found in section 3.

2 Modelling

The modelling requires a description of the bearings's geometry as well as of the fluid pressure distribution. Both are then used to set up the corresponding equations of motion of the whole rotor system.

2.1 Bearing Model

Like depicted in fig. 1, an initially cylindrical journal bearing with inner Radius R_0 is considered to be elastically deformed by an appropriate actuation mechanism in order to obtain an ovally-shaped profile. The deformation should be controlled by a predefined displacement of the upper and lower point respectively.

For simplification reasons it is assumed that the resulting fluid pressure does not influence the bearing deformation at all. This seems rather strict, but in the context of a first investigation indeed reasonable.

The rotational speed of the journal is described by its angular frequency ω , which is also used for the definition of the dimensionless time $\tau = \omega t$.

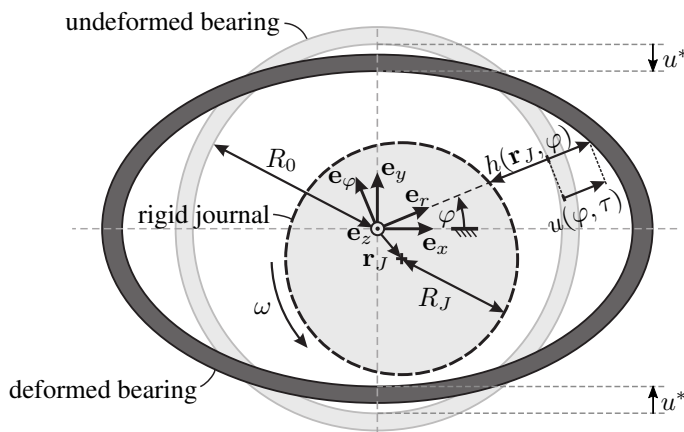


Figure 1: Ovally deformed journal bearing [2]

2.1.1 Elastic Deformation and Bearing Geometry

The bearing is modelled as thin circular beam with rectangular cross-section corresponding to a rather 'short' bearing in the axial e_z -direction. The radial displacement field $\mathbf{u}_r = u\mathbf{e}_r$ thereby depends on the predefined displacements $u^* = -u(\varphi = \pm\pi/2)$ of the upper and lower point respectively, assuming a complete symmetric behaviour (cf. fig. 1). In accordance to the classical BERNOULLI theory, a 1D-stress state is assumed. A detailed derivation of the displacement field can be found in [21].

For the described case of a short, thin cylinder which is deformed at its upper and lower point respectively, the radial displacement field (cf. [21]) is given by the 2π periodic continuation of:

$$u = u^* \left(\frac{2\pi}{\pi^2 - 8} \right) \begin{cases} \frac{4}{\pi} - \varphi \sin \varphi - \cos \varphi & \varphi \in \left[-\frac{\pi}{2}, \frac{\pi}{2} \right] \\ \frac{4}{\pi} - (\pi - \varphi) \sin \varphi + \cos \varphi & \varphi \in \left[\frac{\pi}{2}, \frac{3\pi}{2} \right] \end{cases}. \quad (1)$$

By using the initial bearing clearance $C = R_0 - R_J$ a non-dimensional radial displacement $U = u/C$, is defined, which is assumed to be of the same magnitude as the clearance C , i.e. $U = \mathcal{O}(1)$.

As the deformation should be time-dependent, the following harmonic approach is chosen for the displacement of the upper and lower point of the bearing:

$$U^* = \frac{u^*}{C} = \widehat{U} [1 + \delta_U \cos(\Omega_U \tau)]. \quad (2)$$

The value $\widehat{U} = 0$ for the mean displacement thereby corresponds to the 'classical' bearing with circular profile.

2.1.2 Pressure Distribution

The non-dimensional pressure distribution $\Pi(\varphi, \bar{z})$ is modelled by the non-dimensional form of the REYNOLDS equation (cf. [26]) for a rather short bearing ($\gamma > 1$)

$$\gamma^2 \frac{\partial}{\partial \bar{z}} \left(\frac{\partial \Pi}{\partial \bar{z}} H^3 \right) = 6 \frac{\partial H}{\partial \varphi} + 12 \frac{\partial H}{\partial \tau}, \quad H(X_J, Y_J, \varphi, \tau) = \frac{h}{C} = 1 + U - X_J \cos \varphi - Y_J \sin \varphi \quad (3)$$

on the domain $(\varphi, \bar{z}) \in [0, 2\pi] \times [-1, 1]$ with the corresponding axial boundary conditions $\Pi(\bar{z} = \pm 1) = 0$ and the commonly used parameters

$$\bar{z} = \frac{2z}{B}, \quad \Pi = \frac{C^2}{R_0^2} \frac{p}{\mu\omega}, \quad \gamma = \frac{2R_0}{B}. \quad (4)$$

The axial coordinate is denoted by z , the fluid pressure by p and the dynamic viscosity of the fluid by μ . The coordinates $X_J = x_J/C$ and $Y_J = y_J/C$ result from a rescaling of the journal coordinates (i.e. $\mathbf{r}_J = x_J \mathbf{e}_x + y_J \mathbf{e}_y$) by means of the initial bearing clearance.

As the short-bearing-approach has been applied, eq. (3) can directly be integrated and the pressure reads out to be:

$$\Pi = \frac{3}{\gamma^2} (1 - \bar{z}^2) \frac{-\frac{\partial H}{\partial \varphi} - 2 \frac{\partial H}{\partial \tau}}{H^3}. \quad (5)$$

In a physical sense all negative pressures have to be neglected, such that the following expression is used:

$$\Pi^+ = \frac{1}{2} (\Pi + \|\Pi\|) = \frac{3}{\gamma^2} (1 - \bar{z}^2) \underbrace{\left(\frac{-\frac{\partial H}{\partial \varphi} - 2 \frac{\partial H}{\partial \tau}}{2H^3} + \left\| \frac{-\frac{\partial H}{\partial \varphi} - 2 \frac{\partial H}{\partial \tau}}{2H^3} \right\| \right)}_{=:g} \quad (6)$$

2.1.3 Bearing Forces

With the determined pressure distribution (eq. (6)) the corresponding fluid forces can be calculated by an integration over the journal's surface. As the integration in \bar{z} can directly be performed, the forces are given by:

$$F_x = -F_0 S_m \underbrace{\int_0^{2\pi} g \cos \varphi d\varphi}_{:=f_x}, \quad F_y = -F_0 S_m \underbrace{\int_0^{2\pi} g \sin \varphi d\varphi}_{:=f_y}. \quad (7)$$

The parameter S_m corresponds to the modified Sommerfeld-Number according to the parameter definitions (11) (cf. [26]) and F_0 represents a characteristic force which is used for the non-dimensional representation. As the integrals f_x, f_y cannot be solved analytically, an approximation via a trapezoidal rule with $N_\varphi = 151$ equally distributed sampling points is performed, resulting in

$$f_x \approx \left[\frac{2\pi}{N_\varphi - 1} \sum_{i=1}^{N_\varphi-1} g(\varphi_i) \cos \varphi_i \right], \quad f_y \approx \left[\frac{2\pi}{N_\varphi - 1} \sum_{i=1}^{N_\varphi-1} g(\varphi_i) \sin \varphi_i \right]. \quad (8)$$

2.2 Rotor Model

An elastic Jeffcott rotor system (cf. [14]) is used like depicted in fig. 2. The rotor of mass M is mounted on an elastic shaft with stiffness c_s and is exposed to an additional external viscous damping d_a . Furthermore, the rotor is considered to be perfectly balanced and tilting is not permitted. The rotor's centre of mass coincides with the centre of the shaft, whose position can be described by the vector $\mathbf{r}_R = x_R \mathbf{e}_x + y_R \mathbf{e}_y$ which represents the projection on the $\mathbf{e}_x - \mathbf{e}_y$ -plane.

The shaft is supported by two journal bearings of the described type, whereby additional masses $m \ll M$ are allocated to each journal at the two bearing positions since the non-linear fluid forces cannot be solved explicitly for the corresponding journal velocities.

In the following the case of a vertical rotor is investigated, such that no additional static loads (e.g. through gravity) are considered. As outlined by CHILDS [9], the vertical rotor in cylindrical bearings has no stable equilibria, unless non-cylindrical bearings are used. The vertical rotor is chosen, as for the case of additional static loads and the desired geometry variation, no equilibrium solution exist any more (cf. [3]).

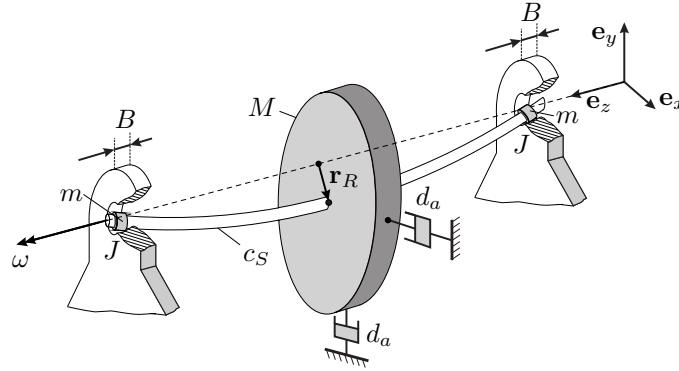


Figure 2: Jeffcott rotor supported by journal bearings

2.2.1 Equations of Motion

The corresponding equations of motion in non-dimensional form (cf. [6]) with $(..)' = d/d\tau(..)$ are given by

$$\begin{aligned} \bar{\omega}^2 X_R'' + \bar{d}_a \bar{\omega} X_R' + \frac{X_R - X_J}{\Gamma} &= 0, & \eta \bar{\omega}^2 X_J'' + \frac{X_J - X_R}{\Gamma} - 2\sigma \bar{\omega} f_x(X_J, Y_J, X_J', Y_J', \tau) &= 0 \\ \bar{\omega}^2 Y_R'' + \bar{d}_a \bar{\omega} Y_R' + \frac{Y_R - Y_J}{\Gamma} &= 0, & \eta \bar{\omega}^2 Y_J'' + \frac{Y_J - Y_R}{\Gamma} - 2\sigma \bar{\omega} f_y(X_J, Y_J, X_J', Y_J', \tau) &= 0 \end{aligned} \quad (9)$$

with the non-dimensional coordinates

$$X_{R/J} = \frac{x_{R/J}}{C}, \quad Y_{R/J} = \frac{y_{R/J}}{C} \quad (10)$$

and the following set of parameters:

$$\bar{\omega}^2 = \frac{MC}{F_0} \omega^2, \quad S_m = \frac{B^3 \mu R_J \omega}{2C^2 F_0}, \quad \sigma = \frac{S_m}{\bar{\omega}}, \quad \eta = \frac{2m}{M}, \quad \Gamma = \frac{F_0}{c_s C}, \quad \bar{d}_a = \sqrt{\frac{C}{MF_0}} d_a. \quad (11)$$

The parameter Γ represents the shaft compliance, \bar{d}_a characterizes the external viscous damping and η describes the mass ratio of the rotor and journal masses. The modified Sommerfeld-Number S_m is used for the definition of the bearing load parameter σ , which is independent of the rotational speed. In the given case of a vertical rotor the characteristic force F_0 represents just a scaling quantity. The rpm-parameter $\bar{\omega}$ is considered to be essential for the following stability investigations. The support reactions from the fluid-solid interaction within the bearings are represented by f_x and f_y from eqs. (8).

The equations of motion (eqs. (9)) can alternatively be represented by the following first-order system

$$\frac{d}{d\tau} \underline{z} = \underline{f}(\underline{z}, \tau), \quad \underline{f}: \mathbb{R}^8 \times \mathbb{R} \rightarrow \mathbb{R}^8, \quad \underline{z} = [X_J, X'_J, X_R, X'_R, Y_J, Y'_J, Y_R, Y'_R]^T. \quad (12)$$

3 Simulation Results

The derived system is systematically investigated by means of numerical solution continuation (MATCONT [11]) as well as transient simulations involving FLOQUET and eigenvalue analysis.

The following section is divided into two parts. The first deals with stability investigations of the rotor system involving 'static' non-cylindrical bearings. Afterwards, the influence of a harmonic geometry variation is investigated. As it is dealt with the vertical rotor, the trivial solution $\underline{z}_0 = \underline{0}$ is of interest for all following investigations.

3.1 Static Bearing Geometry

For the considered case the parametric excitation is switched off, i.e. $\delta_U = 0$.

Focusing on the trivial solution \underline{z}_0 it can be shown that its stability is lost at a certain critical value of the rpm-parameter, corresponding to a subcritical Hopf-Bifurcation. From the bifurcation point unstable limitcycle oscillations start to evolve until a cyclic fold bifurcation, which connects the branch of stable limitcycles to the branch of the unstable ones originating from the Hopf-Bifurcation (cf. fig. 3). A detailed description of this transition can be found in [6].

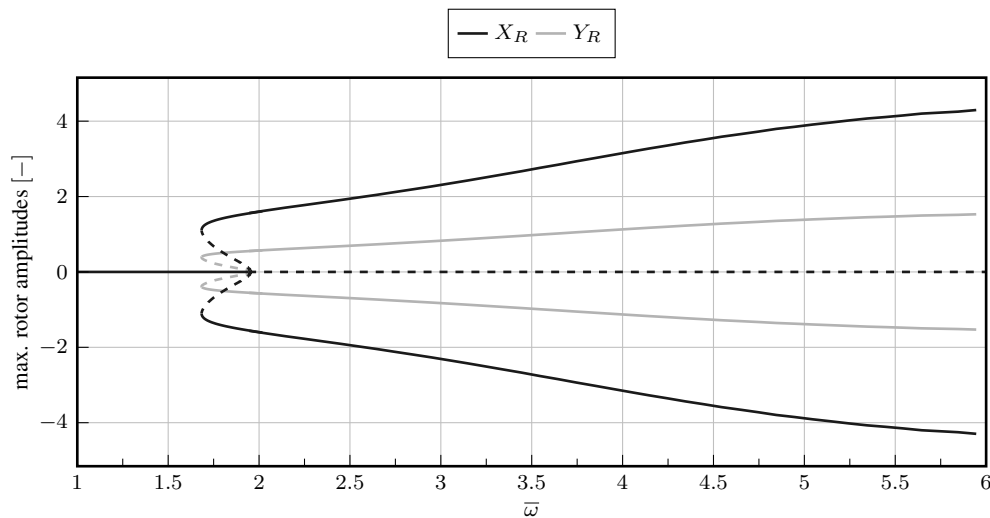


Figure 3: Solution continuation in $\bar{\omega}$ for $\delta_U = 0$ (dashed: unstable solution)

In fig. 4 the stability borders in dependence of the bearing parameter σ can be found for different configurations. If not stated differently, a standard set of parameter values is used as follows:

$$\hat{U} = 0.3, \quad \eta = 0.25, \quad \Gamma = 1, \quad \bar{d}_a = 0.01. \quad (13)$$

The curves correspond to the locations of the Hopf-Bifurcations at which the trivial solution loses its stability. Therefore, in the parameter area above the curve (or 'enclosed' by the curve) the solution is unstable. In the following the system is called to be 'stable' if the trivial solution \underline{z}_0 is stable.

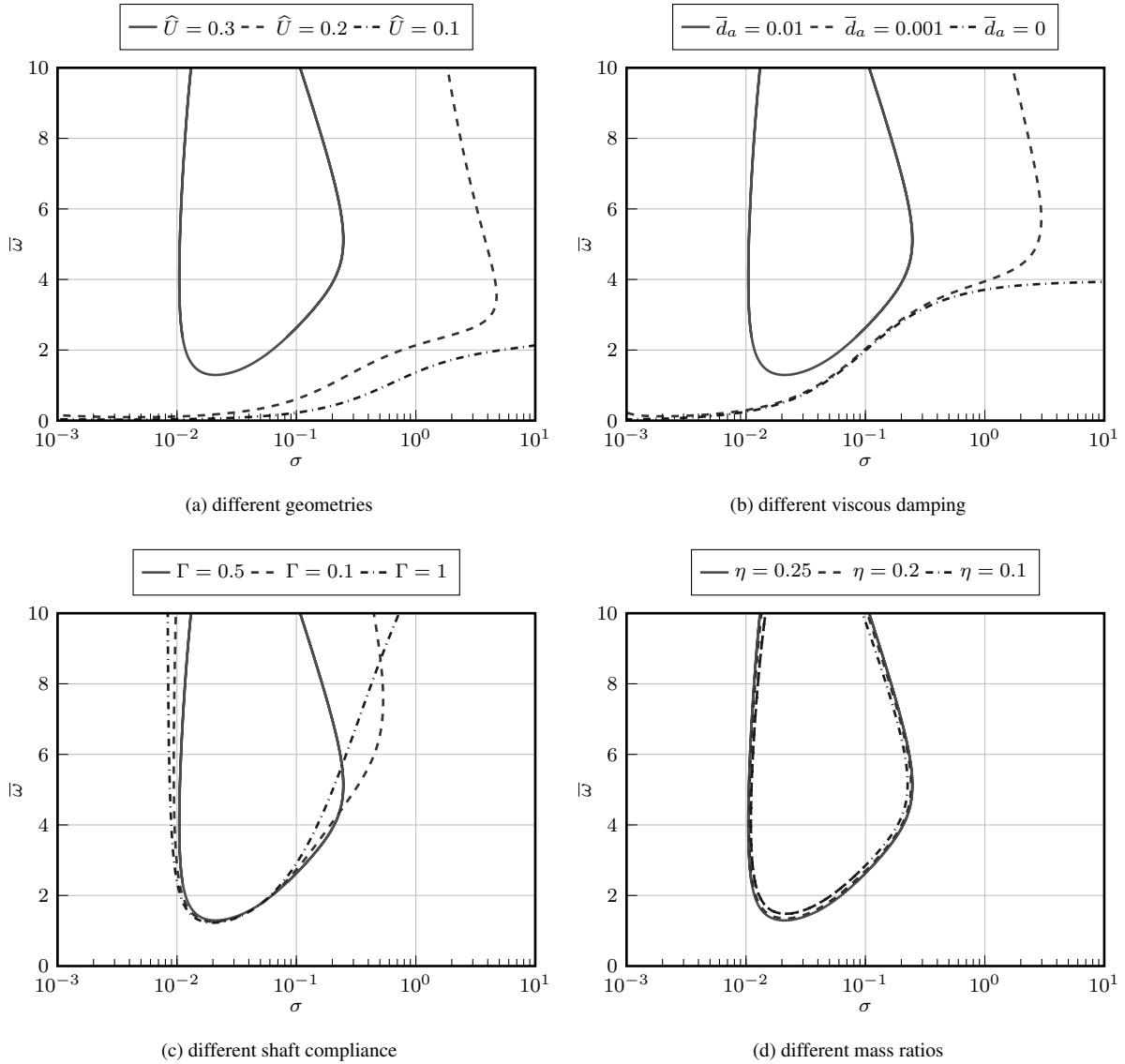


Figure 4: Stability border of trivial solution in $\sigma - \bar{\omega}$ -plane for different cases (a)-(d)

For some parameter configurations (e.g. in fig. 4a for $\hat{U} = 0.3$) a backward turn of the curve can be observed. This phenomenon corresponds to the occurrence of a second Hopf-Bifurcation at higher rpm-values, at which the solution regains its stability. The same behaviour can be observed as well in rotor systems with cylindrical bearings and is therefore considered to be reasonable (cf. [6]).

Concerning the principle character of the system, the following conclusions can be stated. As shown in fig. 4a, a stable region for the vertical rotor can be established by means of bearings with non-circular profiles. By increasing the displacement factor \hat{U} ($\hat{U} \hat{=}$ more oval profile) the stability properties can be further improved. The same qualitative change can be observed for different external damping factors as depicted in fig. 4b.

An increasing shaft compliance has two mentionable effects, which can both be seen in fig. 4c. Firstly, the expansion of the unstable region in σ is reduced. Secondly, the critical value of the rpm-parameter is decreased.

The mass ratio η of journal and rotor does not seem to have a significant influence (cf. fig. 4d) and is therefore considered to be rather irrelevant.

As it can be seen in the depicted cases, there exists a critical range between $\sigma \approx 10^{-2}$ and $\sigma \approx 10^{-1}$, in which the stability is lost at quite small values of the rpm-parameter, no-matter how the parameters are chosen. This is considered to be the critical case for which the described idea of a time-varying bearing geometry should come into play.

3.2 Varying Bearing Geometry

In the following section the geometry variation from eq. (2) with relative amplitude $\delta_U \neq 0$ and frequency Ω_U is used.

As it is shown for the famous MATTHIEU equation in the context of the inverse pendulum problem (e.g. in [5]), a stabilization can be reached by an appropriate parametric excitation. Nevertheless, the problem of self-excitation is not considered in this classical example.

Focusing on systems with multiple degrees of freedom, the problem becomes rather complex, as the different degrees can also interact. NAYFEH [19] describes that there exist several resonance cases in such systems: Internal or external as primary, secondary or combination-type resonances. E.g. in the case of internal resonances, energy is continuously exchanged between the involved modes. If one of these participating modes is damped, the system's energy will be continuously reduced as it is being exchanged.

This conceptual idea was taken by TONDL [27,28] who describes for the simplified case of a linear system, how parametric excitations can be used to obtain a coupling of different system modes, such that an energy exchange between a self-excited mode and another 'damped' mode is enforced, resulting in a suppression of the self-excited oscillations. It turns out that this effect can be reached for certain sets of combination frequencies (cf. [28]). Many adoptions of this stabilization effect can be found as well in literature, e.g. in [12,13].

Based on the described idea, a stability analysis of the trivial solution of the rotor system under the influence of the parametric excitation is performed by means of FLOQUET analysis.

Recalling the previous results from fig. 4 the value $\sigma = 6 \cdot 10^{-2}$ within the critical range of the bearing load parameter is chosen along with the parameter set (13). For this case of a static bearing geometry (i.e. $\delta_U = 0$) the stability of the trivial solution is lost at $\bar{\omega} \approx 1.9$.

Various stability maps in the $\bar{\omega} - \Omega_U$ -parameter plane for different, non-vanishing excitation amplitudes $\delta_U \neq 0$ are depicted in figs. 5 to 7. The shaded areas thereby represent parameter configurations for which the trivial solution is unstable.

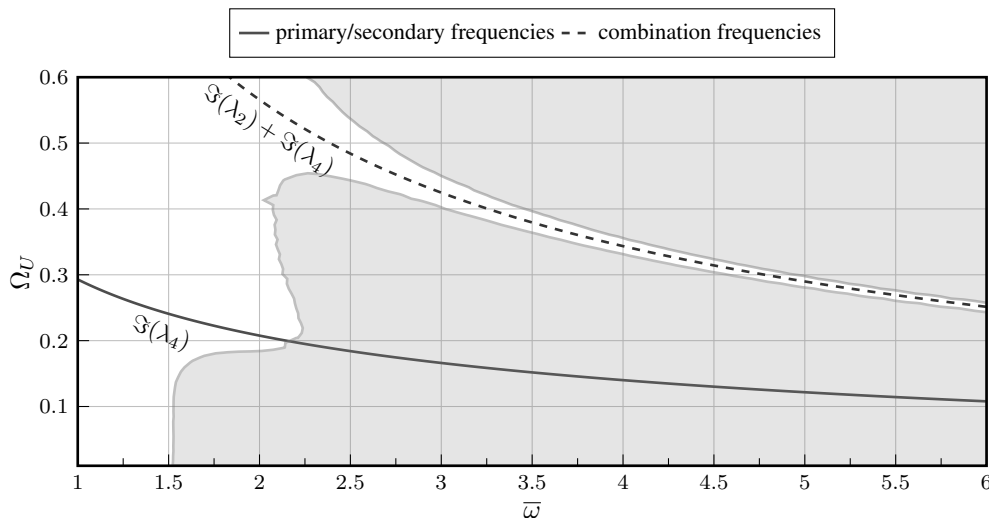


Figure 5: Stability map for $\delta_U = 0.2$ (shaded: unstable)

In fig. 5 the different effects of the applied parametric excitation can be seen. For small excitation frequencies the stable region is decreased to lower rpm values ($\bar{\omega} \approx 1.5$) compared to the case of a static geometry. The results in figs. 6 and 7 emphasize the fact that an increasing amplitude δ_U in the lower frequency domain of the excitation has a destabilizing effect. A recall of the results for the inverse pendulum in [5] could validate this observation. As an overall effect, an increasing frequency Ω_U seems to have some kind of 'dominant' stabilizing effect. The stable region on the left-hand sides of the diagrams is extended to higher rpm values. Assuming no dominant mode interaction in this region, this result could also be explained by the inverse pendulum problem (cf. [5]).

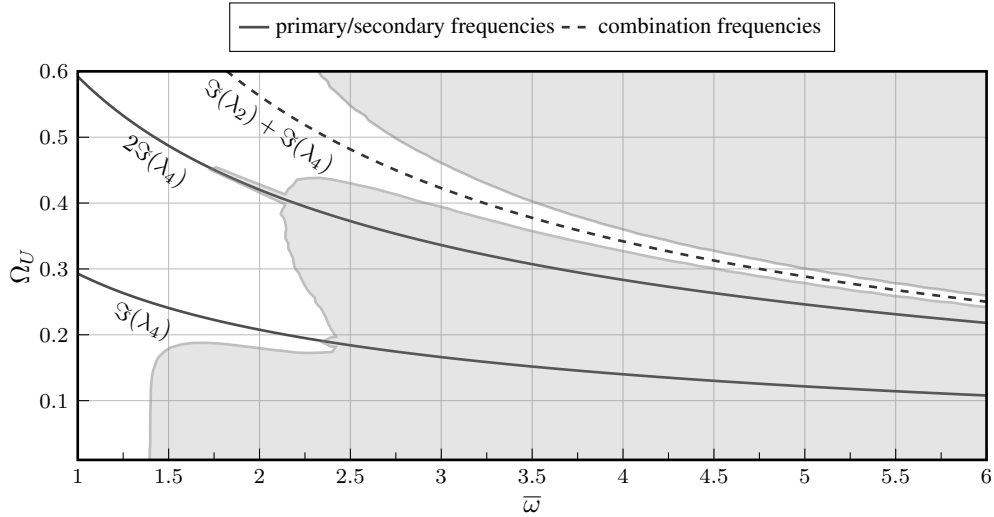


Figure 6: Stability map for stronger excitation $\delta_U = 0.25$ (shaded: unstable)

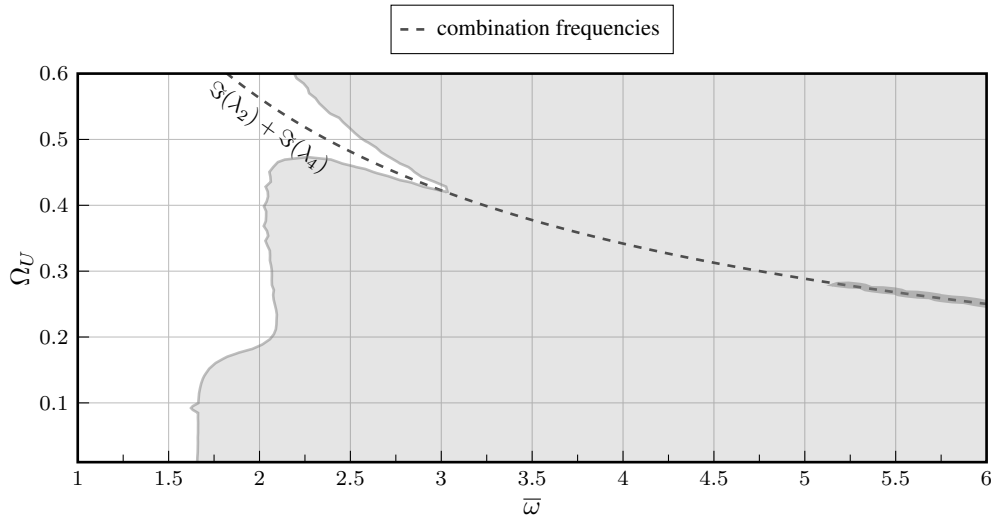


Figure 7: Stability map for weaker excitation $\delta_U = 0.15$ (shaded: unstable)

Before proceeding to further effects, it is focused on the system's behaviour without parametric excitation. Figure 8 depicts the real and imaginary parts of the eigenvalues λ_i of the trivial solution for the static bearing, which have been computed according to the characteristic equation:

$$\det \left(\left. \frac{df(\delta_U = 0)}{dz} \right|_{z_0} - \lambda \mathbf{1} \right) = 0. \quad (14)$$

In the regarded range four pairs of complex conjugated eigenvalues are obtained, whereby $\Im(\lambda_i)$ ($i = 1..4$) denote the positive eigenfrequencies. The eigenvalue λ_4 thereby belongs to the only unstable mode ($\Re(\lambda_4) > 0$) caused by the self-excitation.

Using the computed eigenvalues back in fig. 5, it can be shown that the stable region follows exactly the curve of the combination frequency $\Omega_U = \Im(\lambda_2) + \Im(\lambda_4)$. It is assumed that this frequency links the unstable mode corresponding to λ_4 to another damped mode, such that the above described energy transfer takes place and the self-excited oscillations can be suppressed.

Focusing on figs. 6 and 7 it is obvious that the desired 'coupling' highly depends on a sufficiently large excitation amplitude δ_U . As δ_U can be interpreted as coupling strength, there definitely exist parameter constellations which require a higher coupling strength than others in order to allow the desired stabilization; i.e. in fig. 7 the stable

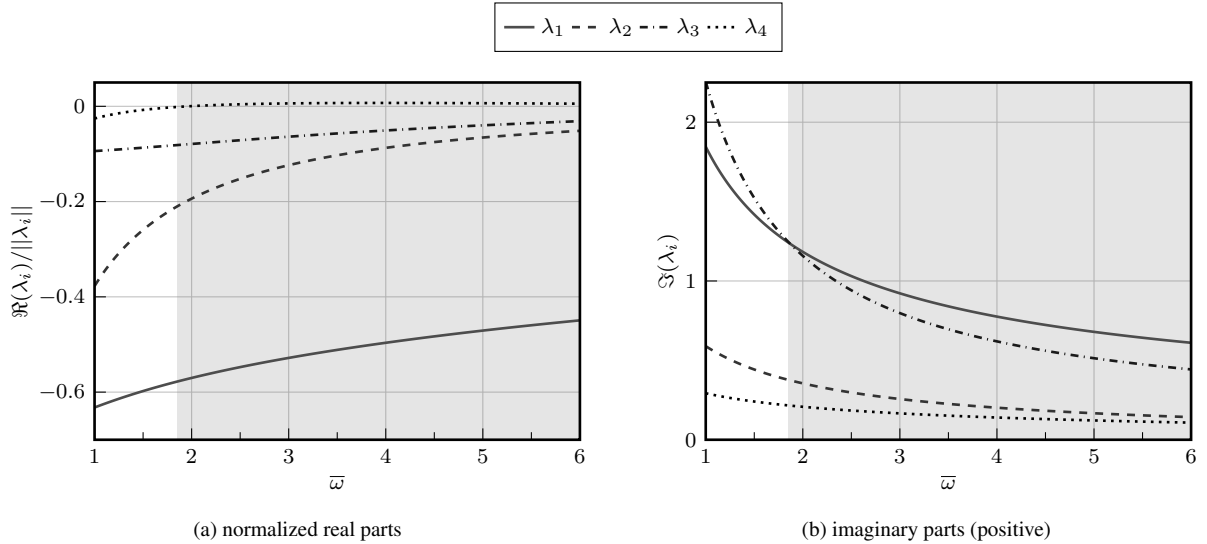


Figure 8: Pairs of conjugated Eigenvalues in dependence of $\bar{\omega}$ for $\delta_U = 0$ (shaded: unstable solution)

region is completely lost between $\bar{\omega} \approx 3$ and $\bar{\omega} \approx 5.2$ in the case of a weaker excitation.

Furthermore, the influence of a secondary parametric resonance can be seen in fig. 6 for a stronger excitation. The frequency of the secondary type $\Omega_U = 2\Im(\lambda_4)$ has a clear destabilizing effect.

The unusual topology of the stability border at this point could be explained by the competitive effects of the secondary resonance and the previously described 'dominant' stabilization caused by an increasing frequency Ω_U .

4 Conclusion and Outlook

A significant influence of journal bearings with non-circular profile on the dynamic behaviour of a Jeffcott rotor system has been shown. Besides the stabilizing effect of a static non-cylindrical geometry in the case of a vertical rotor, also a positive influence of a time-varying bearing geometry has been shown.

In order to assess the stability properties a FLOQUET analysis has been performed in the considered parameter regions. As the parametric excitation enforces some kind of mode-coupling, self-excited oscillations in the higher rpm-ranges can be completely suppressed. In this context a strong dependence on the eigenfrequencies of the corresponding linearised system has been revealed, emphasizing the described approach of a mode coupling.

In case of a horizontal rotor, which involves additional static loads (e.g. through gravity), no equilibrium solution exist anymore and the system performs small periodic oscillations even in parameter ranges without any self-excitation effects. In this special case an investigation by means of a FLOQUET analysis is considered to be rather complicated, if not impossible due to potentially occurring incommensurable frequencies.

Apart from that, the assessment of the stability via a FLOQUET analysis is rather time-consuming as transient simulations have to be performed for a huge set of parameter combinations. Therefore, future works will deal with a more elaborated approach for a systematic investigation by means of an associated spectral system (cf. [25]), which has yielded already promising results in former works (cf. [3, 4]).

Furthermore, the modelling is about to be improved, which comprises an inclusion of an elastic bearing deformation due to the pressure field (cf. [30]) as well as the usage of circumferential terms in the REYNOLDS equation.

REFERENCES

- [1] Allaire, P., Flack, R., et al.: Design of journal bearings for rotating machinery. In: Proceedings of the 10th Turbomachinery Symposium (1981)
- [2] Becker, K.: Ovally deformed journal bearing (2018). DOI 10.5445/IR/1000086134
- [3] Becker, K., Seemann, W.: A Journal Bearing with actively modified geometry for extending the parameter-based stability range of rotor dynamic systems. In: ISROMAC 16 proceedings (2016)
- [4] Becker, K., Seemann, W.: Approximation of quasi-periodic solutions of a rotor in two-lobe bearings with time-varying geometry. PAMM **16**(1), 263–264 (2016)
- [5] Blackburn, J.A., Smith, H., Gro/nbech-Jensen, N.: Stability and hopf bifurcations in an inverted pendulum. American journal of physics **60**(10), 903–908 (1992)

- [6] Boyaci, A.: Zum Stabilitäts-und Bifurkationsverhalten hochtouriger Rotoren in Gleitlagern, vol. 15. Schriftenreihe des Instituts für Technische Mechanik, KIT Scientific Publishing (Ph.D. thesis, 2012)
- [7] Chasalevris, A., Dohnal, F.: A Journal Bearing With Variable Geometry for the Reduction of the Maximum Amplitude During Passage Through Resonance. *Journal of Vibration and Acoustics* **134**(6), 061,005 (2012)
- [8] Chasalevris, A., Dohnal, F.: A journal bearing with variable geometry for the suppression of vibrations in rotating shafts: Simulation, design, construction and experiment. *Mechanical Systems and Signal Processing* **52**, 506–528 (2015)
- [9] Childs, D.W.: *Turbomachinery Rotordynamics: Phenomena, Modeling and Analysis*. John Wiley & Sons (1993)
- [10] Deckler, D., Veillette, R., Braun MJ .and Choy, F.: Simulation and control of an active tilting-pad journal bearing. *Tribology transactions* **47**(3), 440–458 (2004)
- [11] Dhooge, A., Govaerts, W., Kuznetsov, Y.: MATCONT: a MATLAB package for numerical bifurcation analysis of ODEs. *ACM Transactions on Mathematical Software (TOMS)* **29**(2), 141–164 (2003)
- [12] Dohnal, F.: Damping by parametric stiffness excitation: resonance and anti-resonance. *Journal of Vibration and Control* **14**(5), 669–688 (2008)
- [13] Dohnal, F.: General parametric stiffness excitation–anti-resonance frequency and symmetry. *Acta Mechanica* **196**(1-2), 15–31 (2008)
- [14] Gasch, R., Nordmann, R., Pfützner, H.: *Rotordynamik*. Springer-Verlag (2006)
- [15] Krodziewski, J., Sun, L.: Modelling of multi-bearing rotor systems incorporating an active journal bearing. *Journal of Sound and Vibration* **210**(2), 215–229 (1998)
- [16] Kumar, A., Sinhasan, R., Singh, D.: Performance characteristics of two-lobe hydrodynamic journal bearings. *Journal of Tribology* **102**(4), 425–429 (1980)
- [17] Lang, O., Steinhilper, W.: *Gleitlager. konstruktionsbücher* bd. 31 (1979)
- [18] Malik, M.: A comparative study of some two-lobed journal bearing configurations. *ASLE TRANSACTIONS* **26**(1), 118–124 (1983)
- [19] Nayfeh, A., Mook, D.: *Nonlinear oscillations*. John Wiley & Sons (2008)
- [20] Pfau, B., Rieken, M., Markert, R.: Numerische Untersuchungen eines verstellbaren Gleitlagers zur Unterdrückung von Instabilitäten mittels Parameter-Antiresonanzen. In: *First IFToMM DA-CH* (2015)
- [21] Prescott, J.: *Applied elasticity*. Longmans, Green and Co. (1924)
- [22] Przybyłowicz, P.: Active stabilisation of a rigid rotor by piezoelectrically controlled mobile journal bearing system **1**(2), 123–128
- [23] Santos, I.: *Design and evaluation of two types of active tilting pad journal bearings* (1994)
- [24] Santos, I.: Trends in controllable oil film bearings. In: *IUTAM symposium on emerging trends in rotor dynamics*, pp. 185–199. Springer (2011)
- [25] Schilder, F., Vogt, W., Schreiber, S., Osinga, H.: Fourier methods for quasi-periodic oscillations. *International journal for numerical methods in engineering* **67**(5), 629–671 (2006)
- [26] Szeri, A.: *Fluid film lubrication: theory and design*. Cambridge University Press (2005)
- [27] Tondl, A., Ecker, H.: On the problem of self-excited vibration quenching by means of parametric excitation. *Archive of Applied Mechanics* **72**(11-12), 923–932 (2003)
- [28] Tondl, A., Püst, L.: To the parametric anti-resonance application. *Engineering Mechanics* **17**(2), 135–144 (2010)
- [29] Tůma, J., Šimek, J., Škuta, J., Los, J.: Active vibrations control of journal bearings with the use of piezoactuators. *Mechanical Systems and Signal Processing* **36**(2), 618–629 (2013)
- [30] van de Vrande, B.: *Nonlinear dynamics of elementary rotor systems with compliant plain journal bearings*. Technische Universiteit (2001)
- [31] Wu, A., De Queiroz, M.: A new active tilting-pad bearing: Nonlinear modeling and feedback control. *Tribology Transactions* **53**(5), 755–763 (2010)

An extension of the bearing database method to enable nonlinear transient analysis in the standard rotordynamic design evaluation of turbomachinery

Athanasios Chasalevris¹

¹ School of Mechanical Engineering, National Technical University of Athens, 15780, Athens, Hellas,
chasalevris@mail.ntua.gr

Abstract

Fixed profile bearings for industrial applications of medium and high speed are implemented in transient rotordynamic analysis with bearing subroutines called at every discrete time step of integration. Despite the development of bearing numerical solutions in terms of accuracy and time efficiency, the evaluation of bearing impedance forces requires still a considerable net time in transient rotor dynamic analysis of MDOF systems like industrial turbines and turbosystems. The database method renders a severe reduction (up to hundred times compared with direct method) of evaluation time spent on the bearing models in a transient rotor run-up, and has been widely applied in bearings of mostly plain circular profile. The current paper presents the implementation of the method in fixed geometry journal bearings (of complex geometry) for industrial applications. The application covers the generic case of noncircular profile (preloaded pad) with the fluid film thickness functions and boundary conditions for the lubrication problem (Reynolds equation) to include the parameters of the journal mobility (position and velocity) and also the respective bearing profile coordinates. A four parametric database can be established with those parameters to vary in a certain range (-1 to 1) that allows the construction of a database. Enhanced THD bearing models can be implemented through the use of parallel processing for the construction of the database. A 4-D interpolation (linear or Lagrange interpolation) is then applied in the database and the bearing model output (forces and moments) are implemented in the rotordynamic algorithm up to 100 times faster compared to the conventional approach (solution of the lubrication problem at every discrete time step). The method is presented in this paper and is applied in a large medium speed system of a turbine-generator. The resulting run up time is reduced to one third, and this support the consideration of nonlinear transient analysis in standard rotordynamic design evaluation of large rotating machinery.

1 Introduction

In most rotor bearing systems of medium and high speed, the fluid film bearing forces have to be solved at every discrete time step of the integration of system equations when nonlinear transient response is evaluated. This may require a considerable evaluation time spent on bearing subroutines of the rotordynamic algorithm. The evaluation time is a very important matter in rotordynamic design tools as the engineer should be able to try geometrical and physical properties conveniently, in terms of time required to get results for unbalance response and other standard calculations. Due to the fact that the accurate and relatively fast analytical models of finite length journal bearing forces are still cumbersome (and available only for simple bearing profiles) [1,2], and that despite the computational capacity of computers, the numerical bearing models may still require a considerable sum of evaluation time (for an entire rotor run-up), a database model for any complex profile bearing of fixed profile has been proposed to overcome the above shortcomings [3-5].

For all rotor systems supported by fluid film bearings, the linear stability assessment which implements linear bearing stiffness and damping properties (the well-known 8 matrix elements), is not able to predict response at speeds higher than the instability threshold. Further to that, and probably of higher importance, is the fact that the linear theory (linear bearing properties and linear stability assessment) cannot predict that originally stable systems may go unstable when a sudden external excitation is applied. For these major reasons, the nonlinear stability study has attracted more and more attention [4].

The most popular ways to implement nonlinear fluid film forces is the direct solving of the Reynolds equation [6-8], the approximate short and long bearing theory [6-8], and the use of higher order stiffness and

damping coefficients [6-8]. Millions of integration steps are required to evaluate a transient rotor bearing response and the Reynolds equation is repeatedly solved in each of these time steps. Supposing a multi-bearing shaft train, the Reynolds equation should be solved for each bearing. Even for a high speed turbocharger rotor mounted on floating ring bearings, the Reynolds equation should be solved four times at each time step of the transient response (two bearings, and two films at each bearing). The approximate methods are very fast, but their accuracy is not applicable in common bearing profiles e.g. of industrial turbines, as their length to diameter ratio neither corresponds to a short nor a long bearing.

The database technique, developed initially in [9], puts forward a fast and accurate implementation of fluid film forces in rotordynamic algorithms. Application of the method on simple bearing profiles and Jeffcott rotor has proved that the method not only had practically the same accuracy as the direct solving method, but also reduced dramatically the computation time of transient response. Recently, the method was applied in grooved floating ring bearings [10] where it was shown that transient response of turbosystems with simple circular floating rings can be evaluated on such a low time that enables different considerations on the design of such systems.

The key to apply the database technique is on the transformation of the Reynolds equation parameters varying theoretically from $-\infty$ to ∞ (velocity of the journal in two directions) to the variation on a finite range e.g. from -1 to 1. This is described in this paper for the representative case of a fixed lobe bearing of complex geometry (industrial applications) in different way than what presented before [3-5,9,10]. The difference is that 4 parameters are considered in the database, enabling the calculation of oil film forces for a flow on a theoretically arbitrary profile. The key benefit of the current approach is that the database may consider the position of the journal attitude angle with respect to the bearing profile configuration (e.g. scallops) when talking for a fixed profile bearing. Furthermore, with the current approach, the database can be established for the case of floating ring bearings where the floating ring includes radial holes for the communication of oil between inner and outer film, and axial grooves as well. In the current paper, only the fixed lobe bearing profile is considered, and the example of floating ring bearing with axial grooves or radial holes is considered for a future work.

Another benefit of the database method is that a very precise journal bearing model can be considered, including e.g. evaluation using commercial edge tools on THD lubrication principles. Parallel processing can be applied for the a priori to the rotordynamic analysis creation of the database with respect to the 4 parameter variation within finite range intervals (sparse or dense). However, in this paper, a Finite Difference Method (FDM) is used to evaluate the lubricant pressure depending on the four parameters of the database, without the type of the numerical solution to be restrictive for the applicability of the method. Using the database method, a very precise prediction of the bearing performance (e.g. using CFD) can be implemented in a rotordynamic algorithm as fast as a simple solution (e.g. Finite Difference Method using Gumbel boundary condition).

The paper presents the application of the database method in a turbine shaft train consisting of 3 rotors connected with rigid couplings. and 4 oil film bearings with profile which combines partial circular arcs. As a general rule, if two bearings have equal dimensionless geometric parameters (e.g. length to diameter ratio, clearance to radius ratio), then the oil film forces can be deducted from the same database. However, if a dimensional geometrical or physical parameter is different (e.g. dynamic viscosity), then two different databases are needed (one for each dynamic viscosity value). The rotors are modelled using the Transient Transfer Matrix Method (TTMM) [11], and the bearings are modelled using the FDM with the Gumbel's boundary condition applying. The model includes flexible bearing pedestals as lumped mass models on linear springs and dampers.

The results depict the considerable reduction of the evaluation time for a rotor run-up from 0 to 3000RPM to approximately one third of the time needed when bearing forces are implemented directly. The evaluation time spent solely on the call-return of one bearing subroutine is reduced from 0.022s to 0.00038s; the bearing database returns the oil film forces c.a. 100 times faster than the direct method (solution of the Reynolds and calculation of forces). Depending on the rotordynamic problem (type of machine), the bearing database method can reduce the evaluation time of the entire rotordynamic algorithm at a similar level (100 times); this happens for systems with few degrees of freedom, e.g. a rigid rotor mounted on floating ring bearings – simulation of a turbocharger. Depending on the time consumption of the bearing subroutine with respect to the overall calculations, the database method renders a corresponding reduction of the total evaluation time.

2 The database method and its application in journal bearings of fixed profile

A journal bearing of fixed geometry is represented in figure 1. As a matter of generality, the bearing consists of two circular sectors: a) a concentric to the bearing centre $O_B(x_B, y_B)$ circular sector of radius R_B for $\theta_S < \theta < \theta_E$, and b) a circular sector of radius R_L , for $\theta < \theta_S$ or $\theta > \theta_E$, centred at $O_L(x_L, y_L)$. The latter sector is a preloaded lobe (preloaded pad) as its centre does not coincide to the bearing centre. Such a geometric configuration increases the journal bearing effective eccentricity and this is the principle behind the enhanced bearing stability of preloaded bearings [6-7], known also as elliptical bearings or lobe bearings. When the journal

centre $O_j(x_j, y_j)$ does not coincide to the bearing centre O_B , the eccentricity $e = (x_j^2 + y_j^2)^{1/2}$ forms a fluid film thickness h between the sliding surfaces of the journal and the bearing, well approximated by the formulas in equation (1), which can be expressed in dimensionless form as $H = h/c_B$.

$$h = \begin{cases} c_B - (x_j - x_B) \cdot \cos(\theta) - (y_j - y_B) \cdot \sin(\theta), \theta_S \leq \theta \leq \theta_E \\ c_P - (x_j - x_L) \cdot \cos(\theta) - (y_j - y_L) \cdot \sin(\theta), \theta < \theta_S \text{ or } \theta > \theta_E \end{cases} \quad (1)$$

In equation (1), $x_B = y_B = x_L = 0$ (see figure 1), while $y_L \neq 0$; $c_B = R_B - R$ is the bearing clearance (or assembly clearance), and $c_P = R_L - R$ is the pad clearance (or machined pad clearance). It is clear that in figure 1, $c_P > c_B$ (or $R_L > R_B$), and thus the lobe sector is preloaded with a preload $m = 1 - c_B/c_P$. Furthermore, the bearing has a length L_B in Z direction, the lubricant is characterized by a dynamic viscosity μ which for simplicity is assumed constant in this paper (isoviscous flow of the lubricant), and the journal rotates around its centre with a rotating speed Ω (spinning speed). Under dynamic conditions, the journal will perform whirling motion inside the bearing clearance, with velocities \dot{x}_j and \dot{y}_j .

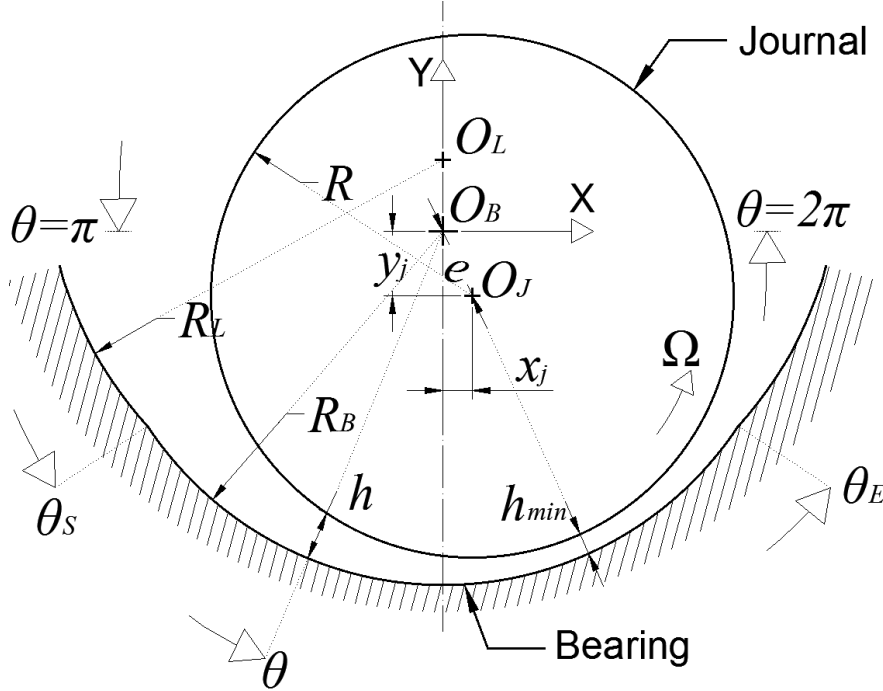


Figure 1: Representation of a fixed geometry journal bearing and its key geometric properties.

The lubrication problem (evaluation of lubricant pressure distribution inside the bearing clearance for laminar isothermal flow) is defined by the Reynolds equation which includes all the previously defined geometric and physical parameters, see equation (2) [6,7].

$$\frac{1}{\mu R^2} \frac{\partial}{\partial \theta} \left(h^3 \frac{\partial p}{\partial \theta} \right) + \frac{h^3}{\mu} \frac{\partial^2 p}{\partial x^2} = 6\Omega \frac{\partial h}{\partial \theta} + 12 \frac{dh}{dt} \quad (2)$$

With the use of equation (1), the right hand side (RHS) of equation (2) is written now after some math as in equation (3).

$$\text{RHS} = (6\Omega x_j - 12\dot{y}_j) \sin \theta - (6\Omega y_j + 12\dot{x}_j) \cos \theta \quad (3)$$

Setting dimensionless variables in equation (4), equation (2) is written in equation (5).

$$\bar{p} = \frac{c_B^2 p}{\mu \Omega R^2}, \varepsilon_x = \frac{x_j}{c_B}, \varepsilon_y = \frac{y_j}{c_B}, \dot{\varepsilon}_x = \frac{\dot{x}_j}{c_B}, \dot{\varepsilon}_y = \frac{\dot{y}_j}{c_B}, \dot{\varepsilon}_x = \frac{\dot{\varepsilon}_x}{\Omega}, \dot{\varepsilon}_y = \frac{\dot{\varepsilon}_y}{\Omega}, k = \frac{2R}{L}, \bar{x} = \frac{2x}{L}, \dot{\phi} = \frac{x_j \dot{y}_j - y_j \dot{x}_j}{\varepsilon_x^2 + \varepsilon_y^2} \quad (4)$$

$$\frac{\partial}{\partial \theta} \left(H^3 \frac{\partial \bar{p}}{\partial \theta} \right) + k^2 H^3 \frac{\partial^2 \bar{p}}{\partial \bar{x}^2} = (6\varepsilon_x - 12\dot{\varepsilon}_y) \sin \theta - (6\varepsilon_y + 12\dot{\varepsilon}_x) \cos \theta \quad (5)$$

The problem on establishing a database for bearing performance directly from the Reynolds equation is that while the input parameters ε_x and ε_y can receive values within the domain $-1 < \varepsilon_x, \varepsilon_y < 1$, the rest input parameters $\dot{\varepsilon}_x, \dot{\varepsilon}_y$ cannot be defined within a specific domain. To overcome this problem, Reynolds equation in the form of equation (5) is divided by $\varepsilon(1 - 2\dot{\phi}')$, where $\varepsilon = e/c_B$, $\dot{\phi}' = \dot{\phi}/\Omega = \dot{\phi}/(c_B^2 \Omega)$. Then, Reynolds

equation can be written in equation (6) with the new variables and functions to be defined in equations (7) and (8).

$$3H^2H_\theta \frac{\partial \bar{p}'}{\partial \theta} + H^3 \frac{\partial^2 \bar{p}'}{\partial \theta^2} + k^2 H^3 \frac{\partial^2 \bar{p}'}{\partial \bar{x}^2} = 6\bar{x}_1 \sin \theta - 6\bar{x}_2 \cos \theta \quad (6)$$

$$\bar{p}' = \frac{\varepsilon \bar{p}}{\varepsilon^2 - 2\varepsilon_x \dot{\varepsilon}_y + 2\varepsilon_y \dot{\varepsilon}_x}, \bar{x}_1 = \frac{\varepsilon(\varepsilon_x - 2\dot{\varepsilon}_y)}{\varepsilon^2 - 2\varepsilon_x \dot{\varepsilon}_y + 2\varepsilon_y \dot{\varepsilon}_x}, \bar{x}_2 = \frac{\varepsilon(\varepsilon_y + 2\dot{\varepsilon}_x)}{\varepsilon^2 - 2\varepsilon_x \dot{\varepsilon}_y + 2\varepsilon_y \dot{\varepsilon}_x} \quad (7)$$

$$H_\theta = \frac{\partial H}{\partial \theta} = \varepsilon_x \sin \theta - \varepsilon_y \cos \theta \quad (8)$$

Reynolds equation (6) can be solved with the four variables \bar{x}_1 , \bar{x}_2 , ε_x , ε_y to receive specific values in the domain (-1,1). The solution can be a numerical solution scheme e.g. Finite Difference Method. Supposing that the FDM is implemented, with a definition of finite difference grid as $N_x \times N_\theta$, the respective intervals are defined as $\Delta x = L_B/N_x$ and $\Delta \theta = (\theta_E - \theta_S)/N_\theta$. The angles θ_S and θ_E can be any angles on the circumference if the corresponding fluid film functions have been defined. Two cases are defined for the evaluation of \bar{p}' :

1) When $1 - 2\dot{\phi}' > 0$, the resulting fluid film forces are given in dimensionless form in equation (9):

$$\begin{Bmatrix} \bar{F}'_{x+} \\ \bar{F}'_{y+} \end{Bmatrix} = \begin{Bmatrix} -\sum_{i=1}^{N_x} \sum_{j=1}^{N_\theta} (\Delta x \cdot \Delta \theta \cdot \bar{p}'_{i,j} \cdot \cos \theta_j) \\ -\sum_{i=1}^{N_x} \sum_{j=1}^{N_\theta} (\Delta x \cdot \Delta \theta \cdot \bar{p}'_{i,j} \cdot \sin \theta_j) \end{Bmatrix} \quad (9)$$

For Gumbel boundary conditions, only $\bar{p}'_{i,j} > 0$ values are implemented in the double sum.

2) When $1 - 2\dot{\phi}' < 0$, the resulting fluid film forces are given in dimensionless form in equation (10):

$$\begin{Bmatrix} \bar{F}'_{x-} \\ \bar{F}'_{y-} \end{Bmatrix} = \begin{Bmatrix} -\sum_{i=1}^{N_x} \sum_{j=1}^{N_\theta} (-\Delta x \cdot \Delta \theta \cdot \bar{p}'_{i,j} \cdot \cos \theta_j) \\ -\sum_{i=1}^{N_x} \sum_{j=1}^{N_\theta} (-\Delta x \cdot \Delta \theta \cdot \bar{p}'_{i,j} \cdot \sin \theta_j) \end{Bmatrix} \quad (10)$$

For Gumbel boundary conditions, only $\bar{p}'_{i,j} < 0$ values are implemented in the double sum.

In both cases 1) and 2) the resulting fluid film forces in dimensional form are defined in equation (11).

$$\begin{Bmatrix} F_x \\ F_y \end{Bmatrix} = \frac{\mu \Omega R^3}{c_B^2} \varepsilon (1 - 2\dot{\phi}') \begin{Bmatrix} \bar{F}'_x \\ \bar{F}'_y \end{Bmatrix} \quad (11)$$

The bearing forces database **dat** can be then constructed simply as in equation (12) where variables ε_x and ε_y vary from the value -0.9 to the value 0.9 within INT = 100 intervals, while variables \bar{x}_1 and \bar{x}_2 vary from the value -0.99 to the value 0.99 within 100 intervals. Further columns can be added in the database corresponding to further outputs like e.g. resulting frictional moment. The number of INT=100 intervals can be sufficient to create a database that corresponds well in the demands for bearing forces under mild dynamic conditions (relatively low response around equilibrium). However, parallel processing can offer higher number of intervals (e.g. 400 or even 600) with the number of intervals to be different for each variable. It makes sense the database **dat** to include combinations of ε_x and ε_y such that they will render $\varepsilon = (\varepsilon_x^2 + \varepsilon_y^2)^{1/2} < 1$.

For the use of the database in a rotordynamic algorithm for transient response analysis a 4-D interpolation should be implemented. The interpolation scheme can be linear or of higher order. The linear 4-D interpolation is presented hereby and the results following in the next sections depict its efficiency.

for i,j,k,m from 1 to INT

$$\begin{aligned} \mathbf{dat}(i, j, k, m, 1) &= \bar{F}'_{y+}(\varepsilon_{x,i}, \varepsilon_{y,j}, \bar{x}_{1,k}, \bar{x}_{2,m}) \\ \mathbf{dat}(i, j, k, m, 2) &= \bar{F}'_{x+}(\varepsilon_{x,i}, \varepsilon_{y,j}, \bar{x}_{1,k}, \bar{x}_{2,m}) \\ \mathbf{dat}(i, j, k, m, 3) &= \bar{F}'_{y-}(\varepsilon_{x,i}, \varepsilon_{y,j}, \bar{x}_{1,k}, \bar{x}_{2,m}) \\ \mathbf{dat}(i, j, k, m, 4) &= \bar{F}'_{x-}(\varepsilon_{x,i}, \varepsilon_{y,j}, \bar{x}_{1,k}, \bar{x}_{2,m}) \end{aligned} \quad (12)$$

next m,k,j,i

At a discrete time moment of transient response, the bearing model should require at least 5 input variables in order to render the output forces and moments: the horizontal and vertical displacement of the journal x_j and y_j , their respective velocities \dot{x}_j and \dot{y}_j , and the rotating speed Ω . When the bearing support motion is included as a parameter in the algorithm, the journal bearing lubrication problem still requires five inputs: two relative displacements and two relative velocities of the journal with respect of the bearing, and the rotating speed. Suppose that a group of $x_j, y_j, \dot{x}_j, \dot{y}_j$, and Ω are rendered from the dynamic problem to the bearing subroutine at the time moment t_1 , then the four variables $\varepsilon_x, \varepsilon_y, \bar{x}_1$, and \bar{x}_2 are computed from equations (4) and (7). If INT is the number of intervals for each variable (as in Table of equation (12)), then the index $a_2, \beta_2, \gamma_2, \delta_2$ (real numbers) of each variable in the database (equation (12)) that corresponds to the actual values $\varepsilon_x, \varepsilon_y, \bar{x}_1, \bar{x}_2$ will be defined in equation (13). Then the side indexes will be defined as $a_1, \beta_1, \gamma_1, \delta_1$ (integers) and $a_0, \beta_0, \gamma_0, \delta_0$ (integers) in equation (13).

$$\begin{pmatrix} a_2 \\ \beta_2 \\ \gamma_2 \\ \delta_2 \end{pmatrix} = \begin{pmatrix} \frac{\varepsilon_x + 0.90 + 2 \cdot 0.90 / (\text{INT} - 1)}{2 \cdot 0.90 / (\text{INT} - 1)} \\ \frac{\varepsilon_y + 0.90 + 2 \cdot 0.90 / (\text{INT} - 1)}{2 \cdot 0.90 / (\text{INT} - 1)} \\ \frac{\bar{x}_1 + 0.99 + 2 \cdot 0.99 / (\text{INT} - 1)}{2 \cdot 0.99 / (\text{INT} - 1)} \\ \frac{\bar{x}_2 + 0.99 + 2 \cdot 0.99 / (\text{INT} - 1)}{2 \cdot 0.99 / (\text{INT} - 1)} \end{pmatrix}, \quad \begin{pmatrix} a_1 \\ \beta_1 \\ \gamma_1 \\ \delta_1 \end{pmatrix} = \begin{pmatrix} \text{ceil}(a_2) \\ \text{ceil}(\beta_2) \\ \text{ceil}(\gamma_2) \\ \text{ceil}(\delta_2) \end{pmatrix}, \quad \begin{pmatrix} a_0 \\ \beta_0 \\ \gamma_0 \\ \delta_0 \end{pmatrix} = \begin{pmatrix} a_1 - 1 \\ \beta_1 - 1 \\ \gamma_1 - 1 \\ \delta_1 - 1 \end{pmatrix} \quad (13)$$

For a 4-D interpolation, $4 \times 4 = 16$ coefficients should be calculated in order to implement the interpolation of the given values in the database [13]. Furthermore, the sign of $1 - 2\dot{\varphi}'$ will indicate if the dimensionless forces should be collected from the $\bar{F}'_{x+}, \bar{F}'_{y+}$ values, or from the $\bar{F}'_{x-}, \bar{F}'_{y-}$ values. The 16 coefficients are defined in equation (14).

$$\begin{aligned} N_1 &= (a_1 - a_2)(\beta_1 - \beta_2)(\gamma_2 - \gamma_0)(\delta_2 - \delta_0), & N_9 &= (a_1 - a_2)(\beta_1 - \beta_2)(\gamma_2 - \gamma_0)(\delta_1 - \delta_2) \\ N_2 &= (a_1 - a_2)(\beta_2 - \beta_0)(\gamma_2 - \gamma_0)(\delta_2 - \delta_0), & N_{10} &= (a_1 - a_2)(\beta_2 - \beta_0)(\gamma_2 - \gamma_0)(\delta_1 - \delta_2) \\ N_3 &= (a_2 - a_0)(\beta_1 - \beta_2)(\gamma_2 - \gamma_0)(\delta_2 - \delta_0), & N_{11} &= (a_2 - a_0)(\beta_1 - \beta_2)(\gamma_2 - \gamma_0)(\delta_1 - \delta_2) \\ N_4 &= (a_2 - a_0)(\beta_2 - \beta_0)(\gamma_2 - \gamma_0)(\delta_2 - \delta_0), & N_{12} &= (a_2 - a_0)(\beta_2 - \beta_0)(\gamma_2 - \gamma_0)(\delta_1 - \delta_2) \\ N_5 &= (a_1 - a_2)(\beta_1 - \beta_2)(\gamma_1 - \gamma_2)(\delta_2 - \delta_0), & N_{13} &= (a_1 - a_2)(\beta_1 - \beta_2)(\gamma_1 - \gamma_2)(\delta_1 - \delta_2) \\ N_6 &= (a_1 - a_2)(\beta_2 - \beta_0)(\gamma_1 - \gamma_2)(\delta_2 - \delta_0), & N_{14} &= (a_1 - a_2)(\beta_2 - \beta_0)(\gamma_1 - \gamma_2)(\delta_1 - \delta_2) \\ N_7 &= (a_2 - a_0)(\beta_1 - \beta_2)(\gamma_1 - \gamma_2)(\delta_2 - \delta_0), & N_{15} &= (a_2 - a_0)(\beta_1 - \beta_2)(\gamma_1 - \gamma_2)(\delta_1 - \delta_2) \\ N_8 &= (a_2 - a_0)(\beta_2 - \beta_0)(\gamma_2 - \gamma_0)(\delta_2 - \delta_0), & N_{16} &= (a_2 - a_0)(\beta_2 - \beta_0)(\gamma_1 - \gamma_2)(\delta_1 - \delta_2) \end{aligned} \quad (14)$$

For the interpolation of \bar{F}'_x , supposing that e.g. $1 - 2\dot{\varphi}' > 0$, 16 values of \bar{F}'_x are picked from the database **dat**, corresponding to all combinations of the integer indexes evaluated in equation (13), as in equation (15).

$$\begin{aligned} \bar{F}'_{x,1} &= \mathbf{dat}(a_0, \beta_0, \gamma_1, \delta_1, 2), \bar{F}'_{x,5} = \mathbf{dat}(a_0, \beta_0, \gamma_0, \delta_1, 2), \bar{F}'_{x,9} = \mathbf{dat}(a_0, \beta_0, \gamma_1, \delta_0, 2), \bar{F}'_{x,13} = \mathbf{dat}(a_0, \beta_0, \gamma_0, \delta_0, 2) \\ \bar{F}'_{x,2} &= \mathbf{dat}(a_0, \beta_1, \gamma_1, \delta_1, 2), \bar{F}'_{x,6} = \mathbf{dat}(a_0, \beta_1, \gamma_0, \delta_1, 2), \bar{F}'_{x,10} = \mathbf{dat}(a_0, \beta_1, \gamma_1, \delta_0, 2), \bar{F}'_{x,14} = \mathbf{dat}(a_0, \beta_1, \gamma_0, \delta_0, 2) \\ \bar{F}'_{x,3} &= \mathbf{dat}(a_1, \beta_0, \gamma_1, \delta_1, 2), \bar{F}'_{x,7} = \mathbf{dat}(a_1, \beta_0, \gamma_0, \delta_1, 2), \bar{F}'_{x,11} = \mathbf{dat}(a_1, \beta_0, \gamma_1, \delta_0, 2), \bar{F}'_{x,15} = \mathbf{dat}(a_1, \beta_0, \gamma_0, \delta_0, 2) \\ \bar{F}'_{x,4} &= \mathbf{dat}(a_1, \beta_1, \gamma_1, \delta_1, 2), \bar{F}'_{x,8} = \mathbf{dat}(a_1, \beta_1, \gamma_0, \delta_1, 2), \bar{F}'_{x,12} = \mathbf{dat}(a_1, \beta_1, \gamma_1, \delta_0, 2), \bar{F}'_{x,16} = \mathbf{dat}(a_1, \beta_1, \gamma_0, \delta_0, 2) \end{aligned} \quad (15)$$

The interpolated values for \bar{F}'_x and \bar{F}'_y are then evaluated from equation (16). For $\bar{F}'_{y,i}$ used in equation (16), equation (15) should be written for the values **dat**(..., ..., ..., ..., 1) in advance.

$$\bar{F}'_x = \sum_{i=1}^{16} N_i \bar{F}'_{x,i}, \quad \bar{F}'_y = \sum_{i=1}^{16} N_i \bar{F}'_{y,i} \quad (16)$$

The benefit of the method is the evaluation time of bearing forces, which is decreased up to c.a. 100 times. A Lagrange interpolation scheme can be also implemented. However, the forces will not obtain that different values compared to the linear interpolation, in order to raise concerns for the type of the interpolation method. Furthermore, the bearing forces included in the database can be calculated with enhanced bearing models such as thermohydrodynamic models (THD models) from any commercial software or other code. The user should bear in mind that 4 variables is the minimum to describe the operating conditions of a non-circular bearing (e.g. lemon bore, 3-4 Lobe, offset halves, partial arc bearing). For the implementation of the method in floating ring

bearings, 4 variables are still required if the floating ring includes holes for the flow of the lubricant from the outer to the inner film. At the case of plain circular floating ring bearing without holes in the ring (or plain circular bearing), 3 variables are enough to create the database [10]. As a generic approach, if the bearing profile is always symmetric with respect to any attitude angle of the journal, then 3 variables are enough to create a database (not the case for the bearing of Figure 1). Furthermore, the method can be applied in squeeze film dampers, and other bearing elements.

3 Application in medium speed system of turbine generator shaft train

The database method in its extended form as described in previous section is applied in a rotor bearing system of an industrial turbine generator for power generation, represented in Figure 2 [12]. The system consists of three rotors and four journal bearings. The profile of the journal bearings consist of a combination of partial arcs. The central partial arc is concentric to the bearing centre (no preload), while the two partial arcs on the sides of the central are preloaded, see Figure 1. The bearings have different L/D ratios, while the ratio of pad clearance to journal radius is equal at all bearings. Therefore, due to the fact that length to diameter ratio is different, all bearings require their database. The lubricant dynamic viscosity is considered equal at all bearings. Thermal effects are not taken into account in the evaluation of bearing performance. However, thermal effects can be considered in the database method as mentioned also in Section 2, but, when a different inlet oil temperature or pressure (in general oil inlet condition) is applied, a new database has to be defined. Furthermore, each bearing is mounted on a flexible pedestal with linear properties of stiffness and damping in horizontal and vertical direction.

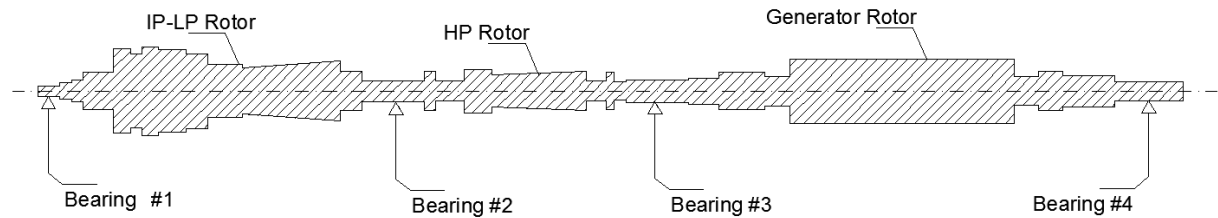


Figure 2: Representation of a turbine generator system with three rotors and four bearings.

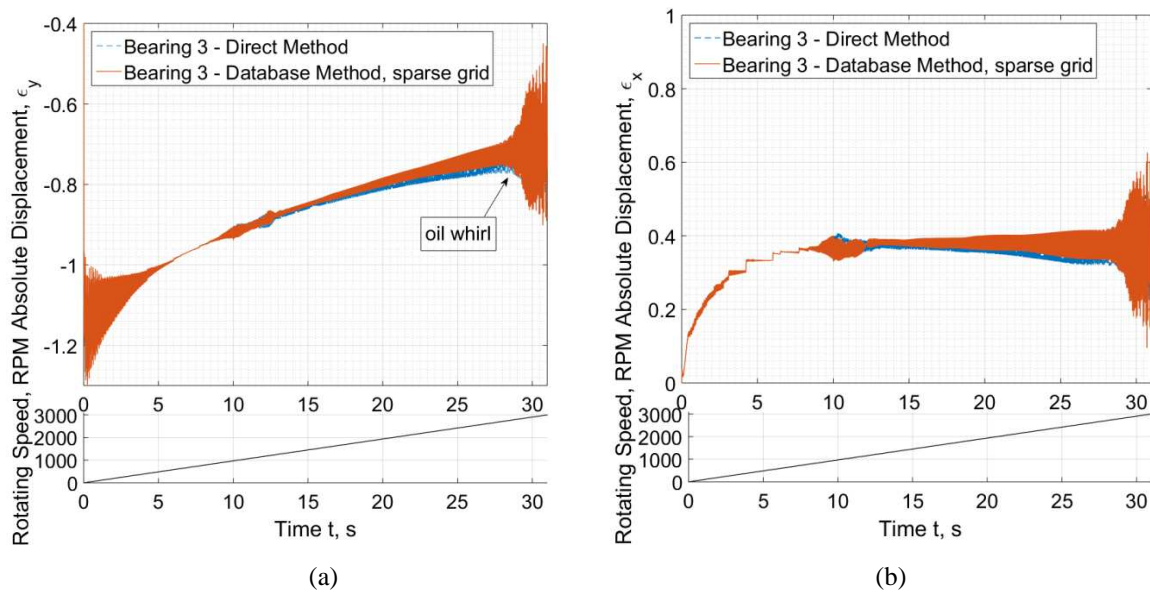


Figure 3: Relative eccentricity a) ϵ_y , and b) ϵ_x of Journal #3 at vertical plane as a function of time during run-up.

A virtual run-up of the rotor system is performed from 0 to 3000RPM with a linearly varying rotating speed for the time duration of 30s. Unbalance excitation is considered in all three rotors in positions so that 1st, 2nd, and 3rd mode of each rotor can be excited, and the unbalance magnitude is defined per ISO. The rotor system response develops some transient phenomena at the beginning of the run-up, as the initial condition locates the system approximately at the center of each bearing. After c.a. 5s these transients have been quenched and the rotor journals continue the normal lift towards the centre of the bearing as the rotating speed increases, see Figure 3a. The first critical speed of the generator rotor appears at c.a. 11s (1100RPM) with a horizontal mode, and at c.a. 13s (1300RPM) for the vertical mode. Only the response at Bearing #3 is considered in Figure 3. In Figure 3b, where the horizontal response is plotted, a stepped progress appears between c.a. 3s and 7s; this is due

to the low relative accuracy of the numerical solver at this stage of response so as the solver to proceed fast to the transient response during passage through resonance which is of more interest for the dynamics of the system. The solver implements dynamic time interval and varying relative accuracy. As the rotor approaches the speed of 2800RPM, instability occurs and the system enters a supercritical Hopf bifurcation, where under constant rotating speed the system whirls at a stable limit cycle of constant shape (extent). However, the rotating speed is increased further (end speed is 3000RPM) so as to achieve a higher response and to study the efficiency of the database method in such a case; this is why an unstable design has been chosen in this paper. Figure 3 depicts that a sparse database of 100 intervals (INT = 100, see equation (12)) is efficient to evaluate an accurate (compared to direct method) response only at relatively low amplitudes. It is clear that after the 15s, a slight divergence appears between the responses evaluated with the two methods for bearing forces. The difference is clearer at Figure 4 where the response is plotted at a narrow time range. In Figure 4a, the sparse grid (INT = 100) is efficient to render an accurate response (close to the response evaluated through the direct method) when the response is low (e.g. at 10s - 1000RPM). When the response amplitude increases (e.g. during instability at 30s), the sparse grid is not sufficient anymore as severe divergence appears between the two methods. A dense grid of e.g. INT = 600 intervals is then required to render an excellent match between the two methods (also INT = 400 can be sufficient but of not that excellent match). The number of INT = 600 intervals is high enough, and the database requires time to be computed. It is redundant to say that the database is calculated in advance of the rotordynamic calculations.

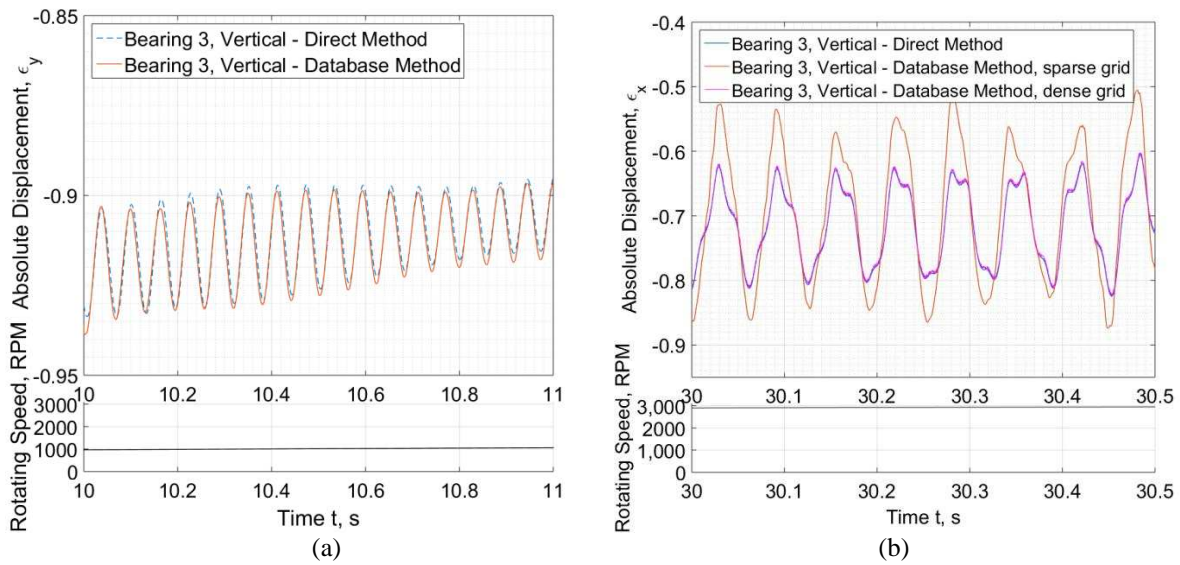


Figure 4: Relative eccentricity ϵ_y , of Journal #3 at vertical plane for narrow time range at a) 10s and b) 30s.

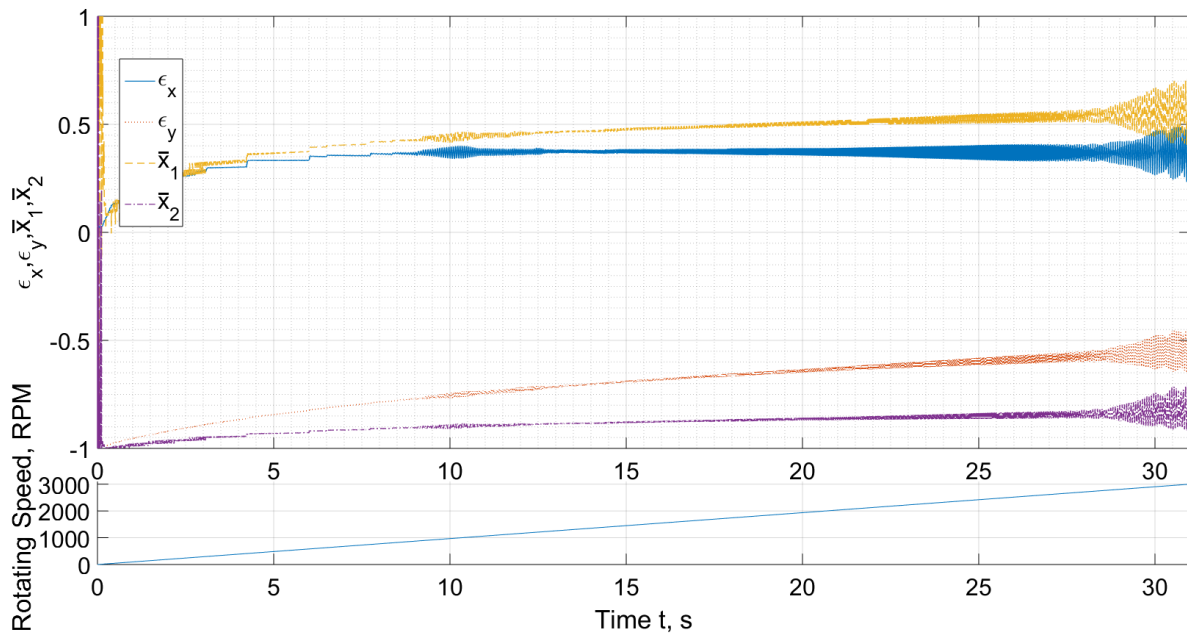


Figure 5: Progress of the four input parameters in the database for Bearing #3 (ϵ_x , ϵ_y , \bar{x}_1 , and \bar{x}_2).

The progress of the four input parameters in the database (ε_x , ε_y , \bar{x}_1 , and \bar{x}_2) is depicted in Figure 5 for the corresponding run-up shown in Figure 3. These four parameters will be always varying in $-1 < \varepsilon_x, \varepsilon_y, \bar{x}_1, \bar{x}_2 < 1$, and therefore, according to Figure 5, somebody can realize that an interval of e.g. $1 / \text{INT} = 0.01$ (sparse grid) might be large compared to $1 / \text{INT} = 0.002$ (dense grid).

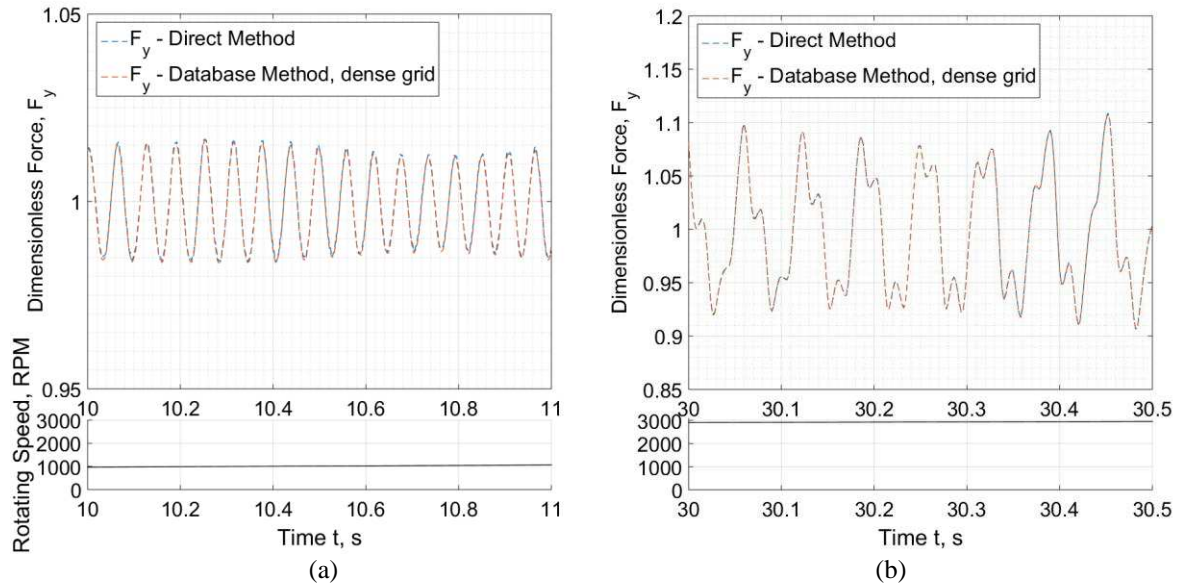


Figure 6: Progress of Bearing #3 vertical fluid film forces (dimensionless) implemented from the database and the direct calculation, at a) 10s and b) 30s.

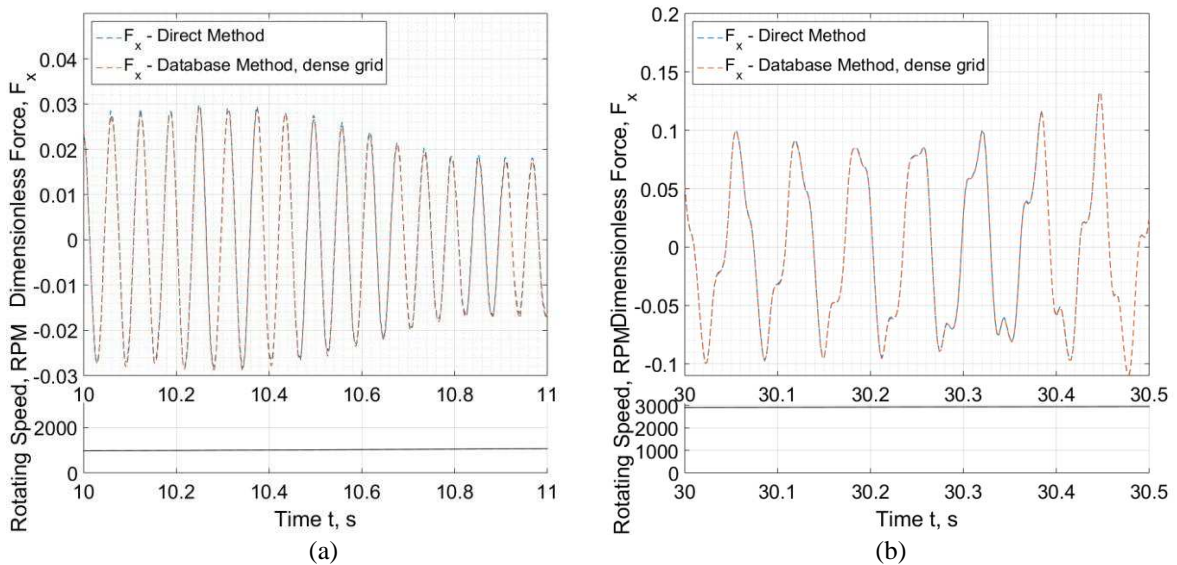


Figure 7: Progress of Bearing #3 horizontal fluid film forces (dimensionless) implemented from the database and the direct calculation, at a) 10s and b) 30s.

Figures 6 and 7 show the efficiency of the database method to predict identical to the direct method forces in all circumstances of small journal whirling around an equilibrium position (e.g. at 10s, see Figures 6a and 7a) or large journal whirling on a limit cycle (e.g. at 30s during instability, see Figures 6b and 7b).

Table 1 depicts the actual benefit of the database method. Bearing forces are returned from the database method subroutine in only 0.00038s while the direct method subroutine will return forces in 0.022 using the same CPU. This is a reduction of approximately 100 times. Furthermore, it has to be highlighted that the database method has the possibility to implement enhanced THD bearing models with any boundary condition or to implement a CFD model for the bearing performance. The time on the database subroutine (from call to return) will be retained at the same low level (e.g. 0.00038s at the specific CPU) whatever the method for the lubrication performance is. Depending on the rotor-bearing system (type of application), low or high number of degrees of freedom is used for the rotor model, and as a result, it may happen that the reduction of the net time spent in the bearing routines is not enough to decrease the total time of a rotor run-up. For instance, a turbocharger transient run-up with a rotor model as a rigid body will experience a tremendous reduction on evaluation time when the

database method is used, as the number of DOFs is low (even 10 DoFs are enough to model such system), and therefore the run-up time is influenced much from the bearing subroutines. At the current example (see Figure 2) the total time for rotor run-up is reduced to c.a. one third by using the database method, from 186hrs to 57hrs.

	Evaluation time needed for the forces of a bearing	Total time for rotor run-up
Direct Method	0.022s	186hrs
Database Method	0.00038s	57hrs

Table 1: Comparison of time needed for response and bearing forces using database method and direct method.

4 Conclusion

Standard rotordynamic design evaluation of large turbomachinery does not include evaluation of nonlinear transient response due to the still high evaluation time which cannot support design procedures. However, in small turbochargers and turbopumps, and generally in high speed turbomachinery, nonlinear transient analysis is mandatory for the accurate prediction of dynamics and therefore of mechanical integrity and operating performance. The evaluation time spent in bearing subroutines is considerable, and this paper aims to support the introduction of bearing database modules with enhanced THD models to the rotordynamics of large and small turbomachinery. Large turbomachinery does not really demand nonlinear transient response for the calculation of unbalance response (linear harmonic analysis yields very similar results in most times), but, the nonlinear stability analysis may be proved very beneficial as slender rotors operate very close to the stability threshold (e.g. 60Hz generators). The present paper aims to provide the tool for a nonlinear rotordynamic analysis with emphasis on the prediction of response on or close to unstable regimes, which today are not avoided on site. With a severe reduction of the evaluation time needed for a run-up, the rotordynamic engineer may compose a DoE with various bearing modules or bearing configurations so as to ensure that the system will not enter unstable regimes, or if it enters to instability, this will not cause severe vibrations and trip of operation. The method can implement enhanced THD bearing models without the evaluation time to be a problem. Regarding the evaluation time of nonlinear transient response of high speed systems (mandatory for their design), this can be severely reduced and perform DoEs (Design of Experiments for the definition of clearances, groove dimensions, bearing length, etc) without time to be a matter, even high the most accurate bearing THD models.

References

- [1] Sfyris, D., and Chasalevris, A. (2012): An exact analytical solution of the Reynolds equation for the finite journal bearing lubrication. *Tribology International*, 55, pp. 46-58
- [2] Chasalevris, A, and Sfyris, D. (2013): Evaluation of the finite journal bearing characteristics, using the exact analytical solution of the Reynolds equation. *Tribology International*, 57, pp. 216-234
- [3] Chen, Z., Jiao, H., Xia, S., Huang, W., and Zhang, Z. (2002): An efficient calculation method of nonlinear fluid film forces in journal bearings. *Trib Trans*, 45(3), pp. 324-329.
- [4] Wen, W., Zhang, Z., and Chen, X. (2001): Application of the non-stationary oil film force database. *Journal of Shanghai University (English Edition)* 5, pp. 230-233
- [5] Wang, Y, Liu, Z., Kang, W., and Yan, J. (2011): Approximate analytical model for the fluid film force of finite length plain journal bearing. *Proc. IMechE Part C: J. Mech. Eng. Sci.* 226, pp. 1345-1355
- [6] Hori, Y. (2006): *Hydrodynamic Lubrication*. Springer-Verlag, Tokyo.
- [7] Szeri, A. (2011): *Fluid Film Lubrication*, 2nd Edition. Cambridge University Press, NY.
- [8] Childs, D. (1993): *Turbomachinery Rotordynamics*. Wiley-Intersciences, New York.
- [9] Wang, W., and Zhang, Z. (1993): Nonlinear oil film force database. *Journal of Shanghai University of Technology* 14 (4), pp. 299-305
- [10] Zhang, C., Men, R., He, H., and Chen, W. (2018): Effects of circumferential and axial grooves on the nonlinear oscillations of the full floating ring bearing supported turbocharger rotor. *IMEchE J Eng Trib*, doi: 10.1177/1350650118800581.
- [11] Liew, A., Feng, N., and Hahn, E. (2004): On using the transfer matrix formulation for transient analysis of nonlinear rotor bearing systems. *Int. J Rot Mach*, 10, pp. 425-431.
- [12] Chasalevris, A., and Guignier, G. (2018): Alignment and rotordynamic optimization of turbine shaft trains using adjustable bearings in real-time operation. *Proc. IMechE Part C: J. Mech. Eng. Sci.* 0(0), pp. 1-21
- [13] Kreysig, E. (1972): *Advanced Engineering Mathematics*, 3rd edition. John Wiley & Sons, Inc.

Active Control

Active vibration control actuator placement for a planetary gearbox based on operational modal analysis

Ellis C. Kessler ¹, Daniel F. Plöger ², Philipp Zech ², Stephan Rinderknecht ²

¹ Virginia Tech Smart Infrastructure Lab, Virginia Tech, 24061, Blacksburg, United States, ellisk1@vt.edu

² Mechatronic Systems in Mechanical Engineering, TU Darmstadt, 64287, Darmstadt, Germany, ploeger@ims.tu-darmstadt.de

Abstract

Operational modal analysis (OMA) is used to place piezoelectric inertial mass actuators optimally on a test rig for active vibration control (AVC). The test-rig can operate small planetary gearboxes at arbitrary speed and load. The estimation of the frequency response functions consists of several steps: Run-ups are performed for roving sensors and stationary reference sensors. From the time signals the spectra are computed. A moving average filter is used in the frequency domain to remove interference caused by the presence of multiple orders in the gearbox vibration. The mode shapes are fitted and then used to derive optimal actuator positions. The placement is validated by applying a narrow-band phase-exact FxLMS-algorithm on the test rig.

1 Introduction

Active vibration control (AVC) enables quiet operation in many applications. Ideally, AVC should be part of the design process of a product. In practice however, it often needs to be applied to existing devices. Here, inertial mass actuators are preferred because they may be placed freely on the surface of the housing or other structural parts. An informed decision on the placement of the actuators requires knowledge of the mode shapes and of the excitation mechanism. These may be computed using finite element analysis, which is difficult for planetary gearboxes. The gear meshing is inherently non-linear and the modulation effects caused by the revolving planet gears further complicate the task. For existing machinery, it is not only easier but also more accurate to rely on operational modal analysis (OMA).

The modulation observed in the vibration of planetary gearboxes has stimulated scientific discussion. The classic paper by McFadden and Smith [13] offers the first useful description of the phenomenon. McNames [14] interprets the vibration as Fourier series. Inalpolat and Kahraman [9] provide a very detailed treatment of the topic, which is not undisputed as Morika et al. [17, 18] show results not consistent with the findings of Inalpolat and Kahraman. The authors recently published an article [25] on the vibration of small planetary gearboxes which further investigates this topic. The conflicting part of the current research concerns the presence of certain orders in the vibration, which is of no consequence for the present investigation. All relevant authors however agree on the representation of gearbox vibration by Fourier series, which will be assumed subsequently.

Several implementations of an AVC system for gearboxes have been proposed in the literature. Active primary or secondary bearings [22, 5] as well as inertial actuators mounted directly on gears [2] can be applied inside the gearbox. Rotating inertial actuators can be used to reduce gearbox shaft vibration [27]. Active struts enable reduction of vibration transmission [12]. Finally, a modulation of the driving electric motor torque can lead to reduced gearbox vibration [1]. While parallel shaft gearboxes have been extensively covered, this is not the case for planetary gearboxes where only few publications with experimental results exist [10]. Especially the complex geometry and modulation mechanisms make the design of an AVC system challenging. Actuators based on piezo stacks are well suited for gear mesh frequencies in the kilohertz range [16, 26]. Adaptive feedforward control can be seen as state of the art approach [20] that permits high vibration reductions. Requirements for an AVC system for small planetary gearboxes have been analyzed experimentally by the authors in [24]. The selection of suitable actuator positions using OMA techniques has not been treated in literature so far.

In order to place the actuators optimally, the structural dynamics of the system must be considered. Methods for optimizing placement of piezoelectric actuators are reviewed by Gupta et al. [6], and range from requiring modal

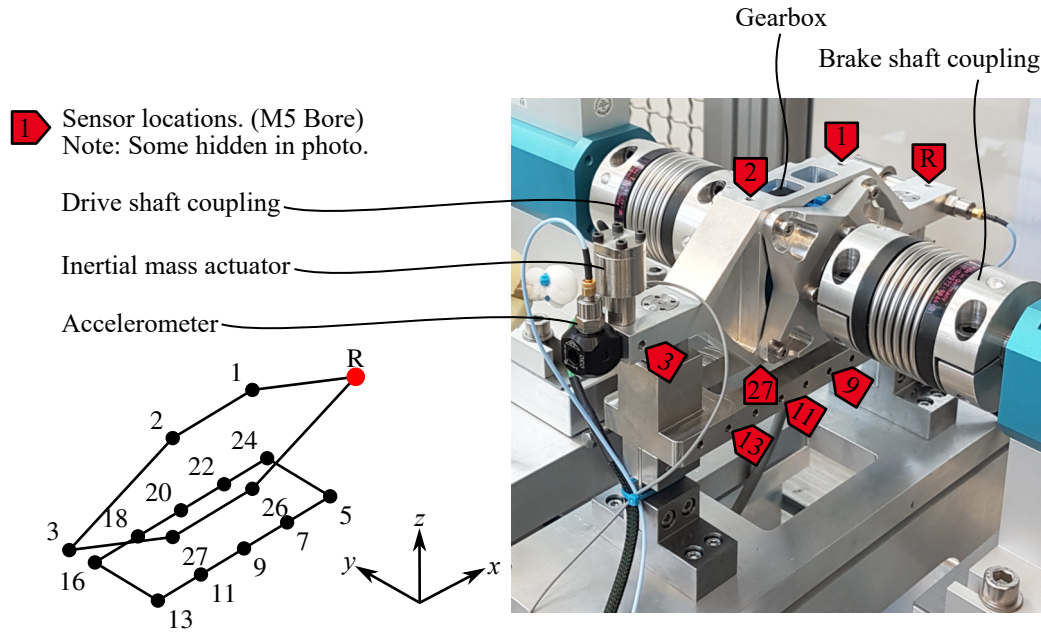


Figure 1: Experimental Set-up for active vibration control. Wireframe view: Sensor locations used for OMA.

parameters to requiring full state space representations of all inputs and outputs of the system. The effort required to model the boundary conditions associated with a revolving planet carrier and the non-linear gear contact is high. In many cases, this makes a finite element or multi-body simulation impractical. Experimental modal analysis also suffers from significant drawbacks. As the gearbox is not truly a linear system, it is difficult to enforce a realistic mesh stiffness between the gears in an experiment unless the gearbox operates at realistic load and speed. Therefore, OMA will be used to estimate modal parameters such as natural frequencies, damping, and mode shapes of the system during operation. However, there are multiple different OMA methods [21, 28] to consider.

In a recent investigation [23], we have found that OMA techniques show good promise for planetary gearboxes. There, we could identify natural frequencies and damping ratios using data recorded from run-up experiments. We used a moving average (MA) filter on recorded vibration spectra to estimate the magnitude of the frequency response functions (FRF) of the test-rig. The drawback of this approach is the loss of phase information. In this contribution, we will show how the method can be extended to estimate complex FRFs, including phase information. These will be used to estimate the mode shapes of the test rig. The knowledge of the natural frequencies and the corresponding mode shapes allows an informed decision on the actuator location. The performance of two different configurations will show the effectiveness of the proposed method.

2 Experimental Set-Up

Figure 1 shows the central components of the test-rig used in this investigation. The test-rig is designed in a modular fashion. It can support various planetary gearboxes, actuator and sensors. By means of an asynchronous motor and an eddy current brake (both outside of the displayed area) the planetary gearbox can run at arbitrary speed and load. These machines are connected via torque sensors by metal bellow couplings to the gearbox. A supporting structure carries the planetary gearbox. It features 28 possible mounting points for sensors or actuators realized as M5 bores. Those which were used in the experiments and which are visible in the photo are marked by numerical identifiers. The exception is the reference position, which is denoted by R. Mounting cubes enable the sensors to be aligned with any direction of the coordinate system. There were two locations (located 26 and 27) where an accelerometer could not be mounted in the x -direction. The x -direction was therefore ignored for these two points. All other measurement locations were measured in all three directions.

In this investigation, piezoelectric accelerometers are primarily used. Beyond these, tri-axial load cells, temperature sensors, microphones, incremental encoders and torque sensors are available. The control algorithm explained in Section 5 uses two piezoelectric inertial mass actuators which may be attached to any of the mounting points as well. It also uses the incremental encoder on the brake shaft to generate the reference signal. Control and recording are executed by a real-time computer.

The inertial mass actuator consists of prestressed low-voltage piezo stacks of type PI P-842.10 with an electric capacitance of 1.5 μF . The inertial mass is designed as a hollow steel cylinder and weighs 80 g. The actuators are driven by switching amplifiers of type PI E-617. The amplifiers feature a switching frequency of 100 kHz and a peak current of 2 A. This qualifies them for the desired frequency range of 1.5 kHz to 5 kHz in which the gear mesh frequency of the test rig may be found.

3 OMA

Due to the highly modulated nature of the vibrations induced by a planetary gearbox, care must be taken to excite all frequencies evenly so that OMA techniques can be applied. First, experiments will not be run at single speeds because steady state operation would excite only isolated frequencies. Instead, run-up experiments will be performed. Run-up experiments consist of starting the gearbox at very low speed and increasing the speed at a constant acceleration up to the a maximum speed. During this procedure, the orders of the gearbox will sweep through the entire frequency band; acting as a multi-sine sweep. However, unlike the procedure used by Janssens et al. [11], in this work order tracking will not be employed. The presence of high orders causes a high slew rate in their associated frequencies which makes order tracking unreliable. In this work the limitations without order tracking can be accepted since the end of order effects which order tracking eliminates are not prevalent. However, the FRF will be under-estimated at high frequencies as the number of contributing orders decreases with increasing frequency. The second part of the procedure to obtain a reliable FRF estimate is to apply a moving average filter to the frequency spectrum estimate in the frequency domain. This flattens out any interference of the orders in the frequency response.

Run-up experiments were conducted for each measurement location with sensors mounted at that location in all three directions. During each experiment, accelerometers were also kept in all three directions at the reference point. They are used as reference sensors. This allows a roving sensor procedure to be implemented while still obtaining phase information between different run-ups. The same processing of data as applied by Zhou et al. [28] is used in this work. The cross spectra between all outputs and the three reference sensors are used as FRF estimates to estimate the modal parameters of the system. In order to find the spectra for each measurement location, first the cross correlation R of the acceleration signals from the measurement location and the reference sensor must be computed. In the following, signals will be considered time series. Thus, the i th term of the acceleration signal for the measurement location is y_i and the i th term of the signal for the reference sensor is r_i . The index variable i assumes values between 1 and the number of acquired samples N . The i th term of the cross correlation is:

$$R_i = \frac{1}{N} \sum_{k=0}^{N-i-1} y_{k+i} r_k . \quad (1)$$

From these cross correlations, the terms of the half spectra S_{yr}^+ can be found through a DFT of these correlations:

$$S_{yr}^+(\omega) = \frac{R_0}{2} + \sum_{k=1}^L R_k e^{-j\omega k \Delta t} , \quad (2)$$

where Δt is the time between samples and L is the maximum number of time lags used to estimate the spectrum. Once the half spectra were calculated, a moving average filter was applied to the complex spectra to remove the mutual interference between the multiple sine sweeps. As the length scale of the interference in the frequency domain is much lower than that of a resonance peak, a clean separation is possible. Finally, the spectra were fitted with an open source least-squares fitting algorithm called ‘vecfit3’ (available online from the Surrogate Modeling lab from Ghent University) [8, 7, 3]. The same workflow as used by commercial least squares OMA programs was followed: spectra estimates were fitted with increasing model orders; stable poles with stable mode shapes were selected and a final least squares fit created the final model [28]. The stabilization diagram is shown in Fig. 2. A total of 22 stable modes were chosen with frequencies ranging from 0.3 kHz to 6 kHz based on stability in frequency, damping, and mode shape over increasing model orders. Fig. 3 shows three example mode shapes, which are within in the frequency range where validation experiments will be run.

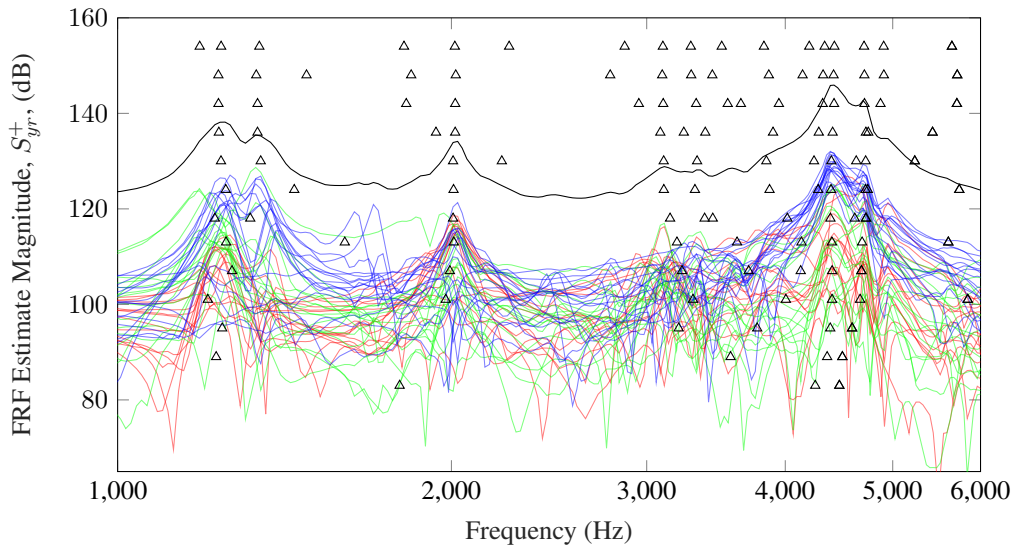


Figure 2: Stabilization diagram showing the estimated FRFs for all measurement locations. Measurements in the x -direction are shown in red, y -direction are shown in green, and z -direction are shown in blue. The sum of all FRFs is also shown in black. The modes identified are shown from model orders 6 to 32 with triangles.

Mode 6: 2013 Hz

Mode 11: 4401 Hz

Mode 12: 4503 Hz

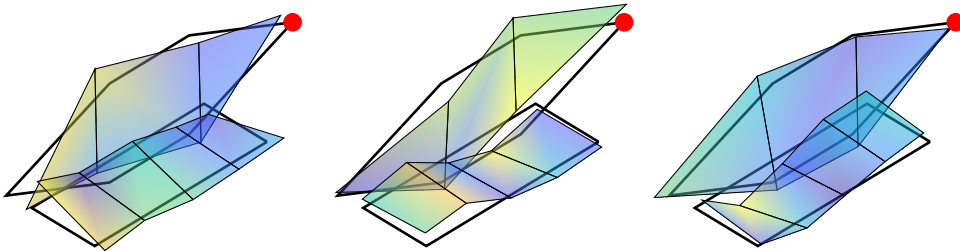


Figure 3: Examples of mode shapes 6, 11, and 12 visualized over a wireframe of the test set-up.

4 Optimization of Actuator placement

In order to find out what frequency range should be considered for active vibration control, a series of stationary speed experiments were conducted ranging from 1000 min^{-1} to 10000 min^{-1} , and ranging from 0 Nm to 30 Nm of torque. For each operating condition, the A-weighted sound pressure was measured using a microphone aimed at the gearbox ($20 \times 10^{-6} \text{ Pa}$ was used as the reference pressure). The maximum dBA recordings for each frequency were combined to represent the loudest condition, and are shown in Fig. 4.

The maximum sound pressure recorded was around 88 dBA. The United States' Occupational Safety and Health Administration (OSHA) sets a limit of 85 dBA, over which workers are required to wear hearing protection if they will be exposed to sound of that level for 8 hours a day [15]. Further, the United States' Environmental Protection Agency has reported a level of 76.4 dBA under which there is no risk for noise induced hearing loss (NIHL) for exposures 8 hours long [4]. This NIHL cutoff is recognized by the World Health Organization as accurate [19]. We will therefore look for the frequency range of any peaks where the sound level surpasses the NIHL limit, and choose to control all modes in that frequency range. In our measurements, the only peaks that surpass the NIHL cutoff are all between 1.8 kHz and 4.8 kHz. We find 8 modes in this range. We selected two different optimization scenarios: the first configuration aims at good vibration control over all modes in the selected frequency range. The second configuration prioritizes the best operation over a smaller frequency range focused at

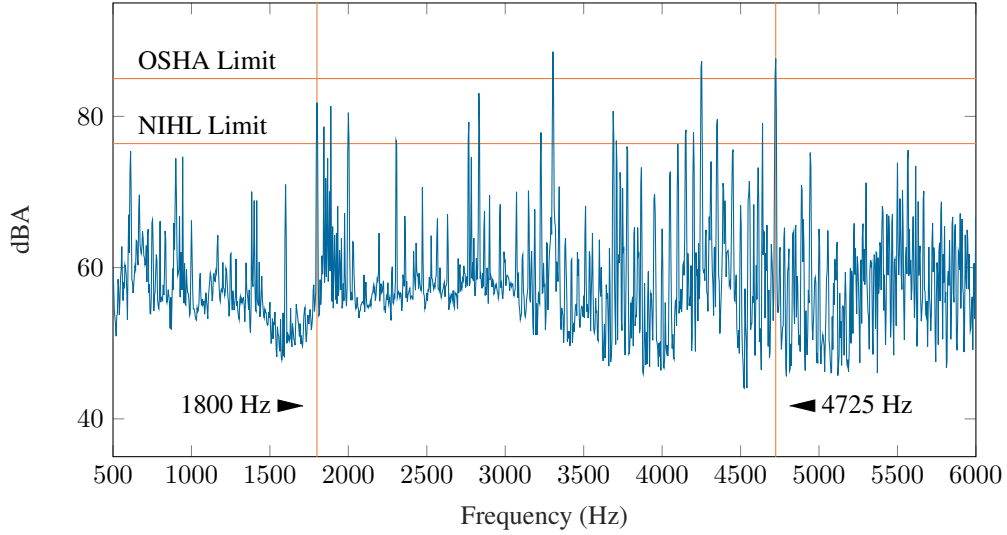


Figure 4: Maximum A-weighted sound pressure for each frequency. OSHA and NIHL limits are shown with horizontal lines, and the frequency range (1800 Hz to 4725 Hz) containing all peaks over the NIHL limit is shown with vertical lines.

higher frequencies. For configuration 1, we seek to control all 8 modes from 1.8 kHz to 4.8 kHz. For configuration 2, we seek to control the 2 modes between 4.3 kHz and 4.6 kHz. This range is centered over the highest peak in the sum of all FRFs, and represents a steady-state operating condition near the top speed of the gearbox.

After choosing the modes which will be controlled, an optimization criterion for determining actuator placements must be chosen. Gupta et. al. give a good overview of various optimization criteria for placement of piezoelectric actuators on smart structures [6]. In our case, two inertial piezoelectric actuators will be placed on the structure. Inertial actuators can be viewed as a point force acting on the structure. Since the OMA provided the mode shapes of the structure, we have chosen to maximize the ability to control the selected modes by maximizing the modal force applied to those modes. Other optimization criteria would require more information, for example a full state-space model of the system with the actuators as inputs. In order to maximize the modal forces input to the modes, the uncoupled system of equations will be considered:

$$\ddot{\mathbf{u}} + \mathbf{\Lambda}\mathbf{u} = \mathbf{\Phi}^T\mathbf{F} = \mathbf{f}, \quad (3)$$

where \mathbf{u} contains the modal coordinates, $\mathbf{\Lambda}$ is a diagonal matrix of the eigenvalues, $\mathbf{\Phi}$ is a matrix of the mode shapes, \mathbf{F} is the force vector input to the physical domain, and \mathbf{f} are the modal forces. The columns of the matrix $\mathbf{\Phi}$ are the mode shapes, ϕ_n , and the values within ϕ_n represent the response (in this case acceleration was measured) of each location during excitement of that mode. If there are N_m modes and N_l measurement locations the mode shape matrix is

$$\mathbf{\Phi} = [\phi_1, \dots, \phi_{N_m}], \quad (4)$$

and each mode shape is a vector,

$$\phi_n = [\phi_{1,n}, \dots, \phi_{N_l,n}]^T. \quad (5)$$

An actuator placed at the location where a mode shape has a maximum value will maximize the modal force input into that mode. Therefore the mode shape value of the mode at an actuator location will be used to represent the modal force put into that mode. For a given frequency range, it is desired that all modes will have a sufficient force input in order to be able to control all modes. The configuration is limited by the minimum modal force input over all modes. This minimum force therefore should be maximized for optimal performance. We consider each

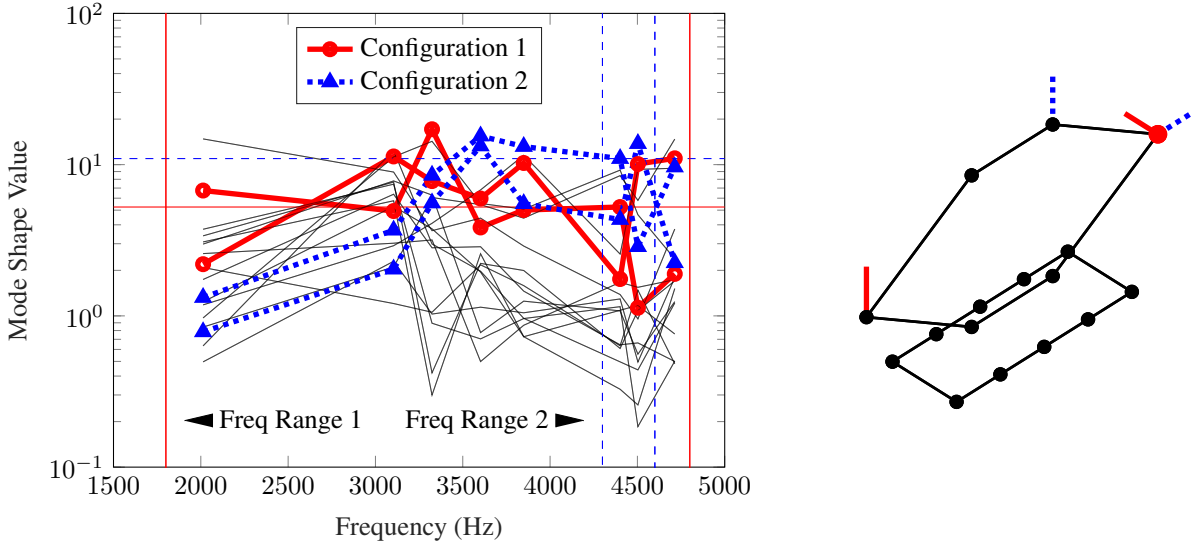


Figure 5: Visualization of the configuration optimization. LEFT: The mode shape values for each actuator location for all modes in the frequency ranges of interest, used to represent the magnitude of the force able to input into each mode from that location. Actuator configuration 1 is shown in red and configuration 2 is shown in blue. The minimum power over the corresponding frequency ranges is also shown with a horizontal line. RIGHT: A visualization showing the location and directions of actuators for both selected configurations.

actuator configuration C a N_a -tuple, where N_a is the number of actuators. For each configuration, the maximum force input into each mode is determined by finding the maximum value, ϕ_{max} , from the mode shape Φ_n at the locations of the N_a actuators in configuration C . This value is taken to be the level of control over that mode. Then, the mode with the minimum input force in the frequency range of interest is found. The control value on this mode is the minimum performance of the configuration over that frequency range. This way, each mode can be well controlled by at least one of the actuators in the optimal configuration, C_{opt} . A visualization of this process is shown in Fig. 5, and the optimization can be represented by the procedure

$$C_{opt} = \arg \max_C \min_{n=1 \dots N_m} \max_{m \in C} \phi_{m,n} . \quad (6)$$

As previously stated, two frequency ranges will be investigated: a large frequency range and a small range in the high end of the whole frequency range. For this discussion the modes will be renamed with their index in the larger frequency range. For example, the first mode in the frequency range (at 2013 Hz) is mode 6 overall, but will be referred to as mode 1 within this range. Table 1 shows a summary of the control over the 8 modes for each configuration, derived from the mode shape values. Configuration 1 has a minimum control value of 5.2 within its frequency range of interest of 1.8 kHz to 4.8 kHz. The second frequency range only contains modes 6 and 7, and has a minimum control value of 11.0 over its frequency range of 4.3 kHz to 4.6 kHz. However if the second configuration is extended to control modes over the whole frequency range, the control value drops to a minimum of 1.3 at the first mode.

5 Validation

The two optimization goals of Section 4 yielded two significantly different actuator configurations. In order to assess the effectiveness of the proposed placement method, the performances of both configurations need to be validated. For that, the actuators were mounted on the test-rig as shown in Figure 1.

The control algorithm used is a narrow-band, phase-exact FxLMS as documented in [26]. This algorithm belongs to the class of adaptive feedforward control. Reference oscillators are fed with the instantaneous angle of the planet carrier. For each vibration order to be canceled a complex valued output weight is adapted online such that the amplitude of the order is driven to zero. Complex look-up tables are used to reduce computational complexity

Table 1: Performance of the chosen configurations. Configuration 1 was optimized for all of the 8 selected modes, configuration 2 was optimized for modes 6 and 7.

Mode	Frequency (Hz)	Configuration 1			Configuration 2		
		Actuator 1	Actuator 2	ϕ_{max}	Actuator 1	Actuator 2	ϕ_{max}
1	2013	6.7	2.2	6.7	0.8	1.3	1.3
2	3104	4.9	11.3	11.3	2.0	3.7	3.7
3	3342	17.1	7.8	17.1	5.6	8.5	8.5
4	3602	3.8	6.0	6.0	13.3	15.4	15.4
5	3849	5.0	10.3	10.3	5.5	13.2	13.2
6	4401	5.2	1.8	5.2	4.3	11.0	11.0
7	4503	1.1	10.1	10.1	13.8	2.9	13.8
8	4714	1.9	11.0	11.0	2.2	9.6	9.6

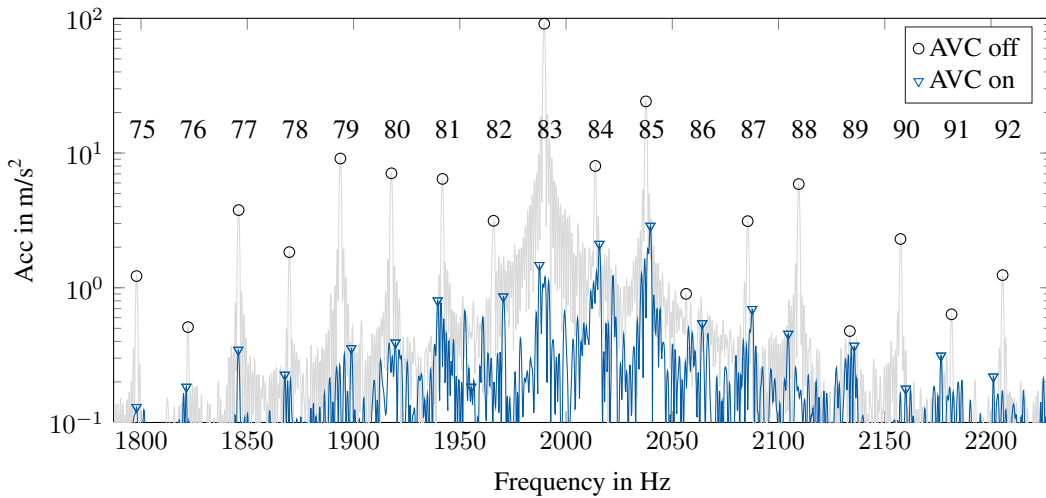


Figure 6: Acceleration spectrum for configuration 1 at position of actuator 1 without and with AVC while driven at low speed. Vibration orders 75 to 92 are controlled.

for secondary path filtering instead of FIR-filters. The control algorithm is implemented with a closed-loop sampling frequency of 50 kHz on the real time system. A total of 18 vibration orders are selected for cancellation in the vicinity of the nominal gear mesh order 84 as depicted in Fig. 6. Further details on the implemented control algorithms are given in [26]. To assess the achieved vibration reduction the ratio W of rms-values for both with and without control is evaluated. It describes the relative remaining vibration with activated control and is calculated using

$$W = \frac{\sqrt{\sum_{k=75}^{92} \text{Acc}_{\text{on}}^2(k)}}{\sqrt{\sum_{k=75}^{92} \text{Acc}_{\text{off}}^2(k)}} \quad (7)$$

where $\text{Acc}(k)$ denotes the acceleration amplitude of the k -th vibration order. The lower the value of W the better the control performance. Each actuator configuration is investigated for the low (gear mesh frequency of 2013 Hz) and high (gear mesh frequency of 4452 Hz) operating speed. The structural model obtained by OMA approach yields three predictions according to Tab. 1:

1. Configuration 1 is well suited for both operating points
2. Configuration 2 is well suited only for the high-speed operating point
3. Configuration 2 should be more efficient than configuration 1 for the high-speed operating point

There are multiple approaches in comparing the performance of the chosen configurations. Generally the performance is related to the reduction in vibration and to the effort needed to achieve this reduction. Well placed

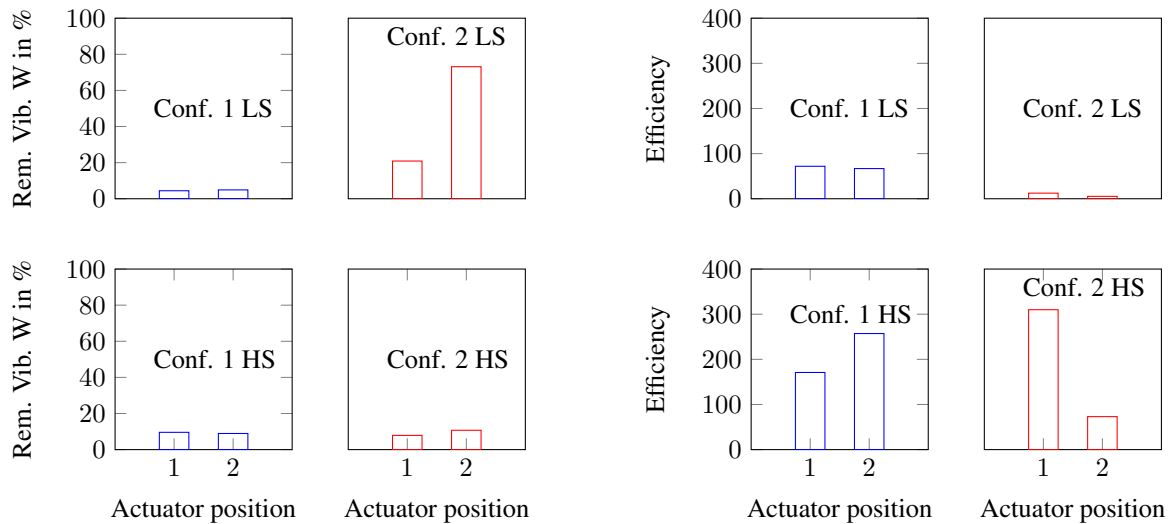


Figure 7: Results for both actuators in both configurations for low-speed (LS) and high-speed (HS) operating points. LEFT: Remaining vibration. RIGHT: Efficiency in $m/s^2/V$ describes ratio between achieved absolute acceleration reduction and used voltage.

actuators should not only yield a significant reduction, but also require a low control voltage in doing so. As the precise control objective depends on the placement of the actuator and their collocated sensor, reductions may not be compared immediately between configurations. Instead, an individual assessment needs to be made for each configuration. The results of the experiments are shown in Fig. 7. Configuration 1 achieves remaining vibrations of 10% or less for both operating speeds. Configuration 2 achieves good performance for high-speed but has problems for low-speed where the remaining vibration is comparatively high. Thus the first two predictions can be clearly confirmed by the experimental results. The first actuator of configuration 2 at high-speed exhibits the highest efficiency. However the efficiency of the second actuator is smaller than for both actuators of configuration 1 at high-speed. Consequently prediction 3 is partly fulfilled.

6 Conclusion

This contribution shows how OMA can be used in the design process of AVC on a real-world system. OMA was chosen to gather information about the system to inform the decision of where to place AVC actuators. The proposed method does not require prior in-depth knowledge of the system or complex modelling techniques. High-quality FRF estimates were obtained despite the highly modulated vibrations caused by the planetary gearbox due to the application of run-up testing and moving average filtering. Least-squares based OMA was applied to the FRF estimates to estimate the natural frequencies and mode shapes of the system. A procedure to choose an optimal actuator configuration was presented which is able to guarantee a minimum level of performance in the targeted frequency range.

Two configurations were investigated using the mode information from OMA and applying the optimization procedure over two frequency ranges. As predicted by the optimization procedure from the modal information, configuration 1 performed well at both operating speeds and configuration 2 only performed well at the high speed.

The success of this contribution to implement effective AVC on a planetary gearbox system shows the applicability of the methods presented. OMA techniques provide a reliable method for determining optimal actuator placement using only measurements of the system in operation. Therefore the methods presented could be straightforwardly applied to an AVC scenario. Finally, the ability to make predictions about the performance of different actuator configurations which were validated using an AVC test-rig show the promise of this method.

7 Acknowledgments

This research was funded in part by a grant from the US National Science Foundation (EEC-1560107).

REFERENCES

- [1] Benzel, T. and Möckel, A. (2014). Multi-channel active gear pair vibration control with an electronically commutated motor as actuator, *2014 IEEE International Electric Vehicle Conference (IEVC)*, pp. 1–8.
- [2] Chen, M. H. and Brennan, M. J. (2000). Active control of gear vibration using specially configured sensors and actuators, *Smart Materials and Structures* **9**(3): 342.
- [3] Deschrijver, D., Mrozowski, M., Dhaene, T. and De Zutter, D. (2008). Macromodeling of Multiport Systems using a Fast Implementation of the Vector Fitting Method, *IEEE Microwave and Wireless Components Letters* **18**(6): 383–385.
- [4] EPA (1974). *Information on Levels of Environmental Noise Requisite to Protect Public Health and Welfare with an Adequate Margin of Safety*, U.S. Environmental Protection Agency.
- [5] Guan, Y. H., Lim, T. C. and Steve Shepard, W. (2005). Experimental study on active vibration control of a gearbox system, *Journal of Sound and Vibration* **282**(3): 713–733.
- [6] Gupta, V., Sharma, M. and Thakur, N. (2010). Optimization Criteria for Optimal Placement of Piezoelectric Sensors and Actuators on a Smart Structure: A Technical Review, *Journal of Intelligent Material Systems and Structures* **21**(12): 1227–1243.
- [7] Gustavsen, B. (2006). Improving the pole relocating properties of vector fitting, *IEEE Trans. Power Delivery* **21**(3): 1587–1592.
- [8] Gustavsen, B. and Semlyen, A. (1999). Rational approximation of frequency domain responses by Vector Fitting, *IEEE Trans. Power Delivery* **14**(3): 1052–1061.
- [9] Inalpolat, M. and Kahraman, A. (2009). A Theoretical and Experimental Investigation of Modulation Sidebands of Planetary Gear Sets, *Journal of Sound and Vibration* **323**(3-5): 677–696.
- [10] Jaenker, P., Kloeppe, V., Konstanzer, P. and Maier, R. (2008). Piezo active vibration and noise control in helicopters, *Proceedings of the 26th international congress of the aeronautical sciences*, pp. 1–10.
- [11] Janssens, K., Kollar, Z., Peeters, B., Pauwels, S. and Van, D. A. (2006). Order-based resonance identification using operational polyMAX.
- [12] Ma, X., Lu, Y. and Wang, F. (2017). Active structural acoustic control of helicopter interior multifrequency noise using input-output-based hybrid control, *Journal of Sound and Vibration* **405**: 187–207.
- [13] McFadden, P. and Smith, J. (1985). An Explanation for the Asymmetry of the Modulation Sidebands about the Tooth Meshing Frequency in Epicyclic Gear Vibration, *Proceedings of the Institution of Mechanical Engineers, Part C: Journal of Mechanical Engineering Science* **199**(1): 65–70.
- [14] McNames, J. (2001). Fourier Series Analysis of Epicyclic Gearbox Vibration, *Journal of Vibration and Acoustics* **124**(1): 150–153.
- [15] McReynolds, M. C. (2005). Noise-induced hearing loss, *Air Medical Journal* **24**(2): 73–78.
- [16] Montague, G. T., Kascak, A. F., Palazzolo, A., Manchala, D. and Thomas, E. (1994). Feedforward control of gear mesh vibration using piezoelectric actuators, *Shock and Vibration* **1**(5): 473–484.
- [17] Morikawa, K., Kumagai, K. and Nishihara, R. (2014). A Study on the Sideband Phenomenon of Planetary Gears, *Transactions of the JSME (in Japanese)* **80**(815): DSM0212–DSM0212.
- [18] Morikawa, K., Kumagai, K., Nishihara, R. and Nemoto, J. (2015). Vibration Behaviour of Stepped Pinion Type Planetary Gears, *Transactions of the JSME (in Japanese)* pp. 15–00310.
- [19] Neitzel, R. and Fligor, B. (2017). *Determination of Risk of Noise-Induced Hearing Loss due to Recreational Sound: Review*, World Health Organization.
- [20] Pasco, Y., Robin, O., Bélanger, P., Berry, A. and Rajan, S. (2011). Multi-input multi-output feedforward control of multi-harmonic gearbox vibrations using parallel adaptive notch filters in the principal component space, *Journal of Sound and Vibration* **330**(22): 5230–5244.
- [21] Peeters, B. and De Roeck, G. (2001). Stochastic System Identification for Operational Modal Analysis: A Review, *Journal of Dynamic Systems Measurement and Control* **123**(4): 659–667.
- [22] Pinte, G., Devos, S., Stallaert, B., Symens, W., Swevers, J. and Sas, P. (2010). A piezo-based bearing for the active structural acoustic control of rotating machinery, *Journal of Sound and Vibration* **329**(9): 1235–1253.
- [23] Plöger, D. F., Jungblut, J., Zech, P. and Rinderknecht, S. (2018). Separation of structural response and excitation characteristics in planetary gearboxes, *Proceedings of ISMA2018*, Leuven, Belgium, pp. 2437–2444.
- [24] Plöger, D. F., Zech, P. and Rinderknecht, S. (2016). Experimental identification of high-frequency gear mesh vibrations in a planetary gearbox, *Proceedings of ISMA2016 International Conference on Noise and Vibration Engineering*, Leuven, Belgium, pp. 911–924.
- [25] Plöger, D. F., Zech, P. and Rinderknecht, S. (2019). Vibration signature analysis of commodity planetary gearboxes, *Mechanical Systems and Signal Processing* **119**: 255–265.
- [26] Zech, P., Plöger, D. F., Bartel, T., Röglin, T. and Rinderknecht, S. (2018). Design of an inertial mass ac-

tuator for active vibration control of a planetary gearbox using piezoelectric shear actuator, *Proceedings of ISMA2018*, Leuven, Belgium, pp. 203–215.

- [27] Zhang, M., Lan, H. and Ser, W. (2005). On comparison of online secondary path modeling methods with auxiliary noise, *IEEE Transactions on Speech and Audio Processing* **13**(4): 618–628.
- [28] Zhou, Z., Wegner, L. D. and Sparling, B. F. (2007). Operational PolyMAX for Estimating the Dynamic Properties of a Stadium Structure During a Football Game, *Shock and Vibration* **14**(4): 16.

Comparative Study of Active Control Applied to a Hydrodynamic Supported Rotor

Matheus Freire Wu¹, **Katia Lucchesi Cavalca**², **Richard Markert**³

¹ Integrated Systems Department, UNICAMP, 13083-860, Campinas, Brazil, matheusfw@fem.unicamp.br

² Integrated Systems Department, UNICAMP, 13083-860, Campinas, Brazil, katia@fem.unicamp.br

³ Institute of Applied Dynamics, TU Darmstadt, 64287, Darmstadt, Germany, markert@ad.tu-darmstadt.de

Abstract

Flexible rotors supported by cylindrical hydrodynamic journal bearings generally face two main problems during operation, crossing the first critical speed and fluid-induced instability. Active control techniques can be applied to mitigate these issues. The main objective of this paper is to compare and experimentally validate different control methods aiming to attenuate the vibration amplitude at the first bending critical speed and stabilize the oil-whip effect by using an active magnetic bearing as actuator. Three different control synthesis methods were employed: classic dynamic H_∞ , μ -synthesis and gain scheduled static H_∞ dependant on the rotational speed. The final performances of the designed controllers were compared by numerical simulation and also with an experimental test rig.

1 Introduction

Hydrodynamic bearings offer a set of advantageous mechanical properties, therefore, they are widely applied by industry, such as in pumps, compressors and turbines. However, the classical cylindrical journal bearing is susceptible to oil-whirl phenomenon, which is known to provoke system fluid-induced instability (oil whip). Usually, the oil-whip occurs above twice the first critical speed and may compromise the machine components integrity due to high lateral amplitude vibration, thus establishing an operational threshold. Many studies can be found suggesting passive solutions for this problem such as geometric modifications, tilting pads and dampers. Nevertheless, in some cases passive solutions may not achieve the growing requirements of modern industry [4] and [10], thus, active methods arise as in hybrid-bearings with piezo or magnetic actuation, active oil injection, smart materials, etc.

In this paper an active magnetic bearing (AMB) is utilized not as a classical load supporting bearing, but rather as an auxiliary active vibration controller. Such approach demands less magnetic force, and therefore, might allow the use of smaller, lighter and more energy-economic hardware. Studies using similar approaches can be found in [3], [4], [10] and [11].

The control methods applied in this paper are all model based. Therefore, finite elements method (FEM) is used to describe the basic system. However, simple linear time invariant (LTI) does not capture the strong rotational speed dependence of journal bearing supported rotors. To deal with this issue, the parametrical variation is considered in uncertainty and linear parametrical varying (LPV) form. The objective is to study and compare the achieved experimental performances of a standard H_∞ to robust (μ -synthesis) and adaptive (gain-scheduled H_∞) controllers. This paper is focused mainly in the practical validation of the proposed methods. More detailed theoretical aspect can be found in [16].

2 Test rig

To validate the proposed control methods an experimental test rig, shown in Figure 1, was utilized. The rotor is composed by a 795 mm length and 8 mm diameter steel shaft, supporting a 0.71 kg steel disc, a 0.92 kg steel journal (for the AMB) and a 1.02 kg brass journal (hydrodynamic journal bearing). The rotor is supported by two self-aligning roller bearings on the motor side, and the journal bearing on the other extremity, according to Figure 1. The journal bearing has 27 mm length, 54 mm diameter, radial gap of 100 μm and is lubricated by ASOLA ZS 10 oil. The first bending critical speed is at 28.5 Hz with this configuration and the oil-whip occurs

at about 60 Hz. The equivalent residual unbalance for the first bending mode is approximately 16.1×10^{-6} kg.m. The acquisition and real-time control are performed by a DSpace board ds1006, which allows to perform the experiments with a frequency rate of 8192 Hz. For a more convenient handle of data, the acquisition was down sampled by 1/16, resulting in a Nyquist frequency of 256 Hz, that is above the maximum rotational speed and range of interest of 90 Hz. The rotor is monitored by pairs of Eddy current displacement sensors placed at the disc, on each side of the magnetic bearing and on each side of the journal bearing. The rotor is powered by a servomotor. And the magnetic control force is performed using an 8 poles AMB, studied in [13], supplied by a Mecos PA 8-50 power amplifier.



Figure 1: Test rig.

3 Rotor modelling

In this section the procedure to obtain the model representations of the rotor utilized in this paper is described. Four different models were utilized for different purposes is described. Firstly, a full standard FEM model, which was utilized for numerical simulations. Secondly, a simple reduced model utilized to calculate a standard H_∞ controller, a third one, considering parametrical uncertainties, which served as base for μ -synthesis controller, and a fourth one, which consists in a polynomial system used to find the LPV controllers.

3.1 FEM rotor modelling

The base for all four models is the finite elements model of the shaft and rigid elements. For that the well-known Nelson's finite elements matrices [8] were employed. With the basic mass (\mathbf{M}_{fem}), stiffness (\mathbf{K}_{fem}), damping (\mathbf{D}_{fem}) and gyroscopic (\mathbf{G}_{fem}) matrices that compose the basic equation of motion of the system, Eq. (1), it can easily be written in space-state form, Eq. (2), which is more convenient for control design and analysis. Where Ω is the rotational speed, \mathbf{w} is the unbalance force and \mathbf{y} represents the sensors readings.

$$\mathbf{M}_{fem} \ddot{\mathbf{q}} + (\mathbf{D}_{fem} + \Omega \mathbf{G}_{fem}) \dot{\mathbf{q}} + \mathbf{K}_{fem} \mathbf{q} = \mathbf{w} \quad (1)$$

$$\mathbf{P} : \begin{cases} \dot{\mathbf{x}} = \mathbf{A} \mathbf{x} + \mathbf{B}_1 \mathbf{w} \\ \mathbf{y} = \mathbf{C}_1 \mathbf{x} + \mathbf{D}_{11} \mathbf{w} \end{cases} \quad (2)$$

with,

$$\mathbf{A} = \begin{bmatrix} \mathbf{I} & \mathbf{0} \\ -\mathbf{M}_{fem}^{-1} \mathbf{K}_{fem} & -\mathbf{M}_{fem}^{-1} (\mathbf{D}_{fem} + \Omega \mathbf{G}_{fem}) \end{bmatrix}, \quad \mathbf{x} = \begin{Bmatrix} \mathbf{q} \\ \dot{\mathbf{q}} \end{Bmatrix} \quad \text{and} \quad \dot{\mathbf{x}} = \begin{Bmatrix} \dot{\mathbf{q}} \\ \ddot{\mathbf{q}} \end{Bmatrix}.$$

The full model was divided in 30 nodes, as shown in Figure 2. Each node has 4 degrees of freedom (DOF), two translations and two rotations. And so, in space-state model it results in order 240. This value can be considered as too high for control applications, both for optimization problems and for real-time implementation. For that reason, the Guyan reduction [5] is employed, allowing to reduce the system while preserving the physical meaning of the remaining DOF making easier to add the varying bearing and gyroscopic parameters.

Literature suggests that best results for Guyan reduction are obtained when preserving nodes with most concentrated masses. Thus, preserving the main nodes for the control (disc, journals and bearings), which provide signals for feedback and performance measurement are quite convenient. And so, only the translation DOF of nodes 4, 10, 18 and 26 were kept. Thereafter, the reduced space-state model presents 16 states, allowing

to describe the first four forward and backward modes. When dealing with cylindrical journal bearing supported rotors, usually one does not expect to need more than the first pairs of modes since the oil-whip effect commonly limits the operation between the first and the second critical speed.

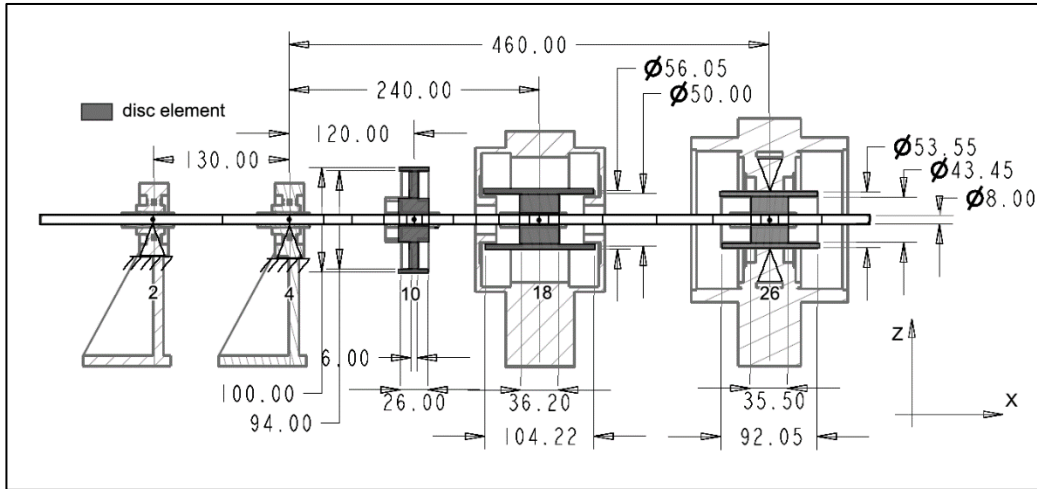


Figure 2: Model of the rotor.

3.2 Bearing coefficients modelling

To express the influence of the bearing coefficients it is utilized the equivalent linear approximation, which is obtained by numerically solving the Reynolds equation via finite volumes [7]. The solution represents the oil film pressure inside the journal bearing at the actual position. By integrating the pressure distribution, one finds the resultant forces applied to the rotating shaft. It is possible to expanding these non-linear force expressions into Taylor series. Generally, the most relevant terms are the ones related to zero and first order. The latter are equivalent to the external stiffness and damping coefficients applied to the rotor which can be directly added to the respective nodes on the FEM model matrices.

Since the solution depends on the rotational speed, the equivalent coefficients are also speed-dependent. Consequently, in addition to the gyroscopic effect, at each rotational speed the rotor dynamics changes. In case of journal bearing supported rotors, this phenomenon is fundamental to represent the fluid-induced instability. In linear approximation, the oil-whip is represented by the occurrence of poles at the right-hand side of the complex plan, which mainly occurs due to the variation of the cross-coupled stiffness coefficients.

To solve the Reynolds equation for each speed step is not computational efficient, therefore a common practice is to find the solution for a set of points distributed along the operational speed range and interpolate the results. In order to take these variations into account when designing the controllers, explained in further sections, one more step is taken in this approximation: it is considered that the equivalent coefficients can be described by polynomial approximations on the rotational speed. In this paper it is adopted a second-degree polynomial, but other degrees can be utilized if necessary. Therefore, the bearing stiffness and damping matrices can be approximated by the format in Eq. (3).

$$\mathbf{K} = \mathbf{K}_0 + \mathbf{K}_1\alpha_1 + \mathbf{K}_2\alpha_1^2 \quad \text{and} \quad \mathbf{D} = \mathbf{D}_0 + \mathbf{D}_1\alpha_1 + \mathbf{D}_2\alpha_1^2 \quad (3)$$

with

$$\alpha_1 = \frac{(\Omega - \Omega_{\min})}{(\Omega_{\max} - \Omega_{\min})}$$

3.3 Uncertain model

A system deviation from the nominal model, or uncertainty, can be described by many different forms, depending on its nature [17]. Here the parametrical uncertainties form is chosen. Following the framework from Figure 3 and the second-degree approximation leads to the augmented Eq. (4), where auxiliary output \mathbf{g} and input \mathbf{h} are added connecting the normalized uncertainty matrix $\mathbf{\Delta}$ to the system \mathbf{P} .

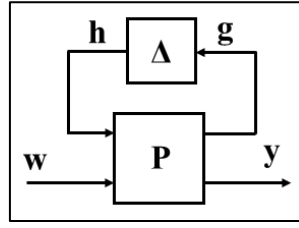


Figure 3: Uncertain loop.

$$\begin{aligned}
 \mathbf{P}: \begin{cases} \dot{\mathbf{x}} = \mathbf{A}_{\text{unc}} \mathbf{x} + \mathbf{B}_h \mathbf{h} + \mathbf{B}_1 \mathbf{w} \\ \mathbf{g} = \mathbf{C}_g \mathbf{x} + \mathbf{D}_g \mathbf{h} \\ \mathbf{y} = \mathbf{C}_1 \mathbf{x} + \mathbf{D}_{11} \mathbf{w} \end{cases} & \quad \mathbf{B}_h = \begin{bmatrix} \mathbf{0} & \mathbf{0} & \mathbf{0} \\ \mathbf{I} & \mathbf{0} & \mathbf{0} \end{bmatrix} \\
 \mathbf{h} = \Delta \mathbf{g} & \quad \mathbf{C}_g = \begin{bmatrix} -\mathbf{M}^{-1} \mathbf{K}_1 & -\mathbf{M}^{-1} [\mathbf{D}_1 + \mathbf{G}_{\text{fem}} (\Omega_{\text{max}} - \Omega_{\text{min}})] \\ -\mathbf{M}^{-1} \mathbf{K}_2 & -\mathbf{M}^{-1} \mathbf{D}_2 \\ \mathbf{0} & \mathbf{0} \end{bmatrix} \\
 & \quad \mathbf{D}_g = \begin{bmatrix} \mathbf{0} & \mathbf{0} & \mathbf{0} \\ \mathbf{0} & \mathbf{0} & \mathbf{0} \\ \mathbf{0} & \mathbf{I} & \mathbf{0} \end{bmatrix} \\
 & \quad \mathbf{A}_{\text{unc}} = \begin{bmatrix} \mathbf{I} & \mathbf{0} \\ -\mathbf{M}_{\text{fem}}^{-1} (\mathbf{K}_{\text{fem}} + \mathbf{K}_0) & -\mathbf{M}_{\text{fem}}^{-1} (\mathbf{D}_{\text{fem}} + \mathbf{D}_0 + \Omega_{\text{min}} \mathbf{G}_{\text{fem}}) \end{bmatrix} \quad \Delta = \begin{bmatrix} \alpha_1 & 0 & 0 \\ 0 & \alpha_1 & 0 \\ 0 & 0 & \alpha_1 \end{bmatrix}
 \end{aligned} \tag{4}$$

3.4 Polynomial model

The polynomial formulation is quite straight forward, and it consists in adding the polynomial stiffness and damping matrices, Eq. (5). For the sake of obtaining less conservative results, it is interesting to homogenise the system writing it in terms of a unitary simplex (6), with $n = 2$, according to the structure in Eq. (7).

$$\mathbf{A}(\alpha) = \mathbf{A}_0 + \mathbf{A}_1 \alpha_1 + \mathbf{A}_2 \alpha_1^2 \tag{5}$$

$$\begin{cases} \mathbf{A}_0 = \begin{bmatrix} \mathbf{I} & \mathbf{0} \\ -\mathbf{M}_{\text{fem}}^{-1} (\mathbf{K}_{\text{fem}} + \mathbf{K}_0) & -\mathbf{M}_{\text{fem}}^{-1} (\mathbf{D}_{\text{fem}} + \mathbf{D}_0 + \Omega_{\text{min}} \mathbf{G}_{\text{fem}}) \end{bmatrix} \\ \mathbf{A}_1 = \begin{bmatrix} \mathbf{0} & \mathbf{0} \\ -\mathbf{M}_{\text{fem}}^{-1} \mathbf{K}_1 & -\mathbf{M}_{\text{fem}}^{-1} (\mathbf{D}_1 + \mathbf{G}_{\text{fem}} (\Omega_{\text{max}} - \Omega_{\text{min}})) \end{bmatrix} \\ \mathbf{A}_2 = \begin{bmatrix} \mathbf{0} & \mathbf{0} \\ -\mathbf{M}_{\text{fem}}^{-1} \mathbf{K}_2 & -\mathbf{M}_{\text{fem}}^{-1} \mathbf{D}_2 \end{bmatrix} \end{cases}$$

$$\alpha \in \Lambda_n \Leftrightarrow \sum_i^n \alpha_i = 1 \tag{6}$$

$$\mathbf{A}(\alpha) = \mathbf{A}_{20} \alpha_1^2 + \mathbf{A}_{11} \alpha_1 \alpha_2 + \mathbf{A}_{02} \alpha_2^2 \tag{7}$$

3 Control

For the main control of the rotor, only the feedbacks from the journal bearing and AMB displacement sensors are considered. Since in real applications usually the availability for sensor placement is limited, although readings of the disc displacements are available, they are utilized only for performance analysis. In addition to the main controller other important elements must be mentioned. To eliminate the offset values, avoiding the onerous procedure to calibrate the center of the journal bearing, the lower frequencies (<1 Hz) components are subtracted from filtered journal bearing signals, as shown in Figure 4. Besides, the journal bearing naturally does not run centered in the gap. It tends to move according to the rotational speed following an arch-like path to the center [9]. If this eccentricity is not considered, extra effort is put into the controller for bringing the journal

bearing to the center. This additional force is not only unnecessary, but might even bring the system to instability since it would change the equivalent bearing coefficients.

Generally, when AMBs are applied in levitation they operate near the modal nodes. Thus the orbits can be small enough to be considered inside the linear region when using the differential configuration [12][13]. In this paper, the AMB is not utilized as a proper bearing since it is not used to provide sustaining force (reducing energy consumption), moreover, it is placed almost at the center of the first mode bending arc. Consequently, at the first critical speed high amplitude orbits are observed inside the AMB, which may reach nonlinear regions. Trying to attenuate the effects of nonlinearities and noise generated by the current amplifier, derivative gains (equivalent to a damping of approximately 50 Ns/m) are included in the ‘control force to voltage’ block. It was also noticed that changing the eccentricity of the AMB could generate considerable deviations in its behavior when operating in high amplitudes due to the magnetic circuit nonlinearities. Therefore, a small integration gain is added which allows to fix the orbit center at the AMB at an initial position, which is practically negligible to the system dynamic. Since the shaft is very flexible the required forces for displacing the AMB center are considered small enough to not have major influence on the journal bearing coefficients. Hence, the main variance of the system dynamics is resultant from the main control block, which implements the methods briefly described in the next subsections.

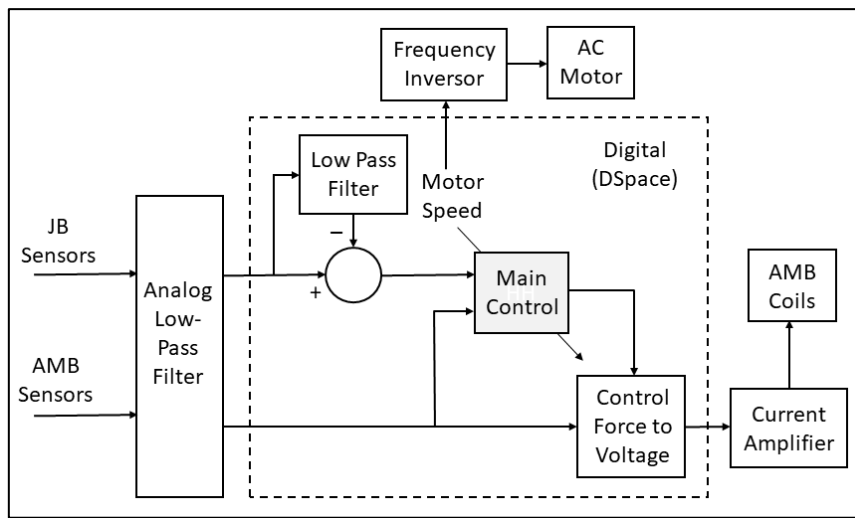


Figure 4: Control Scheme.

3.1 Classic H_∞

The classical framework for designing H_∞ controllers involves creating an augmented system including auxiliary performance output signals \mathbf{z} , as in Eq. (8). The main control objective is to reduce the H_∞ norm from the transfer matrix between the exogenous input signals \mathbf{w} , such as imbalance forces, and performance \mathbf{z} , Eq. (9). The signal \mathbf{z} typically is composed by the actual output that one wants to control (disc node displacement in this paper) and the control force \mathbf{u} .

$$\mathbf{P}_{\text{aug}} : \begin{cases} \dot{\mathbf{x}} = \mathbf{A}\mathbf{x} + \mathbf{B}_1\mathbf{w} + \mathbf{B}_2\mathbf{u} \\ \mathbf{z} = \mathbf{C}_1\mathbf{x} + \mathbf{D}_{11}\mathbf{w} + \mathbf{D}_{12}\mathbf{u} \\ \mathbf{y} = \mathbf{C}_1\mathbf{x} + \mathbf{D}_{21}\mathbf{w} + \mathbf{D}_{22}\mathbf{u} \end{cases} \quad (8)$$

$$\mathbf{u} = \mathbf{K}\mathbf{y}$$

$$\min_{\mathbf{K}} \left(\left\| \mathbf{F}l(\mathbf{P}_{\text{aug}}, \mathbf{K}) \right\|_{\infty} \right) \quad (9)$$

where $\mathbf{F}l$ is the Redheffer star product between the elements.

Since the H_∞ norm can be considered as analogous to the peak of a Bode diagram applied to a MIMO system, when H_∞ control is applied to rotors, it leads to attenuation of the biggest vibration peak, which is generally at the first bending critical speed. However, finding analytical solution for the H_∞ is very challenging. Therefore, many distinct formulation and numerical approaches to obtain suboptimum solutions were developed in the last three decades. Here, the dynamic output-feedback H_∞ control was obtained by the well-known LMI formulation [6], which is implemented in the Matlab Robust Control Toolbox™.

3.2 μ -Synthesis

H_∞ controllers can be casted in a robust approach by considering an uncertain structure as in Figure 3. However, it is known to be a conservative method [17]. To tackle this issue the structured singular value (SSV), or μ , metric was formulated. The general idea is to use the a priori information about the uncertainty structure, explained in section 3.3, to determine the smallest norm that would lead the system to instability, Eq. (10). The SSV is considered a semi-norm and it is rarely possible to determine its precise value. But it was demonstrated that the SSV lays between the systems spectral radius and system maximum singular value, Eq. (11), see [17]. The μ -Synthesis control objective is, therefore, to reduce the μ norm between \mathbf{h} and \mathbf{g} , and \mathbf{w} and \mathbf{z} . Evidently, numerical methods must be applied. The most utilized algorithm to obtain a dynamic output-feedback μ -Synthesis controller is the so-called DK-iteration [14], which iteratively finds a fitting matrix \mathbf{D} , minimizing the upper bound of μ , and then calculates a control \mathbf{K} which minimizes the estimated μ value, Eq. (12). This technique is also implemented in the Matlab Robust Control ToolboxTM.

$$\|\mathbf{P}_{\text{aug}}\|_\mu = \left(\inf_{\Delta \in \mathbf{A}} \{ \bar{\sigma}(\Delta) : \det(\mathbf{I} - \Delta \mathbf{P}_{\text{aug}}) = 0 \} \right)^{-1} \quad (10)$$

$$\rho(\mathbf{P}_{\text{aug}}) \leq \|\mathbf{P}_{\text{aug}}\|_\mu \leq \bar{\sigma}(\mathbf{P}_{\text{aug}}) \quad (11)$$

$$\min_{\mathbf{K}} \left(\|\mathbf{F}l(\mathbf{P}_{\text{aug}}, \mathbf{K})\|_\mu \right) \approx \min_{\mathbf{D}, \mathbf{D}^{-1}} \left(\mathbf{D} \|\mathbf{F}l(\mathbf{P}_{\text{aug}}, \mathbf{K})\|_\infty \mathbf{D}^{-1} \right) \quad (12)$$

3.3 LPV H_∞ control

As stated before, applying H_∞ controllers to rotating machinery problems have two main advantages, reducing the critical speed peak and obtaining robust solutions. For the LVP control, it is chosen to apply the H_∞ control property only to obtain the vibration attenuation, the robustness problem is guaranteed by the quadratic Lyapunov stability in the LMI formulation.

Using the polynomial model from section 2.4, a static output-feedback control is obtained by means of the two-stage LMI formulation described by [1]. In the first stage a generic stabilizing state-feedback gain $\mathbf{K}(\alpha)$ is obtained. In the second stage, a matrix inequality which is not linear is proposed. However, utilizing the result for the first stage as a slack-variable, the second stage also becomes a LMI, which can be easily solved by convex optimization.

Because of the linearization, this procedure does not hold the necessity property. To increase the chances of finding solution it is usually utilized some auxiliary variable in the first stage to allow generating different possibilities for $\mathbf{K}(\alpha)$. Here only one auxiliary variable ε is utilized. Both LMI problems are solved in Matlab using the LMI packer toolboxes Rolmip [15] and the solver SDPT-3 [2]. More details about this implementation can be found in [16].

3.4 Weighting filters

When dealing with multi-objective controllers, a fundamental aspect is the choice of weighting filters. These filters allow to compensate for different units, scales, or ‘‘priority’’ along frequency range and have strong effects over the final performance. They can be placed at different inputs and outputs of the plant for different effects, and the tuning depends on the designer experience. Here, weights are applied to the components of the performance output \mathbf{z} , which is composed by the disc displacement and control force. This allows to demand higher amplitude attenuations at lower frequencies (first critical speed and instability) and low control efforts at higher frequencies, avoiding spill-over. The general formulation for the weighting functions are proper low and high-pass band filters, as in Eq. (13).

$$W_e(s) = g_e \quad W_u(s) = g_u \left(\frac{s + \frac{\omega}{k_u \sqrt{M_u}}}{k_u \sqrt{\varepsilon_u} s + \omega} \right)^k \quad (13)$$

For comparison reasons, the parameters for displacement filters and control force filters W_e and W_u , respectively, are the same for all the designed controllers. Only for the μ -synthesis control g_e and g_u were both multiplied by 10^3 to have approximate the same scale of the uncertainties inputs and outputs.

4 Results

This section is divided in two parts. The first part is focused on the identification and validation of the models. The second part concerns the analysis and comparison of the achieved control performances. For shorter nomenclature the systems will be referred as: open-loop (OL), closed-loop with dynamic H_∞ control (CLhinf), closed-loop with μ -synthesis (CLmu), and for closed-loop with degrees of dependence 0, 1 and 2 (CL0, CL1 and CL2, respectively).

4.1 System identification

Although the starting FEM model achieves relatively good estimation of the expected behaviour, it is necessary to make fine adjustments to get better matching between some key points: frequency and amplitude of the first bending mode as well as instability threshold. The frequency can be adjusted by slightly changing the diameters between shaft and disc elements that composes the additional pieces fixed in the shaft. The on-set stability and amplitude are heavily dependent on the bearing parameters. Some improvement can be achieved by considering reduced length (due to some possible border effect) and small variations in the load (due to assembly misalignments). The calculated bearing parameters and the second-degree polynomial approximation, obtained by least square fitting, are plotted in Figure 5. Extra weighting was considered on higher rotational speeds, since there the instability problem is critical.

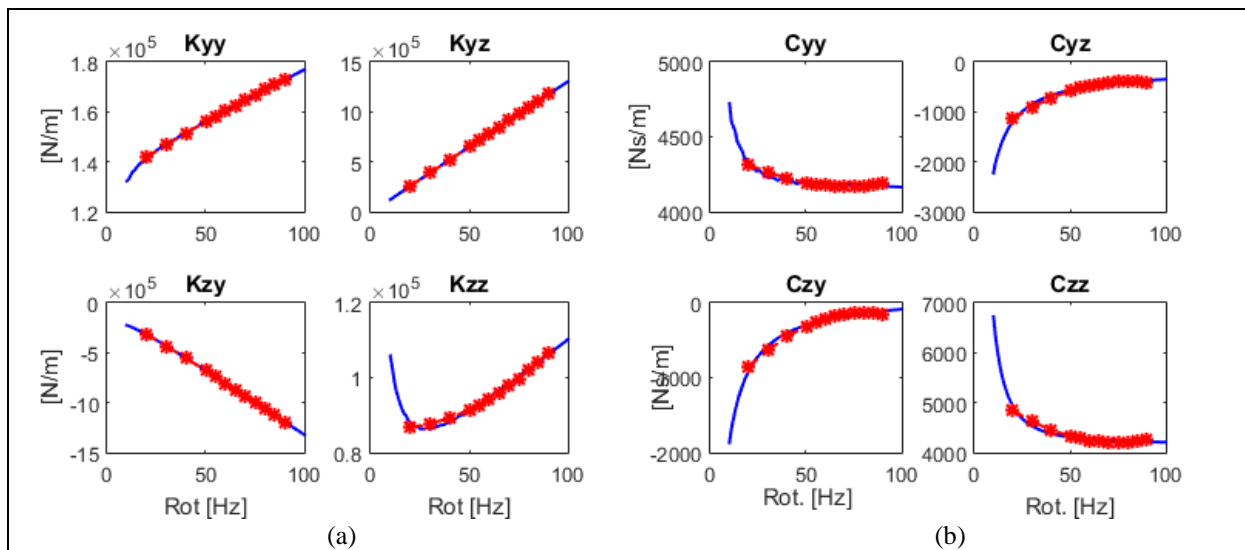


Figure 5: Reynolds (blue) bearing stiffness (a) and damping (b) coefficients, and approximations (red).

To analyse the rotor response to unbalance, measurement acquisitions of 5 s were accomplished with the rotor operating at the values from Table 1. Between each change of speed there was a delay of 4 s to allow the system to achieve stationary condition. Combining all the collected signal spectrum from AMB Z direction displacement is obtained the waterfall diagram from Figure 6.

From the same data, the unbalance response diagram (URD) for the maximum amplitude of the orbit at each rotational speed was also created. Despite showing less details about the signal composition, the URD allows better visualisation when comparing different curves. Figure 7 shows the comparison among the behaviour of the AMB displacement. The critical speed peak at approximately 28.5 Hz is clearly observed in OL curve. The distinct behaviour of the oil-whip is noticed by the OL amplitude amplification at 60 Hz at the URD and is confirmed in Figure 6 by the high amplitude at 0.5x line. In Figure 7 a peak at about 15 Hz is perceptible, and is attributed to assembly misalignment. The peak occurs when the 2x harmonic coincides with the rotor resonance.

To fit the amplitude, the Rayleigh damping coefficient was adjusted proportional to the stiffness, Eq. (14). For this procedure the AMB displacement curve was utilized, which apparently had less non-modelled influences in its response (lower amplitudes outside the critical speed). The result of the modelling can be seen in Figure 7 together with the response with AMB demanding force zero (OLamb). It is possible to state that both the model and the internal AMB control are well calibrated, since the three curves coincide.

In OLamb the anticipation of oil-whip is expected since the integrator force relieve some of the journal bearing load. Regarding the numerical simulation, it is based on a linear model, thus the instability is determined by the first occurrence of positive real part of the eigenvalues. In instability condition the linear model outputs tend to infinity, for this reason, the simulation line of URD is interrupted when a system with unstable poles is generated. In test, the rotor speed is automatically brought back to stable values when the sudden increase of

amplitude is detected. Therefore, in this paper, the URD value at oil-whip condition does not capture the amplitude that would be achieved in regime condition.

$$D_{\text{fem}} = 2.2 \times 10^{-4} K_{\text{fem}} \quad (14)$$

Table 1: Unbalance response rotational speeds

Measurement n°. (init:final)	1:17	18:38	39:45	46:54	55:58	59:64
rotation [Hz] (init:step:final)	10:1:26	27:0.2:31	32:1:38	40:2:56	57:1:62	63:2:69

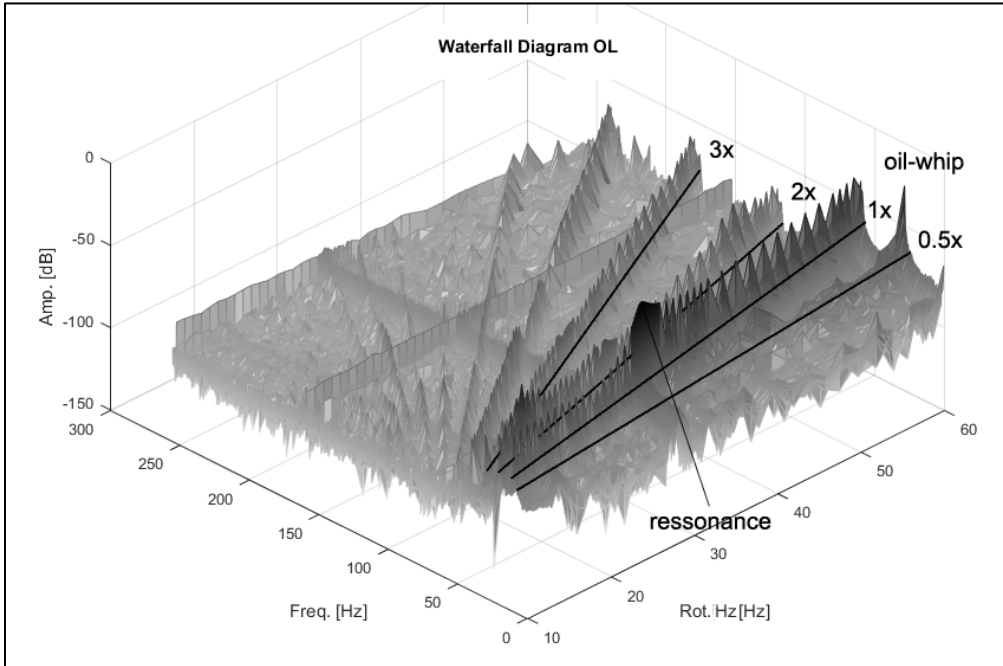


Figure 6: Waterfall diagram of OL at AMB Z direction.

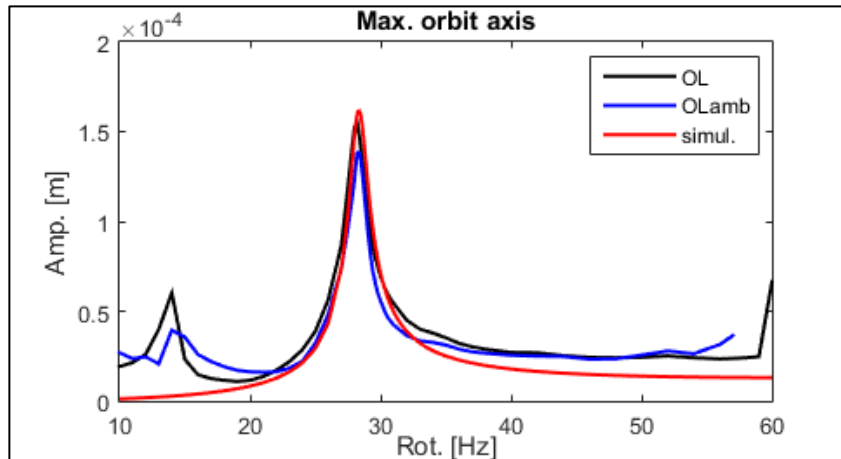


Figure 7: AMB displacement URD of OL, OLamb and Simulation.

4.2 Control performance

The control synthesis, described in section 3, utilized the parameters from Table 2. And the standard H_∞ design considered the reduced rotor model at 28 Hz (critical speed). The simulated URD with the resultant performances is shown in Figure 8. Note that all the controllers should assure stability for the whole considered rotational speed range. And different degrees of attenuation at critical speed were expected. Increasing the degree of dependence of the LPV controllers on the rotational speed rendered better attenuation. However, due to their static structure, the LPV controllers are limited to influence only the stiffness of the system. On the other hand, dynamic controllers are able to create forces with damping properties, and therefore achieving better attenuation at critical speed.

Figure 9 compares the experimental results. The experiment was conducted with rotor speeds up to 89 Hz. All the controllers presented stability for the whole designed range, which accomplishes the extension of the stability region by about 50% of the original stability limit. The test would probably be able to continue above 90 Hz, but due to the significantly high second mode amplitude, regarding the second plane unbalance (not accounted for during simulation) it risked reaching the non-linear region of the AMB, which would likely compromise the rotor stability and integrity. The comparison of the amplitudes shows clearly that a behavior considerably close to that what was simulated was obtained. Better performance was in fact observed by increasing the dependance on the rotational speed, and the dynamic controllers H_∞ and μ -synthesis achieved the best attenuations. Table 3 compares the achieved peak attenuation by the controllers in comparison to the OL.

Table 2: Control synthesis parameters.

	ω (Hz)	k_u	M_u	ε_u	g_u	g_u	ε
CL0	180	4	1	0.01	2×10^{-5}	2×10^{-5}	3.2×10^{-3}
CL1	180	4	1	0.01	2×10^{-5}	2×10^{-5}	3.2×10^{-3}
CL2	180	4	1	0.01	2×10^{-5}	2×10^{-5}	3.2×10^{-3}
CLhinf	180	4	1	0.01	2×10^{-5}	2×10^{-5}	-
CLmu	180	4	1	0.01	2×10^{-2}	1×10^3	-

Table 3: Control performance max(CL)/max(OL).

Attenuation [%]	CL0	CL1	CL2	CLhinf	CLmu
numerical	34.63	47.52	47.52	84.90	85.77
experimental	24.09	30.57	36.91	52.13	55.36

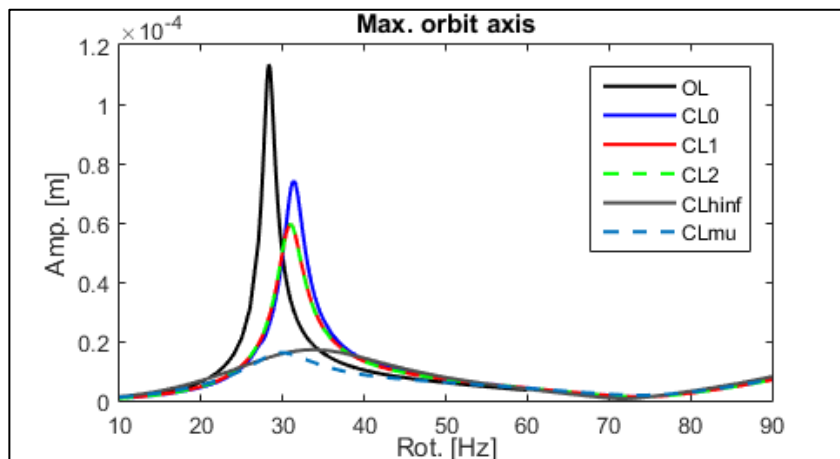


Figure 8: Simulated URD at the Disc for different controllers.

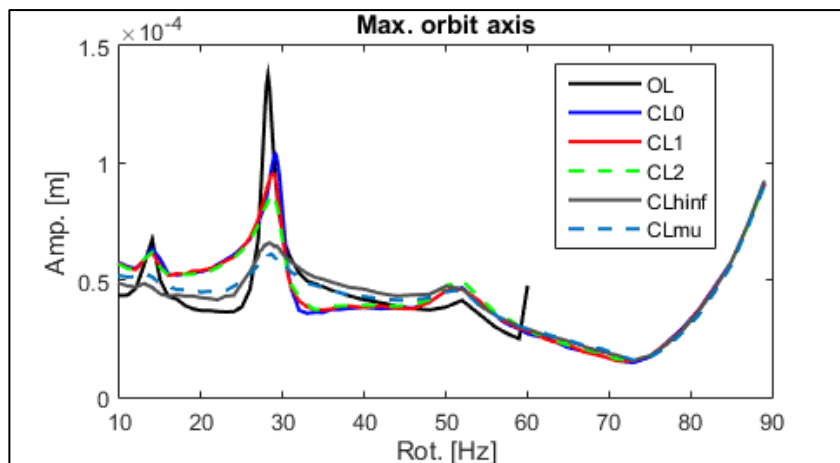


Figure 9: Experimental URD at the disc for different controllers.

5 Conclusion

In this work the flexible rotor dependence on the rotational speed was successfully modelled. Model based controllers were synthesized considering the AMB only for active vibration control purposes. The control performances were validated and compared in an experimental test rig. All proposed methods presented results coherent to those predicted by numerical simulations. Extended rotor stability range was achieved by avoiding oil-whip, while considerably attenuating the first bending critical speed. The LPV controllers showed improvements in performance when the degree of dependence of the rotational speed increased, but due to its static-gain nature, which limit their action to stiffness modification, the capability to suppress the vibration at critical speed were inferior to the dynamic versions of H_∞ and μ -synthesis.

Acknowledgement

The authors would like to thank grants # 2015/20363-6, # 2016/13059-1 and # 2017/15494-0 from the São Paulo Research Foundation (FAPESP) for the financial support, and the TU Darmstadt Institute of Applied Dynamics for the laboratory equipment and infrastructure, necessary for this research, and Bastian Pfau for all the help with the experiment design and theoretical discussions.

References

- [1] Agulhari, C., Oliveira, R. and Peres, P. (2010): Static output feedback control of polytopic systems using polynomial Lyapunov functions. *49th IEEE Conference on Decision and Control*, pp. 6894–901.
- [2] Agulhari, C.M., de Oliveira, R.C.L.F. and Peres, P.L.D. (2012): Robust LMI Parser: a computational package to construct LMI conditions for uncertain systems. *XIX Brazilian Conference on Automation (CBA 2012)*, p. 2298–305.
- [3] Almeida Gonçalves Siqueira, A., Nicoletti, R., Norrick, N., Lucchesi Cavalca, K., Fiori De Castro, H., Bauer, J. et al. (2012): Linear parameter varying control design for rotating systems supported by journal bearings. *Journal of Sound and Vibration*, **331**, pp. 2220–32.
- [4] Becker, F.B., Sehr, M.A. and Rinderknecht, S. (2017): Vibration isolation for parameter-varying rotor systems using piezoelectric actuators and gain-scheduled control. *Journal of Intelligent Material Systems and Structures*, **28**, pp. 1–12.
- [5] Friswell, M.I.M.I., Garvey, S.D. and Penny, J.E.T. (1995): Model reduction using dynamic and iterated IRS techniques. *Journal of Sound and Vibration*, **186**, pp. 311–23.
- [6] Gahinet, P. and Apkarian, P. (1994): A linear matrix inequality approach to Hinf control. *International Journal of Robust and Nonlinear Control*, **4**, pp. 421–48.
- [7] Machado, T.H. and Cavalca, K.L. (2015): Modeling of hydrodynamic bearing wear in rotor-bearing systems. *Mechanics Research Communications*, Elsevier Ltd. **69**, pp. 15–23.
- [8] Nelson, H.D. (1980): A Finite Rotating Shaft Element Using Timoshenko Beam Theory. *Journal of Mechanical Design*, **102**, pp. 793.
- [9] Pinkus, O. Solution of Reynolds' Equation for Finite Journal Bearings. *Transactions of the ASME*, **80**, pp. 858–64.
- [10] Riemann, B., Sehr, M.A., Schittenhelm, R.S. and Rinderknecht, S. (2013): Real gyroscopic uncertainties in robust control of flexible rotors. *Proceedings of the IEEE Conference on Decision and Control*, Florence. p. 3762–9.
- [11] Riemann, B., Araujo, E., Lucchesi, K., Fiori, H. and Castro, D. (2013): Oil whip instability control using m -synthesis technique on a magnetic actuator. *Journal of Sound and Vibration*, Elsevier. **332**, pp. 654–73.
- [12] Schweitzer, G. and Maslen, E.H. (2009): *Magnetic Bearings*. Springer Berlin Heidelberg, Berlin, Heidelberg.
- [13] Skricka, N. and Markert, R. (2002): Improvements of the integration of active magnetic bearings. *Mechatronics*, **12**, pp. 1059–68.
- [14] Stein, G. and Doyle, J.C. (1991): Beyond Singular-Values and Loop Shapes. *Journal of Guidance Control and Dynamics*, **14**, pp. 5–16.
- [15] Toh, K.C., Todd, M.J. and Tütüncü, R.H. (1999): SDPT3 — A Matlab software package for semidefinite programming, Version 1.3. *Optimization Methods and Software*, **11**, pp. 545–81.
- [16] Wu, M.F., Mendes, R.U. and Cavalca, K.L. (2017): Vibration Control of a Journal-Bearing Supported Rotor Using Gain-Scheduled Controller via LMI. *International Symposium on Dynamic Problems of Mechanics*, São Sebastião. p. 10.
- [17] Zhou, K. and Doyle, J.C. (1998): *Essentials of robust control*. Prentice Hall, Upper Saddle River, N.J.

Evaluation of vibration energy harvesters in tilting pad journal bearings

André Rodrigues Garcia da Silveira¹, Gregory Bregion Daniel²

¹Laboratory of Rotating Machinery, UNICAMP, CEP 13083-970, Campinas, Brazil, a193295@g.unicamp.br

²Laboratory of Rotating Machinery, UNICAMP, CEP 13083-970, Campinas, Brazil, gbdaniel@fem.unicamp.br

Abstract

Sensor energy consumption is a growing concern with the advent of the fourth industrial revolution and the arising need of condition monitoring. The necessity of alternative power sources is of increasing interest to the industry and the ambient vibration energy harvesting is a viable technology. The most common energy harvesters disseminated in the literature uses piezoelectric material to transform vibrational energy into electrical energy and therefore is the harvester type considered in this work.

The present work analyzes the feasibility of energy harvesting from a piezoelectric cantilever beam excited by an imposed motion at its tip due to the tilting pad motion. This bending introduces a stiffness in the pad that should be considered in the rotor dynamics with the purpose of assuring that the original behavior is not affected. Consequently, the tilting pad journal model with full coefficients must be used in order to determine the motion of each pad independently.

A Laval rotor was simulated with two tilting pad journal bearings with piezoelectric harvesters coupled with each pad. Changes in beam geometry were investigated and better parameters were determined in order to increase power output. It was possible to conclude that because this application produces 1mW of harvested energy, it is feasible and justifies further studies.

Keywords: Energy harvesting, piezoelectric, vibration, tilting pad

1 Introduction

With the advent of the fourth industrial revolution and the internet of things, there is an increasing necessity of condition monitoring in order to control site production and automate processes. Thus, power sources other than disposable batteries are desired, as batteries are power sources with limited lifespan and may induce machine down time in order to replace drained ones [1]. One alternative technology capable of powering sensors is ambient energy harvesting, being the solar energy harvesting the one with the biggest power-density, followed by thermophotovoltaic and piezoelectric harvesting [2] [3]. Piezoelectric harvesting is typically used to harvest vibrational energy and transform it in electrical energy with some advantages over other harvesting methods, such as ease of application [3], no need of external voltage source and a high electromechanical coupling [4]. This way, the energy harvesting mechanism used in the present paper is the piezoelectric.

Piezoelectric harvesters started being used almost 40 years ago [5], but only in the last decade has the study and development of piezoelectric harvesters increased due to the need of wireless, smart and independent sensors [6]. Typically, the piezoelectric harvester is made in the shape of a beam with two piezoceramic layers (bimorph) that act as capacitor plates. When the piezoelectric material is mechanically loaded, it develops a strain that is responsible for the creation of an electric field that charges this capacitor, thus inducing an electrical current. Due to the vibrational motion, the electrical current and the voltage generated are alternating and they need to be rectified to direct current/voltage through a diode rectifier bridge and a smoothing capacitor, in order to charge batteries or be used by DC sensors [3].

Despite the growing studies related to energy harvesting in recent years, most approaches have application in structural dynamics, with few works related to the dynamics of rotating machines. Regarding the application that will be proposed, this work aims to evaluate the energy harvesting system applied to journal bearings which are one of the most important components used in rotating machines. This component is responsible for the lubrication and support of the shaft that rotates with respect to the housing, in order to avoid the contact and wear between the components. One type of journal bearing is the cylindrical journal bearing that presents some advantages, as reduced price, ease of manufacturing and ease of assembling. However, it is subjected to

destabilizing forces that induce an unstable behavior to the machine in certain critical rotation speeds [7]. A tilting pad journal bearing is composed by a number of pads that are free to rotate and cannot resist external moments. Due to this ability, the destabilizing forces are greatly reduced or eliminated, and this component is not a source of machine instability anymore [8]. Because of this behavior, tilting pad bearings are vastly used in high-speed rotating machines.

Rotating machines are also subjected to unbalance inherent in the rotor that drives the shaft into making an orbit inside the bearing. In a tilting pad bearing, this orbit forces the pads to oscillate with a fixed frequency and amplitude, usually equal to rotor speed and due to constant unbalancing moment, respectively, enabling the use of piezoelectric harvesters in the bearing's pads.

This work brings these effects together, creating a model that evaluates the electrical energy that may be harvested from tilting pad bearings in order to power wireless sensors that are becoming a trend in the fourth industrial revolution era. The objective is to analyze the feasibility of this application, in order to know if the pad vibration generates enough energy to power its monitoring and to analyze the impact in power output due to changes in beam geometry.

2 Methodology

This section aims to present the main concepts and formulations used to model the piezoelectric harvester and the tilting pad bearing behavior. An ideal beam may theoretically oscillate in infinite frequencies and shapes and its displacement is the sum of all vibrations modes. Because each mode has a shape, they induce different strains in the beam material that will be calculated automatically by the model shown in this section. For this paper, all beams are considered to have the same geometry and are installed in the same spot on each tilting pad.

The tilting pad bearing used in this study is described in [9]. Typical applications do not need to consider the pads degrees of freedom and so only uses the reduced order stiffness-damping model. However, this paper aims to study the pad vibration and so the full coefficients model must be used. The guidelines to evaluate these coefficients are described in [8]. The coupling between bearing and piezoelectric harvester is described later in section 2.3. The complete model may be viewed in Figure 1. In this figure, it is possible to see the bearing pad with its pivot point, the bearing support and the piezoelectric beam.

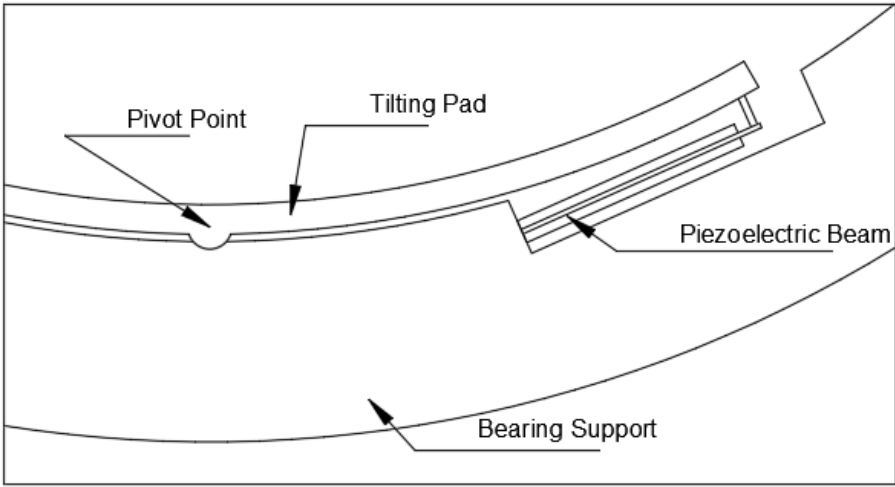


Figure 1 – Application Scheme with the bearing pad and the piezoelectric beam

2.1 Piezoelectric Harvester

The modeling of the piezoelectric harvester is assisted by Figure 2 that shows a bimorph piezoelectric beam, with two layers of piezoceramic material. According to this figure, L_b is the beam length, t_p is the piezoelectric height of each layer, t_s is the substrate height and b is the beam width. In this study, the piezoelectric material has the same width and length of the substrate.

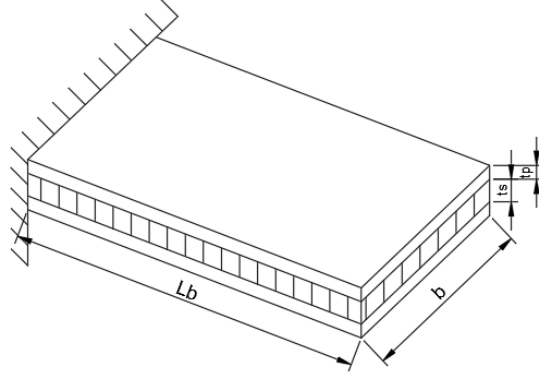


Figure 2 – Beam geometric variables (the hatched region represents the substrate material)

Some of the equations developed in this section were described by Sodano et al [10]. The first step is the deduction of the beam displacement as evaluated by Equation (1).

$$u(x, t) = \sum_{n=1}^N \phi_n(x) r_n(t) = \underline{\phi}(x) \underline{r}(t) \quad (1)$$

Where u is the beam displacement, ϕ_n is the beam mode shape of the n -th natural frequency, r_n is the temporal coordinate of the displacement of the n -th natural frequency and N is the total number of modes being considered in the analysis. According to [11], the mode shape of a cantilever beam is represented by Equation (2). This equation is necessary in order to evaluate the beam properties, such as stiffness and displacement.

$$\phi_n(x) = \cos(\beta_n x) - \cosh(\beta_n x) - \frac{\cos(\beta_n L_b) + \cosh(\beta_n L_b)}{\sin(\beta_n L_b) + \sinh(\beta_n L_b)} [\sin(\beta_n x) - \sinh(\beta_n x)] \quad (2)$$

With β_n being a beam constant, for each mode, that relates inertia to the stiffness. For a cantilever beam, β_n may be found as the result of the Equation (3) with initial estimate equal to $\beta_n = (2n - 1)\pi/2$.

$$\cos(\beta_n L_b) \cosh(\beta_n L_b) + 1 = 0 \quad (3)$$

The following equations were obtained considering Figure 2. The mass, stiffness and damping matrix are diagonal. The mass matrix is defined as the sum of the substrate mass and the piezoelectric material mass shown in Equation (4).

$$\begin{aligned} M &= M_s + M_p = \int \int \int \rho_s \underline{\phi}^T(x) \underline{\phi}(x) dV_s + \int \int \int \rho_p \underline{\phi}^T(x) \underline{\phi}(x) dV_p \\ &= bL_b(t_s \rho_s + 2t_p \rho_p) \begin{bmatrix} 1 & 0 & \dots & 0 \\ 0 & 1 & & 0 \\ \vdots & & \ddots & \vdots \\ 0 & 0 & \dots & 1 \end{bmatrix} \end{aligned} \quad (4)$$

Where ρ_s is the substrate density, ρ_p is the piezoelectric density, V_s is the substrate volume and V_p is the piezoelectric volume. The stiffness matrix is evaluated by Equation (5).

$$\begin{aligned} K &= K_s + K_p = \int \int \int y^2 \underline{\phi}^T(x)'' c_s \underline{\phi}(x)'' dV_s + \int \int \int y^2 \underline{\phi}^T(x)'' c_p \underline{\phi}(x)'' dV_p \\ &= \frac{b}{12} \left(c_s t_s^3 + c_p \left((t_s + 2t_p)^3 - t_s^3 \right) \right) \int_0^{L_b} \begin{bmatrix} \phi_1''^2(x) & 0 & \dots & 0 \\ 0 & \phi_2''^2(x) & & 0 \\ \vdots & & \ddots & \vdots \\ 0 & 0 & \dots & \phi_N''^2(x) \end{bmatrix} dx \end{aligned} \quad (5)$$

Where 'y' is the vertical coordinate, c_s is the Young's Modulus of the substrate, c_p is the Young's Modulus of the piezoelectric material measured at constant electric field, ϕ_n'' is the second derivative of the beam mode shape

The damping matrix is considered as proportional structural, being described by Equation (6).

$$C = \alpha M + \beta K \quad (6)$$

Where α is the Rayleigh coefficient proportional to mass and β is the Rayleigh coefficient proportional to stiffness.

The transition between mechanical and electric energy is made by the factor θ . Each mode has a different value that is considered in the array evaluated by Equation (7). A higher value of θ implies that more energy is traded between mechanical and electrical energies.

$$\underline{\theta} = - \int \int \int y \underline{\phi}^T(x)'' e_p \psi(y) dV_p = e_p b(t_s + t_p) \int_0^{L_b} \begin{bmatrix} \phi_1(x) \\ \phi_2(x) \\ \phi_3(x) \end{bmatrix}'' dx \quad (7)$$

With e_p being the PZT coupling coefficient that relates the stress to the applied electric field and ψ being evaluated by Equation (8).

$$\psi(y) = \begin{cases} -1/t_p, & t_s/2 < y < t_s/2 + t_p \\ 0, & -t_s/2 < y < t_s/2 \\ 1/t_p, & -t_s/2 - t_p < y < -t_s/2 \end{cases} \quad (8)$$

In addition, the two piezoelectric layers of the beam act like a capacitor in parallel with the electrical system [3]. This capacitor is not beneficial, as the harvester should charge it before transferring energy to the electrical sensor. This way, a big capacitance prevents the energy from going from the harvester to the sensor being powered by it and so its value should be minimized. The capacitance is evaluated by Equation (9).

$$C_p = \int \int \int \psi^T(y) \varepsilon \psi(y) dV_p = \frac{2\varepsilon bL}{t_p} \quad (9)$$

Where ε is the dielectric constant measured at constant strain. With every parameter defined, it is possible to evaluate the dynamic motion of the beam, evaluated by Equation (10) along with Equation (11).

$$M\ddot{r}(t) + C\dot{r}(t) + Kr(t) - \theta v(t) = \sum_{i=1}^{n_f} \phi(x_i) f_i(t) \quad (10)$$

$$\theta r(t) + C_p v(t) = q(t) \quad (11)$$

With f_i being the force applied at x_i and n_f being the number of external loads considered. In this case, there is only one load at the end of the beam. In addition, if there is no resonance in higher frequencies, the first frequency mode is responsible for the majority of the vibrational energy. This way, in order to simplify the model without substantial losses, only the first mode will be considered in this analysis.

Considering only one load applied at the end of the beam (see Figure 1) and only the first modal mode, the Equations (10) and (11) may be rewritten as Equations (12) and (13).

$$M\ddot{r}(t) + C\dot{r}(t) + \left(K + \frac{\theta^2}{C_p}\right)r(t) - \frac{\theta}{C_p}q(t) = \phi(L_b)F(t) \quad (12)$$

$$\dot{q}(t) = -\frac{1}{C_p R}q(t) + \frac{\theta}{C_p R}r(t) \quad (13)$$

Where R is the electrical resistance, q is the capacitor charge, \dot{q} is the electrical current and F is the force between the pad and the piezoelectric beam.

2.2 Tilting Pad Bearing

The tilting pad bearing should be incorporated in the finite element method normally using full bearing coefficients. The discretized rotor is represented in Figure 3. The bearings are represented by the red triangles on the second and on the tenth elements and the disk is represented by the yellow pentagon on the sixth element.

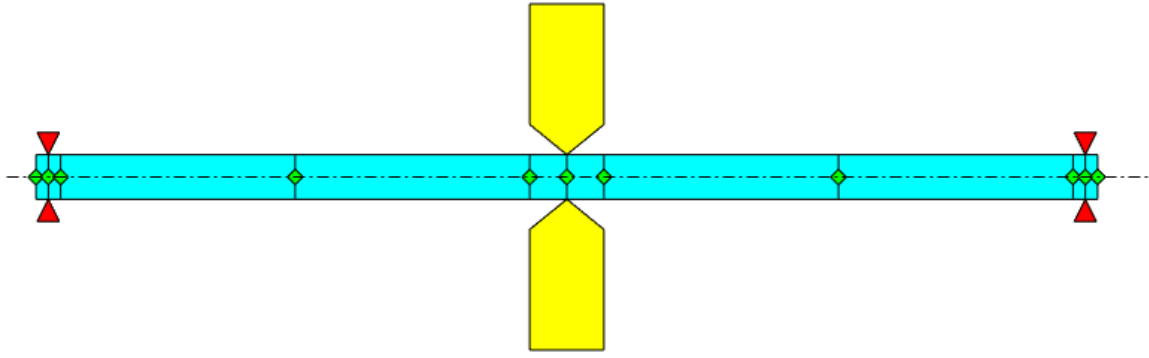


Figure 3 – Rotor scheme with the bearings being evidenced with the triangles and the disk in the center

Normally there is not an external moment in the pads and so the external moment is set to zero, however in the model here presented, there is a moment due to the piezoelectric beam force at the tip of the pad. In the pad equation, this should be considered, so that the bearing equation is shown as Equation (14).

$$\begin{bmatrix} M_e & 0 & 0 & \dots & 0 \\ 0 & M_e & 0 & \dots & 0 \\ 0 & 0 & J_p & & 0 \\ \vdots & \vdots & & \ddots & \\ 0 & 0 & 0 & & J_p \end{bmatrix} \begin{Bmatrix} \ddot{x} \\ \ddot{y} \\ \ddot{\alpha}_1 \\ \ddot{\alpha}_2 \\ \ddot{\alpha}_3 \end{Bmatrix} + \begin{bmatrix} C_{xx} & C_{xy} & C_{x\alpha_1} & \dots & C_{x\alpha_{n_p}} \\ C_{yx} & C_{yy} & C_{y\alpha_1} & \dots & C_{y\alpha_{n_p}} \\ C_{\alpha_1 x} & C_{\alpha_1 y} & C_{\alpha_1 \alpha_1} & & 0 \\ \vdots & \vdots & & \ddots & \\ C_{\alpha_{n_p} x} & C_{\alpha_{n_p} y} & 0 & & C_{\alpha_{n_p} \alpha_{n_p}} \end{bmatrix} \begin{Bmatrix} \dot{x} \\ \dot{y} \\ \dot{\alpha}_1 \\ \vdots \\ \dot{\alpha}_{n_p} \end{Bmatrix} + \begin{bmatrix} K_{xx} & K_{xy} & K_{x\alpha_1} & \dots & K_{x\alpha_{n_p}} \\ K_{yx} & K_{yy} & K_{y\alpha_1} & \dots & K_{y\alpha_{n_p}} \\ K_{\alpha_1 x} & K_{\alpha_1 y} & K_{\alpha_1 \alpha_1} & & 0 \\ \vdots & \vdots & & \ddots & \\ K_{\alpha_{n_p} x} & K_{\alpha_{n_p} y} & 0 & & K_{\alpha_{n_p} \alpha_{n_p}} \end{bmatrix} \begin{Bmatrix} x \\ y \\ \alpha_1 \\ \vdots \\ \alpha_{n_p} \end{Bmatrix} = \begin{Bmatrix} F_x \\ F_y \\ -F_1 L_1 \\ \vdots \\ -F_{n_p} L_{n_p} \end{Bmatrix} \quad (14)$$

Where M_e is the shaft mass seen by the bearing, J_p is the pad moment of inertia, C_{ij} and K_{ij} are the damping and the stiffness of the bearing in direction 'i' with respect to motions in direction 'j', F_i is the force in each direction and L_i is the length between the point of the application of the piezoelectric beam force and the pad pivot for each pad (they are set to be equal in this paper). Note that this model considers each pad as an independent degree of freedom, so that even if the piezoelectric beams are equal, their power output may not be, because each pad vibrates with different amplitudes.

2.3 Complete Model

In order to unify both models, it is necessary to use the same degrees of freedom for both of them. This way, as seen in Figure 4, there is always contact between the piezoelectric beam and the pad, so that it is possible to write Equation (15) that relates r (the piezoelectric beam variable) with α (the tilting pad variable).

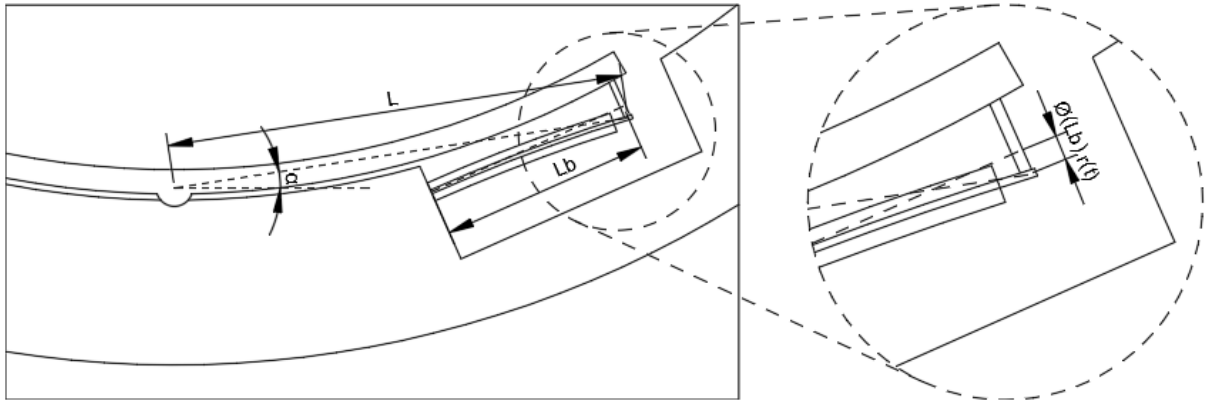


Figure 4 – Evidence that the displacement of the pad tip is equal to the displacement of the beam tip

$$u(L, t) = L\alpha(t) = \phi(L_b)r(t) \rightarrow r(t) = \frac{L}{\phi(L_b)}\alpha(t) \quad (15)$$

So, rewriting Equations (12) and (13) in this coordinate system, the Equations (16) and (17) are obtained as:

$$M \frac{L^2}{\phi^2(L_b)} \ddot{\alpha}(t) + C \frac{L^2}{\phi^2(L_b)} \dot{\alpha}(t) + \left(K + \frac{\theta^2}{C_p} \right) \frac{L^2}{\phi^2(L_b)} \alpha(t) - \frac{\theta L}{\phi(L_b)C_p} q(t) = FL \quad (16)$$

$$\dot{q}(t) + \frac{1}{C_p R} q(t) - \frac{\theta L}{C_p R \phi(L_b)} \alpha(t) = 0 \quad (17)$$

Even if the piezoelectric beams coupled with each pad are equal, because their tip displacement is different, the external moment applied to the pad is different. This way, Equation (16) should be substituted in Equation (14) once for each pad opening one extra degree of freedom to the system for each capacitor charge q_i .

The bearing state-space matrix is shown in Equation (18).

$$\begin{bmatrix} [I] & [0] & [0] \\ [0] & [M_j + M_b] & [0] \\ [0] & [0] & [I] \end{bmatrix} \begin{Bmatrix} \{\dot{x}\} \\ \{\ddot{x}\} \\ \{\dot{q}\} \end{Bmatrix} = \begin{bmatrix} [0] & [I] & [0] \\ -[K_b + K_j] & -[C_b + C_j] & [\theta^*] \\ \frac{[\theta^*]}{R} & [0] & \left[-\frac{1}{C_p R} \right] \end{bmatrix} \begin{Bmatrix} \{x\} \\ \{\dot{x}\} \\ \{q\} \end{Bmatrix} + \begin{Bmatrix} \{0\} \\ \{F_j\} \\ \{0\} \end{Bmatrix} \quad (18)$$

Where I is the identity matrix, M_j , K_j and C_j are the tilting pad journal bearing mass, stiffness and damping matrixes, respectively, defined in Equation (14) and the other matrixes are described from Equation (19) to (23).

$$[M_b] = M \frac{L^2}{\phi^2(L_b)} [I]_{n_p \times n_p} \quad (19)$$

$$[K_b] = \left(K + \frac{\theta^2}{C_p} \right) \frac{L^2}{\phi^2(L_b)} [I]_{n_p \times n_p} \quad (20)$$

$$[C_b] = C \frac{L^2}{\phi^2(L_b)} [I]_{n_p \times n_p} \quad (21)$$

$$[\theta^*] = \frac{\theta L}{\phi(L_b)C_p} [I]_{n_p \times n_p} \quad (22)$$

$$\left[-\frac{1}{C_p R} \right] = -\frac{1}{C_p R} [I]_{n_p \times n_p} \quad (23)$$

Note that these matrixes may be written in this way because all beams are equal and applied at the same spot in the tilting pad. By integrating the bearing model into the finite element method for the rotor, it is possible to evaluate the rotor behavior along with the piezoelectric beam charge and current output. Finally, the mean electrical power output was evaluated by Equation (24):

$$P_{mean} = \frac{\int_t^{t+\Delta t} R \dot{q}(t)^2 dt}{\Delta t} \quad (24)$$

Where P_{mean} is the mean power output and Δt is a time interval big enough to smooth eventual power peaks.

3 Results and Discussion

As previously stated, the purpose of this work is to estimate the power output of a piezoelectric harvester in order to power the tilting pad bearing sensors and to study the feasibility of this application. According to [1], the power output necessary to activate a wireless sensor is 1mW and that was set to be the target power output necessary to ensure the feasibility of this application. Figure 3 shows the Laval rotor considered in these analyses, with the parameters presented in Table 1. This rotor is being excited by an unbalance moment in the disk that introduces a rotating load at both tilting pad bearings, whose parameters are presented in Table 2. Finally, this unbalance is the responsible of the vibration the pads, exciting the piezoelectric beam and generating power. The beam parameters are presented in Table 3.

Table 1 – Rotor parameters used in the computational simulations

Parameters and units	Symbols	Values
Elastic modulus [GPa]	E	200
Poisson's ratio []	ν	0.3
Material density [kg/m ³]	ρ	7850
Shaft external diameter [m]	D_{ex}	0.180
Shaft internal diameter [m]	D_{in}	0.000
Shaft element length (journal bearing) [m]	L_j	0.050
Shaft element length (disk) [m]	L_d	0.150
Shaft element length (other) [m]	L_o	0.975
Rayleigh coefficient for mass matrix []	α	0
Rayleigh coefficient for stiffness matrix []	β	4e-4
Disc width [m]	L_{disk}	0.300
Disc internal diameter [m]	D_{din}	0.180
Disc external diameter [m]	D_{dex}	1.391
Unbalance momentum [kg.m]	$\eta\xi$	0.0175
Rotor speed [rpm]	n	6000

Table 2 – Tilting pad journal bearing parameters used in the computational simulations

Parameters and units	Symbols	Values
Number of pads []	n_p	4
Bearing diameter [m]	D_j	0.180
Bearing length [m]	L_j	0.080
Radial Clearance [μ m]	h_0	260
Viscosity SAE [mPa.s]	μ_{oil}	46
Load configuration	–	Load on pad
Bearing load in vertical direction [N]	F_y	-21580
Bearing load in horizontal direction [N]	F_x	0

Table 3 – Piezoelectric beam parameters used in the computational simulations

Parameters and units	Symbols	Initial values
Distance between force application and pivot [m]	L	0.065
Beam length [m]	L_b	0.020
Beam width [m]	b	0.005
Substrate material thickness [m]	t_s	0.001
Piezoelectric material thickness [m]	t_p	0.0005
Substrate material density [kg/m ³]	ρ_s	9000
Piezoelectric material density [kg/m ³]	ρ_p	7500
Substrate elasticity modulus [GPa]	c_s	105
Piezoelectric elasticity modulus [GPa]	c_p	60.6
Piezoelectric coupling coefficient [C/m ²]	e_p	-16.6
Dielectric constant [nF/m]	ϵ	25.55

Section 3.1 analyzes the rotor model without the piezoelectric beam in order to establish the nominal rotor behavior without the inclusion of the beam. Section 3.2 presents the analysis of the piezoelectric beam alone in

order to find the best geometries and properties that will be used in the complete model and finally section 3.3 joins both models and analyzes its dynamic.

3.1 Dynamic Analysis of the Tilting Pad Bearing without the Piezoelectric Beams

The first analysis made is of the bearing without the piezoelectric beams. This analysis aims to provide information about the current operation status of the equipment. With the addition of the beams, the orbit may not drastically change, in order for the pad not to introduce instabilities in the system. Figure 5 shows the shaft's orbit of the journal inside the tilting pad bearing. It is possible to verify that the bearing is almost centered in the horizontal with a smaller vertical orbit with an ellipsoid overall shape. The horizontal peak-to-peak displacement is $8,0\mu\text{m}$ and the vertical displacement is $1,8\mu\text{m}$.

Regarding the tilting pad displacement, the analysis showed that its tip displacement is $2,2\mu\text{m}$. This value is expected to decrease once the beams are integrated, because they introduce extra damping in the system [3]. Thus, a tip displacement of $2\mu\text{m}$ will be considered in section 3.2 and validated in section 3.3.

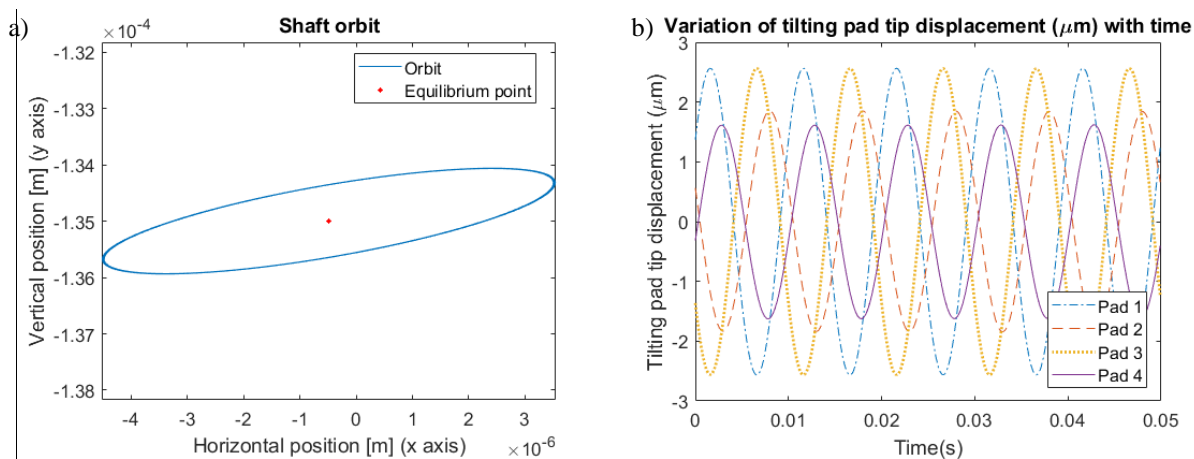


**Figure 5 – a) Shaft orbit of the journal inside the tilting pad bearing without the piezoelectric beams
b) Variation of tilting pad displacement without the piezoelectric beams**

3.2 Piezoelectric beam analysis

The second analysis approached the piezoelectric beam. Some initial parameters were determined in order to analyze which one had more influence in the beam response. These parameters are presented in the first line (Case 1) of the Table 4. With these parameters, it was possible to simulate the power output of the beams considering two beams per pad symmetrically installed (one beam on each side). One important variable for this analysis is the tilting pad tip displacement. If this displacement increases, then the beam is more requested and it yields a bigger strain, producing a bigger power output. Other important variable is the vibration frequency. For the same tilting pad tip displacement, if the frequency increases, the power output tends to increase as well. However, for this equipment, the frequency is set to be the same as the rotation speed since that is the unbalance excitation frequency (only synchronous excitation). As discussed in section 3.1, the tip displacement that will be considered has a value of $2\mu\text{m}$.

In order to analyze the sensibility of each parameter in the power output, each one was doubled one at a time. The results are shown in Table 4. Notice that this analysis also evaluated the stiffness of the beam, because a beam stiffness in the same order of magnitude of the bearing stiffness can affect rotor orbit.

Table 4 – Power output for each configuration considering a pad tip displacement of 2 μ m and four beams per pad for a total of sixteen beams.

Case	L	L _b	b	t _s	t _p	ρ_s	ρ_p	C _s	C _p	e _p	ϵ	Power	Stiffness
Units	m	m	m	m	m	kg/m ³	kg/m ³	GPa	GPa	C/m ²	nF/m	mW	N/m
1	0.065	0.030	0.010	0.001	0.0005	9000	7500	105	60.6	-16.6	25.55	0.1716	231
2	x2											0.1716	925
3		x2										0.0214	29
4			x2									0.343	463
5				x2								0.4766	853
6					x2							0.5796	741
7						x2						0.1716	231
8							x2					0.1716	231
9								x2				0.1716	274
10									x2			0.1720	402
11										x2		0.6862	285
12											x2	0.0858	222
Enhanced	0.065	0.040	0.020	0.002	0.0014	9000	7500	105	60.6	-16.6	25.55	2.1078	2650

As can be seen in Table 4, there are some parameters that does not alter significantly the power output, such as the distance between the pad pivot and the point of application of the beam (L), the material density of both materials (ρ_i) and the elasticity modulus of both materials (c_i). Some changes decreases the power output, such as increases in the beam length and in the dielectric constant (ϵ). Finally, increases in the beam width (b), both material thicknesses (t_i) and in the piezoelectric coupling coefficient (e_p) increases the power output. Since the power output necessary for this application is of 1mW, the parameters were changed in order to achieve this value and the results are shown in the last line of the table with the label “Enhanced”. Note that this is not the optimized configuration, as no optimization algorithms were used. However, future work may use one in order to maximize the power output with proper boundary conditions. These enhanced parameters are the ones shown in Table 3. In addition, the beam stiffness is two orders of magnitude smaller than the bearing stiffness, which should not change the rotor behavior.

This way, the result found in the last line of the table are used in the dynamic analysis of the complete system with the piezoelectric beams, the tilting pad bearing and the rotor.

3.3 Dynamic Analysis of the Complete System

In this section, the complete system is analyzed. The data used in this simulation are described in Table 1, Table 2 and Table 3. The shaft orbit inside the bearing is displayed in Figure 6.

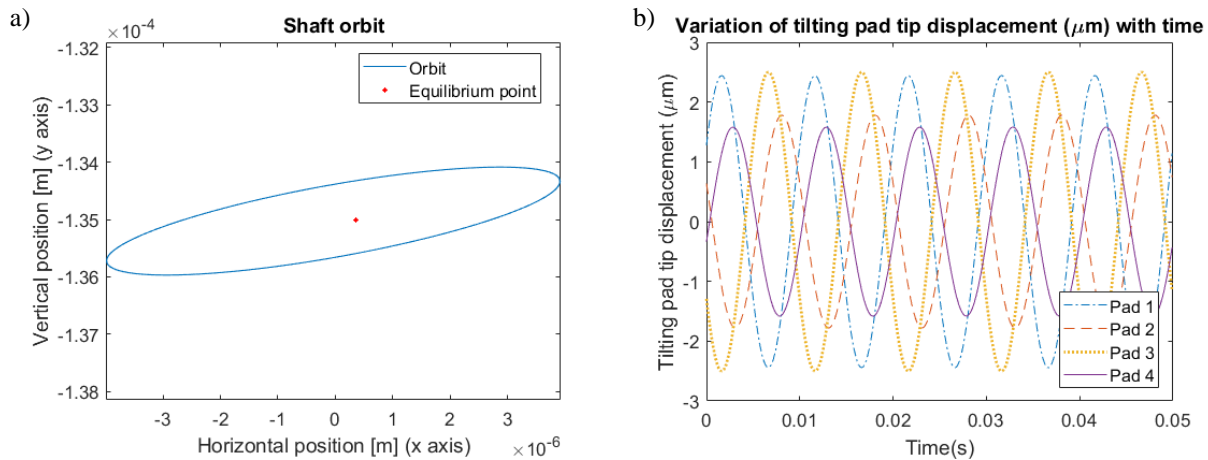


Figure 6 – a) Shaft orbit of the journal inside the tilting pad bearing with the piezoelectric beams. b) Variation of tilting pad displacement with the piezoelectric beams

It is possible to see that the shape of the orbit and the amplitude value of the motion are the same as the ones without the piezoelectric beams. The horizontal peak-to-peak displacement is $7,9\mu\text{m}$ and the vertical displacement is $1,9\mu\text{m}$. The bigger change is that the orbit is not centered in $x_{eq} = -0,5\mu\text{m}$ horizontal position, but has moved to $x_{eq} = 0,4\mu\text{m}$. However, because the journal is still far from the pads this change should not bring a big influence to system dynamic.

The pad tip displacement was reduced, as expected, but to a value of $2,1\mu\text{m}$. With this final displacement, it was possible to evaluate the total power output of the system $P_{output} = 1.16\text{mW}$. According to [1], this is enough to power the sensors, enabling the use of this application.

4 Conclusion

As discussed in the previous section, it is possible to conclude that the objective of this study was successfully achieved. A mathematical model that predicts the power output of a piezoelectric harvester installed in a tilting pad bearing was made and simulated. The simulations predict a power output of the order of 1mW , enough to power a sensor that monitors this bearing.

A sensibility analysis of the piezoelectric beam was made in order to establish which parameters were more important. It was seen that the beam length, the beam width, the layers thicknesses, the dielectric constant and the piezoelectric coupling coefficient are the main variables that alters the power output of the system.

In this paper, no optimization analysis were carried in order to maximize the power output. However, a simple enhancement of the parameters assured the feasibility of the application, justifying further analysis.

Finally, the inclusion of the piezoelectric beam in the bearing does not cause significant changes in the rotor response, showing that the energy harvesting system can be used in this application.

Acknowledgement

The authors thank CNPq (grant 141389/2017-6) and FAPESP (grant 2015/20036-5) for the financial support of this research.

References

- [1] Häggstrom, F. (2015): Energy harvesting for smart-internet-connected bearings. Dissertation, Lulea University of Technology, Lulea..
- [2] Dutoit, N. E., Wardle, B. L. and Kim, S. G. (2005): Design considerations for MEMS-scale piezoelectric mechanical vibration energy harvesters. *Integr. Ferroelectr.*, 71, pp. 121-160..
- [3] Erturk, A. and Inman, D. J. (2011): Piezoelectric energy harvesting. John Wiley & Sons, Chichester..
- [4] Shu, Y. C. and Lien, I. C. (2016): Analysis of power output for piezoelectric energy harvesting systems. *Smart Mater. Struct.*, 15, pp. 1499-1512.
- [5] Roberts, W. M. (1982): US Grant No. US4442372A. New York, United States of America..
- [6] Du, S., Amaratunga, G. A. J. and Seshia, A. A. (2018): A Cold-Startup SSHI Rectifier for Piezoelectric Energy Harvesters with Increased Open-circuit voltage. *IEEE Trans. Power Electron.*, pp. 1-12..
- [7] Frêne, J., Nicolas, D., Degueurce, B., Berthe, D. and Godet, M. (1990): Hydrodynamic lubrication bearings and thrust bearings. Elsevier Science B. V., Amsterdam..
- [8] Dimond, T., Younan, A. and Allaire, P. (2011): A review of tilting pad bearing theory. *Int. J. Rotating Mach.*, 2011, pp. 1-23.
- [9] Daniel, G. B. (2012): Desenvolvimento de um modelo termohidrodinâmico para análises em mancais segmentados. Dissertation, UNICAMP, Campinas..
- [10] Sodano, H. A., Park, G. and Inman, D. J. (2004): Estimation of electric charge output for piezoelectric energy harvesting. *Strain*, 40(2), pp. 49-58..
- [11] Rao, S. S. (2007): Vibration of continuous systems. John Wiley & Sons, New Jersey..

Vibration of rigid rotors supported by hydrodynamic bearings controlled by magnetically sensitive oils

Jaroslav Zapoměl^{1,2}, **Jan Kozánek**³, **Petr Ferfecki**^{4,5}

¹ Department of Applied Mechanics, VŠB-Technical University of Ostrava, 17. listopadu 15, 708 33 Ostrava-Poruba, Czech Republic, jaroslav.zapomel@vsb.cz

² Department of Dynamics and Vibration, Institute of Thermomechanics, Dolejškova 5, 182 00 Prague 8, Czech Republic, zapomel@it.cas.cz

³ Department of Dynamics and Vibration, Institute of Thermomechanics, Dolejškova 5, 182 00 Prague 8, Czech Republic, kozanek@it.cas.cz

⁴ Department of Applied Mechanics, VŠB-Technical University of Ostrava, 17. listopadu 15, 708 33 Ostrava-Poruba, Czech Republic, petr.ferfecki@vsb.cz

⁵ IT4Innovations National Supercomputing Center, VŠB-Technical University of Ostrava, 17. listopadu 15, 708 33, Ostrava-Poruba, Czech Republic, petr.ferfecki@vsb.cz

Abstract

A rotor support element composed of a squeeze film damper and a hydrodynamic bearing is characterized for high loading capacity, high damping, and increased stability of lateral vibration of rotating machines. A simple dynamical analysis shows that minimizing amplitude of the rotor vibration and of the force transmitted between the rotor and its stationary part in a wide interval of running velocities requires to adapt the damping effect in the rotor supports to the current operating speed. It implies it is worth to investigate a new design element that consists of a classical hydrodynamic bearing placed in a magnetorheological squeeze film damper, the damping effect of which can be controlled. Its mathematical model was developed and implemented in the procedures for analysis and stability evaluation of the steady state vibration of rigid rotors. The performed computational simulations show that the magnetorheological damper enables to reduce amplitude of the rotor vibration and of the force transmitted through the support elements in a wide range of operating speeds and to extend the stability limit by controlling the damping force. The proposal of a novel controllable rotor support element, the development of its mathematical model, its implementation into the computational procedures for analysis of oscillation of rotating machines, and learning more on its effect on vibration attenuation are the principal contributions of the carried out research work.

1 Introduction

Unbalance is one of the principle sources of excitation of lateral oscillation of rotating machines and of increase of time varying forces transmitted between the rotor and its stationary part.

The rotors are often mounted in hydrodynamic bearings for their high load capacity, high damping and quiet operation. Their applicability is limited by the critical speed. After its exceeding the oscillation produced by the rotor unbalance becomes unstable and self-excited vibration with large amplitude is developed. The stability limit can be increased if the hydrodynamic bearings are inserted in damping elements.

The analysis reported in [1] shows that the damping effect produced by the damping elements placed in the rotor supports must be adaptable to the current operating speed to achieve the optimum compromise between reducing the vibration amplitude and minimizing the force transmitted between the rotor and its stationary part. In the interval of lower angular speeds the damping should be maximum. For higher velocities the damping should be minimum but still sufficiently high to be able to prevent setting on the self-excited vibration.

The technological solution that makes it possible to adapt the damping effect to the current running speed is represented by magnetorheological squeeze film dampers. There is a number of articles and conference papers that deal with their design, function, experimental investigations and applications for the vibration attenuation of rotating machines [2], [3]. Zapoměl et al. developed the mathematical model of a short squeeze film magnetorheological damper, which is based on representing the magnetorheological oil by a bilinear material

[4]. The results of the study of distribution of magnetic flux in the damper body and of determination of magnetic induction in the lubricating film are reported by Ferfecki et al. [5].

This paper deals with a new semiactive support element that is a combination of a hydrodynamic bearing and a magnetorheological squeeze film damper, with development of its mathematical model and with its implementation into computational procedures for analysis of dynamical behaviour of rigid rotors. Results of the computational simulations show that an appropriate control of the damping effect enables to minimize amplitude of the rotor vibration and of the transmitted force in a wide extent of the operating speeds and increase of the stability limit of the rotor lateral oscillation. The development of a mathematical model of the new support element and learning more on its influence on the rotor vibration are the principle contributions of this paper.

2 Modelling of the support element

The proposed support element (Fig. 1) consists of a magnetorheological squeeze film damper and a hydrodynamic bearing. The principal parts of the damper are two concentric rings between which there is a layer of magnetorheological oil. The inner ring is connected to the damper housing by a spring element (e.g. a cage spring) and to the shaft journal by a hydrodynamic bearing. Lateral oscillation of the rotor squeezes the oil film between the rings, which produces the damping effect. In the damper housing there are embedded electric coils generating magnetic flux passing through the magnetorheological oil. As resistivity against the flow of magnetorheological fluids depends of magnetic induction, the change of the applied current changes the damping force.

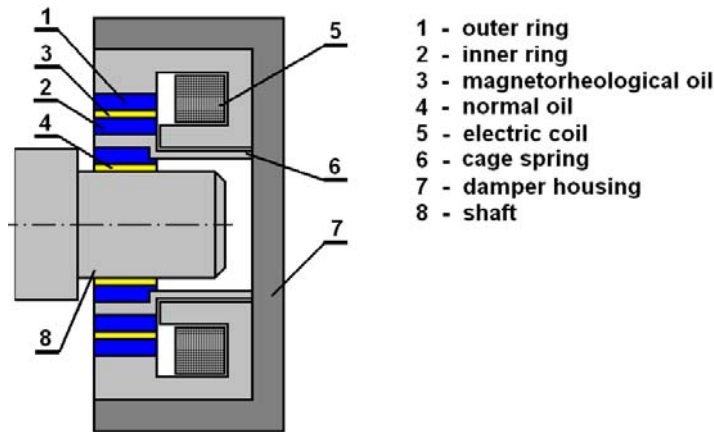


Figure 1: Investigated support element.

The mathematical model of the proposed support element is based on assumptions of the classical theory of lubrication [6]. The hydrodynamic bearing is considered to be of a finite length. The pressure distribution in the oil film is described by the Reynolds equation [6], [7]

$$\frac{1}{R_B^2} \frac{\partial}{\partial \varphi_B} \left(\frac{h_B^3}{\eta_O} \frac{\partial p_{HD}}{\partial \varphi_B} \right) + \frac{\partial}{\partial Z_B} \left(\frac{h_B^3}{\eta_O} \frac{\partial p_{HD}}{\partial Z_B} \right) = 6\omega \frac{\partial h_B}{\partial \varphi_B} + 12\dot{h}_B. \quad (1)$$

p_{HD} is the pressure in oil film of the hydrodynamic bearing, η_O is the normal oil dynamic viscosity, Z_B , φ_B are the hydrodynamic bearing axial and circumferential coordinates, respectively, h_B is the oil film thickness, R_B is the shaft radius, ω is the angular speed of the rotor rotation and $(\dot{})$ denotes the first derivative with respect to time.

The boundary conditions express that the pressure at both ends of the oil film is equal to the pressure in the ambient space and that the pressure at locations of the oil inlets is equal to the input one.

In the developed mathematical model the magnetorheological oil is represented by bilinear theoretical material and the damper is considered to be short and symmetric relative to its middle plane. The pressure distribution in the lubricating layer is governed by the Reynolds equation adapted to bilinear material

$$\frac{\partial}{\partial Z_D} \left(\frac{1}{\eta_C} h_D^3 p'_{MR} \right) = 12\dot{h}_D \quad \text{for} \quad 0 \leq Z_D \leq Z_C, \quad (2)$$

$$\frac{\partial}{\partial Z_D} \left[\frac{1}{\eta} \left(h_D^3 p'_{MR} + 3h_D^2 \tau_y + 8 \frac{\tau_c^3}{p_{MR}'^2} - 12 \frac{\tau_y \tau_c^2}{p_{MR}'^2} \right) - \frac{8}{\eta_c} \frac{\tau_c^3}{p_{MR}'^2} \right] = 12 \dot{h}_D \quad \text{for} \quad \dot{h}_D < 0 \quad \text{and} \quad Z_D > Z_C, \quad (3)$$

where

$$Z_C = -\frac{\tau_c h_D^2}{6\eta_c \dot{h}_D}, \quad (4)$$

$$p'_C = -\frac{2\tau_c}{h_D}. \quad (5)$$

p_{MR} is the pressure in the film of magnetorheological oil, p'_{MR} stands for the pressure gradient in the axial direction, Z is the axial coordinate, h_D is the oil film thickness, τ_y is the yielding shear stress, τ_c is the shear stress at the core border (the core is the region in the oil layer where the velocity rate is low and the oil behaves almost as a solid matter [8]), η_c, η are the dynamic viscosities of the oil inside and outside the core area, respectively, Z_C defines the axial coordinate of the location where the core touches the rings surfaces, and p'_C denotes the pressure gradient in the axial direction at location Z_C .

The boundary conditions express that pressure in the magnetorheological oil at the ends of the lubricating film is equal to the pressure in the ambient space. More details on derivation of equations (2) - (5) and on their solving can be found in [4].

In the developed mathematical model it is assumed that in areas in the oil film where the pressure drops to a critical level a cavitation takes place and that pressure of the medium in cavitated regions remains constant and equal to the pressure in the ambient space p_A

$$p_B = p_{HD} \quad \text{for} \quad p_{HD} \geq p_A, \quad (6)$$

$$p_B = p_A \quad \text{for} \quad p_{HD} < p_A, \quad (7)$$

$$p_D = p_{MR} \quad \text{for} \quad p_{MR} \geq p_A, \quad (8)$$

$$p_D = p_A \quad \text{for} \quad p_{MR} < p_A. \quad (9)$$

The y and z components of the hydraulic bearing force acting on the shaft journal (F_{hdy}, F_{hdz}) and of the magnetorheological damping force acting on the inner damper ring (F_{mry}, F_{mrz}) are calculated by integration of the pressure distribution in the oil films taking into account different pressure profiles in noncavitated and cavitated areas

$$F_{hdy} = -R_B \int_0^{L_B} \int_0^{2\pi} p_B \cos \varphi_B \, d\varphi_B \, dZ_B, \quad (10)$$

$$F_{hdz} = -R_B \int_0^{L_B} \int_0^{2\pi} p_B \sin \varphi_B \, d\varphi_B \, dZ_B, \quad (11)$$

$$F_{mry} = -2R_D \int_0^{\frac{L_D}{2}} \int_0^{2\pi} p_D \cos \varphi_D \, d\varphi_D \, dZ_D, \quad (12)$$

$$F_{mrz} = -2R_D \int_0^{\frac{L_D}{2}} \int_0^{2\pi} p_D \sin \varphi_D \, d\varphi_D \, dZ_D, \quad (13)$$

where R_D is the mean gap radius of the damper, L_B and L_D is the length of the bearing and damper, respectively.

The pressure distribution in the magnetorheological oil film depends of the yielding shear stress. Its dependence of magnetic induction B is approximated by a power function

$$\tau_y = k_y B^{n_y}. \quad (14)$$

Here, k_y and n_y are material constants of the magnetorheological oil.

The damper body is assumed to be consisted of a set of meridian segments and each segment as a divided core of an electromagnet having the gap filled with magnetorheological oil. This idea makes it possible to determine dependence of magnetic induction of the applied current and thickness of the lubricating film

$$B = k_B \mu_0 \mu_{MR} \frac{I}{h_D} . \quad (15)$$

μ_0 is the vacuum permeability, μ_{MR} is the magnetorheological oil relative permeability, I is the applied current, and k_B is the design parameter. More details on determination of the design parameter k_B can be found in [5].

3 The investigated rotor system

The rotor and the stationary part (Fig. 2) of the studied rotor system are rigid. The rotor consists of a shaft and of one disc. The shaft is supported by hydrodynamic bearings mounted in magnetorheological squeeze film dampers at both its ends. The rotor turns at constant angular speed and is loaded by its weight and excited by the disc unbalance. The whole system can be considered as symmetric with respect to the disc middle plane.

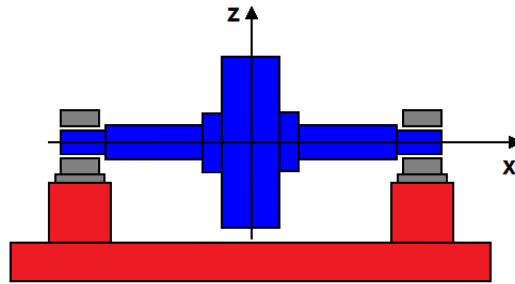


Figure 2: The investigated rotor system.

The task was to study the steady state vibration of the rotor, its amplitude, magnitude of the force transmitted between the rotor and the stationary part and the oscillation stability in dependence of the damping force magnitude.

In the computational model the rotor and the stationary part are represented by absolutely rigid bodies, the hydrodynamic bearings by forces and the dampers by springs and magnetorheological hydraulic forces.

Because of the system symmetry lateral vibration of the rotor system is described by four nonlinear equations

$$m_R \ddot{y}_R + b_P \dot{y}_R = 2F_{hdy} + m_R e_T \omega^2 \cos(\omega t + \psi_T) , \quad (16)$$

$$m_R \ddot{z}_R + b_P \dot{z}_R = 2F_{hdz} + m_R e_T \omega^2 \sin(\omega t + \psi_T) - m_R g , \quad (17)$$

$$0 = -F_{hdy} + F_{mry} - k_D y_D , \quad (18)$$

$$0 = -F_{hdz} + F_{mrz} - k_D z_D . \quad (19)$$

m_R is the rotor mass, b_P is the external damping coefficient, k_D is the cage spring stiffness, e_T , ψ_T are the eccentricity and phase shift of the rotor unbalance, respectively, g is the gravity acceleration, y_R , z_R are the displacements of the rotor centre in the horizontal and vertical directions, y_D , z_D are the displacements of the damper inner ring in the horizontal and vertical directions, t is the time, and $(\ddot{})$ denotes the second derivative with respect to time.

The trigonometric collocation method was used to obtain steady state solution of the governing equations. The vibration stability was evaluated by employing the Floquet theorem. This requires to calculate the transition matrix over the span of time of one period. The oscillation is stable if magnitudes of all its eigenvalues are less than 1. More details on these computational procedures can be found in [7], [9], [10].

4 Results of the computational study

The technical parameters of the studied rotor system are: the rotor mass 450 kg, the coefficient of the rotor linear damping caused by the environment 10 Ns/m, the stiffness of one damper cage spring 4.0 MN/m, the eccentricity and phase shift of the rotor centre of gravity 40 μm , 0.0 rad, the hydrodynamic bearing length/diameter 60/110 mm, the width of the bearing gap 0.1 mm, the oil dynamic viscosity (hydrodynamic bearing) 0.008 Pas, the magnetorheological squeeze film damper length/diameter 40/150 mm, the width of the damper gap 0.8 mm, the magnetorheological oil dynamic viscosity not effected by a magnetic field 0.3 Pas, the

magnetorheological oil dynamic viscosity for very low velocity rate if effected by a magnetic field 300 Pas, the magnetorheological oil proportional and exponential constants 10000, 0.5, respectively, the oil relative permeability 5, the damper design parameter 60.

The task was to analyse behaviour of the studied system for different magnitudes of the operating speed.

Figs. 3 and 4 show orbits of the disc centre and time history of the force transmitted to the stationary part in the vertical direction for three angular speeds of the rotor rotation and two magnitudes of the applied current. Higher damping effect reduces amplitude of the vibration for lower velocities (140, 300 rad/s) but it has little influence on the orbit size for velocity 700 rad/s. The mean value of the transmitted force is not zero, which is caused by the rotor weight. To reduce the force in the interval of higher velocities (300, 700 rad/s) the damping should be minimum.

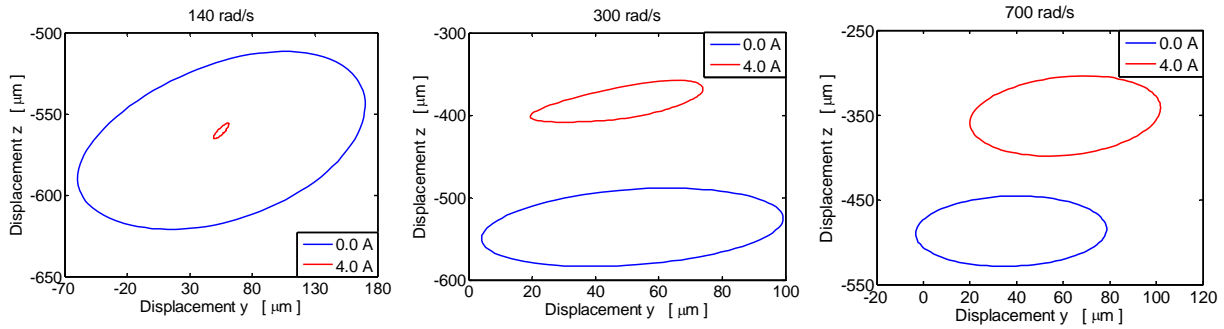


Figure 3: Orbits of the disc centre.

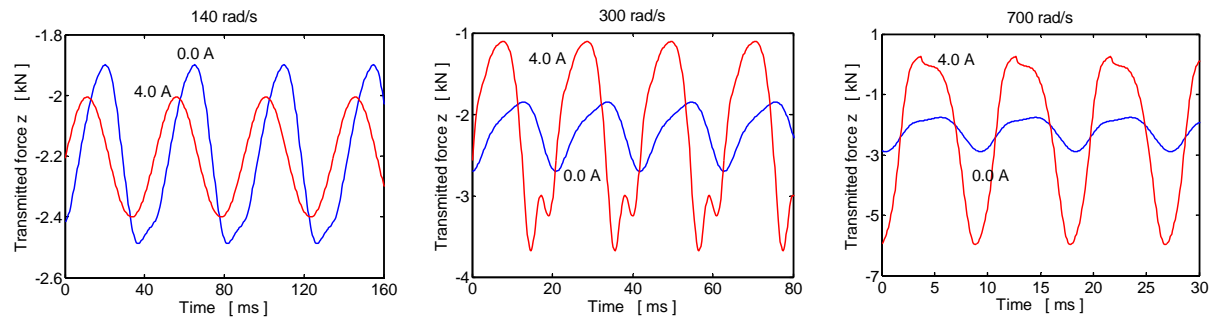


Figure 4: Force transmitted to the stationary part in the vertical direction.

Fig. 5 shows the distribution of images of eigenvalues of the transition matrix set up over the span of time of one period in the Gauss plane. The results are related to the design case when the rotor is supported only by hydrodynamic bearings and turns at angular speed of 900 rad/s. Magnitude of one eigenvalue is greater than 1, which means the steady state response of the rotor on unbalance excitation is instable.

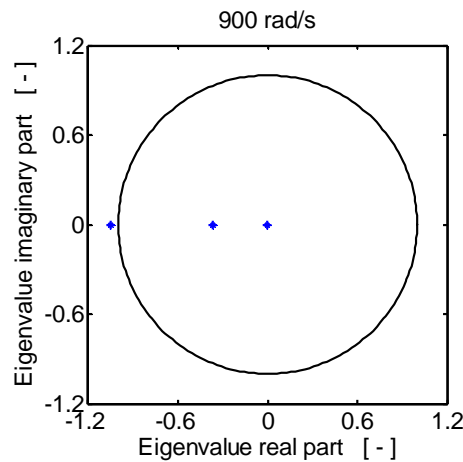


Figure 5: Eigenvalues of the transition matrix - support by hydrodynamic bearings.

Fig. 6 is related to the case when the rotor is supported by hydrodynamic bearings inserted in magnetorheological squeeze film dampers, to the speed of the rotor rotation of 900 rad/s and to two magnitudes of the applied current 0.0, 4.0 A. The figure shows that all eigenvalues of the transition matrix set up over the span of time of one period lie inside a unit circle, which means the rotor vibration is stable. It implies presence of the damping devices increases the stability limit.

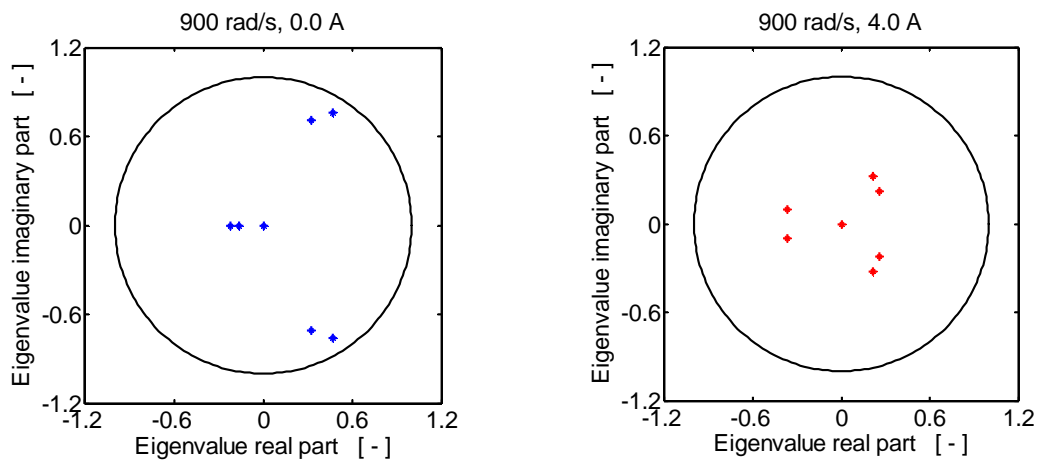


Figure 6: Eigenvalues of the transition matrix - support by hydrodynamic bearings and dampers.

5 Conclusion

The subject of investigation presented in this paper is a new controllable rotor support element consisting of a hydrodynamic bearing inserted in a magnetorheological squeeze film damper. Its mathematical model was developed and implemented in the computational procedures for analysis of the steady state response of a rigid rotor on unbalance excitation and for evaluation of its stability. The simulations proved that application of higher current (higher damping effect) in the interval of lower angular velocities (approximately below the critical speed) arrives at reduction of the amplitude of the rotor vibration and of the force transmitted between the rotor and the stationary part. On the contrary, in the interval of higher velocities higher current leads to increase of the transmitted force. It implies a suitable control of the damping effect enables to achieve optimum compromise between reducing the rotor vibration and minimizing the magnitude of the transmitted force. The stability analysis shows that inserting the hydrodynamic bearings in the damping devices increases the stability limit of the rotor response on unbalance excitation. The advantage of this design solution is that controlling the damping effect is simple, the damping device can work only in the on/off regime in dependence of speed of the rotor rotation. The proposal of the new coupling element, the development of its mathematical model, its implementation into the procedures for dynamical analysis of rigid rotors and learning more on its effect on dynamic properties of rotor systems are the main contributions of this paper.

Acknowledgement

This work has been supported by the Ministry of Education, Youth and Sports within the National Programme of Sustainability (NPU II) project “IT4Innovations excellence in science - LQ1602”, by the grant project of the Czech Science Foundation 19-06666S and by the project of conceptual development of research organizations RVO: 61388998.

References

- [1] Zapoměl, J., Ferfecki, P., Kozánek, J. (2013): Determination of the transient vibrations of a rigid rotor attenuated by a semiactive magnetorheological damping device by means of computational modelling. *Appl. Comput. Mech.*, **7**, pp. 223-234.
- [2] Gong, X., Ruan, X., Xuan, S., Yan, Q., Deng H. (2014): Magnetorheological damper working in squeeze mode. *Adv. Mech. Eng.*, **6**, pp. 1-10.
- [3] T.S. Aravindhan, T. S., Gupta K. (2006): Application of magnetorheological fluid dampers to rotor vibration control. *Adv. Mech. Eng.*, **5**, pp. 369-380.
- [4] Zapoměl, J., Ferfecki, P., Forte, P. (2017): A new mathematical model of a short magnetorheological squeeze film damper for rotordynamic applications based on a bilinear oil representation - derivation of the governing equations. *Appl. Math. Model.*, **52**, pp. 558-575.

- [5] Ferfecki, P., Zapoměl, J., Kozánek, J. (2017): Analysis of the vibration attenuation of rotors supported by magnetorheological squeeze film dampers as a multiphysical finite element problem. *Adv. in Eng. Soft.*, **104**, pp. 1-11.
- [6] Szeri, A. Z. (1980), *Tribology: Friction, Lubrication, and Wear*. Hemisphere Publishing Corporation.
- [7] Zapoměl, J. (2007): *Computer Modelling of Lateral Vibration of Rotors Supported by Hydrodynamical Bearings and Squeeze Film Damper*. VŠB-Technical University of Ostrava, (in Czech).
- [8] Wada, S., Hayashi, H., Haga, K. (1973), Behavior of a Bingham solid in hydrodynamic lubrication, Part 2, Application to step bearing. *Bull. JSME*, **16**(92), pp. 432-440.
- [9] Zhao, J. Y., Linnett, I. W., McLean, L. J. (1994), Stability and Bifurcation of Unbalanced Response of a Squeeze Film Damped Flexible Rotor. *J. Trib.*, **116**, pp. 361-368.
- [10] Nataraj, C., Nelson, H. D. (1989): Periodic Solutions in Rotor Dynamic Systems with Nonlinear Supports: A General Approach. *J. Vib. Acoust. Stress Replib. Des.*, **111**, pp. 187-193.

Control Analysis of Wind Turbine Blade Vibration With SMA Actuators in Thermal Equilibrium

Rodrigo Nicoletti ¹, Robert Liebich ²

¹ São Carlos School of Engineering, University of São Paulo, 13566-590, São Carlos, Brazil, rnicolet@sc.usp.br

² Institut für Maschinenkonstruktion und Systemtechnik, Technische Universität Berlin, 10623, Berlin, Germany, robert.liebich@tu-berlin.de

Abstract

In this work, shape memory alloy (SMA) actuators are applied to wind turbine blades, aiming at reducing blade vibrations during operation. The work is focused on the application of SMA wires in thermal equilibrium on a 5 MW wind turbine blade (61.5 m long). The frequency response function of the SMA wire is modeled considering the thermal conditions of the blade and the constitutive law of the SMA material. This function is included in the state space model of the blade and a PD controller is designed by root locus analysis. The SMA wire geometry is found according to the maximum possible power output in the wind turbine blade. The numerical results show that this strategy is not feasible because the actuation force of the SMA is too small to make a significant effect on the blade dynamics. The necessary number of SMA wires to dynamically affect the blade is impractical.

Nomenclature

A_s	austenite temperature transformation	\mathcal{P}	SMA wire dissipated power
A_S	SMA wire cross section area	R_S	SMA wire radius
C_S	SMA wire specific heat	S	SMA wire heat transfer surface area
d_S	SMA wire diameter	t	time
e_0	bias voltage	T_o	blade surface temperature
E_M	SMA wire Young modulus	T_S	SMA wire temperature
f_S	SMA wire axial force	T_∞	environment temperature
G_P, G_D	proportional and derivative gains	\mathcal{V}	SMA wire volume
\mathbf{G}	gyroscopic matrix of the blade model		
h	heat convection coefficient	Γ	SMA wire operating condition parameter
k	thermal conductivity of the blade material	ε	SMA wire normal strain
\mathbf{K}	stiffness matrix of the blade model	Θ	SMA wire thermal expansion coefficient
l_2	distance from SMA wire to environment	ρ_e	SMA wire electric resistivity
L_S	SMA wire length	ρ_S	SMA wire density
\mathbf{M}	inertia matrix of the blade model	σ	SMA wire normal stress
N_S	number of SMA wires (one side of blade)	ω	frequency

1 Introduction

Vibration problems are among the top five causes of blade failure in the field [1]. The main reasons of such problems are the excessive bending moments, which can cause interlaminar failure and delamination, and high tip deflection, which can make the blades hit the tower [2]. All these failures are due to flapwise motion of the blade, but edgewise vibration can also occur during turbine parking or idling by vortex generation [3], which can cause trailing edge buckling. Trailing edge buckling can also be caused by an excessive weight load on slender blades [4].

Considering these facts, it has been increasingly necessary to include some sort of control device (passive or active) in the blades to mitigate vibration. The simplest approach to reduce blade vibrations is to include a tuned mass damper (passive control device) in the blades. However, in most of the times, wind excitation presents no

dominant frequency and, therefore, a more robust approach shall be looked for. Hence, many different active control devices have been investigated to tackle this problem: jet actuators, trailing edge flaps, microtabs, resonant controllers, active tendons, and active tuned mass dampers, among others, all of them presenting successful results in mitigating blade vibrations. A review of the morphing concepts and materials for wind turbine blade applications can be found in [5].

In this context, a shape memory alloy (SMA) actuator can be used in both control conditions: passive or active. Shape memory alloy is the generic name given to alloys which exhibit the unusual property of a strain-memory which can occur either at constant temperature or on changes of temperature [6]. Active application of SMAs were originally employed in helicopter blades [7]. In this case, SMA wires were used to control tabs in the trailing edge of the blades, aiming at keeping the blades in the same track during operation, thus representing a static operation of the SMA (actuation bandwidth was not a problem). More recently, SMA wires were employed to change the geometry of airfoils [8]. In this case, two antagonistic wires work together to move the trailing edge of an airfoil with successful results but presenting an actuation frequency bandwidth of ~ 0.5 Hz (quasi-static application).

As we see in the literature, the long-time accommodation periods of thermal systems jeopardize the active application of SMAs, thus resulting in low bandwidth actuators. A possible solution to this problem is the adoption of SMAs working in its elastic phase and subjected to variations in temperature that will expand and contract the material. The best results were obtained in [9] with two antagonistic actuators in a pull-push operating condition (frequency bandwidth of 30 Hz). In this work, the feasibility of such strategy is numerically studied in the case of a 61.5 m long wind turbine blade with SMA wires mounted on its outer layers. The frequency response function of the SMA wire is modeled considering the thermal conditions of the blade and the constitutive law of the SMA material. This function is included in the state space model of the blade and a PD controller is designed by root locus analysis. The SMA wire geometry is found according to the maximum possible power output in the wind turbine blade.

2 Model of the SMA Actuator in Thermal Equilibrium

One way of using the SMA as actuators is avoiding the transformation of phase from martensite to austenite, i.e. by working in temperatures below A_s . For that, the SMA will work in its elastic phase, but variations in temperature will extend or contract the SMA wire, thus allowing to act on the structure it is mounted on. In this case, better results are obtained when two antagonistic actuators act together, in a pull-push operating condition [9]. To avoid the long-time accommodation periods of thermal systems that jeopardize actuation bandwidth, a bias electric voltage (e_0) is applied to the antagonistic wires and they work in the thermal equilibrium.

In the present case, the antagonistic SMA wires will be mounted in the top and bottom panels of the wind turbine blade, as shown in Fig. 1. By applying a bias electric voltage e_0 to both SMA wires, such configuration will present the temperature distribution in thermal equilibrium shown in Fig.2.

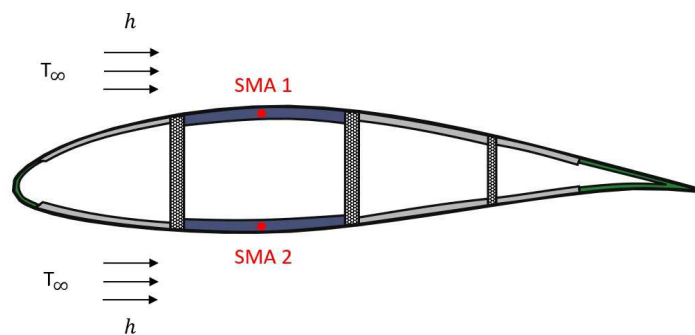


Figure 1: Cross section of the blade with the SMA wires in the top and in the bottom panels (flapwise direction).

Hence, the thermal equilibrium between the SMA wire and the surface of the blade is given by the heat dissipated by the electric voltage and the heat conducted to the blade surface:

$$-\frac{kS}{l_2}(T_S - T_o) + \frac{e_0^2}{R_S} = 0 \quad \Rightarrow \quad T_S = T_o + \frac{l_2 e_0^2}{kSR_S} \quad (1)$$

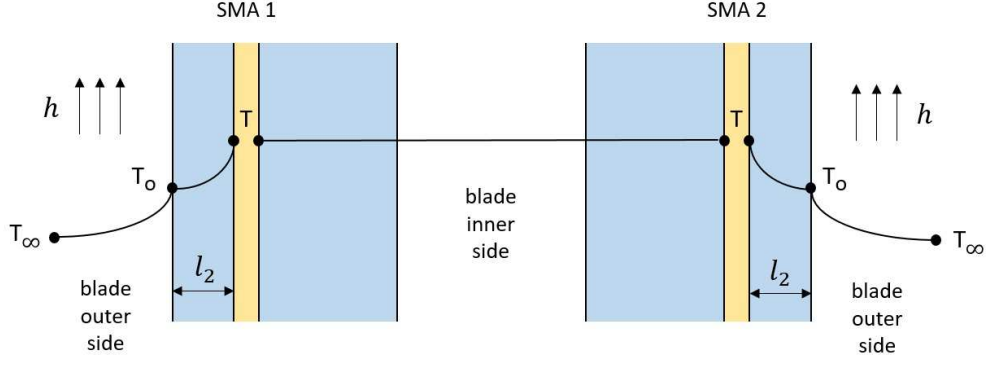


Figure 2: Thermal model of a wind turbine blade with embedded SMA wires in thermal equilibrium.

where S is the heat transfer area of the wire ($S = \pi d_S L_S / 2$, half perimeter area).

In the surface of the blade, the heat conducted in the blade material is in equilibrium with the heat convection of the wind:

$$\frac{k}{l_2} (T_S - T_o) - h (T_o - T_\infty) = 0 \quad \Rightarrow \quad T_o = \frac{kT_S/l_2 + hT_\infty}{h + k/l_2} \quad (2)$$

Hence, from Eqs.(1) and (2) and considering that $S = \pi d_S L_S / 2$ and $R_S = 4L_S \rho_e / \pi d_S^2$, then the temperature of the SMA wire in the thermal equilibrium is:

$$T_S = T_\infty + \left(\frac{l_2}{k} + \frac{1}{h} \right) \frac{d_S e_0^2}{2\rho_e L_S^2} < A_s \quad (3)$$

where ρ_e is the electrical resistivity of the SMA wire.

Hence:

$$\Gamma = \frac{d_S e_0^2}{L_S^2} < \frac{2\rho_e}{l_2/k + 1/h} (A_s - T_\infty) \quad (4)$$

where Γ is a parameter of the operating conditions of the SMA wire (function of the SMA wire diameter and length, and of the bias voltage).

The maximum admissible Γ increases by decreasing the thickness l_2 and the ambient temperature. Considering that higher Γ values allow the adoption of larger SMA wire diameters (d_S) and higher bias voltage (e_0), one can achieve higher force in the SMA actuator with such higher Γ values. Hence, one will adopt in the following analyzes the smallest thickness l_2 of 5 mm. Considering that the maximum admissible Γ value decreases with the ambient temperature, one will adopt in the following analyzes the ambient temperature of 15 °C, for safety reasons (if temperature decreases, the maximum admissible Γ increases).

Hence, considering the data in Table 1, the maximum admissible Γ_{max} value used in the following analysis will be 0.00265 V²/m. Then, we can calculate the necessary length of the SMA wire as a function of its diameter and electric bias voltage:

$$\frac{d_S e_0^2}{L_S^2} \leq \Gamma_{max} \quad \Rightarrow \quad L_S \geq \sqrt{\frac{d_S e_0^2}{\Gamma_{max}}} \quad (5)$$

3 Actuator Frequency Response Function

When the pair of antagonistic actuators operate, an additional electric voltage is added to the bias electric voltage e_0 . Therefore, the thermal equilibrium is disturbed and the temperature in the SMA wire changes, thus resulting in actuation forces. Hence, in the transient thermal regime, we have:

Table 1: Parameters used in the thermal equilibrium analysis of the blade with SMA wires.

parameter	value	unit
electric resistivity of the SMA wire (ρ_e)	80×10^{-8}	$\Omega.m$
start temperature of austenite transformation (A_s) ¹	80	$^{\circ}C$
heat convection coefficient (h)	40	$W/m^2.K$
thermal conductivity of the blade material (k)	0.35	$W/m.K$

¹ high temperature SMA.

$$\rho_S C_S \frac{\partial T}{\partial t} = -\frac{kS}{l_2 \mathcal{V}} (T + T_S - T_o) + \frac{(e + e_0)^2}{R_S \mathcal{V}} \quad (6)$$

If $e \ll e_0$ and considering the equality of the thermal equilibrium in Eq.(1), then:

$$\rho_S C_S \frac{\partial T}{\partial t} = -\frac{kS}{l_2 \mathcal{V}} T + \frac{2e_0}{R_S \mathcal{V}} e \quad (7)$$

Considering that no phase transformation is expected in the SMA material and it will work in its elastic phase, the constitutive law of the SMA material [10] reduces to:

$$\sigma = E_M \varepsilon + \Theta T \quad \Rightarrow \quad T = \frac{f_S}{\Theta A_S} - \frac{E_M}{\Theta} \varepsilon \quad (8)$$

By inserting Eq.(8) into Eq.(7), we have:

$$\dot{f}_S + \frac{kS}{\rho_S C_S l_2 \mathcal{V}} f_S = A_S E_M \dot{\varepsilon} + \frac{A_S E_M k S}{\rho_S C_S l_2 \mathcal{V}} \varepsilon + \frac{2\Theta A_S e_0}{\rho_S C_S R_S \mathcal{V}} e \quad (9)$$

which in Laplace form gives:

$$F(j\omega) = A_S E_M E(j\omega) + \underbrace{\left(\frac{b_0}{j\omega + a_0} \right)}_{H(j\omega)} U(j\omega) \quad (10)$$

where:

$$a_0 = \frac{kS}{\rho_S C_S l_2 \mathcal{V}} = \frac{2k}{\rho_S C_S l_2 d_S} \quad \text{and} \quad b_0 = \frac{2\Theta A_S e_0}{\rho_S C_S R_S \mathcal{V}} = \frac{\pi \Theta d_S^2 e_0}{2\rho_S C_S \rho_e L_S^2} \quad (11)$$

for $A_S = \pi d_S^2/4$, $\mathcal{V} = \pi d_S^2 L_S/4$, $S = \pi d_S L_S/2$, and $R_S = 4\rho_e L_S/\pi d_S^2$.

As one can see in Eq.(10), the actuator force is proportional to the strain and it is a function of the electric voltage in the frequency domain. The amplitude of the force of the actuator in the frequency domain is given by:

$$|H(\omega)| = \frac{b_0}{\sqrt{\omega^2 + a_0^2}} = \frac{\pi \Theta l_2 \Gamma_{max} d_S^2}{2\rho_e e_0 \sqrt{(\omega \rho_S C_S l_2 d_S)^2 + 4k^2}} \approx \frac{\pi \Theta l_2 \Gamma_{max} d_S^2}{2\rho_e e_0 \omega \rho_S C_S l_2 d_S} \quad (12)$$

and the dissipated power in the actuator is given by:

$$\mathcal{P} = \frac{e_0^2}{R_S} = \frac{\pi d_S^2 e_0^2}{2\rho_e L_S} = \frac{\pi \Gamma_{max}^{1/2} e_0 d_S^{3/2}}{4\rho_e} \quad (13)$$

Table 2: Parameters used in the calculation of the amplitude of actuator force and dissipated power.

parameter	value	unit
electric resistivity of the SMA wire (ρ_e)	80×10^{-8}	$\Omega \cdot m$
density of the SMA wire (nitinol) (ρ_S)	6,500	kg/m^3
specific heat of SMA wire (nitinol) (C_S)	836	$J/kg \cdot K$
thermal expansion coefficient of the SMA material (Θ)	0.55	$MN/m^2 \cdot K$
maximum Γ value (Γ_{max})	0.00265	V^2/m
thermal conductivity of the blade material (k)	0.35	$W/m \cdot K$
thickness of blade material (l_2)	5.0	mm
frequency of analysis (ω)	1.0	Hz

By calculating the amplitude of the actuator force at the frequency of 1 Hz (frequency near the first two natural frequencies of the wind turbine blade) and the respective dissipated power in the SMA wire, one obtained the results shown in Fig. 3 for different values of wire diameter and bias electric voltage using parameters listed in Table 2. As one can see, the actuator force increases with higher SMA wire diameters and lower bias electric voltages. The dissipated power in the SMA wire also decreases with lower electric bias voltage. Therefore, the bias electric voltage of $e_0 = 1$ V will be adopted in the following analysis. On the other hand, the dissipated power increases for higher SMA wire diameters, thus showing that higher forces require higher dissipated power in the SMA wires. The maximum actuator force achieved in the analysis ($|H| = 0.38$ N/V @ 1 Hz) occurs for $d_S = 4.5$ mm, $e_0 = 1.0$ V, and $L_S = 1.3$ m. A response force of 0.38 N/V is rather small by taking into account that 15.3 W is dissipated in the SMA wire (a single wire).

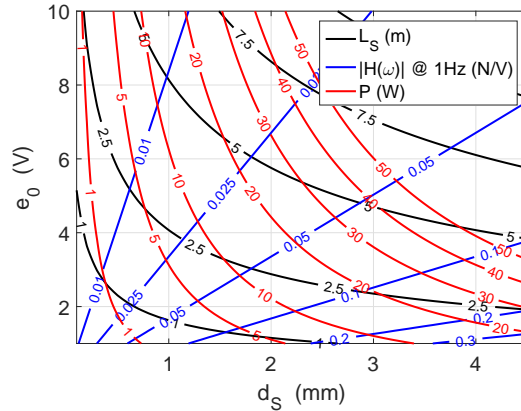


Figure 3: Amplitude of the actuator force at the frequency of 1 Hz and the respective dissipated power in the SMA wire for different values of wire diameter and bias electric voltage.

4 Actuator Design for Maximum Power Output in the Wind Turbine Blade

The problem of mounting antagonistic SMA wires on a wind turbine blade is the dissipated power in the wires. As shown in Fig. 3, the maximum actuation force is obtained with the maximum power dissipation. Hence, one cannot use an infinite number of SMA wires on the blade otherwise the dissipated power would also tend to infinite. Considering that the nominal output power of the turbine is 5 MW, it is interesting to establish a limit to the dissipated power in the actuation system. In this work, one adopted the limit of 1% of the nominal output power of the wind turbine, i.e. a limit of 50 kW.

From Eq.(13), considering two antagonistic SMA wires and knowing that the maximum dissipated power (P_{max}) is 50 kW, one can calculate the maximum number of SMA wires in each side of the blade (N_S) based on the number of actuators along the blade (N_A):

$$N_S = \frac{2 \rho_e \mathcal{P}_{max}}{\pi N_A \Gamma_{max}^{1/2} e_0 d_S^{3/2}} \quad (14)$$

The length of each SMA wires is given by Eq.(5).

The model described in [11] will be used to calculate the maximum tip displacement and the maximum bending angle of the blade, with no wind and no rotation. This is a finite element model of the 61.5 m long blade of the upwind reference turbine [12], considering flapwise translation, edgewise translation, axial translation, and torsion in every node of the model. The actuation forces and moments of the SMA wires on the blade are applied to the nodes of the model, considering that the stress in the SMA wires in the i -th node of the model is:

$$\sigma_i = E_M \varepsilon_i + \frac{\pi \Theta l_2 e_0 d_S^3}{4k \rho_e L_S^2} e_i \quad (15)$$

where $i = 1, 2, \dots, N_A$, and one considered that $\omega = 0$ Hz (static case – see Eq.(12)).

The maximum control voltage e_i is 0.2 V, and the SMA wires are mounted 5 mm apart from the surface of the blade (l_2). Two different configurations of SMA actuators are tested: actuators distributed along the blade ($N_A = 12$, Fig. 4a) and actuators concentrated at the end of the blade ($N_A = 6$, Fig. 4b). Figure 5 presents the results as a function of the SMA wire diameter.

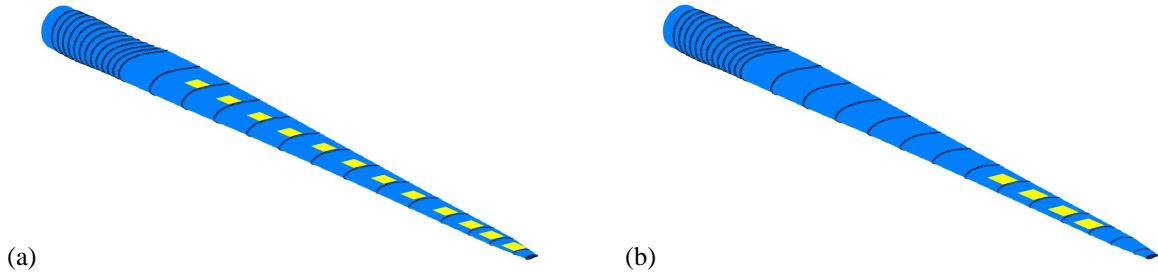


Figure 4: Distribution of antagonistic SMA wires on the blade: (a) along the blade ($N_A = 12$); (b) at the end of the blade ($N_A = 4$).

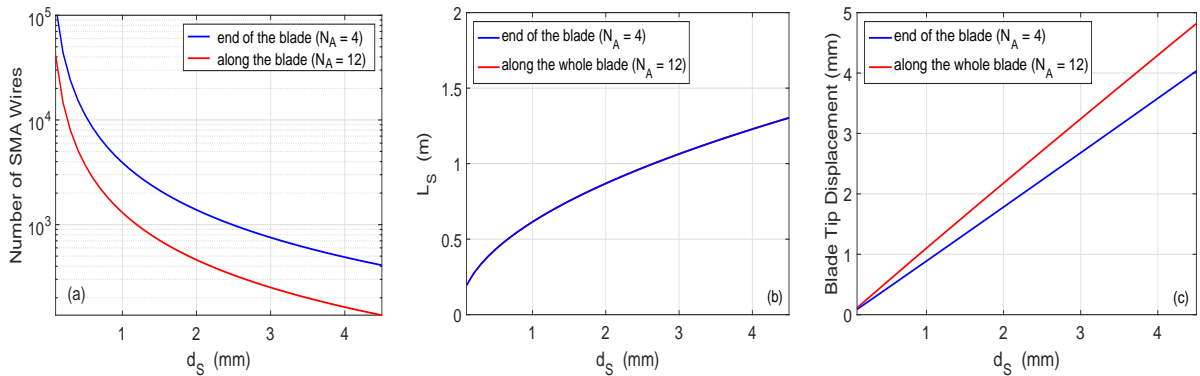


Figure 5: Maximum number of SMA wires, wire length, and maximum blade tip displacement as a function of the SMA wire diameter for a maximum dissipated power in the actuation system of 1% of the turbine output power (50 kW).

As we can see in Fig. 5, the maximum displacements of the blade occur for an SMA wire diameter of 4.5 mm. Better results are obtained by concentrating the actuators at the end of the blade, which is in accordance to previous results [11]. The length of the SMA wires does not depend on the distribution of SMA along the blade. Considering these results, the best set of parameters are: $N_A = 4$ (distribution on the blade), $N_S = 410$ (number of wires in each side of the blade), $d_S = 4.5$ mm (wire diameter), and $L_S = 1.3$ m (wire length).

It is important to emphasize that the above results are valid for static operation ($\omega = 0$ Hz). For dynamic operation, one has to analyze the system in closed loop feedback, considering the dynamics of the controller.

5 Closed-Loop Feedback and Root Locus Analysis

The equation of motion of the blade in Laplace form is:

$$(s^2\mathbf{M} + s\mathbf{G} + \mathbf{K}) X(s) = F_c(s) \quad (16)$$

where $X(s)$ is the vector of degrees-of-freedom of the blade model, and $F_c(s)$ is the vector of control forces.

The control forces come from the SMA wires, whose dynamics is described by Eq.(10), which in Laplace domain is:

$$F_c(s) = -\mathbf{B}A_S E_M \mathbf{C}_1 X(s) - \mathbf{B} \left(\frac{b_0}{s + a_0} \right) U(s) \quad (17)$$

where the forces and moments are embedded in matrix \mathbf{B} , and we considered that there is a linear relationship between the strain and the degrees-of-freedom of the system embedded in matrix \mathbf{C}_1 ($E(s) = \mathbf{C}_1 X(s)$).

The control voltage $U(s)$ comes from the chosen control law. In this work, we adopted a PD-control law, in the form:

$$U(s) = (G_P + sG_D) \mathbf{C}_2 X(s) \quad (18)$$

where G_P and G_D are the proportional and derivative gains of the controller, respectively, and \mathbf{C}_2 is the observation matrix. Hence, we can write:

$$\begin{aligned} & [s^2(s + a_0)\mathbf{M} + s(s + a_0)\mathbf{G} + (s + a_0)\mathbf{K} + \\ & (s + a_0)\mathbf{B}A_S E_M \mathbf{C}_1 + s\mathbf{B}b_0 G_D \mathbf{C}_2 + \mathbf{B}b_0 G_P \mathbf{C}_2] X(s) = \mathbf{0} \end{aligned} \quad (19)$$

which gives:

$$[s^3\mathbf{A}_3 + s^2\mathbf{A}_2 + s\mathbf{A}_1 + \mathbf{A}_0] X(s) = \mathbf{0} \quad (20)$$

where:

$$\begin{aligned} \mathbf{A}_3 &= \mathbf{M} & \mathbf{A}_1 &= a_0 \mathbf{G} + \mathbf{K} + \mathbf{B}b_0 G_D \mathbf{C}_2 + \mathbf{B}A_S E_M \mathbf{C}_1 \\ \mathbf{A}_2 &= a_0 \mathbf{M} + \mathbf{G} & \mathbf{A}_0 &= a_0 \mathbf{K} + a_0 \mathbf{B}A_S E_M \mathbf{C}_1 + \mathbf{B}b_0 G_P \mathbf{C}_2 \end{aligned} \quad (21)$$

From Eq.(20), we have:

$$\mathbf{A}_3 \ddot{\mathbf{q}} + \mathbf{A}_2 \dot{\mathbf{q}} + \mathbf{A}_1 \dot{\mathbf{q}} + \mathbf{A}_0 \mathbf{q} = \mathbf{0} \quad (22)$$

or, in matrix form:

$$\underbrace{\begin{bmatrix} \mathbf{A}_3 & & \\ & \mathbf{A}_3 & \\ & & \mathbf{A}_3 \end{bmatrix}}_{\mathbf{M}} \begin{Bmatrix} \ddot{\mathbf{q}} \\ \dot{\mathbf{q}} \\ \dot{\mathbf{q}} \end{Bmatrix} + \underbrace{\begin{bmatrix} \mathbf{A}_2 & \mathbf{A}_1 & \mathbf{A}_0 \\ -\mathbf{A}_3 & & \\ & -\mathbf{A}_3 & \end{bmatrix}}_{\mathbf{K}} \begin{Bmatrix} \ddot{\mathbf{q}} \\ \dot{\mathbf{q}} \\ \mathbf{q} \end{Bmatrix} = \begin{Bmatrix} \mathbf{0} \\ \mathbf{0} \\ \mathbf{0} \end{Bmatrix} \quad (23)$$

which gives the eigenvalue problem of the system with control feedback:

$$-\mathbb{K}Z = \mathbb{M}Z\lambda \quad (24)$$

where λ is the eigenvalue and Z is the eigenvector.

Considering that the eigenvalue problem of Eq.(24) is composed of matrices three times bigger than those of the mathematical model of the blade, it is interesting to perform a model reduction, in the form:

$$\mathbf{q} = \Phi\eta \quad (25)$$

where Φ is the reduced normal mode matrix composed of chosen eigenvectors, and η is the vector of modal coordinates.

Hence, the eigenvalue problem is reduced to:

$$-\mathbb{K}_r Z_r = \mathbb{M}_r Z_r \lambda \quad (26)$$

whose matrices are given by Eq.(23), but with the following coefficients:

$$\begin{aligned} \mathbf{A}_3 &= \mathbf{M}_r & \mathbf{A}_1 &= a_0 \mathbf{G}_r + \mathbf{K}_r + \mathbf{E}_r + b_0 \mathbf{G}_r^D \\ \mathbf{A}_2 &= a_0 \mathbf{M}_r + \mathbf{G}_r & \mathbf{A}_0 &= a_0 \mathbf{K}_r + a_0 \mathbf{E}_r + b_0 \mathbf{G}_r^P \end{aligned} \quad (27)$$

where:

$$\begin{aligned} \mathbf{M}_r &= \Phi^T \mathbf{M} \Phi & \mathbf{E}_r &= \Phi^T (\mathbf{B} \mathbf{A}_S \mathbf{E}_M \mathbf{C}_1) \Phi \\ \mathbf{G}_r &= \Phi^T \mathbf{G} \Phi & \mathbf{G}_r^D &= \Phi^T (\mathbf{B} \mathbf{G}_D \mathbf{C}_2) \Phi \\ \mathbf{K}_r &= \Phi^T \mathbf{K} \Phi & \mathbf{G}_r^P &= \Phi^T (\mathbf{B} \mathbf{G}_P \mathbf{C}_2) \Phi \end{aligned} \quad (28)$$

Equation (26) is used to calculate the eigenvalues of the system is closed loop to verify the effect of the SMA actuators in the dynamics of the blade. The reduced model of the blade considers the first ten normal modes listed in Table 3. Again, the blade is not subjected to wind and it does not rotate (same model used in the previous sections). A modal damping of 2% is added to the structure. The displacements and velocities of the nodes of the blade where the SMA wires are mounted are used as feedback parameters. The PD-controller gains are considered to be the same for all SMA actuators, and the derivative gain is scaled to be 5% of the proportional gain ($G_D = 0.05 G_P$). The parameters of the SMA actuators are those listed in Table 2, which presented best performance in the static analysis. By solving the eigenvalue problem of Eq.(26) for different values of the proportional gain G_P , we obtained the results shown in Fig. 6.

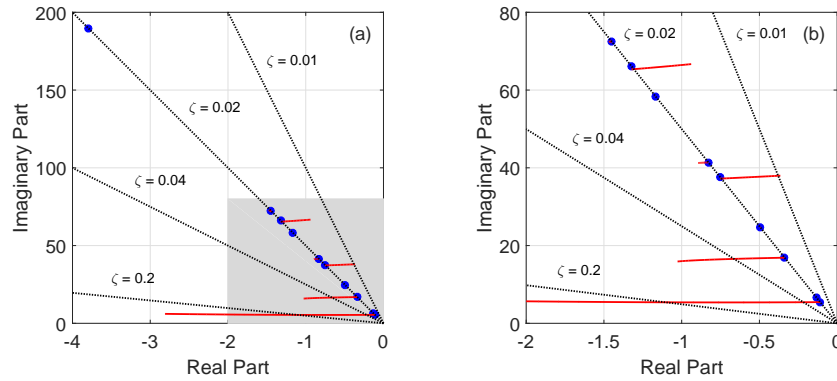


Figure 6: Loci of the eigenvalues of the blade model as a function of the proportional gain ($0 < G_P < 10^8$ V/m): (a) root loci; (b) zoom of shaded area.

Table 3: Normal modes considered in the reduced model of the blade.

mode	frequency (Hz)	type
1	0.868	1st. flapwise bending
2	1.044	1st. edgewise bending
3	2.702	2nd. flapwise bending
4	3.939	2nd. edgewise bending
5	5.987	3rd. flapwise bending
6	6.595	1st. torsion
7	9.284	3rd. edgewise bending
8	10.52	4th. flapwise bending
9	11.53	2nd. torsion
17	30.20	1st. axial

As we can see in Fig. 6, by increasing the proportional gain and, consequently, the derivative gain, the loci of the eigenvalues of the blade model move in the imaginary plane. The first and the third eigenvalues (associated to the first two bending modes in the flapwise direction) move towards higher damping regions. Such effect also happened to the sixth and to the ninth eigenvalues (associated to the first two torsion modes), but with small extent. On the other hand, the fifth and the eighth eigenvalues (associated to the third and fourth bending modes in the flapwise direction) move towards lower damping regions, thus showing that the system may become instable for higher gain values. The second, fourth, and seventh eigenvalues (associated to the first three bending modes in the edgewise direction) and the tenth eigenvalue (associated to the first axial mode) are not affected by the control system.

Hence, it is possible to change the eigenvalues of the blade by mounting the SMA actuators at its upper end. However, by looking at the necessary gain values to achieve such change, one can note that the application is not feasible. For example, the necessary proportional gain to double the amount of damping in the first bending mode of the blade ($\zeta = 0.04$, flapwise direction) is 3.3×10^6 N/V. It means that, if the blade moves 1 mm, the resultant control signal will be 3,300 V, which is much greater than the expected control signal e of 0.2 V from design. By limiting the control signal to 0.2 V, the maximum proportional gain would be 200 N/V (for a blade displacement of only 1 mm), and the resultant damping factor of the first bending mode in flapwise direction would be $\zeta = 0.020012$ (the same, for practical reasons).

6 Conclusion

This paper presents the mathematical modeling and the numerical analysis of the feedback control of a wind turbine blade with SMA wires working in thermal equilibrium. The results show that, the application of antagonistic SMA wires in a wind turbine blade is not feasible. Even adopting the best set of SMA parameters, the actuation force is too small to make any significant effect on the blade dynamics. In order to achieve a significant effect on the blade, it would be necessary a much higher number of SMA actuator and, consequently, much higher energy to operate. Considering that all the results presented here were obtained for a dissipated energy in the SMA actuators of 1% of the total output energy of the turbine, which is already a high value, a further increase in dissipated power would be impractical. And one must not forget that the turbine has three blades (all the previous analyses refer to a single blade).

Acknowledgment

This project was supported by Coordenação de Aperfeiçoamento de Pessoal de Nível Superior (Brazil) and by Alexander von Humboldt Stiftung (Germany) [grant number BEX 0190/15-2].

REFERENCES

- [1] Chou, J.S., Chiu, C.K., Huang, I.K., Chi, K.N. (2013): Failure analysis of wind turbine blade under critical wind loads. *Engineering Failure Analysis*, **27**, pp.99-118.

- [2] Branner, K., Ghadirian, A. (2014): *Database about blade faults*. DTU Wind Energy E-0067, Roskilde.
- [3] Malkin, M., Griffin, D. (2016): *Edgewise vibration and wind turbine blade failure*. Available at www.windtech-international.com/editorial-features/edgewise-vibration-and-wind-turbine-blade-failure (accessed 9 August 2017).
- [4] Jensen, F.M., Kling, A., Sørensen, J.D. (2017): *Change in failure type when wind turbine blades scale-up*. Available at energy.sandia.gov/wp-content/gallery/uploads/2B-A-1-Jensen1.pdf (assessed 9 August 2017).
- [5] Lacednal, X., Daynes, S., Weaver, P.M. (2013): Review of morphing concepts and materials for wind turbine blade applications. *Wind Energy*, **16**(2), pp.283-307.
- [6] Worden, K., Bullough, W.A., Haywood, J. (2003): *Smart technologies*. Singapore: World Scientific Publishing.
- [7] Kennedy, D.K., Straub, F.K., Schetky, L.M., Chaudhry, Z., Roznoy, R. (2004): Development of an SMA actuator for in-flight rotor blade tracking. *Journal of Intelligent Material Systems and Structures*, **15**(4), pp.235-248.
- [8] Abreu, G.L.C.M., Maesta, M.F., Lopes, V.Jr., de Marqui, C.Jr., Faria, C.T., Inman, D.J. (2015): Active angular control of a sectioned airfoil using shape memory alloys and fuzzy controller. *Journal of the Brazilian Society of Mechanical Sciences and Engineering*, **37**(5), pp.1555-1567.
- [9] Susuki, Y., Kagawa, Y. (2010): Active vibration control of a flexible cantilever beam using shape memory alloy actuators. *Smart Materials and Structures*, **19**(8), pp.085014.
- [10] Brinson, L.C. (1993): One-dimensional constitutive behavior of shape memory alloys: thermodynamic derivation with non-constant material functions and redefined martensite internal value. *Journal of Intelligent Material Systems and Structures*, **4**(2), pp.229-242.
- [11] Nicoletti, R., Liebich, R. (2018): Analysis of long wind turbine blades with shape memory alloy wires in super-elastic phase. *Journal of Intelligent Material Systems and Structures*, **29**(15), pp.3108-3123.
- [12] Jonkman, J., Butterfield, S., Musial, W., Scott, G. (2009): *Definition of a 5-MW reference wind turbine for offshore system development*. National Renewable Energy Laboratory, Golden, Report NREL/TP-500-38060.

Experimental and Theoretical Study of an Actively Lubricated LEG Tilting Pad Bearing

Alejandro Cerda Varela¹, **Ilmar Ferreira Santos**², **Jorge González Salazar**³, **Cristóbal Ponce Salazar**¹

¹ Escuela de Ingeniería Mecánica, Pontificia Universidad Católica de Valparaíso, 252000, Valparaíso, Chile, alejandro.cerda@pucv.cl

² Department of Mechanical Engineering, Technical University of Denmark, 2800, Kgs. Lyngby, Denmark, ifs@mek.dtu.dk

³ Departamento de Ingeniería Mecánica, Universidad de La Frontera, 4811230, Temuco, Chile, jorge.gonzalez@ufrontera.cl

Abstract

This work presents theoretical and experimental results regarding the feasibility of introducing an active lubrication concept in tilting pad journal bearings (TPJBs) featuring the leading edge groove (LEG) lubrication system. The modification of the oil flow into each pad supply groove by means of servovalves renders the bearing active, due to the resulting alteration of the oil film pressure field. Experimental results obtained in a suitable test rig enables verification of the concept feasibility at the component level, considering a single tilting pad, load on pad configuration, supporting a rigid rotor. Secondly, theoretical results portray the application of this technology in a 5-pad, load between pad LEG TPJB, aimed at performing active control of vibrations in a flexible rotor setup. The proposed technology exhibits benefits in terms of the ability to excite system dynamics to perform in-situ identification experiments, as well as to reduce the rotor vibration amplitude.

1 INTRODUCTION

Among the different fluid film bearing designs, the oil lubricated tilting pad journal bearing is widely used in the industry. Key features from this machine element are its ability to endure high rotational speed and high load applications, its damping characteristics due to oil film squeeze effect, and its enhanced stability properties [1] when compared to other oil film bearing designs.

Since its introduction during the first half of the 20th century, its basic design has been continuously improved, based on the knowledge gained from theoretical and experimental investigations, as well as the experience gained from their industrial usage. The latest publications related to this bearing design deal with a number of issues: the effect of reduced oil supply rates over its steady state and dynamic behavior [2, 3], the influence of the pivot design over the bearing properties [4], the usage of superconductor materials to incorporate magnetic forces to the bearing load carrying capacity [5], the effect of composite liners installed on the pad surface [6]. The common denominator for these research activities revolves around the need to expand the operational envelope of the tilting pad bearing, enabling it to operate at even higher rotational speed, higher load, lower oil supply rate with a high level of reliability and low power consumption.

Some key parameters that have been the target of the bearing optimization process are the oil film temperature, oil flow consumption and oil shear viscous losses. In order to obtain an energy efficient bearing, it is desirable that all three of these parameters are diminished. Several configurations have been tested, being the so called “directed lubrication” or “leading edge groove” technology one of the alternatives widely implemented in the industry. As its name indicates, it resorts to a deep groove machined close to the pad leading edge to feed the bearing clearance with the lubricant. Its performance has been studied [7, 8, 9, 10] in terms of oil consumption rates and bearing viscous losses, exhibiting significant benefits when compared to other tilting pad bearings lubrication methods.

Together with its characteristics related to energy efficiency, the improvement of the tilting pad bearing dynamic properties has been widely investigated. In general, for rotating machinery that is usually designed to operate in the supercritical rotational speed range, it is desirable that the damping provided by the tilting pad bearing is high

enough to ensure safe crossing of critical speeds, and to counteract the onset of instability due to destabilizing forces acting over the supported rotor [11, 12]. Several strategies can be followed to achieve this objective, being the introduction of the “mechatronic” approach one that has received attention in the late years.

The mechatronic approach consists of the synergetic coupling of traditional mechanical elements with sensors, processing units and actuation elements derived from electronic or electromechanical engineering [13]. In the case of the studied bearing, the presence of the tilting pads entails some advantages for the application of this approach. Among the different designs that have been tested over the years to render the tilting pad bearing “mechatronic” or “active” one can mention: linear and rotational actuators acting over the bearing pads [14, 15, 16], pads with embedded magnetic actuators [17], and pads with controllable oil injection. The later design, denominated “active lubrication” system [18, 19], entails the usage of servovalve controlled injection of pressurized oil into the bearing clearance through nozzles located radially across the bearing pads. The consequent modification of the oil film flow and pressure field gives the possibility to alter the resulting force over the rotor, as a function of the servovalve electrical control signals. An extensive series of studies has dealt with the improvement of the mathematical modelling of such active bearing design [20, 21, 22], as well as with its experimental application to control the dynamics of a rotor system [23, 24, 26, 25] and to perform parameter identification procedures in situ [27, 28].

Within this framework, a recent research effort has focused on attempting to combine the mechatronic characteristics arising from the “active lubrication” technology, with the energy efficient features of the leading edge groove tilting pad bearing. The basic concept entails the introduction of servovalves into the oil supply system for the pad leading edge groove, yielding active regulation of the inlet flow and oil film pressure field. Therefore, the leading edge groove tilting pad bearing can be transformed into a mechatronic machine element in a non-invasive fashion, since only the oil supply system needs to be modified.

Two steps have been accomplished within this research effort. In [29], the mathematical model for the LEG tilting pad bearing with active lubrication was presented, featuring an elastothermohydrodynamic lubrication model, coupled with the dynamics of the servovalve controlled oil supply system. Theoretical results portrayed the viability of the proposed active bearing design. Followingly, in [30] the mathematical model was validated at the component level, in a test rig featuring a single pad, and LEG inlet flow regulated by a single servovalve.

The objective of the current article is to provide insights into the actively lubricated LEG tilting pad bearing technology (ALEG TPJB). Firstly, experimental and theoretical results are presented, depicting the capabilities of the mechatronic pad design as a calibrated actuator. For this purpose, the subject of investigation corresponds to a simplified setup, consisting of a single active LEG tilting pad supporting a rigid rotor in load on pad configuration. Secondly, theoretical results portray the application of the active bearing design in a configuration resembling in a closer manner an industrial application. The studied setup consists of a flexible rotor supported by two TPJBs, featuring 5 pad, load between pads configuration, where one of them features the ALEG system. Active control schemes synthesized via pole placement and LQR techniques are simulated, depicting the feasibility of reducing the rotor vibrations via the proposed mechatronic bearing design.

2 STUDIED SETUPS

2.1 SETUP 1 (DTU-MEK, Denmark)

The first system to be experimentally and theoretically analyzed is the one depicted in Figure 1. Key parameters of the setup are listed in Table 1. It consists of a rigid rotor supported by a single tilting pad in load on pad configuration. The tilting pad features the leading edge groove oil supply configuration. One end of the oil supply line is connected to the groove chamber, and the other one to the exit port of a high response servovalve, governed by electrical signals synthesized in a control unit. Consequently, the groove inlet flow is actively regulated.

The rigid rotor is attached via roller bearings to a lever arm, which features a pivot point and a free side. The free side is used to install displacement sensors and accelerometers to measure indirectly the rotor vertical position. Furthermore, it is used to apply vertical static loading via helical springs, as well as vertical dynamic loading by means of a stinger connected to an electromagnetic shaker. The lever arm is mounted so that the horizontal movement of the rotor is negligible. All analyses are restricted to the frequency range where the lever arm flexible dynamics is not dominant, hence the system is modelled considering only one degree of freedom (arm tilting angle), where the rotor only exhibits vertical motion.

A detailed depiction of the LEG tilting pad can be observed in Figure 1. The pad includes the leading edge groove system to provide the oil supply, via the feedline which is connected to the servovalve exit port to render the system controllable. Since the full amount of the oil supply flow reaching the LEG cavity passes through the servovalve, care must be taken to provide a sufficiently high bias voltage to the control signal. This ensures that the pad does not suffer oil starvation during testing.

Referring to Figure 1, the pad is instrumented with a piezoelectric pressure sensor to measure directly the pressure

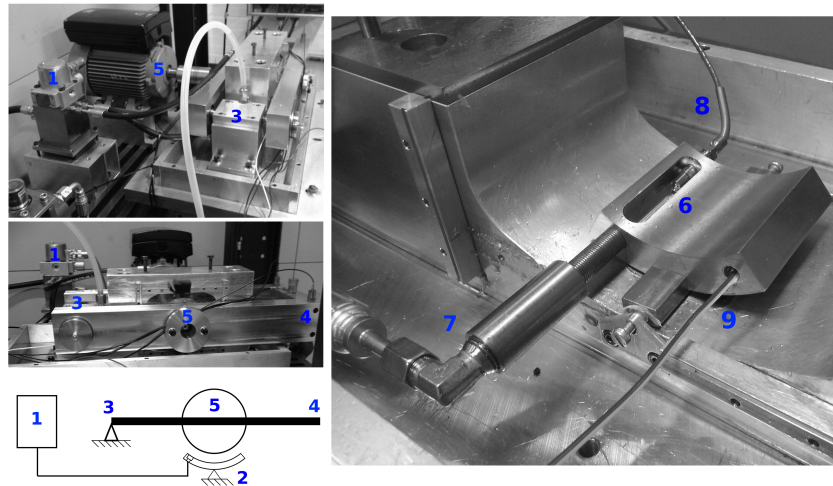


Figure 1: Setup 1: Test rig for the component level study of the ALEG tilting pad. It is composed by: (1) servovalve, (2) LEG tilting pad, (3) leverer arm pivot point, (4) leverer arm free end, (5) rigid rotor, (6) leading edge groove, (7) LEG oil supply line, (8) piezoelectric pressure transducer, (9) thermocouple

within the groove chamber. Furthermore, a thermocouple installed in the pad trailing edge enables to characterize the oil temperature.

2.2 SETUP 2 (PUCV, Chile)

The second system under analysis is depicted in Figure 2. It corresponds to a flexible rotor supported by two identical tilting pad journal bearings featuring the LEG supply configuration. The bearing on the rotor free end includes the ALEG setup. Nevertheless, any of the two bearings are suitable to implement the active system, since the modifications required for it take place outside the bearing itself. The parameters that define the bearing configuration are listed in Table 2. The test rig is currently being assembled and tested, hence for this article only simulation results are presented.

Setup 2 clearly differs from Setup 1, aiming at providing a closer approximation to a real implementation of the studied mechatronic bearing design. It also differs in the manner in which the hydraulic supply system is configured. In Setup 1, the full amount of oil supply reaching the LEG cavity passes through the servovalve mounted in the system, forcing to impose a sufficiently large bias voltage to avoid oil starvation issues. In Setup 2, a “passive” and “active” hydraulic system coexist, enabling to operate the servovalve with zero bias voltage, while preventing oil starvation.

Referring to Figure 3, the passive lubrication system (in black) provides oil supply at all times for each LEG pad. The active lubrication system (in red and blue) enables to modify the oil supply flow reaching each LEG pad via electrical control signals. The output ports of servovalve 1 (SV1, marked in blue) are connected to the supply lines for “upper” pad and the two “lower” ones, whereas servovalve 2 (SV2, marked in red) is associated with pads “left” and “right”. Check valves are installed between the passive and the active lubrication system, in order to prevent counterflow towards the “passive” supply pumps.

The presence of the “passive” supply system enables to operate the servovalves in the vicinities of their closed position (zero bias voltage). Furthermore, the two output ports from the servovalve are connected to “opposite” pads, enabling actuation over the rotor in all relevant directions. For instance, for SV2 a positive voltage signal directs the active flow to the “left” pad, whereas a negative value redirects it to the “right” pad. A similar operation mode is achieved for SV1 and the “upper” and two “lower” pads.

3 MATHEMATICAL MODEL

The mathematical model of the actively lubricated LEG tilting pad bearing technology (ALEG TPJB) has been thoroughly presented in [29, 30]. Consequently, the following presentation is constrained to provide the key points

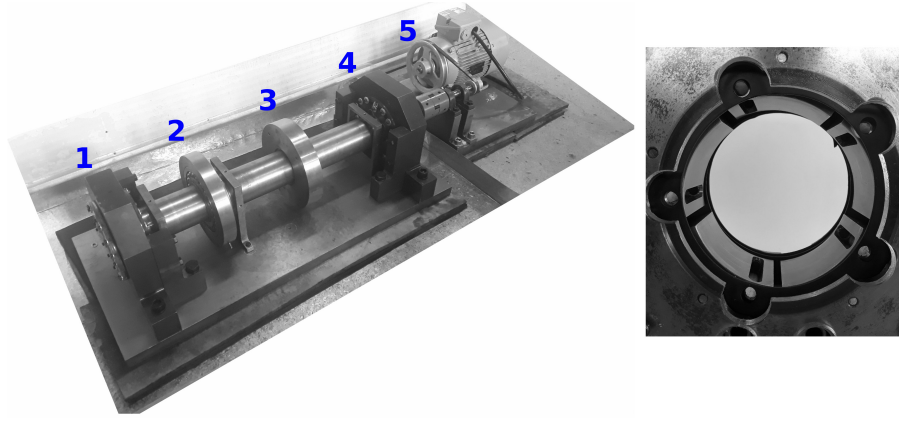


Figure 2: Setup 2: Test rig for the system level study of the ALEG technology. On the right, a detailed view of the pad arrangement in each bearing is provided. The test rig consists of: (1) ALEG TPJB, (2) Excitation Bearing, (3) Unbalance Disk, (4) Passive LEG TPJB, (5) Driving Transmission and Electric Motor

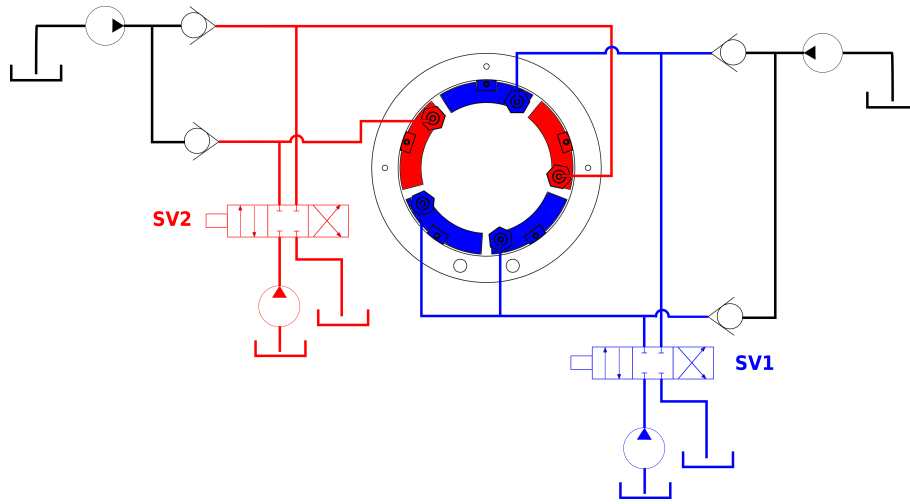


Figure 3: Setup 2: Schematics of the hydraulic system providing the oil supply for the ALEG TPJB.

about its formulation. The reader is advised to refer to the cited publications for an in-depth presentation. The global linearized mathematical model for the two setups under study is formulated with the following structure:

$$\begin{aligned}
 \{\dot{\mathcal{X}}\} &= [\mathcal{A}] \{\mathcal{X}\} + [\mathcal{B}] \{\mathcal{U}\} \\
 \{\mathcal{Y}\} &= [\mathcal{C}] \{\mathcal{X}\} \\
 \{\mathcal{X}\} &= \{\delta \mathbf{x}_r, \delta \mathbf{b}, \delta \mathbf{q}_{x_v}\}^T \\
 \{\mathcal{U}\} &= \{\delta \mathbf{u}_V, \mathbf{f}_r\}^T
 \end{aligned} \tag{1}$$

In Equation (1), the system state vector \mathcal{X} is defined by the degrees of freedom related to the rotor $\delta \mathbf{x}_r$, the tilting pads $\delta \mathbf{b}$, and the servovalves spool driven flow $\delta \mathbf{q}_{x_v}$. The state variables are denoted with the δ operator to indicate that they have been linearized around the steady state equilibrium of the system. The system inputs \mathcal{U} consist of the servovalves control signals $\delta \mathbf{u}_V$ and external excitation forces \mathbf{f}_r applied to perturb the rotor equilibrium position in the experimental setup. The system measurements \mathcal{Y} are provided by the displacement sensors registering the rotor movement at specific positions.

In open loop operation, a predefined servovalve input signal $\delta \mathbf{u}_V$ affects the servovalve flow $\delta \mathbf{q}_{x_v}$, with the consequent modification of the oil supply flow reaching each pad LEG. As a result, the rotor and pads states $\delta \mathbf{x}_r, \delta \mathbf{b}$

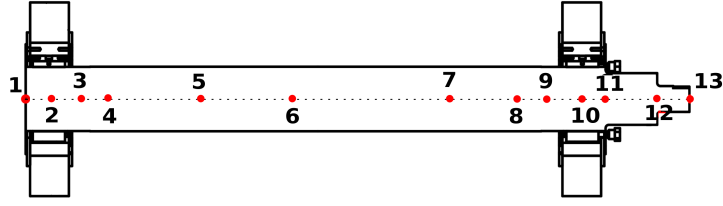


Figure 4: Setup 2: Schematics of the flexible rotor arrangement and node numbering for its finite element discretization.

are altered, due to the modification of the oil film and LEG pressure field. In closed loop operation, the servovalve input signals $\delta \mathbf{u}_V$ are synthesized by means of suitable control gains. Such controller requires the output of an observer, fed with the measured rotor states \mathcal{Y} .

Equation (1) corresponds to a linearized mathematical model, suitable to apply linear control theory. Such model stems from the linearization of the following relationships:

1. *Rotor Model:* The modelling of the rotor states $\delta \mathbf{x}_r$ differs in the two analyzed setups. In Setup 1, Newton Second Law is applied to model the vertical movement of the rigid rotor supported by the tilting pad. The rotor inertia is corrected to account for the tilting frame that supports it. Consequently, a single degree of freedom representation is obtained. In Setup 2, the finite element method considering Euler-Bernoulli beam elements is applied, to obtain a discretized set of equations. The model accounts for the rotor inertial, gyroscopic and lateral flexibility effects. Figure 4 depicts the rotor finite element discretization and further details are provided in Table 3. The ALEG bearing is mounted at node 2 close to the rotor free end, whereas the passive LEG TPJB is located at node 10, close to the driven end. The sensors measuring the rotor horizontal movement are located at nodes 4, 6 and 8. The excitation disk mounted at node 5 is meant to be used in conjunction with an electromagnetic shaker, in order to provide controlled perturbation forces over the rotor. Furthermore, an unbalance disk is mounted at node 7, with the purpose of incrementing the bearing static load and allowing to apply unbalance loads to the rotor.
2. *Tilting Pads Model:* The tilting pads are discretized using the finite element method in two dimensions (radial and circumferential direction), by means of plane stress assumption and second order quadrilateral elements. Linear elasticity equations and boundary conditions related to the tilting motion around the pivot point are imposed. The obtained finite element model is defined by an equivalent mass and stiffness matrix \mathbf{M}_b and \mathbf{K}_b . Such model is then used to obtain mode shapes vectors related to tilting motion, pivot flexibility and first bending mode, which are arranged in a pseudomodal matrix \mathbf{V} . Consequently, the pad dynamics can be modeled in a reduced manner using the pseudo modal reduction scheme [31, 21] considering only three degrees of freedom per pad, arranged in a modal coordinates vector \mathbf{b} as follows:

$$[\mathbf{V}]^T [\mathbf{M}_b] [\mathbf{V}] \{\ddot{\mathbf{b}}\} + [\mathbf{V}]^T [\mathbf{K}_b] [\mathbf{V}] \{\mathbf{b}\} = [\mathbf{V}]^T \{\mathbf{f}_b(\mathbf{p})\} \quad (2)$$

3. *Oil Film Pressure Field:* In order to calculate this field in the circumferential \hat{x} and axial direction \hat{z} of the bearing clearance, the Reynolds Equation for incompressible lubrication is employed:

$$\frac{\partial}{\partial \hat{x}} \left(\frac{h^3}{12\mu} \frac{\partial p}{\partial \hat{x}} \right) + \frac{\partial}{\partial \hat{z}} \left(\frac{h^3}{12\mu} \frac{\partial p}{\partial \hat{z}} \right) = \frac{\Omega R}{2} \frac{\partial h}{\partial \hat{x}} + \frac{\partial h}{\partial t} \quad (3)$$

Boundary conditions are imposed to solve numerically Equation (3) via the finite element method. Zero pressure is imposed at the pad surface limits, except for the one between the bearing clearance and the LEG cavity. In this boundary, the imposed value is equal to the pressure at the LEG cavity plus a correction value due to the Rayleigh step effect. A simplified model developed by [32] is implemented to determine it. The viscosity μ used for Equation (3) is corrected due to thermal effects, based on the oil temperature field

determined by means of a thermal model. Such model is stated following [33], considering the coupled finite element solution of an energy equation for the oil film and heat conduction through the pad via Fourier law. The formulation determines the temperature field in circumferential and radial direction.

4. *Leading Edge Groove Flow and Pressure:* Within the leading edge groove cavity, the mass conservation principle dictates the following relationship:

$$\begin{aligned}
q_V + q_{lead} - q_{trail} - q_{side} &= 0 \\
q_{lead} &= \int_0^{L_{axial}^{LEG}} \left[\frac{\Omega R h}{2} - \frac{h^3}{12\mu} \frac{\partial p}{\partial \hat{x}} \right]_{lead} d\hat{z} \\
q_{trail} &= \int_0^{L_{axial}^{LEG}} \left[\frac{\Omega R h}{2} - \frac{h^3}{12\mu} \frac{\partial p}{\partial \hat{x}} \right]_{trail} d\hat{z} \\
q_{side} &= \int_{L_{lead}^{LEG}}^{L_{trail}^{LEG}} \left[\frac{h^3}{12\mu} \frac{\partial p}{\partial \hat{z}} \right]_{side} d\hat{x}
\end{aligned} \tag{4}$$

Equation (4) dictates that the oil supply flow q_V reaching the LEG through the inlet must be equal to the oil flow entering or leaving the cavity through its leading, trailing and side boundaries. Such flow is modelled by means of the Pouseuille and Couette flows, based on the Reynolds model for incompressible lubrication. Consequently, Equation (3) and (4) must be solved in a coupled manner.

5. *Hydraulic System Model:* the oil supply flow q_V provided by the hydraulic system to the LEG cavity can be modelled as:

$$\begin{aligned}
q_V &= q_V^* + q_{x_V} - K_{pq} p_{port} \\
p_{port} - p_{LEG} &= \frac{8\mu L_{line}}{\pi R_{line}^4} q_V \\
\ddot{q}_{x_V} + 2\xi_V \omega_V \dot{q}_{x_V} + \omega_V^2 q_{x_V} &= \omega_V^2 R_V u_V
\end{aligned} \tag{5}$$

Equation (5) states that the LEG supply flow q_V is modelled following a first order linearization, composed of a steady state flow q_V^* , a servovalve spool driven flow q_{x_V} and pressure dependent term given by the K_{pq} coefficient and the pressure at the servovalve port p_{port} . The pressure difference between the servovalve port p_{port} and the LEG cavity p_{LEG} is quantified following the Hagen-Poiseuille model, whereas the relationship between servovalve spool driven flow q_{x_V} and control signal u_V is given by a second order differential equation that captures the frequency dependant relationship between these parameters.

4 SETUP 1: COMPONENT LEVEL RESULTS

4.1 ALEG Pad as Calibrated Actuator: Theory and Experiment

The first of results deal with the application of the ALEG pad as a calibrated actuator. The experimental and theoretical results aim at evaluating the capability of this mechatronic machine element to generate controllable forces in a wide frequency range. In this case, such forces are applied vertically over the rigid rotor in Setup 1. The experimental arrangement involves fixing the free end of the tilting arm in Setup 1, see Figure 1, with a load cell and an adjustment screw. The arrangement is used to set the rotor vertical position on top of the LEG tilting pad, applying a static load over it. Followingly, a chirp voltage signal is fed to the servovalve, and the resulting force over the rotor is measured indirectly by means of the tilting arm load cell. The postprocessing of these two experimental signals delivers a frequency response function in force/voltage units, that informs how much force is applied over the rotor by the active LEG pad at different frequencies, as well as the phase relationship between input voltage and rotor force.

These experimental frequency response functions can be compared with the ones delivered by the linearized model presented in Equation 1. Since this model includes the dynamics of the hydraulic supply system and the tilting pads, it should be able to portray the frequency dependant relationship between servovalve input voltage and resulting force over the rotor, both in amplitude as well as in phase. The comparison between theory and experiment is provided in Figure 5 and 6. It can be seen that the theoretical model is able to provide a good prediction of the active force generated at the active LEG pad. A critical issue for obtaining good resemblance between theory and experiment is to provide the model with a good estimation of the servovalve cut-off frequency ω_V and the

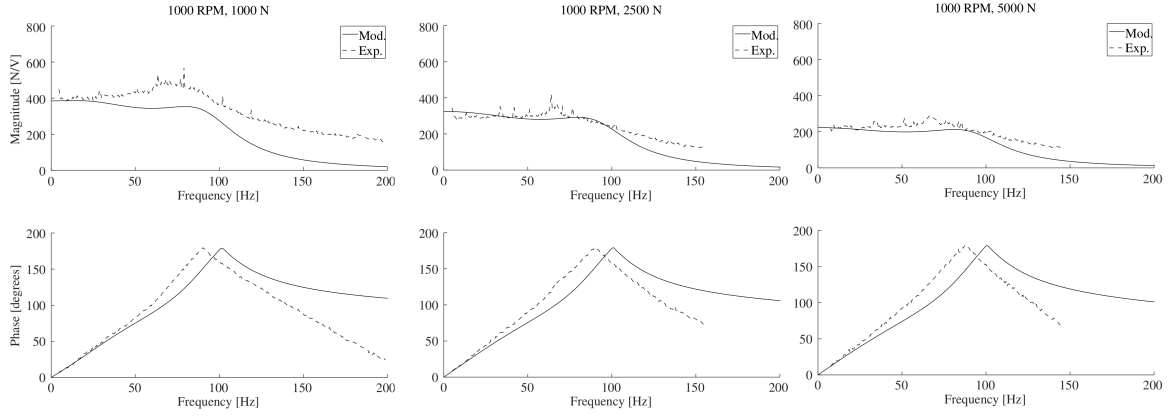


Figure 5: Setup 1: Frequency response function between servovalve input signal and active vertical force over the rotor. A comparison between theoretical model and experimental results is depicted, for rotational speed 1000 RPM and three different static loads over the ALEG pad.

voltage flow linearized coefficient R_V . This is a hidden cost of resorting to a simplified linear model strategy. For higher frequencies, the coherence between theory and experiment diminishes. This is an artifact of the simplified mathematical model that governs the relationship between servovalve spool driven flow and input signal, see Equation 5. The implemented second order model provides better coherence with the servovalve behavior for lower frequencies than higher ones. Furthermore, in the experimental setup the flexibility of the arm becomes relevant as an additional dynamic effect at higher frequencies. Such effect is not accounted for in the theoretical model.

These results prove that the active LEG pad is able to provide measurable forces over the rigid rotor in a wide frequency range. It can be seen that the active force over the rotor tends to diminish for higher static loads, due to predominance of the oil film pressure field in comparison with the pressure developed within the LEG cavity. On the other hand, when varying the rotor rotational speed the frequency dependency between input signal and active force tends to be modified. This is an effect of the alteration of the pad dynamics when incrementing the rotational speed. When analyzing the active bearing as linear system, the pads transfer function is a key component of the global transfer function between servovalve input signal, and rotor resulting force.

4.2 Obtaining Frequency Response Functions by means of the ALEG Pad as Excitation Source

A direct application of the active LEG pad capabilities as a calibrated actuator is to use it as excitation source to perform modal testing in Setup 1. A chirp signal is fed into the servovalve, and the resulting movement of the tilting arm free end is measured by means of displacement sensors. Consequently, a frequency response function can be obtained in displacement/force units, if the active LEG pad calibration function is obtained as portrayed in the previous section. These results can be compared with the benchmark obtained when exciting the tilting arm free end with an electromagnetic shaker equipped with a piezoelectric load cell.

The comparison between the benchmark results and the ones obtained with the active LEG pad as the excitation source are portrayed in Figure 7. It can be observed that the active pad can effectively replace the electromagnetic shaker to perform modal testing in the studied setup, achieving good coherence and good resemblance with the benchmark results. This set of results implies that a bearing equipped with active LEG pads could be employed to perform modal testing in an industrial rotor without the need of installing additional equipment. However, it also requires a good theoretical prediction of the active bearing calibration function, i.e. the transfer function between servovalve input signal and active force over the rotor. This fact justifies the effort in obtaining a good mathematical model of the studied mechatronic bearing.

5 SETUP 2: SYSTEM LEVEL RESULTS

5.1 ALEG Bearing as Calibrated Actuator: theoretical results

The mathematical model for the ALEG bearing can provide a prediction of the active force that can be exerted over the rotor. This model was validated considering the results for Setup 1 presented in the previous section.

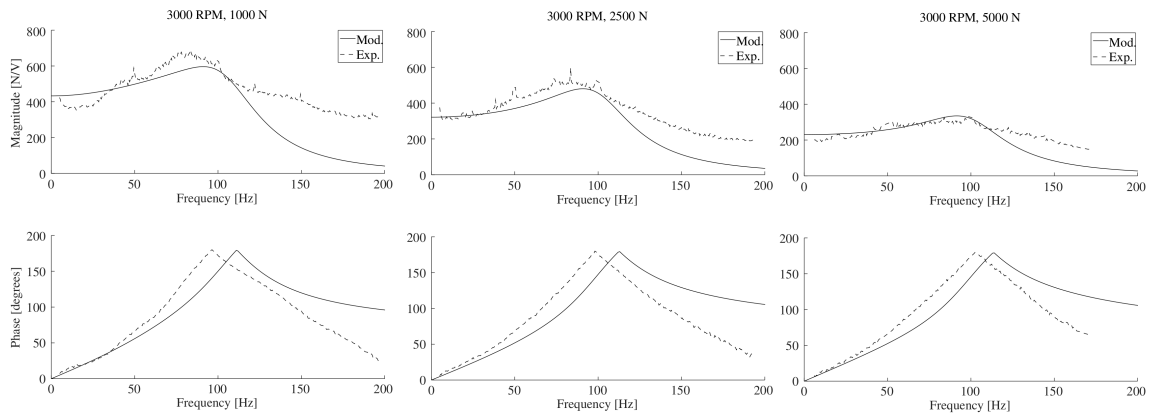


Figure 6: Setup 1: Frequency response function between servovalve input signal and active vertical force over the rotor. A comparison between theoretical model and experimental results is depicted, for rotational speed 3000 RPM and three different static loads over the ALEG pad.

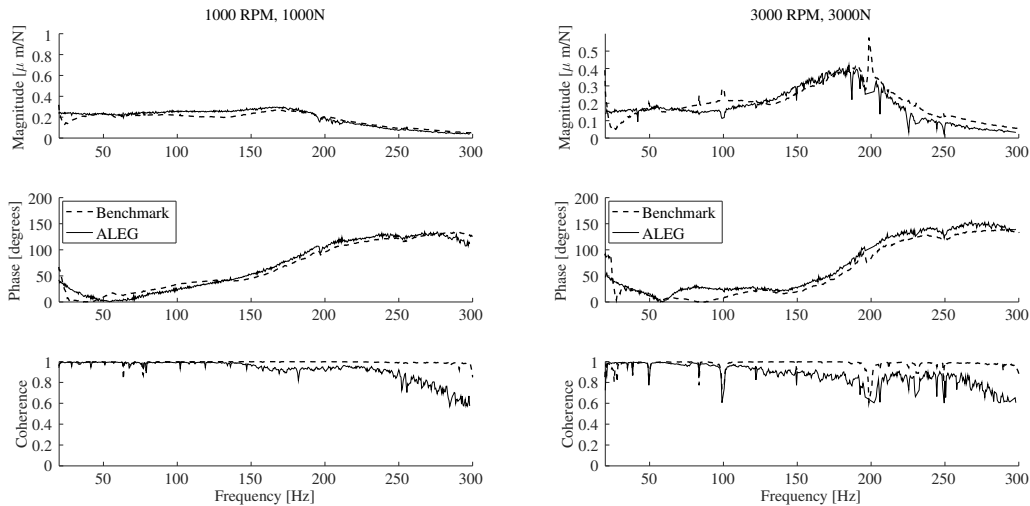


Figure 7: Setup 1: Experimental frequency response function of the rotor vertical displacement versus applied force. Benchmark results are obtained using an electromagnetic shaker as excitation source, whereas the ALEG results resort to the controllable forces generated by the active pad. Two operational conditions are tested, characterized by two rotational speeds and applied static loads.

Hence, it could be inferred that the model should also be able to simulate the behavior of the ALEG bearing in Setup 2, regarding the frequency response functions between servovalve input signal and resulting force, in a similar manner to the analysis presented before for Setup 1.

Figure 8 and 9 portray the frequency response functions for the simulated bearing between servovalve control signals and active force over the rotor. Two different rotational speeds are included in the simulations. In both cases, it can be seen that the hydraulic arrangement illustrated before in Figure 3 enables to obtain almost purely vertical active forces as actuation for servovalve 1, whereas horizontal forces are obtained by means of servovalve 2. In both cases, some actuation is obtained over the “other” direction, but its magnitude is negligible.

In general, an increment of the rotational speed entails a reduction of the active force magnitude. This is due to the increment of the oil film pressure in comparison to the LEG cavity pressure, as well as the reduction of the LEG cavity pressure. Since the journal retrieves oil from the groove at a faster rate for higher rotational speeds, a lower

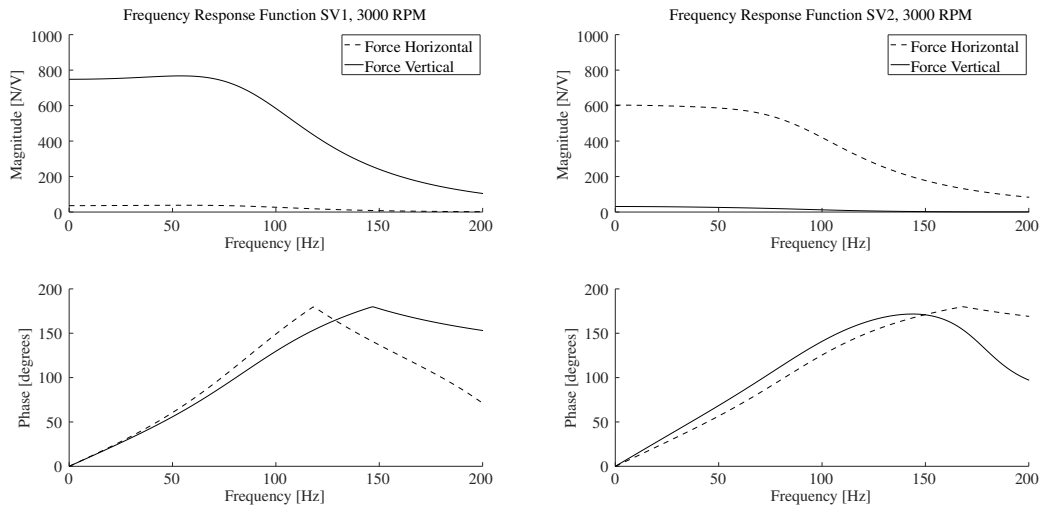


Figure 8: Setup 2: Frequency response function between the two servovalve input signals and active force over the rotor in horizontal and vertical direction. Theoretical model results are depicted for rotational speed of 3000 RPM.

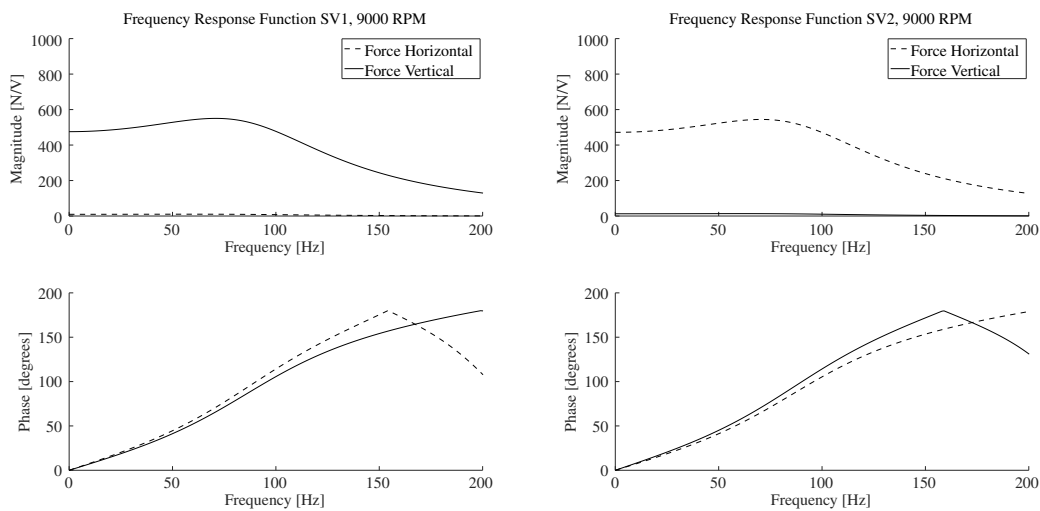


Figure 9: Setup 2: Frequency response function between the two servovalve input signals and active force over the rotor in horizontal and vertical direction. Theoretical model results are depicted for rotational speed of 9000 RPM.

pressure is developed in it for the same active input flow. The simulation indicates that the actuation capabilities of the ALEG bearing extend to a wide frequency range, making it suitable to implement active control strategies to limit the rotor vibrations.

5.2 Active Rotor Vibration Control via ALEG Bearing

In this case, the active LEG bearing actuation capability is aimed at reducing the amplitude of the rotor response around resonant areas. For doing so, suitable control laws must be established to synthesize the servovalves control signals. In particular, two methods are implemented to determine the control law: pole placement and LQR. The study is performed by theoretical means, taking advantage of the linearized state space model already presented in Equation 1.

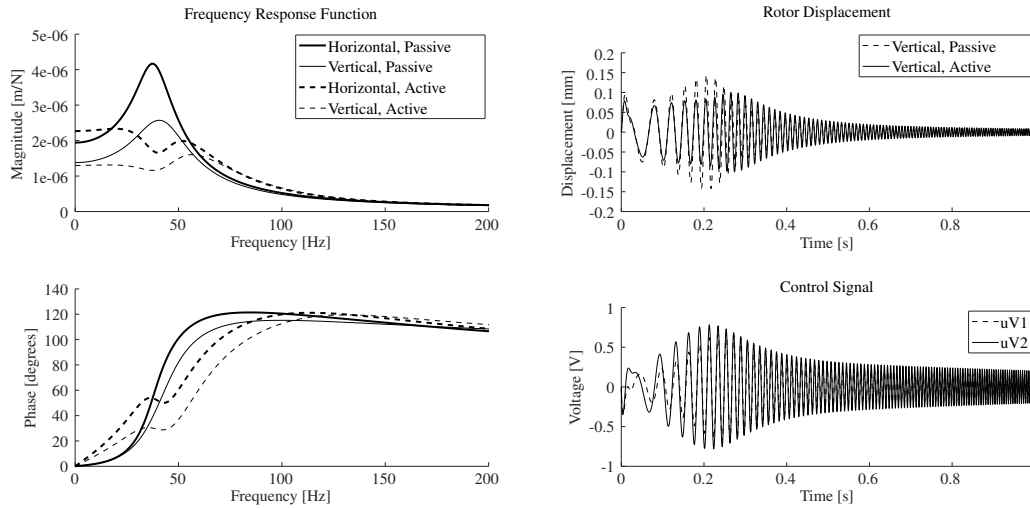


Figure 10: Setup 2: Active rotor vibration control using the ALEG bearing as actuator, for 3000 RPM. Control law synthesized via pole placement.

The simulation is setup by applying simultaneously a perturbation force in horizontal and vertical direction over node 5 of the rotor finite element model. The force corresponds to a chirp of amplitude 50 N and frequency ranging from 5 Hz to 200 Hz. The response is measured in node 4, where displacement sensors are mounted in the experimental setup. The time domain simulation results include displacement in the vertical direction at that node, plus the servovalve signals depicting the control effort necessary to alter the rotor dynamics. The frequency domain results deal with the frequency response function between applied load in vertical and horizontal direction, and the resulting displacements in the same directions (i.e. only the direct terms of the frequency response function are plotted). The control objective is to decrease the rotor response amplitude around the resonant areas, while keeping the servovalve input signals within the $\pm 1V$ range. This is to ensure that the actuation system operates within the linear range of these devices.

Figures 10 and 11 depict the results obtained at two different angular speeds for the passive and active lubrication regimes. In order to close the loop, a pole placement strategy was firstly implemented. The control objective to define the pole placement was to increase by 10% the damping ratio for the poles with damping ratio below 0.5, and to increase their natural frequency in the same order of magnitude, in order to maintain the amplitude of the system response at lower frequencies.

Figure 10 shows that the system frequency response at the resonance around 40 Hz is significantly reduced when the control strategy is implemented. Additionally, the time domain results show that the maximum system response does not surpasses the two tenths of millimeter in the vertical direction nor horizontal (unshown). The control effort is bounded between $\pm 1V$ for both servovalves. Similar results are obtained at 9000 RPM in Figure 11 regarding reduction of system response around resonance, although with an increased control effort which is slightly above $\pm 1V$.

In order to diminish the control effort required to improve the rotor dynamic behavior, a LQR control law is implemented instead of the previous one. For obtaining the LQR control, the weighting matrices are selected in such a way that the control effort does not surpass $\pm 1 V$ and the response from the system poles in the studied range are equally penalized. Figure 12 and 13 show that LQR results are comparable to figures 10 and 11 in terms of reducing the rotor response in the resonant areas. However, some benefits can be observed in terms of reduced control effort, ensuring that the servovalves operate within their linear range.

6 CONCLUSIONS AND FUTURE PERSPECTIVES

This work provided insights into the actively lubricated LEG tilting pad bearing technology (ALEG TPJB), by means of experimental and theoretical results. This technology derived from the extensive previous research effort on the active lubrication concept for TPJBs, and aims at introducing it in a non invasive manner in passive industrial bearings featuring the leading edge groove design.

The main focus of this article was set on presenting the capabilities of this novel mechatronic pad design as a

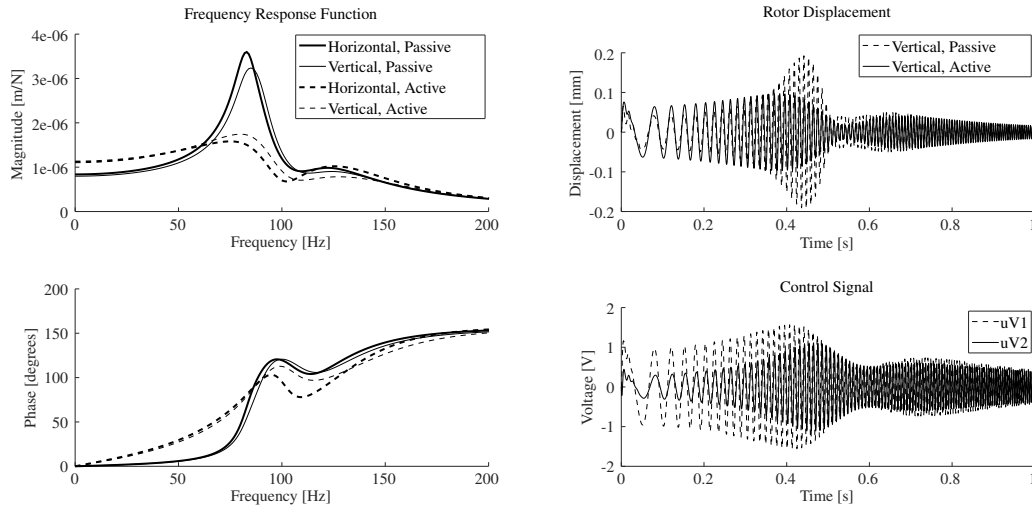


Figure 11: Setup 2: Active rotor vibration control using the ALEG bearing as actuator, for 9000 RPM. Control law synthesized via pole placement.

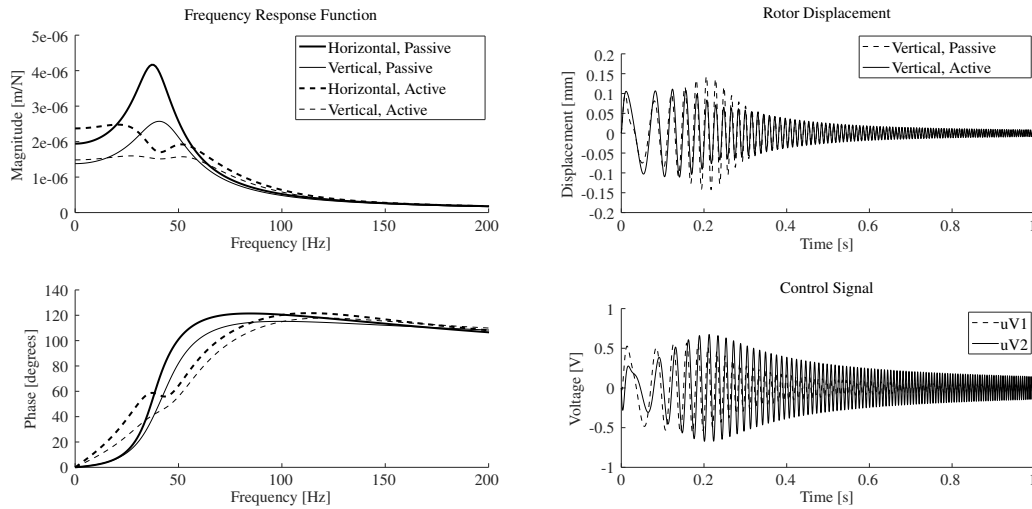


Figure 12: Setup 2: Active rotor vibration control using the ALEG bearing as actuator, for 3000 RPM. Control law synthesized via LQR.

calibrated actuator, at the component and system level. Firstly, a theoretical and experimental study was carried out for an experimental facility representing a component level implementation of the studied bearing design. The obtained results portrayed the feasibility of employing the active LEG pad to apply controllable forces over a rotor in a wide frequency band. A good resemblance between experimental and theoretical results was obtained, particularly for the lower frequency range, regarding the active LEG pad calibration function, i.e. the transfer function between servovalve input signal and resulting force over the rotor. Experimental results also validated the capabilities of the active LEG pad as an actuator for performing in-situ and non invasive modal testing in rotors. Secondly, simulations of a flexible rotor supported by active LEG bearings were performed, in order to portray an industrial application of the studied mechatronic bearing design. No experimental results were included since the test rig is still under assembly process. It was theoretically demonstrated that the 5 pad ALEG bearing is able to exert controllable forces over a rotor in a wide frequency range. Such capability was then applied to simulate the feasibility of reducing the vibration amplitudes of a flexible rotor, when state feedback control strategies are implemented.

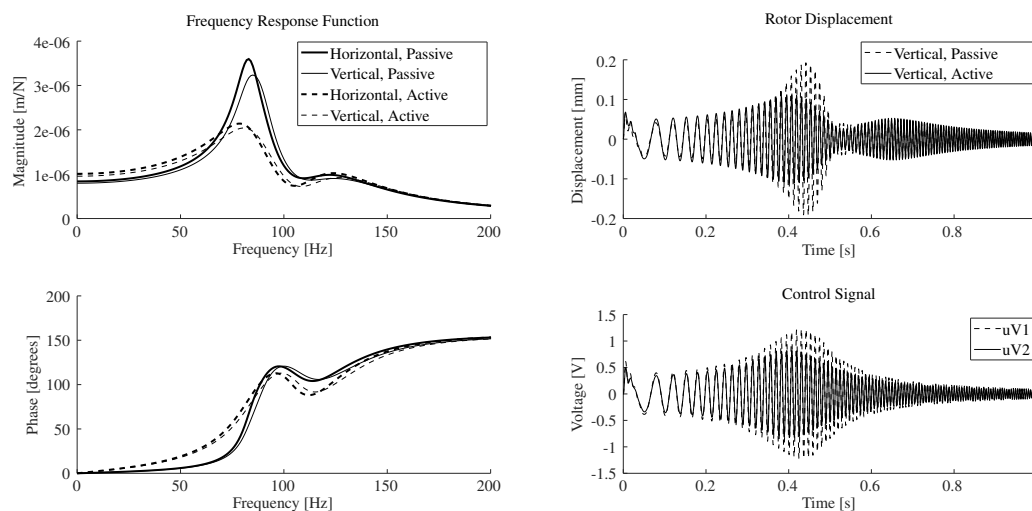


Figure 13: Setup 2: Active rotor vibration control using the ALEG bearing as actuator, for 9000 RPM. Control law synthesized via LQR.

The next step within this research effort is to obtain experimental data to validate the ALEG TPJB concept at the system level, concerning the active vibration control of a flexible rotor supported by this novel mechatronic machine element. The experimental facilities to carry out this objective are currently being assembled at PUCV Chile, and should deliver results to complement the theoretical results presented here for Setup 2.

Acknowledgment

This work has been financed by CONICYT Chile, project FONDECYT Iniciacion No. 11150112

REFERENCES

- [1] R. Lanes, R. Flack, D. Lewis. (1982): Experiments on the stability and response of a flexible rotor in three types of journal bearings. *ASLE Transactions*, **25**, pp. 289–298.
- [2] L. San Andrés, B. Koo, M. Hemmi. (2018): A flow starvation model for tilting pad journal bearings and evaluation of frequency response functions: A contribution toward understanding the onset of low frequency shaft motions. *ASME Journal of Engineering for Gas Turbines and Power*, **140**, 052506.
- [3] B. R. Nichols, R. L. Fittro, C. P. Goyné (2018): Steady-state tilting-pad bearing performance under reduced oil supply flow rates. *ASME Journal of Tribology*, **140**, 051701.
- [4] S. M. Mehdi, K. E. Jang, T. H. Kim (2018): Effects of pivot design on performance of tilting pad journal bearings. *Tribology International*, **119**, pp. 175–189.
- [5] J. Xu, Q. Jia, F. Zhang, X. Yuan, C. Zhang (2018): Fundamental tribological experiments and antifricition design of novel superconducting tilting pad bearing for liquid rocket engine. *Proceedings of the Institution of Mechanical Engineers, Part J: Journal of Engineering Tribology*, **232**, pp. 582–591.
- [6] S. Y. On, Y. S. Kim, J. I. You, J. W. Lim, S. S. Kim (2018): Dynamic characteristics of composite tilting pad journal bearing for turbine/generator applications. *Composite Structures*, **201**, pp. 747–759.
- [7] W. Dmochowski, K. Brockwell, S. DeCamillo, A. Mikula (1993): A study of the thermal characteristics of the leading edge groove and conventional tilting pad journal bearings. *ASME Journal of Tribology*, **115**, pp. 219–226.
- [8] S. L. Edney, G. B. Heitland, S. M. DeCamillo (1998): Testing, analysis, and CFD modeling of a profiled leading edge groove tilting pad journal bearing. *Proceedings of ASME Turbo Expo 1998*, pp. 2–5.

- [9] K. Ikeda, T. Hirano, T. Yamashita, M. Mikami, H. Sakakida (2006): An experimental study of static and dynamic characteristics of a 580mm (22.8 in) diameter direct lubrication tilting pad journal bearing. *ASME Journal of Tribology*, **128**, pp. 146–154.
- [10] K.B. Bang, J.H. Kim, Y.J. Cho (2010): Comparison of power loss and pad temperature for leading edge groove tilting pad journal bearings and conventional tilting pad journal bearings. *Tribology International*, **43**, pp. 1287–1293.
- [11] J. M. Vance (1988): *Rotordynamics of Turbomachinery*. John Wiley & Sons
- [12] D.W. Childs (1993): *Turbomachinery rotordynamics: phenomena, modeling, and analysis*. John Wiley & Sons
- [13] A. Preumont (2006): *Mechatronics: dynamics of electromechanical and piezoelectric systems*. Springer Science & Business Media
- [14] D. C. Deckler, R. J. Veillette, M. J. Braun, F. K. Choy (2004): Simulation and control of an active tilting-pad journal bearing. *Tribology Transactions*, **47**, pp. 440–458.
- [15] A. Wu, M. De Queiroz (2010): A New Active Tilting-Pad Bearing: Non Linear Modeling and Feedback Control. *Tribology Transactions*, **53**, pp. 755–763.
- [16] A. Wu, M. De Queiroz (2007): Model-based control of active tilting- pad bearings. *IEEE/ASME Transactions*, **12**, pp. 689–695.
- [17] H. P. Viveros, R. Nicoletti (2014): Lateral vibration attenuation of shafts supported by tilting-pad journal bearing with embedded electromagnetic actuators. *ASME Journal of Engineering for Gas Turbines and Power*, **136**, 042503.
- [18] I. F. Santos (1994): Design and evaluation of two types of active tilting pad journal bearings. *The Active Control of Vibration*, pp. 79–87.
- [19] I. F. Santos, F. Russo (1998): Tilting-Pad Journal Bearings with Electronic Radial Oil Injection. *ASME Journal of Tribology*, **120**, pp. 583–594.
- [20] I. F. Santos, R. Nicoletti (1999): THD Analysis in Tilting-Pad Journal Bearings using Multiple Orifice Hybrid Lubrication. *ASME Journal of Tribology*, **121**, pp. 892–900.
- [21] A. M. Haugaard, I. F. Santos (2010): Multi-orifice active tilting-pad journal bearings: harnessing of synergetic coupling effects. *Tribology International*, **43**, pp. 1374–1391.
- [22] A. Cerda, B. B. Nielsen, I. F. Santos (2013): Steady state characteristics of a tilting pad journal bearing with controllable lubrication: Comparison between theoretical and experimental results. *Tribology International*, **58**, pp. 85–97.
- [23] R. Nicoletti, I. F. Santos (2003): Linear and Non-Linear Control Techniques Applied to Actively Lubricated Journal Bearings. *Journal of Sound and Vibration*, **260**, pp. 927–947.
- [24] R. Nicoletti, I. F. Santos (2008): Control System Design for Flexible Rotors Supported by Actively Lubricated Bearings. *Journal of Vibration and Control*, **14**, pp. 347–374.
- [25] J. G. Salazar, I. F. Santos (2015): Exploring integral controllers in actively- lubricated tilting-pad journal bearings. *Proceedings of the Institution of Mechanical Engineers, Part J: Journal of Engineering Tribology*.
- [26] J. G. Salazar, I. F. Santos (2015): Feedback-controlled lubrication for reducing the lateral vibration of flexible rotors supported by tilting-pad journal bearings. *Proceedings of the Institution of Mechanical Engineers, Part J: Journal of Engineering Tribology*, **229**, pp. 1264–1275.
- [27] A. Cerda, I. F. Santos (2014): Tilting-Pad Journal Bearings with Active Lubrication Applied as Calibrated Shakers: Theory and Experiment. *ASME Journal of Vibrations and Acoustics*, **136**.
- [28] I. F. Santos, P. Svendsen (2016): Non-invasive parameter identification in rotor dynamics via fluid film bearings: Linking active lubrication and operational modal analysis. *Proceedings of ASME Turbo Expo 2016*.
- [29] A. C. Varela, A. B. García, I. F. Santos (2017): Modelling of LEG tilting pad journal bearings with active lubrication. *Tribology International*, **107**, pp. 250–263.
- [30] A. C. Varela, I. F. Santos (2018): Component level study of an actively lubricated LEG tilting pad bearing: Theory and experiment. *Tribology International*, **120**, pp. 115–126.

- [31] J. Kim, A. Palazzolo, R. Gadangi (1995): Dynamic characteristics of TEHD tilt pad journal bearing simulation including multiple mode pad flexibility model. *ASME Journal of Vibration and Acoustics*, **117**, pp. 123–135.
- [32] V. N. Constantinescu, S. Galetuse (1974): On the possibilities of improving the accuracy of the evaluation of inertia forces in laminar and turbulent films. *ASME Journal of Lubrication Technology*, **96**, pp. 69–77.
- [33] M. Fillon, J.-C. Bligoud, J. Frêne (1992): Experimental study of tilting-pad journal bearings, comparison with theoretical thermoelastohydrodynamic results. *ASME Journal of Tribology*, **114**, pp. 579–587.

Table 1: Parameters for Setup 1

Parameter	Value
Pad inner radius	49.920 mm
Journal radius	49.692 mm
Bearing axial direction length	60 mm
LEG axial length	50 mm
LEG angular position (measured from pad edge)	5 °
LEG circumferential direction width	10 mm
LEG depth	12 mm
Number of pads	1
Pad arc	70 °
Offset	0.5
Load Angle	On pad
Pad thickness	16 mm
Oil type	ISO VG22
Pad material	Brass
Pivot insert material	Steel
Pivot design	Rocker
Oil Supply Pump Maximum Pressure	250 bar
Oil Supply Pump Maximum Flow	2.5 liters per minute
Servo valve cut-off frequency ω_V	150 Hz
Servo valve leakage flow q_V^*	Variable
Servo valve flow pressure coeff. K_{pq}	1e-12 m ³ /(s Pa)
Servo valve flow voltage coeff. R_V	Variable
Servo valve damping ratio ξ_V	0.95

Table 2: Parameters for Setup 2

Parameter	Value
Pad inner diameter	99.840 mm
Journal diameter	99.347 mm
Preload	0.35
Bearing axial direction length	50 mm
LEG axial length	45 mm
LEG angular position (measured from pad edge)	8 °
LEG circumferential direction width	8 mm
LEG depth	10 mm
Number of pads	5
Pad arc	65 °
Offset	0.5
Load Angle	Between pad
Applied Load	500 N
Pad thickness	16 mm
Oil type	ISO VG32
Pad material	Brass
Pivot insert material	Steel
Pivot design	Rocker
Servo valve cut-off frequency ω_{V_1}	150 Hz
Servo valve cut-off frequency ω_{V_2}	150 Hz
Servo valve 1 flow pressure coeff. K_{pq_1}	1e-12 m ³ /(s Pa)
Servo valve 2 flow pressure coeff. K_{pq_2}	1e-12 m ³ /(s Pa)
Servo valve flow voltage coeff. R_{V_1}	Variable
Servo valve flow voltage coeff. R_{V_2}	Variable
Servo valve damping ratio ξ_{V_1}	0.95
Servo valve damping ratio ξ_{V_2}	0.95

Table 3: Finite element discretization for the flexible rotor in Setup 2

Element number #	1	2	3	4	5	6	7	8	9	10	11	12
Diameter [mm]	99.350	99.350	100	100	100	100	100	100	99.350	99.350	80	40
Length [mm]	50	50	20	180	100	200	180	20	50	50	80	50

Magnetic Bearings

Using the Dynamics of Active Magnetic Bearings to perform an experimental Modal Analysis of a Rotor System

Johannes Maierhofer¹, **Max Gille**¹, **Thomas Thümmel**¹, **Daniel Rixen**¹

¹ Chair of Applied Mechanics, Technical University Munich, 85748, Garching, Germany, j.maierhofer@tum.de, max.gille@tum.de, thuemmel@tum.de, rixen@tum.de

Abstract

Classical experimental modal analysis is done using an impulse hammer or a shaker and a few acceleration sensors. The problem is to mount the sensors on a rotating shaft. Even when using contact-less sensors, the problem of exciting without touching the rotor persists. If the rotor is partially or fully supported by Active Magnetic Bearings, the bearings can be used both as actor and sensor.

This contribution shows a first approach of how a full experimental modal analysis of the running rotor without disturbing the machine dynamics could be done. The aim of the method is to use commercial modal analysis systems in combination with the magnetic bearings and their position sensors of the system. The magnetic bearing is used to excite the system with an arbitrary signal coming from the modal analysis system. Contact-less eddy current sensors are used to measure the rotor vibrations.

Special issue of this article is the investigation of the dynamics of the magnetic bearing and how to account for it when analyzing a force signal in the modal analysis system. This signal is needed to calculate the correct transfer functions for the modal analysis algorithm. Therefore, the AMB has to be calibrated and the dynamic behavior has to be considered. This calibration is done numerically as well as experimentally.

1 Introduction

Active Magnetic Bearings (AMB) are commonly used to support rotors in highly demanding environments like undersea compressors or high speed turbo pumps. One request is to monitor the condition of these systems without stopping the rotor for maintenance. Using the concept of experimental modal analysis, it is possible to get some very characteristic properties of the rotor system. Implementing the modal analysis calculation in-situ requires quite some computational resources on the controller. This paper proposes a method where an external modal analysis system is applied to an existing system without the need of major changes in the control system. Using an academic example, the feasibility of the method is shown. Therefore, a test rig with two Active Magnetic Bearings is used. But also, the results show further potential for research and application.

2 Dynamic Model of the Magnetic Bearing

An Active Magnetic Bearing is a machine element that supports a rotating shaft using only magnetic forces. The forces are generated by currents running through coils around a magnetic core enclosing the shaft. To model the Active Magnetic Bearing, it is a common approach to build a quasi static model. Different aspects are discussed in [4]. To calculate the resulting forces from the current, it is common to consider a linearization for the relation between force, current, position.

The AMB used in this investigation is a radial 8-pole heteropolar magnetic bearing, as depicted in fig. 1. It is arranged in a X-shape to load the poles equally under gravity. This assures equal behavior in the horizontal (x) and vertical (y) direction. The current is controlled using a current controller.

This paper tries to use the AMB for exciting a dynamic system in a dynamic bandwidth of frequencies. Therefore, one key aspect is the transfer function between current and generated force. In the following section, this aspect will be discussed theoretically and practically.

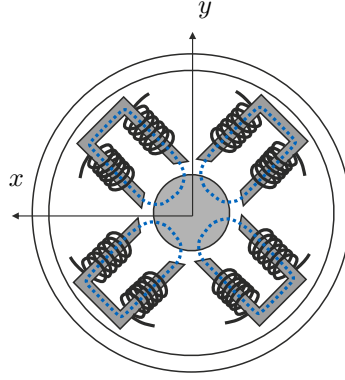


Figure 1: Conceptual diagram of the Active Magnet Bearing in X arrangement

2.1 Theoretical estimations

There are three different effects that have to be thought of when considering dynamics. These are the wave propagation by changing the current in the coils, the eddy currents that occur on changing magnetic fields and the effects of the hysteresis in the material. Similar considerations can be found in [5] and were adapted to the application of Active Magnetic Bearings.

Wave propagation The propagation of an electromagnetic wave is generally determined by transforming the Maxwell equations, as written in eq. (2). Here \mathbf{E} is the electrical field, \mathbf{H} the magnetic field, ϵ is the permittivity, μ the permeability and σ the conductivity of the material. The volumetric charge density is noted as ρ_0 and the surface current density as \mathbf{j}_0 .

$$\epsilon\mu \frac{\partial^2 \mathbf{E}}{\partial t^2} + \mu\sigma \frac{\partial \mathbf{E}}{\partial t} - \Delta \mathbf{E} = -\nabla\left(\frac{\rho_0}{\epsilon}\right) - \mu \frac{\partial \mathbf{j}_0}{\partial t} \quad (1)$$

$$\epsilon\mu \frac{\partial^2 \mathbf{H}}{\partial t^2} + \mu\sigma \frac{\partial \mathbf{H}}{\partial t} - \Delta \mathbf{H} = \text{rot } \mathbf{j}_0 \quad (2)$$

With regard to the investigation of electrodynamic effects, air can be regarded, in good approximation, as vacuum. The permittivity of air deviates only very slightly from the electrical field constant ϵ_0 in vacuum. The specific conductivity is negligibly low ($\sigma_{Air} \approx 0$) due to the lack of particles for charge transfer. Since no external current sources occur in the air, $\mathbf{j}_0 = 0$ applies. These assumptions simplify equation (1) or (2) in the one-dimensional case to:

$$\epsilon_L \mu_L \frac{\partial^2 u}{\partial t^2} - \frac{\partial^2 u}{\partial x^2} = 0 \quad (3)$$

The wave field $u(x, t)$ is a cartesian component of the E or H field. From the D'Alambert's solution of the homogeneous wave equation (3), the velocity of propagation of the wave results in:

$$c = \frac{1}{\sqrt{\epsilon\mu}} \quad \text{i.e. in vacuum: } c_0 = \frac{1}{\sqrt{\epsilon_0\mu_0}} = 2.997 \times 10^8 \frac{\text{m}}{\text{s}} \quad (4)$$

From this, the wavelength λ can be calculated as a function of the frequency f :

$$\lambda_L = \frac{2\pi c_0}{\omega} = \frac{c_0}{f} \quad (5)$$

The electromagnetic waves occurring in the magnetic bearing typically have frequencies in the range of $f_{MG} = 0$ kHz to 1 kHz. To be on the safe side, a maximum frequency $f_{max} = 100$ kHz is assumed. This results in a minimum wavelength for vacuum resp. air of $\lambda_{Lmin} = 3$ m.

For physical estimation of electromagnetic effects in the different domains of the system, dimensionless key values are introduced. The parameter g_1 represents the ratio of wavelength to a definable characteristic length of the domain:

$$g_1 = \left(\frac{\lambda}{L_c}\right)^2 \quad (6)$$

For $g_1 \gg 1$ the problem is purely magnetic or electric.

For $g_1 \approx 1$ the problem is electromagnetic.

For $g_1 \ll 1$ methods of geometrical optics have to be applied.

For Active Magnetic Bearings, the air gap between stator and rotor is defined as the characteristic length. According to $g_1 = \left(\frac{\lambda_{Lmin}}{L_{airgap}}\right)^2 = 9 \times 10^6 \gg 1$, the problem in the air gap is purely magnetic or electric. Therefore, there is no electromagnetic coupling, which is why the displacement current density $\frac{\partial D}{\partial t}$ is negligible. Hence the quasistatic equation with which the magnetic force on the bearing is calculated, remains valid for the application in the air domain.

Eddy Currents Another key value compares the electrical conductivity with the electrical displacement:

$$g_2 = \frac{\sigma}{2\pi f \epsilon} \quad (7)$$

For $g_2 \gg 1$ the approach is electrokinetic.

For $g_2 \approx 1$ the approach is electrodynamic.

For $g_2 \ll 1$ the approach is electrostatic.

The characteristic factor g_2 can also be interpreted as the ratio of conduction current density \mathbf{j} to displacement current density $\frac{\partial \mathbf{D}}{\partial t}$ [3]:

$$\frac{\mathbf{j}}{\dot{\mathbf{D}}} = \frac{\sigma \mathbf{E}}{\epsilon_0 \epsilon_r \dot{\mathbf{E}}} \sim \frac{\sigma}{\epsilon}$$

Since the conductivity σ in air is infinitesimally low, for the air domain we have $g_2 \ll 1$. Therefore, the problem is electrostatic in the air gap. But as there is no potential between the stator and the rotor, there are no forces expected. In the iron and copper domain, where g_2 is getting very big ($g_2 \gg 1$) because of the high conductivity of the materials in the range of $\sigma = 1 \times 10^6 \frac{S}{m}$ to $10 \times 10^7 \frac{S}{m}$, the displacement current density compared to the conduction current density is to be neglected up to very high frequencies, so that the quasi-stationary approach is permissible [3].

If the electrokinetic equation (8) is applied on the iron domain (i.e. the rotor and stator), $\mathbf{j}_{source} = 0$ is valid, since no external power sources are present.

$$\nabla \times \mathbf{H} = \mathbf{j}_{source} + \sigma(\mathbf{E} + \mathbf{v} \times \mathbf{B}) \quad (8)$$

In addition, the assumption that the velocity of the rotor in the bearing is zero $\mathbf{v} = 0$ holds, as the controller should avoid big vibrations of the rotor. With the identity $\nabla(\nabla \times \mathbf{H}) = 0$, it follows that $\nabla(\sigma \mathbf{E}) = \nabla \mathbf{j}_{eddy} = 0$. The electron flow generated by the electric field is therefore solenoidal, i.e. \mathbf{j}_{eddy} is an eddy current. Thus, in the iron domain, eddy currents occur which draw energy from the electromagnetic field.

Due to the high conductivity of iron, penetrating electromagnetic waves are strongly damped. This so-called *skin effect* is characterized by the damping factor α .

$$\alpha = \sqrt{\frac{\sigma \mu \omega}{2}} = \sqrt{\sigma \mu \pi f} \quad (9)$$

or the penetration depth

$$\delta = \frac{1}{\alpha} = \frac{1}{\sqrt{\pi f \sigma \mu}}. \quad (10)$$

The depth of penetration thereby indicates the length after which the electromagnetic field has decayed by a factor of $\frac{1}{e} \approx 37\%$. The following values result for the iron domain: It can be seen that the skin effect increases with

f	$\delta(f)$
1 Hz	3.57 mm
1 kHz	0.11 mm
100 kHz	0.01 mm

Table 1: $\delta(f)$ for iron ($\sigma = 10^7 \frac{S}{m}$ and $\mu = 2000\mu_0$)

increasing frequency. For the AMB this has the most significant influences. By construction, the induced current changes its direction two times during one rotation. Superimposed are the currents induced by the change of the magnetic field due to the position controller. The effect of the rotation happens in the range of 50 Hz, while the effect of the controller is around 1 kHz.

In the following, we assume that the rotor is not rotating. For the eddy currents in the rotor and stator, this means that, in the frequency range $f_{MG} \approx 1$ kHz, they only occur in the boundary layers. Additionally, the iron packages are made of laminated sheet metals that reduce the eddy current further. For that paper, eddy currents are neglected, but future FEM-Simulations will give better insights in the effects of eddy currents.

Hysteresis effects Another dynamic effect in the magnetic bearing is the magnetic hysteresis. This occurs by passing through the magnetization curve of a ferromagnetic material. The so called *Weiss districts* are microscopically small areas of ferromagnetic materials in which the magnetic moments of the atoms are already aligned in parallel, i.e. magnetized, without the application of an external magnetic field. When remagnetizing, energy must be expended to change the orientation of these domains so that the magnetic moments within the entire material point in one direction. This leads to heating of the material. The losses can be measured quantitatively using the hysteresis curve of the respective substance; the area between the hysteresis loop corresponds exactly to the necessary volume-related energy required for complete remagnetization $W_h = V_{fe} A_{BH}$. The area (respectively the energy) expenditure can be thus influenced by the choice of material and the amplitude of the induction B_m [6]. As for this investigation the rotor is not rotating and the controller currents are small, the losses due to the hysteresis effects are neglected.

2.2 Experimental Data

As we saw in the theoretical estimations, the AMB should have a constant transfer function for a non rotating rotor. To obtain experimental data, a test rig was built. The predecessor construction of the test rig is shown in [4]. To investigate the dynamics of the magnetic bearings, the test rig has to be build much stiffer to allow dynamic measurements without deforming the test rig in an unintended way.

To measure the forces, a 6-dof piezo electric force measurement device is used, allowing measuring in a wide frequency range without distortions. Three different measurements with different currents were taken. The current is oscillating around the precurent with the given amplitude in a sinus sweep from 0 Hz to 400 Hz. Then the frequency response function (FRF) between current and force is computed. As fig. 3a shows, there seem to be two peaks in the transfer function.

To check the unexpected result, the test rig was equipped with additional acceleration sensors. On the housing of the bearing, the shaft and the mounting platform where the force sensor is located. Repeating the measurements, fig. 3b show that there is still some movement of the test rig. The main motion is detected in the region of the frequencies where the peaks in the current to force FRF is detected.

The interpretation of the two graphs indicates that the dynamics of the test rig dominates the whole measurements for frequencies higher than 100 Hz. To validate the theoretical estimations it is necessary to even increase

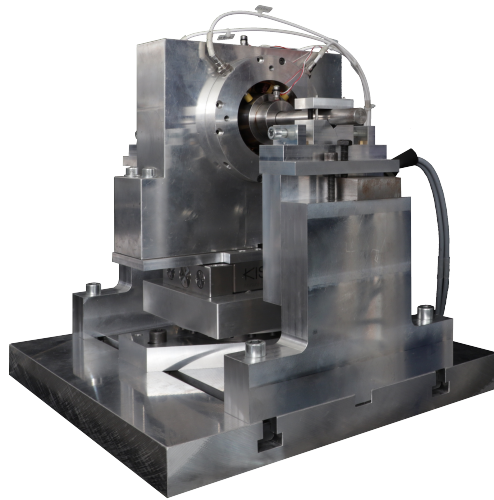


Figure 2: View of the test rig

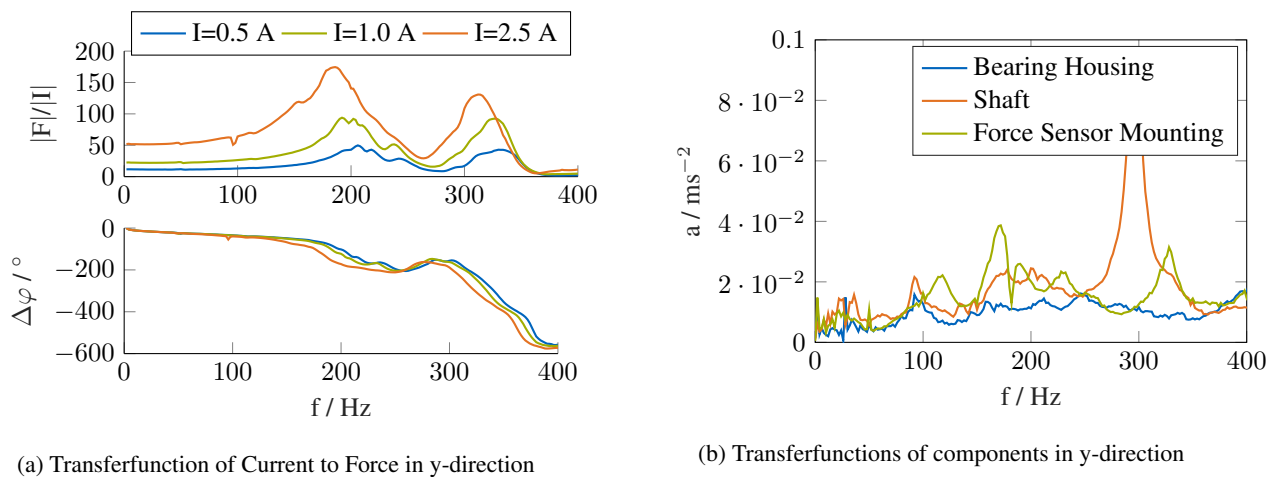


Figure 3: Results of the measurements on the test rig show that the dynamic is dominated by the test rig stiffness

the experimental effort. Concluding this chapter, the dynamics for this magnetic bearing in the desired working point will be neglected up to 200 Hz in a first approximation. Better measurements or a fem simulation could bring more accurate results.

2.3 Modeling the Force of the Magnetic Bearing

Taking together all the results from the previous sections, it is sufficient to model the force of the AMB as a linear function of the current. The position of the shaft is considered to be constant as the disturbing current is very small to not change the rotors stability.

3 Concept of non-intrusive Modal analysis

To bring modal analysis to closed systems with black box controllers it is necessary to bring in an external modal analysis system. The proposed concept of the *non-intrusive modal analysis* is described in the following section and applied to an academic example. The non-intrusive modal analysis uses any built-in actuator to excite a system, even during operation, and using all built-in sensors to perform a modal analysis. Mechatronic systems that have some kind of actuator and any kind of sensor can be used for this method. The minimum requirements are that it is possible to get at least access to the control current and the position values of each actuator.

In fig. 4 the basic components of the academic test rig are shown.

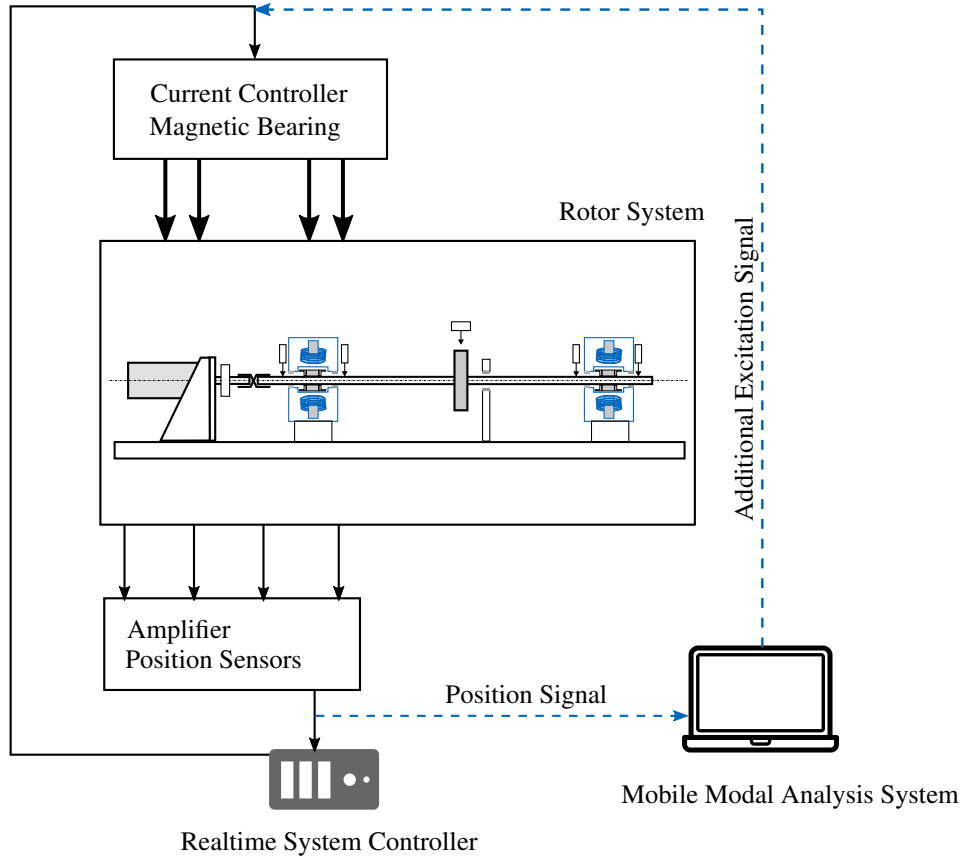


Figure 4: Concept of non-intrusive modal analysis

4 Modal Analysis of a rotor system

This section gives a brief introduction to the test environment and the experiments done. A slender rotor with one disk in the middle is supported by two magnetic bearings. The bearings measure the position of the rotor shaft using eddy current sensors in two planes. A PID controller and an attached amplifier are responsible for controlling the position of the shaft to the middle of the bearing. The controller system is just seen as a black box.

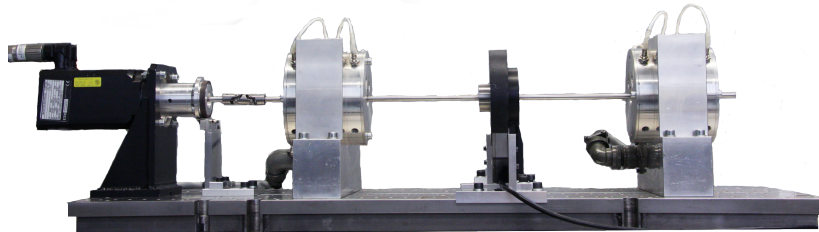


Figure 5: View on the test rig

4.1 Test Environment

For the whole survey, the rotor is never rotating but always levitating in the Active Magnetic Bearings. There will be three different experiments. On the one hand, the classical impact modal analysis and an operational modal analysis with piezo accelerometer sensors. On the other hand, the new approach for the non-intrusive modal analysis under the use of one AMB to excite the system and all the built-in sensors of the test rig to measure the displacements.

The impact measurements are done with 8 3D acceleration sensors (marked in blue) that were fixed on the shaft as seen in fig. 6. Only the x -direction is evaluated. During levitation (a PID-controller is active), the shaft was excited using a manual impact hammer. For the operational measurements the right magnetic bearing was loaded with an sinusoidal sweep force that is additionally applied to the current from the acting PID-controller. As sensors, the acceleration sensors were used. The non-intrusive measurement was also taken with the sweep of the AMB. But this time only the eddy-current sensors of the bearings itself and one additional laser distance sensor in the middle of the rotor are evaluated. The positions of the sensors are marked in green in fig. 6.

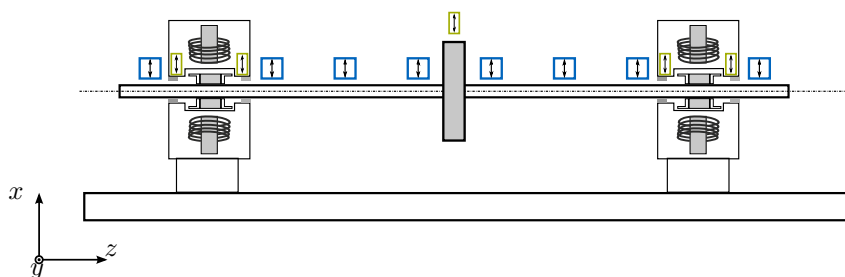


Figure 6: Setup for the modal analysis

For excitation of the structure, we use a sine sweep in a frequency range of 0 Hz to 500 Hz with a duration of 50 s. It is necessary that the duration of the sweep is slow to ensure the system gives a steady-state like response.

4.2 Modal Analysis

The key principle of experimental modal analysis (EMA) is to find the modal parameters of a system to fit the measured data best. To achieve this, FRFs from the sensor nodes to the reference input nodes are computed. These FRFs describe the response (e.g. acceleration or displacement) of the system to a known input force. [2]

$$\alpha_{jk}(\omega) = \sum_{r=1}^N \frac{r A_{jk}}{\omega_r^2 - \omega^2 + i\eta_r \omega_r^2} \quad (11)$$

For the most simple method in the frequency domain, there are mainly three steps to perform. First, individual peaks are chosen in the FRF plots. These are the eigenfrequencies of the modes ω_r . Second, damping is evaluated by the so called 'half-power points'. Using the distance on the frequency axis between this half-power points the modal parameters for the damping η_r are calculated. Third, the modal constant $r A$ is determined by looking at the maximum value of the FRF to fit the generic model to the right scaling. This procedure is done for as many modes N as are to be evaluated to build the modal superposition in eq. (11).

More advanced fitting algorithms (like MDOF, PolyMAX) also consider the neighbor modes to perform the fit of the modal parameter. They may perform better, but the principle idea is similar. It is obvious that one critical part for the result is the quality of the FRF. That means, also the input force has to be known very well.

4.3 Operational Modal Analysis

While in the previous section, we used the virtual force measurement of the magnetic bearing to perform EMA to find mode shapes, we now want to consider a possibility that does not rely on an accurate force measurement. Operational Modal Analysis (OMA) uses only the system's outputs and assumes an excitation with a flat spectrum, ideally white noise. In this case, a very basic OMA technique was tested and used on the same measurements as for the EMA, i.e. the results from a sine sweep excitation. Just as a band-limited noise, the sweep signal has a flat spectrum in the band of interest, such that the central assumption of OMA is fulfilled.

We now want to briefly look into the tested technique [1]: It starts with an n -dof system, whose first eigenfrequencies are well separated. Usually, also a randomness of the excitation in time and space is important when using OMA. Concerning the randomness in time, however, the correlation function of a sine sweep is quite similar to the one of random noise as there is also no recurring pattern in the time signal. The randomness in space, meaning multiple uncorrelated inputs is important to detect closely spaced poles, but on this simple structure, the first few eigenmodes are expected to be well-separated. Thus, it seems reasonable to only use one input in this case. In this case of well separated eigenfrequencies, the system's output in a band around one eigenfrequency is dominated by only one mode shape:

$$\mathbf{y}(t) = \phi q(t) \quad (12)$$

with the vector of displacements $\mathbf{y}(t)$, the dominating eigenvector ϕ in the frequency band of interest and the modal coordinate $q(t)$.

From the measured time data $\mathbf{y}(t)$, one can compute the correlation function matrix $\mathbf{R}(\tau)$ using equation 12:

$$\mathbf{R}(\tau) = E[\mathbf{y}(t)\mathbf{y}(t+\tau)^T] = \phi E[q(t)q(t+\tau)]\phi^T = R_q(\tau)\phi\phi^T$$

with the (scalar) correlation function $R_q(\tau)$ of the modal coordinate. Transforming this last equation into the Fourier space in order to obtain spectral density functions (\mathbf{G}) instead of correlation functions:

$$\mathbf{G}_y(f) = G_q(f)\phi\phi^T \quad (13)$$

We can see clearly, that under the assumptions made above, the spectral density matrix near a resonance frequency is a rank one matrix whose columns (and rows) are the corresponding eigenmode ϕ with varying scaling factors.

The spectral density function is also used to find the resonances of the system by simple peak-picking. After choosing the eigenfrequencies, one evaluates the spectral density matrix at those specific frequencies to find the estimates to the mode shapes according to equation 13.

4.4 Results and Comparison

In this section, the results of the different methods will be explained and compared. In fig. 7 the first three eigenmodes are evaluated for the classical impact measurement, the operational modal analysis and the non-intrusive measurement. The impact measurements are evaluated with LMS Test.LAB 17A using the PolyMAX algorithm. The results for the OMA are computed as described above. The conditions for measuring high quality FRFs are very harsh. All sensors receive some noise from the fact that the rotor is levitating and the PID-controller acting. Also the excitation has to be very low to not disturb the rotor too much.

In general the impact- and the operational modal analysis results fit quite well. On the one hand there were more sensors used, on the other hand inaccuracies due to the calibration of the Active Magnetic Bearing's dynamics are not weighted. This is a clear advantage of the OMA method.

The measurements for the non-intrusive method are also calculated with LMS and the PolyMAX algorithm. These measurements are much more difficult to process. But the results show at least qualitatively the same behavior. The coherence of the single FRFs look very noisy and bad. This is probably because of the vibrations induced by the two PID-controllers. Looking at the MAC-criterion shows a good separation of the identified modes.

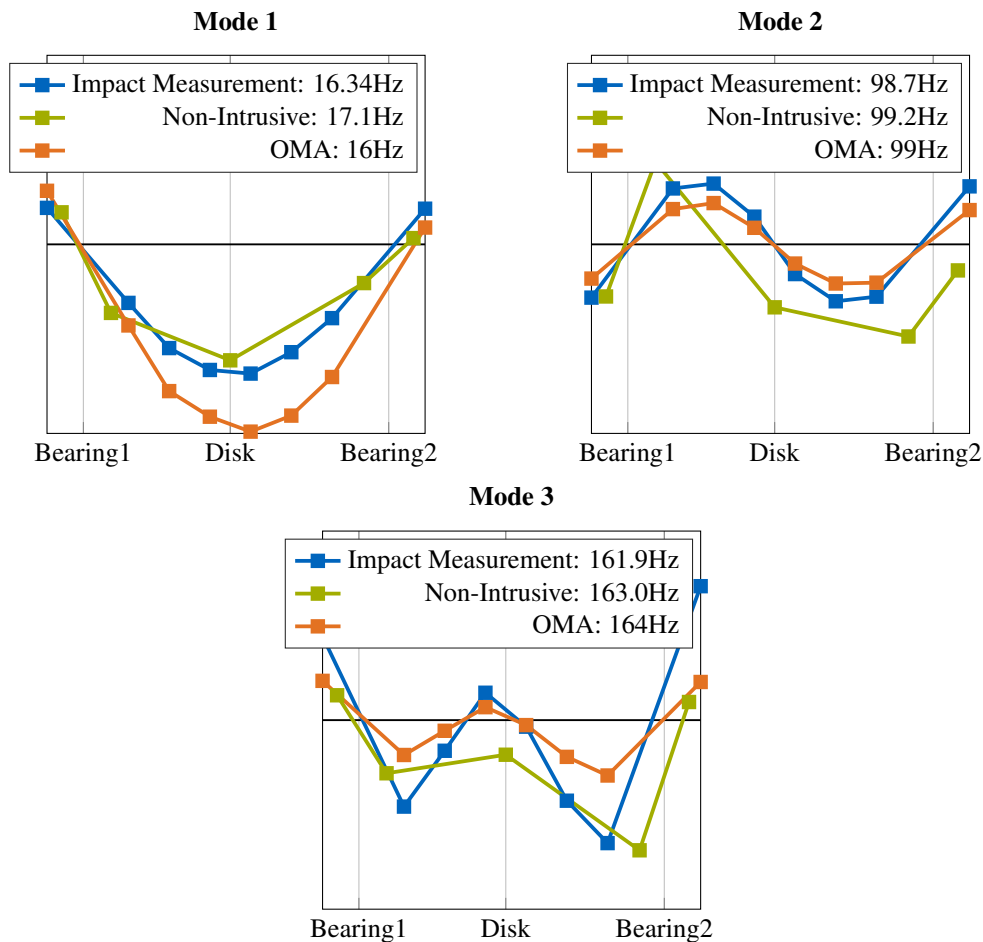


Figure 7: Comparison of the Modeshapes between Impact Testing and Non-Intrusive Modalanalysis and OMA

5 Conclusion

Active Magnetic Bearings provide an elegant way to excite a machinery system to achieve modal measurements. The results of the classical impact measurement and of the operational modal analysis show good similarities. The results with the displacement sensors integrated in the bearing show the same characteristics but are not nearly as good as the measurements with the attached accelerometers. However, using enough sensors that are well placed is critical to achieve good results for the modal analysis. The excitation can be done very well with the Active Magnetic Bearings. Further development needs to be done in further investigation of the dynamics of Magnetic Bearings and to create simple reduced models of it to make use of the driving force for the modal analysis. Also research is necessary to determine the influence of the PID-controller used to levitate the rotor. The signals of the displacement sensors could maybe be filtered to achieve better results.

References

- [1] Brincker, R. and Ventura, C. *Introduction to operational modal analysis*. John Wiley & Sons, 2015.
- [2] Ewins, D. J. *Modal testing: theory and practice*. Vol. 15.
- [3] Küchler, A. *Hochspannungstechnik Grundlagen–Technologie–Anwendung*. 2005. DOI: [10.1007/b138561](https://doi.org/10.1007/b138561).
- [4] Maierhofer, J., Wagner, C., Thümmel, T., and Rixen, D. "Progress in Calibrating Active Magnetic Bearings with Numerical and Experimental Approaches". In: *Mechanisms and Machine Science*. Springer International Publishing, Aug. 2018, pp. 249–261. DOI: [10.1007/978-3-319-99272-3_18](https://doi.org/10.1007/978-3-319-99272-3_18).

- [5] Rochus, V., Rixen, D. J., and Golinval, J.-C. “Monolithic modelling of electro-mechanical coupling in micro-structures”. In: *International Journal for Numerical Methods in Engineering* 65.4 (2005), pp. 461–493. DOI: [10.1002/nme.1450](https://doi.org/10.1002/nme.1450).
- [6] Schweitzer, G., Traxler, A., and Bleuler, H. *Magnetlager: Grundlagen, Eigenschaften und Anwendungen berührungsfreier, elektromagnetischer Lager*. Springer, 1993. DOI: [10.1007/978-3-662-08448-9](https://doi.org/10.1007/978-3-662-08448-9).

The design of a combined, self-stabilizing electrodynamic passive magnetic bearing supporting high-speed rotors

Tomasz Szolc¹, Krzysztof Falkowski²

¹ Institute of Fundamental Technological Research, Polish Academy of Sciences, ul. A. Pawińskiego 5B, 02-106 Warsaw, Poland, tszolc@ippt.pan.pl

² Faculty of Mechatronics and Aerospace of the Military University of Technology, ul. gen. Witolda Urbanowicza 2, 00-908 Warsaw, Poland, Krzysztof.falkowski@wat.edu.pl

Abstract

The purpose of this paper is to create a concept of the structurally simple and operationally robust support of high-speed rotors in the electrodynamic passive magnetic bearings (EDPMB). Since this kind of a magnetic suspension in its fundamental version is dynamically unstable, in order to avoid such an essential disadvantage there is proposed the addition of external damping by the use of the newly designed combined, self-stabilizing electrodynamic passive magnetic bearing. The electromagnetic stiffness- and damping characteristics of the combined EDPMB have been determined for various shaft rotational speeds by means of the advanced 3D finite element method. The dynamic investigations are performed for a single-span, high-speed flexible rotor-shaft. In the computational part a dynamic interaction between the rotor-shaft and the passive magnetic suspension is carried out for a support in the fundamental EDPMBs and in the proposed combined, self-stabilizing passive magnetic bearings. Here, the main attention is focused on asymptotic stability of the both rotor-shaft suspension variants. In addition, for the considered rotor-shaft-bearing system amplitude-frequency characteristics of forced steady-state bending vibrations have been determined. By means of this investigation there is demonstrated a resonance suppression ability using the external damping generated by the proposed combined EDPMBs.

1 Introduction

Electrodynamic passive magnetic bearings (EDPMB) are now viewed as a feasible option when looking for support for high-speed rotors of vacuum pumps, kinetic energy storage flywheels, turbines, turbochargers and many others. Nevertheless, because of the skew-symmetrical visco-elastic properties of such bearings, they are prone to operational instability. In order to avoid this, a sufficient amount of additional external damping should be introduced into the rotor-shaft-bearing system. Such external, rotor-to-stator damping expected to stabilize a support in EDPMBs has been called in [1] “peripheral” damping. The sense of inserting additional damping into a radial EDPMB supporting a rigid rotor is presented in [2] and [3], where they offer a combined passive-active magnetic support for rigid rotor-shafts, as well as in [4] using external damping generated passively. In [5] a vibration energy dissipation allocated for an effective stabilization of the horizontal, flexible rotor-shaft support in EDPMBs has been carried out using three means acting simultaneously, i.e. a simple active magnetic damper, an appropriately soft visco-elastic embedding of the EDPMBs in their housings as well as an optimum selection of the passive magnetic bearing radial stiffness. On the one hand, all the above mentioned approaches used in [2-5] lead to more or less effective stabilization of rotor-shafts suspended in passive magnetic bearings. But on the other hand, they require an application of additional electronic devices or advanced visco-elastic materials which can be expensive, sensitive to exploitation faults or insufficiently resistant to high temperatures.

To reconcile the efficiency of stabilization with a structural simplicity and operational reliability, in this paper a combined design of the EDPMBs supporting a flexible rotor-shaft is proposed. The general idea of a combined electrodynamic passive magnetic suspension of a rotating disk has been initially signalized in [6,7]. Namely, basing on the analytical solution of Maxwell’s equations, it has been proved that a permanent magnet mounted on a shaft rotating relative to the stationary conductor embedded in a bearing housing is a source of ‘in-plane’ viscous and elastic levitation forces without any cross-coupling components. Such an inverse magnet-to-conductor mutual orientation in comparison with that of the classical, fundamental transverse load carrying main EDPMB can be a

source of an effective stabilization of vibrating rotor-shafts suspended in such a passive magnetic support. Thus, the rotating magnet with the stationary conductor assembled on the rotor-shaft in the vicinity of a main support in the form of a conductor rotating relative to the stationary permanent magnet will create a combined, self-stabilizing EDPMB. In comparison with the passive magnetic bearing stabilization methods applied in the literature items cited above, the proposed approach, in addition to an effective stabilization ability, is structurally very simple and assures a robust operation in high-speed rotating machines, particularly in these characterized by small geometrical dimensions.

2 Modelling of the rotor-shaft-bearing system

The object of considerations is a rotor-shaft of the typical automotive engine turbocharger. This rotating element was originally suspended in two floating-ring oil journal bearings which have been virtually substituted by electrodynamic passive magnetic supports. Full geometrical shapes, material constants and inertial parameters of the rotor-shaft are taken from [8]. This rotating system is expected to operate within the rotational speed range 0–210,000 rpm. It consists of the flexible stepped shaft of the total length 0.16 m with attached two heavy disks corresponding respectively to the turbine- and compressor rotor. The considered rotor-shaft is characterized by the entire mass of ca. 0.566 kg and by the bearing span equal to 0.05 m. Such a structure can be very representative for a broad variety of turbochargers applied in internal combustion piston engines as well as for various stationary turbo-compressors working in heavy industry.

2.1 Modelling of the rotor-shaft

In order to obtain sufficiently reliable results of theoretical calculations for the considered flexible rotor-shaft-bearing system, the dynamic analysis will be performed by means of the one-dimensional hybrid structural model consisting of continuous visco-elastic beam finite elements and rigid bodies. In this hybrid model successive cylindrical segments of the stepped rotor-shaft are represented by flexurally deformable cylindrical macro-elements of continuously distributed inertial-visco-elastic properties. With an accuracy that is sufficient for practical purposes the turbine and compressor massive rotors can be substituted by the rigid bodies attached to the respective macro-element extreme cross-sections. Such a hybrid model of the investigated rotor-shaft is presented in Fig. 1a. As it can be noticed, the beam finite elements applied here are not discretized in space and remain naturally continuous, which is the only difference between the hybrid model applied here and the classical one-dimensional finite element model of the same structure.

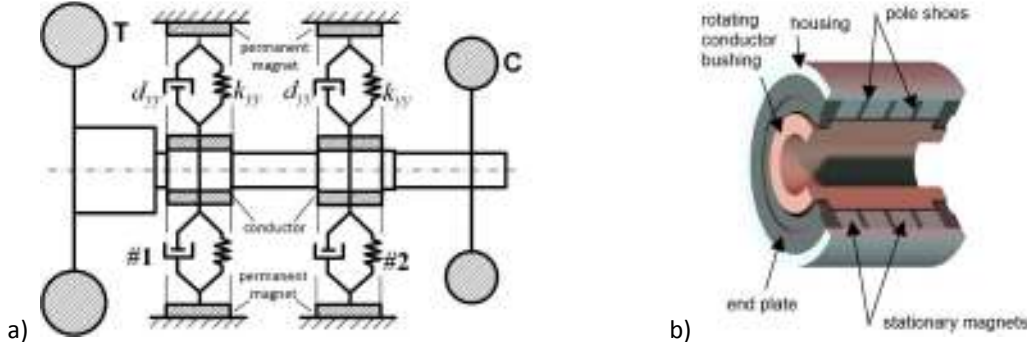


Figure 1: The single-span rotor-shaft supported in the main EDPMBs (a); the view of the main EDPMB (b).

Since the electrodynamic passive magnetic bearings are characterized by relatively much smaller radial stiffness than that of their housings made of metallic materials, a visco-elastic suspension of the rotor-shaft by means of such supports can be described by mass-less springs and dampers attached to the middle cross-sections of the continuous finite macro-elements representing shaft journals, as shown in Fig. 1a. This approach makes possible to represent with a relatively high accuracy kinetostatic and dynamic anisotropic and anti-symmetric bearing properties in the form of constant or variable stiffness and damping coefficients.

2.2 Modelling of the combined electrodynamic passive magnetic bearing

The principle of a classical radial EDPMB operation can be reduced to a mutual, non-contact interaction between a rotating conductor (at room-temperature) and permanent magnets, thus creating a stator, [1], [9-11]. This was initially achieved by a fundamental, transverse load carrying, main bearing support that consist of a conducting sleeve attached to the rotor-shaft journal and permanent magnets embedded in the bearing housing, as illustrated in Fig. 1b. In order to assure a sufficiently high transverse load ability for such a bearing, the permanent magnets must be appropriately mutually placed and also separated by the iron pole shoes in the way resulting in the so called heteropolar or homopolar type of the radial passive magnetic bearing, [1], [10].

Here, a dynamic modelling of the main EDPMBs is intended to calculate their electromagnetic stiffness- and damping characteristics. For this purpose, by means of the advanced 3D finite element code for various shaft rotational speeds it is necessary to calculate the bearing global radial ‘in-plane’ stiffness K regarded as a derivative of the Lorenz force with respect of the conductor-to-stator radial proximity. In the considered case the bearing ‘in plane’ transverse global stiffness K can be defined as:

$$K(\Omega) = -\frac{dF(\Omega)}{d(\Delta r)}, \quad \text{where: } F(\Omega) = \int_V (J \times B) dV \quad (1)$$

is the Lorenz force, J and B denote respectively the current volume- and external magnetic flux densities, Δr is the journal-to-bushing radial proximity, [1], [11], and Ω denotes the current shaft rotational speed. Then, basing on the solution of the Maxwell equations and according to [6], the actual forces acting on a rotating shaft, that depend respectively on radial displacement $\vec{r}(t)$ and velocity $\dot{\vec{r}}(t)$, can be expressed as:

$$\vec{F}_s(\Omega, t) = K(\Omega) \cdot \vec{r}(t) \quad \text{and} \quad \vec{F}_d(\Omega, t) = \frac{K(\Omega)}{\Omega} \cdot \dot{\vec{r}}(t). \quad (2)$$

These forces are mutually perpendicularly oriented in phase and their respective projections on the vertical and horizontal plane result in the following equation of equilibrium with the reaction force of the flexible rotor-shaft:

$$\Gamma([\![v_i]\!]) + \left(\frac{K(\Omega)}{\Omega} \sin \theta\right) \frac{\partial v_i(z, t)}{\partial t} + (K(\Omega) \cos \theta) v_i(z, t) - j \left(\frac{K(\Omega)}{\Omega} \cos \theta\right) \frac{\partial v_i(z, t)}{\partial t} + j (K(\Omega) \sin \theta) v_i(z, t) = 0, \quad (3)$$

where $v_i(z, t) = u_i(z, t) + j w_i(z, t)$ is the lateral journal to bushing displacement with components in the vertical direction $u_i(z, t)$ and in the horizontal direction $w_i(z, t)$, z denotes the rotor-shaft axial co-ordinate, j is the imaginary number, $\theta = \arctan(R/\Omega L)$ is the so called ‘force angle’ expressed as a function of the magnetic bearing coil resistance R and inductance L and $\Gamma([\![v_i]\!])$ denotes the reaction force of the hybrid model i -th beam finite macro-element representing the bearing journal with the cross-sectional shear stiffness GA_i , bending stiffness EI_i , mass moment of inertia ρI_i and the retardation time e , see Fig. 1a. In the case of an application of the Timoshenko beam theory this reaction force is described in the following operator form:

$$\Gamma([\![v_i]\!]) = -\kappa GA_i \left(1 + e \frac{\partial}{\partial t}\right) \frac{\partial}{\partial z} [\![\phi_i(z, t)]\!] + 2j\Omega \rho I_i \frac{\partial^2}{\partial z \partial t} [\![\Delta v_i(z, t)]\!],$$

where $[\![v_i(z, t)]\!]$ and $[\![\phi_i(z, t)]\!]$ denote respectively the partially differentiated complex steps of bending displacements and shear angles on the left- and right-hand side of the bearing planes shown in Fig. 1a. When the Rayleigh rotating beam theory is used, this reaction force can be expressed as:

$$\Gamma([\![v_i]\!]) = \left(EI_i \left(1 + e \left(\frac{\partial}{\partial t} - j\Omega\right)\right) \frac{\partial^3}{\partial z^3} - \rho I_i \left(\frac{\partial^3}{\partial z \partial t^2} - 2j\Omega \rho I_i \frac{\partial^2}{\partial z \partial t}\right)\right) [\![v_i(z, t)]\!].$$

If we denote in (3): $K(\Omega) \cos \theta = k_{xx}(\Omega) = k_{yy}(\Omega)$, $K(\Omega) \sin \theta = k_{xy}(\Omega) = -k_{yx}(\Omega)$, (4)

$(K(\Omega) \sin \theta) / \Omega = d_{xx}(\Omega) = d_{yy}(\Omega)$ and $(K(\Omega) \cos \theta) / \Omega = d_{xy}(\Omega) = -d_{yx}(\Omega)$, (5)

then, $k_{xx}(\Omega) = k_{yy}(\Omega)$ and $d_{xx}(\Omega) = d_{yy}(\Omega)$ become here the coefficients of the ‘in-plane’ horizontal and vertical stiffness- and damping components, respectively. Consequently, the symbols $k_{xy}(\Omega) = -k_{yx}(\Omega)$ and $d_{xy}(\Omega) = -d_{yx}(\Omega)$ denote the coefficients of the cross-coupling stiffness- and damping components which are skew-symmetrical.

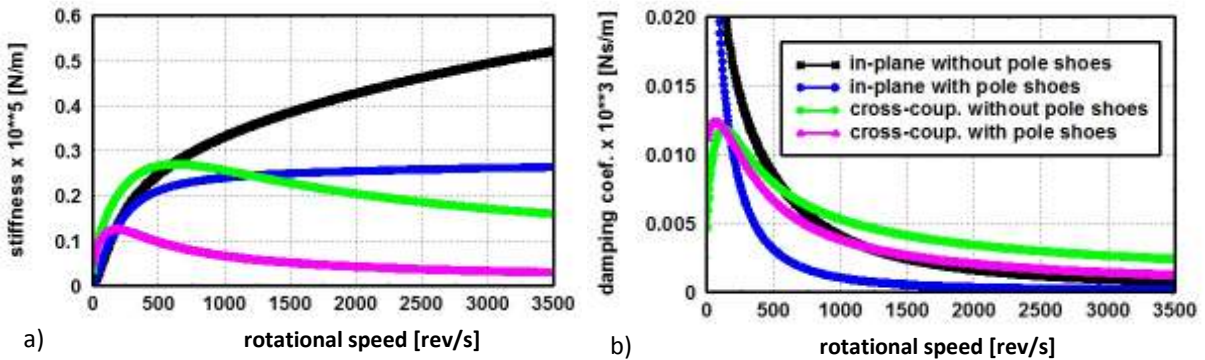


Figure 2: Stiffness (a) and damping (b) characteristics of the EDPMB without- and with magnet pole shoes.

This property is responsible for the mentioned above instability of the rotor-shaft suspension in the classical, main EDPMBs. The plots of these coefficients expressed as functions of the rotor-shaft angular speed Ω are demonstrated in Fig. 2 for the case of the main EDPMB without- and with pole shoes built in the stator permanent magnets. They are qualitatively identical with those obtained in [1,9] for high-speed rotor machines different than investigated here.

In order to make such a passive magnetic support stable, it is necessary to introduce additional ‘in-plane’ damping force components into the rotor-shaft-bearing system. This goal can be realized by means of the so-called ‘‘combined EDPMBs’’. Namely, for this purpose the main, transverse load carrying EDPMB is going to be supplemented with an additional part which consists of the rotating disk made of a permanent magnetic material attached in a given, possibly adjacent shaft segment and the conductor built in the bearing housing, as shown in Fig. 3a. As it follows from the thorough theoretical and experimental analysis performed in [6,7], such an inverse magnet-to-conductor orientation generates ‘in-plane’ visco-elastic forces $\vec{F}(t)$ only, both in the vertical and horizontal direction, according to the following equation:

$$\frac{L}{R} \dot{\vec{F}}(t) + \vec{F}(t) = -D \cdot \dot{\vec{r}}(t), \quad \text{where} \quad D = \frac{n}{2} \frac{\gamma}{R} S \frac{dB}{dr}, \quad (6)$$

L and R denote respectively the conductor inductance and resistance, n is the number of coils creating the conductor, dB/dr denotes the radial magnetic induction gradient in the air gap between the stationary conductor and the rotating disk made of the magnetic material with surface area S and γ is the relationship between the magnetic force and the electric currents induced in the conductor, which follows from the fundamentals of electromagnetism, [6,7]. Since the elastic forces are caused by the usually negligible inductances L of the stationary conductor, they are omitted here. Thus, the actual rotor-to-stator interaction force $\vec{F}(t)$ reduces to the dissipative one and symbol D in (6) becomes here the stabilizing damping coefficient. For the assumed number n of coils with resistances R each, the damping coefficient D has to be determined numerically by means of the 3D finite element model of this additional bearing part expected to stabilize an operation of the entire combined EDPMB.

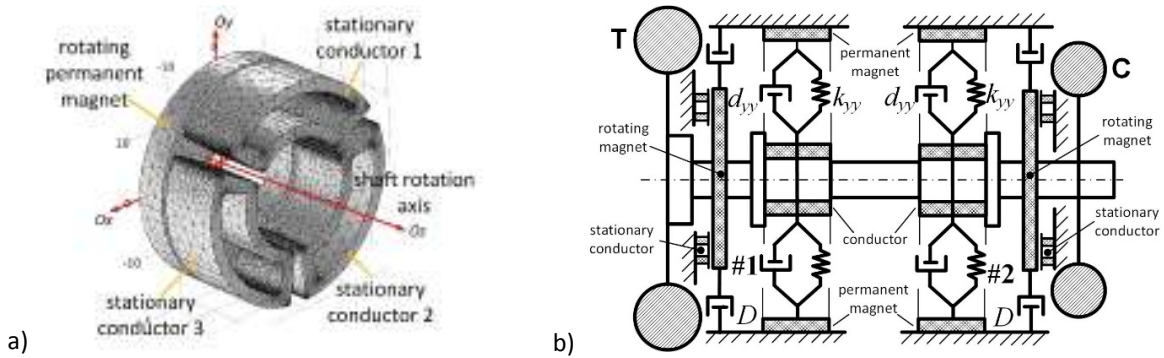


Figure 3: Scheme of the EDPMB damping part (a); the rotor-shaft supported in the combined EDPMBs (b).

3 Solution of the problem

The complete mathematical formulation and solution for the rotor-shaft system hybrid model applied here can be found e.g. in [12] and [13]. In this model the flexural motion of cross-sections of each visco-elastic finite macro-element is governed by the partial differential equations derived using the Timoshenko and Rayleigh rotating beam theory. In such equations there are contained gyroscopic forces mutually coupling rotor-shaft bending vibrations in the vertical and horizontal plane. The analogous coupling effect caused by the system rotational speed dependent shaft material damping, described using the standard body model, is also taken into consideration. Mutual connections of the adjacent finite beam macro-elements are described by means of kinematic conditions of transverse- and angular displacement agreements as well as using dynamic conditions of equilibrium for inertial, elastic, viscous and external transverse forces and bending moments. Equation (3) is an exemplary dynamic condition for transverse forces acting in the cross-section corresponding to the bearing support plane. The solution for the bending vibration analysis has been obtained using the analytical-computational approach demonstrated in details in [12,13]. In the considered case it is to remember that, according to formulae (4)–(6), the visco-elastic bearing support parameters are rotational speed dependent. But for a constant Ω in time, numerical values of all these quantities are also constant. Thus, for each Ω one can solve the differential eigenvalue problem for the orthogonal system. Then, an application of the Fourier solutions in the form of fast convergent series in orthogonal eigenfunctions leads to the set of modal equations

$$\mathbf{M}(\Omega) \cdot \ddot{\mathbf{q}}(t) + \mathbf{C}(\Omega) \cdot \dot{\mathbf{q}}(t) + \mathbf{K}(\Omega) \cdot \mathbf{q}(t) = 0, \quad (7)$$

where: $\mathbf{C}(\Omega) = \mathbf{C}_0(\Omega) + \Omega \cdot \mathbf{C}_g(\Omega)$ and $\mathbf{K}(\Omega) = \mathbf{K}_0(\Omega) + \mathbf{K}_b(\Omega) + \Omega \cdot \mathbf{K}_d(\Omega)$.

The symbols $\mathbf{M}(\Omega)$, $\mathbf{K}_0(\Omega)$ denote respectively the rotational speed dependent diagonal modal mass and stiffness matrices, $\mathbf{C}_0(\Omega)$ is the non-symmetrical damping matrix containing the damping coefficients (5) and (6) of the passive magnetic bearings and $\mathbf{C}_g(\Omega)$ denotes the skew-symmetrical matrix of gyroscopic effects. Skew- or non-symmetrical elastic properties of the bearings are described by matrix $\mathbf{K}_b(\Omega)$. Anti-symmetrical effects due to the standard body material damping model of the rotating shaft are expressed by the skew-symmetrical matrix $\mathbf{K}_d(\Omega)$. Of course, because of the reasons mentioned above, for given constant values of Ω all these matrices are regarded constant. The modal coordinate vector $\mathbf{q}(t)$ consists of the unknown time functions standing in the Fourier solutions. The number of equations (7) corresponds to the number of bending eigenmodes taken into consideration in the frequency range of interest.

In order to determine eigenvalues of the rotor-shaft dynamic model, it is convenient to transform its modal motion equations (7) to analogous equations in the modal state co-ordinates. Then, one can solve a standard eigenvalue problem in which a characteristic non-symmetrical matrix is reduced to the Hessenberg form using the Hausholder transformation. Then, the final computation of the eigenvalue real- and imaginary parts for each bending eigenmode of the considered system is achieved by means of the commonly known QR algorithm, [14].

For constant rotational speeds Ω equations (7) are a system of linear ordinary differential equations with constant coefficients and harmonic external excitation due to residual unbalances. For the harmonic excitation the induced steady-state vibrations are also harmonic with the same synchronous circular frequency Ω . Thus, analytical solutions for the successive modal functions contained in vector $\mathbf{q}(t)$ can be assumed in an appropriate harmonic form. Then, by substituting them into (7), derived here for $\Omega=\text{const}$, one obtains well-known respective systems of linear algebraic equations which can be found e.g. in [13]. By means of this approach amplitude-frequency characteristics of steady-state forced vibrations can be effectively determined.

4 Stability analysis of the rotor-shaft-bearing system

A stability analysis, in the form of determination of rotor-shaft system eigenvalue imaginary and real parts, will be performed initially for two variants of a suspension in the main EDPMBs, i.e. without- and with pole shoes built in the stationary permanent magnets and in the expected rotational frequency range 0-210,000 rpm, which corresponds to 0-3500 rev/s. As it follows from the respective stiffness- and damping coefficient characteristics depicted in Figs. 2a,b, particularly for greater shaft rotational speeds, the variant “without pole shoes” results in significantly bigger coefficient values of the ‘in-plane’ and cross-coupling stiffness- and damping components. This feature shall have a remarkable influence on a system instability, when only the main EDPMBs are used, as shown in Fig. 1a, as well as on its stabilization by means of the combined EDPMBs demonstrated in Fig. 3b. In the case of both support variants, the values of the static rotor-shaft vertical displacement off-set due to the gravitational forces are contained within the bearing radial clearance and they amount between 0.05 and 0.11 mm.

In Fig. 4 there are presented characteristics of the eigenvalue imaginary parts in the form the Campbell diagram for the rotor-shaft suspended in the main EDPMBs without magnet pole shoes. For a better clarity, on the left-hand sides of this diagram also the respective lateral eigenfunctions are depicted. The analogous Campbell diagram determined for the bearing suspension variant “with pole shoes” is almost identical to that shown in Fig. 4 and thus, it has not been presented in a graphical form. Because of the relatively soft suspension in the EDPMBs in relation to the rotor-shaft flexibility, from among the fundamental lateral eigenforms one can distinguish first two similar to ‘rigid-body’ ones. In the considered synchronous external excitation frequency range 0-3500 Hz in the both cases of bearing support variants four lateral eigenforms of the investigated rotor-shaft have been determined, respectively with their backward and forward whirl branches. Moreover, the first two eigenforms are characterized by relatively small damped natural frequencies not exceeding 250 Hz observed for the forward whirl of the second eigenmode, as shown in Fig. 4. Since values of these frequencies fluently start from zero at the zero shaft rotational speed, their plots do not cross the synchronous excitation line 1X. Thanks to this fact, in the cases of the first two eigenmodes critical speeds are practically not observed. However, the only critical speed occurs for the forward precession of the third eigenmode at ca. 1210 rev/s.

In Figs. 5 and 6 there are shown characteristics of the eigenvalue real parts determined for the main EDPMB suspension variants “without-“ and “with pole shoes”, respectively. But here, the appropriately corresponding to each other plots of eigenvalue real parts are characterized by significant qualitative and quantitative differences. First, from the plots illustrated in these figures it follows that not every eigenvalue real parts are negative, what means that the both considered bearing variants pain a lack of stability. Namely, in the case of the support “without pole shoes” the first eigenmode within the entire considered range of rotational speeds is drastically unstable. Moreover, for greater shaft rotational speed values also backward precessions of the third and fourth eigenmode are unstable, see Fig. 5. However, the bearing variant “with pole shoes” built in the permanent magnets results in unstable backward precessions only, but of all four eignemodes. Here, in the case of the first two of them this instability is observed within the entire range of rotational speeds 0–3500 rev/s. But the backward whirls of the third and fourth eigenmodes are unstable at greater rotational speed values, as shown in Fig. 6. In addition, it is worth noting that in the case of the bearing variant “without pole shoes” ca. two times greater maximal positive real part values are observed than these obtained for the variant “with pole shoes”. According to the above, the

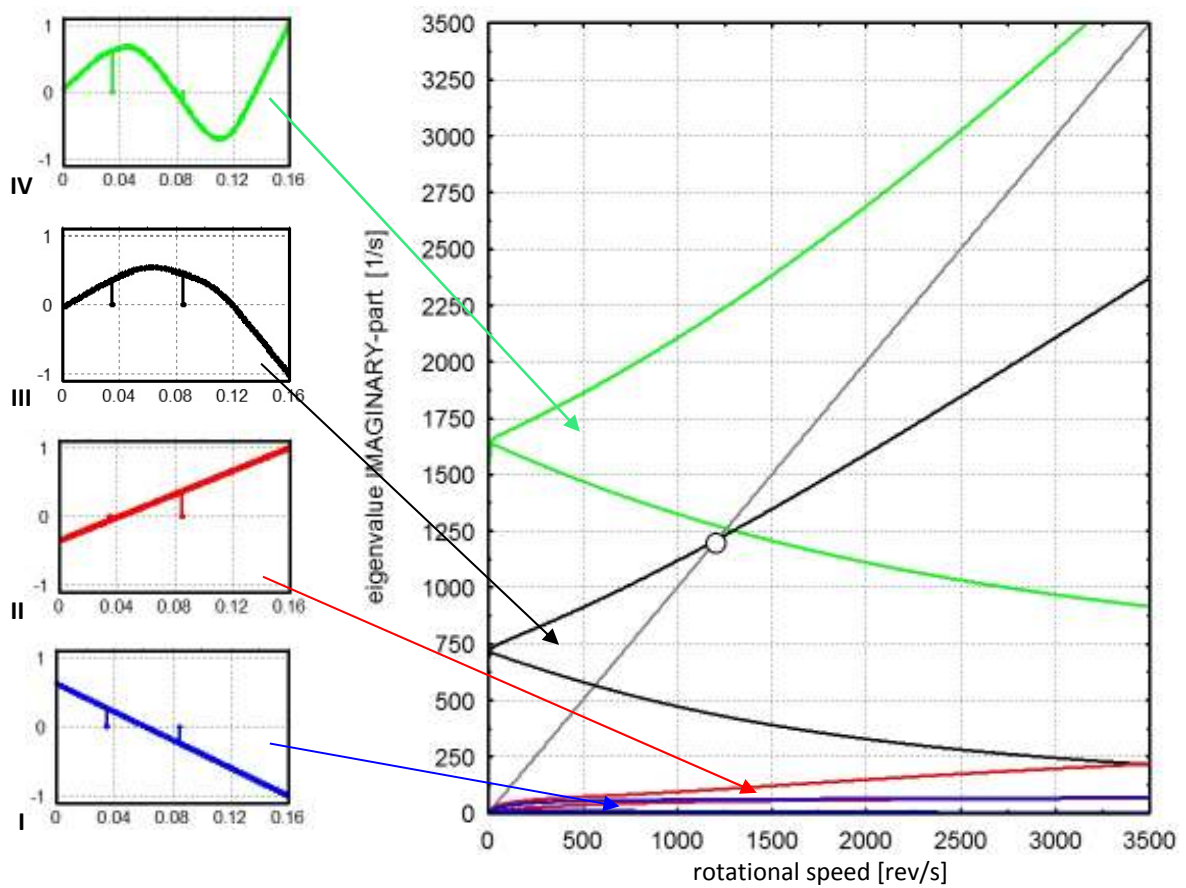


Figure 4: Eigenvalue imaginary parts of the rotor-shaft supported in the EDPMBs without pole shoes.

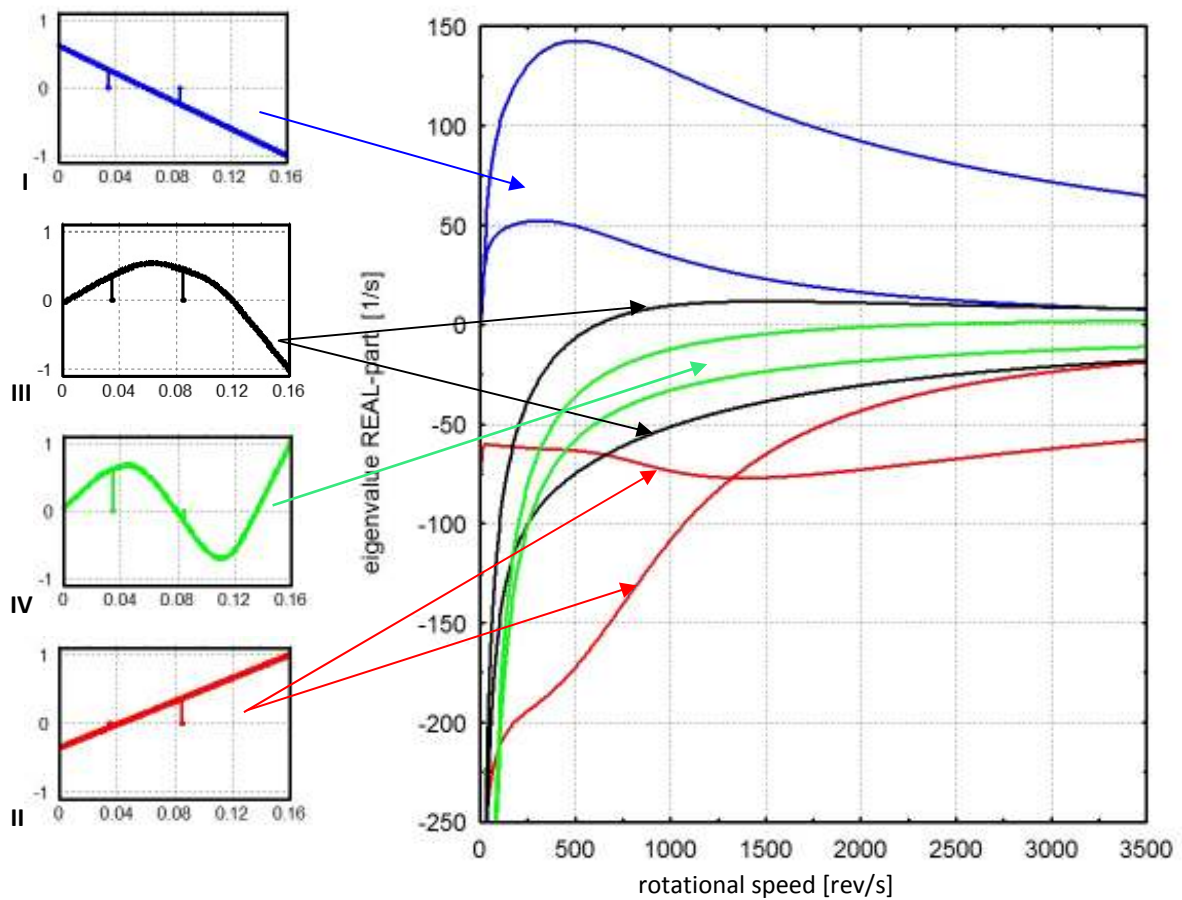


Figure 5: Eigenvalue real parts of the rotor-shaft supported in the EDPMBs without pole shoes.

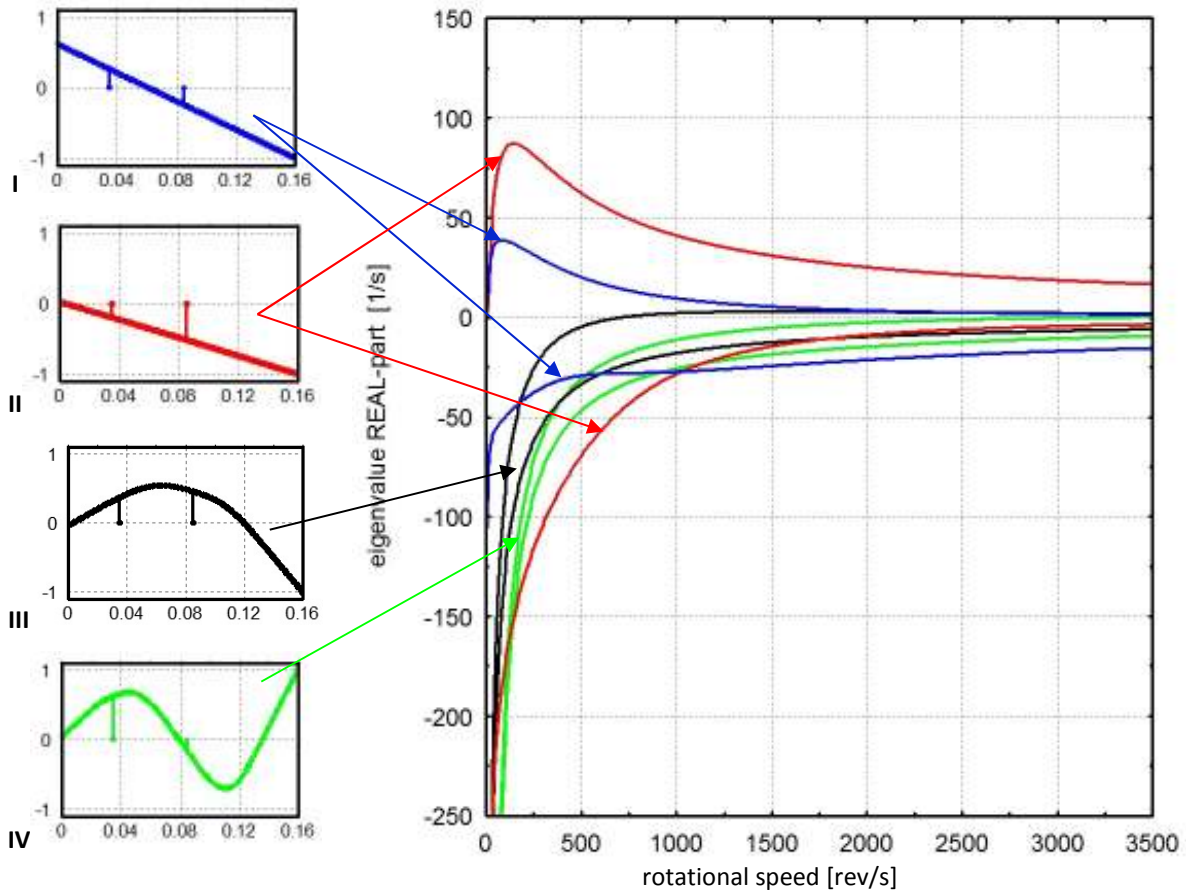


Figure 6: Eigenvalue real parts of the rotor-shaft supported in the EDPMBs with pole shoes.

former variant of the main EDPMBs seems to be more difficult to stabilize than the latter one.

An application of the combined EDPMBs enables us a full stabilization of the considered rotating system if a sufficient magnitude of the additional external damping can be generated by such bearings. For this purpose $n=3$ stationary conductor coils have been designed with the wire diameter 0.5 mm and with 100 windings, each. Then, the overall resistance of this assembly was calculated to be $R=0.0543 \Omega$. In the case of the commercial ring shaped permanent magnets with the standard remanence B_r of 1.24 T that create the rotating disks shown in Fig. 3b, the numerically determined radial induction gradient dB/dr along the diameter of each disk reached 1307 T/m. From results of virtual simulation of the electromechanical interaction between the stationary conductor coils and the rotating magnets it follows that the obtained magnetic force-to-electric current ratio γ was in the range within 7–7.5 N/A, depending on the effective coil placement radius.

Independently, it turned out that if for the main bearing variant “without pole shoes” a numerical value of damping coefficient D defined in (6) was greater than 250 Ns/m, the stabilization effect has been entirely achieved, as it follows from the plots of corresponding the greatest eigenvalue real parts shown in Fig. 7. The analogous stabilization in the case of main bearing variant “with pole shoes” is already obtained when D was greater than 150 Ns/m, which demonstrate the respective plots in Fig. 8. In Figs. 7 and 8 there are presented eigenvalue real part characteristics corresponding to the first eigenmode which is the most sensitive to instability. Numerical values of the real part characteristics of the remaining eigenmodes are even smaller and, of course, always negative. The additional damping generated by the combined EDPMBs to stabilize the considered system does not influence remarkably the eigenvalue imaginary parts of the all four eigenmodes, both in the case of the main bearing variant “without-“ and “with pole shoes”. Thus, the respective plots have not been presented in a graphical form.

Here, in order to achieve the stabilization effects demonstrated in Figs. 7 and 8 by means of the combined EDPMBs with the structure and numerical parameters specified above, the surface area S of the permanent magnets in the form of the rotating disks had to be initially determined. Assuming for this purpose the inner diameter of these disks 0.012 m and the force-to-current ratio $\gamma=7.5$ N/A, the stabilizing damping coefficient D of 250 Ns/m can be obtained using formula (6) for the outer disk diameter greater than 0.0363 m. However, the smaller damping coefficient value of 150 Ns/m, sufficient to stabilize the main bearing variant “with pole shoes”, can be achieved for the outer magnet diameter not exceeding 0.03 m and for the force-to-current ratio γ reaching 7.0 N/A only.

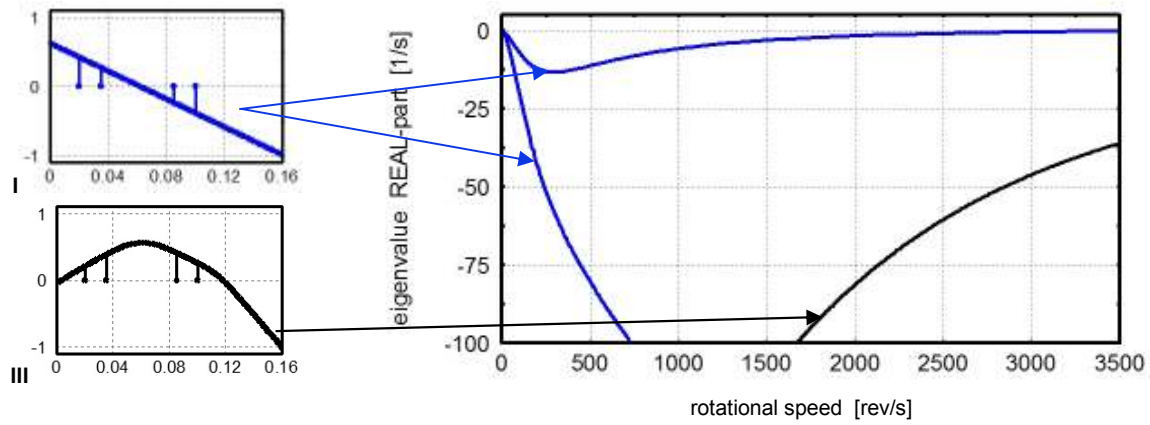


Figure 7: Maximal eigenvalue real parts of the rotor-shaft supported in the combined EDPMBs without pole shoes obtained for the minimal stabilizing damping coefficient D equal to 250 Ns/m.

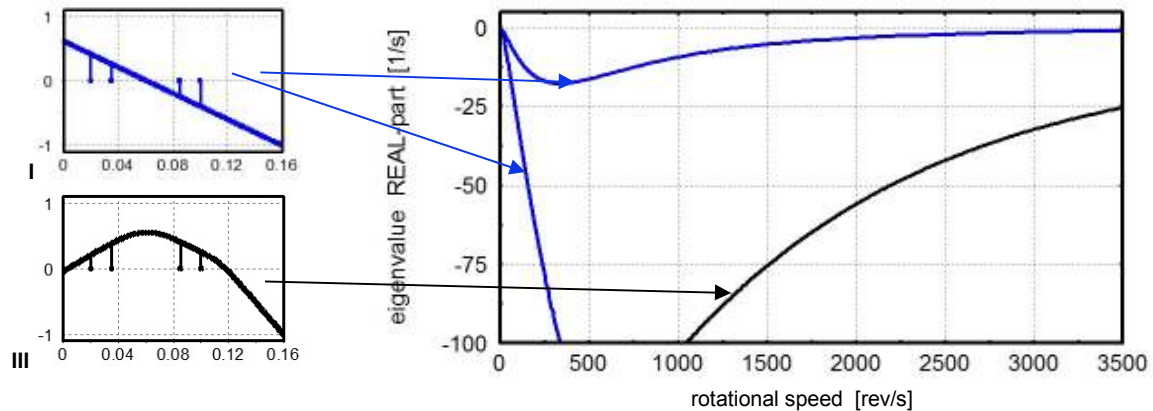


Figure 8: Maximal eigenvalue real parts of the rotor-shaft supported in the combined EDPMBs with pole shoes obtained for the minimal stabilizing damping coefficient D equal to 150 Ns/m.

5 Amplitude-frequency characteristics of the steady-state forced vibrations

In addition to the investigation of eigenvibration properties of the considered rotor-shaft supported in the main and combined EDPMBs, there are going to be compared also amplitude-frequency characteristics of the steady-state forced dynamic responses due to synchronous excitations caused by unavoidable residual unbalances. According to [8], $0.6 \cdot 10^{-6}$ kgm unbalance of the turbine rotor and $0.4 \cdot 10^{-6}$ kgm unbalance of the compressor rotor have been assumed. Here, two unbalance orientations will be investigated, i.e. the commonly called “static unbalance”, when the turbine and compressor rotor unbalances are mutually oriented ‘in phase’, and the “dynamic unbalance”, for which these two unbalances are mutually oriented ‘in anti-phase’. In order to determine the amplitude-frequency characteristics, equations of motion (7) had to be solved analytically for the both mentioned above unbalance orientations and for the two considered kinds of bearing suspension, i.e. in the main and combined bearings, each for a support without- and with permanent magnet pole shoes, and within the investigated rotational speed range 0-210,000 rpm corresponding to the harmonic synchronous excitation frequency band 0-3500 Hz.

Figs. 9 and 10 demonstrate amplitude-frequency characteristics of the steady-state dynamic responses excited by the static and dynamic unbalance of the rotor-shaft supported in the main EDPMBs only. For the case of the static unbalance in Fig. 9a the lateral displacement amplitudes of the turbocharger rotors are depicted and in Fig. 9b the bearing vertical reaction force amplitudes are plotted. In an identical way Figs. 10a and 10b illustrate respectively amplitude-frequency characteristics of the analogous dynamic responses excited by the dynamic unbalance of the rotor-shaft. In all these figures the black and green lines correspond to the bearing support variant “without pole shoes” and the blue and pink lines illustrate the support variant “with pole shoes”.

From the plots presented in Figs. 9 and 10 it follows that the assumed two extremely different from each other unbalance orientations result in completely different dynamic responses of the investigated object qualitatively and quantitatively. Namely, in the case of static unbalance very severe single resonance peaks are observed, both of rotor displacements and bearing forces. These peaks occur at the rotational speed of 1210 rev/s which corresponds to the only critical speed of the considered rotor-shaft for its third eigenmode, see Fig. 4. The analogous peaks obtained in the case of dynamic unbalance are characterized by ca. one order smaller numerical values, as shown in Figs. 10a and 10b. It is worth noting that in the both cases of unbalance orientations, the bearing support variant “without pole shoes” results in significantly smaller response amplitude values than that

“with pole shoes”. This fact can be substantiated by the greater damping magnitudes generated by the main EDPMBs, when their permanent magnets are not equipped with pole shoes, which illustrate the respective damping coefficient characteristics presented in Fig. 2b.

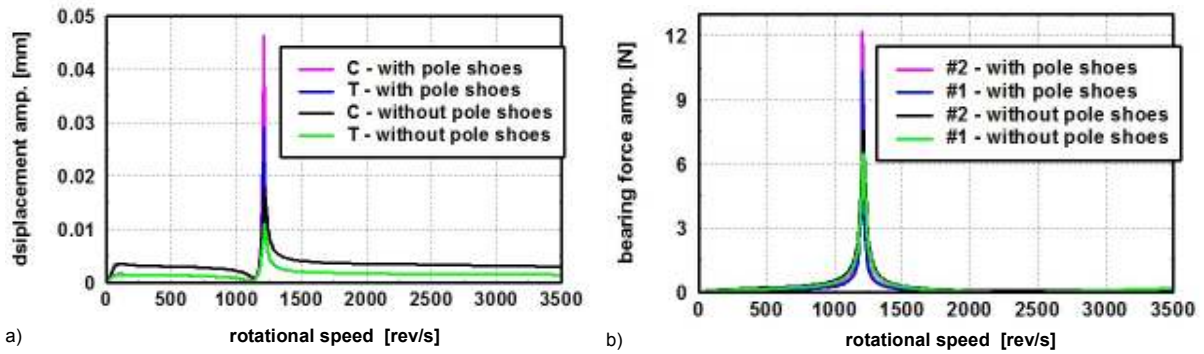


Figure 9: Amplitude characteristics of the turbine- (T) and compressor (C) rotor displacements (a) and of the bearing vertical forces (b) obtained for the support in the main EDPMBs and static residual unbalance.

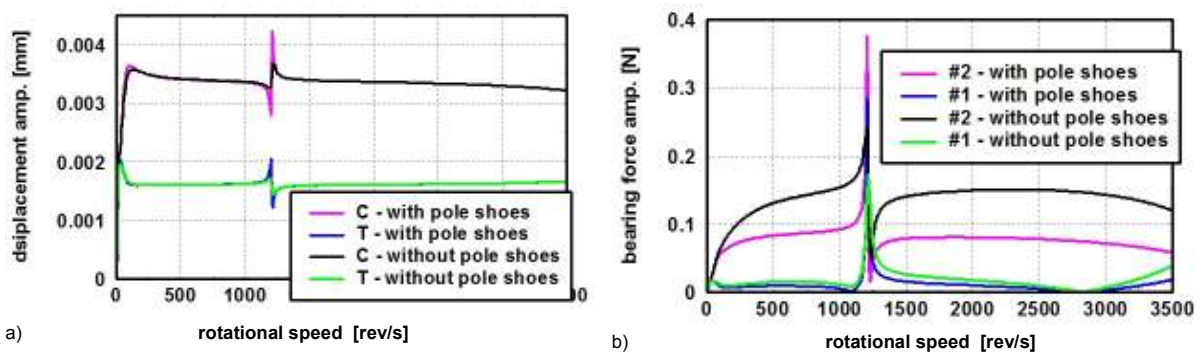


Figure 10: Amplitude characteristics of the turbine- (T) and compressor (C) rotor displacements (a) and of the bearing vertical forces (b) obtained for the support in main EDPMBs and dynamic residual unbalance.

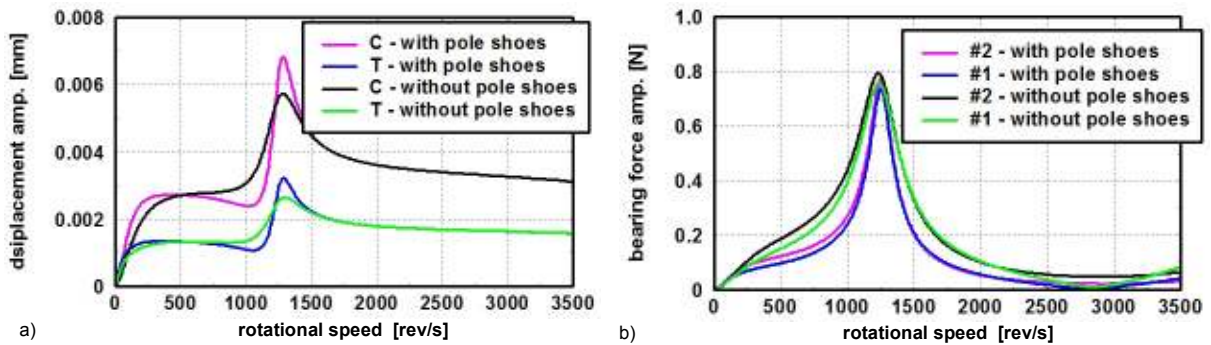


Figure 11: Amplitude characteristics of the turbine- (T) and compressor (C) rotor displacements (a) and of the bearing vertical forces (b) obtained for the support in the combined EDPMBs and static residual unbalance.

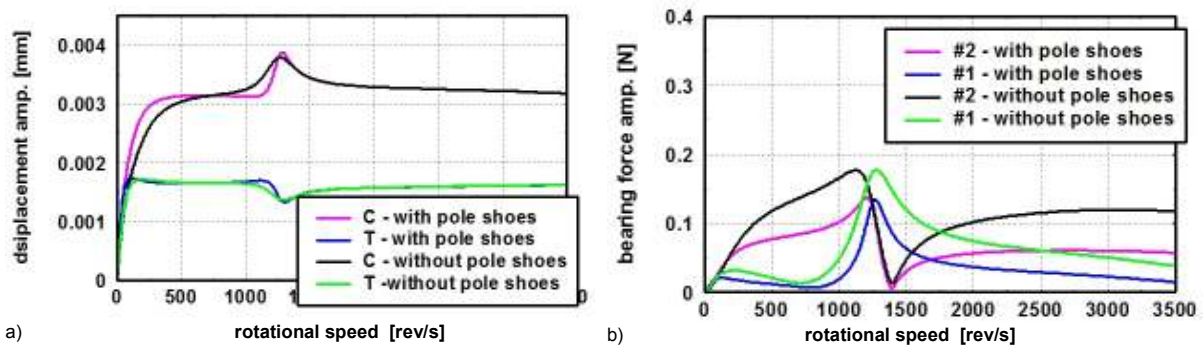


Figure 12: Amplitude characteristics of the turbine- (T) and compressor (C) rotor displacements (a) and of the bearing vertical forces (b) obtained for the support in the combined EDPMBs and dynamic residual unbalance.

However, the magnitudes of the additional external damping generated by the combined EDPMBs that stabilize the considered rotating system, appropriately in the case “without-“ and “with pole shoes”, are high enough to eliminate the resonance associated with the mentioned critical speed. This supplementary advantage of the passive magnetic bearing modified in the proposed way is confirmed by the analogous amplitude-frequency characteristics shown respectively in Figs. 11 and 12.

7 Final remarks and conclusions

In the paper there was proposed a concept of the structurally simple and operationally robust electrodynamic passive magnetic bearing which is able to assure an entirely stable support of high-speed rotor-shaft systems. It turns out that a supplementing of the classical EDPMB with a rotating permanent magnet and a stationary conductor enables us a generation of additional rotor-to-stator external damping with a magnitude sufficient to stabilize all lateral eigenmodes of the rotor-shaft. But for the realistic parameters of the stationary conductor coils and permanent magnets, the greater sufficient magnitude of the additional damping to stabilize the rotor-shaft system, the larger area of magnets in the form of rotating disks is required. Thus, the main EDPMB variant “with pole shoes”, for which less stabilizing damping is necessary, leads to a more compact combined bearing design.

As already known, thanks to a relatively small radial stiffness of the EDPMBs, the first, fundamental eigenmodes are like these of the rigid shaft ones and they are usually not affected by resonances associated with critical speeds. But this is not the case for higher, flexible eigenmodes which can be excited to very severe resonant bending vibrations, as demonstrated by means of results of the dynamic analysis performed here. Luckily, however, it turns out that the external stabilizing damping magnitude generated by the combined EDPMBs is high enough to suppress effectively such resonance effects, as well. This makes the proposed rotor shaft magnetic suspension in the form of combined EDPMBs additionally advantageous.

References

- [1] Lembke, T. A. (2005): Design and analysis of a novel low loss homopolar electrodynamic bearing, Doctoral Thesis, KTH Electrical Engineering, Stockholm.
- [2] Impinna F., Detoni J. G., Tonoli A., Amati N. and Piccolo M. P. (2014): Test and theory of electrodynamic bearings coupled to active magnetic dampers, Proc. of the 14th Int. Symposium on Magnetic Bearings, Linz, Austria: 263-268.
- [3] Cui Q. (2016): Stabilization of electrodynamic bearings with active magnetic dampers, Doctoral Thesis No. 7334, École Polytechnique Fédérale de Lausanne.
- [4] Detoni J. G., Impinna F., Amati N., Tonoli A., Piccolo M. P. and Genta G. (2014): Stability of a 4 degree of freedom rotor on electrodynamic passive magnetic bearings, Proc. of the 14th Int. Symposium on Magnetic Bearings, Linz, Austria, Vol. 14.
- [5] Szolc T., Falkowski K., Henzel M. and Kurnyta-Mazurek P. (2018): The determination of parameters for a design of the stable electro-dynamic passive magnetic support of a high-speed flexible rotor, *Bulletin of the Polish Academy of Sciences, Technical Sciences (in print)*.
- [6] Filatov A.V., Maslen E.H. and Gillies G.T. (2002): A method of noncontact suspension of rotating bodies using electromagnetic forces, *Journal of Applied Physics*, Vol. 91, 2355-2371.
- [7] Filatov A.V., Maslen E.H. and Gillies G.T. (2002): Stability of an electrodynamic suspension, *Journal. of Applied. Physics*, Vol. 92, pp. 3345-3353.
- [8] Göbel S., Daniel Ch., Woschke E. and Strackeljan J. (2015): DoE basierte Sensitivitätsanalyse konstruktiver Lagerparameter eines gleitgelagerten Abgasturboladers, Proc. of the 11th Int. Tagung “Schwingungen in rotierenden Maschinen” (SiRM), Magdeburg, Germany, February 2015, Paper ID-55.
- [9] Amati N., De Lépine X. and Tonoli A. (2008): Modeling of electrodynamic bearings, *ASME Journal of Vibration and Acoustics*, Vol. 130, pp. 061007-1 - 061007-9.
- [10] Detoni J. G., Impinna F., Tonoli A. and Amati N. (2012): Unified modeling of passive homopolar and heteropolar electrodynamic bearings, *Journal of Sound and Vibration*, 331, 4219-4232.
- [11] Szolc T. and Falkowski K. (2015): Dynamic analysis of the high-speed flexible rotors supported on the electrodynamic passive magnetic bearings, *Mechanisms and Machine Science*, Springer Verlag, Vol. 21 Part XI, pp. 1489-1500.
- [12] Szolc T. (2000): On the discrete-continuous modeling of rotor systems for the analysis of coupled lateral-torsional vibrations, *International Journal of Rotating Machinery*, 6(2), pp. 135–149.
- [13] Stocki R., Szolc T., Tazowski P. and Knabel J. (2012): Robust design optimization of the vibrating rotor shaft system subjected to selected dynamic constraints, *Mechan. Syst. and Signal Processing*, 29, 34-44.
- [14] Press W. H., Flannery B. P., Teukolsky S. A. and Vetterling W. T. (1990): *Numerical Recipes – The Art of Numerical Computing* (Fortran Version), Cambridge University press, Cambridge, New York, Sydney.

Overview of Mobile Flywheel Energy Storage Systems State-Of-The-Art

Nikolaj A. Dagnaes-Hansen¹, **Ilmar F. Santos**²

¹ Fritz Schur Energy, 2600, Glostrup, Denmark, nah@fsenergy.com

² Dep. of Mech. Engineering, Technical University of Denmark, 2800, Kgs. Lyngby, Denmark, ifs@mek.dtu.dk

Abstract

The need for low cost reliable energy storage for mobile applications is increasing. One type of battery that can potentially solve this demand is Highspeed Flywheel Energy Storage Systems. These are complex mechatronic systems which can only work reliably if designed and produced based on interdisciplinary knowledge and expertise. This paper gives an overview of state-of-the-art flywheel systems through graphs, tables and discussions. Key performance indicators, technologies, manufacturers, and research groups are presented and discussed. The focus is put on energy density and power of the flywheel systems and on the magnetic bearing technology used to obtain the best performance.

1 Motivation

A crucial component of any electrical grid is energy storage. It is used to smooth out fluctuations in power demand and supply, especially in the case of renewable energy sources such as solar cells and wind turbines. Smaller electrical grids, called micro-grids are found in vehicles such as cars and ships. Here, the demand for higher capacity energy storage is increasing due to the growth in demand of electric and hybrid vehicles.

When dealing with energy storage in transportation, the key performance indicator is the specific energy density e [$\frac{J}{kg}$]. If the system is to function, not only for energy storage, but also as peak shaver, the specific power density p [$\frac{W}{kg}$] must also be regarded. When it comes to a Flywheel Energy Storage System (FESS), the stored kinetic energy is proportional to flywheel mass moment of inertia and the square of flywheel rotational speed. For a modern high-speed FESS, the energy is sought to be increased by maximising rotational speed rather than flywheel size and mass. In this way, power and energy densities are also maximised. The limitations of rotational speed are related to the following:

- For high rotational speeds, the centripetal stresses will at some point cause the flywheel to burst. The speed limit is thus dictated by the maximum tensile strength of the flywheel material.
- The high rotational speed also leads to an undesirable large amount of friction between the flywheel surface and the surroundings. This necessitates the use of a vacuum environment which complicates the use of conventional hydrodynamic and ball bearings due to the vaporisation of bearing lubricant. Furthermore, limitations related to stability, damping, and friction make conventional bearings unsuitable if FESS is to compete with electrochemical batteries on energy density as well as efficiency and reliability.

2 Literature Review

The above listed limitations have until recently caused FESSs to be inferior to electrochemical batteries. However, recent technological advancements within lightweight fibre composites with large tensile strength, motor/generators, and Active Magnetic Bearings (AMBs) have now enabled an increase in rotational speed and consequently high energy and power densities. A sketch of a modern FESS can be seen in Fig. 1.

AMBs first got into the spotlight of FESS applications in the 1960s with the introduction of high-strength fibre composite flywheels that dramatically improved the stress limitations and consequently the limit on rotational speed [15] [32] [71]. This led to the first reports on magnetically suspended flywheels in the start 1970s where aerospace agencies such as NASA among others found them relevant [84] specifically for attitude control [87] [40] [82] [77], energy storage [72], and the combination of the two [62]. Although the above references are primarily focused on experimentally demonstrating the concept, it was from the beginning acknowledged that the

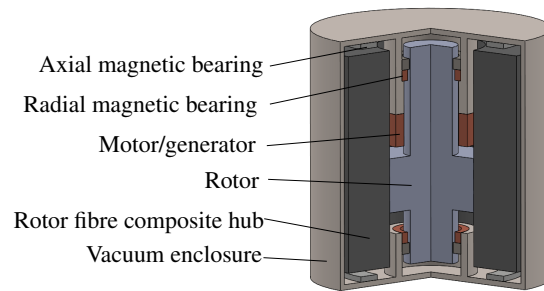


Figure 1: Modern high-speed FESS.

whole system dynamics must be accounted for when designing AMBs: *“Unlike ball bearings, magnetic bearings are an intimate part of the overall design, and cannot be specified in terms of simple mechanical interfaces”* [77]. This is because AMBs use closed-loop control of electromagnetic coils which, as opposed to conventional bearings, introduce additional degrees of freedom into the system. To begin with, however, simple spring-mass-damper models were used to design the AMBs. Through the years, the models improved to more advanced rotor-bearings models accounting for flexible modes and more advanced AMB controls [23]. Consequently, FESS performance has been continuously increasing to a point where too high stresses in the flywheel material again becomes the limiting factor. Experts are looking towards the potential of using new flywheel materials such as graphite in order to further increase rotational speed [10] [75]. Currently, FESSs with energy densities up to 80 Wh/kg have been manufactured [20]. In comparison, modern lithium-ion batteries can contain up to approximately 180 Wh/kg [6]. An overview of the specific energy and power density in different FESSs found in the literature can be seen in Table 1 accompanied by Fig. 2. Items 1 and 2 in the table are both Integrated Power and Attitude Control Systems (IPACs) from NASA, which function as combined energy storage and attitude control for satellites. Items 3-15 are university prototypes (PT). Items 16-22 are commercially available Uninterruptible Power Sources (UPS) and large scale energy storage systems. Items 23-26 are Kinetic Energy Recovery Systems (KERS) for race cars. Item 27 is also aimed for vehicle applications with a highly repetitive duty-cycle such as excavators and commuter trains or buses.

As seen, Li-Ion batteries still have higher energy and power densities than FESSs. However, the flywheels have now reached levels of same orders of magnitude as the electrochemical batteries, which make them a lucrative alternative due to numerous advantages which are listed by the FESS vendor Calnetix in [41] and included here as Table 2. Successful tests of 112,000 discharge cycles are carried out in [8] and the round-trip efficiency is reported as high as 85-95% [14]. In [31], the self-discharge time constant for a 500 Wh FESS is reported to be several days. The NASA G3 IPACS from Table 1 has a total parasitic loss of around 80 W when going full speed storing 2136 Wh.

The FESS examples from Table 1 form only a fraction of all the actors currently involved with the technology – a list of 27 different manufacturers and 28 different research groups are given in [39]. The applications are both stationary systems such as the UPS systems seen in Table 1, storage for renewable energy sources, and mobile systems.

The mobile systems are in particular challenging to design due to vehicle movements, especially because they cause large gyroscopic effects. The gyroscopic loads are proportional to the mass moment of inertia, the rotational speed, and the tilting rate of the flywheel rotational axis, and they will thus inherently be large when a high speed, high inertia flywheel is subject to movements. The flywheel will strongly resist any tilt motions and will reciprocate large forces through the bearings and the rest of the system. This is utilised for satellite attitude control in the IPACS shown in Table 1, but are otherwise regarded as unwanted and are significantly increasing the required load capacity of the bearings. This means that mobile FESSs usually comprise a suspension made of conventional bearings. This is, for example, the case for the KERSs seen in Table 1.

Magnetic suspension is, however, needed if FESSs are to compete on life-time, efficiency, and energy density. As seen for stationary and satellite FESS systems, the proper design of AMBs is based on proper determination of forces and dynamics through rotor-bearing models of varying complexity. This is also the case for a mobile FESS although here, the movement of the foundation (base motions) might have to be accounted for. This includes dynamics of bodies such as the housing as well as accelerations of the vehicle/vessel from e.g. manoeuvring or outer perturbations. The following gives an overview of previous work related to this modelling problem.

	Name	Manufacturer	$e \frac{\text{Wh}}{\text{kg}}$	$e_r \frac{\text{Wh}}{\text{kg}}$	$p \frac{\text{W}}{\text{kg}}$	$p_r \frac{\text{W}}{\text{kg}}$	Ref.
1	G3 IPACS	NASA	35.5	80	54.8	124	[20]
2	G2 IPACS	NASA	5.3	23.1	10.1	44	[1]
3	Uppsala PT	Uppsala Uni.	11.9	18.6	64.4	101	[4] [5]
4	Chemnitz PT	Chemnitz Uni.	3.0	-	375	-	[52]
5	Bialystok PT	Bialystok TU	-	18.5	-	667	[60]
6	Darmstadt PT	TU Darmstadt	-	13.9	-	392	[70]
7	Austin low-cost	Uni. at Austin	2.2	6.0	279	774	[38]
8	Zhejiang PT	Zhejiang Uni.	-	-	-	347	[13]
9	Chiayi PT	C. C. Uni.	-	1.32	-	24.1	[86]
10	500 Wh PT	FZ. Jülich	-	18.7	-	652	[31]
11	Shaftless PT	Texas A&M	-	16.7	-	16.7	[51]
12	Maryland PT	Maryland Uni.	-	14	-	-	[95]
13	Calnetix PT	Uni. at Austin	-	32.7	-	2213	[57]
14	Wien PT	TU Wien	-	3.33	-	6.66	[79]
15	ComFESS	KOYO SEIKO	-	12	-	4	[45]
16	VDC XXE	Calnetix	2.5	13.0	365	1923	[41]
17	XT 250 UPS	ActivePower	-	6.3	-	919	[66] [67]
18	HD 675 UPS	ActivePower	-	3.8	-	875	[65] [67]
19	Powerbridge	Piller Power Sys.	1.0	2.0	400	828	[12] [41]
20	BP 400	Beacon Power	-	22.0	-	88	[68]
21	EnWheel22	Stornetic	-	5.1	-	31	[79] [83]
22	Model 32	Amber Kinetics	7.1	-	1.76	-	[46]
23	KERS GT3R	Porsche	6.6	-	3158	-	[69]
24	KERS E-Tron	Audi	3.6	-	5556	-	[69]
25	KERS MK4	Williams HP	8.3	-	2182	-	[69]
26	KERS F1 sys.	Flybrid Autom.	4.4	22.2	2400	12000	[3]
27	TorqStor	Ricardo	0.56	-	1010	-	[76]
	Prediction	NASA	-	$3 \cdot 10^3$	-	-	[75]

Table 1: Energy and power density, e and p , for different FESSs. The energy and power density only accounting for rotor mass and not housing is also given as e_r and p_r . A prediction made by NASA is also included. It is based on a flywheel rotor made of nanofiber. Abbreviations used in table: Integrated Power and Attitude Control (IPACS), ProtoType (PT), Uninterruptible Power Source (UPS), Kinetic Energy Recovery System (KERS).

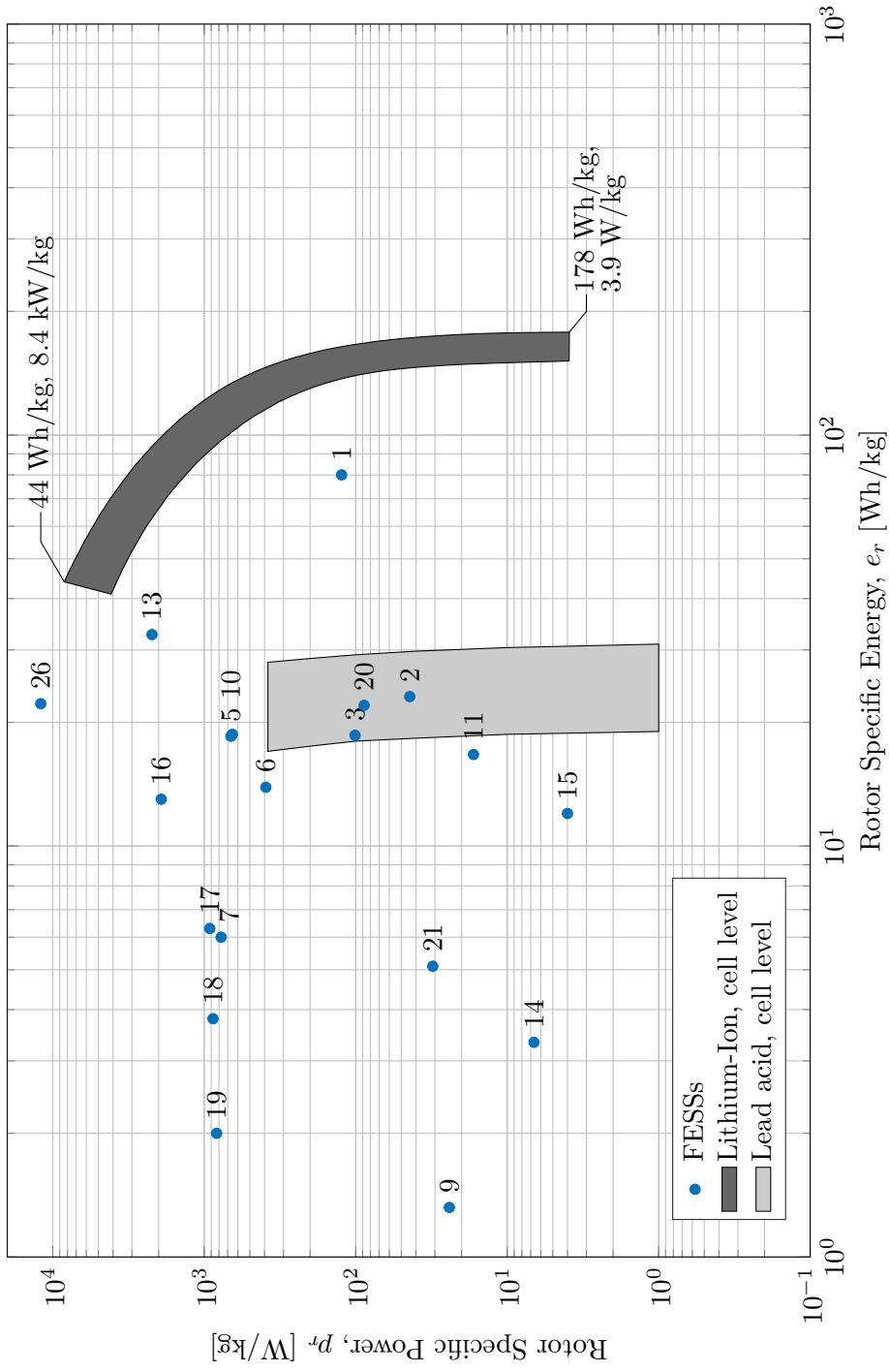


Figure 2: Graphical representation of Table 1. Lithium-ion and lead acid battery data are taken from [6] and included for comparison. Cell level means that electrodes, electrolytes, and separator only are accounted for – no housing or connections.

	Flywheel DC Source	Lead Acid Battery
Maintenance	Minimal/Annual	Frequent/Quarterly
HVAC costs	None	High
Availability (MTBF)	>50,000 hrs	>2,200 hrs
Life expectation	20 years	3-4 years
Installation cost	Low	Medium to High
Hazardous Materials	None	Lead and Acid
Toxic, explosive gas emissions	None	Hydrogen
Footprint	Small	Large to very large
Diagnostics / monitoring	Accurate	Speculative
Disposal requirements	None	Yes
Fire hazard permitting	None	Often
Shelf life	No	Yes

Table 2: Advantages of FESSs as presented by the FESS vendor Calnetix in [41]. Abbreviations used in the table: Heating, ventilation, and air conditioning (HVAC); mean time between failures (MTBF)

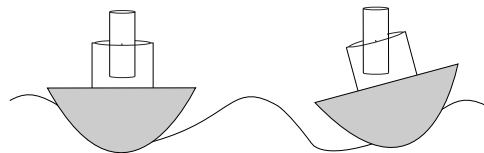


Figure 3: Gimbal-mounted FESS

In 1980, T. McDonald [55] and H. Otaki [63] presented simple gyrodynamic calculations of a vehicle FESS that can be used for bearing design. In 1989, Genta demonstrated the usefulness of using modelling to improve mobile FESS performance [33]. He presents a finite element nonlinear rotor-dynamic model of a kinetic energy storage for a hybrid bus. The flywheel is assumed rigid and the focus is put on the compliant roller element bearings used for suspension. Using the model, structural improvements are introduced to the bearings and supports which results in a system that can run steady in the operation range. One of the first investigations of AMBs for a transportable FESS, rather than roller bearings, is found in [58]. The article focuses on a transit bus application and provides acceleration data from real measurements to quantify bearings loads. The loads are categorised as shock, vibration, and manoeuvring with one important sub-category of manoeuvring: gyrodynamic. They advise that the flywheel spin axis should be vertically oriented and that a passive gimbal mount is used to avoid large gyroscopic loads as seen in Fig. 3. In [35] a gimbal-mounted FESS with magnetic bearings is experimentally tested when subject to perturbations equivalent to 150 % of maximum expected bus frame values. In [29], endurance performance testing of the same experimental test rig is presented. In [73] [80], a FESS is mounted in an active gimbal, installed in a reconfigured golf cart, and successfully used to power the vehicle. For the mitigation of gyroscopic loads, the Toyota Central R&D Laboratory in cooperation with Nagoya University developed a test rig with a FESS in an active gimbal in [61]. For ship applications in particular, no experimental tests have been reported. Calnetix presents the conceptual design of a FESS for naval application in [42] based on the above mentioned FESS for transit bus application which has already proven operational during base motions. The naval Surface Warfare Center together with FESS vendor Beacon Power discuss technical challenges of operating a FESS onboard a ship in [56]. The discussion comprises shock tolerances and the dynamical shipboard environment. In [91], a control algorithm for AMBs is presented which is designed specifically for reducing vibration in marine applications where the AMB-rotor system is subject to wave motions. Comprehensive overviews of literature dealing with AMB-suspended rotors subject to base motions can be found in [44], [91], and [22]. Here, the outer perturbations are handled through tailored control schemes. For FESSs in particular, rather than rotors in general, it can be ascertained from the above mentioned examples on experimental FESS tests, that the gyroscopic forces can easily become too large for the controller to handle and instead the FESS is mounted in a gimbal.

A brief overview of literature concerning the design of magnetic suspension for FESS is given below. Three dif-

ferent types of magnetic bearings are used for flywheel application: Permanent Magnet Bearings (PMBs), AMBs, and high temperature superconducting (HTS) bearings. The latter have the strong advantage of creating a stable equilibrium without any active control. It does, however, only provide low damping on its own [43] and is expected to be used in combination with other forms of damping [2] such as eddy-current dampers (ECDs) or AMBs. Furthermore, HTS bearings rely on operating temperatures around and below 80 K, and finally, the force density and stiffness is about 3 – 4 times larger for AMBs than HTS bearings [90]. The HTS bearings will not be regarded further in this paper due to their lack of damping, their need of a cooling system, and their lower force density.

PMBs

The motivation for looking into pure passive PMBs is that they are used in multiple FESS designs from different independent institutions [89] [92] [53] [86] [88] [70]. Due to the low damping in PMBs, it is a challenge to ensure sufficient axial damping. Also, because PMBs do not provide stable levitation on their own [24], they will contribute with a radial negative stiffness to the system which increases the work load on the radial AMBs. A detailed literature review on PMBs is found in [18].

AMBs

An AMB consists of four components: position sensor, controller, amplifier and electromagnet. In Table 3, an overview of the hardware components chosen for different FESS solutions is given.

The state-of-the-art AMB technology for FESSs is well represented in the NASA IPACS [1]. To increase reliability, each IPACS AMB has six electromagnets. Only three electromagnets are necessary for full control in a plane and thus the AMB has three redundant electromagnets. In case the AMB still fails, backup/touchdown ball bearings are present to catch the rotor. The IPACS backup bearings are designed based on a rotordynamics analysis of the touchdown event. The design is aimed at preventing whirl mode instabilities. O-rings and squeeze-film dampers are used to control stiffness and damping. The backup ball bearings are rated to operate beyond 150 °C making them able to function even when a large amount of heat is dissipated due to friction during touchdown. In IPACS AMBs, the eddy-current energy losses are reduced by using a homopolar configuration and insulated steel sheet laminations. Finally, permanent magnet (PM) bias is used rather than a bias current to avoid ohmic losses from the bias current. The amplifiers are of the pulse width modulated (PWM) type with power filters to reduce current ripples resulting in a low energy loss amplifier solution. This means that only the hysteresis and eddy-current losses are of any significance. For the IPACS G2 AMBs, these losses are estimated to be around 1 W [1] at full speed (525 Wh).

Another way of avoiding ohmic losses from bias currents is to simply avoid using any bias which was done by Rachmanto et al. [73] [80] in a FESS used to power a golf cart. Notably for the AMBs used for this FESS is the air gap between the AMB stator and rotor, which has a recorded low between 0.125 mm [73] and 0.2 mm [74].

With regard to sensors, eddy-current proximity probes are most commonly used as seen in Table 3. However, low-cost inductive sensors are now seeing use in commercial products such as AMB solutions from Calnetix [28]. Even though inductive sensors have lower bandwidth than eddy-current sensors, their bandwidth is still high enough for most FESS applications. They are furthermore easy to co-align axially with the rest of the components as they can be made using the same hardware components as a radial AMB electromagnet. Due to their low cost and their easy coaxial alignment, they are an obvious choice for future commercial FESSs. Low cost eddy-current sensors printed on PCBs are also available under the name of transverse flux sensors [50]. They have been patented by the AMB vendor MECOS [9]. Finally, there are different types of flux sensors, for example one patented by FESS vendor Calnetix [26].

With regard to amplifiers, it can be seen in Table 3 that PWM amplifiers are commonly used. The amplifiers usually have an inner feedback control loop, which controls the current based on current measurements from a hall-effect sensor or a shunt-resistor. This loop is operated with a higher sampling time than the outer position control loop. Alternatively, the inner current control loop and the outer position control loop can be combined into a better performing multiple input, multiple output (MIMO) voltage controller [81] or flux controller [25].

As seen in Table 3, the controller hardware commonly consists of some rapid development platform like dSPACE or National Instruments FPGA or Real-Time hardware. Low-cost digital signal processors (DSPs) e.g. from Texas Instruments (TI) are used for more commercially mature FESSs. Many different forms of control algorithms have been implemented successfully in operational FESSs. From simple decentralised PID-algorithms [4] to model-based MIMO modal control with special focus on damping eigenmodes and dealing with the large gyroscopic effects present in FESSs [21] [37]. Another important controller feature in FESS application is the reliability which can be improved using robust control in [86] [78] [59]. The energy efficiency is also important, thus the controller can be synthesised for minimum control effort as in [60]. Another way to reduce control effort is to use

a nonlinear zero-bias controller as in [7]. Generally speaking, the control effort is reduced by aiming at giving the AMB a low stiffness when used in FESS applications. However, due to the external perturbations present in mobile applications, one should take care to ensure that the controller is not imposing too low stiffness and that it is still reactive during large accelerations. Finally, another obvious AMB feature that can be utilised to reduce the control effort, is unbalance compensation as seen in e.g. [64].

In order to ensure system safety even in the case of AMB failure, experimental tests of drop down events have been carried out [36] [30] [93] as well as analytical predictions such as the above mentioned simulations from NASA [1].

3 Ongoing FESS research at the Technical University of Denmark

As seen in the above literature study, gimbal mounts are commonly used to mitigate the unavoidably large gyroscopic effects present in a mobile FESS. As also seen, mobile FESSs with magnetic bearings have been experimentally demonstrated in only a few research projects, whereas the theoretical basis of the designs are undocumented except for a few simple cases. This raises a number of research questions.

First, to design the AMBs properly, their load-carrying capacity must be accurately determined. The forces provided by the AMBs are frequency-dependent meaning that the force magnitude will depend on how fast the bearing has to provide the force. In this connection:

- Is it possible to theoretically and experimentally quantify the frequency-dependant AMB forces, as well as the other forces in the system, based on the movements of the vehicle? If yes, how accurately?
- Is it possible to quantify the difference in force magnitudes for a gimbal-mounted and non-gimbal-mounted system? If yes, how accurately?

Second, the implementation of a gimbal mount will introduce additional dynamics such as movements of the flywheel housing. This might have negative consequences:

- Will the controller face difficulties in stabilising the flywheel when the housing and gimbal can move and their inertia effects cannot be neglected?
- Are there cases, where the additional dynamics can cause unintended large movements of the gimbal and housing?
- When gimbal-mounted, the system will resemble a gyrocompass which functions by having a rotating disc interacting with the rotation of the Earth. Will the gimbal mount cause the flywheel to behave as a gyrocompass and will this be a problem?

Last, in addition to the AMBs, the magnetic suspension also consists of PMBs. In this connection:

- Is it possible to quantify the forces in the PMBs – both the forces related to axial and radial rotor displacements (stiffness) and related to axial rotor velocities (eddy-current damping)? If yes, how accurately?

These questions have been answered in a number of recent articles [16], [17], [19], and [18]. The dynamic consequences of introducing a passive gimbal mount is dealt with in [16]. A global mathematical model is presented, which couples the dynamics of the flywheel rotor, active and passive magnetic bearings, housing, and a passive gimbal. The original contribution consists of coupling a multi-body model of a gimbal-mounted FESS subject to outer perturbations with the magnetic forces from active and passive magnetic bearings. The magnetic forces are represented in vector form using moving reference frames. The housing and the gimbal are moving and their inertias are included in the model. Their interactions with the rotor-bearing dynamics are investigated. The coil dynamics of the active magnetic bearings are included in the model as well as the controller dynamics. The model is applied to three different test scenarios showing bearing loads as well as rotor and housing movements with and without the gimbal mount.

In [17], the above mathematical model is validated by comparing simulated and experimentally obtained movements of flywheel rotor and housing. The experimental results are obtained using a novel test bench with a modular design making it ideal for testing different types of designs. The AMBs are designed and manufactured in cooperation with FESS manufacturer WattsUp Power and have been produced with high focus on economic feasibility. The original contribution consists of, in addition to the experimental validation, a thorough documentation of the test bench design and a comprehensive set of experimental data, which can be used for other researchers, e.g. for benchmarking and validation.

Name	Sensor	Controller	Amplifier	Electromagnet	Speed	Ref.
2	G2 IPACS	dSPACE, modal control (model based)	PWM	Homopolar, PM-biased, steel sheets	60 kRPM	[1][21]
3	Uppsala PT	FPGA, PID-controlled (SISO)	PWM	Heteropolar, 0.65 mm steel sheets	30 kRPM	[4][5][3]
5	Bialystok PT	DSP, robust control	PWM	Heteropolar, steel sheets	40 kRPM	[60]
6	Darmstadt PT	n/a	n/a	Homopolar, soft magnetic composite	17.5 kRPM	[70]
8	Zhejiang PT	dSPACE	PWM	Heteropolar	20 kRPM	[13][54]
9	Chiayi PT	dSPACE, robust control	PWM	Heteropolar, coreless, Halbach array	10 kRPM	[86]
11	Shaftless PT	dSPACE, MIMO-control	n/a	Homopolar, PM-biased	200 RPM	[51]
12	Maryland PT	Analog	n/a	PM-biased	20 kRPM	[48][47]
13	Calnetix PT	TI DSP, modal control (model based)	PWM	Homopolar, PM-biased, steel sheets	42 kRPM	[57][37][94]
15	ComFESS	AMX095	PWM	Heteropolar, zero-bias	24 kRPM	[45][85]
16	VDC XXE	n/a	n/a	Homopolar, PM-biased, steel sheets	36 kRPM	[11][27][41]
28	Chiba Uni. golf cart PT	NI cPCI	n/a	Homopolar, zero-bias	18 kRPM	[73]

Table 3: Hardware components used for AMBs for different FESS solutions. Abbreviations used in table: Eddy-current (Eddy-cur.), Pulse-Width Modulation (PWM), Rounds Per Minute (RPM), PM-biased, ProtoType (PT), Field-Programmable Gate Array (FPGA), Proportional-Integral-Derivative (PID), Single Input Single Output (SISO), Multiple Input Multiple Output (MIMO), Digital Signal Processor (DSP), National Instruments (NI).

In [19], the above mathematical model and the experimental test bench are used to investigate the forces reciprocated through the system. The AMB bearing loads are given particular focus. The original contribution consists of presenting theoretically and experimentally obtained maximum reaction forces when the foundation is moving. The forces in a gimbal-mounted FESS are compared with the forces when no gimbal mount is present. The differences in force amplitudes are highlighted.

Article [18] deals with the design and test of PMBs. Already established methods for finding bearing stiffness and damping are applied to the specific application of a mobile FESS. The original contribution consists of further developing the established methods with the following:

- The analytical method presented by Lang and Lembke in [49] for evaluating forces and stiffness in a computationally efficient way may have limited applicability due to the assumption that all materials have relative permeability equal to one. This work investigates the limitations of this assumption by comparing the method with a numerical method and with experimental results in a test case where some material with relative permeability much higher than unity is present.
- If the AMB forces are nonlinear within the operational area, the PMBs cannot be modelled using a single linear stiffness. This work presents a semi-analytical method for determining the radial forces in the general 3-dimensional case. The method is accurate for small perturbations and can thus be used to assess the linearity of the radial force. The method is validated experimentally.
- A method for estimating eddy-current damping has been validated against cases where the magnets approximate dipoles in [34]. This work contributes further to the validation of the method in [34] and shows that the method agrees well with experimental results in cases where the magnets cannot be modelled as dipoles. This work also shows how to numerically assess whether self-inductance can be neglected when estimating eddy-current damping.

4 Conclusion

This paper has given an overview of FESS with special focus on mobile applications. The power and energy densities of physical systems produced and tested around the world have been presented and compared to conventional electrochemical batteries. It is seen that the power and energy densities of FESSs are still lower than those of the Li-Ion batteries, although the FESS densities are now reaching the same level of magnitudes. Advantages of FESS over electrochemical batteries have furthermore been presented. An overview of the AMB components used in FESS applications has also been given and discussed. This provides useful insight for choosing the right components when designing the AMBs.

For mobile applications, the gyro dynamics become a challenge and thus only a few research groups have been dealing with FESSs with AMBs. One way to mitigate the gyrodynamic loads are by using a gimbal mount which has also been suggested and tested in the literature.

At the Technical University of Denmark, a mathematical model has been developed that can simulate the dynamics of a FESS suspended in both active and permanent magnetic bearings and gimbal-mounted when subject to base motions. The model has been experimentally validated using a test rig fully resembling the simulated system. The model and the experiments agree in terms of flywheel rotor movements, housing movements, AMB forces and coil currents, and finally PMB forces.

REFERENCES

- [1] G2 flywheel module design. *Collection of Technical Papers - 2nd International Energy Conversion Engineering Conference*, 2:683–695, 2004.
- [2] *Magnetic Bearings: Theory, Design, and Application To Rotating Machinery*. Springer Berlin Heidelberg, 2009.
- [3] Flywheel energy storage for automotive applications. *Energies*, 8(10):10636–10663, 2015.
- [4] Johan Abrahamsson. Kinetic energy storage and magnetic bearings : for vehicular applications. *PhD thesis*, 2014.
- [5] Johan Abrahamsson, Magnus Hedlund, Tobias Kamf, and Hans Bernhoff. High-speed kinetic energy buffer: Optimization of composite shell and magnetic bearings. *IEEE Transactions on Industrial Electronics*, 61(6):3012–3021, 2014.
- [6] International Energy Agency. Technology roadmap, electric and plug-in hybrid electric vehicles, 2009. Available online: https://www.iea.org/publications/freepublications/publication/EV_PHEV_Roadmap.pdf [Accessed Jan. 23th 2018].

- [7] Yuichi Ariga, Kenzo Nonami, and Katsunori Sakai. Nonlinear Control of Zero Power Magnetic Bearing Using Lyapunov's Direct Method. *7th International Symposium on Magnetic Bearings*, pages 293–298, 2000.
- [8] Joseph Beno, Richard Thompson, and Robert Hebner. Flywheel batteries for vehicles. *Proceedings of the IEEE Symposium on Autonomous Underwater Vehicle Technology, Proc IEEE Symp Auton Underwater Veh Technol*, pages 99–101, 2002.
- [9] Philipp Bühler. Device for contact-less measurement of distances in multiple directions: Patent no.: EP1422492A1. *EU Patent*, 2002.
- [10] Jack G. Bitterly. Flywheel technology past, present, and 21st century projections. *IEEE AES Systems Magazine*, (August):13–16, 1998.
- [11] Calnetix. How magnetic bearings work, 2013. Available online: https://www.calnetix.com/sites/default/files/CALNETIX_HOW_MAGNETIC_BEARINGS_WORK.pdf [Accessed June 13th 2018].
- [12] W. R. Canders, H. May, J. Hoffmann, P. Hoffmann, F. Hinrichsen, I. Koch, and D. Röstermundt. Flywheel mass energy storage with hts bearing - development status, 2006. Available online: http://www.eurosolar.org/new/pdfs_neu/electric/IRES2006_Canders.pdf [Accessed Sep. 12th 2016].
- [13] Liangliang Chen, Changsheng Zhu, Meng Wang, and Kejian Jiang. Vibration control for active magnetic bearing high-speed flywheel rotor system with modal separation and velocity estimation strategy. *Journal of Vibroengineering*, 17(2):757–775, 2015.
- [14] D. G. Christopher and R. Beach. Flywheel technology development program for aerospace applications. *IEEE Aerospace and Electronic Systems Magazine*, 2:602–608 vol.2, 1997.
- [15] Robert C. Clerk. The utilization of flywheel energy. In *SAE Technical Paper*. SAE International, January 1964.
- [16] N. Dagnaes-Hansen and I.F. Santos. Magnetically suspended flywheel in gimbal mount - nonlinear modelling and simulation. *Journal of Sound of Vibration*, (432):327–350, 2018.
- [17] N. Dagnaes-Hansen and I.F. Santos. Magnetically suspended flywheel in gimbal mount - test bench design and experimental validation. *Journal of Sound of Vibration. Accepted for submission*, 2018.
- [18] N. Dagnaes-Hansen and I.F. Santos. Permanent magnet thrust bearings for flywheel energy storage systems – analytical, numerical, and experimental comparisons. *IMECH Part C. Submitted*, 2018.
- [19] N. Dagnaes-Hansen and I.F. Santos. Magnetic bearings for non-static flywheel energy storage systems (FESS). In *Proceedings of the 10th International Conference on Rotor Dynamics – IFToMM*, pages 116–131. Springer International Publishing, 2019.
- [20] T. Dever. Presentation: Development of a high specific energy flywheel module, and studies to quantify its mission applications and benefits, 2013. Available online: <http://ntrs.nasa.gov/archive/nasa/casi.ntrs.nasa.gov/20150009522.pdf> [Accessed Sep. 5th 2016].
- [21] Timothy P. Dever, Gerald V. Brown, Ralph H. Jansen, and Kirsten P. Duffy. Modeling and development of a magnetic bearing controller for a high speed flywheel system. *NASA report*, 2005.
- [22] T. Dimond, P. Allaire, S. Mushi, Z. Lin, and S. Y. Yoon. Modal tilt/translate control and stability of a rigid rotor with gyroscopics on active magnetic bearings. *International Journal of Rotating Machinery*, pages 1–10, 2012.
- [23] James R. Downer. Modelling and Control of an Annular Momentum Control Device. *NASA report*, 1988.
- [24] Samuel Earnshaw. On the nature of the molecular forces which regulate the constitution of the luminiferous ether., 1839.
- [25] Jossana Ferreira, Eric Maslen, and Roger Fittro. Transpermeance amplifier applied to magnetic bearings. *Actuators*, 6(1):9 (20 pp.), 9 (20 pp.), 2017.
- [26] Alexai V. Filatov. Noncontact measuring of the position of an object with magnetic flux: Patent no.: US8564281B2. *US Patent*, 2009.
- [27] Alexei V. Filatov. High-aspectratio homopolar magnetic actuator: Patent no.: US0,090,556 A1. *US Patent*, 2010.
- [28] Alexei V. Filatov and Lawrence A. Hawkins. An axial position sensor for active magnetic bearings. *Proceedings of the ASME Turbo Expo*, 3:99–106, 2010.
- [29] M. M. Flynn, J. J. Zierer, and R. C. Thompson. Performance testing of a vehicular flywheel energy system. *SAE Technical Papers*, 2005.
- [30] C. A. L. L. Fonseca, I. F. Santos, and H. I. Weber. Experimental comparison of the nonlinear dynamic behavior of a rigid rotor interacting with two types of different radial backup bearings: Ball and pinned. *Tribology International*, 119:250–261, 2018.

- [31] Johan K Fremerey and Michael Kolk. A 500-Wh POWER FLYWHEEL ON PERMANENT MAGNET BEARINGS. In *Proceedings of ISMST5*, pages 287–295.
- [32] G. Genta. *Kinetic energy storage. Theory and practice of advanced flywheel systems*. Butterworths, 1985.
- [33] G. Genta. Dynamic study of a kinetic energy storage system for a hybrid bus. *Proceedings of the Intersociety Energy Conversion Engineering Conference*, 2:81–86, 1989.
- [34] KD Hahn, EM Johnson, A Brokken, and S Baldwin. Eddy current damping of a magnet moving through a pipe. *American Journal of Physics*, 66(12):1066–1076, 1998.
- [35] L. Hawkins, B. Murphy, R. Hayes, and J. Zierer. Shock and vibration testing of an AMB supported energy storage flywheel. *JSME International Journal*, 46(2):429–435, 2003.
- [36] Lawrence Hawkins, Alexei Filatov, Shamim Imani, and Darren Prosser. Test results and analytical predictions for rotor drop testing of an active magnetic bearing expander/generator. *Journal of Engineering for Gas Turbines and Power-transactions of the ASME*, 129(2):522–529, 2007.
- [37] Lawrence A. Hawkins, Brian T. Murphy, and John Kajs. Analysis and testing of a magnetic bearing energy storage flywheel with gain-scheduled, mimo control. *Proceedings of the ASME Turbo Expo*, 4, 2000.
- [38] C. S. Hearn, M. M. Flynn, M. C. Lewis, R. C. Thompson, B. T. Murphy, and R. G. Longoria. Low cost flywheel energy storage for a fuel cell powered transit bus. *VPPC 2007 - Proceedings of the 2007 IEEE Vehicle Power and Propulsion Conference*, pages 829–836, 2007.
- [39] M. Hedlund, J. Lundin, J. de Santiago, J. Abrahamsson, and H. Bernhoff. Flywheel Energy Storage for Automotive Applications. *Energies*, 8(10):10636–10663, Sep. 2015.
- [40] C. H. Henrikson, J. Lynman, and P. A. Studer. Magnetically suspended momentum wheels for spacecraft stabilization. pages AIAA Paper 74–124. Washington D. C., 1974.
- [41] T. Higuchi and L. Hawkins. Keynote Speeches ISMB 2016. *ISMB presentation*, pages 1–28, 2016.
- [42] Co Huynh, Patrick McMullen, Alexei Filatov, Shamim Imani, Hamid A. Toliyat, and Salman Talebi. Flywheel energy storage system for naval applications. *Proceedings of the ASME Turbo Expo, Proc. ASME Turbo Expo*, 5:25–33, 2006.
- [43] H.K. Jang, D. Song, S.B. Kim, S.C. Han, and T.H. Sung. Study of damping in 5kwh superconductor flywheel energy storage system using a piezoelectric actuator. *Physica C: Superconductivity*, 475:46 – 50, 2012.
- [44] C. Jarroux, J. Mahfoud, R. Dufour, Be. Defoy, and T. Alban. On the dynamics of rotating machinery supported by AMB during base motion. *Proceedings of ISMB15*, pages 1–8, 2016.
- [45] Takahata R. Kubo A. Gachter S. Thoolen F.J.M. Lommen W.G.T. Lathouwers J. Kameno, H. and K. Nonami. Basic design of 1kwh class flywheel energy storage system. *Proceedings of ISMB8*, pages 575–580, 2002.
- [46] Amber Kinetics. Longer duration, lower cost energy storage. Available online: <http://amberkinetics.com/products-2/> [Accessed June 13th 2018].
- [47] James A. Kirk, Dave K. Anand, and David P. Plant. System characterization of a magnetically suspended flywheel. *NASA report*, 1988.
- [48] James A. Kirk, Gregory C. Walsh, Lou P. Hromada, Ronald B. Zmood, and Gary E. Sullivan. Open core composite flywheel. *Proceedings of the Intersociety Energy Conversion Engineering Conference*, 3-4:1748–1753, 1997.
- [49] M. Lang and T. A. Lembke. Design of Permanent Magnet Bearings with high stiffness. *Proceedings of ISMB10*, pages 1–4, 2006.
- [50] René Larsonneur and Philipp Bühler. New Radial Sensor for Active Magnetic Bearings. *Proceedings of ISMB9*, 2004.
- [51] Xiaojun Li, Alan Palazzolo, Dustin Tingey, Xu Han, Patrick McMullen, and Zhiyang Wang. Shaft-less energy storage flywheel. *Proceedings of ASME 9th International Conference on Energy Sustainability, 2015, Vol 2*, 2016.
- [52] Fabian Lorenz and Ralf Werner. Design of a mobile flywheel energy storage driven by a switched reluctance machine. *Proceedings of ISMB15*, pages 1–8, 2016.
- [53] Johan Lundin, Tobias Kamf, Johan Abrahamsson, Juan De Santiago, Magnus Hedlund, and Hans Bernhoff. High Speed Flywheels for Vehicular Applications. *Proceedings of ISMB14*, pages 353–359, 2014.
- [54] Chuan Mao and Changsheng Zhu. Vibration control for active magnetic bearing rotor system of high-speed flywheel energy storage system in a wide range of speed. *2016 IEEE Vehicle Power and Propulsion Conference, VPPC 2016 - Proceedings*, page 7791811, 2016.
- [55] A. T. McDonald. Simplified Gyrodynamics of Road Vehicles with High-Energy Flywheels. *Flywheel Symposium*, pages 240–259, 1980.
- [56] J. McGroarty, J. Schmeller, R. Hockney, and M. Polimeno. Flywheel energy storage system for electric start and an all-electric ship. *2005 IEEE Electric Ship Technologies Symposium*, 2005(0704):400–406, 2005.
- [57] Patrick T. McMullen, Co S. Huynh, and Richard J. Hayes. Combination radial-axial magnetic bearing.

Proceedings of ISMB7, 2000.

- [58] B. Murphy, D. A. Bresie, and J. H. Beno. Bearing Loads in a Vehicular Flywheel Battery. *SAE Special Publications, Electric and Hybrid Vehicle Design Studies, Proceedings of the 1997 International Congress and Exposition*, 1997.
- [59] Arkadiusz Mystkowski. Mu-synthesis for magnetic bearings of flywheel. 9:631–632, 12 2009.
- [60] Arkadiusz Mystkowski. Energy saving robust control of active magnetic bearings in flywheel. *Acta Mechanica et Automatica*, 6(3):72–75, 2012.
- [61] Hideo Nakai, Akinori Matsuda, and Masayuki Suzuki. Development and testing of the suspension system for a flywheel battery. *Control Engineering Practice*, 9(10):1039 – 1046, 2001. Special Section on Control in Defence Systems.
- [62] J. E. Notti and A. Cormack. Integrated power/attitude control system (ipacs) study, volume i - feasibility studies. *NASA CR-2383*, April 1974.
- [63] Hideyuki Otaki. Some analysis of gyroidal effect and the development of a flywheel powered vehicle. *SAE Preprints*, (800835), 1980.
- [64] Junyoung Park, Alan Palazzolo, and Raymond Beach. Mimo active vibration control of magnetically suspended flywheels for satellite ipac service. *Journal of Dynamic Systems Measurement and Control-transactions of the ASME*, 130(4):0410051–04100522, 2008.
- [65] Active Power. CLEANSOURCE® HD675 UPS, 2018. Available online: <http://www.activepower.com/en-US/documents/3970/cleansource-hd675-ups-en.pdf> [Accessed May 31st 2018].
- [66] Active Power. CLEANSOURCE® XT250 UPS, 2018. Available online: <http://www.activepower.com/en-US/documents/3974/cleansource-xt250-ups-en.pdf> [Accessed May 31st 2018].
- [67] Active Power. Flywheel technology, 2018. Available online: <http://www.activepower.com/en-US/5059/flywheel-technology> [Accessed May 31st 2018].
- [68] Beacon Power. 20 MW flywheel energy storage plant. Available online: http://www.sandia.gov/ess/docs/pr_conferences/2014/Thursday/Session7/02_Areseneaux_Jim_20MW_Flywheel_Energy_Storage_Plant_140918.pdf [Accessed May 31st 2018].
- [69] Williams Hybrid Power. Flywheel energy storage, 2013. Available online: http://www.ukintpress-conferences.com/uploads/SPKPMW13R/d1_s1_p2_ian_foley.pdf [Accessed May 31st 2018].
- [70] Lukas Quurck, Michael Richter, Maximilian Schneider, and Daniel Franz. Design and practical realization of an innovative flywheel concept for industrial applications. In *SIRM*, pages 462–470, 2017.
- [71] D. W. Rabenhorst. *Primary Energy Storage and the Super Flywheel*. John Hopkins University Silver Spring MD Applied Physics Lab, September 1969.
- [72] D. W. Rabenhorst. Superflywheel energy storage system. In *Wind Energy Conversion System Workshop (edited by J. M. Savino)*, pages 137–145. Washington D. C. NASA TM-X-69786, June 1973.
- [73] B. Rachmanto, K. Nonami, K. Kuriyama, H. Shimazaki, T. Kagamiishi, and T. Moriya. A study on AMB flywheel powered electric vehicle. *Journal of System Design and Dynamics*, 3(4):659–670, 2009.
- [74] Budi Rachmanto, Kenzo Nonami, Yuki Hiura1, and Takahiro Kagamiishi1. Variable Bias Type AMB Flywheel Powered Electric Vehicle without any Touchdown against LoadDisturbance. *ISMB12*, pages 588–593, 2010.
- [75] C. M. Reid, T. B. Miller, M. A. Hoberecht, P. L. Loyselle, L. M. Taylor, S. C. Farmer, and R. H. Jansen. History of Electrochemical and Energy Storage Technology Development at NASA Glenn Research Center. *Journal of Aerospace Engineering*, 26(2):361–371, apr 2013.
- [76] Ricardo. ‘torqstor’ high efficiency flywheel energy storage, 2014. Available online: <https://ricardo.com/news-and-media/press-releases/ricardo-s-torqstor-receives-sae-2014-world-congr> [Accessed May 31st 2018].
- [77] Ajit V. Sabnis, Joe B. Dendy, and Frank M. Schmitt. A Magnetically Suspended Large Momentum Wheel. *Journal of Spacecraft and Rockets*, 12(7):420–427, 1975.
- [78] Ulrich Schönhoff, J. Luo, G. Li, E. Hilton, Rainer Nordmann, and P. Allaire. Implementation results of mu-synthesis control for an energy storage flywheel test rig. Symposium on Magnetic Bearings <7, 2000, Zürich>: Proceedings. S. 317-322, January 2000.
- [79] Alexander Schulz, Stefan Hartl, Harald Sima, Thomas Hinterdorfer, and Johann Wassermann. Innovative Schwungradspeicher mit hoher Energieeffizienz und Zuverlässigkeit. *Elektrotechnik und Informationstechnik*, 132(8):481–490, 2015.
- [80] F. Shimizu and K. Nonami. Benchmark and Verification of Control Algorithm for Flywheel with Active Magnetic Bearing on Electric Vehicle and Proposal of New SAC Algorithm (ϵ 1 modification and bias variable Γ p approach). *ISMB14*, pages 313–318, 2014.

- [81] R. Siegwart, D. Vischer, R. Larssonneur, R. Herzog, A. Traxler, H. Bleuler, and G. Schweitzer. Control concepts for active magnetic bearings. *1st International Symposium on Magnetic Suspension Technology*, 1991.
- [82] Rainer S. Sindlinger. Magnetic Bearing Momentum Wheels with Vernier Gimballing Capability for 3-Axis Active Attitude Control and Energy Storage. *IFAC Symposium*, 1976.
- [83] Stornetic. Powerful storage system for grid services, 2016. Available online: <https://www.energy-storage-online.de/vis-content/event-energy2017/exh-energy2017.2503879/Energy-Storage-Europe-2017-STORNETIC-GmbH-Paper-energy2017.2503879-RZbpzzbqRveMTsD7LQj53A.pdf> [Accessed June 13th 2018].
- [84] P. A. Studer. Magnetic bearings for spacecraft. *NASA TM X-66111*, January 1972.
- [85] Ryouichi Takahata, Atsushi Kubo, Frans Thoolen, and Kenzo Nonami. Compact flywheel energy storage system. *NEDO*, 2004.
- [86] Chow-Shing Toh and Shyh-Leh Chen. Design, modeling and control of magnetic bearings for a ring-type flywheel energy storage system. *Energies*, 9(12):1051, 2016.
- [87] L. J. Veillette. Design and development of a momentum wheel with magnetic bearings. In *Proceedings of the 8th Aerospace Mechanisms Symposium*. sponsored by NASA, Lockheed Missiles and Space Co., Inc. and California Institute of Technology, Hampton, Va., Oct. 1973.
- [88] Jeffrey Allan Veltri. Flywheel energy system: Patent no.: Us20110298293a1. *US Patent*, 2010.
- [89] WattsUp-Power. Flywheel description, 2018. <http://wattsuppower.com/flywheel/> [Accessed Feb. 16th 2018].
- [90] Frank N. Werfel, Uta Floegel-Delor, Thomas Riedel, Rolf Rothfeld, Dieter Wippich, and Bernd Goebel. Hts magnetic bearings in prototype application. *IEEE Transactions on Applied Superconductivity*, 20(3):874–879, 2010.
- [91] S. Y. Yoon, Z. Lin, T. Dimond, and P. E. Allaire. Control of Active Magnetic Bearing systems on non-static foundations. In *2011 9th IEEE International Conference on Control and Automation (ICCA)*, pages 556–561. IEEE, dec 2011.
- [92] Jamshid Zamany and Martin Speiermann. Flywheel for energy storage systems and energy storage systems comprising the same: Wo2016041987a2. *Patent*, 2015.
- [93] S Zeng. Modelling and experimental study of the transient response of an active magnetic bearing rotor during rotor drop on back-up bearings. *Proceedings of the Institution of Mechanical Engineers, Part I: Journal of Systems and Control Engineering*, 217(6):505–517, 2003.
- [94] Lei Zhu and Larry Hawkins. A model based digital pi current loop control design for AMB actuator coils. *Calnetix homepage*, 2010.
- [95] R.B. Zmood, D. Pang, D.K. Anand, and J.A. Kirk. Improved operation of magnetic bearings for flywheel energy storage system. *Proceedings of the Intersociety Energy Conversion Engineering Conference*, 3:469–474, 1990.

Rotor-fluid Interactions & Instability

Oil Whirl Instability on a Gearbox and Gas Turbine Unbalance.

Sergey Drygin¹, **Nicolas Péton**², **Syauqi Ahmad**³

¹Machinery Diagnostic Technical Leader, Baker Hughes a GE Company (Bently Nevada), 123112, Moscow, Russia, Sergey.Drygin@bhge.com

²MDS Global Director, Baker Hughes a GE Company (Bently Nevada), 44300, Nantes, France, Nicolas.Peton@bhge.com

³Machinery Diagnostic Engineer, Baker Hughes a GE Company (Bently Nevada), 12430, Jakarta, Indonesia, syauqi.ahmad@bhge.com

Abstract

During commissioning a newly installed Gas Turbine Generator (GTG) experienced unusual behavior on October 20th, 2017 when the circuit breakers unexpectedly opened on two separate occasions, resulting in two separate trip related events. Post the circuit breaker related trip events and during subsequent restarts, the gearbox high speed shaft (HSS) drive end bearing (3) direct vibration values were found to breach the OEM assigned Danger set-point (trip value) during early loading, resulting in further vibration related trips.

Review of the post trip event vibration data indicated high levels of sub-synchronous vibration at the gearbox HSS drive end bearing (3) which manifest immediately post synchronization during the initial (early) loading period, with the dominant frequency of vibration measured at 0.41x shaft rotation frequency orders. This dominant gearbox sub-synchronous vibration was attributed to a fluid-based instability issue, with dominant 1x synchronous vibration only measured across the coupling at the gas turbine drive end bearing (gas turbine imbalance symptoms).

It was reasoned that the alignment between the gas turbine and the gearbox had likely changed, with the gearbox possibly twisting and/or deforming during the two-initial high-torque trip related events. Verification of the gas turbine to gearbox alignment should be the first course of action, as part of a full mechanical investigation. If the gearbox had indeed moved and/or deformed during the high-torque circuit breaker related events, gearbox internal alignment related issues would be expected, such as tooth meshing issues, as well as the potential for increased gearbox oil seal clearances and potential bearing damage.

When a full mechanical investigation was finally completed some six weeks post the initial circuit breaker trip related events, a gas turbine to gearbox misalignment condition was indeed confirmed. Additionally, it was verified that the gearbox HSS oil seals had in fact rubbed and all gearbox low speed shaft (LSS) bearings had “wiped” (badly worn bearings). Finally, internal inspection of the gear set revealed abnormal tooth contact.

After the completion of the GTG repair, the gearbox high speed shaft fluid-based instability issue has been fully resolved with the gearbox sub-synchronous frequency no longer evident through the various load ranges. The remaining gas turbine imbalance issue was only then resolved by BHGE, with in-situ trim balancing (one shot balance) was performed, which resulted in a notable decrease in gas turbine 1x synchronous vibration.

Nomenclature

GTG – Gas Turbine Generator
DE Brg – Drive End bearing,
NDE Brg – Non-Drive End bearing,
HSS – High Speed Shaft,
LSS – Low speed shaft,
GB – Gearbox,
FSNL – Full Speed No Load condition.

1 Introduction

BHGE's Machinery Diagnostic Services team was invited to perform vibration data acquisition and subsequent analysis during start-up of a newly commissioned 22 MW GTG unit. The drive train consists of gas turbine driving a step-down gearbox driving a two-pole, air cooled 50 Hz generator (3,000 rpm). The generator rotor is supported by elliptical journal bearings with a rigid design gearbox low speed shaft to generator coupling.

All GTG drive train bearings are monitored via Bently Nevada X/Y Proximity probe systems, orthogonally mounted (45° L & 45° R) and connected to the control panel. Gas turbine rotation is counter-clockwise, when viewed from gas turbine to generator (driver to driven).

The GTG is a newly installed and commissioned unit which experienced unexpected impact due to the 52B circuit breaker unexpectedly opening and closing on two separate occasions on October 20th, 2017, with the unit tripping off-line on both occasions.

After the two separate October 20th, 2017 circuit breaker trip related events, gas turbine and gearbox radial direct vibration values increased with the gearbox high speed shaft drive end bearing values breaching the OEM assigned Danger (trip) set-point. Additionally, the initial start-up gas turbine direct and 1x synchronous vibration values exceeded the OEM Alert set-point (imbalance symptoms).

2 Data collection

Shaft relative vibration data acquisition was performed utilizing a Bently Nevada ADRE 408 DSPi which was connected to all field instrumentation via the control panel. See figure 1.

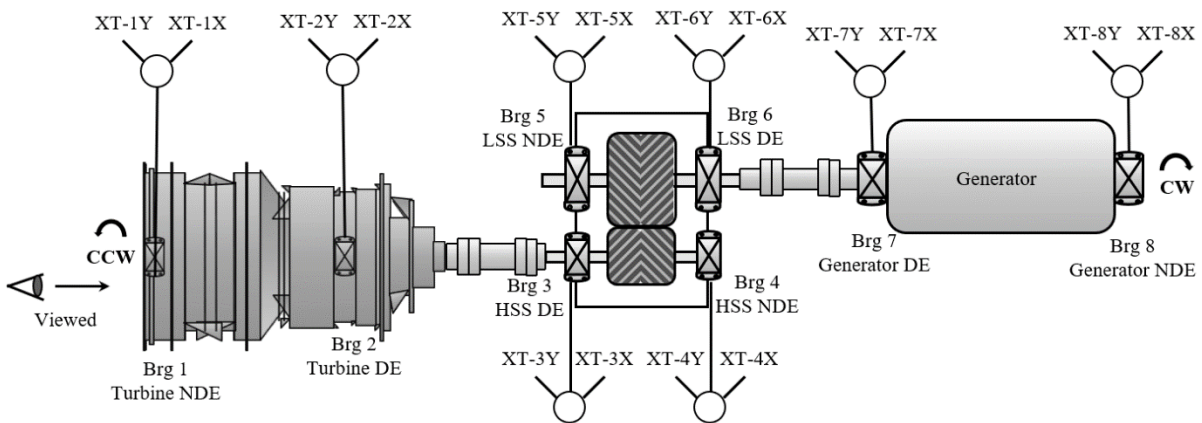


Figure 1: GTG drive train diagram with transducer measurement locations.

After the generator was synchronized and before 2 MW load was achieved, gearbox HSS drive end bearing direct vibration values breached the OEM Danger set-point. Figure 2 presents the HMI direct vibration trends for the October 23rd, 2017 start-up verifying that the GTG tripped off-line with high vibration measured at vibration channel 007A (gearbox HSS drive end bearing 3).

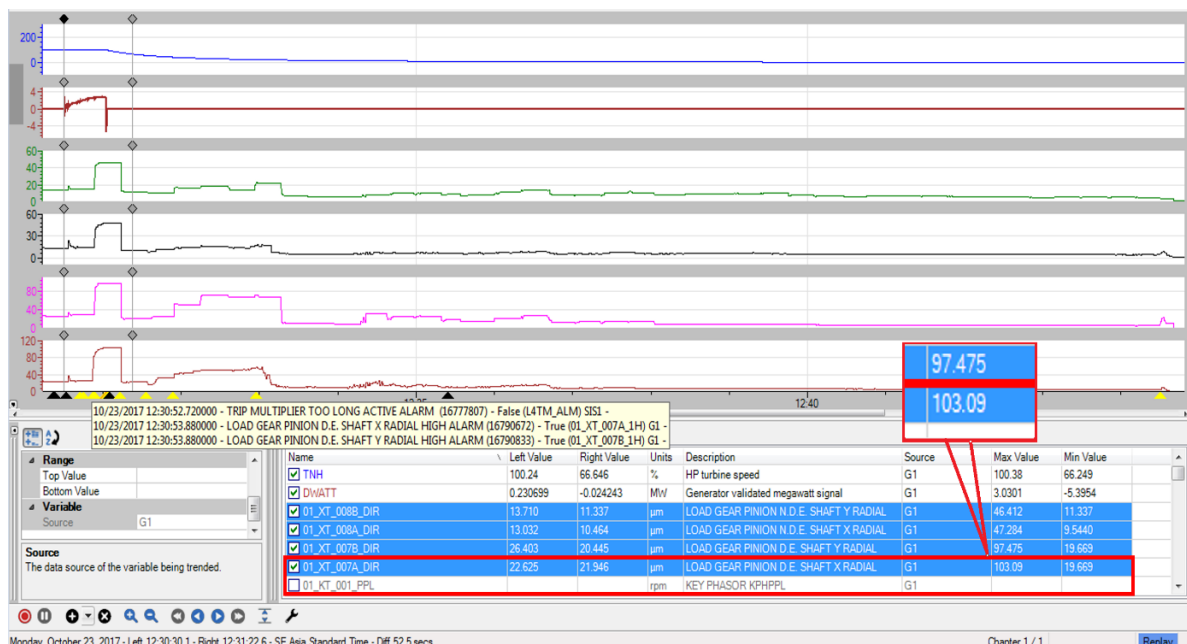


Figure 2: Gearbox shaft relative vibration, historical HMI trends, $\mu\text{m pp}$.

The October 23rd, 2017 vibration trip related event data was reviewed. It was determined that during early loading direct vibration values measured at the gearbox HSS drive end bearing (3) were variable with the corresponding 1x synchronous vibration remaining steady throughout. See Figure 3.

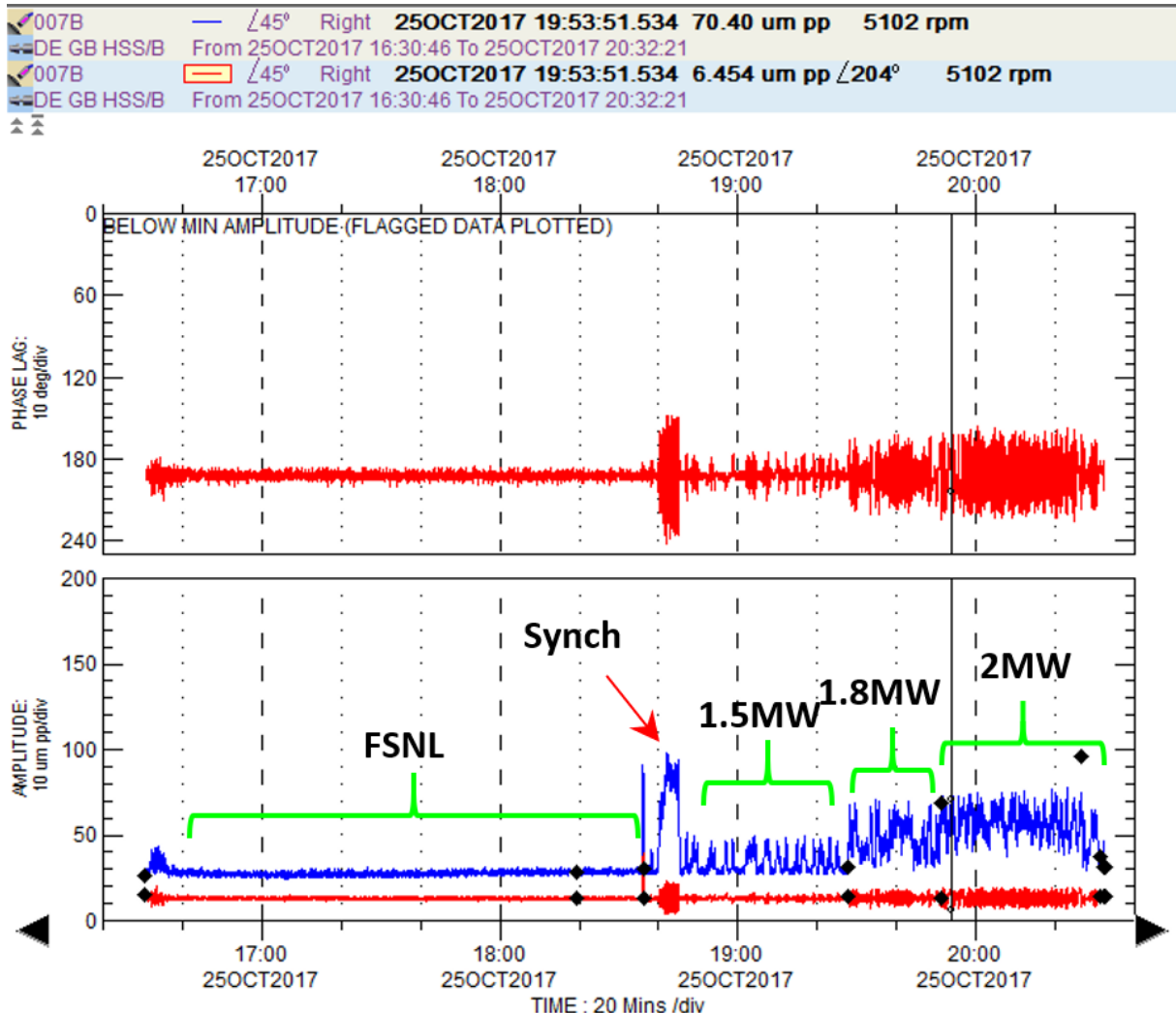


Figure 3: Gearbox shaft relative vibration FSNL, loading up to 2 MW.

Based on ISO 7919-4 (Mechanical vibration of non-reciprocating machines – Measurements on rotating shafts and evaluation criteria – Part 4: Gas turbine sets) standards, the Generator unit vibration levels for the relative vibration transducers were in zone B – machines with vibration within this zone normally considered acceptable for unrestricted long-term operation. However, for newly commissioned machines the vibration within zone A is expected.

3 Data analysis and malfunction investigation.

The maximum gearbox shaft relative vibration direct values were measured during the 2 MW load period. The OEM Danger (trip) set-point for the high-speed shaft bearings is $107 \mu\text{m pp}$. This value was breached hence the unit tripped off-line.

The direct (compensated) orbit/timebase plots for gearbox HSS bearing 3 obtained on October 25th, 2017 presented in Figure 4 are circular with forward precision. The dominant frequency was $< 1/2x$ synchronous (8 Keyphasor dots per 3.5 revolution) with direct values increasing/decreasing in line with load increases/decreases.

Figure 5 presents the full spectrum asynchronous waterfall plots for the two gearbox HSS bearings (3 & 4) during the full speed no load (FSNL) and early loading (2 MW) periods highlighting the dominant sub-synchronous vibration at 0.41x shaft rotation frequency orders.

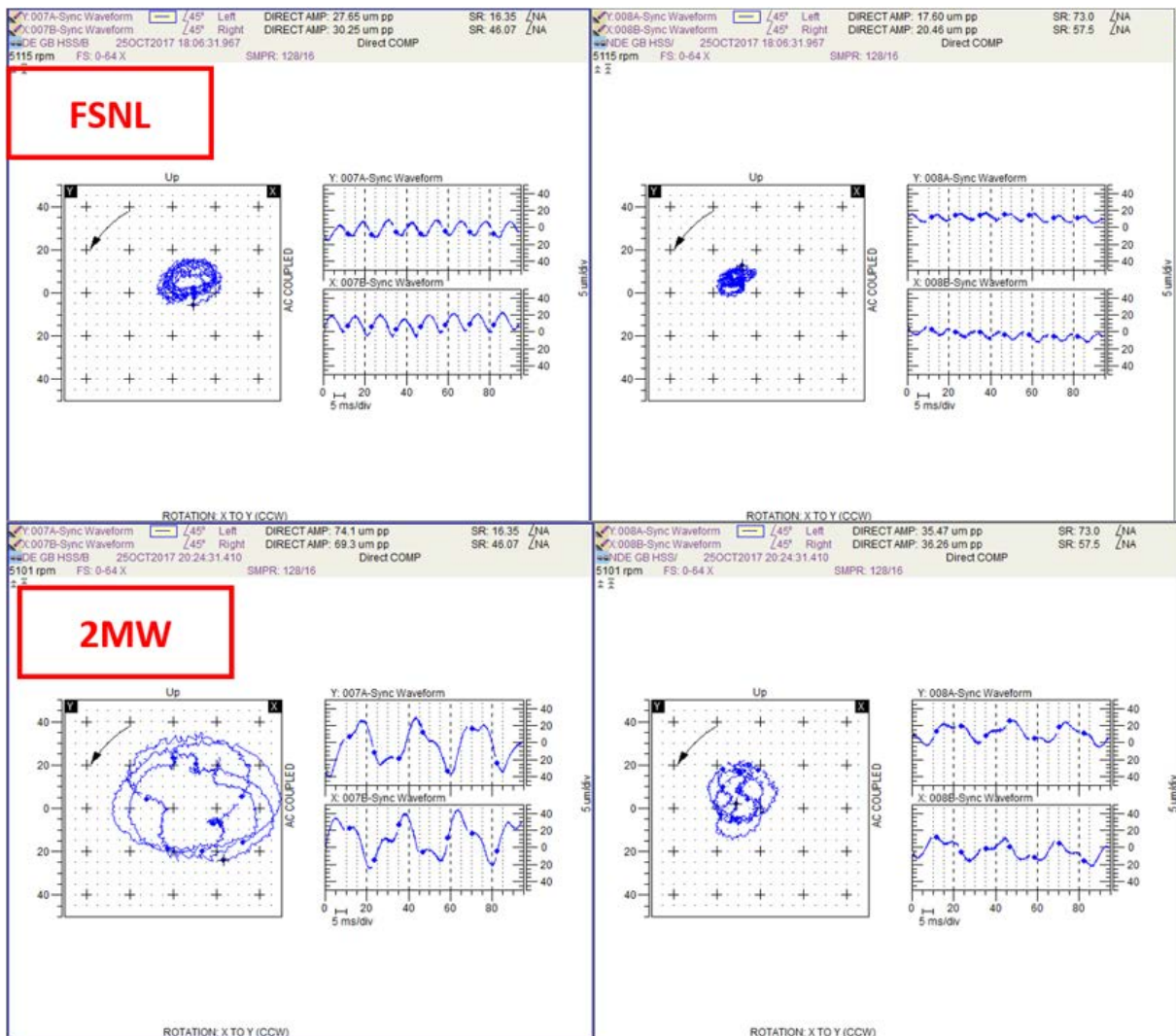


Figure 4: Direct orbit/time base plots (compensated) of bearing #3 during steady state

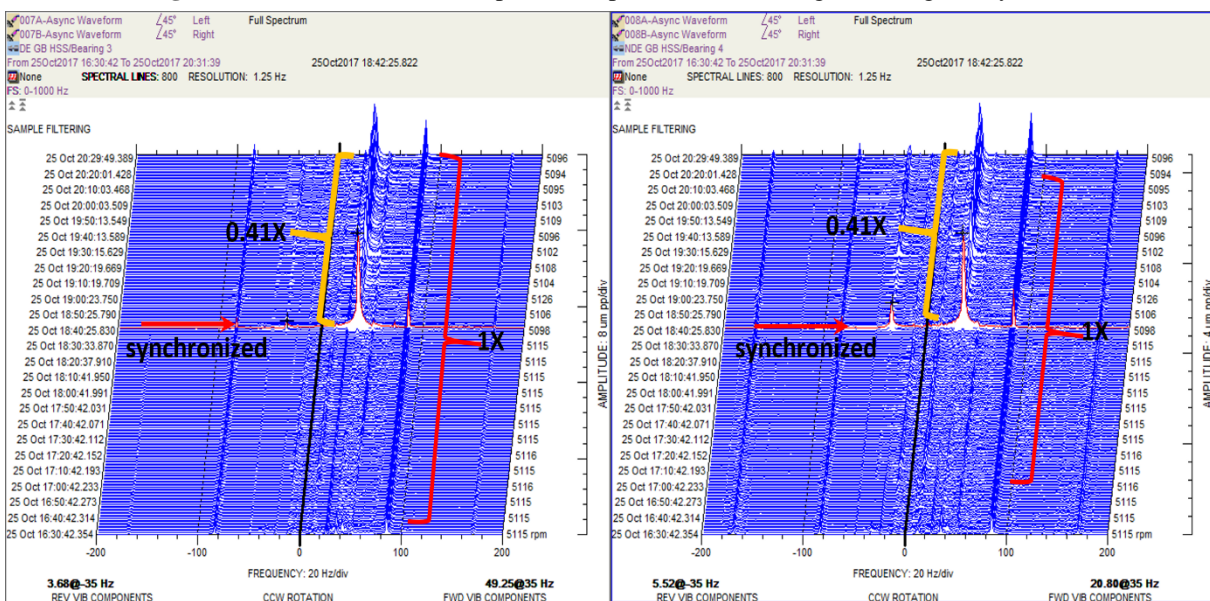


Figure 5: Full spectrum asynchronous waterfall plots for bearing 3 & 4 highlighting the manifestation of

Fluid induced instability (oil whirl) was suspected for the gearbox high speed shaft bearings. Such phenomena could also manifest due to unloading of the high-speed shaft bearings [1,2].

Two gear forces are imposed on the pinion, one is termed the tangential force which acts upward, and one is termed the separating force which acts to push the pinion away from the gear. The magnitudes of both forces are function of transmitted load and hence may vary as the machine condition is changed.

The configuration is a double helical gear. The tangential force is the total transmitted divided by the pitch radius. For the separating force the pressure angle is needed which we don't see on the documentation available. With common pressure angles (around 20 deg.), typically the separating force will work out to be about 1/3 the tangential force. Thrust of course is cancelled when assuming a 50%/50% torque split.

With the rotor weights, the free body diagram can be constructed showing the force acting on each rotor at given speed and load. The pinion weight is 7553 N (769.6 kg) and the gear weight is 62408 N (6361.7 kg). Gear tangential and separation forces due to transmitted torque at 2 MW load were calculated to define both rotors movements in the direction of resulting forces [3]. (Fig.6-7, Equations 1-5):

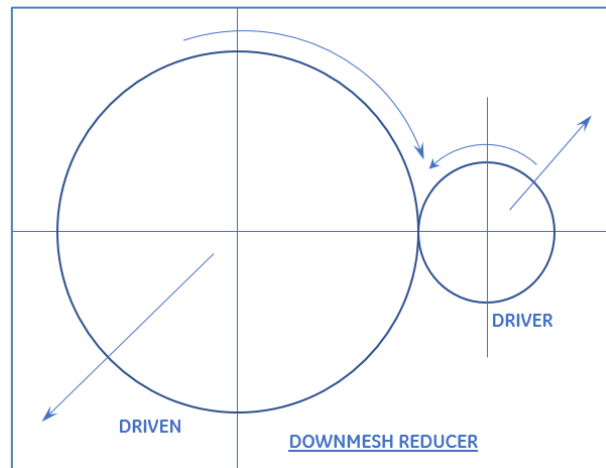


Figure 6: Gear loading (down mesh reducer type)

$$P = \frac{2T}{D}, \quad (1)$$

$$T = \frac{N}{\omega}, \quad (2)$$

$$S = P * \tan \phi, \quad (3)$$

$$F_p = \sqrt{(P - W_p)^2 + S^2}, \quad (4)$$

$$F_G = \sqrt{(P + W_G)^2 + S^2}, \quad (5)$$

where,

P – tangential force, N;

S – separation force, N;

F_p – resultant force on pinion, N;

F_G – resultant force on gear, N;

D – pinion pitch diameter, m;

T – torque, Nm;

N – power, Watt;

ω – pinion speed, rad/s;

φ – is normal pressure angle in degrees;

W_p – pinion weight force, N;

W_G – gear weight force, N.

Tangential force, P = 20587 N;

Separation force, S = 7493 N;

Resultant force on pinion, F_p = 15034 N;

Resultant force on gear, F_G = 83333 N;

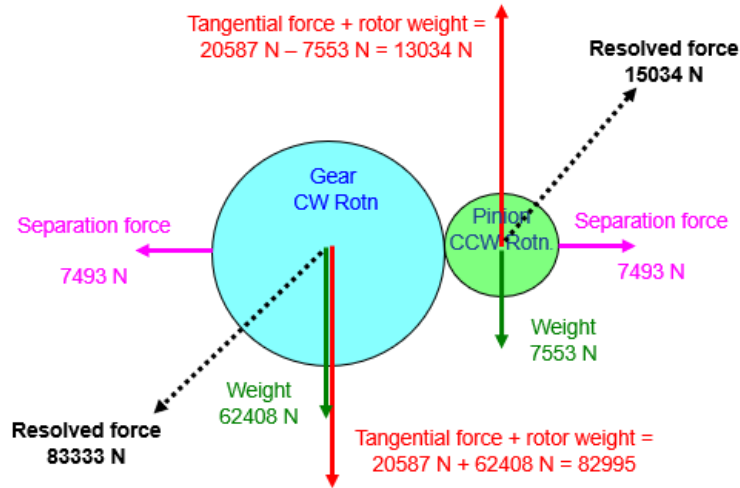


Figure 7: Estimation of designed active gear elements forces at 2MW load condition.

For the rotation shown, the pinion, which is the driver, will tend to lift with the driven gear moving in the opposite downward direction. The summation of the vertical forces on the pinion is the net of the tangential force acting upward with the rotor weight acting downwards. For the gear set in our case, the tangential force and rotor weight both act downward. At 2 MW load it can be shown that the resultant of these forces coupled the rotor weight defines a pinion driven upward and to the right as shown in Figure 7.

Based on the calculations in Figure 6, the gearbox high speed shaft pinion should lift to the upper quadrants of the diametrical bearing clearances. However, as the actual pinion movement is contrary to the expected movement, additional forces acting upon the pinion can be expected hence the pinion movement is deemed as abnormal. For example, preloading due to misalignment or rub condition can overcome the resultant calculated forces presented in figure 6. Thereafter, unexpected (abnormal) pinion operating position can result, as in this instance, with the potential to induce a fluid-based instability condition.

The calculated resultant force on the HSS at 2MW load is about two times that of the gravity force, forcing the pinion to be located in the upper half of the bearing clearance.

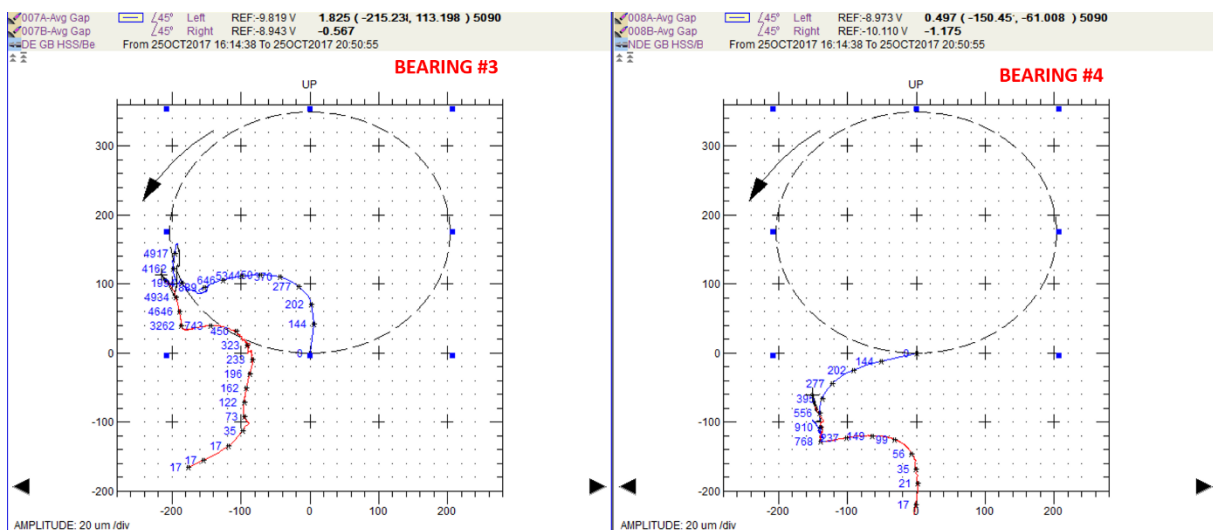


Figure 8: Gearbox HSS shaft bearing 3 & 4 shaft centerline plots during startup (blue), steady state (black) & shutdown (red) operating states

The gearbox HSS shaft centerline plots are presented in Figure 8. Gearbox bearing 3 and 4 high speed shaft startups, full speed no load and early loading (up to 2 MW) operating positions do *not* match the expected positions as per the calculations presented in figure 7, with the high-speed shaft (pinion) moving in the opposite direction to the gear loading calculations (down mesh reduction gear set). Additionally, the “at rest” or zero rpm

high speed shaft positions, required for meaningful shaft centerline plot compensation, could not be accurately determined.

Improper Gearbox bearing loading, coupled with preload forces was suspected. The likely root cause of the suspected radial preload was attributed to gearbox casing deformation resulting in both external and internal gearbox misalignment inducing the high-speed shaft bearing 3 fluid induced instability issue.

the below recommendations were provided to the customer:

- Verify the alignment condition between gas turbine and gearbox high speed shaft.
- Verify the gearbox high speed shaft bearing 3 clearances.
- Investigate potential blockages associated with the lubricating oil path oil paths with emphasis placed in and around the bearing 3 location.
- Verify the internal alignment by performing a contact (blue) test on gear set.

During inspection below malfunctions were found:

- Gas turbine to gearbox high speed shaft misalignment.
- Gearbox high speed shaft oil seal rubs.
- Wiped gearbox low speed shaft (LSS) bearings.
- Distorted/twisted gearbox casing.
- Improper gear tooth contact.

It should be noted that the gearbox HSS bearing clearances remained within OEM specifications with no remedial maintenance activities required.

During corrective maintenance activities, the gas turbine to gearbox and gearbox to generator alignment issues were resolved (re-alignment) as was the gear tooth contact issue. The gearbox high and low speed shaft oil seals were replaced as were both low speed shaft plain bearings. Thereafter, the as per design gear loading was achieved with no evidence of the fluid induced instability phenomena.

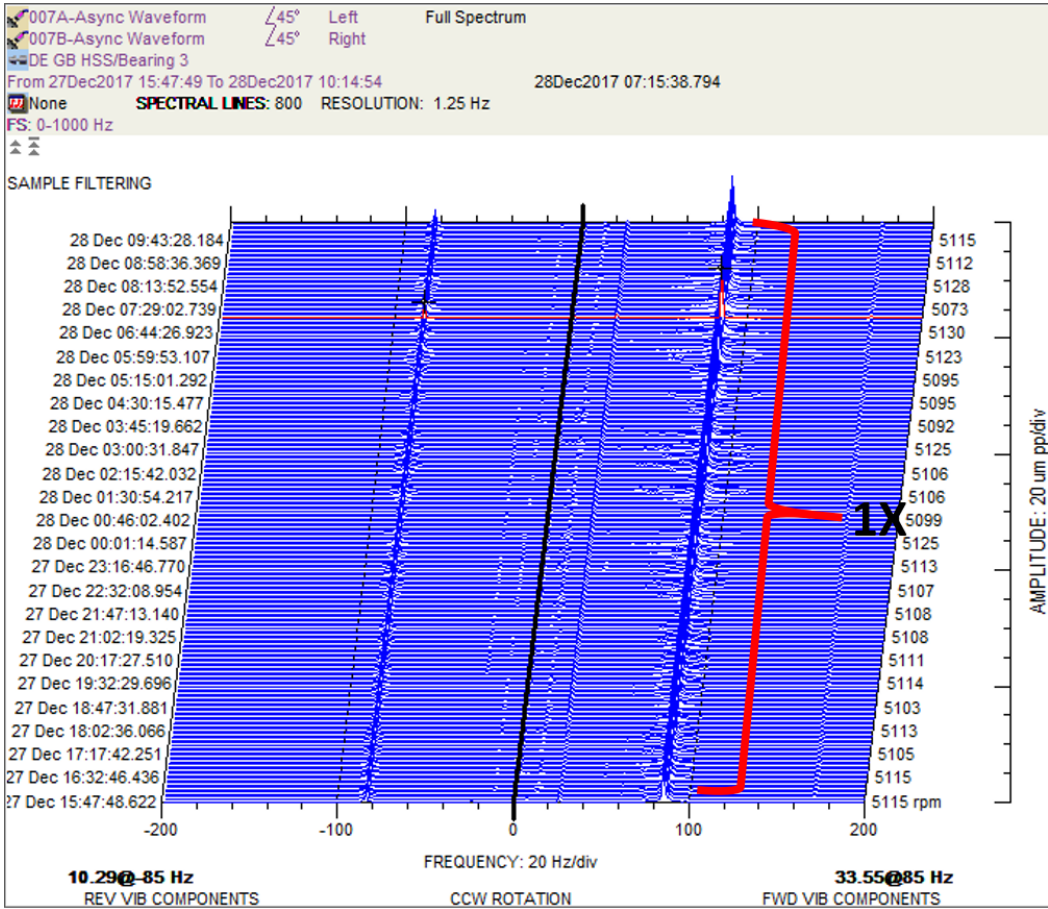


Figure 9: Gearbox high speed shaft bearing 3 full spectrum asynchronous waterfall plot (post gearbox repair).

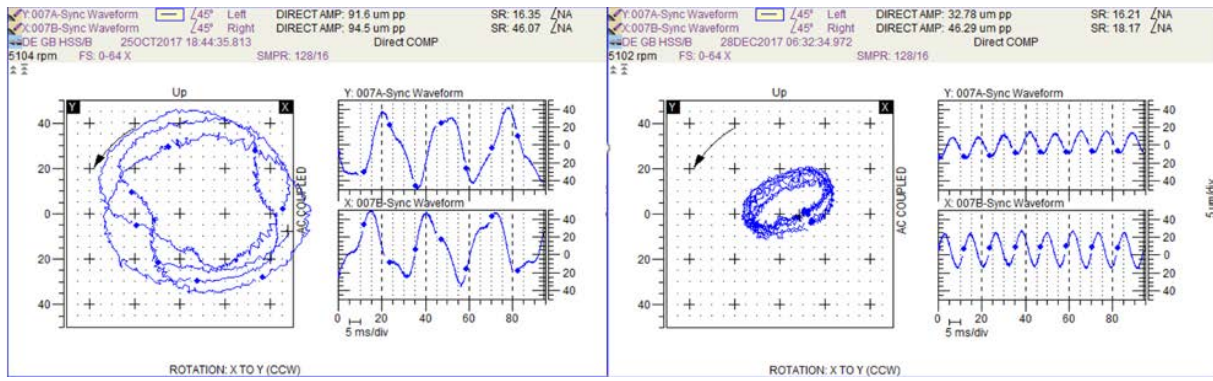


Figure 10: Gearbox high speed shaft bearing 3 compensated direct orbit/time base plots – pre (left hand plot) & post (right hand plot) repair during steady state operation. The dominant pre-repair vibration was $< 1/2x$ synchronous with dominant 1x synchronous vibration only post the repair.

The high levels of gas turbine 1x synchronous vibration (unbalance symptoms) measured during the initial start-up are presented in the figure 11 1x polar plot, with gas turbine bearing (compensated) direct and 1x filtered orbit/time base plots presented in figure 12.

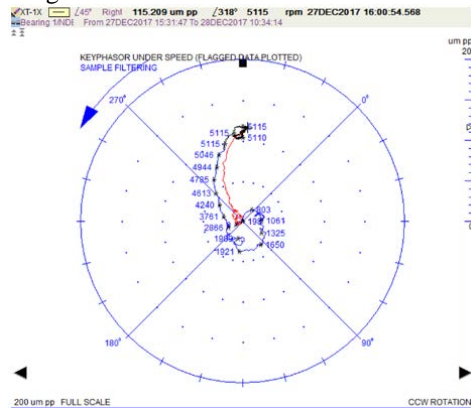


Figure 11: Gas turbine bearing 1 (NDE) 1x compensated polar plot with $> 100 \mu\text{m pp}$ measured during steady state operation (unbalance symptoms)

Blue line data represents a normal start-up

Red line data represents the vibration trip event (abnormal shutdown)

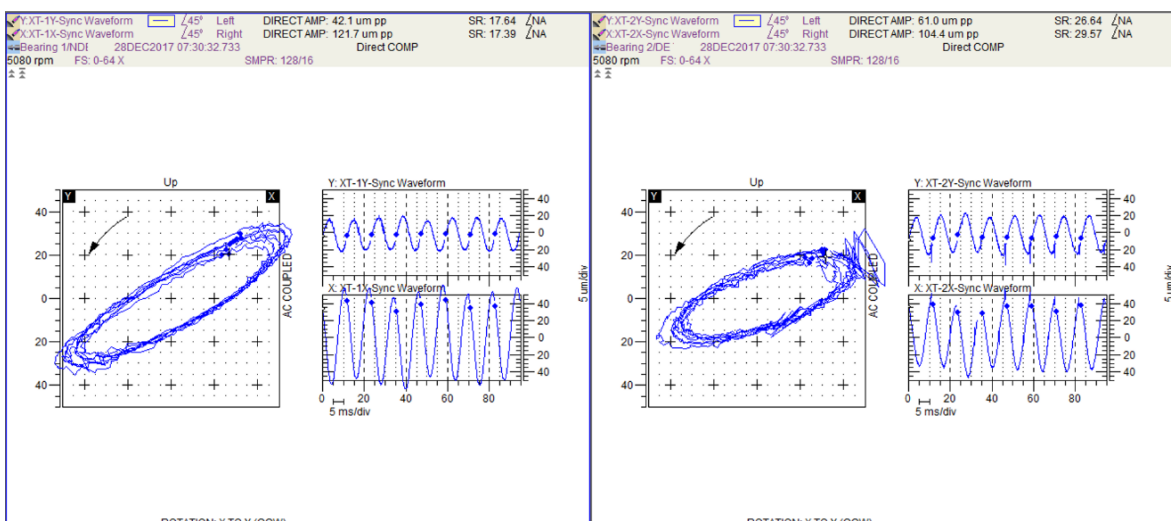


Figure 12: Post repair gas turbine compensated direct orbit/timebase plots are elliptical with forward precession and are indicative of an imbalance condition. This issue was corrected by BHGE by means of in-situ trim balancing (one shot solution)

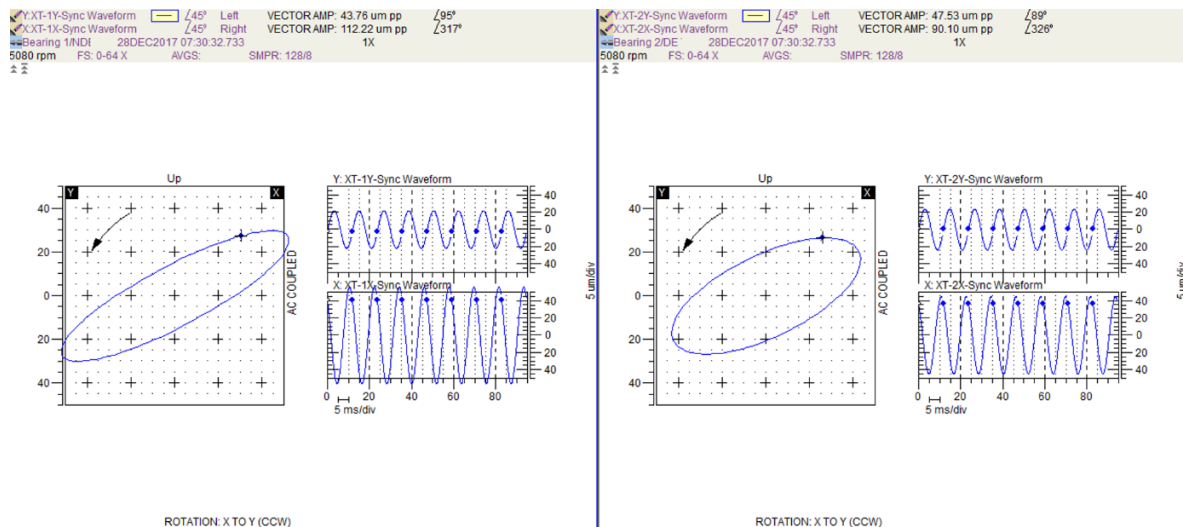


Figure 13: Post repair gas turbine compensated 1x filtered orbit/timebase plots are elliptical with forward precession and are indicative of an imbalance condition. This issue was corrected by BHGE by means of in-situ trim balancing (one shot solution)

Trial weight calculation recommendation:

Rotor weight $\approx 9,100$ kg; balancing speed $\approx 5,110$ rpm; balancing plane radius ≈ 139.7 mm; calibration weight $\approx 10\%$; trial weight ≈ 224 gram @ 135° (ref: XT-1X CW).

In accordance with Gas turbine OEM reference for trim balance:

- Minimum added weight for one hole: 28 grams (short screw without shim)
- Maximum added weight for two holes: 312 grams
- Available weight locations: 14 holes.

Finally, available trial weights were installed on available locations:

- 90 grams on bolt #5 (102.8° from XT-1X CW)
- 90 grams on bolt #6 (128.5° from XT-1X CW).

The two calculated trial weights above were installed on the accessory gearbox coupling hub. This resulted in a significant decrease in 1x synchronous gas turbine vibration, as can be viewed in figures 13 (1x polar plot) and 14 (1x filtered orbit plot). No further trim balancing was required thereafter (one shot solution).

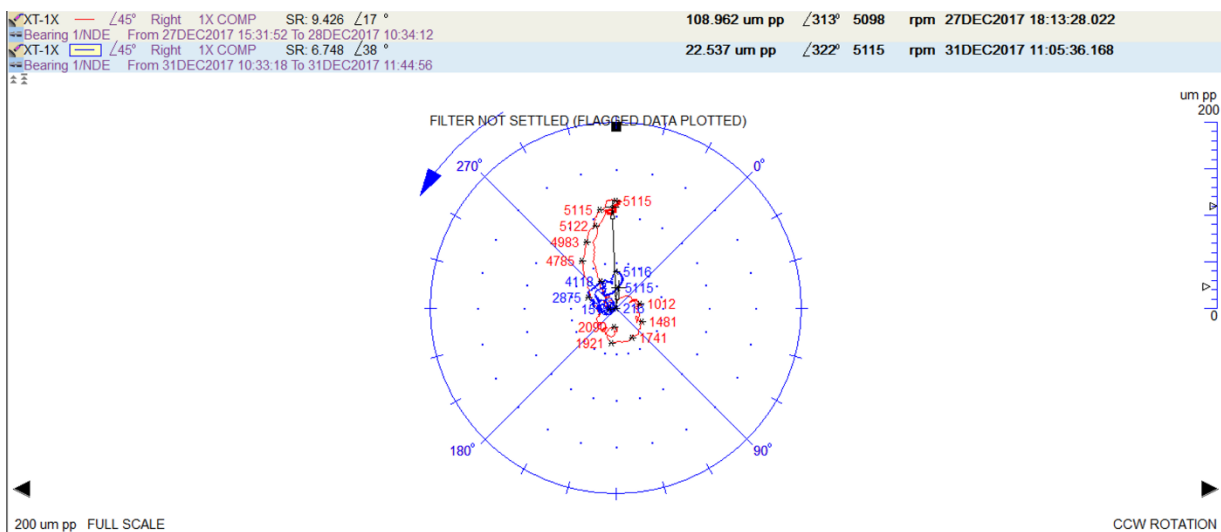


Figure 14: Gas turbine bearing 1 compensated 1x polar plots pre-repair (Red) post balancing (Blue)

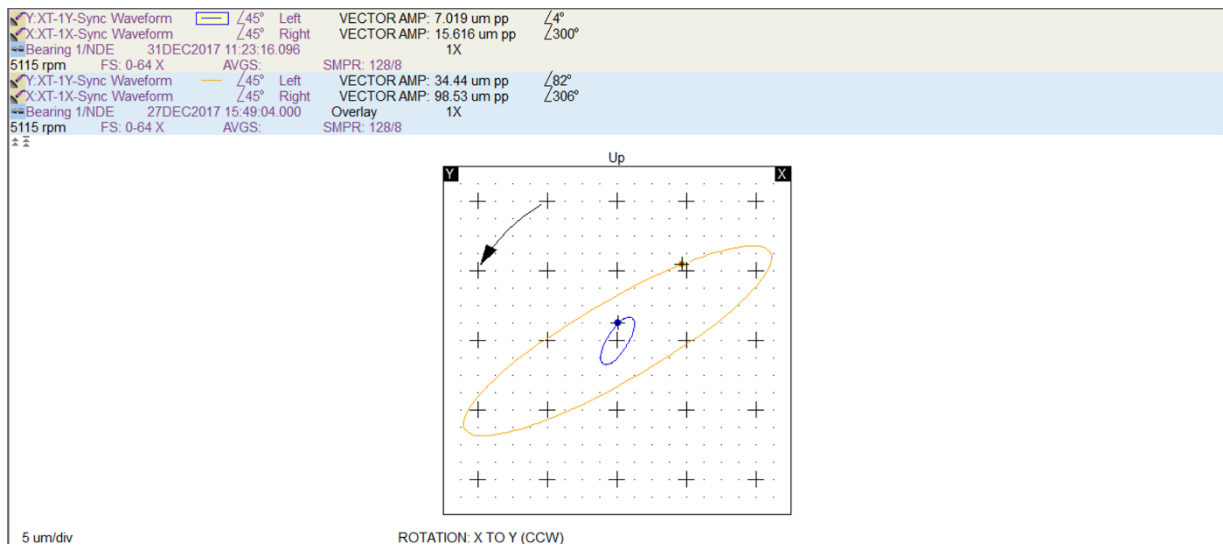


Figure 15: Gas turbine bearing 1 1x filtered (compensated) orbit plots pre-repair (Orange) post balancing (Blue)

4 Conclusions

The October 20th, 2017 circuit breaker related trip events had a negative impact on the drive train gearbox integrity resulting drive train misalignment, gearbox oil seal deterioration and wiped low speed shaft bearing as well as foundation and gear set tooth meshing related issues. During subsequent re-starts, a fluid induced instability condition was diagnosed at the gearbox high speed shaft drive end bearing (3) which was specifically attributed to unloading of the bearing during early loading.

Performing corrective maintenance activities as per BHGE's recommendations, namely gas turbine to gearbox re-alignment and gearbox foundation corrections negated the gearbox high speed shaft fluid-based instability issue. This enabled a successful GTG re-start with subsequent loading/generation thereafter.

The single shot balance solution applied to the gas turbine rotor (accessory gearbox coupling hub) resulted in a significant decrease in 1x synchronous vibration with gas turbine direct vibration reduced to within ISO specifications within the shortest possible time frame.

References

- [1] Robert C. Eisenmann, Sr., P.E. and Robert C. Eisenmann, Jr. (2005): *Vibration Analysis and Troubleshooting for the Process Industries*. Pearson Education, Inc.
- [2] GE Oil & Gas, DS Bently Nevada *Machinery diagnostic technical training. Fluid Induced instability*. (2015)
- [3] GE Oil & Gas, DS Bently Nevada *Advanced Machinery Dynamic technical training. Gears*. (2013)

Optimization of the bearing system for a micro-power turbogenerator with a rotational speed up to 120,000 rpm

Grzegorz Zywica¹, **Lukasz Brenkacz**², **Malgorzata Bogulicz**³

¹ Department of Turbine Dynamics and Diagnostics, Institute of Fluid-Flow Machinery, Polish Academy of Sciences, Fiszera 14, 80-231 Gdansk, Poland, gzywica@imp.gda.pl

² Department of Turbine Dynamics and Diagnostics, Institute of Fluid-Flow Machinery, Polish Academy of Sciences, Fiszera 14, 80-231 Gdansk, Poland, lbrenkacz@imp.gda.pl

³ Department of Turbine Dynamics and Diagnostics, Institute of Fluid-Flow Machinery, Polish Academy of Sciences, Fiszera 14, 80-231 Gdansk, Poland, mbogulicz@imp.gda.pl

Abstract

The paper discusses the selection and optimisation of the bearing system for a high-speed rotor of the turbogenerator with a vapour microturbine. The turbogenerator was designed for the use in a domestic organic Rankine cycle (ORC) system. Its maximum rotational speed is 120,000 rpm, which requires special attention to be given to the bearings. Within the framework of the conducted research, kinetostatic and dynamic properties of the turbogenerator's rotor were analysed, taking into account the following variants for its bearing system: rolling, gas and foil bearings. After analysing the research results, aerostatic gas bearings powered with a low-boiling medium have been finally chosen. The article discusses the results of analyses conducted on the rotor bearings-system for a wide range of rotational speeds. The obtained results are a proof that the turbogenerator's rotor can operate stably even at the maximum rotational speed. Because the selected bearings do not need oil lubrication, it was possible to design the turbogenerator in the oil-free technology.

1 Introduction

The demand for micro-power devices that allow generating thermal and electrical energy grew stronger with the development of distributed power engineering. Among the various energy systems available on the market, ORC (organic Rankine cycle) systems are becoming more and more popular as they enable the production of electricity by using thermal energy both from different renewable and non-renewable resources [1]. For the production of electric energy, such systems use various kinds of expanders, e.g. screw, scroll, vane or piston expanders [17]. Due to their small size and high power density, various types of microturbines are also increasingly employed in ORC systems as expanders [7]. Since the rotors in those microturbines operate at very high rotational speeds, special bearing systems are required.

Even though some advances in the development of foil bearings have been taking place in recent years, such bearings are still regarded as innovative [3,8]. They do not need an external lubrication system and can be lubricated using air or another substance situated in their immediate surroundings. Among various types of foil bearings that can be used in rotating machines, gas foil bearings show enormous potential in vapour microturbines. The working medium from the thermodynamic cycle may serve as a lubricant in gas foil bearings. Such foil bearings can be operated at a high ambient temperature and their rotational speed can exceed 120,000 rpm. Foil bearings are characterised by high durability and exceptional vibration-damping abilities compared to rolling bearings [10,15] that are the most commonly used nowadays. Some modern high-speed machines also use magnetic bearings [5], in particular, active magnetic bearings [14]. However, such application is quite rare due to the high price of the multi-component system of devices that are needed to control the position of the rotor within the gap. Their prices decrease from year to year, opening up an ever-widening range of applications, for example, in microturbines. In the field of bearing systems, the use of slide bearings lubricated with electrorheological and magnetorheological liquids is a novel solution. The use of such liquids allows controlling the properties of the bearing node during its operation [9,13]. In such a system, the electromagnetic field can be used to support the operation of slide bearings, altering their dynamic characteristics and load capacity. As a matter of fact, such bearings are not widely used in practice. What is more, they are not good candidates for the

operation in a high ambient temperature. When discussing innovative bearing systems, shape memory alloys are also worth mentioning. As was shown by Enemark et al. in article [4], such alloys can be used for changing the characteristics of supports in rotor-bearings systems, which also allows us to actively control dynamic properties of the rotor. The authors of this article also have considerable experience in research on high-speed rotors supported on gas bearings with a rigid sleeve [7]. Bearings of this type can use an external lubrication system, which enables a safe start of the rotor and the operation at low rotational speeds (when the aerodynamic lubricating film is not yet stable).

2 Preliminary selection of a bearing system

Before selecting the bearings for the turbogenerator's rotor, analyses of various bearing systems were carried out. At the preliminary stage of the research, both widely available and well-known solutions (which are most commonly used in this type of machines) as well as unconventional foil bearings were analysed. A rolling bearing is a type of bearing which is the most commonly used in engineering. Such bearings are also used in car turbochargers that are operated under similar conditions to those of the analysed turbogenerator. Rotors of turbochargers used in the automotive industry are usually supported on slide bearings lubricated with oil supplied under pressure. However, in the case discussed herein, it was assumed that the turbogenerator would be an oil-free device [12]. Therefore, already at the initial stage of the work, the option of using oil-lubricated bearings was abandoned. Gas bearings are also a very popular solution in high-speed fluid-flow machinery [7]. They can be self-acting (aerodynamic) or aerostatic (which means that they utilise a thin film of high-pressure air to support a load). Compared to rolling bearings they are characterised by lower frictional losses and can be operated at higher rotational speeds. Therefore, gas bearings were considered in further analyses. Additionally, in the framework of preliminary analyses, the possibilities of using gas foil bearings were explored. Bearings of this type have a number of advantages and the research team — of which the authors of this article are members of — has considerable experience in both modelling such bearings [18] as well as conducting experimental research on them [16].

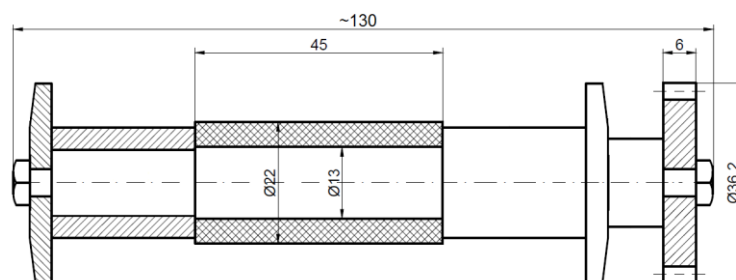


Figure 1: The concept of the rotor's geometry with basic dimensions.

The nominal rotational speed of the turbogenerator's rotor is 100,000 rpm. At this speed, the turbogenerator should have an electric power of approx. 1.5 kW. It was assumed that the maximum rotational speed is equal to 120,000 rpm. Because the turbogenerator will be powered by a low-boiling medium's vapour (instead of steam), the operating temperature will not be high. A low-boiling medium's fresh vapour will be used for powering the turbine and its temperature will be around 150 °C. Regardless of the target bearing system, some dimensions of the rotor were kept constant during the design process. The values that were not changed throughout the whole design process are as follows: dimensions of the generator's rotor (its length as well as its inner and outer diameter) and dimensions of the rotor disc (its length, outer diameter and height of the blades). The initial design of the rotor and the dimensions of its basic components are presented in Fig. 1. The dimensions of the rotor disc result from the previously performed thermal and flow analyses as well as the optimisation of the blade system. The generator's rotor (whose dimensions are presented herein) was selected based on the offer of one of the manufacturers and perfectly met the requirements regarding the rotational speed and the generated power. The remaining dimensions of the shaft were adjusted, given the specificity of individual bearing systems. As far as rolling bearings are concerned, it was necessary to use at least two bearings in order to support both lateral and axial loads. When slide bearings (gas or foil bearings) had been chosen, it was necessary to use at least four bearings, namely two radial bearings and two thrust bearings. It had a direct effect on the geometry of the analysed rotor and the construction of the turbogenerator.

A comprehensive analysis of rolling and gas bearings, as well as a comparison between each of them, can be found in publication [2]. Major advantages and disadvantages of each of the analysed bearing systems, as well as main conclusions resulted from the analyses performed so far, are briefly discussed in the following sections of the article.

2.1 Rolling-element bearings

Rolling bearings are manufactured by many companies, which makes them widely available on the market and their prices are not high. As far as the bearing system for the turbogenerator's rotor is concerned, it is necessary to use bearings designed for special applications that can be operated at very high rotational speeds and at increased temperatures. Such requirements are met by, for example, high precision angular ball bearings. Several manufacturers offer such bearings in a hybrid version, i.e. with balls made of ceramic materials. They can be operated in increased temperatures and under poor lubrication conditions.

The use of rolling bearings in the case discussed herein was associated with the necessity of introducing considerable structural modifications. Since the maximum rotational speed of rolling bearings depends on the diameter of the journal, it was necessary to adapt the rotor design to bearings that can be operated at a speed of 120,000 rpm. The rotor design was ultimately changed in such a way that journals of the bearings had a diameter equal to 8 mm [2]. It enabled the selection of appropriate bearings that have a greater safety margin (in terms of the maximum rotational speed), but at the expense of a significant decrease in the stiffness of the shaft. Unfortunately, it also caused that the critical speed of the rotor decreased so much that it was lower than its nominal speed, which in turn caused a considerable increase in the vibration level. Rolling bearings are characterised by low damping, which worsened the dynamics of the system. Such a rotor could result in big operating problems. As a consequence, the search for better solutions regarding bearing systems for the turbogenerator's rotor went on.

2.2 Gas bearings

When gas bearings are employed in a rotating system they enable its operation at higher rotational speeds compared to oil-lubricated slide bearings. Like in the case of hydrodynamic bearings, the operation of gas bearings can be unstable under certain conditions. Nevertheless, by using appropriate constructional solutions, it is possible to reduce the probability of occurrence of this unfavourable phenomenon. A low load capacity is one of the disadvantages of gas bearings, which results from the low viscosity of gases. The operation of aerodynamic bearings at low rotational speeds is particularly dangerous as damage to the mating surfaces of the journal and the sleeve can occur. This problem can be avoided by using aerostatic bearings supplied with a gas of the suitable pressure.

As far as the investigated turbogenerator's rotor is concerned, preliminary calculations were made for gas bearings whose journals had almost the same diameter as the diameter of the generator's rotor. The length of the radial bearings was equal to the diameter of the journal (i.e. the L/D coefficient was equal to 1.0). Results of the preliminary calculations showed that the rotor supported on aerodynamic gas bearings has very good dynamic properties. Even though the vibration level increased as the rotational speed increased, the vibration amplitude did not surpass a value of 2 μm for throughout the whole tested speed range, i.e. up to a speed of 150,000 rpm [2]. Such good dynamic properties stemmed not only from the high stiffness of the rotor but also from good vibration-damping properties of gas bearings whose operational performance at high speeds was excellent. All in all, the preliminary results confirmed that it is possible to use gas bearings. Such bearings should ensure stable operation of the turbogenerator rotor in a wide range of rotational speeds, but their final geometry should be subject to further, more detailed analyses.

2.3 Gas foil bearings

Owing to their certain advantages, foil bearings are increasingly being used in fluid-flow machines operating under harsh conditions. When they are carefully designed (with appropriately chosen constructional materials), they can be operated at extremely high rotational speeds and at very high temperatures. As a matter of fact, foil bearings are more advanced aerodynamic bearings, in which appropriately shaped thin foils are placed between the journal and the sleeve. Those added elements enable us to affect the dynamic properties of bearings, in particular, to improve their vibration damping capacity. Because the research team, which performed the work described herein, gained considerable experience in researching foil bearings and has in-house software for modelling them, they are considered as one of the possible solutions in the turbogenerator that is still at the design stage.

A greater dynamic stability of the rotor at high rotational speeds could be the major benefit of using foil bearings in the turbogenerator in question. According to results of the calculations made earlier for the rotor supported on classical gas bearings, neither the high vibration level nor the dynamic instability was not a problem in the analysed rotating system. Results of the analysis of the rotor with foil bearings showed that even though achieving a decrease in the vibration level occurring at some speeds was possible, it was only by several per cent. Considering the accuracy of calculations and poor repeatability in manufacturing foil bearings of a given geometry it can be concluded that in the analysed case no substantial benefits resulting from the use of such bearings would be obtained. Additionally, foil bearings have certain drawbacks such as high starting torque

and low accuracy of the rotor alignment. There are no reasonable benefits stemming from the use of foil bearings in the analysed case, mainly due to the operating conditions of the turbogenerator. The rotational speed of the rotor is very high, but the expected temperature in the immediate vicinity of bearings does not surpass a value of 130 °C. Foil bearings cannot show their full potential under such operational conditions. That is why it was decided to finish works relating to the use of foil bearings in the discussed turbogenerator.

3 Optimisation of the gas bearing system

3.1 Numerical model

Computer programs belonging to the MESWIR series, developed at the Institute of Fluid-Flow Machinery of the Polish Academy of Sciences (IMP PAN), were employed for the optimisation of the construction of the rotor and the bearing system. Programs from this software package enable conducting kinetostatic and dynamic analyses of various types of fluid-flow machines, which can be equipped in different types of bearings. This package has been developed for many years [6]. In the last few years, its capabilities have been expanded. Among other things, it is now possible to analyse gas bearings and foil bearings. Characteristics of aerodynamic gas bearings are determined based on an isothermal model. During calculations, the Navier-Stokes momentum equation (assuming constant pressure along the thickness of the lubricating film) and the equation of continuity (without mass transfer) are solved, assuming standard boundary conditions used in the analyses of self-acting gas bearings. Ultimately, pressure distribution is calculated on the basis of the following Reynolds equation for compressible fluids:

$$-\frac{\partial}{R\partial\theta}\left(\frac{\rho h^3}{\mu}\frac{\partial p}{R\partial\theta}\right) - \frac{\partial}{\partial z}\left(\frac{\rho h^3}{\mu}\frac{\partial p}{\partial z}\right) + 12\frac{\partial}{\partial t}(\rho h) + 6\omega\frac{\partial}{\partial\theta}(\rho h) = 0 \quad (1)$$

where:

p – gas pressure, ρ – gas density, h – thickness of the lubrication, R and Θ – the radial and angular coordinates (respectively) in the polar coordinate system, μ - viscosity, z – bearing length, ω – angular speed.

In the discussed case, the model of the turbogenerator's rotor consists of 27 Timoshenko-type beam elements, with six degrees of freedom at each node. The FEM (finite element method) model of the rotor, for one of the analysed geometrical variants, is presented in Fig. 2. In this model, the rotor disc, keep plates of the thrust bearings as well as the generator sleeve were considered. It was assumed that the rotor is supported on two radial bearings whose dimensions were submitted for optimisation. The diameter of the keep plates of the thrust bearings was selected using simplified models of such bearings. The diameter of the rotor disk and of the generator's rotor was constant throughout the whole analysis. The entire shaft was made of steel with a density of 7,860 kg/m³ and the rotor disc was made of aluminium alloy with a density of 2,700 kg/m³.

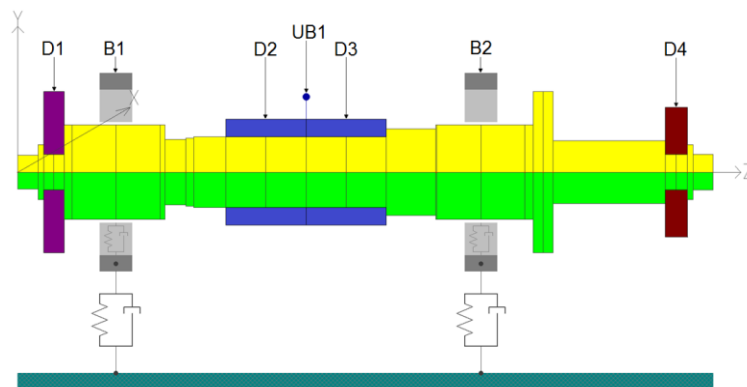


Figure 2: FEM model of the turbogenerator's rotor (D – discs, B – bearings, UB – unbalance).

The numerical model of a gas bearing was used for the purposes of the analysis of the bearing system. In this model, dynamic stiffness and damping coefficients are calculated using the perturbation method. For each bearing, four stiffness coefficients and four damping coefficients (both direct and cross-coupled) were determined for each analysed rotational speed. Vapours of a low-boiling medium — the same medium that drives the microturbine — served as a lubricant for the bearings. This medium has a viscosity of $1.01 \cdot 10^{-3}$ N·s/m² at a temperature of 130 °C. During the analysis of gas bearings, only aerodynamic phenomena were taken into account. This approach allowed us to estimate the lift-off speed of bearings with various dimensions, depending on the operating conditions.

3.2 Determination of the lift-off speed of gas bearings

Already the results of preliminary analyses of the rotor supported on aerodynamic gas bearings show that the rotational speed at which a stable gaseous lubricating film forms itself is too high (for preliminary values of parameters). When both the diameter and the length of each bearing was 16 mm, the lift-off speed (determined by a simulation study) was 27,000 rpm (Fig. 3). This means that the dry or mixed friction takes place between the journal and the sleeve, which, in other words, means that those components of the gas bearings come into physical contact with each other. Although materials of the journal and the sleeve of gas bearings are always selected in such a way that no seizing occurs during short contact between them, longer operation under such conditions can cause permanent damage. Therefore, before the preparation of the manufacturing documentation of the rotor and of the bearings, it was decided to carry out extended research aimed at selecting the bearings' geometry that will enable efficient and failure-free operation of the machine.

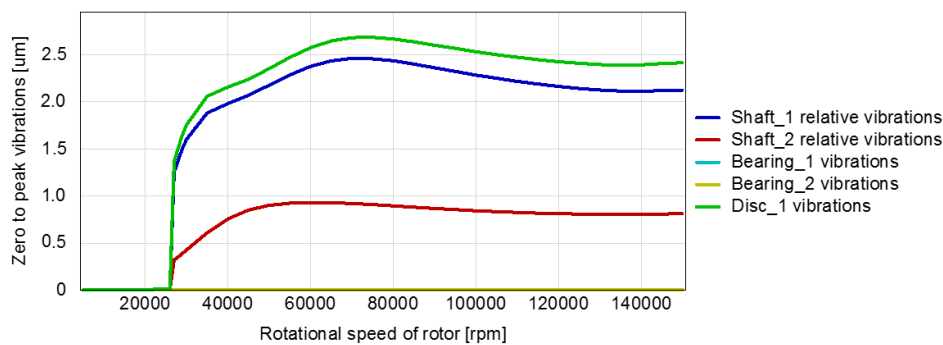


Figure 3: Predicted vibration amplitudes versus rotational speed of the rotor with gas bearings whose diameter and length are equal to 16 mm.

The extended research included the selection of all main dimensions of two radial bearings, with simultaneous selection the diameters of the thrust bearings' keep plates (their inner diameter depended on the diameter of the radial bearings' journals). It was assumed that the optimally selected diameter of the radial bearings' journals has to be in the range of 16 mm to 24 mm. It was also assumed that the bearing length should not be greater than that resulting from the L/D ratio ($L/D=1.2$). The radial clearance of the bearing had to be determined as well. Its value was limited to the range of 12 – 20 μm . The number of possible constructional variants of the bearings was greater than 200. Moreover, in the analysis, it was possible to use different geometry for each of the two bearings due to the fact that the bearings were not evenly loaded (the rotor is not symmetrical). It seemed reasonable because regardless of the diameter of the journals, the load of the bearing situated at the free end of the shaft was about two times smaller than the load of the bearing located between the rotor disc and the generator. The possibility of using two bearings of different dimensions allowed to find a better solution.

The minimum speed at which a stable gaseous lubricating film forms itself (lift-off speed) was the basic criterion for selecting the geometry of the bearings. For each consecutive value of the diameter (16, 18, 20, 22 and 24 mm), series of calculations were carried out in which the length of the bearings and their nominal radial clearance were changed. The minimum rotational speed at which gas bearings started to operate properly was determined for each of the analysed variants. A load of a bearing was assumed to be the force resulting from the static load and transmitted by the support of this bearing. The minimum lift-off speeds of one of the bearings (with a journal diameter of 20 mm) are shown in Fig. 4. Those speeds were obtained for the bearing that was more loaded (by a static force of a value of 2.3 N) than the another bearing. Looking at the graph, it is clear that the lift-off speed decreases as the bearing length increases (but only to its certain value). The lift-off speed also decreases as the radial clearance decreases. In the case presented below (the journal diameter is 20 mm), the lowest lift-off speeds were obtained for bearings whose radial clearances were the lowest and whose lengths were the highest.

When selecting the dimensions of a bearing, attention should also be paid to technological aspects and limitations related to the manufacturing accuracy. A bearing with a greater length and a smaller radial clearance requires higher machining precision and could cause some operational problems. Only after the final geometry was chosen, technological aspects of the manufacturing process were taken into account.

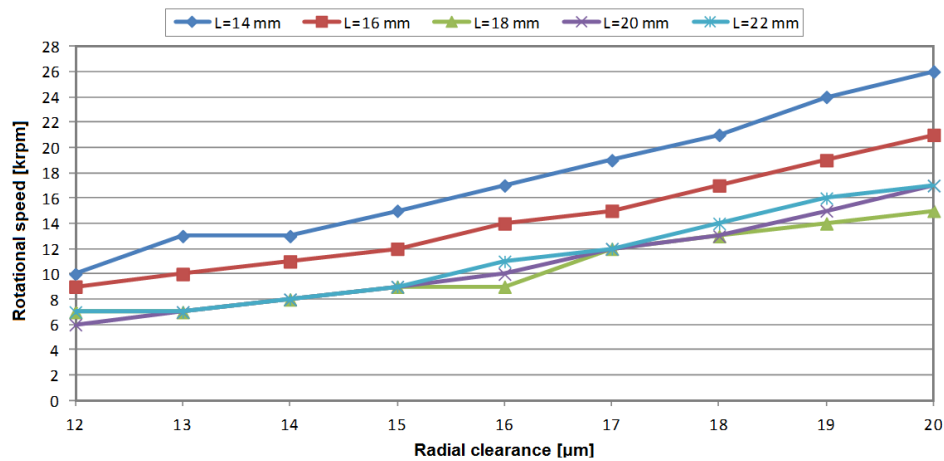


Figure 4: Minimum lift-off speed of the gas bearing with a diameter of 20 mm at the static load equal to 2.3 N versus radial clearance (for different values of the bearing length).

Other criteria for selecting the geometry of gas bearings were the dynamic properties of the rotor and the frictional losses occurring within the bearings themselves. While the dynamic properties of the rotor, which mean (in this case) keeping the rotor vibration at a low level in a wide range of rotational speed, made it possible to indicate the most optimal solutions, the analysis of the frictional losses proved to be of little use. The frictional losses were very slight due to small overall dimensions of the analysed bearings and the low value of the coefficient of friction (which stems from the low viscosity of gases). Changes in the geometry of bearings had a negligible impact on the power losses. Therefore, power losses were not considered during the selection of the target bearing system.

3.3 Characteristics of the optimised rotating system

Conducting many analyses of various variants of gas bearings enabled to select their optimal geometry. Basic dimensions of the bearings are shown in Table 1. It turned out that when the requirements regarding the manufacturing accuracy are met, bearings with a diameter of 24 mm and a length of 22 mm seem to be the best choice. The optimal value of the radial clearance is 20 µm. The choice of such a radial clearance was mainly based on technological aspects. A lower value of the radial clearance would guarantee higher load capacity at lower speeds, but at the same time would necessitate narrower manufacturing tolerance and could cause assembly problems. Lower radial clearance could also cause permanent damage to a bearing due to rubbing of the journal against the sleeve during operation or uneven heating up of these components. The target solution contains two bearings with the same dimensions. In support of that solution, it should be pointed out, first of all, that different dimensions of the bearings provided only a slight improvement in the analysed parameters. What is more, fabrication of two identical bearings is not only less time-consuming but also relatively less expensive.

Table 1: Basic dimensions of gas bearings used in the turbogenerator.

Bearing No.	Radial static load	Diameter	Length	Radial clearance
<i>Bearing 1</i>	1.0 N	24 mm	22 mm	0.02 mm
<i>Bearing 2</i>	2.3 N	24 mm	22 mm	0.02 mm

Based on the optimal dimensions of the bearings and dimensions of the remaining components of the rotor, a 3D CAD model was developed, shown in Fig. 5. This model considers the generator's rotor, the keep plates of the thrust bearings and the impulse microturbine's disc. The bearing sleeves will be made of bronze and the steel journals will be subjected to toughening. In order to ensure sufficient manufacturing accuracy and a low value of the surface roughness, it is planned to grind surfaces of the journals and sleeves during finishing.



Figure 5: Geometry of the optimised rotating system with gas bearings.

The basic dynamic characteristics of the rotor supported on the target bearings are shown in Figs. 6 – 8. Figure 6 presents the vibration amplitudes of chosen components of the rotor versus its rotational speed (in the speed range of 0 – 150,000 rpm). Up to a speed of approx. 60,000 rpm, the vibration level of the rotor goes up as the rotational speed increases. At higher speeds, the vibration level is quite stable. Even though it goes up more for some discs (mainly disc No. 4), its highest value is still low. In the whole speed range, assuming that the residual unbalance complies with the ISO1940 standard, vibration amplitudes of all components of the rotor did not exceed 2 μm . This bears witness to very good dynamic properties of the tested system. Vibration trajectories enabled a better understanding of the dynamic characteristics of the analysed rotor. Selected vibration trajectories of the entire rotor and of the bearing journals are demonstrated in Figs. 7 and 8. Because of the limitation for the number of pages, the vibration trajectories are presented only for two rotational speeds (i.e. 75,000 rpm and 100,000 rpm). These results also bear witness to the stable operation of the rotor supported on the designed gas bearings.

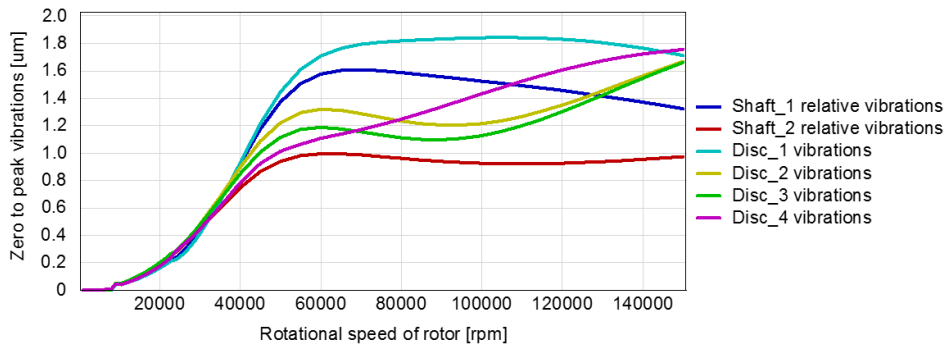


Figure 6: Predicted vibration amplitudes versus rotational speed of the rotor with gas bearings of a diameter and length equal to 24 mm and 22 mm, respectively.

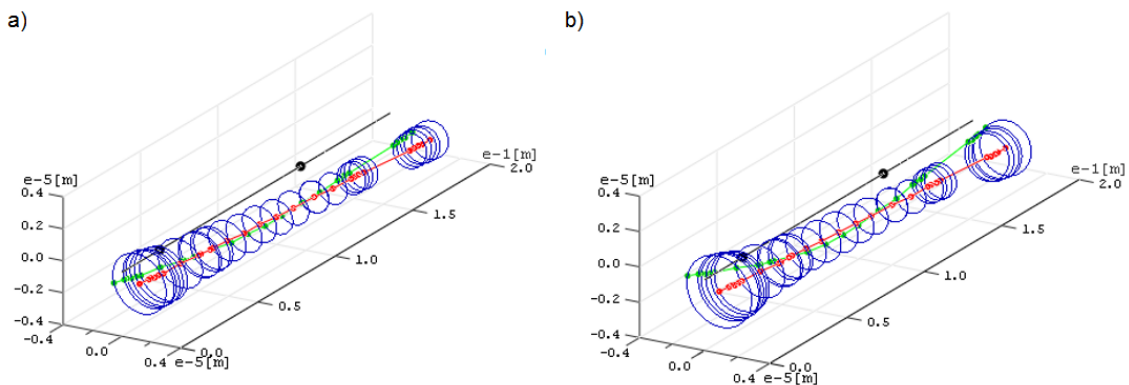


Figure 7: Vibration trajectories for the rotor with gas bearings with a diameter and length equal to 24 mm and 22 mm respectively, at a rotational speed of 75 krpm (a) and 100 krpm (b).

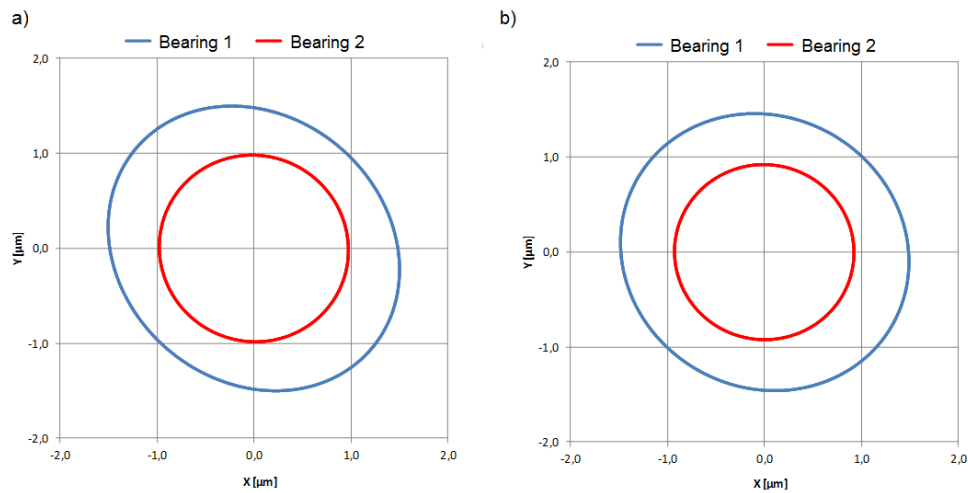


Figure 8: Vibration trajectories for gas bearings with a diameter and length equal to 24 mm and 22 mm respectively, at a rotational speed of 75 krpm (a) and 100 krpm (b).

On the basis of the obtained results, it can be stated that the turbogenerator's rotor can operate reliably at high rotational speeds. However, its characteristics obtained at low speeds gave rise to some concerns. According to the results presented in Fig. 6, a stable gaseous lubricating film, which ensures the required bearing capacity, formed itself at a speed about 8,000 rpm. This means that at lower speeds there will be physical contact between the journal and the sleeve, which could cause damage to the bearing. Therefore, the target construction of the bearings includes additional feed holes that will enable safe start-up and shut-down of the machine. Because of such a light rotor, it was enough to use eight holes with a diameter of less than 0.5 mm, placed evenly around the circumference of each bearing. In the turbogenerator in question, the bearings will be supplied with vapours of the same low-boiling medium that will feed the microturbine. Since the bearings are small in size, the amount of the low-boiling medium needed for their proper operation at low speeds is small. The constructional solution discussed herein has already been used in larger microturbines (with an electric power of 3 kW [7]) and enabled their failure-free operation with negligible efficiency losses.

4 Conclusion

Simulation studies, aimed to select a bearing system for the high-speed turbogenerator that will be operated in a cogeneration system, have been discussed in the article. Preliminary analyses were performed for several bearing systems, including rolling bearings, gas bearings and foil bearings. Due to the very high rotational speed and the lack of possibility to use a conventional lubricating medium, the research work on rolling bearings was finally discontinued. The analysis of foil bearings showed that the rotor would derive little benefit from the use of such bearings. Due to such inconveniences as high starting torque and low alignment accuracy, the possibility of using foil bearings in the new turbogenerator was not considered any more. Preliminary analyses, however, indicated that gas bearings have considerable potential as they enable stable operation of the rotor over a broad speed range. That is why those are the bearings to which more attention has been paid.

Further works were aimed at selecting optimal dimensions of the bearings, particularly in respect of operating conditions of the turbogenerator that will be operated in a cogeneration system. The analyses of gas bearings and the rotor supported on such bearings were carried out using the package of computer programs named MESWIR, developed at the IMP PAN. Out of many possible geometrical variants, bearings with a diameter of 24 mm and a length of 22 mm were finally picked. The optimal value of the radial clearance was 0.02 mm. The choice of this value was linked to certain operational aspects. Therefore, this value is higher than the value of the radial clearance for which the required bearing capacity at the lowest rotational speed was obtained. Due to the large difference in the load of the bearings, the possibility of using two bearings with different dimensions was also taken into account. The calculation results showed, however, that this could cause only a slight improvement in dynamic properties. This fact could not justify the use of a more complex construction of the turbogenerator. The calculation results obtained for the target bearing system indicate a stable operation of the rotor without any dynamic problems. However, due to the lack of conditions for the proper lubrication at low rotational speeds, it was decided that the bearings will be supplied with vapours of a low-boiling medium. Only the small amount of vapour will be sufficient to protect the bearings against damage at low rotational speeds.

The selection of the optimal bearing system resulted in the completion of design works and the preparation of the construction documentation of the new prototype. Currently, the turbogenerator prototype with gas bearings is being prepared for laboratory tests. Only after carrying out experimental research on the designed bearing system the credibility of the simulation results will be verified. After the experimental verification made on the prototype, it is planned to prepare technical documentation of the turbogenerator, which will be intended to serial production.

Acknowledgement

This work has been founded by The Polish Agency for Enterprise Development and from The Smart Growth Operational Programme (European funds) within the project No. POIR.02.03.02-22-0009/15 carried out jointly with the SARK Company.

References

- [1] Bronicki, L.Y. (Editor) (2018): Power Stations Using Locally Available Energy Sources. *Encyclopedia of Sustainability Science and Technology Series*. Springer, New York.
- [2] Brenkacz, L., Zywica, G. and Bogulicz, M. (2019): Selection of the bearing system for a 1 kW ORC microturbine. *Proceedings of the 10-th International Conference on Rotor Dynamics – IFToMM 2018*, Vol. 1, pp. 223-235.
- [3] DellaCorte, C. (2012): Oil-free shaft support system rotordynamics: past, present and future challenges and opportunities. *Mechanical Systems and Signal Processing*, **29**, pp. 67–76.
- [4] Enemark, S., Savi, M. and Santos, I.F. (2015): Experimental analyses of dynamical systems involving shape memory alloys. *Smart Structures and Systems*, **15**(6), pp. 1521-1542.
- [5] Ji, J.C., Hansen, C.H. and Zander, A.C. (2008): Nonlinear dynamics of magnetic bearing systems. *Journal of Intelligent Material Systems and Structures*, **19**(12), pp. 1471–1491.
- [6] Kicinski, J. (2006): *Rotor Dynamics*. IFFM Publisher, Gdansk.
- [7] Kicinski, J. and Zywica, G. (2014): *Steam Microturbines in Distributed Cogeneration*. Springer, Cham.
- [8] Larsen, J.S., Hansen, A.J. and Santos, I.F. (2015): Experimental and theoretical analysis of a rigid rotor supported by air foil bearings. *Mechanics and Industry*, **16**(1), Paper No. 106.
- [9] Peng, J. and Zhu, K.-Q. (2005): Hydrodynamic characteristics of ER journal bearings with external electric field imposed on the contractive part. *Journal of Intelligent Material Systems and Structures*, **16**(6), pp. 493–499.
- [10] Shen, C., Wang, D., Liu, Y., et al. (2014): Recognition of rolling bearing fault patterns and sizes based on two-layer support vector regression machines. *Smart Structures and Systems*, **13**(3), pp. 453–471.
- [11] Soares, C. (2007): *Microturbines (applications for distributed energy systems)*. Butterworth-Heinemann.
- [12] Tkacz, E., Kozanecka, D., Kozanecki, Z. and Miazga, K. (2011): Investigations of oil-free support systems to improve the reliability of ORC hermetic high-speed turbomachinery. *Mechanics and Mechanical Engineering*, **15**(3), pp. 355-365.
- [13] Urreta, H., Leicht, Z., Sanchez, A., et al. (2010): Hydrodynamic bearing lubricated with magnetic fluids. *Journal of Intelligent Material Systems and Structures*, **21**(15), pp. 1491–1499.
- [14] Wu, R.Q., Zhang, W. and Yao, M.H. (2018): Nonlinear dynamics near resonances of a rotor-active magnetic bearings system with 16-pole legs and time varying stiffness. *Mechanical Systems and Signal Processing*, **100**, pp. 113–134.
- [15] Zhao, Y., Zhang, B., An, G., et al. (2016): A hybrid method for dynamic stiffness identification of bearing joint of high speed spindles. *Structural Engineering and Mechanics*, **57**(1), pp. 141–159.
- [16] Zywica, G., Baginski, P. and Banaszek, S. (2016): Experimental studies on foil bearing with a sliding coating made of synthetic material. *ASME Journal of Tribology*, **138**(1), Paper No. 011301.
- [17] Zywica, G., Kaczmarczyk T.Z. and Ihnatowicz, E. (2016): A review of expanders for power generation in small-scale organic Rankine cycle systems: performance and operational aspects. *Proc IMechE Part A: J Power and Energy*, **230**(7), pp. 669-684.
- [18] Zywica, G., Kicinski, J. and Bogulicz, M. (2019): Analysis of the rotor supported by gas foil bearings considering the assembly preload and hardening effect. *Proceedings of the 10-th International Conference on Rotor Dynamics – IFToMM 2018*, Vol. 1, pp. 208-222.

Steam Instability

Sergey Drygin¹, **Nicolas Péton**²

¹Machinery Diagnostic Technical Leader, Baker Hughes a GE Company (Bently Nevada), 123112, Moscow, Russia, Sergey.Drygin@bhge.com

²MDS Global Director, Baker Hughes a GE Company (Bently Nevada), 44300, Nantes, France, Nicolas.Peton@bhge.com

Abstract

This case is a site vibration issue on a Power generation module. The machinery diagnostics Engineer was requested on site to collect startup and steady state data using a multichannel data collector. Power generation module consists of high/intermediate pressure, double flow low pressure stages steam turbine and synchronous generator. The machine train is equipped with online vibration monitoring & protection system. When machine was running at full load condition, vibration at high/intermediate pressure stage of steam turbine suddenly increased and exceeded Alert setpoint. Operation at this condition is unsafe and can be result of serious unit damage.

This case study is designed to outline how the high vibration issue was successfully diagnosed, the root cause for the high vibration found and correction actions recommended.

The review of collected data indicated that vibration amplitudes are rapidly raised up at full load - 163MW. While the unit kept full load, the high vibration situation was suddenly occurred. The dominant of high vibration level – 170 um pp, higher than Alert setpoint was sub synchronous (22.5Hz or 0.375 orders component for full speed, dominated in horizontal direction).

In addition, at unit shut down status, this high vibration situation is disappeared immediately after shutdown command. It is not speed related condition, but load and some operation conditions related. There are no any significant changes in the shaft centerline detected during mentioned 22.5Hz component appearing at Unit full load.

The phase data analysis of filtered 22.5Hz shaft rotation component demonstrating approximately 40 degrees phase leading for drive end bearing plane.

The source of mentioned sub synchronous excitations is steam induced instability – steam whip, detected in HP/LP turbine seals, closer to drive end bearing.

This turbine was initially equipped by antiwhirl packages. It was confirmed that this system is installed or operated not properly, non-original spare parts was installed during last overhaul. It was made by local company and installed without OEM installation guide.

Original antiwhirl package installation was suggested to customer to increase stability threshold and allow unit to operate at full load with acceptable vibration level.

Nomenclature

BHGE - Baker Hughes, a GE company
OEM - Original equipment manufacturer
HIP - High/Intermediate pressure stage
STG - Steam turbine generator
FSNL- Full speed no load
um pp - Micrometers, peak to peak amplitude
RPM - Rotations per minute
DE BRG - Drive end bearing
NDE BRG - Non-drive end bearing

1 Introduction

Baker Hughes, a GE company (BHGE) is the world's first and only full stream provider of integrated oilfield products, services and digital solutions. Bently Nevada is part of the BHGE Measurement & Controls division, it has 60 years history, 134 machinery diagnostic engineers with cumulative experience more than 1000 years worldwide.

BHGE's the machinery diagnostics engineer was requested on site to collect startup and steady state data using a multichannel data collector. Power generation module consists of high/intermediate pressure, double flow low pressure stages steam turbine and synchronous generator. The machine train is equipped with online vibration monitoring & protection system. When machine was running at full load condition, vibration at high/intermediate pressure stage of steam turbine suddenly increased and exceeded Alert setpoint. Operation at this condition is unsafe and can be result of serious unit damage.

This unit was installed in 1999, there are 8163 operating hours and 4585 starts since commissioning. Unit consist of high/intermediate pressure, double flow low pressure stages steam turbine and synchronous generator.

The regular planned outage in 1~31 October 2016 was done as below:

- HP #1, 2, 3, 4 stages: processed to remove cracks from wheel heat grooves & steam balance holes,
- 10 visually identified cracks: 11.2 mm of maximum crack depth (HP 1 stage front),
- estimated growth speed of cracks of 8.75 $\mu\text{m}/\text{cycle}$ (trend analysis),
- correction of HIP turbine rotor bending: 0.30 mm max. \rightarrow 0.05 mm based on mid-span,
- replace to HIP retractable packings (1 anti-swirl conv./14 retr. /2 brush) and N2 conventional packings,
- structural change and removal of sound-absorbing materials to reduce vibrations related to axial resonance of the LP hood

Based on information received from customer, after mentioned outage, the vibration values of HP/IP drive end bearing raised up to 279 μm pp with a main 22.5Hz component during first operation test 1 Nov. On 4th of Nov, the customer had a field balancing at HP/IP stage during FSNL condition, but vibration spike at 22.5 Hz wasn't significantly affected and remained at high amplitude (213 μm pp). After this, two more attempts were made to start the unit:

- at the first start up, STG was tripped at 1635rpm because of high vibration (up to 231 μm pp).
- at the second start up, STG starting procedure was changed with 60 minutes holding time at 300 rpm, then the vibration amplitude raised up to 175 μm pp at 1688rpm and 137 μm pp at FSNL,
- after synchronization, for 10 minutes, a 22.5Hz sub synchronous component was noticed with direct values raising up to 223 μm pp.
- when load was 33MW, this sub synchronous component decreased to 78 μm pp.

2 Data collection

Scope of the visit was to collect vibration data during start up, steady state operation at different operating modes (different load conditions) and shutdown to understand the root cause of the problem.

During visit other measurements were performed: the shafts relative vibration was collected by multichannel data collector, using permanently installed probes connected to protection system racks. Following measurements were used for analysis:

- Stopped unit.
- Cold startup.
- Unit at steady state operation at full speed no load.
- Unit at steady state operation at full speed with loading up to nominal load.
- Unit planned shutdown.

Train diagram with measurement point location is presented in fig.1

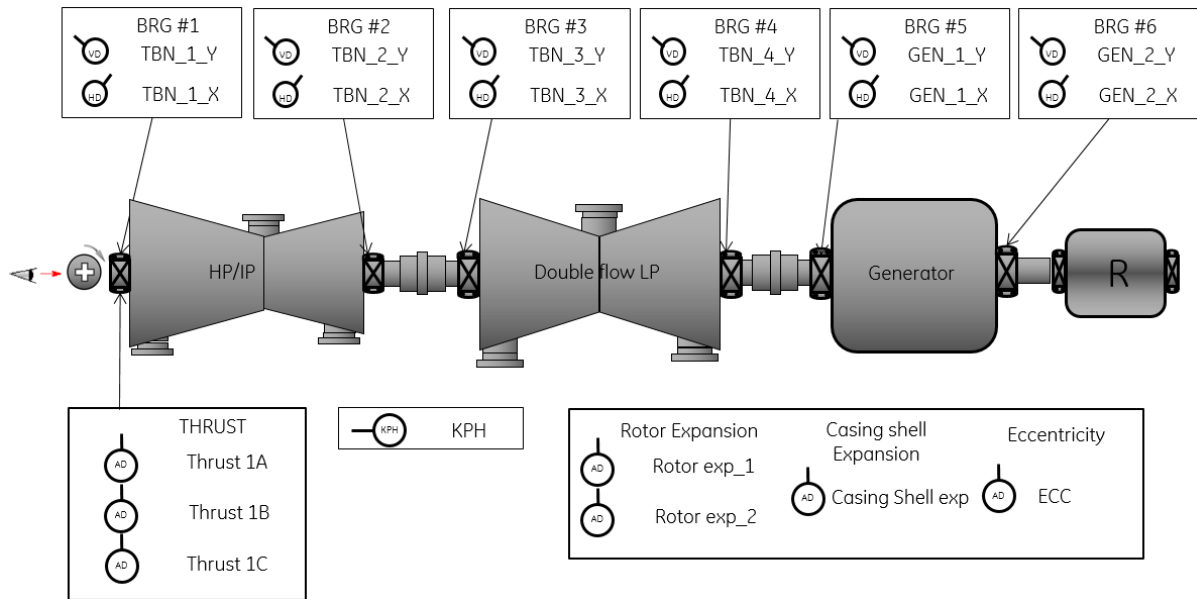


Figure 1: Train diagram with permanently installed transducers, connected to monitoring system.

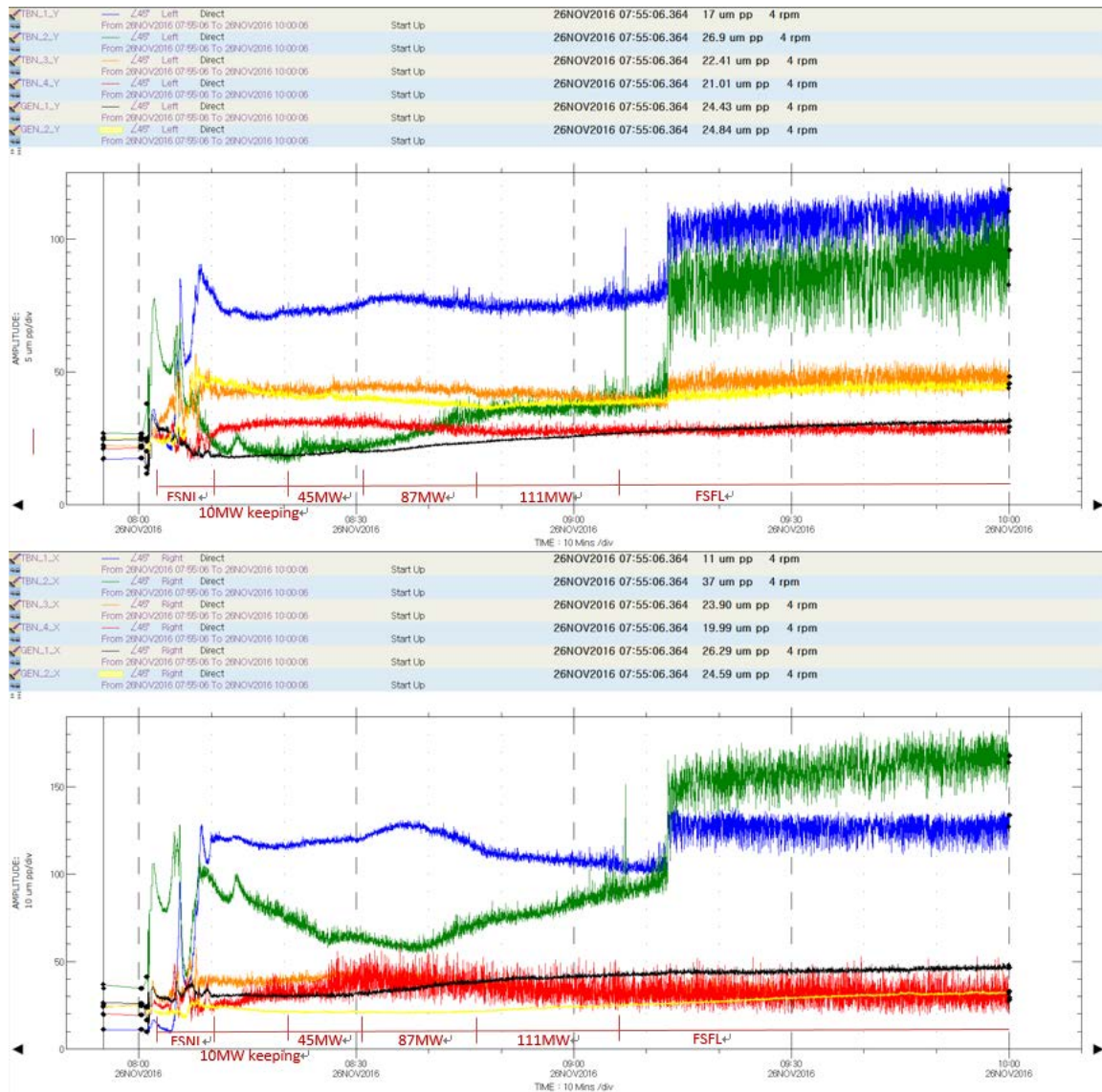


Figure 2: Direct trend, shaft relative vibration during startup, loading and operation at nominal load. Vibration suddenly increased at full load.

HP/IP direct shaft relative vibration trend analysis for unit startup and loading up to nominal load on 26th of Nov 2016 indicated that vibration amplitudes of BRG#1,2 were rapidly raising up at full load(163MW). While the unit was kept at full load, high vibration event suddenly occurred. The direct vibration amplitude of BRG#2 increased by 63um pp, increased by 22 um pp for BRG#1. This vibration increase was not due to 1X component (See fig.2, 3 for details). The 1X component did not change during that event.

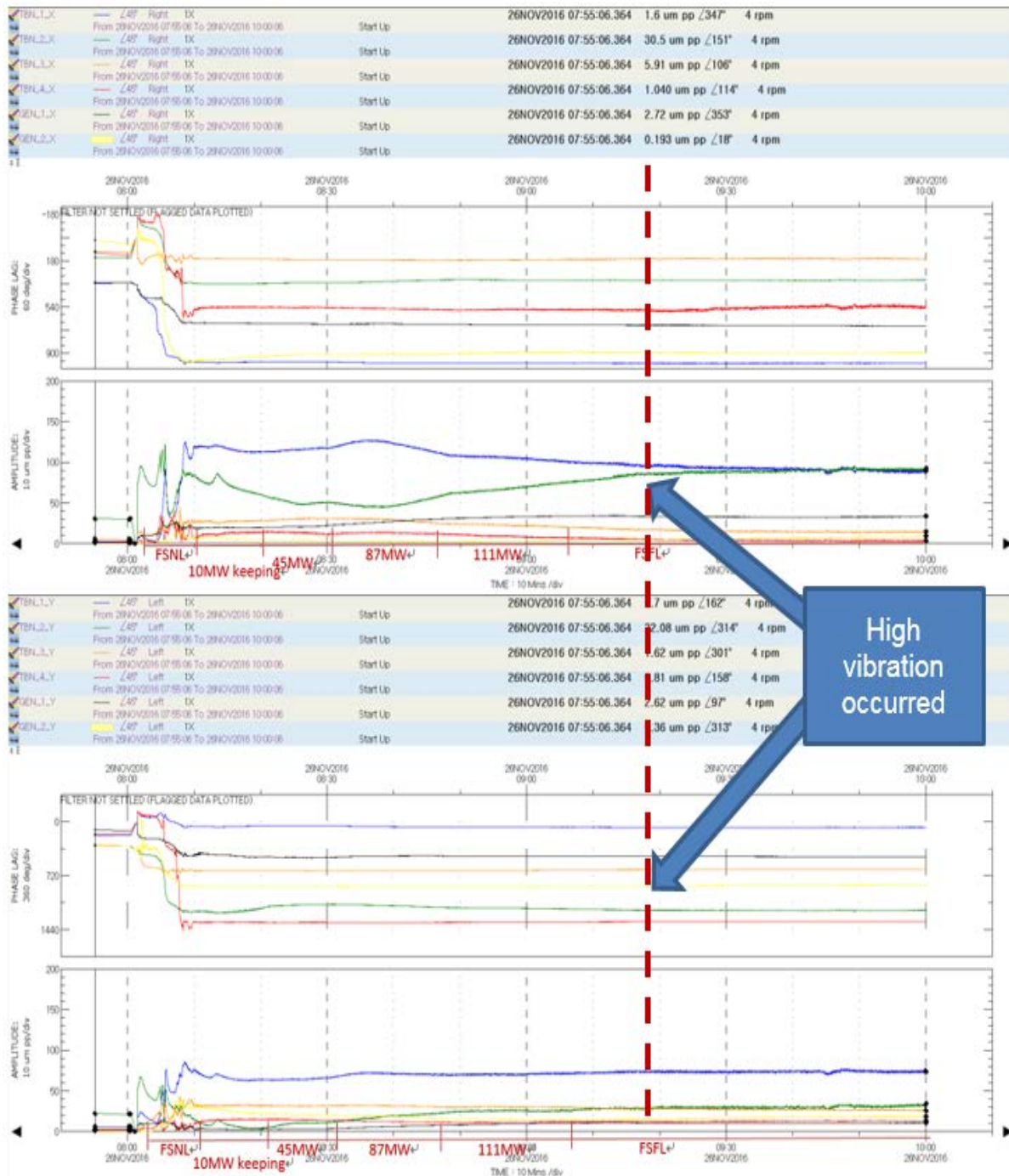


Figure 3: Trend of 1X filtered component, shaft relative vibration during startup, loading and operation at nominal load. There aren't any changes in 1X component when the direct level increased.

In addition, at unit shut down status, this high vibration level subsynchronous component disappeared immediately after shut down command - at 3540 RPM (fig. 4). It was concluded that vibration spike at 22.5 Hz nature was not speed related, but load and some operation conditions related.

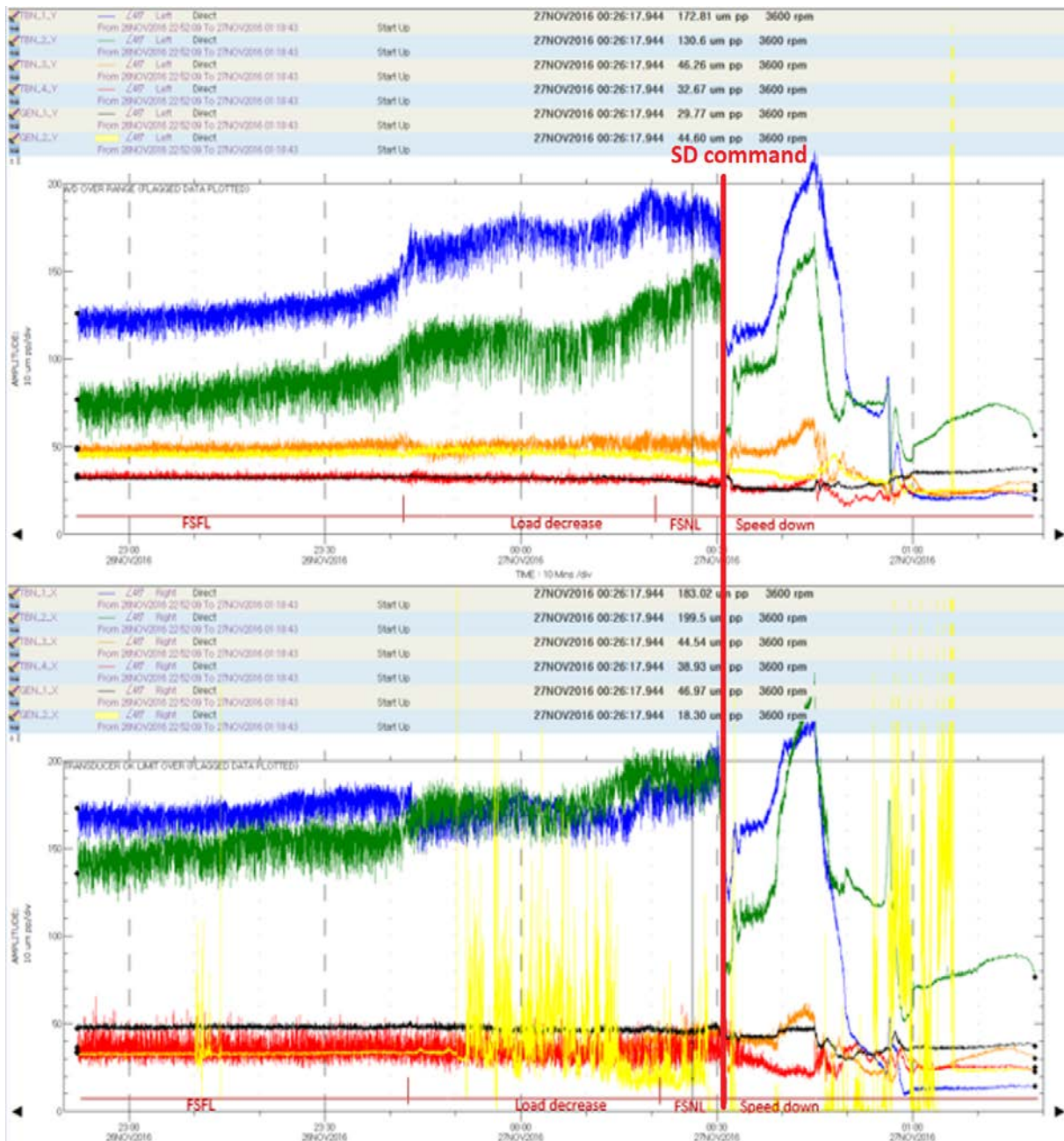


Figure 4: Trend of direct shaft relative vibration during unit shutdown.

(The yellow spikes - generator NDE bearing X probe should be ignored – it is temporary line connection issue, because of using BNC T connectors to split signal for different system usage).

3 Data analysis and malfunction investigation.

The analysis of full spectrum waterfall plot indicated that the dominant component was 22.5 Hz with forward precession. This subharmonic was close to 0.375X component of generator nominal operation speed (fig. 5). It could be noticed on the full spectrum of BRG#2 that this 22.5Hz component was appearing and disappearing. The filtered 0.375X component trend lines indicated that this sub synchronous component was suddenly raising like the direct trend while the Unit was already at the full load (fig 6).

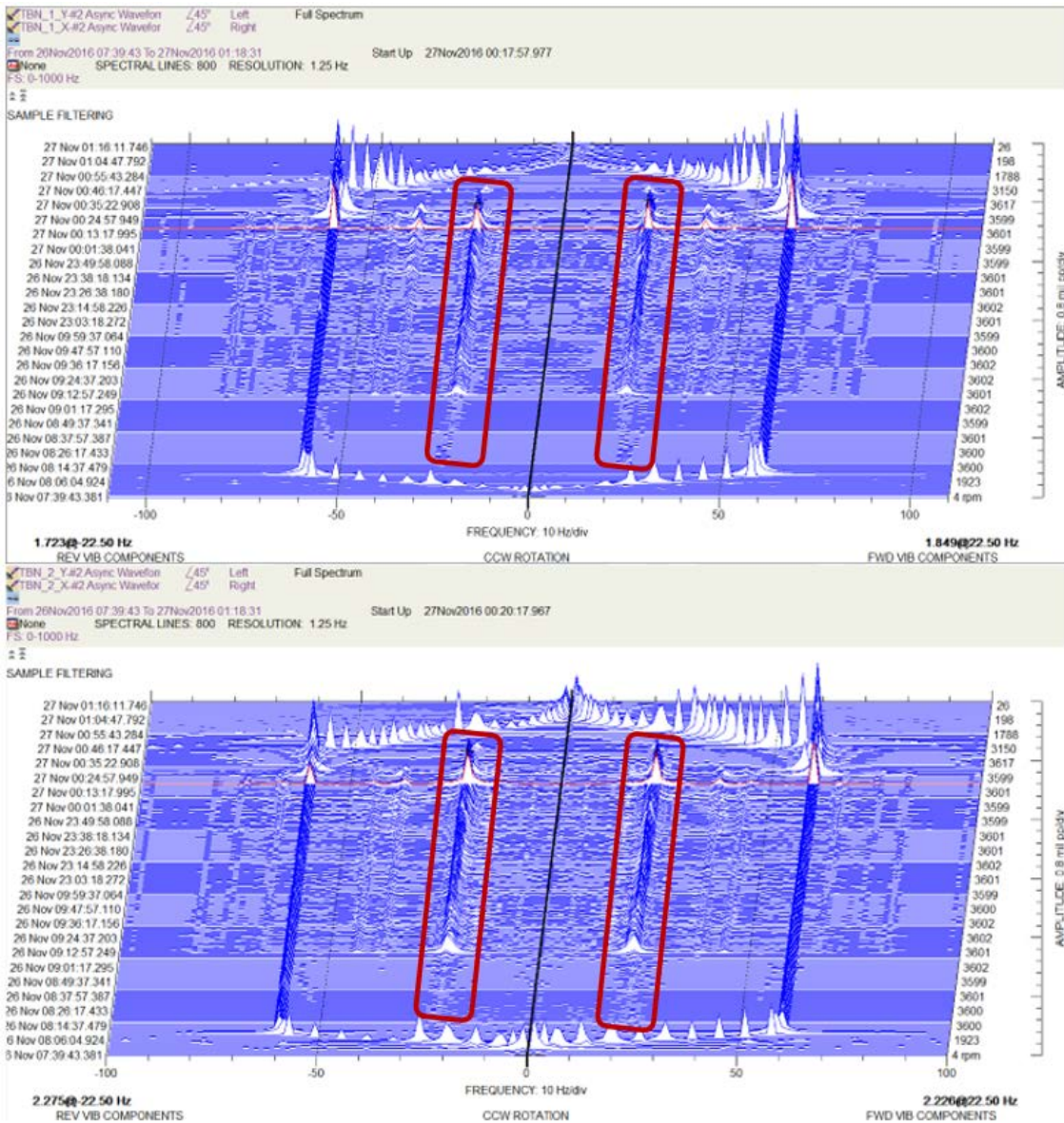


Figure 5: Full spectrum waterfall shaft relative vibration during Unit startup, loading and shutdown. Amplitude changes for 22.5Hz component during Unit operation.

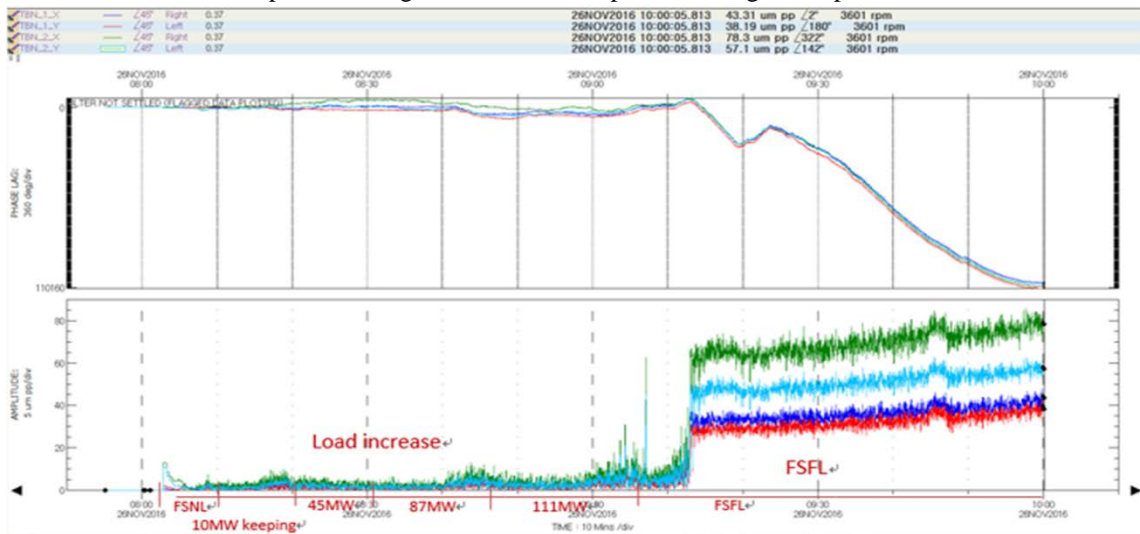


Figure 6: Trend of 0.375X filtered component, shaft relative vibration during startup, loading and operation at nominal load. Vibration amplitude suddenly increased at nominal load.

The shutdown trend of 0.375X component is also showing almost the same trend behavior as the one of the direct trend. The amplitude of this component decreased significantly just after shutdown (fig. 7).

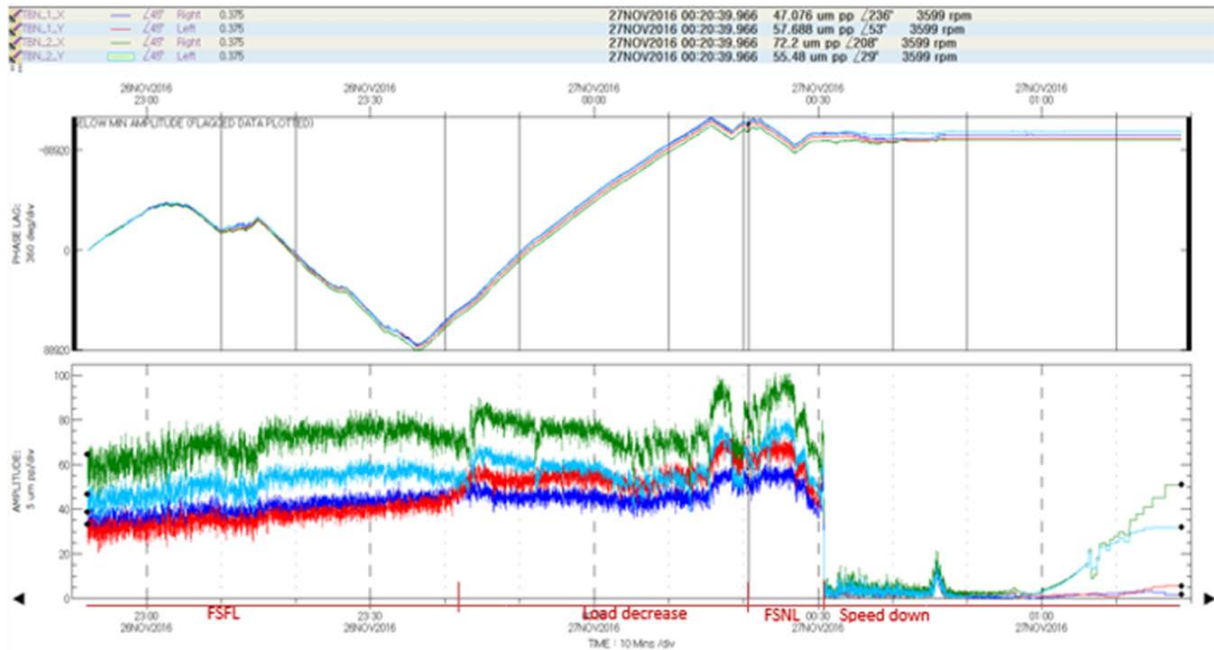


Figure 7: Trend of 0.375X filtered component, shaft relative vibration during Shutdown. High vibration level subsynchronous component disappeared immediately after shut down command.

The phase data analysis of filtered 0.375X shaft rotation component was demonstrating app. 40 degrees phase leading for BRG#2 (fig. 8). From this analysis it could be assumed that the source of instability was close to BRG#2. This analysis of the sub synchronous component relative phase made it possible to assume the location of the source of instability. The source of instability was on the side of the plane with the leading phase, BRG#2 plane. Final conclusion would be possible made only using modeling, based on rotor design.

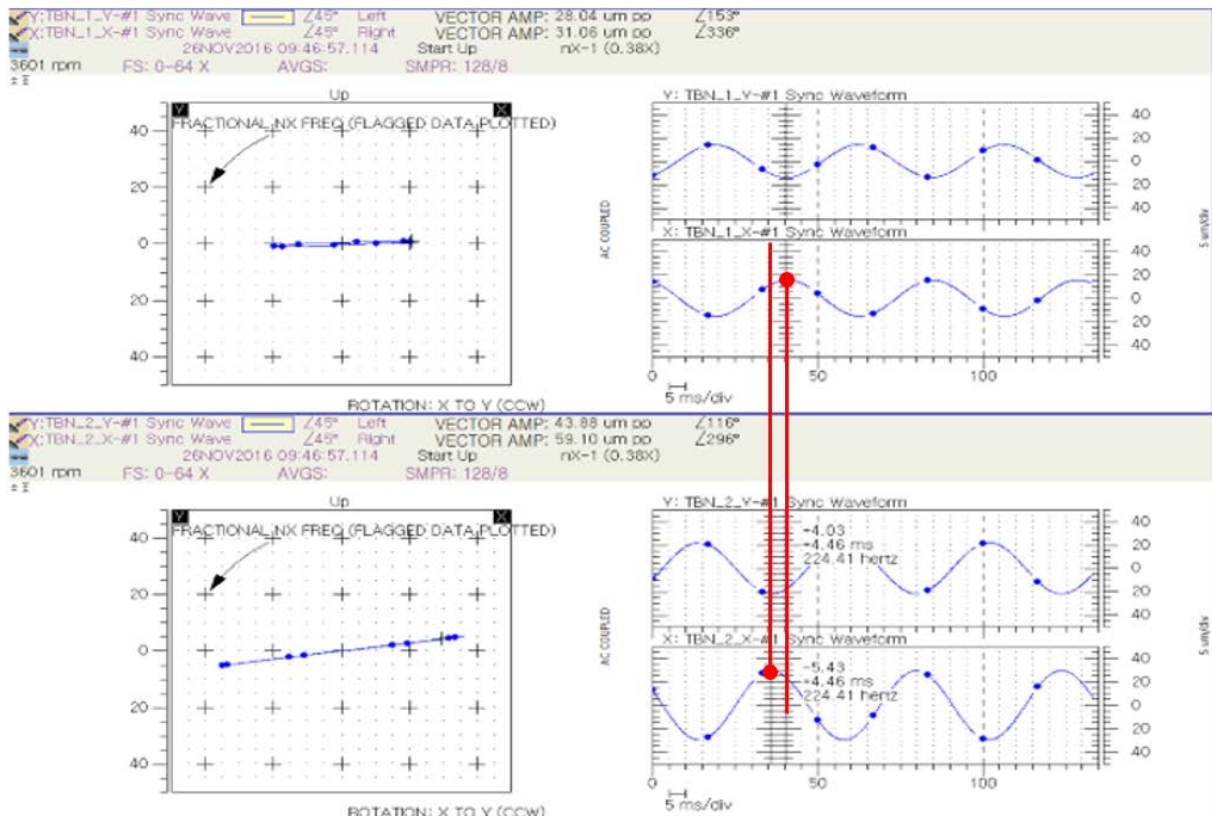


Figure 8: Orbit plot for of 0.375X filtered component, shaft relative vibration during High vibration event at full load. 40 degrees phase leading for BRG#2 plane detected.

No significant changes in the shaft centerline was detected when the 22.5Hz component appeared at FSFL and disappeared during SD (fig. 9).

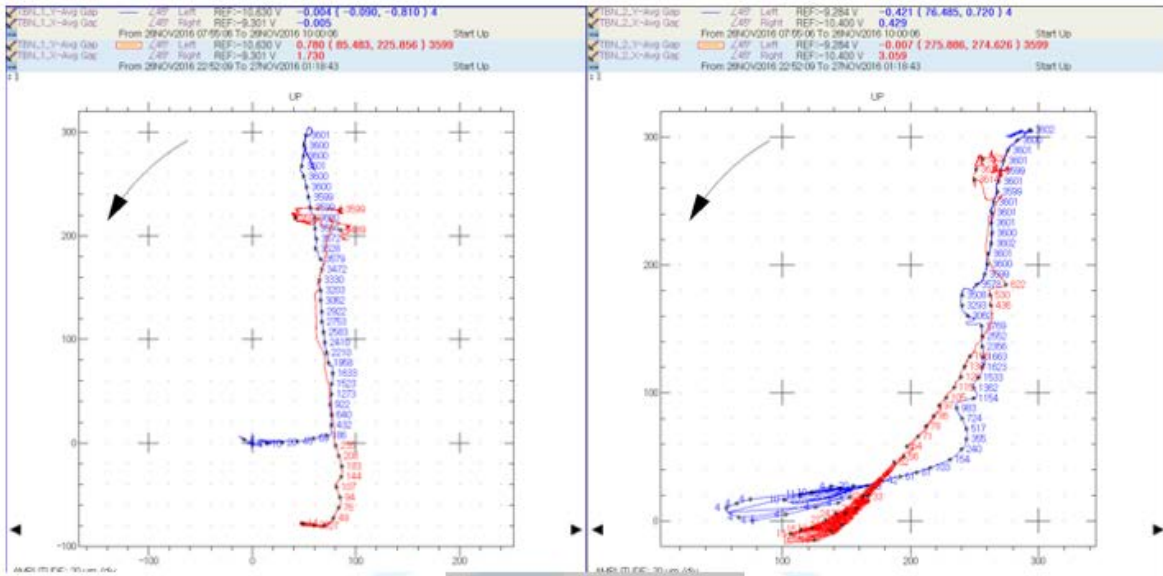


Figure 9: Shaft centerline plots for HP/IP turbine bearings, Blue - Unit startup, Red - shutdown. Stable shaft centerline position during steady state operation mode.

There was clear sign of discussed 22.5Hz component in the waterfall plot after overhaul condition, whereas before overhauling it was absent (Fig. 10). This historical data presented by customer was using legacy condition monitoring software. Based on data collected by customer prior overhaul there were no any abnormalities, mechanical malfunctions, abnormal bearing load conditions detected for this unit.

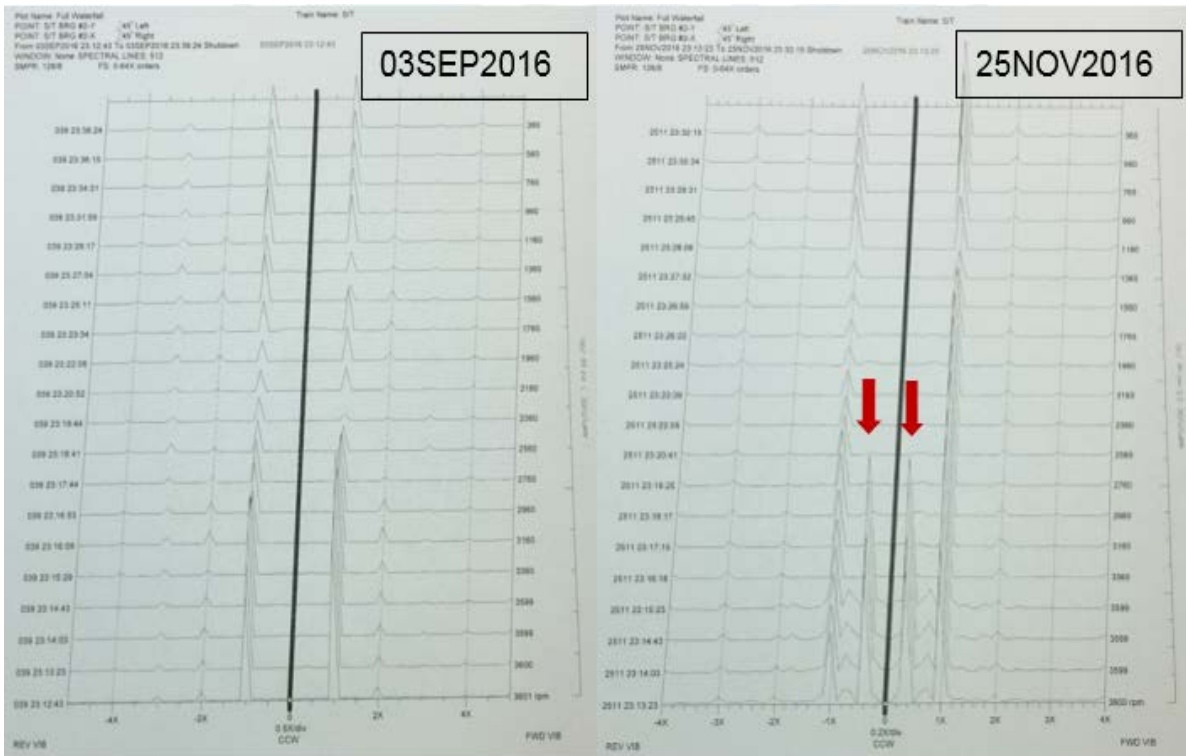


Figure 10: Full cascade plots of BRG#2. Left-before overhaul, right-after overhaul.

When reading historical report, it was found the following comment “Replace to HIP retractable packings (1 antiswirl conv./14 retr. /2 brush) and N2 conventional packings.”. This high vibration situation had not occurred before ST outage (2016 10.01 ~ 10.31 class A).

The HP / IP stage of this steam turbine is equipped with anti-swirl system (fig. 11), which is designed to prevent the circular motion of steam in the seals. Based on the data provided, it is possible to derive a conclusion about the malfunctioning of this anti-swirl packages.

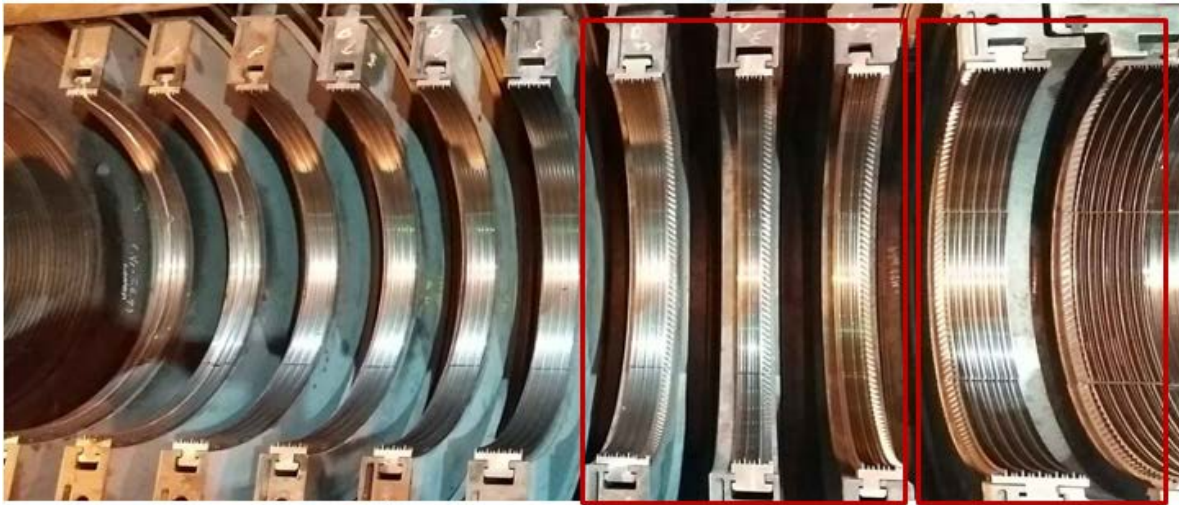


Figure 11: Replaced Original Anti-swirl packages.

When the machine becomes unstable, the source of the instability is the steam in motion. By definition, the frequency of the steam in motion will be $\lambda\Omega$ (the average circumferential steam velocity ratio times the rotative speed). Typically, λ is less than one-half synchronous speed. Under this condition, the Keyphasor dots on the orbit will appear to be rotating opposite sense of rotation of the shaft on the scope. This effect is an illusion and can best be explained using illustration (fig.12). The Keyphasors appear to be moving on the orbit and appear to be moving opposite the direction of vibration when the frequency is less than $1/2X$. The sequence of the blank/bright on the orbit and the direction of precession from the timebase shows that the vibration is forward precessing. The forward precession is reasonable because the exciting force is the circumferential flow of the fluid matched with the shaft rotation. The steam circular flow in the seals, that is moving at the frequency equal to the rotor's natural frequency excites the rotor's 1st horizontal natural frequency and these forces increase at higher load/steam flow and disappeared just after steam cut during shutdown process.

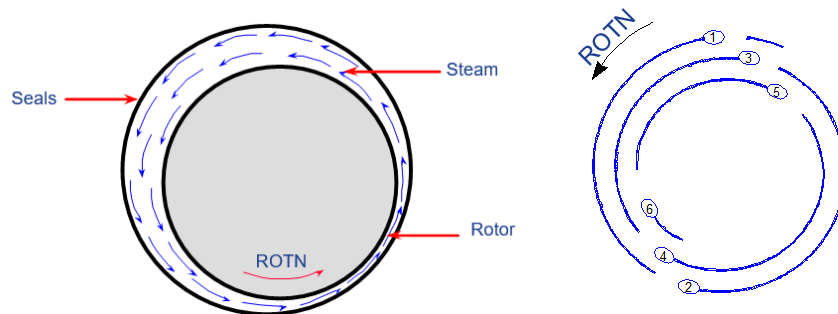


Figure 12: Examples of steam in circumferential motion (left) and Orbit plot (right), approximately two Keyphasor dots occurring within each cycle of vibration, changing their position slowly from cycle to cycle.

4 Conclusions.

The reason for this investigation was the increased shaft relative vibration level of the steam turbine after the planned overhaul. The STG BRG#1,2 direct level reached the Danger setpoint of 229 um pp established by the turbine manufacturer.

A sudden increase in the level of vibration during the operation of the turbine at nominal load is recorded. The dominated component of vibration was 22.5 Hz (0.375 harmonic of the rotor nominal speed). The amplitude of this component decreased significantly just after shutdown command.

The HP / IP stage of this steam turbine is equipped with anti-swirl system, which is designed to prevent the circular motion of steam in the seals. Based on the data provided, it is possible to derive a conclusion about the malfunctioning of this anti-swirl packages.

This analysis of the sub synchronous component relative phase makes it possible to assume the location of the source of instability. The source of instability was on the side of the plane with the leading phase, BRG#2 plane.

Based on presented data analysis it was recommended to inspect installed HP/IP steam turbine stage anti-swirl system, as it was expected that this system was installed or operated not properly. Original anti-swirl package installation had been suggested to the customer to increase stability threshold and allow Unit to operate at full load with acceptable vibration level.

Below are short-term and long-term solutions, accepted by customer:

- short term - to limit unit load, operate below stability threshold, MW;
- long term: steam turbine replacement by new, same model unit.

After one year of operation with limited load turbine was replaced by a new one.

This case is a good example of how proper machinery diagnostic service, based on deep machinery diagnostic service team's theoretical knowledge and practical skills, allowed reasonable corrections actions to be taken on site based on correct analysis.

References

- Robert C. Eisenmann, Sr., P.E. and Robert C. Eisenmann, Jr. (2005): *Vibration Analysis and Troubleshooting for the Process Industries*. Pearson Education, Inc.
- GE Oil & Gas, DS Bently Nevada *Machinery diagnostic technical training. Fluid Induced instability*. (2015)
- GE Oil & Gas, DS Bently Nevada *Advanced machinery dynamic training*. (2015)

Advanced Numerical Tools & Nonlinearities

Numerical Schemes for Quasi-Periodic Oscillations and Synchronisation in Rotordynamics

Simon Bäuerle¹, Hartmut Hetzler²

¹ Institute of Mechanics, University of Kassel, 34125 Kassel, Germany, baeuerle@uni-kassel.de

² Institute of Mechanics, University of Kassel, 34125 Kassel, Germany, hetzler@uni-kassel.de

Abstract

Quasi-periodic oscillations are a typical phenomenon in rotordynamics: unbalance induced rotor motions can become unstable e.g. due to self-excitation adding another frequency to the synchronous one. In general, the irrational quotients of two or more frequencies lead to an infinitely long period duration making time integration inexpedient for computing stationary solutions. To circumvent this problem, methods have been proposed in literature, which transform the time argument to a higher dimensional, but finite coordinate space. An often encountered problem in continuing these solutions along e.g. the rotational speed is synchronisation. This can lead to a failure of these methods since the dimension of the coordinate space is suddenly reduced due to the entrained frequency. In this contribution, this problem is approached numerically. A modified *Newton*-scheme is presented which identifies synchronisation automatically. The algorithm in combination with a *Fourier-Galerkin* method is demonstrated for a forced *van-der-Pol* oscillator and a *Jeffcott*-rotor with a visco-elastically supported seal.

1 Introduction

Many systems in nature and technique contain more than one source of excitation: the occurrence of solar flares is influenced by energy load/unload releases and magnetohydrodynamic processes [19]. Another example is the electrical activity in the gastrointestinal tract, which is dictated by different muscle sections, each having its own frequency [15]. In electronics, frequency mixer circuits are driven by multiple external input signals with different frequencies [8]. Such multiple excitation mechanisms can also be found in the field of rotordynamics: material damping, non-circular shafts, fluid forces in journal bearings/ seals and the ever-present mass unbalance. These different sources of excitation might enforce stationary system responses with distinct frequencies. In general, these frequencies do not maintain a fixed ratio to each other under system parameter variations. For example: a frequency due to excitation by mass unbalance and a self-excited frequency due to forces in journal bearings (oil whirl) do not maintain a fixed ratio when the rotor speed is changed. Furthermore, such frequencies do not have to be whole-number multiples of each other: in this case they are incommensurable. If a signal is in addition not sensitive to its initial conditions (which would be the case of chaos [5]), then it is called quasi-periodic.

These distinct kinds of solutions have been known since the 19th century, when integrable *Hamiltonian* systems were investigated: here, quasi-periodic solutions emerge naturally since the angle variables can be viewed as a torus of n -th dimension [2]. One important consequence from a practical point of view is, that the incommensurability of the frequencies leads to an infinitely long period duration. Thus, the choices of methods for computing stationary quasi-periodic solutions are limited, since standard methods like time integration are not able to fully characterise the solution and classical shooting methods are not applicable.

During the last 80 years, different classes of specialised solution methods were developed to address this problem. *Krylov* and *Bogoliubov* started in the 1930's amongst others to investigate quasi-periodic solutions of weakly non-linear systems by usage of perturbation methods (for a review article see [1]). Probably the first numerical method was developed by *Brommundt* in 1970 [6], where he approximated quasi-periodic solutions by neighbouring periodic solutions. In 1981, *Chua* and *Ushida* used the *Spectral Harmonic Balance Method*¹ to characterize signals known from time simulation by multifrequent *Fourier* series.

Using *Poincaré* maps and sections is another approach: periodic orbits appear as points, whereas quasi-periodic

¹*Spectral Harmonic Balance* often describes the generalization of the *Harmonic Balance Method* for quasi-periodic solutions.

solutions densely fill out a closed curve². In 1985, *Kaas-Peterson* defined probably the first method for quasi-periodic solutions. The advantage of these methods is, that statements on solution stability can be formulated relatively 'easy'.

One important group of methods (referred to as *Tori of ODEs* by [23]) tackles the problem of infinitely long solution periods w.r.t. the time coordinate t by introducing multiple new coordinates. As a consequence the definition domain is now higher-dimensional but finite and one has, therefore, to solve partial differential equations for the invariant (solution) manifold rather than an ordinary one. In 1987 *Samoilenko* used a multidimensional *Fourier* series [22], whereas *Dieci et al.* [9] used a leap-frog scheme in 1991 to solve the mentioned PDEs. Both parametrized the manifold with radii and angles (torus coordinates), whereby the angles are not constant. *Schilder et al.* introduced in 2005 a new parametrization of the work of *Samoilenko* which leads to constant angles. *Schilder et al.* solved the resulting PDEs with finite differences [23] and with a *Fourier-Galerkin* series in 2006 [24], which is the approach used in this publication.

The investigation of quasi-periodic motions in rotordynamics with the aforementioned methods started - as far as the authors are aware - in 1993 with publications from *van der Heijden* [11] on drill string dynamics and *Zhao et al.* [26] on squeeze film damper supported stiff rotors. Both used *Poincaré* maps to access the behaviour. One of the first uses of the now popular *Spectral Harmonic Balance Method* (aka *Fourier-Galerkin Method*) in rotordynamics was by *Kim et al.* in 1996/1997 [13, 14] who looked at a *Jeffcott* rotor with bearing clearances. The same system was also investigated in more recent publications by *Guskov et al.* in 2008 [10] and *Peletan et al.* in 2014 [21], who automatically selected harmonic multiples.

2 Theory and Method

2.1 Mathematical Background

Incommensurability p frequencies γ_j are said to be rationally independent (incommensurable) to each other, if $\mathbf{a}^\top \boldsymbol{\gamma} = \sum_{j=1}^p a_j \gamma_j = 0$, with the coefficients being integers $\mathbf{a} \in \mathbb{Z}^p$, holds only for $\mathbf{a} = [0, 0, \dots, 0]^\top$. In a signal with at least two incommensurable frequencies no finite period length can be found.

Quasi-periodic function A function $\mathbf{x}(\boldsymbol{\gamma}^\top t) = \mathbf{x}(\gamma_1 t, \gamma_2 t, \dots, \gamma_p t) \in \mathbb{R}^{q \times 1}$ is called quasi-periodic, if $\boldsymbol{\gamma}$ is a vector containing p incommensurable frequencies and if the function is periodic in each single frequency with the other ones fixed.

Base frequencies The incommensurable frequencies $\boldsymbol{\gamma} \in \mathbb{R}^p$ of a quasi-periodic function $\mathbf{x}(\boldsymbol{\gamma}^\top t)$ are called base frequencies, if there is no other set of frequencies $\tilde{\boldsymbol{\gamma}} \in \mathbb{R}^s$ with $s < p$ for which $\mathbf{x}(\boldsymbol{\gamma}^\top t) = \mathbf{x}(\tilde{\boldsymbol{\gamma}}^\top t)$ holds. Please note, that $\boldsymbol{\gamma}$ is not unique.

Torus function, torus and coordinates A function $\mathbf{u}(\boldsymbol{\theta}) = \mathbf{u}(\theta_1, \theta_2, \dots, \theta_p) \in \mathbb{R}^{q \times p}$, $\theta_i \in [0, 2\pi)$, $i = 1, \dots, p$ is called torus function. The image of that function is a manifold and called a p -torus. $\boldsymbol{\theta}$ are called torus coordinates and the domain of the function \mathbf{u} coordinate torus.

Density If the torus function \mathbf{u} is a solution or an invariant manifold, respectively, then the solution trajectories of the corresponding quasi-periodic function $\mathbf{x}(\boldsymbol{\gamma}^\top t)$ are lying on that torus and fill this torus densely [5]. This is, broadly speaking, one of the properties which allows the investigation of quasi-periodic motions by torus functions.

Stone-Weierstraß approximation theorem The theorem states in particular that a torus function $\mathbf{u}(\boldsymbol{\theta})$ can be approximated by a multidimensional *Fourier* series \mathbf{u}_N (cf. eq. (6)) since $\lim_{N \rightarrow \infty} \|\mathbf{u} - \mathbf{u}_N\|_0 = 0$ holds. Due to the fact, that $\mathbf{x}(\boldsymbol{\gamma}^\top t)$ fills $\mathbf{u}(\boldsymbol{\theta})$ densely, $\mathbf{x}(\boldsymbol{\gamma}^\top t)$ can be approximated by a quasi-periodic *Fourier-series* \mathbf{x}_N (cf. eq. (2)), since there exists a N for which $\sup_{t \in \mathbb{R}} \|\mathbf{x} - \mathbf{x}_N\| < \varepsilon$ holds for any $\varepsilon > 0$ [16].

2.2 Fourier-Galerkin Method

The ordinary differential equation

$$\mathbf{M} \ddot{\mathbf{x}} + \mathbf{B} \dot{\mathbf{x}} + \mathbf{K} \mathbf{x} + \mathbf{f}(\dot{\mathbf{x}}, \mathbf{x}, \boldsymbol{\Omega} t) = \mathbf{0}, \quad (1)$$

is considered, where \mathbf{M} , \mathbf{B} and \mathbf{K} are the mass, velocity- and position-proportional matrices, $\mathbf{x} \in \mathbb{R}^q$ is a solution vector, \mathbf{f} is a vector containing all non-linear and explicitly time-dependent terms and $\boldsymbol{\Omega} = [\Omega_j]^\top$, $j = 1, \dots, m$ is a vector containing all m non-autonomous incommensurable base frequencies. Suppose that (1) has a quasi-periodic solution with p incommensurable base frequencies $\boldsymbol{\gamma} = [\Omega_j, \omega_k]^\top$, $j = 1, \dots, m$, $k = (m + 1), \dots, p$, where ω_k are autonomous incommensurable base frequencies (e.g. due to self-excitation). This solution is approximated with a

²Depending on the number of base frequencies, several appropriate *Poincaré* maps might be needed.

generalised truncated *Fourier* series

$$\mathbf{x}_N(t) = \mathbf{c}_0 + \sum_{\|(\mathbf{H})_n\| \leq R} [\mathbf{c}_n \cos((\mathbf{H})_n^\top \gamma t) + \mathbf{s}_n \sin((\mathbf{H})_n^\top \gamma t)], \quad (2)$$

where the approximation is reasonable, since the *Stone-Weierstraß* approximation theorem holds. $\mathbf{c}_0, \mathbf{c}_j, \mathbf{s}_j$ are *Fourier* coefficient vectors and $(\mathbf{H})_n$ is the n -th column of the harmonic multiples matrix $\mathbf{H} \in \mathbb{Z}^{(p \times N)}$, where

$$\mathbf{H} = \begin{bmatrix} 1 & 0 & 1 & 2 & \dots \\ 0 & 1 & 1 & 1 & \dots \end{bmatrix} \quad \cos(\mathbf{H}_4^\top \gamma t) = \cos([2 \ 1] \begin{pmatrix} \Omega \\ \omega \end{pmatrix} t) = \cos(2\Omega t + \omega t) \quad (3)$$

shows an example for two base frequencies. The scalar N is the number of possible combinations, which meet the condition $\|(\mathbf{H})_n\| \leq R$ (multi-index). The torus coordinates (also called hyper time) $\boldsymbol{\theta} = \theta_j \ j = 1, \dots, p$ and the implied differential operator are defined by

$$\boldsymbol{\theta} = \gamma t \quad \rightarrow \quad \frac{d}{dt} = \sum_{j=1}^p \gamma_j \frac{\partial}{\partial \theta_j} = \boldsymbol{\gamma}^\top \boldsymbol{\partial}_\theta. \quad (4)$$

Inserting (4) into equations (1) and (2) gives

$$\mathbf{M} [\boldsymbol{\gamma}^\top \boldsymbol{\partial}_\theta]^2 \mathbf{u}(\boldsymbol{\theta}) + \mathbf{B} [\boldsymbol{\gamma}^\top \boldsymbol{\partial}_\theta] \mathbf{u}(\boldsymbol{\theta}) + \mathbf{K} \mathbf{u}(\boldsymbol{\theta}) + \mathbf{f}([\boldsymbol{\gamma}^\top \boldsymbol{\partial}_\theta] \mathbf{u}(\boldsymbol{\theta}), \mathbf{u}(\boldsymbol{\theta}), [\theta_1, \dots, \theta_m]^\top) = \mathbf{0} \quad (5)$$

$$\mathbf{u}_N(\boldsymbol{\theta}) = \mathbf{c}_0 + \sum_{\|(\mathbf{H})_n\| \leq R} [\mathbf{c}_n \cos((\mathbf{H})_n^\top \boldsymbol{\theta}) + \mathbf{s}_n \sin((\mathbf{H})_n^\top \boldsymbol{\theta})]. \quad (6)$$

Equations (5) are partial differential equations and $\mathbf{u}(\boldsymbol{\theta}), \mathbf{u}_N(\boldsymbol{\theta}) : \mathbb{R}^p \mapsto \mathbb{R}^{q \times p}$. Describing an invariant manifold³, equations (5) are often referred to as invariance equations. The transformation to torus coordinates is a valid operation since \mathbf{x} lies densely in \mathbf{u} , which applies to equations (5) and (6) equally, as does the *Stone-Weierstraß* approximation theorem. Inserting the *Fourier* series (6) into PDEs (5) defines the residuum vector

$$\mathbf{R}(\boldsymbol{\theta}) = \mathbf{M} [\boldsymbol{\gamma}^\top \boldsymbol{\partial}_\theta]^2 \mathbf{u}_N(\boldsymbol{\theta}) + \mathbf{B} [\boldsymbol{\gamma}^\top \boldsymbol{\partial}_\theta] \mathbf{u}_N(\boldsymbol{\theta}) + \mathbf{K} \mathbf{u}_N(\boldsymbol{\theta}) + \mathbf{f}([\boldsymbol{\gamma}^\top \boldsymbol{\partial}_\theta] \mathbf{u}_N(\boldsymbol{\theta}), \mathbf{u}_N(\boldsymbol{\theta}), [\theta_1, \dots, \theta_m]^\top). \quad (7)$$

By projecting \mathbf{R} to the subspace spanned by the base functions $\{1, \{\cos((\mathbf{H})_n^\top \boldsymbol{\theta}), \sin((\mathbf{H})_n^\top \boldsymbol{\theta})\}, n = 1, \dots, N\}$

$$\frac{1}{(2\pi)^p} \int_{\boldsymbol{\theta}} \mathbf{R}(\boldsymbol{\theta}) d\boldsymbol{\theta} = \mathbf{0}, \quad \left\{ \frac{1}{(2\pi)^p} \int_{\boldsymbol{\theta}} \mathbf{R}(\boldsymbol{\theta}) \cos((\mathbf{H})_n^\top \boldsymbol{\theta}) d\boldsymbol{\theta} = \mathbf{0}, \quad \frac{1}{(2\pi)^p} \int_{\boldsymbol{\theta}} \mathbf{R}(\boldsymbol{\theta}) \sin((\mathbf{H})_n^\top \boldsymbol{\theta}) d\boldsymbol{\theta} = \mathbf{0} \right\} n = 1, \dots, N \quad (8)$$

$q \times (2N + 1)$ equations are attained to determine the $q \times (2N + 1)$ *Fourier* coefficients. Here, $\int_{\boldsymbol{\theta}} (\cdot) d\boldsymbol{\theta}$ is a multiple integral over all p dimensions of the coordinate torus in the intervals $[0, 2\pi)$. The projection of the linear parts can be performed analytically, whereas the projections of the non-linear terms \mathbf{f} is in general not explicitly available. In fact, the projection via multiple integrals over a finite interval $[0, 2\pi)$ instead of one integral over an infinite time period is the pay-off for the transformation from a one- to a p -dimensional space. Since the $p - m$ autonomous frequencies ω_k are also unknowns, additional equations are needed. Due to the fact, that solutions modelled by autonomous differential equations are translational invariant (which means that a time or phase shifted solution of the equation is also a solution) so-called phase condition can be implied. There are multiple possibilities to formulate such equations. Here, the integral *Poincaré* condition [24]

$$\frac{1}{(2\pi)^p} \int_{\boldsymbol{\theta}} \left\langle \frac{\partial \tilde{\mathbf{u}}}{\partial \theta_j}, \mathbf{u} \right\rangle d\boldsymbol{\theta} = 0 \quad j \in [m + 1, p], \quad (9)$$

³ In this context, an invariant manifold is a solution to a dynamical system and constitutes a hyperplane in phase space, where trajectories stay on that plane if they started on it [25].

is used, where $\langle(\cdot)\rangle$ is the scalar product between functions. This condition can be derived by demanding a minimal deviation between the current solution \mathbf{u} and a close neighbouring solution⁴ $\tilde{\mathbf{u}}$ w.r.t. time or phase translation of the autonomous solution [20]. The now closed algebraic equation system

$$\mathbf{b} = \begin{cases} \mathbf{K}\mathbf{c}_0 + \frac{1}{(2\pi)^p} \int_{\theta} \mathbf{f} d\theta = \mathbf{0} \\ \left[\mathbf{K} - ((\mathbf{H})_n^\top \gamma)^2 \mathbf{M} \right] \mathbf{c}_n + (\mathbf{H})_n^\top \gamma \mathbf{B} \mathbf{s}_n + \frac{1}{(2\pi)^p} \int_{\theta} \mathbf{f} \cos((\mathbf{H})_n^\top \theta) d\theta = \mathbf{0} \\ -(\mathbf{H})_n^\top \gamma \mathbf{B} \mathbf{c}_n + \left[\mathbf{K} - ((\mathbf{H})_n^\top \gamma)^2 \mathbf{M} \right] \mathbf{s}_n + \frac{1}{(2\pi)^p} \int_{\theta} \mathbf{f} \sin((\mathbf{H})_n^\top \theta) d\theta = \mathbf{0} \end{cases} n \in [1, N] \quad (10)$$

$$\frac{1}{(2\pi)^p} \int_{\theta} \left\langle \frac{\partial \tilde{\mathbf{u}}_N}{\partial \theta_j}, \mathbf{u}_N \right\rangle d\theta = 0 \quad j \in [m+1, p]$$

has $q \times (2N + 1) + (p - m)$ equations for $q \times (2N + 1)$ unknown *Fourier* coefficients and $(p - m)$ unknown autonomous frequencies.

Implementation The method was implemented in MATLAB using a *Newton*-type solver and the *Alternating Frequency Time Method* [7]: the *AFT* uses n -dimensional *FFT* to efficiently compute the projection of the non-linear forces \mathbf{f} on the (in this case complex) base functions. In contrast to the original *AFT*, the term \mathbf{f} is not evaluated with the inverse *FFT* of the *Fourier* coefficients but rather with an explicitly set up *Fourier* series.

2.3 Synchronisation

Within this publication, synchronisation (also called entrainment) is understood as the phenomenon, where one autonomous base frequency disappears in a signal \mathbf{x} over a finite parameter interval due to frequency aka phase locking. The p -torus is reduced to a $p - 1$ torus. This can happen e.g. via a *Neimark-Sacker* bifurcation or a *Saddle-Node* bifurcation of maps (both leading from a quasi-periodic to a periodic solution).

Synchronisation in solutions approximated by *Fourier-Galerkin* Methods are problematic when the solution is continued along a parameter. In general, the exact location of a synchronisation point is not known. Running into or over (in a numerical sense) such a point whilst continuing renders the used ansatz *Fourier* series inadequate since it is still build up with the synchronised and now vanished base frequency. This leads to numerical problems in terms of ill-conditioned Jacobian matrices.

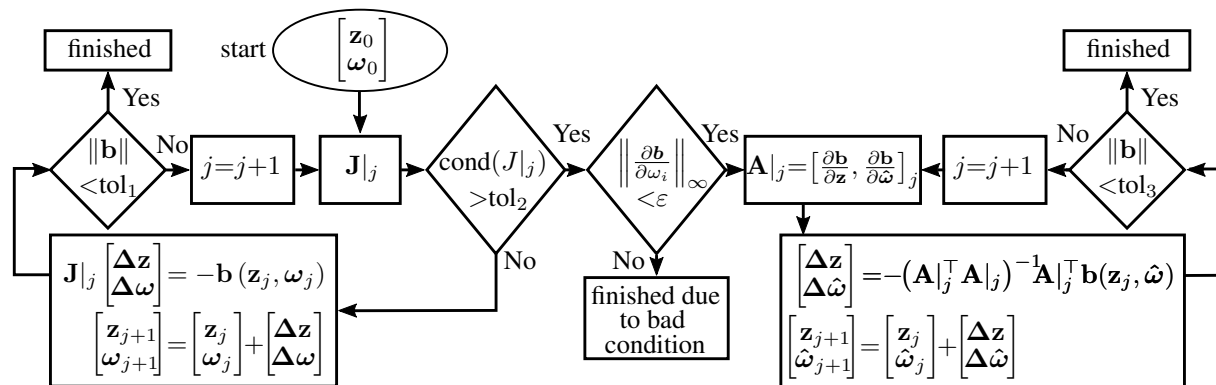


Figure 1: Flow chart of a *Newton*-like algorithm capable of dealing with synchronised frequencies.

Example To illustrate the problem and a solution strategy, the *Fourier-Galerkin* Method is exemplarily applied to an arbitrary ODE. A solution \mathbf{u} is now continued having a non- and an autonomous base frequency $\gamma = (\Omega, \omega)^\top$. Ω is the bifurcation parameter. The solution is a 2-torus (quasi-periodic) for $\Omega = \Omega_1$ and loses a base frequency due to synchronisation at $\Omega = \Omega_2$ rendering it a 1-torus (periodic). Suppose the synchronisation point was passed unnoticed and the solution \mathbf{u} at Ω_2 is falsely tried to be approximated with a 2-dimensional *Fourier* series

$$\mathbf{u}_2 = \mathbf{c}_0 + \mathbf{c}_1 \cos(\theta_1) + \mathbf{c}_2 \cos(\theta_2) + \mathbf{s}_1 \sin(\theta_1) + \mathbf{s}_2 \sin(\theta_2). \quad (11)$$

⁴Such a solution is always known within this scheme, since it can be computed by the initial conditions for the *Newton*-algorithm. These initial conditions are either known from a preceding continuation step or from an appropriate initialisation.

Applying a *Newton*(-like) algorithm to $\mathbf{b}(\mathbf{c}_0, \mathbf{c}_1, \mathbf{c}_2, \mathbf{s}_1, \mathbf{s}_2, \omega) = \mathbf{0}$ (cf. eq. (10)) to solve for $[\mathbf{c}_0, \mathbf{c}_1, \mathbf{c}_2, \mathbf{s}_1, \mathbf{s}_2, \omega]^\top = [\mathbf{z}, \omega]^\top$ gives in the j -th *Newton* iteration

$$\mathbf{J}|_j \begin{bmatrix} \Delta \mathbf{z} \\ \Delta \omega \end{bmatrix} = -\mathbf{b}(\mathbf{z}_j, \omega_j), \quad \begin{bmatrix} \mathbf{z}_{j+1} \\ \omega_{j+1} \end{bmatrix} = \begin{bmatrix} \mathbf{z}_j \\ \omega_j \end{bmatrix} + \begin{bmatrix} \Delta \mathbf{z} \\ \Delta \omega \end{bmatrix}, \quad (12)$$

where \mathbf{J} is the *Jacobi* matrix. This algorithm will break down for $\Omega = \Omega_2$ due to poor condition of \mathbf{J} , since

$$\mathbf{J}|_j = \begin{bmatrix} \frac{\partial \mathbf{b}}{\partial \mathbf{z}} & \frac{\partial \mathbf{b}}{\partial \omega} \end{bmatrix}_j, \quad \left\| \frac{\partial \mathbf{b}}{\partial \omega} \right\|_\infty < \varepsilon \quad (13)$$

is valid at a specific iteration \tilde{j} . The inequality $\left\| \frac{\partial \mathbf{b}}{\partial \omega} \right\|_\infty < \varepsilon$ with the maximum norm $\|(\cdot)\|_\infty$ is fulfilled if the biggest element is smaller than $\varepsilon \ll 1$. For $\Omega = \Omega_2$ the solution \mathbf{u} does no longer depend on ω . The associated *Fourier* coefficients become consequently very small $\mathbf{c}_2 \approx \mathbf{0}$, $\mathbf{s}_2 \approx \mathbf{0}$. The projected residuum \mathbf{b} does therefore no longer vary w.r.t. ω leading to $\left\| \frac{\partial \mathbf{b}}{\partial \omega} \right\|_\infty < \varepsilon$ and, thus, to a poor condition of the matrix.

Implementation The flow-chart of an algorithmic solution to that problem can be seen in figure 1. For convenience only, a *Newton* algorithm is used. With the starting values \mathbf{z}_0, ω_0 the Jacobian $\mathbf{J}|_0$ is evaluated. The condition number $\text{cond}(\mathbf{J}|_0)$ is computed and the algorithm continues in the well known fashion, as long as the condition number stays below a tolerance tol_2 . If it is not meeting the tolerance criteria in some j -th iteration, then the algorithm checks whether there is one column of $\mathbf{J}|_j$, where all absolute values of the contained numbers are smaller than a tolerance ε . In that case, the corresponding column $\frac{\partial \mathbf{b}}{\partial \omega_i}$ is deleted, where ω_i is the relevant, now synchronised frequency. $\hat{\omega}$ are the remaining $(p - m) - 1$ autonomous frequencies. The matrix $\mathbf{A}|_j = \begin{bmatrix} \frac{\partial \mathbf{b}}{\partial \mathbf{z}} & \frac{\partial \mathbf{b}}{\partial \hat{\omega}} \end{bmatrix}_j$ is now set up without the relevant column and the *Moore-Penrose* inverse $\mathbf{A}|_j^+ = (\mathbf{A}|_j^\top \mathbf{A}|_j)^{-1} \mathbf{A}|_j^\top$ is used to compute the new iterated solution vector $[\mathbf{z}_{j+1}, \hat{\omega}_{j+1}]^\top$. This is repeated until $\|\mathbf{b}\| < \text{tol}_3$ is fulfilled. The advantages of this approach are besides its relatively simple implementation, the ability to determine the synchronised frequency as well as to distinguish between a bad conditioned Jacobian due to synchronisation or due to some other reasons.

3 Results

3.1 Forced *van-der-Pol* Oscillator

In a first example, the discussed methods from section 2 are applied to the forced *van-der-Pol* oscillator

$$\ddot{x} - \mu(1 - x^2)\dot{x} + x = \Gamma \cos(\Omega t), \quad (14)$$

where a small non-linearity $\mu = 0.1$ and a strong forcing $\Gamma = 1.2$ is assumed. The non-autonomous frequency Ω is the bifurcation parameter. Equation (14) posses parameter regimes with stable quasi-periodic and unstable periodic solutions (self-excited frequency ω , forced frequency Ω) and parameter regimes with stable periodic solutions due to synchronisation (forced frequency Ω) (cf. e.g. [12]). An analysis of a great part of the dynamics of the *van-der-Pol* oscillator can be found in [17]. In order to investigate these two regimes the two invariance equations

$$\Omega^2 \frac{d^2 u}{d\theta_1^2} - \mu(1 - u^2)\Omega \frac{du}{d\theta_1} + u = \Gamma \cos(\theta_1) \quad (15)$$

$$\Omega^2 \frac{\partial^2 u}{\partial \theta_1^2} + \omega \Omega \frac{\partial^2 u}{\partial \theta_1 \partial \theta_2} + \omega^2 \frac{\partial^2 u}{\partial \theta_2^2} - \mu(1 - u^2) \left[\Omega \frac{\partial u}{\partial \theta_1} + \omega \frac{\partial u}{\partial \theta_2} \right] + u = \Gamma \cos(\theta_1) \quad (16)$$

are solved with the stated *Fourier-Galerkin* method. The synchronisation algorithm enables to decide within the continuation where to solve which equation by detecting synchronised solutions. The result of the continuation can be seen in figure 2. Here, the orbital radius in phase space $\rho = \sqrt{u^2 + (\boldsymbol{\gamma}^\top \partial_{\boldsymbol{\theta}} u)^2}$ is plotted against the non-autonomous frequency Ω . The area contained between the minimal $\min(\rho_{qp})$ and the maximal radius $\max(\rho_{qp})$ of the quasi-periodic orbits (plotted in green) is colour-filled. In contrast, the area between the minimal $\min(\rho_p)$

and the maximal radius $\max(\rho_p)$ of the stable/ unstable periodic solution (straight blue line/ dashed blue line) is not filled. Black crosses or black dotted lines display solutions from sufficiently long time simulations with high accuracy and small time-steps as a reference. Leaving the synchronised area at $\Omega \approx \frac{1}{3}$ for the moment aside, it can be seen that the quasi-periodic solution vanishes in a *Neimark-Sacker* bifurcation at $\Omega \approx 0.37$. Here, two of the computed *Floquet* multipliers enter the unit circle with non-vanishing imaginary parts. The autonomous frequency ω gets locked on the non-autonomous frequency Ω . The periodic solution becomes stable at that point and shows a resonance phenomenon around the eigenfrequency. The stability of the periodic solution is lost in a second *Neimark-Sacker* bifurcation.

Figure 3 and 4 show the periodic solution at $\Omega = 1$ (red line in figure 2) in phase space and torus coordinates, respectively. Figures 5 and 6 show the solutions at $\Omega = 1.75$ (red line in figure 2). In figure 5, the *Fourier* series solution, evaluated here with respect to time t , and the time simulation fill the manifold densely. The benefit of the *Fourier-Galerkin* method can be seen in figure 6, where the green surface representing the 2-torus solution is plotted as defined by the multidimensional *Fourier* series. This manifold contains the complete information of the solution. The exact maximum and minimal amplitude can be easily determined, which would be one of the main application-based interests. The black dotted trajectories of the time simulation would fill the manifold densely for $t \rightarrow \infty$. The forced *van-der-Pol* oscillator does not only show a synchronisation phenomenon around $\Omega = 1$ but also a supercritical synchronisation or so-called 1:3-synchronisation⁵ at $\Omega = \frac{1}{3}$,

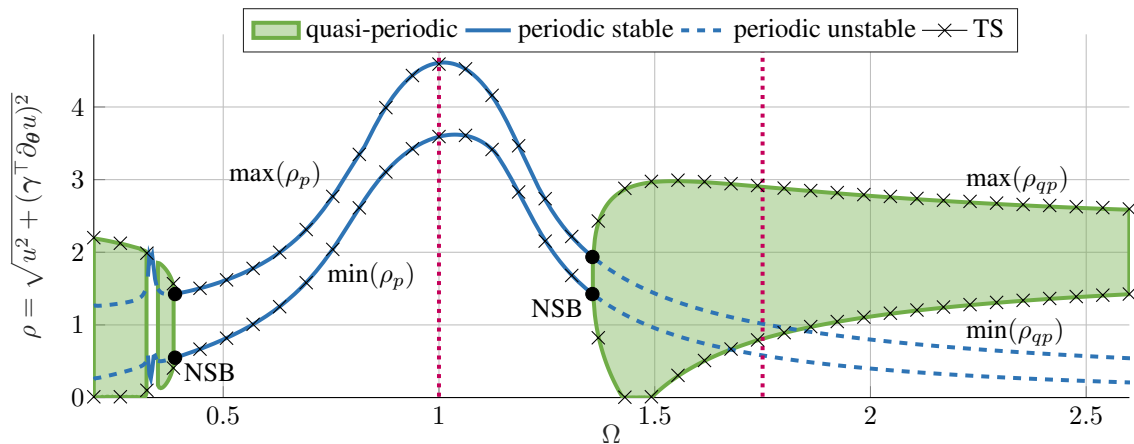


Figure 2: Bifurcation diagram of the forced *van-der-Pol* oscillator; minimal $\min(\rho_{(\cdot)})$ and maximal radius $\max(\rho_{(\cdot)})$ of the orbit in phase space of quasi-/periodic solutions are plotted. NSB: *Neimark-Sacker* Bifurcation.

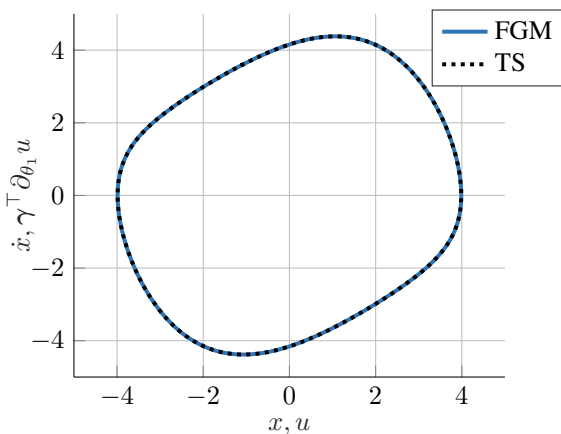


Figure 3: Periodic/ synchronised solution of the forced *van-der-Pol* oscillator at $\Omega = 1$ in phase space: Fourier-Galerkin Method (blue/ FGM) and time simulation (dotted black/ TS).

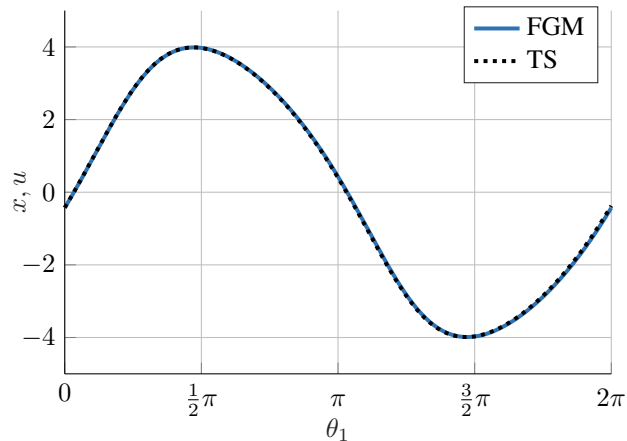


Figure 4: Periodic/ synchronised solution of the forced *van-der-Pol* oscillator at $\Omega = 1$ in torus space: Fourier-Galerkin Method (blue/ FGM) and time simulation (dotted black/ TS).

⁵In literature, the term '1:3 resonance' is also common. However, 'synchronisation' is used here to avoid confusion with the phenomenon of super-elevation of amplitudes near eigenfrequencies.

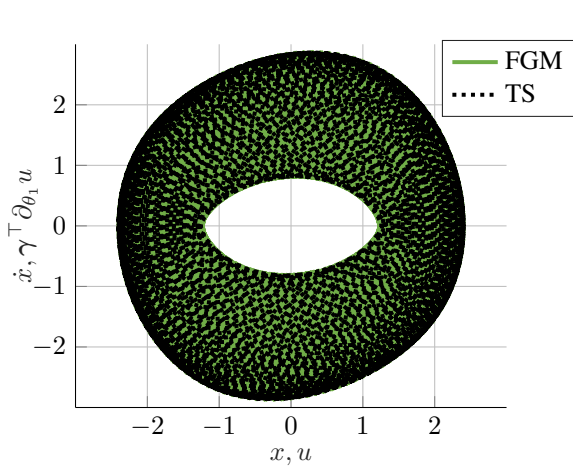


Figure 5: Quasi-periodic solution of the forced *van-der-Pol* oscillator at $\Omega = 1.75$ in phase space: Fourier-Galerkin Method (green/ FGM) and time simulation (dotted black/ TS) fill space densely.

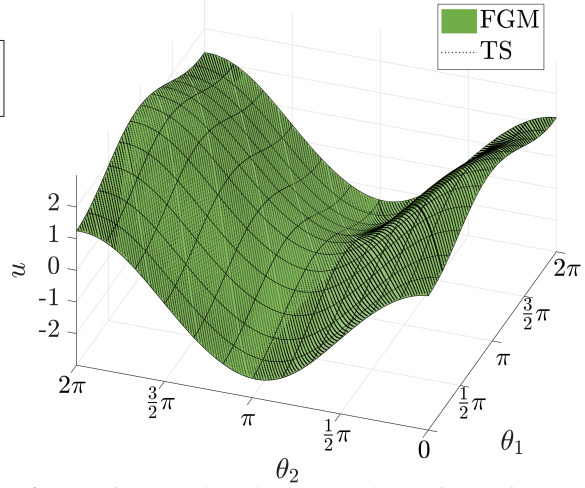


Figure 6: Quasi-periodic solution of the forced *van-der-Pol* oscillator at $\Omega = 1.75$ in torus space: Fourier-Galerkin Method (green/ FGM). Time simulation (dotted black/ TS) fills manifold densely for $t \rightarrow \infty$.

which can be seen in figure 7. Here, the autonomous frequency ω synchronises on three times the non-autonomous frequency Ω . The synchronisation takes again place in a *Neimark-Sacker* bifurcation. In order to illustrate the operating principle of the synchronisation algorithm, figure 8 shows the course of the condition number $\text{cond}(\mathbf{J}|_j)$ over the iteration number of the *Newton* algorithm for the last two continuation steps (black/ grey line) before the first *Neimark-Sacker* bifurcation and the first step after (red line), respectively. The course of the red line shows, that the *Newton* algorithm starts with comparatively low condition numbers. In the third iteration the condition number grows considerably: the algorithm checks (in this case) the last column of the Jacobian $\mathbf{J}|_3$ and detects a synchronisation. The last column is eliminated and the solution of the overdetermined algebraic equation system is computed by means of the *Moore-Penrose* Inverse. The next continuation step is then executed with invariance equation (15) for periodic manifolds.

The *van-der-Pol* oscillator exhibits also a 3:1 synchronisation in an interval around $\Omega = 3$, which is not shown. For this case the autonomous frequency ω synchronises on $\frac{1}{3}\Omega$, which is the new, lowest base frequency. Without modification, the *Fourier-Galerkin* Method as stated in section 2.2 cannot approximate this type of solutions, since the wrong base frequency is chosen. It would require an entry in the matrix of harmonic multiples \mathbf{H} of $\frac{1}{3}$.

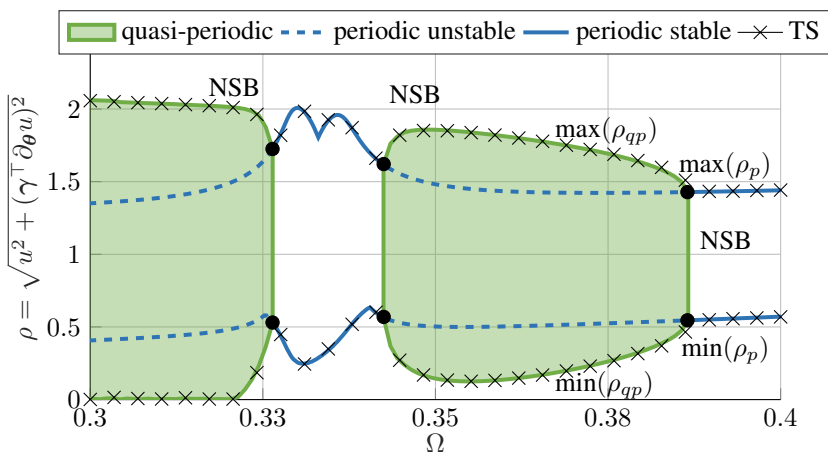


Figure 7: Detail of fig. 2: 1:3 synchronisation forced *van-der-Pol* oscillator; minimal $\min(\rho_{(\cdot)})$ and maximal radius $\max(\rho_{(\cdot)})$ of the orbit in phase space of quasi-/periodic solutions are plotted. NSB: *Neimark-Sacker* Bifurcation.

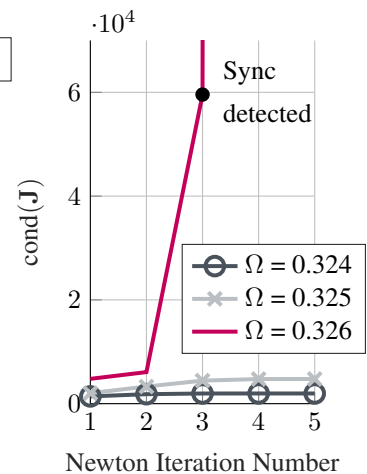


Figure 8: Condition number of the *Jacobian* \mathbf{J} over *Newton* iteration. Black/grey line and red line indicate behaviour before and after synchronisation point.

3.2 Jeffcott-rotor with visco-elastically supported seal

The second example is an unbalanced *Jeffcott(Laval)*-rotor with a rigid seal ring, which is visco-elastically supported. Figure 9 shows the minimal model. The leakage flow in the seal is assumed to be fully turbulent and *Jeffcott*-rotor and seal are modelled linearly. The fluid forces \mathbf{F}_f due to the leakage flow are modelled non-linearly in the position vector $\mathbf{x} = (\mathbf{x}_R^T, \mathbf{x}_S^T)$ by means of the *Muszynska* model [18]. This leads to the equations of motion

$$\begin{bmatrix} \mathbf{M}_R & \mathbf{0} \\ \mathbf{0} & \mathbf{M}_S \end{bmatrix} \ddot{\mathbf{x}} + \begin{bmatrix} \mathbf{D}_R & \mathbf{0} \\ \mathbf{0} & \mathbf{D}_S \end{bmatrix} \dot{\mathbf{x}} + \begin{bmatrix} \mathbf{K}_R & \mathbf{0} \\ \mathbf{0} & \mathbf{K}_S \end{bmatrix} \mathbf{x} = \dots \\ \tilde{e}\Omega^2 \begin{pmatrix} \cos(\Omega t) \\ \sin(\Omega t) \\ 0 \end{pmatrix} + \begin{pmatrix} \mathbf{F}_f(\mathbf{x}) \\ -\mathbf{F}_f(\mathbf{x}) \end{pmatrix}, \quad (17)$$

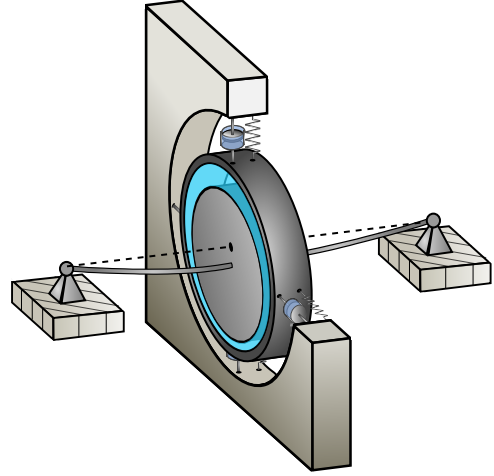


Figure 9: *Jeffcott*-rotor, rigid seal ring visco-elastically supported.

where \mathbf{M} , \mathbf{D} and \mathbf{K} are the mass, velocity- and position-proportional matrices. The subscript R indicates rotor-related and the subscript S seal-related variables and parameters. The normed mass unbalance \tilde{e} is responsible for the external forcing with the (non-autonomous) rotor speed Ω . Dependent on

Ω and \tilde{e} the fluid forces \mathbf{F}_f lead to self-excitation with the autonomous frequency ω . A more in-depth model description can be found in [3]. The invariance equations for the periodic and quasi-periodic solutions are defined accordingly to equation (6). In figure 10 the rotor radius⁶ is plotted over the normed rotor speed Ω for a normed rotor damping of $D_R = 0.05$. Due to the symmetry of the system, the rotor orbits are always point symmetric. The black crosses mark exemplary results of time simulations. The solution shows a resonance phenomenon at the first eigenfrequency. Increasing Ω , the solution loses its stability in a first *Neimark-Sacker* bifurcation. The solution then resynchronises in a second *Neimark-Sacker* bifurcation. This point is detected by the described algorithm. The synchronisation interval coincides with an area around the second eigenfrequency, where the seal ring shows increased amplitudes due to resonance [3]. In a third *Neimark-Sacker* bifurcation the system loses its stability again and large quasi-periodic limit cycles occur. Figure 11 shows the same system except for a vanishing rotor damping $D_R = 0$ and a slightly different parameter setting [4]. The solution behaviour stays qualitatively the same except for the first quasi-periodic regime: increasing Ω from the first *Neimark-Sacker* bifurcation on, the solution exhibits a Secondary Fold Bifurcation (Fold Bifurcation of Maps). The branch reverses, the quasi-periodic solutions becomes unstable (green filled area/ dotted boundary) and vanishes in a second *Neimark-Sacker* Bifurcation. Depending on the technique which is used to continue the solution curve, the synchronisation algorithm detects either the Secondary-Fold Bifurcation (constant predictor) or the *Neimark-Sacker* Bifurcation, if the curve is continued around the Secondary-Fold Bifurcation/ turning point (tangent predictor/ pseudo-arc-length parametrization).

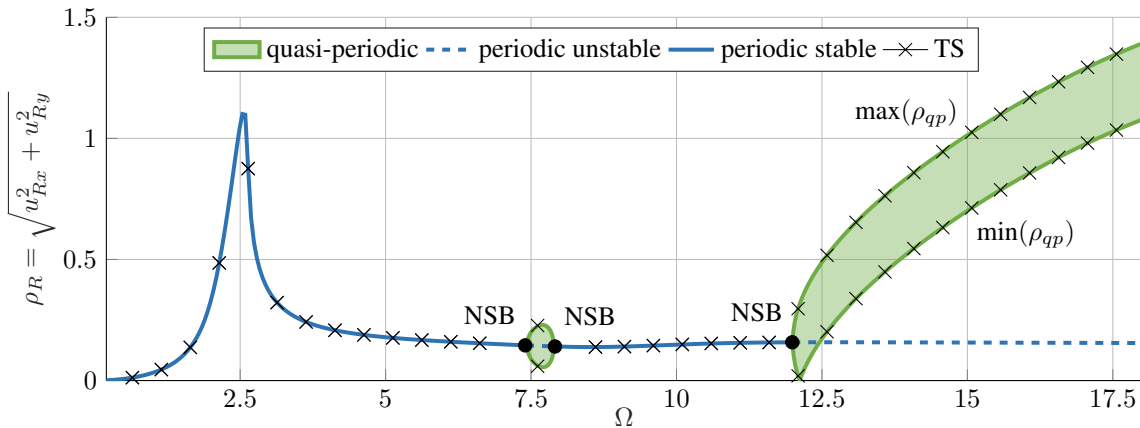


Figure 10: Bifurcation diagram for the *Jeffcott*-rotor with flexible seal for a normed rotor damping of $D_R = 0.05$; minimal $\min(\rho_{(\cdot)})$ and maximal radius $\max(\rho_{(\cdot)})$ rotor radius of quasi-/periodic solutions are plotted. Seal radius is not shown. NSB: *Neimark-Sacker* Bifurcation.

⁶The bifurcation path of the seal motion is not shown in this contribution.

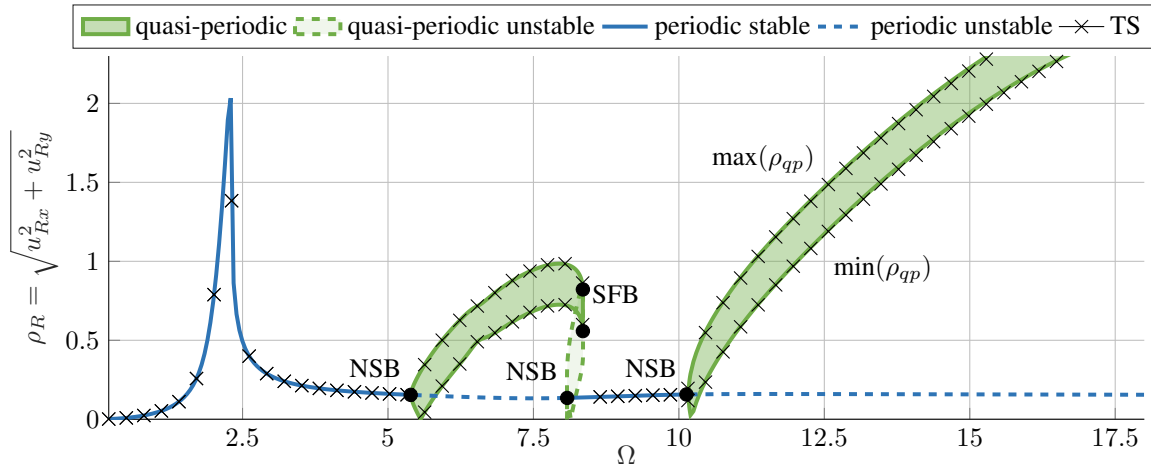


Figure 11: Bifurcation diagram for the *Jeffcott*-rotor with flexible seal for a normed rotor damping of $D_R = 0$; minimal $\min(\rho_{(\cdot)})$ and maximal radius $\max(\rho_{(\cdot)})$ rotor radius of quasi-/periodic solutions are plotted. Seal radius is not shown. NSB: *Neimark-Sacker Bifurcation*; SFB: *Secondary Fold Bifurcation*; source [4]

4 Conclusion

This contribution presented a *Fourier-Galerkin* Method, an extension for synchronised solutions and some results of the application to the forced *van-der-Pol* oscillator and to a *Jeffcott*-rotor model with visco-elastically supported seal.

The presented *Fourier-Galerkin* Method is able to approximate periodic and quasi-periodic solutions, whereby autonomous and non-autonomous frequencies in the signal can be handled. The autonomous case demands the additional consideration of phase conditions. The problem of synchronisation/ entrainment of autonomous frequencies in quasi-periodic solutions has been treated with a numerical approach: synchronisation points are detected by monitoring the *Jacobi* matrix of the used *Newton* algorithm. In case of synchronisation, the convergence of the algorithm is ensured by forming an overdetermined equation system and using the *Moore-Penrose* inverse.

The algorithms have been applied to the forced *van-der-Pol* oscillator, where periodic and quasi-periodic as well as the transitions via a 1:3 and a 1:1 synchronisation could be approximated. The results for the *Jeffcott*-rotor model showed resonances, quasi-periodic regimes and synchronisation. The stable solutions of the *Fourier-Galerkin* Method compared well to results from time integration.

REFERENCES

- [1] Andrianov, I. V. and Awrejcewicz, J. (2001): New trends in asymptotic approaches: Summation and interpolation methods. *ASME APPL MECH REV*, **54**(1), pp. 69–63.
- [2] Argyris, J.H., Faust, G., Haase, M. and Friedrich, R. (2015): *An Exploration of Dynamical Systems and Chaos: Completely Revised and Enlarged Second Edition*. Springer, Berlin.
- [3] Bäuerle, S. and Hetzler, H. (2017): Non-linear dynamics of a rotor system with compliant seal. In *Proc. Int. Symp. on Transp. Phenom. and Dyn. of Rot. Mach.*, Lahaina, USA, Dec. 16-21.
- [4] Bäuerle, S. and Hetzler, H. (2018): Approximation of Periodic and Quasi-Periodic Motions of a Rotor System with Visco-elastic Seal Support by Using a Fourier-Galerkin-Method. *PAMM - to be published*.
- [5] Broer, H. W. Huitema, G. B. and Sevryuk, M. B. (2009): *Quasi-periodic motions in families of dynamical systems: order amidst chaos*. Springer, Berlin.
- [6] Brommundt, E. (1970): Approximate solutions of quasiperiodic differential equations. *J MATH ANAL APPL*, **30**(2), pp. 252-263.
- [7] Cameron, T. M. and Griffin, J. H. (1989): An alternating frequency/time domain method for calculating the steady-state response of nonlinear dynamic systems. *J APPL MECH*, **56**(1), pp. 149-154.
- [8] Chua, L. and Ushida, A. (1981): Algorithms for Computing Almost Periodic Steady-State Response of Non-linear System to Multiple Input Frequencies. *IEEE CAS*, **28**(10), pp. 953-971.

- [9] Dieci, L. Lorenz, J. and Russell, R. D. (1991): Numerical calculation of invariant tori. *SIAM J SCI COMPUT*, **12**(3), pp. 607-647.
- [10] Guskov, M. Sinou, J. J. and Thouverez, F. (2007): Multi-dimensional harmonic balance applied to rotor dynamics. In *ASME 2007 Int. Design Eng. Tech. Conf. and Comp. and Info. in Eng. Conf.*. Las Vegas, USA, Sep. 4-7, pp. 1243-1249).
- [11] Van Der Heijden, G. H. (1993): Bifurcation and chaos in drillstring dynamics. *CHAOS SOLITON FRACT*, **3**(2), pp. 219-247.
- [12] Jordan D. W. and Smith P. (1999). *Nonlinear ordinary differential equations: an introduction to dynamical systems*. Oxford University Press Inc., New York.
- [13] Kim, Y. B. and Noah, S. T. (1996): Quasi-periodic response and stability analysis for a non-linear Jeffcott rotor. *JSV*, **190**(2), pp. 239-253.
- [14] Kim, Y. B. and Choi, S. K. (1997): A multiple harmonic balance method for the internal resonant vibration of a non-linear Jeffcott rotor. *JSV*, **208**(5), pp. 745-761.
- [15] Linkens, D. (1974): Analytical solution of large numbers of mutually coupled nearly sinusoidal oscillators. *IEEE CAS*, **21**(2), pp. 294-300.
- [16] Marx, B. and Vogt, W. (2011): *Dynamical Systems - Theory and Numerics* (in German). Spektrum Akademischer Verlag, Heidelberg.
- [17] Mettin, R. Parlitz, U. and Lauterborn, W. (1993): Bifurcation structure of the driven van der Pol oscillator. *INT J BIFURC CHAOS*, **3**(6), pp. 1529-1555.
- [18] Muszynska A. (1986): Whirl and Whip Rotor Bearing Stability Problems. *JSV* **110**(3). pp. 443-462.
- [19] Nakariakov, V. M. and Melnikov, V. F. (2009): Quasi-periodic pulsations in solar flares. *SPACE SCI REV*, **149**(1-4), pp. 119-151.
- [20] Nayfeh, A. and Balachandran, B. (1993): *Applied Nonlinear Dynamics*. John Wiley & Sons Inc., New York.s
- [21] Peletan, L. et al. (2014): Quasi-periodic harmonic balance method for rubbing self-induced vibrations in rotor-stator dynamics. *NONLINEAR DYNAM*, **78**(4), pp. 2501-2515.
- [22] Samoilenko, A. M. (1991): *Elements of the mathematical theory of multi-frequency oscillations*. Springer Science & Business Media, Dordrecht.
- [23] Schilder, F. Osinga, H. M. and Vogt, W. (2005): Continuation of quasi-periodic invariant tori. *SIAM J APPL DYN SYST*, **4**(3), pp. 459-488.
- [24] Schilder, F. et al. (2006): Fourier Methods for Quasi-Periodic Oscillations. *INT J NUMER METH ENG*, **67**(5), pp. 629-671.
- [25] Wiggins, S. (2013): *Normally hyperbolic invariant manifolds in dynamical systems*. Springer Science & Business Media, New York.
- [26] Zhao, J. Y. and Hahn, E. J. (1993): Subharmonic, quasi-periodic and chaotic motions of a rigid rotor supported by an eccentric squeeze film damper. *PROC INST MECH ENG C*, **207**(6), pp. 383-392.

Numerical Description of a Rotor Supported by Gas Polymer Bearings for Time Domain Simulations - Implementation and Parametrization of the Structure Model

Gregor Schilling¹, **Katja Bäuerlein**¹, **Robert Liebich**¹

¹ Engineering Design and Product Reliability, Technical University Berlin, 10623, Berlin, Germany, gregor.schilling@tu-berlin.de

Abstract

Gas Polymer Bearings (GPBs) have a wide range of usability as replacements for common Gas Foil Journal Bearings (GFBs). The most important benefit of these kind of bearings is the simple manufacturing process and the wide range of suitable materials for many applications for example in organic rankine cycle processes and turbomachinery in food industry. The present work examines the implementation of a viscoelastic model of the structure to describe the behavior of polymer materials and their frequency dependent stiffness and damping characteristic. The model is based on discrete rheological elements and embedded into a transient model of a rotor bearing system (RBS). Following the model description, the parametrization process of the rheological elements is explained. Finally the results of transient simulations of a rotor-bearing-system are presented and discussed with regards to the parametrization process.

1 Introduction

In the field of rotating machinery at high speeds hydrodynamic air bearings have many advantages in comparison to common rolling bearings or oil based hydrostatic and hydrodynamic bearings. The most important benefits are the simple bearing system design without additional lubrication components, the low abrasive wear and the high degree of efficiency in case of the small friction torque. Due to the low viscosity of gases, air bearings exhibit a lower load capacity and damping ratio in comparison to oil lubricated bearings. Another problem is the occurrence of nonlinear sub- and super harmonic vibrations, which can lead to instabilities in the system behavior.

In order to avoid these disadvantages bearings with an elastic air film support, called Gas Foil Bearings (GFB) were developed. The elastic deformation under the impact of the pressure field leads to an optimized gap geometry and increases the bearable load capacity. Furthermore, friction processes during dynamic deformation generate additional, external damping with positive effects on system stability and the rotor vibration level, ref. Heshmat et al [1].

Dellacorte et al [2] made a comparison between bearings with different realizations of the deformable bearing housings up to 1998. The most appreciable solutions were the Leaf (LFB) and the bump-type Bearings (BFB). While Leaf type bearings use the bending stiffness of thin metal sheets, the bump-type bearings make use of a corrugated metal foil. Dellacorte et al. [2] have shown that the steady progression leads to more than four times higher load capacities. These results indicate the high influence of the structure properties for possible operating ranges.

San Andres et al [3] investigated concepts based on a metal mesh as a replacement for the most frequently used bump foils. Metal Mesh Foil Bearings (MMFB) have the advantage of continuous distributed stiffness and damping properties in circumferencial and axial direction. An experimental performance analysis of a BFB and a MMFB with similar size performed by San Andres et al.[4] in 2012 revealed better damping characteristics for the metal mesh type. The determined loss factor as indicator for the external mechanical damping of the MMFB was two times higher than the loss factor of the contemplated BFB. In 2003 Lee et al [5] tried to improve the performance of a common BFB of the first generation by integrating a viscoelastic material between top and bump foil. The Viscoelastic Foil Bearing (VEFB) had superior damping characteristics. Especially near the first bending critical speed and in the range beyond, the magnitude of the rotor amplitudes could be intensively reduced.

Sim and Park [6] executed measurements on an electrical drive with three different bearing types. First conventional BFBs, as second Gas Polymer Bearings (GPB) with a polymer layer instead of the bump foil and as third a hybrid version like Lee et al [5] investigated were used for the rotor support. The results of the experiment are similar to these from Lee. The integration of the polymer layer had positive effects for the dynamic of the driven rotor. The greatest loss factors could be determined for the GPB. It is obvious that viscoelastic materials, especially polymers, offer other benefits, for example a simple manufacturing and the possibility to set material characteristics specifically.

Despite the higher performance of improved structures it is still complicated to conceptualize a system with GFBs. Numerical simulations and measurements have to be conducted. Today, focus in research on GFBs is to build high efficient numerical models to simulate the rotordynamic behavior in order to increase the speed of development processes and reduce its costs. For GPBs only experimental studies are available. Several models for simulations with bump-type-bearings in frequency and time domain were developed up until today. However, numerical models for GPBs do not exist yet. The objective of the present work is to implement a model for transient simulations of a rotor supported by GPBs and to give a description of the frequency domain based parametrization method.

2 Theory

The description of the nonlinear behavior of polymer materials is an important part of research. The dynamic characteristics generally depend on the deformation magnitude and its velocity. Furthermore, the material temperature has a high impact on the polymer properties. With respect to the dominating radial load, which is initialized by the pressure field, all crosswise deformations of the polymer layer will be neglected. Commonly used characterization methods for one-dimensional models consider the material response on harmonic excitation. Based on this, frequency-dependent stiffness and damping coefficients can be determined. Figure (1) illustrates coefficients for a perfluoro-caoutchouc (FFKM), which are based on a master curve by Bormann [7].

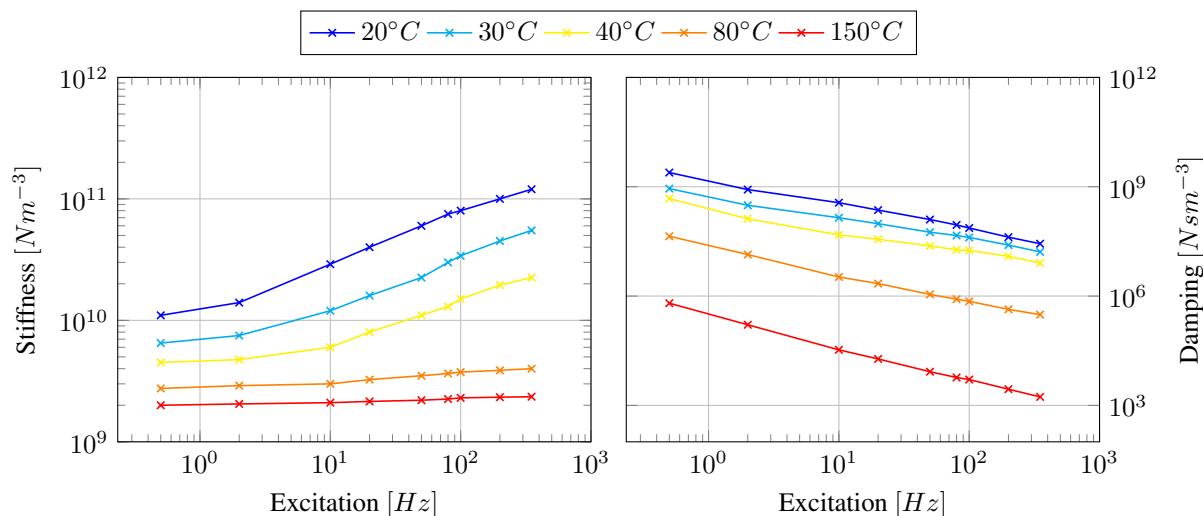


Figure 1: Frequency-dependent stiffness and damping coefficients of a perfluoro-caoutchouc based on a measurement published by Bormann [7]: (left) stiffness coefficients , (right) damping coefficients

The following statements apply in general for polymer materials:

- The stiffness coefficients are increasing with the frequency.
- The damping coefficients are decreasing with the frequency.
- An increase in temperature reduces the stiffness and damping performance.
- For a constant frequency, a higher deformation magnitude results in lower stiffness and higher damping coefficients.

Model Pre-Limitations

The following structure model is an early and simple implementation for the viscoelastic behavior of polymer structures. It considers the frequency dependence of the stiffness and damping coefficients, under the assumption of one-directional displacements without element couplings. Because the model is isothermal, new sets of parameters have to be generated for different temperatures. Due to the small ratio between deformation and layer thickness the dependence of the deformation magnitude is neglected.

3 Structure Model

In order to describe the nonlinear behavior of polymers under dynamic loads, discrete rheological elements are commonly used. These complex elements consist of linear basic elements, like the Hookean (HE) and the Newton element (NE). While the HE corresponds to a linear stiffness the NE represents a linear damper. A nonlinear material behaviour can be modeled by creating networks of these basic elements. A high number of complex networks is available for effects like crawling and relaxation. Based on the generalized Kelvin-Voigt model (GKV) and the generalized Maxwell model (GM) depicted in Figure (2), it is possible to create the behavior of any complex network of HE's and NE's.

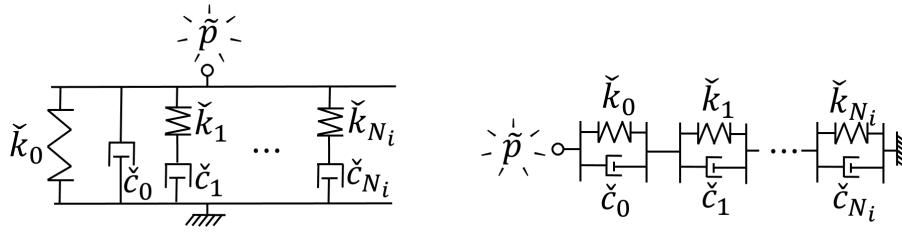


Figure 2: Complex rheological elements with inner parameters for the discrete springs and dampers under the load of a pressure field: (left) Generalized Maxwell Model, (right) Generalized Kelvin-Voigt Model

3.1 Parametrization - Frequency Domain

In order to approximate the frequency dependence for the stiffness and damping coefficients a complex stiffness (with respect to the Complex Shear Module, ref. Popov [8]), can be defined,

$$K^*(\omega) = K'(\omega) + jK''(\omega) \quad (1)$$

where the stiffness and damping coefficient for a specific frequency can be calculated from the real and imaginary part.

$$\tilde{k}(\omega) = \text{Re}\{K^*(\omega)\} \quad , \quad \tilde{c}(\omega) = \text{Im}\{K^*(\omega)\}/\omega \quad (2)$$

With the complex stiffness of the HE and the NE,

$$K_{HE}^* = \tilde{k} \quad , \quad K_{NE}^* = j\omega\tilde{c} \quad (3)$$

where $\tilde{k} = kh_0/p_a$ and $\tilde{c} = ch_0\Omega/p_a$ are the discrete normalized stiffness and damping values of the basic elements, p_a is the ambient pressure and h_0 is the nominal gap. For the GM and GKV network

$$K_{GM}^*(\omega) = \left[\tilde{k}_0 + \sum_{i=1}^{N_{re}} \frac{\tilde{k}_i \tilde{c}_i^2 \omega^2}{\tilde{k}_i^2 + \tilde{c}_i^2 \omega^2} \right] + j \left[\tilde{c}_0 \omega + \sum_{i=1}^{N_{re}} \frac{\tilde{k}_i^2 \tilde{c}_i \omega}{\tilde{k}_i^2 + \tilde{c}_i^2 \omega^2} \right] \quad (4)$$

and

$$K_{GKV}^*(\omega) = \left(\sum_{i=0}^{N_{re}} \frac{1}{\check{k}_i + j\omega\check{c}_i} \right)^{-1} \quad (5)$$

can be obtained. Thus, the given Eqs. (4) and (5) in combination with Eq. (2) enable a comparison between model and measured data. For an initial set of $2N_{re}$ inner parameters \check{k}_i and \check{c}_i with $i = 0, \dots, N_{re}$ the local mismatch for each frequency can be determined. It is reasonable to avoid a different weighting for the measured stiffness \bar{k} and damping \bar{c} in the parametrization process. The local difference at ω_k has to be normalized by the measured values \bar{k}_k or \bar{c}_k . A high global accordance can be achieved by adding up the local relative errors. To enable a comparison of global errors from measured data sets with different grid sizes the global error is divided by the number of frequency grid points K . The resulting, nonlinear minimization problem is defined in Equation (6).

$$Err = \frac{1}{K} \left[\sum_{k=1}^K \left(\check{k}_k - \bar{k}_k \right) \frac{1}{\bar{k}_k} + \sum_{k=1}^K \left(\check{c}_k - \bar{c}_k \right) \frac{1}{\bar{c}_k} \right] \implies \min \quad (6)$$

In the $2n$ -dimensional parameter space a high number of local minimums are located, therefore gradient based minimization methods are not suitable. As solver for the problem, metaheuristic methods like genetic algorithms (GA) or particle swarm optimizer are to prefer.

3.2 Time Domain

In contrast to the frequency domain model, with only one external degree of freedom (DOF), the time domain model needs several inner DOFs. In Figure (3) the extension of the GM and GKV is depicted. For each DOF

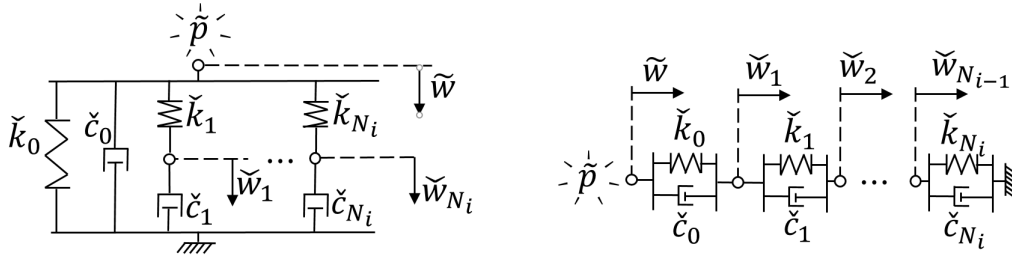


Figure 3: Complex rheological elements with inner parameters for the discrete springs and dampers and inner degrees of freedom, under the load of a pressure field: (left) Generalized Maxwell Model, (right) Generalized Kelvin-Voigt Model

an equilibrium in forces leads to an equation of motion. The Equations (7) up to (9) build a system of ordinary differential equations (ODE) for the GM, which can be solved by common ODE solvers.

$$\check{p} = \check{k}_0\check{w} + \check{k}_1(\check{w} - \check{w}_1) + \dots + \check{k}_i(\check{w} - \check{w}_i) + \check{c}_0\dot{\check{w}} \quad (7)$$

$$0 = \check{k}_1(\check{w}_1 - \check{w}) + \check{c}_1\dot{\check{w}}_1 \quad (8)$$

\vdots

$$0 = \check{k}_n(\check{w}_n - \check{w}) + \check{c}_n\dot{\check{w}}_n \quad (9)$$

The same procedure for the GKV results in the system of the Equations (10) up to (13).

$$\tilde{p} = \tilde{k}_0(\tilde{w} - \tilde{w}_1) + \tilde{c}_0(\dot{\tilde{w}} - \dot{\tilde{w}}_1) \quad (10)$$

$$0 = \tilde{k}_1(\tilde{w}_1 - \tilde{w}_2) + \tilde{c}_1(\dot{\tilde{w}}_1 - \dot{\tilde{w}}_2) - \tilde{k}_0(\tilde{w} - \tilde{w}_1) - \tilde{c}_0(\dot{\tilde{w}} - \dot{\tilde{w}}_1) \quad (11)$$

⋮

$$0 = \tilde{k}_{n-1}(\tilde{w}_{n-1} - \tilde{w}_n) + \tilde{c}_{n-1}(\dot{\tilde{w}}_{n-1} - \dot{\tilde{w}}_n) - \tilde{k}_{n-2}(\tilde{w}_{n-2} - \tilde{w}_{n-1}) - \tilde{c}_{n-2}(\dot{\tilde{w}}_{n-2} - \dot{\tilde{w}}_{n-1}) \quad (12)$$

$$0 = \tilde{k}_n \tilde{w}_n + \tilde{c}_n \dot{\tilde{w}}_n - \tilde{k}_{n-1}(\tilde{w}_{n-1} - \tilde{w}_n) - \tilde{c}_{n-1}(\dot{\tilde{w}}_{n-1} - \dot{\tilde{w}}_n) \quad (13)$$

For both elements the ODE system has the form of Equation (14), with $\mathbf{K}^{(e)}$ and $\mathbf{C}^{(e)}$ as resulting stiffness and damping matrices. The vector \mathbf{w} contains the displacement of the external DOF, which has an impact on the height of the air film. The other DOFs are the inner ones, which do not interact with the fluid film or the rotor. The load vector \mathbf{f} contains the external load initiated by the pressure field.

$$\mathbf{f}^{(e)} = \mathbf{C}^{(e)} \dot{\mathbf{w}}^{(e)} + \mathbf{K}^{(e)} \mathbf{w}^{(e)} \quad (14)$$

4 Transient Model

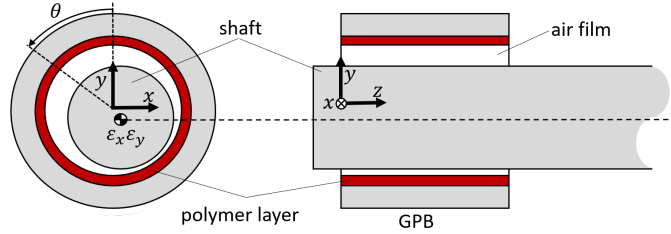


Figure 4: Schematic model of a rotor supported by GPBs

In Figure (4) a rotor supported by GPBs is schematically illustrated. Under the assumption of symmetry, only one bearing and half of the shaft have to be considered. The following model is based on the work of Bonello and Pham [9], who introduced a state variable ψ that allows a simultaneous time integration of the whole rotor-bearing-system. As a model for the fluid film a dimensionless form of the Reynolds Equation (15) is used. The definitions for ψ and the normalized pressure \tilde{p} , gap height \tilde{h} , time τ and the axial coordinate Z are presented in Equation (16).

$$\frac{\partial \psi}{\partial \tau} = \frac{1}{\Lambda} \left\{ \frac{\partial}{\partial \Theta} \left[\psi \left(\tilde{h} \frac{\partial \psi}{\partial \Theta} - \psi \frac{\partial \tilde{h}}{\partial \Theta} \right) \right] + \frac{\partial}{\partial Z} \left[\psi \left(\tilde{h} \frac{\partial \psi}{\partial Z} - \psi \frac{\partial \tilde{h}}{\partial Z} \right) \right] \right\} - \frac{\partial \psi}{\partial \Theta} \quad (15)$$

$$\psi = \tilde{p} \tilde{h} \quad , \quad \tilde{p} = \frac{p}{p_a} \quad , \quad \tilde{h} = \frac{h}{h_0} \quad , \quad \tau = \frac{\Omega}{2} t \quad , \quad Z = \frac{L}{R} \quad (16)$$

To create a system of ODEs from the partial differential equation (15), finite difference formulas were used to approximate the derivatives. The discretization of Equation (15), with N_Θ and N_Z grid points in circumferential and axial direction, can be written in a vectorized form, see Equation (17). It has to be mentioned that all vectors have to be multiplied elementwise.

$$\begin{aligned} \frac{d\psi}{d\tau} = & \frac{1}{\Lambda} \left(\tilde{h} \left(\frac{\partial \psi}{\partial \Theta} \frac{\partial \psi}{\partial \Theta} + \frac{\partial \psi}{\partial Z} \frac{\partial \psi}{\partial Z} \right) + \tilde{h} \psi \left(\frac{\partial^2 \psi}{\partial \Theta^2} + \frac{\partial^2 \psi}{\partial Z^2} \right) \right. \\ & \left. - \psi \left(\frac{\partial \tilde{h}}{\partial \Theta} \frac{\partial \psi}{\partial \Theta} + \frac{\partial \tilde{h}}{\partial Z} \frac{\partial \psi}{\partial Z} \right) - \psi^2 \left(\frac{\partial^2 \tilde{h}}{\partial \Theta^2} + \frac{\partial^2 \tilde{h}}{\partial Z^2} \right) \right) - \frac{\partial \psi}{\partial \Theta} \end{aligned} \quad (17)$$

The differential equation for the rotor is defined in Equation (18), where the vector $\boldsymbol{\varepsilon} = \{\varepsilon_x, \varepsilon_y\}^T$ contains the displacement of the shaft center normalized by the nominal gap h_0 . The tilting DOFs are neglected under the assumption of a symmetric system.

$$\frac{d^2}{d\tau^2}\boldsymbol{\varepsilon} = \frac{4}{m_r h_0 \Omega^2}(\mathbf{f}_f + \mathbf{f}_u + \mathbf{f}_p) \quad (18)$$

The motion of the rotor depends on the three force components on the right hand side of the system. The vector \mathbf{f}_f contains the gravitational force and \mathbf{f}_u gives the effect of the unbalance, see. Equations (19). Both forces are rotor specific ones,

$$\mathbf{f}_f = \{0, m_r g\}^T, \quad \mathbf{f}_u = \hat{F}_u \{\sin(2\tau), \cos(2\tau)\}^T \quad (19)$$

whereas the vector \mathbf{f}_p contains the gas forces induced by the pressure field, see Equation (20).

$$\mathbf{f}_p = -p_a R^2 \int_0^{2\pi} \int_0^{R/L} \left\{ \frac{\psi}{\tilde{h}} - 1 \right\} \begin{bmatrix} \cos(\Theta) \\ \sin(\Theta) \end{bmatrix} dZ d\Theta \quad (20)$$

The second order equation (18) has to be transformed into state space to enable a later use of standardized ODE solvers, ref. Equation (21).

$$\frac{\partial}{\partial \tau} \begin{pmatrix} \boldsymbol{\varepsilon} \\ \dot{\boldsymbol{\varepsilon}} \end{pmatrix} = \begin{pmatrix} \dot{\boldsymbol{\varepsilon}} \\ \frac{4}{m_r h_0 \Omega^2}(\mathbf{f}_f + \mathbf{f}_u + \mathbf{f}_p) \end{pmatrix} \quad (21)$$

As approximation for the structure behavior, a Nonlinear Viscoelastic Foundation Model (NVEFM) is realized by a single GM or GKV element for each angular mesh position. At a discrete node the load for each structure element corresponds to the mean value of the pressure in axial direction. The ODE system of the structure given in Equation (22) is an assembly of the element formulation in analogy to Equation (14),

$$\mathbf{f}_S = \mathbf{C}_S \dot{\mathbf{w}}_S + \mathbf{K}_S \mathbf{w}_S \quad (22)$$

with

$$\mathbf{f}_S = \{f_{1,1}^e, f_{1,2}^e, \dots, f_{1,N_Z}^e, \dots, f_{N_\Theta,1}^e, \dots, f_{N_\Theta,N_Z}^e\}^T, \quad (23)$$

$$\mathbf{w}_S = \{w_{1,1}^e, w_{1,2}^e, \dots, w_{1,N_Z}^e, \dots, w_{N_\Theta,1}^e, \dots, w_{N_\Theta,N_Z}^e\}^T, \quad (24)$$

$$\text{diag}(\mathbf{C}_S) = \{\mathbf{C}_{1,1}^e, \mathbf{C}_{1,2}^e, \dots, \mathbf{C}_{1,N_Z}^e, \dots, \mathbf{C}_{N_\Theta,1}^e, \dots, \mathbf{C}_{N_\Theta,N_Z}^e\}, \quad (25)$$

$$\text{diag}(\mathbf{K}_S) = \{\mathbf{K}_{1,1}^e, \mathbf{K}_{1,2}^e, \dots, \mathbf{K}_{1,N_Z}^e, \dots, \mathbf{K}_{N_\Theta,1}^e, \dots, \mathbf{K}_{N_\Theta,N_Z}^e\}. \quad (26)$$

In order to transform the system to the same form as Equation (17) and (21), the Equation (22) has to be rewritten as follows:

$$\dot{\mathbf{w}}_S = \mathbf{C}_S^{-1}(\mathbf{f}_S - \mathbf{K}_S \mathbf{w}_S). \quad (27)$$

The normalized height of the gap at each discrete point of the fluid film grid can be calculated with Equation (28). It defines the gap geometry for the fluid film and depends on the rotor displacements and the structure deformation. The simultaneous coupling of the system is defined by Equation (28) in combination with Equation (20) for all $a = 1 \dots N_\Theta$ and $b = 1 \dots N_Z$.

$$\tilde{h}_{a,b} = 1 - \varepsilon_x \cos(\Theta_a) - \varepsilon_y \sin(\Theta_a) + \tilde{w}_{a,b} \quad (28)$$

Boundary Conditions

The objective with subsequent bearing prototypes is to manufacture the bearings by an injection molding process with a closed loop top foil. The absence of the fixture point is considered by using a continuous, circular condition for the mesh ends in circumferential direction, ref. Equations (29) and (30).

$$\psi_{N_{\Theta}+1,b} = \psi_{1,b} \quad b = 1 \dots N_Z \quad (29)$$

$$\tilde{h}_{N_{\Theta}+1,b} = \tilde{h}_{1,b} \quad b = 1 \dots N_Z \quad (30)$$

At the bearing edges, constant ambient pressure is assumed, for that reason the edges are removed from the fluid film and structure mesh. Nevertheless the assumption of the constant ambient pressure has to be considered for the derivatives, for all $a = 1 \dots N_{\Theta}$ the Equation (31) is used in the finite difference formulas.

$$\psi_{a,N_Z+(1)} = \tilde{h}_{a,N_Z+(1)} \quad , \quad \psi_{a,1-(1)} = \tilde{h}_{a,1-(1)} \quad (31)$$

The gap function at the bearing edges, see Equations (32) and (33), depends on the deformation of the structure. By the assumption of ambient pressure, theoretically there is no deformations at the edges. However, for the purpose of considering the axial bending stiffness of the top foil, a constant deformation in axial direction is implemented.

$$\tilde{h}_{a,N_Z+(1)} = 1 - \varepsilon_x \cos(\Theta) - \varepsilon_y \sin(\Theta) + \tilde{w}_{a,N_Z+(1)} \quad (32)$$

$$\tilde{h}_{a,1-(1)} = 1 - \varepsilon_x \cos(\Theta) - \varepsilon_y \sin(\Theta) + \tilde{w}_{a,1-(1)} \quad (33)$$

5 Numerical results

The results presented are based on the data set of the FFKM at a temperature of $T = 20^{\circ}C$ and were calculated for a material thickness of $t_L = 2mm$. As solver for the minimization problem, a genetic algorithm was used. Figure (5) shows the resulting coefficients for a GM and a GKV model with a number of $2N_{de} = 14$ discrete springs and dampers. In general the increasing character of the stiffness and the decreasing behavior of the damping are well represented by both models.

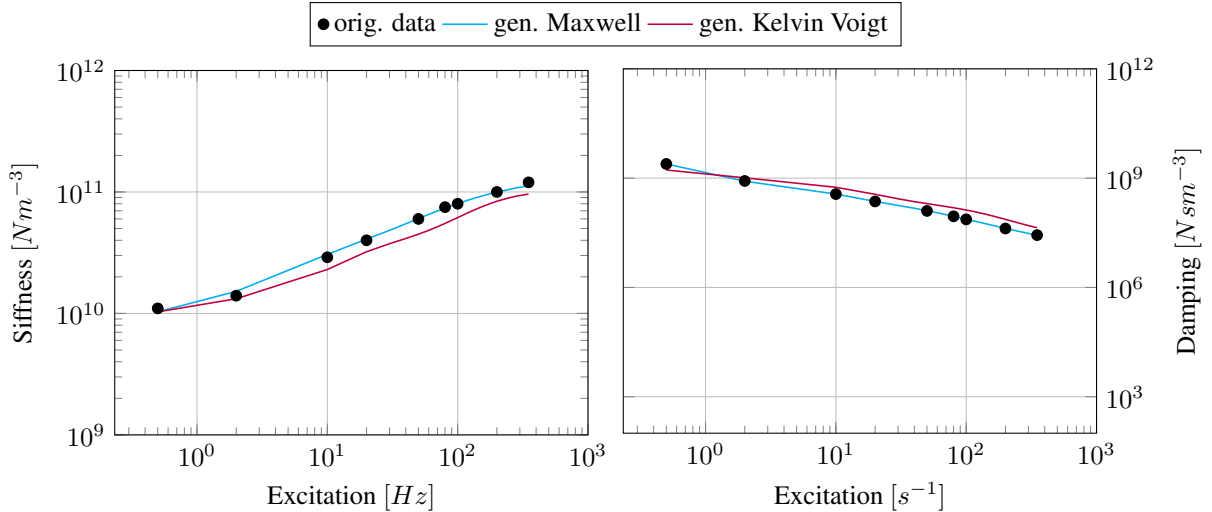


Figure 5: Frequency dependent stiffness and damping coefficients generated by the GM and the GKV models in comparison to the original measured coefficients: (left) stiffness, (right) damping

In Figure (6) the local, relative discrepancy of the coefficients from the original data is depicted. For each excitation frequency the local error for the GM is less than 10%. The parameter set for the GKV has a higher discrepancy to the measured data. The local relative errors are only in the same decade of the measured data. The

approximation quality has to be improved in future development. For both models it is theoretically possible to approximate the data set in the same quality, but due to the series build character of the GKV it is more difficult to find suitable parameters. Inside of the GM model each pair, consisting of a discrete spring and damper, has a specific character in the frequency domain without influence on other pairs. Furthermore, it is possible to control the activation frequency for a discrete spring by its damping parameter. In contrast every change of a parameter inside of the GKV can in- or decrease the effect of other pairs.

As mentioned before, the mountainous landscape character of the minimization problem in Equation (6) leads to parameter sets, that represent local minimums. Regarding to the stochastically generated initial population, it is unlikely to regenerate the exact same solution twice. Nevertheless, the dynamic behavior of two sets with nearly the same global error level is very similar. A higher number of discrete elements can lead to a better concurrence between model and measured data, but also increases the numerical effort in the time domain. Furthermore it becomes more difficult to define the parameter ranges for the sampler and the optimizer. On the experimental side, the measurement of more data points in frequency domain even has a positive effect.

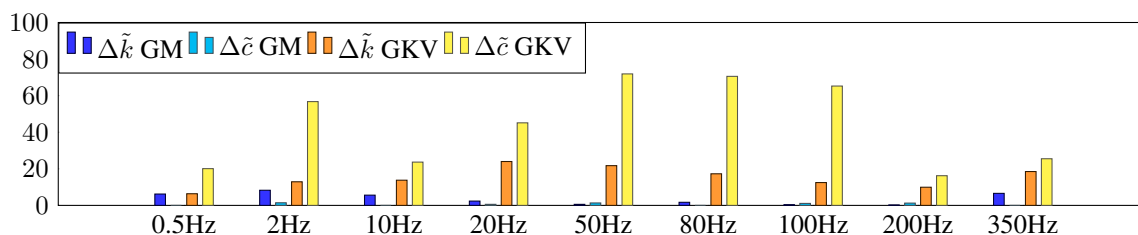


Figure 6: Overview of the local model discrepancy, for the generalized Maxwell Model and the Generalized Kelvin-Voigt Model, relative to the coefficients of the measured coefficients from literature

The transient model pertains to the properties listed in Table (2), while the generated parameter sets for the GM and the GKV are listed in Table (1). The mesh size for the fluid film is $N_\Theta \times N_Z$ with $N_\Theta = 72$ and $N_Z = 24$. The structure contains N_Θ generalized elements. The resulting trajectories describe the motion of the rotor falling from the center position at a constant rotational speed. As solver for the ODE system an explicit 3rd-order Runge-Kutta-Method with embedded step control was used.

i	GM		GKV	
	\tilde{k}_i	\tilde{c}_i	\tilde{k}_i	\tilde{c}_i
0	1.362E+09	1.605E+07	2.950e+010	1.612e+010
1	4.150E+10	1.110E+08	1.182e+011	2.380e+007
2	5.767E+09	2.988E+09	2.505e+010	1.690e+009
3	1.735E+10	4.522E+08	1.062e+009	6.466e+010
4	6.400E+09	3.303E+09	4.816e+010	2.623e+010
5	1.125E+10	1.135E+08	8.855e+010	5.186e+008
6	3.946E+10	3.120E+07	7.500e+010	3.527e+010

Table 1: Damping and stiffness parameters for the generalized Maxwell-Model

RBS parameter			
half of rotor mass	m_r	5.0	kg
bearing radius	R	20	mm
bearing length	L	40	mm
nominal clearance	h_0	50	μm
air viscosity	μ	19.5	N/mm^2
ambient pressure	p_a	0.1	MPa
FFKM thickness	t_L	2	mm

Table 2: Damping and stiffness parameter for the generalized Maxwell-Model

Figure (7) illustrates the trajectories for the RBS without unbalance for different rotational speeds. Despite the difference in the approximation quality, both models show a similar behaviour for each case. In the simulation for

12krpm on the left side, the center of the rotor moves quickly to its equilibrium position. Shortly before the spiral movement of the rotor ends, a creep effect can be detected. These effects are typical for polymers. Regarding the model, this effect is caused by the gradually decreasing influence of the discrete dampers. Thus, for the GM the static equilibrium position of the rotor center is the same, as for a simulation with only the parameter k_0 . The simulations with 18krpm and 24krpm show, that the magnitude of the shaft motion increases with the rotor

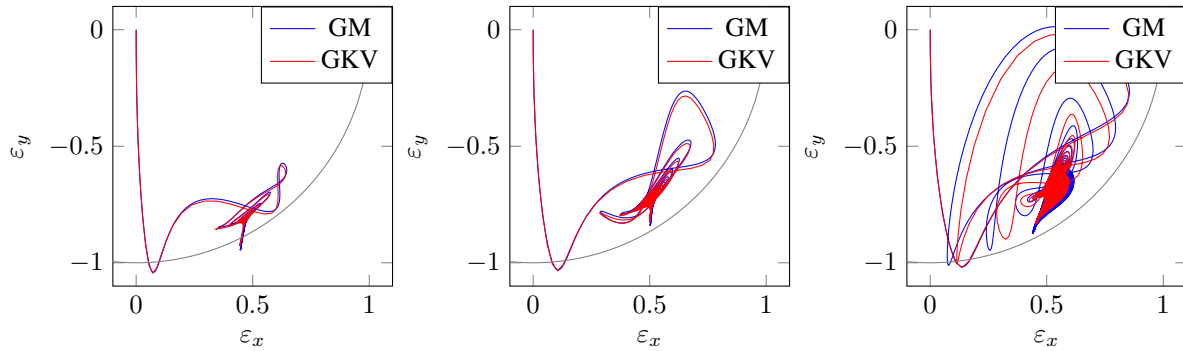


Figure 7: Trajectories of the shaft center under different rotational speeds: (left) at 12000rpm, (middle) at 18000rpm, (right) at 24000rpm

speed. In case of 24krpm the center does not reach an equilibrium, because of sub harmonic vibrations. In Figure (8) the normalized shaft displacement ϵ_x in horizontal direction over time is illustrated for 18krpm, 24krpm and 25krpm. The initial vibration for 18krpm disappears quickly, whereas the vibration for 24krpm rises. As shown in the lower figure, for higher speeds the motion of the shaft becomes dominated by a subharmonic vibration, after a short period of time.

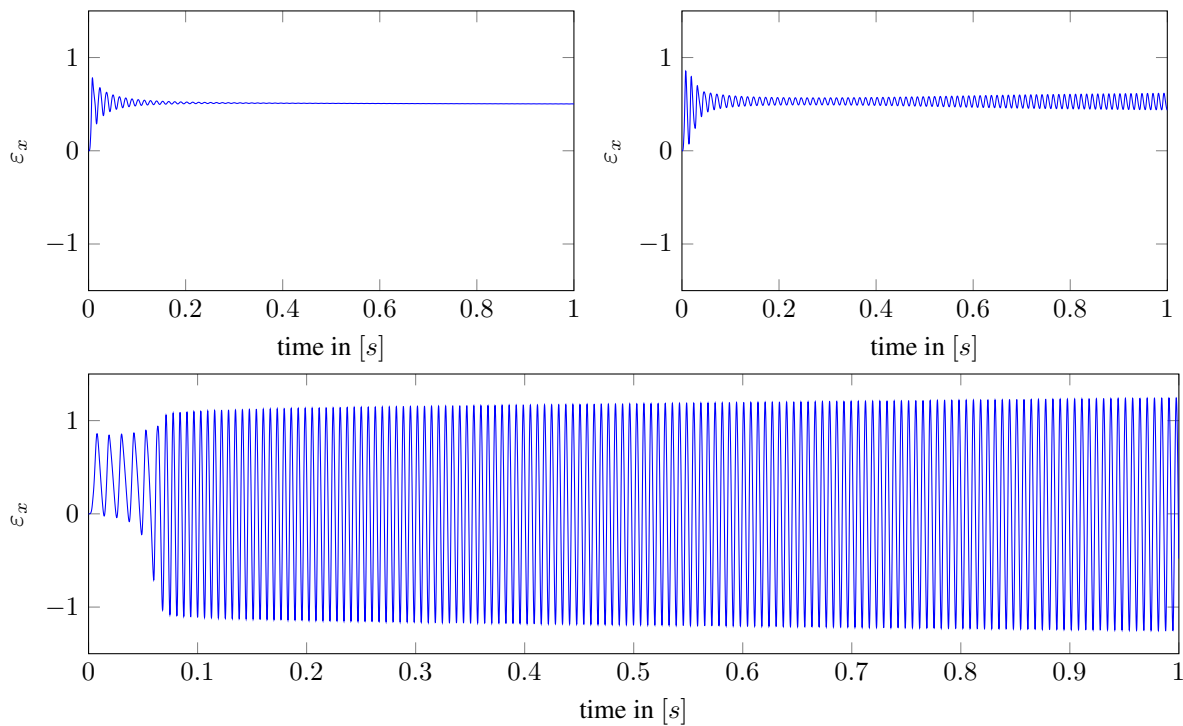


Figure 8: Time signals for the motion component in horizontal direction: (upper left) at 18000rpm, (upper right) at 24000rpm, (bottom) at 25000rpm

6 Conclusion

This paper’s overall contribution has been the implementation of a structure model for analysis of rotors supported by Gas Polymer Bearings in the time domain. The developed Nonlinear Viscoelastic Foundation Model uses generalized rheological elements to include the frequency dependent behaviour of polymers. Furthermore, the description of a procedure to generate suitable parameter sets for the structure model was subject of this paper. Due to the neglected temperature and amplitude dependencies, the presented NVEFM has to be seen as an early basic model, which has to be expanded in future. For the enhancements it is essential to perform an experimental material study with respect to the required information density.

The next phase of research includes the set up of a test rig to build a data basis, to validate the material models on the measured data and to develop GPB-prototypes for rotordynamic analysis.

REFERENCES

- [1] Heshmat, H., 1994. “Advancements in the performance of aerodynamic foil journal bearings: High speed and load capability”. *Journal of Tribology*, **116**(2), S. 287.
- [2] Dellacorte, C., and Valco, M. J., 2000. “Load capacity estimation of foil air journal bearings for oil-free turbomachinery applications”. *Tribology Transactions*, **43**(4), jan, S. 795–801.
- [3] San Andrés, L., Chirathadam, T. A., and Kim, T.-H., 2010. “Measurement of structural stiffness and damping coefficients in a metal mesh foil bearing”. *Journal of Engineering for Gas Turbines and Power*, **132**(3), S. 032503.
- [4] San Andrés, L., and Chirathadam, T. A., 2012. “A metal mesh foil bearing and a bump-type foil bearing: Comparison of performance for two similar size gas bearings”. *Journal of Engineering for Gas Turbines and Power*, **134**(10), S. 102501.
- [5] Lee, Y.-B., Kim, T.-H., Kim, C.-H., Lee, N.-S., and Choi, D.-H., 2004. “Dynamic characteristics of a flexible rotor system supported by a viscoelastic foil bearing (VEFB)”. *Tribology International*, **37**(9), sep, S. 679–687.
- [6] Sim, K., and Park, J., 2017. “Performance measurements of gas bearings with high damping structures of polymer and bump foil via electric motor driving tests and one degree-of-freedom shaker dynamic loading tests”. *Journal of Engineering for Gas Turbines and Power*, **139**(9), apr, S. 092504.
- [7] Bormann, A., 2005. *Elastomerringe zur Schwingungsberuhigung in der Rotordynamik: Theorie, Messungen und optimierte Auslegung*. Fortschritt-Berichte VDI: Reihe 11, Schwingungstechnik. VDI-Verlag.
- [8] Popov, V. L., 2017. *Contact Mechanics and Friction*. Springer Berlin Heidelberg.
- [9] Bonello, P., and Pham, H., 2014. “The efficient computation of the nonlinear dynamic response of a foil–air bearing rotor system”. *Journal of Sound and Vibration*, **333**(15), jul, S. 3459–3478.

Nomenclature

p	pressure	\mathbf{K}	stiffness matrix
k, K	stiffness	\mathbf{C}	damping matrix
c	damping coefficient	\mathbf{f}	force vector
w	structure deformation	$\boldsymbol{\varepsilon}$	rotor displacement vector
h	gap height		
m_r	rotor mass	$\tilde{(\cdot)}$	normalized external value
L	axial bearing length	$\hat{(\cdot)}$	normalized inner value
R	bearing radius	$\hat{(\cdot)}^*$	complex value
ε	norm. rotor displacement	$\bar{(\cdot)}$	measured normalized value
Λ	$= 6\mu\Omega/p_a(R/h_0)^2$	$\dot{(\cdot)}$	time derivative
μ	air viscosity		
ω	excitation frequency	Z, Θ	polar coordinates
Ω	rotational speed	x, y	cartesian coordinates
ψ	ph couple value		

Quasiperiodic Motions in Unbalanced Rotor Systems with simultaneous Self- or Forced Excitation

Robert Fiedler¹, Hartmut Hetzler²

¹ Institute of Mechanics, University of Kassel, 34125, Kassel, Germany, robert.fiedler@uni-kassel.de

² Institute of Mechanics, University of Kassel, 34125, Kassel, Germany, hetzler@uni-kassel.de

Abstract

The occurrence of quasiperiodic motions in nonlinear rotor dynamical systems with unbalance is often reported in the literature. Typical, such motions stem from simultaneously acting vibrational excitations which are uncorrelated. This work presents a numerical approach to calculate invariant manifolds for quasiperiodic motions in dynamical systems. Basically, this approach is based on a reparametrization from physical time to the separated time scales of the individual excitation mechanisms. Eventually this yields a description of the invariant manifold in the extended phase space by means of a partial differential equation, which is discretized using a finite-difference-scheme. Being a special case with only one time scale, periodic motions can also be analyzed. The approach is applied to two rotor dynamical examples from literature which feature a superposition of unbalance and additional self- or forced excitation stemming from another source.

1 Introduction

In an abstract view, rotating machines contain bodies which undergo complex spatial motion at usually high speeds and which are often influenced by manifold multiphysical interactions. Consequently, the dynamics of such machinery is very complex and demands for a thorough analysis in order to guarantee safe operation.

As a consequence of the rotational motion, real machinery exhibits unbalance effects which are directly correlated to the rotation speed. Thus, practically any rotor system will show vibrations that contain the rotation frequency. On the other hand, there is a huge variety of forces and excitation mechanisms which may produce vibrations at frequencies that differ from the rotation frequency of the rotor. Typical examples are

- forced vibrations due to unbalanced magnetic pull (UMP) [3, 4, 10, 24]
- non-smooth forced vibrations due to rotor-stator-contact [1, 5, 6, 8, 13, 12, 17, 23, 18]
- self-excited vibrations due to co-rotating damping (internal damping) [11, 14]
- self-excited vibrations due to nonlinear bearing or sealing forces [2].

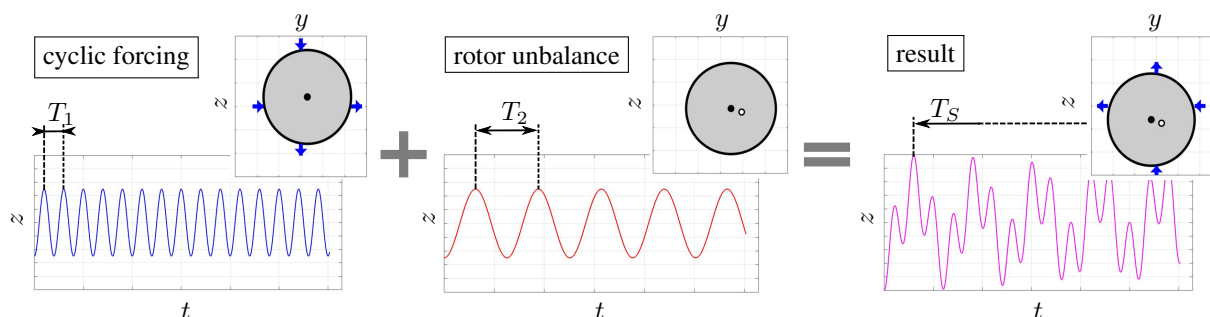


Figure 1: On the systematical occurrence of quasiperiodic motion in rotordynamics

If only one mechanism is active or if – under rather special conditions – two or more mechanisms of vibrational excitation synchronize, periodic motions may result. For such periodic cases, a variety of analytical and numerical

methods exists to calculate stationary solutions (the so-called invariant manifolds): common tools are FOURIER-GALERKIN methods, shooting methods or time-marching techniques for instance. However, if multiple individual mechanisms affect the system simultaneously, and synchronization does not occur, the resulting motion usually will not be periodic anymore (cf. figure 1) and standard approaches to directly find periodic solutions will fail. As a consequence of non-periodicity, such motions do not exhibit a finite period time and any trajectory of finite length will only fill a fraction of the invariant manifold. Due to the lack of alternative methods, for such non-periodic cases many authors resorted to direct time integration techniques in order to analyze the system behavior [5, 6, 18, 1, 24, 10]. Although necessary when analyzing the transient behavior [8, 4], this is obviously not the most efficient method investigating stationary solution since the interval of time integration has to be sufficiently large in order to eliminate transitory motion and approximate the invariant manifold. An additional drawback of direct time integration approaches is that only attractively stable motions may be found. This paper presents an approach to directly calculate the invariant manifold which circumvents the problems arising from the infinite time interval of non-periodic vibrations stemming from multiple cyclic motions. To this end, a partial differential equation describing the invariant manifold is derived and solved using a finite-differences-scheme.

2 Quasiperiodicity: basic theory and methods

In this section only some basic aspects of quasiperiodic motions will be explained. A brief summary of established methods for the calculation of quasiperiodic motions will finish this section. Further details on the mathematical background as well as the presented methods may be found in [20, 19, 15] for instance. Consider an autonomous ordinary differential equation (ODE)

$$\dot{\mathbf{z}} = \mathbf{f}(\mathbf{z}, \boldsymbol{\gamma}), \quad \mathbf{z} \in \mathbb{R}^n, \quad \boldsymbol{\gamma} \in \mathbb{R}^m, \quad (1)$$

where \mathbf{z} represents the state vector, $\boldsymbol{\gamma}$ is a parameter vector and $\mathbf{f}(\mathbf{z}, \boldsymbol{\gamma})$ is a sufficiently smooth vector field. For a given $\boldsymbol{\gamma}$ equation (1) may exhibit different stationary solutions which are assumed to be either periodic or quasiperiodic. Chaotic motions will not be considered in the following. Let be $\tilde{\mathbf{z}}_S(t)$ one of these stationary solutions for a given $\boldsymbol{\gamma}$. In case of an attractively stable solution the determination can simply be achieved using a time marching technique for sufficiently long integration time. Analyzing an arbitrary coordinate \tilde{z}_i , $i \in 1, \dots, n$ with the Fast-FOURIER Transformation, a typical result may look like depicted in figure 2. The signal in figure 2

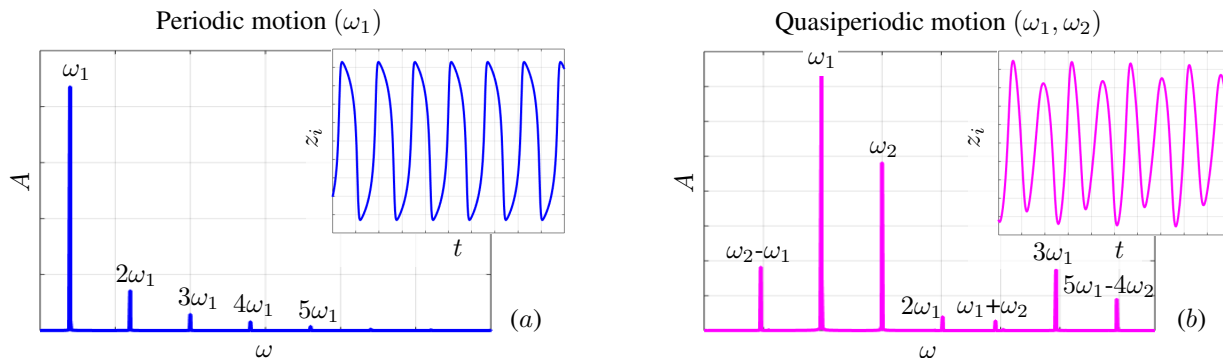


Figure 2: Schematic spectra of (a) periodic motions and (b) quasiperiodic motions (e.g.: fig.8 in [17], fig.7 in [23], fig.8 in [24], fig.5 in [10], fig.2 in [13])

(a) is a non-harmonic periodic signal which has one base frequency and higher harmonic terms. In contrast to this periodic motion figure 2 (b) outlines the essential characteristics of a quasiperiodic motion: here, two (or more) basis frequencies are observed which have no common multiplier¹. Such frequencies are referred to as

¹Through the presence of multiple internal (basis) frequencies and nonlinearities, combinations of those frequencies can be present in the spectrum.

'incommensurable frequencies', meaning that the ratio of frequencies is an irrational number (e.g. $\omega_1 = 1, \omega_2 = \pi$). The mathematical condition reads

$$\langle \mathbf{k}, \boldsymbol{\omega} \rangle = \sum_{l=1}^p k_l \omega_l = 0 \quad \forall \mathbf{k} \in \mathbb{Z}^p, \quad (2)$$

meaning that by determining a minimal number of frequencies not fulfilling equation (2) a basis of the quasiperiodic motion is found. Due to the incommensurability of frequencies the solution can be rewritten $\tilde{\mathbf{z}}_S(t) \rightarrow \mathbf{z}_S(\omega_1 t, \dots, \omega_p t)$. Noteworthy is that in case of a periodic solution $\mathbf{z}_S(\omega_1 t)$ corresponds to a solution parametrized on dimensionless time. It can be motivated that due to incommensurable frequencies each $\omega_i t$ describes an independent time domain. In the broadest sense this approach is similar to the method of multiple time scales [16] but without small parameter. The parametrization and time derivation read

$$\begin{aligned} \mathbf{z}_S(\omega_1 t, \dots, \omega_p t) &\rightarrow \mathbf{z}_S(\theta_1, \dots, \theta_p); \\ \theta_1 &= \omega_1 t \\ &\vdots \\ \theta_p &= \omega_p t \end{aligned} \quad \frac{d(\cdot)}{dt} = \frac{\partial(\cdot)}{\partial \theta_1} \frac{d\theta_1}{dt} + \dots + \frac{\partial(\cdot)}{\partial \theta_p} \frac{d\theta_p}{dt} = \frac{\partial(\cdot)}{\partial \theta_1} \omega_1 + \dots + \frac{\partial(\cdot)}{\partial \theta_p} \omega_p, \quad (3)$$

where $\theta_1, \dots, \theta_p$ are 2π periodic variables. By using this parametrization a carrier of the quasiperiodic motion can be defined, the torus (cf. figure 3)

$$\mathbb{T}^p = \left\{ \boldsymbol{\theta} \mid \boldsymbol{\theta} = [\theta_1, \dots, \theta_p]^\top, \theta_i \in \mathbb{R} \bmod 2\pi, i = 1, \dots, p \right\}. \quad (4)$$

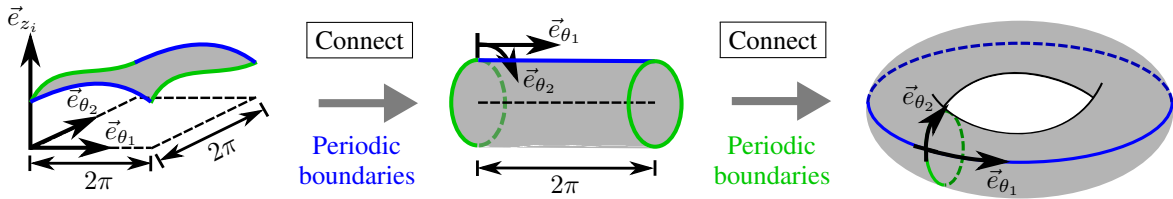


Figure 3: Parametrization of a coordinate z_i on a \mathbb{T}^2 with subsequent bending of the space.

Some important characteristics hold for the torus. Because of incommensurable frequencies, a quasiperiodic solution fills the surface of the torus densely and ensures a unique solution on every point of it (for further details see [20]). It is important to note, that a torus is merely the carrier (parametrization) of a quasiperiodic motion. The resultant solution is described with a manifold

$$\mathcal{M} = \{(\boldsymbol{\theta}, \boldsymbol{\gamma}, \mathbf{z}) \mid \mathbf{z} = \mathbf{z}(\boldsymbol{\theta}, \boldsymbol{\gamma}), \boldsymbol{\theta} \in \mathbb{T}^p, \boldsymbol{\gamma} \in \mathbb{R}^m, \mathbf{z} \in \mathbb{R}^n\} \subset \mathbb{T}^p \times \mathbb{R}^m \times \mathbb{R}^n, \quad (5)$$

where the manifold is embedded in the phase space, parametrized on a torus. Furthermore holds that the manifold is invariant, meaning that solutions on the manifold stay on it². In addition a nearly always made assumption is that analyzed manifolds are isolated (normal hyperbolic) solutions³.

To calculate an invariant manifold the parametrization has to change from time to the torus coordinates. Different concepts for the argumentation of this transition can be found in the literature, for example describing the flow in the tangential space $\mathcal{T}_{(\boldsymbol{\theta}, \boldsymbol{\gamma}, \mathbf{z})} \mathcal{M}$ of the manifold [15], but with a substitution of the time derivation from equation (3) in equation (1) the **invariance equation**

$$\frac{\partial \mathbf{z}}{\partial \theta_1} \omega_1 + \dots + \frac{\partial \mathbf{z}}{\partial \theta_p} \omega_p = \mathbf{f}(\mathbf{z}, \boldsymbol{\gamma}), \quad (6)$$

²A periodic solution is also a manifold parametrized on a \mathbb{T}^1 and a fixed point is a manifold parametrized on a \mathbb{T}^0 .

³This condition is a generalization of hyperbolic equilibrium points.

can be obtained, whereby the equation consists of a system of partial differential equations (PDE) (for more details see [19, 22, 21]). Since $[\omega_1, \dots, \omega_p]$ in equation (6) are the internal frequencies of the quasiperiodic motion, it is advantageous to distinguish between known frequencies Ω_i ⁴ (e.g. rotation speed of unbalance) and unknown frequencies ω_j (e.g. self-excitation).

$$\sum_{i=1}^m \frac{\partial \mathbf{z}}{\partial \theta_i} \Omega_i + \sum_{j=m+1}^p \frac{\partial \mathbf{z}}{\partial \theta_j} \omega_j = \mathbf{f}(\mathbf{z}, \gamma) \quad (7)$$

The analysis of equation (7) is in the case of $m = p$ (just known frequencies are present) without any further considerations possible, since the PDE has n unknowns ($[z_1, \dots, z_n]$) and the same number of equations. If $m < p$ (unknown frequencies are present) the system of PDE has $k = p - (m + 1)$ more unknowns than equations. A well known special case of this problem is a dynamical system with a periodic solution resulting from self-excitation ($m = 0, p = 1$). The equations of motion with dimensionless time read

$$\frac{d\mathbf{z}}{d\theta_1} \omega_1 = \mathbf{f}(\mathbf{z}, \gamma), \quad \int_0^{2\pi} \mathbf{f}(\mathbf{z}_0, \gamma)^\top \cdot \mathbf{z} \, d\theta_1 = 0, \quad (8)$$

whereby the second equation is an integral POINCARÉ phase condition, which fixes the free phase θ_1 resulting from the unknown frequency ω_1 . Furthermore, \mathbf{z}_0 represents a nearby solution (for example obtained by a previous continuation step). In other words, the invariance equation describes the periodic solution uniquely but due to self-excitation the zero point of the phase is not unique.

Generalizing this idea to quasiperiodic motions under the consideration of torus coordinates (different time scales), a phase condition has to be added for every free phase [22] and the projection on the vector field $(\mathbf{f}(\mathbf{z}_0, \gamma)^\top \cdot \mathbf{z})$ has just to fix the phase in the direction of the associated torus coordinate (time scale). The equations for describing a quasiperiodic motion on a finite interval read:

Equation system: general formulation

$$\begin{aligned} \sum_{i=1}^m \frac{\partial \mathbf{z}}{\partial \theta_i} \Omega_i + \sum_{j=m+1}^p \frac{\partial \mathbf{z}}{\partial \theta_j} \omega_j = \mathbf{f}(\mathbf{z}, \gamma) & \quad \boldsymbol{\theta} \in \mathbb{T}^p, \quad \boldsymbol{\gamma} \in \mathbb{R}^m, \quad \mathbf{z} \in \mathbb{R}^n \\ \int_0^{2\pi} \dots \int_0^{2\pi} \left(\frac{\partial \mathbf{z}_0}{\partial \theta_j} \right)^\top \cdot \mathbf{z} \, d\theta_1 \dots d\theta_p = 0, & \quad j = m + 1, \dots, p. \end{aligned} \quad (9)$$

With this system of equations the problem of solving an ODE on an infinite, one dimensional time interval can be transformed to solving a PDE on finite, multidimensional intervals (time scales), the torus coordinates θ_i .

In the literature two methods are mainly used to solve equation (9). The first one is a generalization of the FOURIER-GALERKIN method (FGM), whereby instead of one internal frequency, multiple internal frequencies are taken into account [21, 17]. Problems can arise from the initialization of the FOURIER coefficients and the number of ansatz functions which are taken into account. Roughly speaking, with a higher degree of nonlinearities more terms of the FOURIER series have to be taken into account resulting in large calculation costs. Methods to overcome this problem in a certain degree base on a selection of harmonic terms, whereby a Fast-FOURIER Transformation is applied to the residuum identifying missing terms in the ansatz functions [9, 17]. The second approach used to solve equation (9) base upon a finite-difference method (FDM) [7, 22]. A typical drawback of this method is the geometry of the discretized area, but since the area is well known through the parametrization on the 2π periodic torus the method is well suited. The discretization of the phase condition can be handled point wise [21]. In this work all further results are calculated with a FDM algorithm implemented in MATLAB, whereby the derivatives approximation is of third order and the nonlinear system solver FSOLVE is used.

⁴In the context of autonomous equations known frequencies describe the increasing velocity of corresponding phase space coordinates, whereby in the invariance equations are those coordinates the torus coordinates ($z_k = \Omega_i t = \theta_i$, under the assumption of internal frequencies).

3 Application to model problems from the literature

In this section two example problems from literature are re-examined using the approach described above. Since the results in the reference sources have been obtained using different methods, the following examples may serve as a validation of the presented approach. In order to facilitate validation, the choice of parameters and variable names has been adopted from the original publications.

The first one is a simple model of the lateral vibrations of a rotor of an electric generator with unbalanced magnetic pull (UMP) [24]: In this example one cyclic excitation stems from the unbalance, the other one is related to the UMP: in this example both excitation frequencies are known and predetermined. The second example is a rotor-to-stator contact system [17], where one frequency is predetermined and the second one, if present, is unknown since it results from self-excited vibration.

3.1 Generator rotor with unbalanced magnetic pull (UMP)

The considered model stems from [24], whereby merely all significant information for an implementation are mentioned⁵. The rotor is modeled as a JEFFCOTT-rotor and the magnetic field is modeled by means of the air-gap

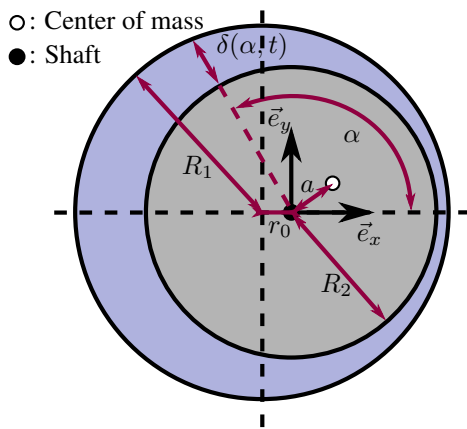


Figure 4: Geometry of the generator.

$$\delta(\alpha, t) \approx \delta_0 - r_0 \cos(\alpha) - r \cos(\alpha - \theta), \quad (10)$$

where $\delta_0 = R_1 - R_2$ is the air-gap of a centered rotor, r_0 is the static eccentricity, (r, θ) are the Polar coordinates of the shaft deflection concerning to the Cartesian coordinates (x, y) and α is a air-gap coordinate (cf. figure 4).

3.1.1 Modeling

Since the rotor is modeled as a JEFFCOTT rotor, the left hand side of the equation is linear. The right hand side consists of a linear part, due to unbalance, and a nonlinear part, due to electromagnetic forces. The dimensionless equation of motion read

$$\begin{bmatrix} 1 & 0 \\ 0 & 1 \end{bmatrix} \begin{bmatrix} \ddot{X} \\ \ddot{Y} \end{bmatrix} + \begin{bmatrix} 2\xi & 0 \\ 0 & 2\xi \end{bmatrix} \begin{bmatrix} \dot{X} \\ \dot{Y} \end{bmatrix} + \begin{bmatrix} 1 & 0 \\ 0 & 1 \end{bmatrix} \begin{bmatrix} X \\ Y \end{bmatrix} = \begin{bmatrix} \Pi\lambda^2 \cos(\lambda T) \\ \Pi\lambda^2 \sin(\lambda T) \end{bmatrix} + \begin{bmatrix} \frac{F_x^{\text{ump}}}{m\omega_n^2\delta_0} \\ \frac{F_y^{\text{ump}}}{m\omega_n^2\delta_0} \end{bmatrix}, \quad (11)$$

where $T = \omega_n t$ is the dimensionless time concerning to the natural angular frequency of the rotor $\omega_n^2 = \frac{k}{m}$ and $F_x^{\text{ump}}, F_y^{\text{ump}}$ are the resultant forces of UMP in \vec{e}_x - and \vec{e}_y -direction. These forces

$$F_x^{\text{ump}} = R_2 L \int_0^{2\pi} \sigma(\alpha, t) \cos(\alpha) d\alpha; \quad F_y^{\text{ump}} = R_2 L \int_0^{2\pi} \sigma(\alpha, t) \sin(\alpha) d\alpha \quad (12)$$

⁵If more detailed descriptions are required or of interested see [24].

⁶E.g. is a motion with $\omega_1 = 2$ and $\omega_2 = 0.999999999999$ better approximated as a quasiperiodic than as a periodic motion.

can be determined by integrating the horizontal and vertical component of the MAXWELL stress $\sigma(\alpha, t)$ on the surface of the rotor. Under some assumptions (see [24]) the MAXWELL stress

$$\sigma(\alpha, t) = \frac{B(\alpha, t)^2}{2\mu_0} \quad (13)$$

can be described with the radial component of the magnetic flux density $B(\alpha, t)$ and the magnetic permeability of the vacuum μ_0 . To calculate the magnetic flux density

$$B(\alpha, t) = \Delta_{\text{mmf}}(\alpha, t)\Lambda(\alpha, t), \quad \text{where} \quad \Delta_{\text{mmf}}(\alpha, t) = F_c \cos(\lambda_0 T - p\alpha) \quad (14)$$

$$\Lambda(\alpha, t) = \frac{\mu_0}{\delta(\alpha, t)}$$

the fundamental magnetomotive force (MMF) of the air-gap Δ_{mmf} , whereby F_c is the amplitude of the MMF, p is the number of pole-pair and λ_0 is the dimensionless supply frequency, and the air-gap permeance $\Lambda(\alpha, t)$ are needed. Note that the second excitation mechanism is the MMF.

3.1.2 Continuation of stationary motion

According to the literature, the parameters are chosen to $2\xi = 0.0156$, $\Pi = 0.2273$, $m = 18.15$ kg, $k = 1.526 \cdot 10^6 \frac{\text{N}}{\text{m}}$, $\delta_0 = 2.2 \cdot 10^{-3}$ m, $R_2 = 59 \cdot 10^{-3}$ m, $L = 0.1551$ m, $\mu_0 = 4\pi \cdot 10^{-7} \frac{\text{H}}{\text{m}}$, $F_c = 684$ A, $\lambda_0 = 1.0835$ and $p = 1$. The static eccentricity r_0 is given in percent of δ_0 and is analyzed for different values. After transforming equation (11) into the phase space, the invariance equations (9) of this problem read

Equation system: generator rotor with unbalanced magnetic pull

$$\frac{\partial \mathbf{z}}{\partial \theta_1} \Omega_1 + \frac{\partial \mathbf{z}}{\partial \theta_2} \Omega_2 = \mathbf{f}(\mathbf{z}, \gamma) \quad \boldsymbol{\theta} = [\theta_1, \theta_2] \in \mathbb{T}^2, \quad \gamma = \lambda \in \mathbb{R}^1, \quad \mathbf{z} = [X, Y, \dot{X}, \dot{Y}] \in \mathbb{R}^4, \quad (15)$$

where both frequencies are given ($\Omega_1 = \lambda$, $\Omega_2 = \lambda_0$) and the continuation parameter is the normalized rotation frequency of the rotor. Since both frequencies are given, no phase condition is required.

To obtain results, the position of the rotor (r, θ) has to be updated in each calculation step of the nonlinear solver to get the current air-gap shape (equation (10)). Furthermore, the resultant forces of UMP from equation (12) have to be evaluated in each calculation step. Since the resulting manifolds are relatively smooth, an approximation with 21×23 elements is sufficient. In figure 5 are the invariant submanifold⁷ of the maximal deflection radius

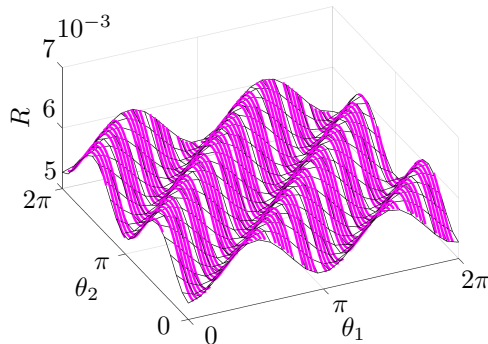


Figure 5: Invariant manifold of the rotor radius compared to a time simulation ($r_0 = 0$, $\lambda = 0.11$).

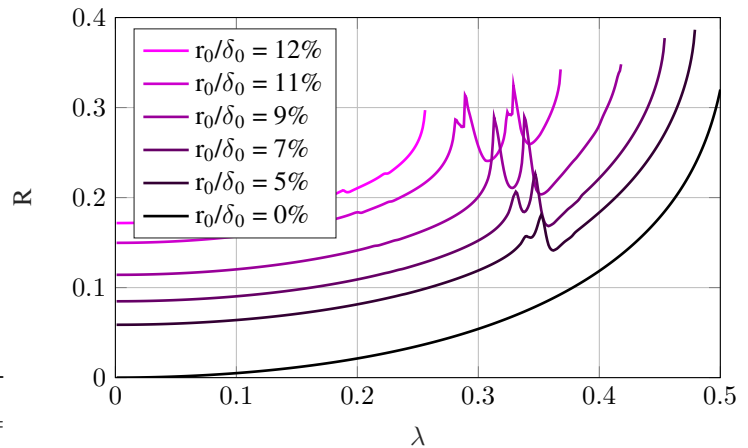


Figure 6: Continuation of λ for different static eccentricities

⁷The whole manifold is defined as $\mathcal{M} \subset \mathbb{T}^2 \times \mathbb{R}^4$ for a fixed λ and would require a six dimensional plot to be depicted, since z_1, z_2, z_3, z_4 have to be plotted against θ_1, θ_2 .

($R = \sqrt{z_1^2 + z_2^2}$) and the results of a finite, stationary time simulation depicted. The solution of the time simulation lies on the predicted manifold and if the time interval is enlarged, the trajectory would fill the manifold densely (cf. chapter 2). According to the source, the investigation will focus on the under critical operating regime. Looking in figure 6 at $r_0/\delta_0 = 0\%$ the classical behavior can be identified. Due to a centric rotor the maximal deflection is at low rotation frequencies small, since the unbalance excites the rotor weakly and the resultant forces of UMP are also weak. As soon as the frequency increases, the maximal deflection grows. When a static eccentricity is considered interesting phenomena occur. First, although small deflections for low rotating frequencies are expected, the resultant deflections are large. The origin of this behavior is founded in the resultant forces of the UMP since through a static eccentricity the forces are exciting the rotor strongly from the beginning⁸. Second, as soon as a certain deflection is reached, the continuation cannot find any solutions. This stems from the pull properties of the resultant UMP forces, since once the rotor comes in a certain distance to the stator it gets pulled against the stator resulting in fatal failure of the machinery. The last interesting phenomena is the presence of extensive deflections at $\lambda \approx 0.32$. With an increasing static eccentricity the two peaks begin to take shape and enlarge with higher values of static eccentricity. At $r_0/\delta_0 = 11\%$ the peaks have split again, but due to large deflections at $r_0/\delta_0 = 12\%$ the large amplitudes are sufficient to let the rotor come into contact with the stator whereby the operating regime lessens significantly. The reason for this behavior lies in the resultant forces of the UMP and continuing investigations will be carried out in further work.

3.2 Rotor-to-stator contact system

The considered model is taken from [12], whereby it has already been investigated from [17] in terms of quasiperiodic motions by means of a multifrequent FOURIER-GALERKIN method. This model⁹ is used to describe rotor to stator interaction by means of a penalty contact using a dry friction COULOMB approach (cf. figure 7). This model can exhibit four classical types of stationary solutions resulting from different constellations of the

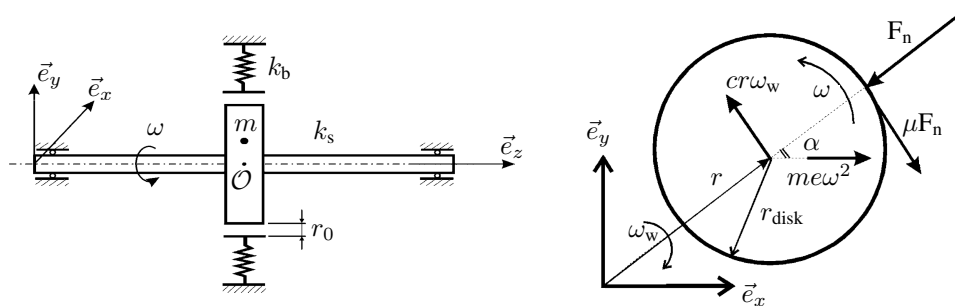


Figure 7: Schematic depiction of the rotor-to-stator contact system with a rigid and circular stator (source [12]).

external forcing due to unbalance and internal forcing due to circulatory terms arising from dry friction. The four types are: **1. No-rub** The rotor is not in contact with the stator. This can be model as an unbalanced JEFFCOTT rotor, the motion is circular and periodic. **2. Full annular rub**: The rotor is in permanent contact with the stator. This can be considered by adding circulatory and corresponding stiffness terms, the motion is circular and periodic. **3. Partial rub**: The rotor switches between in contact and out of contact states. Adding a HEAVISIDE function the rubbing terms can be active or neglected, the motion is quasiperiodic. **4. Dry whip**: The rotor can rub or roll on the inner surface of the stator. Consider a counter rotation oscillation of the rotor (due to self-excitation) to the rotor rotation itself (cf. figure 7: ω_w and ω). A relative velocity between the stator and rotor results whereby its sign determine the direction of friction forces, the motion is quasiperiodic.

⁸Orbits concerning to this motion can be found in [24]

⁹If more detailed descriptions are required or of interested see [12, 13, 17].

3.2.1 Modeling

Since this model is taken from the literature the parameters and variables are chosen after [17] to simplify the consultation of the source. The dimensionless equations of motion modeling the mentioned four steady states read

$$\begin{bmatrix} 1 & 0 \\ 0 & 1 \end{bmatrix} \begin{bmatrix} X'' \\ Y'' \end{bmatrix} + \begin{bmatrix} 2\zeta & 0 \\ 0 & 2\zeta \end{bmatrix} \begin{bmatrix} X' \\ Y' \end{bmatrix} + \begin{bmatrix} \beta & 0 \\ 0 & \beta \end{bmatrix} \begin{bmatrix} X \\ Y \end{bmatrix} + \Theta(R) \begin{pmatrix} 1 - \frac{R_0}{R} \\ \mu \operatorname{sign}(V_{\text{rel}}) \end{pmatrix} \begin{bmatrix} X \\ Y \end{bmatrix} = \begin{bmatrix} \Omega^2 \cos(\Omega\tau) \\ \Omega^2 \sin(\Omega\tau) \end{bmatrix}, \quad (16)$$

where

$$R = \sqrt{X^2 + Y^2}, \quad \Theta(R) = \begin{cases} 0, & R < R_0 \\ 1, & R \geq R_0 \end{cases}, \quad V_{\text{rel}} = R_{\text{disk}}\Omega + R\omega_b. \quad (17)$$

The HEAVISIDE function considers the nonlinearities in fact instantaneous, but due to the term $(1 - R/R_0)$ a continuous changeover is warranted. Furthermore, it is noteworthy that the dimensionless dry whip frequency ω_b is negative

$$\omega_b = - \left(\frac{\zeta}{\mu} + \sqrt{\beta + \left(\frac{\zeta}{\mu} \right)^2} \right) \quad (18)$$

and corresponds to the unstable natural frequency of the coupled rotor-stator system (cf. [13]).

3.2.2 Continuation of stationary motion

According to the literature, the parameters are chosen to $2\zeta = 0.1$, $\beta = 0.04$, $R_0 = 1.05$, $R_{\text{disk}} = 20R_0$ and $\mu = 0.2$. To investigate the different types of behavior and define a reference solution a time integration is carried out (cf. figure 9). Doing a quasi stationary run up simulation the four described states can be identified. Noteworthy is a jump phenomena occurring between the partial rub and the dry whip motion at $\Omega \approx 0.46$ suggesting a bifurcation. Since a simple JEFFCOTT rotor is the basis of this model it can be deduced, that a no-rub motion has to exist at higher rotational speeds. Starting on this motion and doing a run down simulation two more jump phenomena can be observed. The first one between the no rub and dry whip motion at $\Omega \approx 0.86$ and the second the other way around at $\Omega \approx 0.04$. The questions arising are how are the periodic motions connected and can the quasiperiodic motion be continued efficiently. After transforming equation (16) into phase space some distinctions have to be made. The continuation starts with the no-rub periodic motion, whereby the invariance equation (9) of these solutions read:

Equation system: rotor-to-stator contact system (periodic solution)

$$\frac{d\mathbf{z}}{d\theta_1} \Omega_1 = \mathbf{f}(\mathbf{z}, \gamma) \quad \theta_1 \in \mathbb{T}^1, \gamma = \Omega \in \mathbb{R}^1, \mathbf{z} = [X, Y, X', Y'] \in \mathbb{R}^4. \quad (19)$$

Like mentioned in chapter 2 a periodic solution is just a special case of a quasiperiodic motion with one internal frequency ($\Omega_1 = \Omega$) and can therefore be calculated with the used framework. Here, a phase condition is not required since the frequency is predetermined. During the continuation the FLOQUET multipliers are monitored to analyze the stability and identify (possible) arising quasiperiodic solutions through a NEIMARK-SACKER bifurcation¹⁰. If quasiperiodic solutions are present the invariance equation (9) of this type of solutions read

Equation system: rotor-to-stator contact system (quasiperiodic solution)

$$\begin{aligned} \frac{\partial \mathbf{z}}{\partial \theta_1} \Omega_1 + \frac{\partial \mathbf{z}}{\partial \theta_2} \omega_2 = \mathbf{f}(\mathbf{z}, \gamma) \quad \boldsymbol{\theta} = [\theta_1, \theta_2] \in \mathbb{T}^2, \gamma = \Omega \in \mathbb{R}^1, \mathbf{z} = [X, Y, X', Y'] \in \mathbb{R}^4 \\ \int_0^{2\pi} \int_0^{2\pi} \left(\frac{\partial \mathbf{z}_0}{\partial \theta_2} \right)^\top \cdot \mathbf{z} \, d\theta_1 d\theta_2 = 0. \end{aligned} \quad (20)$$

¹⁰Often referred to as a HOPF bifurcation of maps.

In the case of quasiperiodic solutions a phase condition is required, since ω_2 is a frequency arising from self-excitation. Note again, that the projection of the phase condition is just carried out on the differentiation of the time scale θ_2 , since this scale represents the free phase. Furthermore, a common task in the literature is the determination of a nearby solution \mathbf{z}_0 and an initial guess for the nonlinear solver at the internalization of the continuation¹¹. In this contribution it is implemented with a time simulation. The results of the continuation are depicted in figure

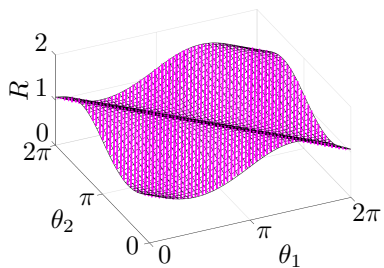


Figure 8: Invariant manifold of the rotor radius compared to a finite time simulation ($\Omega = 0.33$).

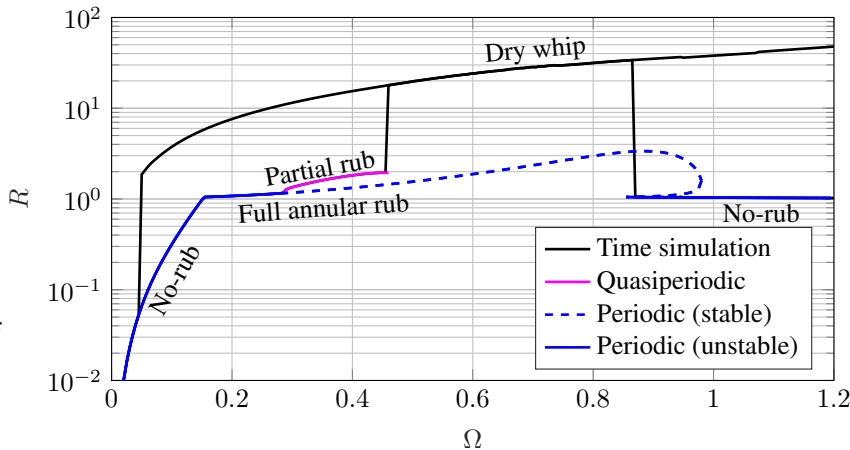


Figure 9: Continuation of Ω compared to time integrations.

9, where $R = \sqrt{X^2 + Y^2}$ is the maximal rotor amplitude. Starting with a periodic no-rub motion the transition to the full annular rub happens when the rotor comes in contact with the stator. The full annular rub gets unstable at $\Omega \approx 0.29$ through a NEIMARK-SACKER bifurcation and a quasiperiodic motion arises, the partial rub. Since the invariance equation holds also for unstable solution, the periodic branch can be continued. It regains stability when the amplitudes of the full annular decrease and the rotor is no longer in contact with the stator. The quasiperiodic branch of the partial rub can also be continued until it stops existing. The stationary results are in good accordance with the time integrations and the literature [17]. In figure 8 an approximated invariant submanifold of the partial rub motion and a time simulation are depicted. The trajectory fills the manifold densely when the time interval increases. The stationary solutions of the dry whip motion are not investigated in context of this contribution and will be considered in further works.

4 Conclusion

In this work a brief summary of the systematic appearance of quasiperiodic motion in rotor dynamical applications is given. It has been shown that quasiperiodic oscillations are often found in the literature but usually analyzed with time marching techniques. This circumstance originated due to the lack of established programs to continue quasiperiodic motions. Furthermore, the basic theory of formulating equations to calculate quasiperiodic on finite boundaries is given. In this context the connection between periodic and quasiperiodic solutions concerning internal frequencies is stressed out and put into one framework. The two main approaches, used in the literature, to solve the resulting system of PDE are outlined (FOURIER-GALERKIN method (FGM) and finite-difference method (FDM)) whereby the FDM is used in this work. The method is applied to two examples from the literature covering the main concepts of quasiperiodic occurrence in unbalanced rotor systems. The first one is a generator rotor with unbalanced magnetic pull (UMP), where both frequencies are predetermined. The investigation led to interesting behavior when considering static eccentricities of the rotor, like lessen of the operation regime. The second considered model is a rotor-to-stator contact system in which one frequency is predetermined and the other one not. Concerning to this investigation it is shown that the stationary quasiperiodic solutions can be predicted correctly, which is verified by time simulations. Furthermore, it is shown that periodic solution are included in the framework of quasiperiodic motions.

Although the presented method is merely applied to relatively small models, the framework is easily applicable to larger dynamical systems.

¹¹During a continuation one can use the solution of a previous continuation step.

REFERENCES

- [1] An, X., Zhou, J., Xiang, X., Li, C., and Luo, Z. (2009): Dynamic response of a rub-impact rotor system under axial thrust. *Archive of Applied Mechanics*, **79**(11), pp. 1009–1018.
- [2] Bonello, P., Brennan, M. J., and Holmes, R. (2002): Non-linear modelling of rotor dynamic systems with squeeze film dampers an efficient integrated approach. *Journal of Sound and Vibration*, **249**(4), pp. 743–773.
- [3] Bonnett, A. H., and Soukup, G. C. (1992): Cause and analysis of stator and rotor failures in three-phase squirrel-cage induction motors. *IEEE Transactions on Industry applications*, **28**(4), pp. 921–937.
- [4] Boy, F., and Hetzler, H. (2018): A Co-energy Based Approach to Model the Rotordynamics of Electrical Machines. In *International Conference on Rotor Dynamics*. Rio, Brazil, Sept. 23–27, pp. 190–204.
- [5] Edwards, S., Lees, A. W., and Friswell, M. I. (1999): The influence of torsion on rotor/stator contact in rotating machinery. *Journal of Sound and Vibration*, **225**(4), pp. 767–778.
- [6] Feng, Z. C., and Zhang, X. Z. (2002): Rubbing phenomena in rotor–stator contact. *Chaos, Solitons and Fractals*, **14**(2), pp. 257–267.
- [7] Fiedler, R. and Hetzler, H. (2017): Numerical approximation of invariant manifolds for dynamical systems with simultaneous self- and forced excitation. In *Proceedings of the 9th European Nonlinear Dynamics Conference*. Budapest, Hungary, June 25–30, ID 279
- [8] Grāpis, O., Tamus, V., Ohlson, N. G., and Andersons, J. (2006): Overcritical high-speed rotor systems, full annular rub and accident. *Journal of sound and vibration*, **290**(3-5), pp. 910–927
- [9] Grolet, A., and Thouverez, F. (2012): On a new harmonic selection technique for harmonic balance method. *Mechanical Systems and Signal Processing*, **30**, pp. 43–60.
- [10] Guo, D., Chu, F., and Chen, D. (2002): The unbalanced magnetic pull and its effects on vibration in a three-phase generator with eccentric rotor. *Journal of sound and Vibration*, **254**(2), pp. 297–312.
- [11] Hetzler, H. and Boy, F. (2017): Internal dissipation and self-excited oscillations in rotating machinery: internal friction vs. internal viscous damping, In *Proceedings of the 17th International Symposium of Rotating Machinery ISROMAC*. Maui/Hawaii, USA, December 16–21.
- [12] Jiang, J. (2009): Determination of the global responses characteristics of a piecewise smooth dynamical system with contact. *Nonlinear Dynamics*, **57**(3), pp. 351–361.
- [13] Jiang, J., and Ulbrich, H. (2005): The physical reason and the analytical condition for the onset of dry whip in rotor-to-stator contact systems. *Journal of vibration and acoustics*, **12**(6), pp. 594–603.
- [14] Kandil, M.A.: On Rotor Internal Damping. *dissertation thesis*, Imperial College, London, UK.
- [15] Marx, B., and Vogt, W. (2010): *Dynamische Systeme: Theorie und Numerik*. Springer-Verlag.
- [16] Nayfeh, A. H., and Mook, D. T. (2008): *Nonlinear oscillations*. John Wiley & Sons.
- [17] Peletan, L., Baguet, S., Torkhani, M., and Jacquet-Richardet, G. (2014): Quasi-periodic harmonic balance method for rubbing self-induced vibrations in rotorstator dynamics. *Nonlinear Dynamics*, **78**(4), pp. 2501–2515.
- [18] Popprath, S., and Ecker, H. (2007): Nonlinear dynamics of a rotor contacting an elastically suspended stator. *Journal of Sound and Vibration*, **308**(3-5), pp. 767–784.
- [19] Samoilenko, A. M., and Petryshyn, R. (2004): *Multifrequency oscillations of nonlinear systems* (Vol. 567). Springer Science & Business Media.
- [20] Samoilenko, A. M. (1991): *Elements of the mathematical theory of multi-frequency oscillations* (Vol. 71). Springer Science & Business Media.
- [21] Schilder, F., Vogt, W., Schreiber, S., and Osinga, H. M. (2006): Fourier methods for quasiperiodic oscillations. *International journal for numerical methods in engineering*, **67**(5), pp. 629–671.
- [22] Schilder, F., Osinga, H. M., and Vogt, W. (2005): Continuation of quasi-periodic invariant tori. *SIAM Journal on Applied Dynamical Systems*, **4**(3), pp. 459–488.
- [23] Sinha, S. K. (2013): Rotordynamic analysis of asymmetric turbofan rotor due to fan blade-loss event with contact-impact rub loads. *Journal of Sound and Vibration*, **332**(9), pp. 2253–2283.
- [24] Xu, X., Han, Q., and Chu, F. (2016): Nonlinear vibration of a generator rotor with unbalanced magnetic pull considering both dynamic and static eccentricities. *Archive of Applied Mechanics*, **86**(8), pp. 1521–1536.

Model correlation for special types of rotor systems

Gudrun Mikota¹, **Horst Ecker**²

¹ Institute of Machine Design and Hydraulic Drives, Johannes Kepler University Linz, A-4040 Linz, Austria, gudrun.mikota@jku.at

² Institute of Mechanics and Mechatronics, Vienna University of Technology, A-1060 Wien, Austria, horst.ecker@tuwien.ac.at

Abstract

The correlation between theoretical and experimental modal models can be quantified by the Modal Assurance Criterion, which has also been used for rotor systems. However, the conclusions drawn from the Modal Assurance Criterion may not be valid for non-symmetric systems since the underlying orthogonality relations are violated. Therefore, a Rotor Correlation Criterion is proposed, which incorporates right and left eigenvectors, eigenvalues, and mass and stiffness matrices. Applications of model correlation for test data assessment, sensor placement, mode pairing, and model updating are discussed in the context of rotors. For two numerical examples, the modified correlation approach is compared to the Modal Assurance Criterion. Considering the availability of experimentally determined left eigenvectors, these examples deal with a damped rotor under special support conditions and a purely gyroscopic rotor under more general conditions.

1 Introduction

The Modal Assurance Criterion (MAC) [2] is widely used to assess the correlation between theoretical and experimental modal models. If the mass or stiffness weighted MAC of a non-rotating structure is proportional to the identity matrix, mode shapes are perfectly correlated. For many structural models, the weighting matrix is not essential, and a similar MAC is obtained without weighting. The unweighted MAC only requires the mode shapes, which suggests that it could be suited for any type of system. However, the properties of the MAC depend on the underlying orthogonality relations, which are violated by non-symmetric models. Since the system matrices of rotors are in general non-symmetric, there is no guarantee that the usual conclusions from the MAC are still valid.

For a flexible rotor in journal bearings, the main MAC diagonal of theoretical and experimental modes has been calculated in [6]. Four out of ten values were below the recommended limit of 0.9 and could not be improved by model updating. Moreover, significant differences appeared between the MAC values of right and left eigenvectors. In this case, model correlation would have required a modified approach.

For the model correlation of rotor systems, one might consider the modal matching array from [1], which is defined for general second-order systems. It incorporates right and left eigenvectors as well as all system matrices. In a comparison between theoretical and experimental modal models, approximate mass and stiffness matrices will be available, while damping will hardly be known; this discourages the use of the modal matching array, which also involves rather complex calculations. The difficulty of obtaining left eigenvectors from experiments has been discussed in [3]. For purely gyroscopic rotors [7, 8] or special support conditions [9, 10], they can be calculated from right eigenvectors so that the rotor only has to be excited in one degree of freedom. In this paper, the results from [9, 10] are used to ensure the practical applicability of a modified correlation approach.

Besides the comparison between theoretical and experimental modal models, the MAC is used in other applications such as the validation of experimental modal models [2], optimal sensor placement [11], and the objective function for model updating algorithms [12]. Future success in the model updating of rotor systems will depend on an efficient treatment of these issues and requires an appropriate approach to model correlation.

This paper is based on a general orthogonality relation for non-symmetric systems. It proposes a correlation criterion that incorporates right and left eigenvectors, eigenvalues, and mass and stiffness matrices. Various applications of model correlation are discussed with an emphasis on their importance for rotors. The advantage of the modified correlation approach is demonstrated by numerical examples. These examples consider special types of rotor systems for which appropriate experiments are feasible. They investigate various applications of model correlation for a rotor in damped isotropic bearings and a rotor in undamped bearings with minor anisotropy.

2 Modified correlation criterion

To derive the required orthogonality relation, the equation of motion

$$\mathbf{M}\ddot{\mathbf{u}} + (\mathbf{C} + \mathbf{G})\dot{\mathbf{u}} + (\mathbf{K} + \mathbf{N})\mathbf{u} = \mathbf{0} \quad (1)$$

for an autonomous rotor system with the displacement vector \mathbf{u} , the symmetric mass matrix \mathbf{M} , the symmetric damping matrix \mathbf{C} , the skew-symmetric gyroscopic Matrix \mathbf{G} , the symmetric stiffness matrix \mathbf{K} , and the skew-symmetric circulatory matrix \mathbf{N} is transformed into

$$\mathbf{A} \begin{bmatrix} \dot{\mathbf{u}} \\ \ddot{\mathbf{u}} \end{bmatrix} + \mathbf{B} \begin{bmatrix} \mathbf{u} \\ \dot{\mathbf{u}} \end{bmatrix} = \mathbf{0} \quad (2)$$

where

$$\mathbf{A} = \begin{bmatrix} \mathbf{C} + \mathbf{G} & \mathbf{M} \\ \mathbf{M} & \mathbf{0} \end{bmatrix} \quad (3)$$

and

$$\mathbf{B} = \begin{bmatrix} \mathbf{K} + \mathbf{N} & \mathbf{0} \\ \mathbf{0} & -\mathbf{M} \end{bmatrix}. \quad (4)$$

Equation (2) leads to the first order right eigenvalue problem

$$(\lambda_n \mathbf{A} + \mathbf{B}) \boldsymbol{\theta}_{rn} = \mathbf{0}, \quad (5)$$

in which both eigenvalues λ_n and right eigenvectors $\boldsymbol{\theta}_{rn}$ appear as complex conjugate pairs. The first order left eigenvalue problem

$$\boldsymbol{\theta}_{ln}^T (\lambda_n \mathbf{A} + \mathbf{B}) = \mathbf{0}^T \quad (6)$$

yields the same eigenvalues λ_n and the left eigenvectors $\boldsymbol{\theta}_{ln}$, which also appear as complex conjugate pairs. In general, right and left eigenvectors do not coincide.

If Eq. (5) is premultiplied by the transpose of the left eigenvector $\boldsymbol{\theta}_{lm}$, one obtains

$$\boldsymbol{\theta}_{lm}^T (\lambda_n \mathbf{A} + \mathbf{B}) \boldsymbol{\theta}_{rn} = 0. \quad (7)$$

Expressing Eq. (6) for the index m and postmultiplying by the right eigenvector $\boldsymbol{\theta}_{rn}$ results in

$$\boldsymbol{\theta}_{lm}^T (\lambda_m \mathbf{A} + \mathbf{B}) \boldsymbol{\theta}_{rn} = 0. \quad (8)$$

For $m \neq n$, the combination of Eqs. (7) and (8) proves the orthogonality relation

$$\boldsymbol{\theta}_{lm}^T \mathbf{B} \boldsymbol{\theta}_{rn} = 0. \quad (9)$$

The right and left eigenvectors $\boldsymbol{\psi}_{rn}$ and $\boldsymbol{\psi}_{lm}$ of the system (1) satisfy the relations

$$(\lambda_n^2 \mathbf{M} + \lambda_n(\mathbf{C} + \mathbf{G}) + \mathbf{K} + \mathbf{N}) \boldsymbol{\psi}_{rn} = \mathbf{0} \quad (10)$$

and

$$\boldsymbol{\psi}_{lm}^T (\lambda_m^2 \mathbf{M} + \lambda_m(\mathbf{C} + \mathbf{G}) + \mathbf{K} + \mathbf{N}) = \mathbf{0}^T, \quad (11)$$

respectively. It follows from Eqs. (3-6), (10), and (11) that

$$\boldsymbol{\theta}_{rn} = \begin{bmatrix} \boldsymbol{\psi}_{rn} \\ \lambda_n \boldsymbol{\psi}_{rn} \end{bmatrix} \quad (12)$$

and

$$\boldsymbol{\theta}_{lm} = \begin{bmatrix} \boldsymbol{\psi}_{lm} \\ \lambda_m \boldsymbol{\psi}_{lm} \end{bmatrix}. \quad (13)$$

With Eqs. (4), (12), and (13), the orthogonality relation (9) becomes

$$\boldsymbol{\psi}_{lm}^T (\mathbf{K} + \mathbf{N}) \boldsymbol{\psi}_{rn} - \lambda_m \lambda_n \boldsymbol{\psi}_{lm}^T \mathbf{M} \boldsymbol{\psi}_{rn} = 0, \quad (14)$$

which constitutes the basis of the correlation criterion proposed in this paper.

In the various applications of model correlation, two sets A and B of both right and left eigenvectors are considered. They may be obtained from theory or by experiment and sometimes they coincide. Omitting the circulatory matrix for brevity, Eq. (14) suggests the abbreviation

$$S_{mAnB} = \boldsymbol{\psi}_{lmA}^T \mathbf{K} \boldsymbol{\psi}_{rnB} - \lambda_{mA} \lambda_{nB} \boldsymbol{\psi}_{lmA}^T \mathbf{M} \boldsymbol{\psi}_{rnB}; \quad (15)$$

using Eq. (15), the elements of the Rotor Correlation Criterion (RCC) matrix are defined as

$$\text{RCC}_{mn} = \frac{|S_{mAnB}| \cdot |S_{nBmA}|}{|S_{mA mA}| \cdot |S_{nB nB}|}. \quad (16)$$

If the two sets of eigenvectors A and B coincide, an auto-RCC is obtained, which should be close to the identity matrix. In theory, it yields the identity matrix if the circulatory matrix remains in Eq. (15).

Section 4 uses the elements of the classical MAC matrix for comparison. They are given by

$$\text{MAC}_{mn} = \frac{|\boldsymbol{\psi}_{rmA}^H \boldsymbol{\psi}_{rnB}| \cdot |\boldsymbol{\psi}_{rnB}^H \boldsymbol{\psi}_{rmA}|}{|\boldsymbol{\psi}_{rmA}^H \boldsymbol{\psi}_{rmA}| \cdot |\boldsymbol{\psi}_{rnB}^H \boldsymbol{\psi}_{rnB}|}, \quad (17)$$

which is based on the orthogonality relation

$$\boldsymbol{\psi}_{rm}^T \mathbf{M} \boldsymbol{\psi}_{rn} = 0 \quad (m \neq n) \quad (18)$$

for undamped symmetric systems [4].

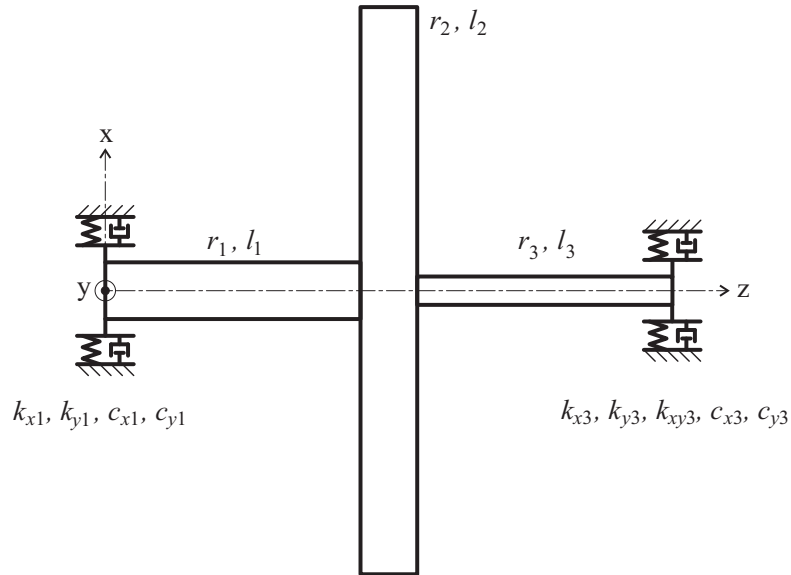


Figure 1: Schematic of a flexible rotor.

3 Applications of model correlation

In structural dynamics, the MAC has a wide range of applications; typical uses are listed in [2]. Some applications of model correlation will be essential for modal testing and model updating of rotor systems. In practical cases, access to a rotor is limited and vibration measurements are restricted to a small number of degrees of freedom. The preparation of measurement points may cause a considerable effort, which should be made for optimal positions to avoid repeated trials. This issue is addressed by optimal sensor placement. For non-rotating systems, an appropriate method has been described in [11]. It considers the auto-MAC matrix of Finite Element mode shapes that are sampled at the selected sensor positions. This matrix should come close to identity. For rotor systems, it can be replaced by the RCC matrix. In the RCC formula, right and left eigenvectors have to be sampled at the selected sensor positions, and mass and stiffness matrices must be reduced to the measured degrees of freedom.

In view of the practical difficulties that arise with excitation and measurement under rotation, an experimental modal rotor model should be validated to ensure the quality of measurements. The validation of experimental modal models was an original intention of the MAC [2]. For non-rotating systems, it requires an auto-MAC matrix of experimental mode shapes, which can be calculated in the absence of a theoretical model. If the RCC matrix is calculated for the validation of experimental mode shapes from a rotor system, the formula also requires experimental left eigenvectors as well as a first estimate of reduced mass and stiffness matrices. It seems easier to use the MAC, but this may lead to misjudgement. For an experimental modal rotor model, the auto-RCC matrix should be near identity.

The validation and, if possible, the successful correction of a physical model may be considered as the ultimate goal of modal testing. Once the quality of measurements has been ensured, the correlation between theoretical and experimental modal models can be used to validate the physical model. For non-rotating systems, the MAC matrix of theoretical and experimental mode shapes should have main diagonal values above 0.9 and off-diagonal values below 0.1 to ensure a good correlation [4]. For rotor systems, the RCC matrix can be used in a similar way. Reduced mass and stiffness matrices can be estimated from the theoretical model.

Model updating aims at the correction of physical model parameters. The objective function can be composed of theoretical and experimental eigenvalues, eigenvectors, or the correlation criterion itself [12]. For a reasonable definition of this function, it is essential to identify matching mode pairs, which are indicated by the correlation criterion. If the MAC is used for rotor mode pairing, the objective function may be misleading and model updating may fail. The RCC should be used instead. In an iterative approach, reduced mass and stiffness matrices could be recalculated from updated model parameters.

4 Numerical examples

The rotor under consideration is depicted in Fig. 1. The non-symmetric rotor system consists of a rigid disc attached to a flexible shaft, which is supported by a bearings at both ends. In the examples, two different configurations of these bearings will be considered. The coordinate system in Fig. 1 is aligned with the principal axes of the left bearing with stiffness constants in directions x and y denoted as k_{x1} and k_{y1} ; respective damping constants c_{x1} and c_{y1} are used in the first example. The left shaft section with radius r_1 and length l_1 is described by its mass $m_1 = \rho l_1 r_1^2 \pi$ and transverse area moment of inertia $J_1 = r_1^4 \pi / 4$; ρ denotes the mass density. The mass of the disc with radius r_2 and thickness l_2 is $m_2 = \rho l_2 r_2^2 \pi$. Its transverse and polar mass moments of inertia are $I_{t2} = \rho l_2 r_2^4 \pi / 4$ and $I_{p2} = \rho l_2 r_2^4 \pi / 2$, respectively. For the right shaft section with radius r_3 and length l_3 , $m_3 = \rho l_3 r_3^2 \pi$ and $J_3 = r_3^4 \pi / 4$. The stiffness constants of the right bearing are denoted as k_{x3} and k_{y3} . Respective damping constants c_{x3} and c_{y3} are used in the first example. Below, a cross-coupled stiffness k_{xy3} appears in the second example.

To keep the model simple, each of the two shaft sections is described by a beam element neglecting shear deflection [5]. The displacement vector is defined as

$$\mathbf{u} = [x_1 \ \beta_1 \ x_2 \ \beta_2 \ x_3 \ \beta_3 \ y_1 \ \alpha_1 \ y_2 \ \alpha_2 \ y_3 \ \alpha_3]^T \quad (19)$$

with translations $x_1, y_1, x_2, y_2, x_3, y_3$ and rotations $\alpha_1, \beta_1, \alpha_2, \beta_2, \alpha_3, \beta_3$ at the left bearing (index 1), the disc center (index 2), and the right bearing (index 3); α and β describe rotations about the x - and y -axes, respectively. The mass matrix associated with the displacement vector \mathbf{u} reads

$$\mathbf{M} = \begin{bmatrix} \mathbf{M}_x & \mathbf{0} \\ \mathbf{0} & \mathbf{M}_y \end{bmatrix} \quad (20)$$

with

$$\mathbf{M}_x = \mathbf{M}_2 + \frac{1}{420} \begin{bmatrix} 156m_1 l_1 & 22m_1 l_1^2 & 54m_1 l_1 & -13m_1 l_1^2 & 0 & 0 \\ 22m_1 l_1^2 & 4m_1 l_1^3 & 13m_1 l_1^2 & -3m_1 l_1^3 & 0 & 0 \\ 54m_1 l_1 & 13m_1 l_1^2 & 156(m_1 l_1 + m_3 l_3) & -22(m_1 l_1^2 - m_3 l_3^2) & 54m_3 l_3 & -13m_3 l_3^2 \\ -13m_1 l_1^2 & -3m_1 l_1^3 & -22(m_1 l_1^2 - m_3 l_3^2) & 4(m_1 l_1^3 + m_3 l_3^3) & 13m_3 l_3^2 & -3m_3 l_3^3 \\ 0 & 0 & 54m_3 l_3 & 13m_3 l_3^2 & 156m_3 l_3 & -22m_3 l_3^2 \\ 0 & 0 & -13m_3 l_3^2 & -3m_3 l_3^3 & -22m_3 l_3^2 & 4m_3 l_3^3 \end{bmatrix} \quad (21)$$

and

$$\mathbf{M}_y = \mathbf{M}_2 + \frac{1}{420} \begin{bmatrix} 156m_1 l_1 & -22m_1 l_1^2 & 54m_1 l_1 & 13m_1 l_1^2 & 0 & 0 \\ -22m_1 l_1^2 & 4m_1 l_1^3 & -13m_1 l_1^2 & -3m_1 l_1^3 & 0 & 0 \\ 54m_1 l_1 & -13m_1 l_1^2 & 156(m_1 l_1 + m_3 l_3) & 22(m_1 l_1^2 - m_3 l_3^2) & 54m_3 l_3 & 13m_3 l_3^2 \\ 13m_1 l_1^2 & -3m_1 l_1^3 & 22(m_1 l_1^2 - m_3 l_3^2) & 4(m_1 l_1^3 + m_3 l_3^3) & -13m_3 l_3^2 & -3m_3 l_3^3 \\ 0 & 0 & 54m_3 l_3 & -13m_3 l_3^2 & 156m_3 l_3 & 22m_3 l_3^2 \\ 0 & 0 & 13m_3 l_3^2 & -3m_3 l_3^3 & 22m_3 l_3^2 & 4m_3 l_3^3 \end{bmatrix}, \quad (22)$$

where

$$\mathbf{M}_2 = \begin{bmatrix} 0 & 0 & 0 & 0 & 0 & 0 \\ 0 & 0 & 0 & 0 & 0 & 0 \\ 0 & 0 & m_2 & 0 & 0 & 0 \\ 0 & 0 & 0 & I_{t2} & 0 & 0 \\ 0 & 0 & 0 & 0 & 0 & 0 \\ 0 & 0 & 0 & 0 & 0 & 0 \end{bmatrix}. \quad (23)$$

Note that signs are changed between Eqs. (21) and (22). The damping matrix is given by

$$\mathbf{C} = \begin{bmatrix} \mathbf{C}_x & \mathbf{0} \\ \mathbf{0} & \mathbf{C}_y \end{bmatrix} \quad (24)$$

with

$$\mathbf{C}_x = \begin{bmatrix} c_{x1} & 0 & 0 & 0 & 0 & 0 \\ 0 & 0 & 0 & 0 & 0 & 0 \\ 0 & 0 & 0 & 0 & 0 & 0 \\ 0 & 0 & 0 & 0 & 0 & 0 \\ 0 & 0 & 0 & c_{x3} & 0 & 0 \\ 0 & 0 & 0 & 0 & 0 & 0 \end{bmatrix} \quad \text{and} \quad \mathbf{C}_y = \begin{bmatrix} c_{y1} & 0 & 0 & 0 & 0 & 0 \\ 0 & 0 & 0 & 0 & 0 & 0 \\ 0 & 0 & 0 & 0 & 0 & 0 \\ 0 & 0 & 0 & 0 & 0 & 0 \\ 0 & 0 & 0 & c_{y3} & 0 & 0 \\ 0 & 0 & 0 & 0 & 0 & 0 \end{bmatrix}. \quad (25)$$

The gyroscopic matrix reads

$$\mathbf{G} = \begin{bmatrix} \mathbf{0} & \mathbf{G}_0 \\ -\mathbf{G}_0^T & \mathbf{0} \end{bmatrix} \quad (26)$$

with

$$\mathbf{G}_0 = \begin{bmatrix} 0 & 0 & 0 & 0 & 0 & 0 \\ 0 & 0 & 0 & 0 & 0 & 0 \\ 0 & 0 & 0 & 0 & 0 & 0 \\ 0 & 0 & 0 & -I_{p2}\Omega & 0 & 0 \\ 0 & 0 & 0 & 0 & 0 & 0 \\ 0 & 0 & 0 & 0 & 0 & 0 \end{bmatrix}, \quad (27)$$

in which Ω denotes the rotational speed. The stiffness matrix is given by

$$\mathbf{K} = \begin{bmatrix} \mathbf{K}_x & \mathbf{K}_{xy} \\ \mathbf{K}_{xy}^T & \mathbf{K}_y \end{bmatrix} \quad (28)$$

with

$$\mathbf{K}_x = \begin{bmatrix} k_{x1} & 0 & 0 & 0 & 0 & 0 \\ 0 & 0 & 0 & 0 & 0 & 0 \\ 0 & 0 & 0 & 0 & 0 & 0 \\ 0 & 0 & 0 & 0 & 0 & 0 \\ 0 & 0 & 0 & k_{x3} & 0 & 0 \\ 0 & 0 & 0 & 0 & 0 & 0 \end{bmatrix} + E \begin{bmatrix} 12\frac{J_1}{l_1^3} & 6\frac{J_1}{l_1^2} & -12\frac{J_1}{l_1^3} & 6\frac{J_1}{l_1^2} & 0 & 0 \\ 6\frac{J_1}{l_1^2} & 4\frac{J_1}{l_1} & -6\frac{J_1}{l_1^2} & 2\frac{J_1}{l_1} & 0 & 0 \\ -12\frac{J_1}{l_1^3} & -6\frac{J_1}{l_1^2} & 12\left(\frac{J_1}{l_1^3} + \frac{J_3}{l_3^3}\right) & -6\left(\frac{J_1}{l_1^2} - \frac{J_3}{l_3^2}\right) & -12\frac{J_3}{l_3^3} & 6\frac{J_3}{l_3^2} \\ 6\frac{J_1}{l_1^2} & 2\frac{J_1}{l_1} & -6\left(\frac{J_1}{l_1^2} - \frac{J_3}{l_3^2}\right) & 4\left(\frac{J_1}{l_1} + \frac{J_3}{l_3}\right) & -6\frac{J_3}{l_3^2} & 2\frac{J_3}{l_3} \\ 0 & 0 & -12\frac{J_3}{l_3^3} & -6\frac{J_3}{l_3^2} & 12\frac{J_3}{l_3^3} & -6\frac{J_3}{l_3^2} \\ 0 & 0 & 6\frac{J_3}{l_3^2} & 2\frac{J_3}{l_3} & -6\frac{J_3}{l_3^2} & 4\frac{J_3}{l_3} \end{bmatrix}, \quad (29)$$

$$\mathbf{K}_y = \begin{bmatrix} k_{y1} & 0 & 0 & 0 & 0 & 0 \\ 0 & 0 & 0 & 0 & 0 & 0 \\ 0 & 0 & 0 & 0 & 0 & 0 \\ 0 & 0 & 0 & 0 & 0 & 0 \\ 0 & 0 & 0 & k_{y3} & 0 & 0 \\ 0 & 0 & 0 & 0 & 0 & 0 \end{bmatrix} + E \begin{bmatrix} 12\frac{J_1}{l_1^3} & -6\frac{J_1}{l_1^2} & -12\frac{J_1}{l_1^3} & -6\frac{J_1}{l_1^2} & 0 & 0 \\ -6\frac{J_1}{l_1^2} & 4\frac{J_1}{l_1} & 6\frac{J_1}{l_1^2} & 2\frac{J_1}{l_1} & 0 & 0 \\ -12\frac{J_1}{l_1^3} & 6\frac{J_1}{l_1^2} & 12\left(\frac{J_1}{l_1^3} + \frac{J_3}{l_3^3}\right) & 6\left(\frac{J_1}{l_1^2} - \frac{J_3}{l_3^2}\right) & -12\frac{J_3}{l_3^3} & -6\frac{J_3}{l_3^2} \\ -6\frac{J_1}{l_1^2} & 2\frac{J_1}{l_1} & 6\left(\frac{J_1}{l_1^2} - \frac{J_3}{l_3^2}\right) & 4\left(\frac{J_1}{l_1} + \frac{J_3}{l_3}\right) & 6\frac{J_3}{l_3^2} & 2\frac{J_3}{l_3} \\ 0 & 0 & -12\frac{J_3}{l_3^3} & 6\frac{J_3}{l_3^2} & 12\frac{J_3}{l_3^3} & 6\frac{J_3}{l_3^2} \\ 0 & 0 & -6\frac{J_3}{l_3^2} & 2\frac{J_3}{l_3} & 6\frac{J_3}{l_3^2} & 4\frac{J_3}{l_3} \end{bmatrix}, \quad (30)$$

and

$$\mathbf{K}_{xy} = \begin{bmatrix} 0 & 0 & 0 & 0 & 0 & 0 \\ 0 & 0 & 0 & 0 & 0 & 0 \\ 0 & 0 & 0 & 0 & 0 & 0 \\ 0 & 0 & 0 & 0 & 0 & 0 \\ 0 & 0 & 0 & 0 & k_{xy3} & 0 \\ 0 & 0 & 0 & 0 & 0 & 0 \end{bmatrix}, \quad (31)$$

where E denotes the modulus of elasticity. Again, signs are changed between Eqs. (29) and (30).

For a mixture of translations and rotations, the MAC cannot be calculated since this would require an addition of squared lengths and squared angles. The model is therefore reduced to the translational coordinates

$$\mathbf{x} = [x_1 \ x_2 \ x_3 \ y_1 \ y_2 \ y_3]^T \quad (32)$$

by a static condensation [5]. The matrix \mathbf{S} sorts the displacement vector \mathbf{u} so that

$$\begin{bmatrix} \mathbf{x} \\ \mathbf{a} \end{bmatrix} = \mathbf{S} \mathbf{u} \quad (33)$$

with the remaining coordinates \mathbf{x} and the condensed coordinates

$$\mathbf{a} = [\beta_1 \ \beta_2 \ \beta_3 \ \alpha_1 \ \alpha_2 \ \alpha_3]^T. \quad (34)$$

The stiffness matrix associated with the sorted displacement vector is partitioned in 6×6 blocks according to

$$(\mathbf{S}^{-1})^T \mathbf{K} \mathbf{S}^{-1} = \begin{bmatrix} \mathbf{K}_{xx} & \mathbf{K}_{xa} \\ \mathbf{K}_{ax} & \mathbf{K}_{aa} \end{bmatrix}, \quad (35)$$

and the static relationship can be expressed by

$$\begin{bmatrix} \mathbf{x} \\ \mathbf{a} \end{bmatrix} = \begin{bmatrix} \mathbf{I}(6 \times 6) \\ -\mathbf{K}_{aa}^{-1} \mathbf{K}_{ax} \end{bmatrix} \mathbf{x}. \quad (36)$$

Using the reduction matrix

$$\mathbf{R} = \mathbf{S}^{-1} \begin{bmatrix} \mathbf{I}(6 \times 6) \\ -\mathbf{K}_{aa}^{-1} \mathbf{K}_{ax} \end{bmatrix}, \quad (37)$$

the condensed system matrices are given by $\mathbf{R}^T \mathbf{M} \mathbf{R}$, $\mathbf{R}^T \mathbf{C} \mathbf{R}$, $\mathbf{R}^T \mathbf{G} \mathbf{R}$, and $\mathbf{R}^T \mathbf{K} \mathbf{R}$.

4.1 Rotor in damped isotropic bearings

The first example considers a rotor system whose parameters are given by $r_1 = 10$ mm, $l_1 = 100$ mm, $r_2 = 100$ mm, $l_2 = 20$ mm, $r_3 = 5$ mm, $l_3 = 100$ mm, $\rho = 7860$ kg m⁻³, $E = 2.1 \cdot 10^{11}$ N m⁻², $k_{x1} = k_{y1} = 30E J_1/l_1^3$, $k_{x3} = k_{y3} = 0.1k_{x1}$, $k_{xy3} = 0$, $c_{x1} = c_{y1} = 0.01\sqrt{k_{x1}m_2/2}$, $c_{x3} = c_{y3} = 0.01\sqrt{k_{x3}m_2/2}$, and $\Omega = 20000$ rpm. Both the original and the reduced model comply with the conditions in [9, 10]. This means that the calculation of the RCC does not require additional measurements for the experimental determination of left eigenvectors.

To compare theoretical MAC and RCC matrices, the eigenvalue problem is solved for the reduced model. The auto-RCC of the reduced model yields the identity matrix. The respective auto-MAC matrix is given by

$$\text{MAC : } \begin{bmatrix} \mathbf{1.0000} & 0.0000 & 0.2532 & 0.0000 & 0.0153 & 0.0000 \\ 0.0000 & \mathbf{1.0000} & 0.0000 & 0.2735 & 0.0000 & 0.0400 \\ 0.2532 & 0.0000 & \mathbf{1.0000} & 0.0000 & 0.1249 & 0.0000 \\ 0.0000 & 0.2735 & 0.0000 & \mathbf{1.0000} & 0.0000 & \mathbf{0.4306} \\ 0.0153 & 0.0000 & 0.1249 & 0.0000 & \mathbf{1.0000} & 0.0000 \\ 0.0000 & 0.0400 & 0.0000 & \mathbf{0.4306} & 0.0000 & \mathbf{1.0000} \end{bmatrix} .$$

Since this matrix contains large off-diagonal values, it should not be used for the validation of an experimental modal rotor model. Otherwise, perfect measurements might be dismissed.

If the eigenvalue problem is solved for the original model and eigenvectors are sampled at the translational degrees of freedom, the question of sensor placement can be addressed. There is little alternative to measuring six translations, which results in the auto-RCC matrix

$$\text{RCC : } \begin{bmatrix} \mathbf{1.0000} & 0.0000 & 0.1488 & 0.0000 & 0.0009 & 0.0000 \\ 0.0000 & \mathbf{1.0000} & 0.0000 & 0.0848 & 0.0000 & 0.0511 \\ 0.1488 & 0.0000 & \mathbf{1.0000} & 0.0000 & 0.0488 & 0.0000 \\ 0.0000 & 0.0848 & 0.0000 & \mathbf{1.0000} & 0.0000 & \mathbf{0.6426} \\ 0.0009 & 0.0000 & 0.0488 & 0.0000 & \mathbf{1.0000} & 0.0000 \\ 0.0000 & 0.0511 & 0.0000 & \mathbf{0.6426} & 0.0000 & \mathbf{1.0000} \end{bmatrix} ;$$

relaxing the limit for off-diagonal values to 0.2, it can be concluded that the omission of rotations is acceptable for the lowest five modes. In contrast, the auto-MAC matrix becomes

$$\text{MAC : } \begin{bmatrix} \mathbf{1.0000} & 0.0000 & \mathbf{0.9827} & 0.0000 & 0.0155 & 0.0000 \\ 0.0000 & \mathbf{1.0000} & 0.0000 & 0.0007 & 0.0000 & 0.0040 \\ \mathbf{0.9827} & 0.0000 & \mathbf{1.0000} & 0.0000 & 0.0028 & 0.0000 \\ 0.0000 & 0.0007 & 0.0000 & \mathbf{1.0000} & 0.0000 & 0.8001 \\ 0.0155 & 0.0000 & 0.0028 & 0.0000 & \mathbf{1.0000} & 0.0000 \\ 0.0000 & 0.0040 & 0.0000 & 0.8001 & 0.0000 & \mathbf{1.0000} \end{bmatrix} ;$$

this would mean that the omission of rotations cannot be accepted at all.

It is now assumed that experimental right eigenvectors are available for a rotor system whose actual model parameters differ from those of the theoretical model. The stiffness constants of the right bearing are $k_{x3} = k_{y3} = 0.06k_{x1}$ in this assumption. Experimental left eigenvectors can be obtained by changing the signs in the lower halves of the right eigenvectors [9, 10]. The RCC matrix of theoretical and experimental modal models reads

$$\text{RCC : } \begin{bmatrix} \mathbf{0.9744} & 0.0000 & 0.0000 & 0.0000 & 0.0000 & 0.0000 \\ 0.0000 & \mathbf{0.9971} & 0.0000 & 0.0000 & 0.0000 & 0.0000 \\ 0.0005 & 0.0000 & \mathbf{0.9939} & 0.0000 & 0.0000 & 0.0000 \\ 0.0000 & 0.0000 & 0.0000 & \mathbf{1.0039} & 0.0000 & 0.0019 \\ 0.0127 & 0.0000 & 0.0035 & 0.0000 & \mathbf{0.9874} & 0.0000 \\ 0.0000 & 0.0016 & 0.0000 & 0.0045 & 0.0000 & \mathbf{0.9892} \end{bmatrix} .$$

Its main diagonal indicates a better correlation than the main diagonal of the MAC matrix

$$\text{MAC : } \begin{bmatrix} \mathbf{0.9946} & 0.0000 & 0.1876 & 0.0000 & 0.0153 & 0.0000 \\ 0.0000 & \mathbf{0.9839} & 0.0000 & 0.1595 & 0.0000 & 0.0400 \\ 0.2191 & 0.0000 & \mathbf{0.9629} & 0.0000 & 0.1247 & 0.0000 \\ 0.0000 & 0.3471 & 0.0000 & \mathbf{0.8429} & 0.0000 & 0.4317 \\ 0.0384 & 0.0000 & 0.2776 & 0.0000 & \mathbf{1.0000} & 0.0000 \\ 0.0000 & 0.1042 & 0.0000 & 0.7483 & 0.0000 & \mathbf{1.0000} \end{bmatrix} ,$$

which underestimates the theoretical model. This demonstrates that the MAC may not be able to recognize the quality of a theoretical rotor system model.

4.2 Rotor in undamped bearings with minor anisotropy

In the second example, $c_{x1} = c_{y1} = c_{x3} = c_{y3} = 0$, and $k_{xy3} = 0.0005k_{x3}$. All the other parameters are the same as in the first example. Both the original and the reduced model comply with the conditions in [7]. Again, the calculation of the RCC does not require additional measurements for the experimental determination of left eigenvectors. While the auto-RCC of the reduced model yields the identity matrix, the auto-MAC matrix

$$\text{MAC : } \begin{bmatrix} \mathbf{1.0000} & 0.0000 & 0.2532 & 0.0000 & 0.0126 & 0.0027 \\ 0.0000 & \mathbf{1.0000} & 0.0000 & 0.2699 & 0.0070 & 0.0328 \\ 0.2532 & 0.0000 & \mathbf{1.0000} & 0.0000 & 0.1029 & 0.0220 \\ 0.0000 & 0.2699 & 0.0000 & \mathbf{1.0000} & 0.0845 & \mathbf{0.3931} \\ 0.0126 & 0.0070 & 0.1029 & 0.0845 & \mathbf{1.0000} & 0.0000 \\ 0.0027 & 0.0328 & 0.0220 & \mathbf{0.3931} & 0.0000 & \mathbf{1.0000} \end{bmatrix}$$

would not allow for a fair assessment of measurements. If the eigenvalue problem is solved for the original model, the auto-RCC matrix with eigenvectors sampled at the translational degrees of freedom reads

$$\text{RCC : } \begin{bmatrix} \mathbf{1.0000} & 0.0000 & 0.1488 & 0.0000 & 0.0007 & 0.0003 \\ 0.0000 & \mathbf{1.0000} & 0.0000 & 0.0843 & 0.0138 & 0.0361 \\ 0.1488 & 0.0000 & \mathbf{1.0000} & 0.0000 & 0.0347 & 0.0134 \\ 0.0000 & 0.0843 & 0.0000 & \mathbf{1.0000} & 0.1815 & \mathbf{0.4737} \\ 0.0007 & 0.0138 & 0.0347 & 0.1815 & \mathbf{1.0000} & 0.0000 \\ 0.0003 & 0.0361 & 0.0134 & \mathbf{0.4737} & 0.0000 & \mathbf{1.0000} \end{bmatrix}.$$

In contrast, the respective auto-MAC matrix

$$\text{MAC : } \begin{bmatrix} \mathbf{1.0000} & 0.0000 & \mathbf{0.9827} & 0.0000 & 0.0112 & 0.0043 \\ 0.0000 & \mathbf{1.0000} & 0.0000 & 0.0006 & 0.0011 & 0.0029 \\ \mathbf{0.9827} & 0.0000 & \mathbf{1.0000} & 0.0000 & 0.0020 & 0.0008 \\ 0.0000 & 0.0006 & 0.0000 & \mathbf{1.0000} & 0.2336 & 0.6058 \\ 0.0112 & 0.0011 & 0.0020 & 0.2336 & \mathbf{1.0000} & 0.0000 \\ 0.0043 & 0.0029 & 0.0008 & 0.6058 & 0.0000 & \mathbf{1.0000} \end{bmatrix}$$

would not recommend the omission of rotations.

Experimental right eigenvectors shall now be available for a reduced shaft stiffness according to $J_1 = 0.7r_1^4\pi/4$. Experimental left eigenvectors can be obtained as the complex conjugates of the right eigenvectors [8]. The RCC matrix of theoretical and experimental modal models then reads

$$\text{RCC : } \begin{bmatrix} \mathbf{0.9999} & 0.0000 & 0.0000 & 0.0000 & 0.0003 & 0.0000 \\ 0.0000 & \mathbf{0.9973} & 0.0000 & 0.0000 & 0.0000 & 0.0003 \\ 0.0000 & 0.0000 & \mathbf{0.9963} & 0.0000 & 0.0074 & 0.0009 \\ 0.0000 & 0.0002 & 0.0000 & \mathbf{0.9996} & 0.0227 & 0.1876 \\ 0.0000 & 0.0002 & 0.0016 & 0.0001 & \mathbf{0.7813} & 0.0090 \\ 0.0000 & 0.0011 & 0.0003 & 0.0003 & 0.0075 & \mathbf{0.7811} \end{bmatrix}.$$

Its main diagonal indicates a worse correlation than the main diagonal of the MAC matrix

$$\text{MAC : } \begin{bmatrix} \mathbf{1.0000} & 0.0000 & 0.2123 & 0.0000 & 0.0135 & 0.0016 \\ 0.0000 & \mathbf{0.9899} & 0.0000 & 0.2339 & 0.0036 & 0.0307 \\ 0.2514 & 0.0000 & \mathbf{0.9789} & 0.0000 & 0.0994 & 0.0118 \\ 0.0000 & 0.3102 & 0.0000 & \mathbf{0.9806} & 0.0479 & 0.4028 \\ 0.0133 & 0.0151 & 0.1938 & 0.1090 & \mathbf{0.9889} & 0.0102 \\ 0.0028 & 0.0706 & 0.0415 & 0.5071 & 0.0105 & \mathbf{0.9889} \end{bmatrix},$$

which overestimates the theoretical model. This demonstrates that the MAC may approve a theoretical rotor system model that does not comply with measurements.

5 Conclusions

It has been demonstrated by numerical examples that the Modal Assurance Criterion may not be suited for rotor systems. A Rotor Correlation Criterion has been defined as an alternative. Its advantage concerning the validation of experimental modal models, sensor placement, and the correlation between theoretical and experimental modal models has been demonstrated numerically. Since the Rotor Correlation Criterion requires left eigenvectors, the examples discuss rotors for which a relationship between right and left eigenvectors is known. Model correlation for other rotors would be facilitated if more general results on the determination of left eigenvectors were available.

REFERENCES

- [1] Alkhfaji, S.S. and Garvey, S.D. (2011): Modal correlation approaches for general second order systems: Matching mode pairs and an application to Campbell diagrams. *JSV*, **330**, pp. 5615–5627.
- [2] Allemang, R.J. (2003): The modal assurance criterion – twenty years of use and abuse. *Sound and Vibration*, **37**(8), pp. 14–21.
- [3] Bucher, I. and Ewins, D.J. (2001): Modal analysis and testing of rotating structures. *Phil. Trans. R. Soc. Lond. A*, **359**, pp. 61–96.
- [4] Ewins, D.J. (2000): *Modal Testing: Theory, Practice, and Application*. Second Edition, Research Studies Press Ltd., Baldock, Hertfordshire, England.
- [5] Géradin, M. and Rixen, D. (1994): *Mechanical Vibrations: Theory and Application to Structural Dynamics*. Masson, Paris.
- [6] Lindemann, S. (2008): *Model Updating an einem biegeelastischen Rotor (Model updating of a flexible rotor)*. Ph.D. Dissertation, Kassel University, Kassel, Germany.
- [7] Meirovitch, L. (1974): A new method for the solution of the eigenvalue problem for gyroscopic systems. *AIAA Journal*, **12**(10), pp. 1337–1342.
- [8] Meirovitch, L. and Ryland, G. (1979): Response of slightly damped gyroscopic systems. *JSV*, **67**(1), pp. 1–19.
- [9] Mikota, G. (2017): Modal analysis of rotors under special support conditions. In *Proc. 12th Int. Conference on Vibrations in Rotating Machines, SIRM 2017*. Graz, Austria, Feb. 15-17, pp. 165–172.
- [10] Mikota, G. (2017): Modal analysis of rotors under special support conditions. *Technische Mechanik*, **37**(2-5), pp. 250–257.
- [11] Schedlinski, C. and Link, M. (1996): An approach to optimal pick-up and exciter placement. In *Proc. 14th Int. Modal Analysis Conference, IMAC*. Dearborn, Michigan, USA, Feb. 12-15, pp. 376–382.
- [12] Zárate, B.A. and Caicedo, J.M. (2008): Finite element model updating: Multiple alternatives. *Engineering Structures*, **30**, pp. 3724–3730.

SHBT based modeling of a composite hollow shaft regarding its dynamic behavior prediction

Paulo C. P. F. Barbosa¹, Vergílio T. S. Del Claro^{1,2}, Marcelo S. Sousa Jr.¹, Aldemir A. Cavalini Jr.¹, Valder Steffen Jr.¹

¹ LMEst – Structural Mechanics Laboratory, Federal University of Uberlândia, School of Mechanical Engineering, João Naves de Ávila Avenue, 2121, Uberlândia, MG, 38408-144, Brazil, paulo.barbosa@ufu.br, vergilio.claro@ufu.br, marcelo.samora@ufu.br, aacjunior@ufu.br; vsteffen@ufu.br

² DTU Mekanik – Denmark Technical University, Mechanics Department, Nils Koppels Allé, DTU Building 404, Office 005, 2800 Kongens Lyngby, Denmark

Abstract

Composite materials have been extensively used in engineering applications over the past few decades, enabling new possibilities in engineering design. These materials appear to be an interesting solution for many rotating machinery applications, due to their associated low weight and high strength. For the modeling of composite shafts, simplified theories are often used. In the present contribution, a finite element model based on the Simplified Homogenized Beam Theory (SHBT) was used to predict the dynamic behavior of a thick-walled composite hollow shaft. The finite element model of the shaft is based on the Timoshenko beam theory and considers the contribution of the shear stress in the dynamic model. For the purpose of validation, a test rig with a thick-walled carbon-epoxy composite hollow shaft, two aluminum disks, and two self-aligning ball bearings was experimentally tested and numerically simulated. The developed model was updated based on the experimentally measured frequency response functions, obtained from the rotor test rig. Numerical and experimental unbalance responses were compared, considering two rotation speeds of the test rig. Results show promising outcomes from the model, for it precisely predicts the first critical speed and the corresponding unbalance responses, both in time and frequency domains.

1 Introduction

Rotor dynamics is one of the areas with interest in the use of composite shafts since they are a viable solution to overcome the intrinsic limitations of metal shafts [1]. The low weight of composite shafts allows for faster acceleration and deceleration when compared with conventional rotating machines [2], and also reduces effects related to rotational inertia. However, in supercritical operations (flexible rotors) the vibration responses associated with the shaft bending, dynamic stress, stability, and fatigue should be carefully evaluated [3].

In composite material shafts, it is possible to change stiffness and damping properties by manipulating some characteristics, such as adjusting fiber and matrix composition, fiber orientation, number of layers, stacking sequence, layer thickness, and other geometric properties [4]. This allows for critical velocities to be conveniently changed according to the project requirements for the rotor system. Additionally, it is possible to attenuate the vibration amplitudes when the system undergoes critical speeds [1], depending on the structural damping properties of the composite [5]. The internal structural damping can significantly affect the dynamic behavior of composite shafts. It can reduce the vibration amplitude of the shaft at critical speeds, but also make the system unstable [1, 6]. In rotors with metallic shafts, the internal damping influence can be omitted in most cases, nevertheless, in composite shafts, it can be up to twice as large as on a metal shaft [7]. In this context, the characterization of the internal damping is important to the design of rotating machines, aiming to establish a safe operating condition [8, 9].

Various recent finite element formulations based on homogeneous beam theory, equivalent layer theories and the costly layerwise models have been recently proposed for the analysis of composite materials [10, 11, 12, 13, 14]. The Equivalent Modulus Beam Theory (EMBT) [15, 16] can be effectively used for the modeling of tubular

composite shafts, and even be extended to represent rotating dynamics accordingly. However, the EMBT model has some limitations, mainly regarding the coupling of the vertical and horizontal directions, most evident in composite asymmetric rotors [17]. A Layerwise Beam Theory (LBT) [9] presents an excellent prediction of the composite shaft dynamics in rotating applications, but nevertheless have an exponentially higher computational cost, given the complexity of the beam element it utilizes. LBT is a degeneration of the Layerwise Shell Theory (LST), considering that the cross-section of the beam suffers no distortion whatsoever [16]. Even alternate solutions, such as the Rayleigh-Ritz method, were recently used in the modeling of composite shafts [8]. An intermediary approach, which could provide accurate results and low computational cost, was therefore researched, resulting in some modified EMBT models [4] and in the Simplified Homogenized Beam Theory (SHBT) [18].

In this study, the SHBT model [18] was used to model the dynamic behavior and unbalance response in sub-critical speeds of an experimental test rig with a thick-walled carbon fiber composite shaft. The adopted model allows for modeling any stacking sequence of the plies, considers the structural damping of the composite, and also takes into account the shear stress acting transversely on the shaft.

Aiming to present original experimental results and provide a proper confirmation of the proposed methodology results, an experimental validation was performed. An experimental test rig composed by a multilayered thick-walled carbon-epoxy composite hollow shaft, two aluminum disks, and two self-aligning ball bearings was assembled. Various experimental measurements were carried out, acquiring displacement and acceleration data both in the vertical and horizontal directions of the two disks by means of two pairs of proximity probes.

2 Rotor model

2.1 Equations of motion

The formulation of the composite shaft will follow that developed by [19], obtaining a differential equation that represents the dynamic behavior of a flexible onboard rotor operating in a steady state condition [4]. In this formulation, the shaft is characterized by its strain and kinetic energies, the disks and unbalance mass by their kinetic energy only, and the bearings by the virtual work produced by their lift forces. Therefore, to produce the Equations of Motion for the rotor one must proceed accordingly to the Lagrange formulation.

2.2 Composite shaft kinetic and potential energies

The kinetic and potential energies for the composite shaft and the potential energy for the metallic disk need to be determined. As such and explained beforehand, the Lagrange model for the composite shaft rotor becomes Eq. (1):

$$\frac{d}{dt} \left(\frac{\partial T}{\partial \dot{q}_i} \right) - \frac{\partial T}{\partial q_i} + \frac{\partial U}{\partial q_i} = Q_i \quad (1)$$

where T and U are the kinetic and potential energies, respectively, and Q_i is the generalized efforts.

Concerning the shaft contribution to the overall dynamics, a beam element considering shear stresses is adopted with 4 Degrees of Freedom (DoFs) per node, being 2 linear displacements (u and w), and 2 rotations (θ and φ), resulting in 8 DoFs per element, this element is able to represent the coupling between u and w directions. Formulating the shape functions for the said element [19], the rotation θ is the partial derivative of w relative to y , and in a similar fashion, the rotation φ is the negative partial derivative of u relative to y . The transverse strain fields for each element are described by a third degree polynomial, as in Eq. (2):

$$\begin{cases} u = N_1 \mathbf{q}_u \\ w = N_2 \mathbf{q}_w \end{cases}, \text{ where } \begin{cases} \mathbf{q}_u = \{u_1, \varphi_1, u_2, \varphi_2\} \\ \mathbf{q}_w = \{w_1, \theta_1, w_2, \theta_2\} \end{cases} \begin{cases} N_1 = \left\{ 1 - \frac{3y^2}{L^2} + \frac{2y^3}{L^3}, -y + \frac{2y^2}{L} - \frac{y^3}{L^2}, \frac{3y^2}{L^2} - \frac{2y^3}{L^3}, \frac{y^2}{L} - \frac{y^3}{L^2} \right\} \\ N_2 = \left\{ 1 - \frac{3y^2}{L^2} + \frac{2y^3}{L^3}, y - \frac{2y^2}{L} - \frac{y^3}{L^2}, \frac{3y^2}{L^2} - \frac{2y^3}{L^3}, -\frac{y^2}{L} + \frac{y^3}{L^2} \right\} \end{cases} \quad (2)$$

being N_1 and N_2 the shape functions to the beam element. The shaft kinetic energy becomes Eq. (3):

$$T_S = \frac{\rho S}{2} \int_0^L (\dot{u}^2 + \dot{w}^2) dy + \frac{\rho I}{2} \int_0^L (\dot{\varphi}^2 + \dot{\theta}^2) dy + 2\rho I \Omega^2 + 2\rho I \Omega \int_0^L \dot{\varphi} \dot{\theta} dy \quad (3)$$

being ρ the linear density for the composite shaft, S the transverse section area and I the transverse section area inertia.

As for the shaft strain energy during the rotating motion, it is obtained from the analysis of the strain ε and stress σ terms. Assuming that the shaft itself is symmetric, considering that the shaft cross section remains circular, and that C is the shaft geometric center, one can determine a physical model where the static system is (X, Y, Z)

and the rotating one is (x, y, z) . The point C coordinates are (u, w) in the static system and (u^*, w^*) in the rotating one, also, the rotation of one system relative to the other is given by Ωt [19]. Disregarding axial stresses, the shaft strain becomes Eq. (4):

$$U = \frac{EI}{2} \int_0^L \left[\mathbf{q}_u^t \frac{d^2 N_1^t}{dy^2} \frac{d^2 N_1^t}{dy^2} \mathbf{q}_u + \mathbf{q}_w^t \frac{d^2 N_2^t}{dy^2} \frac{d^2 N_2^t}{dy^2} \mathbf{q}_w \right] dy \quad (4)$$

where E is the shaft elasticity modulus and I its inertia. By applying the Lagrange equation (Eq. (1)) into Eq. (4), one can obtain the stiffness matrix \mathbf{K} , $\partial U / \partial \mathbf{q} = \mathbf{K} \mathbf{q}$.

2.3 Disk potential energy

In this contribution, the disk is considered rigid, as it is not the main focus of this work. The stationary coordinate system is represented by $R_0 = (X, Y, Z)$, and the mobile system, attached to the disk geometric center, by $R = (x, y, z)$. The disk have 4 DoFs, two lateral displacements u and w , and two rotations θ and φ . From that one can obtain the node displacement vector $\mathbf{q}_D = \{u, w, \theta, \varphi\}^t$ and, assuming a symmetric disk and that θ and φ are sufficiently small to be disregarded, one can simplify the disk kinetic energy into Eq. (5):

$$T_D = \frac{1}{2} m_D (\dot{u}^2 + \dot{w}^2) + \frac{1}{2} I_D (\dot{\theta}^2 + \dot{\varphi}^2) + \frac{1}{2} I_{Dy} (\Omega^2 + 2\Omega\dot{\varphi}\theta) \quad (5)$$

where m_D stands for the disk mass, I_{Dx} , I_{Dy} and I_{Dz} for the inertias relative to R corresponding axes and ω_x , ω_y and ω_z the angular velocities, also relatives to R corresponding axes, and the gyroscopic effect is given by $I_{Dy} \Omega \dot{\varphi} \theta$. According to [3], and the formulation in the present contribution, the disk is added to the general model by coupling its influences to a single beam node, adding the components into the shaft model global matrices.

2.4 Bearing virtual work and Unbalanced mass kinetic energy

Regarding the bearings, these components are modeled as stiffness and viscous damping coefficients (k and c respectively), and are introduced in the movement equations of the composite rotor through the virtual work of the lift forces acting on the shaft. As for the unbalanced mass, it is represented by a punctual mass m_u , located at a distance d from the shaft geometrical center, that have coordinates u and w . Both developments can be further explained by reference [21], and will ultimately be introduced into the equations of motion, resulting in Eq. (6). This is the equation of motion of the proposed model, already introducing the dissipative effects associated with composite materials [18]:

$$\mathbf{M} \ddot{\mathbf{q}} + [\mathbf{D} + \Omega \mathbf{D}_g + \mathbf{D}_i] \dot{\mathbf{q}} + [\mathbf{K} + \dot{\Omega} \mathbf{K}_{st} + \Omega \mathbf{K}_i] \mathbf{q} = \mathbf{W} + \mathbf{F}_u + \mathbf{F}_m \quad (6)$$

where \mathbf{M} is the mass matrix, \mathbf{D} is the damping matrix associated with the bearings and \mathbf{D}_g represents the gyroscopic effect. All boldfaced terms are in the global level of the FE formulation. The vector \mathbf{d} represents the generalized displacements of the shaft (lateral displacements) and \mathbf{W} is the rotation speed. \mathbf{W} stands for the weight of the rotating parts and \mathbf{F}_u represents the unbalance forces. \mathbf{D}_i and \mathbf{K}_i are the internal damping and the stiffness matrices, respectively, both associated with the composite material.

2.6 Internal damping:

The internal damping is represented by using a Kelvin-Voigt rheological model [18], where the stiffness is represented by $\sigma_1 = E \varepsilon_1$, and the damping by $\sigma_2 = \eta \dot{\varepsilon}_2$. The representative element of this approach is a spring-damper parallel association, in which the spring is the elastic fraction of the deformation, following Hooke's law, and the damper is assumed to be linear, with a resulting stress expressed as a function of the strain rate [25]. The relationship between the stress σ and the deformation ε of the Kelvin-Voigt [22] model is given by $\sigma = E \varepsilon + \eta \dot{\varepsilon}$, where $\sigma = \sigma_1 + \sigma_2$ and $\varepsilon = \varepsilon_1 + \varepsilon_2$. Here, η is the viscosity and $\dot{\varepsilon}$ is the deformation rate. The relaxation time α is given by the relation: $\alpha = \eta / E$. The internal dissipative effects of the composite are described by Eq. (7):

$$\begin{aligned} \delta W &= \int_0^L \int_S \alpha E \left[x^2 \frac{\partial^2 \dot{u}^*}{\partial y^2} \frac{\partial^2 \delta u^*}{\partial y^2} + xz \frac{\partial^2 \dot{u}^*}{\partial y^2} \frac{\partial^2 \delta w^*}{\partial y^2} + xz \frac{\partial^2 \dot{w}^*}{\partial y^2} \frac{\partial^2 \delta u^*}{\partial y^2} + x^2 \frac{\partial^2 \dot{w}^*}{\partial y^2} \frac{\partial^2 \delta w^*}{\partial y^2} \right] dS dy \\ \delta W &= -F_i^t \delta \mathbf{q}, \quad \text{where:} \\ F_i &= -\alpha EI \int_0^L \left[\left(\frac{d^2 N_1^t}{dy^2} \frac{d^2 N_1}{dy^2} + \frac{d^2 N_2^t}{dy^2} \frac{d^2 N_2}{dy^2} \right) \dot{\mathbf{q}} + \Omega \left(\frac{d^2 N_2^t}{dy^2} \frac{d^2 N_1}{dy^2} - \frac{d^2 N_1^t}{dy^2} \frac{d^2 N_2}{dy^2} \right) \mathbf{q} \right] dy \end{aligned} \quad (7)$$

2.7 Homogenization method:

This method considers equivalent properties for each beam section, calculated by SHBT homogenization. A new coordinate system (1, 2, 3) is developed, where it is guided with direction 1 parallel to the fibers, direction 2 orthogonal to them and direction 3 normal to the plane of the composite. Here, a transversely orthotropic material

is considered, having 5 mechanical constants. Assuming that each individual ply is thin enough to be a plate/shell element, and therefore under a plane stress state, its mechanical properties matrix can be described by Eq. (8):

$$\mathbf{Q} = \begin{bmatrix} \frac{E_1}{1-\nu_{12}\nu_{21}} & \frac{E_2\nu_{12}}{1-\nu_{12}\nu_{21}} & 0 \\ \frac{E_1\nu_{12}}{1-\nu_{12}\nu_{21}} & \frac{E_2}{1-\nu_{12}\nu_{21}} & 0 \\ 0 & 0 & G_{12} \end{bmatrix} = \begin{bmatrix} Q_{11} & Q_{12} & 0 \\ Q_{21} & Q_{22} & 0 \\ 0 & 0 & Q_{66} \end{bmatrix} \quad (8)$$

being E , G , and ν , associated to directions 1 and 2 of the new coordinate system.

After this procedure, the SHBT is applied to determine the equivalent properties to be used in the element-level matrices of Eq. (6). It permits to consider the structural damping and shear stress in the beam elements and also allows for any stacking sequence. The SHBT model [18] considers a homogenized flexural stiffness with Young's modulus \tilde{E}_k^y and inertia moment of area I_k for each ply k of the composite material, as shown in Eq. (9):

$$\begin{cases} I_k = \frac{\pi}{4}(R_k^4 - R_{k-1}^4) \\ E_k^y = \left[\frac{\cos^4(\theta_k)}{E_1} + \frac{\sin^4(\theta_k)}{E_2} + \cos^2(\theta_k)\sin^2(\theta_k) \left(\frac{1}{G_{12}} - \frac{2\nu_{21}}{E_2} \right) \right]^{-1} \end{cases} \Rightarrow EI = \sum_{k=1}^N E_k^y I_k \quad (9)$$

Regarding to the shear stresses, the following Eq. (10) give the undamped components:

$$\begin{cases} S^k = \pi(R_k^2 - R_{k-1}^2) \\ G_{12}^k = \left[4\cos^2(\theta_k)\sin^2(\theta_k) \left(\frac{1}{E_1} + \frac{1}{E_2} + 2\frac{\nu_{21}}{E_1} \right) + \frac{(\cos^2(\theta_k) - \sin^2(\theta_k))^2}{G_{12}^k} \right]^{-1} \end{cases} \Rightarrow GS_k = \sum_{k=1}^N G_{12}^k S^k \quad (10)$$

where GS_k is the equivalent term for the whole beam element. In order to obtain the equivalent damped bending stiffness matrix, Eq. (11) is utilized:

$$\alpha EI_k = \sum_{k=1}^N \tilde{E}_y^k I^k \Rightarrow \begin{cases} \mathbf{Q}^\psi = \begin{bmatrix} \psi_{11}Q_{11} & \psi_{11}\nu_{21}Q_{11} & 0 \\ \psi_{22}\nu_{21}Q_{11} & \psi_{22}Q_{22} & 0 \\ 0 & 0 & \psi_{12}Q_{66} \end{bmatrix}, \text{ in } (X, Y, Z), \text{ and:} \\ \bar{\mathbf{Q}}^\psi = \mathbf{T}\mathbf{Q}^\psi\mathbf{T}^t, \text{ in } (1, 2, 3), \text{ where:} \\ \mathbf{T} = \begin{bmatrix} \cos^2(\theta_k) & \sin^2(\theta_k) & 2\sin(\theta_k)\cos(\theta_k) \\ \sin^2(\theta_k) & \cos^2(\theta_k) & -2\sin(\theta_k)\cos(\theta_k) \\ -\sin(\theta_k)\cos(\theta_k) & \sin(\theta_k)\cos(\theta_k) & \cos^2(\theta_k) - \sin^2(\theta_k) \end{bmatrix}. \end{cases} \quad (11)$$

The resulting matrix $\bar{\mathbf{Q}}^\psi$ is used to determine the equivalent damped stiffness modulus, as given by Eq. (12):

$$\begin{cases} \mathbf{c} = [\bar{\mathbf{Q}}^\psi]^{-1} \\ \tilde{E}_y^k = [\mathbf{c}(2,2)]^{-1} \end{cases} \quad (12)$$

3 Experimental setup:

The experimental setup is represented by an overhung rotor [23] as shown in Figure 1. It is composed of a horizontal composite tube and two aluminum disks, supported by two self-aligning bearings. Relative to the end of the aluminum coupling that connects the motor to the shaft, the center of the rotor components are given by the following distances: a) Bearing #1, 80 mm; b) Disk #1, 145 mm; c) Bearing #2, 680 mm; d) Disk #2, 885 mm.

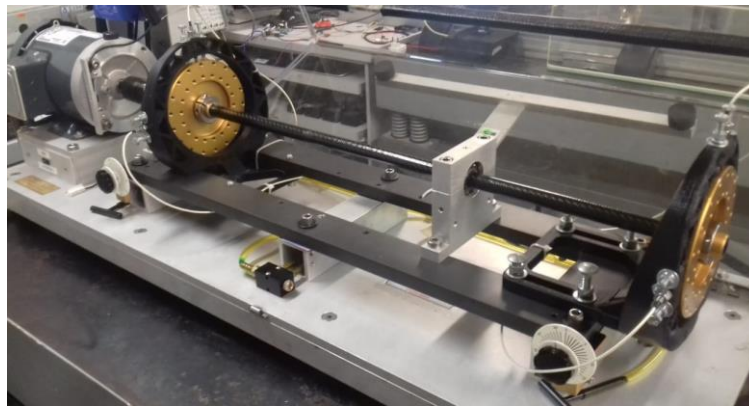


Figure 1: Composite rotor test rig.

The composite shaft is made of special high-modulus and pre-impregnated carbon fiber plies, presenting twenty layers with the following stacking sequence: [0, 0, 0, 0, 90, 90, 45, -45, 0, 0, 0, 45, -45, 90, 90, 0, 0, 0, 0, 0/90] (degrees of inclination, relative to the Y direction of Fig. 3), from the most internal to the most external ply. The last layer is made of a crossed mesh, with woven filaments (fibers at 0 and at 90 degrees). The geometric properties of the shaft and its plies are shown in Table 1.

Table 1: Geometric properties of the shaft

Shaft Properties	Length [m]	Outer diameter [m]	Inner diameter [m]	Density [kg/m ³]
Value	0.9070	0.0180	0.0128	1667

The disks were positioned using adjustable sleeves for a better grip and placement. The bearings are self-aligning ball bearings, also positioned along the shaft using sleeves and locking nuts. The system was mounted in bipartite pillows and locked in place using bolts, equally placed using a torque wrench. The motor used is run by a digital controller, set to 1000 and 1400 RPM. This system features a laser encoder, effectively measuring the system rotating speed without contact. The system stabilized its rotating speed slightly below the set velocity (no variations greater than ± 5 RPM around the dynamically stable speeds were measured).

4 Numerical model

By using the previously described formulation, the SHBT based FEM model was assembled to represent the test rig, having 39 beam elements. A simple description is given by Figure 2.

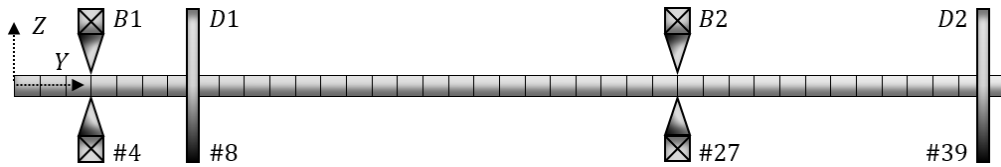


Figure 2: FEM model for the experimental test rig. The numbers below the figure represent the corresponding element.

For updating some of the rotor system physical properties, such as the Young's and shear modulus of the shaft, unbalanced mass and bearing coefficients, a fine-tuning was performed by solving a typical inverse problem. The chosen objective function is based on the difference between the numerical and experimental frequency response functions. In this case, the Differential Evolution (DE) approach was used [15, 24], as shown in Table 2:

Table 2: Shaft parameters, bearing stiffness and damping coefficients, and unbalance masses

Variable	Minimum Limit	Optimized Value at 992 RPM	Optimized Value at 1387 RPM	Maximum Limit
Young's modulus 0 ⁰ [Pa]	70x10 ⁹	103.67x10 ⁹	103.68x10 ⁹	150x10 ⁹
Young's modulus 90 ⁰ [Pa]	70x10 ⁹	127.05x10 ⁹	127.06x10 ⁹	150x10 ⁹
Young's modulus 0 ⁰ 90 ⁰ [Pa]	20x10 ⁹	47.49x10 ⁹	47.50x10 ⁹	80x10 ⁹
In-plane shear modulus [Pa]	1x10 ⁸	8.98x10 ⁸	8.98x10 ⁸	10x10 ⁹
In-plane shear modulus 0 ⁰ 90 ⁰	1x10 ⁸	3.04x10 ⁹	3.05x10 ⁹	10x10 ⁹
Major Poisson's ratio	0.05	0.3050	0.3051	0.5
Major Poisson's ratio 0 ⁰ 90 ⁰	0.05	0.2802	0.2803	0.5
η_1	1x10 ⁻⁸	2.67x10 ⁻⁷	2.67x10 ⁻⁷	1x10 ⁻⁵
η_2	1x10 ⁻⁸	7.11x10 ⁻⁶	7.12x10 ⁻⁶	1x10 ⁻⁵
η_3	1x10 ⁻⁸	6.58x10 ⁻⁶	6.58x10 ⁻⁶	1x10 ⁻⁵
Bearing #1 - k _{xx} [N/m]	1x10 ³	866.77x10 ³	866.77x10 ³	1x10 ⁷
Bearing #1 - k _{zz} [N/m]	1x10 ³	182.37x10 ³	182.37x10 ³	1x10 ⁷
Bearing #1 - d _{xx} [Ns/m]	1x10 ²	64.58x10 ³	64.58x10 ³	1x10 ⁶
Bearing #1 - d _{zz} [Ns/m]	1x10 ²	6.86x10 ³	6.86x10 ³	1x10 ⁶
Bearing #2 - k _{xx} [N/m]	1x10 ³	10.01x10 ³	10.01x10 ³	1x10 ⁷
Bearing #2 - k _{zz} [N/m]	1x10 ³	10.00x10 ³	10.00x10 ³	1x10 ⁷

Bearing #2 - d_{xx} [Ns/m]	1×10^2	9.06×10^3	9.06×10^3	1×10^6
Bearing #2 - d_{zz} [Ns/m]	1×10^2	1.02×10^3	1.02×10^3	1×10^6
Mass unbalance - disk #1 [Kg]	1×10^{-6}	2.10×10^{-3}	1.82×10^{-3}	1×10^{-2}
Phase - disk #1 [rad]	0	4.30	5.88	2π
Mass unbalance - disk #2 [Kg]	1×10^{-6}	6.72×10^{-5}	4.58×10^{-5}	1×10^{-2}
Phase - disk #2 [rad]	0	3.49	5.19	2π

5 Results

5.1 Frequency Response Functions

First, a *free-free* condition was considered by suspending the shaft through low stiffness nylon cords, attached to its extremities. The second condition was obtained with the system fully assembled, bolted in the bearing pillows and with the motor attached via an aluminum coupling. In both cases, an impact hammer and two accelerometers were used measuring the vibration responses in the *X* and *Z* directions for each disk. It is noteworthy that only the first two frequencies were of interest and only they were adjusted in the model, as seen in Figure 3 and Table 3.

Table 3: Numeric model and experimental data comparison, featuring: a) numeric frequency values for the 3 first natural frequencies; b) experimental values of the 3 first natural frequencies; c) numerical amplitude values for the 3 first natural frequencies; d) empirical amplitude values for the 3 first natural frequencies

	Mode and direction	a) Numeric freq. value [Hz]	b) Test rig freq. value [Hz]	c) Numeric amp. [N/m]	d) Test rig amp. [N/m]
Free-free condition	Mode 1 X	164.7	162.8	7.024×10^{-4}	9.033×10^{-4}
	Mode 1 Z	164.7	162.8	7.512×10^{-4}	9.748×10^{-4}
	Mode 2 X	449.9	449.8	2.183×10^{-5}	3.465×10^{-4}
	Mode 2 Z	449.3	499.9	1.623×10^{-5}	3.648×10^{-4}
Assembled condition	Mode 1 X	63.2	63.2	1.407×10^{-3}	1.096×10^{-3}
	Mode 1 Z	63.2	63.2	1.727×10^{-3}	1.365×10^{-3}
	Mode 2 X	188.2	188.2	1.721×10^{-4}	2.992×10^{-4}
	Mode 2 Z	188.2	188.2	2.459×10^{-5}	2.674×10^{-5}

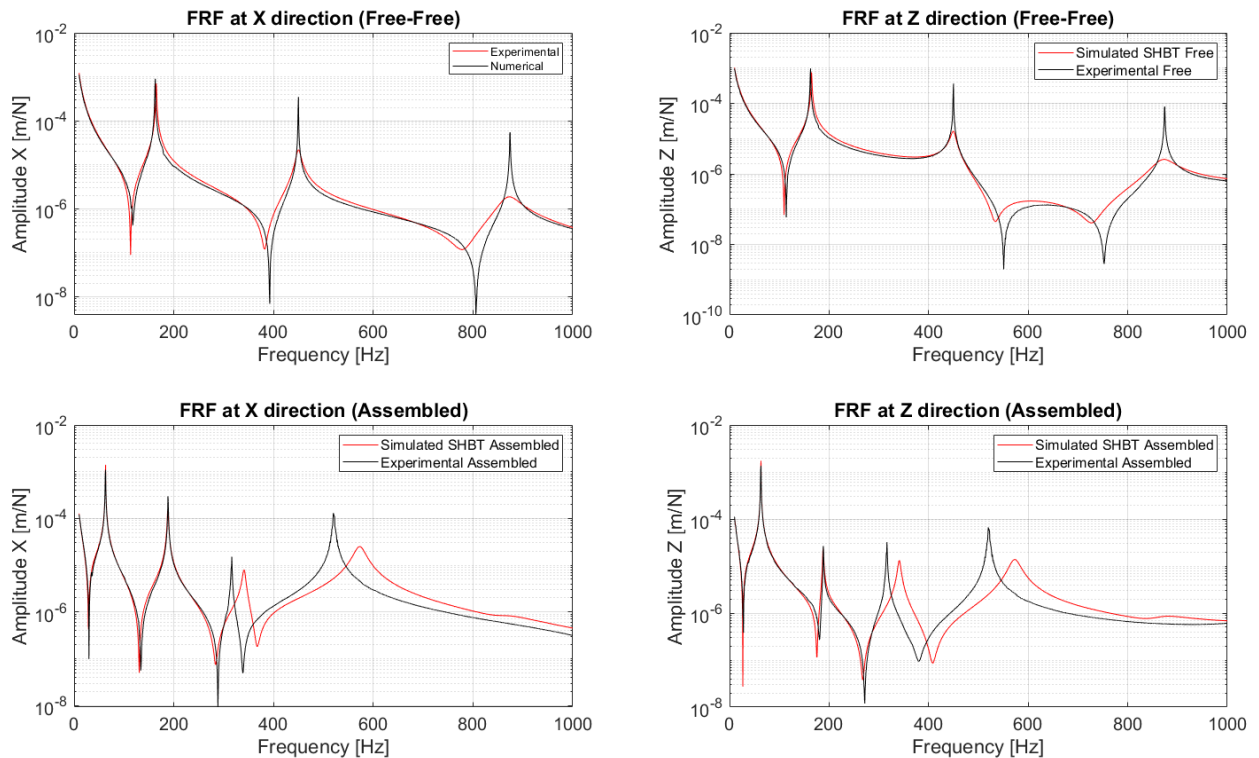


Figure 3: FRF for the free suspended shaft and for the assembled system, in *X* and *Z* directions

5.2 Time signal data acquisition and Order analysis

After assembling the complete machine and performing the FRFs, the settled system was run at two conditions, 1000 and 1400 RPM, for 2 hours each. At steady-state condition, the rotating speeds the system settled in were 992 and 1387 RPM, respectively. In total, four proximity probes were used for each analysis, again measuring the response in the X and Z directions for each disk. Table 4 presents the comparative results.

Table 4: Numeric model and experimental (proximity probes) results in comparison, featuring: a) phase lag between experimental and numeric time signal data; b) order analysis numeric amplitude values for the $1X$ peak; c) order analysis experimental test rig amplitude values for the $1X$ peak

	Disk and direction	a) Phase lag [rad]	b) Numeric amp. [mm]	c) Test rig amp. [mm]
$\Omega = 992$ RPM	Disk 1 - Horizontal	0.07	4.002×10^{-5}	4.103×10^{-5}
	Disk 1 - Vertical	0.61	6.563×10^{-5}	5.274×10^{-5}
	Disk 2 - Horizontal	0.00	1.186×10^{-4}	1.154×10^{-4}
	Disk 2 - Vertical	0.00	1.612×10^{-4}	1.450×10^{-4}
$\Omega = 1387$ RPM	Disk 1 - Horizontal	0.05	4.821×10^{-5}	4.837×10^{-5}
	Disk 1 - Vertical	0.64	6.392×10^{-5}	6.749×10^{-5}
	Disk 2 - Horizontal	0.04	2.537×10^{-4}	2.480×10^{-4}
	Disk 2 - Vertical	0.58	2.462×10^{-4}	3.386×10^{-4}

5.3 Rotor orbits

Figure 4 presents the overlaid orbits, for both the numeric response and experimental measurements.

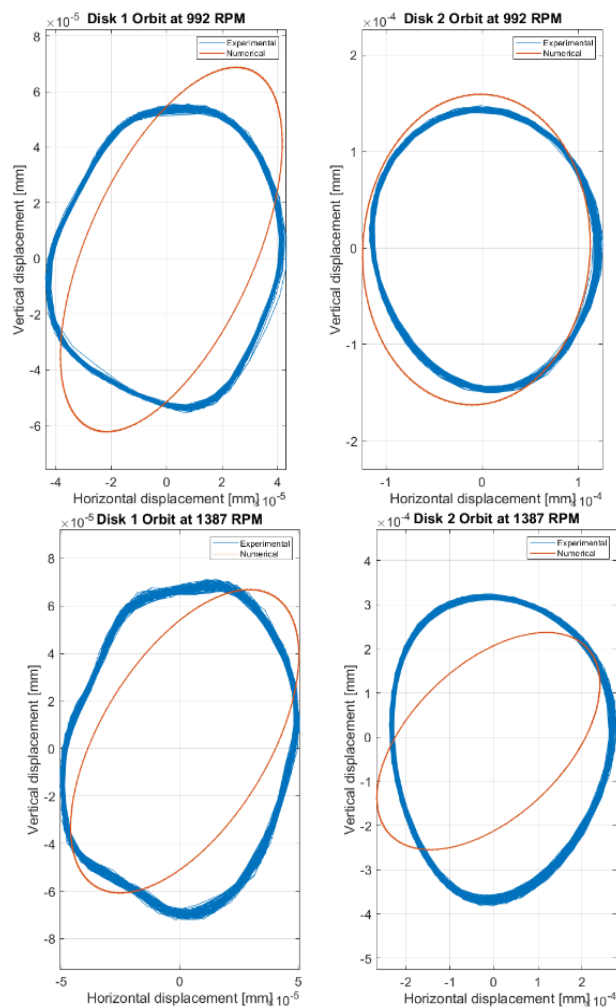


Figure 4: Orbit analysis for both disks, comparing numerical and experimental results, where blue lines are experimental and red lines, numeric results

5.4 Campbell diagram

Having an adjusted model, a Campbell diagram was produced numerically. Due to safety concerns, given the unstable behavior of the system at high speeds, this analysis was not performed experimentally. The 1st backward speed was determined at 26.97 Hz, while the 1st forward speed is present at 27.30 Hz, for this rotor system, as presented in Figure 5.

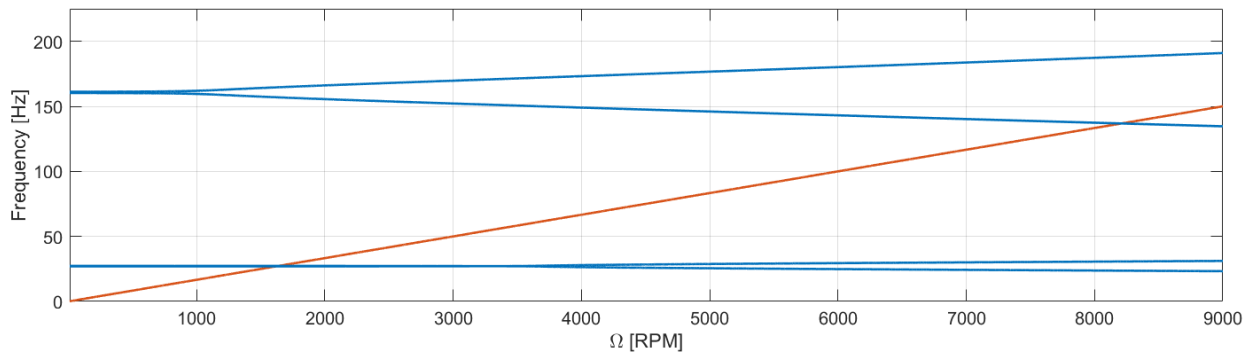


Figure 5: Campbell diagram for the assembled rotating machine

6 Conclusions

In this contribution, a numerical model was proposed to represent the dynamic behavior of rotating machines with thick-walled composite shafts. The formulation was able to precisely predict the dynamic of the experimental test rig. Even though the proposed methodology accounts for additional physical characteristics, the resulting FEM model is still sufficiently simple to be subject to optimization procedures via heuristic optimization methods. The computational cost of the proposed model is on par with similar simplified models, such as the Rayleigh-Ritz and the EMBT models, while better representing the physical characteristics of the rotor system.

In regard to the experimentation performed, the tests were executed in a controlled environment, with stabilized temperature and on steady-state conditions for the machine. Appropriate running time was allowed for the bearings and eventual pre-stresses to settle in place, resulting in a better experimental similarity to conditions found in standard industrial machinery. The motor and controller were able to provide stable torque, to keep the machine operating steadily in the set conditions, allowing for the data acquisition to run smoothly.

Specifically, on the FRFs results, it can be seen that for lower frequencies the model predictions tend to match those of the experiment, while for higher frequencies there is a loss in precision due to damping misinterpretation.

Some notable features can be obtained from the optimized values of the physical parameters of the test rig, displayed in Table 2. Particularly on the bearing parameters, one observes the following: a) the bearings show an unusually low stiffness; b) also the bearings have a high damping, which will affect the general behavior of the shaft.

On the time signal comparison, a clear agreement, and some other characteristics can be noted. Primarily, the amplitude and phase of the horizontal measurements show no significant discrepancies from the model results, for both rotation speeds of 992 and 1387 RPM. Notably, the modeled response tends to be slightly off the experimental response phase in the vertical direction. This effect is believed to be due to high order directional coupling effects of the composite, which were neglected in the present formulation.

The phase lag can be more clearly observed in the orbits, where the numerically generated orbits tend to be more ovalized than the experimentally determined ones. In addition, the orbits show that higher order signals are seen in the experimental results, however they do not appear in the numerical data. These higher order signals appear at two and three times the rotating speed Ω (2Ω and 3Ω) of the rotor, and similarly to metallic shafts, mostly come from the same origins: ordinarily due to the experimental test rig presenting small geometrical and fabrication imperfections, such as warping of the shaft, misalignment of the disks, eventual residual stress inside the composite mesh, imperfections in the epoxy curing process, bearing clearances and other smaller factors. Nevertheless, both the numerical and experimental responses have the same order of magnitude.

7 Acknowledgments

The authors are thankful for the financial support provided to the present research effort by CNPq (574001/2008-5 and 304546/2018-8), FAPEMIG (TEC-APQ-3076-09, TEC-APQ-02284-15, and TEC-APQ-00464-16), and CAPES through the INCT-EIE and PDSE programs.

References

- [1] Silveira, M. E. (2001): “Análise do Comportamento Dinâmico de Rotores em Eixos Bobinados”. 97 p. Master’s thesis, Federal University of Santa Catarina, Florianópolis, Brazil.
- [2] Brush, M. (1999): “Still Spinning After All These Years: A Profile of the Ultracentrifuge”. *The Scientist*, v. 13, p. 16-18, Out.
- [3] Gupta, K. (2015): “Composite Shaft Rotor Dynamics: An Overview”. In: Proceedings of VETOMAC, X, Manchester. *Vibration Engineering and Technology of Machinery*. p. 79-94.
- [4] Barbosa, P. C. P. F.; Cavalini Jr., A. A.; Steffen Jr., V. (2018): “Analysis of the dynamic behavior of composite shafts on rotating machines”. 43p. Master’s thesis, Federal University of Uberlândia, Brazil.
- [5] Mendonça, W. R. P.; Medeiros, E. C.; Pereira, A. L. R.; Mathias, M. H. (2017): ” The dynamic analysis of rotors mounted on composite shafts with internal damping”, *Composite Structures*, Volume 167, p. 50-62.
- [6] Bucciarelli, L. L. (1982): “On the Instability of Rotating Shafts Due to Internal Damping”, *Journal of Applied Mechanics*, Volume 49, Issue 2, Pages 425-428.
- [7] Wasilkoski, C. M. (2006): “Comportamento Mecânico dos Materiais Poliméricos”. 82p. PhD Thesis, Federal University of Paraná, Brazil.
- [8] Del Claro, V. T. S.; Barbosa, P. C. P. F.; Cavalini Jr., A. A.; Steffen Jr., V. (2017): “A shell based fem model for thick walled composite rotors”, COBEM-2017-2118, 24th ABCM International Congress of Mechanical Engineering, December 3-8, Curitiba, PR, Brazil.
- [9] Sino, R.; Baranger, A. B.; Chatelet, A. G.; Jacquet, A. (2008): “Dynamic analysis of a rotating composite shaft”, *Composites Science and Technology*, Volume 68, Pages 337–345.
- [10] Wettergreen, H.L.; Olsson, K.O. (1996): “Dynamic Instability of a Rotating Asymmetric Shaft with Internal Viscous Damping Supported in Anisotropic Bearings”. *Journal of Sound and Vibration*, v. 195, p. 75-84.
- [11] Arab, S. B.; Rodrigues, J. D.; Bouaziz, S.; Haddar, M. (2017): “A finite element based on Equivalent Single Layer Theory for rotating composite shafts dynamic analysis”, *Composite Structures*, Volume 178, Pages 135-144.
- [12] Arab, S. B.; Rodrigues, J. D.; Bouaziz, S.; Haddar, M. (2017): “Dynamic analysis of laminated rotors using a layerwise theory”, *Composite Structures*, Volume 182, Pages 335-345.
- [13] Milazzo, A. (2014): “Refined equivalent single layer formulations and finite elements for smart laminates free vibrations”, *Composites Part B: Engineering*, Volume 61, Pages 238-253.
- [14] Milazzo, A. (2014): “Layer-wise and equivalent single layer models for smart multilayered plates”, *Composites Part B: Engineering*, Volume 67, Pages 62-75.
- [15] Storn, R.; Price, K. (1997): “Differential Evolution: A Simple and Efficient Heuristic for Global Optimization Over Continuous Spaces.” *Journal of Global Optimization*, V. 11, p. 341-359.
- [16] Singh, S.P.; Gupta, K. (1996): “Composite shaft rotordynamic analysis using a layerwise theory”, *Journal of Sound and Vibration*, Volume 191(5), Pages 739-756.
- [17] Gubran, H. B. H.; Gupta, K. (2005): “The effect of stacking sequence and coupling mechanisms on the natural frequencies of composite shafts”, *Journal of Sound and Vibrations*, Volume 282(1-2), Pages 231-248.
- [18] Sino, R. (2007): “Comportement Dynamique et Stabilité des Rotors: Application aux Rotors Composites”. 157 p. PhD Thesis, INSA - Lyon, Lyon.
- [19] Lalanne, M.; Ferraris, G. (1998): “Rotordynamics Prediction in Engineering”. New York: J. Wiley and Sons, 266p.
- [20] Reddy, J. N. (2017): “Energy Principles and Variational Methods in Applied Mechanics”, Wiley, 3rd Edition, 760p. ISBN: 978-1-119-08737-3.
- [21] Cavalini Jr, A. A. (2013): “Detection and identification of incipient transversal cracks in flexible and horizontal shafts of rotating machines”. 270p. PhD Thesis, Federal University of Uberlândia, Brazil.
- [22] Tsai, S. W. (1988): “Composites design”, 4th Edition, Ohio, USA, Dayton.
- [23] Friswell, M. I.; Penny, E. T.; Garvey, D.; Lees, W. (2010): “Dynamics of Rotating Machines”, Cambridge Aerospace Series, Cambridge University Press, 544p. ISBN: 978-0-521-85016-2.
- [24] Lobato, F. S.; Steffen Jr., V. (2017): “Multi-Objective Optimization Problems: Concepts and Self-Adaptive Parameters with Mathematical and Engineering Applications”, Springer International Publishing, 160p. ISBN: 978-3-319-58565-9.
- [25] Singh, S. P.; Gupta, K. (1994): “Free damped flexural vibration analysis of composite cylindrical tubes using beam and shell theories”, *Journal of Sound and Vibration*, Volume 172(2), p. 171-190.

Validation of the generalized polynomial chaos expansion to approximate the stochastic frequency response of a multi-fault rotor

Gabriel Y. Garoli¹, **Lais B. Visnadi**², **Helio F. de Castro**³

Laboratory of Rotating Machines, School of Mechanical Engineering - UNICAMP, 13083-860, Campinas, Brazil, yujigaroli@fem.unicamp.br¹, lais.visnadi@fem.unicamp.br², heliofc@fem.unicamp.br³

Abstract

The application of the rotor machines is made in different types of industry. These equipments are subject to many faults, which should be studied, so an early diagnosis can be done. The quantified parameters of the faults by identification methods have uncertainties, which should be considered in the mathematical model. The deterministic problem, become a stochastic problem. A common approach for this problem is the Monte Carlo method, which consists of the evaluation of a large number of random samples and, then, do a statistical analysis. The method is simple to implement and allows use deterministic solver. However, the processing cost is high due to the large number of samples needed. The generalized Polynomial Chaos Expansion can approximate stochastic processes and resumes the problem into evaluate the expansion coefficients. The Stochastic Collocation method is straightforward to implement and allows the use of a deterministic solver, as well. This method needs less samples than the Monte Carlo one. In this work, the validation of the polynomial expansion to approximate the stochastic response of a rotor system with faults is made. This approximation of the stochastic response presents satisfactory convergence with a smaller processing time.

1 Introduction

Rotor machineries are used in different segments of the industry. Therefore, the knowledge of its behaviour and faults are fundamental. Mathematical models and experiments are developed to understand such machines. These are generally approached by the Finite Elements method. Nelson and McVaugh [7] used the Timoshenko beam to approximate the shaft of the rotor system. Their model includes the gyroscopic effect, as well. These machines, generally, are supported by hydrodynamic bearings and their effects have to be considered in the model of the system.

The rotating machines are subject to faults. Generally, these faults are identified by the vibration levels of the system. In case of a fault, the vibration amplitude tends to increase and can damage the machine. According to [2], the most common faults are the unbalance mass, bowed shaft and crack.

The unbalance fault is the most studied one, due to its presence in almost every rotor system. The bowed shaft can be caused by a thermal distortion or, even, a prolonged high unbalance force. The force caused by a bent shaft is similar to the one caused by a unbalance mass. They are slightly different, although. Therefore, it is necessary to recognize this difference and correctly identify the fault in question.

A crack on the shaft can be caused by fatigue or failures. The "breathing" movement of the crack cause a signature vibration on the system response. Al-Shudeifat [1] studied this signature vibration. The author uses the harmonic method to model the dynamic effects of the crack.

If the rotor system is connected to another one, a shaft or a engine, this connection is made by a coupling. This element is subject to the misalignment, both angular and parallel. Lees [5] presents model for rigidly coupled rotors. The author considered two rotors connected by bolts and develop the forces and stiffness on the system from displacement of the bolts edges.

The quantification methods of the faults parameters has inherent uncertainties. These has to be added in the mathematical model for robustness. Therefore, it is necessary a stochastic model. The solution of the stochastic problem is generally evaluated by the Monte Carlo method. It is straightforward and easy to implement, after the uncertainties are already modelled. First, samples are generated, then they are simulated by a deterministic solver. Finally, a statistical analysis is made with the results. The convergence of the method is guaranteed by the Law of

Large Numbers and the Central Limit Theorem. However, a large number of samples is needed. If the deterministic solver has a reasonable processing cost, the Monte Carlo simulation will take a very high computational cost.

The generalized Polynomial Expansion is proposed to approximate the stochastic response of the system. Wiener [9] presented the "Homogeneous Chaos", which was the approximation of Gaussian process through a series of Hermite polynomials. Then, this idea was expanded by Xiu and Karniadakis [10] into more polynomial families. This approximation by a polynomial expansion, resumes the stochastic problem into evaluate the expansion coefficients.

The evaluation of the expansion coefficients can be done by the Stochastic Collocation method. The method needs a deterministic solver, as the Monte Carlo one. However, samples are not random generated, they respect a quadrature rule. Then, the expansion coefficients are calculated by solving a linear system. The Stochastic Collocation method need less samples than the Monte Carlo one. Nonetheless, if the number of random variables is large, the number of samples will be similar for both methods.

In this work, it is proposed the study of the effects of the faults uncertainties in the stochastic response of a rotor system. The harmonic method will be used to approach the dynamical response of the system and the unbalance, bent shaft, cracked shaft and misalignment faults will be considered. The stochastic response will be approximated by the generalized polynomial chaos expansion and the coefficients evaluated by the Stochastic Collocation method. To validate the usage of the proposed method, it results will be compared with Monte Carlo stochastic response.

2 Rotor system and faults models

2.1 General equation of a rotor system

The studied system is presented in Fig.1. The system consists of two rotors connected by a series of N bolts. Each rotor is supported by two journal bearings and has a rigid disc at the middle of the shaft, equidistant from the bearings. Only one rotor will be considered bent and with a transversal crack. Both will be considered unbalanced. Table 1 presents the parameters of the model.

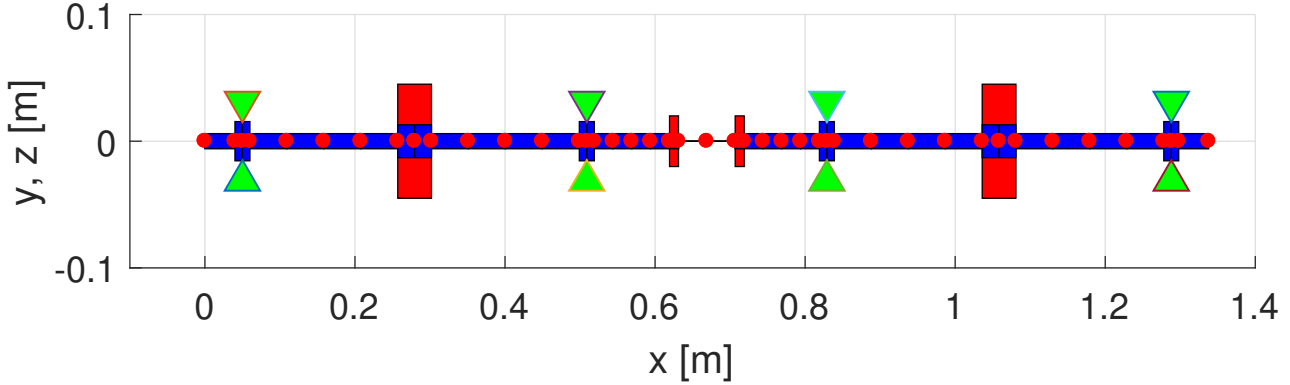


Figure 1: Studied rotor system

The rotor system is modelled by the Finite Elements Method. The formulation is the same as presented by [7]. Each node has 4 degrees of freedom, displacements and rotations in the vertical and horizontal axis. After the damping, mass and stiffness matrix of each element are calculated, the final equation of motion of the system is shown by Eq. 1.

$$\mathbf{M} \cdot \ddot{\mathbf{q}} + (\mathbf{C} + \omega \mathbf{G}) \cdot \dot{\mathbf{q}} + \mathbf{K} \cdot \mathbf{q} = \mathbf{f} \quad (1)$$

with $\mathbf{M}, \mathbf{C}, \mathbf{G}, \mathbf{K}$ as the mass, damping, gyroscopic and stiffness global matrices, \mathbf{f} as the forces applied in the system, which includes the forces caused by the faults and gravity. $\ddot{\mathbf{q}}, \dot{\mathbf{q}}, \mathbf{q}$ are the acceleration, velocity and displacement of the degrees of freedom and ω is the rotating speed of the shaft.

Table 1: Model Parameters

Parameters	Dimensions	Parameters	Dimensions
Length of each shaft	$631.5 \cdot 10^{-3} \text{ m}$	Diameter of the coupling discs	0.04 m
Diameter of the shaft	0.012 m	Number of bolts N	4
Inner diameter of the discs	0.012 m	Axial stiffness of the bolt k_a	$5 \cdot 10^3 \text{ N/m}$
Outer diameter of the discs	0.09 m	Transversal stiffness of the bolt k_b	$13 \cdot 10^3 \text{ N/m}$
Thickness of the discs	$45 \cdot 10^{-3} \text{ m}$	Unbalance moment me_{unb}	$50 \cdot 10^{-6} \text{ kg} \cdot \text{m}$
Young modulus of elasticity E	$2.1 \cdot 10^{11} \text{ N} \cdot \text{m}^2$	Unbalance force phase ψ_{unb}	0°
Shear modulus G	$0.796 \cdot 10^{11} \text{ N} \cdot \text{m}^2$	Maximum amplitude of the bent shaft	$22.57 \cdot 10^{-6} \text{ m}$
Density ρ	7860 kg/m^3	Bent shaft force phase ψ_b	0°
Bearing diameter	0.031 m	Parallel displacement at the coupling	$2.03 \cdot 10^{-3} \text{ m}$
Radial clearance of the bearing	90 μm	Angular displacement at the coupling	0.2°
Viscosity of the lubricant oil	0.04 Pa \cdot s	Non-dimensional crack depth μ	0.2

2.2 Hydrodynamic Bearings model

The hydrodynamic bearings are included in the model by the stiffness and damping coefficients, as proposed by Lund [6]. The model of the short bearing, developed by Ocvirk[8], is considered. By solving the Reynolds equation, it is possible to obtain the horizontal and vertical forces acting in the shaft (Eq. 2 as functions of the eccentricity ratio of the shaft ε , the attitude angle φ and rotational speed of the shaft ω . The Equations 2 to 4 were proposed by [4]

$$\begin{aligned} F_x &= F_\eta f_x(\varepsilon, \dot{\varepsilon}, \dot{\varphi}) \cos(\varphi) - F_\eta f_y(\varepsilon, \dot{\varepsilon}, \dot{\varphi}) \sin(\varphi) \\ F_y &= F_\eta f_x(\varepsilon, \dot{\varepsilon}, \dot{\varphi}) \sin(\varphi) + F_\eta f_y(\varepsilon, \dot{\varepsilon}, \dot{\varphi}) \cos(\varphi) \end{aligned} \quad (2)$$

$$\varepsilon = \frac{e}{h_0} \quad F_\eta = \frac{\eta L^3 \omega R}{2h_0^2} \quad (3)$$

$$\begin{aligned} f_x(\varepsilon, \dot{\varepsilon}, \dot{\varphi}) &= \left(1 - \frac{2\dot{\varphi}}{\omega}\right) \cdot \frac{2\varepsilon^2}{(1 - \varepsilon^2)^2} + \pi \frac{\dot{\varepsilon}}{\omega} \cdot \frac{1 + 2\varepsilon^2}{(1 - \varepsilon^2)^{5/2}} \\ f_y(\varepsilon, \dot{\varepsilon}, \dot{\varphi}) &= \left(1 - \frac{2\dot{\varphi}}{\omega}\right) \cdot \frac{\varepsilon}{(1 - \varepsilon^2)^{3/2}} - \frac{\dot{\varepsilon}}{\omega} \cdot \frac{4\varepsilon}{(1 - \varepsilon^2)^2} \end{aligned} \quad (4)$$

which, h_0 is the radial clearance, L and R are, respectively, the length and radius of the bearing.

By partially differentiating Eq. 4 with respect to the horizontal and vertical displacements and its velocities, it is obtained the stiffness and damping coefficients, respectively. Therefore, the dynamical coefficients can be included in the respective matrix in the positions that correspond with the bearings location.

2.3 Rotor machineries faults

Brief definitions and mathematical models are present in this section. It will be considered a rotor system with unbalance, bend, crack, parallel and angular misalignment.

2.3.1 Unbalance

The unbalance is the most common fault presented in rotor machines. It is when the center of mass of the shaft or an disk is not in the rotating axis of the system. This fault is, generally, modeled as a eccentric mass in a disk or shaft of the rotor. The force caused by the unbalance of the system is presented in Eq. 5 with constant rotating speed.

$$\mathbf{f}_{unb} = me_{unb} \cdot \omega^2 \cdot [\cos(\omega t + \psi_{unb}) \sin(\omega t + \psi_{unb}) 0 0]^T \quad (5)$$

which me_{unb} as the equivalent unbalance moment and ϕ_{unb} as the phase of the unbalance force.

2.3.2 Bowed shaft

The bow in a shaft can be caused by many situations, such as different temperatures on different parts of the shaft or it is stored bi-supported for a long period. In this work, the bow will be represented by its maximum amplitude. The Equation 6 presents the motion equation of a rotor system with a bent shaft.

$$\mathbf{M}_r \cdot \ddot{\mathbf{q}}_r + \mathbf{C}_r \cdot \dot{\mathbf{q}}_r + \mathbf{K}_r \cdot (\mathbf{q}_r + \mathbf{y}_{b_r}) = \mathbf{f}_r \quad (6)$$

The subscript r refers to the rotating frame. The vector \mathbf{y}_{b_r} is the displacements caused by the bent rotor and it has the form below, which y_{b_k} is the displacement of the k th node, in the rotating frame, and n is the total number of nodes of the model. These displacements are interpolated from the maximum amplitude and its location on the shaft. This deformation can be expressed by the force:

$$\mathbf{f}_{b_r} = \mathbf{K}_r \cdot \mathbf{y}_{b_r}, \quad \mathbf{y}_{b_r} = [y_{b_1} \ y_{b_2} \ \cdots \ y_{b_n}]^T \quad (7)$$

Using a transformation matrix, the force can be in the fixed frame and rewrite with the form:

$$\mathbf{f}_b = \mathbf{f}_{b_c} \cdot \cos(\omega t + \psi_b) + \mathbf{f}_{b_s} \cdot \sin(\omega t + \psi_b) \quad (8)$$

2.3.3 Cracked rotor

It will be considered a traversal crack. The crack removes material of the shaft, which change the area moments of inertia of the shaft. Therefore, the stiffness of the shaft change in the section where the crack is located. A brief presentation of the mathematical model developed by [1] is shown below.

The stiffness matrix can be written similarly to the asymmetric shaft. The area moments of inertia of the cracked element on the centroidal fixed axes \bar{Y}_f and \bar{Z}_f are calculated using the centroidal area moments of inertia on the rotating frame $\bar{Y}\bar{Z}$.

$$\begin{aligned} I_{\bar{Y}_f}(t) &= \frac{I_{\bar{Y}} + I_{\bar{Z}}}{2} + \frac{I_{\bar{Y}} - I_{\bar{Z}}}{2} \cos(2\omega t) + I_{\bar{Y}\bar{Z}} \sin(2\omega t) \\ I_{\bar{Z}_f}(t) &= \frac{I_{\bar{Y}} + I_{\bar{Z}}}{2} + \frac{I_{\bar{Y}} - I_{\bar{Z}}}{2} \cos(2\omega t) - I_{\bar{Y}\bar{Z}} \sin(2\omega t) \\ I_{\bar{Y}_f\bar{Z}_f}(t) &= -\frac{I_{\bar{Y}} - I_{\bar{Z}}}{2} \sin(2\omega t) + I_{\bar{Y}\bar{Z}} \cos(2\omega t) \end{aligned} \quad (9)$$

with:

$$\begin{aligned} I_{\bar{Y}} &= I_Y - A_{ce} \cdot e^2, \quad I_{\bar{Z}} = I_Z \\ A_{ce} &= R^2(\pi - \cos^{-1}(1 - \mu) + (1 - \mu)\sqrt{\mu(2 - \mu)}) \\ e &= \frac{2R^3}{3A_{ce}}(\mu(2 - \mu))^{\frac{3}{2}} \end{aligned}$$

which A_{ce} is the area of the cracked cross-section and e is the centroid location on Z axis. I_Y and I_Z are the area moments of inertia of the cracked element cross-section about the rotating axe YZ and are given by

$$\begin{aligned} I_Y &= \frac{\pi R^4}{4} + \frac{R^4}{4}((1-\mu)(2\mu^2 - 4\mu + 1)\gamma + \sin^{-1}(1-\mu)) \\ I_Z &= \frac{\pi R^4}{4} - \frac{R^4}{12}((1-\mu)(2\mu^2 - 4\mu - 3)\gamma + 3\sin^{-1}(\gamma)) \end{aligned} \quad (10)$$

which $\gamma = \sqrt{\mu(1-\mu)}$ and $\mu = h/R$ is the non-dimensional crack depth and h is the crack depth in the radial direction. The stiffness matrix of the cracked element in the rotating frame is:

$$\mathbf{K}_{crack} = \frac{E}{l^3} \cdot \begin{bmatrix} 12I_{\bar{Y}} & 0 & 0 & 6lI_{\bar{Y}} & -12lI_{\bar{Y}} & 0 & 0 & 6lI_{\bar{Y}} \\ 0 & 12I_{\bar{Z}} & -6lI_{\bar{Z}} & 0 & 0 & -12I_{\bar{Z}} & -6lI_{\bar{Z}} & 0 \\ 0 & -6lI_{\bar{Z}} & 4l^2I_{\bar{Z}} & 0 & 0 & 6lI_{\bar{Z}} & 2l^2I_{\bar{Z}} & 0 \\ 6lI_{\bar{Y}} & 0 & 0 & 4l^2I_{\bar{Y}} & -6I_{\bar{Y}} & 0 & 0 & 2l^2I_{\bar{Y}} \\ -12lI_{\bar{Y}} & 0 & 0 & -6lI_{\bar{Y}} & 12I_{\bar{Y}} & 0 & 0 & -6lI_{\bar{Y}} \\ 0 & -12lI_{\bar{Z}} & 6lI_{\bar{Z}} & 0 & 0 & 12I_{\bar{Z}} & 6lI_{\bar{Z}} & 0 \\ 0 & -6lI_{\bar{Z}} & 2l^2I_{\bar{Z}} & 0 & 0 & 6lI_{\bar{Z}} & 4l^2I_{\bar{Z}} & 0 \\ 6lI_{\bar{Y}} & 0 & 0 & 2l^2I_{\bar{Y}} & -6I_{\bar{Y}} & 0 & 0 & 4l^2I_{\bar{Y}} \end{bmatrix} \quad (11)$$

Using the transformation matrix that alter the frame from the rotating one to the fixed one, the stiffness matrix can be write in the static frame. The stiffness matrix of the cracked can be write as the form of Eq. 12, as shown in [1].

$$\mathbf{K}_{crack} = \mathbf{K}_{crack_0} + \mathbf{K}_{crack_c} \cdot \cos(2\omega t) + \mathbf{K}_{crack_s} \cdot \sin(2\omega t) \quad (12)$$

Therefore, assembling these matrices in the global system equation, the effect of the crack in the rotor system.

2.3.4 Misalignment

The model proposed by Lees[5] is used to model the parallel misalignment. Two parallel rotors are coupled by N_b bolts, each one with transversal stiffness k_b . The rotors have a relative vertical displacement of δ_b . On the first rotor, the bolts are distributed in a circle of radius r_b concentric with the shaft. In the second rotor, there is the same circle with an off-set of δ_b . It will be considered that both rotors are in the same rotating speed. Therefore, it will not have torsional deflection.

The stiffness of the coupling is presented by Eq. 13 and the force due to the parallel misalignment is presented by Eq. 14.

$$\mathbf{K}_{par} = N_b \cdot k_b \cdot \begin{bmatrix} 1 & 0 & 0 & 0 \\ 0 & 1 & 0 & 0 \\ 0 & 0 & 0 & 0 \\ 0 & 0 & 0 & 0 \end{bmatrix} \quad (13)$$

$$\mathbf{f}_{par} = N_b k_b \delta_b \cdot [\sin(\omega t) \ 1 - \cos(\omega t) \ 0 \ 0]^T \quad (14)$$

The angular misalignment it is composed of two discs with a angular offset α_b . Due to this angular displacement, it is considered that one bolt has a stiffness of $k_a + k'$ and the others has k_a .

The stiffness due of the misalignment coupling and its force is presented by the Eqs. 15 and 16, respectively.

$$\mathbf{K}_{ang} = \frac{1}{2}(3k_a + k')r_b^2 \begin{bmatrix} 0 & 0 & 0 & 0 \\ 0 & 0 & 0 & 0 \\ 0 & 0 & 1 & 0 \\ 0 & 0 & 0 & 1 \end{bmatrix} + \frac{1}{2}k'r_b^2 \begin{bmatrix} 0 & 0 & 0 \\ 0 & 0 & 0 \\ 0 & 0 & \cos(2\omega t) & \sin(2\omega t) \\ 0 & 0 & \sin(2\omega t) & -\cos(2\omega t) \end{bmatrix} \quad (15)$$

$$\mathbf{F}_{ang} = -\frac{1}{2}\alpha_b r_b^2 [0 \ 0 \ 3k_a + k' + k' \cos(2\omega t) \ k' \sin(2\omega t)]^T \quad (16)$$

2.4 Solution of the system equation

Let the solution of the Eq. 1 and the forces be expressed as Fourier series:

$$\begin{aligned} \mathbf{q} &= \mathbf{A}_0 + \sum_{k=1}^n \mathbf{A}_k \cdot \cos(k\omega t) + \mathbf{B}_k \cdot \sin(k\omega t) \\ \mathbf{f} &= \mathbf{f}_0 + \sum_{k=1}^n \mathbf{f}_{s_k} \cdot \cos(k\omega t) + \mathbf{f}_{c_k} \cdot \sin(k\omega t) \end{aligned} \quad (17)$$

and, therefore, the matrix \mathbf{K} can be wrote as:

$$\mathbf{K} = K_0 + K_{c_k} \cos(k\omega t) + K_{s_k} \sin(k\omega t) \quad (18)$$

Therefore, the Equation 1 is reformulated for the linear system presented by Eq.19.

$$[\mathbf{H}] \cdot \{\mathbf{AB}\} = \{\mathbf{F}\} \quad (19)$$

which:

$$[\mathbf{H}] = \begin{bmatrix} \mathbf{K}_0 & 0 & 0 & 0.5\mathbf{K}_c & 0.5\mathbf{K}_s & 0 & 0 & 0 & 0 & \dots & 0 & 0 \\ 0 & \mathbf{K}_0 - \omega\mathbf{M} + 0.5\mathbf{K}_c & \mathbf{K}_0 - \omega\mathbf{M} + 0.5\mathbf{K}_s & 0 & 0 & 0.5\mathbf{K}_c & 0.5\mathbf{K}_s & 0 & 0 & \dots & 0 & 0 \\ 0 & -\mathbf{K}_0 + \omega\mathbf{M} + 0.5\mathbf{K}_s & \mathbf{K}_0 - \omega\mathbf{M} + 0.5\mathbf{K}_c & 0 & 0 & -0.5\mathbf{K}_s & 0.5\mathbf{K}_c & 0 & 0 & \dots & \vdots & \vdots \\ K_c & 0 & 0 & \mathbf{K}_0 - 2\omega\mathbf{M} & 2\omega\mathbf{C} & 0 & 0 & 0.5\mathbf{K}_c & 0.5\mathbf{K}_s & \ddots & 0 & 0 \\ K_s & 0 & 0 & -2\omega\mathbf{C} & \mathbf{K}_0 - 2\omega\mathbf{M} & 0 & 0 & -0.5\mathbf{K}_s & 0.5\mathbf{K}_c & \ddots & 0.5\mathbf{K}_c & 0.5\mathbf{K}_s \\ 0 & 0.5\mathbf{K}_c & 0.5\mathbf{K}_s & 0 & 0 & \mathbf{K}_0 - 3\omega\mathbf{M} & 3\omega\mathbf{C} & 0 & 0 & \ddots & -0.5\mathbf{K}_s & 0.5\mathbf{K}_c \\ 0 & -0.5\mathbf{K}_s & 0.5\mathbf{K}_c & 0 & 0 & -3\omega\mathbf{C} & \mathbf{K}_0 - 3\omega\mathbf{M} & 0 & 0 & \ddots & 0 & 0 \\ \vdots & \ddots \\ 0 & 0 & 0 & 0 & \dots & 0 & 0.5\mathbf{K}_c & 0.5\mathbf{K}_s & 0 & 0 & \mathbf{K}_0 - n\omega\mathbf{M} & n\omega\mathbf{C} \\ 0 & 0 & 0 & 0 & \dots & 0 & -0.5\mathbf{K}_s & 0.5\mathbf{K}_c & 0 & 0 & -n\omega\mathbf{C} & \mathbf{K}_0 - n\omega\mathbf{M} \end{bmatrix}$$

$$\begin{aligned} \{\mathbf{AB}\} &= [A_0 \ A_1 \ B_1 \ A_2 \ B_2 \ \dots \ A_n \ B_n]^T \\ \{\mathbf{F}\} &= [f_0 \ f_{s_1} \ f_{c_1} \ f_{s_2} \ f_{c_2} \ \dots \ f_{s_n} \ f_{c_n}]^T \end{aligned}$$

Solving the system for $\{\mathbf{AB}\}$, the static position, the dynamic response and its harmonic components can be calculated.

3 Uncertainties analysis

In this work, it will be considered uncertainties in the faults parameters. Therefore, it will be needed a stochastic model and, then, evaluate the stochastic response of the problem.

The Monte Carlo method is generally used to solve stochastic problems, due to its easy implementation and accuracy in response. Which consists of: modelling the uncertainties, it can be used common ones as the Gaussian distribution, Gamma distribution, etc.; Generate samples based on these distributions; Simulate each sample; And proceed with a statistical analysis. However, if the solver used to simulate each sample is computationally expensive, the Monte Carlo simulations will have a huge processing cost.

It is proposed the Stochastic Collocation method with generalized Polynomial Chaos Expansion (gPCE). The stochastic response is approximated by a polynomial series and the stochastic problem resumes into evaluate the expansion coefficients.

3.1 Generalized Polynomial Chaos Expansion

The gPCE was first presented as the "Homogeneous Chaos" by [9]. The author proposed to approximate Gaussian processes via a series of Hermite polynomials. Later, Xiu and Karniadakis [10] spread the concept for more polynomials families. The theory of the gPCE is briefly presented below.

The stochastic response is dependent of random variables λ and deterministic variables \mathbf{p} . It will be approximated by a truncated polynomial series, as in Eq.20.

$$\mathbf{q}_N^P = \sum_{i=1}^M \hat{\mathbf{q}}_i(\mathbf{p}) \cdot \Phi_i(\lambda) \quad (20)$$

which P is the maximum degree of the polynomial and N is the number of random variables. M is give Eq.21 :

$$M = \binom{N+P}{N} \quad (21)$$

For multi-variables problems, $N \geq 2$, the polynomials basis is constructed with uni-variable basis and a tensor product, presented in Eq. 22

$$\Phi_N^P = \bigotimes_{|\mathbf{d}| \leq P} \phi^{i, d_i} \quad (22)$$

which $\mathbf{d} = [d_1, d_2, \dots, d_N]$ is the vector of the degrees of each uni-variable polynomial for each term of the series, d_i is the degree of the polynomial i in that term of the expansion. Therefore, the stochastic problem resumes into evaluate the expansion coefficients $\hat{\mathbf{q}}_i(\mathbf{p})$. To do so, the Stochastic Collocation will be used.

3.2 Stochastic Collocation method

The Stochastic Collocation method is a non-intrusive stochastic method, which permits the usage of a deterministic solver. The method consists in evaluating the deterministic problem in chosen nodes and, then, evaluate the expansion coefficients through a linear system.

To define which node will be calculated the deterministic problem, the sparse grid method is used. The method have the same accuracy as the case of using the full grid, but with less nodes. After all the simulations, the expansion coefficients can be evaluated solving the overdetermined system, i.e. $Q > M$, represented by Eq. 23.

$$\begin{bmatrix} \Phi_1(\lambda^{(1)}) & \dots & \Phi_M(\lambda^{(1)}) \\ \vdots & \ddots & \vdots \\ \Phi_1(\lambda^{(Q)}) & \dots & \Phi_M(\lambda^{(Q)}) \end{bmatrix} \cdot \begin{Bmatrix} \hat{\mathbf{q}}_1(\mathbf{p}) \\ \vdots \\ \hat{\mathbf{q}}_M(\mathbf{p}) \end{Bmatrix} = \begin{Bmatrix} \hat{\mathbf{q}}(\lambda^{(1)}, \mathbf{p}) \\ \vdots \\ \hat{\mathbf{q}}(\lambda^{(Q)}, \mathbf{p}) \end{Bmatrix} \quad (23)$$

which $\lambda^{(i)}$ are the pre-chosen nodes. The system is solved by hte minimum square method. Therefore, with the expansion coefficients evaluated, statistical data can be calculated. The mean and the variance calculus are represented by Eq.24.

$$\begin{aligned} E[\mathbf{q}_N^P] = \mu &= \int \rho(\lambda) \cdot \sum_{i=1}^M \hat{\mathbf{q}}_i(\mathbf{p}) \cdot \Phi_i(\lambda) = \hat{\mathbf{q}}_1(\mathbf{p}) \\ E[(\mathbf{q}_N^P - \mu)^2] = \sigma^2 &= \int \rho(\lambda) \cdot \left(\sum_{i=1}^M \hat{\mathbf{q}}_i(\mathbf{p}) \cdot \Phi_i(\lambda) - \mu \right)^2 = \sum_{i=2}^M \hat{\mathbf{q}}_i^2(\mathbf{p}) \end{aligned} \quad (24)$$

4 Numerical example

The effects of the uncertainties on the system response are presented in this section. The approximation by the polynomial expansion will be validated by comparing it with the stochastic dynamical response evaluated by Monte Carlo simulations.

4.1 Stochastic model

The rotor system was presented in section 2.1. It is considered that the unbalance moment, maximum amplitude of the shaft bow, parallel displacement and angular displacement at the coupling and non-dimensional crack depth have uncertainties. The means of the parameter are presented in table 2.1 and it is considered a 5% variance coefficient. The fault parameters do not have negative values. Therefore, the Gamma distribution is considered. Equation 25 presents the relation of the shape α and scale β parameters with the mean μ and variance σ^2 , necessary to construct a Gamma distribution.

The generalized Laguerre should be used, due to the choice of the Gamma distribution. The polynomial family uses the shape parameter to be constructed. However, the shape parameters has high values, because of the low coefficient of variation value. To avoid this, the memoryless transformation is used. Making possible the usage of the Hermite polynomials. The theory of the method can be seen in [3]

$$\alpha = \frac{\mu^2}{\sigma^2}, \quad \beta = \frac{\sigma^2}{\mu^2} \quad (25)$$

4.2 Comparison of the methods

It was simulated six cases to validate the usage of the polynomial approach. Two cases consist of the rotor subjected to the unbalance and the bowed shaft, separately, with uncertainties. Other three cases the rotor system is subject to the unbalance without uncertainties and the crack or the misalignment (angular and parallel) with uncertainties. And a final case with all faults with uncertainties.

For the cases with only one fault parameter uncertain, it was simulated 1000 samples for the Monte Carlo method and 65 samples and a maximum polynomial degree of 3 for the stochastic collocation. The Monte Carlo simulations took about 20 hours and the stochastic collocation simulations took 80 minutes. For the case of the five fault parameters with uncertainties, it was simulated 6000 samples for the Monte Carlo method and 801 samples and a maximum polynomial degree of 3 for the stochastic collocation. The Monte Carlo simulations took about 125 hours and the stochastic collocation ones took about 18 hours.

4.2.1 One fault parameter with uncertainty

First it is compared the stochastic response evaluated by the Monte Carlo method and the stochastic collocation for the cases of only one fault parameter has uncertainties.

The Figures 2 to 9 present the unbalance response of the shaft in the first bearing with a zoom in the peak of the first critical speed. Some faults have influence in higher harmonic components of the response, which is the case of the cracked shaft, Figures 4 to 6, and angular misalignment fault, Figures 8 and 9. Therefore, it is presented more components for these faults. The unbalance (Fig. 2), bowed shaft (Fig. 3) and parallel misalignment (Fig. 7) have almost no influence in the higher components of the response, so these components are neglected. The Figures 2 to 9 show the mean and a confidence interval of three standard deviation evaluated by both methods for the amplitude of the response. The phase did presented a very small influence to the uncertainties, because of that they are not presented in this work.

Figure 2 presents the unbalance response when the rotor is subjected to only to the unbalance fault with uncertainties. The mean and the envelope evaluated by the stochastic collocation method has similar values to the ones evaluated by the Monte Carlo simulations. The 5% variance ratio has higher influence on the variance of the response when compare with others stochastic responses, illustrated by the distance between the mean and the envelope. Figure 3 presents the unbalance respond when the rotor is subjected to only to the bowed shaft fault with uncertainties. The same is observed as in the case when the rotor is subjected only to the unbalance fault. It is observed as well, how similar are the response of the system for these faults, which difficult the differentiation of them in fault identification methods.

Figures 4 to 6 present the unbalance respond when the rotor is subjected to the crack shaft fault with uncertainties and unbalance. Again, the stochastic response evaluated by the stochastic collocation is very similar to the one evaluated by the Monte Carlo simulations. The second and third harmonic components have some influence of the variance ratio. However, the first component has almost none. This fact, highlight the importance of considered more harmonics components when working with a rotor system with cracked shaft.

Figure 7 presents the unbalance respond when the rotor is subjected to the parallel misalignment fault with uncertainties and the unbalance. The same as the case when the rotor is subjected only to the unbalance and only to the bowed shaft, similar stochastic responses and higher influence of the variance ratio. However, for the case of the angular misalignment (Figs. 8 and 9) the stochastic responses still are very similar, but the variance ration has almost none influence in the variance of the response.

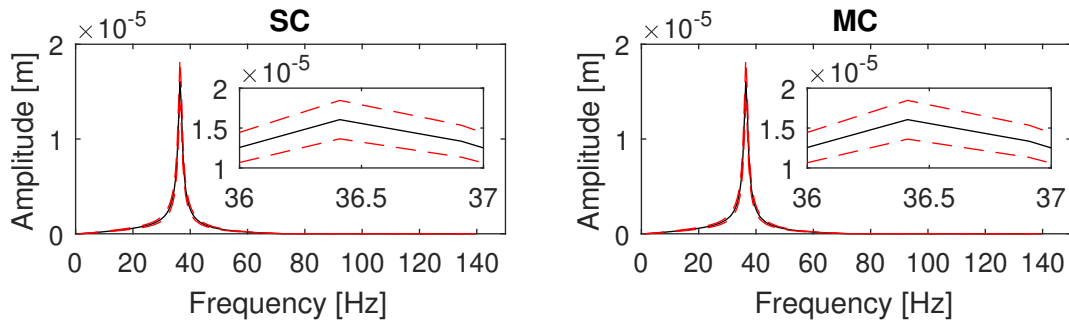


Figure 2: Frequency response of the shaft in the first bearing subjected only to unbalance with uncertainty - first harmonic component

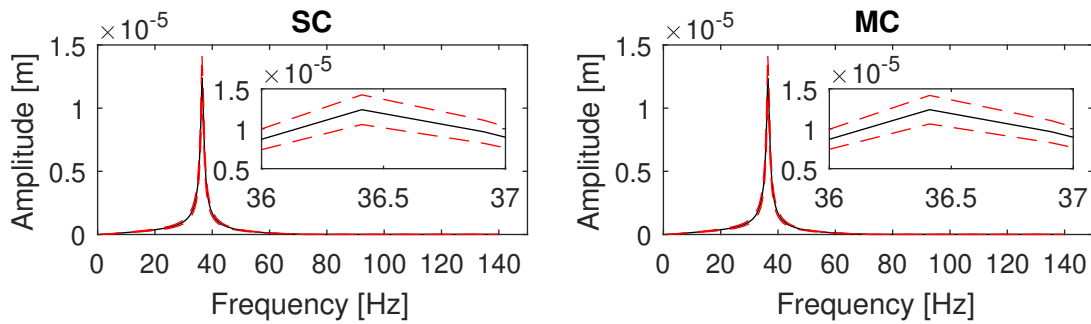


Figure 3: Frequency response of the shaft in the first bearing subjected only to bowed shaft with uncertainty - first harmonic component

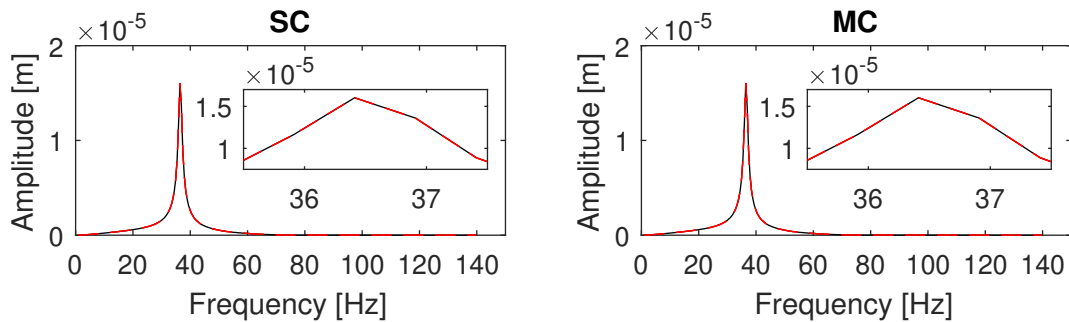


Figure 4: Frequency response of the shaft in the first bearing subjected to cracked shaft with uncertainty and unbalance - first harmonic component

4.2.2 All faults with uncertainties

The case that the rotor system are subjected to all faults considered in this work: unbalance, bowed shaft, cracked shaft, angular and parallel misalignment. It will be considered uncertainties in the parameters of these faults.

Figures 10 to 12 present the stochastic response of the rotor system. Again, the results of the stochastic collocation are very similar to the ones evaluated by the Monte Carlo method. The the variance of the second harmonic component has almost no influence of the variance ratio of the input parameters with uncertainties. The first and third harmonic components has a higher influence.

5 Conclusion

The generalized polynomial chaos expansion was proposed to approximate the stochastic response of a multi-fault rotor system. The stochastic collocation method was use to evaluate the expansion coefficients. The poly-

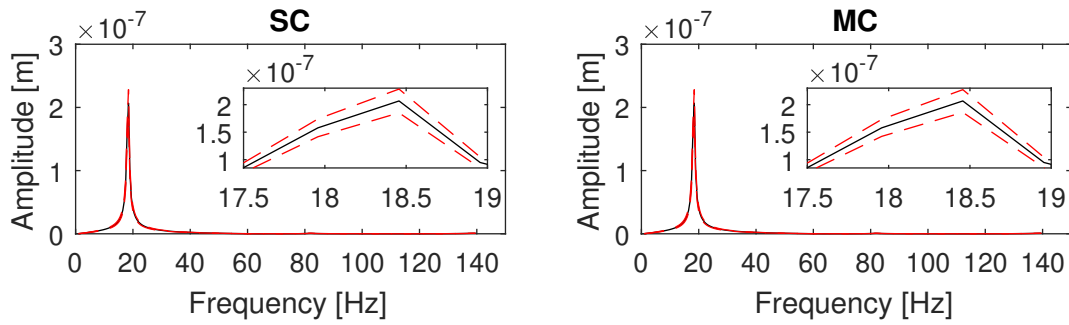


Figure 5: Frequency response of the shaft in the first bearing subjected to cracked shaft with uncertainty and unbalance - second harmonic component

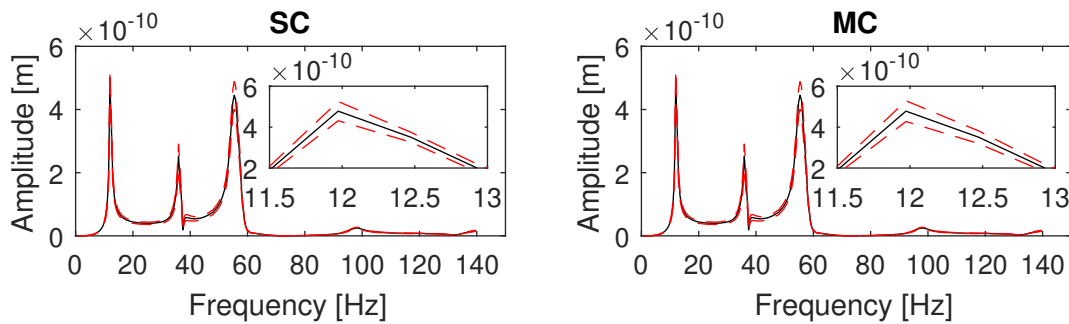


Figure 6: Frequency response of the shaft in the first bearing subjected to cracked shaft with uncertainty and unbalance - third harmonic component

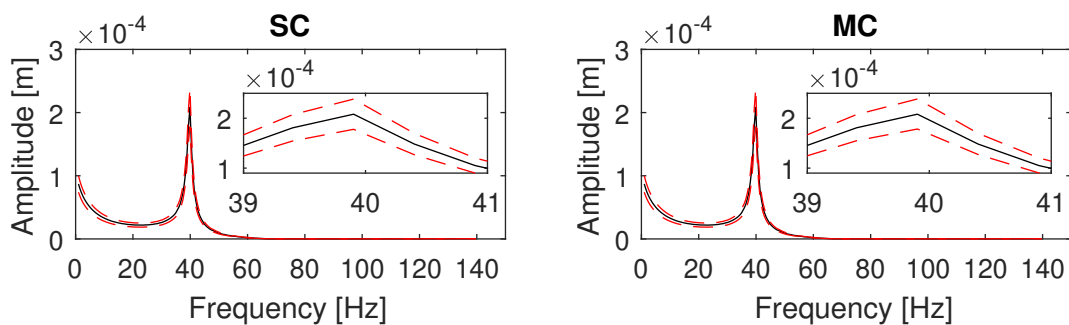


Figure 7: Frequency response of the shaft in the first bearing subjected to parallel misalignment with uncertainty and unbalance - first harmonic component

nomial approximation was compared to the results evaluated by the Monte Carlo method. It was simulated six cases. Two of them consist of the rotor system subjected to the unbalance with uncertainties and bowed shaft with uncertainties, separately. Three of them consist of the rotor system subjected to cracked shaft, parallel and angular misalignment, all with uncertainties and each one together with unbalance. And the last one has all the faults of this work with uncertainties considered.

The results evaluated by the stochastic collocation method are very similar to the ones evaluated by the Monte Carlo method. Which means, that the means and interval of confidence evaluated of each method has a small difference. Therefore, the polynomial approximation with the stochastic collocation is a valid method to evaluate the stochastic frequency response of a faulty rotor. The method presents good accuracy and it is faster than the Monte Carlo method.

The first component of the cracked shaft and the first and second components of the angular misalignment have a almost no envelope. However, for the majority of the frequency responses and higher components, the uncertainties has some influence on.

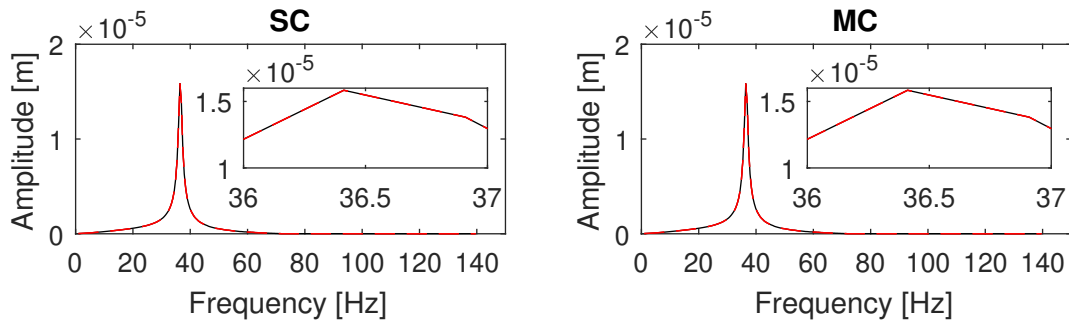


Figure 8: Frequency response of the shaft in the first bearing subjected to angular misalignment with uncertainty and unbalance - first harmonic component

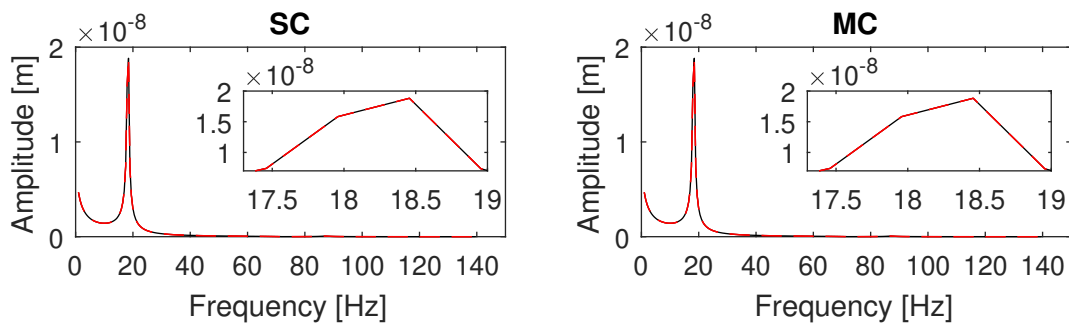


Figure 9: Frequency response of the shaft in the first bearing subjected to angular misalignment with uncertainty and unbalance - second harmonic component

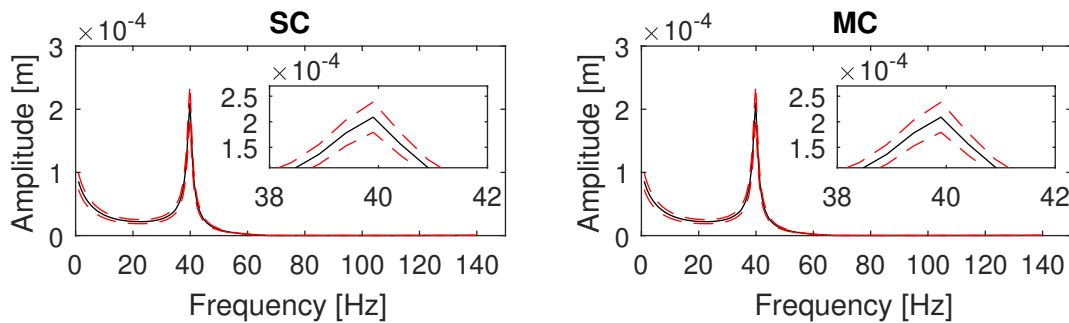


Figure 10: Frequency response of the shaft in the first bearing subjected to all faults with uncertainties - first harmonic component

For the case of all faults with uncertainties, all harmonic components evaluated by the stochastic collocation are very similar with the ones evaluated by the Monte Carlo method.

Overall, the approximation by the generalized polynomial chaos expansion of the stochastic frequency response has a good convergence for the case of a multi-faulty rotor. And can be an alternative of the Monte Carlo method, due to this last one takes a high computational cost.

Acknowledgment

The author would like to thank FAPESP (grant 2015/20363-6, grant 2016/13223-6 and grant 2018/02976-9) for the financial support of the research.

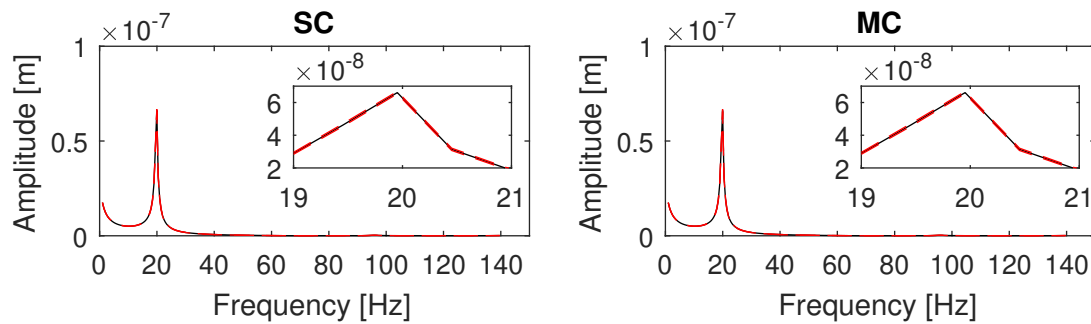


Figure 11: Frequency response of the shaft in the first bearing subjected to all faults with uncertainties - second harmonic component

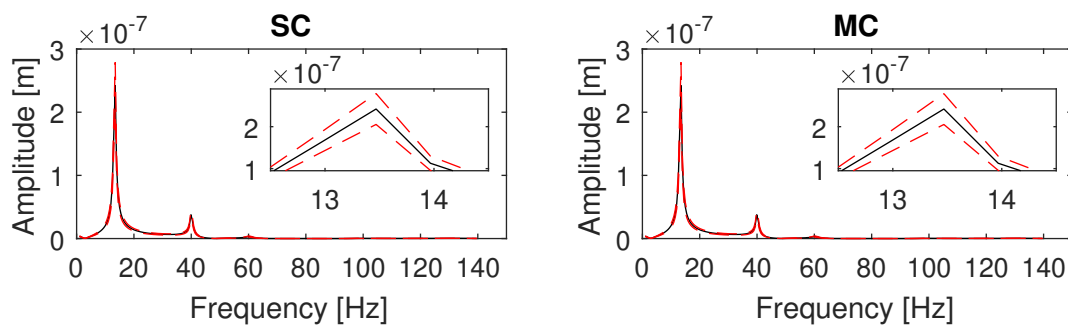


Figure 12: Frequency response of the shaft in the first bearing subjected to all faults with uncertainties - third harmonic component

REFERENCES

- [1] AL-Shudeifat (2013), M. A., On the finite element modelling of the asymmetric cracked rotor, *JSV*, **332**, pp. 2795–2807.
- [2] Edwards, S., Lees, A. W., Friswell, M. I. (1998), Fault Diagnosis of Rotating Machinery, *Shock and Vibration Digest*, **30**(1), pp. 4–13
- [3] Howard, R. M. (2002), *Principles of Random Signal Analysis and Low Noise Design: The Power Spectral Density and Its Applications*, publish online Wiley Online Library,
- [4] Krämer, E. (1993), *Dynamics of Rotors and Foundations*, Springer-Verlag. Chapter 6, pp. 84–85.
- [5] Lees, A. W. (2007), Misalignment in rigidly coupled rotors, *JSV*, **305**(1-2), pp. 261–271.
- [6] Lund, J. W. (1964), Spring and Damping Coefficients for the Tilting-Pad Journal Bearing. *ASLE Transactions*, **7**, pp. 342–352
- [7] Nelson, H. D., McVaugh, J. M. (1976), The Dynamics of Rotor-Bearing Systems Using Finite Elements. *Journal of engineering for Industry*, **98**(2), p.593-600
- [8] Ocvirk, W. (1952), Short bearing approximation for full journal bearings, National Advisory Committee for Aeronautics, Technical Note 2808, Cornell University
- [9] Wiener, N. (1938), The Homogeneous Chaos, *Amer. J. Math*, **60**, p. 897-936
- [10] Xiu, D., Karniadakis, G. (2002), The Wiener–Askey polynomial chaos for stochastic differential equations, *SIAM J. Sci. Comput.*, **24**(2) p. 619-644

Rotor-foundation Dynamics

On the Multiphysics Modelling of Rotor-Bearing-Foundation Dynamics & the Model-Based Control Design of Active Fluid Film Bearings

Michael Gani¹, **Ilmar F. Santos**²

¹ DTU MEK, Technical University of Denmark, 2800, Kgs. Lyngby, Denmark, micgani@mek.dtu.dk

² DTU MEK, Technical University of Denmark, 2800, Kgs. Lyngby, Denmark, ifs@mek.dtu.dk

Abstract

Tilting-pad journal bearings (TPJB) are commonly used by the industry in turbomachinery due to their excellent stability properties. The main drawback is the lack of damping at high rotational speeds, which can be overcome by using a squeeze-film damper attached to their housing (passive approach) or active radial oil injection (mechatronic approach). TPJB with *active oil injection* (ATPJB) uses high-pressure oil to adjust the rotor position and increase damping. Modelling these controllable bearings is not a trivial task from the viewpoint of fluid dynamics and strong fluid film forces couple the lateral movements of the rotor to the bearing housing and foundation. In this framework the entire rotor-bearing-foundation system must be considered and the coupled dynamics modelled. In this paper the complex coupling between rotor, bearing, and foundation dynamics is described by a multi-physics model instead of approaching the foundation dynamics via equivalent impedance.

Individual components of a test-rig composed of a flexible rotor, ATPJB, pedestals, and flexible foundation are discretised using FE methods in MatLab and ANSYS, based on the geometrical and material properties of each component. By implementing solid 3D models in ANSYS and using Craig-Bampton reduction, the accuracy and efficiency of the model is evaluated. *Experimental modal analysis* (EMA) is used to measure the natural frequencies, damping ratios and mode shapes of the coupled rotor-bearing-foundation system. The results are used to validate the mathematical multi-physics model.

The theoretical and experimental results fit with a high degree of accuracy, the first 7 theoretical and experimental natural frequencies and mode shapes deviate less than 8%. More tuning and optimisation of the model is recommended, particularly the coupling between ATPJB and other components. Nevertheless the current model provides useful insights to how these rotor-bearing-foundation systems can be described and is a step closer towards regulating the ATPJB using model-based control design.

1 Introduction

In this paper a finite-element based approach to modelling rotor-bearing-foundation systems is presented as an alternative to equivalent impedance methods. The demand for more efficient energy solutions in rotating machinery has pushed the development of active bearings, that can overcome the limits and disadvantages of conventional passive bearings. *Active tilting-pad journal bearings* (ATPJB) that combine passive hydrodynamic lubrication with active hydrostatic lubrication is a promising solution to this problem. In ATPJBs hydrostatic lubrication is achieved by injecting oil at high-pressure through inlets in the tilting pads which can be controlled to adjust the rotor position and increase damping. A theoretical model of this concept was presented by Santos and Russo [14] and later expanded with thermohydrodynamic theory by Santos and Nicoletti [15]. For model-based control of ATPJBs, accurate and efficient mathematical models of the machine dynamics must be developed to calculate the system dynamics in real time. Because of strong fluid film forces in the ATPJB there is a strong coupling between rotor, bearing housing, and foundation. If the foundation is sufficiently flexible the foundation dynamics must be included in the model to obtain a reasonable accuracy. An example presented by Vance et al. [18] shows that the omission of foundation dynamics can cause critical speeds to be missed entirely. Based on several numerical examples, Krämer [8] concluded that the coupling between rotor and foundation can significantly affect the natural frequencies, resonance amplitudes and stability lines with a flexible foundation. This suggests that a fully coupled

rotor-bearing-foundation multi-physical model is necessary to model systems with ATPJBs.

Nelson and McVaugh [9] presented a finite-element procedure for modelling rotor-bearing system consisting of rigid discs, rotor segments and linear bearings. This rotor-bearing model was coupled with the ATPJB model in [16] to investigate the theoretical limits and feasibility of active lubrication and shows how the ATPJB can successfully be coupled with a rotor model. The influence of the foundation is typically included in rotor-bearing-foundation models by using equivalent impedance. An early schematic of the impedance method is given by Bachschmid et al. [2] where the impedance of three different foundations is coupled with a rotor to study the effect on critical speeds. The impedance is defined as the forces transmitted from the foundation to the bearings and can be obtained either experimentally or analytically. Because the impedance coefficients are frequency dependent and time consuming to measure directly, a lot of research has been devoted to alternative ways of defining them. These include modal analysis [3], frequency response functions [17], numerical analysis [6], and finite-element methods [10]. A similar method based on the foundation receptance is given by Gasch [7], which requires experimental measurements of the foundation to include its effects in a numerical rotor-bearing model. One of the main benefits of the impedance method is that very few extra *degrees of freedom* (DOFs) are added to the system. In some situations experimental measurement of the impedance may also reduce the modelling work significantly. The impedance method allows for steady-state analysis in the frequency domain. Nevertheless, it cannot be used for time-domain analysis and stability calculations which are required to design and regulate the ATPJB. Nevertheless, it cannot be used for time-domain analysis and stability calculations which are required to design and regulate the ATPJB. Alternative hybrid methods also exist that combine numerical and experimental techniques to determine equivalent inputs from the foundation. In an effort to reduce the computational effort a hybrid approach using a combination of the transfer matrix and modal analysis to model rotor-bearing-foundation systems was developed by Zhang et al. [20]. This method relies on measurements of the foundation and avoids modelling issues for structures with complicated interactions to the environment.

The novelty of the rotor-bearing-foundation model presented lies in the “physics-based” approach to modelling the foundation, rather than impedance or hybrid methods, and using reduction techniques to minimize the computational cost. The model is derived having an experimental setup in mind, i.e. a test-rig composed of a flexible rotor, an ATPJB, pedestals, and a flexible foundation. The purpose of the model is to aid the design of a model-based controller for the ATPJB, which requires calculation of system stability and time-domain analysis. Due to the limitations of the equivalent impedance method for this type of applications, a finite-element approach is used to include the effects of the foundation. Finite-element models of the foundation are generally avoided in rotor-bearing-foundation models due to the computational cost, but by implementing the Craig-Bampton reduction technique [11] it is possible to reduce the model to a reasonable size. The model is then compared to experimental results coming from experimental modal analysis carried out using the test-rig. It is important to emphasize that the main goal of the work is to achieve the reduced rotor-bearing-foundation model, not to design the ATPJB controller. Such a model should have a minimum of DOFs and be able to describe the system dynamics in the range of up to 200 Hz.

2 Test Facility and Experimental Modal Testing

The test-rig is designed to test ATPJBs under realistic circumstances that could be found in industrial compressors. Figure 1 shows the test-rig setup during this work. Call-outs show the important components of which test-rig that are relevant to understand its operational principle. These components are all fixed on the foundation with ‘T’ shaped slots (T-slot plate). A coordinate system is shown on the figure, representing the global coordinate system in the model. The x-axis goes in the axial direction of the rotor, the y-axis is perpendicular to the rotor in the horizontal direction and the z-axis is perpendicular to the foundation.

At the left end (drive end) the drive motor is located. It is coupled to a drive coupling using a V-belt to drive the rotor. The drive coupling is connected to the rotor via a flexible coupling that uses a special joint so only rotation is transmitted. It decouples the dynamics of the drive motor from the rotor while maintaining the ability to transmit rotation. The ball bearing which supports the left end of the rotor is housed in the blue pedestal, located right after the coupling point between rotor and flexible coupling. Three sensor pedestals are mounted on the test-rig, two of them between the ball bearing and magnetic bearing, and one of them at the far right end. These can be used to measure the horizontal and vertical displacements of the rotor but were not used in this work. Because their size and mass is very small relative to the foundation and other components, these pedestals are neglected in the mathematical model. After the second sensor pedestal, a magnetic bearing is located and can be used to

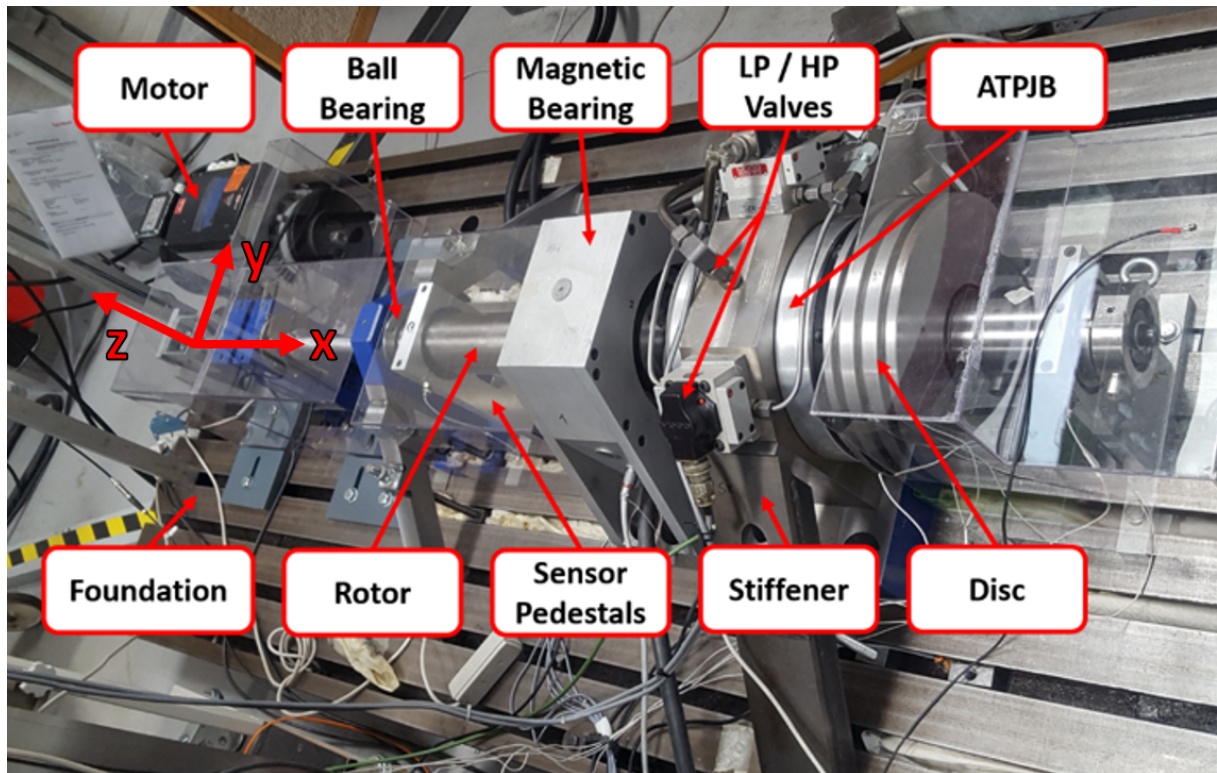


Figure 1: Photo of the test-rig with call-outs to major components.

excite the rotor without being in contact with it. Directly to the right of the magnetic bearing the rotor is supported by the ATPJB, housed in a large grey pedestal. This bearing provide hydrodynamic lubrication by injecting oil using a low-pressure pump and hydrostatic lubrication by using a high-pressure pump. Both of these pumps are located next to the foundation but are not shown in the picture. The two diagonally mounted valves supply the high-pressure oil and the vertically mounted valve provides the low-pressure oil. Finally at the right end of the rotor discs can be mounted. The most important components when modelling the test-rig dynamics are the ones relating the foundation to the rotor. They consist of the rotor, the discs that can be mounted on it, the ATPJB, the pedestals coupling the rotor and foundation, the stiffeners, the foundation, and the damping mat. The estimated geometrical and physical properties of these components are listed in Table 1. The specified values are used in the modelling described in Section 3.

In order to verify the model, experimental modal analysis is carried out to get insights into the test-rig dynamics. Impact testing is used as the measure the response of the test-rig as it requires very little setup and is convenient for the given conditions. The equipment consists of a Brüel&Kjær impact hammer type 8202 with a Manfred Weber M68D1 charge amplifier, a Brüel&Kjær accelerometer type 4730 with a charge amplifier type 2635, and a National Instruments DAQ. For a high spatial resolution the foundation is divided into a 4×15 grid and the rotor is divided into 7 points, as shown on Figure 2. The blue and green dots indicate where the test-rig is struck by the impact hammer and the red dot indicates where the accelerometer is mounted. Data from three experiments is used in order to verify the model at different stages. For the first experiment the entire test-rig is suspended in the air using a crane, ensuring 'free-free' boundary conditions and eliminating the damping mat from the measurements, shown on Figure 3. In the second experiment the test rig is resting on the damping mat, adding damping to the system. For the third experiment vibration data is obtained, with the test-rig resting on the damping mat and the rotor is driven at 1000 RPM.

Each set of measurements is analysed using signal processing and modal analysis to find the natural frequencies, mode shapes, and modal parameters of the test-rig under the given conditions. This is done by calculating the *frequency response function* (FRF) of the measured signals and then using the *single degree of freedom* (SDOF) method on the peaks in the frequency domain via least squares method [5].

Table 1: Estimated geometrical and physical properties of the test-rig components.

Component	Property	Value	Material
Rotor	Length	1150 mm	Steel
	Diameter	90 mm	
	Mass	49.3 kg	
Disc 1	Thickness	80mm	Steel
	Mass	37.3 kg	
Disc 2	Thickness	100 mm	
	Mass	48.5 kg	
	Diameter	295 mm	
Ball Bearing Pedestal	Top Dimensions	50 × 160 × 250 mm	Steel
	Base Dimensions	150 × 280 × 50 mm	
	Mass	28.5 kg	
Ball Bearing Stiffeners	Outer Dimensions	50 × 50 × 500 mm	Steel
ATPJB Pedestal	Top Dimensions	100mm × 300mm × 300mm	Aluminium
	Base Dimensions	150mm × 480mm × 50mm	
	Mass	70.0 kg	
ATPJB Stiffeners	Outer Dimensions	100mm × 50mm × 500mm	Steel
Foundation	Outer Dimensions	3500mm × 1100mm × 105mm	Cast Iron
	Mass	3000.0 kg	

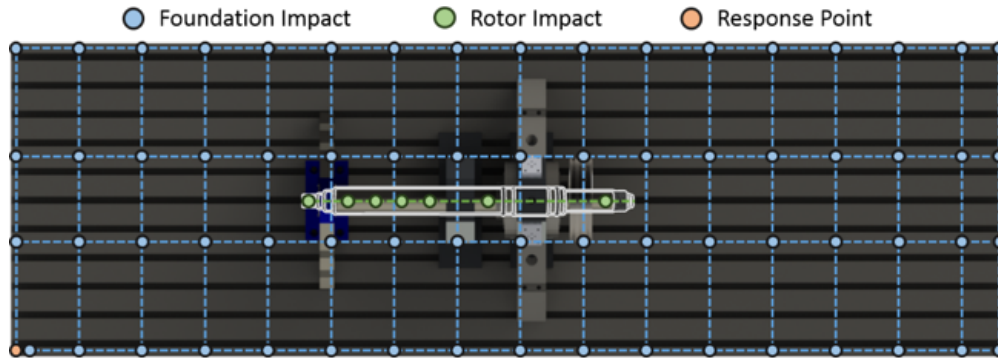


Figure 2: Sketch of all measurement points on the test rig.

3 Dynamic Modelling

The most significant components of the test-rig that must be included in the model are a) rotor and disc, b) ATPJB, c) pedestals, d) stiffeners, and e) foundation.

3.1 Rotor, Disc and Ball Bearing

The rotor, disc and ball bearing are modelled using the finite-element method presented by Nelson and McvVaugh[9]. This means that the rotor consists of 2-node beam elements with 4 DOFs per node that are assembled to form the entire rotor. Each node can translate in the y and z direction and rotate about the y and z axes. These DOFs are given by the vector $\mathbf{q}_n^r = \{V, W, \beta, \Gamma\}$. The radius and length of different elements r_e and l_e varies slightly to match the actual dimensions of the rotor. The disc consists of a single node with the same 4 DOFs as the rotor. It is assumed to be rigid and only contributes with mass and gyro. The ball bearing is modelled as a linear spring which is simply added to the DOFs of the rotor where it is attached. The equations of motion for the rotor and disc are given in (1) and (2) where \mathbf{M} is the mass matrix, \mathbf{K} is the stiffness matrix, \mathbf{G} is the gyroscopic matrix, \mathbf{q} is the displacement vector, \mathbf{Q} is the force vector, Ω is the angular velocity. The superscripts r and d refer to the rotor and

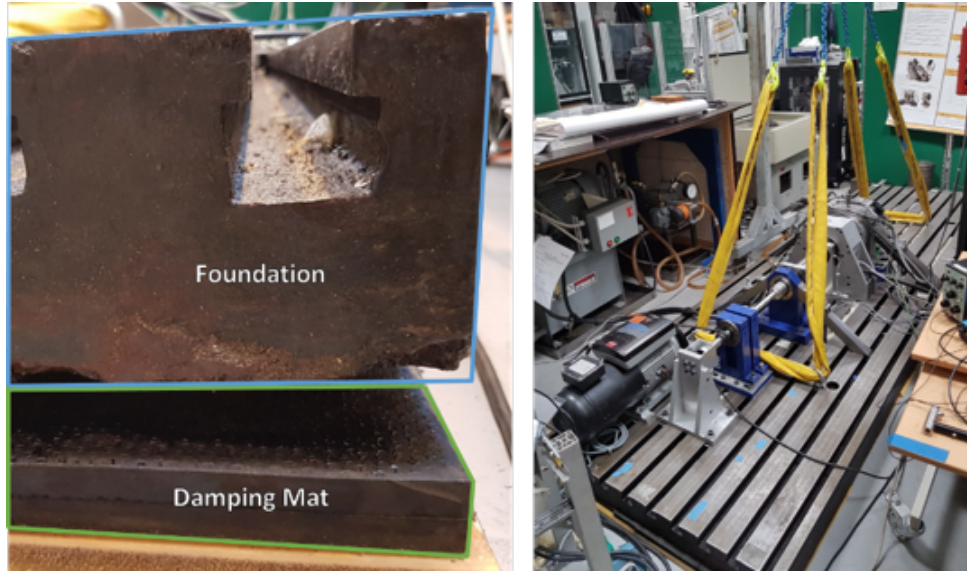


Figure 3: Photo of the test-rig in 'free-free' conditions.

disc respectively.

$$\mathbf{M}^r \ddot{\mathbf{q}}^r - \Omega \mathbf{G}^r \dot{\mathbf{q}}^r + \mathbf{K}^r \mathbf{q}^r = \mathbf{Q}^r \quad (1)$$

$$\mathbf{M}^d \ddot{\mathbf{q}}^d + \Omega \mathbf{G}^d \dot{\mathbf{q}}^d = \mathbf{Q}^d \quad (2)$$

The rotor and disc model was validated with 22 elements using experimental results from a 'free-free' measurements of the rotor natural frequencies with disc 1 mounted on it. The results showed less than 5% deviation for the first three natural frequencies which were within the range of interest. The total number of DOFs in this model is 92.

3.2 ATPJB

The full derivation of the ATPJB model is given in the work by Santos and Russo [14], Santos and Nicoletti [15], and Varela et al. [19]. The DOFs of a 1-pad ATPJB subsystem are defined as vertical and horizontal translations of the rotor $\{X'_J, Y'_J\}$ and rotation and two translations of the tilting pads $\{\alpha', \xi', \eta'\}$. For a 4-pad ATPJB this results in a total of 20 DOFs. In order to couple these with the global rotor-bearing-foundation model, the translational DOFs related to the rotor and pad are rotated to the global coordinates and added together, resulting in a total of 8 DOFs for the ATPJB element $\mathbf{q} = \{X_J, Y_J, \alpha_1, \alpha_2, \alpha_3, \alpha_4, \xi, \eta\}$. The resulting equations of motions for the ATPJB is given in equation (3) where \mathbf{C} is the damping matrix.

$$\mathbf{M}^{atpjb} \ddot{\mathbf{q}}^{atpjb} + \mathbf{C}^{atpjb} \dot{\mathbf{q}}^{atpjb} + \mathbf{K}^{atpjb} \mathbf{q}^{atpjb} = \mathbf{Q}^{atpjb} \quad (3)$$

3.3 Pedestals

Both pedestals were modelled using rectangular 2-node beam elements with 6 DOFs per node, x,y,z translation and rotations as illustrated on Figure 4. These are given by the vector $\mathbf{q}_n^r = \{X, Y, Z, R_x, R_y, R_z\}$. The equations of motion for the pedestals are derived by turning the governing differential equation for a beam (strong formulation) into an integral equation (weak formulation). This equation states the deformation at the nodes and uses shape functions to interpolate between them. Completing the integration gives the equations of motion (4) with the mass matrix \mathbf{M} , stiffness matrix \mathbf{K} , displacements \mathbf{q} , forces \mathbf{Q} , and the superscript p' refers to the pedestal in its local coordinate system.

$$\mathbf{M}^{p'} \ddot{\mathbf{q}}^{p'} - \mathbf{K}^{p'} \mathbf{q}^{p'} = \mathbf{Q}^{p'} \quad (4)$$

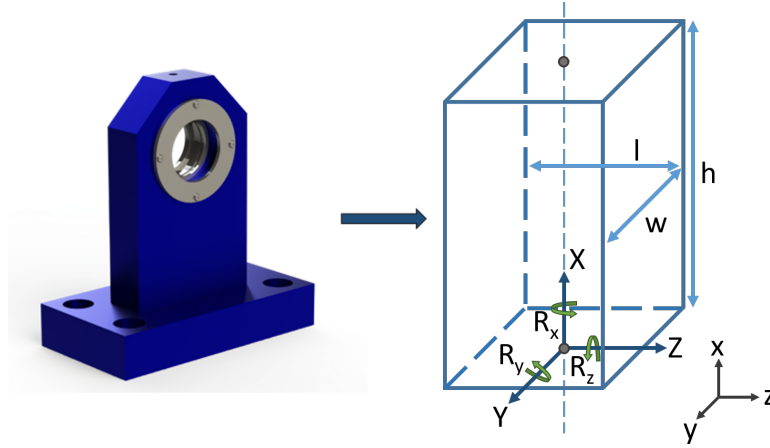


Figure 4: Sketch of a 2-node beam element with 12-DOFs.

The prime indicates the these are defined in a local coordinate system. A coordinate transformation matrix is defined that transforms the xyz-coordinates to the global coordinate system which is then assembled into the full pedestal element transformation matrix (5). The transformation equation to rotate the pedestal DOFs is given by (6).

$$\mathbf{T}_{y,\pi/2} = \begin{bmatrix} \cos(\pi/2) & 0 & \sin(\pi/2) \\ 0 & 1 & 0 \\ -\sin(\pi/2) & 0 & \cos(\pi/2) \end{bmatrix}, \quad \mathbf{T}_{y,\pi/2}^p = \begin{bmatrix} \mathbf{T}_{y,\pi/2} & 0 & 0 & 0 \\ 0 & \mathbf{T}_{y,\pi/2} & 0 & 0 \\ 0 & 0 & \mathbf{T}_{y,\pi/2} & 0 \\ 0 & 0 & 0 & \mathbf{T}_{y,\pi/2} \end{bmatrix} \quad (5)$$

$$\mathbf{K}^p = (\mathbf{T}_{y,\pi/2}^p)^T \mathbf{K}^{p'} \mathbf{T}_{y,\pi/2}^p \quad (6)$$

Note that in the full model assembly, it is assumed that the pedestal nodes can only be displaced in the DOFs of the component they are coupled with. This means that the $\{X, R_x\}$ DOFs are eliminated from the node coupled with the rotor. For nodes coupled with the foundation (described later) and ATPJB the $\{R_x, R_y, R_z\}$ and $\{X, R_x, R_y, R_z\}$ DOFs are eliminated. This results in 7×7 dynamic matrices for the ball bearing pedestal and 5×5 dynamic matrices for the ATPJB pedestal.

3.4 Stiffeners

To develop the equations of motion and system matrices for the stiffeners they are viewed as two dimensional bar elements in the yz-plane, shown on Figure 5. Each stiffener can deform axially in each node in their local

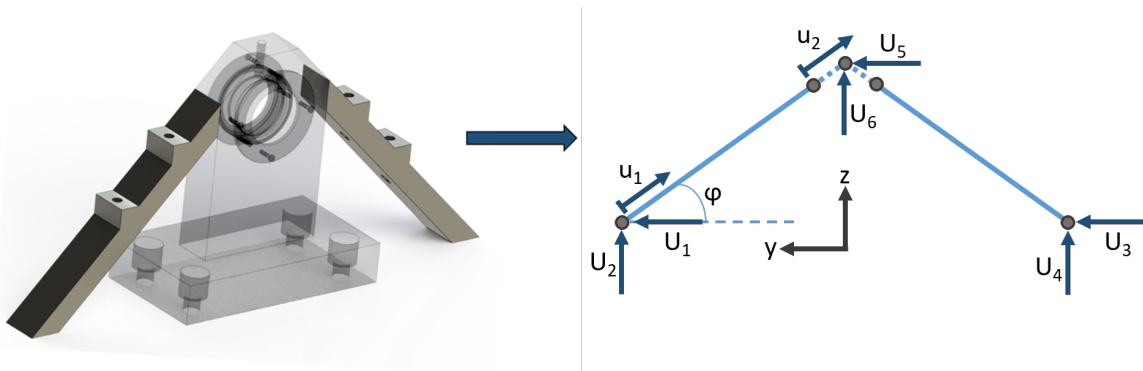


Figure 5: Sketch of the stiffener element.

coordinate systems, as indicated by u_1, u_2 for the left stiffener. By transforming the local stiffness matrix for each bar to the global coordinate system, as shown in equations (7) and (8) for the left stiffener, they can be added together to form a single 3-node bar element with 2 DOFs per node $\mathbf{q}_n^s = \{U_1, U_2\}$. The superscript s'_i refers to the left stiffener in its local coordinate system and s_l refers to the left stiffener in the global coordinate system.

$$\mathbf{K}_1^{s'_i} = \frac{E^s A^s}{l^s} \begin{bmatrix} 1 & 0 & -1 \\ 0 & 0 & 0 \\ -1 & 0 & 1 \end{bmatrix}, \quad \mathbf{T}_1^{s_l} = \begin{bmatrix} -\cos \theta & \sin \theta & 0 & 0 & 0 & 0 \\ 0 & 0 & 0 & 0 & 0 & 0 \\ 0 & 0 & 0 & 0 & \cos \theta & \sin \theta \end{bmatrix} \quad (7)$$

$$\mathbf{K}_1^{s_l} = (\mathbf{T}_1^{s_l})^T \mathbf{K}_1^{s'_i} \mathbf{T}_1^{s_l} \quad (8)$$

This process is repeated for the mass matrix, giving the equations of motions for each stiffener element (9), where the dynamic matrices are of size 6×6 .

$$\mathbf{M}^s \ddot{\mathbf{q}}^s - \mathbf{K}^s \mathbf{q}^s = \mathbf{Q}^s \quad (9)$$

3.5 Foundation

The foundation is modelled using three different types of elements, Kirchoff plate elements, Mindlin plate elements and 3D elements. A description of both types of plate elements can be found in [4] and a description of the SOLID186 element used for the 3D model is given in the ANSYS documentation [1]. The results on Table 2 show that neither Kirchoff or Mindlin plate elements are suitable to model the foundation while the 3D model is very accurate for the first 12 modes (only 7 are shown in the table). Therefore the 3D foundation model is implemented in the rotor-bearing-foundation model.

Table 2: Comparison of measured natural frequencies and calculated natural frequencies for a T-slot plate using Kirchoff elements, Mindling elements and 3D elements.

Mode	Experiment [Hz]	Plate - Kirchoff [Hz]		Plate - Mindlin [Hz]		3D - SOLID186 [Hz]	
ω_{n_1}	94.1	146.1	55.3%	119.0	26.5%	94.7	0.7%
ω_{n_2}	160.0	159.1	-0.6%	153.8	-3.9%	154.8	-3.3%
ω_{n_3}	218.6	218.0	-0.3%	281.9	13.5%	224.5	2.7%
ω_{n_4}	248.4	334.9	34.8%	287.2	31.3%	244.7	-1.5%
ω_{n_5}	285.2	365.2	28.0%	356.4	25.0%	287.3	0.7%
ω_{n_6}	439.6	448.5	2.0%	429.3	-2.3%	426.4	-3.0%
ω_{n_7}	578.6	597.2	3.2%	534.5	3.3%	594.5	2.7%

Based on the results of a convergence study, the final size of the foundation 3D model consisted of 41.020 nodes or approximately 820.000 DOFs. To cut down on computational effort Craig-Bampton reduction is used to reduce the model. Because both the static and dynamic modes are included in the reduction the dynamic properties of the foundation are still preserved with a high degree of accuracy. The static modes Ψ are computed from equation (10) where the subscript i indicates inner nodes and b indicates boundary nodes. The dynamic modes consist of the modal matrix Φ which is obtained when solving the eigenvalue problem given by (11). The reduction matrix

is given by (12) and the reduced stiffness matrix is given by (13).

$$\Psi = -\mathbf{K}_{ii}^{-1}\mathbf{K}_{ib} \quad (10)$$

$$(\mathbf{K}_{ii} - \lambda_j^2\mathbf{M}_{ii}) = \mathbf{0} \quad (11)$$

$$\mathbf{R} = \begin{bmatrix} \Psi & \Phi \\ \mathbf{I} & \mathbf{0} \end{bmatrix} \rightarrow \begin{Bmatrix} \mathbf{q}_i \\ \mathbf{q}_b \end{Bmatrix} = \mathbf{R} \begin{Bmatrix} \mathbf{q}_b \\ \eta \end{Bmatrix} \quad (12)$$

$$\mathbf{K}_r = \mathbf{R}^T\mathbf{K}\mathbf{R} \quad (13)$$

The nodes included in the reduction are chosen based on the geometric locations where the pedestals and stiffeners are fastened on the foundation. Additional boundary nodes are chosen in a grid pattern for the drive motor in the upper left, and in a grid pattern across the bottom of the foundation to add springs and dampeners representing the damping mat. The amount of damping and stiffness added by the mat is controlled by adjusting the value added to these nodes. This is illustrated on Figure 6 which is generated from a MatLab program that imports and reduces the ANSYS foundation model. The colored dots indicate nodes that are included as boundary nodes in the reduction. The size of the reduced matrices is equal to the number of boundary nodes in the reduction n_b plus the amount

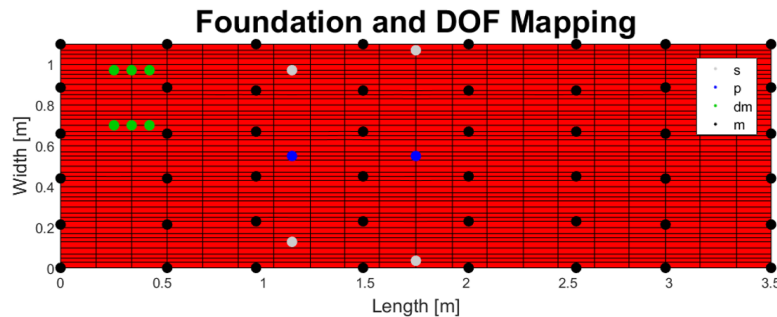


Figure 6: Plot of the foundation bottom mesh and DOFs picked for CB reduction.

of modes in the modal matrix j . Using this method the number of DOFs in the foundation model can easily be reduced to the order of 100 DOFs without significant loss of accuracy, while reducing the computational effort extensively. One should note that the reduced matrix will be dense and, in some cases, can outweigh the benefits of the reduced size. To plot the mode shapes the full system must be reconstructed so the physical displacements can be found.

3.6 Model Assembly

The global model is assembled by adding together the dynamic matrices of all components of the rotor-bearing-foundation system. For components that are coupled the DOFs will be mapped on to each other and summed. This means that the total size of the global matrices is equal to the number of unique DOFs in all the components.

The unique DOFs shown are the rotor DOFs, the ATPJB pad rotation DOFs, the y and z translation DOFs of the top ATPJB pedestal node and finally the reduced foundation DOFs. Both stiffeners and the ball bearing pedestal are coupled to these DOFs and therefore do not have their own unique placement in the matrix. A plot of the matrix entries in the global stiffness matrix assembled in MatLab is shown on Figure 7. The resulting equation of motion for the rotor-bearing-foundation system is given by (14) where the superscript g refers to the global system. By solving the eigenvalue problem of this equation the natural frequencies and mode shapes are extracted.

$$\mathbf{M}^g\ddot{\mathbf{q}}^g + (\mathbf{C}^g - \Omega\mathbf{G}^g)\dot{\mathbf{q}}^g + \mathbf{K}^g\mathbf{q} = \mathbf{0} \quad (14)$$

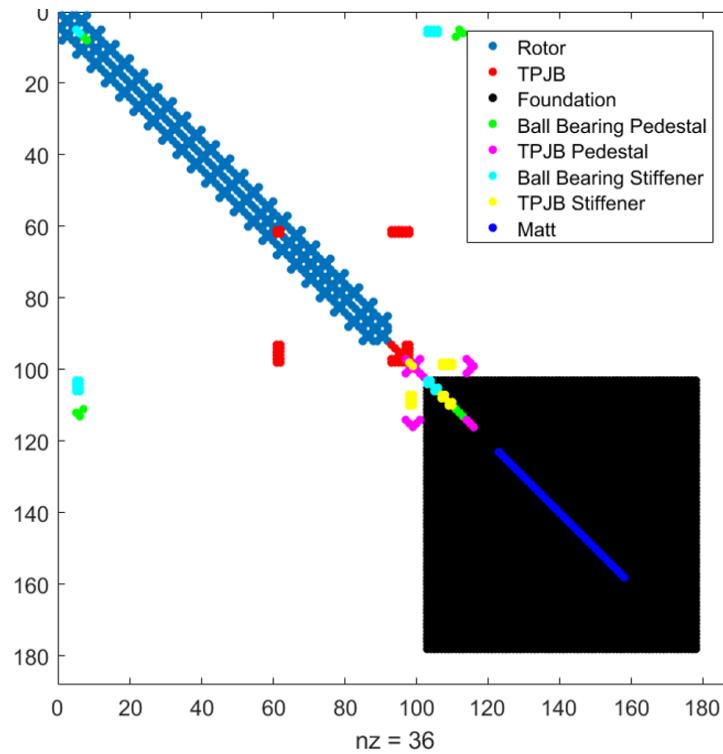


Figure 7: Example showing the component mapping in the global stiffness matrix.

4 Theoretical and Experimental Results

For all three cases, the first 3 experimentally measured mode shapes and corresponding calculated mode shapes are shown on Figure 8a and 8b. From these figures it is very clear that the predicted foundation mode shapes match those measured experimentally. The measured mode shapes also show the coupled rotor-foundation motions which confirms that the foundation should not be neglected in the model. Although not shown here, a total of 7 measured mode shapes were found to match the predicted mode shapes very well in the interval of 20-200 Hz for all three cases.

Table 3 compares the natural frequencies of the model to the experimental data under the three sets of conditions for the 7 modes. These show that with exception of the third mode in the '1000-RPM' experiment, the natural frequencies calculated by the model are very accurate, with deviations under 8%. This shows that a reduced finite-element model of the foundation is a viable method of including foundation dynamics in a rotor-bearing-foundation system. The damping ratios are compared on Table 4 and also show a reasonable degree of accuracy, especially for the 'damping-mat' experiment. For these results the damping values of the mat were adjusted to fit the results from the experiment. For the '1000-RPM' experiment the damping parameters were not changed, although a similar accuracy could likely be reached by adjusting them further.

To be useful when designing a model-based controller for the ATPJB [12, 13] the rotor-bearing-foundation model must be very computationally efficient. When using the reduced finite-element foundation model it is therefore important to include a suitable amount of modes and boundary DOFs in the reduction, to have a reasonable accuracy and model size. In the original results the reduced foundation model contained 348 DOFs and it can be shown that the number of DOFs can be reduced to a total of 190 without significantly affecting the natural frequencies in the 'damping-mat' case. The change in natural frequencies is given on Table 5. This is achieved by reducing the number of foundation nodes coupled with the damping mat and only including 20 modes in the reduction. The number of coupling points with the stiffeners, pedestals and drive motor is not changed. Using reduction methods on the rotor-bearing part of the model could potentially further reduce the number of DOFs. By reducing the number of DOFs the average solution time of the eigenvalue problem is reduced by 48.4%, i.e. from 0.33 seconds to 0.17 seconds.

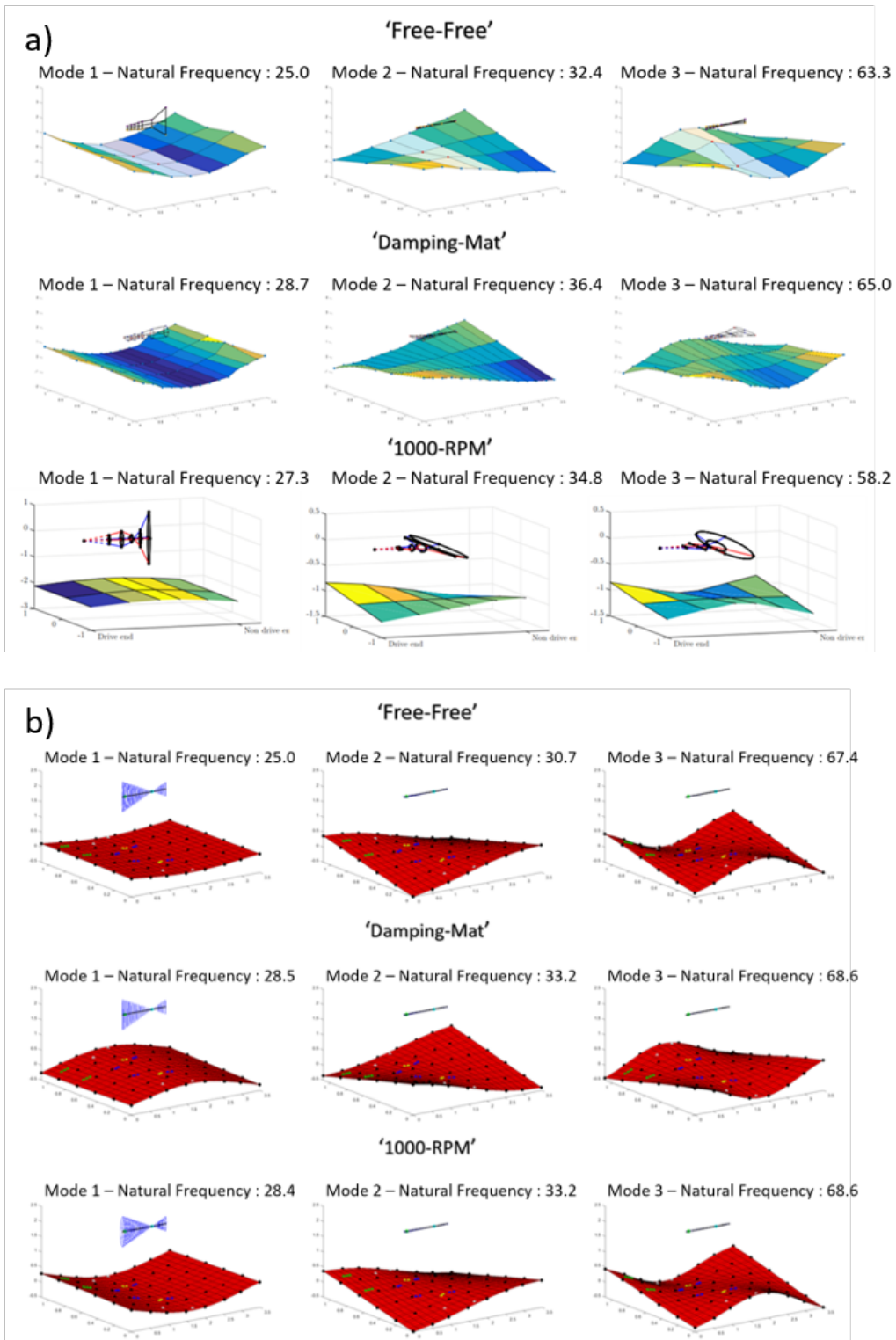


Figure 8: First three mode shapes for all three cases. a) measured mode shapes, b) calculated mode shapes.

5 Model Limitations and Necessity of Further Improvements

While rotor and foundation dynamics is accurately described by means of the finite-element method the pedestal and stiffener model needs further refinement. It should be stressed that in the presented results, the Young's modulus used for the pedestals and stiffeners is set to $E_p = 10^6 \frac{N}{m^2}$ to avoid a locking issue with the foundation modes. Because the pedestal and stiffener elements consist of very few nodes the stiffness is very

Table 3: Comparison of calculated and measured natural frequencies for three different cases.

Mode	RFB-3D Model [Hz]	'Free-Free' Experiment [Hz]	Discrepancy [%]
ω_{n_1}	25.0	25.0	0.2
ω_{n_2}	30.7	32.4	-5.3
ω_{n_3}	67.4	63.3	6.4
ω_{n_4}	70.4	70.8	-0.6
ω_{n_5}	117.7	122.9	-4.1
ω_{n_6}	131.2	129.3	1.5
ω_{n_7}	138.7	139.4	-0.5
Mode	RFB-3D Model [Hz]	'Damping-Mat' Experiment [Hz]	Discrepancy [%]
ω_{n_1}	28.5	28.7	-0.8
ω_{n_2}	33.2	36.4	-8.7
ω_{n_3}	68.6	65.0	5.6
ω_{n_4}	71.5	72.1	-0.8
ω_{n_5}	118.5	123.6	-4.1
ω_{n_6}	131.9	129.0	2.2
ω_{n_7}	139.3	138.0	1.0
Mode	RFB-3D Model [Hz]	'1000-RPM' Experiment [Hz]	Discrepancy [%]
ω_{n_1}	28.4	27.3	4.1
ω_{n_2}	33.3	34.8	-4.5
ω_{n_3}	68.6	58.2	17.9
ω_{n_4}	71.5	70.8	1.0
ω_{n_8}	118.5	124.8	-5.0
ω_{n_9}	139.3	136.8	1.9
$\omega_{n_{10}}$	184.8	180.0	2.7

Table 4: Comparison of calculated and measured damping ratios for the 'damping-mat' and '1000-RPM' cases.

Damping Ratio	RFB-3D Model [Hz]	'Damping-Mat' Experiment [Hz]	Discrepancy [%]
ξ_1	0.042	0.045	-7.3
ξ_2	0.046	0.043	6.7
ξ_3	0.023	0.026	-12.7
ξ_4	0.021	0.020	4.5
ξ_5	0.015	0.017	-7.3
ξ_6	0.012	0.012	-5.0
ξ_7	0.012	0.025	-51.6
Damping Ratio	RFB-3D Model [Hz]	'1000-RPM' Experiment [Hz]	Discrepancy [%]
ξ_1	0.042	0.043	-2.6
ξ_2	0.046	0.139	-66.8
ξ_3	0.023	0.055	-58.7
ξ_4	0.021	0.026	-19.2
ξ_8	0.015	0.026	-41.2
ξ_9	0.012	0.020	-39.5
ξ_{10}	0.011	0.019	-40.5

high compared to the foundation nodes. This creates an artificial increase in stiffness in the connections between foundation, pedestals, and stiffeners, splitting some of the mode shapes in two. By lowering the stiffness the issue is resolved, although the value is not realistic. This also appears to decouple the rotor from the foundation as seen on the calculated mode shapes on Figure 8. With exception of the first mode, the comparison shows that the rotor mode shapes do not match very well. In the model there is no motion of the rotor for any modes above the first, which contradicts the measurements that show different kinds of rotor motion for most modes. These limitations

Table 5: Comparison of discrepancies for the 'damping-mat' experiment with different reduced foundation model sizes.

Mode Shape	Discrepancy - 348 DOFs [%]	Discrepancy - 190 DOFs [%]
ω_1	-0.8	3.2
ω_2	-8.7	-4.4
ω_3	5.6	7.4
ω_4	-0.8	0.4
ω_5	-4.1	-2.8
ω_6	2.2	2.6
ω_7	1.0	1.7

clearly show that the pedestal and stiffener models must be revisited. Pedestals and stiffeners should be modelled using 3D solid elements as done for describing the foundation dynamics, as illustrated on Figure 9, followed by a reduction of the DOFs. The rotor will be coupled to the pedestals which are already connected to the foundation and stiffeners through the 3D model. This will reduce the number of DOFs in the system and should solve the coupling issue.

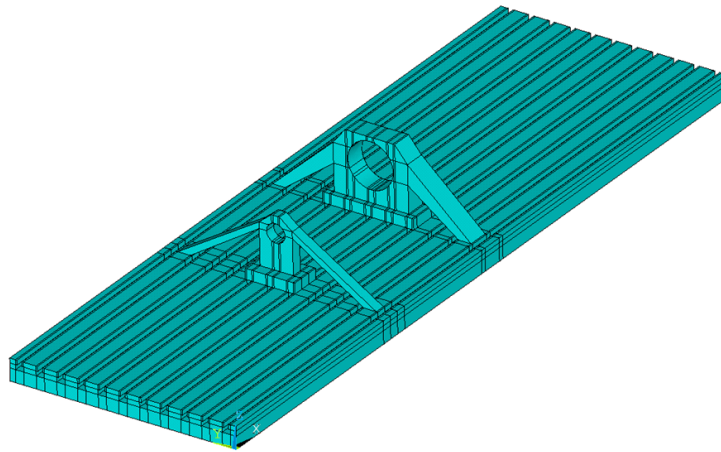


Figure 9: 3D model of foundation, pedestals and stiffeners in ANSYS.

6 Conclusion and Future Aspects

In this paper a mathematical rotor-bearing-foundation model of an ATPJB test-rig was presented and validated through experimental measurements. The foundation was implemented using a finite-element approach with Craig-Bampton reduction to manage the computational cost, instead of the conventional equivalent impedance methods. Even though the foundation looks like a plate it was found that plate elements were not suitable for describing its dynamics. Instead a full 3D model was necessary, using 20-node brick elements. By using experimental data from a similar T-slot plate, the dynamic foundation model was validated, with the first 12 natural frequencies being within 5% of measured values.

The natural frequencies and damping ratios of the rotor-bearing-foundation model were compared to experimentally measured values for three cases, 'free-free', 'damping-mat' and '1000-RPM'. The first seven natural frequencies were found to be within 8% of the measured values in all three cases (with exception of one mode), suggesting a very good model accuracy. The mode shapes were also compared and found to be very accurate. The solution time for the eigenvalue problem of the model could be cut in half by reducing the number of DOFs and modes included in the foundation reduction, without significant changes to the natural frequencies. The smallest model size tested was 190 DOFs. This can likely be optimised further by including pedestals and stiffeners as 3D elements followed by Craig-Bampton reduction. The accuracy and efficiency of the model should be tested for designing model-based controllers for the ATPJB in the near future.

REFERENCES

- [1] ANSYS Documentation, https://www.sharcnet.ca/Software/Ansys/16.2.3/en-us/help/ans_elem/Hlp_E_SOLID186.html
- [2] Bachschmid, N., Pizzigoni, B., and Di Pasquantonio, F. (1977): Method For Investigating the Dynamic Behaviour of a Turbomachinery Shaft on a Foundation. *ASME Pap*, (77).
- [3] Cheli, F., Diana G., Curami A., and Vania A. (1985) *On the Use of Modal Analysis to Define the Mechanical Impedance of a Foundation*. American Society of Mechanical Engineers
- [4] Cook R.D., Malkus D.S., Plesha M.E., Witt R.J., (2002) *Concepts and Applications of Finite Element Analysis*. John Wiley Sons, United States.
- [5] Ewins, D. J. (2008): *Modal Analysis and Modal Testing*. Handbook of Noise and Vibration Control, pp. 565–574.
- [6] Feng, N. S. and Hahn, E. J. (1995): Including Foundation Effects on the Vibration Behaviour of Rotating Machinery. *Mechanical Systems and Signal Processing*, **9**(3), pp. 243–256.
- [7] Gasch, R. (1976): Vibration of Large Turbo-Rotors in Fluid Film Bearings on an Elastic Foundation. *ASME, J. Vib., Acoust., Stress, and Reliab.*, **47**(1), pp. 53–73.
- [8] Krämer, E. (1993): *Dynamics of Rotors and Foundations*. Springer-Verlag Berlin Heidelberg.
- [9] Nelson, H. D. and McVaugh, J. M. (1976): The Dynamics of Rotor-Bearing Systems Using Finite Elements. *ASME J. Eng. Ind.* **98**(2) pp. 593–600.
- [10] Rouch, K. E., McMains, T. H., and Stephenson, R. W. (1989): Modeling of Rotor-Foundation Systems Using Frequency-Response Functions in a Finite Element Approach. *American Society of Mechanical Engineers, Design Engineering Division*, **18-1**, pp. 157–166.
- [11] Roy Craig, Jr. (2000); Coupling of Substructures for Dynamic Analyses - An Overview. *41st Structures, Structural Dynamics, and Materials Conference and Exhibit*.
- [12] Salazar, J. G. and Santos, I. F. (2017): Active Tilting-Pad Journal Bearings Supporting Flexible Rotors: Part I – The Hybrid Lubrication. *Tribology International*, **107**, pp. 94–105.
- [13] Salazar, J. G. and Santos, I. F. (2017): Active Tilting-Pad Journal Bearings Supporting Flexible Rotors: Part II – The Model-Based Feedback-Controlled Lubrication. *Tribology International*, **107**, pp. 106–115.
- [14] Santos, I. F. and Russo, F. H. (1998): Tilting-Pad Journal Bearings with Electronic Radial Oil Injection. *ASME, J. Tribol.*, **120**(3), pp. 583–594.
- [15] Santos, I. F. and Nicoletti, R. (1999): THD Analysis in Tilting-Pad Journal Bearings Using Multiple Orifice Hybrid Lubrication. *ASME, J. Tribol.*, **121**(4), pp. 892–900.
- [16] Santos, I. F., Nicoletti, R., and Scalabrin, A. (2004): Feasibility of Applying Active Lubrication to Reduce Vibrations in Industrial Compressors. *Journal of Engineering for Gas Turbines and Power*, **126**(4), pp. 848–854.
- [17] Stephenson, R. W. and Rouch, K. E (1992): Generating Matrices of the Foundation Structure of a Rotor System from Test Data. *Journal of Sound and Vibration*, **154**(3), pp. 467–484.
- [18] Vance, J. M., Murphy, B. T., and Tripp, H. A. (1987): Critical Speeds of Turbomachinery: Computer Predictions vs. Experimental Measurements - Part II: Effect of Tilt-Pad Bearings and Foundation Dynamics. *ASME, J. Vib., Acoust., Stress, and Reliab.* **109**(1) pp. 8–14.
- [19] Varela, A. C., Nielsen, B. B., and Santos, I. F. (2013) Steady State Characteristics of a Tilting Pad Journal Bearing with Controllable Lubrication: Comparison Between Theoretical and Experimental Results. *Tribology International*, **58**(1), pp. 85–97.
- [20] Zhang, Z. G., Zhang, Z. Y., Jing, B., and Hua, H. X. (2016): A Hybrid Approach for Modelling Dynamic Behaviours of a Rotor-Foundation System. *Journal of Physics: Conference Series*. **744**, 012136

Investigation on the rotor-bearing-foundation interaction

Leonardo Biagiotti Saint Martin^{1a}, Ricardo Ugliara Mendes^{1b}, Katia Lucchesi Cavalca^{1c}

¹ Laboratory of Rotating Machinery, Department of Integrated Systems, University of Campinas (UNICAMP),
13083-860, Campinas, Brazil

^a lbsmartin@fem.unicamp.br

^b rumqld@gmail.com

^c katia@fem.unicamp.br

Abstract

Rotor-foundation dynamic interaction is one of the major concerns in scientific and industrial fields. The stronger the rotor-foundation coupling and/or the more flexible the foundation, the greater the effects of this dynamic interaction. To investigate this issue, two methods are proposed in this work to approach rotor-foundation interaction. The first method concerns the identification of the mechanical impedance matrix of the complete system. This method requires a square modal matrix with as many natural modes of the foundation as there are degrees of freedom shared by rotor and foundation. The second method, called mixed coordinates, proposes a more comprehensive use of experimental information since the modal matrix must not be square. In fact, the modal matrix for this approach can only contain identified natural modes of the foundation within the frequency operation range of the machine. The comparison between these two approaches is presented in this paper for a rotor (simulated in physical and directional coordinates) connected by hydrodynamic bearings to a steel plate that is coupled to an inertial table by four rigid pillars in its corners. The results are relevant to better understand coupling effects in complex identification problems, namely, fault detection and identification in rotating systems.

1 Introduction

The rotor-foundation dynamical interaction is a classical issue in scientific and industrial applications of rotating machines [1-10,17,19]. Especially in the last four decades, engineers and researchers have worked to accomplish a better understanding of the coupling of rotor-foundation systems and its effects. From the point of view of the rotor, a flexible foundation may alter the resonant frequencies and/or amplitudes of the machine. From the point of view of the foundation, the forces transmitted from the rotor may not be properly damped, imposing dangerous vibrations not just to the foundation, but also to the surrounding buildings [10]. Therefore, this paper aims to contribute to this field of research proposing the analysis of a rotor-foundation system via two different methods: the mechanical impedance matrix technique and the mixed coordinates technique.

In the first method, the mechanical impedance matrix (a square matrix) of the foundation is built via numerical finite element simulation or via experimental modal analysis. This matrix is assembled with the rotor and the bearings in a global set of equations and the resultant system is solved in the time or the frequency domain [1,2,9,17]. This technique has the disadvantage of being mandatory to identify as many natural modes of the foundation as there are degrees of freedom (DOF) shared simultaneously by rotor and foundation (i.e. the total number of coupling degrees of freedom).

As an alternative to that strict limitation of the impedance matrix method, the mixed coordinates method proposes a transformation in the foundation representation: instead of being associated to physical coordinates, the foundation is represented by modal or principal coordinates. This coordinate transformation is achieved via the modal matrix (i.e. the matrix of the eigenvectors of the foundation) and since this matrix may not be square it is feasible to work with as many identified or known modes as possible [2-8,17,19].

Finally, to better understand the coupling effects on the rotor, another transformation is proposed: instead of being represented by physical coordinates, the rotor will be represented by directional coordinates. Directional coordinates allow a clear identification of the rotor precession movement direction, facilitating the comprehension of several phenomena present in rotating machine, mainly associated to anisotropic effects inserted in the global system by the bearings and by the foundation [4,13].

2 Theoretical development

In this section, a brief review of the theoretical development regarding the methods for coupling the foundation to the rotor is carried out. The section contemplates two coordinate changes: the first from physical to modal coordinates for the foundation, and the second from physical to directional coordinates for the rotor.

2.1 Impedance matrix: physical representation of the foundation

In the present work, the rotor was modeled by finite Timoshenko beam elements that consider the shear and the secondary effect of rotatory inertia. For this kind of element, 4 DOF (2 translational and 2 rotational) in a plane parallel to the bearing's planes were adopted for each node (see [2,16,17]). This process led to a general displacement vector for the i -th node defined as follows.

$$\mathbf{x}_i^{(r)} = \{y_i^{(r)} \quad z_i^{(r)} \quad \theta_{y_i}^{(r)} \quad \theta_{z_i}^{(r)}\}^T \quad (1)$$

Two subsequent nodes define one element in a way that if the rotor is discretized in n_r nodes, there are $n_r - 1$ elements. Once the displacement vector was established for the rotor, its equation of motion could be written.

$$\mathbf{M}^{(r)}\ddot{\mathbf{x}}^{(r)} + (\mathbf{C}^{(r)} + \Omega\mathbf{G}^{(r)})\dot{\mathbf{x}}^{(r)} + \mathbf{K}^{(r)}\mathbf{x}^{(r)} = \mathbf{f}^{(r)} \quad (2)$$

In Equation (2), $\mathbf{M}^{(r)}$, $\mathbf{C}^{(r)}$, $\mathbf{G}^{(r)}$ and $\mathbf{K}^{(r)}$ are, respectively, rotor matrices of mass, damping, gyroscopic effect and stiffness (all of order $4n_r \times 4n_r$). $\mathbf{f}^{(r)}$ is the vector of forces acting on the rotor (the unbalance force is accounted for within this vector).

For the rotor damping, a proportional structural approach was made. Therefore, the matrix $\mathbf{C}^{(r)}$ is a linear combination of the matrices $\mathbf{M}^{(r)}$ and $\mathbf{K}^{(r)}$ through constants $\alpha^{(r)}$ and $\beta^{(r)}$, respectively.

$$\mathbf{C}^{(r)} = \alpha^{(r)}\mathbf{M}^{(r)} + \beta^{(r)}\mathbf{K}^{(r)} \quad (3)$$

For the foundation, another mesh of finite elements was proposed. Only horizontal and vertical displacements were considered (angular displacements were neglect since the connecting points with the rotor were the bearings), resulting in 2 DOFs per node. Thus, if one considers a foundation discretized in n_b nodes, the general vector of displacements for the foundation would be as follows (displacements on the axial direction of the rotor were neglected).

$$\mathbf{x}^{(f)} = \{y_1^{(f)} \quad z_1^{(f)} \quad \dots \quad y_{n_b}^{(f)} \quad z_{n_b}^{(f)}\}^T \quad (4)$$

And the equation of motion for the foundation could be established considering $\mathbf{M}^{(f)}$, $\mathbf{C}^{(f)}$ and $\mathbf{K}^{(f)}$, respectively, the foundation matrices of mass, damping and stiffness (all of order $2n_b \times 2n_b$). $\mathbf{f}^{(f)}$ is the vector of forces acting on the foundation.

$$\mathbf{M}^{(f)}\ddot{\mathbf{x}}^{(f)} + \mathbf{C}^{(f)}\dot{\mathbf{x}}^{(f)} + \mathbf{K}^{(f)}\mathbf{x}^{(f)} = \mathbf{f}^{(f)} \quad (5)$$

The damping matrix of the foundation also was composed according to the structural proportional damping technique [2].

$$\mathbf{C}^{(f)} = \alpha^{(f)}\mathbf{M}^{(f)} + \beta^{(f)}\mathbf{K}^{(f)} \quad (6)$$

For the complete rotor-foundation system, the displacement vector is composed by the respective displacement vectors from the rotor and the foundation.

$$\mathbf{x} = \begin{Bmatrix} \mathbf{x}^{(r)} \\ \mathbf{x}^{(f)} \end{Bmatrix} \quad (7)$$

Analogously, the complete rotor-foundation equation of motion would be:

$$\mathbf{M}\ddot{\mathbf{x}} + \mathbf{C}\dot{\mathbf{x}} + \mathbf{K}\mathbf{x} = \mathbf{f} \quad (8)$$

It's well known from literature [18] that, for hydrodynamic bearings, a first-order Taylor expansion is proposed to approximate the complete solution of the Reynold's equation for the oil pressure distribution field within the bearings. Through this technique, equivalent direct and cross-coupled damping and stiffness coefficients, rotational speed Ω dependent, are obtained for each bearing. Thus, the linearized force transmitted from the j -th bearing to the i -th rotor node as a function of rotor displacements is [17]:

$$\mathbf{F}_j^{(br)}(\Omega) = - \begin{bmatrix} k_{yyj}^{(b)}(\Omega) & k_{yzj}^{(b)}(\Omega) & 0 & 0 & y_i^{(r)} & c_{yyj}^{(b)}(\Omega) & c_{yzj}^{(b)}(\Omega) & 0 & 0 & \dot{y}_i^{(r)} \\ k_{zyj}^{(b)}(\Omega) & k_{zzj}^{(b)}(\Omega) & 0 & 0 & z_i^{(r)} & -c_{zyj}^{(b)}(\Omega) & c_{zzj}^{(b)}(\Omega) & 0 & 0 & \dot{z}_i^{(r)} \\ 0 & 0 & 0 & 0 & \theta_{y_i}^{(r)} & 0 & 0 & 0 & 0 & \dot{\theta}_{y_i}^{(r)} \\ 0 & 0 & 0 & 0 & \theta_{z_i}^{(r)} & 0 & 0 & 0 & 0 & \dot{\theta}_{z_i}^{(r)} \end{bmatrix} \begin{Bmatrix} y_i^{(r)} \\ z_i^{(r)} \\ \theta_{y_i}^{(r)} \\ \theta_{z_i}^{(r)} \end{Bmatrix} \quad (9)$$

$$\mathbf{F}_j^{(br)}(\Omega) = -\mathbf{K}_j^{(br)}(\Omega)\mathbf{x}_i^{(r)} - \mathbf{C}_j^{(br)}(\Omega)\dot{\mathbf{x}}_i^{(r)} \quad (10)$$

On the other hand, if there is a force transmitted from the foundation to the rotor, there is a reaction from the rotor to the foundation (also transmitted through the bearings). Therefore, the linearized force transmitted from the bearing to the j -th foundation node as a function of foundation displacement is:

$$\mathbf{F}_j^{(bf)}(\Omega) = - \begin{bmatrix} k_{yyj}^{(b)}(\Omega) & k_{yzj}^{(b)}(\Omega) \\ k_{zyj}^{(b)}(\Omega) & k_{zzj}^{(b)}(\Omega) \end{bmatrix} \begin{Bmatrix} y_j^{(f)} \\ z_j^{(f)} \end{Bmatrix} - \begin{bmatrix} c_{yyj}^{(b)}(\Omega) & c_{yzj}^{(b)}(\Omega) \\ c_{zyj}^{(b)}(\Omega) & c_{zzj}^{(b)}(\Omega) \end{bmatrix} \begin{Bmatrix} \dot{y}_j^{(f)} \\ \dot{z}_j^{(f)} \end{Bmatrix} \quad (11)$$

$$\mathbf{F}_j^{(bf)}(\Omega) = -\mathbf{K}_j^{(bf)}(\Omega)\mathbf{x}_j^{(f)} - \mathbf{C}_j^{(bf)}(\Omega)\dot{\mathbf{x}}_j^{(f)} \quad (12)$$

Equations (9)-(12) consider the force through the bearings as function of the rotor displacements only or as function of the foundation displacements only. Naturally, the resultant bearing forces are function of the relative displacements between rotor and foundation, and thus this force can be only estimated by the difference between equations (10) and (12).

From equations (9)-(12), the missing elements in the global matrices of equation (8) can finally be assembled.

$$\mathbf{K}^{(rr)}_{4n_r \times 4n_r} = \text{diag}(\dots \mathbf{K}_j^{(br)}(\Omega) \dots), \quad \mathbf{K}^{(ff)}_{2n_b \times 2n_b} = \text{diag}(\dots \mathbf{K}_j^{(bf)}(\Omega) \dots) \quad (13)$$

$$\mathbf{K}^{(fr)}_{2n_b \times 4n_r} = \begin{bmatrix} \dots & \dots & \dots & \dots & \dots & \dots & \dots \\ \dots & k_{yyj}^{(b)}(\Omega) & k_{yzj}^{(b)}(\Omega) & 0 & 0 & \dots & \dots \\ \dots & k_{zyj}^{(b)}(\Omega) & k_{zzj}^{(b)}(\Omega) & 0 & 0 & \dots & \dots \\ \dots & \dots & \dots & \dots & \dots & \dots & \dots \end{bmatrix}, \quad \mathbf{K}^{(rf)}_{4n_r \times 2n_b} = \mathbf{K}^{(fr)T} \quad (14)$$

Naturally, the process is analogous for the damping terms $\mathbf{C}^{(rr)}$, $\mathbf{C}^{(ff)}$, $\mathbf{C}^{(fr)}$, and $\mathbf{C}^{(rf)}$; and, therefore, they will be omitted here for brevity. With all terms established and neglecting the inertia effects of the oil-film within the bearings, the global matrices for the complete rotor-bearings-foundation system can be obtained as follows.

$$\mathbf{M} = \begin{bmatrix} \mathbf{M}^{(r)} & \mathbf{0} \\ \mathbf{0} & \mathbf{M}^{(f)} \end{bmatrix} \quad (15)$$

$$\mathbf{C} = \begin{bmatrix} \mathbf{C}^{(r)} + \Omega \mathbf{G}^{(r)} + \mathbf{C}^{(rr)} & -\mathbf{C}^{(rf)} \\ -\mathbf{C}^{(fr)} & \mathbf{C}^{(f)} + \mathbf{C}^{(ff)} \end{bmatrix} \quad (16)$$

$$\mathbf{K} = \begin{bmatrix} \mathbf{K}^{(r)} + \mathbf{K}^{(rr)} & -\mathbf{K}^{(rf)} \\ -\mathbf{K}^{(fr)} & \mathbf{K}^{(f)} + \mathbf{K}^{(ff)} \end{bmatrix} \quad (17)$$

For the vector of external forces in equation (8), it's assumed that no external force is applied to the foundation. The only forces acting on the foundation are those transmitted from the rotor through the bearings. Therefore, this vector of forces can be rewritten.

$$\mathbf{f} = \begin{Bmatrix} \mathbf{f}^{(r)} \\ \mathbf{f}^{(f)} \end{Bmatrix} = \begin{Bmatrix} \mathbf{f}^{(r)} \\ \mathbf{0} \end{Bmatrix} \quad (18)$$

2.2 Mixed coordinates: modal representation of the foundation

In subsection 2.1 the global system of equations (equation (8)) was assembled considering that the mass, damping, and stiffness of the foundation were previously known or could be determined (e.g. the impedance matrix of the foundation analytically or experimentally obtained). To solve the complete rotor-bearing-foundation system in the frequency domain, the global matrices should be squared (to be invertible). Since the rotor matrices are already square, the foundation matrices should also be square. Thus, for any approach chosen, it would be necessary to know as many natural modes of the foundation as there are coupling degrees of freedom (i.e. $2n_b$). Otherwise, numerical techniques should be employed to approach the problem (e.g. matrix pseudo-inverse technique), bringing still more uncertainties to the solution.

However, the method presented in this subsection overcomes this strict limitation of the previous method, resulting in square global mass, damping and stiffness matrices without being mandatory to find or determine $2n_b$ natural modes for the foundation. Consequently, the present method is a powerful tool [2-8,17,19] to use the

empirical data available for the foundation together with an analytical model of the rotor and the bearings to analyse the complete system.

Considering Φ the modal or eigenvector matrix, each column of Φ is an eigenvector associated with one natural mode of the foundation. The rows of Φ represents the degrees of freedom considered for the foundation. If l is the number of natural modes, then the order of Φ would be $(2n_b \times l)$.

$$\Phi = \begin{bmatrix} y_{1,1}^{(f)} & \cdots & y_{1,l}^{(f)} \\ z_{1,1}^{(f)} & \cdots & z_{1,l}^{(f)} \\ \vdots & \vdots & \vdots \\ y_{n_b,1}^{(f)} & \cdots & y_{n_b,l}^{(f)} \\ z_{n_b,1}^{(f)} & \cdots & z_{n_b,l}^{(f)} \end{bmatrix} \quad (19)$$

With the modal matrix, the physical coordinates of the foundation, $\mathbf{x}^{(f)}$, may be expressed as a function of its principal or modal coordinates, $\mathbf{q}^{(f)}$. Analogously, the foundation force vector associated with physical coordinates, $\mathbf{f}^{(f)}$, may be converted to a generalized force vector, $\mathbf{w}^{(f)}$ [2].

$$\mathbf{x}^{(f)} = \Phi \mathbf{q}^{(f)} \Leftrightarrow \mathbf{q}^{(f)} = \Phi^{-1} \mathbf{x}^{(f)} \quad (20)$$

$$\mathbf{f}^{(f)} = \Phi^T \mathbf{w}^{(f)} \Leftrightarrow \mathbf{w}^{(f)} = \Phi^T \mathbf{f}^{(f)} \quad (21)$$

Substituting equations (20) and (21) in equation (8), the terms in equations (15)-(17) become:

$$\bar{\mathbf{M}} = \begin{bmatrix} \mathbf{M}^{(r)} & \mathbf{0} \\ \mathbf{0} & \bar{\mathbf{M}}^{(f)} \end{bmatrix} \quad (22)$$

$$\bar{\mathbf{C}} = \begin{bmatrix} \mathbf{C}^{(r)} + \Omega \mathbf{G}^{(r)} + \mathbf{C}^{(rr)} & -\mathbf{C}^{(rf)} \Phi \\ -\Phi^T \mathbf{C}^{(fr)} & \bar{\mathbf{C}}^{(f)} + \Phi^T \mathbf{C}^{(ff)} \Phi \end{bmatrix} \quad (23)$$

$$\bar{\mathbf{K}} = \begin{bmatrix} \mathbf{K}^{(r)} + \mathbf{K}^{(rr)} & -\mathbf{K}^{(rf)} \Phi \\ -\Phi^T \mathbf{K}^{(fr)} & \bar{\mathbf{K}}^{(f)} + \Phi^T \mathbf{K}^{(ff)} \Phi \end{bmatrix} \quad (24)$$

In equations (22)-(24), $\bar{\mathbf{M}}^{(f)}$, $\bar{\mathbf{C}}^{(f)}$ and $\bar{\mathbf{K}}^{(f)}$ are modal matrices of mass, damping and stiffness respectively. The relations among these matrices and the original ones (in physical coordinates) are stated in equations (25)-(27). It must be remarked that the process of pre-multiplying by Φ^T and post-multiplying by Φ results in diagonalized matrices [17].

$$\bar{\mathbf{M}}^{(f)} = \Phi^T \mathbf{M}^{(f)} \Phi = \text{diag}(m_1^{(f)}, \dots, m_l^{(f)}) \quad (25)$$

$$\bar{\mathbf{C}}^{(f)} = \Phi^T \mathbf{C}^{(f)} \Phi = \text{diag}(c_1^{(f)}, \dots, c_l^{(f)}) \quad (26)$$

$$\bar{\mathbf{K}}^{(f)} = \Phi^T \mathbf{K}^{(f)} \Phi = \text{diag}(k_1^{(f)}, \dots, k_l^{(f)}) \quad (27)$$

The global rotor-bearings-foundation system, synthetically described in equation (28) and expressed in terms of mixed coordinates, can be solved in the frequency domain no matter the quantity of identified modes for the foundation (i.e. the number of columns in the modal matrix Φ).

$$\bar{\mathbf{M}} \begin{Bmatrix} \ddot{\mathbf{x}}^{(r)} \\ \dot{\mathbf{q}}^{(f)} \end{Bmatrix} + \bar{\mathbf{C}} \begin{Bmatrix} \dot{\mathbf{x}}^{(r)} \\ \mathbf{q}^{(f)} \end{Bmatrix} + \bar{\mathbf{K}} \begin{Bmatrix} \mathbf{x}^{(r)} \\ \mathbf{q}^{(f)} \end{Bmatrix} = \begin{Bmatrix} \mathbf{f}^{(r)} \\ \mathbf{0} \end{Bmatrix} \quad (28)$$

2.3 Directional coordinates for the rotor

Subsections 2.1 and 2.2 presented two different approaches to write the equation of motion for the complete rotor-bearings-foundation system that could be solved either in time or frequency domains. However, the core difference between those subsections was precisely the coordinate system chosen to represent the foundation dynamic behavior. The impedance matrix interprets the foundation with physical coordinates. The mixed coordinates technique proposes a representation of the foundation by modal coordinates. This subsection presents a new interpretation of the rotor dynamics with directional coordinates [4,13].

According to [13], a transformation matrix $\mathbf{T}_i^{(r)}$ capable of converting the physical coordinates of the i -th rotor node to directional coordinates is given by equation (29), where j is the complex unit ($j^2 = -1$).

$$\mathbf{T}_i^{(r)} = \begin{bmatrix} 1 & 1 & 0 & 0 \\ -j & j & 0 & 0 \\ 0 & 0 & 1 & 1 \\ 0 & 0 & -j & j \end{bmatrix} \quad (29)$$

Then, the global transformation matrix $\mathbf{T}^{(r)}$ is:

$$\mathbf{T}^{(r)}_{(4n_r+l) \times (4n_r+l)} = \text{diag}(\dots \mathbf{T}_i^{(r)} \dots) \quad (30)$$

And the relations between the physical rotor coordinates $\mathbf{x}^{(r)}$ and directional coordinates $\mathbf{p}^{(r)}$, and also between the force $\mathbf{f}^{(r)}$ in physical coordinates and its correspondent $\mathbf{r}^{(r)}$ in directional coordinates are:

$$\mathbf{x}^{(r)} = \mathbf{T}^{(r)} \mathbf{p}^{(r)} \Leftrightarrow \mathbf{p}^{(r)} = \mathbf{T}^{(r)-1} \mathbf{x}^{(r)} \quad (31)$$

$$\mathbf{f}^{(r)} = \mathbf{T}^{(r)} \mathbf{r}^{(r)} \Leftrightarrow \mathbf{r}^{(r)} = \mathbf{T}^{(r)-1} \mathbf{f}^{(r)} \quad (32)$$

Substituting equations (31) and (32) in equation (8), the terms in equations (15)-(17) become:

$$\mathbf{M}_T = \begin{bmatrix} \mathbf{T}^{(r)-1} \mathbf{M}^{(r)} \mathbf{T}^{(r)} & \mathbf{0} \\ \mathbf{0} & \mathbf{M}^{(f)} \end{bmatrix} \quad (33)$$

$$\mathbf{C}_T = \begin{bmatrix} \mathbf{T}^{(r)-1} (\mathbf{C}^{(r)} + \Omega \mathbf{G}^{(r)} + \mathbf{C}^{(rr)}) \mathbf{T}^{(r)} & -\mathbf{T}^{(r)-1} \mathbf{C}^{(rf)} \\ -\mathbf{C}^{(fr)} \mathbf{T}^{(r)} & \mathbf{C}^{(f)} + \mathbf{C}^{(ff)} \end{bmatrix} \quad (34)$$

$$\mathbf{K}_T = \begin{bmatrix} \mathbf{T}^{(r)-1} (\mathbf{K}^{(r)} + \mathbf{K}^{(rr)}) \mathbf{T}^{(r)} & -\mathbf{T}^{(r)-1} \mathbf{K}^{(rf)} \\ -\mathbf{K}^{(fr)} \mathbf{T}^{(r)} & \mathbf{K}^{(f)} + \mathbf{K}^{(ff)} \end{bmatrix} \quad (35)$$

And the global equation of motion for the complete system in directional coordinates,

$$\mathbf{M}_T \begin{Bmatrix} \ddot{\mathbf{p}}^{(r)} \\ \ddot{\mathbf{x}}^{(f)} \end{Bmatrix} + \mathbf{C}_T \begin{Bmatrix} \dot{\mathbf{p}}^{(r)} \\ \dot{\mathbf{x}}^{(f)} \end{Bmatrix} + \mathbf{K}_T \begin{Bmatrix} \mathbf{p}^{(r)} \\ \mathbf{x}^{(f)} \end{Bmatrix} = \begin{Bmatrix} \mathbf{r}^{(r)} \\ \mathbf{0} \end{Bmatrix} \quad (36)$$

Analogously, substituting equations (31) and (32) into equation (28), the terms (22)-(24) become:

$$\bar{\mathbf{M}}_T = \begin{bmatrix} \mathbf{T}^{(r)-1} \mathbf{M}^{(r)} \mathbf{T}^{(r)} & \mathbf{0} \\ \mathbf{0} & \bar{\mathbf{M}}^{(f)} \end{bmatrix} \quad (37)$$

$$\bar{\mathbf{C}}_T = \begin{bmatrix} \mathbf{T}^{(r)-1} (\mathbf{C}^{(r)} + \Omega \mathbf{G}^{(r)} + \mathbf{C}^{(rr)}) \mathbf{T}^{(r)} & -\mathbf{T}^{(r)-1} \mathbf{C}^{(rf)} \Phi \\ -\Phi^T \mathbf{C}^{(fr)} \mathbf{T}^{(r)} & \bar{\mathbf{C}}^{(f)} + \Phi^T \mathbf{C}^{(ff)} \Phi \end{bmatrix} \quad (38)$$

$$\bar{\mathbf{K}}_T = \begin{bmatrix} \mathbf{T}^{(r)-1} (\mathbf{K}^{(r)} + \mathbf{K}^{(rr)}) \mathbf{T}^{(r)} & -\mathbf{T}^{(r)-1} \mathbf{K}^{(rf)} \Phi \\ -\Phi^T \mathbf{K}^{(fr)} \mathbf{T}^{(r)} & \bar{\mathbf{K}}^{(f)} + \Phi^T \mathbf{K}^{(ff)} \Phi \end{bmatrix} \quad (39)$$

And the global equation of motion, equation (28), becomes equation (40).

$$\bar{\mathbf{M}}_T \begin{Bmatrix} \ddot{\mathbf{p}}^{(r)} \\ \ddot{\mathbf{q}}^{(f)} \end{Bmatrix} + \bar{\mathbf{C}}_T \begin{Bmatrix} \dot{\mathbf{p}}^{(r)} \\ \dot{\mathbf{q}}^{(f)} \end{Bmatrix} + \bar{\mathbf{K}}_T \begin{Bmatrix} \mathbf{p}^{(r)} \\ \mathbf{q}^{(f)} \end{Bmatrix} = \begin{Bmatrix} \mathbf{r}^{(r)} \\ \mathbf{0} \end{Bmatrix} \quad (40)$$

Both equations, (36) and (40), can be solved in the frequency domain.

3 Rotor, bearings and foundation characterization

Once the equations of motion for the problem are established, the geometrical and physical features, and the finite element discretization of all elements (rotor, bearings, and foundation) may be presented.

3.1 Rotor and bearings characteristics

The rotor simulated in this paper has a steel shaft with a total length of 1.08 m, a diameter of 30 mm and proportional structural damping coefficients $\alpha^{(r)} = 0$ e $\beta^{(r)} = 1.60 \times 10^{-4}$ s. It is supported by four hydrodynamic bearings with 30 mm diameter, 18 mm length and radial clearance of 90 μm . The distances between the bearings are 0.28 m, 0.39 m and, 0.33 m. In the half distance between each pair of bearings there is a solid disc of length 47 mm, outer diameter of 95 mm and mass of 2.57 kg.

The rotor is discretized in a total of 23 nodes, and the discs influences are concentrated in their corresponding nodes, as illustrated in figure 1.

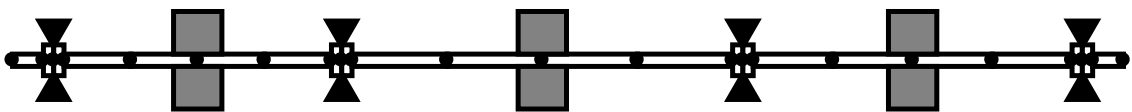


Figure 1: Finite element model of the rotor.

3.2 Foundation characteristics

The foundation is composed by a 1170 mm length, 280 mm width, and 10 mm thick, steel plate with holes for the assembly of the bearing housings and other auxiliary equipment needed in the test rig. The plate is supported by four pillar structures (one at each corner of the plate). The pillars are the connection elements consisting of hollow cylinders (outer diameter of 60 mm, inner diameter of 40 mm and 100mm length) that act as support columns joining the plate to an inertial structure. The ensemble of plate and pillars was simulated in commercial software of mechanical analysis (CREO 2.0[®]) and a large mesh was automatically created by the software. The result of this simulation was a set of 3D linear and angular displacements of all nodes of the finite element mesh. Next, a careful revision of the resultant modes was carried out to separate only modes that really could affect the rotor dynamic behavior (i.e. modes in axial direction were excluded). Then, 4 nodes, in the positions of each bearing, were selected and their information was separated and used to determine the mass, damping, and stiffness matrices of the foundation, which would compose the complete system equation of motion (equation (8)).

Figure 2 illustrates the plate and pillars set. For damping matrix of the foundation, the proportional structural damping coefficients $\alpha^{(f)} = 0$ e $\beta^{(f)} = 1.00 \times 10^{-5}$ s were adopted.

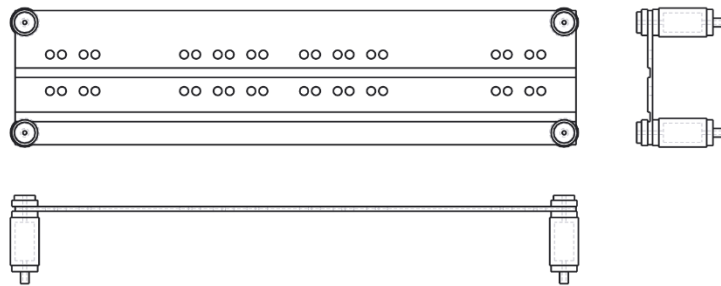
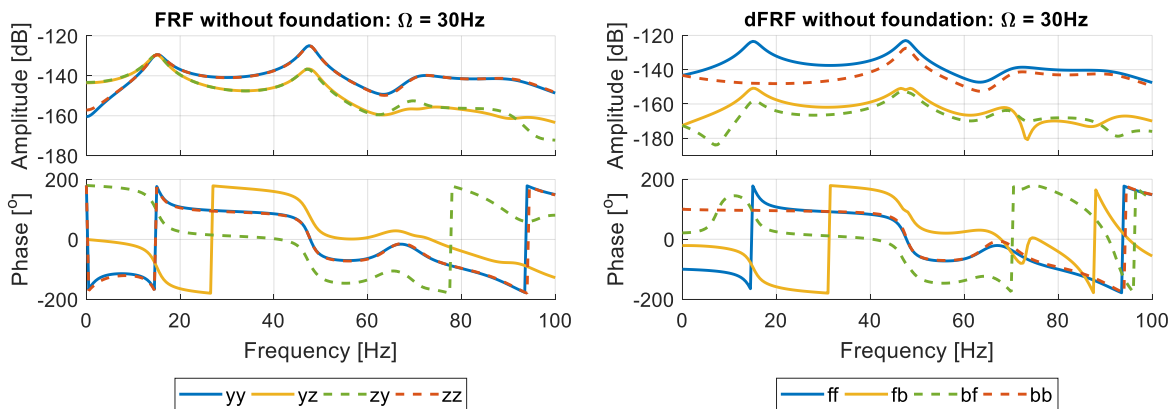


Figure 2: Foundation composed by a thin plate and 4 hollow pillars.

4 Numerical results

Initially, a comparison between the rotor responses with and without the foundation is presented to evidence the influence of the foundation in the dynamic behavior of the rotor. Figure 3 presents the rotor dynamics (including the bearings) for a rotation of 30 Hz in two comparative representations: physical coordinates and directional coordinates, while figure 4 presents the same comparison, now including the foundation via impedance matrix. The results presented consider the transfer function between an excitation applied at node 12 (second disc) and measured at node 3 (first bearing).

The representation of the rotor in directional coordinates (figure 3b) clearly separates the direct response (purely forward and purely backward) from the crossed terms, thus evidencing the anisotropy effects in the system. This valuable information is masked in physical coordinates (figure 3a). In Figure 3b, for instance, it can be seen how the direct terms (ff and bb) stand out from the crossed terms, revealing a low level of anisotropy. The same behaviour cannot be readily inferred from the response in physical coordinates (Figure 3a).



(a) Physical coordinates.

(b) Directional coordinates.

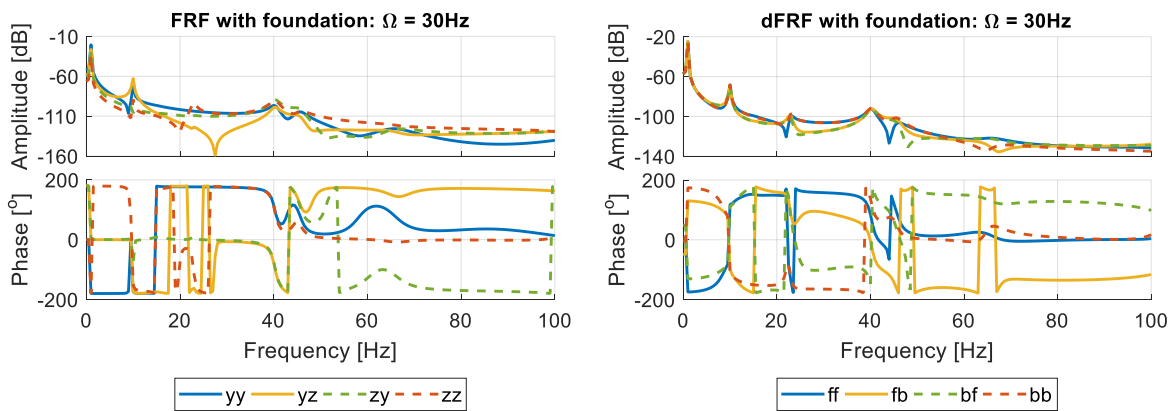
Figure 3: FRF (a) and dFRF (b) of the rotor and bearings at a rotation speed of 30Hz.

It is clear from Figure 3b that the subsystem rotor-bearings has three main peaks within the range 0Hz-100Hz (considering the ff and bb curves): the first about 15Hz in the ff curve is related to the oil-whirl and the two peaks about 48Hz (one in the ff and one in the bb curves) are the first forward and first backward bending modes.

When the foundation is included in the system (figure 4), the anisotropy level of the system is increased. This effect is evidenced by the crossed terms fb and bf which become as high as the direct terms ff and bb in Figure 4b. With the increase of the system anisotropy, the possibility of having backward whirl when the rotor is excited by pure forward excitation (such as unbalance) also increases. Operate the rotor in backward whirl is not desired since it can lead to fault by fatigue; thus, reinforcing the importance of considering foundation effects in rotor dynamics analyses. The analysis of the system response in direction coordinates is also beneficial in fault detection and identification since many faults, such as bearing wear, increase the anisotropy of the system (see e.g. [11,12,14,15]).

The frequency positions of the main amplitude peaks are considerably changed when the subsystem foundation is coupled (figure 4) and even new amplitude peaks arise, totaling 5 amplitude peaks for the complete rotor-bearings-foundation system about 1Hz, 10Hz, 23Hz, 40.5Hz and 45.5Hz.

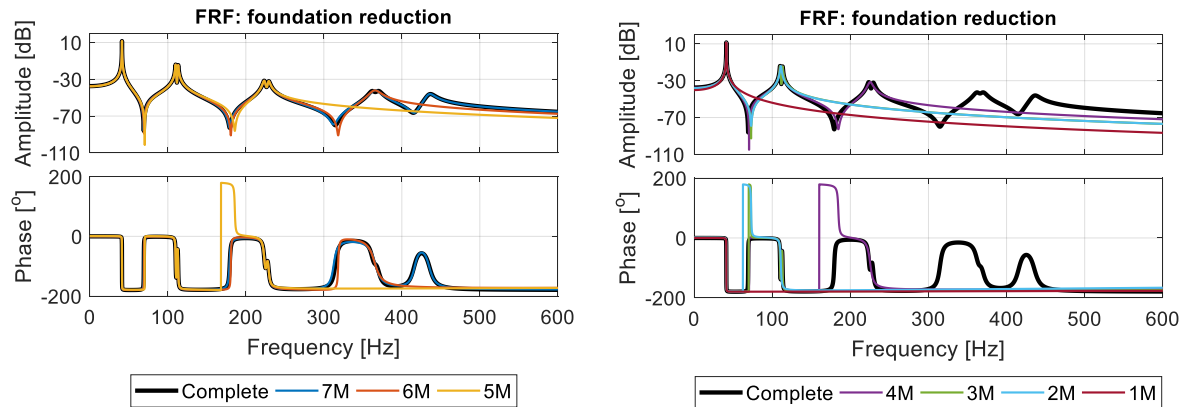
However, one will not find a pure natural frequency from the subsystem rotor-bearing or from the subsystem foundation in the resonances of the complete system (figure 4). As expected, the complete system is a complex combination of the dynamics of its component subsystems.



(a) Physical coordinates.

(b) Directional coordinates.

Figure 4: FRF (a) and dFRF (b) of the rotor, bearings, and foundation at a rotation speed of 30Hz.



(a) Complete vs. reduced models (considering 5 to 7 modes).

(b) Complete vs. reduced models (considering 1 to 4 modes).

Figure 5: Modal reduction of the foundation through an energy criterion. In the legends, 7M is the model reduced to 7 natural modes via mixed coordinates technique, and so on.

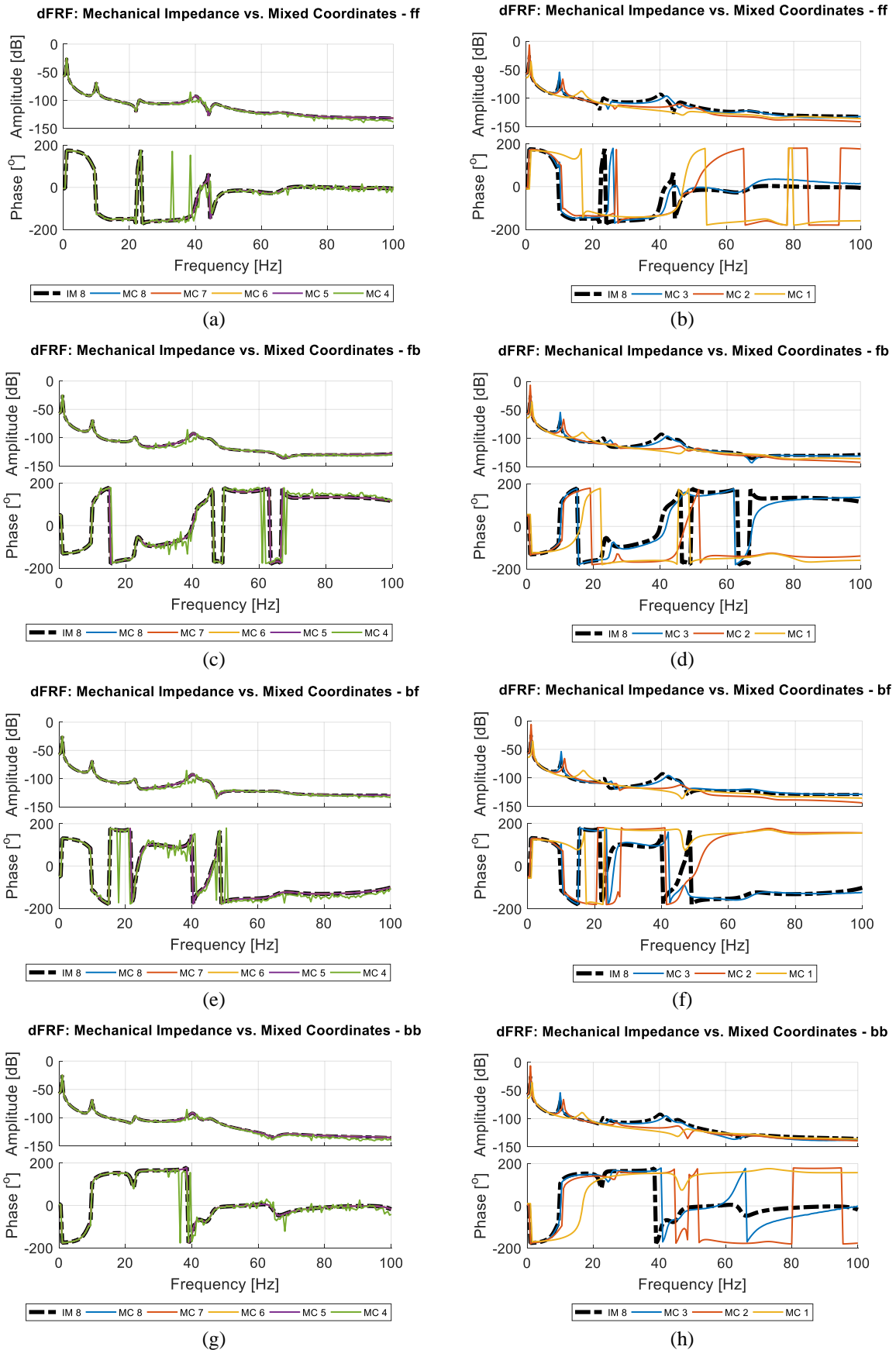


Figure 6: Rotor-bearings-foundation system obtained via impedance matrix (8 modes for the foundation) and via mixed coordinates technique (1 to 8 modes for the foundation). Rotation speed of 30Hz.

Figure 5 compares the FRFs (considering an excitation applied at node 12 and measured at node 3) of the complete foundation subsystem with 8 DOFs (2 per bearing) considering the original 8 modes and its reduced versions. At each step of the reduction process one natural mode of the foundation (the one with less energy) was removed. The original resonance frequencies of the foundation were at 41.2Hz, 110.0Hz, 113.3Hz, 223.7Hz, 229.1Hz, 362.4Hz, 369.6Hz and 435.5Hz. At last, figure 6 presents a comparison between the full-system response, in directional coordinates at the rotational speed of 30Hz, with the complete model of the foundation (8 modes) and with its reduced versions (figure 5).

For the three first reduced models (foundation with 7, 6 and 5 modes) practically no information was lost in the complete system dFRFs, as it can be seen in figures 6a, 6c, 6e, and 6g. The fifth reduction (foundation with 3 modes) preserved the original two first natural frequencies in the right positions, but the amplitude (mainly in the second peak) was considerably increased; figures 6b, 6d, 6f, and 6h. The sixth reduction (foundation with 2 modes) could also maintain the first peak in the right frequency position but altered its amplitude. The last reduction (foundation with 1 mode) could only approximate in frequency and amplitude the original first resonant peak. Therefore, only four modes would be enough for the foundation in the system analysis.

5 Conclusion

The present work demonstrated the influence of a flexible foundation in the dynamic response of a rotating machine. Moreover, the resultant system (composed by rotor, bearings, and foundation) response is not a simple combination of the responses of its constituent elements.

It was also shown that the directional coordinates better evidence the anisotropy effects introduced in the complete model by the hydrodynamic bearings and by the foundation. This representation clarifies the direction of the rotor precession motion and allows for a better comprehension of its dynamics.

For the foundation, the modal coordinates representation proved to be a strong tool when dealing with coupled rotor-foundation systems. This technique allows the use of any number of identified natural modes for the foundation together with a numerical model of the rotor and the bearings. Besides, the results presented in this paper showed that, even for a number of identified modes equals to the half of the total number of connection DOFs, no information was lost in the complete system dynamics. It is remarked that the number of foundation modes to be considered depends on a complex relation between the frequency range of interest, and the relative stiffness and damping of each foundation mode and the rotor modes.

The present work made a careful review of the theoretical development necessary to obtain a global equation of motion for a coupled system composed by two subsystems: rotor-bearings and foundation considering physical and directional coordinates for the rotor and physical and modal coordinates for the foundation.

Acknowledgment

Authors would like to sincerely thank grant #2015/20363-6 from the São Paulo Research Foundation (FAPESP) and CNPq for the financial support for this research.

References

- [1] Bachschmid, N., Bernante, R., Frigeri, C. (1982): Dynamic analysis of a 660 MW turbogenerator foundation. In *Proc. IFToMM*. Rome, Italy, Sept., pp. 129–138.
- [2] Cavalca, K. L. (1993): *L'interazione tra rotori e struttura portante: metodologie per la sua modellazione*. Dissertation, Politecnico di Milano, Milan.
- [3] Cavalca, K. L., Cavalcante, P. F., Okabe, E. P. (2005): An investigation on the influence of the supporting structure on the dynamics of the rotor system. *Mechanical Systems and Signal Processing*, **15**, pp. 157–174.
- [4] Cavalca, K.L., Okabe, E. P. (2010): On the analysis of rotor-bearing-foundation systems. In *Proc. IUTAM Symposium on Emerging trends in rotor dynamics*. New Delhi, India, Marc. 23-26, pp. 89–101.
- [5] Cavalcante, P. F., Cavalca, K. L. (1998): A method to analyse the interaction between rotor-foundation system. In *Proc. IMAC*. Santa Barbara, USA, Febr. 2-5, pp. 775–781.
- [6] Cheli, F., Cavalca, K. L., Dedini, F. G., Vania, A. (1992): Supporting structure effects on rotating machinery vibrations. In *Proc. IMechE*. pp. 543–548.
- [7] Curami, A., Vania, A. (1985): An application of modal analysis techniques. *L'energia Elettrica*, **LXII**(7), pp. 294–307.
- [8] Diana, G., Cheli, F., Vania, A. (1988): A method to identify the foundation modal parameters through measurements of the rotor vibrations. In *Proc. IMechE*. Cambridge, UK, pp. 217–222.
- [9] Gasch, R. (1976): Vibration of large turbo-rotors in fluid-film bearings on an elastic foundation. *Journal of Sound and Vibration*, **47**(1), pp. 53–73.

- [10] Liu, W., Novak, M. (1995): Dynamic behaviour of turbine-generator-foundation systems. *Earthquake Engineering and Structural Dynamics*, **24**, pp. 339–360.
- [11] Machado, T. H., Cavalca, K. L. (2015): Modeling of hydrodynamic bearing wear in rotor-bearing systems. *Mechanics Research Communications*, **69**, pp. 15-23.
- [12] Machado, T. H., Mendes, R. U., Cavalca, K. L. (2016): Directional frequency response applied to wear identification in hydrodynamic bearings. *Mechanics Research Communications*, **74**, pp. 60-71.
- [13] Mendes, R. U. (2016): *Validação experimental de modelo para identificação de parâmetros de falha por desgaste em mancais lubrificados*. Dissertation, Universidade Estadual de Campinas, Campinas.
- [14] Mendes, R. U., Machado, T. H., Cavalca, K. L. (2016): Evaluation of a model based identification method for hydrodynamic bearing wear. In *Proc. of the IMechE 12th International Conference on Vibrations in Rotating Machinery (VIRM11)*. Manchester, United Kingdom, Sept. 13-15, pp. 593-602.
- [15] Mendes, R. U., Machado, T. H., Cavalca, K. L. (2017): Experimental wear parameters identification in hydrodynamic bearings via model based methodology. *Wear*, 372-373, pp. 116-129.
- [16] Nelson, H. D., McVaugh, J. M. (1976): The dynamics of rotor-bearing systems using finite elements. *Journal of Engineering for Industry*, pp. 593–600.
- [17] Pennacchi, P., Bachschmid, N., Vania, A., Zanetta, G. A., Gregori, L. (2006): Use of modal representation of the supporting structure in model-based fault identification of large rotating machinery: Part 1 – theoretical remarks. *Mechanical Systems and Signal Processing*, **20**, pp. 662–681.
- [18] Saint Martin, L. B., Alves, D. S., Cavalca, K. L. (2018): EMC – Reduction of rotor vibration amplitude using PID tuning methods. In *Proc. of the 10th IFToMM*. Rio de Janeiro, Brazil, Sept. 23-27, pp. 74–88.
- [19] Tuckmantel, F. W. S., Cavalca, K. L., Castro, H. F., Felscher, P., Markert, R. (2011): An analysis on the supporting structure representative model in rotating systems. In *Proc. of the 10th ICOVP*. Prague, Czech Republic, pp. 589–596

Dynamics of a Flexible Mobile Flywheel Energy Storage System – Theoretical Modeling and Analysis

Frederik T. Hansen¹, **Nikolaj A. Dagnaes-Hansen**², **Ilmar F. Santos**³

¹ Dept. of Mechanical Eng., Technical University of Denmark, 2800, Kgs. Lyngby, Denmark, frederik.troels.hansen@gmail.com

² Fritz Schur Energy, 2600, Glostrup, Denmark, nah@fsenergy.dk

³ Dept. of Mechanical Eng., Technical University of Denmark, 2800, Kgs. Lyngby, Denmark, ifs@mek.dtu.dk

Abstract

Flywheel energy storage systems (FESSs) based on active and passive magnetic bearings (MBs) have a huge energy storing potential in mobile applications. Under such operating conditions the FESS is exposed to gyroscopic forces, which can be handled by mounting the FESS in a passive gimbal. The purpose of this article is to investigate the coupled dynamics among the flexible bodies: gimbal, housing, and rotor in a FESS. This is carried out by theoretical modal analysis of each body and the FESS by utilizing the finite element (FE) method. Modeling of the bodies are carried out in ANSYS MAPDL using SOLID186 elements. The model of the FESS has been built by assembling the FE models of the bodies, representing the MB forces by linear springs using the MATRIX27 element. The first six natural frequencies and mode shapes have been identified for the gimbal, housing, and rotor occurring in the range of 195-801 Hz, 2882-4580 Hz, and 1346-6504 Hz respectively. The model of the FESS indicates 23 natural frequencies in the range 0-2000 Hz. Decoupled vibrations are noticed, such as isolated vibrations corresponding to the fifth mode shape for the gimbal and the first bending mode for the rotor. Coupled vibrations are also observed between the gimbal, housing, and rotor for which the active MB controllers must be designed taking such dynamics into account.

1 Introduction

Today's modern society is still highly dependent on fossil fuels in terms of oil and natural gasses [7]. These are typically extracted from the ground by drilling. Often, this is carried out offshore where drillships are used in locations with very deep water and where drilling depths of up to 12.000 meters are needed [8]. During the drilling process, huge amounts of energy are sometimes wasted which are desired to store instead.

The risks of explosive gas emissions and fire hazards in a potential battery used to store the energy on the drillships should be minimized, which can be achieved by storing the excess energy as kinetic energy in a flywheel. These type of batteries are called flywheel energy storage systems (FESSs).

The amount of kinetic energy stored is increasing quadratically with rotational speed of the flywheel and the life time is expected to be up to 20 years for such systems [3]. To compete with other battery types, the rotational speeds of FESSs must be very large and the friction and wear should be very low to achieve a high energy density. This can be achieved by implementation of magnetic bearings for supporting the flywheel instead of traditional ball bearings or hydrodynamic based bearings.

Support of the flywheel in the axial direction can be achieved by permanent magnetic bearings and active magnetic bearings can be utilized for radial support of the flywheel. When the FESS is installed in a mobile setting like a ship, it will be imposed to large gyroscopic forces, which in most cases are difficult to handle for active magnetic bearings. In [9] and [10] it is suggested how manoeuvring, vibrations, and gyrodynamic imposed to the FESS can be removed by implementing a passive gimbal mount. To investigate the coupled dynamics of a passive gimbal mounted rotor supported by active magnetic bearings, a test-rig has been designed at the Technical University of Denmark.

The flywheel energy storage system considered consists of a tilting frame, a gimbal, a housing, and a rotor. The gimbal frame is implemented into the test-rig with the sole purpose of removing gyroscopic forces, which is desired if the FESS described is to be implemented in mobile applications. Furthermore, magnetic bearings are mounted inside the housing to keep the rotor levitated and positioned in the centre. The energy is supplied to the system

by blowing air on a compressor wheel mounted on the top of the rotor and thus, the energy is stored in the rotor which acts as the flywheel. A picture of the test-rig can be observed in figure 1 where only the top of the rotor can be seen and the compressor wheel is not mounted.

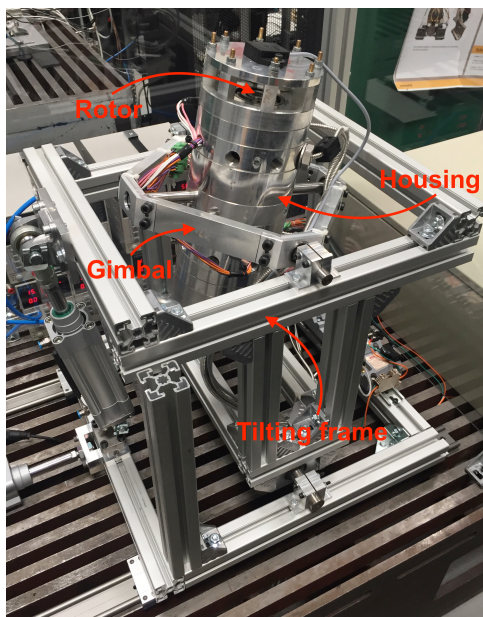


Figure 1: Flywheel energy storage system

A mathematical model has been developed of the FESS in [3] where the multi-body dynamics of the gimbal, housing, and rotor is coupled to the forces from the magnetic bearings. In this model the parts have been assumed rigid. However, results [4] indicates that there might be an influence on the dynamics from the fact that the parts are flexible and not rigid. The purpose of this article is to investigate the flexibility effects on the dynamics of the FESS and the coupled vibrations between the flexible bodies through a theoretical modal analysis.

2 Finite Element Model

Theoretical results in terms of natural frequencies and mode shapes are determined by setting up mathematical models for the considered structures. These mathematical models are designed by utilizing the finite element method through the commercial program ANSYS. The finite element model of the FESS consists of individual FE models of the gimbal, housing, and rotor which are assembled together.

During the investigation of the flexibility effects, the FESS will only be modeled with the rotor levitated but not rotating. Thus, gyroscopic forces are not considered. Furthermore, damping is neglected and contact modeling between the assembled parts in the housing and rotor is not taken into account. It is assumed through out the report that all materials are isotropic and homogeneous. The main materials used in the model are aluminum and steel. In table 1 Young's modulus, E , Poisson's ratio, ν , and the density, ρ , for the steel and aluminum types considered are listed provided from [1],[2].

Material	E [GPa]	ν	ρ [kg/m ³]
Aluminum	71	0.33	2770
Steel	210	0.3	7830

Table 1: Material properties for aluminum and steel

In the following the FE model of the gimbal, housing and rotor as well as the final global model of the FESS is considered. The tilting frame will not be taken into account. All parts are modeled using the SOLID186 element type, which is a quadrilateral 20 node solid element with 3 DOF: translation in x , y , and z -direction. The inter-part connections are modeled using linear springs through the MATRIX27 element type, which is an arbitrary element

in ANSYS that can be used to relate the movement of two nodes to each other by defining the element type as a stiffness matrix. When analyzing the gimbal, housing, and rotor individually, they are assumed in a free condition. Moreover, the global model of the FESS is assumed clamped at the locations where the gimbal is mounted to the tilting frame (see figure 1). Further information regarding the FE models of the gimbal, housing, rotor, and FESS can be found in [6].

2.1 Gimbal

In order to represent the gimbal model using FEM, a simplification of the physical structure is carried out. Bolt holes for the gimbal parts and connecting bolts are neglected. These are instead represented by contact surfaces. In figure 2a the simplified structure of the gimbal is shown, consisting of four side parts (blue), four corner parts (red), and eight contacts regions (green). Furthermore, the global coordinate system for the model is shown. It should be noted that two different corner parts are used, the ones connecting the gimbal to the housing and the ones to the tilting frame with reference to figure 1, however, their geometries are close to similar.

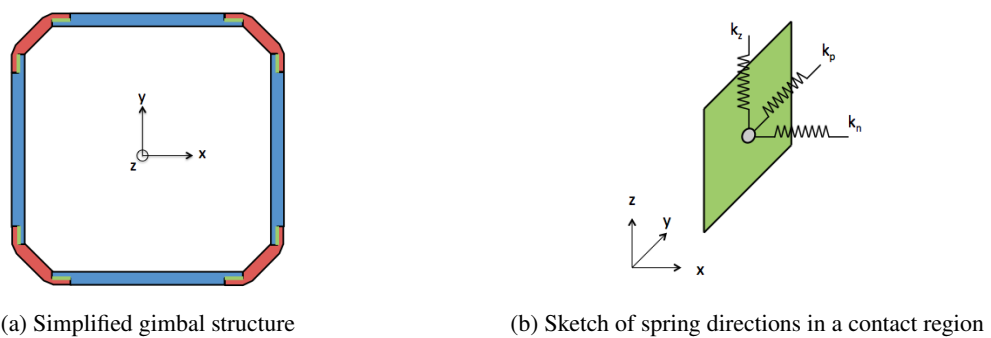


Figure 2: Contact regions in gimbal

The contact regions are modeled using linear springs relating the translation DOF in the coincident nodes from the corner parts and side parts. One spring is used for each translational DOF as shown on figure 2b. Here k_n is the spring stiffness assigned to the spring relating the translational DOF in the normal direction to the contact surface. The spring stiffnesses k_p and k_z are assigned to the springs relating the translational DOF in the parallel direction and global z -direction respectively.

The spring stiffnesses are determined by adjusting them to obtain a minimum sum of squares fit between the six first theoretical and experimental obtained natural frequencies. Details on the experimental obtained natural frequencies can be found in [1] and the obtained stiffnesses are:

$$k_n = 2\,871\,000 \text{ N/m} \quad k_p = 3\,065\,000 \text{ N/m} \quad k_z = 1\,748\,000 \text{ N/m} \quad (1)$$

A convergence study has been carried out to assure that a suitable amount of elements is used to describe the gimbal and the FE model consists of 7098 elements with 98892 DOF.

2.2 Housing

The housing consists of multiple parts assembled together with contact surfaces perpendicular to the axial direction. A picture of the CAD model of the housing can be observed in figure 3a. In order to simplify the physical structure of the housing the following assumptions are made. The active magnetic bearings (AMB) actuator geometries are approximated as cylinders. The ball bearings can be described as steel cylinders. The permanent magnetic bearings (PMB) are made only of aluminum. The bearings are perfectly connected to the housing parts. The housing can be modeled as one solid part and the mounting holes for the house parts can be neglected. Based on these assumptions the simplified geometry of the housing can be observed in figure 3b as a section view.

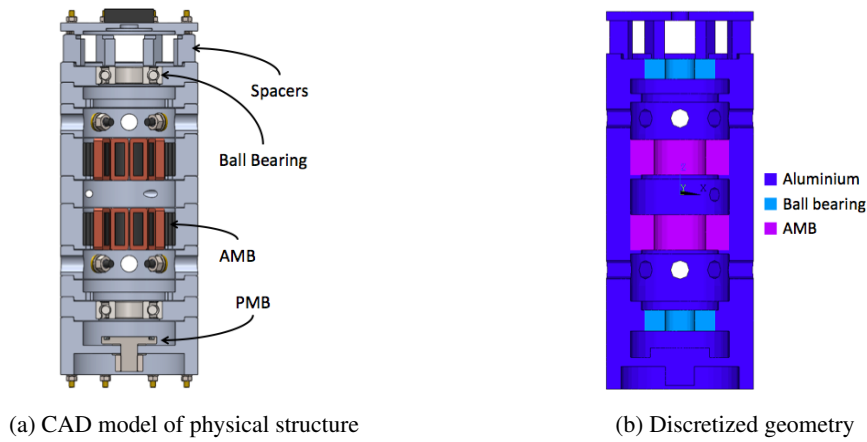


Figure 3: Housing

On the figure the global coordinate system is shown which is aligned with the global coordinate system for the gimbal model. Furthermore, the ball bearing volumes, AMB volumes, and aluminum volumes are designated. The overall material properties for the AMB volumes are estimated by volume fractions of copper and steel from the CAD model. A convergence study has been carried out and the housing FE model consists of 8568 elements with 133023 DOF.

2.3 Rotor

The rotor consists of a steel shaft where aluminum hubs and stacked steel sheet hubs (identical to the AMB stator steel component) are pres-fitted onto. Furthermore, the PMB rotor part is mounted by a bolt. A cross sectional view of the CAD model of the rotor can be observed in figure 4a. In order to describe the physical structure of the rotor, it is modeled as one solid part and the compressor wheel is neglected. The simplified geometry of the rotor is shown in figure 4b.

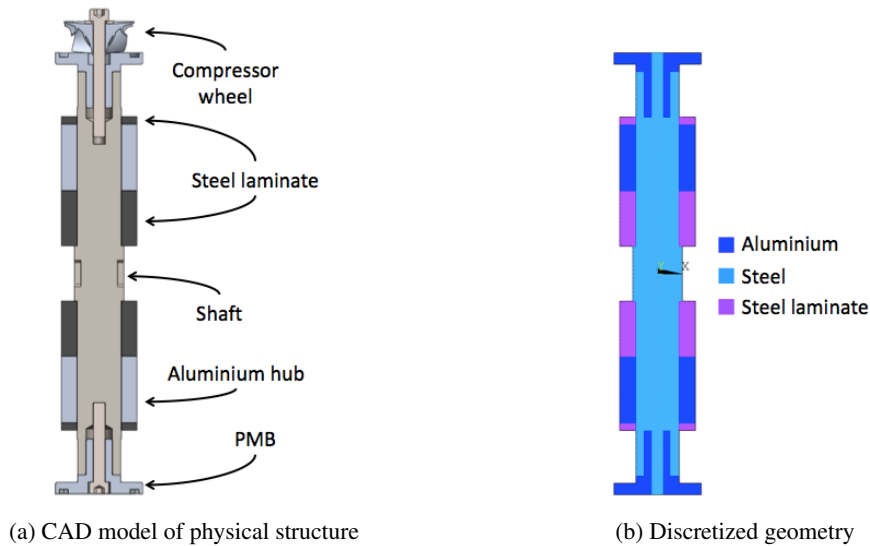


Figure 4: Rotor

On the figure the different materials are designated. The steel laminates are not modeled but instead the mass contribution from the steel sheets are added by increasing the density on the steel shaft segments where the laminates are attached by scaling with the steel sheet laminate volume. This adjustment were carried out to obtain better results compared to experimental ones. It should be noted that the top part of the rotor is identical to the

PMB rotor part and therefore, the rotor is symmetric around the (x,y) -plane w.r.t. the global coordinate system. A convergence study of the rotor FE model yielded 5816 elements with a total of 74283 DOF to be sufficient.

2.4 Global model

The FE models of the gimbal, housing and rotor are assembled into the global FE model of the FESS. This is carried out by implementing the ball bearings, magnetic bearings, and the steel rods connecting the housing to the gimbal. In order to simplify the inter-part connections, the connection of the gimbal corner part to the surroundings is regarded as clamped, the ball bearings and magnetic bearings are represented by linear springs, and the steel rods are perfectly connected to the housing. Based on these assumptions, the physical FESS is simplified such that it can be represented by the mechanical model illustrated in figure 5. Here the springs in the gimbal corner part holes represent the ball bearings, and the springs between the housing and rotor represent the magnetic bearings.

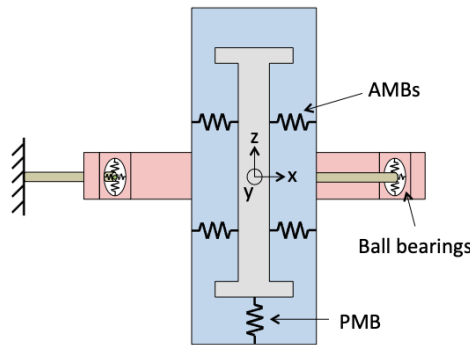


Figure 5: Mechanical model of the FESS

The steel rods are modeled using SOLID186 elements, and a suitable mesh is assured by a convergence study. The ball bearings are modeled by linear springs in the radial direction and axial direction. Four connection points in the radial direction are chosen at every 90 degrees. This is carried out with the purpose of "spreading out" the ball bearing effect into the corner parts. Furthermore, this connection is carried out at three points in the axial direction as shown on figure 6.

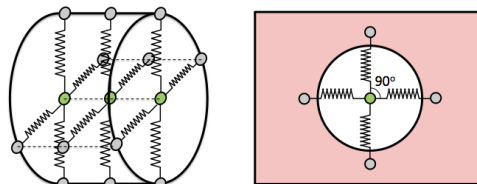


Figure 6: Ball bearing spring arrangement

The ball bearing stiffnesses are not available and therefore, to make sure that these do not affect the results, a convergence study has been carried out yielding a stiffness of $k_{BB} = 1 \times 10^{11}$ N/m. The ball bearing stiffnesses can then be adjusted to fit experimental results for future aspects.

The AMBs are implemented in the same manner as the ball bearings, however, only with one supporting point for each AMB and are only supporting the rotor in the radial direction with a spring stiffness from [5] to be:

$$k_{r,AMB} = 284/2 \text{ kN/m} \quad (2)$$

The PMB is modeled by springs connected between a node in the bottom of the housing model and a node in the PMB part on the rotor model by linear springs with stiffness:

$$k_{z,PMB} = 15 \text{ kN/m} \quad k_{r,PMB} = -12 \text{ kN/m} \quad (3)$$

It should be noted that the stiffness obtained for the PMB cannot change. This is not the case for the AMBs, as this depends on the controller settings. However, fixed stiffnesses for the AMB springs are used in the model.

3 Results

Theoretical natural frequencies and corresponding mode shapes for the gimbal, housing, rotor, and global FESS model have been obtained and are represented in the following. Furthermore, experimental results are available for the gimbal and rotor, which the theoretical results are compared to.

3.1 Gimbal

In table 2 the experimental and theoretical obtained natural frequencies for the gimbal and the discrepancies between the two are listed. The experimental results are obtained from [1].

	Freq. no.	f_1 ,	f_2	f_3	f_4	f_5	f_6
Experimental	[Hz]	193.4	384.9	426	767-778	767-778	~801
Theoretical	[Hz]	195.4	380.5	426	772	775	801
ERROR	[%]	1.03	1.14	0	0.65-0.77	0.39-1.04	0

Table 2: Experimental and theoretical natural frequencies for gimbal

It is observed from the discrepancies that a good agreement between the experimental and theoretical results are obtained. This indicates that the FE model represents the behaviour of the real physical structure well. The theoretical obtained mode shapes for the third and fifth natural frequency for the gimbal is shown in figure 7.

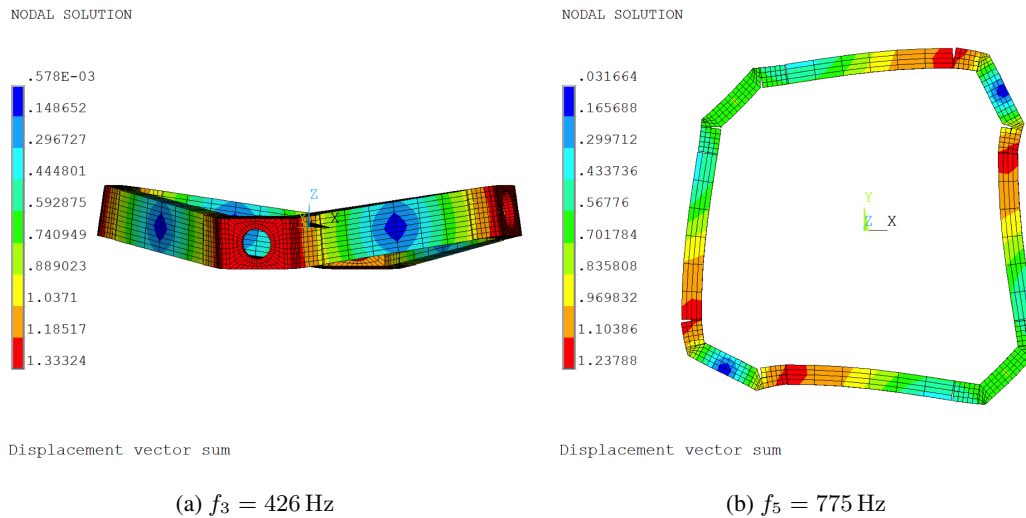


Figure 7: Third and fifth theoretical mode shape for gimbal

3.2 Housing

In table 3 the theoretical obtained natural frequencies for the housing are listed. As indicated by the table experimental results are not available.

Frequency	f_1	f_2	f_3	f_4	f_5	f_6
Mode type [Hz]	bend.	bend.	tor.	bend.	bend	long.
Theoretical [Hz]	2882	2903	3741	4299	4316	4580

Table 3: Theoretical natural frequencies for housing

It is observed that the first natural frequency for the housing is rather large and therefore, the flexibility effects for the housing might not become of interest in the global FE model of the FESS. Due to a lack of experimental results, the housing model was not adjusted further. In figure 8 two selected mode shapes for the housing are illustrated.

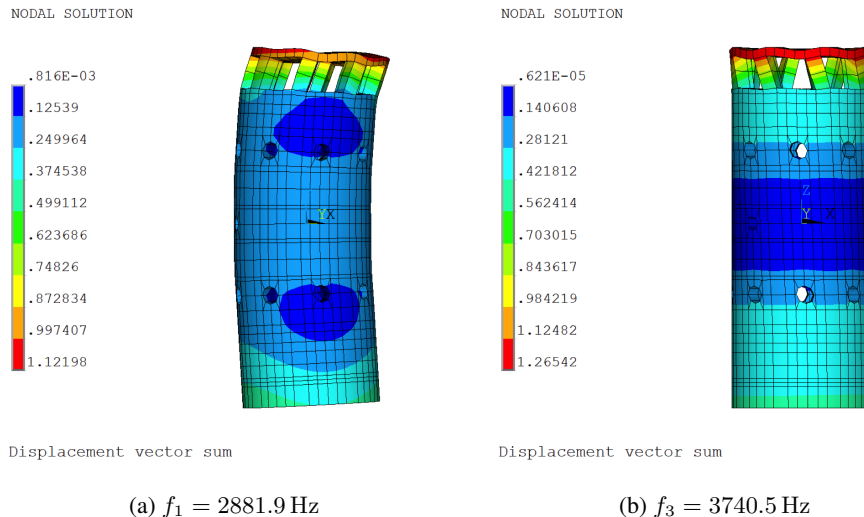


Figure 8: First and third theoretical mode shape for housing

From the figures, it is observed that the mode shapes behave in the same manner as the first two bending modes for a beam in free condition. Furthermore, it is observed that the spacers in the top of housing appear to be the most flexible part of the housing.

3.3 Rotor

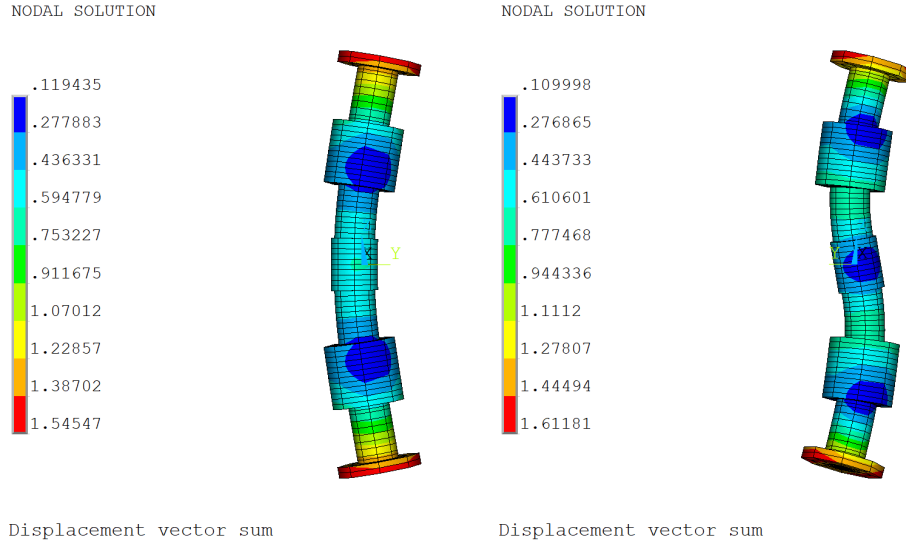
In table 4 the experimental and theoretical obtained natural frequencies for the rotor and the discrepancies between the two are listed. The experimental results are obtained by frequency response functions (FRF) based on experimental data, where the response of the rotor at different points is measured by an accelerometer under impact from a hammer with the input measured by a force transducer.

From table 4 it is seen that fairly low discrepancies are obtained, however, they are not in same order of magnitude as for the gimbal. Better theoretical results might be obtained if inter-part contact were modeled as well. In order to do so, more detailed experimental results are needed to justify these modifications.

Frequency	f_1	f_2	f_3	f_4	f_5	f_6
Experimental [Hz]	1237	1237	3023	3023	4797	4797
Theoretical [Hz]	1347	1347	3224	3224	3644	6504
Error [%]	8.81	8.81	4.19	4.19	32.39	35.58

Table 4: Experimental and theoretical natural frequencies for rotor

It should be noted that the FE model of the rotor has mainly been updated according to the first natural frequency, since this frequency were verified by two experiments: based on the before mentioned FRF and under excitation of the rotor using the AMBs. In figure 9 the first two mode shapes for the rotor is shown.



(a) $f_1 = 1347$ Hz (b) $f_3 = 3224$ Hz
Figure 9: First and third theoretical mode shape for rotor

As for the case with the housing, the first two bending mode shapes look very similar to the first two bending modes for a slender beam.

3.4 Global Model

In table 5 the theoretical obtained natural frequencies for the global model of the FESS are listed. It is observed that a total of 23 natural frequencies are occurring in the interval from 0 to 2000 Hz.

Freq.	f_1	f_2	f_3	f_4	f_5	f_6	f_7	f_8	f_9	f_{10}	f_{11}	f_{12}
[Hz]	0	0	10.10	26.33	27.79	59.75	64.25	68.51	68.87	111.4	270.8	365.1
Freq.	f_{13}	f_{14}	f_{15}	f_{16}	f_{17}	f_{18}	f_{19}	f_{20}	f_{21}	f_{22}	f_{23}	-
[Hz]	504.4	641.8	801.0	1086	1095	1226	1238	1347	1347	1396	1693	-

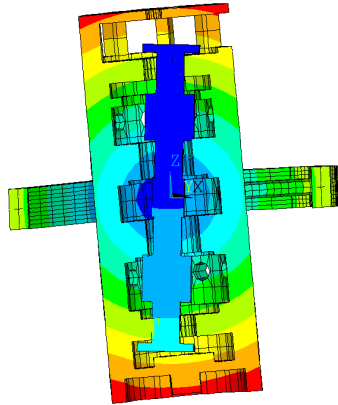
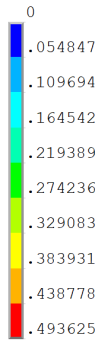
Table 5: Theoretical natural frequencies for the global model of the FESS in the range of 0-2000 Hz

The first two natural frequencies occur at 0 Hz. The first mode is a rigid body mode for the housing and rotor rotating together about the ball bearing axis. The second mode is the rotor rotating about the centre axis, which is a movement the magnetic bearings allow. In figure 10 a few selected mode shapes are shown.

In general, it is observed that a lot of the mode shapes appearing in the interval 0-2000 Hz are non-rigid body motions, which means that the flexibility effects play a role in the mode shapes. This is especially true for the gimbal, steel rods, and rotor, whereas the housing behaves more as a rigid body. Therefore, a more simple rigid model of the housing might be sufficient in the global model.

The mode shape corresponding to the sixth natural frequency is shown in figure 10a, where the gimbal and housing is vibrating together with the rotor almost standing still. Here the flexibility effects of the bodies do not play a large role in the mode shape. However, the flexibility effects are clearly seen on the 11th mode shape in figure 10c. Here a kind of bending mode for the steel rods is observed where the housing is twisted around the global z-axis. This mode clearly illustrates a scenario of coupled vibrations where energy is exchanged between the housing and gimbal. As illustrated by this mode shape the steel rods tends to be the most flexible part in the FESS. Furthermore, a strong coupling between gimbal and housing is often seen in the mode shapes.

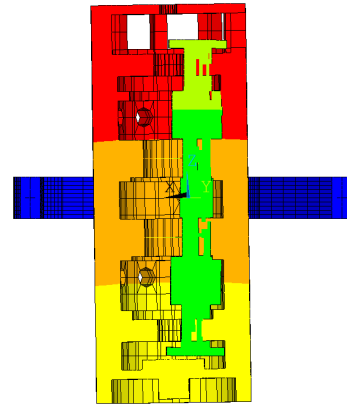
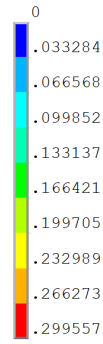
NODAL SOLUTION



Displacement vector sum

(a) $f_6 = 59.75$ Hz

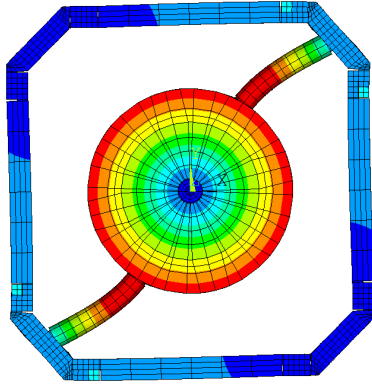
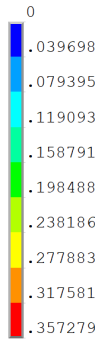
NODAL SOLUTION



Displacement vector sum

(b) $f_{10} = 111.4$ Hz

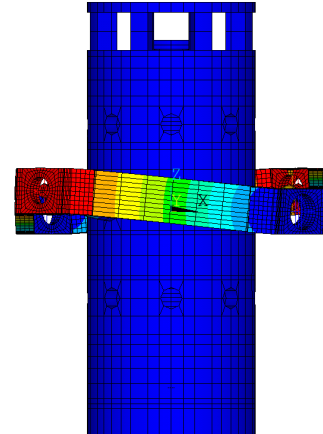
NODAL SOLUTION



Displacement vector sum

(c) $f_{11} = 270.8$ Hz

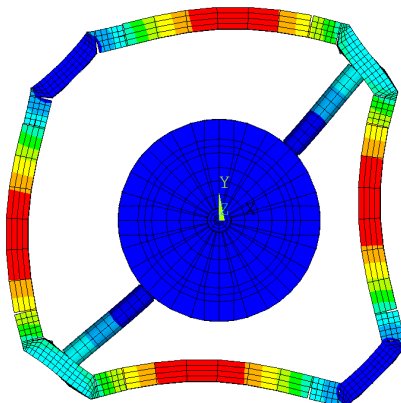
NODAL SOLUTION



Displacement vector sum

(d) $f_{14} = 641.8$ Hz

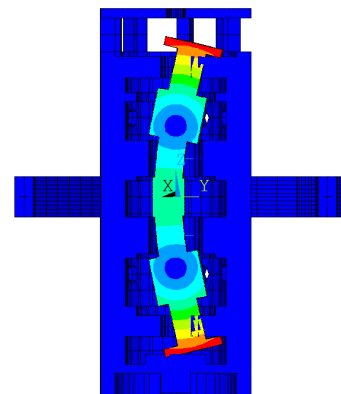
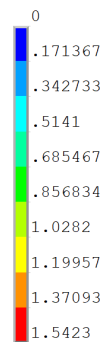
NODAL SOLUTION



Displacement vector sum

(e) $f_{17} = 1095$ Hz

NODAL SOLUTION



Displacement vector sum

(f) $f_{20} = 1347$ Hz

Figure 10: Selected theoretical mode shapes for global model of the FESS

In general, the coupling between the housing and rotor is weak. As an exception mode shape 10 shows coupled vibrations between the housing and rotor. In contrast to this, mode shape 20 serves as a great example of decoupled vibrations. Here the rotor is solely vibrating along with a natural frequency and mode shape corresponding to the first natural frequency and mode shape of the rotor itself in free condition as shown on figure 9a. "Isolated" mode shapes are not only observed for the rotor only but also the gimbal. This is seen in the 14th and 17th mode shape where only the gimbal is vibrating. These two modes look similar to the third and fifth mode shape for the gimbal model shown in figure 7. However, the frequencies are a lot higher which indicates that the vibrations are still affected by the coupling to the other parts and the implementation of the BC. Further details on the results and illustrations of all the mode shapes can be found in [6]. Finally it should be mentioned that in order to verify the mode shapes and natural frequencies obtained by the FE models a experimental modal analysis should be carried out.

4 Conclusion and Future Aspects

Theoretical natural frequencies and mode shapes have been obtained for the gimbal, housing, and rotor individually. Six natural frequencies have been identified in the range of 0 to 800 Hz for the gimbal with the first natural frequency occurring at 193.4 Hz. Furthermore, a maximum discrepancy of 1.14% between the theoretical and experimental natural frequencies were obtained, which indicates that the FE model of the gimbal represents the physical structure well.

A FE model of the housing has been developed and six theoretical natural frequencies have been identified in the range of 0-4580 Hz with the first natural frequency occurring at 2882 Hz. However, the flexibility effects of the housing do not appear to be relevant in the interval from 0 to 2000 Hz in the global model due to the high natural frequencies for the housing. The FE model of the rotor indicates the first natural frequency to occur at 1347 Hz, which yields a discrepancy of 8.81% compared to the experimental obtained first natural frequency. However, further adjustments of the rotor were not carried out due to lack of experimental data.

The theoretical results for the global FE model of the FESS indicate that the flexibility effects have an influence on the dynamics of the FESS, since some of the components are not behaving as rigid bodies in the mode shapes. Furthermore, coupled vibrations also occur between the flexible bodies for which the AMBs must be properly designed taken these into account.

A FE model of the FESS has been designed, however, the FE model should be validated according to experimental results. Therefore experimental modal analyses (EMAs) should be carried out to determine the natural frequencies and mode shapes experimentally. It is suggested that an EMA is carried out for the gimbal, housing, and rotor separately so the components in the FESS can be validated individually and an EMA of the FESS for validating the global model of the FESS.

Furthermore, aspects such as reducing the model in terms of number of DOF could be of relevance in order to simplify the model. Finally, gyroscopic forces could be introduced by simulating the FESS under operational conditions, that is, by giving the flywheel/rotor an angular velocity. This will affect the natural frequencies and mode shapes obtained for the system. The FE model of the FESS under operational conditions should be validated by experimental results as well. Therefore, a operational modal analysis should be carried out.

REFERENCES

- [1] Andersen, A. [2017]. Design of Gimbal Mounting for Offshore Flywheel Applications – Theory & Experiment. Bachelor Thesis, Department of Mechanical Engineering, Technical University of Denmark, Kgs. Lyngby.
- [2] CES EduPack [Computer software]
- [3] Dagnaes-Hansen, N. and Santos, I.F. [2018]. Magnetically suspended flywheel in gimbal mount – nonlinear modelling and simulation. *Journal of Sound and Vibration*, (432):327–350.
- [4] Dagnaes-Hansen, N. and Santos, I.F. [2018]. Magnetically suspended flywheel in gimbal mount – test bench design and experimental validation. *Journal of Sound and Vibration*. Accepted for submission.
- [5] Dagnaes-Hansen, N. and Santos, I.F. [2019]. Magnetic bearings for non-static flywheel energy storage systems (FESS). In *Proceedings of the 10th International Conference on Rotor Dynamics – IFToMM*, pages 116–131. Springer International Publishing.

- [6] Hansen, F.T. [2018]. Flexibility Effects on the Dynamics of Gimbal Mounted Flywheels – Theory & Experiment. Master Thesis, Department of Mechanical Engineering, Technical University of Denmark, Kgs. Lyngby.
- [7] Energistyrelsen, Energistatistik 2016. Available online: <https://ens.dk/sites/ens.dk/files/Statistik/estat2016.pdf> [Accessed June 21st 2018].
- [8] Maersk Drilling, The drilling industry. Available online: <https://www.maerskdirilling.com/en/about-us/the-drilling-industry> [Accessed June 21st 2018].
- [9] Flynn, M.M. and Zierer, J.J. and Thompson, R.C. [2005]. Performance Testing of a Vehicular Flywheel Energy System. Advanced Hybrid Vehicle Powertrains, SAE Technical Papers 2005.
- [10] Hawkins, L. and Murphy, B. and Zierer, J. and Hayes, R. [2003]. Shock and Vibration Testing of an AMB Supported Energy Storage Flywheel. JSME International Journal Series C, (46):429–435.

Balancing

Balancing high-speed gyroscopic systems at low rotation speeds

Izhak Bucher, Shachar Tresser, Amit Dolev

Dynamics Laboratory, Mechanical Engineering, Technion Israel Institute of Technology, Haifa 3200003, Israel

Abstract

The present paper describes a method to balance flexible high-speed rotating systems using data measured at low rotation speeds. The method required external, non-synchronous excitation that blends the effect of imbalance and any high frequency mode to isolate the projection of imbalance on a specific mode and therefore on the vibration at a specific critical rotation speed. The latter is accomplished using a digital signal processor (DSP) synthesizing an excitation is applied to the system such that it amplifies the desired parts.

The projection of the distributed mass imbalance along a rotating shaft produces the effective modal forces that affect the level of vibration at critical speeds. Unfortunately, one can measure and identify the effect of mass imbalance on at high speeds only by rotating the system at a frequency close to the relevant critical speed.

The paper describes a formulation for gyroscopic system and will discuss the controlled sensitivity to imbalance and the anticipated accuracy for a realistic system. Some simulated and experimental result will be shown and discussed.

Nomenclature

If you use lots of symbols in your paper it might be a good idea to make a table or list and include it here. If not needed just delete this section and define symbols and acronyms the first time they appear.

1 Introduction

High-speed systems pass several critical speeds during their normal operation and therefore several modes of vibration need to be balanced, one mode at a time. The balancing process consists of measuring the effect of mass imbalance on the particular mode being balanced. By placing a set of corrective masses at designated locations such the projection of imbalance on the corresponding mode is zero the effect excitation due to imbalance on this mode is eliminated. Once a certain mode is balanced, speed can be increased to get to the next critical speed and a set of corrective masses is placed such that they do not spoil the balancing of previously balanced modes, while eliminating the imbalance of this mode. The calculation of the corrective masses employs traditionally either influence coefficients or modal balancing techniques.

When it is not possible to rotate the system at sufficiently high-speed during balancing one must resort to a method such as presented here. Although more complex, the proposed method can predict the corrective masses at higher rotation speed related mode while rotating at a constant speed, and these can be balanced simultaneously. To find the effective imbalance on each mode, trial masses need to be placed on the system for every mode being balanced and a set of corrective masses can be computed.

The response of the structure to these forces, comprises a combination of all of the mode shapes, where each mode is excited proportionally to the projection of the distributed imbalance on it [1,2], and by the vicinity of the spin speed to its corresponding natural frequency. The response of the structure is minimized by a mass balancing procedure, where small correction masses are added or removed from the structure. These corrective masses are calculated from measured vibrations [3–6]. High-speed machinery usually operates above one critical speed or more, where the rotor exhibits bending, such rotors are usually balanced by either the “Influence Coefficient Method” or “Modal Balancing” [3–11]. Since all of the aforementioned methods are based on vibration readings, they require the rotor to be rotated close to critical speeds.

When it is impossible to run the system to be balanced at the operating speed during the balancing stage, a different method needs to be introduced. Such a method was previously introduced, whereby a tunable parametric amplifier, which employs a dual frequency excitation and a hardening, Duffing-type nonlinearity, was recently introduced for non-rotating systems [12,13].

The dual frequency parametric excitations consist of a principal parametric resonance term, which results in great amplification of the response, and of a combination resonance term, which yields sensitivity to an external force. The nonlinearity keeps the system from producing excessive vibration levels and leads to oscillations with steady amplitudes. The mentioned amplifier was applied to a rotating system, to selectively detect the projection of the imbalance on different modes, while rotating much slower than their critical speeds [12,13]. In [13], the imbalance was identified both numerically and experimentally with an accuracy higher than 90% in a single balancing iteration, but the formulation and implementation were limited to 2 degrees of freedom, non-gyroscopic system.

The paper includes a brief summary of the proposed balancing method of [19], and of the results which were obtained. Following, in Sections 2-3, gyroscopic effects are added to the model. Finally, in Section 3 simulations are shown to verify the analytic model, and the proposed balancing scheme, which includes both gyroscopic effects and use of only two actuators. The numeric example also demonstrates that rigid rotor balancing is not suitable for flexible rotors.

2 Modelling, mathematical background and suggested procedure

Considering a high-speed rotating system undergoing mass balancing. The system has means to apply external forces via of electromagnetic actuators that deflect a flexible mount through a thin rod. The vibratory response is measured at the actuators and along the shaft. A representative system is depicted in Fig.1.

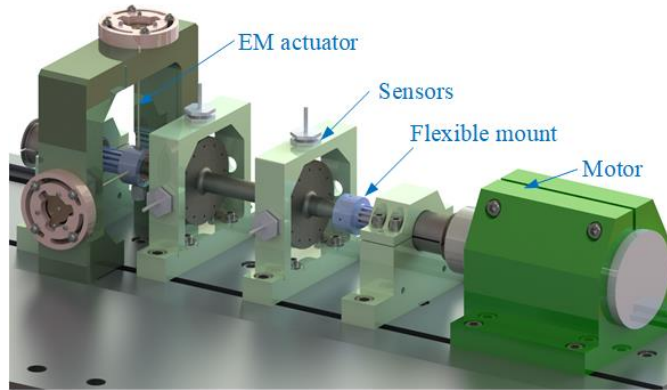


Figure 1: Cad model of a representative fast-rotor undergoing mass balancing using the proposed method.

Unlike traditional mass balancing approaches, the proposed method actively applies forces not synchronous with the rotation speed, based on the specific mode being balanced and, on the data, measured from the vibrations of the structure. The proposed method applies several forces according to

$$f_i = -\left\{\gamma_{a,i} \cos(\omega_a t - \varphi_a) + \gamma_{b,i} \cos(\omega_b t - \varphi_b)\right\} x_i - k_{3,i} x_i^3 . \quad (1)$$

Here, $\gamma_{a,i}$, ω_a , φ_a , $\gamma_{b,i}$, φ_b and $k_{3,i}$ are tunable parameters and x_i is the measured displacement of the rotor at the i th location and where f_i are the applied forces. The frequencies of the parametric excitations are set such that one is the principal parametric resonance, leading to high oscillations, and the other is a combinations type resonance, coupling the response to the imbalance [12-17]

$$\omega_a = 2\omega_n + 2\varepsilon\sigma, \quad \omega_b = \omega_n - \Omega + \varepsilon\sigma . \quad (2)$$

The symbol σ is a detuning parameter, and ε is a small non-dimensional number, $0 < \varepsilon \ll 1$.

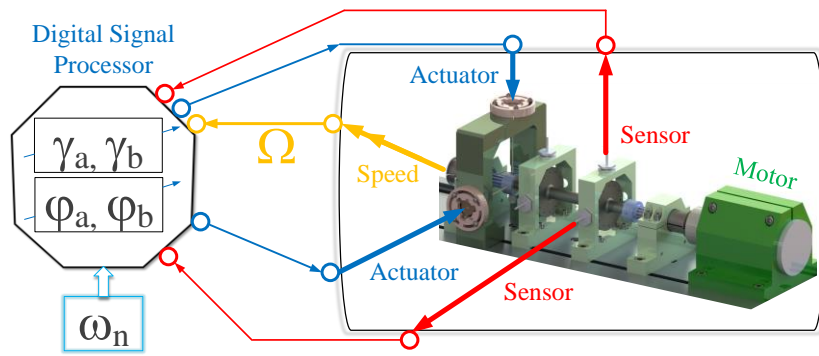


Figure 2: Block-diagram of the overall system showing the flow of signals and their meaning.

As shown in Fig.2, the external forces are generated by a digital signal processor (DSP) that implements the amplification scheme based on the expression in (1) reported in detail in [12-17]. The input to the algorithm is the specific critical speed one wishes to perform mass balancing for, ω_n . The excitation signal that extracts the imbalance for this particular mode of vibration consists of 3 parts, all realized in a form of time-dependent nonlinear feedback, geared to extract the sought information. Within the DSP, several gain and phase parameters are set to obtain the highest sensitivity and find the magnitude and phase of imbalance. The main difficulty in identifying the effect of imbalance on a higher speed related mode is that the signal is weak and is composed of the contribution of several modes. The external forces produce a response that is greatly dominated by the contribution of the imbalance to the target mode of vibration. A multiple time-scale asymptotic analysis helps in producing a concise expression for the measured response. It has been shown (see [12-17]) that the proposed excitation scheme in (1) gives rise to an asymptotic expression for the steady-state vibratory response amplitude, a_{n0} , at the selected mode's frequency - ω_n

$$a_{n0} = \frac{-\Lambda_n \gamma_{b_n} \sin(\psi_{n0} + \varphi_n + \varphi_b)}{\gamma_{a,n} \sin(2\psi_{n0}(t_1) + \varphi_a) - 4\zeta_n}. \quad (3)$$

Here Λ_n represents the projection of distributed mass imbalance on the relevant mode of vibration - ϕ_n , which is the effective imbalance of the selected mode to be balanced (see [15]). And ψ_{n0} is the phase of the response at steady state (see [12-17]), due to the additional excitation and φ_n is the phase with no external forces.

As $\gamma_{a,n}, \gamma_{b_n}, \varphi_a, \varphi_b$ are all tunable within the DSP (see Fig. 2.) the measured response amplitude can be controlled by, say, sweeping the phase, φ_b of one of the external force components. As it turns out, a_{n0} is periodic in φ_b with a period of π . By sweeping, φ_b twice with and without a trial mass, the mass imbalance magnitude and phase can be identified.

The abovementioned result and analysis, ignored the coupling to other modes, assuming they are not excited and the gyroscopic effect was neglected too. The new formulation presented below considers both these effects.

3 MDOF gyroscopic system modelling, analysis of the proposed approach

Assuming small damping and feedback forces, the equations of motion for a constant speed of rotation, written in complex vector form, are:

$$\mathbf{M}\ddot{\mathbf{q}} + (\varepsilon\mathbf{C} + \Omega\mathbf{G})\dot{\mathbf{q}} + \mathbf{K}\mathbf{q} = \Omega^2\mathbf{f}_u e^{i\Omega t} + \varepsilon(\mathbf{f}_{nl} + \mathbf{f}_{pe}) \triangleq \mathbf{f}(t), \quad (4)$$

Here, \mathbf{M} , \mathbf{C} , \mathbf{G} and \mathbf{K} are the mass, damping, gyroscopic and stiffness matrices respectively, $\mathbf{f}_u, \mathbf{f}_{pe}$ and \mathbf{f}_{nl} are the imbalance, parametric excitation and nonlinear force vector respectively, \mathbf{q} is the vector of degrees of freedom, and Ω the rotation speed. The equation of motion (EOM) can be written in the state-space as:

$$\mathbf{A}\dot{\mathbf{r}} + \mathbf{B}\mathbf{r} = \begin{Bmatrix} \mathbf{f}(t) \\ \mathbf{0} \end{Bmatrix}, \quad (5)$$

where

$$\mathbf{A} = \begin{bmatrix} \mathbf{M} & \mathbf{0} \\ \mathbf{0} & \mathbf{K} \end{bmatrix}, \mathbf{B} = \begin{bmatrix} \mathbf{G} + \varepsilon\mathbf{C} & \mathbf{K} \\ -\mathbf{K} & \mathbf{0} \end{bmatrix}, \mathbf{r} = \begin{Bmatrix} \dot{\mathbf{q}} \\ \mathbf{q} \end{Bmatrix}, \mathbf{r} \in \mathbb{R}^{2M \times 1}. \quad (6)$$

As will be shown later on, the solution is based on the multiple-scales expansion, hence the modal analysis is done by neglecting damping. As shown in [2], the system (5) (with damping neglected) admits pairs of equal and

pure imaginary eigenvalues, whose corresponding eigenvectors are linearly independent. The $2N$ eigenvectors, which are expressed by:

As shown in [2], the system (5) (with damping neglected) admits pairs of equal and pure imaginary eigenvalues, whose corresponding eigenvectors are linearly independent. The $2N$ eigenvectors, which are expressed by:

$$\tilde{\phi}_r = \mathbf{w}_r + i\mathbf{z}_r, \quad (7)$$

and are collected in columns of a real matrix $\tilde{\Phi} \in \mathfrak{R}^{2N \times 2N}$, where:

$$\tilde{\Phi} = [\mathbf{w}_1 \quad \mathbf{z}_1 \quad \dots \quad \mathbf{z}_N]. \quad (8)$$

In this paper the tilde sign is used for eigenvectors and modal matrices expressed in the state-space. The response may be expressed as a superposition of all eigenvectors as:

$$\mathbf{r} = \sum_{s=1}^N \xi_s(t) \mathbf{w}_s + \eta_s(t) \mathbf{z}_s = \tilde{\Phi} \chi(t), \quad \chi(t) = \{\xi_1(t) \quad \eta_1(t) \quad \dots \quad \xi_N(t) \quad \eta_N(t)\}^T \quad (9)$$

As shown in [2], the eigenvectors are orthonormalized with respect to the matrix \mathbf{A} , so that

$$\mathbf{I} \dot{\chi}(t) + \omega^* \chi(t) = \tilde{\Phi}^T \left\{ \begin{matrix} \mathbf{f}(t) \\ 0 \end{matrix} \right\} \triangleq \left\{ \begin{matrix} f_1 \\ f_2 \end{matrix} \right\}, \quad \omega^* = \mathbf{diag} \left(\begin{bmatrix} 0 & -\omega_n \\ \omega_n & 0 \end{bmatrix} \right). \quad (10)$$

For undamped systems, the eigenvectors represent whirling motions, and can be written as (assuming that the coordinate system coincides with the principle axes of stiffness) [25]:

$$\mathbf{w}_j + i\mathbf{z}_j = \begin{Bmatrix} \lambda_j \phi_j \\ \phi_j \end{Bmatrix} = \begin{Bmatrix} i\omega_j \phi_j \\ \phi_j \end{Bmatrix}, \quad \phi_j = \begin{Bmatrix} \phi_j^x \\ i\phi_j^y \end{Bmatrix} \in \mathbb{R}^{2N \times 1}. \quad (11)$$

By substituting (11) into (8), the modal matrix is (shown for the corresponding columns of the j^{th} mode)

$$\mathbf{w}_j = \begin{pmatrix} 0 \\ -\omega_j \phi_j^y \\ \phi_j^x \\ 0 \end{pmatrix}, \quad \mathbf{z}_j = \begin{pmatrix} \omega_j \phi_j^x \\ 0 \\ 0 \\ \phi_j^y \end{pmatrix} \quad (12)$$

The projection of any force vector $\mathbf{F}(t)$ on the j^{th} mode is:

$$\mathbf{F}(t) = \begin{Bmatrix} f_1 \\ f_2 \end{Bmatrix} = \begin{bmatrix} 0 & -\omega_j \phi_j^{yT} & \phi_j^{xT} & 0 \\ \omega_j \phi_j^{xT} & 0 & 0 & \phi_j^{yT} \end{bmatrix} \begin{Bmatrix} \mathbf{f}_x \\ \mathbf{f}_y \\ 0 \\ 0 \end{Bmatrix} = \begin{Bmatrix} -\omega_j \phi_j^{yT} \mathbf{f}_y \\ \omega_j \phi_j^{xT} \mathbf{f}_x \end{Bmatrix} \quad (13)$$

At this point, the formulation deviates from the previous results ([2]) as additional terms need to be added. Equation (10) can be written as a 2nd order modal EOM, assuming isotropic supports for sake of brevity

$$\begin{aligned} \ddot{\xi}_j + \omega_j^2 \xi_j &= -\omega_j \phi_j^{yT} \dot{\mathbf{f}}_y + \omega_j^2 \phi_j^{xT} \mathbf{f}_x \\ \ddot{\eta}_j + \omega_j^2 \eta_j &= \omega_j \phi_j^{xT} \dot{\mathbf{f}}_x + \omega_j^2 \phi_j^{yT} \mathbf{f}_y \end{aligned}, \quad (14)$$

and from (10)

$$\xi_j = \frac{-\dot{\eta}_j + f_2}{\omega_j}, \quad \eta_j = \frac{\dot{\xi}_j - f_1}{\omega_j}. \quad (15)$$

Defining the external forces comprising of the parametric excitation, nonlinear forces and imbalance forces

$$\begin{Bmatrix} \mathbf{f}_x \\ \mathbf{f}_y \end{Bmatrix} = \begin{Bmatrix} \mathbf{f}_{\text{pex}} \\ \mathbf{f}_{\text{pey}} \end{Bmatrix} + \begin{Bmatrix} \mathbf{f}_{\text{nlx}} \\ \mathbf{f}_{\text{nly}} \end{Bmatrix} + \begin{Bmatrix} \mathbf{f}_{\text{ux}} \\ \mathbf{f}_{\text{uy}} \end{Bmatrix} = -\varepsilon \left(\mathbf{K}_p(t) \begin{Bmatrix} \mathbf{x} \\ \mathbf{y} \end{Bmatrix} + k_3 \begin{Bmatrix} \mathbf{x}^3 \\ \mathbf{y}^3 \end{Bmatrix} \right) + \Omega^2 \{ \mathbf{f}_u(t) \}. \quad (16)$$

The parametric excitation matrix, $\mathbf{K}_p(t)$ is chosen to decouple (mostly) the n^{th} mode from the rest. Combining (14),(15) and (16) and adding light modal damping with negligible effect on the eigenvectors one obtains two modal equations, one in the x and the other in the y direction

$$\begin{aligned}\ddot{\xi}_n + 2\varepsilon\omega_n\zeta_n\dot{\xi}_n + \omega_n^2\xi_n &= -\omega_n\boldsymbol{\phi}_n^{yT} \left(\dot{\mathbf{f}}_{\text{uy}} + \varepsilon \left(\dot{\mathbf{f}}_{\text{pey}} + \dot{\mathbf{f}}_{\text{nly}} \right) \right) + \omega_n^2\boldsymbol{\phi}_n^{xT} \left(\mathbf{f}_{\text{ux}} + \varepsilon \left(\mathbf{f}_{\text{pex}} + \mathbf{f}_{\text{nlx}} \right) \right) \\ \ddot{\eta}_n + 2\varepsilon\omega_n\zeta_n\dot{\eta}_n + \omega_n^2\eta_n &= \omega_n\boldsymbol{\phi}_n^{xT} \left(\dot{\mathbf{f}}_{\text{ux}} + \varepsilon \left(\dot{\mathbf{f}}_{\text{pex}} + \dot{\mathbf{f}}_{\text{nlx}} \right) \right) + \omega_n^2\boldsymbol{\phi}_n^{yT} \left(\mathbf{f}_{\text{uy}} + \varepsilon \left(\mathbf{f}_{\text{pey}} + \mathbf{f}_{\text{nly}} \right) \right).\end{aligned}\quad (17)$$

At this point one must resort to asymptotic solution methods, and the multiple time-scales approach is utilized here. Using the following, standard, multiple scales expansion [16,21]

$$\xi(t) \approx \xi_0(t_0, t_1) + \varepsilon\xi_1(t_0, t_1), t_i = \varepsilon^i t. \quad (18)$$

The EOM are arranged by orders of magnitude:

$$\begin{aligned}O(\varepsilon^0): \quad (\mathbf{ID}_0^2 + \mathbf{diag}(\omega_n^2))\xi_0 &= \Omega^2\mathbf{f}_m \\ O(\varepsilon^1): \quad (\mathbf{ID}_0^2 + \mathbf{diag}(\omega_n^2))\xi_1 &= -(\mathbf{C}_m D_0 + \mathbf{K}_{p_m}(t_0))\xi_0 - \mathbf{f}_{\text{nlm}} - 2\mathbf{ID}_0 D_1 \eta_0.\end{aligned}\quad (19)$$

Here the subscript m is used for vectors and matrices expressed in the modal coordinates.

At this point it proves useful and convenient to introduce some simplifying assumptions:

- (a) Forward modes are denoted by even numbers, and backward modes by odd numbers;
- (b) The j^{th} forward mode is the excited mode (the mode to be balanced) and is denoted by the subscript $2j$, and the j^{th} backward mode (twined with the excited mode) is denoted by the subscript $2j-1$;
- (c) The system is axisymmetric, and therefore the modes represent circular whirls and are related by [26]

$$\boldsymbol{\phi}_{2n}^y = -\boldsymbol{\phi}_{2n}^x = -\boldsymbol{\phi}_{2n}, \quad \boldsymbol{\phi}_{2n-1}^y = \boldsymbol{\phi}_{2n-1}^x = \boldsymbol{\phi}_{2n-1}; \quad (20)$$

- (d) The spin speed is significantly lower than the critical speed of all modes, so the forward and backward mode shapes of all modes are quite similar (even when the natural frequencies exhibit gyroscopic split):

$$\boldsymbol{\phi}_{2n} \approx \boldsymbol{\phi}_{2n-1}; \quad (21)$$

- (e) No combination resonance nor sub-harmonic resonance exist, so the spin speed and natural frequencies should comply with [15]:

$$\omega_i \neq 3\Omega, 2\omega_k \pm \Omega, \omega_k \pm \omega_j \pm \Omega, 3\omega_k, 2\omega_k \pm \omega_j, 2\Omega \pm \omega_j, \omega_j \pm \omega_k \pm \omega_l. \quad (22)$$

- (f) Modes which are much higher than the excited mode are neglected (i.e. $\omega_i > 10\omega_{2j}$).

Following the routine solution cascade method of solution [15], the steady-state response of the n^{th} mode is:

$$\xi_{0n} = A_n(t_1)e^{i\omega_n t_0} + \frac{\Lambda_n}{2}e^{i(\Omega t_0 - \varphi_n)} + cc, \quad \eta_{0n} = I \left(A_n(t_1)e^{i\omega_n t_0} + (-1)^{(n+1)} \frac{\Lambda_n}{2}e^{i(\Omega t_0 - \varphi_n)} \right) + cc. \quad (23)$$

where $\Lambda_n \propto \boldsymbol{\phi}_n^T \mathbf{f}_u$ is the response to imbalance and cc represents the complex conjugate of previous terms.

The projection of imbalance on the backward and forward modes is similar so:

$$\varphi_{2j-1} \approx \varphi_{2j}, \quad (24)$$

In this case, the steady state amplitude, denoted by a_{2j} , may be simplified to:

$$a_{2j} \approx \frac{\gamma_b R \cos(\psi + \varphi_{2j} + \varphi_b - \theta)}{\gamma_a \cos(2\psi + \varphi_a + \pi/4) - 2\sqrt{2}\zeta_{2j}}. \quad (25)$$

where

$$\begin{aligned}R &= \sqrt{(\Lambda_{2j} + \Lambda_{2j-1})^2 + (\Lambda_{2j} - \Lambda_{2j-1})^2} = \Lambda_{2j} \sqrt{1 + \Gamma^2} \\ \tan(\theta) &= \frac{\Lambda_{2j} + \Lambda_{2j-1}}{\Lambda_{2j} - \Lambda_{2j-1}} = \frac{1 + \Gamma}{1 - \Gamma}, \quad \Gamma = \frac{\Lambda_{2j-1}}{\Lambda_{2j}}.\end{aligned}\quad (26)$$

The ratio Γ depends only on the natural frequencies and the spin speed.

$$\Gamma = \frac{\Lambda_{2j-1}}{\Lambda_{2j}} = \frac{\omega_{2j-1}}{\omega_{2j}} \frac{\omega_{2j} - \Omega}{\omega_{2j-1} + \Omega}, \quad (27)$$

Clearly, (27) indicates that the measured response (25) is dominated by the forward mode.

The response (25) can be measured at a range of frequencies around the design mode's natural frequency, ω_{2j} . It turns out that there is a tradeoff between signal's (response) strength and sensitivity to imbalance. This sensitivity is measured by two expressions

$$S_\Lambda = \frac{\partial a_j}{\partial \Lambda}, S_\varphi = \frac{\partial a_j}{\partial \varphi}. \quad (28)$$

Where S_Λ measured the change in amplitude to the imbalance mass and S_φ the change in measured response due to change in the angular location of the effective imbalance mass.

2 Suggested Balancing Procedure

Once the levels of and frequency of excitation has been set to the optimal values, the value of the parametric excitation's phase φ_b can be swept, until minimal amplitude is reached, denoted by φ_{b0} . The location of the modal imbalance φ_j is found according to the numerator of (25), and has two possible solutions, 180 degrees apart:

$$\varphi_{2j} = \theta - \psi_0 - \varphi_{b0} + n\pi, \quad n = 0, 1 \quad (29)$$

By placing a modal trial mass of Δf_m , the true location and magnitude of the imbalance can be found. The total modal imbalance at the trial run is

$$|\tilde{f}_m| e^{-i\tilde{\varphi}_j} = |f_m| e^{-i\varphi_j} + \Delta f_m e^{-i(\varphi_j + \alpha)}. \quad (30)$$

The phase $\tilde{\varphi}_j$ is found by sweeping φ_b , until a minimal (or maximal) amplitude is reached (again, two possible solutions 180 degrees apart). The maximal change in φ_j is achieved when the modal trial mass is placed 90 degrees apart from φ_j . The true location of φ_j (and $\tilde{\varphi}_j$) are the ones for which the imbalance at the trial run lies between φ_j and α . The magnitude of the modal imbalance is calculated by the following expression, and shown graphically in Fig.3:

$$f_m = \frac{|\Delta f_m| \sin(\pi - \alpha - \Delta\varphi_j)}{\sin(\Delta\varphi_j)}. \quad (31)$$

The imbalance identification is illustrated graphically in Fig.3, as if it is a single plane system. In fact it is related to a multi-plane balancing as it is performed in the modal domain using the modal vector to project its distribution on the real system.

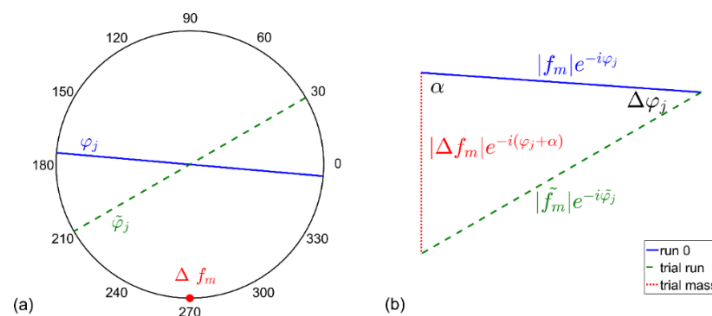


Figure 3: Graphical representation of the trial mass measurement and imbalance calculation

3 Numerical example

The analytical model was verified numerically for the system shown in Fig.4, which comprises of a rotor mounted on bearings having substantial stiffness compared to the shaft, and subjected to the external forces of (1). The numerical example demonstrates the use of the new balancing method, which is also compared to results that would have been obtained if the rotor was balanced by a commercial balancing machine as a rigid body.

The response is measured at four locations along the shaft, as shown in Fig.4. **Error! Reference source not found.** The properties of the rotor are given in Appendix A. The system was modelled by finite elements, using Timoshenko beams and concentrated mass elements. The numerical simulations comprised of numerical integration of (17), without any assumptions or neglects.

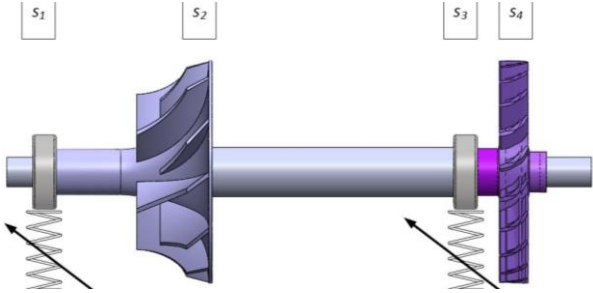


Figure 4: CAD Model of the rotor in the numerical example. The parametric excitation and cubic spring are applied at the bearing, represented by tunable springs. Sensors are placed at the locations indicated by s_1, \dots, s_4 .

The model has a total of 36 DOFs (18 at each plane). The Campbell diagram of the rotor is shown Fig.5, showing the operating speed and the speed at which the balancing procedure is carried out using dashed lines.

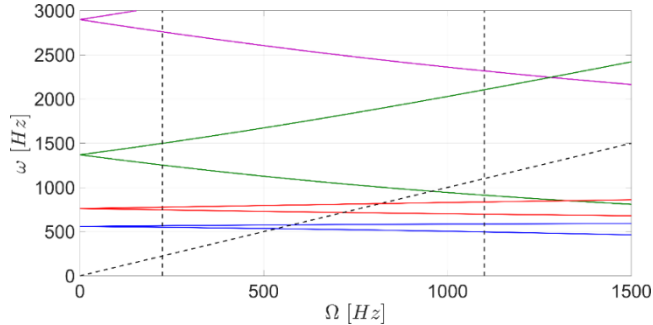


Figure 5: Campbell diagram. Operating speed and balancing speed shown by vertical dashed lines. Line of resonance shown by inclined dashed line

The rotor is to be balanced by using two balancing planes, since the operating speed is above two critical speeds and substantially below the third. Although the rotor requires balancing of the first two modes, there are four dominant modes contributing to the imbalance response at the balancing speed, hence four sensors are required (the natural frequency of the fifth mode is over 5300 Hz). The mode shapes at the balancing speed are shown in **Error! Reference source not found.** (only forward whirling modes are shown). The analytical solution considers a total of eight relevant modes (four backward and four forward).

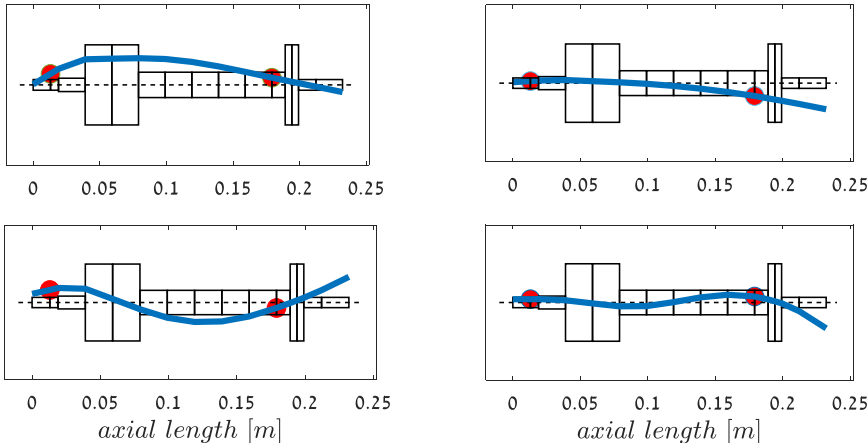


Figure 6: First 4 forward mode shapes at the balancing speed. Bearings locations shown by \bullet . $\omega_2 = 567 [Hz]$ (a), $\omega_4 = 777 [Hz]$ (b), $\omega_6 = 1499 [Hz]$ (c), $\omega_8 = 3048 [Hz]$ (d).

In order to fine-tune the external excitation frequency, the parametric excitation is tuned according to (2) by sweeping the detuning parameter, σ . The response amplitude curves vs the detuning frequency for both modes are shown in Fig.7 (for Run 0). Sweeping through the phase of the excitation φ_b is performed for a detuning value of $\sigma/\omega_{2j} = -0.3$, and so is the calibration process.

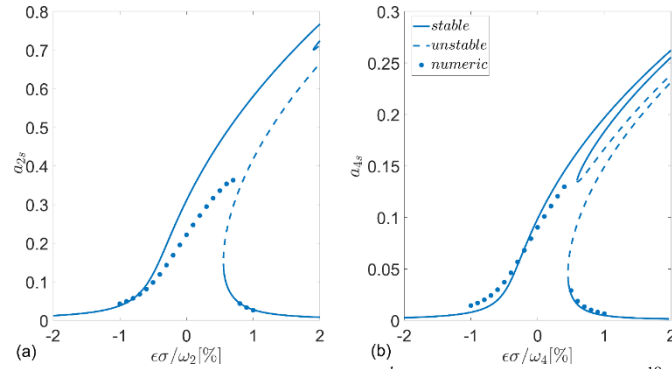


Figure 7: Response amplitude curve for $\zeta_{2j} = 1, \gamma_{2j,2j}^a = \gamma_{2j,2j}^b = 1.02\zeta_{2j}, k_3 = 2 \cdot 10^{18}$ 1st forward mode (a) and 2nd forward mode (b).

It should be mentioned that the optimal detuning frequency is a compromise between high amplitude (good signal to noise) and sensitivity to imbalance. Returning to (28), one can plot the sensitivity of imbalance phase

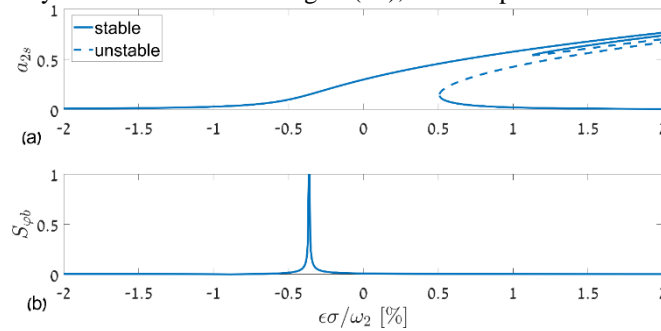


Figure 8: Response curve of the 1st forward whirling mode for the example shown here (a). Sensitivity to the phase φ or angular location of the imbalance.

Figure 8 shows that one should choose a compromise between signal amplitude and sensitivity and indeed, the preferred frequency region where the imbalance identification takes place is close to the maximal sensitivity.

3.1 Balancing simulation results

The results of the process of sweeping through φ_b are shown Fig.9, and summarized in Tables 1,2 **Error! Reference source not found.** It should be emphasized that the numerical simulation includes the whole model with no approximations takes place. Although balancing is carried out at low speed such that the effect of gyroscopics is not fully effective and the modes separation is partial, and there are only 2 excitation locations and 4 sensors, the procedure seems successful.

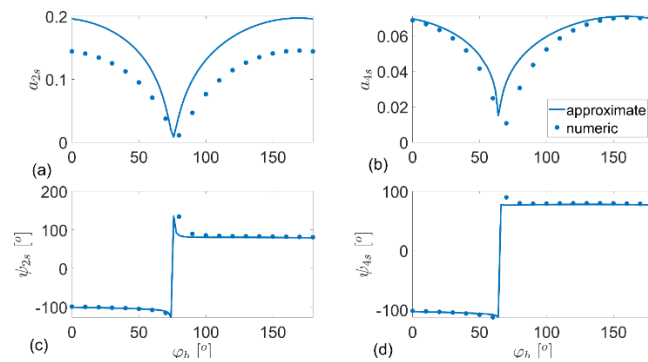


Figure 9: Sweep through φ_b at the first run. Amplitude of the 1st mode (a), Amplitude of the 2nd mode (b), phase of the 1st mode (c) and phase of the 2nd mode (d). The continuous line presents the analytical, asymptotic approximation and the dotted line presents the numerically simulated full model.

Table 1: Results of sweeping through φ_b . All phases in degrees.

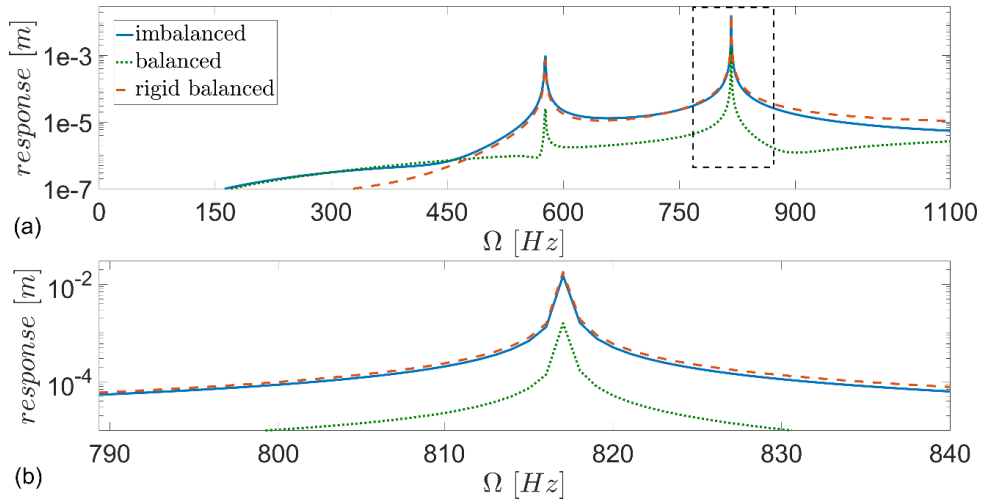
Mode		φ_{b0}	ψ_{γ_j}	φ_{calib}	Evaluated $\varphi_{\gamma_j}^*$	True φ_{γ_j}	Modal Trial mass
1 st fw	Run 0	170	85	-1.9	-163/17	-160	0
	Trial run	12	-95	-1.9	174.9/354.9	178	$4 \cdot 10^{-10} \exp(1.9i)$
2 nd fw	Run 0	170	84	-49	-160/22	-154	0
	Trial run	120	84	-49	-110/70	-103	$4 \cdot 10^{-10} \exp(2i)$

The procedure described in (30),(31) is carried out and the simulated imbalance is identified

Table 2: Projection of imbalance on the modes

Mode	Evaluated imbalance	True imbalance	Relative error
1 st fw	$10.047 \cdot 10^{-10} e^{-i\frac{197\pi}{180}}$	$10.1 \cdot 10^{-10} e^{-i\frac{200\pi}{180}}$	5.3 [%]
2 nd fw	$3.36 \cdot 10^{-10} e^{-i\frac{160\pi}{180}}$	$3.18 \cdot 10^{-10} e^{-i\frac{154\pi}{180}}$	12 [%]

Once the calculated correcting mass are applied, the simulated response to imbalance obtains the following form

**Figure 7:** Imbalance response - displacement at the plane of the rear bearing (a), zoom view at the 2nd critical speed (b).

Balancing the rotor as a rigid body would have improved the response of the rotor at low speeds, where the rotor is truly rigid, but as the spin speed increases, the balancing masses become less effective, and even deteriorate the rotors response. The presented balancing method improves the rotors response throughout the entire speed range, and by more than 90% at the critical speeds.

4 Conclusions

This paper presents a method to balance high frequency flexible modes, without the need to rotate the rotor to high speeds. The method is based on the method presented in previous work [16–19], which includes a dual frequency parametric excitation and a cubic stiffness term. The frequencies of the parametric excitation are selected such as to excite a desired mode, while rotating significantly below its natural frequency, while the nonlinear stiffness keeps the response bounded. The present paper presents solutions to two main weaknesses that arose in [17]: (i) A method that allows the excitation to be orthogonal to undesired modes, even when only actuators can be implemented only in two planes. (ii) Including gyroscopic effects, to cases where the spin speed needs to be increased in order to increase the forces caused by imbalance, hence improving the sensitivity of the balancing procedure.

The analytical model was verified by numerical simulations, where vibration levels were decreased by approximately 90%.

References

- [1] I. Bucher, D.J. Ewins, Modal analysis and testing of rotating structures, *Philos. Trans. R. Soc. London A Math. Phys. Eng. Sci.* 359 (2001) 61–96.
- [2] M. Géradin, D. Rixen, *Mechanical vibrations: theory and application to structural dynamics*, Third, John Wiley & Sons, 2015.
- [3] G. Genta, *Dynamics of rotating systems*, Springer Science & Business Media, 2007.
- [4] T.Y. Ishida, Yukio, *Linear and nonlinear rotordynamics: a modern treatment with applications*, John Wiley & Sons, 2013.
- [5] M.S. Darlow, *Balancing of high-speed machinery*, Springer Science & Business Media, 2012.
- [6] W.C. Foiles, P.E. Allaire, E.J. Gunter, Review: Rotor Balancing, *Shock Vib.* 5 (1998) 325–336. doi:10.1155/1998/648518.
- [7] W.D. Pilkey, J.T. Bailey, Constrained balancing techniques for flexible rotors, *J. Mech. Des.* 101 (1979) 304–308.
- [8] R.M. Little, W.D. Pilkey, A linear programming approach for balancing flexible rotors, *J. Eng. Ind.* 98 (1976) 1030–1035.
- [9] C.D. Untaroiu, P.E. Allaire, W.C. Foiles, Balancing of flexible rotors using convex optimization techniques: optimum Min-Max LMI influence coefficient balancing, *J. Vib. Acoust.* 130 (2008) 21006.
- [10] M.S. Darlow, A.J. Smalley, A.G. Parkinson, Demonstration of a unified approach to the balancing of flexible rotors, *J. Eng. Power.* 103 (1981) 101–107.
- [11] R.E.D. Bishop, A.G. Parkinson, On the use of balancing machines for flexible rotors, *J. Eng. Ind.* 94 (1972) 561–572.
- [12] A. Dolev, I. Bucher, A parametric amplifier for weak, low-frequency forces, in: *11th Int. Conf. Multibody Syst. Nonlinear Dyn. Control*, ASME, Boston, 2015.
- [13] A. Dolev, I. Bucher, Tuneable, non-degenerated, nonlinear, parametrically-excited amplifier, *J. Sound Vib.* 361 (2016) 176–189. doi:10.1016/j.jsv.2015.09.048.
- [14] S. Tresser, I. Bucher, A method for balancing high speed rotors from low rotation speed data using parametric excitation, in: *Vib. Rotating Mach. - Virm 11*, 2016: pp. 769–783.
- [15] S. Tresser, A. Dolev, I. Bucher, Dynamic balancing of super-critical rotating structures using slow-speed data via parametric excitation, *J. Sound Vib.* 415 (2018) 59–77.
- [16] A. Dolev, I. Bucher, Optimizing the dynamical behavior of a dual-frequency parametric amplifier with quadratic and cubic nonlinearities, *Nonlinear Dyn.* (2018) 1–20.
- [17] S. Tresser, A. Dolev, I. Bucher, Balancing High-Speed Rotors at Low Rotation Speeds Using Parametric Excitation, in: *Int. Conf. Rotor Dyn.*, Springer, 2018: pp. 327–339.
- [18] J.T. Sawicki, G. Genta, Modal uncoupling of damped gyroscopic systems, *J. Sound Vib.* 244 (2001) 431–451.
- [19] P.R. Houlston, *Active vibration control of rotating machines*, (2007).
- [20] P.R. Houlston, S.D. Garvey, A.A. Popov, Modal control of vibration in rotating machines and other generally damped systems, *J. Sound Vib.* 302 (2007) 104–116.
- [21] A.H. Nayfeh, D.T. Mook, *Nonlinear Oscillations*, John Wiley & Sons, 2008.
- [22] L. Meirovitch, G. Ryland, Response of slightly damped gyroscopic systems, VIRGINIA POLYTECHNIC INST AND STATE UNIV BLACKSBURG DEPT OF ENGINEERING SCIENCE AND MECHANICS, 1979.
- [23] L. Meirovitch, H. Baruh, Optimal control of damped flexible gyroscopic systems, *J. Guid. Control. Dyn.* 4 (1981) 157–163.
- [24] M.B. Wagner, A. Younan, P. Allaire, R. Cogill, Model reduction methods for rotor dynamic analysis: a survey and review, *Int. J. Rotating Mach.* 2010 (2010).
- [25] W. Wang, J. Kirkhope, New eigensolutions and modal analysis for gyroscopic/rotor systems, Part 2: perturbation analysis for damped systems, *J. Sound Vib.* 175 (1994) 171–183.
- [26] W. Wang, J. Kirkhope, New eigensolutions and modal analysis for gyroscopic/rotor systems, part 1: undamped systems, *J. Sound Vib.* 175 (1994) 159–170.
- [27] L. Meirovitch, H. Oz, Modal-space control of distributed gyroscopic systems, *J. Guid. Control. Dyn.* 3 (1980) 140–150.

2 planes generator balancing with support of lateral analysis

Guillaume Christin¹, **Nicolas Peton**²,

¹MDS Services, GE Measurement and Control, 44300, Nantes, France, guillaume.christin@bhge.com

²MDS Services, GE Measurement and Control, 44300, Nantes, France, nicolas.peton@bhge.com

Abstract

On October 2017 at a power plant, a machine train consisting of a gas turbine (LM6000), a gearbox and a generator rotating at 3000rpm, faced a short circuit issue on the grid and the unit tripped. 10 days later the level of vibration of the generator reached the level of alarm. The 17th of October 2017, a first vibration survey done by a third party recommended to check the alignment of the machine train. All foundation nuts were found well tightened and there was no obvious sign of generator movement. The generator was re-aligned with no success: the level of vibration was still over the alarm level. Then BHGE (Baker Hughes a GE Company) Machinery Diagnostic Services team was invited to investigate the vibration issue. Relative vibration data were collected from the Bently Nevada's Rack 3500 monitor buffered outputs. Each of the generator bearings was monitored by Bently Nevada XY proximity probe pair and shaft was rotating counter clockwise, when viewed from the driver (Gas Turbine) to the driven (Generator).

The analysis of the data concluded that the high level of vibration of the generator was due to an unexpected residual unbalance of a second mode since 1X filtered vectors were opposite of phase from one side to another side of the machine. One could understand to have unbalance evolution over the time for a gas turbine or a compressor (due to dirty gas or blade worn for example). However, it was not expected to have an evolution of the residual unbalance for a generator. Even if the root cause of this unbalance could have not been identified, it was decided to balance the generator. A modal method and 2 balancing planes were used to successfully decrease the level of vibration from 75 μ m pp to 20 μ m pp.

At the same time a lateral analysis of the generator using XLTRC² software was carried out to check that the generator had a vibration behavior as expected by design. In fact, a high 1X response was identified and it led to an unbalance issue. However, an evolution of the generator dynamic stiffness (bearing, shaft or bearing support) could have also increased the 1X vector amplitude. The transient data measured at the generator were compared with the theoretical ones. The damped critical speed map allowed to identify important characteristics of the generator vibration behavior.

An important characteristic, was the fact that the frequency of the "pivotal mode" was increasing with the speed and was following the 1X frequency without crossing the 1X line. This was confirmed with measurement. Several other parameters were confirmed. Finally, an unbalance response was calculated with the software that allowed us to draw the conclusion that measurement and theoretical response were matching well. This comparison between measurement and theoretical behavior allowed us to be confident with the fact that the root cause was a real modification of the unbalance of the generator and/or a slight increase of the bearing clearances. The customer decided to wait for the next overhaul for a complete inspection of the generator and the machine train was re-connected to the grid.

1 Introduction

At a power plant, a machine train consists of a gas turbine (LM6000), a gearbox and a generator rotating at 3000rpm. faced on October 2017 a short circuit issue on the grid and the unit tripped. 10 days later the level of vibration of the generator reached the level of alarm (75µm pp). The 17th October 2017, a first vibration survey done by a third party recommended to check the alignment of the machine train. All foundation nuts were found well tighten and there was no obvious sign of generator movement. The generator was re-aligned with no success, the level of vibration (80µm pp) was still over the alarm level. BHGE Machinery Diagnostic Services team was then invited to investigate vibration issue.

2 Analysis of the vibration data

Relative vibration data were collected from the Bently Nevada's Rack 3500 monitor buffered outputs. Each of the generator bearings were monitored by Bently Nevada XY proximity probe pair and shaft was rotating counter clockwise, when viewed from the driver (Gas Turbine) to the driven (Generator).

The data were collected for two identical runs consisting of a cold start up, a steady state at full speed no load (FSNL), a steady state at full speed full load (FSFL) and a shutdown. From these data, it was observed that the vibration signal was mainly due to synchronous component (1X) and the 1X component was increasing with the speed. The behaviour of the machine was the same during both start up and both shutdowns, which means that the vibration behaviour of the generator was repeatable. It was also observed that the orbit shapes were ellipticals with a forward precession and that the shaft reached a normal position inside the bearing at nominal speed. All these characteristics indicated that the high level of vibration of the generator was most probably due to an unexpected residual unbalance.

However, if the level of synchronous vibration ($\overrightarrow{d_{Synch}}$) increases it can be due to an increase of the residual unbalance ($\overrightarrow{F_{Unbalance}}$) or a diminution of the synchronous dynamic stiffness (see Eq 1).

$$\overrightarrow{d_{Synch}} = \frac{\overrightarrow{F_{Unbalance}}}{\text{Synchronous Dynamic Stiffness}} \quad (1)$$

One could suspect to have an unbalance evolution over the time for a gas turbine or a compressor (due to dirty gas or blade worn for example). However, it was not expected to have an evolution of the residual unbalance for a generator. Even if the root cause of this unbalance could have not been identified, it was decided to balance the generator to reduce the level of synchronous vibration. In parallel, a lateral analysis was carried out (with XLTRC² software) to confirm that the synchronous dynamic stiffness of the machine had not significantly changed. This point was important in order for the customer to be confident to wait the next scheduled overhaul for inspection. The next chapter will describe the balancing activity and the result of the lateral analysis compare to the measurements.

3 Balancing of the generator

As explained previously, it was suspected that the level of 1X vibration at full speed was mainly due to a residual unbalance. To determine if two planes are needed to balance such a machine, the first thing to do is to compare the phase relationship between DE 1X vectors and NDE 1X vectors. Obviously, this comparison needs to be done for probes which are installed at the same angular position. The objective is to understand which lateral rotor mode dominates the dynamic behaviour of the rotor. An alternative is presented in figure 3, the DE 1X forward vector and the NDE 1x forward vectors are compared. As a reminder, a 1X filtered orbit is obtained from the 1X filtered vectors of a pair of orthogonal proximity probes. An orbit will be always circular or elliptical. From mathematics, an ellipse is the sum of a vector rotating in one direction and a vector rotating in the opposite direction. The 1X forward vector, which is rotating with the same direction of rotation of the shaft, can be filtered out. As the unbalance force is forward and synchronous, the vibration response of the unbalance force is the 1X forward vector. Principally, the 1X reverse vectors is mainly due to the anisotropy of the support stiffness. This technic allows us to focus on the 1X forward synchronous response of the unbalance force. From polar plots (figure 3), it appears that the 1X forward vectors from one to another side of the machine are opposite of phase. At nominal speed, the 2nd lateral rotor mode dominates the dynamic behaviour of the rotor and the residual response of the first mode seems to be negligible. In such a case, there are several balancing methods such as influence vector, Static-Couple method and modal methods that could be applied. Since a generator has a quasi-symmetric design the modal method can be applied. The advantage of this method is that one trial run can be saved and consequently limits the unavailable time of the machine for the customer. Moreover, the vibration behaviour of the generator was quasi-similar between FSFL and FSNL so it was decided to balance the unit at FSNL. This method saves also time and cost to balance the unit.

The modal method considers that each mode of the machine is independent, consequently each mode could be balance independently without any effect on the other one. One way to be able to implement such a method is to install two similar weights at the same time on both balancing plane of the machine (DE and NDE). Let's

consider a simple symmetric machine with two discs equally spaced from DE and NDE bearing. The first mode is cylindrical, and the second mode is pivotal. Assuming two similar weights are installed at the same angular location on both balancing plane of the machine (DE & NDE), the first mode (cylindrical) will be unbalance since both weights will act in the same direction. However, the second mode (conical) will not be affected since the weights will act in opposite direction and will cancel each other as it can be visible on figure 1.

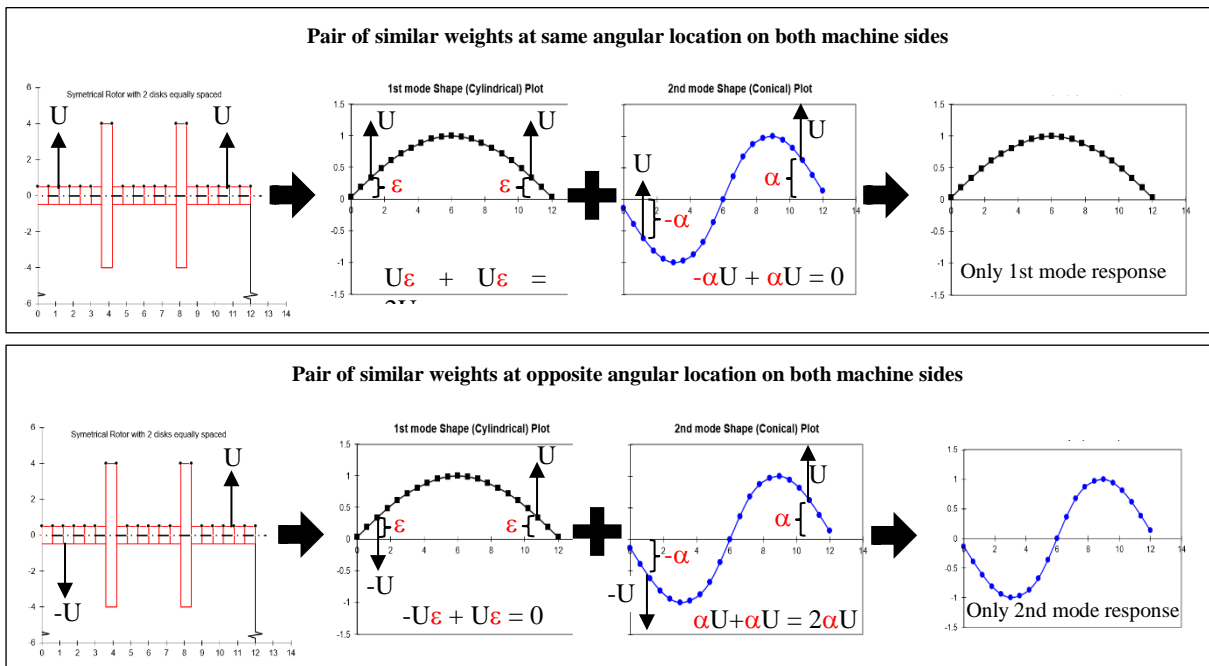
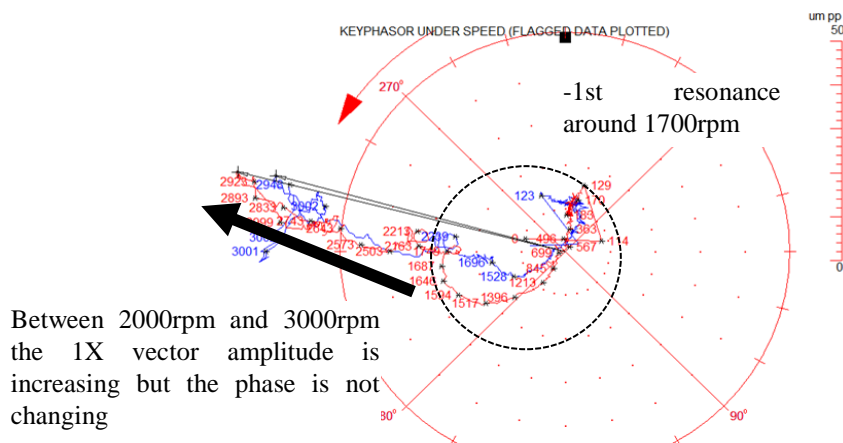


Figure 1: Illustration of modal method (dual weights) applied on symmetric machine.

Selecting a trial weight can be a dangerous task. In many cases, the vibration on the machine is already high, and adding an excessive trial weight at a wrong location could increase the vibration amplitudes. So, a good practice is to at least get a correct trial weight location to be opposite at the actual residual unbalance location and add enough weight to get some response. This selection is not easy unless a reasonable amount of information is known about the machine. Adequate trial weight would be enough weight to produce a 10% change in vibration vector based on the original vibration. For this generator, both balancing planes at DE and NDE planes have a groove just under the blades of the cooling fans. A total trial weight of 400g was used. Before defining the angular location of the trial weights, it is important to remind that the high spot (1X response in displacement) and the heavy spot (unbalance) are in phase when the machine is running well below a resonance. Looking at the polar plot (Figure 3), it can be observed that a first resonance is crossed around 1800rpm. From 2500rpm to 3000rpm the 1X vector amplitude increases but the 1X phase stays almost constant. It means that at 3000rpm the machine operates below the 2nd resonance since there is no phase shift visible that could indicate that the machine operates close or after the resonance.

GEN DE X	∠45° Right	66.4 um pp	2985 rpm
Generator			
GEN DE X	∠45° Right	74.79 um pp	2983 rpm
Generator			



3.1 Trial run with dual mass opposite of phase.

From the previous statement, and because only the second mode had to be balanced, it was decided to install the trial weights opposite to the 1X vectors. One trial weight of 200g was installed at 90° CW from the angular reference (45°R) on the DE balancing plane and another one of 200g was installed at the opposite location (270° CW) on the NDE balancing plane (See figure 4).

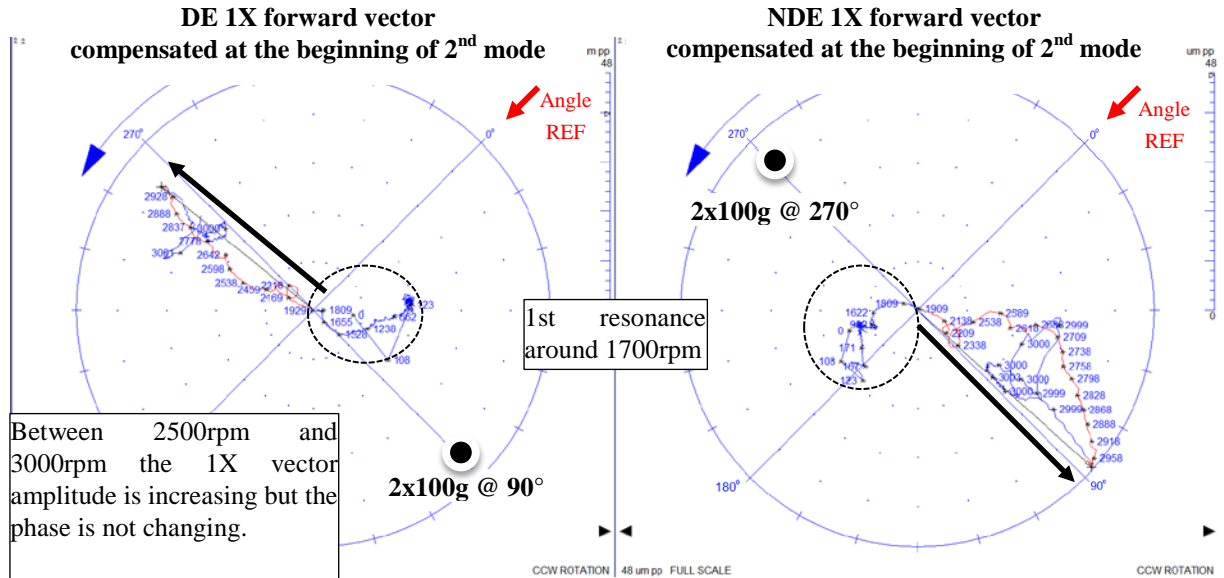


Figure 3: 1X forward polar plot for DE and NDE generator proximity probes (compensated around 2000rpm)

The polar plots (figure 4) show that the weight had an influence on the vibration since the 1X amplitude and the 1X angle changed. Both C vectors, which are the response of the trial weight only, are almost opposite of phase as expected. Consequently, a calculation was done to find the final weights. The principle is to calculate the amplitude and the angular location of the final weights for the C vectors to be opposite and equal to the original 1X vectors. This step is not explained here since this method is well known and it is not the purpose of this paper.

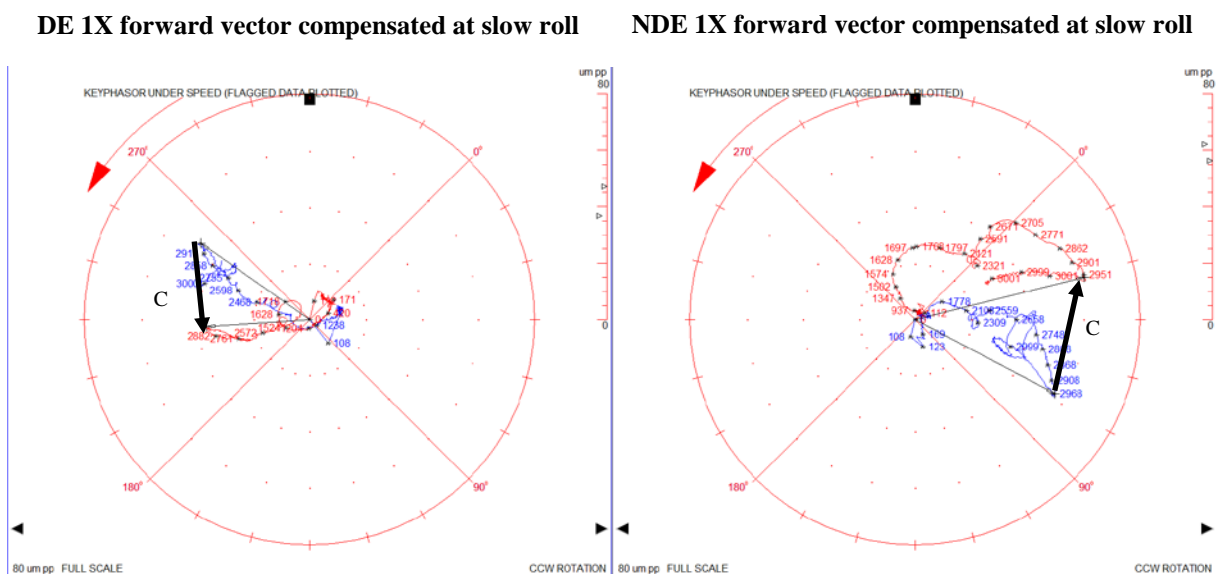


Figure 4: 1X forward polar plot for DE and NDE generator proximity probes. BLUE curve is the reference run and RED curve is the trial run.

One final weight of 300g was installed at 20° CW from the angular reference (45°R) on the DE balancing plane and another one of 300g was installed at the opposite location (200° CW) on the NDE balancing plane

(See figure 5). As it can be seen of the next polar plot, the balancing activity was a success since the 1X vibration level decrease by 95 % for DE side and 70% for NDE side.

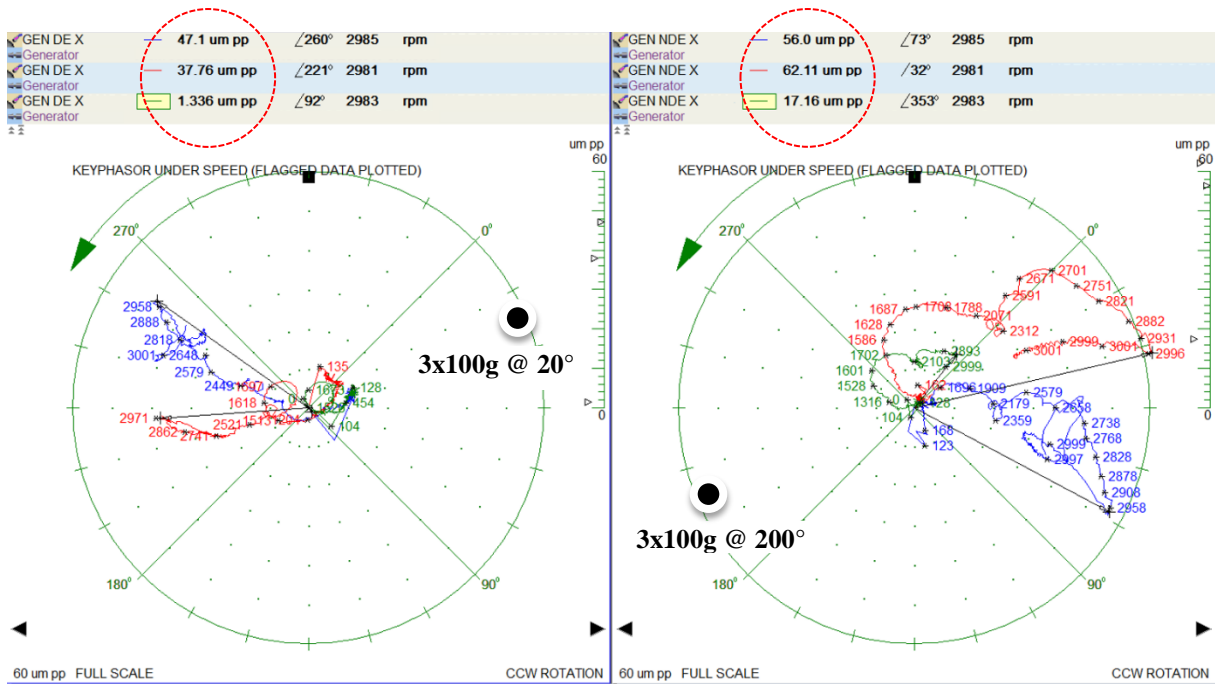


Figure 5: 1X forward polar plot for DE and NDE generator proximity probes. BLUE curve is the reference run; RED curve is the trial run; GREEN run is the final run.

4 Rotor modelling and lateral analysis

The need to do the lateral analysis on site was supported by the fact that the residual unbalance of a generator is not expected to change over time. The 1X vectors augmentation could also be due to a diminution of synchronous dynamic stiffness. Moreover, the synchronous response of the generator for the trial weights was not exactly as expected. As explained in the previous chapter, well below a resonance the high spot and the heavy spot are in phase. According to the data, at 3000rpm the generator is running below the 2nd resonance so the C vectors, which is the response due to only the trial weight, should have been in phase with the trial weight. However, the result shows that the C vectors lags the trial weights by approximately 70°. It means that the machine is close to the 2nd resonance at full speed instead of being well below. Again, from the analysis of the measurement it is impossible to have such conclusion. The lateral analysis will help us to understand this point.

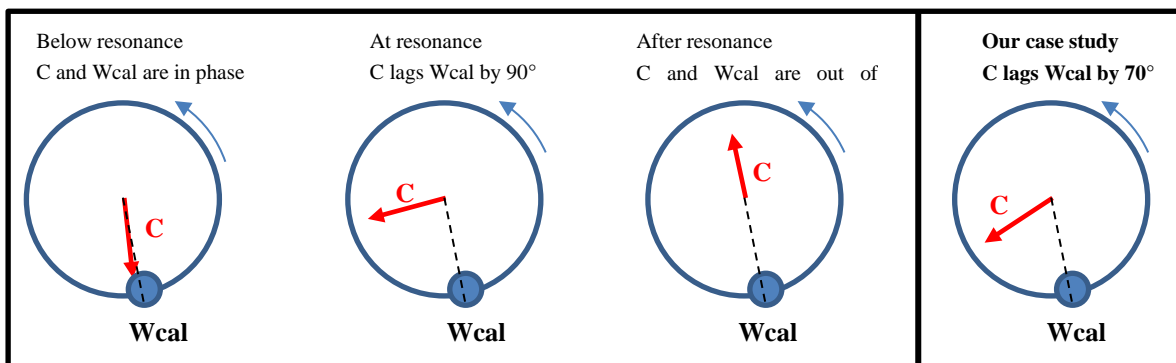


Figure 6: Relationship between C vectors and trial weight in respect to running speed and compared to the resonance.

3.1 Model of the rotor and Undamped Critical Speed Map.

The original lateral analysis of the generator was not available at site in the OEM documentation. However, a drawing with all shaft generator sections, material, local masses, local inertias and bearings information was available.

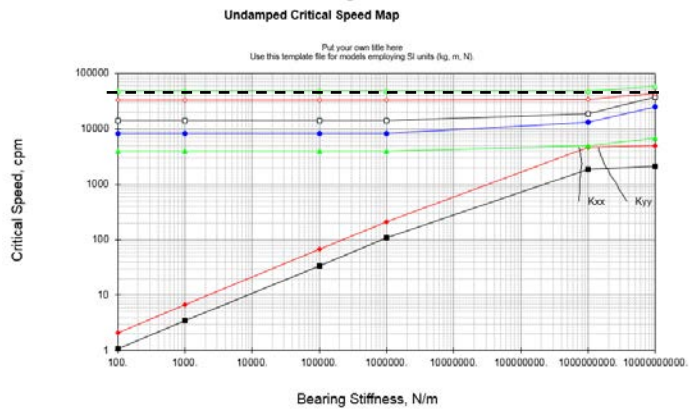


Figure 7: Geometry of the generator rotor as seen in XLTRC², and Undamped Critical Speed Map

The Undamped Critical Speed (UCS) map shows the evolution of the critical speeds versus the bearing stiffness. As it can be seen on Figure 7, both first modes are bearing stiffness dependent. From UCS, it can be concluded that the generator should have two critical speeds around 1850 rpm and 4500 rpm in horizontal direction and two critical speeds around 2000 rpm and 5000 rpm in vertical direction.

3.1 Comparison between Damped Critical Speed Map and measurements.

The type of bearing, the diametral clearances, the bearing length and the type of oil were known. All this information was sufficient to calculate the evolution of the bearing stiffness and damping with the rotor speed. The Damped Critical Speed (DCS) map was then calculated to show the evolution of the natural frequencies versus the rotor speed (Figure 8). Several “key” points are labelled on the figure 8. They correspond to intersections between synchronous lines (1X or 2X) and natural frequencies.

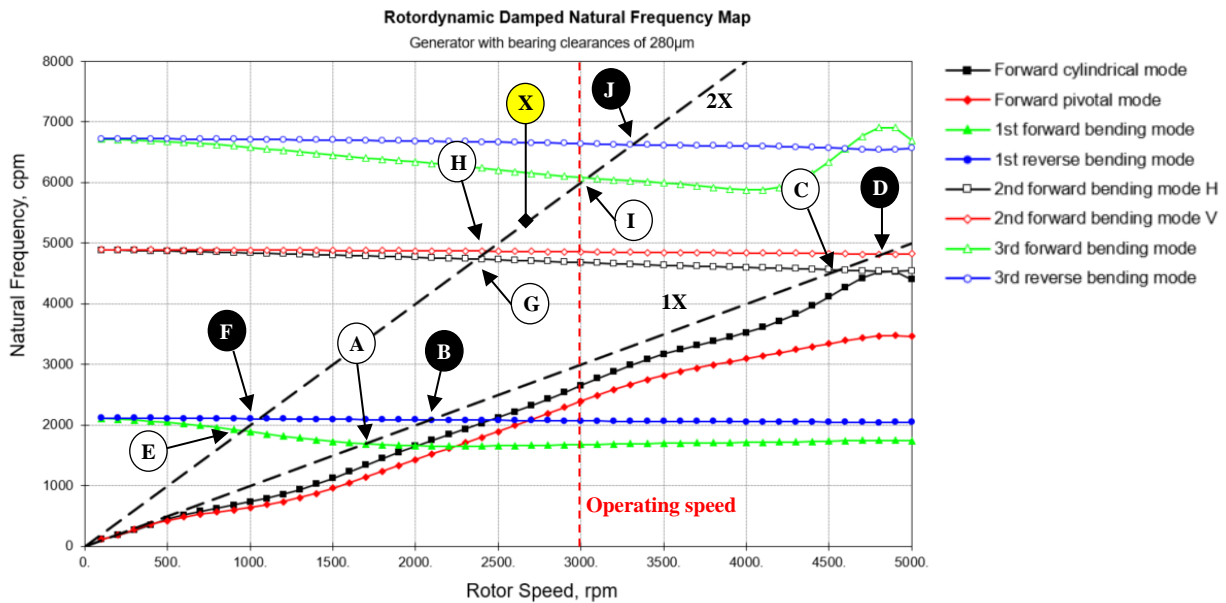


Figure 8: Damped Critical Speed Map of the generator with nominal bearing clearances of 280µ m pp.

The points B, D, F and J corresponds to intersections with reverse modes, which are not interesting for this historical case. The point A shows the intersection between the 1X line and the 1st forward bending mode at a rotor speed close to 1680rpm. This information is coherent with the measurements that indicate also a resonance around 1680rpm with the 1X vectors in phase from one side to another side of the generator (See figure 9). Then, the 1X line crosses the 2nd forward bending mode around 4500rpm (point C). From the measurement, it is impossible to confirm this last characteristic since the maximum operating speed is 3000rpm. To be sure that the model of the rotor is correct, it is necessary to find other similarity between the measurements and the calculation.

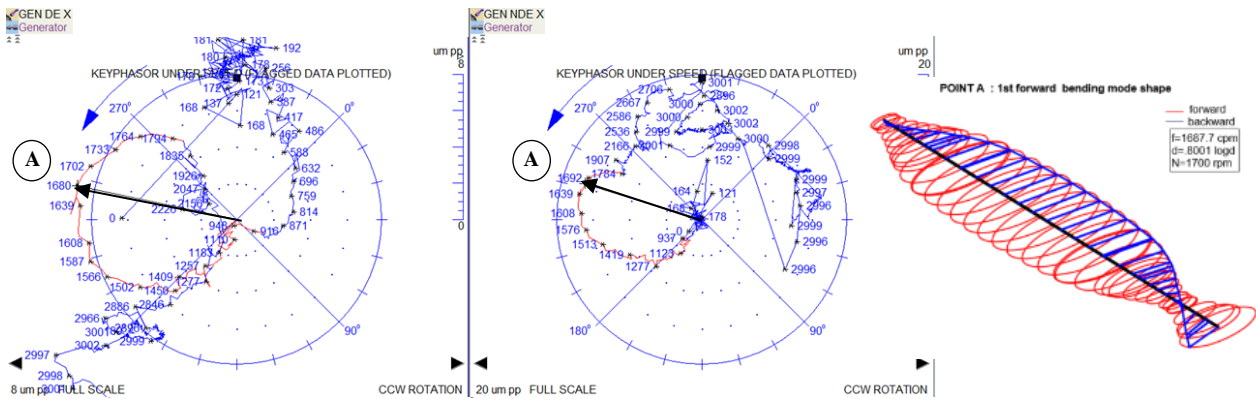


Figure 9: 1X polar plots for DE and NDE proximity probes of the generator during start up after the balancing job. Both loops (red) with a maximum amplitude around 1680rpm are in phase.

The other points that were used to validate the model are located on the 2X line. From theory, it is known that 2X vibration can be present if a preload (constant and unidirectional force) acts on a rotor that has stiffness anisotropy. For this case, both conditions are true since a 2 poles generator has a rotor design with a significant stiffness anisotropy and the gravity is a constant unidirectional force that acts on the rotor. Moreover, this level of 2X vibration is amplified when the rotor speed is close to half a critical speed. Therefore, the point E and G were used for comparison. Point E shows that the 2X line cross the 1st forward bending mode around 950rpm. The 2X polar plots (figure 10) shows a resonance around 900rpm with 2X vectors almost in phase from one side to another side of the machine. Again, the measurement and the calculation are closed.

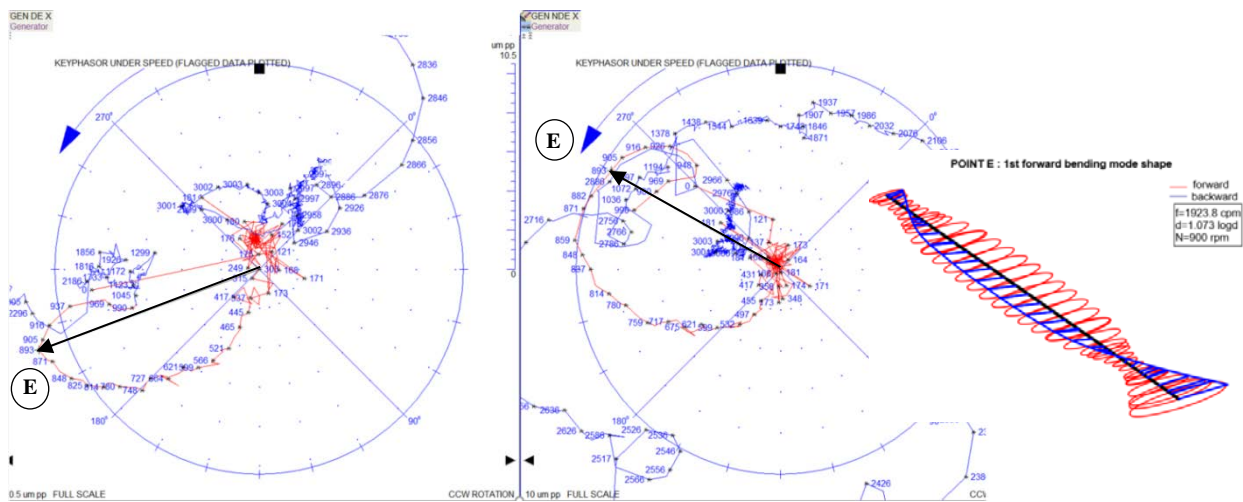


Figure 10: 2X polar plots for DE and NDE proximity probes of the generator during start up after the balancing activity. Both loops (red) with a maximum amplitude around 900 rpm are almost in phase.

Point G and H shows that the 2X line crosses respectively the 2nd forward bending mode in horizontal direction at 2300rpm and in vertical direction at 2400rpm. The 2X polar plot (figure 11) for NDE side shows that there is a typical loop of split resonance between 2300rpm and 2400rpm. However, on DE side there is no loop. Looking at the mode shape (figure 11), it can be noticed that the DE probe is located close to a node whereas the deflection is important at NDE probe location. To conclude Point G and H seem to validate the model rotor as well.

The 2X polar plots (figure 11) do not show a resonance at 3000rpm (point I) but they show a resonance at 2680rpm which was named point X. Looking at the DCS map, it can be observed that there is an intersection

between the 2X line and a resonance at 3000rpm (Point I) instead of 2680rpm (point X). Therefore, measurements and calculation do not match for point I.

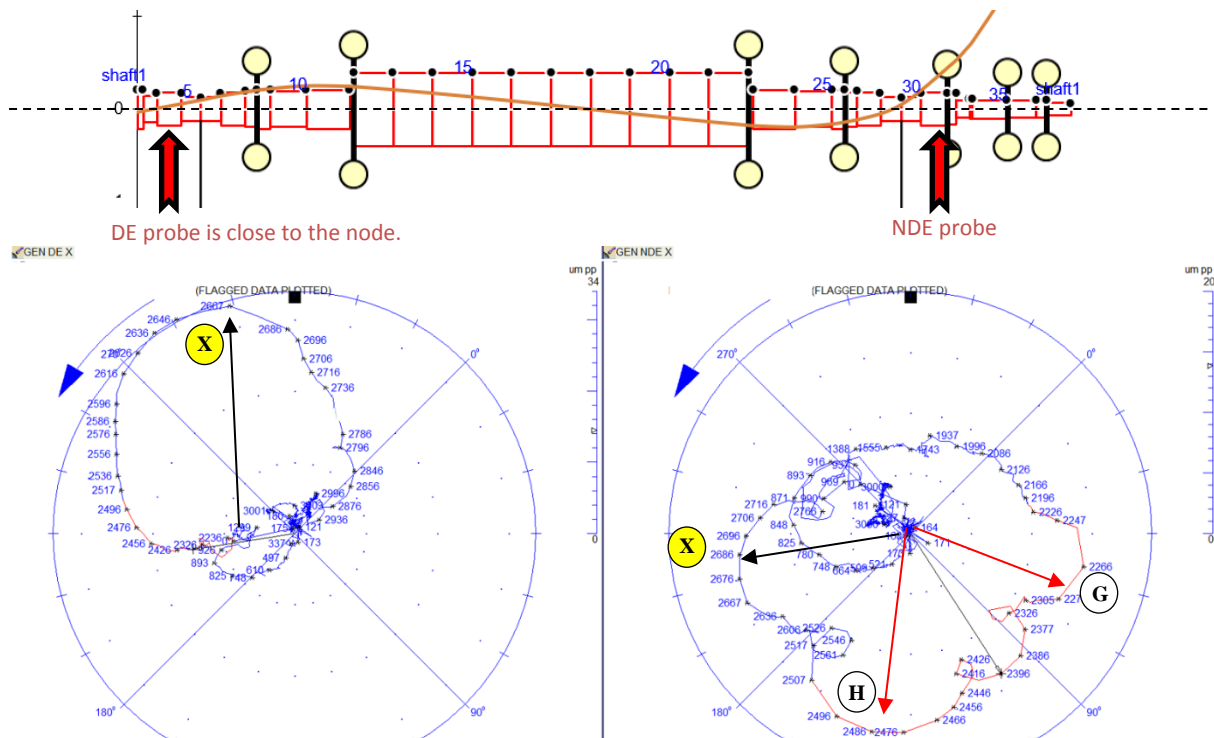


Figure 11: 2X polar plots for DE and NDE proximity probes of the generator during start up. At NDE side a typical split resonance loop is visible between 2300rpm and 2500rpm.

To have a DCS map which matches also with point X and I, it was decided to increase the bearing clearances until the 2X line matches the 3rd forward bending mode close to 2680rpm. The bearing diametrical clearances were increased from 280µm to 325µm. This point will be reminded in the conclusion of this article. It is interesting to note that an increase of the clearances has an impact mainly on the 3rd forward bending mode, the forward cylindrical mode and the forward pivotal mode. The points A, C, D, E, G and H are still at the same position. The point X and I are now identical, and they fit with the measurement as seen on 2X polar plots (figure 11).

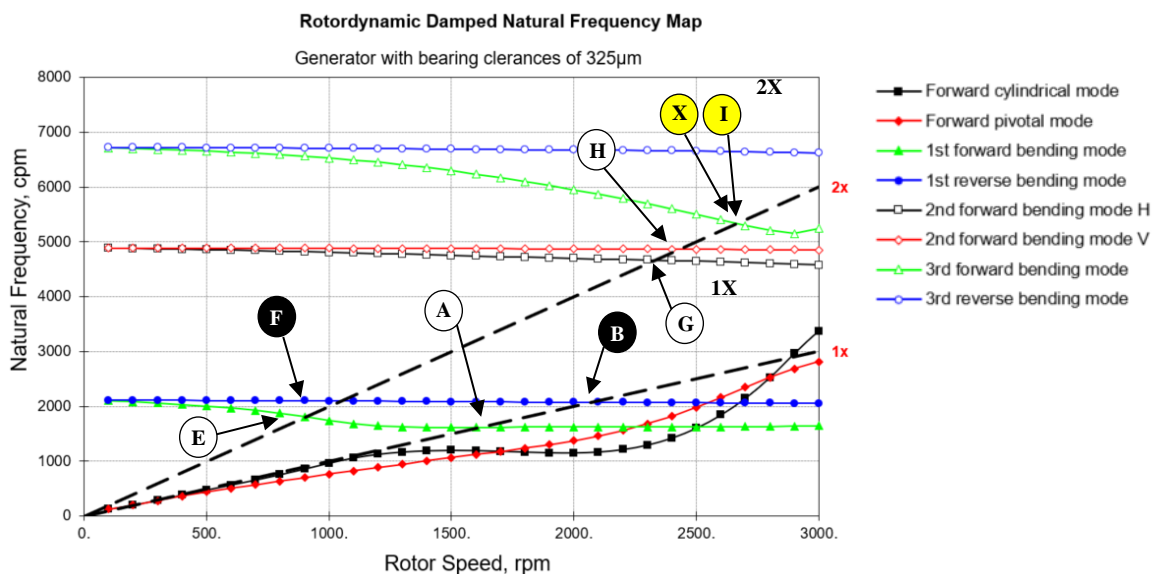


Figure 13: DCS map, Mode shape of forward pivotal mode and Mode shape of cylindrical mode.

To conclude, assuming that the bearing clearances are slightly bigger than expected, the comparison between the resonances determined from the measurements and the resonances calculated by the model are very close for all the points (A, E, G, H and I).

It allows us to be confident with the rotor model and it confirms that the forward bending modes are well estimated.

Hence, the point C (figure 8), which is the intersection between the 1X line and the 2nd forward bending mode at 4500 rpm, can be consider as well calculated in the DCS map. As a reminder, the DCS map was calculated to understand why the data from 1X polar plots indicate that from 2500rpm to 3000rpm the rotor seems to operate well below a “2nd mode”, whereas the result of the balancing activity indicates that at 3000rpm the rotor is close to a “2nd mode” resonance. For sure, the 2nd forward bending mode (point C) is too far from the operating speed to explain the phenomena describes previously. At 3000rpm the machine operates well below the 2nd forward bending mode, so the phase relationship between the unbalance and the heavy spot for this mode should be in phase.

Since DCS map is trustable, it is interesting to look into details at the evolution of the mode named “Forward cylindrical mode” and “Forward pivotal mode”. It can be observed that the natural frequencies of those both modes are always close to the 1X line from zero rpm to operating speed. From the measurement, it seems that the effect of the forward cylindrical mode is negligible on the vibration behaviour. It is most probably due to the facts that the cylindrical mode was well balanced and its damping (log dec ~ 7) is much more significant than the pivotal mode (log dec ~3.5). Let’s focus on the evolution of the forward pivotal mode which is shown on figure 14. The blue line and the red line are respectively the forward pivotal mode assuming 280µm and 325µm. It can be observed that there is always a gap of 600rpm between the 1X line and the natural frequency of the forward pivotal mode (280µm) (figure 12). The result of increasing the clearances up to 325µm, moved the natural frequency of the forward pivotal mode closer to the 1X line. At 2000rpm there is gap of 600rpm and then the gap slightly decreases to reach 200rpm at operating speed. It means that between 2000rpm and 3000 rpm the shaft operates always “close” to the resonance of the forward pivotal mode. In this speed range, it makes sense to have a quasi-constant phase relationship between the heavy spot and the high spot. Furthermore, the phase lag of 70° observed between the heavy spot and the high spot during the balancing activity can be explained since at 3000rpm the machine operates close to the resonance of the forward pivotal mode. The clearances of 325µm would have for effect for the machine to operate closer to the resonance at 3000 rpm than with clearances of 280µm.

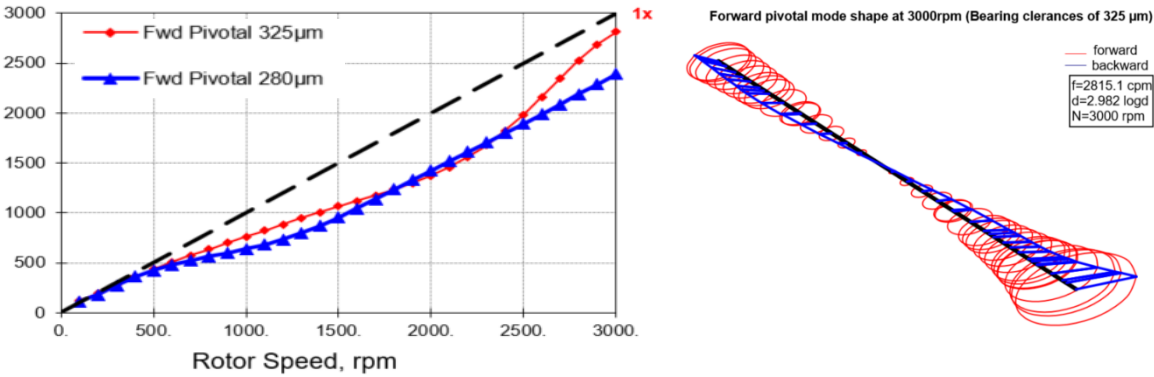


Figure 14: DCS map with evolution of the natural frequency of the forward pivotal mode assuming bearing clearances of 280µm (BLUE curve) and 325µm clearances (RED curve). On right, forward pivotal mode shape for 325µm clearance at 3000rpm

3.1 Comparison between simulated synchronous response and measurement.

Finally, several synchronous forced responses were simulated to check the 1X response at DE and NDE probes locations. Only the synchronous response with one imbalance of 300g installed at the DE balancing plane is presented in this article. It allows to excite cylindrical, pivotal and bending modes. As it can be observed on figure 15 the 1X vectors behaviours are similar between measurement and simulation. From 2500rpm to 3000rpm it is observed that the 1X vectors are opposite of phase, the 1X amplitude increases and the 1X phase is almost constant. These characteristics are seen on measurement and simulation.

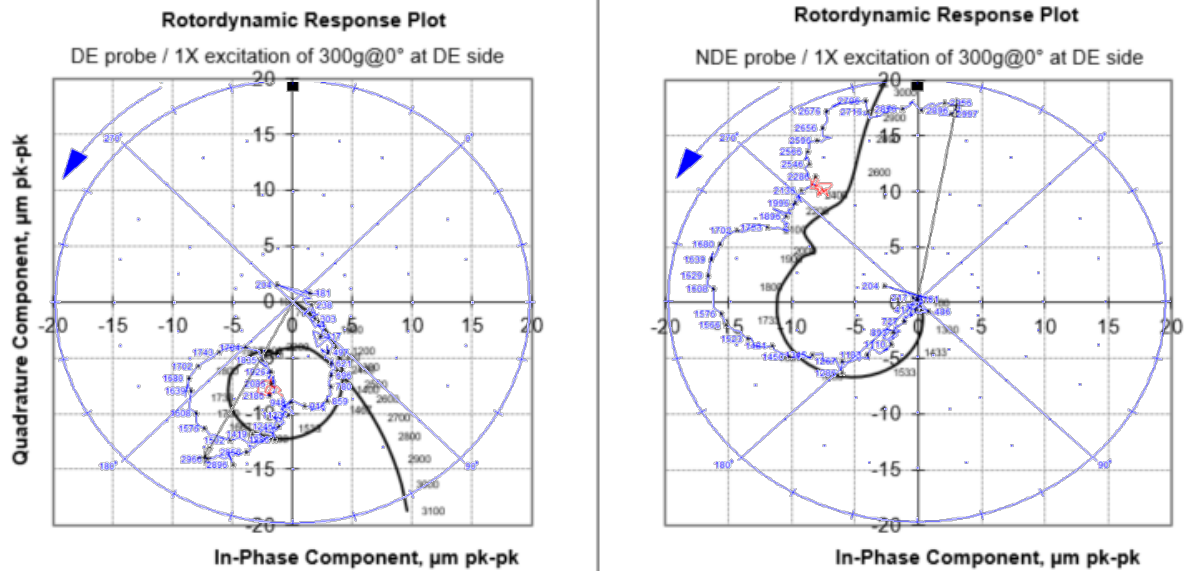


Figure 15: 1X polar plots for DE and NDE probes. The 1X vectors obtained from simulation are the black curves and the 1X vectors from measurements are the Blue curves.

5 Conclusion

It is important to always remember that if the 1X level of vibration increases, it can be due to an increase of the unbalance force or a diminution of the synchronous dynamic stiffness. The analysis of the data didn't show any sign of malfunction, so a modal method was carried out to balance the generator and it was a success to reduce the synchronous level of vibration (1X) by 70% with only 3 runs. However, it was unexpected for a generator to have a change of the residual unbalance. Thus, to continue the diagnostic a lateral analysis was carried out. It helped to confirm that the stiffness of the generator shaft was as expected since the 1st forward bending mode and 2nd forward bending mode crossed the synchronous lines as expected compare to the measurements. Moreover, several natural frequencies were dependant of the bearing clearances (Stiffness and damping dependant). The increase of the bearing clearances had two main effects. The first one was to decrease the 3rd forward bending mode and the second one was to move the forward pivotal mode close to the 1X line. To have a rotor model that matches the measurement it was necessary to increase the bearing clearances from 280µm to 325µm. For a constant residual unbalance, if a natural frequency moves close to an excitation frequency (1X in this case) then the response amplitude would be larger than before. It means that one of the root cause that lead to the increase of the 1X level of vibration could be a worn bearing. For this case, it was concluded that an increase of the bearing clearances by 45µm was acceptable and the customer could continue to safely operate the machine train until the next outage. One year later, the level of vibration was similar than after the balancing activity and no issue were reported. The bearings are supposed to inspected at next maintenance opportunity.

References

- [1] Donald E.Bently with Charles T.Hatch): *Fundamentals of Rotating Machinery Diagnostics*. Edited by Bob Grissom.
- [2] Erik Swanson, Chris D. Powell and Sorin Weissman (May 2005) : *A Practical Review of Rotating Machinery Critical Speeds and Modes*. SOUND AND VIBRATION.

Low Speed Balancing via Parametric Combination Resonance

Ricardo Ugliara Mendes¹, Fadi Dohnal²

¹Laboratory of Rotating Machinery, University of Campinas (UNICAMP), 13083-970, Campinas, Brazil, rumqld@gmail.com

²Division for Mechatronics Lienz, UMIT, Private University for Health Sciences, Medical Informatics and Technology, 9900 Lienz, Austria, fadi.dohnal@umit.at

Abstract

Recently, a low speed modal balancing method in which the rotor needs to rotate up to the first critical speed only was proposed. Once the rotor is at the first critical speed, energy can be transferred to higher modes via parametric excitation at the combination resonance frequencies. This procedure allows obtaining the response of higher modes without the need to accelerate the unbalanced rotor up to higher critical speeds; thus, reducing the time consumed in the balancing procedure and avoiding high levels of vibration when the unbalance is critical. Similar to the traditional balancing procedure, it is important that the rotor measurements present a high signal-to-noise ratio (SNR), so that the modal responses are obtained effectively. The main issue of the proposed method is that the parametric excitation needs to be tuned carefully, in terms of frequency and amplitude, to realize a sufficient transfer of energy to higher modes and to increase the SNR of these modes. In this context, this work analyses the energy transfer sensitivity to the parametric excitation frequency and amplitude. The analyses are performed through numerical simulations of a flexible rotor with three critical speeds in its operational range and sustained by active magnetic bearings.

1 Introduction

Rotating machines are largely used in many industrial sectors due to their broad range of applications, and rotor balancing is a well-established and common procedure. A complete review of the balancing methods can be found in [13], [6] and [11].

Nowadays, most of the methods used are based on the influence coefficient method, which consist of adding test masses in each balancing plane, and measuring the rotor response near to the critical speeds. The measurements taken are used to calculate influence coefficients and to obtain the final correction masses. The inherent disadvantage of the traditional balancing method is the time consumed during run-up/run-down cycles, once the rotor must be stopped and re-accelerated for every test mass added.

An attempt to mitigate this problem was presented in [17], where a model-based approach was used to determine the influence coefficients for a rotor train of a power plant. The drawback of this approach is that many errors are involved due to inaccuracies of the model, mainly due to non-modelled dynamics.

Another possibility to overcome the limitations presented is to apply parametric excitation at very specific frequencies. This triggers high-frequency modes which become visible at low rotor speed, i.e. without the need to accelerate the rotor close to higher critical speeds. Parametric excitation is mathematically described similarly to Eq. 1; where k_p is the nominal value of the parameter and ε is its amplitude variation.

If the parametric excitation frequency $\nu^{kl,n}$ is tuned properly, the effect over the system may have a destabilizing or a stabilizing characteristic. In Eq. 2, the parametric excitation frequency is called a principal parametric resonance for $k=l$, and a parametric combination resonance for $k \neq l$; where ω_k and ω_l are the k -th and l -th damped natural frequencies of the system, and n denotes the parametric resonance order.

$$K_p(t) = k_p \left(1 + \varepsilon \sin(\nu^{kl,n} t) \right) \quad (1)$$

$$\nu^{kl,n} = |\omega_k \mp \omega_l| / n, \quad k, l = 1, 2, \dots \quad (2)$$

The vast majority of the literature was dedicated to the destabilizing effect of parametric excitation (see e.g. [2], [4], [12], [23], [24], and [15]), and Tondl [18] was the first to study the beneficial effect of parametric excitation by using it to suppress self-excited vibrations. The author mathematically formulated the conditions for full vibration suppression in [19]. Later, other authors ([1], [7], and [10]) presented such conditions using an alternative approach. In the works of [8] and [9], active magnetic bearings (AMB) were used to implement the parametric excitation and increment the system damping. Recently, [5] extended this concept to rotors in fluid-film bearings.

A balancing method based on parametric excitation was developed in the works of [3], [20], [21], and [22]. The authors applied a parametric excitation to transfer energy from the first rotational speed harmonic, due to unbalance, to the mode to be balanced, similar to the effect obtained in the parametric combination resonance. Simultaneously, an unstable response of the correspondent mode is induced to amplify its vibration also using a parametric excitation at the principal parametric resonance of the correspondent mode, and a non-linear force is applied to limit the vibration amplitude.

Recently, a simpler approach using parametric excitation was presented in [14]. In the proposed balancing method, the test masses are also used and, instead of accelerating the rotor close to each critical speed of interest, the rotor is accelerated only up to the first critical speed. Once the rotor is close to the first critical speed, there is no need to amplify the mode response or to use a nonlinear term to control any instability or to limit the vibration amplitude. The responses of higher modes are obtained by transferring energy from the first mode to higher modes using parametric excitation at combination resonance frequencies. The parametric excitation is induced in the active magnetic bearings (AMBs), which support the rotor, by a time-periodic PID controller in analogy to [8].

However, the parametric excitation applied in the system should be carefully tuned to maximize the energy transferred to the system. The main parameters to be adjusted are the amplitude ε and the excitation frequency $\nu^{kl,n}$. This work presents a short review of the method developed in [14], and analyzes the influence of both parameters mentioned in the energy transfer. The results present were obtained from numerical simulations of a simple rotor sustained by two active magnetic bearings.

2 Balancing via Parametric Excitation

The similarities between the balancing method proposed by [14] and the traditional influence coefficients method are illustrated by the Campbell Diagram presented in Fig. 1; which corresponds to the rotor simulated in this work, presented in section 4.

As previously mentioned, the traditional balancing procedure consists of placing single test masses at the pre-defined balancing planes. For each mass, the rotor is accelerated as close as possible to each critical speed of the modes to be balanced. That means that, in the traditional balancing, the rotor operates over the 1x line (black dashed line in the Campbell Diagram – Fig. 1) and the measurements are taken at the red dots (critical speeds). The measurements acquired are used to calculate the influence coefficients, which are used to obtain the correction masses. In summary, the rotor must be accelerated up to the last critical speed to be balanced and stopped once per balancing plane, and once with the residual unbalance.

In the proposed balancing method, the rotor is accelerated at the first critical speed only (red dashed line). Once this rotational speed is reached and the response of the first critical speed is measured, parametric excitation at the combination resonance frequencies is used to induce a kinetic energy transfer to the higher modes (blue triangles); to one mode at time. Thus, the higher modes responses can be obtained without the need to accelerate the rotor further than the first critical speed. After the measurements are obtained, the processes of calculating influence coefficients and correction masses are the same used in the traditional balancing method. A limitation of the proposed method, in its present form, is that the relations between the responses of the system obtained via parametric excitation (blue triangles) and by accelerating the rotor up to the correspondent critical speed (red dots) must be known. The implication of such limitation is that the method is only worth if more the one similar rotor must be balanced, than the same relations obtained for the first rotor can be used by the following ones. A detailed description of the method and its limitations are found in [14].

3 Analysis Procedure

The objective of the analysis performed is to evaluate the sensitivity of the kinetic energy transfer between modes when the system is subjected to parametric excitation at the combination resonance frequencies. In the balancing procedure, it is desired that the maximum amount of energy is transferred to the mode under analysis, resulting in a higher signal-to-noise ratio. Similarly, in the case which parametric excitation is used to increase the system damping, it is desired that as much energy as possible is transferred to the heavily damped mode.

In the simulations performed, the system was rotating at the first critical speed (65.93 rad/s) and kinetic energy was transferred to the higher modes (blue triangles at the Campbell Diagram – Fig. 1), at 241.45 rad/s and 429.23 rad/s, by inducing a parametric excitation simultaneously in both directions of both bearings.

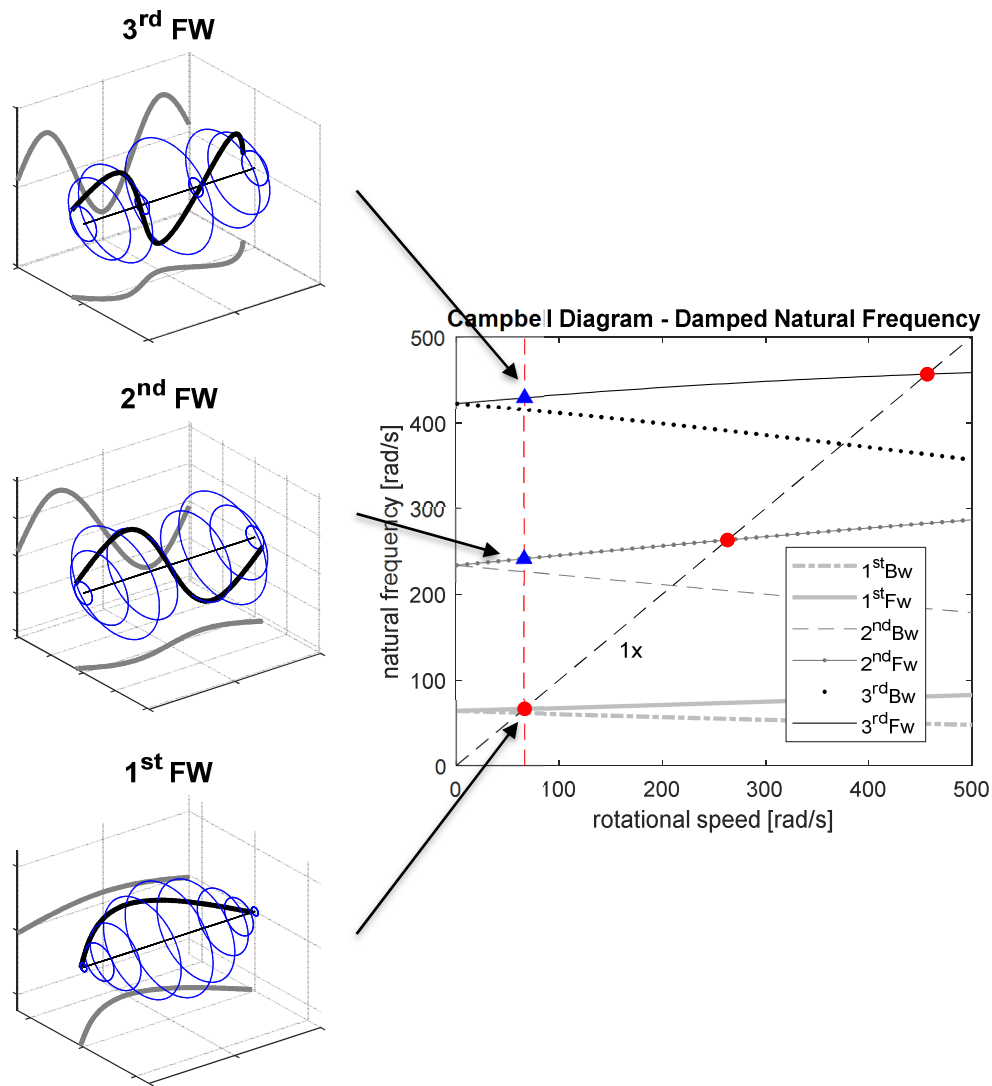


Figure 1: Campbell diagram of the simulated rotor illustrating the similarities between the traditional method and the method proposed by [14].

The procedure to obtain the results presented is summarized in Fig. 2. It starts by initializing the variables of the simulation such as the rotational speed (the first critical speed), the sampling time of the simulation, and the parameters of the parametric excitation. Other parameters that must be set to precisely calculate the DFT of the response signal in the desired frequency are the settling time and the number of periods to be considered; these parameters are used to compute the simulation time.

Next, the simulation is performed and the displacements in the AMBs are obtained. Before calculating the DFT, the transient response is discarded from the results (only steady state response is considered) and Hanning window is applied. Finally, the DFT is calculated at the frequency of interest from the windowed signal.

The results presented correspond to the horizontal displacement at the first active magnetic bearing (node 1). The displacement in the vertical direction and the displacements in the second bearing presented similar results and were omitted.

4 Rotor Model

The simulated rotor, presented in Fig. 1, is composed of a steel shaft of 400 mm length and 3.2 mm diameter. The shaft model is divided into 8 elements (red numbers), resulting in 9 nodes (black numbers); the model considers rotatory inertia, gyroscopic moments, and transverse shear effects [16]. The damping matrix of the rotor is proportional to its stiffness matrix by a factor of $1.5 \cdot 10^{-5}$ s.

Five aluminium discs are distributed along the shaft: two at each end where the active magnetic bearings are placed (nodes 1 and 9), one at the shaft midspan (node 5), and two discs placed at 75 mm from each bearing (nodes

3 and 7). Due to the complex geometry of the discs, each disc is modelled using three disc elements according to Table 1.

The properties considered for aluminium and steel are found in Table 2; and the unbalance distribution considered is presented in Table 3. Nodes 2, 4, 6, and 8 are in the midspan between the discs.

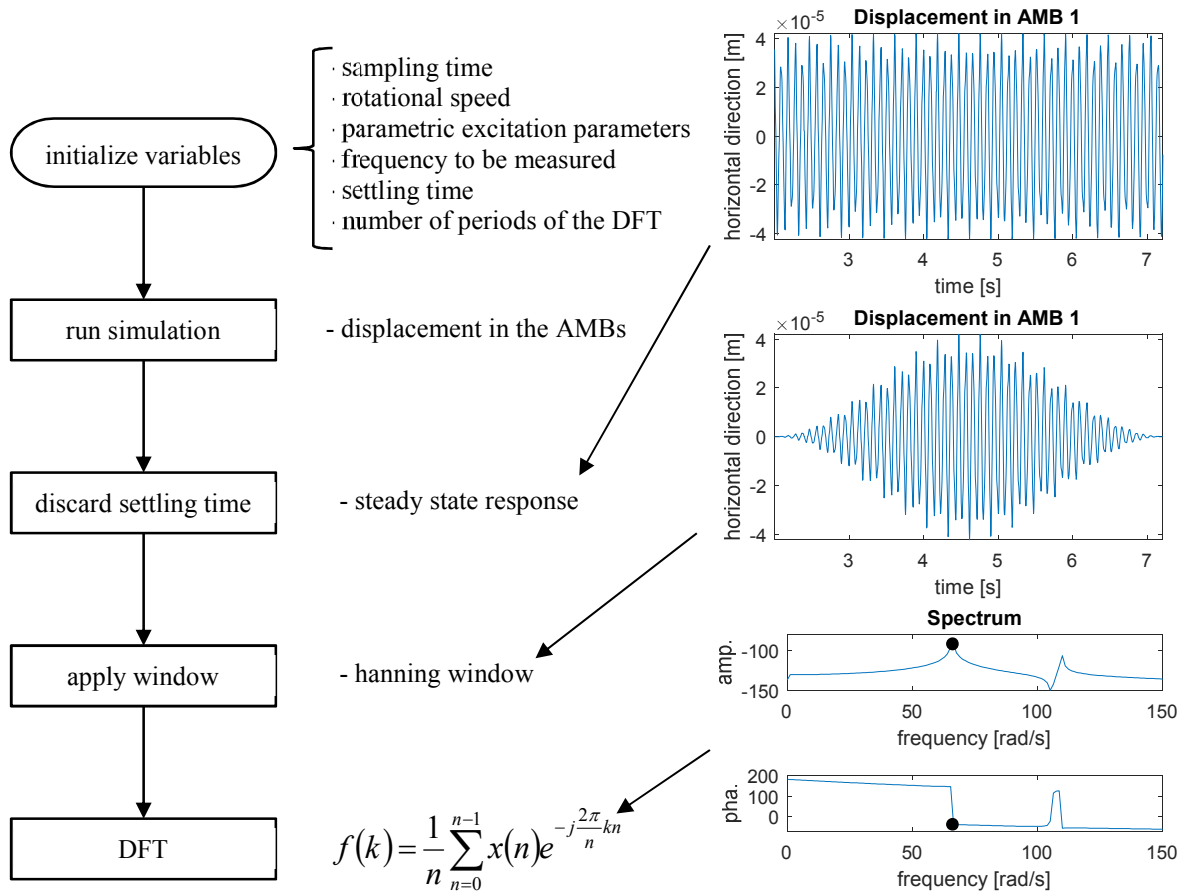


Figure 2: Procedure to obtain the simulated results for the analysis.

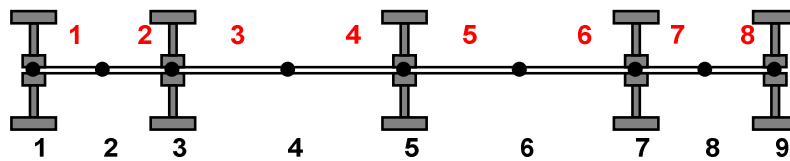


Figure 3: Finite element model of the rotor considered in the analysis.

The bearings have a nominal gap g_0 of 0.5 mm, a constructive constant K_m of $4 \cdot 10^{-6} \text{ N.m}^2/\text{A}^2$ and work with a bias current i_0 of 0.04 A. A linearized magnetic force F_m was considered, as presented in Eq. 3 and [8]; where K_c is the actuator-gain and K_x is the open-loop stiffness. Each axis of the AMBs is governed by a PID controller, according to Eq. 4; where $K_p = 1760$, $K_i = 20000$, $K_d = 36.5$ and $T_f = 0.002$.

Table 1: Dimensions of the rigid disc elements composing each of the five discs of the system.

Property	1st element	2nd element	3rd element
Inner Diameter	3.2 mm	16 mm	50 mm
Outer Diameter	16 mm	50 mm	63 mm
Length	12 mm	4 mm	24 mm

Table 2: Properties of materials.

Material	Elastic Modulus	Poisson's Coefficient	Shear Modulus	Density
Steel	$2.05 \cdot 10^{11}$ N/m ²	0.3	$0.796 \cdot 10^{11}$ N/m ²	7850 kg/m ³
Aluminium	$6.90 \cdot 10^{10}$ N/m ²	-	-	2766 kg/m ³

Table 3: Dimensions of the discs composing the AMB journals and the central mass.

Disc	Node	Mass	Eccentricity	Angular Position
1	1	0.1 g	25 mm	0°
2	3	0.2 g	25 mm	230°
3	5	0.2 g	25 mm	120°
4	7	0.1 g	25 mm	180°
5	9	0.3 g	25 mm	270°

The Campbell Diagram of the closed-loop system is presented in Fig. 1 along with the mode shapes. The rotor operational speed is 600 rad/s. During acceleration, the rotor crosses three critical speeds due to the first three forward bending modes, at 65.93 rad/s, 263.15 rad/s, and 456.48 rad/s, respectively, as marked by the red dots in Fig. 1. The natural frequencies of the second and third modes when the rotor is running at the first critical speed (represented by the blue triangles) are, respectively, 241.45 rad/s and 429.23 rad/s. Unbalance is a forward excitation, thus, only forward critical speeds are considered; moreover, the rigid modes are not considered because their modal damping is higher than 0.97.

$$F_m = K_c i_x + K_x x, \quad \text{where} \quad K_c = \frac{4K_m i_0}{g_0^2}, \quad \text{and} \quad K_x = \frac{4K_m i_0^2}{g_0^3} \quad (3)$$

$$C(s) = K_p + \frac{K_i}{s} + \frac{K_d s}{T_f s + 1} \quad (4)$$

To transfer kinetic energy between modes during the balancing procedure, the parametric excitation is realized by a periodic change in the AMBs stiffness in analogy to [8]. This is implemented by a periodic open-loop control of the proportional constant $K_p(t)$ in Eq. 4, similar to equation Eq. 1. The parametric excitation is applied in both directions of both bearings. The parametric combination frequencies applied are $\nu_a^{12,1} = 175.52$ rad/s (for an energy transfer from the first to the second mode) and $\nu_a^{13,1} = 363.30$ rad/s (for an energy transfer from the first to the third mode).

5 Results and Discussion

The sensitivity analysis performed considered two parameters: the amplitude of the parametric excitation ϵ and the frequency of the parametric excitation ν . The parametric excitation amplitude was evaluated from 0.1 to 0.9. In this analysis, ν is treated as a percentage of the nominal value of the combination resonance frequencies of each mode. It was considered an interval of 80% (0.8) to 120% (1.2) around each parametric resonance frequency ($\nu_a^{12,1} = 175.52$ rad/s for the second mode, and $\nu_a^{13,1} = 363.30$ rad/s for the third mode). It is important to recall that the parametric excitation was applied in both directions of both bearings with the same amplitude, frequency and phase. The results regarding the energy transfer from the first to the second mode are presented in Figs. 4a and 4b, and regarding the energy transfer from the first mode to the third mode are presented in Figs. 4c and 4d.

From the results obtained for both modes (Figs. 4a and 4c), it can be concluded that, for a given parametric excitation frequency, the response amplitude of the mode receiving energy increases linearly with the increase of the amplitude of the parametric excitation. However, the increase rate in amplitude changes as the parametric excitation frequency changes. In the specific case where AMBs are used to induce the parametric excitation, it is important to analyse if the resulting current due to the amplitude used (ϵ) does not lead the bearing to a magnetic saturation; which could drive the system unstable.

The front views of both surfaces are presented in Figs. 4b and 4d. The result of the second mode (Fig. 4b) shows that, when the parametric excitation is applied precisely at the combination resonance frequency ($\nu = \nu_a^{12,1}$), the energy transfer from the first mode to the second mode is a little lower than if a small detuning is applied to

the excitation frequency. If the parametric excitation frequency is set to 90 % of the nominal value ($\nu = 0.9\nu_a^{12,1}$), the amplitude of the second mode increases only by a factor of 1.085, considering a parametric excitation amplitude of $\varepsilon = 0.5$ (red line in Fig. 4a and b). The result obtained for the third mode (Fig. 4d), however, show that the energy transfer is 4 times higher if the parametric excitation frequency is set to 90% of the nominal value ($\nu = 0.9\nu_a^{13,1}$); a parametric excitation amplitude of $\varepsilon = 0.5$ (red line in Fig. 4c and d) was considered. Therefore, the parametric excitation frequency may have an important influence in the energy transfer depending on the mode receiving energy and, thus, needs to be tuned properly for each mode.

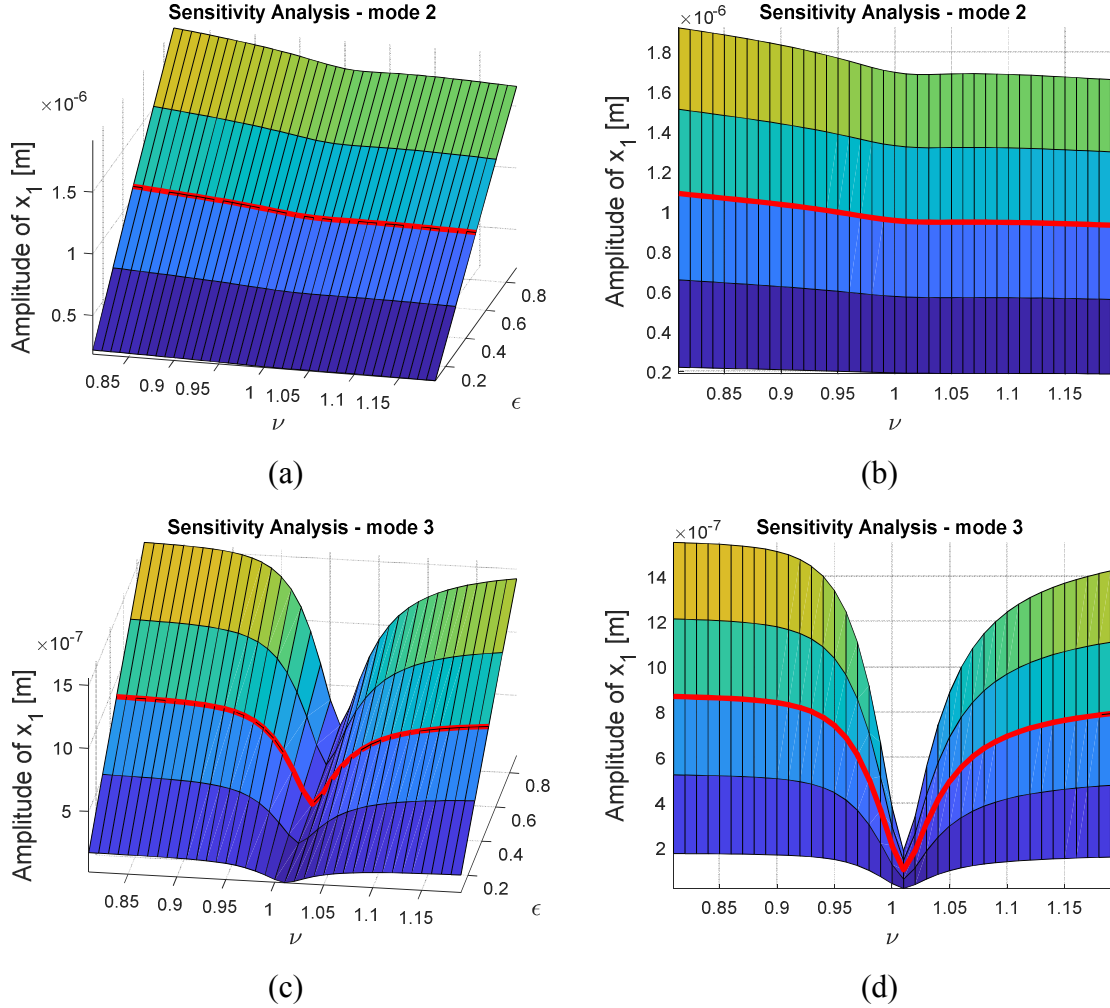


Figure 4: Horizontal displacement at the AMB at node 1 in the presence of parametric excitation as a function of ε and ν : (a) and (b) second mode; (c) and (d) third mode.

Finally, a phase shift in the time-periodicity of the bearings is introduced in order to analyse the influence of the controllability on the induced energy transfer. The speed-dependent mode shapes in Fig. 1 suggest that mode 2 is excited the best if the bearings are moved synchronously with a phase shift of 180 degrees. In terms of parametric excitation this translates to

$$\begin{aligned}
 \text{bearing 1: } K_{p,1}(t) &= k_p \left(1 + \varepsilon \sin(\nu^{kl,n} t) \right), \\
 \text{bearing 2: } K_{p,2}(t) &= k_p \left(1 + \varepsilon \sin(\nu^{kl,n} t) + \pi \right)
 \end{aligned} \tag{5}$$

This change results in the corresponding sensitivity maps shown in Fig. 5. Contrary to Fig. 4, vibration energy is transferred now between mode 1 and 2 instead of mode 1 and mode 3.

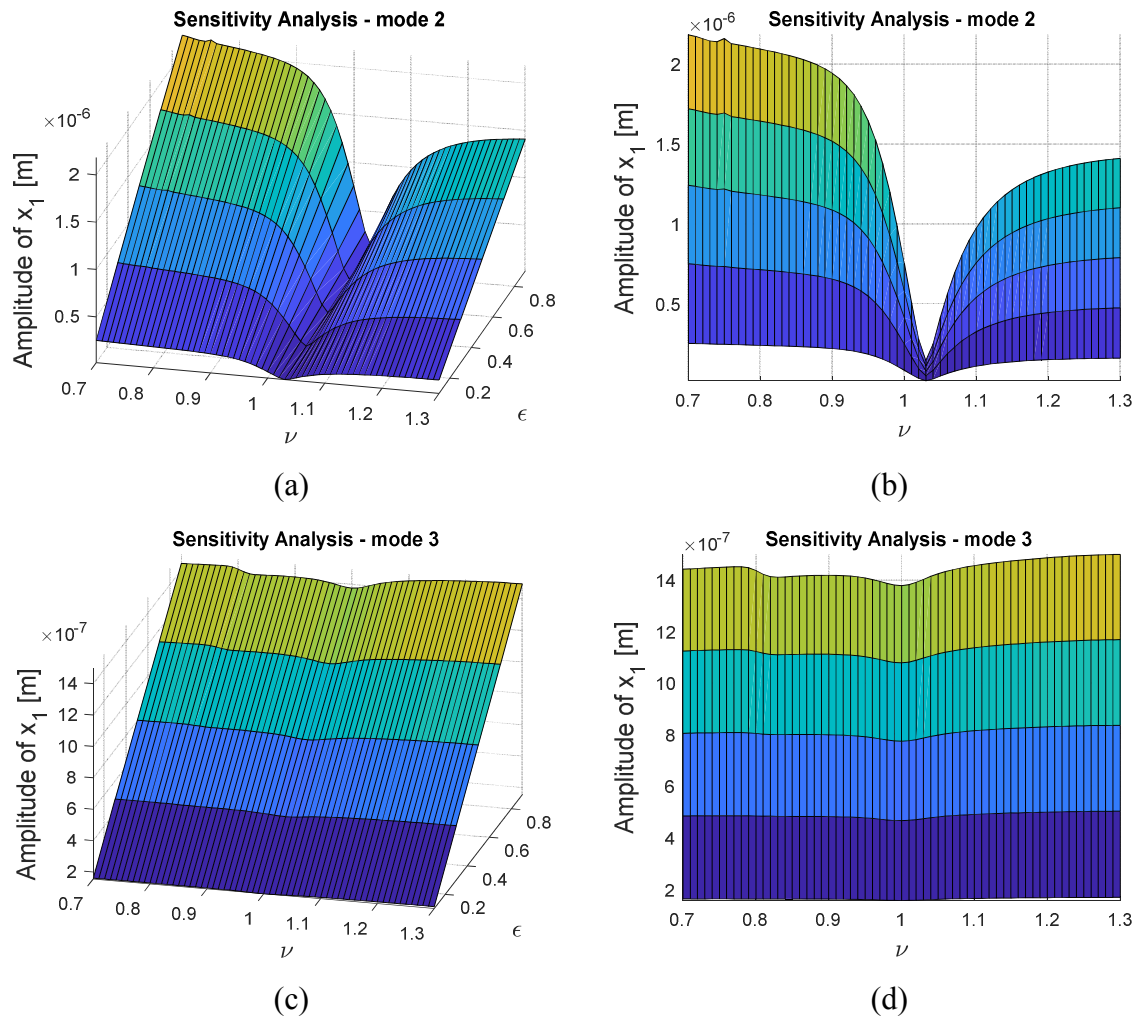


Figure 5: Horizontal displacement at the AMB at node 1 in the presence of parametric excitation with a phase shift of 180° between bearings as a function of ϵ and ν : (a) and (b) second mode; (c) and (d) third mode.

6 Conclusion

The beneficial effect of parametric excitation at different combination resonances is related to the effect similar to a kinetic energy transfer between modes. Whether it is used to increase system damping or for rotor balancing, the parametric excitation must be properly tuned to maximize this energy transfer. Specifically, in the case of rotor balancing, a higher energy transfer ensures a higher signal-to-noise ratio, which directly influence the quality of the measurements used in the balancing procedure.

This work analysed the sensibility of the energy transfer between modes in the presence of parametric excitation in a horizontal rotor sustained by AMBs. The results have shown that the parametric excitation frequency and amplitude should be carefully tuned to maximize the energy transfer between modes. As demonstrated by the simulations, in the case studied, depending on the mode receiving energy a proper frequency tuning resulted in a response 4 times higher. The results also have shown that a higher amplitude for the parametric excitation results in a higher response. However, it is important to recall that the parametric excitation amplitude should be limited to avoid magnetic saturation in the bearings; which could drive the system unstable.

Acknowledgement

The first author would like to thank grants #2015/20363-6 and #2018/05703-3, São Paulo Research Foundation (FAPESP), for the financial support for this research. The second author would like to thank for the financial support within EFRE-LEADER-Project "Campus Technik Lienz".

References

- [1] Abadi, A. (2003): *Nonlinear Dynamics of Self-excitation in Autoparametric Systems*, PhD Thesis, Utrecht University, Utrecht.
- [2] Bolotin V. V. (1964): *Dynamic stability of elastic systems*. Holden-Day, San Francisco.
- [3] Bucher, I., Tresser, S., Dolev, A. (2017): Detecting imbalance of high-speed rotors with dual frequency parametric excitation. In *Proceedings of the International Conference on Computational & Experimental Engineering and Science – ICCES2017*, Funchal, Madeira Island, Portugal, June 26-30.
- [4] Cartmell, M. (1990): *Introduction to linear, parametric and nonlinear vibrations*. Chapman and Hall, London.
- [5] Chasalevris, A., Dohnal, F. (2016): Enhancing stability of industrial turbines using adjustable partial arc bearings. *Journal of Physics: Conference Series*, **744** (012152), pp. 1-13.
- [6] Darlow, M. S. (1989): *Balancing of High-Speed Machinery*. Springer-Verlag, New York.
- [7] Dohnal, F. (2003): *Application of the averaging method on parametrically excited 2dof-systems*. Technical Report, Institute for Machine Dynamics and Measurement, Vienna University of Technology, Austria.
- [8] Dohnal, F. (2012): *A contribution to the mitigation of transient vibrations. Parametric anti-resonance: theory, experiment and interpretation*. Habilitation thesis, Technical University Darmstadt, Germany.
- [9] Dohnal, F., Markert, R. (2011): Enhancement of external damping of a flexible rotor in active magnetic bearings by time-periodic stiffness variation. *J Syst Des Dyn*, **5**, pp. 856–65.
- [10] Fatimah, S., Verhulst, F. (2003): Suppressing flow-induced vibrations by parametric excitation. *Nonlinear Dynamics*, **23**, pp.275–297.
- [11] Foiles, W. C., Allaire, P. E., Gunter, E. J. (1998): Review: Rotor balancing. *Shock and Vibration*, **5**, pp. 325-336.
- [12] Hsu, C. S. (1963): On the parametric excitation of a dynamic system having multiple degrees of freedom. *J Appl Mech Trans ASME*, **30**, pp. 367–70.
- [13] Kellenberger, W. (1987): *Elastisches Wuchten* (in German). Springer-Verlag, Berlin.
- [14] Mendes, R.U., Dohnal, F. (2018): Modal Balancing Using Parametric Combination Resonance. In *Proceedings of the 10th International Conference on Rotor Dynamics – IFToMM Vol. 4*, Rio de Janeiro, Brazil, Sept. 23-27, pp. 129-144.
- [15] Nayfeh, A. H., Mook, D. T. (1995): *Nonlinear oscillations*. John Wiley and Sons, New York.
- [16] Nelson, H. D. (1980): A Finite Rotating Shaft Element Using Timoshenko Beam Theory. *Journal of Mechanical Design*, **102**, pp. 793-803.
- [17] Nordmann, R., Knopf, E., Abrate B. (2018): Numerical Analysis of Influence Coefficients for On-Site Balancing of Flexible Rotors. In *Proceedings of the 10th International Conference on Rotor Dynamics – IFToMM Vol. 4*, Rio de Janeiro, Brazil, Sept. 23-27, pp. 157-172.
- [18] Tondl, A. (1978): *On the Interaction between Self-excited and Parametric Vibrations*. Monographs and Memoranda, Vol. 25, National Research Institute for Machine Design, Prague.
- [19] Tondl, A. (1998): To the problem of quenching self-excited vibrations. *Acta Technica CSAV*, **43**, pp. 109-116.
- [20] Tresser, S., Bucher, I. (2016): A method for balancing high-speed rotors using low rotation speed measured data through parametric excitation. In *Proc. of the IMechE 12th International Conference on Vibrations in Rotating Machinery (VIRM11)*. Manchester, United Kingdom, Sept. 13-15, pp. 769-783.
- [21] Tresser, S., Dolev, A., Bucher, I. (2017): Dynamic balancing of super-critical rotating structures using low-speed data via parametric excitation. *Journal of Sound and Vibration*, **415**, pp. 59-77.
- [22] Tresser, S., Dolev, A., Bucher, I. (2018): Balancing high-speed rotors at low rotation speeds using parametric excitation. In *Proceedings of the 10th International Conference on Rotor Dynamics – IFToMM Vol. 4*, Rio de Janeiro, Brazil, Sept. 23-27, pp. 327-339.
- [23] Yakubovich, V. A., Starzhinskii, V. M. (1975): *Linear differential equations with periodic coefficients*, vol. 1 and 2, Wiley, London.
- [24] Yamamoto, T., Saito, A. (1970): On the vibrations of summed and differential types under parametric excitation. *Memoirs of the Faculty of Engng, Nagoya Univ. Japan*, **22**, pp. 54–123.

Case Studies & Application Tools

Case Study on resolving high vibration on a vertical motor

Sanker Ganesh¹, Mustafa Shalabi²

¹ Machinery Diagnostic Technical Leader, Baker Hughes a GE Company (Bently Nevada), Doha, Qatar, sanker.ganesh@bhge.com

²Lead Machinery Diagnostics Engineer, Baker Hughes a GE Company (Bently Nevada), 31261, Dhahran, Saudi Arabia, Mustafa.shalabi@bhge.com

Abstract

This case is about a single stage vertical pump installed in Acetic Acid area in a petrochemical plant. The unit is vertical HP reactor feed pump (High speed single stage, 230 Kw, 12338 rpm & 3.444 gear ratio) driven by induction motor through a flexible shim pack coupling.

High vibration levels were observed on the motor, pump and structure for more than 2 years with 1X dominant vibration (1X of motor). Assuming that the issue was of complete structural issue even though this motor had been running well in the past, some structural modifications had been carried out at site without any proper engineering calculations. The modifications included welding a total mass of 100 Kg on the structure in addition to the installation of braces to the structure which did not yield any positive results. A systematic structural measurement along with the Operating Deflection Shape carried out at site with the help of experts did not reveal any significant issue with the structure itself except for the structural natural frequency slightly closer to the running frequency of the motor. The timely right decision by the experts to carry out an onsite balancing on the motor which was intended to remove the excitation force yielded good results which exposed additionally a mistake in the balancing activities carried out by a local vendor at work shop.

This case study is designed to outline how the high vibration issue was successfully diagnosed using various tests at site including the operating deflection shape, the root cause for the high vibration and finally how it was mitigated.

Nomenclature

- BHGE - Baker Hughes, a GE company.
- HP - High Pressure.
- Kw - Kilowatt.
- Rpm - Revolutions Per Minute.
- Kg - Kilogram.
- ODS - Operating Deflection Shape.
- Fig – Figure.
- SU/SD - Start Up/Shut Down.
- OB - Outboard.
- IB - Inboard.
- V - Vertical.
- H - Horizontal.
- A - Axial.
- Str - Structure.
- Hz - Hertz.

1 Introduction

BHGE Machinery Diagnostic Services team was requested to perform vibration measurement and evaluation of the HP reactor feed pump installed in Acetic Acid area at one of the customers in the Middle East. The unit is vertical HP reactor feed pump (single stage, 230 Kw, 12338 rpm & 3.444 gear ratio) driven by induction motor (260 Kw, 3585 rpm, ball bearings) through a flexible shim pack coupling. The unit rotates in the counter-clockwise direction when looking from top of the motor. As reported from the customer, high vibration levels were observed on the motor, pump and structure for more than 2 years with 1X dominant vibration (1X of motor). Onsite trials were done to reduce the vibration problem by welding total mass of 100 Kg on the structure in addition to installing additional braces to the structure to change the natural frequency of the system however, vibration levels remained at higher values.

2 Data collection

In order to diagnose the problem, the Bently Nevada™ data acquisition unit was connected to temporary velometers installed on the motor, pump and structure with reference to a temporary laser keyphasor. SCOUT140 portable data collector was used to collect data for ODS & impact test purposes.

The scope of the job is defined by the following objectives:

- Collect and analyze the transient and steady state data.
- Analyze the vibration data and assess the machine condition.
- Collect steady state data on the motor and structure for operating deflection shape ODS.
- Provide recommendations on further action as and if necessary.

Machine train diagram with measurement point locations is presented in Fig. (1).

Figure 1: Machinery Arrangement & Structure Measurement Locations

2.1 Coupled Run (as found)

On 16th January 2017, the unit was started up and reached full speed. The unit remained at full speed for about 4 hours to collect data of ODS points. High vibration levels were observed at full speed on the motor and pump along with the structure especially at the upper surface of the structure, moreover extremely high vibration levels were observed while passing the 2nd critical speed as observed from Fig. (2). The motor transient SU/SD data analysis via polar plot confirmed the high residual unbalance response.

Motor polar plots during transient SU showed exactly 180 degrees phase difference (out of phase) between motor OB and IB bearings while passing the 2nd critical and at full speed as observed from Fig. (2).

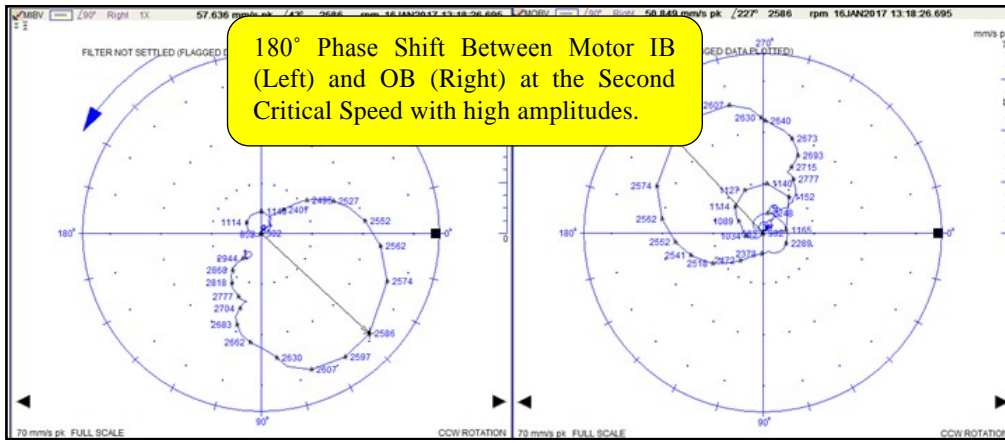


Figure 2: Motor Coupled Run Startup Polar Plot showing high amplitude at second critical speed

3 Data analysis and malfunction investigation

During steady state, the structure was vibrating with high amplitude levels especially at the points nearest to the upper surface of the structure as shown in Fig. (3) (see Fig. (1) for the measurement locations), moreover each side of the structure was vibrating in phase (same phase) and opposite side of the structures were vibrating in out of phase (180 degree phase difference) as shown in Fig. (4) so the structure was vibrating in a circular motion shape (slightly elliptical due to weak stiffness in one side).

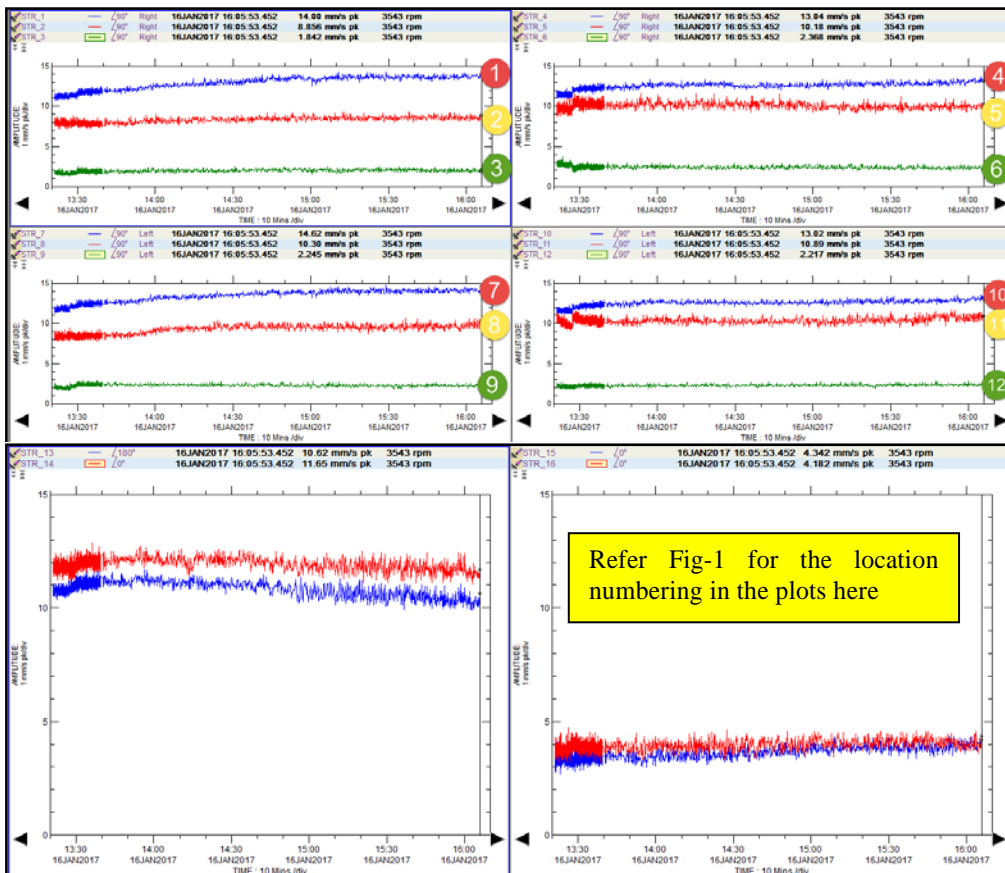


Figure 3: Structure Vibration Trend at Measurement Locations 1 to 16 shown in Fig.(1)

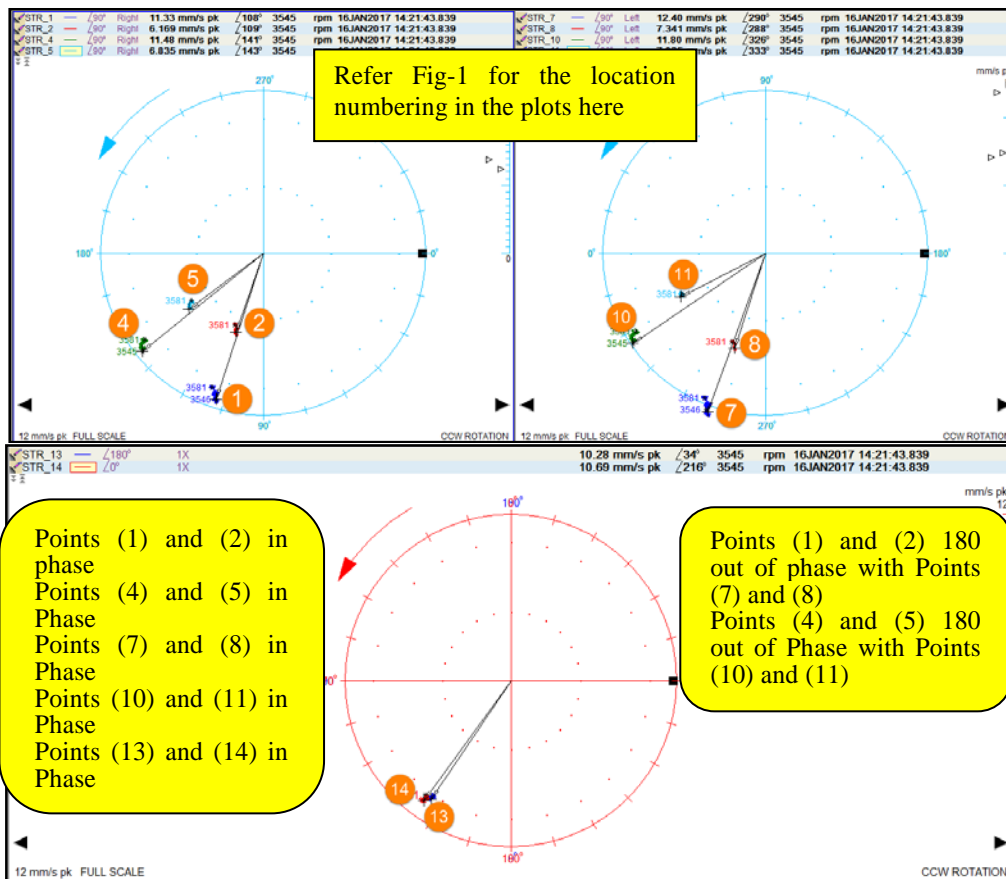


Figure 4: Structure Phase Relationship during Steady State at Measurement Locations 1 to 14 shown in Fig. (1)

3.1 Original Solo Run (as found)

On 17th January 2017, the unit was started up for solo run test and reached full speed. The unit remained at full speed for about 4 hours to collect ODS data. High vibration levels were observed at full speed on the motor and pump along with the structure especially at the upper surface of the structure similar to the coupled run test. Moreover, extremely high vibration levels were observed while passing the 2nd critical speed as shown in Fig. (5), the motor transient SU/SD data analysis via polar plot also confirmed the high residual unbalance response.

Motor polar plots during transient SU showed exactly 180 degrees phase difference (out of phase) between motor OB and IB bearings while passing the 2nd critical and at full speed as shown in Fig. (5).

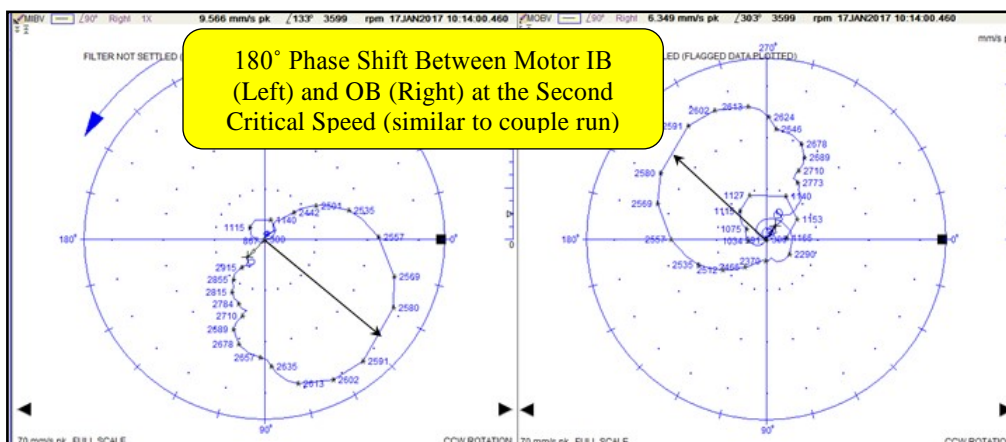


Figure 5: Motor Solo Run Startup Polar Plot

3.2 Solo Run (after adding trial balance weight on the hub)

On 17th January 2017, Polar plot from IB- V was used for balancing calculations and a calibration balance weight of 178 grams was installed at 247 degrees on the motor hub (2 bolts were added to the hub) resulted significant decrease in vibration levels subsiding well below acceptable levels as seen in Fig. (6) and Fig. (7).

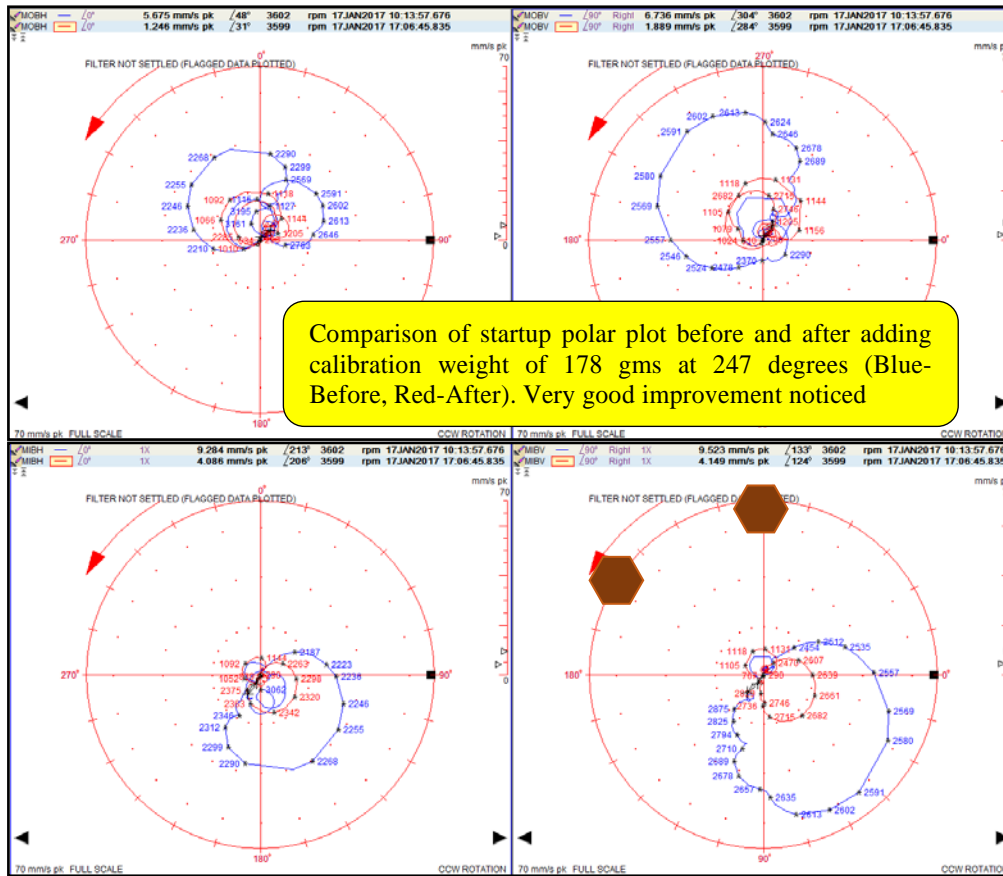


Figure 6: Motor Radial Sensors Startup Polar Plot (Blue-as found condition, Red-after calibration weights Addition)

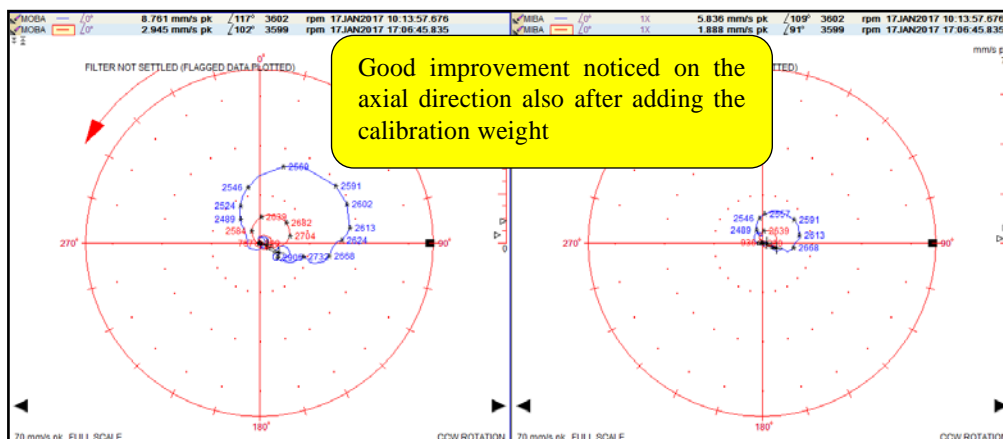


Figure 7: Motor Axial Sensors Startup Polar Plot Comparison (Blue-as found condition, Red-After Balancing Weights Addition)

3.3 Solo Run (after removing existing wrong balance weights on the cooling fan)

On 18th January 2017, it was decided to install the final balance weight on the motor cooling fan since the requirement for final correction weight was little bit more than the calibration run and there was no more

place to add weights in the coupling. Hence motor cooling fan was inspected, after opening the cooling fan cover, it was discovered that there were already some balancing weights which were found exactly opposite to the required location (three fans had one bolt each) with almost the same amount as per the calculation. This observation confirmed that those balance weights were the source of unbalance response. So, the balancing weights originally added at the motor cooling fan was removed. Then, the unit was started up and reached full speed. Normal and acceptable casing vibration levels were observed on all locations of the machine train component (motor, pump & structure) as seen in Fig. (8).

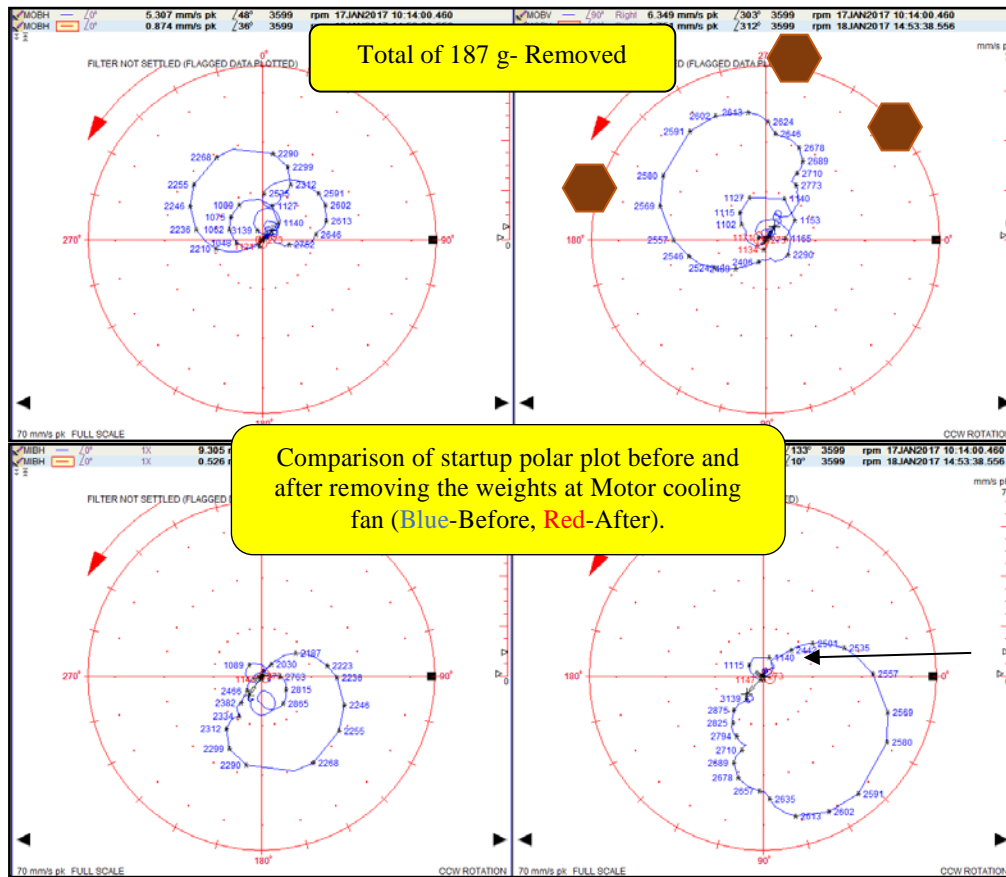


Figure 8: Motor Radial Sensors Startup Polar Plot (Blue-as found condition, Red-After Balancing Weights removal)

3.4 Coupled Run (after balancing)

On 19th January 2017 and after removing the wrong existing balance weights from the motor cooling fan blades (seen in Fig. (9)), the unit was started up and reached full speed. The unit revealed normal and acceptable casing vibration levels on all the unit component (motor, pump & structure) as can be seen in Fig. (10) and (11) at all conditions (critical speed and steady state).

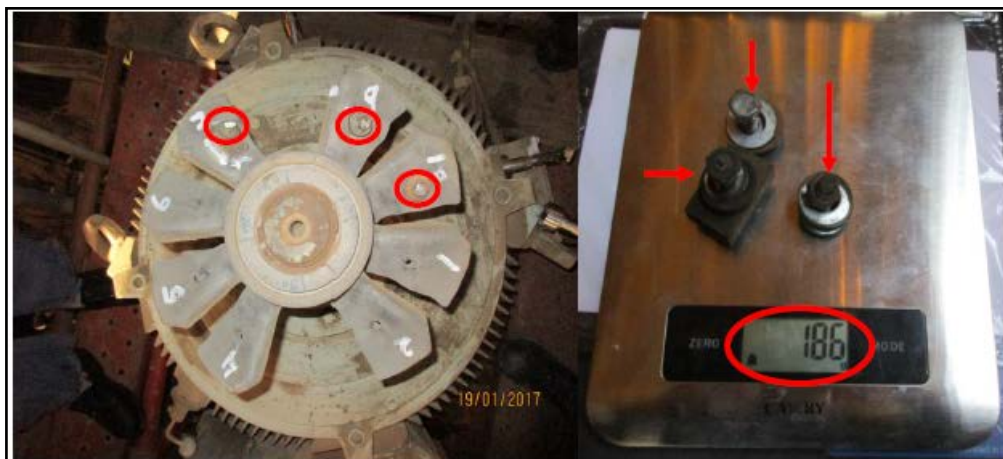


Figure 9: Existing wrong balance weights (removed from the cooling fan)

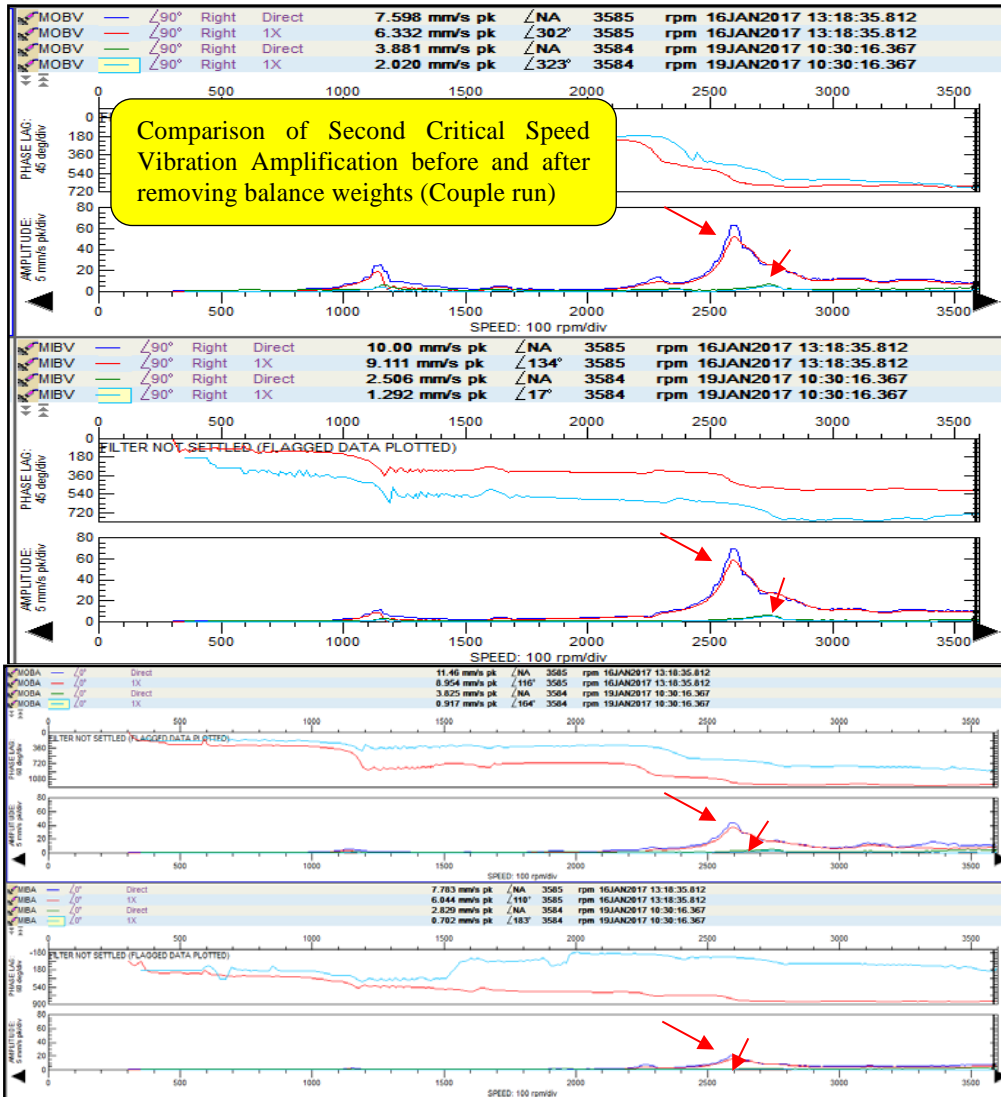


Figure 10: Motor Startup Bode Plot Comparison (dark blue-direct vibration as found condition, red-1X vibration as found condition, green-direct vibration after balancing weights removed, light blue-1X vibration after balancing weights removed)

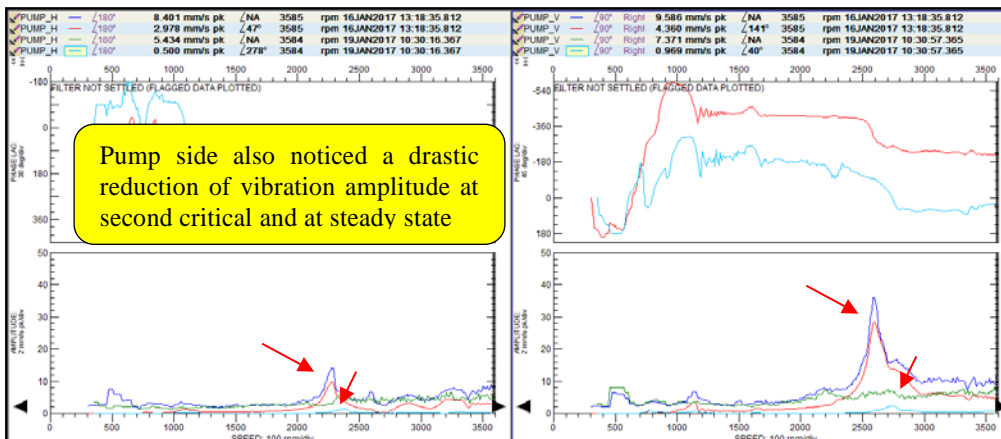


Figure 11: Pump Startup Bode Plot Comparison (dark blue-direct vibration as found condition, red-1X vibration as found condition, green-direct vibration after balancing weights removed, light blue-1X vibration after balancing weights removed)

3.5 Impact Test

It was decided to conduct a modal impact test to verify for any natural frequencies on the structure close to the running speed. The impact modal test conducted on 19th Jan 2017 showed excitation of natural frequency at 55 Hz (close to the steady state running speed of the motor) at structure point#5 as seen in Fig. (13) (See Fig. (12) for test locations).

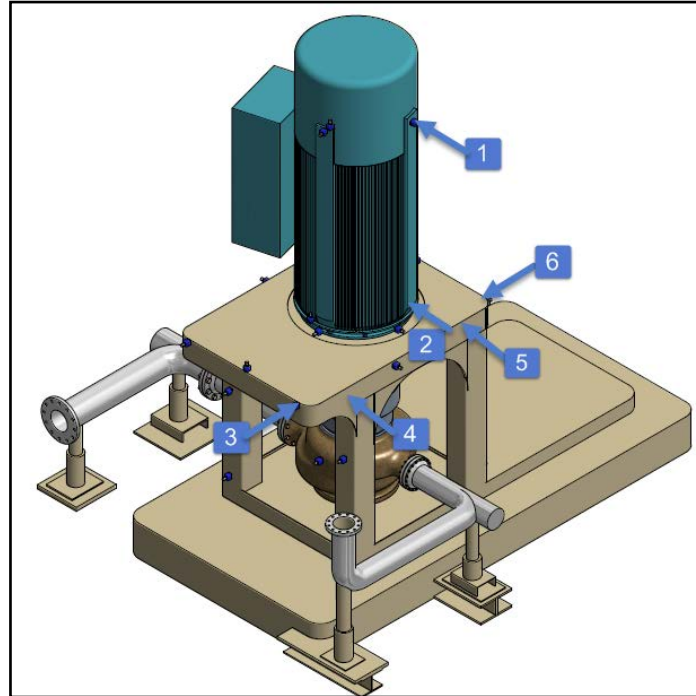


Figure 12: Impact Test Locations

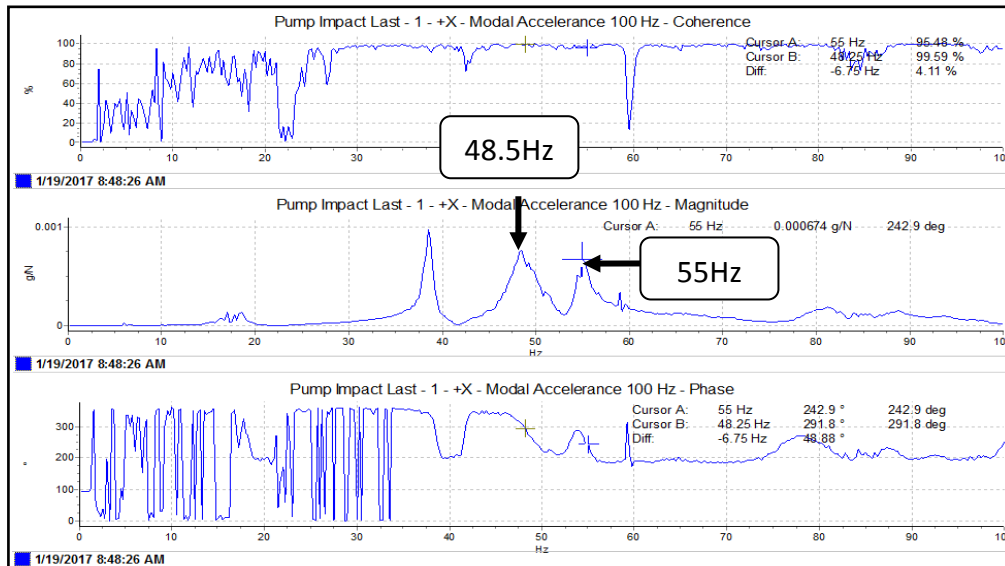


Figure 13: Impact Test at Point#5

mm/sec Peak		Coupled Run Before Balancing		Solo Run Before Balancing		Solo Run After Balancing		Coupled Run After Balancing	
		Overall	1X _{motor}	Overall	1X _{motor}	Overall	1X _{motor}	Overall	1X _{motor}
Motor	OBH	9.6	5.8	6.6	4.9	3	1.8	2.9	1.5
	OBV	8	6.5	6.9	5.8	3.2	2.4	2.9	2.4
	OBA	9.2	6.2	8.6	7	2.4	0.8	2.5	0.6
	IBH	10.7	9.8	10.5	9.9	2.8	2.1	3	2.5
	IBV	11	10.2	11	10.2	2.6	1.7	2.5	1.9
	IBA	6.3	3.8	5.8	4.3	1.6	0.7	2.2	0.4

Pump	H	6.3	2.6	3.6	3.1	1	0.6	3.8	0.7
	V	8.5	5.1	5.4	4.7	1.3	0.6	4.3	1.3
Structure	Str#1	12.9	11.2	11.5	11.2	2.2	1.6	3.1	1.8
	Str#2	8.5	6.2	6.7	6.2	1.6	0.9	3.6	1
	Str#3	1.3	0.2	0.4	0.2	0.3	0	1.1	0
	Str#4	12.5	11.2	11.6	11.2	2.7	2.3	3.3	2.6
	Str#5	9.1	6.7	7.3	6.7	2	1.5	4.7	1.7
	Str#6	1.7	0.5	0.7	0.5	0.3	0.1	1.4	0.1
	Str#7	13.7	12.4	12.6	12.4	2.2	1.8	2.8	2
	Str#8	9.8	7.3	7.8	7.3	1.7	0.9	2.6	1.1
	Str#9	1.4	0.7	1	0.7	0.3	0	0.8	0.1
	Str#10	12.7	11.5	11.9	11.5	2.7	2.4	3.2	2.7
	Str#11	10.2	6.8	7.3	6.8	1.8	1.2	4	1.5
	Str#12	1.6	0.7	0.9	0.7	0.4	0.1	1.2	0.1
	Str#13	10.1	10.1	10.4	10.3	2.4	2	3.1	2.5
	Str#14	11.2	10.5	10	9.9	2.3	1.9	3.4	2.4
	Str#15	3.1	0.9	1.5	0.9	1.2	0.4	2.9	0.3
	Str#16	4.1	0.9	2.4	1.2	1.1	0.5	2.2	0.4

Table 1: Vibration comparison at steady state for different scenarios

4 Conclusions.

Based on a detailed evaluation of the acquired information, it was concluded that extremely high vibration levels were observed on the motor, pump and structure with 1X of motor dominant frequency mainly due to motor rotor residual unbalance.

In-situ balancing reduced vibration levels on all the location of machine train components to acceptable values by removing the wrong existing balance weights from the motor cooling fan (see Table (1) for complete comparison of the vibration of the machine and structure before and after the balancing), however it is recommended to closely monitor the vibration levels on the motor and pump bearings since the unit was subjected to high vibration levels for an extended period.

It should be mentioned that the source of the unbalance mass was on the motor OB (top bearing), however the higher vibration values were observed on the upper surface of the structure. This was actually due to the fact that the structure resonance frequency was found close to operating speed frequency which amplified the vibration of the structure at operating speed of the machine, therefore it is recommended to review the structural design with the OEM to shift the structure resonance frequency for at least 20% above or below the operating speed frequency.

ODS showed circular motion due to unbalance response in addition to slightly structure twisting motion; after balancing, the twisting motion remained due to the natural frequency of 55 Hz as indicated from the impact test data.

It should be considered to change the motor cooling fan with a new one as the existing fan is missing two blades.

Table (2) shows the comparison of ODS files during steady state and different scenarios. The ODS animations will be played during the presentation.

	Coupled Run Before Balancing	Solo Run Before Balancing	Coupled Run After Balancing
ODS	Coupled Run Before Balancing_59Hz.wmv	Solo Run Before Balancing_59Hz.wmv	Coupled Run After Balancing_59Hz.wmv
	Coupled Run Before Balancing_55Hz.wmv	Solo Run Before Balancing_55Hz.wmv	Coupled Run After Balancing_55Hz.wmv
Comments	Circular + twisting motion	Circular + twisting motion	Twisting motion

Table 2: Operational Deflection Shape Comparison during Steady State

References

GE Oil & Gas, DS Bently Nevada *Machinery diagnostic technical training. Balancing.* (2015)

GE Oil & Gas, DS Bently Nevada *Advanced machinery dynamic training. Structural Analysis using ODS & Modal* (2015)

Case study on resolving structural vibration issues on a multi stage pump

Nicolas Péton¹, Sanker Ganesh²

¹ MDS Global Director, Baker Hughes a GE Company (Bently Nevada), 44300, Nantes, France,
nicolas.peton@bhge.com

² Machinery Diagnostics Technical Leader, Baker Hughes a GE Company (Bently Nevada), Doha, Qatar,
sanker.ganesh@bhge.com

Abstract

There are three multistage pumps supplied as part of a new project where these pumps are being used for transporting diesel from one location to another. Earlier, the transportation of diesel was carried out by using trucks by road at this facility. The availability of these pumps are critical to make sure that the diesel transportation happens smoothly without the need to use the truck services. The machine train is equipped with online vibration monitoring & protection system with online diagnosis software.

During the commissioning, it was noticed that these pumps were not able to reach the full speed of 3040 rpm (50.7Hz) and tripping on high vibration at the pump casing. The operation of these pumps were limited with the speed restrictions using the VFD system. The data review from the online diagnostics system revealed that these pumps were tripping on high vibration due to the excitation of pump vane pass frequency (195 Hz), when the pump was reaching the speed of 2340 rpm (39Hz). Further tests concluded that the pump casing natural frequency was matching with the vane pass frequency of 195 Hz.

This case study is designed to outline how the high vibration issue was successfully diagnosed, the root cause for the high vibration and finally how it was mitigated using some of the structural analysis techniques (modal analysis, Operating Deflection Shape etc). Lessons learned are also discussed on the discovery methodology using expert system available at site, project point of view as well as from design point of view, which will be very much useful for the audience.

Nomenclature

BHGE - Baker Hughes, a GE company
Hz - Hertz
VFD - Variable Frequency Drive
l/s - Litres/sec
Kw - Kilowatt
Rpm - Revolutions Per Minute
DE - Drive End
NDE - Non-Drive End
Rms - root mean square
ODS - Operating Deflection Shape
Fig - Figure
FRF - Frequency Response Function
OEM - Original Equipment Manufacturer

1 Introduction

Baker Hughes, a GE company (BHGE) is the world's first and only full stream provider of integrated oilfield products, services and digital solutions. Bently Nevada is part of the BHGE Measurement & Controls division, it has 60 years history, 134 machinery diagnostic engineers with cumulative experience more than 1000 years worldwide.

BHGE Machinery Diagnostic Services team was requested to perform vibration measurement and evaluation of the shipper pump installed at a customer site in the Middle East. These pumps are being used for transporting diesel from one location to another. Earlier, the diesel transportation was carried out by trucks. The availability of these pumps is very critical.

The unit is a four-stage centrifugal pump (Flow capacity 285 l/s) driven by a variable speed motor (2600 Kw) through a flexible shim pack coupling. The maximum continuous speed of the pump is 3040 rpm whereas the maximum rated speed is 3229 rpm. The pump installed with 4 proximity probes (two probes on the DE and two on the NDE) for monitoring the shaft vibration. In addition, one casing probe is installed at pump NDE side vertically and this probe is connected to a protection system for high vibration trips. For the continuous monitoring and analysis, the pump is connected to an online diagnostics software.

During commissioning, these pumps were not able to reach the maximum continuous speed of 3040 rpm and were tripping on high casing vibration at Pump NDE side while crossing the speed range of 1800 to 2300 rpm.

The original Alarm/Danger set points of 0.17/0.26 in/s rms were revised and increased to 0.26/0.35 in/s rms respectively to avoid the trip.

When the machine was reaching the speed of 2340 rpm (39 Hz), the pumps were tripping on high casing vibration with 195 Hz dominant frequency which is matching with the pump vane pass frequency (Number of impeller vanes – 5).

Since the issue has existed in all the pumps, one of the pumps (Pump A) was selected as pilot to carry out a detailed analysis including ODS to identify the root cause and the rectifications. Once the issue is resolved, it was planned to implement the solutions to other pumps also.

2 Data collection

In order to diagnose the root cause of high casing vibration problem, the data was reviewed from the online diagnostic software for the analysis of shaft vibration and bearing temperature. In addition to SCOUT140 portable data collector for ODS & impact test purposes. The data in this report has been selected from all the recorded data and is limited to the most relevant plots only.

The scope of the job is defined by the following objectives:

Collect and analyze the transient and steady state vibration data.

Collect steady state data on the pump structure for operating deflection shape ODS.

Provide recommendations on further action as and if necessary.

Machine train diagram is presented in Fig.1

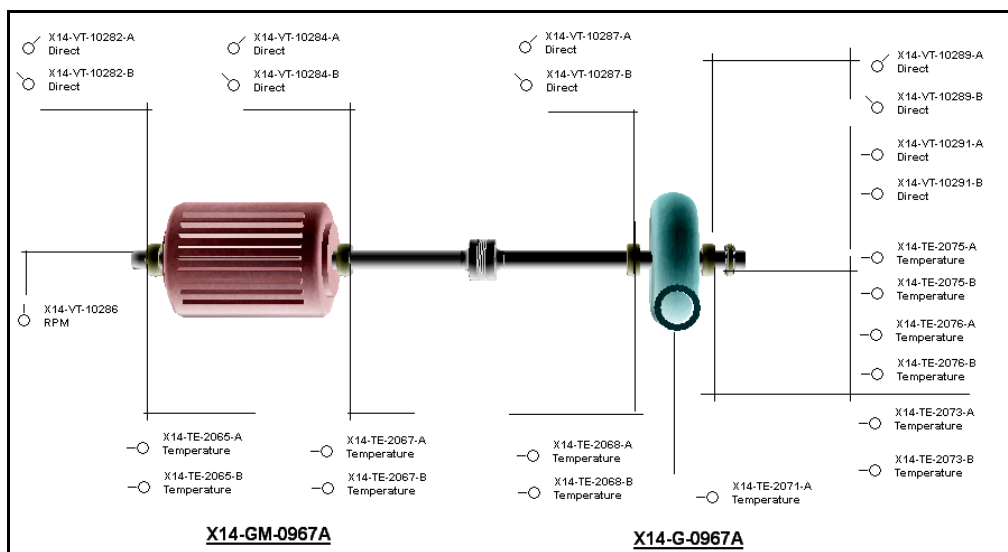


Figure1: Machine Train Diagram

With the revised alarm/Danger set points, the pump trial run was taken to review the vibration behavior. The review of shaft vibration levels on the Motor and pump revealed acceptable vibration levels of less than 1 mils PP up to the speed of 2780 rpm (See Fig 2 and 3). However, the pump casing direct vibration levels were increasing and crossing the original alarm set point of 0.17 in/s rms (See Fig-4), while crossing the speed zone of 1800 – 2300 rpm with the increase of 5X component (See Fig-5 & 6) due to excitation of vane pass frequency (Number of impeller vanes – 5).

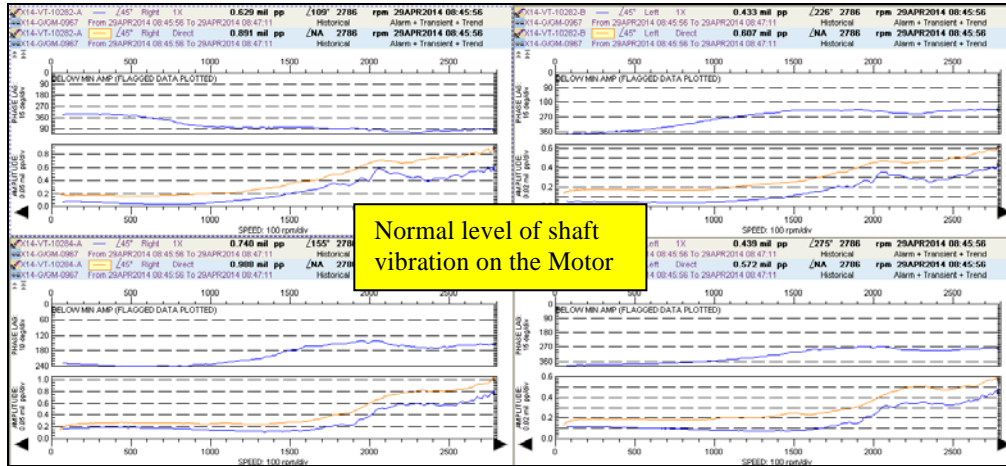


Figure 2: Motor shaft vibration Startup Bode Plot

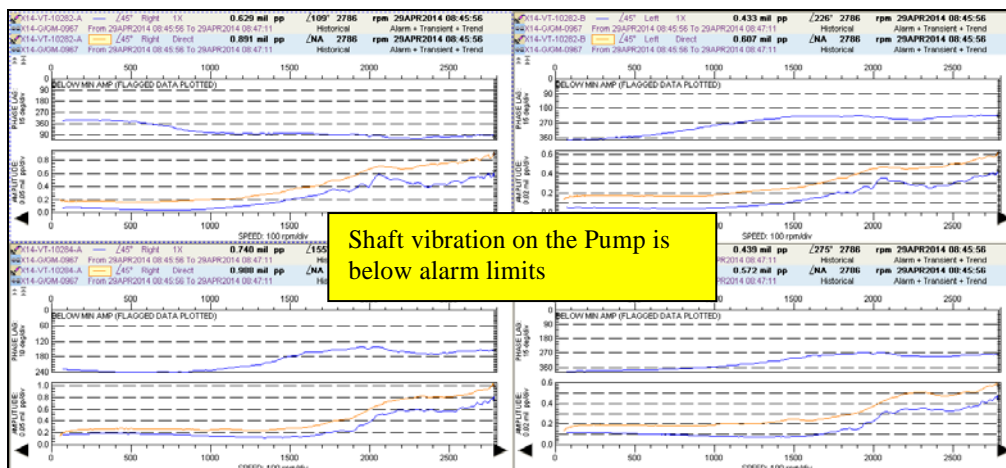


Figure 3: Pump shaft vibration Startup Bode Plot

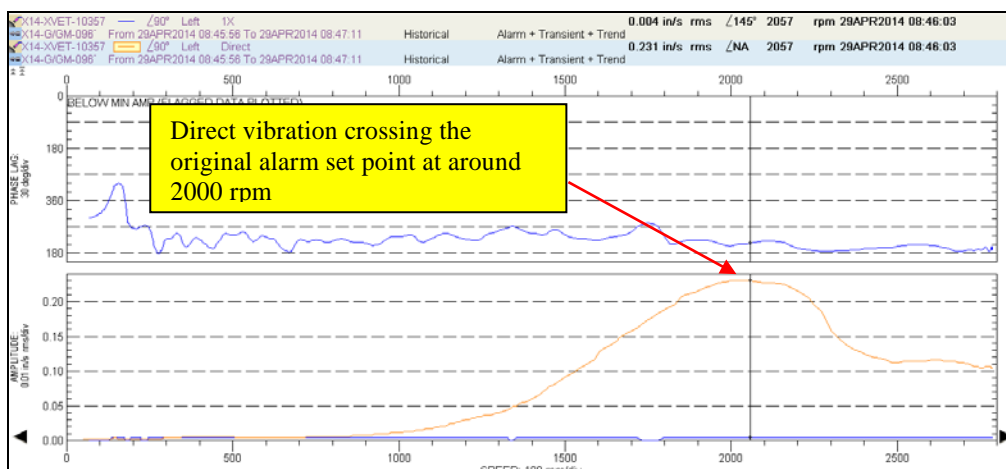


Figure 4: Pump NDE seismic vibration Startup Bode plot – Direct vibration crossing the original Alarm set point

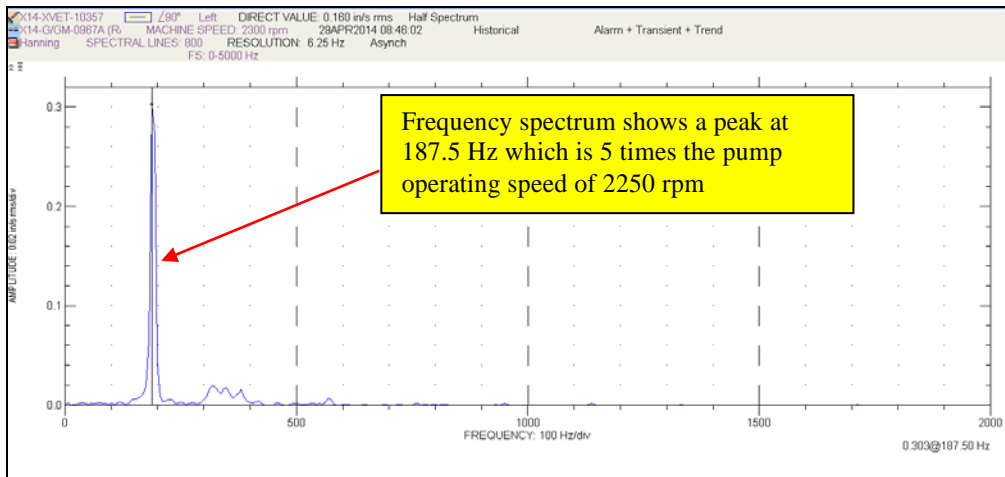


Figure 5: Half spectrum captured at 2300 speed shows dominant 5X component

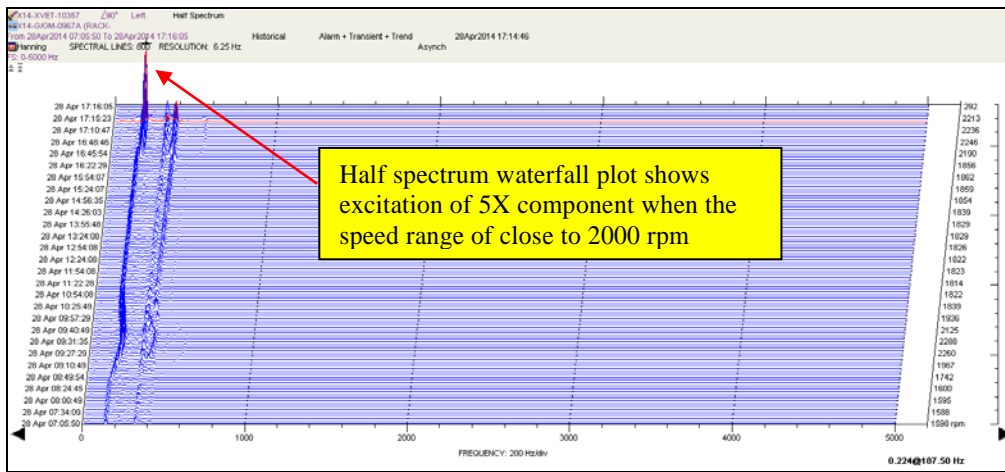


Figure 6: Half spectrum waterfall shows excitation of 5X component while startup as well as shutdown while reaching the speed range of 1800 to 2300 rpm.

3 Data analysis and malfunction investigation.

To identify the root cause for the excitation of pump vane pass frequency (5X), it was decided to conduct a bump test on the pump bearing housing to see if there are any correlation between the pump vane pass frequency and the pump casing natural frequency. The bump test on the bearing housing at Pump NDE clearly showed a natural frequency at 198 Hz, which is matching with the pump vane frequency of 198 Hz (Fig-7). This is the direction at which the pump has a vibration sensor for online monitoring. The bump test carried out on Horizontal direction of pump NDE plus the DE bearing of both Vertical and Horizontal did not show a similar excitation at 198 Hz (Fig-8)

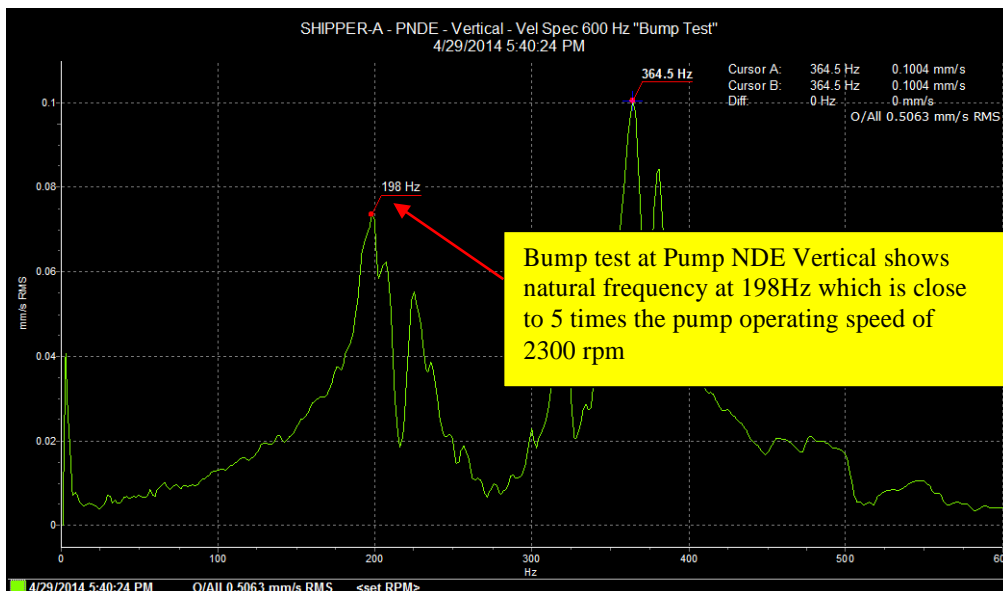


Figure 7: Bump test spectrum at Pump NDE Vertical



Figure 8: Bump test spectrum at Pump NDE Horizontal

The Operating Deflection Shape (cross spectrum) performed at 2380 rpm shows the motion of vibration at the rotating speed at 39.6 Hz and 198 Hz (5X) showed horizontal deflections (Fig-10 & 11).

The Operating Deflection Shape (ODS FRF) performed at 3140 rpm shows the motion of vibration at rotating speed at 52.3 Hz and 261.2/262 Hz (5X) showed vertical deflections. (Fig-12 & 13)

The ODS using cross spectrum is very sensitive to change in load levels (and so amplitude levels) between measurement sets.

Both ODS from cross spectrum and ODS FRF show a horizontal deflection at running speed. (Fig 10 & 12).

Both ODS from cross spectrum and ODF FRF show a vertical deflection at 5 times running speed. (Fig 11 & 13).

At 52.3 Hz the most dominant motion is seen in the horizontal direction.

The actual animations will be shown during the conference presentation.

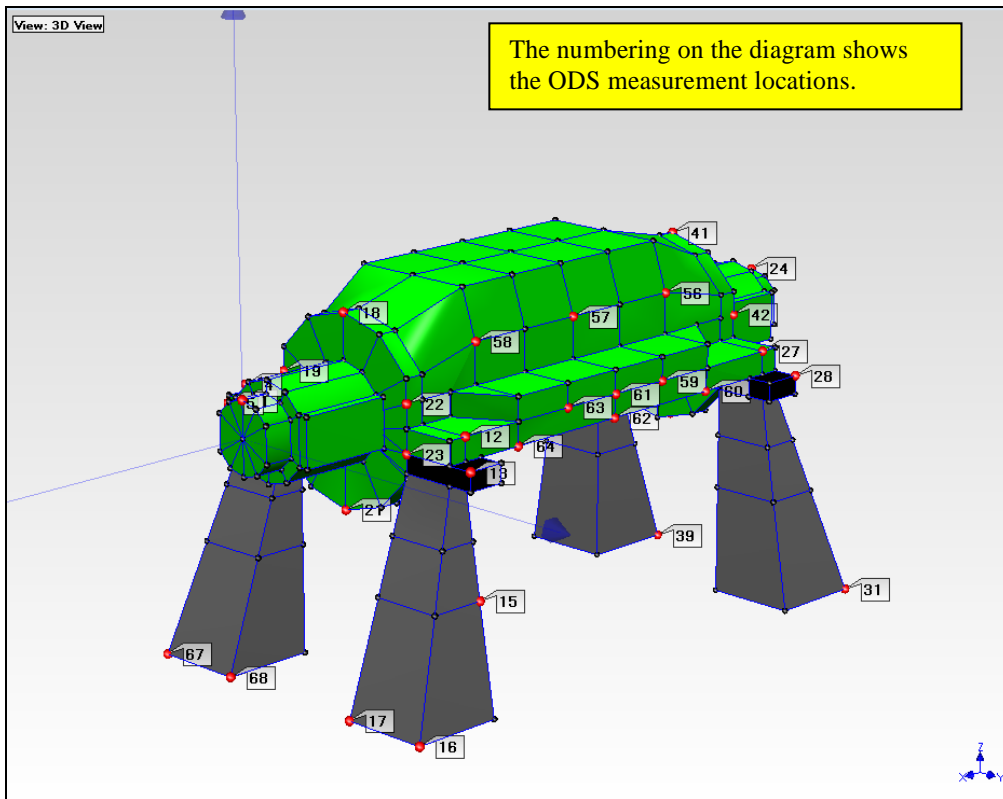


Figure 9: ODS measurement locations

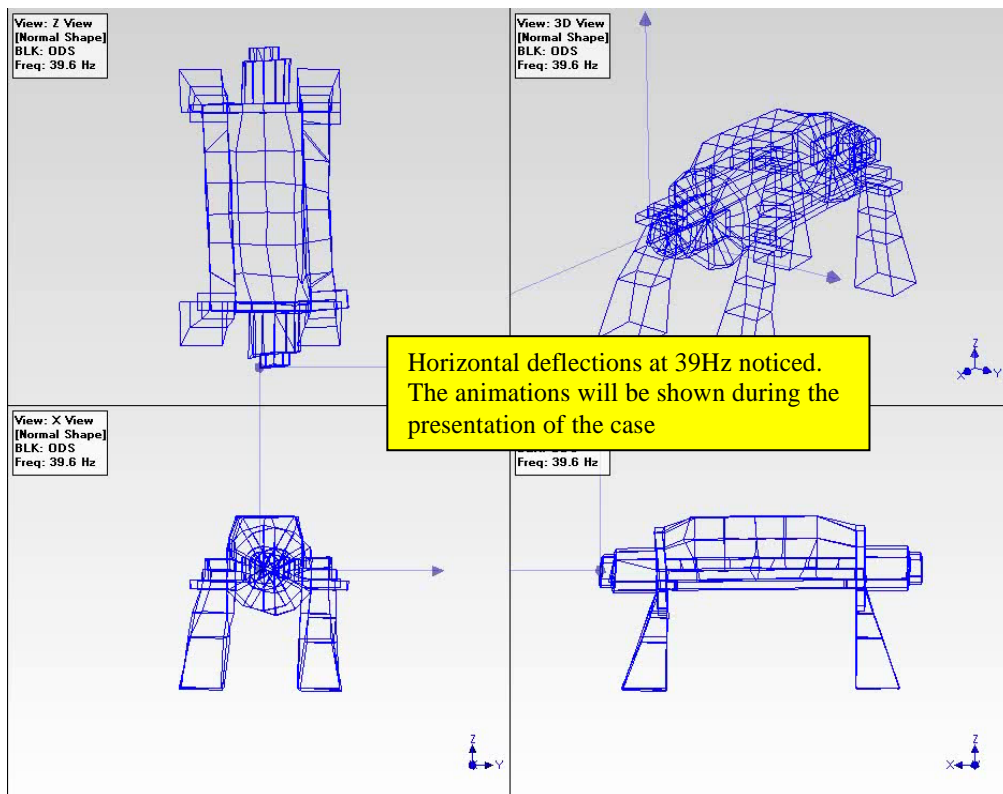


Figure 10: ODS Animation (using cross spectrum) with running speed=2380 rpm (39.67 Hz)

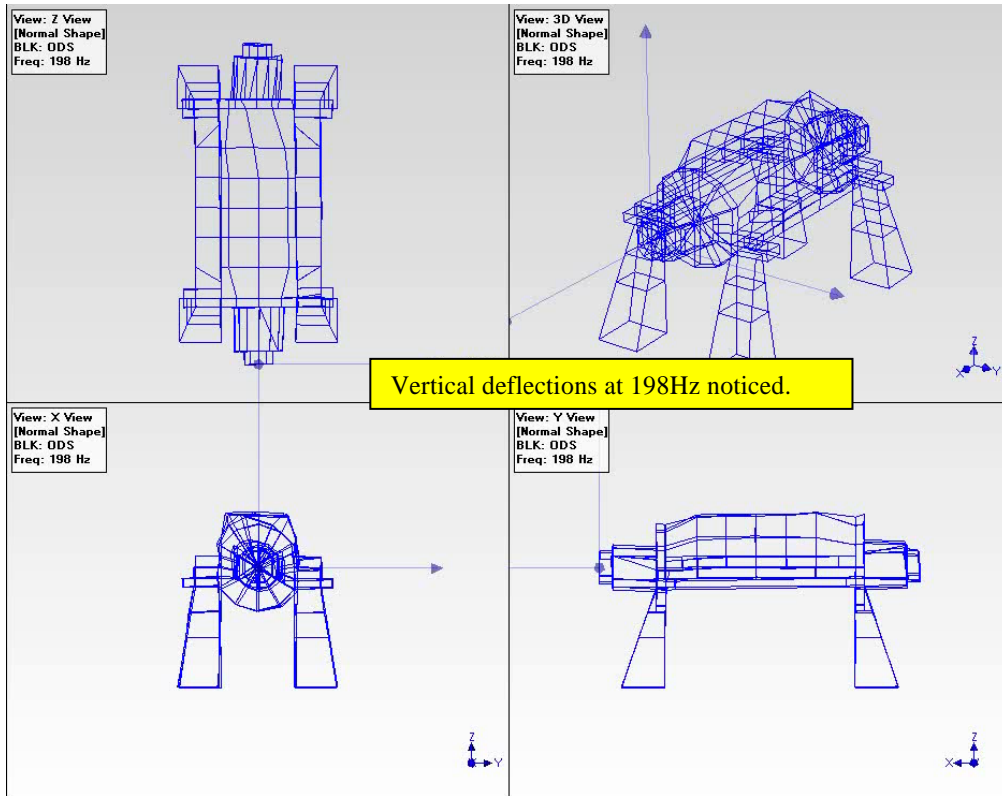


Figure 11: ODS Animation (using cross spectrum) at 198 Hz (5X).

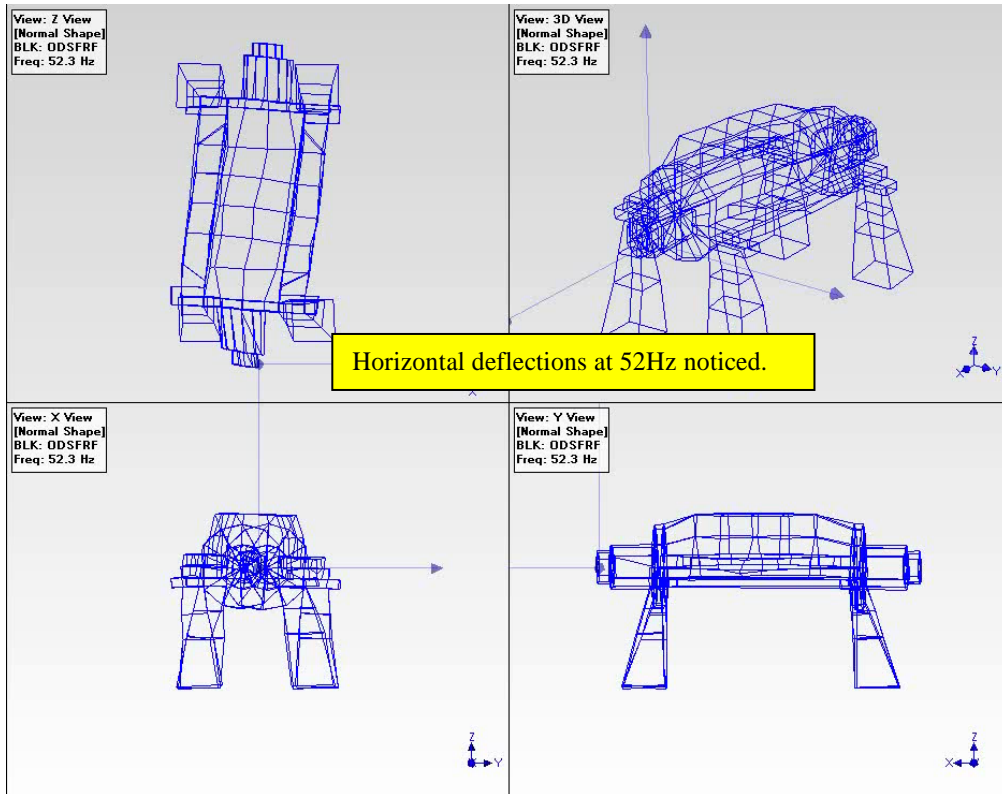


Figure 12: ODS Animation (ODS FRF) with running speed=3140 rpm (52.3 Hz)

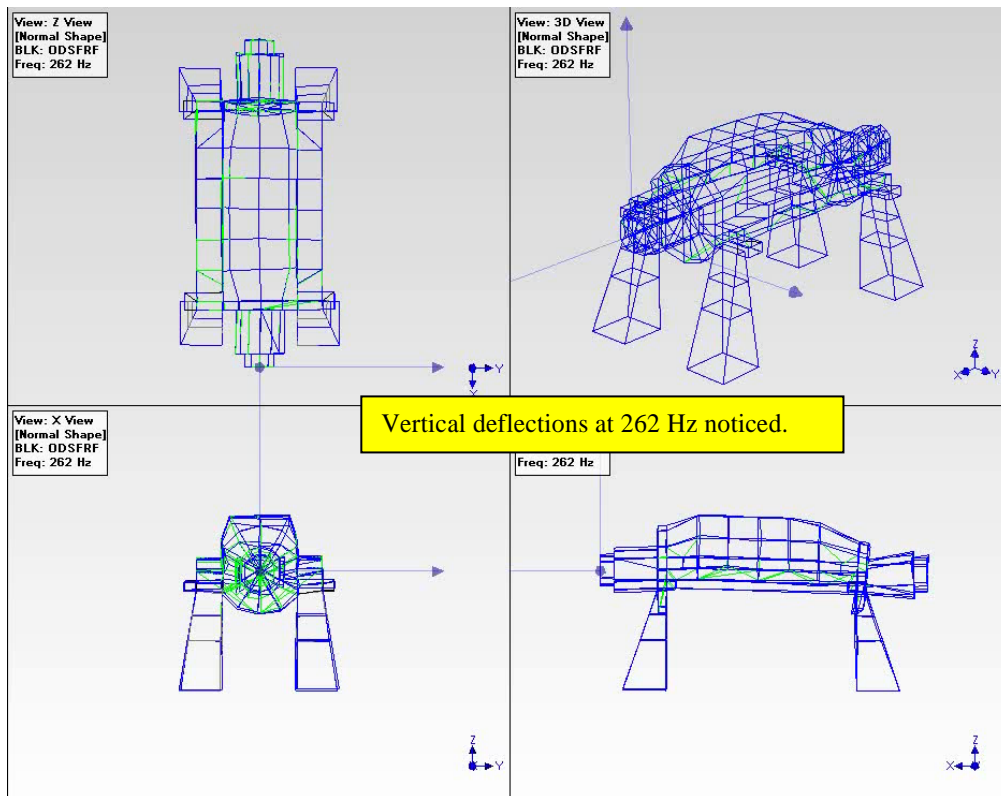


Figure 13: ODS Animation (ODS FRF) with running at 5X or 262 Hz (1X=3140 rpm)

4 Conclusions.

The conclusions from the ODS analysis is as follows:

- The pedestal of the pump support structure appears to be the weak point in the vertical and horizontal direction.
- The left drive end pedestal appears to cause a problem in the vertical direction.
- The Non-Drive End Bearing appears to move much more in the vertical direction than the Drive end bearing.
- Recommendation would be to modify the pedestals of the pumps and check the Non-drive end bearing housing.

Based on the above conclusions, the pump pedestal was modified by pump OEM as per the picture below (Fig 14 & 15)



Figure 14: Old Pump Support Pedestal:

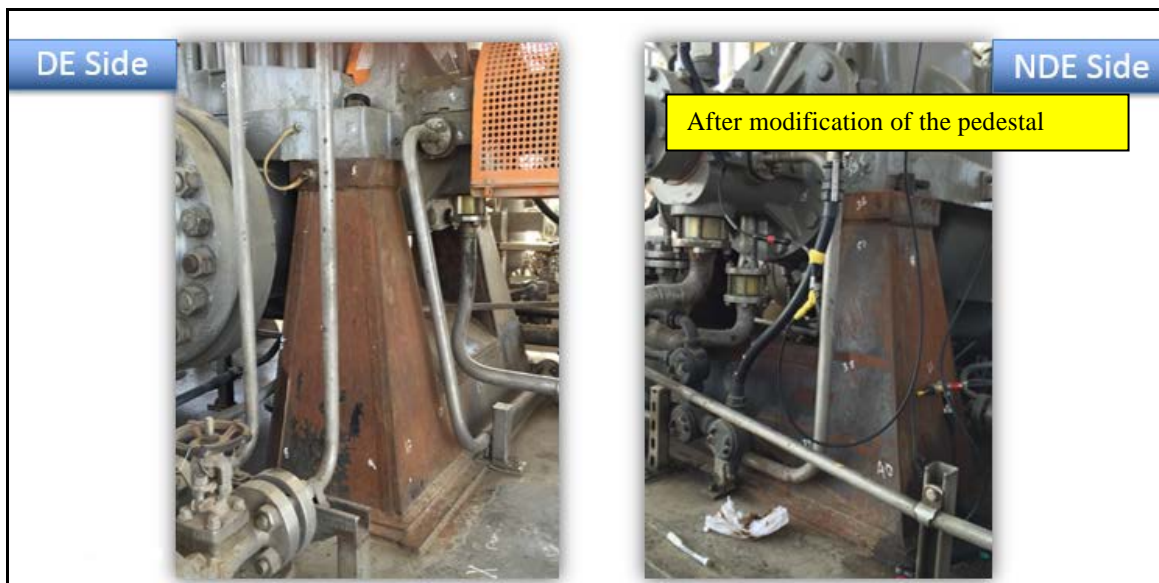


Figure 15: New Pump Support Pedestal:

Following the pump pedestal modification, the bump test, ODS measurement and the pump trial was taken to verify the effectiveness of the modification.

The bump test showed a significant shift in the natural frequency from 198 Hz to 260 Hz (Fig-16). The startup Bode plot showed a significant improvement of vibration level (almost 50% reduction) which helped in reaching the full speed without any alarm (Fig-17).

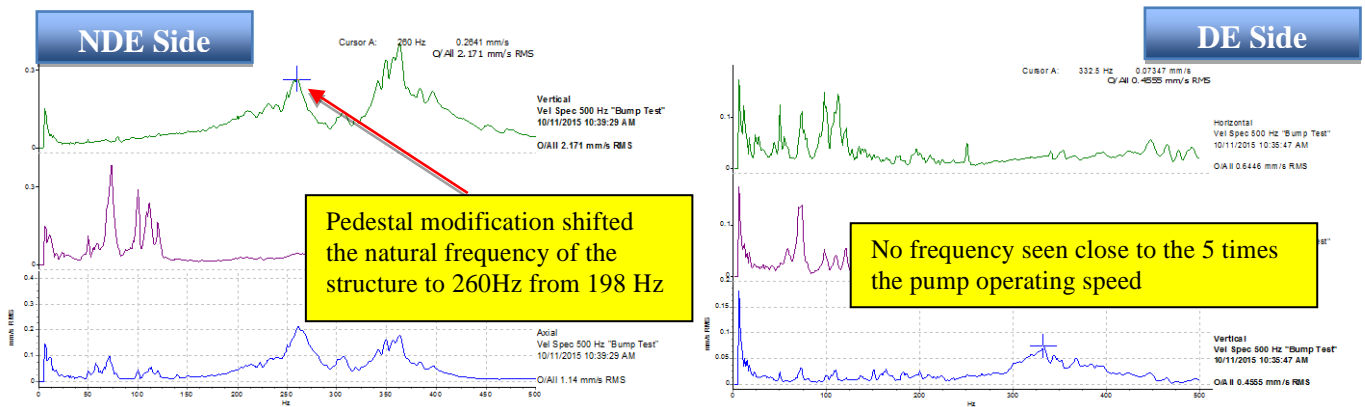


Figure 16: Bump test post pedestal modification shows shifting of natural frequency

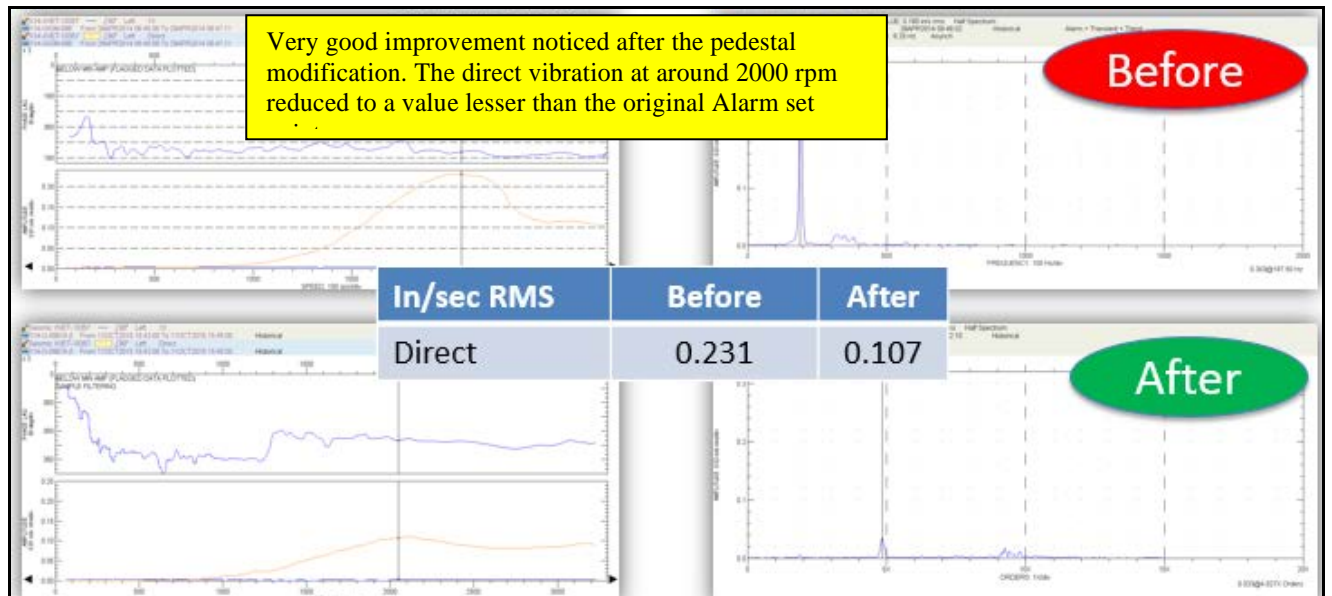


Figure 17: Startup Bode plot comparison before and after the modification shows very good improvement in the vibration levels

References

- GE Oil & Gas, DS Bently Nevada *Machinery diagnostic technical training. Balancing.* (2015)
- GE Oil & Gas, DS Bently Nevada *Advanced machinery dynamic training. Structural Analysis using ODS & Modal* (2015)

Turbocharger dynamic analysis: concept-phase simulation in frequency domain

Tigran Parikyan¹, **Saša Bukovnik**²

^{1,2} Advanced Simulation Technologies, AVL List GmbH, Hans-List-Platz 1, 8020, Graz, Austria

¹ tigran.parikyan@avl.com, ² sasa.bukovnik@avl.com

Abstract

The subject of the paper is to present the capabilities of rotor modeling and of “rotor-bearings” system simulation in the early concept phase of turbocharger calculation project, considering 3D frequency domain linearized dynamics solution using software tool AVL EXCITE™ Designer. The resonances of main bearing forces and moments resulting from the forced response are compared to the critical speeds predicted by gyroscopic modal analysis. The behavior of rotor when passing through critical speeds is illustrated.

Nomenclature

N – number of vibrating nodes in the model, with 6 degrees of freedom (DOF) per each node;

\mathbf{M} – mass matrix;

\mathbf{K} – stiffness matrix of rotor elastically supported in bearings;

\mathbf{D} – viscous damping matrix;

\mathbf{G} – gyroscopic/Coriolis matrix;

\mathbf{C} – centrifugal matrix;

\mathbf{H} – viscoelastic (hysteretic) damping matrix

\mathbf{q} , $\dot{\mathbf{q}}$, $\ddot{\mathbf{q}}$ – vectors of translational/rotational displacement, velocity, acceleration as functions of rotation angle;

\mathbf{f} – vector of excitation force/moment as function of rotation angle;

\mathbf{q}_n – complex-value vector of translational/rotational displacements in the n th harmonic order;

\mathbf{f}_n – complex-value vector of forces/moments in the n th harmonic order.

$\omega_n = n\Omega$ – harmonic frequency of n th order;

Ω – angular velocity of the rotor;

j – imaginary unit.

1 Introduction

Turbocharger dynamic analysis is an example of AVL strategy for developing multi-level simulation software *EXCITE™*: there are two modes of operation, one for concept phase (*Designer*) and the other one – for detailed analysis phase (*Power Unit*), with a common GUI, shared data set and equivalent modelling of flexible bodies, but based on different calculation principles.

In the concept phase, simulation is based on restricted set of input data and is performed in frequency domain. It must not be very accurate, but is usually very fast and robust, thus giving an opportunity to perform multiple runs while varying some of the few design parameters. The goal at this early stage of calculation project is the coarsely optimized primary layout of mechanical system [18], [19].

The subsequent analysis phase is based on the full set of input data available and is performed in time domain to take all the non-linear properties and physical effects into account. It must be very accurate, but is not very fast as a rule. The goal here is to verify and eventually to refine/tune the primary layout, as well as to calculate the absolute levels of stresses, pressures, etc. for the final assessment of the system performance [2].

Only the combination of these two levels represents a complete workflow and assures a time-efficient execution of calculation project while targeting at the same quality requirements.

It is important to note, that the modelling depth on both levels is often application related, i.e. it is driven by the types of the mechanical sub-systems analyzed, as well as by the availability of measured or pre-calculated data.

2 Literature survey

There is a number of publications on modal analysis of rotors, including those of turbochargers, taking the spin effects into account [1]-[9], where the critical speeds (resonance points) are being found considering Campbell diagram. In [2]-[6], [9]-[12], forward and backward whirl effects are additionally analyzed, and journal orbits in absolute and in rotating coordinate systems are considered. Stability issues have received much attention in [2]-[8], [11]-[14]. For the analysis, the “rotor-bearing” systems are modelled both in 2D [3], [9] and in 3D [3], [16]. Both time integration [3], [4], [8] and [13] and frequency response [4], [15] and [17] are used to solve the equations of motion.

The theoretical groundwork for developing a software tool for gyroscopic modal analysis and frequency-domain forced response of rotating structures, as well as the corresponding application cases are described in [16] and [17]. Based on these previous developments, the present paper focuses on application of these methods to simulate the dynamics of automotive turbochargers. For practice-oriented modelling, specific requirements on modeling of turbocharger rotors using coaxial and compound shafts, are taken into account.

3 Turbocharger rotor modeling

Turbocharger rotors have complex geometry, especially the compressor and turbine wheels (see **Figure 1**). Therefore, for obtaining accurate results depending on specific application (e.g. durability of blades, gas flow, acoustics) the modeling has to be done taking the real shape of the rotor into account, which is mostly attained by using 3D CAD and subsequent volumetric FE-modeling.

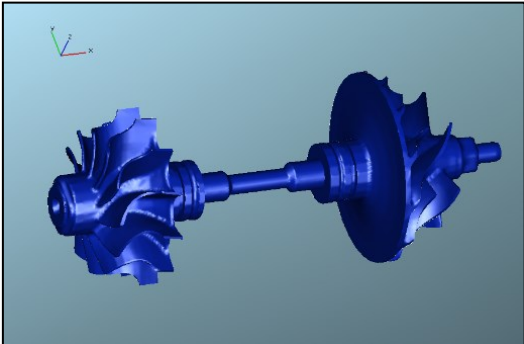


Figure 1: Turbocharger rotor 3D CAD model.

In other applications not directly related to the actual shape of the rotor wheels (e.g. bearing dynamic load estimation), an approximation of the rotor shape with cylindrical steps, which are then transformed into equivalent quality rotor mass and stiffness characteristics, can be a reasonable alternative.

Here the turbocharger rotor is modeled using a pre-processor called *Shaft Modeler* that is integrated into AVL EXCITE™. This approach uses analytical calculation of the lumped mass parameters resulting from mass discretization, and of the stiffness parameters of elastic elements connecting these mass points, based on Timoshenko beam theory, without involving any volumetric FE-modeling.

For building up a rotor model, the user puts in geometric and material parameters of cylindrical steps (with or without central bore), constituting the rotor shaft. The turbine and compressor wheels are also approximated by cylindrical steps. Figure 2 below shows an example of such a modeling.

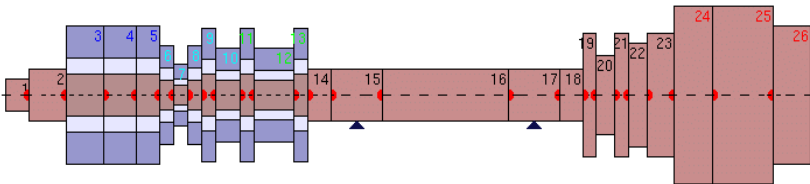


Figure 2: Model of turbocharger rotor

Taking the specific design based requirements for modeling of turbocharger rotors into account, some advanced modeling options of *shaft-in-shaft* elements are also foreseen (Figure 3).

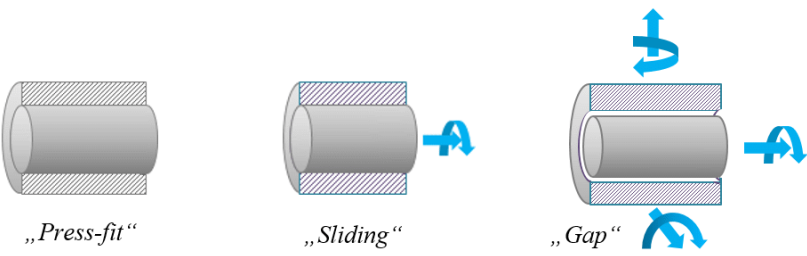


Figure 3: Modeling options of “shaft-in-shaft” element

In course of assembling, the pre-processor transforms the data mentioned above into a bar-mass model as shown in Figure 4, which consists of 6 DOF nodes representing mass lumps, connected by elastic elements.

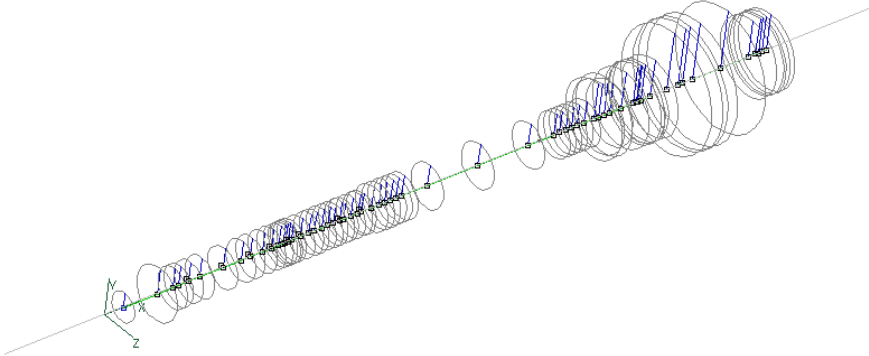


Figure 4: Bar-mass model of turbocharger rotor after assembling

4 Turbocharger rotor modal analysis

To evaluate the intrinsic dynamic properties of the „rotor-bearing“ system, its modal analysis has to be performed.

Here, we consider undamped gyroscopic modal analysis of the turbocharger rotor in bearings, which is governed by the solution of the following linear system:

$$\mathbf{M}\ddot{\mathbf{q}} + \mathbf{G}\dot{\mathbf{q}} + (\mathbf{K} + \mathbf{C})\mathbf{q} = \mathbf{0} \tag{1}$$

The methods to solve such equations are well described in the literature (see, e.g. [16]).

The critical speed diagrams (Figure 5) show the eigenfrequencies of gyroscopic modes vs rotor speed. Lines of different color track the modes of the same whirl and shape type. In the relative coordinate system, the whirl changes its sign (dashed color lines) when passing through the critical speed (marked with U1..U3 and vertical lines) [16].

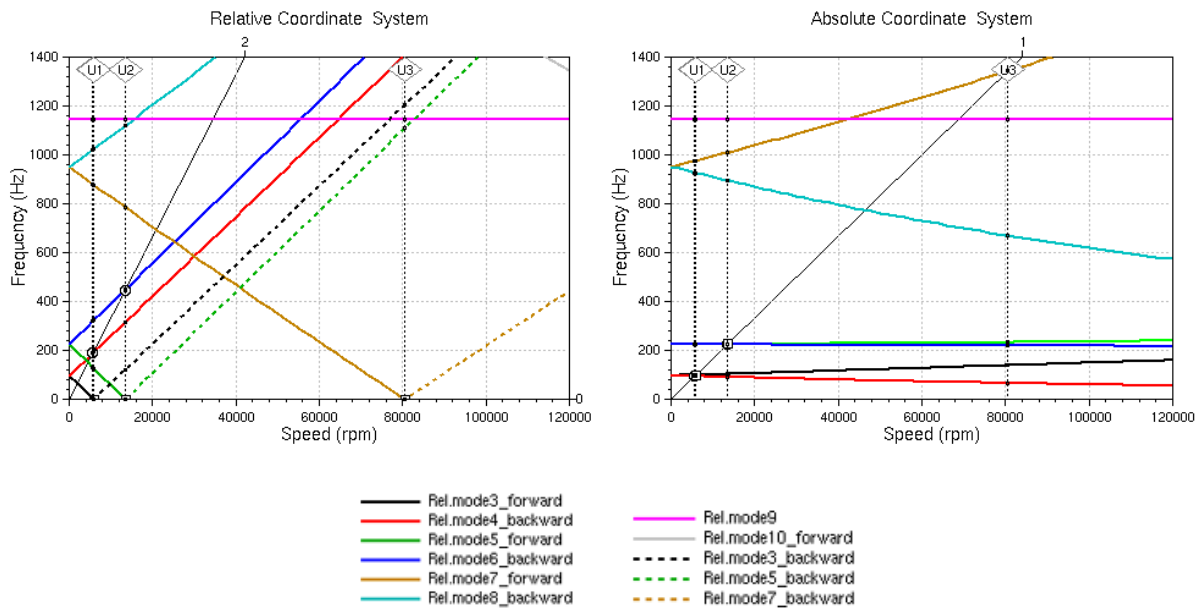


Figure 5: Critical speed diagram of gyroscopic modal analysis of turbocharger (in relative and in absolute coordinate systems)

At each critical speed, one of the eigenvalues of the effective stiffness matrix ($\mathbf{K} + \mathbf{C}$) becomes zero, which means that the additional (negative) stiffness coefficients due to rotor spin effects become equal to some stiffness coefficients of the „rotor-bearings“ system. An example of such eigenvalue analysis of the effective stiffness matrix ($\mathbf{K} + \mathbf{C}$) is shown in Figure 6.

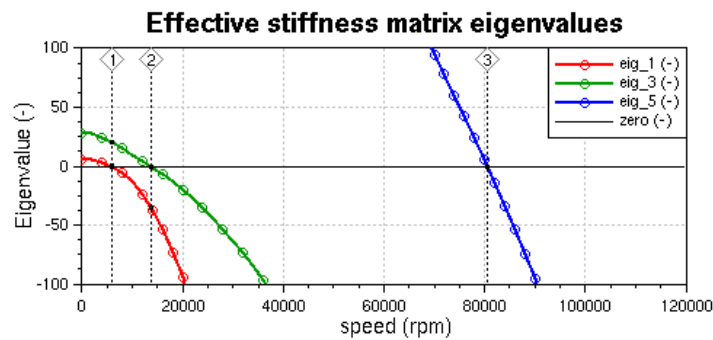


Figure 6: Eigenvalues of the effective stiffness matrix ($\mathbf{K} + \mathbf{C}$) vs. speed

The numerical values of critical speed and corresponding frequencies in relative and in absolute coordinate systems are summarized in Table 1.

Table 1: Resonances in relative and in absolute coordinate systems

Resonances (REL)		Resonances (ABS)	
Speed	Frequency	Speed	Frequency
rpm	Hz	rpm	Hz
5965.6	0.0	5965.6	99.4
13524.5	0.0	13524.5	225.4
80561.9	0.0	80561.9	1342.7

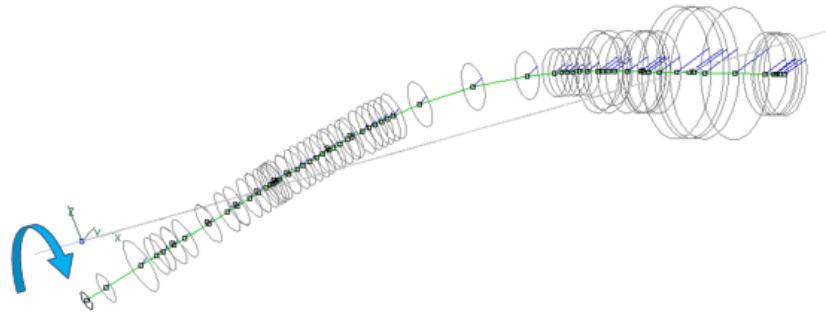


Figure 7: One of the forward-whirl bending modes of the turbo charger rotor

5 Turbocharger “rotor-bearings” system forced response

In general case, a system of 6N linear equations describes the dynamic vibrations of a system with 6N degrees of freedom (DOF), which can be written in rotor coordinate system rotating with constant speed as:

$$\mathbf{M}\ddot{\mathbf{q}} + (\mathbf{D} + \mathbf{G})\dot{\mathbf{q}} + (\mathbf{K} + \mathbf{C} + j\mathbf{H})\mathbf{q} = \mathbf{f} \quad (2)$$

To solve the system of equations (2) in frequency domain, we split it up into n harmonics:

$$[-\omega_n^2\mathbf{M} + j\omega_n(\mathbf{D} + \mathbf{G}) + (\mathbf{K} + \mathbf{C} + j\mathbf{H})]\mathbf{q}_n = \mathbf{f}_n \quad (3)$$

The main application case considered in practice, is the steady state rotation of the turbocharger rotor having residual unbalances, i.e. rotation under the action of inertia load, without any other external loads applied on it. That means, that the linear system (3) has to be solved for the 0th harmonic order only, representing the kinetostatic equilibrium condition (which is equivalent to the 1st harmonic order in absolute coordinate system):

$$[j\Omega\mathbf{D}_0 + (\mathbf{K} + \mathbf{C})]\mathbf{q}_0 = \mathbf{f}_0 \quad (4)$$

Here we consider an example of simulation of rotor supported by two radial slider bearings having the same linear stiffness and viscous damping coefficients. The compressor and the turbine wheel both have residual unbalance at 180°. Under action of inertia load, the rotor bends and rotates at constant speed without vibration. This rotor bending induces forces and moments in bearings, which show some resonances in the operation speed range (Figure 8).

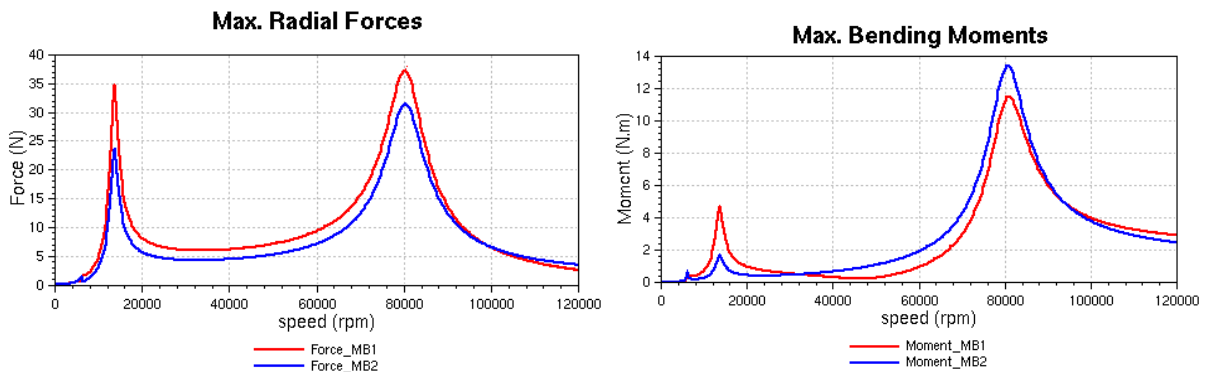


Figure 8: Main bearing forces and moments vs speed

These resonances show a very good match with the critical speeds shown in Table 1 – some slight differences are due to damping used in forced response.

The rotor bent line is shown in **Figure 9** for the speeds around the critical one at about 13 527 rpm. As expected, near this speed, the rotor bending line (axial view) re-orient by passing from values near 180° at sub-critical speed, through 270° (or -90°) at the resonance, and near 0° at super-critical speeds.

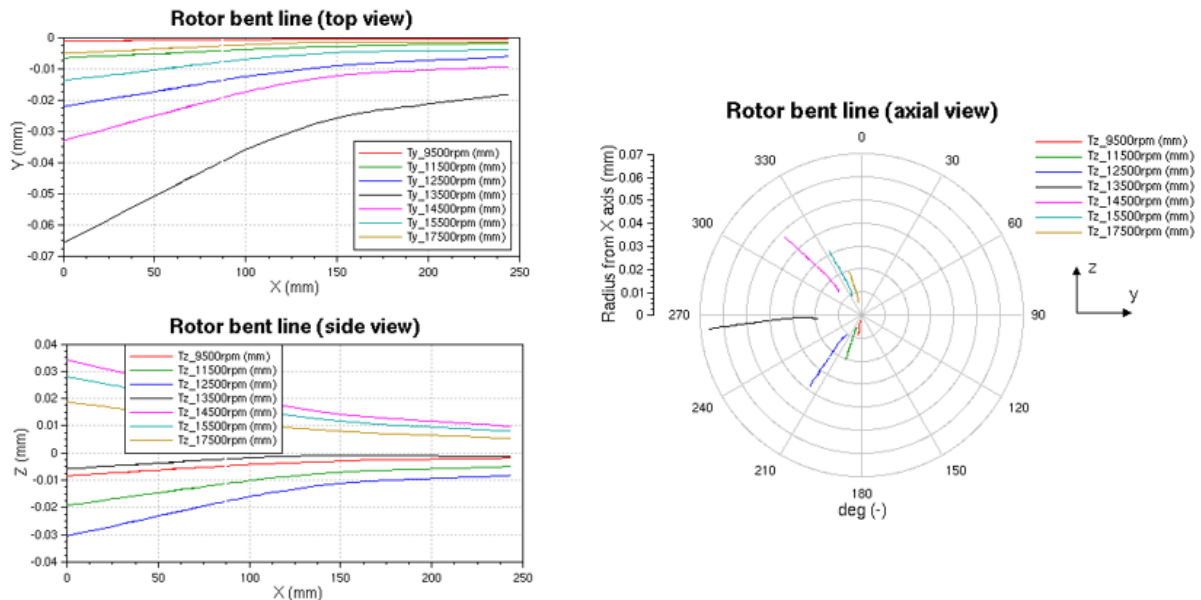


Figure 9: Rotor bent line (in projections) when passing through resonance.

7 Conclusion and outlook

To evaluate turbocharger dynamics, including bearing loads in the early concept phase of calculation project, the rotor can be sufficiently well represented as 3D bar-mass model. This is attained by an automatic pre-processor assembling such a model based on geometric and material data, and definition of residual unbalances as non-structural masses. Extended options to model “shaft-in-shaft” elements are also covered by the tool to fulfill the design requirements specific to turbocharger rotors.

As a result of gyroscopic modal analysis, critical speeds diagram is presented, which tracks mode lines featuring the same whirl and mode shape. The critical speeds are shown to correspond to the singularities of effective stiffness matrix taking the rotor spin effects into account.

As a result of forced response in frequency domain performed by own software tool, main bearing forces and moments are evaluated showing resonances at critical speeds predicted by the gyroscopic modal analysis. The rotor bent line is calculated, showing an expected behavior when passing through resonances.

Further extensions of the software tools are planned in the following directions:

- 1) for modal analysis: taking viscous and hysteretic damping into account;
- 2) for forced response: modeling semi-floating and floating short and long bushings, as well as non-linearities in bearing stiffness and damping characteristics.

References

- [1] Boricean, C. C. and Radu, Gh. A. (2012): *Diesel engine turbochargers: analysis and testing*, Bulletin of Transilvania University Brasov, Series I: Engineering Sciences, **5 (54)** No. 1, pp. 1–6.
- [2] Bukovnik, S. et al. (2017): *Turbocharger dynamic analysis: Advanced design simulation in time domain using CFD predicted thermal boundary conditions*, 12th International Conference on Vibrations in Rotating Machines (SIRM 2017), Paper S16-3, p.440-451.
- [3] Cavalcante, P. F., Cavalca, K. L. and Okabe E. P. (2002): *A model of rotor-hydrodynamic bearings systems on flexible structures*, XX IMAC Conference, Paper S10P05, pp. 265-270.
- [4] Downham, E. (1958): *The influence of plain bearings on shaft whirling*, London.

- [5] Eling, R., van Ostayen, R. and Rixen D. (2013): *Dynamics of Rotors on Hydrodynamic Bearings*, Proc. of COMSOL Conference, Rotterdam.
- [6] Fischer, J. and Strackeljan, J. (2006): *FEM-simulation and stability analyses of high speed rotor systems*, 7th IFToMM Conference on Rotor Dynamics, Vienna, Austria, Paper-ID 184.
- [7] Friswell, M. I. et al. (2010): *Dynamics of Rotating Machines*, Cambridge Univ. Press.
- [8] Fryšček, T. (2012): *Rotor dynamics of modern turbochargers*, **VII**(2), pp. 40-50.
- [9] Gasch, R., Nordmann, R. and Pfützner, H. (2002): *Rotordynamik*, Springer.
- [10] von Groll, G. and Ewins, D. J. (2000): *Frequency Domain Analysis in Rotor/Stator Contact Problems*, Seventh International Congress on Sound and Vibration, **4**, Paper 660, pp.1-8.
- [11] Gunter Jr., E. J. (1972): *Rotor-bearing stability*, Proc. of the First Turbomachinery Symposium, Texas A & M University Press, pp.119-141.
- [12] Jones, S. (2005): *Finite elements for the analysis of rotor-dynamic systems that include gyroscopic effects*, Ph.D. thesis, Brunel University.
- [13] Kessler, Ch. L. (1999): *Complex modal analysis of rotating machinery*, Ph.D. dissertation, Univ. of Cincinnati.
- [14] Nelson, F. C. (2007): *Rotor dynamics without equations*, Intl. Journal of COMADEM, **10**(3), pp. 2-10.
- [15] Nguyen-Schäfer, H. (2015): *Rotordynamics of Automotive Turbochargers*, 2nd Edition, Springer.
- [16] Parikyan, T. (2016): *Complex modes analysis for powertrain and driveline applications*, International Conference on Noise and Vibration Engineering (ISMA 2016), Paper No. 77.
- [17] Parikyan, T. and Resch, T. (2012): *Statically indeterminate main bearing load calculation in frequency domain for usage in early concept phase*, ASME Paper ICEF2012-92164.
- [18] *EXCITE™ Designer Theory Manual*, AVL (2018).
- [19] *Shaft Modeler with AutoSHAFT Users Guide*, AVL (2018).

Application of MADYN 2000 to rotor dynamic problems of industrial machinery

Joachim Schmied¹

¹ DELTA JS, CH-8005, Zurich, Switzerland, jschmied@delta-js.ch

Abstract

The special requirements of rotor dynamics engineering are illustrated by means of different examples of turbomachines. The properties of magnetic bearings and the more common fluid film bearings are pointed out in the examples of two turbo compressors. The importance of the correct consideration of bearing support properties is shown for a turbine generator train. The impact of seal forces is demonstrated for the turbo compressor supported on fluid film bearings. Two of the considered seals are honeycomb seals. Bearings and seals can have frequency and speed dependent characteristics; complex supports have non-negligible couplings between bearings and are frequency dependent as well. The consequences of the coupling of lateral and torsional vibrations in gears are illustrated for a gear compressor with three pinions. All examples have a practical background from troubleshooting and engineering work, although they do not exactly correspond to real cases.

Nomenclature

B	Width of bearings
d	Damping coefficient of bearings or seals
D	Diameter of bearings
	Damping ratio
f	Frequency
k	Stiffness coefficient of bearings or seals
m	Pad preload of fluid film bearings

1 Introduction

Rotors are structures with special properties due to their rotation (causing e.g. the gyroscopic effect), due to their bearings (fluid film bearings, magnetic bearings) and in many cases due to surrounding fluids (seal forces). Therefore, rotor dynamics requires special engineering tools although the structural properties of the rotors and their supports could well be modeled by any general finite element program.

Tools for rotor dynamics and bearings have been developed for many years. Nordmann, Nelson and Gasch introduced the finite element method to rotor dynamics (see [1] to [4]). Glienicke and Lund developed the basics for fluid film bearings (see [5] and [6]), which were further refined by many researchers.

The recent development of magnetic bearings, which are now more and more introduced in industrial applications of turbomachines, required an extension of existing rotordynamic tools to model the specific characteristics of this bearing type and the controllers. Spirig et al. [7] give insight into the control design process for three practical examples. This process has been further developed in the meantime and standards for design goals have been created as explained by Schmied et al. [8].

The bearing properties and resulting rotor dynamic behaviors for support on classical tilting pad fluid film bearings and magnetic bearings are illustrated for two turbo compressor examples.

The impact of the dynamics of a casing as bearing support is shown for the example of a turbine generator train with fluid film bearings.

The interaction of fluid forces in seals with rotors has been investigated by Nordmann [9] and Childs [10] to name two of the most well-known researchers in this area. A few years ago, fluid forces were mainly modeled as stiffness and damping coefficients. Recently it is more and more recognized thanks to more sophisticated analysis tools and measurements, that this approach is too restrictive. Honeycomb seals for example can have more complex

frequency dependent characteristics as shown by Kleynhans et al. [11]. Still, the rotor dynamic tools for the consideration of fluid forces are not as established as for fluid film bearings and strongly simplified engineering approaches are frequently used, for example the procedure described in the standard by the American Petroleum Institution [12] as stability level I analysis. In this paper an approach is described for a high-pressure turbo compressor, which could be used as stability level II analysis.

In train arrangements with gears the lateral and torsional vibrations are coupled. The influence of this coupling, which is not considered in standard analyses, is shown for a gear compressor.

All analyses in this paper were carried out with the general rotor dynamic program MADYN 2000. Its capabilities are described in detail by Schmied in [13]. The fluid film bearing module in MADYN 2000 is based on more than 30 years research in the German consortium FVV (Forschungsvereinigung Verbrennungskraftmaschinen / Research Association for Combustion Engines). Fuchs [14] comprehensively describes the status at the beginning of the century, which has been further developed, but basically is still valid today. The magnetic bearing module has been developed over several years based on practical needs starting with the industrial applications of magnetic bearings in turbo compressors. The developers of the module were involved from the very beginning of this area. Early applications are described by Schmied and Nijhuis et al. in [15] and [16].

2 Description of the examples

Four rotor arrangements are considered in this paper, which are described in the following chapters.

The rotor structures are modeled with finite elements according to the Timoshenko beam theory considering the shear deformation and gyroscopic effects as described by Nordmann [1], Nelson et al. [2], Gasch [4], Lund et al. [6] and Krämer [17]. Each cross section can consist of superimposed cross sections with different mass and stiffness diameter as well as different material properties. The contours shown in the rotor plot represent the resulting mass diameter with the density of the basis cross section, which is normally steel.

Stiff shrunk parts on the rotor, e.g. impellers, can be modeled as rigid parts. They are represented by mass, equatorial and polar moments of inertia. In the rotor plots they are drawn as equivalent disks. In case only the mass is given and no moments of inertias they are drawn as spheres. These parts can be fixed rigidly to the shaft, or if necessary, flexibly for example to consider disk or blade vibration modes. To model a blade mode, it may be necessary to split the mass into a rigidly mounted mass and a flexibly mounted mass representing the effective modal mass.

Several analytical results of the examples will be shown: Campbell diagrams, i.e. damped natural vibration modes at different speeds, and the response to unbalance loads. The damping in the Campbell diagrams is described as damping ratio, which can easily be transformed to an amplification factor in resonance. The damping from the Campbell diagram is unequivocal and accurate in contrast to the damping from an unbalance response received by the half power width method, as it is described in for example in the standard American Petroleum Institution [12]. The stability can also be assessed by the damping ratio; an unstable rotor has a negative damping ratio.

2.1 Turbo compressor supported on fluid film bearings with seals

The model of the turbo compressor is shown in figure 1. Its maximum speed is 12'000 rpm and the total rotor weight 220 kg. This example will also be used to demonstrate the impact of seal fluid forces. The location of the two considered labyrinth seals and honeycomb seals with the highest gas density are shown in the figure.

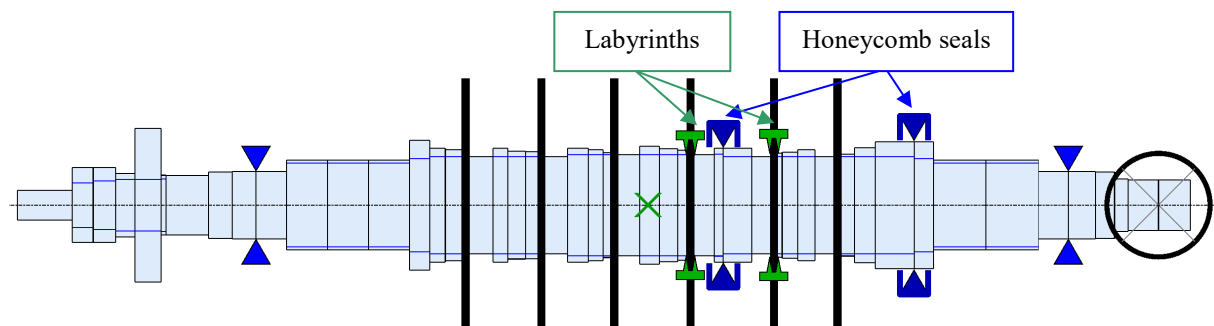


Figure 1: Compressor rotor on fluid film bearings with seals.

The geometry of the 4 tilting pad bearings is illustrated in figure 2. The bearing has a load between pads arrangement. The pads have a central support.

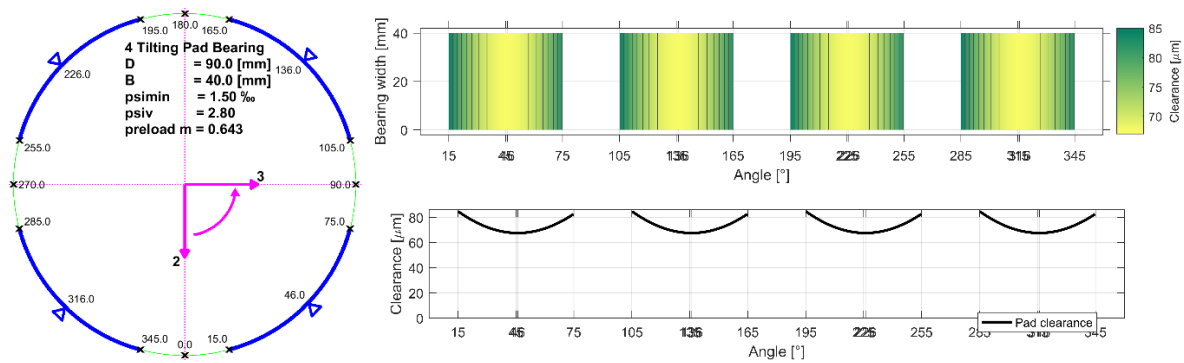


Figure 2: Radial fluid film bearing geometry and clearance plot.

2.2 Turbo compressor on magnetic bearings

The model of the turbo compressor is shown in figure 3. Its maximum speed is 12'600 rpm and the total rotor weight 550 kg. The bearings are represented by their sensor and actuator. The triangle in the plot indicates the actuator location, the bar the sensor location.

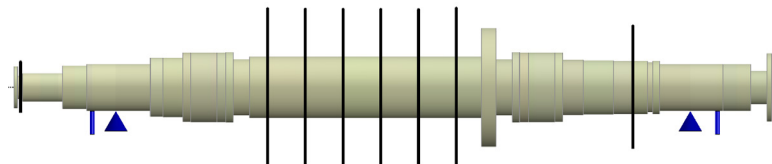


Figure 3: Turbo compressor on magnetic bearings.

2.3 Turbine generator train

The model of the turbine generator train is shown in figure 4. Its nominal speed is 3'000rpm. Turbine and generator are supported on fixed pad fluid film bearings.

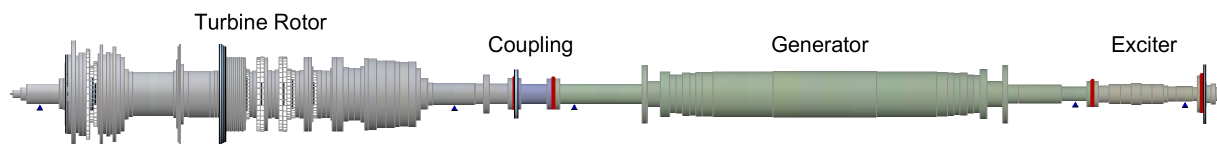


Figure 4: Turbine generator shaft train.

The turbine rotor casing is considered as a state space model, which is gained from the natural modes of a finite element model of the casing. The method is described by Krüger in [18]. In the present case ANSYS was used to receive the state space matrices in a so called spm-file, which can directly be imported to MADYN 2000 as explained by Schmied in [19]. When importing the state space matrices to MADYN 2000 a structural damping can be defined, in our example it is 1%. The ANSYS system does not have any damping. The amplitudes of the transfer functions of the coupled turbine casing can be seen in figure 5.

Each column in figure 5 corresponds to the location/direction of an excitation and each row to the location/direction of the response. Locations are the turbine NDE (left, STA 4) and DE (right STA 100) bearings and directions are 2 (vertical) and 3 (horizontal). The couplings of the casing between the two bearings are rather strong, i.e. their amplitude has the same order of magnitude as the amplitude of the direct transfer functions on the diagonal, whereas the couplings between the directions is weak.

The generator and exciter have simple spring, mass supports. Each support has a resonance in horizontal and vertical direction in the range of three times operating speed. Such support models are used in traditional rotor dynamic analyses. In case a support has only one relevant resonance in each direction and the coupling between supports is negligible, such a model is sufficient.

For the turbine such a support model was also used originally. It proved to be insufficient as we will see later in this paper.

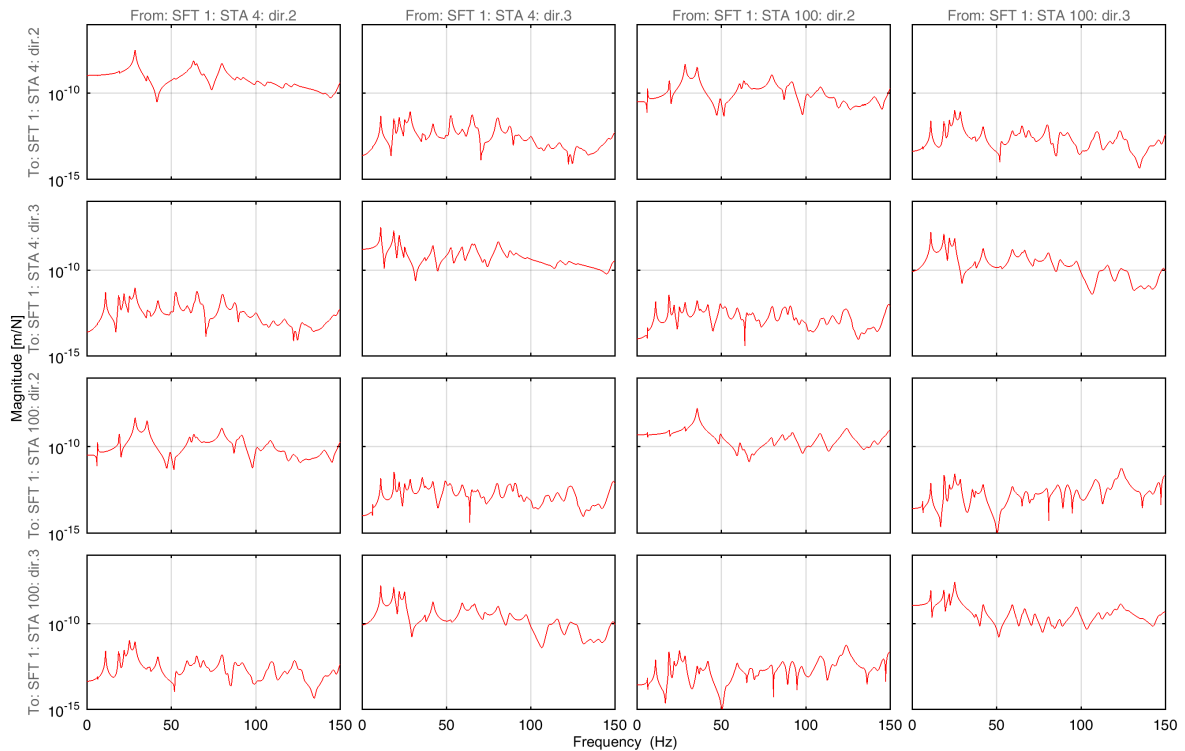


Figure 5: Transfer functions of the turbine casing.

In a shaft train consisting of two rotors with two bearings each and coupled with a solid coupling the static bearing load and thus the bearing characteristics depend on the alignment, which may change due to thermal growths of supports and casings. MADYN 2000 allows static analyses for different alignments and finding an optimal alignment for minimum forces in the coupling flanges. In this example the influence of different alignments is relatively small due to the high weight of the rotors and the flexibility of the solid coupling.

2.4 Gear compressor

The model of the gear compressor consisting of a bull gear and three pinions is shown in figure 7. All rotors are supported on fluid film bearings, the pinions on tilting pad bearings and the bull gear on cylindrical bearings. The meshing is modelled as explained in the figure next to the model plot. The spring is aligned with the tooth contact force. Its direction is indicated by the magenta line.

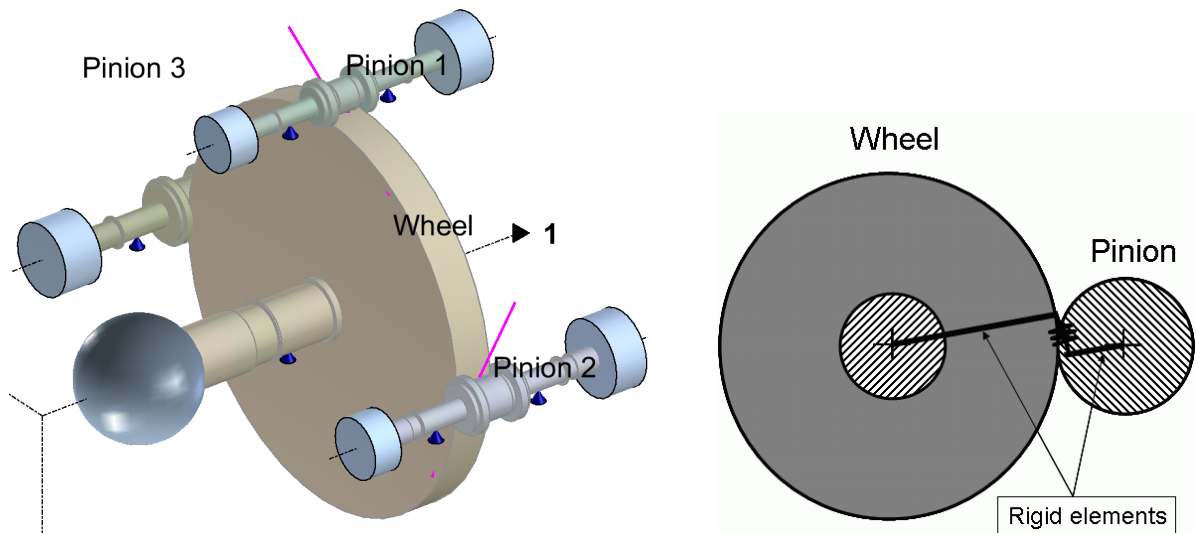


Figure 6: Gear compressor with explanation of the gear mesh model.

3 Rotor dynamic behaviour with fluid film bearings and magnetic bearings

3.1 Rotor on fluid film bearings

The stiffness and damping coefficients of the fluid film bearings in the 2-3 coordinate system of figure 2 are shown in figure 7 together with the static position in the bearing at different speed (Gümbel curve). Due to the pad arrangement the bearing is isotropic, i.e. the coefficients in 2- and 3-direction are equal. Moreover, there are no cross-coupling terms. The coefficients of the two bearings are almost the same. For this reason, the results of only one bearing is shown.

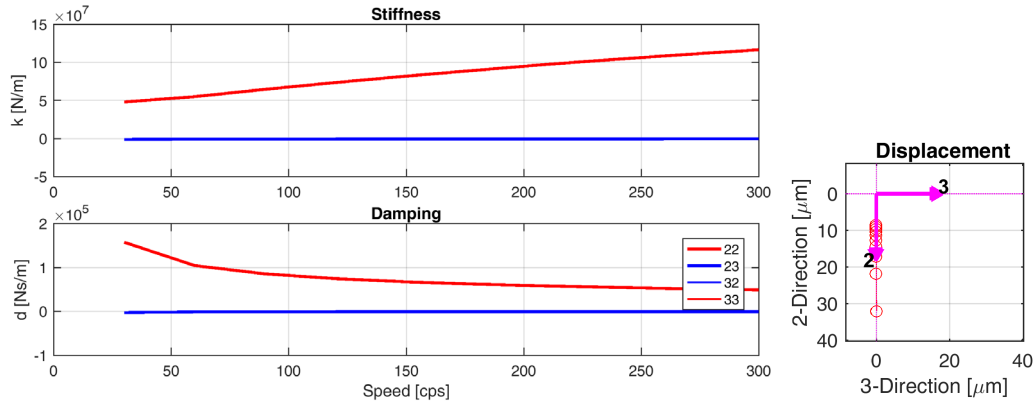


Figure 7: Stiffness and damping coefficients of the fluid film bearing with Gümbel curve.

The coefficients of fluid film bearings are load dependent (the load in the present case is the rotor weight) and speed dependent. However, for tilting pad bearings they can additionally be frequency dependent, i.e. the stiffness and damping at a certain speed for vibrations with non-synchronous frequencies is different. This effect can be considered by a full model of the tilting pad bearing, i.e. keeping the tilting angles in the bearing model and not reducing them, what is normally done under the assumption, that tangential pad forces are negligible. A full model can be represented in state space form with the rotor displacement and velocities as inputs, the radial forces as outputs and the pad tilting angles and their derivatives in time as states. More details are described by Schmied et al. [20]. The non-synchronous coefficients of the same bearing at the nominal speed of 210 rps are shown in figure 8. The synchronous coefficients are highlighted with data tips. They correspond to the coefficient in figure 7 at 210 cps. For lower frequencies at this speed the stiffness increases and the damping decreases. These trends tend to reduce the damping of modes in the sub-synchronous frequency range.

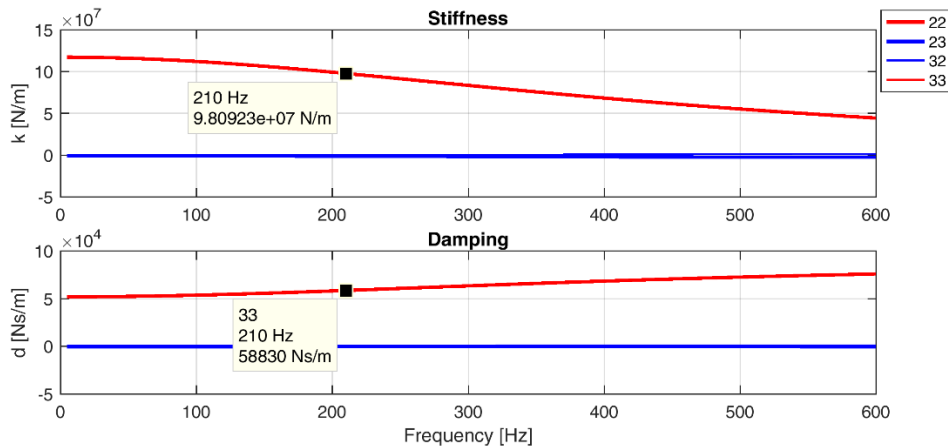


Figure 8: Non-synchronous stiffness and damping coefficients at nominal speed of 210 rps.

The Campbell diagram (natural frequencies and damping ratios as a function of speed) calculated with the full model i.e. correct non-synchronous characteristics is shown in figure 9. The dashed line for the damping is for mode 2 calculated with bearing coefficients neglecting the frequency dependence, i.e. in the traditional way. It can be seen, that the damping with the correct non-synchronous characteristics is indeed lower at nominal speed, as expected from the trends in figure 8. The damping reduces from 10.6% to 8.2%.

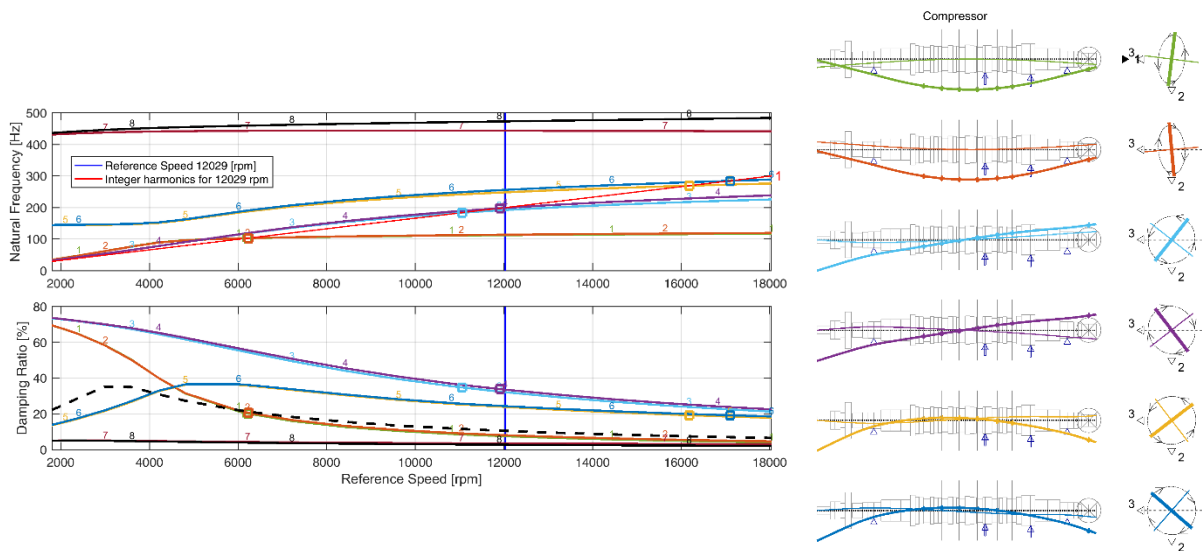


Figure 9: Campbell diagram (dashed line damping mode 2 with syn. coeff.) and mode shapes in critical speeds

The mode shapes in critical speeds can also be seen in figure 9 in compact form. MADYN 2000 has another 3-dimensional presentation of modes. In the compact form they are shown in two planes at the instant when the maximum deflection occurs. The first plane is determined by the maximum deflection and the rotor axis and the second plane is perpendicular to this plane. The first plane is indicated by the bold line in the 2-3 coordinate system and the second plane by the thin line. The whirling direction is also indicated in the figure. A circular forward whirling orbit has the value +1 and a circular backward whirling mode the value -1. Elliptic orbits have values between 0 and +1 and -1 respectively.

The rotor runs clearly above its first bending. The tilting mode is very close to the nominal speed. It has a large damping ratio of more than 30%, thus this resonance is not a problem. Standards such as API allow running in a resonance, if the damping is above 20% corresponding to an amplification factor smaller than 2.5.

3.2 Rotor on magnetic bearings

In figure 10 the bearing characteristics of the magnetic bearings are shown as transfer functions describing the relation between the rotor displacement at the sensor and the actuator force. The characteristics are highly frequency dependent. However, they do not change with speed. The hardware consisting of sensor, amplifier and actuator, the controller and digitization effects are included in the transfer functions. The hardware causes a continuous phase lag with increasing frequency, i.e. a reduction of damping. The ranges with bold lines indicate where the bearings have a damping characteristic (phase angles between 0 and 90 degree or below -180 degree). The eigenvalues (natural frequency and damping ratio) of the complete system (bearing and rotor) at maximum speed are also shown in figure 10. The transfer functions are determined to a large extent by the controllers. The design of a controller requires extensive engineering effort. It is described for example by Schmied et al. [8]. Goals of the design are to receive a robust, stable system with enough damping in the speed range. Robustness must be fulfilled against system changes (the model deviates to some extent of the real system) and against noise in the magnetic bearing system, which requires the gain to remain below a certain level.

The mode shapes in two perpendicular planes as described for figure 9 are shown in figure 11. The shapes move on circles, because the bearings are completely isotropic.

It can be seen, that all modes below maximum speed are well damped and that all modes in the higher frequency range are stable. Some modes are not determined by the rotor but by the controller, which augments the system and causes additional modes.

Compared to the rotor on fluid film bearings the behaviour is quite different. There are two pairs of forward and backward whirling well damped rigid body modes at low frequencies. They appear due to low bearing stiffness in this frequency range, which can be recognized in the transfer function in figure 10. The transfer function has a value well below 10^8 N/m. This is lower than the stiffness of the fluid film bearing of the other rotor, despite the fact, that the rotor for fluid film bearings is considerable smaller. The first bending modes occur at 155Hz and 162Hz, respectively. Their shape corresponds more to a free - free bending mode shape. In the present case this mode is within the speed range and the damping of more than 20% allows running in resonance.

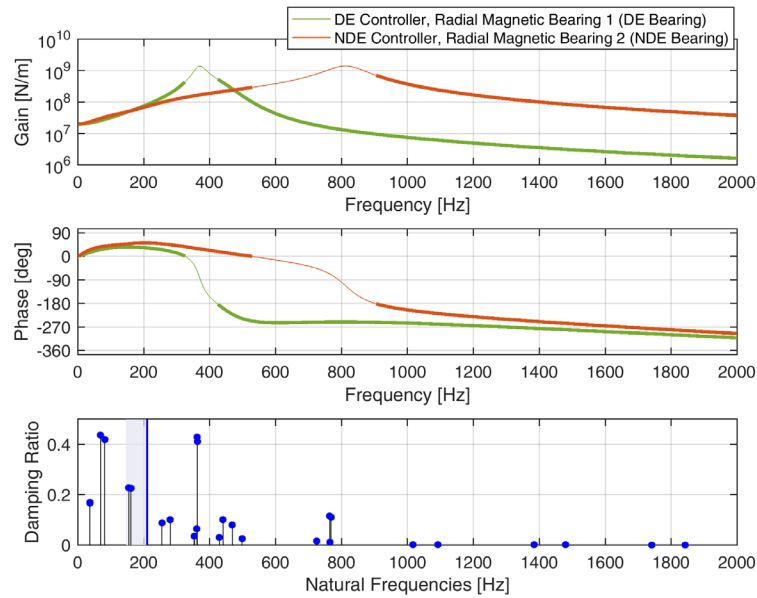


Figure 10: Magnetic bearing transfer functions and eigenvalues (damping and natural frequencies)

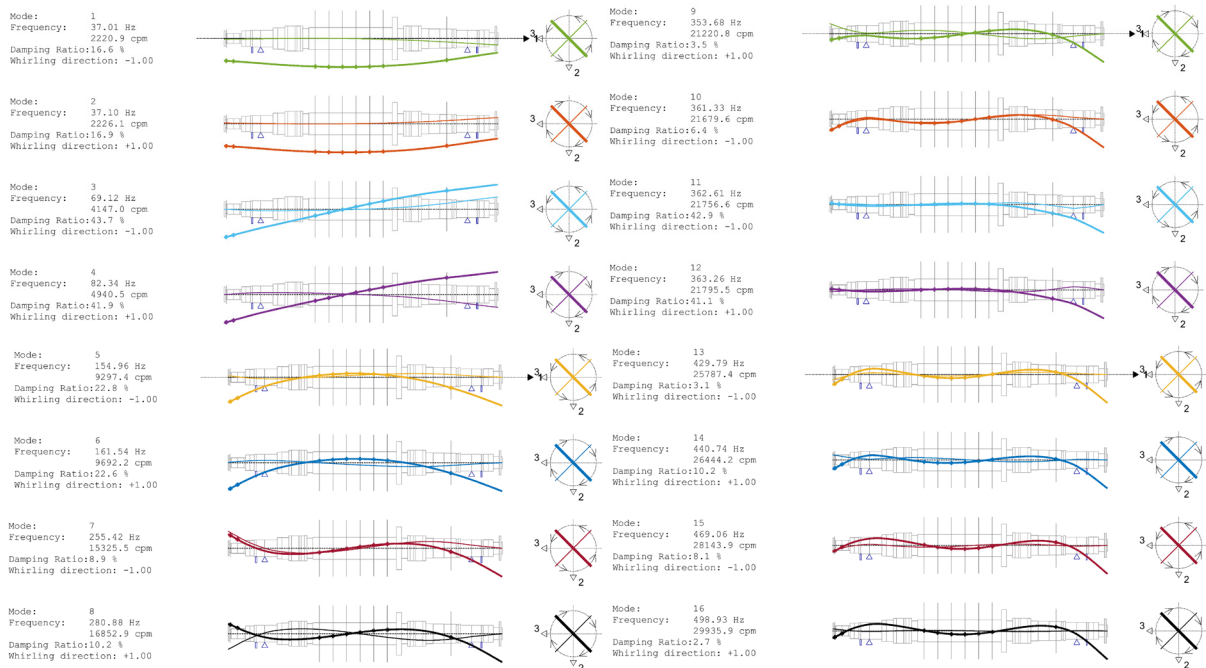


Figure 11: Natural modes nominal speed.

4. The influence of bearing supports

The Campbell diagram of the turbine generator shaft train including the turbine casing and the spring mass supports for the generator and exciter bearings is shown in figure 12. The number of modes is huge, because the system has many turbine casing modes. Some of the turbine modes couple with the rotor, some not. In figure 12 two examples of modes in critical speeds are shown: one mode which is mainly a casing mode, and another coupled rotor casing mode. The casing mode has no relative displacement between rotor and casing displacement in contrast to the coupled mode. Casing modes are also characterized by their damping of 1%, which is the structural casing damping. Casing modes, which couple with the rotor, have a different damping; normally it is higher, because some of the bearing damping is transferred.

The Campbell diagram of a coupled rotor casing systems can be complex. Unbalance response analyses are a big help to find the relevance of modes and their resonances. Some of the casing modes for example may be difficult to excite, due to their shape or due to their big effective mass. The relative vibrations at the turbine bearings of a response to an unbalance are shown in figure 13 for the model with the complex casing characteristics and a

model with simple bearing support. A comparison of the two responses reveals the importance of a correct casing model. The resonances are completely different. The traditionally still widely used simple supports are not always suitable.

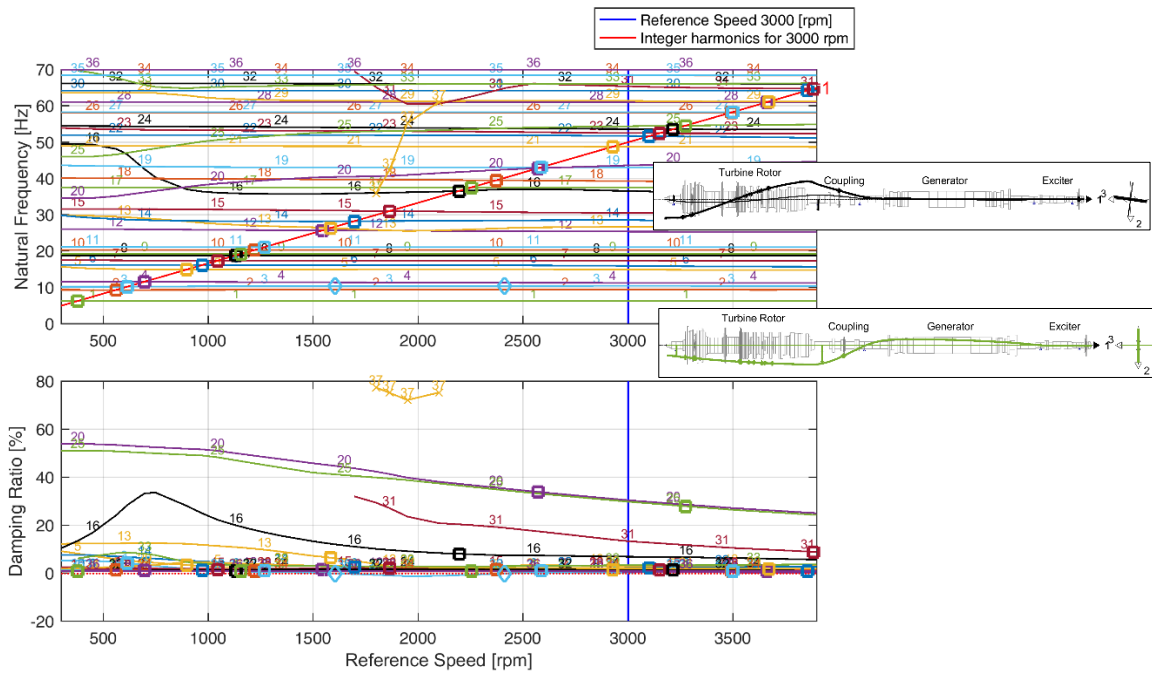


Figure 12: Campbell diagram with two exemplary critical mode shapes (dominated by casing and coupled).

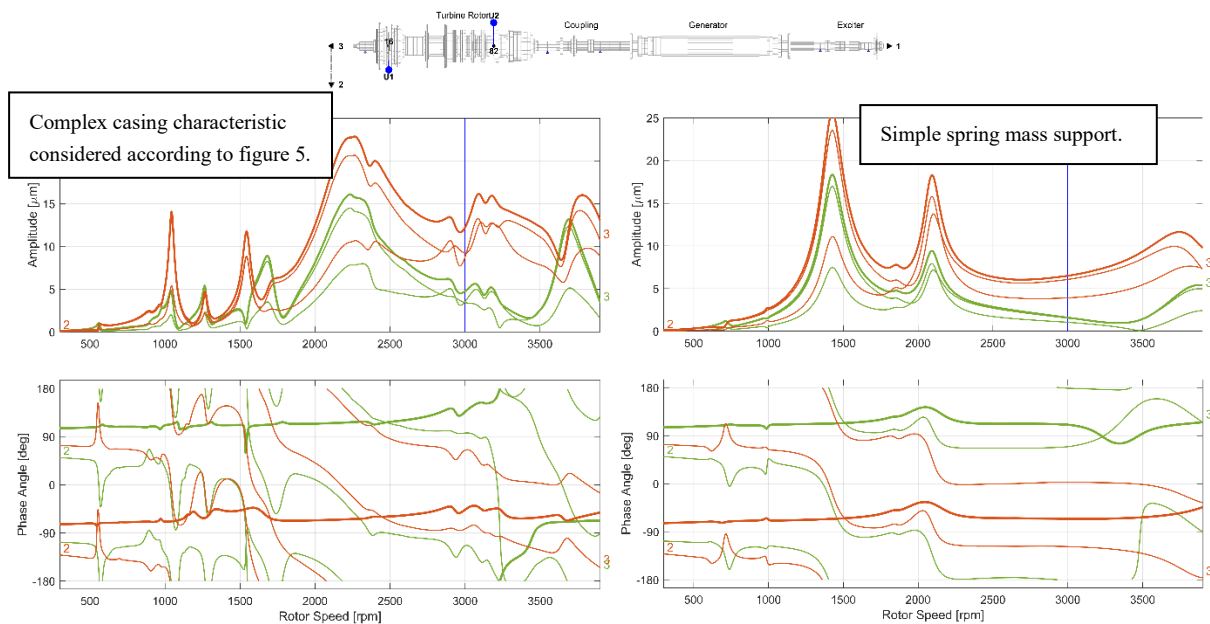


Figure 13: Unbalance load and response (relative vibrations at turbine bearings).

5. The impact of seal forces

The tangential and radial seal forces of the labyrinths of the rotor in figure 3 for a circular unit shaft orbit are shown in figure 14. They are the forces from the seal on the rotor, i.e. positive tangential forces destabilize forward whirling modes and positive radial forces are in the same direction as the orbit radius, i.e. they bring the rotor out of centre and thus soften the system.

The labyrinth seal forces were calculated with a Navier Stokes solver described by Weiser in [21]. The tangential as well as radial force show a slight curvature caused by inertia effects. To include them in the model, mass coefficients are necessary. In the present case the inertia effect is small.

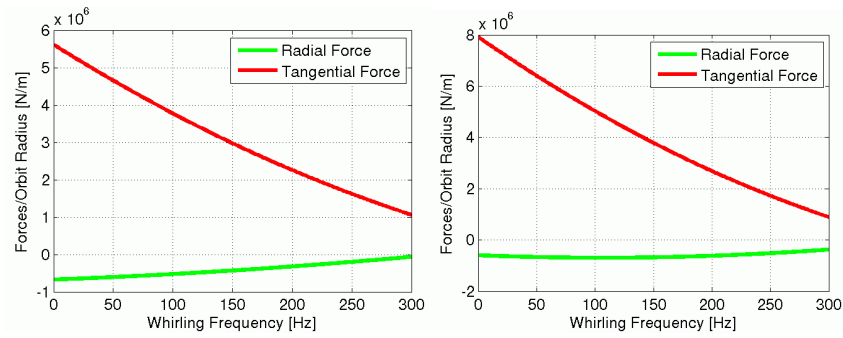


Figure 14: Radial and tangential labyrinth seal forces

The frequency at which the tangential force is zero, the so-called swirl frequency, allows a rough assessment, which rotor modes are destabilized by the seals: Forward whirling modes with lower frequencies will be subjected to a damping reduction. For the labyrinth seals this frequency is beyond the shown frequency range to 300Hz.

The honeycomb seal forces in figure 15 for circular backward (neg. frequency) and forward (pos. frequency) orbits are strongly frequency dependent. They were calculated according to the method described by Kleynhans in [11] and cannot be simply modelled by stiffness, damping and mass coefficients. They must be modelled by transfer functions in a similar way as magnetic bearings.

The swirl frequencies of the balance piston and interstage seal are around 50Hz and 70Hz, respectively.

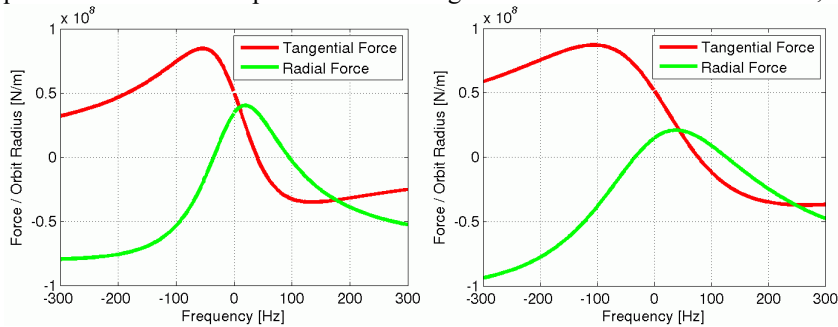


Figure 15: Radial and tangential honeycomb seal forces

The eigenvalues of the system with and without the seals are shown in figure 16. The seals are considered in two steps for a better interpretation of the results. In a first step only the labyrinth seals are considered and in a second step all seals.

The labyrinth seals mainly influence the forward and backward whirling first bending mode. The damping of the forward mode is decreased, of the backward mode increased. The other modes are almost not affected.

The impact of the honeycomb labyrinth seals is very big in a frequency range up to 250Hz. The system with honeycomb seals is well damped. This is due to the large stiffening effect at higher frequencies (negative radial force) and the relatively low swirl frequency.

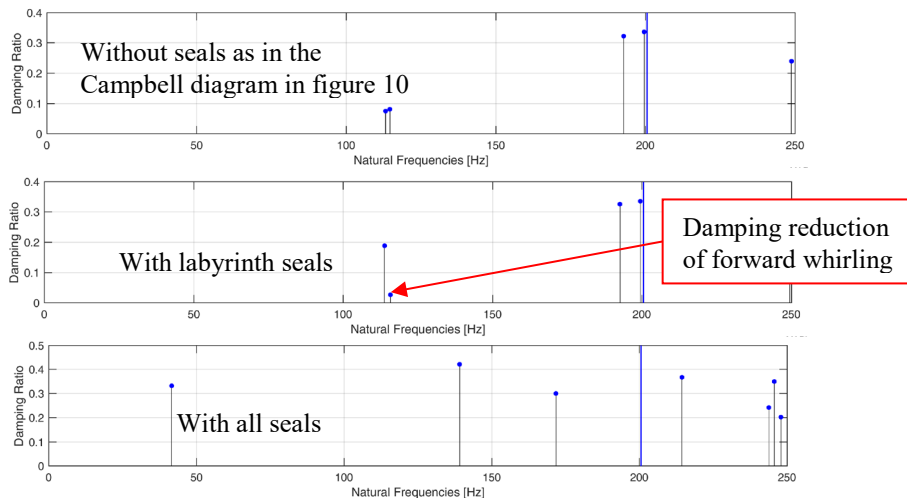


Figure 16: Eigenvalues at nominal speed without and with consideration of seal forces

6. Coupling of torsional and lateral vibrations in gears

The coupling of lateral and torsional vibrations in gears is normally not considered. An additional coupling with axial vibrations can also occur. Lateral torsional coupling is of interest for the following reasons:

Due to the lateral vibration component the radial bearings can influence the damping of the torsional vibration modes. Normally they add damping, but they can also destabilize as reported for example by Viggiano et al. in [22]. This reference also contains a comparison of measured and calculated stability thresholds, verifying this type of analysis.

Lateral excitations such as the unbalance can excite torsional vibrations and vice versa torsional excitations excite lateral vibrations. By means of a coupled model this can be simulated.

The natural vibration modes of a lateral torsional coupled model can be different from those of the decoupled systems. For our example this is shown in figure 17, where a selection of modes of the standalone pinion 1 are shown together with modes of the coupled system, which are dominated by this pinion.

Some modes practically do not change due to the coupling as the mode at 118 Hz. On the other side completely new modes can appear as the mode at 173 Hz and modes can couple as the torsional mode at 345 Hz and the lateral mode at 419 Hz of the pinion, which are combined to a coupled lateral torsional mode at 360 Hz.

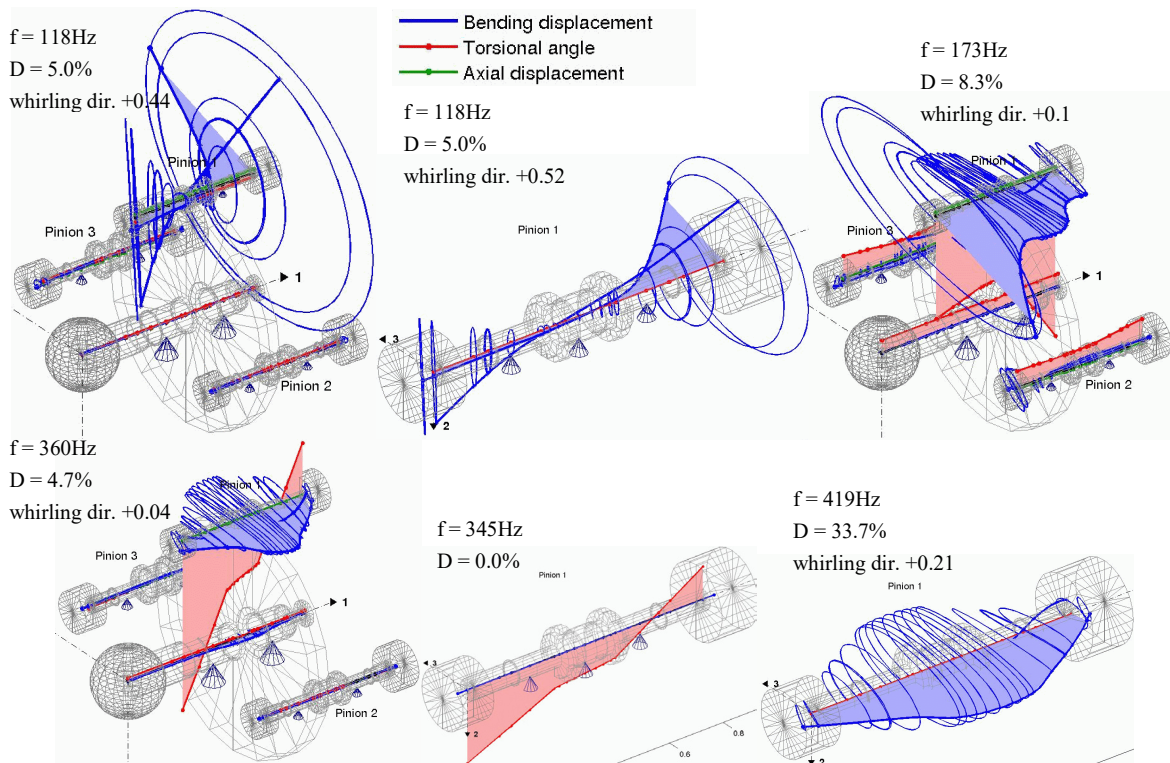


Figure 17: Lateral and torsional modes of pinion 1 of the coupled and uncoupled system

7 Conclusion

The requirements of a modern tool for rotor dynamic analyses are demonstrated for four examples, covering different types of bearings, the influence of casing dynamics, seal forces acting on rotors and coupled vibrations as they can occur in gears.

Some of the requirements are new due to new bearing technologies (e.g. magnetic bearings) or new research results (e.g. the frequency dependence of seal forces and tilting pad bearings). In both cases the forces caused by rotor displacements are strongly frequency dependent and cannot be simply modelled by stiffness, damping and mass coefficients.

To cover these needs MADYN 2000 uses state space representation for frequency dependent bearings. State space matrices are also used for the import of complex support structures. For support structures the input to the system are forces and the outputs displacements and velocities, whereas for the bearings the inputs are displacements and velocities and the outputs forces.

References

- [1] Rainer Nordmann (1974). *Ein Näherungsverfahren zur Berechnung der Eigenwerte und Eigenformen von Turborotoren mit Gleitlagern, Spalterregung, äusserer und innerer Dämpfung*. Dissertation Technische Hochschule Darmstadt.
- [2] H.D. Nelson, J.M. McVaugh (1976). The Dynamics of Rotor-Bearing Systems using Finite Element. *ASME Trans., Journal of Industry*, Vol. 98(2), pp.593-600.
- [3] H.D. Nelson (1980). A Finite Rotating Shaft Element using Timoshenko Beam Theory. *Trans. ASME, Journal of Mechanical Design*, Vol. 102(4), pp.793-803.
- [4] Rainer Gasch (1976). Vibration of Large Turbo-Rotors in Fluid Film Bearings on an Elastic Foundation. *Journal of Sound and Vibration*, Vol. 120, pp.175-182.
- [5] Joachim Glienicke (1966). *Feder- und Dämpfungskonstanten von Gleitlagern für Turbomaschinen und deren Einfluss auf das Schwingungsverhalten eines einfachen Rotors*. Dissertation Technische Hochschule Karlsruhe.
- [6] J. Lund, K. Thomsen (1978). A Calculation Method and Data for the Dynamics of Oil Lubricated Journal Bearings in Fluid Film Bearings and Rotor Bearings System Design and Optimization. *ASME*, New York (1978), pp. 1-28.
- [7] M. Spirig, J. Schmied, P. Jenckel, U. Kanne (2002). Three Practical Examples of Magnetic Bearing Control Design Using a Modern Tool. *ASME Journal of Engineering for Gas Turbines and Power*, October 2002, Vol. 124, pp. 1025-1031.
- [8] J. Schmied, A. Kosenkov (2013). Practical Control Design for Rotor on Magnetic Bearings by Means of an Efficient Tool. *Proceedings of ASME Turbo Expo*, San Antonio, Texas, USA.
- [9] R. Nordmann, F.J. Dietzen (1987). Calculating Rotordynamic Coefficients of Seals by Finite-Difference Techniques. *ASME Journal of Tribology*, July 1987, Vol. 109, pp. 388-394.
- [10] Dara Childs (1993). *Turbomachinery Rotordynamics*. Wiley Inter Science Publication, New York, Chichester, Brisbane, Toronto, Singapore.
- [11] G.F. Kleynhans, D. Childs, (1996). The Acoustic Influence of Cell Depth on the Rotordynamic Characteristics of Smooth Rotor / Honeycomb-Stator Annular Gas Seals. *ASME paper No. 96-GT-122*, presented at the ASME Turbo Expo, Birmingham, UK, 1996.
- [12] American Petroleum Institution (2002). Axial and Centrifugal Compressors and Expander-compressors for Petroleum, Chemical and Gas Industry. *API Standard 617*, 7th edition.
- [13] Joachim Schmied (2017). *MADYN 2000 Documentation Version 4.4*. Internal document DELTA JS, Zurich, Switzerland.
- [14] Andreas Fuchs (2002). *Schnellaufende Radialgleitlagerungen im instationären Betrieb*. Dissertation Technische Universität Braunschweig.
- [15] Joachim Schmied (1990). Experience with Magnetic Bearings Supporting a Pipeline Compressor. *Proceedings 2nd Symposium on Magnetic Bearings*, Tokyo, Japan.
- [16] A.B.M. Nijhuis, J. Schmied, R.R. Schultz (1999). Rotordynamic Design Considerations for a 23MW Compressor with Magnetic Bearings. *IMEchE Fluid Machinery Symposium*, The Hague, Netherlands.
- [17] Erwin Krämer (1984). *Maschinendynamik*. Springer Verlag, Berlin, Heidelberg, New York, Tokyo.
- [18] Thomas Krüger, Sauro Liberatore, Eric Knopf (2013). Complex Substructures And Their Impact On Rotordynamics. *Proceedings of SIRM 2013 – 10th International Conference on Vibrations in Rotating Machines*, Berlin, Germany.
- [19] Joachim Schmied, Marco Perucchi (2017). Coupled Rotor-Bearing-Casing Analysis. *22nd Swiss CADFEM ANSYS Simulation Conference*, Switzerland.
- [20] J. Schmied, A. Fedorov, B.S. Grigoriev (2010). Non-Synchronous Tilting Pad Bearing Characteristics. *Proceedings of the 8th IFTOMM International Conference on Rotordynamics*, KIST, Seoul, Korea.
- [21] H.P. Weiser (1989). *Ein Beitrag zur Berechnung dynamischer Koeffizienten von Labyrinthdichtungssystemen bei turbulenter Durchströmung mit kompressiblen Medien*. Dissertation TU Kaiserslautern.
- [22] F. Viggiano, J. Schmied (1996). Torsional Instability of a geared compressor shaft train. *IMEchE paper C508/013*.

Vibration analysis of a rotor of an electrical rotating machine with stochastically distributed input parameters

Marcel S. Prem¹, **Michael Klanner**², **Katrin Ellermann**³

¹ Institute of Mechanics, Graz University of Technology, Austria, marcel.prem@tugraz.at

² Institute of Mechanics, Graz University of Technology, Austria, michael.klanner@tugraz.at

³ Institute of Mechanics, Graz University of Technology, Austria, ellermann@tugraz.at

Abstract

In modern engineering, the use of advanced materials is state of the art. Due to material combinations and complex manufacturing processes, calculations based on constant input values are not very accurate. In electrical machines, especially in the laminated rotor stack, different materials are used. Due to the manufacturing process, the steel sheets in the rotor stack are not perfectly planar. This, as well as the resin and air in the gap, affects the contact conditions between the different sheets of the stack. As a result, the stiffness of the stack may show significant local fluctuations, which influences the dynamic properties.

This paper analyzes the influence of the Young's modulus of the laminated rotor stack by varying one specific parameter in the rotor stack. Afterwards, heterogeneous material parameter series are generated by a series expansion method called Karhunen-Loève expansion. The series with different statistical attributes are used as input parameters. To determine the influence of the variations of the input parameters, a modal analysis is used to analyze the eigenfrequencies, especially the first bending mode. The numerical model is a 3D FE model with about 1.5 million nodes.

The aim of the paper is to show the influence of the Young's modulus on the eigenfrequency. Furthermore, the heterogeneity is represented in contrast to the homogeneous reference calculation. The influence of the deviation of the series along the rotor and the mathematical method to describe the resulting value of a heterogeneous system is shown.

Nomenclature

$\xi(\theta)$	Random variable
μ	Mean value of random variables
σ^2	Variance of random variables
σ	Standard deviation of random variables
\mathbf{x}	Position vector in the random field
$C_{HH}(\mathbf{x}, \mathbf{x}')$	Autocovariance function of two local positions
$\rho(\mathbf{x}, \mathbf{x}')$	Correlation function
$H(\mathbf{x})$	Random field
λ	Eigenvalue
$\phi(\mathbf{x})$	Eigenfunction
δ	Kronecker delta

1 Introduction

Modal analysis of electrical machines, especially of the rotor, is a very common technique in the design phase of a machine. Different material combinations in the rotor, especially in the laminated rotor stack, and the manufacturing processes lead to varying parameters. Due to the lamination, the stiffness parameters of the laminated rotor stack is significantly less than the parameters of the solid component [2]. With respect to the combination of materials, the influence of Young's modulus on the eigenfrequencies need to be determined. In practice, these fluctuations of parameter values in the laminated rotor stack are often neglected.

After the examination of the basic influence of the Young's modulus on the eigenfrequencies, the influence of the deviation of the parameter needs to be determined. During the last decades, one method called Monte Carlo Simulation (MCS) became increasingly popular for the investigation of systems with random influences. MCS was developed in the 1940's [10] and uses variable input parameters, which are constant (homogeneous) along the model, to describe the statistical behavior of the model. Modelling each steel sheet and its contact conditions separately would result in a very large computational effort. In order to reduce this to a manageable load, a homogenization of the rotor is used. Therefore, constant input parameters with a statistical distribution are generated. A large number of input parameters is needed to describe the statistical properties correctly. These requirements increase the computational load for detailed MCS enormously.

Increasing computational performance and mathematically advanced methods allow for the calculation of more physically realistic models with a manageable effort. In the following, MCS is used in two ways: first, a "homogeneous model" is analyzed in order to derive basic dynamical features of the rotor. In a second step, local parameter fluctuations are included to analyze the effect of local parameter changes on the dynamics. We will call the later the "heterogeneous model". If fluctuations are taken into account, several possibilities to generate fluctuating random fields exist. A random field is a parameter configuration of variable values, which follows a mathematical description. The process of the generation of a random field is named discretization. A discretization method is a mathematical process to simplify a complex system to a mathematical system by approximation. Sudret and Der Kiureghian divide the possibility of representing heterogeneity (generate random fields) in three main categories [13] named point discretization methods, average discretization methods and the series expansion methods.

Point discretization methods use single random variables to describe a part of a global domain. A representative method for this type of discretization is the so called midpoint method. It was introduced by Der Kiureghian and Ke (1988) [1]. The method uses one single random variable to describe one subdomain, which is a spatial division of the global domain. The random variable is located in the centroid of the local subdomain. This method uses standard random variables to illustrate the stochastic influence. The advantages are the simple generation of a random variable and the fast implementation of the system. The disadvantages are the non-linked variables and the high load of preliminary work. Based on the non-linked random variables, systems, which are physically not realistic, can be generated. The high preliminary work is caused by the knowledge of the system and the individually generation of random fields. For example, if the system varies, the whole random field must be generated again.

Average discretization methods use a high number of random variables to include all the information of the statistics. To minimize the computational load, the values are averaged. A representative method of this kind of discretization is the so-called spatial average method, which was introduced by Vanmarcke and Grigoriu (1983) [15]. This method divides a global domain into subdomains. Afterwards, the random variables are generated along the global domain. As a simplification, all variables inside one subdomain are averaged. Based on the values near the edges of the subdomain, a small influence of the variables between two neighboring subdomains is given.

Series expansion methods were presented by Spanos and Ghanem (1989) [12], Zhang and Ellingwood (1994) [16] and Li and Der Kiureghian (1993) [5]. They are based on continuous parameter distributions. The initial point of series expansion methods are the correlation functions. These functions represent the correlation, and furthermore the manipulation, of two points in a domain. Li and Der Kiureghian (1993) give an overview of the most important correlation functions in [5]. For example, in the Karhunen-Loève expansion method Spanos and Ghanem (1989) used the decomposition of the correlation function to generate weighting factors and distribution functions. Based on this information the series expansion is formed, which reflect the variation of the parameters. The values along the series are controlled by the correlation function. Based on this advantage, physically realistic systems are generated. The size of a system has no influence on the generated random fields due to the effect of the continuous series generation. A disadvantage is the high effort to generate random field series.

2 Theoretical background

In this section, the theoretical background of Gaussian distributed random fields and series expansions is explained. First, a short overview of Gaussian distributed random variables is given and the series expansion is explained in detail, focusing on the decomposition and the generation of the series.

2.1 Gaussian distributed random fields

A Gaussian random variable ξ is a variable depending on the Gaussian distribution function [14]

$$f_{\xi}(\xi; \mu, \sigma) = \frac{1}{\sqrt{2\pi\sigma^2}} \exp\left(-\frac{(\xi - \mu)^2}{2\sigma^2}\right), \quad \xi \in \mathbb{R} \quad (1)$$

where μ is the mean value and σ^2 is the variance. A random field is generated by a discretization method. A discretization method is a mathematical process to simplify a complex system to a mathematical system by approximation. Sudret and Der Kiureghian [13] categorize this methods as point discretization method, average discretization method and series expansion method. Further series expansion methods will be explained in detail.

2.2 Series expansion methods

There are several methods to generate random fields. In this paper, the fluctuation of the input parameter (random field) is generated by a series expansion method called Karhunen-Loève expansion (KLE). The main advantage of series expansion methods is the continuity and the resulting independence of the numerical system. Discrete methods need information on the size of the system and the number of divisions to generate a suited random field. Series expansion methods generate continuous series independence of the numerical system. Another advantage of series expansion methods is the correlation between the values inside the series. Hence, physically systems can be generated, while unsteady behavior can exist in discrete random fields.

The KLE was developed by Karhunen (1947) [4] and Loève (1948) [6]. Spanos and Ghanem introduced the method for engineering problems (1989) [12]. The KLE is a method to represent random fields as continuous series based on a linear combination of orthogonal functions. These functions are the eigenfunctions of a Fredholm integral equation resulting from the spectral decomposition of the autocovariance function $C_{HH}(\mathbf{x}, \mathbf{x}')$ [3]. The autocovariance function $C_{HH}(\mathbf{x}, \mathbf{x}')$ describes the parameter variation between two local positions \mathbf{x} and \mathbf{x}' in the random field.

In this paper, the Gaussian function is used to correlate the random variables. The correlation function $\rho(\mathbf{x}, \mathbf{x}')$ is defined with [5]

$$\rho(\mathbf{x}, \mathbf{x}') = \exp\left(-\frac{|\mathbf{x} - \mathbf{x}'|^2}{a^2}\right) \quad (2)$$

while \mathbf{x} and \mathbf{x}' represent the local positions in the random field. The correlation length a describes the influence of the parameters with $0 < a < \infty$. By multiplying the correlation function with the variance $\sigma(\mathbf{x})$ the autocovariance function $C_{HH}(\mathbf{x}, \mathbf{x}')$ is generated with

$$C_{HH}(\mathbf{x}, \mathbf{x}') = \sigma(\mathbf{x})\sigma(\mathbf{x}')\rho(\mathbf{x}, \mathbf{x}') = \mathbb{E}[(H(\mathbf{x}) - \boldsymbol{\mu})(H(\mathbf{x}') - \boldsymbol{\mu})] \quad (3)$$

where $\mathbb{E}[\]$ is the expectation value of the values inside the brackets and $H(\mathbf{x})$ is the value of the random field at the position \mathbf{x} .

To decompose the autocovariance function $C_{HH}(\mathbf{x}, \mathbf{x}')$ Mercer's theorem is used. Mercer's theorem was introduced in 1909 [9] and is defined by

$$k(\mathbf{x}_1, \mathbf{x}_2) = \sum_{i=1}^{\infty} \lambda_i \phi_i(\mathbf{x}_1) \phi_i(\mathbf{x}_2) \quad (4)$$

with $k(\cdot, \cdot)$ as a continuous symmetric function, λ as the eigenvalue and $\phi(\mathbf{x})$ as the eigenfunction in dependence of the local position \mathbf{x} at the random field. Due to the fact that $C_{HH}(\mathbf{x}, \mathbf{x}')$ is continuous symmetric the decomposition with Mercer's theorem is following [12]

$$C_{HH}(\mathbf{x}, \mathbf{x}') = \sum_{i=1}^{\infty} \lambda_i \phi_i(\mathbf{x}) \phi_i(\mathbf{x}') \quad (5)$$

The eigenvalues λ_i and the eigenfunction $\phi_i(\mathbf{x})$ are the solution of the homogeneous Fredholm integral equation of the second kind given by [12]

$$\int_{\Omega} C_{HH}(\mathbf{x}, \mathbf{x}') \phi_i(\mathbf{x}) d\mathbf{x}' = \lambda_i \phi_i(\mathbf{x}) \quad (6)$$

Based on the attributes of the autocovariance function (symmetric and positive definite), the eigenfunctions are orthogonal to [12]

$$\int_{\Omega} \phi_n(\mathbf{x}) \phi_m(\mathbf{x}) d\mathbf{x} = \delta_{mn} \quad (7)$$

with δ_{mn} as Kronecker delta. Spanos and Ghanem [11] show the connection between the random field and the decomposed covariance kernel function with

$$H(\mathbf{x}, \theta) = \mu(\mathbf{x}) + \sum_{i=1}^{\infty} \sqrt{\lambda_i} \phi_i(\mathbf{x}) \xi_i(\theta) \quad (8)$$

with $\xi_i(\theta)$ as uncorrelated Gaussian standard random variables. Loève (1977) [7] showed that if $H(\mathbf{x}, \theta)$ is a process with gaussian random variables, the series converges. In addition, the autocovariance function can be decomposed into a series of weighted functions, multiplied with standard gaussian random variables with zero mean and standard deviation. Due to the fact of a finite number of series, the approximated random field $\tilde{H}(\mathbf{x}, \mathbf{x}')$ with the truncation factor M can be written to

$$H(\mathbf{x}, \theta) \approx \hat{H}(\mathbf{x}, \theta) = \mu(\mathbf{x}) + \sum_{i=1}^M \sqrt{\lambda_i} \phi_i(\mathbf{x}) \xi_i(\theta) \quad (9)$$

while $\tilde{H}(\mathbf{x}, \mathbf{x}')$ represents the approximated random field.

3 Description of the model

In the following section, the rotor and the methods to generate the FE model are explained in detail.

In this paper, a rotor of a wind engine is analysed. The machine is an asynchronous induction machine which contains a shaft, the bridges, a laminated rotor stack including windings and the end plates. In Figure 1, the principle sketch of the rotor is shown. In Figure 2, the cross-section of the laminated rotor stack is illustrated. The stack is split into the laminated core stack, which consists of non-planar thin metal sheets and a mix of air and resin in the interspaces, the spacer ribs and the windings. For simplification the end windings end in the end plates. The bridges on the shaft, in combination with the spacer ribs, are used to cool the rotor during the usage.

The rotor bearing is modelled as a fixed-floating bearing. The bearings are linear isotropic springs with a stiffness value of $2 \cdot 10^8 \frac{N}{m^2}$.

The 3D FE model is generated with ANSYS®18.1. The model contains linear homogeneous structural solid elements and includes about 1.5 million nodes. The rotor stack diameter is 900 mm with a length of 2650 mm.

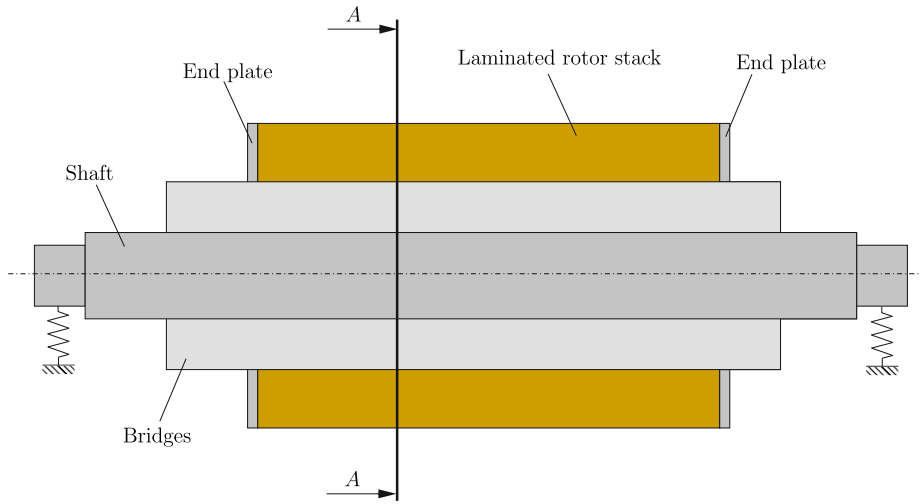


Figure 1: Design of the rotor

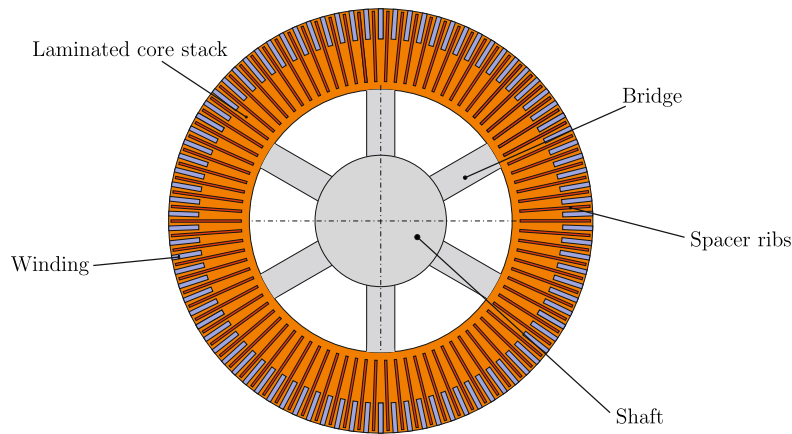


Figure 2: Section A of the rotor

4 Parameter description

In this section, the material parameters relevant for the eigenfrequency of the rotor are explained, which includes the homogeneous parameters as well as the heterogeneous parameters. The numerical values are collected in Table 1.

The calculations for the homogenous model contain constant parameter values in all components of the rotor. The shaft, the bridges and the spacer ribs use an isotropic material model. All the components are made of steel, so the standard values of the Young's modulus, the poisson ratio and the density are applied. The windings are modelled by a combination of the material parameters of copper and resin. Also, in this case the isotropic material model is used. The laminated rotor stack consists of a combination of steel, air and resin (see Figure 3). The air and resin must be taken into account because of the resulting inclusions between two steel sheets. The materials in the laminated rotor stack have an influence on the stiffness along the rotor axis and also orthogonal to the axis. Hence, an isotropic material model is used because of the influence of the matrix material (resin) in all directions. The value of the Young's modulus is lower than the value for solid steel, but Poisson's ratio and the density are equivalent to steel. In the homogeneous calculations, Young's modulus is varied between $E_{min} = 2 \cdot 10^8 \frac{N}{m^2}$ and $E_{max} = 2 \cdot 10^{11} \frac{N}{m^2}$ to show the influence of Young's modulus on the eigenfrequency. The density is equal to the density of steel to allocate upcoming phenomena to the variation of Young's modulus.

Table 1: Material parameters

	Shaft	Bridges	Spacer ribs	Windings	Laminated core stack
Young's modulus E_x [$\frac{N}{m^2}$]	$200 \cdot 10^9$	$200 \cdot 10^9$	$200 \cdot 10^9$	$70.9 \cdot 10^9$	mean value = $20 \cdot 10^9$ (statistically distributed in heterogeneous model)
Poisson ratio ν_{xy} [-]	0.3	0.3	0.3	0.2996	0.3
Density ρ [$\frac{kg}{m^3}$]	7850	7850	7850	6123.2	7850

Table 1 shows the used material parameters to calculate the eigenfrequencies of the rotor. The material parameter of the shaft, the bridges and windings based on Mair (2016) [8]. The spacer ribs are made of steel, thus the same value is used as for the shaft and the bridges. For Young's modulus of the laminated core stack a mean value of $20 \cdot 10^9 \frac{N}{m^2}$ is used.

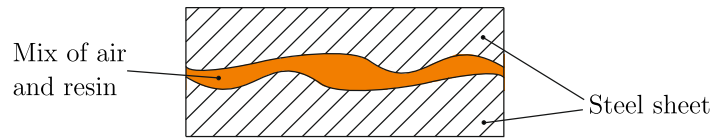


Figure 3: Principle sketch of the laminated core stack

The calculations for the heterogeneous model include the variation of parameter values along the laminated core stack. All other material parameters are equal to the homogeneous model. The variation is generated with the KLE method explained in Section 2. The Gaussian function (see equation 2) is used as the correlation function $\rho(\mathbf{x}, \mathbf{x}')$ with a supposed correlation length of $a = 0.5$. Due to the unknown composition of the material parameters and the influence of the manufacturing process a deviation of Young's modulus of 25% is assumed.

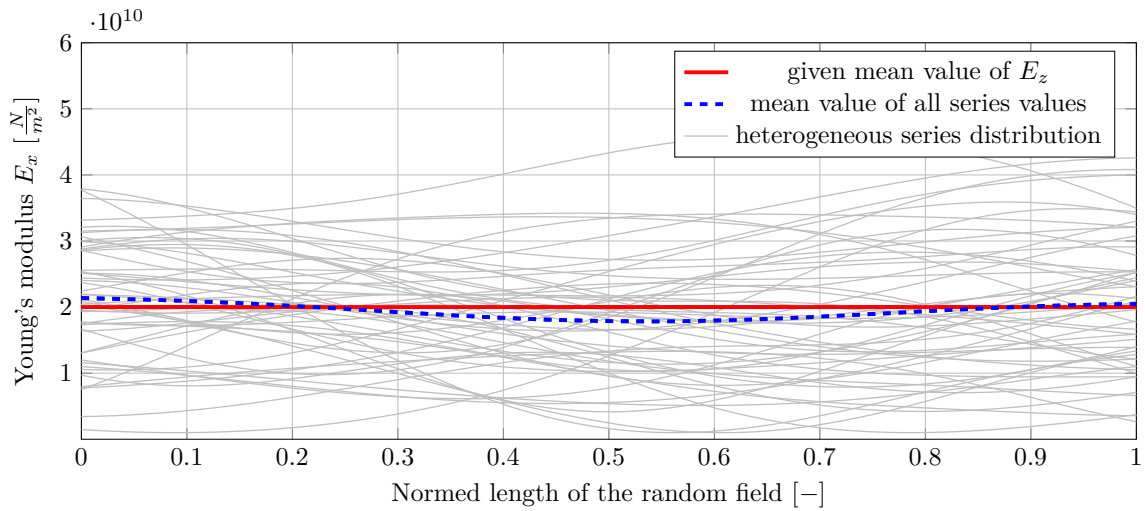


Figure 4: Series representation of 5% fluctuation

Figure 4 shows the series expansion where Young's modulus varies along the normed rotor axis for the different elements of the series: each thin line represents one possible Young's modulus variation. The mean values of all series expansions and the series itself are Gaussian distributed. The statistical error between the mean of this series and the given mean is 3.21%.

To calculate the eigenfrequency of the rotor, the FE model divides the continues series into as many parts as elements in rotor axis direction exist. Inside the elements the Young's modulus is constant. Due to this manipulation, the mean value of the series is not identical to the arithmetic mean. Each element poses as a spring with local constant stiffness values. The springs are connected in serial direction, so the resulting mean value is defined by

$$E_{res} = n \cdot \frac{1}{\sum_{i=1}^n \frac{1}{E_i}} \quad (10)$$

while n is the number of elements and E_i as the local value of Young's modulus.

5 Computational Results

In the first step, the influence of Young's modulus on the first eigenfrequency is analysed. For the homogeneous model, Young's modulus varies between $E_{min} = 2 \cdot 10^8 \frac{N}{m^2}$ and $E_{max} = 2 \cdot 10^{11} \frac{N}{m^2}$ for different rotor stacks.

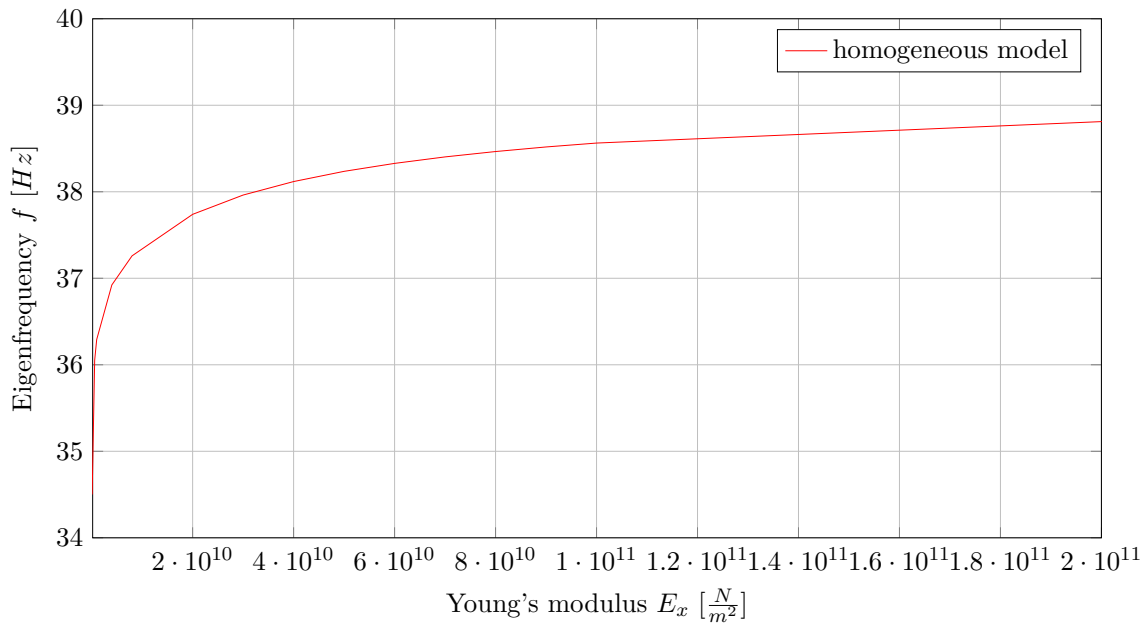


Figure 5: First eigenfrequency with variation of the Young's modulus of a homogeneous model

Figure 5 shows the influence of the Young's modulus on the first eigenfrequency. In practice the stiffness of the laminated rotor stack is often disregarded (due to the low value of the stiffness of the rotor stack) and only mass is included in the model. Due to this simplification, the first eigenfrequency is lower as compared to the models which include the stiffness. Within the range of parameter values considered, the eigenfrequency changes approximately 11.4% due to the effect of Young's modulus. So the theory that Young's modulus and all parameters have no influence in the first eigenfrequency cannot be confirmed.

As a next step, variations of Young's modulus along the axis of the rotor are included. A series of heterogeneous rotor models is generated and the first eigenfrequency is determined. As a reference, this eigenfrequency is compared to the eigenfrequency of a homogeneous rotor for which Young's modulus is the mean of the moduli of the heterogeneous model. Figure 6 shows the influence of the heterogeneity of the variable Young's modulus.

Depending on the series deviation, the gap between the heterogeneous and the reference calculation fluctuates. It is shown, that with nearly the same resulting Young's modulus different first eigenfrequencies are calculated due to the fluctuation of the series of the Young's modulus along the rotor axis.

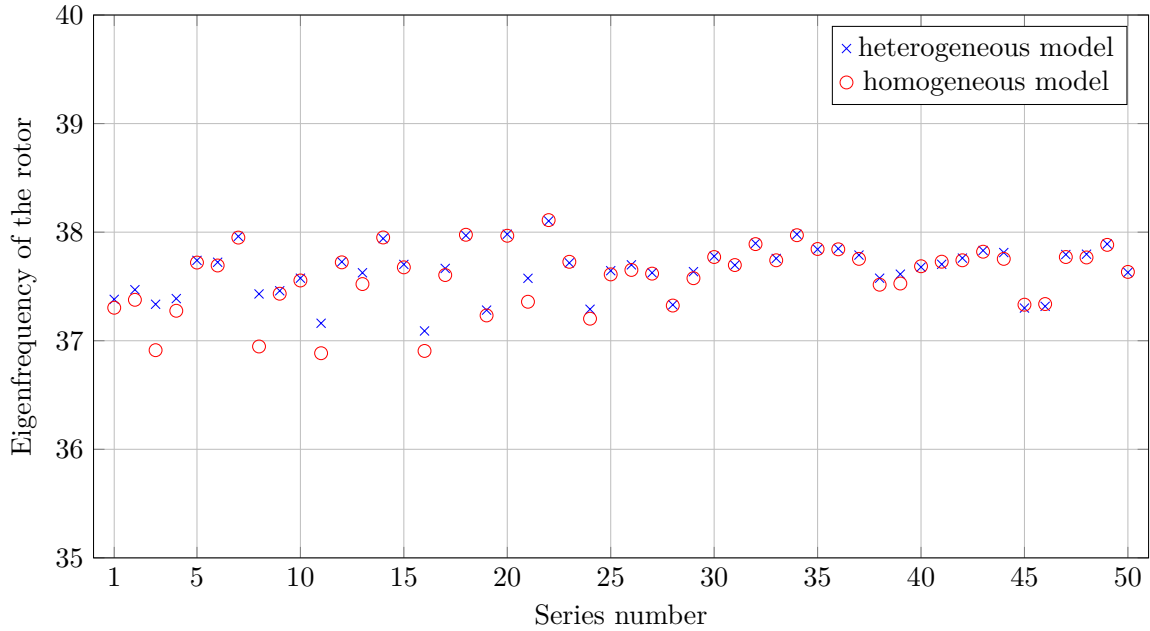


Figure 6: Influence of heterogeneous input parameters

For comparison, the different results for heterogeneous rotor models are shown in Figure 7 and compared to the results of the homogeneous rotor model (reference calculation).

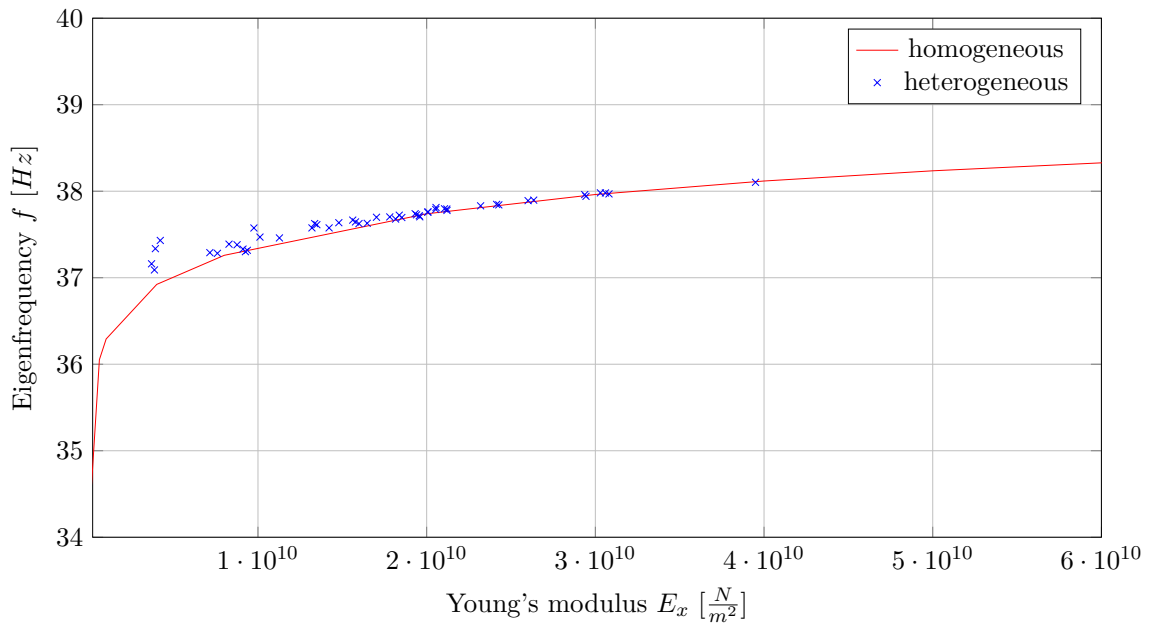


Figure 7: Eigenfrequencies for homogeneous vs. heterogeneous rotor models

The heterogeneous calculations with a resulting Young's modulus which is lower than $2 \cdot 10^{10} \frac{N}{m^2}$ show higher eigenfrequencies than the reference calculations. However, the heterogeneous calculations with values which are higher than $2 \cdot 10^{10} \frac{N}{m^2}$ are very similar to the reference results.

This phenomenon is based on the deviation of the series fluctuation. Softer parts of a rotor with a low value of Young's modulus affect the mean significantly, but these softer parts do not change the eigenfrequency of the otherwise stiff rotor significantly.

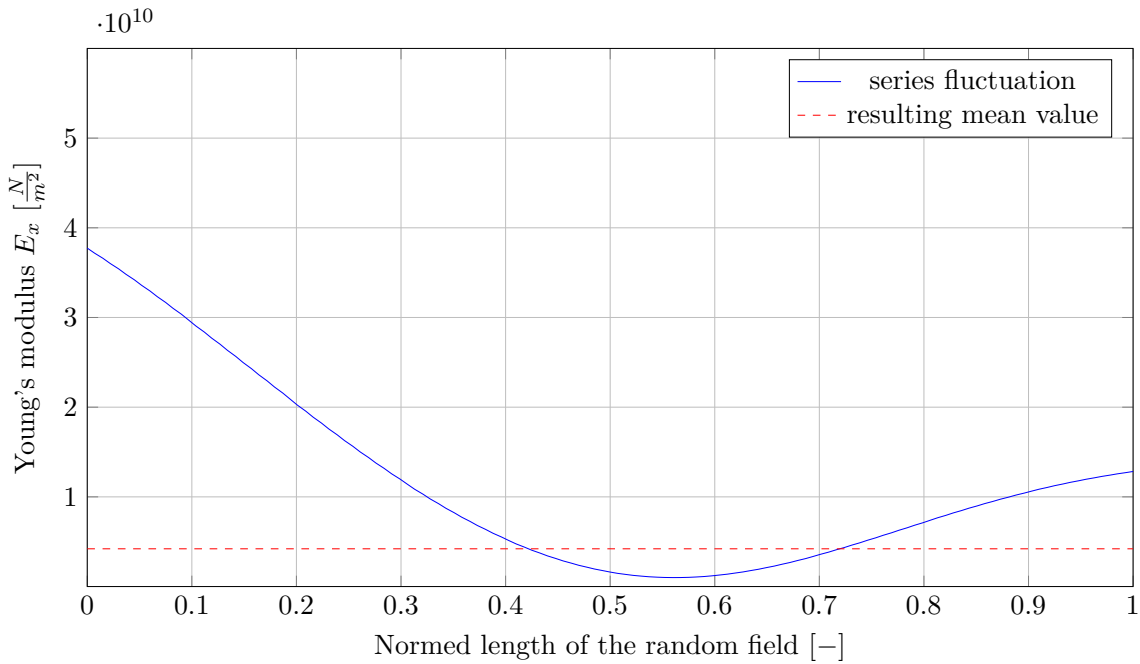


Figure 8: Example of a series fluctuation

As an example, series number 8 is plotted in Figure 8. The deviation of low and high Young's modulus values is statistically given. The first eigenfrequency of this series is $37.43Hz$, the homogeneous model with the same mean of Young's modulus has its first eigenfrequency at $36.93Hz$. This variation, due to the heterogeneous series expansion, is 1.35% in relation to the homogeneous model.

Referencing Young's modulus to the same result of the first eigenfrequency, series number 8 has a resulting Young's modulus of $4.2 \cdot 10^9 \frac{N}{m^2}$. The homogeneous reference calculation with the same first eigenfrequency has a resulting Young's modulus of $12.3 \cdot 10^9 \frac{N}{m^2}$. So a system with the same first eigenfrequency has a deviation of the Young's modulus of 65.85%, due to the difference of a calculation between a heterogeneous and a homogeneous system.

6 Conclusion

This paper shows of the influence of Young's modulus of a laminated rotor stack on the first eigenfrequency. Two effects are considered: Variations of Young's modulus in a homogeneous rotor model and heterogeneous rotor models which include the variations of Young's modulus along the length of the axis. In the second case, a mean value of Young's modulus can be defined and used for a reference calculation with the homogeneous model.

The calculations show that rotors with softer sections may have a relatively low mean value of Young's modulus, but the effect of the soft section on the eigenfrequency is not very significant. On the other hand, for rotors with a high mean value of Young's modulus, the difference between the homogenous and the heterogenous model is negligible.

REFERENCES

- [1] DER KIUREGHIAN, A., AND KE, J.-B. The stochastic finite element method in structural reliability. *Probabilistic Engineering Mechanics* 3, 2 (1988), 83–91.
- [2] GARVEY, S. The vibrational behaviour of laminated components in electrical machines. In *Fourth International Conference on Electrical Machines and Drives* (1989), pp. 266–231.
- [3] GHANEM, R., AND SPANOS, P. *Stochastic finite elements. A spectral approach. Revised Edition*. Dover Civil and Mechanical Engineering, Mineola, New York, 2012.
- [4] KARHUNEN, K. *Über lineare Methoden in der Wahrscheinlichkeitsrechnung*. Annales Academiae scientiarum Fennicae. Series A. 1, Mathematica-physica. Kirjapaino oy. sana, Helsinki, 1947.
- [5] LI, C.-C., AND DER KIUREGHIAN, A. Optimal discretization of random fields. *Journal of Engineering Mechanics* 119, 6 (1993), 1136–1154.
- [6] LOÈVE, M. *Fonctions aléatoires du second ordre. Processus stochastiques et mouvement Brownien*. Gauthier-Villars, Paris, 1948.
- [7] LOÈVE, M. *Probability theory*, vol. 4th Edition. Springer-Verlag, New York, 1977.
- [8] MAIR, M. *Nonlinear Structural Rotor Vibrations in Electrical Machines*. PhD thesis, Graz University of Technology, 2016.
- [9] MERCER, J. Functions of positive and negative type, and their connection the theory of integral equations. *Philosophical Transactions Of The Royal Society* 83 (1909).
- [10] METROPOLIS, N., AND ULAM, S. The Monte Carlo Method. *Journal of the American statistical association* 44, 247 (1949), 335–341.
- [11] SPANOS, P., BEER, M., AND RED-HORSE, J. Karhunen-love expansion of stochastic processes with a modified exponential covariance kernel. *Journal of Engineering Mechanics* 113, 7 (2007), 773–779.
- [12] SPANOS, P., AND GHANEM, R. Stochastic finite element expansion for random media. *Journal of Engineering Mechanics* 115, 5 (1989), 1035–1053.
- [13] SUDRET, B., AND KIUREGHIAN, A. D. Stochastic Finite Element Methods and Reliability: A State-of-the-Art Report. Tech. Rep. UCB/SEMM-2000/08, Structural Engineering, Mechanics and Materials Department of Civil & Environmental Engineering, University of California, Berkeley, 2000.
- [14] VANMARCKE, E. *Random Fields: Analysis and Synthesis*. World Scientific, Singapore, 2010.
- [15] VANMARCKE, E., AND GRIGORIU, M. Stochastic finite element analysis of simple beams. *Journal of Engineering Mechanics* 109, 5 (1983), 1203–1214.
- [16] ZHANG, J., AND ELLINGWOOD, B. Orthogonal series expansions of random fields in reliability analysis. *Journal of Engineering Mechanics* 120, 12 (1994), 2660–2677.

DTU Mechanical Engineering
Section of Solid Mechanics
Technical University of Denmark

Nils Koppels Allé, Bld. 404
DK-2800 Kgs. Lyngby
Denmark
Phone (+45) 4525 4250
Fax (+45) 4525 1961

www.mek.dtu.dk

February 2019
ISBN: 978-87-7475-568-4